Canadian Bulletin of Fisheries and Aquatic Sciences 212

STORM SURGES

Meteorological Ocean Tides

T.S. MURTY

Fisheries and Oceans
Pêches et Océans

Canada

Storm Surges —
Meteorological Ocean Tides

The *Canadian Bulletins of Fisheries and Aquatic Sciences* are designed to interpret current knowledge in scientific fields pertinent to Canadian fisheries and aquatic environments.

The *Canadian Journal of Fisheries and Aquatic Sciences* is published in annual volumes of monthly issues. *Canadian Special Publications of Fisheries and Aquatic Sciences* are issued periodically. These series are available from authorized bookstore agents and other bookstores, or you may send your prepaid order to the Canadian Government Publishing Centre, Supply and Services Canada, Ottawa, Ont. K1A 0S9. Make cheques or money orders payable in Canadian funds to the Receiver General for Canada.

BULLETIN 212
(La version française est en préparation)

Storm Surges —
Meteorological Ocean Tides

T. S. MURTY

Forecast Methods Section
Institute of Ocean Sciences
Department of Fisheries and Oceans
Sidney, B.C. V8L 4B2

DEPARTMENT OF FISHERIES AND OCEANS
Ottawa 1984

Available in Canada through

Authorized Bookstore Agents
and other bookstores

or by mail from

Canadian Government Publishing Centre
Supply and Services Canada
Ottawa, Canada K1A 0S9

Catalogue No. Fs 94-212E
ISBN 0-660-11663-4
ISSN 0706-6503

Canada: $34.95
Other Countries: $41.95

Price subject to change without notice

Printed in Canada
by
Friesen Printers Ltd.
Altona, Manitoba, Canada
R0G 0B0
Contract No. 30KT.FP802-4-0247

Contents

PREFACE vii

ABSTRACT / RÉSUMÉ ix

CHAPTER 1. INTRODUCTION AND GENERAL CONSIDERATIONS

1.1 Introduction to Oceanographical Aspects of Storm Surges 1
1.2 Global Weather Systems 6
1.3 Air Masses, Fronts, Cyclones, and Anticyclones 11
1.4 Regional Weather Systems 16

CHAPTER 2. THE MATHEMATICAL PROBLEM AND FINITE-DIFFERENCE SOLUTIONS FOR TWO-DIMENSIONAL NUMERICAL MODELS

2.1 Formulation of the Storm Surge Equations 33
2.2 Two-Dimensional Models 45
2.3 Finite-Difference Techniques for Marching Problems, Computational Stability 49
2.4 Formulation of the Storm Surge Equations Using the Concept of Ekman Number and Proudman Number 53
2.5 Numerical Integration Using Conjugate Richardson Lattices ... 59
2.6 Staggered and Nonstaggered Grid Schemes 64
2.7 Numerical Dispersion, Parasitic Waves, Filtering, and Aliasing 67
2.8 Finite-Differencing of the Time Derivative 73
2.9 The Courant–Friedrichs–Lewy (C–F–L) Stability Criterion .. 78
2.10 Energy Calculation as a Test of Computational Stability 89
2.11 Treatment of Open Boundaries 91
2.12 Treatment of the Nonlinear Advective Terms 94
2.13 Moving Boundary Models and Inclusion of Tidal Flats 102
2.14 Nested Grids and Multiple Grids 110
2.15 Stretched Coordinates and Transformed Grid Systems 113

CHAPTER 3. OTHER NUMERICAL SOLUTIONS

3.1 Three-Dimensional Models 123
3.2 Two-and-a-Half-Dimensional Models and Improved Treatment of Bottom Stress 130
3.3 One-and-a-Half-Dimensional Models 144
3.4 One-Dimensional Models 148
3.5 Combination of Two-Dimensional and One-Dimensional Models 161
3.6 Finite-Element and Irregular-Grid Finite-Difference Models ... 166

CHAPTER 4. DIFFERENT APPROACHES TO THE STORM SURGE PROBLEMS

4.1 Analytical Methods 185
4.2 Empirical Methods 210
4.3 Graphical Techniques 225
4.4 Statistical Techniques 236
4.5 Electronic Analog Models 247
4.6 Instrumentation, Laboratory Experiments, and Hydraulic Models 253
4.7 Hybrid Models 268

Contents (concluded)

CHAPTER 5. SPECIAL HYDRODYNAMIC PROBLEMS

5.1 Resonance, Edge Waves 271
5.2 Tidal Regimes in the Oceans and Coastal Water Bodies 312
5.3 Interaction Between Storm Surges and Tides 328
5.4 Interaction Between Storm Surges and Wind Waves 356
5.5 Influence of Ice and Stratification on Storm Surges 363

CHAPTER 6. METEOROLOGICAL PROBLEMS

6.1 Extratropical Cyclones 377
6.2 Tropical Cyclones 394
6.3 Cyclones of the Pacific Ocean 420
6.4 Cyclones of the Atlantic Ocean 436
6.5 Cyclones of the Indian Ocean 450
6.6 Wind Stress and Atmospheric Pressure Gradients 481
6.7 Meteorological Problems Associated with Storm Surges in Canada 493
6.8 Meteorological Problems Associated with Storm Surges in the United States 506
6.9 Meteorological Problems Associated with Storm Surges in Europe 530
6.10 Meteorological Problems Associated with Storm Surges Elsewhere than in Canada, the United States, and Europe 561
6.11 Mesoscale Weather Systems 578

CHAPTER 7. CASE STUDIES OF STORM SURGES ON THE GLOBE

7.1 Storm Surges in Canada 587
7.2 Storm Surges in the United States 621
7.3 Storm Surges in Europe 733
7.4 Storm Surges Elsewhere than in Canada, the United States, and Europe 790

REFERENCES 851

Preface

In the decade, 1970–79, approximately half a million people were killed by storm surges on the globe. I felt that a reference book summarizing the state of the art on the various aspects of storm surges would be of use to researchers as well as to people dealing with the practical aspects. Since, to my knowledge, no book is available on this topic, it will also serve as a guide to the storm surge literature.

The relative coverage given to various topics is based to some extent on my own research interests, but to a major extent on the total available space, so that the printing costs could be kept within reasonable limits. I apologize for the relatively inadequate coverage given to South America, Africa, eastern Europe, and the USSR, as I had no easy access to their literature.

I thank my colleagues Dr. R. F. Henry and Mr. F. G. Barber for their encouragement and help in various forms. This work was begun when I was working at the Marine Environmental Data Service in Ottawa. I thank Dr. N. J. Campbell, Dr. J. R. Wilson, Mr. G. L. Holland, and Dr. G. Godin for various courtesies. I express my gratitude to Dr. C. R. Mann, Director General of the Institute of Ocean Sciences, and to Dr. J. Garrett, Head of Ocean Physics, for enabling me to use the Institute's resources. I thank Dr. N. C. Kraus for reviewing the manuscript prior to publication, Mr. Peter Burke for editorial help, Ms Jill Anderson for typing, and Mrs. Coralie Wallace for drafting.

I thank the following societies and associations for granting me permission to reproduce material from their publications: Academic Press; Accademia Nazionale Dei Lincei; American Association for the Advancement of Science; American Geophysical Union; American Meteorological Society; American Society of Civil Engineers; American Society of Limnology and Oceanography; Amoy University, China; Archiv für Meteorologie Geophysik und Bioklimatologie; Arctic Institute of North America; Australian Academy of Sciences; Australian Bureau of Meteorology; Australian Government Publishing Service; Bangladesh Atomic Energy Commission; Bangladesh Meteorological Department; Blackwell Scientific Publications; Bollettino di Geofisica Teorica ed Applicata; Colorado State University, USA; Crane, Russak Publishers; Deutsches Hydrographisches Institut; Elsevier Publishing Company; Flinders University, Australia; Gordon and Breach Science Publishers; Holt, Rinehart and Winston Publishers; Hydraulics Research Station, Wallingford, U.K.; India Meteorological Department; Institute of Civil Engineers, U.K.; Institute of Oceanographic Sciences, U.K.; International Association for Great Lakes Research; International Association for Hydraulics Research; International Hydrographic Bureau; Japan Meteorological Agency; MacMillan Press; Marine Technology Society, USA; McGill University; McGraw-Hill Publications; Massachusetts Institute of Technology; Museum National d'Histoire Naturelle, France; National Academy of Sciences, USA; National Bureau of Standards, USA; National Oceanic and Atmospheric Administration, USA; Netherlands Meteorological Department; New York Academy of Sciences; New York Sea Grant Institute; New Zealand Journal of Geology and Geophysics; Oceanographical Society of Japan; Pergamon Press; Plenum Publishing Corp.; Sears Foundation for Marine Research; Springer Verlag; Superintendant of Documents, USA; Tetra Tech Inc., Pasadena, California; Texas A&M University; The Royal Astronomical Society; The Royal Meteorological Society; The Royal Society; The Swedish Meteorological Society; University of Bonn; University of Buenos Aires; University of Chicago; University of Florida; University of Hamburg; University of Oslo; University of Louisiana Press; University of Quebec at Rimouski; UNESCO; U.S. Army Corps of

Engineers; U.S. Geological Survey; Wiley-Interscience; World Meteorological Organization.

The material is arranged as follows. In Chapter 1, general concepts about storm surges are introduced, and some oceanographic background as to where, when, and how storm surges occur is discussed. Also, the global weather systems, with particular emphasis on North America, are considered. In Chapter 2, the storm surge equations are formulated, and two-dimensional numerical methods for solving these equations are considered in detail. In Chapter 3, numerical solutions, other than two-dimensional, are considered. Chapter 4 deals with all other types of approaches to the storm surge problems, and a section on laboratory experiments and hydraulic models is included. Chapter 5 discusses special hydrodynamic problems and Chapter 6 is devoted to a discussion of the meteorological problems. Chapter 7 includes case studies of storm surges in various water bodies on the globe. It also contains a considerable amount of information of practical interest. References are listed after Chapter 7. No list of mathematical symbols is provided, because it was found necessary to use the same symbol to represent different parameters at different times. However, the mathematical notation is adequately explained in the text. A subject index is not provided because it is felt that the table of contents includes sufficient details.

SIDNEY, B.C. T. S. MURTY

Abstract

MURTY, T. S. 1984. Storm surges—meteorological ocean tides. Can. Bull. Fish. Aquat. Sci. 212: 897 p.

This bulletin is an attempt to synthesize current knowledge on storm surges. The bulletin is directed mainly to researchers and would-be researchers in this topic; nevertheless, sufficient material of practical interest is included for those who have a general interest in this topic. The book deals with all the meteorological and oceanographical aspects of storm surges and makes extensive use of numerical finite-difference methods. In addition, analytical methods, empirical methods, graphical techniques, statistical techniques, finite-element methods, and laboratory and hydraulic models are discussed. Case studies of storm surges in various water bodies on the globe are treated in considerable detail.

Résumé

MURTY, T. S. 1984. Storm surges—meteorological ocean tides. Can. Bull. Fish. Aquat. Sci. 212: 897 p.

Le présent travail est une synthèse de l'état actuel de nos connaissances sur les ondes de tempêtes. Il s'adresse surtout aux chercheurs actuels ou potentiels oeuvrant dans ce domaine. Il contient néanmoins suffisamment de matériel pratique pour ceux que le sujet intéresse généralement. L'ouvrage traite de tous les aspects météorologiques et océanographiques des ondes de tempêtes et fait largement appel aux méthodes de différences finies. On y examine en outre les méthodes analytiques, empiriques, graphiques, statistiques, d'éléments finis, de même que des modèles de laboratoire et hydrauliques. Sont également analysés en détail les dossiers d'ondes de tempêtes dans diverses masses d'eau du globe.

Chapter 1

Introduction and General Considerations

1.1 Introduction to Oceanographical Aspects of Storm Surges

Storm surges are oscillations of the water level in a coastal or inland water body in the period range of a few minutes to a few days, resulting from forcing from the atmospheric weather systems. By this definition, the so-called wind-generated waves (often referred to as wind waves) and swell, which have periods of the order of a few to several seconds, are excluded. The term "storm surge" is commonly used in European literature, especially in the literature pertaining to the water level oscillations in the North Sea. In North American literature, the terms "wind tides" and "storm tides" are also used to refer to the same phenomenon.

Unfortunately, the term "wind tides" has occasionally been used in aeronomy to refer to atmospheric tides (which have the same astronomical origin as oceanic tides). Hence, the term will not be used here. The term "storm tide" is used in North American literature in a confusing manner: at times it is used in the same sense as storm surge, and at other times it is used to denote the sum of the storm surge and the astronomical tide. Here, the term will be used only in the latter sense. As an alternative to the term "storm surges," the term "meteorological ocean tides" will be used. In some sense, storm surges are similar to astronomical tides: although storm surges are not periodic in the sense that tides are, they do exhibit certain periodicities, and since the forcing functions are due to meteorological causes, it is not inappropriate to call them meteorological ocean tides. Here, the word "ocean" is used to denote a water body of any scale, and not necessarily the oceans. In Russian literature (e.g. see Lappo and Rozhdestvenskiy 1979), the term "meteorological ocean tide" is commonly used.

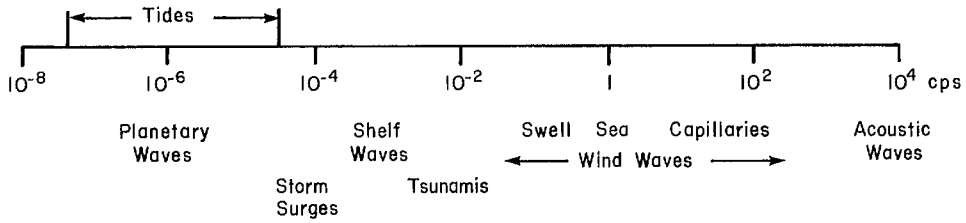

FIG. 1.1. Frequencies of oceanic wave motion in cycles per second (cps). (Platzman 1971)

The spectrum of ocean waves is shown schematically in Fig. 1.1, and it can be seen that storm surges are centered at about 10^{-4} cycles per second (cps or Hz), which gives a period of about 3 h. However, depending mainly on the topography of the water body and secondarily on other parameters, such as the direction of movement of the storm, strength of the storm, stratification of the water body, presence or absence of ice cover, nature of tidal motion in the water body, etc., the periods in the water level oscillations may vary considerably. Even in the same water body, storm surge records at different locations can exhibit different periods.

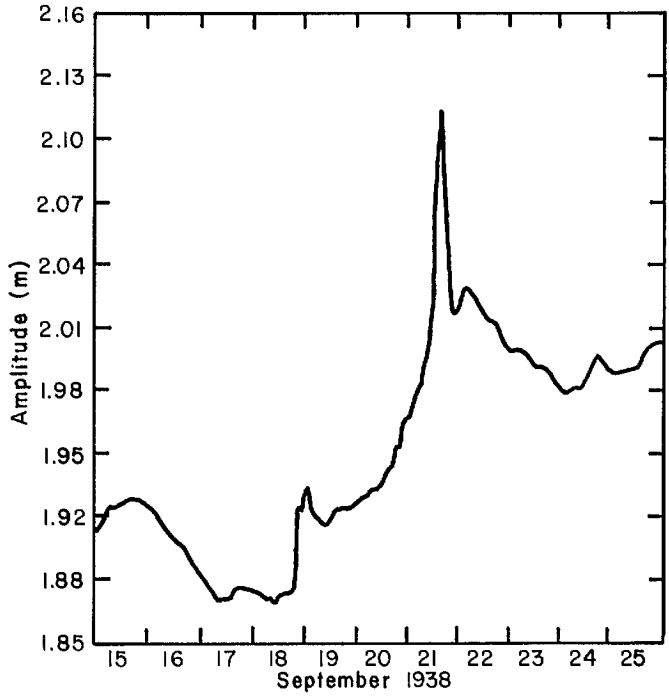

FIG. 1.2. Storm surge at Forest Hills, New York. (Paulsen et al. 1940)

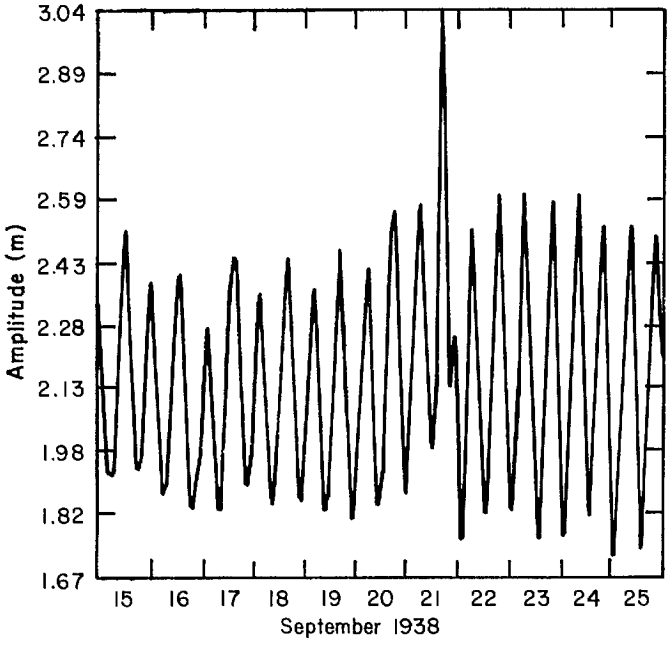

FIG. 1.3. Storm surge at Rockaway Park, New York. (Paulsen et al. 1940)

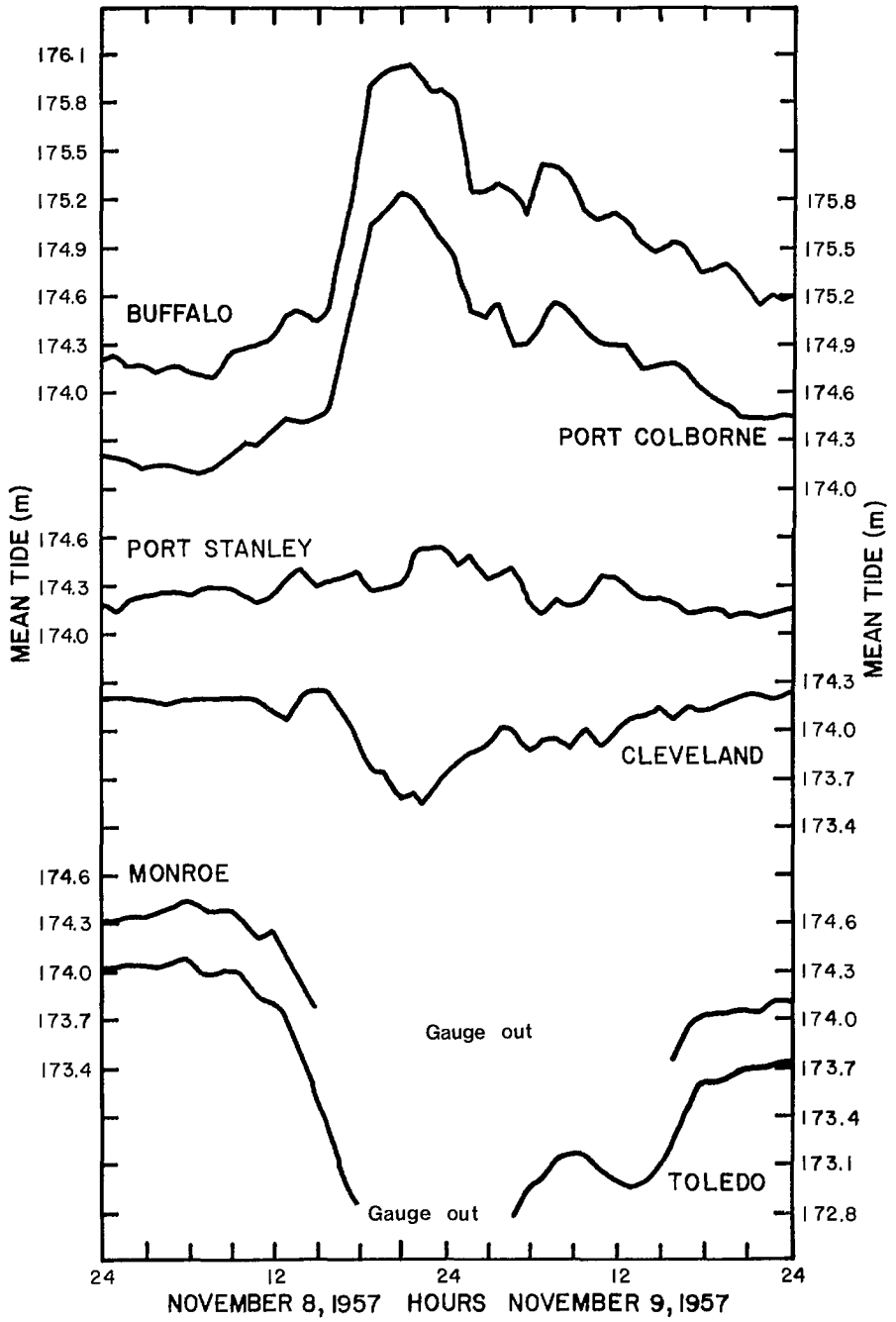

FIG. 1.4. Observed storm surges at six locations on Lake Erie. Mean tides are shown on the left ordinate for Buffalo, Port Stanley, and Monroe and on the right ordinate for Port Colborne, Cleveland, and Toledo. Mean tides are metres above the Great Lakes Datum with reference to the mean tide at New York. (Hunt 1959)

Although storm surges belong to the same class known as long waves, as do astronomical tides and tsunamis, there are at least two important differences. First, whereas tides and tsunamis occur on the oceanic scale, storm surges are simply a coastal phenomenon. Second, significant tsunamis and tides cannot occur in a completely closed small coastal or inland water body, but storm surges can occur even in completely enclosed lakes, or in canals and rivers.

In Fig. 1.2–1.4, examples are shown of storm surge profiles with several different periods. For example, the profile at Forest Hills, NY, is shown in Fig. 1.2, and a period of about 2.5 d can be seen. The same storm generated a surge at Rockaway, NY, with periods of the order of 1 d or less (Fig. 1.3). Thus, even nearby locations can exhibit considerably differing periods. The surge profiles at six locations on Lake Erie due to an extratropical storm in November 1957 are shown in Fig. 1.4. It can be seen that surges with ranges of up to 8 ft (2.4 m) occurred at Buffalo, Port Colborne, and Toledo, whereas at Port Stanley the range of the surge was less than 2 ft (0.61 m). Also, whereas the period of the surge at Buffalo and Port Colborne was about 7–8 h, the period at Port Stanley was about 3 h.

One may ask why large surges occur at Buffalo, Toledo, and Port Colborne and only small surges are recorded at Port Stanley. The answer is that the range of the surge depends on the topography in the region of the tide station and the location of the tide station relative to the storm track. It will be shown later in detail, mathematically, how topography, position with reference to storm track, forcing from the weather systems, plus a host of secondary factors determine the range of the storm surge at a given location in a specified water body. But it can be stated that shallow water bodies generally experience surges with greater ranges. Lake Erie, being the shallowest (on the average) among the five Great Lakes of North America, experiences surges of maximum amplitude among the Great Lakes. Lake Okeechobee in Florida also gives rise to significant storm surges. The east coast and the Gulf of Mexico coast of the United States have been, not infrequently, subjected to destructive storm surges. Nineteen cases of hurricanes that killed more than 50 people in the United States during the period 1900–72 are listed in Table 1.1. It is generally recognized that most of the deaths occurred as a result of the storm surge generated by the hurricane.

Surges on the east and south coasts of the United States are generated by tropical storms referred to as "hurricanes." Similar tropical storms in the Pacific are referred to as "typhoons." (The Japanese refer to them also as "Reppus.") In Australia, they are called "willy-willies," in the Phillipines, "Baguios," and in Arabia, "Asifat." Tropical cyclones in the Indian Ocean, Bay of Bengal, and the Arabian Sea are popularly referred to as "depressions," although there is a strict classification based on maximum wind speed attained in the weather system. It may be of interest to note that the word "cyclone" comes from the Greek word "kyklon," which means "to whirl around." Most of the storm surges on the east coast of the United States are generated by hurricanes; however, significant storm surges due to extratropical weather systems also occur.

In Canada, storm surges are almost always due to extratropical weather systems. Storm surges with ranges up to a few metres occur in the St. Lawrence Estuary, in James Bay (southern extension of Hudson Bay), and in Frobisher Bay. Storm surges occur in the Canadian Arctic and in Alaska, but storm surge is a very rare phenomenon on the west coasts of Canada and the United States. On those coasts, water level variations are mainly caused by wind waves and swell.

Another area on the globe where destructive surges occur is the North Sea. Considerable literature exists on the surges along the east coast of the United Kingdom and the

TABLE 1.1. Some of the most disastrous hurricanes of the twentieth century affecting the United States.

Date	Name of hurricane	Area affected	No. of people killed	Damage in millions of dollars
Sept. 8, 1900	—	Storm surge at Galveston greater than 6.5 m	6000	30
Sept. 20, 1909	—	Louisiana coast (Grand Isle)	353	—
Sept. 29, 1915	—	Mississippi Delta (New Orleans)	284	—
Sept. 14, 1919	—	Florida Keys, Corpus Christi (Texas)	600–900	20
Sept. 20, 1926	—	Miami and Pensacola to Southern Alabama	243	—
Sept. 16, 1928	—	Palm Beach, Okeechobee	2000	25
Sept. 1, 1935	Labor Day storm	Florida Keys (winds greater than 332 $km \cdot h^{-1}$)	408	76
Sept. 21, 1938	—	New England and Long Island	600	306
Aug. 7–11, 1940	—	Southeastern United States (Georgia to Tennessee)	50	—
Sept. 14–15, 1944	—	Atlantic coast	390	—
Sept. 19, 1947	—	Florida, Louisiana, Mississippi	51	—
Aug. 31, 1954	Carol	North Carolina to New England	60	500
Oct. 13–17, 1954	Hazel	South Carolina to New York	95	—
Aug. 16–20, 1955	Diane	Northeast United States	184	1000
June 27, 1957	Audrey	Texas to Alabama (4-m surge inundated Louisiana 40 km inland)	390	150
Sept. 9–11, 1960	Donna	Florida, New York, New England	50	387
Sept. 7–12, 1961	Carla	Texas	46	408
Sept. 8, 1965	Betsy	Florida, Louisiana, mid-Atlantic States, New England	75	1421
Aug. 15–16, 1969	Camille	Louisiana, Mississippi, Virginia (7.4-m surge on Pass Christian, Mississippi)	>250	1421
Mid-June, 1972	Agnes	Florida, Virginia, Maryland, Pennsylvania, North Carolina to New York	122	2100
Late Aug.– early Sept. 1979	David and Frederic	Alabama, Mississippi, Florida	5	2300

coasts of the Netherlands and Federal Republic of Germany. Storm surges also occur in the Irish Sea.

Japan is frequently affected by storm surges due to typhoons. The Bay of Bengal coasts of India and Bangladesh have been subjected to very severe storm surges not infrequently. It will be seen later that the peculiar topography (i.e. triangular or V-shaped basin), shallowness of the water body, together with a large tidal range make storm surges on the Bay of Bengal coast more dangerous than in any other region of the globe.

It is recognized by now that the storm surge problem is an air–sea interaction problem; i.e. the atmosphere forces the water body, which responds by generating oscillations of the water level with various frequencies and amplitudes. Our present interest is confined to that part of the oscillation between a few minutes and a few days. Study of the storm surge problem will begin with a consideration of the global weather systems.

1.2 Global Weather Systems

To understand global weather systems, it is convenient to begin with the so-called "general circulation of the atmosphere," which refers to the motion of the atmosphere in an average sense, both in space and time. Before discussing the general circulation, it is appropriate to introduce certain nomenclature. There are two important characteristics of the atmosphere. The pressure decreases with height in a monotonic fashion, as can be seen from the ordinate on the right side of Fig. 1.5. The units of pressure are millibars. (Another internationally used unit is the kilopascal, 1 kPa = 10 mb.) On the average, the atmospheric pressure at sea level is 1013.2 mb. The height scale (kilometres) is shown on the left side. For general interest, the maximum heights of three mountain peaks, namely, Mount Everest, Mont Blanc, and Ben Nevis, are included. The heights of different cloud types are also indicated.

The second important characteristic is the change of temperature with height, indicated by the curve in Fig. 1.5. The temperature reverses several times with increasing height, and this gives rise to three warm and two cold regions. The warm regions are near the earth's surface, at a height between 40 and 60 km, and above 150 km (i.e. more or less the top of the atmosphere). The first cold region extends from about 10 to 35 km and the second cold region from about 80 to 90 km. The exact distribution of temperature with height depends on latitude and, to a certain extent, on the season.

It can be seen that the temperature decreases from the earth's surface as far as the tropopause. The atmosphere below the tropopause is called the troposphere, and the region immediately above the troposphere is referred to as the stratosphere. The electrical conductivity of air above the 80-km level is much greater than that at lower levels, especially during sunlight hours. This region of the atmosphere, called the ionosphere, allows radio waves to propagate great distances.

For weather and climate purposes, as well as for the atmospheric forcing of storm surges, interest here will be primarily in the troposphere and, to a lesser extent, in the lower part of the stratosphere. The ionosphere will be of no direct interest. Earlier, the term "general circulation of the atmosphere" was introduced. In practice, this term is used to describe the more or less permanent wind and pressure systems of the troposphere and the lower stratosphere.

If the surface of the earth were perfectly smooth, i.e. lacking orographical features, and uniformly covered with water, then the long-term average pattern of winds, temperature, and precipitation would not show any variation with longitude but would exhibit only zonal bands (i.e. variation with latitude only). A general examination of weather charts shows that although the influence of the distribution of land and water and such orographical features as mountains have a significant influence on the patterns of meteorological parameters, a zonal pattern (i.e. some uniformity in the east–west direction) is nevertheless evident. For a first approximation, the longitudinal variations will be ignored and only the patterns in the east–west direction will be considered.

It has been known since the early days of meteorological measurements that the tropical areas of the globe receive more radiation from the sun than they radiate into space, whereas the higher latitudes receive less than they radiate. The observed average temperature distributions are maintained through motion on various scales in the atmosphere. The rate of heat flow from lower latitudes towards the pole increases from the equator to about 35° latitude; it then decreases because the higher latitude regions retain some of this imported heat.

If the earth were stationary (i.e. not rotating), this exchange of heat could be achieved

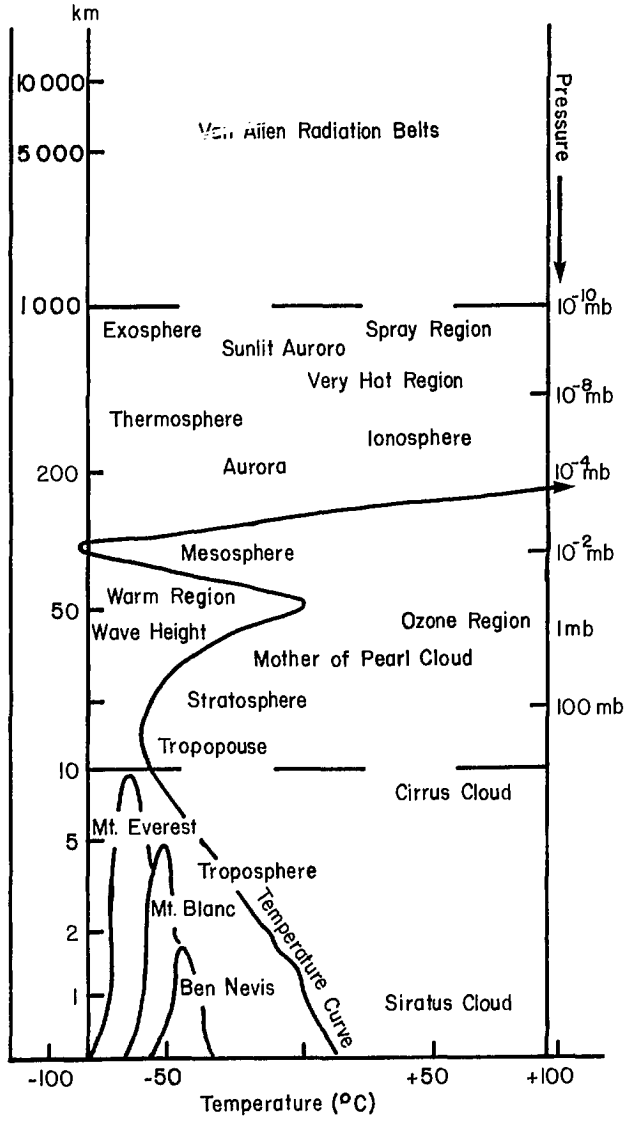

FIG. 1.5. Vertical structure of the atmosphere. (Dobson 1963)

through a meridional circulation between the equator and the pole. This circulation can be visualized as consisting of a single cell with upward motion (up to the tropopause) over the equator, then south to north motion aloft from the equator to the pole (in the Northern Hemisphere), and sinking motion at the pole and north to south motion from the pole to the equator at ground level. However, with rotation of the earth, a simple circulation such as this is not possible because of the requirement of the conservation of angular momentum.

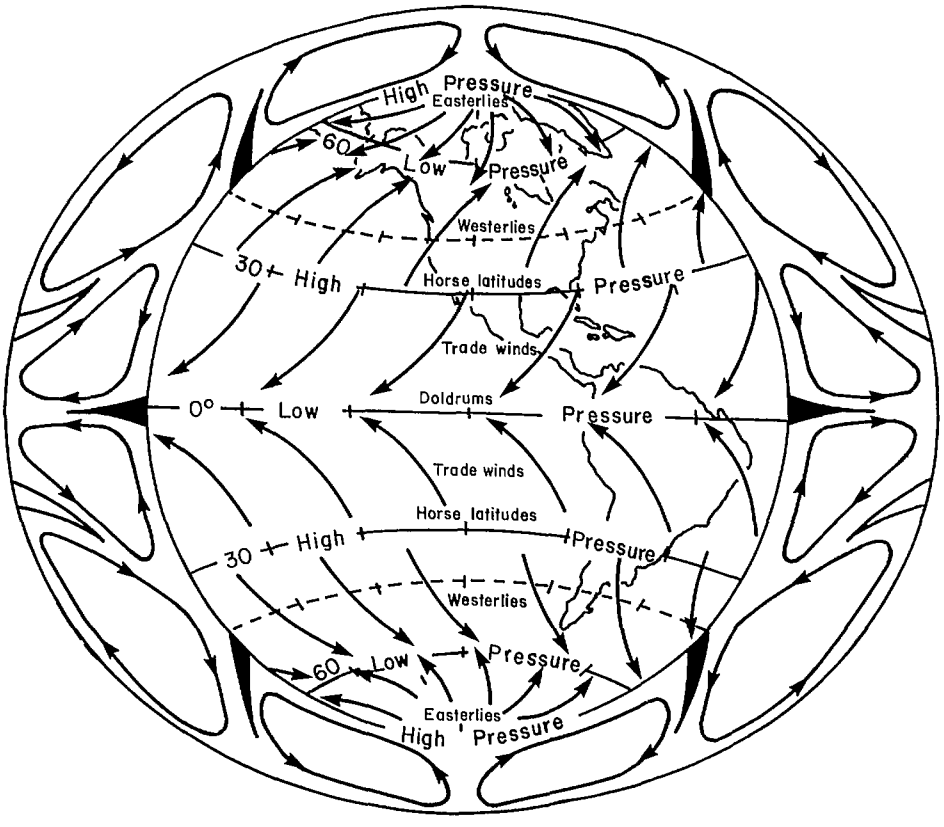

FIG. 1.6. Schematic representation of observed zonal winds near the earth's surface.

Angular momentum is proportional to the angular velocity and the square of the distance of the air parcel from the axis of rotation. For a uniformly rotating earth and atmosphere, the total angular momentum must remain constant. The angular momentum is greatest at the equator and decreases with increase of latitude, becoming zero at the pole. Suppose a large mass of air changes its position so that its distance from the axis of rotation also changes; then its angular velocity must change so that its angular momentum does not change. Barry and Chorley (1970) estimated that a mass of air traveling from 42 to 46° latitude should increase its speed relative to the earth's surface by 29 $m \cdot s^{-1}$ to conserve angular momentum. However, in practice, this increase is opposed by other forces such as friction, but it is important to note that many of the observed features of the general circulation are due to the poleward transfer of angular momentum on a rotating earth. A simple meridional (i.e. north–south) circulation is not possible on a rotating earth because the northward-moving air mass would be deflected eastward and the southward-moving air westward, and thus zonal (i.e. east–west) motions would set in. Heat exchange between the equatorial and polar regions could be achieved through a system of vortices and/or waves.

A generalized scheme for global pressure and wind distributions, taking into account heat budget and conservation of angular momentum, is shown in Fig. 1.6. Note that in

drawing this diagram, no attention was paid to the distribution of continents and oceans or to the great mountain chains. In this diagram, only the Western Hemisphere is shown. Near the ground, in the areas close to the equator, trade winds converge into the doldrums while at the same time being deflected westward. The descending air in the subtropics spreads horizontally and gains anticyclonic vorticity. Because of this, high-pressure belts are found in the subtropics. The circulation systems between the equator and 35° latitude (i.e. in the areas of the tropics and subtropics) are fairly steady and large.

However, the middle and higher latitude regions have large baroclinicity[1] as compared with the tropics, and the temperature range is much greater than in the tropics. Here, great amounts of potential energy are converted into kinetic energy, thus creating the wind systems. Because of this, the extratropics have traveling weather systems known as cyclones and anticyclones that appear, respectively, as centers of low and high pressures on the surface weather charts. However, in upper air charts (e.g. a height of 3 km), one rarely sees centers of low and high pressures; one sees large waves usually moving from west to east superimposed on a strong zonal current. The core of this zonal current is called the jet stream.

Next, the possible modification of the hypothetical wind systems due to the influence of the distribution of continents and oceans will be considered briefly. The insolation does not vary significantly over the year near the equator, but the variation increases with latitude. The conductive capacity of the land is very much smaller than that of the oceans, and for this reason, the annual range of temperature is greater over the continents than over the oceans. Thus, the temperature difference between oceans and continents varies little over the year near the equator and more in the higher latitude regions.

This contrast in the heat capacity of land and water gives rise to the low and high pressure centers. In spring, the land is heated more rapidly than the oceans, and extensive low pressure areas develop over land and relatively high pressures persist over the oceans. In fall, the continents cool more rapidly than the oceans, and high pressure centers develop over the land areas. Since the temperature difference between continents and oceans is greater in winter, the low pressure centers over the continents in summer are less pronounced than the high pressure areas over the continents in winter.

Large mountain ranges can modify the distribution of these low and high pressure centers considerably. Petterssen (1969) mentioned that North America may be considered as a triangle with its base in the Arctic and its apex in the tropics. Thus, it is completely open to exchange of heat with the Atlantic Ocean, but the Rocky Mountains (hereafter referred to as the Rockies) obstruct the heat exchange with the Pacific. Because of this, the high pressure center in winter and the low pressure center in summer are located to the east of the mountain ranges.

In Fig. 1.6, the global wind and pressure patterns are presented through the traditional method of zonal belts. It should be realized that these zonal belts do not actually exist over the globe in such a well-defined fashion except, possibly, in the Southern Hemisphere between 50 and 60° latitude. However, over certain areas of the earth, the sea level pressure field and surface winds have more or less persistent distribution over the year. There are seven regions of persistent high pressure and six regions of persistent low pressure (Rumney 1969).

---

[1] When lines of equal pressure (isobars) and lines of equal density (isosteric lines) are parallel to each other, the atmosphere is said to be barotropic. When they are inclined to each other, the atmosphere is said to be baroclinic. The degree of inclination determines the baroclinicity.

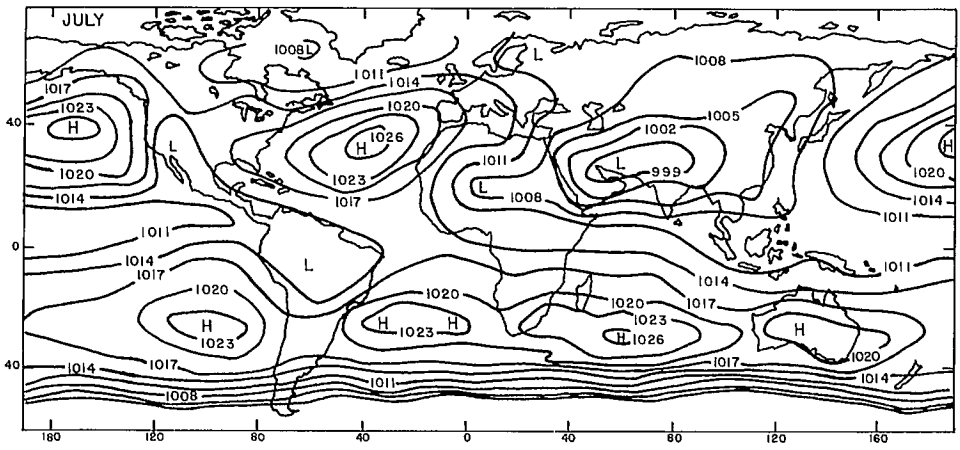

FIG. 1.7. Global sea level pressure (millibars) distribution in July.

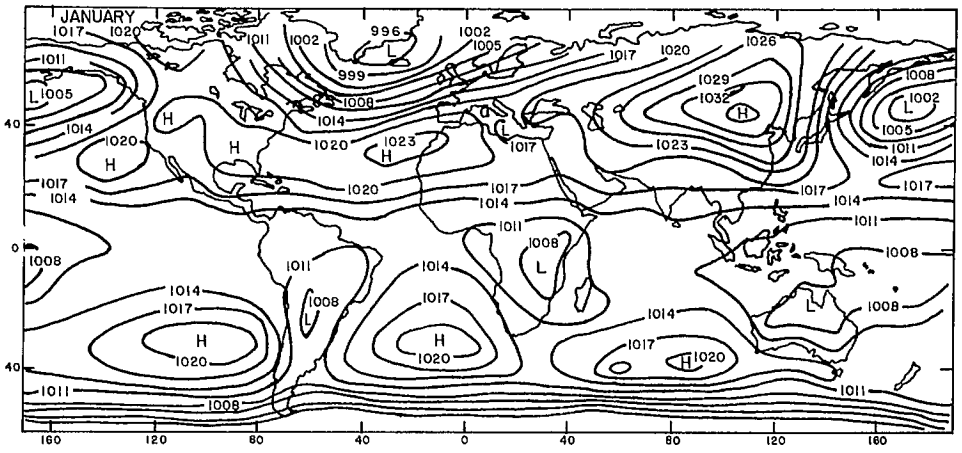

FIG. 1.8. Global sea level pressure (millibars) distribution in January.

The sea level pressure distribution for the months of July (representative of summer in the Northern Hemisphere) and January (representative of winter) is shown in Fig. 1.7 and 1.8, respectively. The high pressure centers are over the eastern Atlantic and Pacific, north and south of the equator, South Indian Ocean, Arctic Ocean, and Antarctica. Occasionally, names are given to these centers. For example, the one over the eastern Pacific is called the "Hawaiian High" and the one over the eastern Atlantic is called the "Azores High." The low pressure centers are the "Icelandic Low" (over the North Atlantic), the "Aleutian Low" (over the North Pacific), one each in the Atlantic, Pacific, and Indian oceans in a shifting zone along the equator, and one in the Southern Ocean near Antarctica.

With reference to Fig. 1.7 and 1.8, the following remarks may be made. Pressure is higher and the gradients are steeper in the winter hemisphere (i.e. the hemisphere that has

winter at that time), and the pressure centers shift northward in July and southward in January (Trewartha 1968). The pressure belts in the subtropics are more or less continuous in the winter hemisphere, whereas in the summer hemisphere, the continuity is broken by the heated continents. Between the subtropical high and the subpolar lows lies the main zone of traveling cyclones and anticyclones. The high and low pressure areas are called centers of action, because their strength over a given period (e.g. week, month, or season), as compared with long-term averages, is an indication of the departure of the weather from its average.

1.3 Air Masses, Fronts, Cyclones, and Anticyclones

An air mass is a large body of air with dimensions of the order of at least 1000 km, whose properties, especially temperature and relative humidity, do not change significantly within the mass. The border region between two air masses usually has a width of about a few tens of kilometres and is called a frontal zone (referred to simply as a front). Since the frontal regions are typified by strong variations in temperature and moisture, they are also regions in which potential energy of the air masses becomes changed into the kinetic energy of the cyclonic systems.

It has been shown that the major pressure and wind systems are located over either the oceans or the continents but not in the transition zones. Because of its large conducting capacity, the air that is associated with these systems will acquire the physical properties of the underlying surface. The sources that produce air masses are aptly termed "air mass sources." Air masses are not stationary, and once an air mass begins to move, its structure changes depending on the properties of the underlying surface. If the new surface is colder than the air mass, then the air mass loses heat and becomes more stable. On the other hand, if the surface is warmer, the air mass acquires heat and becomes less stable.

The Norwegian School of Meteorologists developed the polar frontal theory of cyclones. The basic structure of a cyclone, which forms from the convergence of two air masses, is shown schematically in Fig. 1.9. The first air mass is relatively warm and moist and has as its source a subtropical region. The second one is colder and has a polar air mass source. In the initial stages of development of the cyclone, a tongue of warm air extends northward between these two air masses. The narrow region separating the air masses is the front and is referred to as the polar front, since it represents the southern edge of the polar air mass.

A warm front is one along which cold air is displaced by warm air, and a cold front is one in which the reverse is true; a stationary front is one that does not move.

In the frontal theory of cyclones, the initial stage is characterized by a quasi-stationary front separating a warm and a cold air mass. The next stage involves the development of wave motion on the front, with the subsequent development of a low pressure center. At this stage of cyclogenesis, the cyclone is referred to as nascent. In the next stage, the warm front is overtaken by the cold front, and this process is called occlusion. With the progress of the occlusion process, the warm air is lifted to higher levels and becomes replaced at the lower levels by colder and heavier air. Because of this, the center of gravity of the air mass is lowered, and large amounts of potential energy are released. This potential energy is converted into kinetic energy of the wind systems that surround the cyclone center.

Petterssen (1969) stated that an extratropical cyclone is usually accompanied by three or four similar cyclones to form a series, or a family. The first member of this family is an occluded cyclone, the second member is partly occluded, and the trailing member is

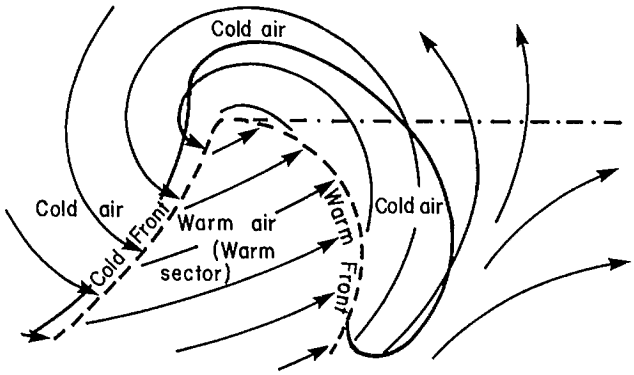

FIG. 1.9. Cyclone model of the Norwegian Meteorological School.

an incipient cyclone wave. While the leading cyclone dissipates slowly, new cyclones develop on the trailing front. Because of this, the group, as a whole, moves slower than an individual member. While the first cyclone is in the higher latitudes, the subsequent cyclones take more southerly paths, and in the rear of the frontal member, cold air moves southward into the substropics. This phenomenon is called a polar outbreak and will lead to the development of an arctic cyclone. At times, on the surface weather charts, it is difficult to recognize a coherent cyclone family. This is especially true in North America because of the influence of the Rockies. Coherent cyclone families, with three to six members, travel eastward over the northern oceans with a period of 3–8 d.

Anticyclones, as the name implies, are opposite to cyclones, i.e. they are centers of high pressure. Their intensities are lower than those of cyclones, they exhibit a more irregular behavior than cyclones, and as a rule, they move slower. Petterssen (1969) gave the following classification for anticyclones. (1) Subtropical highs: vast, elongated, and deep (in height) anticyclones located in the subtropics. These are highly persistent, are either stationary or slowly moving, and can be seen on practically any weather chart. (2) Polar continental highs: anticyclones that develop predominantly over northern continents during winter. In North America, they develop mainly in Alaska and western Canada (east of the Rockies) and move towards the Atlantic Ocean in a southeasterly to easterly direction. Once they enter the Atlantic Ocean, they cannot maintain their identity and get absorbed in the subtropical anticyclone. (3) Highs within the cyclone series: small anticyclones that lie between individual members of a cyclone family. Sometimes, these are simply wedges of high pressure that travel at the edges of huge subtropical anticyclones. (4) Polar-outbreak highs: either the last member of a cyclone family or follow any intense cyclone family.

Next, the geographical distribution of cyclones and anticyclones will be discussed. Cyclones occur preferentially in the higher middle latitudes. In the Northern Hemisphere, the maximum cyclone frequency occurs at approximately 60°N in summer and 50°N in winter. Note that the subtropical anticyclones and the equatorial convergence zone also have a similar 10° latitude seasonal shift. In the Southern Hemisphere, the belt of maximum cyclone frequency is more continuous and lies between 50 and 60° latitude.

Petterssen (1969) presented diagrams of percentages of cyclone and anticyclone centers. Based on these diagrams, the following important points may be noted for cyclone activity in the Northern Hemisphere during winter. Over the Pacific Ocean, there is a wide

zone of cyclonic activity stretching from southeast Asia to the Gulf of Alaska. During winter, most of these cyclones travel in a northeastward direction and converge in the Gulf of Alaska. However, some of the storms, especially those that form on the mid-Pacific polar front, travel on a more southerly track and reach the California coast. Most of the Pacific cyclones cannot cross the Rockies; however, some of them redevelop on the eastern side of the Rockies. There are three areas where such a redevelopment occurs frequently. (1) The region east of Sierra Nevada: the cyclones generated here are usually weak. (2) East of the Rockies in Colorado: many of the cyclones originating here (usually referred to as Colorado cyclones) achieve great intensities and travel to the central and eastern parts of North America. They usually travel northeastward toward the Great Lakes. (3) East of the Canadian Rockies, in Alberta: these Alberta storms are also intense, and associated with their eastward travel, cold air moves southward over the Great Plains.

During winter, the Great Lakes region is also a region of high cyclone frequency, for several reasons. This region can originate storms because the water is warmer than the surrounding land. Secondly, this is a region where the storm-tracks from the Alberta and Colorado lows converge. Occasionally, storms that develop over the Gulf of Mexico travel northward towards the Great Lakes.

Over the Atlantic Ocean, storms usually develop on the Atlantic polar front (Fig. 1.10). One of the most favored regions is the coast of Virginia and to the area east of the southern Appalachians. These are referred to as the East Coast Storms or the Cape Hatteras Storms, and while moving along the Gulf Stream, they achieve great intensity, and finally they become stagnant near Iceland or between Greenland and Labrador. On the Atlantic–Arctic front, many cyclones either form or redevelop, and they generally move in the direction of the Barents Sea.

During the summer period for the Northern Hemisphere, there are mainly two belts of high frequencies of storm occurrence. The northern belt surrounding the Arctic is irregular and consists of cyclones with fronts. The southerly belt is over the warm continents of the subtropics. The more or less permanent heat low over the continents accounts for the high frequency found over southern California, Nevada, Arizona, and northern Mexico. At the higher levels, there is an anticyclone with strong subsidence, and because of this, clouds and weather systems are absent in the second belt.

Next, the geographical distribution of the anticyclones in the Northern Hemisphere will be briefly discussed. There is a belt over the oceans with a maximum occurrence frequency off the subtropical west coasts. In the eastern North Pacific, strong frequencies occur. The greatest frequency occurs over Nevada, Utah, and Idaho, and the frequency is generally high over the Rockies and also from Alaska to the Great Plains. These anticyclones are shallow and cold and are of the polar continental type. The frequency is high near the Atlantic coast but is low in the region of the Great Lakes.

Regarding the distribution of the anticyclonic centres in the Northern Hemisphere during summer, note that the belt of subtropical anticyclones is now farther north than in winter. The occurrence frequency is again significant in the eastern Pacific but is low in the western Pacific because of the summer monsoon. There are two maxima over North America. The first one is over Nebraska and Kansas, which is a grouping of weak highs. The second one, over the Great Lakes, arises because anticyclones from the Kansas–Nebraska area travel eastward and become stagnant over the cold waters of the Great Lakes.

Earlier, a front was defined as a sloping zone of transition between two air masses of different density. Although a front is several kilometres wide, it is narrow compared with the horizontal dimensions of the air masses. On weather charts, fronts appear as lines

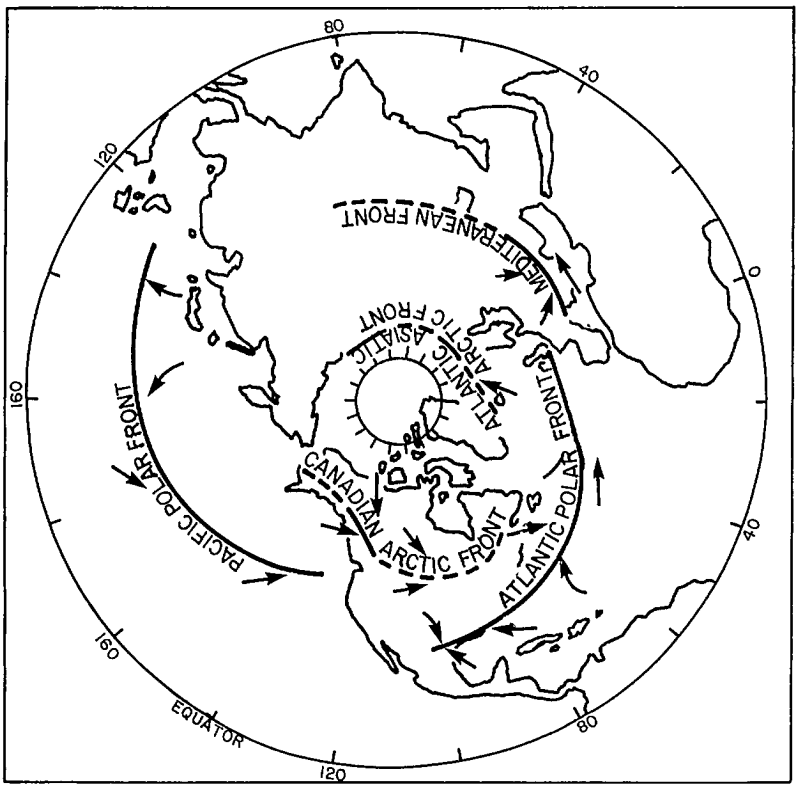

FIG. 1.10 Major frontal zones in the Northern Hemisphere during winter. (Barry and Chorley 1970)

of discontinuity in wind and temperature. At the front, there is a kink in the isobars (i.e. lines of equal pressure), directed from low to high pressures.

Next, the principal frontal zones on the globe will be identified. Although fronts are not usually stationary, certain regions nevertheless consistently show high frequency of fronts, these regions being the areas of confluence between the main air mass sources discussed earlier. Figure 1.10 shows the major frontal zones in the Northern Hemisphere during winter. In the Atlantic Ocean region, one has the Atlantic polar front, which is the confluence region between the polar continental and the tropical maritime air mass sources, and the opposing currents indicated maintain the front. Quite often, the Atlantic polar front extends eastward over Europe. Its position varies quite drastically in the meridional direction; i.e. it can be anywhere from the West Indies to Portugal in the south to the Great Lakes and Iceland in the north (Petterssen 1969). This frontal zone is responsible for the cyclones that bring precipitation over a wide belt from the eastern part of the North American continent to northwest Europe.

A second important frontal zone is formed by the Atlantic–Arctic fronts, which are in the confluence region between the arctic source region and the polar maritime air. The storms that form on this frontal zone usually travel from Iceland along the northern part of Norway to the Barents Sea. A third important frontal zone is the Mediterranean front,

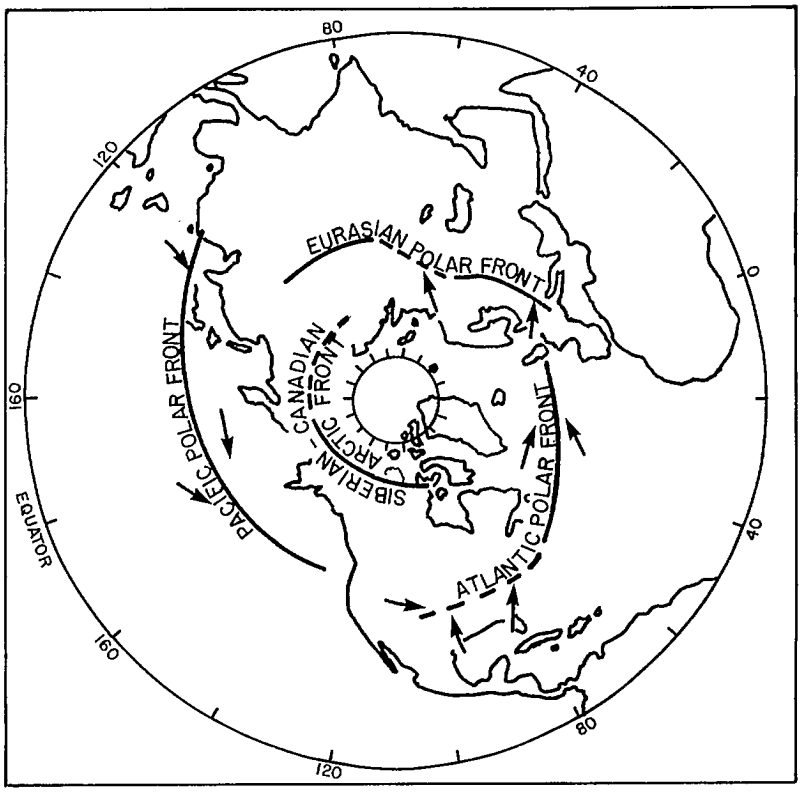

FIG. 1.11 Major frontal zones in the Northern Hemisphere during summer. (Barry and Chorley 1970)

which forms at the confluence of the cold air from Europe and the mild air from North Africa and Mediterranean Sea area. The cyclones that develop here usually travel in a northeasterly direction to southern parts of the USSR. However, some travel eastward to northwest India.

Over the North Pacific Ocean, there are usually two polar fronts, the one nearest the Arctic coast being the more pronounced. Most of the North Pacific storms form along this frontal zone and travel towards the Gulf of Alaska, but some of them take a southerly route to California and northern Mexico. The Pacific–Arctic front usually extends towards the Great Lakes, and many of the storms between the Great Lakes and the Rockies develop on this front. Cold air from the Arctic may reach as far south as Texas, or even northern Mexico, in the rear of these storms. It has already been mentioned that Pacific cyclones usually cannot cross the Rockies, but they redevelop to the east of these mountains in such preferred areas as Alberta, Colorado, and Oklahoma.

The frontal zone distribution during the summer period for the Northern Hemisphere is shown in Fig. 1.11. Since, in summer, the differences in the properties of the various air masses are not as pronounced as in winter, one can find permanent frontal zones only in the Arctic region. The polar fronts over the western Atlantic and Pacific are usually 10° farther north in summer as compared with their winter positions. There are new frontal

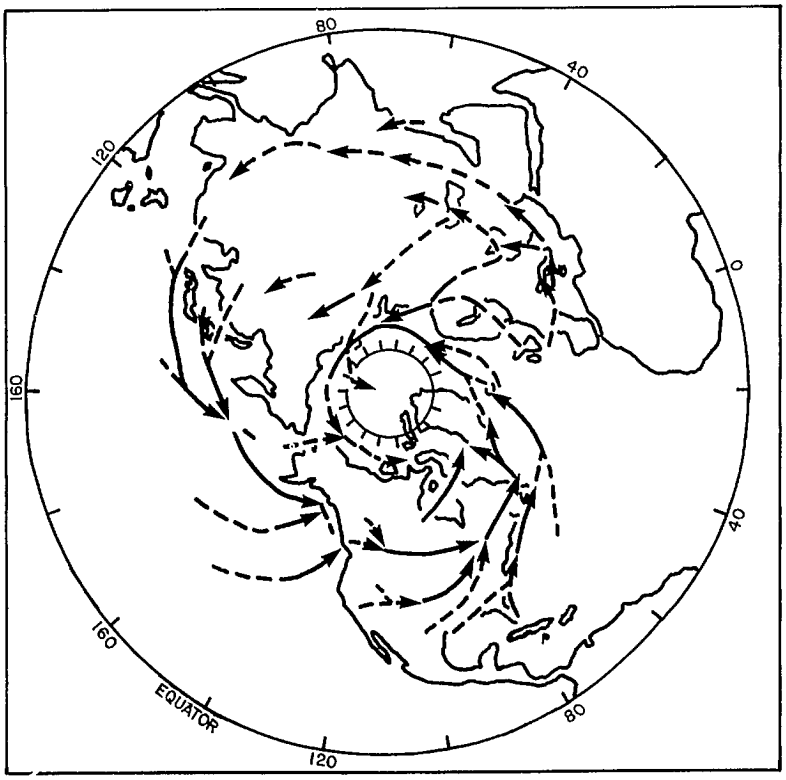

FIG. 1.12. Major depression tracks for the Northern Hemisphere in January. Tracks represented by broken lines are less certain than those represented by solid lines. (Klein 1957)

zones over Eurasia and over the middle part of North America. These new zones are due to the prevailing meridional temperature gradient and the large scale orographical influences. The Arctic front, in summer, is formed along the Arctic coasts of Siberia and North America and is associated with the snow (and ice) boundaries of the higher latitudes.

The principal tracks of the depressions in the Northern Hemisphere for the winter period are shown in Fig. 1.12. Note that these tracks basically reflect the influence of the major frontal zones.

1.4 Regional Weather Systems

In this section, the regional weather systems of North America, South America, Europe, Africa, Asia, Australia, and the oceanic regions will be briefly considered. The detailed meteorological problems associated with storm surges will be considered in Chapter 6.

WEATHER SYSTEMS OF NORTH AMERICA

During both winter and summer, the mean pressure field at the midtropospheric level

shows a prominent trough over the eastern part of North America. The origin of this can be traced to the influence of the Rockies on the upper westerlies, but in winter, the strongly baroclinic zone along the east coast of North America is also responsible. Over the midwestern states, cyclones generally move in a southeast direction, bringing continental polar air southward, whereas along the Atlantic coast the cyclones travel northeastward. If the upper air trough is far to the west of its average position, then depressions form ahead of it over the South Central States (Petterssen 1969) and move in a northeasterly direction towards the lower St. Lawrence.

Considering January as a typical month for the winter period, the surface pressure chart shows an extension of the subtropical high over the southwest part of the United States (this high being referred to as the "Great Basin High") and a polar anticyclone over the Mackenzie River area. On both the Atlantic and Pacific coasts, the pressure is low because of the Icelandic and Aleutian lows. Because of heating over the land, the Icelandic low is split and a secondary low appears over the northeastern part of Canada. The cyclone frequency is maximum on the Pacific coast and in the Great Lakes area during winter, whereas in the Great Plains, the maximum frequency is in spring and early summer. On the average, in the month of December, the Gulf of Alaska has the maximum frequency

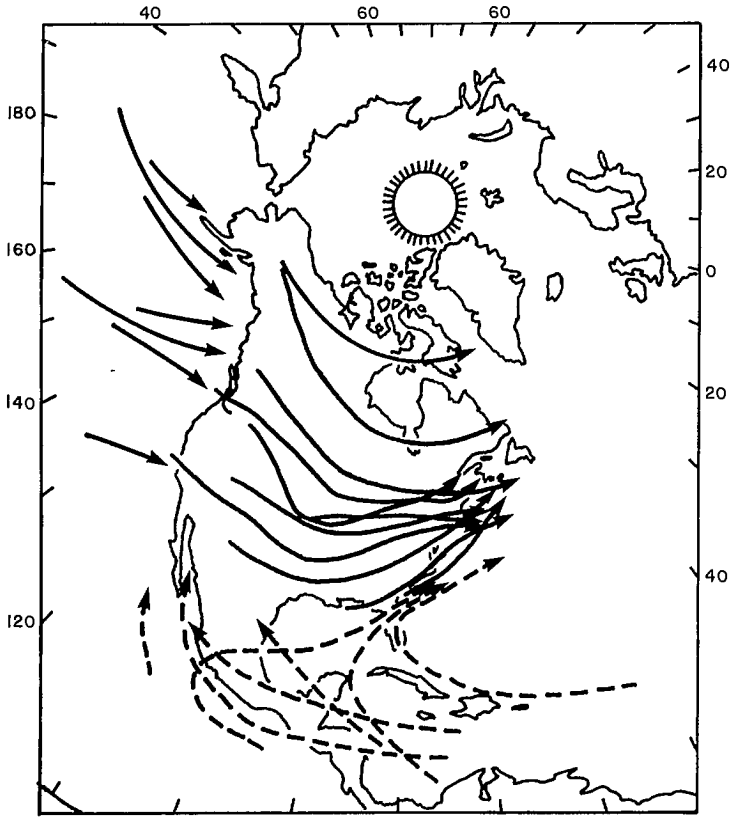

FIG. 1.13. Cyclone tracks of North and Central America. Solid lines represent extra-tropical cyclones and broken lines represent tropical cyclones.(Haurwitz and Austin 1944)

of lows and the Great Basin region has the maximum frequency of highs, as compared with any other region in the Northern Hemisphere.

In winter, there are three main depression tracks across North America. (1) Depressions from the west move eastward between 45 and 50°N. (2) Some depressions first travel southeastward as far as the Central States and then travel northeastward towards New England and the Gulf of St. Lawrence. Depressions developing over the Pacific cross the western mountains as upper troughs and redevelop in the lee of the mountains in Alberta and Colorado. (3) Depressions form on the polar front off the east coast of the United States and move northeastward towards Newfoundland.

In the summer period, the frequency of depressions originating in the east coast is less, and the tracks of depressions from the west are somewhat northward as compared with their winter positions. The tracks pass over Hudson Bay, Ungava Bay, Labrador, or the Gulf of St. Lawrence. The maritime frontal zone that gives rise to these depressions is not pronounced.

In early April, the Aleutian low (which is located approximately at 55°N, 165°W during September to March) splits into two; one center is over the Gulf of Alaska and the other is over northern Manchuria. Cyclogenesis increases in Alberta and Colorado. By the end of June, the subtropical high pressure cells in the Northern Hemisphere are displaced northward, and because of this, the depression tracks also move northward.

The essential features of the sea level circulation in the eastern and central parts of the United States and Canada can be determined from sea level pressure maps. However, due to the presence of mountains and rugged orographical features in the west, sea level pressure gradients do not accurately reflect the wind distribution. Because of the presence of high coastal mountains, the Aleutian low pressure system does not extend far inland. Haurwitz and Austin (1944) stated that because the inland pressures are reduced to sea level, they appear quite high compared with those over the surrounding ocean, and this sea level correction gives rise to steep fictitious pressure gradients in northern British Columbia and southern Alaska. Due to the presence of several fjords and the banking effect produced by the coastal mountains, the average surface winds do not agree with the mean isobaric pattern.

Weather Systems of Central America

Central America, as defined here, is the region from Mexico to the equator. The main mountain range in Central America is the Sierra Madre in Mexico. This region generally lies between the subtropical belt of high pressure and the equatorial belt of low pressure. The prevailing winds are easterly and the migratory low pressure centers generally move from east to west. Thus, these secondary circulations are significantly different from those of middle and high latitudes. The strong cyclones that travel over Mexico and Central America are tropical hurricanes, the tracks of which are shown in Fig. 1.13 (Haurwitz and Austin 1944). The following is a summary of the average conditions associated with these tracks in Mexico. (a) The Antillean hurricanes recurve in the eastern part of the Gulf of Mexico, and the hurricane season is August to October. During August, the recurvature occurs farther north than during October. (b) A frequently observed track is over the Caribbean Sea, the Yucatan Peninsula, and then over the northeast coast of Mexico or along the coast of Texas. (c) Occasionally, the hurricanes, after crossing the Yucatan Peninsula, travel over Central Mexico and arrive at the Pacific coast and then travel northwestward. (d) Similar to c across Central America, and then the track is towards the northwest, parallel to the Pacific coast and passing over the Gulf of California. (e) These

storms develop over the southeast Pacific and travel towards the Gulf of Mexico. Some tropical cyclones also form south of the Revillagigedo Islands.

Thus, two main classes of cyclones can be noted: (1) hurricanes that develop over the warm waters of the Caribbean Sea and the Atlantic Ocean and (2) storms that develop or rejuvenate over the eastern Pacific near the Central American coast. During summer (June to August), the West Indies storms generally travel inland or recurve farther west than during fall (September to November). This difference in behavior is due to the strong subtropical anticyclone in midsummer, which prevents the recurvature of a storm until it arrives at an area of southerly winds. In autumn, the Atlantic high is less permanent, and a hurricane can recurve northward into a trough of low pressure over the western Atlantic. In winter, due to the southward displacement of the westerlies, extratropical cyclones are found in relatively low latitudes.

Alaka (1976) provided details about the Atlantic hurricanes. The locations at which Atlantic tropical storms reached hurricane intensity during the period 1901–63 are shown in Fig. 1.14 (Dunn and Miller 1960). The monthly distribution of Atlantic hurricanes during the period 1881–1972 is given in Fig. 1.15.

Bryson and Hare (1974) stated that, on the average, 5–10 tropical storms and hurricanes affect North America and Caribbean regions per year; but there was only 1 in 1914 and as many as 21 in 1933. During the peak hurricane season of August to October, the preferred regions of hurricane formation are the trade wind belt east of the Antilles (including the Canary Islands) and the southwestern parts of the Gulf of Mexico and Caribbean.

Weather Systems of South America

The most important orographical feature of South America is the continuous chain of high mountains, known as the Andes, which extend from Venezuela to Cape Horn. Another topographical feature is that South America does not have prominent coastal indentations (such as Hudson Bay, Gulf of St. Lawrence, and Gulf of Mexico in North America) or large inland lakes.

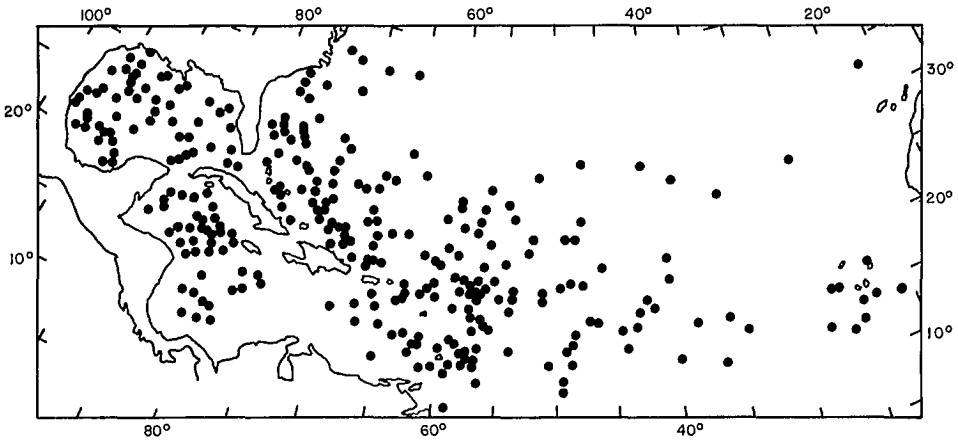

Fig. 1.14. Locations at which Atlantic tropical storms reached hurricane intensity during the period 1901–63. (Dunn and Miller 1960)

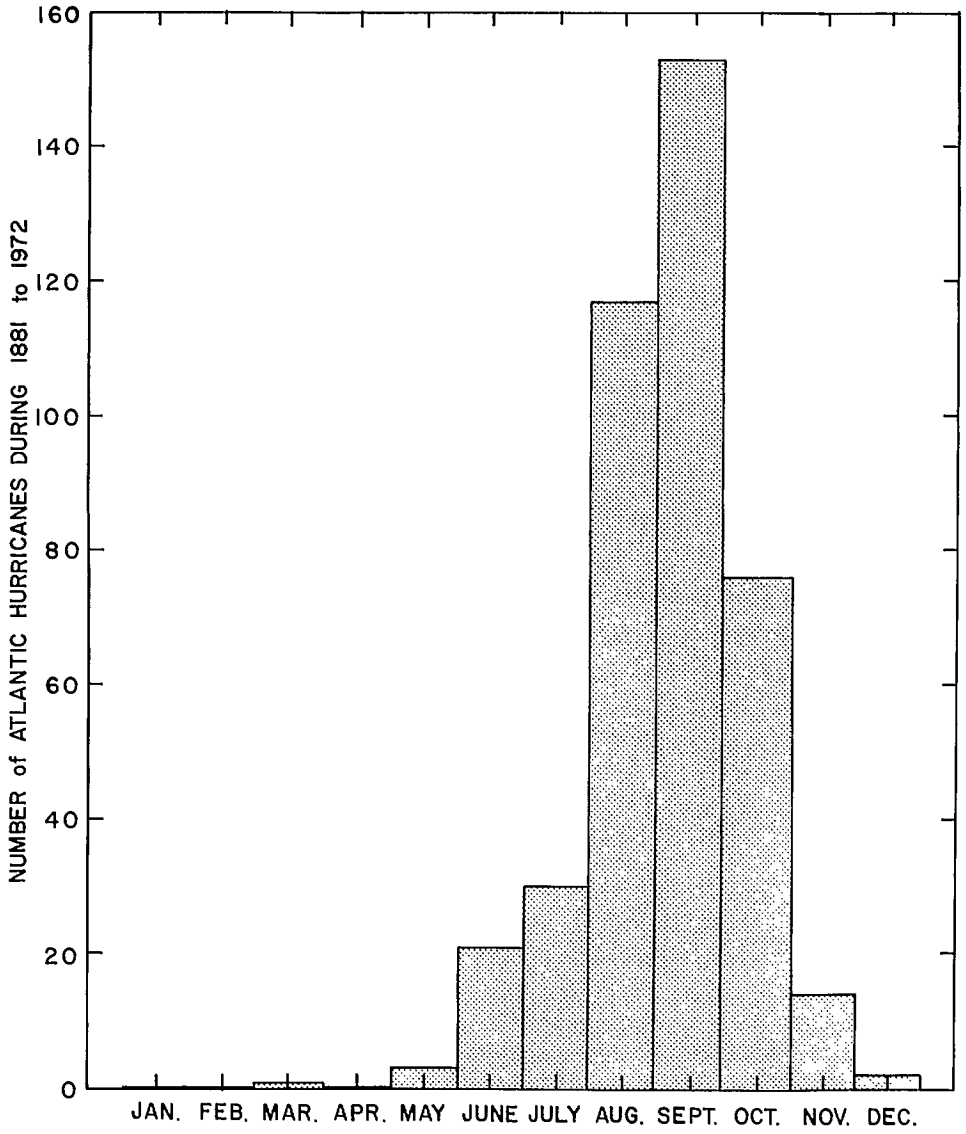

FIG. 1.15. Total number of Atlantic hurricanes during the period 1881–1972 distributed by month.

A more or less persistent feature is the presence of two semipermanent anticyclones, one over the Atlantic and the other over the Pacific, near the east and west coasts, respectively. A circumpolar zone of low pressure extends to about 45°S, with the mean pressure trough located slightly east of South America (Haurwitz and Austin 1944). South of Cape Horn, there are deep semipermanent cyclones of the Weddel and Belgique seas. One main difference between the Northern and Southern hemispheres is that, whereas in the Northern Hemisphere the low pressure areas are deeper in winter (than in summer), the reverse situation occurs in the Southern Hemisphere.

Because of continental heating, a thermal low is located over Paraguay in January. However, during July, this area comes under the influence of a weak anticyclone. The southern edge of the Northern Hemisphere's Atlantic anticyclone stretches as far south as the north coast of South America. Throughout the year, a trough of low pressure lies near the equator.

At frequent intervals, the circumpolar zone of low pressure is traversed by cyclones, which move from northwest to southeast. Cold anticyclones usually follow these cyclones and move from southwest to northeast. Generally, over northern Argentina, these anticyclones are preceded by the deepening of a cyclone, which moves southeastward on to the Atlantic Ocean.

TABLE 1.2. Cyclone frequency (% of the total annual occurrence) at 15°W longitude (Atlantic Ocean). (Haurwitz and Austin 1944)

Latitude	Winter	Spring	Summer	Autumn	Year
30–35°N	1.7	2.0	0.4	2.0	6.1
35–40°N	3.0	3.9	1.1	3.8	11.8
40–45°N	3.3	4.2	2.3	3.1	12.9
45–50°N	2.1	3.0	3.7	2.7	11.5
50–55°N	2.3	3.7	4.5	2.4	12.9
55–60°N	3.0	4.5	6.0	4.1	17.6
60–65°N	3.2	5.1	5.0	5.4	18.7
65–70°N	1.9	2.1	2.2	2.3	8.5
30–70°N	20.5	28.5	25.2	25.8	100.0

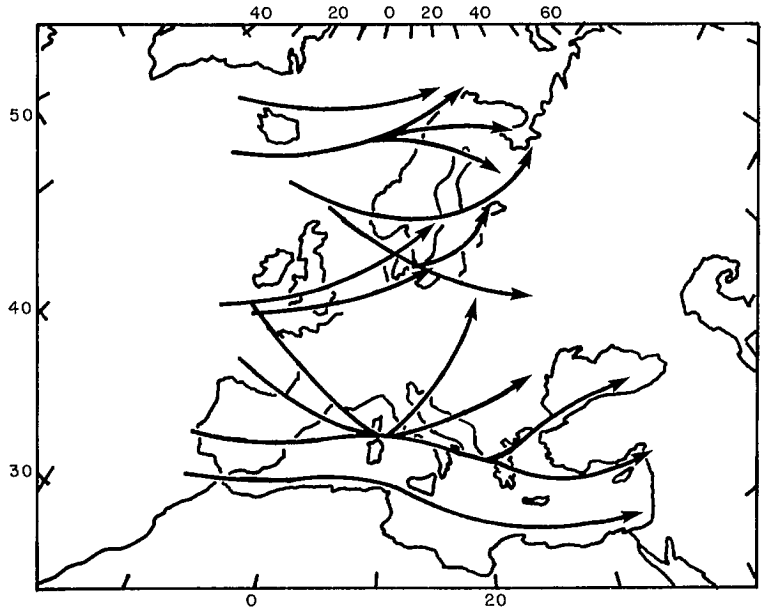

FIG. 1.16. Cyclone tracks across Europe. (Haurwitz and Austin 1944)

Weather Systems of Europe (Excluding the USSR)

Orographically, Europe is quite different from South America. (a) In Europe, there is no extensive high mountain chain in a north–south direction. (b) There are several large indentations to the coastline, e.g. the Black Sea, the Aegean Sea, the Adriatic Sea, the North Sea, the Baltic Sea, the Gulf of Bothnia, the Gulf of Finland, and the Bay of Biscay. Haurwitz and Austin (1944) conveniently grouped the important mountain chains as follows: (1) the Scandinavian mountains, oriented in a general southwest–northeast direction, (2) the Pyrenees (separating France and Spain), which have peaks higher than 9000 ft (2743 m), (3) the Alps, which are the highest mountain chain in Europe and extend in a general west–east direction from southern France to southeastern Austria, and (4) the Apennines, which extend almost the entire length of Italy.

In winter, the cyclones that travel across North America, or those that develop on the Atlantic front, travel south of Iceland in a general northeasterly direction towards Norway. The latitudinal variation of cyclones that approach the west coast of Europe for the different seasons of the year is listed in Table 1.2. The cyclone tracks across Europe are shown in Fig. 1.16 (according to Haurwitz and Austin 1944). This difference in frequency is more pronounced in summer than in winter.

Some of the cyclones that traverse Europe have traveled over the Atlantic Ocean. Others develop over Europe itself and the adjacent seas. For example, secondary cyclones develop south of the Scandinavian range, and these are referred to as the Skagerrak cyclones. Other regions where deepening of an old primary cyclone may occur are the Adriatic Sea and the Gulf of Genoa. The cyclones that traverse Southern Europe either originate over the Atlantic and deepen over the warm waters surrounding Italy or form in the Mediterranean Sea. According to Wallen (1970), the cyclones of Europe have a duration of usually 8 d but at times up to 17 d. Figure 1.17 shows the frequencies of cyclones in winter and summer for Europe.

Weather Systems of Asia (Including the USSR)

Haurwitz and Austin (1944) recognized the following mountain chains as the important orographical features of Asia. (1) The Himalaya mountains extend from west to east in northern India; some of the highest peaks on the globe are in this mountain chain. For example, Mount Everest is over 29 000 ft (8839 m) in height. (2) Between the Himalayas and the Kunlun chain to the north lies the high plateau of Tibet, which contains a number of smaller mountain chains. (3) A more or less continuous series of mountains, oriented in the southwest–northeast direction, stretches from the Arabian Sea to Mongolia. The most important ranges are the Hindu Kush and the Tien Shan. (4) Starting at the Tibetan plateau, the land slopes gradually down towards the Arctic Ocean. Several mountain ranges exist in Mongolia and Siberia. Important ones are the Altai and Yablonova ranges. (5) In the southeast direction, a minor ridge extends towards the Gulf of Siam.

In southwestern Asia, land with elevations in excess of 2000 ft (610 m) contains mountain ranges such as the Caucasus, extending from the Caspian Sea to the Black Sea. The Urals form a north–south mountain chain. There are also smaller mountain chains on the east coast of the USSR and in Japan, Indonesia, Southern India, and Arabia. The Asian continent has several large indentations, e.g. the Red Sea, the Persian Gulf, the Arabian Sea, the Bay of Bengal, the Gulf of Siam, the Gulf of Tonkin, the China Sea (Pohai Sea), the Sea of Japan, the Okhotsk Sea, the Kara Sea, etc.

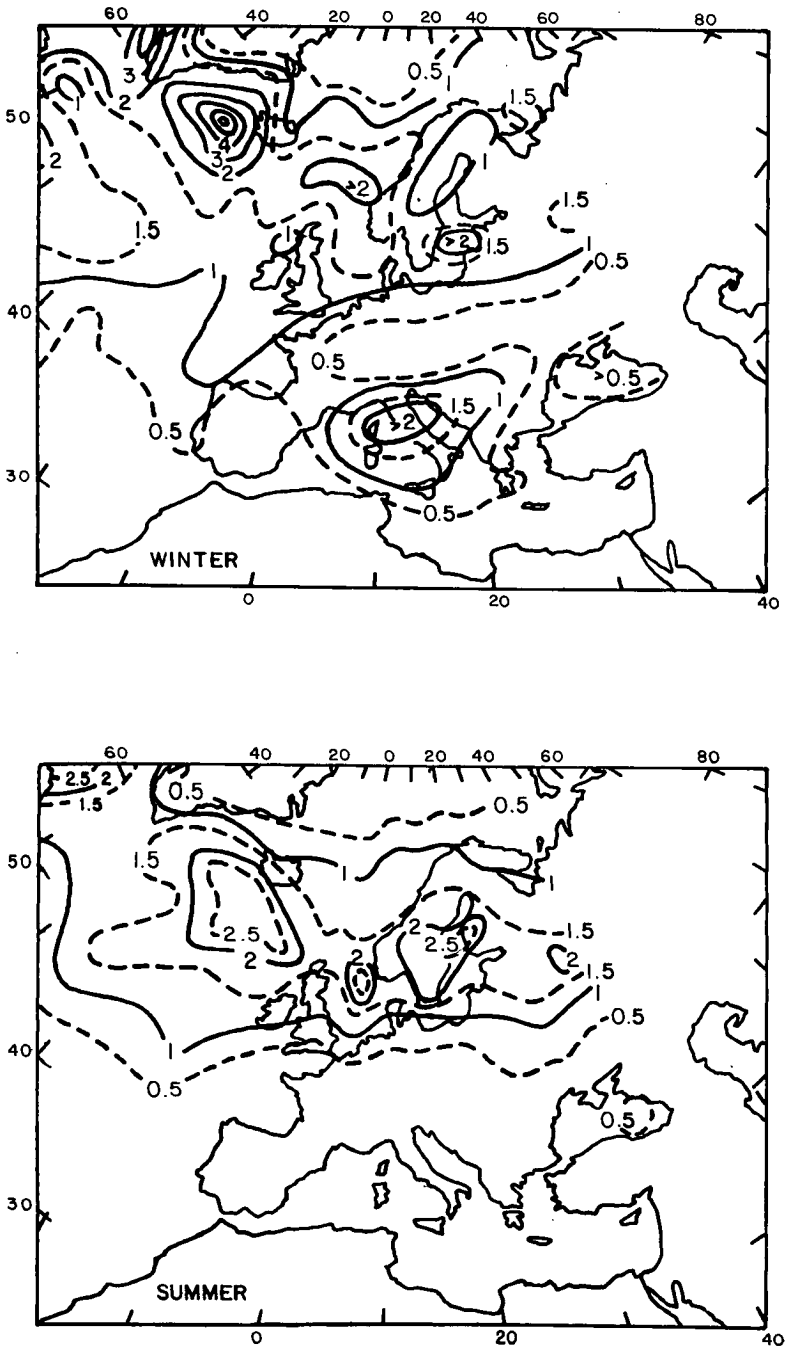

FIG. 1.17. Average frequency of cyclones with central pressures less than 1000 mb during a winter season (top) and a summer season (bottom). (Haurwitz and Austin 1944)

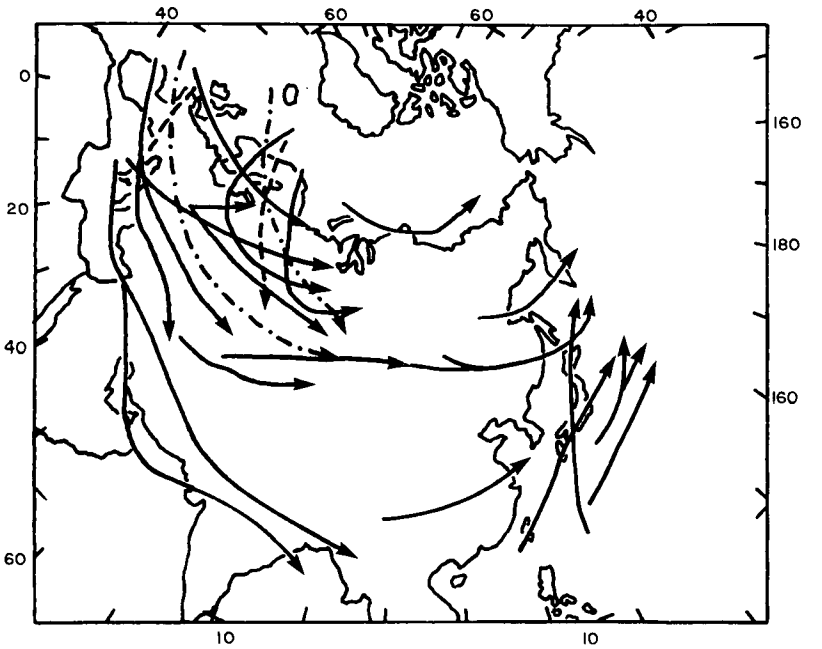

FIG. 1.18. Extratropical cyclone tracks across Asia. Tracks represented by broken lines are less certain than those represented by solid lines. (Haurwitz and Austin 1944)

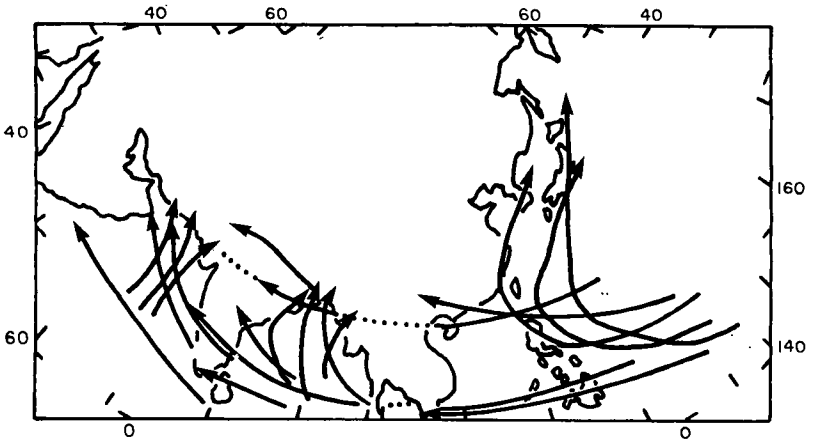

FIG. 1.19. Tropical cyclone tracks across Asia. (Haurwitz and Austin 1944)

The tracks of extratropical and tropical cyclones across Asia are shown in Fig. 1.18 and 1.19, respectively. The approximate percentage distribution of tropical cyclones in the Arabian Sea and the Bay of Bengal is given in Table 1.3. Note that whereas in the Arabian Sea the maximum percentage is during May to June, in the Bay of Bengal, it is in September to October. In Chapter 6 and section 7.4, the Arabian Sea and Bay of Bengal cyclones and the resulting storm surges will be discussed in more detail. Special attention

TABLE 1.3. Bimonthly distribution (approximate %) of tropical cyclones in the Arabian Sea and the Bay of Bengal. (Haurwitz and Austin 1944)

Water body	Jan.– Feb.	Mar.– Apr.	May– June	July– Aug.	Sept.– Oct.	Nov.– Dec.
Arabian Sea	1	11	50	1	11	26
Bay of Bengal	1	2	17	29	34	17

TABLE 1.4. Average number of tropical cyclones per month within 5–30°N and 105–150°E (based on data for the period 1884–1953). Note that this area is in the northwestern Pacific Ocean east of the Philippines and southeast of Japan. (Watts 1969)

Month	Average No.	Month	Average No.
January	0.3	August	4.4
February	0.1	September	4.4
March	0.1	October	3.0
April	0.3	November	2.1
May	1.0	December	0.9
June	1.5		
July	3.8	Year	21.9

will be given to the Bay of Bengal surges because these account for almost half of the lives lost globally.

The weather systems of northern and eastern Asia will now be considered. The monthly distribution of tropical cyclones in the southwestern Pacific and China Sea is given in Table 1.4. This table is based on data for the period between 1884 and 1953, inclusive, and shows an average of about 22 tropical cyclones per year, most of them occurring between July and October (Arakawa 1969). During July to September, tropical cyclones frequently travel over the coasts of China and Korea; however, the southern parts of China experience these sometimes as early as May and as late as mid-November. Between mid-November and April, tropical cyclones rarely traverse the mainland of China.

During the main cyclone season (i.e. July to September) for this area most of the cyclones form over the warm north equatorial current between Luzon and the Marianas, and they proceed west–northwest. About half of these persist in this direction until they reach the South China coast, but the other half recurve northward towards Korea and Japan. The number of tropical cyclones passing through each square of 2.5° latitude and longitude over the Northwest Pacific and China seas during the month of August for the period 1884–1953 is shown in Fig. 1.20. Broken lines show the areas of maximum activity.

The number of typhoons traversing different coastal sections during the period 1884–1955 is listed in Table 1.5. The most vulnerable area is the Fukien–Taiwan sector. As elsewhere on the globe, most of the deaths in China and surrounding areas due to typhoons occur as a result of the storm surge. For example, in 1881, about 300 000 people died at Haiphong. In 1922, about 60 000 people died at Swatow, and in September 1937, about 11 000 people died in Hong Kong. Usually, the surge at Hong Kong does not exceed 2 m, but surges three times greater have occurred nearby (Arakawa 1969).

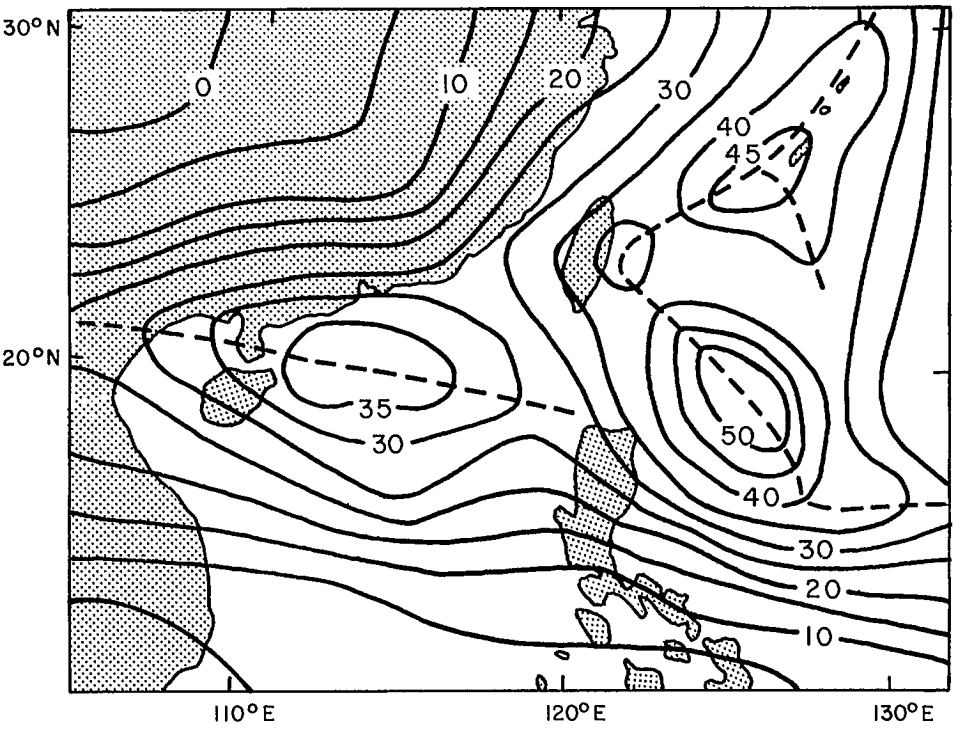

FIG. 1.20. Total number of tropical cyclones over a part of the Northwest Pacific Ocean and the Sea of China during the month of August for the period 1884–1953. Areas of maxima are represented by broken lines. (Arakawa 1969)

TABLE 1.5. Number of typhoons crossing the Southeast Asian coast during 1884–1955. (Watts 1969)

Coastal region	No. of typhoons
Kora and further east	87
Liaoning to Shantung Peninsula	39
Shantung Peninsula to Shanghai	22
Shanghai to Wenchow	34
Wenchow to Foochow	30
Foochow to Swatow	90
Swatow to Canton	43
Canton to Hainan	93
Total	438

Another area where tropical cyclones (and storm surges) cause great destruction and loss of life is in the Philippines. This country is situated in a region that has one of the greatest frequencies of tropical cyclones on the globe. The average number per year is about 22. Figure 1.21 shows the monthly distribution of these. It can be seen that the main cyclone season is July to November, with the maximum in October. Although the

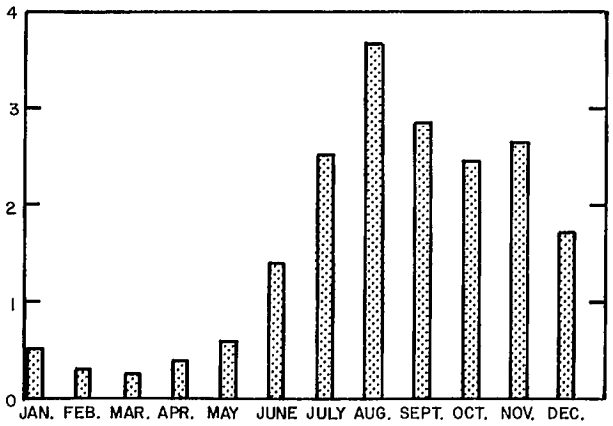

FIG. 1.21. Mean monthly frequency of tropical cyclones affecting the Philippines. (Arakawa 1969)

Philippine region has the highest number of tropical cyclones per year, the destruction and deaths due to storm surges are greatest in Bangladesh, which accounts for about 40% of the deaths over the whole globe. This will be discussed in greater detail in section 7.4.

Considered next are the weather systems of the USSR. Lydolph (1977) mentioned that during winter, the strong dominance of a high pressure cell over Eurasia causes the majority of fronts and cyclone tracks to be located along the edges of the land mass. In winter, the polar front generally lies south of the USSR. This front has two branches: the western branch lies in the Mediterranean–Asia Minor–Middle East area, and an eastern segment lies off the coast of China and across Japan, stretching into the Aleutians. Many cyclones that affect the weather over the Soviet Union develop on the western segment. The cyclones forming in the eastern Mediterranean usually move northeastward across the Black Sea, the Caucasus, Ukraine, the lower Volga, and western Siberia. Cyclones developing in the Middle East travel into Soviet Central Asia. Cyclones forming along the eastern branch of the polar front in winter travel north of the Soviet Union.

Thus, many of the cyclones affecting the USSR in winter either originate in the Icelandic low area or in the Mediterranean Sea. The Barents Sea also acts as a region of cyclogenesis and redevelopment. The Black Sea and the Caspian Sea also act as areas of cyclogenesis during winter. Other areas of cyclogenesis are western Siberia, the Baltic Sea, and southern Finland. In the Far East, cyclogenesis occurs over the northern part of the Okhotsk Sea (sea level pressures as low as 970 mb occur). However, in the Far East, most of the cyclogenesis occurs over Japan and the Sea of Japan. These cyclones affect southern portions of the Kamchatka Peninsula, Sakhalin Island, and Kuril Islands.

In winter, one of the stormiest areas in the USSR is the Ob Estuary region where cyclones traveling from the west along the Arctic coast meet those from the southwest traveling along the Black and Caspian seas. During spring, the center of maximum cyclone frequency shifts eastward from the Barents Sea to the Ob Gulf. In summer, the location of maximum cyclone frequency shifts southeastward into central Siberia south of the Taymyr Peninsula. In summer, the frequency of cyclones over the Black and Caspian seas diminishes considerably. In the Far East, the Aleutian low becomes weak, and the Amur Valley becomes a region of strong cyclogenesis.

Generally speaking, cyclones are more evenly distributed across the USSR land mass

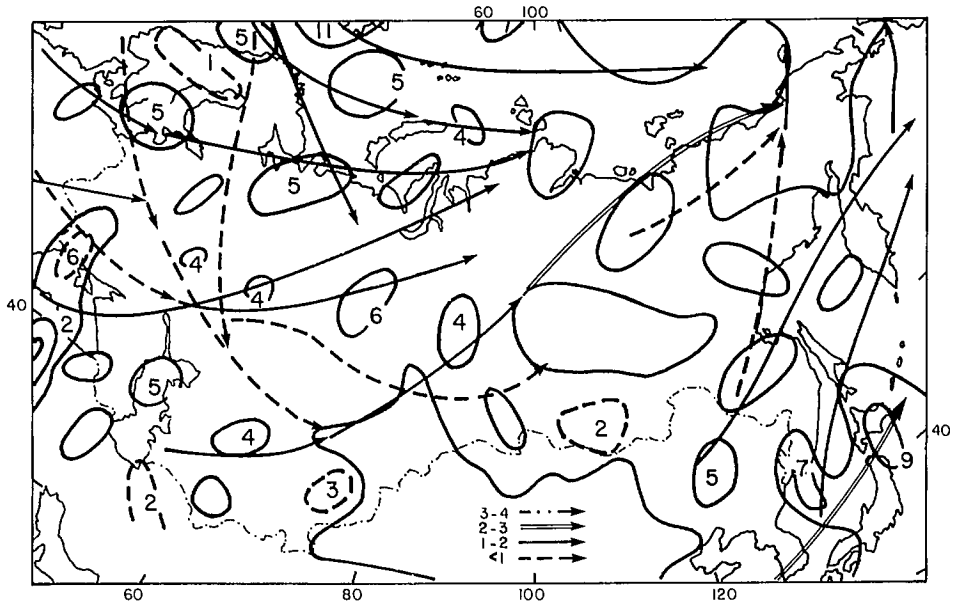

FIG. 1.22. Total number of cyclones during a 20-yr period over the Soviet Union during the month of January. The principal tracks of cyclones are also shown. (Lydolph 1977)

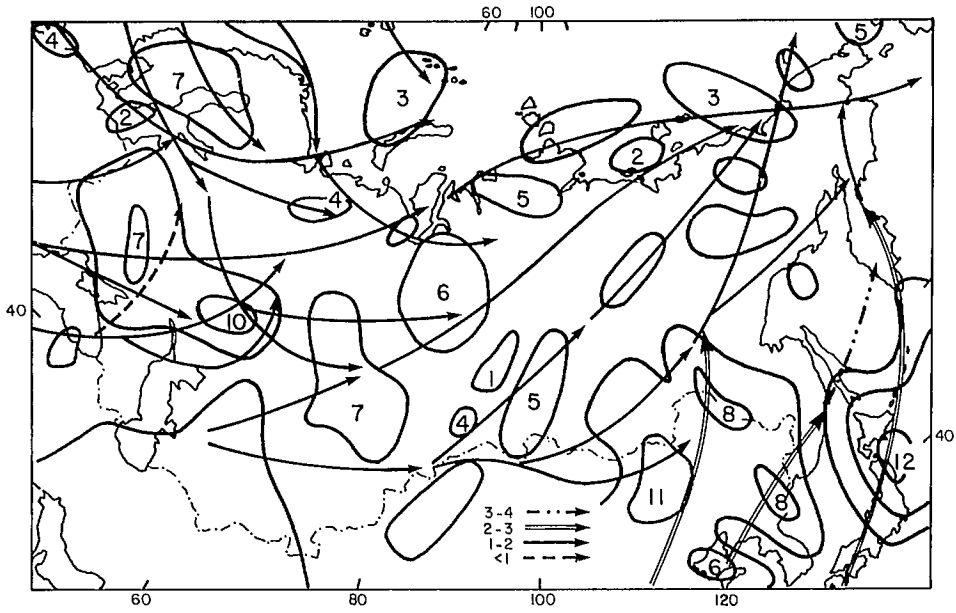

FIG. 1.23. Total number of cyclones during a 20-yr period over the Soviet Union during the month of July. The principal tracks of cyclones are also shown. (Lydolph 1977)

in summer. In winter, most of the cyclones affecting the USSR originate outside the country, whereas in summer, most of the cyclogenesis occurs in the USSR itself. In summer, areas of high cyclogenesis are the Amur Valley, the Urals, western Siberia, and northcentral Kazakhstan.

Generally, the movement of cyclones and fronts over the USSR is slower than over the eastern part of North America. Also, there is frequent stagnation for a day or more. On the average, about 32 cyclones per year affect central Asia. The frequencies of cyclogenesis and the main routes of cyclones in January and July are shown in Fig. 1.22 and 1.23, respectively.

Weather Systems of Africa

The continent of Africa is devoid of high mountain chains and large indentations to its coastline. Haurwitz and Austin (1944) recognized the following mountain chains as having some influence on the weather patterns. In the northwest part of the continent, the Atlas Mountains and the Algerian Plateau separate the coast and the desert to the south. A few peaks in Morocco extend over 10 000 ft (3050 m) in height. The huge Sahara Desert varies in elevation considerably, with a few peaks over 8000 ft (2440 m), such as the Ahaggar and Tibesti. The main mountain ranges of this continent are somewhat irregularly situated between Zambia (formerly Northern Rhodesia) and the Red Sea. Near Lake Victoria, and in Ethiopia, some peaks are over 12 000 ft (3660 m). Smaller mountain ranges (Drakensberg Mountains) exist in the southeast; the Auaz Mountains in the southwest, the Cameroon Mountains in Cameroon, and the Ankaratra Mountains in Madagascar (Malagasy Republic) are other examples.

The only indentations along the coastline are the gulfs of Guinea, Gabès, Sidra, and Aden. The only lakes of any significant size are Rudolf, Victoria, and Nyasa.

Because of its situation in low latitudes, Africa is not significantly influenced by disturbances originating in the polar front. The cyclones originating in the main frontal zones affect only a small portion of Africa. Those developing over the Atlantic Ocean frequently move in a northeast direction and, after entering the Mediterranean Sea, move eastward. The average track of the cyclones follows the Mediterranean coast. A few cyclones, however, traverse southern Morocco and southern Algeria.

Only on rare occasions do tropical disturbances occur over the African coast. The region of intense tropical cyclonic activity in Africa is the region of Madagascar (Malagasy Republic) and the surrounding area in the southwest Indian Ocean. During January to April, cyclogenesis is intense and occurs usually east of the Seychelles at about 10°S. Most of these cyclones recurve about the latitude of Madagascar. The majority recurve to the east of this island. During March and April, some of these tropical cyclones follow a southward path along the east coast of Africa and become converted to extratropical lows. The monthly frequency of these cyclones is listed in Table 1.6.

Griffiths (1972) provides the following information about the weather systems of Africa, with particular reference to those of Egypt. During winter, the Mediterranean Sea is a center of cyclogenesis. These Mediterranean depressions mainly affect northern parts of Egypt. During spring (March to May), the tracks of the Mediterranean depressions shift southward, and during this season, these are referred to as the "desert" or "Khamsin" depressions. The frequency of these varies from two to six per month. Also, these depressions, in spring, are smaller in size than the winter depressions.

During summer, the depressions do not traverse Egypt. In fall (October to November), Khamsin-type depressions move across Egypt. Compared with the spring depres-

TABLE 1.6. Monthly distribution (totals) of cyclones in the Mozambique Channel area during the period 1848–1966. (Griffiths 1972)

Month	No.	Month	No.
January	28	April	6
February	30	May–November	3
March	18	December	15

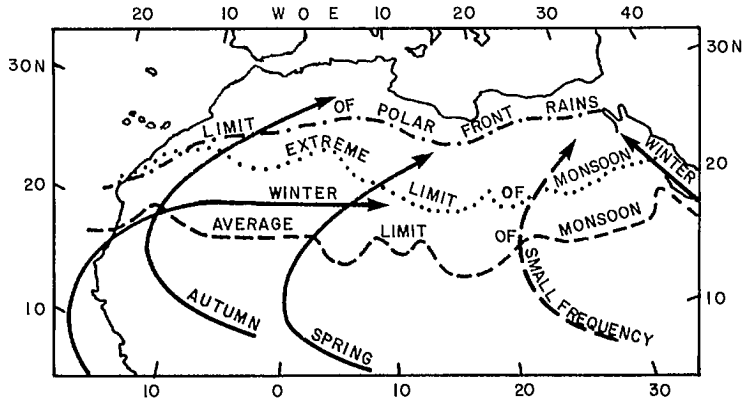

FIG. 1.24. Most frequent trajectories of the Sudan–Sahara disturbances. (Griffiths 1972)

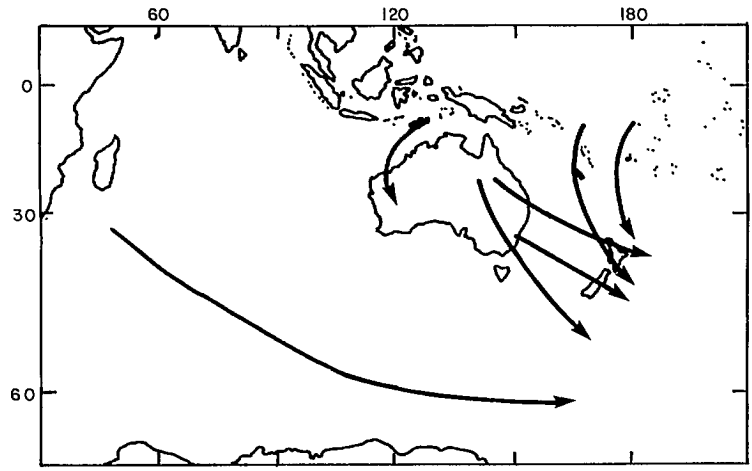

FIG. 1.25. Cyclone tracks across Australia and New Zealand. (Haurwitz and Austin 1944)

sions, these are weaker and move more slowly towards the east. The most frequent trajectories of the so-called Sudan–Sahara disturbances are shown in Fig. 1.24.

Weather Systems of Australia and New Zealand

The weather systems of this region will be discussed first generally (following Haurwitz and Austin 1944), followed by a consideration of certain details of the Australian weather systems (following Gentilli 1971).

There are no high mountain chains in the mainland of Australia, and the only significant indentations to the coastline are the Great Australian Bight and the Gulf of Carpentaria. However, Tasmania is mountainous. New Zealand is also relatively mountainous.

The tracks of cyclones across Australia and New Zealand are shown in Fig. 1.25. Cyclones developing along the polar front off South Africa usually move southeastward to the south of New Zealand. Also, stationary cold fronts over Queensland lead to cyclones that move in a general southeasterly direction, either to the north of New Zealand or across North Island of New Zealand. Cyclones developing over New South Wales travel across South Island of New Zealand. Sometimes, cyclones develop along the south coast of Australia.

Tropical disturbances that develop north of Australia have parabolic trajectories and travel to the northwest coast of Australia. During summer, tropical cyclones developing over the western Pacific recurve and traverse New Zealand in the form of deep, extratropical cyclones. Hurricanes recurving near Australia influence New Zealand, whereas those that recurve farther to the east do not. There is also a secondary family of summer cyclones that develops on the secondary front across southeastern Australia.

Gentilli (1971) stated that, because of its shape, Australia is the only continent that has roughly the same frequency of tropical cyclones on both the east and west coasts. Data for the period 1870–1955 show that, on the average, Northern Territories and Queensland together experience about 3.3 tropical cyclones per year, whereas the west coast average is 2.1. As far as the monthly distribution is concerned, western Australia experiences the highest frequency during December to April.

Generally, in the Australian region, tropical cyclones originate in the belt of 4–20° latitude (north and south). One significant feature of tropical cyclones in the region of Australia is their relatively short tracks. Those originating in the Timor Sea travel in a southwest direction with a speed ranging from 8 to 24 $km \cdot s^{-1}$.

Weather Systems of the Oceanic Regions

Since tropical and extratropical cyclogenesis depends on the positions of the various frontal zones, the positions of these will be briefly summarized. The intertropical front lies in the low pressure belt between the large anticyclones of both hemispheres, whereas the polar fronts are mainly located off the east coasts of the continents, and the Arctic and Antarctic fronts lie in the troughs that extend from the high latitude deep cyclones (Haurwitz and Austin 1944).

The cyclones of the middle and high latitudes generally develop as wave disturbances on the polar front. Since the position of the front varies considerably, the positions of cyclogenesis also vary with the season. In the Northern Hemisphere, most of these cyclones move in a northeasterly direction towards the Aleutian and Icelandic lows, whereas in the Southern Hemisphere, they move southeastward toward the circumpolar

low. The seasonal variation is more pronounced in the Northern Hemisphere. In summer, cyclogenesis usually occurs farther north; the cyclones move slower and they are shallower than the winter cyclones.

Tropical cyclones develop in the intertropical front beyond 5° latitude in the summer hemisphere. Tropical cyclones are a rare phenomenon in the South Atlantic and eastern part of the South Pacific. Their frequency in the North Indian Ocean is quite different from elsewhere. In the Arabian Sea and the Bay of Bengal, they occur mainly in the periods between the southwest and the northeast monsoon seasons. Other water bodies where tropical cyclones occur are the waters surrounding the Philippines, the China Sea, the Solomon Islands, New Hebrides and the Society Islands, the areas off the west coasts of North America and Central America, the Caribbean Sea, the waters surrounding the Malagasy Republic (Madagascar), and the area off the northwest coast of Australia (Haurwitz and Austin 1944). These tropical cyclones move westward in low latitudes and then towards the northeast in the Northern Hemisphere (and towards the southeast in the Southern Hemisphere), in the higher latitudes. Rather irregular trajectories can occur in many areas, especially in the Arabian Sea and the Bay of Bengal.

Chapter 2

The Mathematical Problem and Finite-Difference Solutions for Two-Dimensional Numerical Models

2.1 Formulation of the Storm Surge Equations

In numerical models for storm surges, the equations most frequently used are linearized versions of the Navier–Stokes equations in vertically integrated form. These equations will be derived making use of an approach given by Fofonoff (1962). Although at times a spherical polar coordinate system will be used, in the initial development, only Cartesian coordinates will be used, making use of a right-handed rectangular coordinate system with the origin located at the undisturbed level of the free surface.

The coordinate system is such that the x-axis points towards east, the y-axis points towards north, and the z-axis points upwards. The components of velocity along these three axes will be respectively denoted by u, v, and w. For convenience and brevity, we will also use a tensor summation notation, in which the axes are denoted by x_1, x_2, and x_3 and the velocity components by u_1, u_2, and u_3. In this notation, an index appearing twice in a term implies summation over all three index values.

The equation expressing the conservation of momentum can be written as

$$\rho \frac{\partial u_i}{\partial t} + \rho u_j \frac{\partial u_i}{\partial x_j} + 2\rho \epsilon_{ijk} \Omega_j u_k = -\frac{\partial P}{\partial x_i} - \rho g \delta_{3i} + \frac{\partial \sigma_{ij}}{\partial x_j} \tag{2.1}$$

where ρ is the density of water, t is time, P is the pressure field, Ω_j is the component of the earth's rotation, and σ_{ij} are the components of stress due to molecular viscosity. Also note that $\epsilon_{ijk} = +1$ if i, j, k are in cyclic order, $\epsilon_{ijk} = -1$ if i, j, k are in anticyclic order, and $\epsilon_{ijk} = 0$ if any pair or all three indices have the same value; $\delta_{3i} = 1$ for $i = 3$ and $\delta_{3i} = 0$ for otherwise.

If μ is the molecular viscosity, then the stress tensor, σ_{ij}, can be expressed in terms of the rate of deformation of a fluid element by the motion

$$\sigma_{ij} = \mu \left(\frac{\partial u_i}{\partial x_j} + \frac{\partial u_j}{\partial x_i} \right) \tag{2.2}$$

The conservation of mass can be expressed through the continuity equation

$$\frac{\partial \rho}{\partial t} + \frac{\partial \rho u_j}{\partial x_j} = 0 \tag{2.3}$$

For any other property of the fluid (e.g. temperature, salinity, etc.), the general form of the conservation equation is

$$\frac{\partial}{\partial t}(\rho \phi) + \frac{\partial}{\partial x_j}(\rho \phi u_j) = -\frac{\partial F_j}{\partial x_j} + q \tag{2.4}$$

Here, F_j are the components of flux of the property ϕ due to internal forces or pressures and q is the total internal source of the property ϕ. Note that eq. 2.1 and 2.3 are special forms of eq. 2.4.

Separation of the Equations into Steady and Time-Dependent Forms

The above equations cannot be solved exactly, except in a few simple cases. To make the equations tractable, several simplifying assumptions have to be made. The first is to separate the equations into two sets: one set expressing the mean motion and the other describing the time-dependent motion (i.e. departure from the mean). Because of the nonlinear nature of the above equations, this separation cannot be achieved as two independent equations, and one has to contend with two sets, in each of which terms expressing interactions between mean and time-dependent motions appear.

Multiplying eq. 2.3 by u_i and adding to eq. 2.1 and using eq. 2.2 after ignoring compressibility of the water in the frictional terms gives

$$\frac{\partial}{\partial t}(\rho u_i) + \frac{\partial}{\partial x_j}(\rho u_i u_j) + 2\rho\epsilon_{ijk}\,\Omega_j u_k = -\frac{\partial P}{\partial x_i} - \rho g \delta_{3i} + \mu \frac{\partial^2 u_i}{\partial x_j \partial x_j} \tag{2.5}$$

Basically, eq. 2.4 and 2.5 are similar. To achieve the abovementioned separation, eq. 2.3 and 2.5 are averaged with respect to time. To do this, the averaging process is denoted by a bar:

$$\bar{\phi} = \lim_{T\to\infty}\left(\frac{1}{2T}\int_{-T}^{T}\phi dt\right) \tag{2.6}$$

The averaging process of eq. 2.5 and 2.3 gives

$$\frac{\partial \overline{\rho u_i u_j}}{\partial x_j} + 2\epsilon_{ijk}\,\Omega_j\,\overline{\rho u_k} = -\frac{\partial \bar{P}}{\partial x_i} - \overline{\rho g}\,\delta_{3i} + \mu \frac{\partial^2 \bar{u}_i}{\partial x_j \partial x_j} \tag{2.7}$$

and

$$\frac{\partial \overline{\rho u_j}}{\partial x_j} = 0 \tag{2.8}$$

Noting that the time-dependent motion has zero mean by definition, the time-dependent equations are obtained by subtracting eq. 2.7 from eq. 2.5 and eq. 2.8 from eq. 2.3.

$$\frac{\partial \rho u_i}{\partial t} + \frac{\partial(\rho u_i u_j - \overline{\rho u_i u_j})}{\partial x_j} + 2\epsilon_{ijk}\,\Omega_j(\rho u_k - \overline{\rho u_k}) = \frac{-\partial(P - \bar{P})}{\partial x_i} - (\rho - \bar{\rho})\,g\,\delta_{3_i} + \mu \frac{\partial^2(u_i - \bar{u}_i)}{\partial x_j \partial x_j} \tag{2.9}$$

and

$$\frac{\partial \rho}{\partial t} + \frac{\partial(\rho u_j - \overline{\rho u_j})}{\partial x_j} = 0 \tag{2.10}$$

The next step is to express the velocity, pressure, and density fields as steady and time-dependent components: $u_i = \bar{u}_i + u_i'$. Conventionally, however, U_i is used for $\bar{u}_i$. Thus,

$$\begin{aligned} u_i &= U_i + u_i' \\ P &= \mathcal{P} + P' \\ \rho &= \bar{\rho} + \rho' \end{aligned} \tag{2.11}$$

where $\overline{u_i'}$, $\bar{P}'$, and $\bar{\rho}'$ are zero. The term $\overline{\rho u_i u_j}$ in eq. 2.9 becomes

$$\overline{\rho u_i u_j} = \bar{\rho} U_i U_j + \overline{\rho u_i' u_j'} + \overline{\rho' u_j'} U_i + \overline{\rho_i u_i'} U_j + \overline{\rho' u_i' u \rho_j'}$$

In water bodies, generally speaking, variations in the density field are very small in proportion to the mean density, whereas the fluctuations in the velocity field can be of the same order as the mean velocity. Thus, the terms containing correlations between fluctuations of density and velocity are small compared with the terms containing correlations between velocity components. Thus, we will ignore the density fluctuations in the acceleration terms. However, the correlation between density and velocity fluctuations can be significant in the other equations where velocity correlations do not appear. Especially in the continuity equation, the correlations between density and velocity fluctuations may be important.

Reynolds stress tensor is defined as

$$R_{ij} \equiv -\bar{\rho}\,\overline{u_i' u_j'} \tag{2.12}$$

R_{ij}' is defined as

$$R_{ij}' \equiv -\bar{\rho}(u_i' u_j' - \overline{u_i' u_j'}) \tag{2.13}$$

Then, eq. 2.7 and 2.8 can be written as

$$\bar{\rho} U_j \frac{\partial U_i}{\partial x_j} - \frac{\partial R_{ij}}{\partial x_j} + 2\epsilon_{ijk}\Omega_j \bar{\rho} U_k = -\frac{\partial P}{\partial x_i} - \bar{\rho} g \delta_{3i} + \mu \frac{\partial^2 U_i}{\partial x_j \partial x_j} \tag{2.14}$$

and

$$\frac{\partial \bar{\rho} U_j}{\partial x_j} = 0 \tag{2.15}$$

These are the equations for the mean flow. The equations for the time-dependent motion are

$$\bar{\rho} \frac{\partial u_i'}{\partial t} + \bar{\rho} U_j \frac{\partial u_i'}{\partial x_j} + \bar{\rho} u_j' \frac{\partial U_i}{\partial x_j} - \frac{\partial R_{ij}'}{\partial x_j} + 2\epsilon_{ijk}\Omega_j \bar{\rho} u_k' = \frac{-\partial P'}{\partial x_i} - \rho' g \delta_{3i} + \mu \frac{\partial^2 u_i'}{\partial x_j \partial x_j} \tag{2.16}$$

and

$$\frac{\partial \rho'}{\partial t} + \frac{\partial \rho u_j'}{\partial x_j} = 0 \tag{2.17}$$

One can see from eq. 2.14 that the influence of the time-dependent flow upon the mean motion is expressed completely by Reynolds stress tensor, R_{ij}. However, in the time-dependent equations, the interactions are contained in many terms and are of three different types: (a) convection of fluctuating momentum by the steady flow, (b) convection of the steady-state momentum by the fluctuating flow, and (c) divergence of momentum-flux variations of the purely time-dependent flow.

The time-dependent equations 2.16 and 2.17 permit motions with all frequencies. In principle, one can carry out a second averaging process making use of an averaging time that is small compared with the period of the motion under consideration. Thus, one can separate the slow motion from the high-frequency turbulence. If this averaging is carried out on eq. 2.16 and 2.17, all the terms except R_{ij} can be simply replaced by their averages,

because they are linear. The finite average of R_{ij} (i.e. average with reference to a finite time step) is the difference between the finite and the steady-state average of $\bar{\rho} u_i' u_j'$. Contributions to both of these from the perturbations with periods shorter than the finite averaging time step will be roughly the same, and when the difference is taken, they will cancel each other.

If the Reynolds stresses in the steady-state equations 2.14 are interpreted as a dissipating mechanism, then one has to consider the divergence of the finite average of R_{ij} as a source of momentum, and longer period motions principally contribute to this source. This means that the time-dependent motion of a prescribed time scale can receive momentum mainly from longer time scales and lose momentum to shorter time scales.

Turbulence plays an important role in the dissipative process in water bodies. However, it cannot be easily incorporated into the momentum equations. Usually, the dissipative action due to turbulence is taken into account by asusming that the Reynolds stresses are proportional to the strain rate of the mean flow. In analogy to molecular viscosity, this proportionality constant is referred to as eddy viscosity. Considering the fact that the horizontal dimensions of a water body are usually much larger than its vertical dimensions, eddy viscosities of widely differing values might be necessary for the horizontal and vertical directions. Sometimes, in the horizontal plane, different eddy viscosity values might have to be used in the x and y direction (e.g. narrow water bodies). Equation 2.12 can be written as

$$(2.18) \qquad R_{ij} = -\overline{\bar{\rho} u_i' u_j'} = \mu(j) \frac{\partial U_i}{\partial x_j} + \mu(i) \frac{\partial U_j}{\partial x_i}$$

Here, $\mu(i) = \mu_H$ for $i,j \neq 3$ and $\mu(j) = \mu_V$ for $i,j = 3$.

The parameters μ_H and μ_V are referred to as horizontal and vertical eddy viscosities, respectively.

Nondimensionalization

To nondimensionalize the time-dependent equations 2.16 and 2.17, the following parameters are introduced: a horizontal scale L, a characteristic depth H for the vertical scale, and similar scale parameters U_0 for the mean velocity in the horizontal direction, u_0 for the perturbation current in the horizontal direction, W_0 for the mean current in the vertical direction, and w_0 for the fluctuating current in the vertical direction. Because of the continuity equations 2.15 and 2.17, one can write

$$(2.19) \qquad W_0 \sim \frac{U_0 H}{L} \text{ and } w_0 \sim \frac{u_0 H}{L}$$

Let s denote a characteristic value of the surface slope of the water body. Then, a typical value of the pressure gradient is $\rho_0 g s$. The balance between the pressure gradient and Coriolis forces can be expressed by choosing U_0 so that

$$(2.20) \qquad f_0 U_0 = gs$$

where f_0 is a typical value of the Coriolis parameter and is equal to $2\Omega_3$. Also, the following nondimensional parameters are defined:

$$\text{Rossby number} = R_o = \frac{U_0}{f_0 L}$$

(2.21) $$\text{Reynolds number} = R_e = \frac{\rho_0 U_0 L}{\mu}$$

$$\text{Froude number} = F_r = \frac{U_0^2}{gH}$$

Note that

(2.22) $$\frac{1}{\rho'} = \alpha' = \frac{\rho_0}{\bar{\rho}} \sim 1$$

where α' is the specific volume.

Further,

(2.23) $$r'_{ij} \equiv \frac{R_{ij}}{\rho_0 u_0^2}$$

where a prime denotes a dimensionless variable. Finally, a characteristic time scale, T_0, and a characteristic density difference, $\Delta\rho_0$, will be introduced and internal Froude number, F'_r, defined:

(2.24) $$F'_r \equiv \frac{U_0^2 \rho_0}{\Delta\rho_0 g H}$$

With the understanding that the time-dependent variables are denoted by a double prime, the two horizontal equations of motion (expressed in tensor notation), the vertical equation of motion, and the continuity equation take the following forms:

(2.25) $$\frac{1}{f_0 T_0}\frac{\partial u''_i}{\partial t'} + R_o\left[U'_j\frac{\partial u''_i}{\partial x'_j} + u''_j\frac{\partial U'_i}{\partial x_j} - \left(\frac{u_0}{U_0}\right)\frac{\partial r''}{\partial x'_j}\right] + \epsilon_{ijk}\,\Omega'_j\,u''_k = -\alpha'\frac{\partial P''}{\partial x'_i} + \frac{R_o}{R_e}\left[\nabla^2 u''_i + \left(\frac{L}{H}\right)^2\frac{\partial^2 u''_i}{\partial x'^2_3}\right],\quad i = 1, 2$$

(2.26) $$F'_r\left(\frac{u_0}{U_0}\right)\left(\frac{H}{L}\right)^2\left[\frac{1}{(U_0/L)T}\frac{\partial u''_3}{\partial t'} + U'_j\frac{\partial u''_3}{\partial x'_j} + u''_j\frac{\partial U'_3}{\partial x'_j} - \left(\frac{u_0}{U_0}\right)\frac{\partial r''_{3j}}{\partial x'_j}\right] + \frac{\rho_0 u_0 f_0}{\Delta\rho_0 g} \times \epsilon_{ijk}\Omega'_j u''_k = -\frac{\partial P''}{\partial x'_3} - \rho'' + \frac{F'_r}{R_e}\left(\frac{u_0}{U_0}\right)\left(\frac{H}{L}\right)^2\left[\nabla^2 u''_3 + \left(\frac{L}{H}\right)^2\frac{\partial^2 u''_3}{\partial x'^2_3}\right]$$

(2.27) $$\frac{\Delta\rho_0}{\rho_0}\frac{1}{(U_0/L)T_0}\frac{\partial\rho''}{\partial t'} + \frac{\partial\rho' u''_j}{\partial x'_j} = 0$$

where

$$\nabla^2 \equiv \frac{\partial^2}{\partial x_1^2} + \frac{\partial^2}{\partial x_2^2}$$

Next, the significance of the three nondimensional parameters, namely, the Rossby number, the Reynolds number, and the Froude number (defined by eq. 2.21 and 2.22), will be considered. The Rossby number is the ratio of the nonlinear acceleration terms to the Coriolis terms. In most storm surge studies, the Rossby number is assumed to be small

compared with unity, and thus the nonlinear acceleration terms are ignored; however, it will be shown in later sections that, in some special cases, these terms are important and have to be retained.

The importance of these nondimensional parameters for the steady state will be briefly discussed before discussing their relevance for the time-dependent flow (for the nondimensional forms of the steady-state equations, see Fofonoff 1962, p. 330, eq. 17–19). If the magnitude of the perturbation in the velocity field is greater than the mean flow (i.e. $u_0/U_0 > 1$), then the Reynolds stresses become important. The other instance in which they are important is when their variation is great over distances small compared with the characteristic length of the steady-state flow (i.e. when $\partial r'_{ij}/\partial x_j > 1$).

The other parameters, namely, the Reynolds number, R_e, and the Froude number, F_r, will have values or order unity for very small horizontal and vertical scales of motion. Thus, in the steady state, molecular viscosity and vertical accelerations can be justifiably neglected. Hence, the balance of forces in the vertical direction can be represented fairly accurately by the hydrostatic equation, which in nondimensional form is

$$\alpha' \frac{\partial P'}{\partial x'_3} + 1 = 0 \tag{2.28}$$

In the equations of motion, it is convenient to use eddy viscosity coefficients instead of Reynolds stresses. The magnitudes of the eddy viscosity coefficients can be related to the Reynolds stresses through the following (nondimensional) equation:

$$\left(\frac{u_0}{U_0}\right)^2 \frac{\partial r'_{ij}}{\partial x'_j} = \frac{1}{R'_e}\left[\nabla^2 U'_i + \frac{\mu_V}{\mu_H}\frac{L^2}{H^2}\frac{\partial^2 U'_i}{\partial x'^2_3}\right] \tag{2.29}$$

where

$$R'_e \equiv \frac{\rho_0 U_0 L}{\mu_H} \tag{2.30}$$

In analogy to molecular viscosity, R_e can be treated as the Reynolds number for eddy viscosity. If the frictional forces are comparable with the acceleration terms, then R_e must be of order unity, i.e.

$$\mu_H \sim \rho_0 U_0 L \sim \rho_0 \left(\frac{U_0}{L}\right) L^2$$

Since L is a characteristic horizontal scale of the flow, U_0/L represents the strain rate of the mean flow. Similarly, friction due to vertical shear is important if

$$\mu_V \sim \mu_H \left(\frac{H}{L}\right)^2 \sim \rho_0 \left(\frac{U_0}{L}\right) H^2$$

The eddy viscosity terms are more important than the acceleration terms if R_e is less than the Rossby number, R_o. This happens when $\mu_H > \rho_0 f_0 L^2$.

Next, the time-dependent eq. 2.25–2.27 will be considered. In eq. 2.25, the local acceleration term (time-derivative term) is of order unity provided that the time scale of the perturbation is of the order of half-pendulum day or less.[2]

When $f_0 T_0 \ll 1$, the Coriolis terms are insignificant compared with the acceleration terms, and balance is achieved between pressure gradient forces and acceleration terms.

[2]Half-pendulum day is equal to $2\pi/f_0$. At the equator, it is ∞ and at the poles is equal to π/Ω, where Ω is the angular velocity of the earth's rotation.

Hence, short-period fluctuations (i.e. $T_0 < 2\pi/f_0$) are referred to as inertiogravitational oscillations. For long periods (i.e. $T_0 > 2\pi/f_0$), the balance is mainly between the pressure gradient terms and the Coriolis terms. As in the case of steady-state motion, in time-dependent motion molecular friction can be neglected. The variations in the pressure field are mostly due to variations of density and slope of the water surface, and the hydrostatic equations satisfactorily represent this (the cases in which the hydrostatic equations may not be satisfactory will be considered later).

Traditional Linear Storm Surge Equations and Boundary Conditions

We will develop the linear storm surge equations most commonly used, following Welander (1961). It is convenient to switch from the tensor notation, used above, to a scalar notation. Assume that the water is homogenous and incompressible, and that friction due to vertical shear is much more important than horizontal friction. At this stage, the hydrostatic approximation has not been made, nor any assumption concerning Rossby number. Then, the equations of motion in a right-handed Cartesian coordinate system can be written as

$$\frac{\partial u}{\partial t} + u\frac{\partial u}{\partial x} + v\frac{\partial u}{\partial y} + w\frac{\partial u}{\partial z} - fv = -\frac{1}{\rho_0}\frac{\partial P}{\partial x} + \frac{1}{\rho_0}\frac{\partial \tau_x}{\partial z} \tag{2.31}$$

$$\frac{\partial v}{\partial t} + u\frac{\partial v}{\partial x} + v\frac{\partial v}{\partial y} + w\frac{\partial v}{\partial z} + fu = -\frac{1}{\rho_0}\frac{\partial P}{\partial y} + \frac{1}{\rho_0}\frac{\partial \tau_y}{\partial z} \tag{2.32}$$

$$\frac{\partial w}{\partial t} + u\frac{\partial w}{\partial x} + v\frac{\partial w}{\partial y} + w\frac{\partial w}{\partial z} = -\frac{1}{\rho_0}\frac{\partial P}{\partial z} - g \tag{2.33}$$

The continuity equation is

$$\frac{\partial u}{\partial x} + \frac{\partial v}{\partial y} + \frac{\partial w}{\partial z} = 0 \tag{2.34}$$

where u, v, and w are the velocity fields in the x, y, and z directions, f is the Coriolis parameter, g is gravity, ρ_0 is the uniform density of water, P is the pressure, and τ_x and τ_y are the x and y components of the frictional stress.

With reference to the origin of the coordinate system located at the undisturbed level of the free surface ($z = 0$), the free surface can be denoted by $z = h(x, y, t)$ and the bottom by $z = -D(x, y)$. Let τ_{S_x} and τ_{S_y} denote the tangential wind stress components and let P_a be the atmospheric pressure on the water surface. Then, the following boundary conditions must be satisfied. At the free surface $z = h$:

$$\tau_x = \tau_{S_x},\ \tau_y = \tau_{S_y} \tag{2.35}$$

and

$$p = P_a \tag{2.36}$$

Since the free surface has to follow the fluid, we have an additional condition given by

$$\frac{\partial h}{\partial t} + u\frac{\partial h}{\partial x} + v\frac{\partial h}{\partial y} = w \text{ at } z = h \tag{2.37}$$

At the bottom, all the velocity components have to vanish. Thus,

$$u = v = w = 0 \text{ at } z = -D \tag{2.38}$$

The traditional storm surge equations are derived by performing the two operations of vertical integration and linearization. To perform the vertical integration, we define the x and y components of the horizontal transport as follows:

$$(2.39) \quad M \equiv \int_{z=-D}^{h} u dz \text{ and } N \equiv \int_{z=-D}^{h} v dz$$

Integrating the horizontal equations of motion 2.31 and 2.32 and the continuity equation 2.34 with respect to z from $z = -D$ to h and using the boundary conditions defined by eq. 2.35–2.38 gives

$$(2.40) \quad \frac{\partial M}{\partial t} + \frac{\partial}{\partial x}\widetilde{u^2} + \frac{\partial}{\partial y}\widetilde{uv} - fN = -\frac{1}{\rho_0}\int_{z=-D}^{h} \frac{\partial P}{\partial x} dz + \frac{1}{\rho_0}(\tau_{S_x} - \tau_{B_x})$$

$$(2.41) \quad \frac{\partial N}{\partial t} + \frac{\partial}{\partial x}\widetilde{uv} + \frac{\partial}{\partial y}\widetilde{v^2} + fM = -\frac{1}{\rho_0}\int_{z=-D}^{h} \frac{\partial P}{\partial y} dz + \frac{1}{\rho_0}(\tau_{S_y} - \tau_{B_y})$$

$$(2.42) \quad \frac{\partial h}{\partial t} + \frac{\partial M}{\partial x} + \frac{\partial N}{\partial y} = 0$$

where τ_{B_x} and τ_{B_y} are the x and y components of the bottom stress τ_B. In eq. 2.40 and 2.41, the following notation was used:

$$(2.43) \quad \frac{\partial}{\partial x}\widetilde{u^2} = \frac{\partial}{\partial x}\int_{-D}^{h} \widetilde{u^2} dz$$

$$\frac{\partial}{\partial y}\widetilde{uv} = \frac{\partial}{\partial y}\int_{-D}^{h} uv dz$$

Next, the hydrostatic approximation will be made ignoring the nonlinear acceleration terms. To justify this, two assumptions are made: (a) the amplitude of the surge is small compared with the water depth and (b) and horizontal scale of the surge is large compared with the water depth. Following Charnock and Crease (1957), the following scale analysis can be performed to ascertain the relative importance of the various terms. Let L and H represent the characteristic horizontal scale and depth, respectively. The vertical velocity varies from zero at the bottom to about Z/T at the surface where Z is a characteristic amplitude of the surge and T is a characteristic period. The horizontal velocity is of the order of $L/H \cdot Z/T$.

From eq. 2.31 and 2.33, the pressure field is eliminated to obtain the following equation:

$$(2.44) \quad \frac{\partial^2 u}{\partial t \partial z} + \frac{\partial^2}{\partial x \partial z} u^2 + \frac{\partial^2}{\partial y \partial z} uv + \frac{\partial^2}{\partial z^2} uw - f\frac{\partial v}{\partial z}$$

$$1 \qquad \frac{Z}{H} \qquad \frac{Z}{H} \qquad \frac{Z}{H} \qquad fT$$

$$= \frac{\partial^2 w}{\partial t \partial z} + \frac{\partial^2}{\partial x^2} uw + \frac{\partial^2}{\partial x \partial y} vw + \frac{\partial^2}{\partial x \partial z} w^2$$

$$\left(\frac{H}{L}\right)^2 \quad \frac{Z}{H}\left(\frac{H}{L}\right)^2 \quad \frac{Z}{H}\left(\frac{H}{L}\right)^2 \quad \frac{Z}{H}\left(\frac{H}{L}\right)^2$$

In eq. 2.44, the order of magnitude of each term relative to the first term is indicated under the term. If $(H/L)^2$ is small, all the terms on the right side of eq. 2.44 can be neglected. This means that the amplitude of the surge is, at most, equal to the water depth. Ignoring these terms amounts to the hydrostatic approximation. If Z/H is small, one can ignore the three nonlinear terms on the left side of eq. 2.44.

The pressure terms can be evaluated as follows:

$$\frac{\partial P}{\partial x} = g\rho_0 \frac{\partial h}{\partial x} + \frac{\partial P_a}{\partial x} \tag{2.45}$$

On vertical integration

$$\int_{-D}^{h} \frac{\partial P}{\partial x}\, dz \sim g\rho_0 D \frac{\partial h}{\partial x} + D \frac{\partial P_a}{\partial x} \tag{2.46}$$

Note that, here, h relative to D is ignored, which is consistent with the above approximations. Under the above simplifications, eq. 2.40 and 2.42 finally reduce to the so-called linear storm surge prediction equations:

$$\frac{\partial M}{\partial t} - fN = -gD \frac{\partial h}{\partial x} - \frac{D}{\rho_0} \frac{\partial P_a}{\partial x} + \frac{1}{\rho_0} (\tau_{S_x} - \tau_{B_x}) \tag{2.47}$$

$$\frac{\partial N}{\partial t} + fM = -gD \frac{\partial h}{\partial y} - \frac{D}{\rho_0} \frac{\partial P_a}{\partial y} + \frac{1}{\rho_0} (\tau_{S_y} - \tau_{B_y}) \tag{2.48}$$

$$\frac{\partial h}{\partial t} + \frac{\partial M}{\partial x} + \frac{\partial N}{\partial y} = 0 \tag{2.49}$$

For convenience, hereafter, the subscript on the density field will be omitted.

In these linear storm surge prediction equations, the dependent variables are the transport components M and N and the water level h. The forcing functions are the atmospheric pressure gradients given by $\partial P_a/\partial x$ and $\partial P_a/\partial y$ and the wind stress components τ_{S_x} and τ_{S_y}. The retarding force is the bottom stress. At this stage, there are more unknowns than the available equations. To get a closed system of equations, the bottom stress must be expressed in terms of the known parameters, such as the volume transports.

Bottom Stress

Here, parameterization of the bottom stress, based on Simons (1973), will be discussed; in Chapter 6, the bottom stress problem in conjunction with the surface stress problem will be discussed. Let $\boldsymbol{V}_B$ denote the velocity vector near the bottom. Then, the bottom stress τ_B can be expressed as

$$\tau_B = \rho k |\boldsymbol{V}_B| \boldsymbol{V}_B \tag{2.50}$$

where k is a nondimensional coefficient referred to as skin friction; the value of k is about 2.5×10^{-3}. If one assumes a uniform velocity distribution in the vertical, and noting that the horizontal transport vector $\boldsymbol{M}$ is given by

$$\boldsymbol{M} \equiv (M, N) = \int_{-D}^{h} \boldsymbol{V}_B\, dz = \int_{-D}^{h} (u, v)\, dz \tag{2.51}$$

one obtains

$$\frac{\tau_B}{\rho} = BM \text{ where } B \equiv \frac{k|M|}{(D+h)^2} \tag{2.52}$$

In most storm surge studies, either for obtaining analytical solutions or for economizing on computer time in numerical models, the bottom stress relation 2.50 is linearized by assuming typical values either for the average velocities or the transport components. For a model of Lake Ontario, Simons (1973) assumed average velocities of the order of 10 $cm \cdot s^{-1}$ in the shallow waters and about 1 $cm \cdot s^{-1}$ in the deep waters of the lake. Thus, B varies from $0.0025/D$ to $0.025/D$ in C.G.S. units. Rao and Murty (1970) used a value of $0.01/D$ for B in their model for Lake Ontario.

Instead of the average velocity field, one can examine the mass transport, which varies more smoothly. For Lake Ontario, Simons (1973) gave a value of 2×10^4 to 4×10^4 $cm^2 \cdot s^{-1}$ in shallow as well as deep water, and this leads to $B = 50/D^2$ to $100/D^2$ in C.G.S. units. Another approach to prescribing the bottom stress is to specify the vertical turbulent diffusion of momentum by a constant eddy viscosity ν. Platzman (1963) deduced a bottom friction coefficient as a function of the Ekman number, $D\sqrt{f/2\nu}$, in such a way that $B \to 0$ for great depths and $B = 2.5\nu/D^2$ for shallow water. For Lake Erie, Platzman took $\nu = 40$ $cm^2 \cdot s^{-1}$, which gives $B = 100/D^2$ in C.G.S. units.

Thus, the alternatives for the bottom friction can be summarized:

$$\begin{aligned}
&\text{linear form } B = \frac{a}{D} && a \sim 0.01 \text{ cm} \cdot \text{s}^{-1} \\
&\text{quasilinear form } B = \frac{b}{D^2} && b \sim 100 \text{ cm}^2 \cdot \text{s}^{-1} \\
&\text{nonlinear form } B = \frac{k|V|}{D^2} && k \sim 0.0025
\end{aligned} \tag{2.53}$$

In most early storm surge studies, the linear form has been used. Fischer (1959) used the quasilinear form, whereas Hansen (1956) and Ueno (1964) used the nonlinear forms.

Simons (1973) suggested that the procedure of using the Ekman solution implies a reduction of the pressure gradient force by a factor 5/6 and an increase in the wind stress by a factor of 1.25 for the shallow part of the water body. In addition, a slight rotation of the pressure gradient force and bottom stress are involved. Jelesnianski (1970) developed an integral operator for the bottom stress which incorporates the time history of the forcing in the form of a convolution integral, which implies a time lag between wind stress or slope of the free surface and bottom stress.

Welander (1957) showed that the local velocity profile and hence the bottom stress can be expressed as certain integrals over the time history of the local surface slope and local forcing functions, and from these one can derive a single integrodifferential equation for the free surface elevation. Since this equation is difficult to solve, one has to resort to other approaches.

Welander (1961) distinguished among the following three types of surges: (1) the transient surge, (2) the quasisteady surge with vertical circulation, and (3) the quasisteady surge with horizontal circulation. Note that the bottom stress is defined as the force acting from the water on the bottom. For type 1 surge, there is a partially developed frictional layer at the bottom, and the bottom stress is in the same direction as the flow and its magnitude is inversely proportional to the period of the surge (Lamb 1953).

Type 2 surge corresponds to a one-dimensional surge in a channel. Since the water

circulates in a vertical cell and the bottom stress is in a direction opposite to the surface flow (i.e. opposite to the wind stress, generally speaking), it can be seen from Ekman's (1905, 1923) theory that the magnitude of the bottom stress is half that of the wind stress for a constant value of the friction coefficient. Type 3 surge occurs in steady state, and the flow direction is essentially the same at all depths at a given horizontal position, and the water circulates horizontally. For small depths, the bottom stress is in the direction of the flow. For depths comparable with or greater than the Ekman depth, D_E, defined by

$$D_E \equiv \pi \sqrt{\frac{2\nu}{f}} \tag{2.54}$$

where ν is the vertical eddy viscosity and f is the Coriolis parameter, the influence of the earth's rotation is important and there is a component of the stress perpendicular to the direction of the transport and directed to its left in the Northern Hemisphere. Note that the Ekman depth, D_E, is of the order of 100 m (in the oceans) at higher latitudes and increases towards the equator because of the decrease of the Coriolis parameter, f.

The bottom stress for these three types of surges can be expressed sufficiently accurately by a linear bottom stress law of the type

$$\frac{1}{\rho}(\tau_{B_x}, \tau_{B_y}) = R(M, N) \tag{2.55}$$

where R is a prescribed friction coefficient, which generally depends on the water depth. Harris (1967) critically examined the bottom stress problem as a part of a general evaluation of the importance of several terms in the storm surge equations (e.g. wave setup). His analysis, as well as other considerations of bottom stress, will be discussed later. Kabbaj and LeProvost (1980) used a perturbation approach to include quadratic bottom friction.

Forcing Terms and Lateral Boundary Conditions

In eq. 2.47 and 2.48, the forcing terms are the gradients of the atmospheric pressure, $\partial P_a/\partial x$ and $\partial P_a/\partial y$, and the components of the wind stress, τ_{S_x} and τ_{S_y}. In Chapter 6, the meteorological problems will be considered in detail; here, the forcing terms will be discussed briefly. In principle, the atmospheric pressure gradients can be prescribed either from observations or from the prognosis of numerical weather prediction models. However, the wind stress is not routinely measured and must be deduced from wind observations or predicted winds. The wind stress is usually expressed as

$$\tau_S = \rho_a k |V_a| V_a \tag{2.56}$$

where ρ_a is the density of air (1.2×10^{-3} gm $\cdot$ cm^{-3}) and V_a is the wind velocity at the anemometer level. The parameter k is the drag coefficient (nondimensional) and is usually given a value of about 3×10^{-3} (Platzman 1958a; Ueno 1964). However, Simons (1973) suggested that for the Great Lakes, a more appropriate value for k is about 1.2×10^{-3}.

Next follows a brief consideration of the lateral boundary conditions to be specified so that the system of equations described by eq. 2.47 and 2.49 is complete (details of the lateral boundary conditions will be discussed later). The main lateral boundary condition is that the transport normal to the coastline is zero, i.e.

$$M \cos \phi + N \sin \phi = 0 \tag{2.57}$$

where ϕ is the angle between the x-axis and the normal to the coastline. If it is assumed that the depth of the water is zero at the shoreline, then the tangential component of the volume transport vector must also be zero. The boundary condition in the open part of the water body is more difficult to prescribe. Since the contribution to the storm surges comes mainly from the shallow water region, a generally followed procedure is to locate the outer boundary in the deep water and assume that the water level perturbation there is zero. However, this may not be satisfactory in certain situations, as will be shown later.

Storm Surge Equations in Spherical Polar Coordinates

When storm surge calculations are made for large expanses on the globe, it is more appropriate to use spherical polar coordinates than the traditional Cartesian coordinates. Proudman (1954c) wrote the following linear equations for tides and storm surges in a spherical polar coordinate system.

$$\frac{\partial M}{\partial t} = fN - \frac{gD\,\partial h}{a\cos\phi\,\partial\chi} - \frac{D}{\rho_0 a\cos\phi}\frac{\partial P_a}{\partial\chi} + \frac{1}{\rho_0}(\tau_{S_\chi} - \tau_{B_\chi}) \tag{2.58}$$

$$\frac{\partial N}{\partial t} = -fM - \frac{gD}{a}\frac{\partial h}{\partial\phi} - \frac{D}{\rho_0 a}\frac{\partial P_a}{\partial\phi} + \frac{1}{\rho_0}(\tau_{S_\phi} - \tau_{B_\phi}) \tag{2.59}$$

$$\frac{\partial h}{\partial t} + \frac{1}{a\cos\phi}\left[\frac{\partial M}{\partial\chi} + \frac{\partial}{\partial\phi}(N\cos\phi)\right] = 0 \tag{2.60}$$

Here, a is the radius of the earth, χ is the east longitude, and ϕ is the latitude.

Map Scale Factor

In numerical models of storm surges, ordinarily a Cartesian grid is used on a Mercator projection. Let the origin of a coordinate system be at latitude ϕ_0 with the x-axis pointing northward and the y-axis pointing westward. Let ϕ and χ represent the north latitude and the west longitude, respectively. Let M and N be the transport components towards north and west, and let a be the radius of the earth, Ω the angular velocity of earth's rotation, D the water depth, ρ the water density, P_a the atmospheric pressure, h the deviation of the water level from its equilibrium position, τ_{S_χ} and τ_{S_ϕ} the wind stress components, and τ_{B_χ} and τ_{B_ϕ} the bottom stress components. We have the following relationships:

$$x = a\cos\phi_0 \ln\tan\left(\frac{\pi}{4} + \frac{\phi}{2}\right)\Big/S$$

$$y = a\cos\phi_0\,\chi/S$$

where S is the map scale at latitude ϕ_0. The traditional storm surge equations can be written as

$$\frac{\partial M}{\partial t} = 2\,\Omega\sin\phi\cdot N - \frac{g(D+h)}{a}\frac{\partial h}{\partial\phi} - \frac{(D+h)}{\rho a}\frac{\partial P_a}{\partial\phi} + \frac{1}{\rho}(\tau_{S_\phi} - \tau_{B_\phi})$$

$$\frac{\partial N}{\partial t} = -2\,\Omega\sin\phi\cdot M - \frac{g(D+h)}{a\cos\phi}\frac{\partial h}{\partial\chi} - \frac{(D+h)}{\rho a\cos\phi}\frac{\partial P_a}{\partial\chi} + \frac{1}{\rho}(\tau_{S_\chi} - \tau_{B_\chi})$$

$$\frac{\partial h}{\partial t} = -\frac{1}{a\cos\phi}\left[\frac{\partial}{\partial\phi}(M\cos\phi) + \frac{\partial N}{\partial\chi}\right]$$

One can account for S in the evaluation of Δx and Δy. When $S = 1$, these equations assume the following forms in the x and y coordinates.

$$\frac{\partial M}{\partial t} = 2\,\Omega \sin\phi \cdot N - \frac{g(D+h)}{\cos\phi}\cos\phi_0 \frac{\partial h}{\partial x} - \frac{(D+h)}{\rho}\frac{\cos\phi_0}{\cos\phi}\frac{\partial P_a}{\partial x} + \frac{1}{\rho}(\tau_{S_x} - \tau_{B_x})$$

$$\frac{\partial N}{\partial t} = -2\,\Omega \sin\phi \cdot M - g(D+h)\frac{\cos\phi_0}{\cos\phi}\frac{\partial h}{\partial y} - \frac{(D+h)}{\rho}\frac{\cos\phi_0}{\cos\phi}\frac{\partial P_a}{\partial y} + \frac{1}{\rho}(\tau_{S_y} - \tau_{B_y})$$

$$\frac{\partial h}{\partial t} = -\frac{\cos\phi_0}{\cos\phi}\left[\frac{\partial M}{\partial x} + \frac{\partial N}{\partial y}\right] + \frac{M\tan\phi}{a}$$

The factor $\cos\phi_0/\cos\phi$ associated with each spatial gradient term corrects for the latitudinal scale change. Without this correction, gradients will be underestimated at points north of ϕ_0 and overestimated at locations south of ϕ_0. The term $M \tan\phi/a$ is a correction term to the horizontal divergence due to the convergence of the meridians on the globe.

If the Cartesian grid is inclined to the meridians at an angle ϕ, the above equations remain unchanged, except that $M \tan\phi/a$ must be replaced by $M_n \tan\phi/a$, where M_n is the northward component of the velocity (i.e. $M \cos\phi - N \sin\phi$).

Shuman and Stackpole (1968) discussed appropriate finite-difference forms including a map scale factor and showed that the computational stability of the calculations is very much dependent on the manner in which the map scale factor is introduced and the form in which the dynamic terms of the equations are written.

Taylor (1975) discussed various map projections that are suitable for oceanographic applications and also listed a computer program to print any coastline on the globe on several different projections on any desired scale.

2.2 Two-Dimensional Models

In this section, numerical finite-difference solutions for two-dimensional models for storm surges and tides will be discussed. Since two-dimensional models are the ones most commonly used, these models will be studied before proceeding to three-dimensional and one-dimensional models. Since the storm surge problem involves propagation of long gravity waves, this section will begin with a general discussion of propagation problems, followed by consideration of numerical models for solving the partial differential equations of the type encountered in storm surge models. In the following discussion, arguments developed by Crandall (1956) will be made use of.

Propagation problems in continuous systems arise not only in fluid dynamics but also in other fields of science. For example, Crandall (1956) discussed the following problems, all of which fall into the category of propagation problems: (a) cooling of a rod, (b) boundary-layer wake, (c) unsteady transverse motion of a beam, (d) transverse motion of a taut string, and (e) expansion of a gas behind a piston. The five problems were posed such that there are two independent variables, and the solution domains have the open

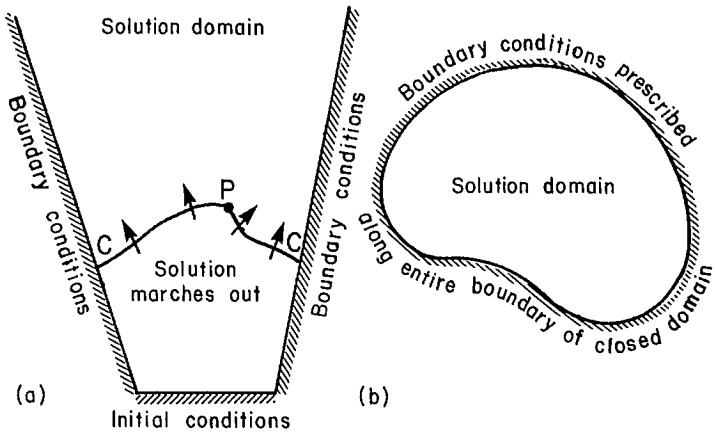

FIG. 2.1. (a) Propagation problem is solved in an open domain; (b) equilibrium problem is solved in a closed domain. (Crandall 1956)

shape shown in Fig. 2.1a in contrast with the closed domain shown in Fig. 2.1b, this latter domain being characteristic of equilibrium problems.

Initial conditions must be specified throughout the domain, and boundary conditions must be specified at the open boundary at all times. (Generally speaking, boundary conditions must also be specified at the closed boundary at all times.) It will be shown below that the governing equations for propagation problems are either hyperbolic or parabolic whereas for the equilibrium problems, they are elliptic. Crandall (1956, p. 352) formulated the general propagation problem in the following manner:

> The problem is to march out the solution of a governing system of partial differential equations of hyperbolic or parabolic type from prescribed conditions on an open boundary.

The following is a pair of simultaneous first-order differential equations:

$$A_1 \frac{\partial u}{\partial x} + B_1 \frac{\partial u}{\partial y} + C_1 \frac{\partial v}{\partial x} + D_1 \frac{\partial v}{\partial y} = 0 \tag{2.61}$$

$$A_2 \frac{\partial u}{\partial x} + B_2 \frac{\partial u}{\partial y} + C_2 \frac{\partial v}{\partial x} + D_2 \frac{\partial v}{\partial y} = 0 \tag{2.62}$$

Here, u and v are the dependent variables, x and y are the independent variables, and the coefficients A_1, A_2, B_1, B_2, C_1, C_2, D_1, and D_2 are functions of u and v but not of x and y. Usually, the system of eq. 2.61 and 2.62 is nonlinear, but since the coefficients are not functions of x and y, one can make it linear by treating u and v as the independent variables and x and y as the dependent variables. Hence, the system of eq. 2.61 and 2.62 is referred to as a "reducible system."

Assume that the system of eq. 2.61 and 2.62 is being solved in the domain shown in Fig. 2.1a and that the solution up to curve CPC is known. At P, the continuously differentiable values of u and v along CPC are known, as well as all of their derivatives in the directions pointing towards the interior of the curve. The following question is asked: is the behavior of the solution above P completely determined by the solution below CPC, or is additional information at the boundaries of C required? To answer this, consider the following argument.

Let S be a direction in which the distance is measured; then one can write

$$\frac{\partial u}{\partial S} = \frac{\partial u}{\partial x}\frac{\partial x}{\partial S} + \frac{\partial u}{\partial y}\frac{\partial y}{\partial S} \tag{2.63}$$

$$\frac{\partial v}{\partial S} = \frac{\partial v}{\partial x}\frac{\partial x}{\partial S} + \frac{\partial v}{\partial y}\frac{\partial y}{\partial S} \tag{2.64}$$

The above question can be reformulated: for a solution of eq. 2.61 and 2.62, do the values of u and v along CPC uniquely determine the derivatives?
Here, S measures the distance along CPC. Define

$$\begin{aligned} du &\equiv \frac{\partial u}{\partial S}\,dS \\ dv &\equiv \frac{\partial v}{\partial S}\,dS \\ dx &\equiv \frac{\partial x}{\partial S}\,dS \\ dy &\equiv \frac{\partial y}{\partial S}\,dS \end{aligned} \tag{2.65}$$

The set of equations 2.61–2.64 written at P can be expressed in the following compact form:

$$\begin{bmatrix} A_1 & B_1 & C_1 & D_1 \\ A_2 & B_2 & C_2 & D_2 \\ dx & dy & 0 & 0 \\ 0 & 0 & dx & dy \end{bmatrix} \begin{bmatrix} \partial u/\partial x \\ \partial u/\partial y \\ \partial v/\partial x \\ \partial v/\partial y \end{bmatrix} = \begin{bmatrix} 0 \\ 0 \\ du \\ dv \end{bmatrix} \tag{2.66}$$

Since u and v are known at P, the coefficients A_1, A_2, D_1, and D_2 are also known. If the curve CPC is specified (i.e. its direction), then dx and dy are known. When u and v are known along CPC, then du and dv are also known. The system (eq. 2.66) constitutes a set of four simultaneous linear algebraic equations for the four unknowns, $\partial u/\partial x$, $\partial u/\partial y$, $\partial v/\partial x$, and $\partial v/\partial y$. Two possibilities exist. If the determinant of matrix 2.66 $= 0$, there is an indefinite set of solutions; there may be discontinuities in the solutions on either side of CPC. If the determinant $\neq 0$, there is a unique solution.

To find out under what conditions the determinant of this matrix can be zero, it is expanded to give

$$\begin{aligned} (A_1C_2 - A_2C_1)\,(dy)^2 - (A_1D_2 - A_2D_1 + B_1C_2 - B_2C_1)\,dx\,dy \\ + (B_1D_2 - B_2D_1)\,(dx)^2 = 0 \end{aligned} \tag{2.67}$$

One can consider this as a quadratic equation for the slope dy/dx. If the direction of CPC at P is such that it has a slope satisfying eq. 2.67, then the derivatives of u and v are not uniquely determined by the values of u and v along CPC. Such a direction is called a characteristic direction.

Let the discriminant $(A_1D_2 - A_2D_1 + B_1C_2 - B_2C_1)^2 - 4(A_1C_2 - A_2C_1)\,(B_1D_2 - B_2D_1)$ be denoted by D; then the following is true. If D is positive, eq. 2.67 gives two real slopes; the system of eq. 2.61 and 2.62 is hyperbolic (there are two real characteristic

directions at P). If $D = 0$, eq. 2.67 gives one real slope; the system of eq. 2.61 and 2.62 is parabolic (there is only a single characteristic direction at P). If D is negative, eq. 2.67 gives a pair of complex slopes; the system of eq. 2.61 and 2.62 is elliptic (there are no real characteristic directions at P).

Similar analysis can be made for the following single second-order quasilinear equation:

$$(2.68) \qquad a\frac{\partial^2\psi}{\partial x^2} + b\frac{\partial^2\psi}{\partial x\,\partial y} + c\frac{\partial^2\psi}{\partial y^2} = f$$

in which a, b, c, and f are functions of x, y, ψ, $\partial\psi/\partial x$, and $\partial\psi/\partial y$. The characteristic directions are determined from the following quadratic equation:

$$(2.69) \qquad a(dy)^2 - bdxdy + c(dx)^2 = 0$$

Thus, if $b^2 - 4ac$ is positive, eq. 2.68 is hyperbolic; if $b^2 - 4ac = 0$, eq. 2.68 is parabolic; if $b^2 - 4ac$ is negative, eq. 2.68 is elliptic.

A technique referred to as the method of characteristics, which will be dealt with in more detail in later sections, will be briefly outlined. Assume that the system given by eq. 2.61 and 2.62 is hyperbolic in the domain under consideration. Thus, at every point there are two roots, $(dy/dx)_\alpha$ and $(dy/dx)_\beta$, to the quadratic eq. 2.67. A curve having a slope $(dy/dx)_\alpha$ at each of its points is an α-characteristic and a curve with a slope $(dy/dx)_\beta$ is a β-characteristic. There are thus two families of characteristics filling the domain as shown in Fig. 2.2.

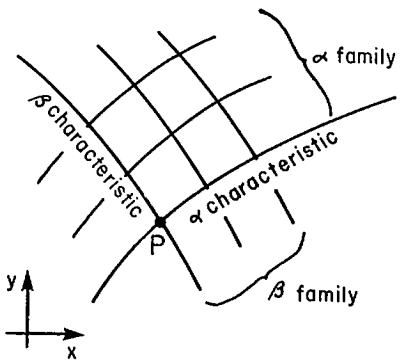

FIG. 2.2. α and β characteristics in a given domain. The slopes of the characteristics are $(dy/dx)_\alpha$ and $(dy/dx)_\beta$, respectively. (Crandall 1956)

It has been shown that the characteristics are loci of possible discontinuities in the derivatives of a solution. In eq. 2.66, if a characteristic direction is considered such that the determinant is zero, then, when the right-hand column is substituted for any column on the left-hand side, the resulting determinant must also be zero. Thus, replacing the fourth column on the left with the column on the right and equating the determinant to zero results in the following:

$$(2.70) \qquad (A_1B_2 - A_2B_1)du + [(A_1C_2 - A_2C_1)\,dy/dx - (B_1C_2 - B_2C_1)]\,dv = 0$$

From eq. 2.67, one can obtain (dy/dx) as a root, and when this is substituted into eq. 2.70, the latter becomes an ordinary differential equation for u and v along the α-characteristic. A similar equation can be obtained along the β-characteristic. Thus, for solving hyperbolic systems, one can first locate the characteristic curves and then integrate the ordinary differential eq. 2.70 along these characteristics. This technique is referred to as the method of characteristics.

Before closing this section, reference is made to a paper by Richardson (1925) in which he respectively refers to the propagation and equilibrium problems as "marching problems" and "jury problems." Crandall (1956, p. 351) stated:

> In propagation problems, the solution marches out from initial conditions guided in transit by side boundary conditions. In equilibrium problems, the entire solution is judged by a jury demanding simultaneous satisfaction of all the boundary conditions and all the internal requirements.

2.3 Finite-Difference Techniques for Marching Problems, Computational Stability

Beginning in the late 1940's, several finite-difference techniques were developed by people working in the field of meteorology with the aim of predicting the weather through numerical solutions of the governing partial differential equations. Thus, in this section, the discussion will have some meteorological connotations and will be based on the discussion by Phillips (1960).

In the partial differential equations governing storm surges (see section 2.1), there are three independent variables, namely, the two horizontal coordinates, x and y, and time t. In the finite-difference technique, these are replaced with the following relationships:

$$\begin{aligned} x &= x_0 + j\Delta x \\ y &= y_0 + k\Delta y \\ t &= t_0 + n\Delta t \end{aligned} \tag{2.71}$$

where j, k, and n are integers, Δx and Δy are grid spaces in the x and y directions, and Δt is the time increment (time step). In the original partial differential equations, the partial derivatives are replaced by partial differences. Let $S = S(x, y, t)$ represent any dependent variable (in the storm surge equations this will be any of the two components, M or N, or the water level deviation, h).

For example, one can use a centered difference for the time derivative and write

$$\frac{\partial S(x,y,t)}{\partial t} = \frac{S(x,y,t+\Delta t) - S(x,y,t-\Delta t)}{2\Delta t} = \frac{(S_{j,k,n+1} - S_{j,k,n-1})}{2\Delta t} \tag{2.72}$$

Thus, one can replace all the partial derivatives (space and time) with partial differences and determine the dependent variables at time step $(n + 1)$, knowing the values of the variables at previous time steps.

Let Z_n be a multidimensional vector whose components are the grid point values of all the unknowns at time step n. Then, one can write, symbolically,

$$Z_{n+1} = L(Z_n, Z_{n-1}) \tag{2.73}$$

where L is an operator (could be nonlinear).
This is the finite-difference analog of a "marching problem" in which the dependent variable at a given time step can be determined knowing its values at previous time steps (Richardson 1922). Instead of the centered difference scheme used in eq. 2.72, one can use an uncentered scheme (forward-difference) such as

$$\frac{\partial S(x,y,t)}{\partial t} = \frac{(S_{j,k,n+1} - S_{j,k,n})}{\Delta t} \tag{2.74}$$

In the discussions that follow, it will be seen that many different finite-difference schemes are possible and that the accuracy of the computation (numerical integration) depends on the grid increments, Δx and Δy, the time step, Δt, and the finite-difference scheme used.

Lax and Richtmeyer (1956) and Richtmeyer (1957) discussed the convergence of a finite-difference solution of a linear initial value problem to the true solution of the differential equation and stated the following theorem (usually referred to as the Lax theorem):

> Given a properly posed initial value problem (linear) and a finite difference approximation to it that satisfies the consistency condition, stability of the difference equations is the necessary and sufficient condition for convergence.

For details of "properly posed problem" and "consistency condition," see Lax and Richtmeyer (1956) and Richtmeyer (1957).

By convergence, it is meant that the finite-difference solution for $t = T$ converges to the true solution for $t = T$ as the space and time increments tend to zero. If the finite-difference scheme is unstable, then solutions with unlimited amplitude may be generated. The contributions of Lax and Richtmeyer are very useful because the more difficult problem of proving convergence is reduced to the simpler problem of stability and consistency. The weakness of their theorem is that it applies only to linear equations. It is worthwhile to note that all stability criteria developed to date for the storm surge models are for the linear problem only.

Next, the phenomenon of computational instability in marching problems will be explained. For this purpose, although not directly relevant to the storm surge problem, we will make use of the so-called one-dimensional advection equation (Phillips 1960):

$$\frac{\partial u}{\partial t} = -c\frac{\partial u}{\partial x} \tag{2.75}$$

Here, x and t are the independent variables, $u = u(x, t)$, and c is a constant. The true solution of eq. 2.75 is (Phillips 1960)

$$u(x, t) = u(x - ct, 0) \tag{2.76}$$

A centered finite-difference scheme for eq. 2.75 is

$$u_{j,n+1} = u_{j,n-1} - \mu(u_{j+1,n} - u_{j-1,n}) \tag{2.77}$$

where

$$\mu \equiv c\frac{\Delta t}{\Delta x} \tag{2.78}$$

and j and n, respectively, are the indices for x and t.

For the initial time step, $n = 0$ to 1, one has to use an uncentered step such as

$$u_{j,1} = u_{j,0} - \frac{\mu}{2}(u_{j+1,0} - u_{j-1,0}) \tag{2.79}$$

We assume that the initial state is periodic in x, with a wavelength L. Then,

$$u(x, 0) = \exp\left(\frac{2\pi i x}{L}\right) \tag{2.80}$$

Then, eq. 2.76 becomes

$$u(x, t) = \exp\frac{2\pi i}{L}(x - ct) \tag{2.81}$$

The solution of the difference equations (2.77–2.79) is

$$u_{j,n} = e^{imj}\left[\frac{(1 + \cos\alpha)}{2\cos\alpha} e^{-i\alpha n} - \left(\frac{1 - \cos\alpha}{2\cos\alpha}\right)(-1)^n e^{i\alpha n}\right] \tag{2.82}$$

where

$$m \equiv \frac{2\pi\Delta x}{L} \tag{2.83}$$

and α is defined such that

$$\sin\alpha = \mu \sin m = c\frac{\Delta t}{\Delta x}\sin\left(\frac{2\pi\Delta x}{L}\right) \tag{2.84}$$

From eq. 2.82 one can see that the finite-difference solution consists of two types of waves. The amplitude of the first wave is given by

$$\frac{1 + \cos\alpha}{2\cos\alpha}$$

and it moves with a phase speed c' given by

$$c' = \frac{c\alpha}{\mu m} = \frac{c \sin^{-1}(\mu \sin m)}{\mu m} \tag{2.85}$$

where α is real. The difference between $\alpha/(\mu m)$ and unity is a measure of the truncation error of eq. 2.77. For details on the truncation error, see Ökland (1958) and Gates (1959). The second type of wave has an amplitude given by

$$\frac{1 - \cos\alpha}{2\cos\alpha}$$

and it moves in the opposite (i.e. wrong) direction, and it changes sign at each time step. Platzman (1958b) referred to this second type of wave as a "computational wave" and he suggested that this wave exists due to the fact that eq. 2.77 is a second-order equation whereas eq. 2.85 is first order.

From eq. 2.84 one can write

$$\alpha = \frac{\pi}{2} + i\cos^{-1}(\mu \sin m) \tag{2.86}$$

provided

$$\mu \sin m > 1$$

Then it can be seen that eq. 2.82 contains a factor that increases with n (i.e. in time) without limit and thus the stability condition required for convergence is violated. Indeed,

it can be seen from eq. 2.77−2.79 that stability is possible provided

$$(2.87) \quad |\mu| = \left| c \frac{\Delta t}{\Delta x} \right| < 1$$

where the two vertical bars denote absolute value of the quantity contained in between. For the two-dimensional case (horizontal coordinates x and y), the stability criterion is

$$(2.88) \quad (|C| + |V|) \frac{\Delta t}{\Delta x} < 1$$

where C and V are the maximum velocity components in the x and y directions.

It can be seen from eq. 2.77 that, except for the initial time step given by eq. 2.78, values of $u_{j,n}$ where $j + n$ is odd do not require values of $u_{j,n}$ at those points where $j + n$ is even. Thus, eq. 2.77 involves two almost independent computations and hence is not an efficient scheme. Indeed, Platzman (1958b) showed tht the two independent sets of $u_{j,n}$ each satisfy the following difference equation:

$$(2.89) \quad u_{j,n+2} + 2u_{j,n} + u_{j,n-2} = \mu^2(u_{j+2,n} - 2u_{j,n} + u_{j-2,n})$$

which is somewhat analogous to the wave equation

$$(2.90) \quad \frac{\partial^2 u}{\partial t^2} = U^2 \frac{\partial^2 u}{\partial x^2}$$

Thus, the first-order eq. 2.75 is artificially raised to second order during the central finite-differencing, and this can cause computational instability in nonlinear cases (i.e. when U in eq. 2.90 is not a constant but makes eq. 2.90 nonlinear) even when the (linear) stability criterion (eq. 2.87) is satisfied (Phillips 1959). Miyakoda (1962) showed that similar computational instability could occur even for linear equations with variable coefficients. Phillips (1959) showed that wavelengths shorter than four grid intervals can grow exponentially with n. Thus, energy can accumulate in short wavelengths; to suppress this, smoothing must be used.

Obukhov (1957) showed that smoothing is equivalent to adding a diffusion term $\partial^2 u/\partial x^2$ to the right side of eq. 2.75. An alternative to the centered difference scheme of eq. 2.77 is the following uncentered scheme:

$$(2.91) \quad \begin{aligned} u_{j,n+1} &= u_{j,n} - \mu(u_{j,n} - u_{j-1,n}) \text{ for } \mu > 0 \\ u_{j,n+1} &= u_{j,n} - \mu(u_{j+1,n} - u_{j,n}) \text{ for } \mu < 0 \end{aligned}$$

The solution of this first-order difference scheme with the same initial condition (eq. 2.80) is

$$(2.92) \quad u_{j,n} = e^{imj} [1 - 2\mu(1 - \mu)(1 - \cos m)]^{n/2} e^{-i\beta n} \text{ for } \mu > 0$$

where

$$(2.93) \quad \beta \equiv \tan^{-1} \left\{ \frac{\mu \sin m}{[1 - \mu(1 - \cos m)]} \right\}$$

If one lets m take all possible values, then the stability criterion is simply $0 \leq \mu \leq 1$. The phase speed, c'', of the wave is

$$(2.94) \quad c'' = \frac{c\beta}{\mu m} = \frac{c \tan^{-1} \left[\frac{\mu \sin m}{1 - \mu(1 - \cos m)} \right]}{\mu m}$$

For $1/2 < \mu < 1$, we have $c'' > c$, whereas from eq. 2.85, it can be seen that $c'' < c$ for all possible μ values that are permitted. Hence, by combining eq. 2.77 and 2.91, one can reduce the truncation errors. Note that this treatment of the computational error did not take into account the influence of the lateral boundaries.

2.4 Formulation of the Storm Surge Equations Using the Concept of Ekman Number and Proudman Number

Following Platzman (1963), the so-called Ekman (1905, 1923) equations in a rotating frame of reference are

$$\frac{\partial u}{\partial t} = -g\frac{\partial h}{\partial x} + fv + \frac{\partial}{\partial z'}\left(\nu\frac{\partial u}{\partial z'}\right) \tag{2.95}$$

$$\frac{\partial v}{\partial t} = -g\frac{\partial h}{\partial y} - fu + \frac{\partial}{\partial z'}\left(\nu\frac{\partial v}{\partial z'}\right) \tag{2.96}$$

$$\frac{\partial h}{\partial t} = -\frac{\partial M}{\partial x} - \frac{\partial N}{\partial y} \tag{2.97}$$

where

$$(M, N) \equiv \int_{-D}^{h} (u, v)\, dz' \tag{2.98}$$

Here, x and y are the horizontal Cartesian coordinates with origin at the undisturbed level of the free surface, z' is the vertical coordinate (positive upward), $z' = -D(x, y)$ is the bottom depth, $z' = h(x, y, t)$ is the deviation of the free surface from its equilibrium position, u and v are the horizontal velocity components in the x and y directions, M and N are the horizontal volume transports through a section of unit width between the bottom and the free surface, g is gravity, f is the Coriolis parameter, and ν is the kinematic eddy viscosity.

For convenience, Platzman (1963) defined the following complex notation:

$$\begin{aligned} U &\equiv (u + iv)D \\ \boldsymbol{M} &\equiv M + iN \\ \nabla h &\equiv \frac{\partial h}{\partial x} + i\frac{\partial h}{\partial y} \\ P &= -gD\nabla h \end{aligned} \tag{2.99}$$

where ∇h is the slope vector and P is the horizontal pressure gradient force on a unit column. Note that, although U and $\boldsymbol{M}$ have the same dimensions, $\boldsymbol{M}$ is independent of z', whereas U depends on z'. One can define a dimensionless vertical coordinate z as

$$z \equiv \frac{z'}{D} \tag{2.100}$$

Then

$$\boldsymbol{M} = \bar{U} = \int_{-1}^{0} U dz \tag{2.101}$$

where the bar means an integral over the complete range of z. In eq. 2.101, a slight approximation is involved in that the upper limit in the integral should be, strictly speaking, h'/D rather than zero.

Assuming ν to be independent of z and multiplying eq. 2.95 and 2.96 by D and eq. 2.97 by $-gD\nabla$ gives

$$\frac{\partial U}{\partial t} = P - ifU + n_\nu \frac{\partial^2 U}{\partial z^2} \tag{2.102}$$

$$\frac{\partial P}{\partial t} = gD \text{ div } \boldsymbol{M} \tag{2.103}$$

where div = divergence and

$$n_\nu \equiv \frac{\nu}{D^2} \tag{2.104}$$

Note that n_ν has the dimensions of frequency and may be considered as a typical decay rate associated with viscosity in boundary layer flow. Also note that the Coriolis parameter, f, is a typical frequency associated with rotation and is referred to as the gyroscopic frequency. Equations 2.102 and 2.103 not only contain the gyroscopic frequency, f, but also contain a gravitational frequency defined by

$$n_g = k\sqrt{gD} \tag{2.105}$$

where k is a wave number corresponding to a horizontal wavelength.

Platzman (1963) defined an Ekman number ϵ and a Proudman number α as follows:

$$\epsilon \equiv \left(\frac{1}{2} f/n_\nu\right)^{1/2} = D\left(\frac{f}{2\nu}\right)^{1/2} \tag{2.106}$$

$$\alpha \equiv \left(\frac{n_\nu}{n_g}\right)^2 = \frac{\nu^2}{k^2 g D^5} \tag{2.107}$$

The Ekman number may be considered as a dimensionless representation of the depth of the water body, whereas the square root of the Proudman number may be regarded as a dimensionless representation of the basin length.

Boundary layer thicknesses D_f and D_g associated with the effects of rotation and gravity are defined as follows:

$$D_f \equiv \sqrt{\frac{\nu}{f}}$$

$$D_g \equiv \sqrt{\frac{\nu}{n_g}} \tag{2.108}$$

Then one can write

$$\epsilon = \frac{D}{\sqrt{2}\, D_f} \tag{2.109}$$

$$\alpha = \left(\frac{D_g}{D}\right)^4 \tag{2.110}$$

Another interpretation for the Ekman and Proudman numbers can be given as follows: the ratio of the Coriolis forces to viscous forces is $2\epsilon^2$ (i.e. the ratio of the second term to the third term on the right side of eq. 2.102) and the ratio of the gravitational aspect of the inertial forces to viscous forces (i.e. ratio of $\partial U/\partial t$ to the third term on the right of eq. 2.102). Let

$$\boldsymbol{R} \equiv R + iS \tag{2.111}$$

be the ratio of the tangential wind stress at the surface to the water density ρ. Then, the condition of the continuity of stress at the air–water interface can be written as

$$\frac{\partial U}{\partial z} = \frac{1}{n_v}\boldsymbol{R}(x, y, t) \text{ at } z = 0 \tag{2.112}$$

The condition of no slip at the bottom can be written as

$$U = 0 \text{ at } z = -1 \tag{2.113}$$

However, the no-slip boundary condition can be replaced by a more general condition:

$$U = -s\frac{\partial U}{\partial z} \tag{2.114}$$

which simply states that velocity and stress are parallel at the bottom. This means that near the bottom there is a transition from the Ekman boundary layer to the logarithmic boundary layer (i.e. the eddy viscosity must approach zero):

$$\begin{aligned} &s = 0 \text{ (for no slip at the bottom)} \\ &s \to \infty \text{ (stress approaches zero at the bottom)} \end{aligned} \tag{2.115}$$

Although, in principle, use of the general condition (eq. 2.114) is no more difficult than the no-slip condition (eq. 2.113), it requires the specification of an additional parameter s. For this reason, Platzman used only the no-slip condition and pointed out that for calculation of the free surface fluctuations, since only the vertically integrated flow is of interest, details of the vertical variation of the eddy viscosity are not important.

Next, after Platzman, the following is defined:

$$\sigma^2 \equiv 2i\,\epsilon^2 + \frac{1}{n_v}\frac{\partial}{\partial t} \tag{2.116}$$

Then, eq. 2.102 becomes

$$\frac{\sigma^2 U}{\partial z^2} - \sigma^2 U = -\frac{P}{n_v} \tag{2.117}$$

The solution of eq. 2.117 is

$$U = U_P + U_R \tag{2.118}$$

where

$$U_P = \frac{1}{n_v} Q_P(z, \sigma)P \tag{2.119}$$

and

$$U_R = \frac{1}{n_v} Q_R(z, \sigma)\boldsymbol{R} \tag{2.120}$$

Here,

$$(2.121)\quad Q_P(z,\sigma) \equiv \frac{1}{\sigma^2}\left[1 - \frac{\cosh(\sigma z)}{\cosh\sigma}\right]$$

$$(2.122)\quad Q_R(z,\sigma) \equiv \frac{\sinh[\sigma(z+1)]}{\sigma\cosh\sigma}$$

Here, one can regard U_P as a slope current and U_R as a wind current.

The volume transport $\boldsymbol{M}$ can be expressed as

$$(2.123)\quad \boldsymbol{M} = \boldsymbol{M}_P + \boldsymbol{M}_R = \bar{U}$$

Noting that a bar denotes vertical integration from $z = -1$ to $z = 0$, the following is written:

$$(2.124)\quad \begin{aligned} \boldsymbol{M}_P &= \frac{1}{n_v}\bar{Q}_P(\sigma)P \\ \boldsymbol{M}_R &= \frac{1}{n_v}\bar{Q}_R(\sigma)\boldsymbol{R} \end{aligned}$$

where

$$(2.125)\quad \begin{aligned} \bar{Q}_P(\sigma) &\equiv \frac{1}{\sigma^2}\left(1 - \frac{1}{\sigma}\tanh\sigma\right) \\ \bar{Q}_R(\sigma) &= \frac{1}{\sigma^2}(1 - \operatorname{sech}\sigma) \end{aligned}$$

If the steady-state value of σ^2 is denoted by σ_0^2, then

$$(2.126)\quad \sigma_0^2 = 2i\epsilon^2 = \frac{if}{n_v}$$

When σ is replaced by σ_0, $\bar{Q}_P$ and $\bar{Q}_R$ in eq. 2.125 assume constant values. Then, from eq. 2.125, the expressions for steady-state transport and wind transport, originally given by Ekman (1905), are derived.

To deal with the transient state, the following is written:

$$(2.127)\quad \sigma^2 = \sigma_0^2 + \lambda$$

where

$$(2.128)\quad \lambda \equiv \frac{1}{n_v}\frac{\partial}{\partial t} = \frac{D^2}{\nu}\frac{\partial}{\partial t}$$

Then, from eq. 2.124 and 2.125

$$(2.129)\quad n_v\boldsymbol{M} = \bar{Q}_P(\sigma)P + \bar{Q}_R(\sigma)\boldsymbol{R}$$

Define

$$(2.130)\quad G(\sigma) \equiv \frac{\sigma\tanh\sigma}{\left(1 - \frac{1}{\sigma}\tanh\sigma\right)}$$

and

$$H(\sigma) \equiv \frac{\left(\frac{1}{\sigma}\tanh\sigma - \operatorname{sech}\sigma\right)}{\left(1 - \frac{1}{\sigma}\tanh\sigma\right)} \tag{2.131}$$

Then, from eq. 2.124, 2.125, and 2.129

$$n_v\left[\sigma^2 + G(\sigma)\right]\boldsymbol{M} = P + \left[1 + H(\sigma)\right]\boldsymbol{R} \tag{2.132}$$

Note that the operators, $G(\sigma)$ and $H(\sigma)$, are more convenient than $\bar{Q}_P(\sigma)$ and $\bar{Q}_R(\sigma)$.

The G and H functions can be expanded in terms of λ as follows:

$$\begin{aligned} G(\sigma) &= \sum_{n=0}^{\infty} G_n(\sigma_0)\,\lambda^n \\ H(\sigma) &= \sum_{n=0}^{\infty} H_n(\sigma_0)\,\lambda^n \end{aligned} \tag{2.133}$$

where

$$\begin{aligned} G_n(\sigma_0) &\equiv \frac{1}{n!}\left[\left(\frac{d}{d\sigma^2}\right)^n G(\sigma)\right]_{\sigma=\sigma_0} \\ H_n(\sigma_0) &\equiv \frac{1}{n!}\left[\left(\frac{d}{d\sigma^2}\right)^n H(\sigma)\right]_{\sigma=\sigma_0} \end{aligned} \tag{2.134}$$

Note that $G_n(\sigma_0)$ and $H_n(\sigma_0)$ are functions only of the Ekman number, ϵ, through the relation

$$\sigma_0 = (1 + i)\epsilon \tag{2.135}$$

It can be shown that the λ expansions converge rapidly.

To deal with an arbitrary Ekman number, define

$$\begin{aligned} \xi &\equiv \frac{1}{\sigma}\tanh\sigma \\ \eta &\equiv \operatorname{sech}\sigma \end{aligned} \tag{2.136}$$

Then,

$$\begin{aligned} G(\sigma) &= \frac{\sigma^2\xi}{(1 - \xi)} \\ H(\sigma) &= \frac{(\xi - \eta)}{(1 - \xi)} \end{aligned} \tag{2.137}$$

Then the first two coefficients in the λ expansion of $G(\sigma)$ and $H(\sigma)$ are

$$\begin{aligned} G_0(\sigma_0) &= \frac{\sigma_0^2\xi_0}{1 - \xi_0} \\ G_1(\sigma_0) &= \frac{1 + \xi_0 - (2 + \sigma_0^2)\xi_0^2}{2(1 - \xi_0)^2} \end{aligned} \tag{2.138}$$

$$H_0(\sigma_0) = \frac{(\xi_0 - \eta_0)}{(1 - \xi_0)}$$

(2.139)

$$H_1(\sigma_0) = \frac{(1 - \xi_0 - \sigma_0^2\xi_0^2) - [-(1 + \sigma_0^2)\xi_0]\eta_0}{2\sigma_0^2(1 - \xi_0)^2}$$

Platzman (1963) assumed that the characteristic time scale of the wind stress field is not small in comparison with the characteristic decay time (which is of the order of n_v^{-1}) due to eddies. Then, the norm of λ in eq. 2.126 is of order one or less, and one can reasonably hope that eq. 2.137 can be approximated by ignoring all terms with powers of λ higher than one in the expansions for $G(\sigma)$ and $H(\sigma)$. This approximate equation is

$$\text{(2.140)} \quad \frac{\partial \boldsymbol{M}}{\partial t} = BP - ifA\boldsymbol{M} + \left(C + \frac{J}{if}\frac{\partial}{\partial t}\right)\boldsymbol{R}$$

where

$$\text{(2.141)} \quad A \equiv \frac{\left(1 + \frac{G}{\sigma_0^2}\right)}{(1 + G_1)}$$

$$\text{(2.142)} \quad B \equiv \frac{1}{(1 + G_1)}$$

$$\text{(2.143)} \quad C \equiv \frac{1 + H_0}{(1 + G_1)}$$

$$\text{(2.144)} \quad J \equiv \frac{\sigma_0^2 H_1}{(1 + G_1)}$$

The coefficients A, B, C, and J are dependent on the depth, D, through

$$\sigma_0 = (1 + i)\epsilon$$

and can be computed once and for all (there is no difficulty due to the complex nature of these coefficients). Note that the real part of A contains the rotation effects and the imaginary part of A includes friction. Equation 2.140 is a first-order (in time) differential equation in $\boldsymbol{M}$.

Take the real and imaginary parts of eq. 2.140 and let subscripts r and i denote real and imaginary quantities, respectively. Then

$$\text{(2.145)} \quad \frac{\partial M}{\partial t} = -gD\left(B_r\frac{\partial h}{\partial x} - B_i\frac{\partial h}{\partial y}\right) + f(A_rN + A_iM) + (C_rR - C_iS)$$

$$\text{(2.146)} \quad \frac{\partial N}{\partial t} = -gD\left(B_r\frac{\partial h}{\partial y} + B_i\frac{\partial h}{\partial x}\right) - f(A_rM - A_iN) + (C_rS + C_iR)$$

and

$$\text{(2.147)} \quad \frac{\partial h}{\partial t} = -\frac{\partial M}{\partial x} - \frac{\partial N}{\partial y}$$

In writing these equations, the water level, h, is reintroduced through the following definition:

$$P = -gD\nabla h \tag{2.148}$$

and the term involving J, being small, is omitted.

Equations 2.145–2.147 form a set of prediction equations for the three variables M, N, and h. Note that these equations are linear with variable coefficients (the coefficients depend on the depth, D, which is space dependent). We assume that R and S (i.e. the x and y components of the wind stress divided by the water density ρ) are prescribed in space and time. Although by elimination one can obtain prediction equations individually for the transports and the water level, this is not necessarily convenient in the numerical integration.

2.5 Numerical Integration Using Conjugate Richardson Lattices

The finite-difference forms for eq. 2.145–2.147 make use of two interlocking lattices (Platzman 1958b), as shown in Fig. 2.3. The grid points are located at

$$\begin{aligned} x &= \tfrac{1}{2} j\Delta s,\ j = 0, 1, 2, \ldots \\ y &= \tfrac{1}{2} k\Delta s,\ k = 0, 1, 2, \ldots \\ t &= \tfrac{1}{2} n\Delta t,\ n = 0, 1, 2, \ldots \end{aligned} \tag{2.149}$$

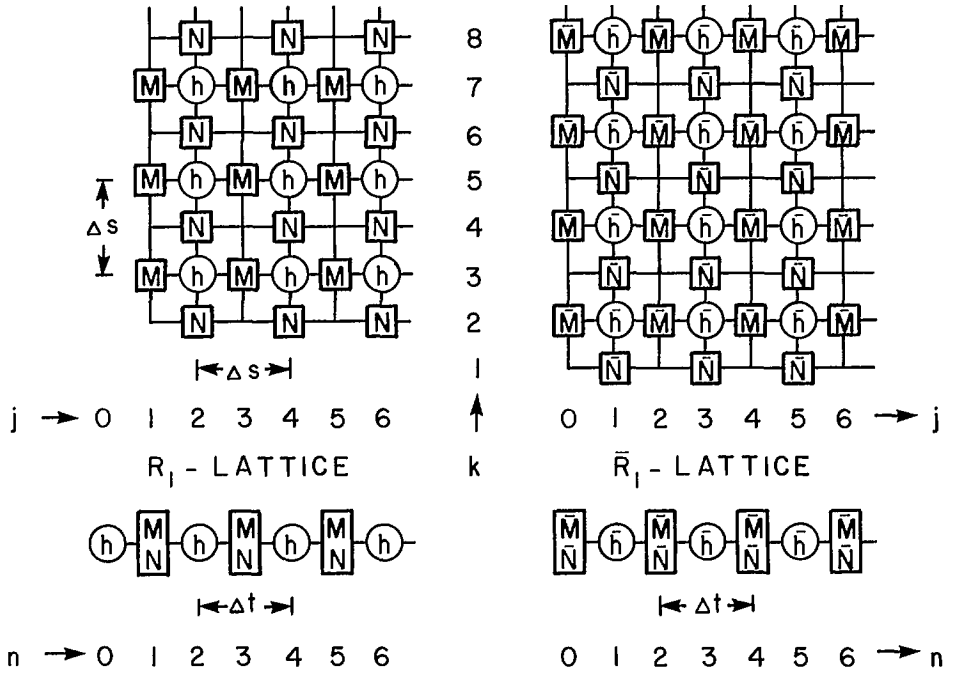

FIG. 2.3. Conjugate Richardson lattices. (Platzman 1963)

To explain the grid arrangement, in eq. 2.145 and 2.146 we omit certain terms temporarily: the A_r terms involving the Coriolis force, the C terms involving the inhomogeneous parameters, and the B_i terms. Then the reduced forms of eq. 2.145–2.147 are

$$\frac{\partial M}{\partial t} \sim -gDB_r \frac{\partial h}{\partial x} + fA_iM \tag{2.150}$$

$$\frac{\partial N}{\partial t} \sim -gDB_r \frac{\partial h}{\partial y} + fA_iN \tag{2.151}$$

$$\frac{\partial h}{\partial t} = -\frac{\partial M}{\partial x} - \frac{\partial N}{\partial y} \tag{2.152}$$

If the dependent variables M, N, and h are arranged as shown on the left side of Fig. 2.3, for the terms in eq. 2.150–2.152 no space interpolation will be needed provided central differences are used in space. Richardson (1922) called this scheme "a lattice reproducing process." Note that in this arrangement (shown on the left side of Fig. 2.3) $j + k$ is odd for the h field and even for the M and N field.

It is shown in the lower left part of Fig. 2.3 that the M and N fields are defined only for odd values of n, whereas the h field is defined only for even values of n. Then, if one uses central differences for the time derivative, time interpolation is not needed in evaluating any term. This scheme is referred to by Richardson as "step-over" differencing, because in reproducing itself at $t + \Delta t/2$ from the known values at $t - \Delta t/2$ using eq. 2.152, the h field steps over the M and N fields which are known at time t. It can be seen from eq. 2.150 and 2.151 that the M and N fields step over the h field.

It can be shown that the step-over procedure is computationally unstable for the dissipation terms (i.e. those involving A_i) and computationally neutral for the pressure gradient terms. Platzman (1963) pointed out that this difference is due to the fact that whereas the dissipation terms are governed by a first-order (in time) equation representing decay, the pressure gradient terms (along with the divergent terms in the continuity equation) are governed by a second-order equation which characterizes wave motion. As a consequence of this, in computing the M and N fields at time step $t + \Delta t/2$, the dissipation terms in eq. 2.150 and 2.151 are evaluated from the values at $t - \Delta t/2$. Platzman refers to this as a "step-on procedure."

The Richardson lattice shown on the left side of Fig. 2.3 may be called an "odd lattice" because $(j + k + n)$ is odd for all grid points. As can be seen from Table 2.1, indeed there are eight distinct Richardson lattices (four having odd parity and four with even parity). The reason there are eight such lattices is the following.

On the left side of Fig. 2.3 for the h field, j is even, k is odd, and n is even. An equiparity submesh is one in which all j values have the same parity, all k values have the same parity, and all n values have the same parity. It can be seen that each of the same independent variables, M, N, and h, of a Richardson lattice lies on an equiparity submesh. One can generate eight equiparity submeshes by giving each of the three indices, j, k, and n, either even or odd parity. These eight equiparity submeshes listed in Table 2.1 are arranged in four conjugate pairs (two equiparity submeshes are referred to as "conjugate" if their respective j values have opposite parity, k values have opposite parity, and n values have opposite parity).

By locating the M, N, and h fields on suitable combinations of the eight equiparity submeshes, eight Richardson lattices may be formed, as shown in Table 2.2, in which they are arranged in four conjugate pairs (two Richardson lattices are said to be conjugate if

TABLE 2.1. The four pairs of conjugate submeshes (O, odd; E, even). (Platzman 1963)

Identity	j	k	n	$j + k + n$
O_1	O	E	E	O
E_1	E	O	O	E
O_2	E	O	E	O
E_2	O	E	O	E
O_3	E	E	O	O
E_3	O	O	E	E
O_4	O	O	O	O
E_4	E	E	E	E

TABLE 2.2. The four pairs of conjugate Richardson lattices, in terms of the submeshes defined in Table 2.1. (Platzman 1963)

Identity	M	N	h
R_1	O_4	O_3	O_2
$\bar{R}_1$	E_4	E_3	E_2
R_2	O_3	O_4	O_1
$\bar{R}_2$	E_3	E_4	E_1
R_3	O_2	O_1	O_4
$\bar{R}_3$	E_2	E_1	E_4
R_4	O_1	O_2	O_3
$\bar{R}_4$	E_1	E_2	E_3

their respective M, N, and h fields are located on conjugate equiparity submeshes). In Fig. 2.3, the left side is the mesh R_1 and the right side is the mesh $\bar{R}_1$ (see Table 2.2), and together they form a pair of conjugate Richardson lattices.

Platzman (1963) pointed out that for any one of the eight Richardson lattices of Table 2.2, any finite-difference scheme that used the "step-over" process for the pressure gradient terms in eq. 2.150 and 2.151 and the divergence terms in eq. 2.152 and "step-on" process for the dissipation terms in eq. 2.150 and 2.151 provides a lattice-reproducing process.

Next, the complete equations, eq. 2.145–2.147, are compared with the reduced equations, eq. 2.150–2.152. The Coriolis terms and the A_r and B_i terms that involved the pressure gradients must be considered. Since the Coriolis terms represent wave motion, these will be treated by a step-over process. Also, to evaluate the Coriolis terms, M values are needed at the grid points where N is defined and vice versa. Thus, for evaluation of the Coriolis terms, the conjugate Richardson lattice shown on the right side of Fig. 2.3 is required.

In other words, let R_1 be the lattice on which the dependent variables M, N, and h are to be predicted. For evaluating the Coriolis terms, the M and N fields on the lattice $\bar{R}_1$ must be known (these will be designated as $\bar{M}$ and $\bar{N}$). Platzman treated the $\bar{M}$ and $\bar{N}$ fields as additional prognostic fields and predicted $\bar{M}$, $\bar{N}$, and $\bar{h}$ on lattice $\bar{R}_1$ simultaneously, with the prediction of M, N, and h on the R_1 lattice. (Note that because of the conjugate relationship, for the evaluation of the Coriolis terms on the $\bar{R}_1$ lattice, one must know the M and N fields on the R_1 lattice.)

Thus, the finite-difference scheme described here gives rise to a lattice-reproducing process with respect to any pair of conjugate Richardson lattices of Table 2.2. This scheme in fact couples the two lattices through the Coriolis terms. Hansen (1956) and Fischer (1959), in their studies on the tides and surges in the North Sea, treated the Coriolis terms using a step-on process rather than a step-over process. This means that they also used two Richardson lattices but they are not conjugate (they used lattices R_1 and R_2 of Table 2.2). It can be shown that their scheme is computationally unstable when Coriolis forces are included.[3] In shallow water, one may suppress the instability through dissipation terms, and in deep water through smoothing. However, when conjugate lattices are used, the scheme is computationally neutral, even when Coriolis terms are present.

[3] Fischer (1965b) modified his original scheme to suppress the instability.

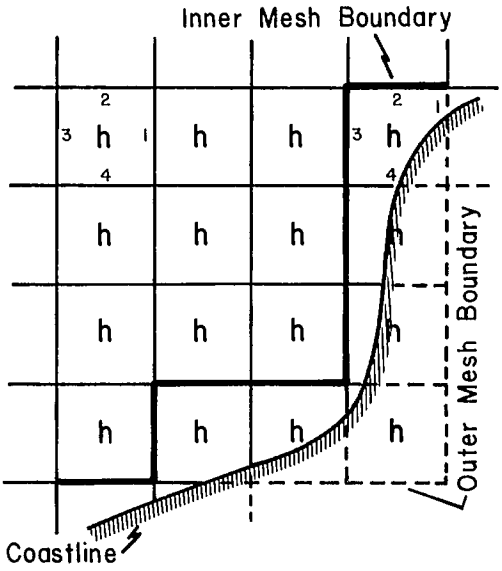

FIG. 2.4. Mesh elements for the h field of R_1 lattice. Upper left is a typical interior element; upper right is a typical boundary element. (Platzman 1963)

To include the B_i terms, for consistency one requires another pair of conjugate Richardson lattices, R_2 and $\bar{R}_2$. However, this considerably extra effort is not justified for the B_i terms, which are not significant generally. Hence, Platzman treated the B_i terms as step-on terms because one can obtain the required h values from the $\bar{R}_1$ lattice. This also provides another (weak) coupling between the two lattices, R_1 and $\bar{R}_1$, in addition to the coupling provided by the Coriolis terms.

The next step is to incorporate the boundary conditions. A typical arrangement of h points on the R_1 lattice is shown in Fig. 2.4. The heavy solid line separates interior elements from boundary elements, and the polygonal line is referred to as the inner mesh boundary. The broken line encloses all mesh elements and is called the outer mesh boundary.

Platzman (1958a) used the inner (or the outer) mesh boundary as a vertical coastline because the boundary conditions then become rather simple: $M = 0$ if the segment is parallel to the y-axis and $N = 0$ if the segment is parallel to the x-axis. These boundary conditions do not require any changes in the finite-difference forms. However, the disadvantage of this scheme is that the truncation errors are maximal at the coastline where, in principle, one would like to have minimum errors because observational data are available mostly at the coastline.

In a later paper, Platzman (1963) used a somewhat different procedure. One can integrate the continuity equation over an h element (whether interior or not) and, thus, express the right side as a line integral of the volume transport across the boundary of the element. Then, if one assumes no transport across the coastline, one gets

$$(2.153)\quad \frac{\partial h}{\partial t}\, a = -M_1 \Delta S_1 - N_2 \Delta S_2 + M_3 \Delta S_3 + N_4 \Delta S_4$$

where h is the average value over the element. The subscripts identify the four sides in the

scheme at the upper left and upper right in Fig. 2.4. For an interior element:

$$a = (\Delta S)^2$$

$$\Delta S_1 = \Delta S_2 = \Delta S_3 = \Delta S_4 = \Delta S \tag{2.154}$$

Then, eq. 2.153 reduces to the central-difference scheme. For a boundary element, since the sum of the length of sides is less than ΔS, $a < (\Delta S)^2$. Central-differencing was used for $\partial/\partial t$, and eq. 2.153 was used as the finite-difference form for the continuity equation. The area and side lengths of each boundary element were determined to provide as input.

For evaluating eq. 2.153, prediction of M or N on truncated sides of boundary h elements is required. However, this is not convenient with the momentum equations. Hence, Platzman obtained a prediction equation for the component of volume transport parallel to the coastline in each boundary h element. One can compute M or N from this tangential component through multiplication by the cosine or sine of the angle between the x-axis and the segment of coastline interior to the boundary element. This angle could be determined for each boundary h element as part of the input data.

Platzman (1963) performed stability analysis under various conditions. His results will be summarized, omitting the details. The computational stability limit imposed upon Δt by boundary layer decay in the absence of gravitational and rotational effects is

$$P\Delta t \leq 1 \tag{2.155}$$

where

$$P \equiv \frac{5}{4} n_\nu = \frac{5\nu}{4D^2} \tag{2.156}$$

Define

$$(\Delta t)_\nu = \frac{1}{P} = \frac{4}{5}\frac{D^2}{\nu} \tag{2.157}$$

Then, the stability criterion is given by

$$\Delta t < (\Delta t)_\nu \tag{2.158}$$

The condition given by eq. 2.155 is necessary for viscogravitational as well as for viscous modes but sufficient only for the latter.

Define

$$\beta \equiv P\Delta t = \frac{5}{4}\frac{\nu \Delta t}{D^2} \tag{2.159}$$

$$\gamma \equiv \frac{5}{3} gD \left(\frac{\Delta t}{\Delta S}\right)^2 S \tag{2.160}$$

where

$$S \equiv \frac{1}{2}\left(\sin^2 \frac{1}{2} k\Delta S + \sin^2 \frac{1}{2} l\Delta S\right) \tag{2.161}$$

where k and l are such that, for viscogravitational modes, the typical solution is

$$\begin{aligned} M &= M_0 e^{\sigma t} \sin(kx) \cos(ly) \\ N &= N_0 e^{\sigma t} \cos(kx) \sin(ly) \\ h &= h_0 e^{\sigma t} \cos(kx) \cos(ly) \end{aligned} \tag{2.162}$$

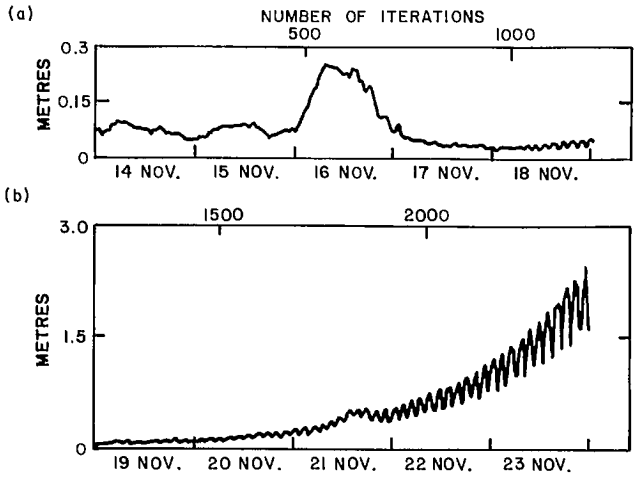

FIG. 2.5. Lattice dispersion for a 10-d period of a storm surge calculation for Lake Erie. (a) First 5 d; (b) second 5 d. Note that the ordinate scales for Fig. 2.5a and 2.5b differ by a factor of 5. (Platzman 1963)

For viscogravitational modes, the sufficient condition for stability is

$$\beta + \gamma \leq 1 \tag{2.163}$$

This is more stringent than the necessary condition

$$\beta \leq 1 \quad \text{because} \quad \gamma > 0 \tag{2.164}$$

This stability analysis did not take into account the boundary conditions and the variable coefficients.

Next, the question of lattice dispersion, which is a measure of the truncation error, will be briefly considered. On the grid R_1 for each point of the h field, a corresponding value of the $\bar{h}$ field on lattice $\bar{R}_1$ is obtained by taking the arithmetic mean of the immediate four neighbours to h (let h' denote this arithmetic mean). Note that since h and $\bar{h}$ are not known at the same time steps, one has to allow a lag of $\Delta t/2$ between h and h'. Platzman (1963) defined lattice dispersion as the root mean square value of $(h' - h)$ over all points of the h field.

The lattice dispersion for one particular storm surge calculation in Lake Erie, performed by Platzman (1963), is shown in Fig. 2.5a for the first 5 d and in Fig. 2.5b for the next 5 d. (Note that the ordinate scales in Fig. 2.5a and 2.5b differ by a factor of 5.) As can be seen, during the first 4 d the lattice dispersion is insignificant (about 0.06 m). On the 5th d, the dispersion began to exhibit an oscillation with continuously increasing amplitude. Thus, the truncation errors make the computation unstable. Platzman (1963) suggested that the somewhat irregular treatment of the momentum equations at the boundaries is the source of this instability.

2.6 Staggered and Nonstaggered Grid Schemes

The Richardson lattice, described above, is a "staggered grid" because the variables are staggered in space on the grid. The leapfrog scheme for integration in time is also a

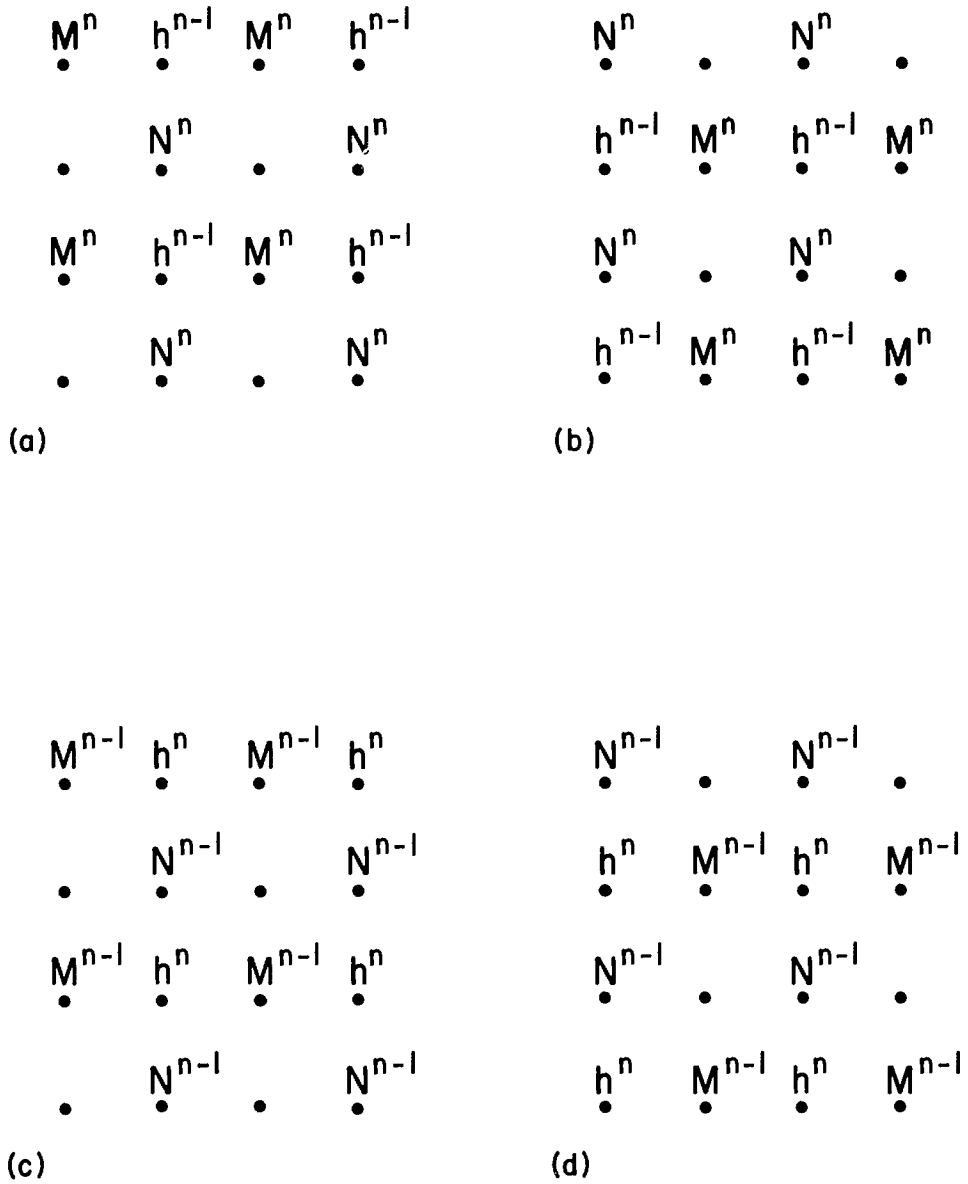

FIG. 2.6. Various staggered (in space and time) grids for the central-difference scheme. (a) Basic scheme; (b) space supplement of Fig. 2.6a; (c) time supplement of Fig. 2.6a; (d) space–time supplement of Fig. 2.6a. Subscript n denotes time step.

staggered scheme (in time). Nonstaggered grids in space and time integration were used in storm surge calculations until the early 1960's. Discussion will begin with the simplest staggered grid schemes associated with central finite-difference.

Away from the boundaries, central-differencing is the most convenient manner of space discretization. However, near (and at) the boundaries, special attention is required;

one can place fictitious points outside the boundary or use one-sided difference schemes. One of the simplest central difference schemes is shown in Fig. 2.6a. However, this scheme is not convenient for the evaluation of advective terms and the Coriolis terms. For convenient evaluation of these terms, multiple-lattice grids have been used. Simons (1980) suggested coupling the grid in Fig. 2.6a with its space supplement shown in Fig. 2.6b or its time supplement shown in Fig. 2.6c or its space–time supplement shown in Fig. 2.6d. Note that scheme in Fig. 2.6d corresponds to the conjugate lattice developed by Platzman (1963).

In double-lattice grids, both the transport variables are defined at the same location, which leads to a combination of the conuugate lattices in Fig. 2.6a and 2.6d as originally proposed by Eliassen (1956). Lilly (1961) used a time interpolation for the Coriolis terms for the space-supplemental lattices in Fig. 2.6a and 2.6d.

Single-lattice grids are useful in situations in which Coriolis terms and nonlinear advective terms are not important. However, for larger bodies of water in which the earth's rotational effects have to be considered, the truncation errors due to the spatial averaging (that will be required to compute the Coriolis terms) on a single lattice deserve attention.

One could form double-lattice grids by combining the space-supplemental lattices in Fig. 2.6a and 2.6b or the conjugate lattices in Fig. 2.6a and 2.6d (Simons 1980). The spatial representation of either of these is the same and is shown in Fig. 2.7a. The chief advantage of a double-lattice grid over a single-lattice grid is that no spatial averaging will be required for most of the terms in the equations of motion and continuity. The main drawback of a double-lattice grid is that the surface gravity waves travel independently in each lattice and the lattices tend to become decoupled progressively with time, especially for water bodies with irregular boundaries (practically all natural water bodies have irregular boundaries). The Coriolis terms and the nonlinear advective terms will tend to keep the two lattices coupled; however, as was shown by Platzman (1958b), some spurious results may be obtained in addition to computational instability.

The phenomenon of grid dispersion can become quite a serious hindrance in calculations with double-lattice grids, and various smoothing (in space) operators were developed. Later, some of these operators used by Shuman (1957), Harris and Jelesnianski (1964), and others will be discussed. An alternative to space-smoothing is the introduction of an artificial viscosity (also referred to as pseudo or virtual viscosity) which, in effect, works in a similar manner to a horizontal eddy diffusion of momentum (Obukhov 1957). Rotation of the basic coordinate system to give a new system, x_r and y_r, and then evaluating the Laplacian operator for diffusion along the rotated coordinates has also been used in an attempt to couple the two lattices (e.g. Simons 1980).

Another approach to keep the two lattices coupled was made by Janjic (1974). Janjic added an artificial diffusion term, not to the momentum equations as is traditionally done, but to the continuity equation. This term was made proportional to the difference between the two Laplacians of the free surface height field. The first Laplacian is calculated on the x and y coordinates and, hence, involves only one lattice, and the second Laplacian is evaluated along the rotated coordinates, x_r and y_r, and thus involves both lattices. In principle, if there are no truncation errors, both Laplacians should be identical. However, in practice, this will not be so, and the artificial diffusion term will be nonzero; this will smooth the surface height field and tend to keep the lattices coupled.

Several authors (e.g. Lauwerier 1962; Leith 1965; Heaps 1969) have used rotated coordinates and evaluated all the derivatives in the relevant equations along these coordinates. However, it should be pointed out (Lauwerier 1962; Simons 1973) that any improvements in the elimination of grid dispersion is not only due to the evaluation of all the

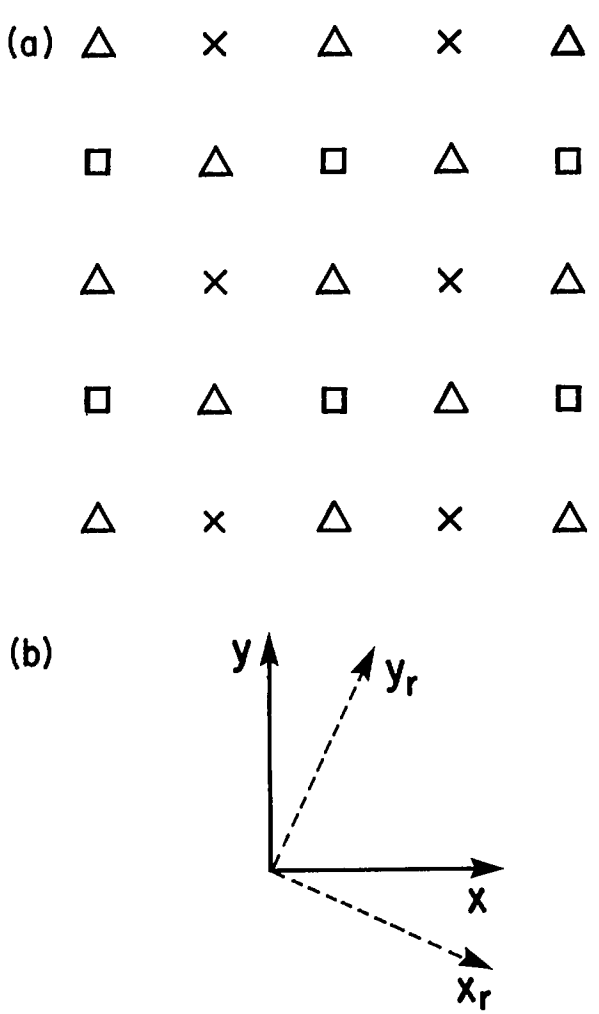

FIG. 2.7. (a) Double-lattice grid. △, locations where the transport components, M and N, are defined; ×, surface height field belonging to one lattice; □, surface height field belonging to a second lattice. (b) Rotated coordinates.

derivatives along the rotated coordinates but also to the orientation of the grid relative to the boundaries of the water body.

One of the examples of a computation involving multiple lattices is that of Harris and Jelesnianski (1964) in which the two transport components and the surface height field were defined at all the grid points at every time step (this is a combination of eight lattices).

2.7 Numerical Dispersion, Parasitic Waves, Filtering, and Aliasing

Earlier, the linear advective equation 2.75 was considered, which has a solution in

the form of a single harmonic component (Mesinger and Arakawa 1976):

$$(2.165) \quad u(x, t) = Re\,[U(t)\, e^{ikx}]$$

provided

$$(2.166) \quad \frac{dU}{dt} + ikcU = 0$$

where Re denotes the real part. Equation 2.166 is referred to as the oscillation equation and

$$(2.167) \quad c = \frac{\nu}{k}$$

is the phase speed of the waves, k is the wave number, and ν is the wave frequency. There is no dispersion because $u(x, t)$ is advected without change of shape along the x-axis with a constant speed c (all wavelengths propagate with the same phase speed).

Suppose in eq. 2.75 the space derivative is represented by a central finite-difference, leading to the following differential-difference equation:

$$(2.168) \quad \frac{\partial u_j}{\partial t} + c\,\frac{(u_{j+1} - u_{j-1})}{2\Delta x} = 0$$

This has a solution in the form of a single harmonic component

$$(2.169) \quad u_j(t) = Re\,[U(t)\, e^{ikj\Delta x}]$$

provided

$$(2.170) \quad \frac{dU}{dt} + ik\left[\frac{c\,\sin(k\Delta x)}{k\Delta x}\right] U = 0$$

In this case, waves propagate with the phase speed

$$(2.171) \quad c^* = c\,\frac{\sin(k\Delta x)}{k\Delta x}$$

which is a function of the wave number, k. Thus, the spatial finite-differencing created a dispersion of the waves, which will be referred to as numerical dispersion.

It can be seen that, as $k\Delta x$ increases (starting from zero), the phase speed c^* decreases monotonically from c, and c^* becomes zero for the shortest resolvable wavelength $2\Delta x$ (Δx is the grid interval) when $k\Delta x = \pi$. Thus, the propagation speed for all waves is less than the true phase speed, c, and the departure of c^* from c increases as the wavelength decreases.

For the linear advection equation 2.75, the group velocity is given by

$$(2.172) \quad c_g = \frac{d}{dk}(kc) = 0$$

Hence, the group velocity, c_g, is equal to the phase velocity, c, and is constant. However, for the differential-difference equation 2.168, the group velocity is given by (Mesinger and Arakawa 1976):

$$(2.173) \quad c_g^* = \frac{d}{dk}(kc^*) = c\,\cos(k\Delta x)$$

Hence, as $k\Delta x$ increases from zero, the group velocity, c_g^*, decreases monotonically from c_g, and c_g^* is equal to $-c_g$ at the shortest resolvable wavelength, $2\Delta x$.

To summarize, central-differencing of the space derivative term in the linear advection equation causes both the phase and group velocities to decrease as the wave number increases. Waves having lengths less than $4\Delta x$ have negative group velocity (which means that wave packets travel in a direction opposite to that of individual waves). Since this wave-packet motion is inconsistent with the expected behavior of the advection equation, such waves are referred to as parasitic waves.

One can think of various uncentered space-difference schemes to remove parasitic waves. The following scheme can be written for the linear advection equation:

$$\frac{\partial u_j}{\partial t} + c\frac{(u_j - u_{j-1})}{\Delta x} = 0 \text{ for } c > 0$$

(2.174)

$$\frac{\partial u_j}{\partial t} + c\frac{(u_{j+1} - u_j)}{\Delta x} = 0 \text{ for } c < 0$$

This scheme is called an upstream-difference scheme because the differences are calculated on the side from which the advection velocity arrives at the point under consideration. A scheme that involves evaluation from the opposite side will be referred to as a downstream-difference scheme. When an upstream-difference scheme is used, no perturbation can propagate in a direction opposite to that of advection. Hence, no parasitic waves can form.

One may ask the question whether there is anything to be gained by retaining the central finite-difference scheme but using a higher order difference form. Using a Taylor expansion, one can approximate the term $\partial u/\partial x$ by

$$\text{(2.175)} \quad \frac{(u_{j+1} - u_{j-1})}{2\Delta x} = \frac{\partial u}{\partial x} + \frac{1}{3!}\frac{\partial^3 u}{\partial x^3}(\Delta x)^2 + O(\Delta x)^4$$

One can replace Δx with $2\Delta x$ in eq. 2.175 and write

$$\text{(2.176)} \quad \frac{(u_{j+2} - u_{j-2})}{4\Delta x} = \frac{\partial u}{\partial x} + \frac{4}{3!}\frac{\partial^3 u}{\partial x^3}(\Delta x)^2 + O(\Delta x)^4$$

A fourth-order accurate scheme, which is formed by a linear combination of eq. 2.175 and 2.176 and in which the truncation errors due to eq. 2.175 cancel those due to eq. 2.176, is the following:

$$\text{(2.177)} \quad \frac{4}{3}\frac{(u_{j+1} - u_{j-1})}{2\Delta x} - \frac{1}{3}\frac{(u_{j+2} - u_{j-2})}{4\Delta x} = \frac{\partial u}{\partial x} + O(\Delta x)^4$$

Using eq. 2.177 for the linear advection equation 2.175 gives

$$\text{(2.178)} \quad \frac{\partial u_j}{\partial t} + c\left[\frac{4}{3}\frac{(u_{j+1} - u_{j-1})}{2\Delta x} - \frac{1}{3}\frac{(u_{j+2} - u_{j-2})}{4\Delta x}\right] = 0$$

Proceeding as above, the phase speed can be written as

$$\text{(2.179)} \quad c^{**} = c\left[\frac{4}{3}\frac{\sin(k\Delta x)}{k\Delta x} - \frac{1}{3}\frac{\sin(2k\Delta x)}{2k\Delta x}\right]$$

Small values of k, from eq. 2.171 and 2.179, give

$$c^* = c\left[1 - \frac{1}{3!}(k\Delta x)^2 + \ldots\right]$$

(2.180)

$$c^{**} = c\left[1 - \frac{4}{5!}(k\Delta x)^4 + \ldots\right]$$

It can be seen that for large and medium wavelengths, the fourth-order scheme is more accurate. However, for short wavelengths, even though the advection speed is better represented by the fourth-order scheme, the numerical dispersion is greater. The main drawback of higher order differencing schemes is the requirement of additional grid rows, which leads to computation modes in space similar to computational modes in time, and makes the prescription of boundary conditions rather difficult. Also, the computational effort increases considerably.

Some of the space-differencing schemes have been referred to as the filter factor forms in the literature (Schuman 1957; Harris and Jelesnianski 1964). For a dependent variable, $F(x)$, the standard central-difference form is

$$\frac{dF(x)}{dx} = \frac{F(x + \Delta x) - F(x - \Delta x)}{2\Delta x} + \epsilon_2 \tag{2.181}$$

where

$$\epsilon_2 = \frac{d^3F}{dx^3}\frac{(\Delta x)^2}{3!} \tag{2.182}$$

A three-point forward-difference form is

$$\frac{dF}{dx} = \frac{1}{2\Delta x}[-3F(x) + 4F(x + \Delta x) - F(x + 2\Delta x)] + \epsilon_3 \tag{2.183}$$

where

$$\epsilon_3 \equiv \frac{4}{3!}\frac{d^3F}{dx^3}(\Delta x)^2 \tag{2.184}$$

For a function $F = F(x, y)$:

$$\begin{aligned}\frac{\partial F}{\partial x} = \frac{1}{\Delta S(4a + 2b)}\{a[&F(x + \Delta x, y + \Delta y) - F(x - \Delta x, y + \Delta y) \\ &+ F(x + \Delta x, y - \Delta y) - F(x - \Delta x, y - \Delta y)] \\ &+ b[F(x + \Delta x, y) - F(x - \Delta x, y)]\}\end{aligned} \tag{2.185}$$

where $\Delta x = \Delta y = \Delta S$.

In a simplified form, eq. 2.185 can be written as

$$\frac{\partial F}{\partial x} = \frac{1}{\Delta S(4a + 2b)}\begin{bmatrix} -a & 0 & a \\ -b & 0 & b \\ -a & 0 & a \end{bmatrix} F(x, y) \tag{2.186}$$

Note that if $a = 0$ and $b = 1$, eq. 2.186 reduces to the central-difference form, eq. 2.181. Shuman used $a = 1$ and $b = 2$ and called it the filter factor form for the following reason.

Computational instability, when it occurs, usually appears as an unlimited growth of energy in the water body. (The criteria for avoiding or suppressing computational instability will be considered later.) Truncation errors and round-off errors are greatest for the higher order harmonics. Hence, instability might be suppressed by eliminating or dampening the higher harmonics. This process is referred to as smoothing or filtering. Shuman (1957) and Holloway (1958) suggested that the following numerical filter

$$\bar{F}(x) = \frac{1}{4}[F(x - \Delta x) + 2F(x) + F(x + \Delta x)] \tag{2.187}$$

will eliminate the harmonic with a wavelength of $2\Delta x$ (which is the most troublesome) without causing significant phase shifts. The two-dimensional version of eq. 2.187, which can be obtained by setting $a = 1$ and $b = 2$ in eq. 2.186, is referred to as the filter factor form. Lauwerier (1962) used $a = 1$ and $b = 0$ and showed that this form has many superior qualities not possessed by the central difference form.

The advection equation will again be used to introduce the problems associated with aliasing. However, rather than the linear form, the nonlinear form will be used:

$$\frac{\partial u}{\partial t} + u\frac{\partial u}{\partial x} = 0 \tag{2.188}$$

This equation is referred to as the shock equation by Shuman (1974). Platzman (1964) wrote the general solutions as

$$u = f(x - ut) \tag{2.189}$$

where f is an arbitrary function. It will be shown that the finite-difference form of eq. 2.188 will give rise to errors due to the inability of a discrete scheme to resolve wavelengths shorter than $2\Delta x$ (or wave numbers greater than $k_{max} = \pi/\Delta x$).

With reference to Fig. 2.8, consider a function $u(x)$ given by

$$u = \sin(kx) \tag{2.190}$$

for $k < k_{max}$. From eq. 2.190:

$$u\frac{\partial u}{\partial x} = k \sin(kx) \cos(kx) = \frac{1}{2} k \sin(2kx) \tag{2.191}$$

For wave numbers in the range $1/2\, k_{max} < k \leq k_{max}$, the nonlinear term $u(\partial u/\partial x)$ will give rise to a wave number that lies in a range that cannot be resolved by the grid.

The situation for $k > k_{max}$ (Mesinger and Arakawa 1976) is examined. With reference to Fig. 2.8, let $L = 4/3\ \Delta x$ (the solid line shows this wave). If the values of the function at the two grid points shown by black dots are known, one cannot distinguish this wave from the wave shown by the broken line. Thus, all wavelengths that cannot be resolved by the grid will be misrepresented (or aliased) as longer wavelengths.

Next, the results are generalized to the case when u consists of a number of harmonic components:

$$u = \sum_n u_n \tag{2.192}$$

The term $u(\partial u/\partial x)$ will contain products of harmonics of different wavelengths, such as $\sin(k_1 x) \sin(k_2 x)$. The following trigonometric identity can be easily obtained:

$$\sin(k_1 x) \sin(k_2 x) = \frac{1}{2}[\cos(k_1 - k_2)x - \cos(k_1 + k_2)x] \tag{2.193}$$

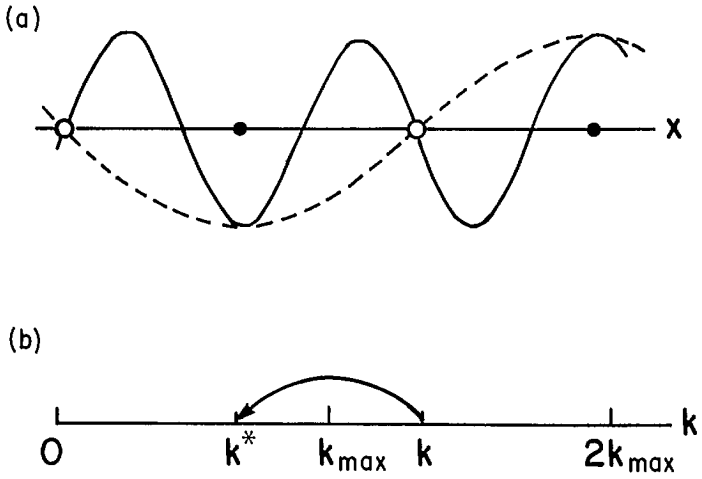

FIG. 2.8. (a) Wave of length $4\Delta x/3$ misrepresented by the finite-difference grid as a wave of length $4\Delta x$; (b) misrepresentation of a wave number $k > k_{max}$. (Mesinger and Arakawa 1976)

Hence, even if initially all wave numbers, k, are less than or equal to k_{max}, through nonlinear interaction, waves with $k > k_{max}$ will develop, and aliasing will occur. One can also write

$$\sin(kx) = \sin[2k_{max} - (2k_{max} - k)]x \tag{2.194}$$

It can be seen from Fig. 2.8b that a wave number k will be misrepresented as a wave number $2k_{max} - k$.

Next, visualization of the consequences of aliasing is attempted. To do this, it can be assumed that the dependent variables of concern here are made up of a series of harmonic components. The energy spectrum of these various components determines the relative contributions of different scales to the dependent variable. Aliasing errors will create a spurious inflow of energy at wave numbers that are not much less than k_{max} and, with the progress of time, the energy of these components grows in a rapid manner. Phillips (1959) referred to this as nonlinear instability. Miyakoda (1962) showed that similar instability could occur even for linear equations with variable coefficients.

Next, possible schemes for prevention or suppression of nonlinear instability are considered. Orszag (1971) showed that aliasing errors could be eliminated by filtering out wave numbers $k > 2/3\,k_{max}$. Another approach for the suppression of the shortest waves is the Lax and Wendroff (1960) scheme, and this approach was suggested by Richtmeyer (1963). Kasahara (1969) suggested that it is sufficient to use the Lax–Wendroff scheme intermittently after long intervals of time integration using other simpler schemes. A third approach for eliminating nonlinear instability is to use a Lagrangian formulation (Leith 1965; Krishnamurti et al. 1973). Although nonlinear instability might be suppressed, there are several highly undesirable features with Lagrangian schemes (the worst one being the drastic distortion of the basic grid after a few time steps of integration); these schemes will therefore not be considered.

The most sophisticated methods are the conservation schemes developed by Arakawa (1966, 1972) and Arakawa and Lamb (1981). These schemes, by retaining the conservation (in the finite-difference forms) of some integral properties of the original differ-

ential equations, eliminate nonlinear instability, as well as the spurious inflow of energy to the short waves, rather than artificially suppressing their amplitudes. In these conservation schemes the average values of enstrophy (half the vorticity squared) and the kinetic energy do not change, nor does the average wave number.

For a review of the finite-difference schemes and their conservation properties, see Grammelvedt (1969).

2.8 Finite-Differencing of the Time Derivative

The time-derivative terms in the storm surge equations are the time derivatives of the horizontal transport components M and N in the momentum equations and the time derivative of the free surface height h in the continuity equation. Since the terms $\partial M/\partial t$, $\partial N/\partial t$, and $\partial h/\partial t$ all have the same form, discussion will be based on a general relationship of the following form:

$$\frac{\partial U}{\partial t} = F(U, t), \qquad U = U(t) \tag{2.195}$$

The reason a total time derivative d/dt is used rather than a partial derivative $\partial/\partial t$ is that, here, $U = U(t)$ only and its space dependence is not considered, since, earlier, the problem of space-differencing was already considered. In this section, liberal use will be made of the works of Mesinger and Arawaka (1976) and Simons (1980).

Several time-differencing schemes are available: two-level schemes without iteration, two-level schemes with iteration, three-level schemes, etc. Discussion will begin with two-level schemes without iteration. In this, three different schemes are well known: the Euler (or forward), backward, and trapezoidal schemes.

In the Euler or forward scheme, the time derivative is approximated as

$$\begin{aligned} U_{n+1} &= U_n + \Delta t \cdot F_n \\ F_n &= F(U_n) \end{aligned} \tag{2.196}$$

This is a first-order accurate scheme with a truncation error of $O(\Delta t)$, and it is an uncentered scheme because F is not centered in time.

In the backward scheme

$$\begin{aligned} U_{n+1} &= U_n + \Delta t \cdot F_{n+1} \\ F_{n+1} &= F(U_{n+1}) \end{aligned} \tag{2.197}$$

This scheme, as written here, is implicit, because F depends on U_{n+1}, which must be determined. In the case of partial differential equations, this will require iteration because a set of simultaneous equations (one for each grid point) must be solved. The truncation error of this scheme is also of $O(\Delta t)$.

In the trapezoidal scheme

$$U_{n+1} = U_n + \frac{1}{2}\Delta t\,(F_n + F_{n+1}) \tag{2.198}$$

As can be seen, this is also an implicit scheme, but its truncation error is of $O(\Delta t)^2$. Next, two iterative schemes will be discussed, but still involving two time levels only.

In the Matsuno or Euler backward scheme, the first step is the regular Euler scheme

(2.199) $U_{(n+1)^*} = U_n + \Delta t \cdot F_n$

This value of $U_{(n+1)^*}$ is used to determine $F_{(n+1)^*}$ through

(2.200) $F_{(n+1)^*} = F(U_{(n+1)^*})$

This value of $F_{(n+1)^*}$ is used in a backward step to compute U_{n+1}:

(2.201) $U_{n+1} = U_n + \Delta t \cdot F_{(n+1)^*}$

As can be seen, this is a first-order accurate scheme and is explicit.

The Heun scheme is a development from the trapezoidal scheme and can be expressed as

$$\begin{aligned} U_{(n+1)^*} &= U_n + \Delta t \cdot F_n \\ U_{n+1} &= U_n + \Delta t/2\,(F_n + F_{(n+1)^*}) \end{aligned} \tag{2.202}$$

This is also an explicit scheme, but is of second-order accuracy.

All the time-differencing schemes introduced thus far can be used for the first time step, as well as all the subsequent time steps in the numerical integration. However, the three-level schemes cannot be used for the first time step. The most common of the three-level schemes has already been introduced, namely, the leapfrog scheme (also called the midpoint rule or step-over rule). In this scheme:

(2.203) $U_{n+1} = U_{n-1} + 2\Delta t \cdot F_n$

with a truncation error of $O(\Delta t)^2$.

The Adams–Bashforth scheme

(2.204) $U_{n+1} = U_n + \Delta t \left(\frac{3}{2} F_n - \frac{1}{2} F_{n-1}\right)$

is second-order accurate. Another scheme, referred to as the Milne–Simpson scheme, involves fitting a parabola to the values of F_{n-1}, F_n, and F_{n+1} which will lead to an implicit scheme. Young (1968) discussed 13 different time-differencing schemes. For a discussion on the conservation of the energy of low-frequency waves in iterative time integration schemes see Kondo et al. (1982). It is also possible to construct complicated schemes in which space- and time-differencing are treated in a manner that cannot be described separately.

Next, the stability properties of some of these schemes will be discussed. This can be done only when the form of the function $F(U, t)$ is known. The oscillation equation 2.166 will be considered assuming

(2.205) $F = i\omega U$

where $i = \sqrt{-1}$ and ω is the frequency. In this notation, the oscillation equation becomes

(2.206) $\frac{dU}{dt} = i\omega U,\ U = U(t)$

Note that U could be complex, but ω is real.

The general solution of eq. 2.206 is

(2.207) $U(t) = U(0)\, e^{i\omega t}$

In the finite-difference form, taking $t = n\Delta t$

$$U(n\Delta t) = U(0)\, e^{in\omega\Delta t}$$

If the solution is considered in a complex plane, the argument rotates by $\omega\Delta t$ in each time step, Δt, but the amplitude does not change.

The stability of the various schemes can be ascertained using the Von Neumann method in which we define a variable λ through

(2.208) $$U_{n+1} = \lambda U_n$$

Let

(2.209) $$\lambda = |\lambda| e^{i\theta}$$

Then, the solution to eq. 2.207 becomes

(2.210) $$U_n = |\lambda|^n U^{(0)} e^{in\theta}$$

Here, θ is the phase change in each time step. Since the amplitude of the correct solution does not change, the condition for stability is $|\lambda| \leq 1$. Hence, for the following values of λ:

(2.211) $$\lambda \begin{cases} > 1, \text{ unstable} \\ = 1, \text{ neutral} \\ < 1, \text{ damping or dissipative} \end{cases}$$

Thus, we can refer to λ as the amplifcation factor. One can also compare the phase change, θ, with that for the correct solution, i.e. $\omega\Delta t$. The relative phase change of the numerical solution is given by $\theta/(\omega\Delta t)$:

(2.212) $$\frac{\theta}{\omega\Delta t} \begin{cases} > 1, \text{ accelerating} \\ = 1, \text{ no effect on phase speed} \\ < 1, \text{ decelerating} \end{cases}$$

For accuracy in the computation, it is desirable to have

(2.213) $$\lambda \sim 1 \text{ and } \frac{\theta}{\omega\Delta t} \sim 1$$

The computational mode introduced earlier violates these conditions. For these modes, the numerical solution does not approach the true solution as ΔS (i.e. grid size) $\rightarrow 0$ and $\Delta t \rightarrow 0$.

The Euler (or forward) scheme, the backward scheme, and the trapezoidal scheme can be represented by the following equation:

(2.214) $$U_{n+1} = U_n + \Delta t\, (\alpha F_n + \beta F_{n+1})$$

A consistency condition will be

(2.215) $$\alpha + \beta = 1$$

and the following is true for each scheme:

(2.216)
Euler scheme $\alpha = 1, \quad \beta = 0$

Backward scheme $\alpha = 0, \quad \beta = 1$

Trapezoidal scheme $\alpha = \frac{1}{2}, \quad \beta = \frac{1}{2}$

From eq. 2.206 and 2.214

(2.217) $U_{n+1} = U_n + i\omega\Delta t(\alpha U_n + \beta U_{n+1})$

This equation must be solved for U_{n+1} to evaluate λ. Following Mesinger and Arakawa (1976), define

(2.218) $P \equiv \omega\Delta t$

Then, from eq. 2.217 and 2.218:

(2.219) $$\lambda = \frac{1}{(1 + \beta^2 P^2)}(1 - \alpha\beta P^2 + iP) = \frac{1 + i\alpha P}{1 - i\beta P}$$

Using eq. 2.216 and 2.219, the following is true for each scheme:

(2.220) Euler scheme $\lambda = 1 + iP$

(2.221) Backward scheme $$\lambda = \frac{1}{(1 + P^2)}(1 + iP)$$

(2.222) Trapezoidal scheme $$\lambda = \frac{1}{\left(1 + \frac{1}{4}P^2\right)}\left(1 - \frac{1}{4}P^2 + iP\right)$$

From eq. 2.219, the following is true for each scheme:

(2.223) Euler scheme $|\lambda| = (1 + P^2)^{1/2}$

(2.224) Backward scheme $|\lambda| = (1 + P^2)^{-1/2}$

(2.225) Trapezoidal scheme $|\lambda| = 1$

From eq. 2.223–2.225, it can be seen that the Euler scheme is unstable and the backward scheme is stable for any Δt. The trapezoidal scheme is neutral.

Next, two-level iterative schemes will be considered, namely, the Matsuno and the Heun schemes. The finite-difference forms for these schemes can be written as

$$U_{n+1} = U_n + \Delta t\,[\alpha F_n + \beta F_{(n+1)^*}]$$

(2.226) $$U_{(n+1)^*} = U_n + \Delta t\, F_n$$

$$\alpha + \beta = 1$$

The following is true for each scheme:

(2.227) Matsuno scheme $\alpha = 0, \quad \beta = 1$

Heun scheme $\alpha = \frac{1}{2}, \quad \beta = \frac{1}{2}$

Applying this to the oscillation equation and proceeding as above gives

(2.228) $\lambda = 1 - \beta P^2 + iP$

From eq. 2.227 and 2.228 the following is true for each scheme:

$$\text{Matsuno scheme } \lambda = 1 - P^2 + iP$$
$$\text{Heun scheme } \lambda = 1 - \frac{1}{2}P^2 + iP \tag{2.229}$$

Evaluating $|\lambda|$ gives the following for each scheme:

$$\text{Matsuno scheme } |\lambda| = (1 - P^2 + P^4)^{1/2}$$
$$\text{Heun scheme } |\lambda| = \left(1 + \frac{1}{4}P^4\right)^{1/2} \tag{2.230}$$

Thus, the Matsuno scheme is stable if $|P| \leq 1$. Hence, one must use a small Δt so that

$$\Delta t \leq \frac{1}{|\omega|} \tag{2.231}$$

It can be seen that the Heun scheme is always unstable, similar to the Euler scheme. In practice, both these schemes can be used, provided Δt is not large.

Next, three-level schemes will be considered. The leapfrog scheme, when applied to the oscillation equation, gives

$$U_{n+1} = U_{n-1} + i2\omega\Delta t \cdot U_n \tag{2.232}$$

Since this is a three-level scheme, we must specify a computational initial condition U^1 in addition to the physical initial condition U^0. This value of U^1 must be obtained from some two-level scheme.

From Eq. 2.208 write

$$U_n = \lambda U_{n-1}$$
$$U_{n+1} = \lambda^2 U_{n-1} \tag{2.233}$$

From eq. 2.232 and 2.233, $\lambda^2 - i2P\lambda - 1 = 0$, which is a quadratic equation. The two values of λ are given by

$$\lambda_1 = \sqrt{1 - P^2} + iP$$
$$\lambda_2 = -\sqrt{1 - P^2} + iP \tag{2.234}$$

Note that as $P \to 0$, $\lambda_1 \to 1$ and $\lambda_2 \to -1$. Hence, solutions associated with λ_1 are the physical modes, and those associated with λ_2 are the computational modes. Thus, although the leapfrog scheme is a convenient scheme with second-order accuracy and is neutral within the stability range of $|\omega\Delta t| \leq 1$, its main drawback is the occurrence of a neutral computational mode. This computational mode exhibits a tendency to amplify slowly in the case of nonlinear equations. Lilly (1965) suggested that an occasional use of a two-level scheme, interspersed with a three-level scheme, eliminates the trouble with the computational mode.

The Adams–Bashforth scheme applied to the oscillation equation gives

$$U_{n+1} = U_n + i\omega\Delta t\left(\frac{3}{2}U_n - \frac{1}{2}U_{n-1}\right) \tag{2.235}$$

From eq. 2.233

$$\lambda^2 - \left(1 + i\frac{3}{2}P\right)\lambda + \frac{i}{2}P = 0$$

The solutions are

$$\lambda_1 = \frac{1}{2}\left(1 + i\frac{3}{2}P + \sqrt{1 - \frac{9}{4}P^2 + iP}\right)$$

(2.236)

$$\lambda_2 = \frac{1}{2}\left(1 + i\frac{3}{2}P - \sqrt{1 - \frac{9}{4}P^2 + iP}\right)$$

As $P \to 0$, $\lambda_1 \to 1$ and $\lambda_2 \to 0$. Thus, the solution associated with the computational mode is damped (as opposed to neutral for the leapfrog scheme) and, hence, there is no trouble from this mode.

It can be shown that the physical mode of the Adams–Bashforth scheme is always unstable. However, fortunately, as in the Heun scheme, the amplification is only a fourth-order term (i.e. $O(\Delta t)^4$) and, hence, the scheme can be used with small values of Δt. The reader is referred to Lilly (1965), Kurihara (1965), and Young (1968) for the evaluation of some other schemes.

2.9 The Courant–Friedrichs–Lewy (C–F–L) Stability Criterion

The Courant–Friedrichs–Lewy (C–F–L) stability criterion for integration in time can be formally derived as follows: assuming a constant advecting velocity c the equations of motion and continuity for the one-dimensional case are

$$\frac{\partial u}{\partial t} + c\frac{\partial u}{\partial x} + g\frac{\partial h}{\partial x} = 0$$

(2.237)

$$\frac{\partial h}{\partial t} + c\frac{\partial h}{\partial x} + D\frac{\partial u}{\partial x} = 0$$

where D is the uniform water depth and h is the free surface height.

Multiply the second part of eq. 2.237 by an arbitrary parameter λ, and add the result to the first equation to give

$$\frac{\partial}{\partial t}(u + \lambda h) + (c + \lambda D)\frac{\partial u}{\partial x} + (g + \lambda c)\frac{\partial h}{\partial x} = 0 \quad (2.238)$$

Following Mesinger and Arakawa (1976), choose λ so that

$$\frac{g + \lambda c}{c + \lambda D} = \lambda \quad (2.239)$$

The solutions of eq. 2.239 are

$$\lambda = \pm\sqrt{\frac{g}{D}} \quad (2.240)$$

Substitution of eq. 2.240 into eq. 2.238 gives

$$\left[\frac{\partial}{\partial t} + (c + \sqrt{gD}\frac{\partial}{\partial x}\right]\left[u + \sqrt{\frac{g}{D}}h\right] = 0$$

(2.241)

$$\left[\frac{\partial}{\partial t} + (c - \sqrt{gD}\frac{\partial}{\partial x}\right]\left[u - \sqrt{\frac{g}{D}}h\right] = 0$$

Thus, eq. 2.237 is equivalent to a system of two advection equations given by eq. 2.241. This means that the parameter $(u + \sqrt{g/D}\,h)$ is advected with a velocity of $c + \sqrt{gD}$

and the parameter $(u - \sqrt{g/D}\,h)$ is advected with a velocity $c - \sqrt{gD}$, both in the positive x direction.

Using a leapfrog scheme for eq. 2.241 and proceeding as above for the advection equation, we get the following stability criterion:

$$(2.242) \quad (c + \sqrt{gD})\frac{\Delta t}{\Delta x} \leq 1$$

which is referred to as the C−F−L condition. Since, usually (in the atmosphere), c is an order of magnitude less than the phase speed of external gravity waves, one often neglects c and writes

$$(2.243) \quad \sqrt{gD}\,\frac{\Delta t}{\Delta x} < 1$$

In the two-dimensional case, it can be shown that the stability condition is

$$(2.244) \quad \sqrt{2gD}\,\frac{\Delta t}{\Delta x} < 1$$

Here, we assume that $\Delta y = \Delta x$. The parameter $(\sqrt{2gD}\,\Delta t/\Delta x)$ is referred to as the Courant number.

Some Efficient Grid Schemes

In the literature on numerical weather prediction, the five different grids shown in Fig. 2.9 have been used frequently. Mesinger and Arakawa (1976) gave a detailed discussion of the properties of these grids. The simplified two-dimensional system for surface gravity waves, assuming the water depth, D, to be constant, can be written as (in the primitive equation form before vertical integration)

$$(2.245) \quad \begin{aligned} &\frac{\partial u}{\partial t} - fv = -g\frac{\partial h}{\partial x} \\ &\frac{\partial v}{\partial t} + fu = -g\frac{\partial h}{\partial y} \\ &\frac{\partial h}{\partial t} + D\left(\frac{\partial u}{\partial x} + \frac{\partial v}{\partial y}\right) = 0 \end{aligned}$$

Use of centered space-differencing with lattice E of Fig. 2.9 and the leapfrog scheme for the time-differencing is one way of constructing an efficient scheme.

A space−time combination grid is shown in Fig. 2.10. If all the variables were computed at each time level, as explained above, there would be two independent solutions (i.e. the solutions with the variables shown in Fig. 2.10 will be independent of the solutions involving the variables not shown on the space−time grid). However, one can obtain the second grid by a translation of the first grid along the line $y = x$. Hence, one can conclude that the space−time lattice obtained by using the lattice shown in Fig. 2.9e at every time step is really a superposition of two basic lattices of the type of Fig. 2.10. Eliassen (1956) suggested that if system 2.245 is solved on only one of the basic lattices, then there will be no computational mode and, hence, considerable saving in computer time, since the computational effort is reduced to half.

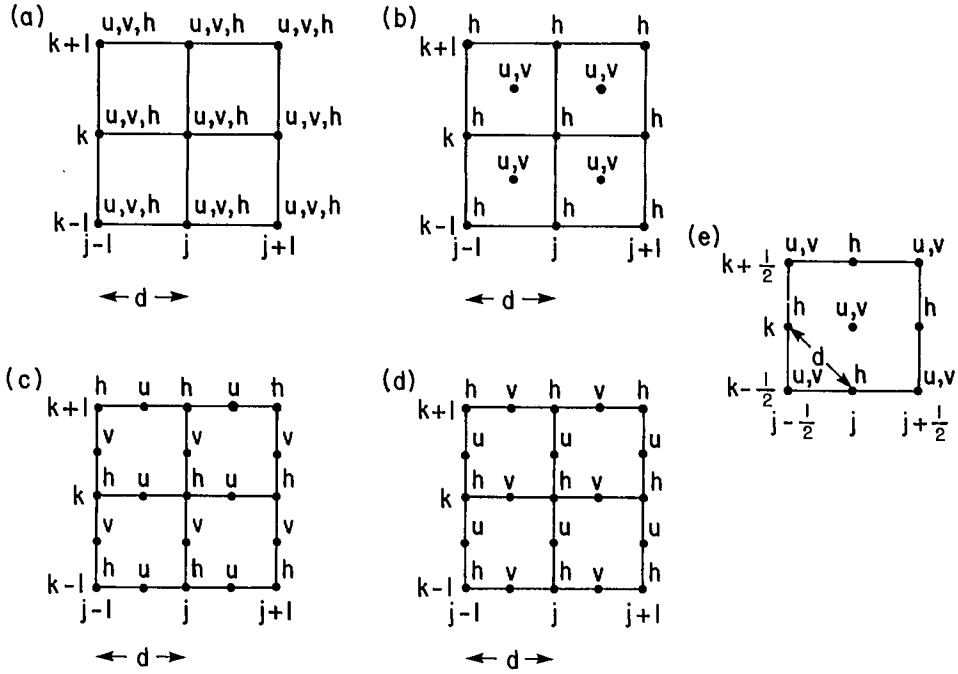

FIG. 2.9. Five different types of grids used in numerical weather prediction models. (Mesinger and Arakawa 1976)

However, Platzman (1963) suggested that the basic Eliassen grid of Fig. 2.10 is really a combination of two Richardson lattices introduced earlier (i.e. height field calculated at one time level and velocity component calculated at the next time level). It is easy to verify that a single Richardson grid is a time-staggered version of the lattice shown in Fig. 2.9c, and this can be used for system 2.245. However, on an Eliassen grid (i.e. Fig. 2.10), there are two independent solutions for system 2.245 and the only coupling between these solutions is through the Coriolis terms.

Next, two computationally efficient explicit schemes will be compared: (1) the forward–backward scheme and (2) leapfrog time-differencing by the Eliassen grid. In both these schemes, computational effort is reduced by using different integration procedures for the height gradient terms in the momentum equations and the divergence term in the continuity equation. Mesinger and Arakawa (1976) referred to these terms as the gravity wave terms.

Economy of computation is achieved in the forward–backward scheme by first integrating the gravity wave terms of either the equations of motion or of continuity forward and the terms of the other equation backward in time. It can be shown that this scheme is stable and allows (from the C–F–L criterion point of view) twice the size of a time step permitted by the leapfrog scheme.

The second method has already been discussed. Both methods halve the computational effort (as compared with a standard leapfrog method) by avoiding the calculation of the computational mode. Between these two methods, the forward–backward method is superior because all the variables are defined at all grid points at every time step,

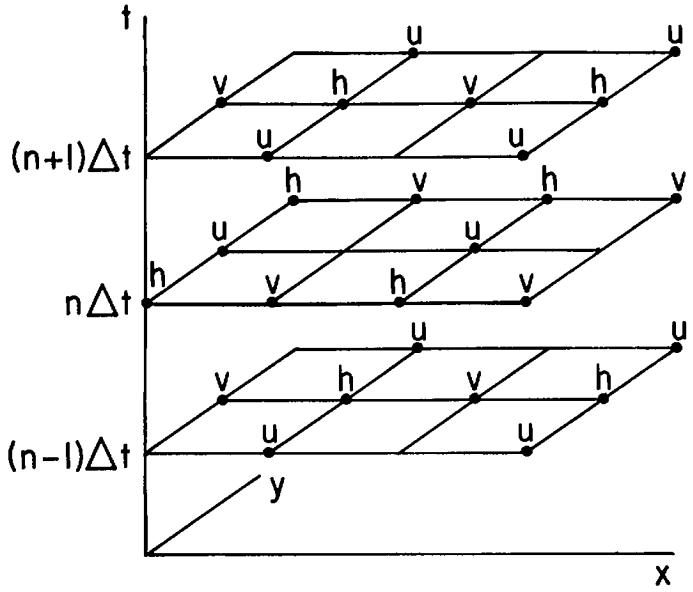

FIG. 2.10. A grid staggered in space and time for use with the leapfrog scheme associated with centered space differencing. (Mesinger and Arakawa 1976)

which makes the programming easy. It could also be modified so that the two-grid interval noise (to be defined later) is eliminated.

For the storm surge problems, the forward–backward scheme has been used by Fischer (1959) and Sielecki (1968), Lauwerier (1962), and Heaps (1969). Welander (1961) referred to this as the half-implicit scheme. Fischer (1959) showed that the forward time-differencing applied to the Coriolis terms makes this scheme unstable. Later, Fischer (1965b) showed how to make this scheme stable.

Another computationally economic explicit scheme was that of Shuman et al. (1975), referred to as the SBC scheme. In this scheme, the surface height field is evaluated at time level $n + 1$, using the leapfrog scheme, and then the momentum equations are integrated using this height field averaged over the time interval $2\Delta t$ through the trapezoidal rule:

$$\frac{1}{4}h_{n-1} + \frac{1}{2}h_n + \frac{1}{4}h_{n+1}$$

This scheme is similar to the forward–backward scheme as far as the stability criterion and the physical solution are concerned. Because of the averaging of the height field, one can use time staggering, even though this is a three-level scheme.

Even though the computationally economic schemes described here permit twice the time step that is required by the C–F–L criterion, the time step is still quite small. For this reason, implicit schemes have been considered as an alternative to the explicit schemes because these schemes are stable for any size of the time step. In the simplest implicit scheme (the trapezoidal rule), the finite-difference form for system 2.245 with the Coriolis terms omitted could be written as

$$u_{n+1} = u_n - g\Delta t\frac{1}{2}(\delta_x h_n + \delta_x h_{n+1})$$

$$v_{n+1} = v_n - g\Delta t\frac{1}{2}(\delta_y h_n + \delta_y h_{n+1}) \tag{2.246}$$

$$h_{n+1} = h_n - D\Delta t\frac{1}{2}[(\delta_x u + \delta_y v)_n + (\delta_x u + \delta_y v)_{n+1}]$$

where the notation δ_x is defined by

$$\delta_x h = \frac{1}{2\Delta x}[h(x + \Delta x, y) - h(x - \Delta x, y)] \tag{2.247}$$

with similar formulae for other variables. It can be shown that this scheme is unconditionally stable and neutral.

Although one can use a larger time step in implicit schemes than in explicit schemes, the main disadvantage of the implicit schemes lies in the necessity of solving a set of simultaneous solutions. For example, in system 2.246, one can apply the operators δ_x and δ_y, respectively, to the first two equations of system 2.246 and substitute these results in the third equation to obtain an equation for the height field. This equation must be solved simultaneously (unlike in the explicit schemes) over the computational region, for instance, by relaxation methods (Crandall 1956).

An alternative is the "alternating direction implicit (ADI)" schemes. In these schemes, basically in each time step, one first evaluates the derivatives along one horizontal coordinate and then along the second coordinate. This splitting will permit the solution of simultaneous equations for a single row or column, which makes the computation economical. For the gravity wave problems, this has been used by Leendertse (1967) and Abbott et al. (1973).

Several other schemes are available for efficiently inverting large matrices. For example, Noye (1977) described a scheme in which a sparse matrix can be converted into a dense matrix, thereby achieving economy in the computational effort.

Usually, Coriolis terms, advection terms, and other terms are omitted more often in implicit schemes than in explicit schemes due to inherent difficulties in the implicit methods. Kwizak and Robert (1971) used a semi-implicit scheme in which these terms are computed explicitly, whereas the rest of the integration proceeds through an implicit scheme.

Although the semi-implicit scheme is one way of making an implicit scheme more efficient, there are better methods available, which are referred to as the "splitting methods." Splitting methods are preferable to semi-implicit methods in that, with the latter, even though the explicit and the implicit parts may be individually stable, there is no assurance that the total scheme will be stable.

To explain the splitting scheme, consider the following simple one-dimensional system:

$$\begin{aligned} &\frac{\partial u}{\partial t} + c\frac{\partial u}{\partial x} + g\frac{\partial h}{\partial x} = 0 \\ &\frac{\partial h}{\partial t} + c\frac{\partial h}{\partial x} + D\frac{\partial u}{\partial x} = 0 \end{aligned} \tag{2.248}$$

Here, the advection terms are made linear by replacing u with a constant c.

Within a given time step, one could first solve the system of advection equations:

$$\frac{\partial u}{\partial t} + c\frac{\partial u}{\partial x} = 0$$
$$\frac{\partial h}{\partial t} + c\frac{\partial h}{\partial x} = 0 \tag{2.249}$$

Let these provisional values (or intermediate values) be represented by u^* and h^*. These values then can be used to solve for the system

$$\frac{\partial u^*}{\partial t} + g\frac{\partial h^*}{\partial x} = 0$$
$$\frac{\partial h^*}{\partial t} + D\frac{\partial u^*}{\partial x} = 0 \tag{2.250}$$

This procedure can be repeated in every time step. The main advantage of the splitting method is that one can use a larger time step for the slower process, such as advection, and a smaller time step for other processes. Its main disadvantage is a greater truncation error than in other schemes. Brown and Pandolfo (1978) devised a scheme to merge two finite-difference schemes with unequal time steps. Basically, this is done by introducing an additional time level and at the expense of increasing the storage requirements.

Two-Grid Interval Noise

Mesinger and Arakawa (1976) have drawn attention to the important problem of "two-grid interval noise," which is the phenomenon of false stationary waves appearing as neutral solutions of the difference equations. Only with the lattice of Fig. 2.9c will this not occur. When the earth's rotation effects are included, the two-grid interval waves appear with incorrect low frequencies as inertial waves (on the lattice of Fig. 2.9d, they will appear stationary). Usually, by using dissipative schemes with a maximum dissipation for the two-grid interval noise and through additional horizontal diffusion, this is controlled. Arakawa (1972) suggested intermittent use of uncentered space-differencing for the gravity wave terms (defined earlier) alternately on opposite sides of the central point. Mesinger (1973) developed a scheme to suppress two-grid interval noise, which is suitable for centered differencing schemes.

Lilly (1965) showed that two-grid interval noise can also occur in time for the leapfrog scheme (i.e. for three time-level schemes). One scheme that was used in numerical weather prediction to suppress two-grid interval noise in time is the intermittent use of a two-level time-differencing scheme. However, this has the disadvantage that the solution that is eliminated is done arbitrarily. An alternative approach is the use of a time filter (Robert 1966).

Propagation Factors

Leendertse (1967) defined "propagation factor" as the ratio of the numerical and analytical solutions for long-wave propagation problems. Usually, the propagation factor is a complex number and thus characterizes the wave deformation in amplitude as well as in phase. Sobey (1970) used the propagation factor in a dimensionless form to compare the following four different finite-difference schemes that have been used in two-dimensional models of long-wave propagation.

Of these four schemes, two are explicit schemes and were originally proposed by Heaps (1969) and Reid and Bodine (1968). The remaining two are implicit schemes and

were proposed by Leendertse (1967) and Abbott (1969). Sobey's (1970) comparison of these four schemes is based on the application of these schemes to the simple system of equations representing two-dimensional propagation of long gravity waves given by system 2.245 and neglecting the earth's rotation. Here, u and v are the vertically averaged values of the velocity components in the x and y directions and D is the uniform depth of the water body. The analytical solution of this system was referred to as the real or physical wave by Sobey (1970). A solution of this system in the form of a Fourier series is

$$\bar{U} = \sum_m \overline{U_m}^* e^{i(\beta_m t + \sigma_m S)} \tag{2.251}$$

where $\bar{U} = (u, v, h)^T$ is the analytic solution, $\overline{U_m}^* = (u_m^*, v_m^*, h_m^*)^T$ is the amplitude of the mth component, β_m is the real wave frequency for the mth component, σ_m is the wave number of the mth component, and S is the coordinate dimension of the direction of wave propagation. The superscript T denotes a transpose vector.

It will be assumed that the direction of wave propagation is oriented at angle γ_m to the positive x-axis. Then, the components of the wave number can be defined as

$$\begin{aligned} \sigma_{1m} &= \sigma_m \cos \gamma_m \\ \sigma_{2m} &= \sigma_m \sin \gamma_m \end{aligned} \tag{2.252}$$

Since this is a linear system, all one has to consider is only one component of the Fourier series (i.e. from eq. 2.251):

$$\bar{U} = \bar{U}^* \, e^{i(\beta t + \sigma_1 x + \sigma_2 y)} \tag{2.253}$$

Substituting eq. 2.253 into system 2.245 (with $f = 0$) gives the following three equations, written for convenience in the matrix notation:

$$\begin{vmatrix} i\beta & 0 & i\sigma_1 gD \\ 0 & i\beta & i\sigma_2 gD \\ i\sigma_1 & i\sigma_2 & i\beta \end{vmatrix} \begin{vmatrix} u^* \\ v^* \\ h^* \end{vmatrix} = 0 \tag{2.254}$$

The determinant of the coefficient matrix, equated to zero, gives the cubic equation

$$(i\beta)^3 + \sigma^2 gDi\beta = 0$$

The solutions are

$$\begin{aligned} \beta_1 &= 0 \\ \beta_{2,3} &= \pm\sigma\sqrt{gD} \end{aligned} \tag{2.255}$$

Let $\bar{U}_{j,k,n}$ represent the finite-difference solution at $j\Delta x$, $k\Delta y$, and $n\Delta t$. The grid used by Heaps (1969) is shown in Fig. 2.11, whereas the grid used by the others considered in this study is shown in Fig. 2.12. Actually, Heaps (1969) used a spherical polar coordinate system, and what is shown here is the equivalent Cartesian coordinate grid.

The finite-difference forms for the Heaps (1969) scheme are

$$\frac{(u_{j,k,n+1} - u_{j,k,n})}{\Delta t} + g\frac{(h_{j+1,k+1,n} - h_{j-1,k+1,n} + h_{j+1,k-1,n} - h_{j-1,k-1,n})}{4\Delta S} = 0 \tag{2.256}$$

$$\frac{(v_{j,k,n+1} - v_{j,k,n})}{\Delta t} + g\frac{(h_{j+1,k+1,n} - h_{j+1,k-1,n} + h_{j-1,k+1,n} - h_{j-1,k-1,n})}{4\Delta S} = 0 \tag{2.257}$$

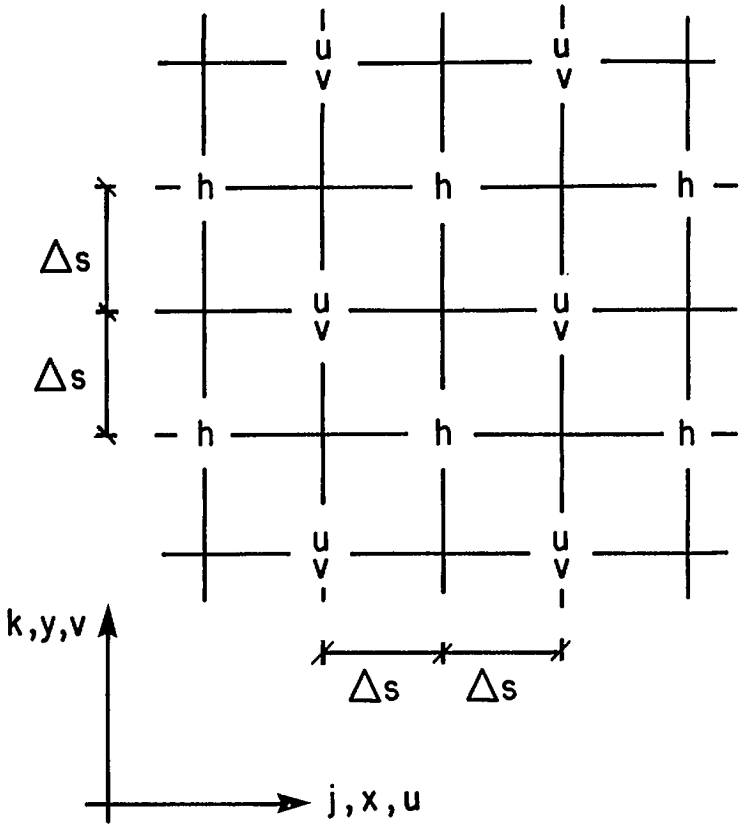

FIG. 2.11. Finite-difference grid used by Heaps (1969).

$$(2.258)\quad \frac{(h_{j,k,n+1} - h_{j,k,n})}{\Delta t} + D\frac{(u_{j+1,k+1,n+1} - u_{j-1,k+1,n+1} + u_{j+1,k-1,n+1} - u_{j-1,k-1,n+1})}{4\Delta S} + D\frac{(v_{j+1,k+1,n+1} - v_{j+1,k-1,n+1} + v_{j-1,k+1,n+1} - v_{j-1,k-1,n+1})}{4\Delta S} = 0$$

In this case, all the eigenvalues of the amplification matrix are within the unit circle on the imaginary plane, provided

$$(2.259)\quad gD\left(\frac{\Delta t}{\Delta S}\right)^2 (\sin^2 \sigma_1 \Delta S \cos^2 \sigma_2 \Delta S + \cos^2 \sigma_1 \Delta S \sin^2 \sigma_2 \Delta S) < 4$$

The stability condition becomes

$$(2.260)\quad gD\left(\frac{\Delta t}{\Delta S}\right)^2 < 4$$

For the Reid and Bodine (1968) scheme, the finite-difference forms are

$$(2.261)\quad \frac{(u_{j,k,n+1} - u_{j,k,n})}{\Delta t} + g\frac{(h_{j+1,k,n} - h_{j-1,k,n})}{2\Delta S} = 0$$

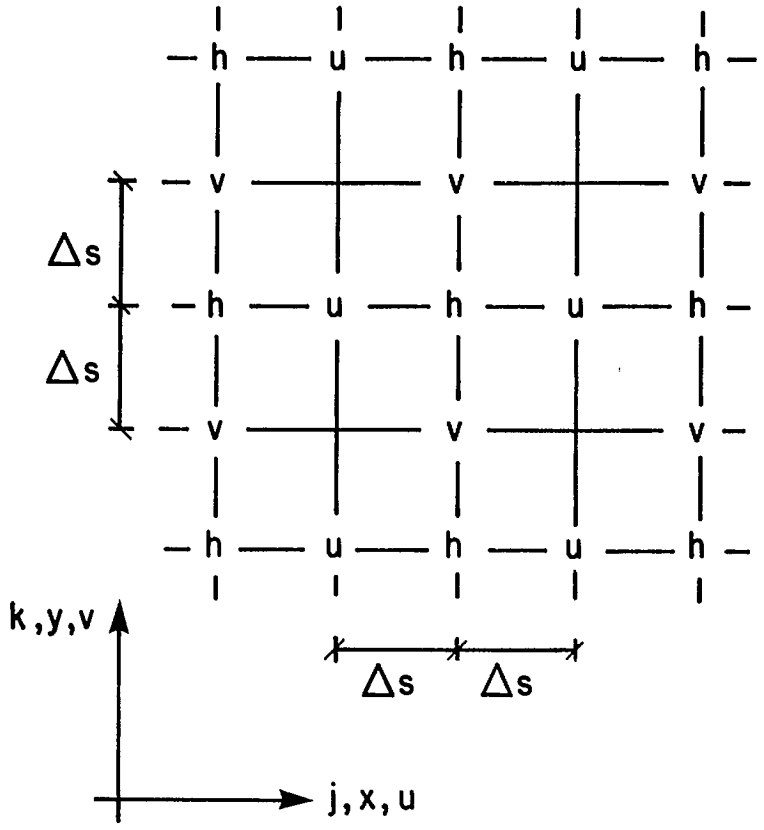

FIG. 2.12. Finite-difference grid used by Reid and Bodine (1968), Leendertse (1967), and Abbott (1969).

$$(2.262)\quad \frac{(v_{j,k,n+1} - v_{j,k,n})}{\Delta t} + g\frac{(h_{j,k+1,n} - h_{j,k-1,n})}{2\Delta S} = 0$$

$$(2.263)\quad \frac{(h_{j,k,n+1} - h_{j,k,n})}{\Delta t} + D\left[\frac{(u_{j+1,k,n+1} - u_{j-1,k,n+1})}{2\Delta S} + \frac{(v_{j,k+1,n+1} - v_{j,k-1,n+1})}{2\Delta S}\right] = 0$$

In this case, all the eigenvalues of the amplification matrix lie on the unit circle in the imaginary plane, provided

$$gD\left(\frac{\Delta t}{\Delta S}\right)^2 (\sin^2 \sigma_1 \Delta S + \sin^2 \sigma_2 \Delta S) \leq 4$$

The stability condition becomes

$$(2.264)\quad gD\left(\frac{\Delta t}{\Delta S}\right)^2 < 2$$

Leendertse (1967) used a leap-frog scheme, and the finite-difference forms are

$$(2.265)\quad \frac{(u_{j,k,n+1/2} - u_{j,k,n})}{\frac{1}{2}\Delta t} + g\frac{(h_{j+1,k,n+1/2} - h_{j-1,k,n+1/2})}{2\Delta S} = 0$$

$$(2.266)\quad \frac{(v_{j,k,n+1/2} - v_{j,k,n})}{\frac{1}{2}\Delta t} + g\frac{(h_{j,k+1,n} - h_{j,k-1,n})}{2\Delta S} = 0$$

$$(2.267)\quad \frac{(h_{j,k,n+1/2} - h_{j,k,n})}{\frac{1}{2}\Delta t} + D\left[\frac{(u_{j+1,k,n+1/2} - u_{j-1,k,n+1/2})}{2\Delta S} + \frac{(v_{j,k+1,n} - v_{j,k-1,n})}{2\Delta S}\right] = 0$$

$$(2.268)\quad \frac{(u_{j,k,n+1} - u_{j,k,n+1/2})}{\frac{1}{2}\Delta t} + g\frac{(h_{j+1,k,n+1/2} - h_{j-1,k,n+1/2})}{2\Delta S} = 0$$

$$(2.269)\quad \frac{(v_{j,k,n+1} - v_{j,k,n+1/2})}{\frac{1}{2}\Delta t} + g\frac{(h_{j,k+1,n+1} - h_{j,k-1,n+1})}{2\Delta S} = 0$$

$$(2.270)\quad \frac{(h_{j,k,n+1} - h_{j,k,n+1/2})}{\frac{1}{2}\Delta t} + D\left[\frac{(u_{j+1,k,n+1/2} - u_{j-1,k,n+1/2})}{2\Delta S} + \frac{(v_{j,k+1,n+1} - v_{j,k-1,n+1})}{2\Delta S}\right] = 0$$

All the eigenvalues of the amplification matrix lie on the unit circle and the scheme, being implicit, is unconditionally stable.

Abbot (1969) also used the leapfrog scheme, and his finite-difference equations become

$$(2.271)\quad \frac{(u_{j,k,n+1} - u_{j,k,n})}{\Delta t} + g\frac{(h_{j+1,k,n+1/2} - h_{j-1,k,n+1/2})}{2\Delta S} = 0$$

$$(2.272)\quad \frac{(h_{j,k,n+1/2} - h_{j,k,n})}{\frac{1}{2}\Delta t} + \frac{D}{2}\left[\frac{(u_{j+1,k,n+1} - u_{j-1,k,n+1})}{2\Delta S} + \frac{(u_{j+1,k,n} - u_{j-1,k,n})}{2\Delta S} + \frac{2(v_{j,k+1,n} - v_{j,k-1,n})}{2\Delta S}\right] = 0$$

$$(2.273)\quad \frac{(v_{j,k,n+1} - v_{j,k,n})}{\Delta t} + \frac{g}{2}\left[\frac{(h_{j,k+1,n+1} - h_{j,k-1,n+1})}{2\Delta S} - \frac{(h_{j,k+1,n} - h_{j,k-1,n})}{2\Delta S}\right] = 0$$

$$(2.274)\quad \frac{(h_{j,k,n+1} - h_{j,k,n+1/2})}{\frac{1}{2}\Delta t} + \frac{D}{2}\left[\frac{(u_{j+1,k,n+1} - u_{j-1,k,n+1})}{2\Delta S} - \frac{(u_{j+1,k,n} - u_{j-1,k,n})}{2\Delta S} + \frac{2(v_{j,k+1,n+1} - v_{j,k-1,n+1})}{2\Delta S}\right] = 0$$

In this case, all the eigenvalues of the amplification matrix lie on or within the unit circle in the imaginary plane. Again, being an implicit scheme, this is unconditionally stable.

The numerical solutions will be referred to as the computed wave. For the four schemes described above, a Fourier series solution is assumed:

$$(2.275)\quad \bar{U} = \bar{U}^* e^{i(\beta' n\Delta t + \sigma_1 J\Delta S + \sigma_2 k\Delta S)}$$

where β' is a complex number of dimension of time^{-1} and is such that Re (β') is the frequency of the computed wave and Im (β') is a measure of the amplitude deformation. Also, let

$$(2.276)\quad \phi = e^{i\beta'\Delta t}$$

Leendertse (1967) defined a complex propagation factor T as the ratio of the com-

puted wave to the real wave after an interval of time in which the real wave propagates over its wavelength L. Thus,

$$T = \frac{e^{i(\beta' t + \sigma S)}}{e^{i(\beta t + \sigma S)}}$$

But

$$t = 2\pi/\beta$$

and

$$S = 2\pi/\sigma$$

Hence,

$$T = e^{i2\pi}[(\beta'/\beta) - 1] \tag{2.277}$$

The system of equations represented by 2.245 (with $f = 0$) has three waves. The first wave represents the steady-state flow for the whole field. It can be shown that, for this wave, for the four schemes considered:

$$\beta_1' = 0$$

Hence,

$$T_1 = 1 \tag{2.278}$$

The second and third waves represent, respectively, the positive and negative characteristics of the system. When a finite-difference scheme is stable:

$$T_2 = T_3 = T \tag{2.279}$$

Concern will be with this value of T. The modulus of T represents the amplitude error of the propagated wave, and the phase error of the wave is given by the argument of T.

It can be shown that

$$|T| = |e^{-\mathrm{Im}(\beta' \Delta t)}|^{\nu} \tag{2.280}$$

where ν is the number of time steps necessary to propagate the real wave over one wavelength. Hence,

$$\nu = \frac{\text{period}}{\Delta t} = \frac{2\pi}{\beta \Delta t} = \frac{2\pi}{\sigma \Delta S} \Big/ \left(\sqrt{gD}\,\frac{\Delta t}{\Delta S}\right)$$

Hence,

$$\mathrm{Arg}\, T = 2\pi\left[\frac{\mathrm{Re}\,(\beta' \Delta t)}{\beta \Delta t} - 1\right] \tag{2.281}$$

Equation 2.281 can be evaluated for the four schemes discussed above.

For convenience of comparing the four schemes, the following dimensionless parameters are defined:

$$\text{Dimensionless celerity} = \sqrt{gD}\,\frac{\Delta t}{\Delta S}$$

$$\text{Dimensionless grid size} = \frac{L}{\Delta S} = \frac{2\pi}{\sigma \Delta S}$$

where $\sigma\Delta S$ is a dimensionless wave number.

The results could be summarized as follows. The explicit scheme of Reid and Bodine (1968), when stable, offers slight advantages over the other schemes. However, if the stability criteria are not met, this scheme exhibits extreme amplitude distortions. The explicit difference scheme of Heaps (1969) exhibits a slow, creeping instability and the wave deformation becomes serious with increase of the dimensionless celerity. Both implicit schemes exhibited satisfactory wave deformation.

Until now, grids with square elements (i.e. $\Delta x = \Delta y = \Delta S$) have been considered. Bennett (1977) used a numerical model in which $\Delta x \neq \Delta y$, and he referred to this as a rectangular element model.

2.10 Energy Calculation as a Test of Computational Stability

Earlier, we have seen that the criteria for computational stability can be established rigorously only for linear equations with constant coefficients. Harris and Jelesnianski (1964) used the criterion of finite energy in the system as a measure of computational stability.

After ignoring bottom friction and the meteorological forcing terms, the energy, E, in the system is given by

$$E = \frac{\rho}{2} \int_A \left[gh^2 + \frac{(M^2 + N^2)}{D} \right] dA \tag{2.282}$$

where A is the surface area of the water, ρ is the water density, h is the free surface height, and M and N are the x and y components of the volume transport, respectively.

The energy, E, is determined in the numerical model through

$$E = \frac{E^* \rho (\Delta S)^2}{2} \tag{2.283}$$

where the finite-difference form for E^* is

$$\begin{aligned} E^* = {} & \sum_{i=1}^{L-1} \sum_{j=1}^{W-1} \{g(h_{i,j})^2 + [(M_{i,j})^2 + (N_{i,j})^2]/D_{i,j}\} + \frac{1}{2} \sum_{j=1}^{W-1} \{g[(h_{0,j})^2 + (h_{L,j})^2] \\ & + [(M_{0,j})^2 + (N_{0,j})^2]/D_{0,j} + [(M_{L,j})^2 + (N_{L,j})^2]/D_{L,j}\} \\ & + \frac{1}{2} \sum_{i=1}^{L-1} \{g[(h_{i,0})^2 + (h_{i,w})^2] + [(M_{i,0})^2 + (N_{i,0})^2]/D_{i,0} \\ & + [(M_{i,w})^2 + (N_{i,w})^2]/D_{i,w}\} + \frac{g}{4} \{(h_{0,0})^2 + (h_{0,W})^2 + (h_{L,0})^2 + (h_{L,w})^2\} \end{aligned} \tag{2.284}$$

Here, the grid points in the x direction range from 0 to L, the grid points in the y direction range from 0 to W, $\Delta x = \Delta y = \Delta S$, and $D_{i,j}$ is the water depth at i,j.

Sielecki (1968) introduced a finite-difference scheme involving forward time differences and examined the energetics of this scheme. She pointed out that in uncentered time-difference schemes even on a nonstaggered space grid measures have to be taken to calculate the energy at any given time correctly.

Sielecki (1968) used the linearized storm surge equations, retained the Coriolis terms and the atmospheric pressure gradient terms, but ignored the wind stress terms and the bottom friction terms. Then, for the set

$$\frac{\partial h}{\partial t} = -\frac{\partial M}{\partial x} - \frac{\partial N}{\partial y}$$

$$\text{(2.285)} \quad \frac{\partial M}{\partial t} = fN - gD\frac{\partial h}{\partial x} - \frac{D}{\rho}\frac{\partial P_a}{\partial x}$$

$$\frac{\partial N}{\partial t} = -fM - gD\frac{\partial h}{\partial y} - \frac{D}{\rho}\frac{\partial P_a}{\partial y}$$

the following finite-difference forms were used:

$$h_{j,k,n+1} = h_{j,k,n} - \frac{\Delta t}{2\Delta S}(M_{j+1,k,n} - M_{j-1,k,n} + N_{j,k+1,n} - N_{j,k-1,n})$$

$$\text{(2.286)} \quad M_{j,k,n+1} = M_{j,k,n} + f\Delta t N_{j,k,n} - \frac{g\Delta t}{2\Delta S} D_{j,k}(h_{j+1,k,n+1} - h_{j-1,k,n+1}) - \frac{\Delta t}{\rho} D_{j,k}\left(\frac{\partial P_a}{\partial x}\right)_{j,k,n+1}$$

$$N_{j,k,n+1} = N_{j,k,n} - f\Delta t M_{j,k,n+1} - \frac{g\Delta t}{2\Delta S} D_{j,k}(h_{j,k+1,n+1} - h_{j,k-1,n+1}) - \frac{\Delta t}{\rho} D_{j,k}\left(\frac{\partial P_a}{\partial y}\right)_{j,k,n+1}$$

Her grid is such that M and N are defined at the same grid points. At the intermediate points in both x and y directions, h is evaluated. Although system 2.286 looks like a combination of explicit and implicit schemes, when evaluated in the order indicated, it is an explicit scheme. This scheme is also quite economical in storage, because the dependent variables have to be stored only at two time levels (and not three), and the scheme is economical in computer time because M and N are evaluated only at even $j + k$ and h only at odd $j + k$.

The stability condition is given by

$$gD_{\max}\left(\frac{\Delta t}{\Delta S}\right)^2 \leq \frac{4 - f^2(\Delta t)^2}{2 - f\Delta t} = 2 + f\Delta t$$

For practical purposes, this condition reduces to

$$\text{(2.287)} \quad \frac{\Delta t}{\Delta S} \leq \sqrt{\frac{2}{gD_{\max}}}$$

The energy relation for system 2.285 is

$$\text{(2.288)} \quad \frac{\partial}{\partial t}\iint_S \left[\frac{(M^2 + N^2)}{2D} + \frac{g}{2}h^2\right] dx\, dy + \frac{1}{\rho}\iint_S P_a \frac{\partial h}{\partial t}\, dx\, dy + \oint_C \left(gh + \frac{P_a}{\rho}\right)\boldsymbol{Mn}\, dl = 0$$

Here, S is the surface area of the water body and C is its contour. For a closed basin, the third term involving the normal transport components becomes zero. Let the length (in the x direction) and width (in the y direction) of the water body be $(R - 1)\Delta S$ and $(T - 1)\Delta S$. Then, the first part of the first term in eq. 2.288 becomes

$$(2.289)\quad \frac{2}{(\Delta S)^2/2}\iint_S \frac{M^2}{2D}\,dx\,dy \approx \left(\frac{M_{1,1}^2}{D_{1,1}} + \frac{M_{1,T}^2}{D_{1,T}} + \frac{M_{R,1}^2}{D_{T,1}} + \frac{M_{R,T}^2}{D_{R,T}}\right) + 2\sum_{k=1}^{(T-3)/2}\left(\frac{M_{1,2k+1}^2}{D_{1,2k+1}} + \frac{M_{R,2k+1}^2}{D_{R,2k+1}}\right) + 2\sum_{j=1}^{(R-3)/2}\left(\frac{M_{2j+1,1}^2}{D_{2j+1,1}} + \frac{M_{2j+1,T}^2}{D_{2j+1,T}}\right) + 4\sum_{j=1}^{(R-3)/2}\sum_{k=1}^{(T-3)/2}\left(\frac{M_{2j+1,2k+1}^2}{D_{2j+1,2k+1}}\right) + 4\sum_{j=1}^{(R-1)/2}\sum_{k=1}^{(T-1)/2}\left(\frac{M_{2j,2k}^2}{D_{2j,2k}}\right)$$

The finite-difference forms for the other terms can be written similarly.

However, there is difficulty associated with the time-derivative terms. In the finite-difference scheme 2.286, certain terms were evaluated at step n and others at step $n+1$, and the scheme is different for the different dependent variables. Hence, to obtain a finite-difference scheme consistent with eq. 2.288, define

$$(2.290)\quad (EN)_n = \frac{[3(E_{\mathrm{KIN}})_{n-1} + (E_{\mathrm{KIN}})_n]}{4} + \frac{[(E_{\mathrm{POT}})_{n-1} + 3(E_{\mathrm{POT}})_n]}{4}$$

where

$$(2.291)\quad E_{\mathrm{KIN}} = \frac{1}{2}\sum_j\sum_k \frac{(M_{j,k}^2 + N_{j,k}^2)}{D_{j,k}}(\Delta S)^2$$

$$E_{\mathrm{POT}} = \frac{g}{2}\sum_j\sum_k h_{j,k}^2(\Delta S)^2$$

2.11 Treatment of Open Boundaries

At times, storm surge calculations might have to be performed in a limited region of a large water body. This problem could be tackled in at least two different ways. In one approach, one can perform the calculations in the large water body of which the smaller water body is a part and then use the results for the area of interest. However, this approach is not economical and may not even be possible for certain water bodies. Also, there may be a problem with the resolution, since one has to model a larger water body. In the second approach, artificial open boundaries can be introduced around the area of interest and the calculations can be performed in the limited region of interest. However, along these artificial open boundaries, certain conditions have to be introduced, and without proper considerations, these conditions might make the results in the interior region inaccurate.

The commonly used practice of putting zero surface elevation at the sea boundary is not at all satisfactory, because this amounts to perfect reflection at the sea boundary. A better approximation (Heaps 1974; Henry and Heaps 1976) is to assume that all outward traveling waves are normal to the boundary and to calculate the volume transports M (or N) from the water level h at the nearest interior grid point; i.e. $M = [g(D + h)]h^{1/2}$. This is the so-called radiation condition.

Reid (1975) corrected a misconception commonly held (e.g. Forristall 1974) in applying open boundary conditions. Forristall (1974, p. 2722) stated "At shallow water (lateral) boundary points, the derivative of velocity perpendicular to the boundary is set equal to zero so that the transport across the boundary may be calculated from the adjacent flow. This condition is designed to let long waves pass unimpeded through the artificial boundary."

Reid showed that, although such a condition will permit flow of fluid to or from the system, it will produce total reflection of long waves and not zero reflection as Forristall stated.

To show this, following Reid (1975), assume a simple harmonic wave of frequency ω incident at an angle θ relative to the x-axis. Owing to this, the transport for $x \geq 0$ is

$$M_i = A_i \cos [\omega t + k(x \cos \theta + y \sin \theta)]$$

where A_i is the local incident amplitude for transport and k is a local wave number which is determined by the frequency, the local water depth, D, and the Coriolis parameter, f. In case of reflection, the transport for $x \geq 0$ will be in the form

$$M_r = A_r \cos [\omega t + k(-x \cos \theta + y \sin \theta) + \phi]$$

where A_r is the reflected amplitude for transport and ϕ is a relative phase angle.

The boundary condition under consideration is

$$\frac{\partial M}{\partial x} = 0 \text{ at } x = 0$$

where M is the total transport in the x direction, i.e. $(M_i + M_r)$ on the positive (interior) side of the open boundary. It can be seen that for a nontrivial A_i and $0 \leq |\theta| < \pi/2$:

$$A_r = A_i \text{ and } \phi = 0$$

Hence, the above boundary condition leads to total reflection with no phase change for the reflected M field.

Reid (1975) suggested that to permit wave transmission through the open boundary, one has to force the normal component of transport to be in phase with the water level deviation. The outward flux of energy J through a unit length of vertical boundary, from the bottom to the surface, is $J = \rho(gh + 1/2q^2)Q_n$ where Q_n is the volume transport through a unit width of boundary taken positive outwards, h is the surface elevation, ρ is the water density, and q is the speed of the fluid. For the radiation of energy it is required that the average value of J over one wave cycle be positive. If $h \gg q^2/2g$, then the necessary condition is that hQ_n be positive at the boundary. Hence, a boundary condition of the type (used by Reid and Bodine 1968) $Q_n = ch$, where c is a positive coefficient (having dimensions of velocity), permits proper radiation of energy through the open boundary.

Wurtele et al. (1971) developed boundary conditions that will allow disturbances to travel out of the computational region with negligible reflection at the open boundaries. In developing these boundary conditions the concept of Riemann invariants has been used. These conditions in one and two space dimensions have been used to study the flow around a sea mound, island arc, and on a shelf, and comparison was made with the Sommerfeld's (1949) radiation condition as described by Vastano and Reid (1967).

Wurtele et al. (1971) coupled the meteorological forcing terms into the single term (F_x, F_y) and began with the simple system

$$\frac{\partial h}{\partial t} = -\left(\frac{\partial M}{\partial x} + \frac{\partial N}{\partial y}\right)$$

$$\frac{\partial M}{\partial t} = -gD\frac{\partial h}{\partial x} + F_x \tag{2.292}$$

$$\frac{\partial N}{\partial t} = -gD\frac{\partial h}{\partial y} + F_y$$

Let Δ denote a forward-difference operator, δ specify a central-difference operator, and indices j, k, and n are such that

$$x, y, t = (j\Delta x, k\Delta y, n\Delta t)$$

Also let $\Delta x = \Delta y = \Delta S$. Then the finite-difference forms of system 2.292 are

$$\Delta_n \eta_{j,k,n} = -\frac{\Delta t}{2\Delta S}(\delta_j M_{j,k,n} + \delta_k N_{j,k,n})$$

$$\Delta_n M_{j,k,n} = -gD_{j,k}\frac{\Delta t}{2\Delta S}\delta_j h_{j,k,n+1} \tag{2.293}$$

$$\Delta_n N_{j,k,n} = -gD_{j,k}\frac{\Delta t}{2\Delta S}\delta_k h_{j,k,n+1}$$

For the case of uniform depth and zero external forces, Garabedian (1964) gave the following analytic solution for the water level h:

$$h(x, y, t) = \frac{1}{c}\frac{\partial}{\partial t}\frac{1}{2\pi}\iint \frac{G_1(x + \zeta_1, y + \zeta_2)}{\sqrt{c^2t^2 - \zeta_1^2 - \zeta_2^2}}\, d\zeta_1\, d\zeta_2 + \frac{1}{2\pi c}\iint \frac{G_2(x + \zeta_1, y + \zeta_2)}{\sqrt{c^2t^2 - \zeta_1^2 - \zeta_2^2}}\, d\zeta_1\, d\zeta_2 \tag{2.294}$$

where $\zeta_1^2 + \zeta_2^2 < c^2t^2$, $c = \sqrt{gD}$, $G_1 = h(x, y, 0)$, and $G_2 = \dfrac{\partial h}{\partial t}(x, y, 0)$.

Equation 2.294 gives the solution at any point and time as an area integral over the circular domain of dependence cut from the initial data plane by the characteristic cone

$$(x - x_0)^2 + (y - y_0)^2 - c(t - t_0)^2 = 0$$

and (x_0, y_0, t_0) denotes the initial state. In the one-dimensional case, eq. 2.294 reduces to the d'Alembert solution

$$h = \frac{1}{2}[G_1(x + ct) + G_1(x - ct)] + \frac{1}{2}\int_{-ct}^{ct} G_2(x + \xi)\, d\xi \tag{2.295}$$

It can be seen that (in the two-dimensional case) once the disturbance arrives at any point in the computational region, irrespective of how concentrated it might be originally, it will not simply vanish at this point. If this location under consideration is an open boundary, the disturbance outside that boundary will influence the solution in the region interior to the boundary. Thus, the interior solution is quite dependent on the condition applied at the open boundary. Similar results hold for the one-dimensional case. These results are for the case $G_1 \neq 0$, $G_2 \neq 0$. However, if $G_2 = 0$, a concentrated disturbance progresses without change of shape and an arbitrary point returns to its original state after the passage of the disturbance.

For the one-dimensional case, system 2.292 reduces to

$$\frac{\partial M}{\partial t} = c^2\frac{\partial h}{\partial x} \tag{2.296}$$

$$\frac{\partial h}{\partial t} = -\frac{\partial M}{\partial x} \tag{2.297}$$

Equation 2.297 $\times\, c \pm$ eq. 2.296 gives

$$\frac{\partial}{\partial t}(M + ch) + c\frac{\partial}{\partial x}(M + ch) = 0$$

(2.298)

$$\frac{\partial}{\partial t}(M - ch) - c\frac{\partial}{\partial x}(M - ch) = 0$$

Equation 2.298 states that the linear Riemann invariants $M \pm ch$ are respectively conserved along the directions

$$\frac{\partial x}{\partial t} = \pm c$$

The characteristics $x \pm ct$ could be drawn to intersect the open boundaries at $x = 0$ and L. The boundary conditions are

$$M + ch = 0 \text{ at } x = 0$$

(2.299)

$$M - ch = 0 \text{ at } x = L$$

These conditions represent the influence of the outer region on the interior region. If h is determined at each boundary ($x = 0$ and L) by a one-sided space-difference, then M may be determined from system 2.299. In the two-dimensional case, the condition becomes

(2.300) $(M^2 + N^2) - ch = 0$

at all the boundaries.

2.12 Treatment of the Nonlinear Advective Terms

Until now, only the linearized versions of the storm surge equations have been considered. In shallow-water areas and in the computation of the horizontal motion, at times the nonlinear advective terms might have to be included. Charnock and Crease (1957) showed through dimensional analysis that the nonlinear advective terms become important when the free surface height is of the same order of magnitude as the water depth.

Flather and Heaps (1975) developed a model for Morecambe Bay allowing for the inclusion of the nonlinear advective terms. In the depth-averaged form, the equations of motion and continuity are

(2.301) $$\frac{\partial u}{\partial t} + u\frac{\partial u}{\partial x} + v\frac{\partial u}{\partial y} - fv + \frac{ku(u^2 + v^2)^{1/2}}{H} + g\frac{\partial h}{\partial x} = 0$$

(2.302) $$\frac{\partial v}{\partial t} + u\frac{\partial v}{\partial x} + v\frac{\partial v}{\partial y} + fu + \frac{kv(u^2 + v^2)^{1/2}}{H} + g\frac{\partial h}{\partial y} = 0$$

(2.303) $$\frac{\partial h}{\partial t} + \frac{\partial}{\partial x}(Hu) + \frac{\partial}{\partial y}(Hv) = 0$$

Total water depth $= H = D + h$ and $D =$ undisturbed water depth.

The depth mean currents are defined as

$$u = \frac{1}{H}\int_{-D}^{h} u'\,dz,\ v = \frac{1}{H}\int_{-D}^{h} v'\,dz$$

where $u'$and v' are horizontal current components at depth z below the sea surface. To write the depth-averaged forms for the advective terms, we assume that the currents do not

vary significantly in the vertical direction, i.e.

$$\int_{-D}^{h} u'^2\,dz = Hu^2,\ \int_{-D}^{h} v'^2\,dz = Hv^2$$

$$\int_{-D}^{h} u'v'\,dz = Huv$$

Initially

(2.304) $u = v = 0$ and $h = 0$ at $t = 0$

The grid is similar to that shown in Fig. 2.12.

The scheme for the nonlinear advective terms used by Flather and Heaps (1975) is somewhat different from the schemes used by other authors, e.g. Lax and Wendroff (1960), Crowley (1970), and Sielecki and Wurtele (1970). The scheme to be described below is based on the angled derivative approach suggested by Roberts and Weiss (1966). To explain this approach, following Flather and Heaps (1975), the simple nonlinear one-dimensional advection equation will be considered:

(2.305) $$\frac{\partial u}{\partial t} + u\frac{\partial u}{\partial x} = 0$$

The finite-difference form of this can be written as

(2.306) $$\frac{[u_i(t+\Delta t) - u_i(t)]}{\Delta t} + \bar{u}_i(t)\left\{\frac{1}{2}[u_i(t+\Delta t) + u_{i+1}(t)] - \frac{1}{2}[u_{i-1}(t+\Delta t) + u_i(t)]\right\}\Big/ 2\Delta S = 0$$

where

$$\bar{u}_i = \frac{1}{4}(u_{i-1} + 2u_i + u_{i+1})$$

Here, $2\Delta S$ is the distance between successive u values (or successive v or successive h values). Here, it is assumed that before computing $u_i(t+\Delta t)$, $u_j(t)$ for $1 \le j \le m$ and $u_j(t+\Delta t)$ for $1 \le j \le i-1$ are already known. The finite-difference approximation for $\partial u/\partial x$ is called the angled derivative and is correctly centered in space and time.

In the next step, the direction of integration is reversed so that integration is performed in the direction of decreasing i. Then, the finite-difference approximation is

(2.307) $$\frac{[u_i(t+\Delta t) - u_i(t)]}{\Delta t} + \bar{u}_i(t)\left\{\frac{1}{2}[u_i(t) + u_{i+1}(t+\tau)] - \frac{1}{2}[u_{i-1}(t) + u_i(t+\Delta t)]\right\}\Big/ 2\Delta S = 0$$

provided $u_j(t)$ for $1 \le j \le m$ and $u_j(t+\Delta t)$ for $i+1 \le j \le m$ are known. Equations 2.306 and 2.307 can be rearranged to give explicit forms for $u_i(t+\Delta t)$.

Flather and Heaps (1975) described two different ways of extending the angled derivative approach to include all the nonlinear advective terms. In the first method, the variations in the components of the depth-averaged current over one time step due to advection alone are calculated, and these are added to the variations caused by other terms.

Before writing the finite-difference forms, for convenience, define

$$d_i = \frac{1}{2}(H_i + H_{i+1})$$

$$\mathcal{D}_i = \max\,(d_i, H_0)$$

$$e_i = \frac{1}{2}(H_i + H_{i+m})$$

$$E_i = \max\,(e_i, H_0)$$

$$\widetilde{u_i} = \frac{1}{4}(u_{i+1} + u_i + u_{i+m+1} + u_{i+m})$$

$$\widetilde{v_i} = \frac{1}{4}(v_{i-m} + v_{i-m+1} + v_i + v_{i+1})$$

H_0 is a prescribed minimum depth for the denominator in the frictional terms which could otherwise lead to a singularity at $H = 0$. Since $\mathcal{D}_i$ is the maximum value of d_i or H_0, it cannot be smaller than H_0. Similar arguments hold for E_i. The reason for prescribing a minimum depth is (besides avoiding possible division by zero) to cut off frictional damping before it becomes too great (due to very small water depth) and the boundary layer considerations on which the quadratic bottom friction is formulated are no longer applicable. Let there be l rows and m columns in the grid.

The finite-difference forms for the tentative values of u and v are denoted by an asterisk. Then,

$$\text{(2.308)}\quad \frac{[u_i^*(t+\Delta t) - u_i(t)]}{\Delta t} = f\,\widetilde{v_i}(t) - k u_i^*(t+\Delta t)\frac{[u_i^2(t) + \widetilde{v_i}^2(t)]^{1/2}}{D_i(t)} - \frac{g[h_{i+1}(t+\Delta t) - h_i(t+\Delta t)]}{2\Delta S}$$

$$\text{(2.309)}\quad \frac{[v_i^*(t+\Delta t) - v_i(t)]}{\Delta t} = -f\,\widetilde{u_i}^*(t+\Delta t) - \mathrm{k} v_i^*(t+\Delta t)\frac{[\widetilde{u_i}^2(t) + v_i^2(t)]^{1/2}}{E_i(t)} - \frac{g[h_i(t+\Delta t) - h_{i+m}(t+\Delta t)]}{2\Delta S}$$

For odd time steps with increasing i, the following are final forms for u_i and v_i:

$$\text{(2.310)}\quad \frac{[u_i(t+\Delta t) - u_i^*(t+\Delta t)]}{\Delta t} = -\frac{1}{4\Delta S}\overline{u_i}^*(t+\Delta t)[u_{i+1}^*(t+\Delta t) - u_i^*(t+\Delta t) + u_i(t+\Delta t) - u_{i-1}(t+\Delta t)] - \frac{1}{8\Delta S}\{[v_{i-m}^*(t+\Delta t) + v_{i-m+1}^*(t+\Delta t)] \times [u_{i-m}(t+\Delta t) - u_i(t+\Delta t)] + [v_i^*(t+\Delta t) + v_{i+1}^*(t+\Delta t)] \times [u_i^*(t+\Delta t) - u_{i+m}^*(t+\Delta t)]\}$$

and

$$\text{(2.311)}\quad \frac{[v_i(t+\Delta t) - v_i^*(t+\Delta t)]}{\Delta t} = -\frac{1}{8\Delta S}\{[u_i^*(t+\Delta t) + u_{i+m}^*(t+\Delta t)] \times [v_{i+1}^*(t+\Delta t) - v_i^*(t+\Delta t)] + [u_{i-1}^*(t+\Delta t) + u_{i+m-1}^*(t+\Delta t)] \times [v_i(t+\Delta t) - v_{i-1}(t+\Delta t)]\} - \frac{1}{4\Delta S}\bar{v}_i^*(t+\Delta t)[v_{i-m}(t+\Delta t) - v_i(t+\Delta t) + v_i^*(t+\Delta t) - v_{i+m}^*(t+\Delta t)]$$

The term for $\overline{u_i}$ has been defined. Define $\overline{v_i}$:

$$\overline{v_i} = \frac{1}{4}(v_{i-m} + 2v_i + v_{i+m}) \tag{2.312}$$

Equations similar to 2.310 and 2.311 are true for even time steps with decreasing i. The finite-difference form for the continuity equation is

$$\frac{[h_i(t + \Delta t) - h_i(t)]}{\Delta t} = -[d_i(t)u_i(t) - d_{i-1}(t)u_{i-1}(t) + e_{i-m}(t)v_{i-m}(t) - e_i(t)v_i(t)]/2\Delta S \tag{2.313}$$

In the second method, Flather and Heaps (1975) included the advection terms directly and gave the following finite-difference forms:

$$\begin{aligned}[u_i(t+\Delta t) - u_i(t)]/\Delta t = &-\frac{1}{4\Delta S}\overline{u_i}(t)[u_{i+1}(t) - u_i(t) + u_i(t+\Delta t) \\ &- u_{i-1}(t+\Delta t)] - \frac{1}{8\Delta S}\{[v_{i-m}(t) + v_{i-m+1}(t)][u_{i-m}(t + \Delta t) - u_i(t + \Delta t)] \\ &+ [v_i(t) + v_{i+1}(t)][u_i(t) - u_{i+m}(t)]\} + f\,\widetilde{v_i}(t) - ku_i(t + \Delta t) \\ &\times \frac{[u_i^2(t) + \widetilde{v_i}^2(t)]^{1/2}}{\mathcal{D}_i(t)} - g[h_{i+1}(t + \Delta t) - h_i(t + \Delta t)]/2\Delta S\end{aligned} \tag{2.314}$$

and

$$\begin{aligned}[v_i(t + \Delta t) - v_i(t)]/\Delta t = &-\frac{1}{8\Delta S}\{[u_i(t) + u_{i+m}(t)][v_{i+1}(t) - v_i(t)] \\ &+ [u_{i-1}(t) + u_{i+m-1}(t)][v_i(t + \tau) - v_{i-1}(t + \Delta t)]\} \\ &- \frac{1}{4\Delta S}\bar{v}_i(t)[v_{i-m}(t + \Delta t) - v_i(t + \Delta t) + v_i(t) - v_{i+m}(t)] \\ &- f\,\widetilde{u_i}(t + \Delta t) - kv_i(t + \Delta t)\frac{[\widetilde{u_i}^2(t) + v_i^2(t)]^{1/2}}{E_i(t)} \\ &- g[h_i(t + \Delta t) - h_{i+m}(t + \Delta t)]/2\Delta S\end{aligned} \tag{2.315}$$

Equations 2.314 and 2.315 are for the odd time steps for increasing i and with u calculated before v. For even time steps, for decreasing i, v will be calculated before u.

One word of caution: since not all the values of the variables required to compute from the above equations are defined adjacent to open boundaries, one has to ignore the advective terms within a distance of $2\Delta S$ from these boundaries. For a calculation for Morecambe Bay, Flather and Heaps found some instability (in the form of grid scale oscillations) originating from the corner of the open boundary. This instability was removed by omitting the nonlinear advective terms within a distance of $6\Delta S$ from the open boundaries. Leendertse (1967) excluded the nonlinear advective terms in a distance of $2\Delta S$ from land boundaries to suppress instability.

Henry (1982) encountered a similar instability in a calculation of the circulation in Bridport Inlet and suppressed the instability by using a procedure similar to that of Flather and Heaps (1975).

Crean (1978) modified the scheme of Flather and Heaps (1975) in three ways by (a)

using the vertically integrated forms of the equations (i.e. transport components) rather than the depth-averaged forms, (b) using the flux forms for the nonlinear advective terms, and (c) including the horizontal frictional terms. Crean (personal communication) found it necessary to include horizontal friction to control the slight instability due to the inclusion of the nonlinear advective terms (he called this instability noodling). He defined noodling as small grid scale fluctuations in the direction of velocity vectors occurring in the areas where nonlinear advective terms are important. The question of computation of the second derivatives near the boundary (to evaluate the horizontal frictional terms) is avoided by setting the horizontal friction coefficient, ν_H, to zero near the boundaries. This means that in the shallow areas near the coast, bottom stress is dominant over lateral stress.

The forms of the equations of motion used by Crean (1978) are as follows:

$$\frac{\partial M}{\partial t} + \frac{\partial}{\partial x}\left(\frac{M^2}{H}\right) + \frac{\partial}{\partial y}\left(\frac{MN}{H}\right) - fN + \nu_H\left(\frac{\partial^2 M}{\partial x^2} + \frac{\partial^2 M}{\partial y^2}\right) + gH\frac{\partial h}{\partial x} + \frac{KM\sqrt{M^2 + N^2}}{H^2} = 0 \tag{2.316}$$

$$\frac{\partial N}{\partial t} + \frac{\partial}{\partial x}\left(\frac{MN}{H}\right) + \frac{\partial}{\partial y}\left(\frac{N^2}{H}\right) + fM + \nu_H\left(\frac{\partial^2 N}{\partial x^2} + \frac{\partial^2 N}{\partial y^2}\right) + gH\frac{\partial h}{\partial y} + \frac{KN\sqrt{M^2 + N^2}}{H^2} = 0 \tag{2.317}$$

$$\frac{\partial h}{\partial t} + \frac{\partial M}{\partial x} + \frac{\partial N}{\partial y} = 0 \tag{2.318}$$

where $H = D + h$ is the total water depth, D is the undisturbed water depth, K is a bottom friction coefficient, and ν_H is the horizontal eddy viscosity. The grid is similar to that used by Flather and Heaps (1975) and Hansen (1962). The finite-difference form for the x-momentum equation is

$$\frac{(M_{j,n+1} - M_{j,n})}{\Delta t} = f\bar{\bar{N}}_{j,n} - \frac{g\bar{H}^x_j}{\Delta S}(h_{j+1,n+1} - h_{j,n+1}) - \frac{KM_{j,n}(M^2_{j,n} + \bar{\bar{N}}^2_{j,n})^{1/2}}{(\bar{H}^x_j)^2} - \left[\frac{(\bar{M}^x_{j,n})^2}{\frac{1}{2}(\bar{H}^x_j + \bar{H}^x_{j+1})} - \frac{(\bar{M}^x_{j-1,n})^2}{\frac{1}{2}(\bar{H}^x_{j-1} + \bar{H}^x_j)}\right]\frac{1}{\Delta S} - \left(\frac{\bar{M}^y_{j,n}\bar{N}^x_{j-m,n}}{\bar{\bar{H}}_j} - \frac{\bar{M}^y_{j+m}\bar{N}^x_{j,n}}{\bar{\bar{H}}_{j-m}}\right)\frac{1}{\Delta S} + \frac{\nu_{H_j}}{(\Delta S)^2}(M_{j-m,n} + M_{j+m,n} + M_{j-1,n} + M_{j+1,n} - 4M_{j,n}) \tag{2.319}$$

The finite-difference form for the y-momentum equation is

$$\frac{(N_{j,n+1} - N_{j,n})}{\Delta t} = -f\bar{\bar{M}}_j - \frac{g\bar{H}^y_{j-m}}{\Delta S}(h_{j,n+1} - h_{j-m,n+1}) - KN_{j,n}(\bar{\bar{M}}^2_{j,n} + N^2_{j,n})^{1/2}/(\bar{H}^y_{j+m})^2 - \left(\frac{\bar{M}^y_{j+m,n}\bar{N}^x_{j,n}}{\bar{\bar{H}}_{j+m}} - \frac{\bar{M}^y_{j+m-1,n}\bar{N}^x_{j-1,n}}{\bar{\bar{H}}_{j+m-1}}\right)\frac{1}{\Delta S} - \left[\frac{(\bar{N}^y_{j,n})^2}{\frac{1}{2}(\bar{H}^y_j + \bar{H}^y_{j+m})} - \frac{(\bar{N}^y_{j+m,n})^2}{\frac{1}{2}(\bar{H}^y_{j+m} + \bar{H}^y_{j+2m})}\right]\frac{1}{\Delta S} + \frac{\nu_{H_j}}{(\Delta S)^2}(N_{j-m,n} + N_{j+m,n} + N_{j-1,n} + N_{j+1,n} - 4N_{j,n}) \tag{2.320}$$

where

$$\bar{M}_j^x = \frac{1}{2}(M_j + M_{j+1})$$

$$\bar{M}_j^y = \frac{1}{2}(M_j + M_{j-m})$$

$$\bar{\bar{H}}_j = \frac{1}{4}(H_j + H_{j-m} + H_{j-m+1} + H_{j+1}) \tag{2.321}$$

$$\bar{\bar{M}}_j = \frac{1}{4}(M_j + M_{j+m} + M_{j+m-1} + M_{j-1})$$

$$\bar{\bar{N}}_j = \frac{1}{4}(N_j + N_{j-m} + N_{j-m+1} + N_{j+1})$$

The finite-difference form for the continuity equation is

$$\frac{(h_{j,n+1} - h_{j,n})}{\Delta t} = -\frac{(M_{j,n} - M_{j-1,n} + N_{j-m,n} - N_{j,n})}{\Delta S} \tag{2.322}$$

The stability criterion is

$$\Delta t \leq \frac{\Delta S}{\sqrt{2gH_{\max}}}$$

Falconer (1980) introduced a conditionally stable three time level implicit scheme including the nonlinear advective terms. This scheme is especially suitable for narrow-entrance harbors and estuaries where the nonlinear instability problems associated with rapidly changing velocity fields might be very important.

The equations of motion and continuity in the depth-averaged form are as follows:

$$\frac{\partial U}{\partial t} + \alpha\left(\frac{\partial U^2}{\partial x} + \frac{\partial UV}{\partial y}\right) - fV + g\frac{\partial h}{\partial x} + \frac{gU(U^2 + V^2)^{1/2}}{(D + h)C^2} - \frac{\rho'\gamma WW_x}{(D + h)} - \nu_H\left(\frac{\partial^2 U}{\partial x^2} + \frac{\partial^2 U}{\partial y^2}\right) = 0 \tag{2.323}$$

$$\frac{\partial V}{\partial t} + \alpha\left(\frac{\partial VU}{\partial x} + \frac{\partial V^2}{\partial y}\right) + fU + g\frac{\partial \eta}{\partial y} + \frac{gV(U^2 + V^2)^{1/2}}{(D + h)C^2} - \frac{\rho'\gamma WW_y}{(D + h)} - \nu_H\left(\frac{\partial^2 V}{\partial x^2} + \frac{\partial^2 V}{\partial y^2}\right) = 0 \tag{2.324}$$

$$\frac{\partial h}{\partial t} + \frac{\partial}{\partial x}[(D + h)U] + \frac{\partial}{\partial y}[(D + h)V] = 0 \tag{2.325}$$

where α is a correction factor for the nonuniformity of the vertical velocity profile, C is a Chezy roughness coefficient, ρ' is the ratio of the density of air to that of water, γ is a wind resistance coefficient, and W, W_x, and W_y are the absolute wind velocity and its x and y components, respectively. Note that in eq. 2.323 and 2.324 the fifth and sixth terms represent the bottom stress and the wind stress, respectively.

Assume that the velocity profile in the vertical plane can be represented by the logarithmic velocity distribution:

$$u = \frac{U^*}{k}\ln(D + z) + \text{constant} \tag{2.326}$$

where U^* is the shear velocity and k is the Von Karman constant. Then,

$$\alpha = 1 + \frac{g}{C^2 k^2}$$

and define

$$(2.327)\quad l = k(D + z)\left[1 - \frac{(D + z)}{(D + h)}\right]^{1/2}$$

where l is the mixing length and z is the vertical coordinate, positive upward. The depth-averaged horizontal eddy viscosity, ν_H, is given by

$$\nu_H = \frac{\beta\sqrt{g}(D + h)(U^2 + V^2)^{1/2}}{C}$$

where

$$\beta = k/6$$

The finite-difference equations are expressed in the alternate direction implicit (ADI) form with two successive operations in time during each time step. For the first part from $n\Delta t$ to $(n + 1/2)\,\Delta t$, the terms involving U and h of the continuity and the x-momentum equation are expressed implicitly whereas the terms involving V are expressed explicitly. For the second part, i.e. during $(n + 1/2)\Delta t$ to $(n + 1)\Delta t$, the terms involving V and h of the continuity equation and the y-momentum equation are expressed implicitly whereas the previous implicit values of U are now represented explicitly. The grid used is similar to that in Fig. 2.12.

In this scheme (to be described below) the only terms requiring special attention are the convective acceleration terms. These are represented in such a manner that their locations depend on the direction of the velocity component perpendicular to the axis direction under consideration (see Fig. 2.12). This scheme allows momentum ρU and ρV to be evaluated correctly at the position where the momentum originates and this momentum is conserved in the finite-difference equations. Define

$$(2.328)\quad h_{j,k,n} = h(j\Delta x,\ k\Delta y,\ n\Delta t)$$

$$(2.329)\quad \bar{h}^x_{j,k} = \frac{1}{2}(h_{j+1/2,k} + h_{j-1/2,k})$$

$$(2.330)\quad h_{\max} = h_{j+n/2,k} - h_{j-n/2,k}$$

$$(2.331)\quad \bar{\bar{h}}_{j,k} = \frac{1}{4}(h_{j-1/2,k-1/2} + h_{j-1/2,k+1/2} + h_{j+1/2,k-1/2} + h_{j+1/2,k+1/2})$$

For the first part of a given time step, the finite-difference equations are

$$(2.332)\quad h_{n+1/2} = h_n - \frac{\Delta t}{2\Delta S}\frac{\partial}{\partial x}[(\bar{D}^y + \bar{h}^x)U]_{n+1/2} - \frac{\Delta t}{2\Delta S}\frac{\partial}{\partial y}[(\bar{D}^x + \bar{h}^y)V]_{n-1} \text{ at } j,\ k$$

$$(2.333)\quad U_{n+1/2} = U_{n-3/2} - \frac{\alpha 2\Delta t}{\Delta S}\left[\frac{\partial}{\partial x}(U^2)_{n-1/2} + \frac{\partial}{\partial y}\langle\overline{UV}\rangle^x_{n-1/2}\right] + 2\Delta t f \bar{\bar{V}}_n$$
$$- \frac{2\Delta t}{\Delta S} g\left(\frac{\partial h}{\partial x}\right)_{n+1/2} - \Delta t\, g\,(U_{n+1/2} + U_{n-3/2})\left[\frac{|U_{n-1/2}| + |\bar{\bar{V}}_n|}{(\bar{D}^y + \bar{h}^x)(\bar{C}^x)^2}\right]$$
$$+ \frac{2\Delta t \rho' \gamma W W_x}{(\bar{D}^y + \bar{h}^x)} + \frac{\nu_H 2\Delta t}{(\Delta S)^2}\left[\frac{\partial^2}{\partial x^2}U_{n-1/2} + \frac{\partial^2}{\partial y^2}U_{n-1/2}\right.$$
$$\left. - 2(U_{n+1/2} + U_{n-3/2})\right] \text{ at } j + \frac{1}{2},\ k$$

where

$$\frac{\partial}{\partial y}\langle \overline{UV^x} \rangle_{n-1/2} = U_{j+1/2,k+1/2+p,n-1/2}(\bar{V}^x)_{j+1/2,k+1/2,n} - U_{j+1/2,k-1/2+q,n-1/2}(\bar{V}^x)_{j+1/2,k-1/2,n}$$

with p and q having half-integer values such that

$$p = \left(\frac{-V}{2|V|}\right)_{j+1/2,k+1/2}$$

$$q = \left(\frac{-V}{2|V|}\right)_{j+1/2,k-1/2}$$

For the second part of the time step,

(2.334) $$h_{n+1} = h_{n+1/2} - \frac{\Delta t}{2\Delta S}\frac{\partial}{\partial x}[(\bar{D}^y + \bar{h}^x)U]_{n-1/2} - \frac{\Delta t}{2\Delta S}\frac{\partial}{\partial y}[(\bar{D}^x + \bar{h}^y)V]_{n+1} \text{ at } j,\ k$$

(2.335) $$V_{n+1} = V_{n-1} - \frac{\alpha 2\Delta t}{\Delta S}\left[\frac{\partial}{\partial x}\langle \bar{U}^y V\rangle_n + \frac{\partial}{\partial y}V_n^2\right] - 2\Delta t f \bar{\bar{U}}_{n+1/2} - \frac{2\Delta t}{\Delta S} g \left(\frac{\partial h}{\partial y}\right)_{n+1}$$
$$- \Delta t\, g\,(V_{n+1} + V_{n-1})\left[\frac{|U_{n+1/2}| + |V_n|}{(\bar{D}^x + \bar{h}^y)(\bar{C}^y)^2}\right] + \frac{2\Delta t \rho' \gamma W W_y}{(\bar{D}^x + \bar{h}^y)}$$
$$+ \nu_H \frac{2\Delta t}{(\Delta S)^2}\left[\left(\frac{\partial^2 V}{\partial x^2}\right)_n + \left(\frac{\partial^2 V}{\partial y^2}\right)_n - 2(V_{n+1} + V_{n-1})\right] \text{ at } j,\ k + 1/2$$

where

$$\frac{\partial}{\partial x}\langle \bar{U}^y V\rangle_n = \bar{U}^y_{j+1/2,k+1/2,n+1/2} V_{j+1/2+p,k+1/2,n} - \bar{U}^y_{j-1/2,k+1/2,n+1/2} V_{j-1/2+q,k+1/2,n}$$

and

$$p = \left(\frac{-U}{2|U|}\right)_{j+1/2,k+1/2}$$

$$q = \left(\frac{-U}{2|U|}\right)_{j-1/2,k+1/2}$$

The above equations can be solved by the Gauss elimination method.

Davies (1976) included nonlinear advective terms in the equations of motion and continuity written in the spherical polar coordinate form:

(2.336) $$\frac{\partial U}{\partial t} + \frac{U}{R\cos\phi}\frac{\partial U}{\partial \chi} + \frac{V}{R\cos\phi}\frac{\partial}{\partial \phi}(U\cos\phi) - fV + \frac{KU(U^2 + V^2)^{1/2}}{H} + \frac{g}{R\cos\phi}\frac{\partial h}{\partial \chi} = 0$$

(2.337) $$\frac{\partial V}{\partial t} + \frac{U}{R\cos\phi}\frac{\partial V}{\partial \chi} + \frac{V}{R}\frac{\partial V}{\partial \phi} + \frac{U^2\tan\phi}{R} + fU + \frac{KV(U^2 + V^2)^{1/2}}{H} + \frac{g}{R}\frac{\partial h}{\partial \phi} = 0$$

(2.338) $$\frac{\partial h}{\partial t} + \frac{1}{R\cos\phi}\left[\frac{\partial}{\partial \chi}(HU) + \frac{\partial}{\partial \phi}(HV\cos\phi)\right] = 0$$

where χ and ϕ are the east longitude and north latitude, respectively, R is the radius of

the earth, $H = D + h$ is the total water depth, and K is the bottom friction coefficient. The depth mean currents, U and V, are given as

$$U = \frac{1}{D + h} \int_{-D}^{h} u(z)dz$$

$$V = \frac{1}{D + h} \int_{-D}^{h} v(z)dz$$

The angled derivative approach of Flather and Heaps (1975) was used by Davies (1976) in solving these equations.

Book et al. (1975) developed "flux-corrected" transport schemes for the proper inclusion of the nonlinear advective terms. In this scheme, any artificial diffusion added to the advection term in the first step is subtracted in the subsequent step. Lam (1977) compared various schemes of this type and showed that a central-difference scheme produces oscillations of great amplitude, whereas a one-sided upstream-differencing scheme shows a large false diffusion. However, the one-sided upstream-differencing scheme combined with a flux-corrected transport scheme gave reliable results.

2.13 Moving Boundary Models and Inclusion of Tidal Flats

Moving boundary models have been developed to allow for the climbing of the surge on the coastline as well as to include tidal flats, which become submerged during flood and dry during ebb.

Omitting the nonlinear advective and Coriolis terms, Reid and Bodine (1968) developed a technique for the inclusion of tidal flats. The coastal boundary that follows the grid lines can advance or retreat in discrete steps as the water level rises or falls. To allow for flooding of dry land and to simulate submerged barriers, empirical formulae based on the concept of flow over weirs were used, and application was made to storm surges in Galveston Bay, TX.

Leendertse (1970) and Leendertse and Gritton (1971) developed an alternating direction implicit technique of allowing for tidal flats, with application to Jamaica Bay, NY. In this model also, the boundary moves along grid lines in discrete steps. However, the condition for dry area is more stringent than a simple zero local water depth (the stringent condition was used to suppress most of the computational noise due to the movements of the boundary). The programming effort is quite cumbersome, especially due to the implicit scheme used. Other works that dealt with this problem are those of Ramming (1972), Abbott et al. (1973), Backhaus (1976), Runchal (1975), and Wanstrath (1977a, 1977b).

The model of Flather and Heaps (1975) has already been introduced in the section on nonlinear terms. For the calculations in which tidal flats are to be included, they omitted the advective terms and used a simple explicit scheme. The conditions they used depended on an examination of the local water depth and the slope of the water level. Use of the condition on the water level slope especially suppresses the unrealistic movements of the boundary. As in the models of Reid and Bodine (1968) and Leendertse and Gritton (1971), the water–land boundary follows grid lines in discrete time steps.

Before the calculation of currents u and v in the x and y directions at each time step, each grid point was tested to see if it was wet (i.e. positive water depth) or dry (zero water depth). If the point was dry, then the current was prescribed as zero. For wet points, u and v were computed from the relevant equations.

Yeh and Yeh (1976) developed a moving boundary model; i.e. the boundary between dry land and the water can move with time using an ADI technique. Since the technique was found to be numerically inefficient, Yeh and Chou (1979) developed an explicit technique. They showed that the moving boundary (MB) model gives storm surge amplitudes that could be 30% smaller than those given by a fixed boundary (FB) model, and observations are in better agreement with the results of the MB model. In other words, FB models that assume a fixed vertical wall at the water–land boundary could overestimate the surge by about 30%.

Yeh and Chou (1979) used the following forms of the equations:

$$\frac{\partial u}{\partial t} + u\frac{\partial u}{\partial x} + v\frac{\partial u}{\partial y} - qu - fv = -g\frac{\partial h}{\partial x} - \frac{1}{\rho}\frac{\partial P_a}{\partial x} + \frac{(\tau_{S_x} - \tau_{B_x})}{\rho(D + h)} \tag{2.339}$$

$$\frac{\partial v}{\partial t} + u\frac{\partial v}{\partial x} + v\frac{\partial v}{\partial y} - qv + fu = -g\frac{\partial h}{\partial y} - \frac{1}{\rho}\frac{\partial P_a}{\partial y} + \frac{(\tau_{S_y} - \tau_{B_y})}{\rho(D + h)} \tag{2.340}$$

$$\frac{\partial h}{\partial t} + \frac{\partial}{\partial x}[u(D + h)] + \frac{\partial}{\partial y}[v(D + h)] = 0 \tag{2.341}$$

where u and v are the velocities in the x and y directions and q is the discharge per unit volume (other symbols as previously defined).

At the seaward open boundary water level h is taken as the sum of the tide plus the inverse barometer effect. The land–water boundary advances or retreats according to the rise or recession of the surge level, i.e.

$$\vec{V}\cdot\vec{n} = 0 \text{ at } S[x, y, h(t)] = 0 \tag{2.342}$$

where $\vec{V}$ is the velocity vector, $\vec{n}$ is the unit vector normal to the curve S, and $S[x, y, h(t)]$ is the water–land interface which is determined by the solution. Note that at the water–land boundary the normal velocity is taken as zero; however, this boundary is not fixed but is allowed to move freely depending on the surge elevation. This is done by varying the boundary lines on units of the grid (thus making discrete changes). However, this may give rise to computational instability problems. Hence, in very shallow areas, the bottom friction was increased (which is physically justified). Yeh and Yeh (1976) stated that the criteria upon which the location of water–land interfaces are based are relatively simple (see the original paper for details).

The first set of numerical experiments were for the Gulf of Mexico. The surge as calculated by the MB and FB models at Eugene Island is shown in Fig. 2.13. Three differences exist between the results for both models. With the MB model (a) the maximum amplitude is about 30% lower, (b) the curve is flatter, and (c) the peak surge occurs later. The observed surge (not shown here) is in better agreement (mainly at the peak) with the MB model results.

A second set of experiments was performed for the Hurricane Carla storm surge of September 1961. A third set of experiments was performed for the south coast of Maine. The surge from a northeaster on February 3, 1972, was simulated. A maximum surge at 1.13 m was observed at Portland, ME. In this case, both models gave almost identical surges because of the steep slope in the inland areas and the small amplitude of the surge. Lynch (1980) suggested that these models should be referred to as "sequence of fixed boundary simulations." Yeh and Chou (1981) preferred the term "discrete moving boundary."

Tetra Tech Inc. (1978) developed coastal flooding storm surge models which included the nonlinear advective terms, Coriolis terms, wind stress, atmospheric pressure

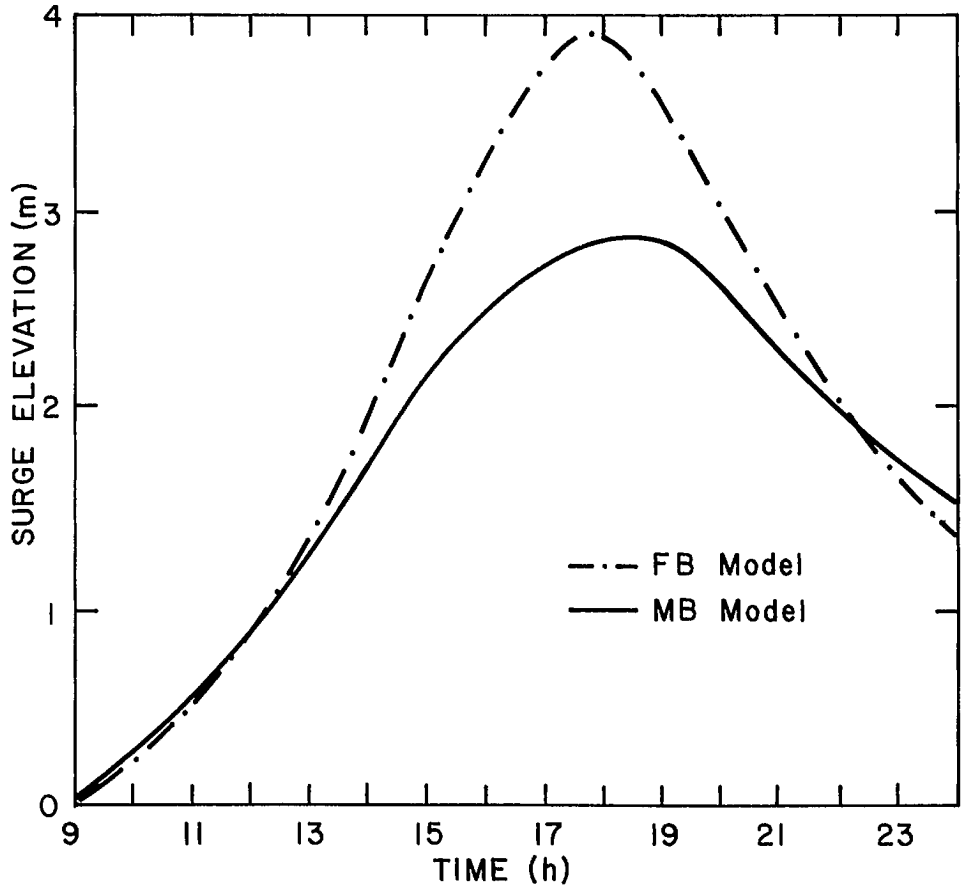

FIG. 2.13. Computed storm surge at Eugene Island, U.S.A., using fixed boundary (FB) and moving boundary (MB) models. (Yeh and Chou 1979)

gradients, and bottom stress. Certain aspects of this model and the main results will be covered in section 7.2. Here, discussion will be confined to the treatment of the land–water boundary. Usually, the landslope onshore is much greater than the slope of the ocean floor. In such situations, the coastal surge is assumed to propagate overland to its corresponding contour level (when the distance to that contour line is much less than one grid interval). However, there are certain regions, such as western Florida, where the onshore slope is very small and the limiting contour interval may be several kilometres inland. For such cases, a one-dimensional run-up model is used at various traverses. Johns et al. (1981) used a moving boundary model for the Bay of Bengal.

Sielecki and Wurtele (1970) developed a moving boundary scheme in which the lateral boundary of the fluid is determined as a part of the solution. They tested the validity of their scheme by comparing the results of some simple numerical experiments with the results from analytical solutions. Actually, their scheme consists of three different methods: (a) Lax–Wendroff scheme (Lax and Wendroff 1960) as modified by Richtmeyer (Richtmeyer 1963); (b) using the principle of energy conservation as formulated by Arakawa (1966); (c) using the quasi implicit character of the difference equations.

Sielecki and Wurtele (1970) wrote the equation of continuity and the equations of motion in a form that is somewhat different from the traditional forms:

$$\frac{\partial H}{\partial t} + \frac{\partial M}{\partial x} + \frac{\partial N}{\partial y} = 0 \tag{2.343}$$

$$\frac{\partial M}{\partial t} + \frac{\partial}{\partial x}(Mu + GH^2) + \frac{\partial}{\partial y}(Nu) - fN = gH\frac{\partial D}{\partial x} \tag{2.344}$$

$$\frac{\partial N}{\partial t} + \frac{\partial}{\partial x}(Mv) + \frac{\partial}{\partial y}(Nv + GH^2) + fM = gH\frac{\partial D}{\partial y} \tag{2.345}$$

where $D(x, y)$ is the undisturbed water depth, $h(x, y, t)$ is the free surface ($H = D + h$), u and v are the velocity components in the x and y directions, M and N are the transport components ($M = Hu$, $N = Hv$), and $G = g/2$.

For use with the modified Lax–Wendroff scheme, a nonstaggered grid was used. For any dependent variable let

$$\begin{aligned} \Delta_j \phi_{j,k,n} &= \phi_{j+1,k,n} - \phi_{j-1,k,n} \\ \Delta_k \phi_{j,k,n} &= \phi_{j,k+1,n} - \phi_{j,k-1,n} \\ \bar{\phi}_{j,k,n} &= \frac{1}{4}(\phi_{j+1,k,n} + \phi_{j-1,k,n} + \phi_{j,k+1,n} + \phi_{j,k-1,n}) \end{aligned} \tag{2.346}$$

and

$$\Delta x = \Delta y = \Delta S$$

Let

$$\epsilon = \frac{\Delta t}{2\Delta S} \tag{2.347}$$

The time integration of scheme I consists of two parts, in a given time step. In the first part:

$$h_{j,k,n+1} = \bar{h}_{j,k,n} - \epsilon(\Delta_j M_{j,k} + \Delta_k N_{j,k}) \tag{2.348}$$

$$M_{j,k,n+1} = \bar{M}_{j,k,n} - \epsilon\left[\Delta_j\left(\frac{M_{j,k,n}}{H_{j,k,n}}\right)^2 + G\Delta_j(H^2_{j,k,n}) + \Delta_k\left(\frac{M_{j,k,n}N_{j,k,n}}{H_{j,k,n}}\right)\right] + f\Delta t N_{j,k,n} + \epsilon g H_{j,k,n-1}\Delta_j D_{j,k} \tag{2.349}$$

$$N_{j,k,n+1} = \bar{N}_{j,k,n} - \epsilon\left[\Delta_j\left(\frac{M_{j,k,n}N_{j,k,n}}{H_{j,k,n}}\right) + \Delta_k\left(\frac{N^2_{j,k,n}}{H_{j,k,n}}\right) + G\Delta_k(H_{j,k,n})^2\right] - f\Delta t M_{j,k,n} + \epsilon g H_{j,k,n-1}\Delta_k D_{j,k} \tag{2.350}$$

In the second part:

$$H_{j,k,n+2} = H_{j,k,n} - 2\epsilon(\Delta_j M_{j,k,n+1} + \Delta_k N_{j,k,n+1}) \tag{2.351}$$

$$M_{j,k,n+2} = M_{j,k,n} - 2\epsilon\left[\Delta_j\left(\frac{M^2_{j,k,n+1}}{H_{j,k,n+1}}\right) + G\Delta_j(H^2_{j,k,n+1}) + \Delta_k\left(\frac{M_{j,k,n+1}N_{j,k,n+1}}{H_{j,k,\ n+1}}\right)\right] + 2f\Delta t N_{j,k,n+1} + 2\epsilon g H_{j,k,n}\Delta_j D_{j,k} \tag{2.352}$$

$$(2.353)\quad N_{j,k,n+2} = N_{j,k,n} - 2\epsilon\left[\Delta_j\left(\frac{M_{j,k,n+1}N_{j,k,n+1}}{H_{j,k,n+1}}\right) + \Delta_k\left(\frac{N^2_{j,k,n+1}}{H_{j,k,n+1}}\right) + G\Delta_k(H^2_{j,k,n+1})\right] - 2f\Delta t M_{j,k,n+1} + 2\epsilon g H_{j,k,n}\Delta_k D_{j,k}$$

Scheme II is formulated using Arakawa's (1966) approach. The staggered grid for this scheme is shown in Fig. 10 of Sielecki and Wurtele (1970). Also, define

$$\Delta_j\phi_{j,k,n} = \phi_{j+1/2,k,n} - \phi_{j-1/2,k,n}$$

$$\Delta_k\phi_{j,k,n} = \phi_{j,k+1/2,n} - \phi_{j,k-1/2,n}$$

$$\delta_j\phi_{j,k,n} = \frac{1}{2}(\phi_{j+1/2,k,n} + \phi_{j-1/2,k,n})$$

$$\delta_k\phi_{j,k,n} = \frac{1}{2}(\phi_{j,k+1/2,n} + \phi_{j,k-1/2,n})$$

$$(2.354)\quad M_{j,k+1/2} = (\delta_j H_{j,k+1/2})\delta_k(u_{j,k+1/2})$$

$$N_{j+1/2,k} = (\delta_k H_{j+1/2,k})(\delta_j v_{j+1/2,k})$$

$$U_{j+1/2,k} = \frac{1}{2}(\delta_j M_{j+1/2,k+1/2} + \delta_k M_{j+1/2,k-1/2})$$

$$V_{j,k+1/2} = \frac{1}{2}(\delta_k N_{j-1/2,k+1/2} + \delta_k N_{j+1/2,k+1/2})$$

$$\bar{H}_{j,k} = \frac{1}{2}(\delta_j H_{j,k+1/2} + \delta_j H_{j,k-1/2})$$

As with scheme I, this scheme has two parts in each time step. In the first part:

$$(2.355)\quad H_{j+1/2,k+1/2,n+1} = H_{j+1/2,k+1/2,n} - 2\epsilon\Delta_j M_{j+1/2,k+1/2,n} + \Delta_k N_{j+1/2,k+1/2,n}$$

$$(2.356)\quad \bar{H}_{j,k,n+1}\tilde{u}_{j,k,n+1} = H_{j,k,n}u_{j,k,n} - 2\epsilon\{\Delta_j[U_{j,k,n}\delta_j u_{j,k,n} + G\delta_k(H_{j,k,n+1})] + \Delta_k(V_{j,k,n}\delta_k u_{j,k,n})\} + \bar{H}_{j,k,n+1}(f\Delta t v_{j,k,n} + 2\epsilon g\Delta_j D_{j,k})$$

$$(2.357)\quad \bar{H}_{j,k,n+1}\tilde{v}_{j,k,n+1} = \bar{H}_{j,k,n}v_{j,k,n} - 2\epsilon\{\Delta_j(\tilde{U}_{j,k,n+1}\delta_j v_{j,k,n}) + \Delta_k[V_{j,k,n}\delta_k v_{j,k,n} + G\delta_j(H_{j,k,n+1})]\} + \bar{H}_{j,k,n+1}(-f\Delta t\tilde{u}_{j,k,n+1} + 2\epsilon g\Delta_k D_{j,k})$$

In the second part:

$$(2.358)\quad \bar{H}_{j,k,n+1}u_{j,k,n+1} = \bar{H}_{j,k,n}u_{j,k,n} - 2\epsilon[\Delta_j U_{j,k,n}\delta_j\tilde{u}_{j,k,n+1} + G\delta_k(H^2_{j,k,n+1}) + \Delta_k(V_{j,k,n}\delta_k\tilde{u}_{j,k,n+1})] + \bar{H}_{j,k,n+1}(f\Delta t\tilde{v}_{j,k,n+1} + 2\epsilon g\Delta_j D_{j,k})$$

and

$$(2.359)\quad \bar{H}_{j,k,n+1}v_{j,k,n+1} = \bar{H}_{j,k,n}v_{j,k,n} - 2\epsilon\Delta_j\{(\tilde{U}_{j,k,n+1}\delta_j\tilde{v}_{j,k,n+1}) + \Delta_k[V_{j,k,n}\delta_k\tilde{v}_{j,k,n+1} + G\delta_j(H_{j,k,n+1})]\} + H_{j,k,n+1}(f\Delta t u_{j,k,n+1} + 2\epsilon g\Delta_k D_{j,k})$$

where the symbol $\sim$ over a variable denotes a temporary value. Note that in this scheme, the water level is calculated in the first half-step itself, whereas the final values of the currents are computed in the second half-step.

Scheme III also consists of two half-steps. In the first half-step:

$$h_{j,k,n+1} = h_{j,k,n} - \epsilon\{\Delta_j[(D_{j,k} + h_{j,k,n})u_{j,k,n}] + \Delta_k[(D_{j,k} + h_{j,k,n})v_{j,k,n}]\} \quad (2.360)$$

$$\tilde{u}_{j,k,n+1} = u_{j,k,n}(1 - \epsilon\Delta_j u_{j,k,n}) + v_{j,k,n}(f\Delta t - \epsilon\Delta_k u_{j,k,n}) - g\epsilon\Delta_j h_{j,k,n+1} \quad (2.361)$$

$$\tilde{v}_{j,k,n+1} = v_{j,k,n}(1 - \epsilon\Delta_k v_{j,k,n}) + u_{j,k,n+1}(-f\Delta t - \epsilon\Delta_j v_{j,k,n}) - g\epsilon\Delta_k h_{j,k,n+1} \quad (2.362)$$

In the second half-step, only the final values of the velocity components are computed:

$$u_{j,k,n+1} = u_{j,k,n}(1 - \epsilon\Delta_j\tilde{u}_{j,k,n+1}) - \epsilon v_{j,k,n}\Delta_k\tilde{u}_{j,k,n+1} + f\Delta t\tilde{v}_{j,k,n+1} - g\epsilon\Delta_j h_{j,k,n+1} \quad (2.363)$$

and

$$v_{j,k,n+1} = v_{j,k,n}(1 - \epsilon\Delta_k\tilde{v}_{j,k,n+1}) - \epsilon\tilde{u}_{j,k,n+1}\Delta_j\tilde{v}_{j,k,n+1} - f\Delta t u_{j,k,n+1} - g\epsilon\Delta_k h_{j,k,n+1} \quad (2.364)$$

In eq. 2.360–2.364 the symbols used for the finite-differencing follow eq. 2.346 and 2.347.

Sielecki and Wurtele (1970) faced no difficulty in the calculation for the case when water level is falling at the shore. On the other hand, when the water level is rising, a new underground point may have to be included. To determine the position of the new shoreline, one has to know the slope of the free surface at the present shoreline. To eliminate computational noise, the slope of the free surface at the shoreline was estimated from the last two underwater points to the first underground point (for details, see the original paper).

Reid and Whitaker (1976) and Reid et al. (1977b) allowed for vast stretches of vegetation and marsh grass (such as in Lake Okeechobee in Florida) in storm surge models. They showed that when the marsh grass extends above the water surface, a single canopy flow regime results, whereas when the vegetation does not extend above the water surface, a two-layer regime exists. Flooded marsh areas are treated as an ensemble of subgrid scale obstacles.

For submerged vegetation the model is similar to a two-layer system. The interfacial stress is formulated in terms of a coupling coefficient and the flow differential. The friction due to individual canopies is parameterized through a drag coefficient and the dimensions of the elements. When the canopy elements are not submerged, a sheltering factor is introduced.

Reid and Whitaker (1976) assumed that the obstacles are rigid elements of width w and height b and are oriented normal to the flow. It was also assumed that they are distributed evenly over the bottom. For water depth $D > b$, the vertically integrated equation of motion for the lower layer is

$$\frac{\partial Q_1}{\partial t} + gb\nabla h = \tau_C - \tau_B - F_C \quad (2.365)$$

For the area above the obstacles:

$$\frac{\partial Q_2}{\partial t} + g(D - b)\nabla h = \tau_S - \tau_C \quad (2.366)$$

where subscripts 1 and 2 refer, respectively, to the lower and upper layers. Here, h is the total water depth, τ_C is the interfacial stress, τ_B is the bottom stress, and F_C is any external force. Q_1 and Q_2 respectively denote the transports in the lower and upper layers.

Let

$$Q = Q_1 + Q_2 \quad (2.367)$$

From eq. 2.365–2.367:

$$\frac{\partial Q}{\partial t} + gD\nabla h = \tau_S - \tau_B - F_C \tag{2.368}$$

For the total water column, the continuity equation is

$$\frac{\partial h}{\partial t} + \nabla Q = 0 \tag{2.369}$$

Let u_1 and u_2 be the depth-averaged velocities for the two layers; then, the stresses (in quadratic form) are

$$\tau_B = f_1|u_1|u_1 \tag{2.370}$$

$$\tau_C = f_2|u_2 - u_1|(u_2 - u_1) \tag{2.371}$$

Note that coefficients f_1 and f_2 are nondimensional.

Let N be the number of obstacles per unit horizontal area and C_D be a dimensionless drag coefficient. The resistance per unit horizontal area to the flow in the lower layer is

$$F_C = C_D wbN|u_1|u_1 \tag{2.372}$$

If $D \leq b$, then the interfacial stress τ_C vanishes, and in eq. 2.372 one has to replace b with D.

When $D < b$, one has to introduce a sheltering coefficient S to model the modification of the wind stress due to the canopy. Reid and Whitaker (1976) wrote

$$S = \frac{1}{\left(1 + \dfrac{C_D NwH(C)}{K}\right)} \tag{2.373}$$

where

$$\begin{aligned} H(C) &= b - D \text{ if } D < b \\ H(C) &= 0 \text{ if } D \geq b \end{aligned} \tag{2.374}$$

and K is a wind stress coefficient. The assumption here is that the wind stress is continuous at elevation b and that a quadratic form holds for the resistance to the wind provided by the individual elements. Note that eq. 2.373 for the dimensional coefficient S is valid for $D < b$ and $S \to 1$ as $NwH(C) \to 0$.

The scheme for the numerical integration of these equations is similar to that of Platzman (1963) and Reid and Bodine (1968). This model was applied to calculate the storm surge in Lake Okeechobee, FL, due to the 1950 October storm. Earlier, Whitaker et al. (1973) showed that the dense marsh in the southwest quadrant of the lake has significant influence on the circulation. Their attempts to modify the bottom friction factor for the vegetation area proved to be useless. The water level computed with the inclusion of the canopy agreed well with observed values.

Walton and Christensen (1980) developed a model for storm surges propagating onto a shore and applied this study to a hurricane storm surge on the west coast of Florida. Their theory includes a friction factor which varies spatially and depends not only on the local depth but also on the roughness elements and their spacings. The bottom stress com-

ponents τ_{B_x} and τ_{B_y} are expressed as follows:

$$\tau_{B_x} = \frac{F\rho|Q|M}{8D^2}$$
$$\tau_{B_y} = \frac{F\rho|Q|N}{8D^2} \tag{2.375}$$

where $D(x,y)$ is the undisturbed water depth, ρ is the density of water, F is a Darcy–Weisbach friction factor, M and N are the transports in the x and y directions, and $Q = (M^2 + N^2)^{1/2}$.

The friction factor, F, can be determined for the offshore regions knowing the sand roughness of the bed, the Reynolds number, the Froude number, and the Strouhal number. However, for the shore region, F cannot be easily determined. The Darcy–Weisbach formula for the energy loss, ΔE, in a water column of depth D is

$$\Delta E = \frac{F V_m^2}{2g} \frac{L}{4D} \tag{2.376}$$

where V_m is the spatially averaged velocity and L is the length over which the energy loss is determined. The commonly used expression for the shear (or friction) velocity V_* is

$$\frac{V_m}{V_*} = \sqrt{\frac{8}{F}} \tag{2.377}$$

For the travel of the storm surge over land, the following logarithmic distribution is assumed:

$$\frac{V}{V_*} = 8.48 + 2.5 \ln\left(\frac{y}{K} + 0.0338\right) \tag{2.378}$$

where V is the local velocity, y is the distance from the bed to the location where local velocity is under consideration, and K is the Nikuradse's equivalent sand roughness. The mean velocity, V_m, theoretically occurs at $y = 0.368D$ from the bed; then, from eq. 2.377 and 2.378:

$$F = \frac{1.28}{\left[\ln\left(\frac{10.94D}{K} + 1\right)\right]^2} \tag{2.379}$$

Equation 2.379 for F can be used for the overland travel of the storm surge. However, if vegetation and (man-made) structures are present, additional considerations are necessary.

Consider the travel of a storm surge over a vegetated area; let the density of distribution of the trees per unit area be m and let δ be the average diameter of these trees. The energy loss, ΔE, can be written as

$$\Delta E = \frac{F V_m^2}{2g} \frac{L}{4D}(1 - \epsilon) + m\delta D C_D \frac{V_m^2}{2g} \tag{2.380}$$

where ϵ is the fraction of the land occupied by the obstructions and C_D is a drag coefficient. An equivalent friction factor F_e can be introduced as follows:

$$F_e = F(1 - \epsilon) + 4m\delta D C_D \tag{2.381}$$

and one can write

$$\epsilon = \frac{\pi}{4}\delta^2 m \tag{2.382}$$

$$F_e = \frac{1.28\left(1 - m\frac{\pi}{4}\delta^2\right)}{\left[\ln\left(\frac{10.94D}{K} + 1\right)\right]^2} + 4m\delta D C_D \tag{2.383}$$

For larger values of the Reynolds number (i.e. greater than 5×10^5), $C_D \sim 0.4$. Let S be the average spacing between the trees (obstacles). Then

$$m = \frac{1}{S^2} \tag{2.384}$$

Walton and Christensen (1980) wrote for a regular hexagonal pattern:

$$m = \frac{2.31}{S^2} \tag{2.385}$$

Averaging eq. 2.384 and 2.385 gives

$$m = \frac{1.65}{S^2} \tag{2.386}$$

Equation 2.383 then becomes

$$F_e = \frac{1.28\left[1 - 1.3\left(\frac{\delta}{S}\right)^2\right]}{\left[\ln\left(\frac{10.94D}{K} + 1\right)\right]^2} + 2.65\left(\frac{\delta}{S}\right)\left(\frac{D}{S}\right) \tag{2.387}$$

Here, the first term represents the roughness and the second term denotes the effect of the vegetation and structures. As mentioned earlier, this study was applied to a hurricane-generated surge on the west coast of Florida. As expected, inclusion of the friction factor reduced the peak surge and delayed it. The calculated results compare well with observations.

2.14 Nested Grids and Multiple Grids

In this section, the use of multiple grids, such as combinations of coarse and fine grids, to model storm surges in a water body will be considered. The philosophy behind using multiple grids is to be able to reduce the total computational effort by placing a coarse grid in the deep (and offshore) region and couple this with a finer grid in the shallow coastal area.

In connection with storm surge studies in the Beaufort Sea, Henry (1975) and Henry and Heaps (1976) used a combination of coarse and fine grids but the grids were not coupled dynamically. Examples of studies in which the grids are dynamically coupled are those of Abbott et al. (1973), Ramming (1976), Simons (1978), and Johns and Ali (1980).

Greenberg (1975, 1976, 1977, 1979) used a combination of grids in his numerical model for tides in the Bay of Fundy. Following Greenberg, a technique will be considered merging different mesh sizes for the simplified case of a rectangular basin of uniform depth D using the linearized version of the relevant equations. Rather than the traditional manner of using volume transports, Greenberg used depth-mean currents U and V in the x and y directions, defined as

$$U \equiv \frac{1}{D}\int_0^D u(z)\,dz, \qquad V \equiv \frac{1}{D}\int_0^D v(z)\,dz \tag{2.388}$$

Then, the equation of continuity is

$$\frac{\partial h}{\partial t} + \frac{\partial}{\partial x}(DU) + \frac{\partial}{\partial y}(Dv) = 0 \tag{2.389}$$

The equations of motion are

$$\frac{\partial U}{\partial t} + \frac{kU}{D} - fV = -g\frac{\partial h}{\partial x} + \frac{\tau_{S_x}}{\rho D} \tag{2.390}$$

$$\frac{\partial V}{\partial t} + \frac{kV}{D} + fU = -g\frac{\partial h}{\partial y} + \frac{\tau_{S_y}}{\rho D} \tag{2.391}$$

where $h(x, y, t)$ is the water level deviation from the equilibrium position and τ_{S_x} and τ_{S_y} are the wind stress components in the x and y directions, respectively.

Noting that indices j, k, and n refer to x, y, and t, the finite-difference forms of eq. 2.388, 2.389, and 2.390 are as follows:

$$h_{j,k,n+1} = h_{j,k,n} - D\Delta t\left[\frac{(U_{j,k,n} - U_{j-1,k,n})}{\Delta x} + \frac{(V_{j,k-1,n} - V_{j,k,n})}{\Delta y}\right] \tag{2.392}$$

$$U_{j,k,n+1} = \frac{1}{\left(1 + \frac{k\Delta t}{2D}\right)}\left[U_{j,k,n}\left(1 - \frac{k\Delta t}{2D}\right) + f\Delta t\hat{V}_{j,k,n} - \frac{g\Delta t}{\Delta x}(h_{j+1,k,n+1} - h_{j,k,n}) + \frac{\Delta t}{\rho D}\tau_{S_x}\right] \tag{2.393}$$

$$V_{j,k,n+1} = \frac{1}{\left(1 + \frac{k\Delta t}{2D}\right)}\left[V_{j,k,n}\left(1 - \frac{k\Delta t}{2D}\right) - f\Delta t\hat{U}_{j,k,n+1} - \frac{g\Delta t}{\Delta y}(h_{j,k,n+1} - h_{j,k+1,n+1}) + \frac{\Delta t}{\rho D}\tau_{S_y}\right] \tag{2.394}$$

where

$$U_{j,k,n} \equiv \frac{1}{4}(U_{j-1,k,n} + U_{j,k,n} + U_{j-1,k+1,n} + U_{j,k+1,n}) \tag{2.395}$$

$$\hat{V}_{j,k,n} \equiv \frac{1}{4}(V_{j,k-1,n} + V_{j+1,k-1,n} + V_{j,k,n} + V_{j+1,k,n}) \tag{2.396}$$

Initially, U, V, and h were prescribed to be zero. The boundary conditions are $U = V = 0$ on all the boundaries. In addition to the usual C−F−L stability criterion, Greenberg (1977) gave another condition, namely

$$\Delta t < \frac{2}{f} \tag{2.397}$$

where f is the Coriolis parameter, which is satisfied easily.

The scheme for coupling grids is shown in Fig. 2.14. The fine-grid calculations of the mixed grid commence at row $(q + 1)$ of the coarse grid and row r of the fine grid. To be able to calculate h and U on the rth row, one must know V on the $(r - 1)$th row.

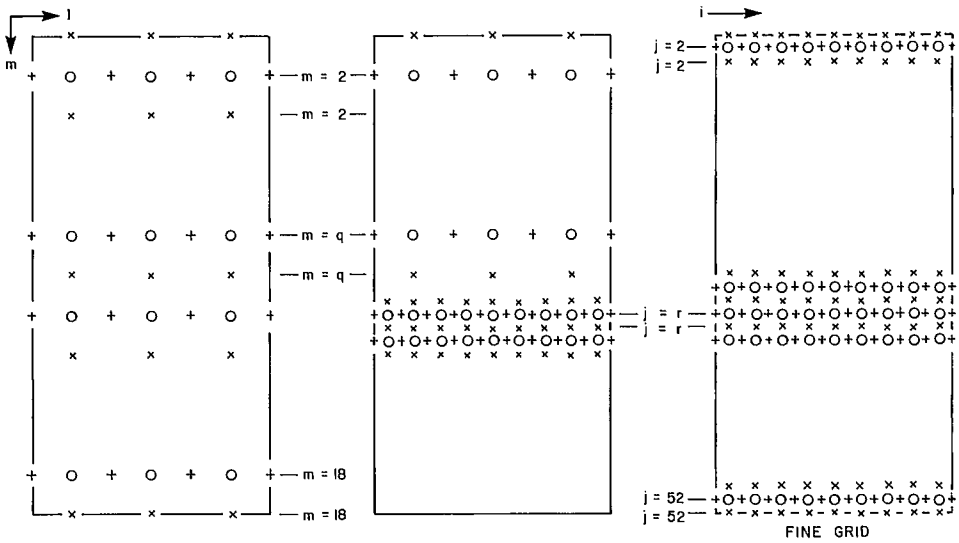

FIG. 2.14. Scheme for coupling grids in a multiple-grid computation. (Greenberg 1977)

However, eq. 2.394 does not give these values directly. Hence, one must interpolate (linearly) the qth row of the coarse grid and the rth row of the fine grid for the V values. Thus, for example,

$$
\begin{aligned}
V_{2,r-1} &= \frac{1}{2}\left[V_{2,r} + V_{2,q} + \frac{1}{3}(V_{2,q} - V_{3,q})\right] \\
V_{j,r-1} &= \frac{1}{2}(V_{l,q} + V_{j,r})
\end{aligned}
\tag{2.398}
$$

Similarly, for the computations of V in the qth row of the coarse part of the mixed grid, one must know U and h on the rth row of the fine grid. Thus:

$$\hat{U}_{l,q} = \frac{1}{4}(U_{l-1,q} + U_{l,q} + U_{j-2,r} + U_{j+1,r}) \tag{2.399}$$

$$h_{l,q} = \frac{1}{3}(h_{j-1,r} + h_{j,r} + h_{j+1,r}) \tag{2.400}$$

The coarse-grid computations are done for the first q rows and the fine-grid calculations commence along the $(q+1)$th row of the coarse grid (this row is referred to as the rth row of the fine grid). Greenberg (1977) gave the following sequence for the calculation of h, U, and V at step $(n+1)\Delta t$ knowing the values at step $n\Delta t$.

1) Interior $h_{l,m}$ of the coarse grid area are determined for $m = 2(1)q$ using eq. 2.392.
2) Interior $h_{j,k}$ of the fine grid are calculated for $k = r(1)k_{\max}$ ($k_{\max} = 52$ in Fig. 2.14) using eq. 2.392.
3) Interior $U_{l,m}$ are determined for $m = 2(1)q$ using eq. 2.393.
4) Interior $U_{j,k}$ are calculated for $k = m(1)k_{\max}$ using eq. 2.393.
5) Interior $V_{l,m}$ are computed for $m = 2(1)q - 1$ using eq. 2.394.
6) Interior $V_{l,q}$ are calculated using eq. 2.394 and 2.399.
7) Interior $V_{j,k}$ are determined for $k = r(1)k_{\max} - 1$ from eq. 2.394.
8) $V_{j,r-1}$ are interpolated using eq. 2.398.

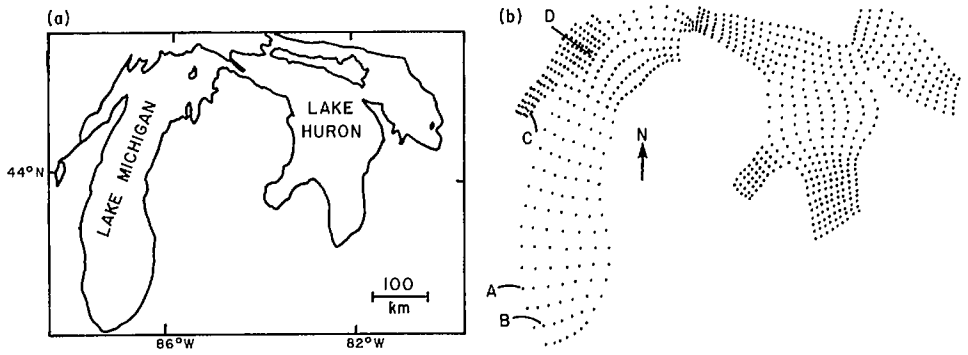

FIG. 2.15. (a) Basins of lakes Michigan and Huron joined at the Straits of Mackinac. (b) Curvilinear mesh for the basins of lakes Michigan and Huron. Note that the North Channel has been excluded. Points A, B, C, and D are special locations where observations were available for comparison with theory. (Birchfield and Murty 1974)

Greenberg made further calculations with the inclusion of the nonlinear terms because these terms might be important in understanding the interaction between tide and storm surge. He found that when the nonlinear terms are present, the damping due to frictional terms is less. For details on the computational scheme when nonlinear (advective) terms and quadratic bottom friction terms are included, see Greenberg (1977). This report also includes details of the finite-difference forms, for the calculation of energy, and the stability criterion.

2.15 Stretched Coordinates and Transformed Grid Systems

Birchfield and Murty (1974) used a stretched coordinate system to study wind-generated circulation in the combined system of Lake Michigan, Straits of Mackinac, and Lake Huron. Although this study did not examine storm surges, the technique is applicable to simulation of storm surges in two water bodies connected by narrow straits. The system studied here is shown in Fig. 2.15a and the curvilinear grid used is shown in Fig. 2.15b. The curvilinear grid is mapped onto a plane in which the irregular basin is transformed into a series of connected rectangles (Fig. 2.16). An equispaced grid was used in the connected rectangle system, and all the calculations are performed conveniently in this system; however, for easy interpretation the results of the output are printed in the geographical format.

Birchfield and Murty (1974) began with the formulation of Platzman (1963) described earlier. The main difference is that, whereas Platzman used a no-slip condition at the bottom, these authors permitted slip. Their model has certain similarities to the model of Jelesnianski (1967).

Equations 2.145–2.147 could be integrated in time under the following boundary conditions:

$$(2.401)\quad \frac{\nu}{D^2}\frac{\partial V}{\partial z} = T \text{ at } z = 0$$

and

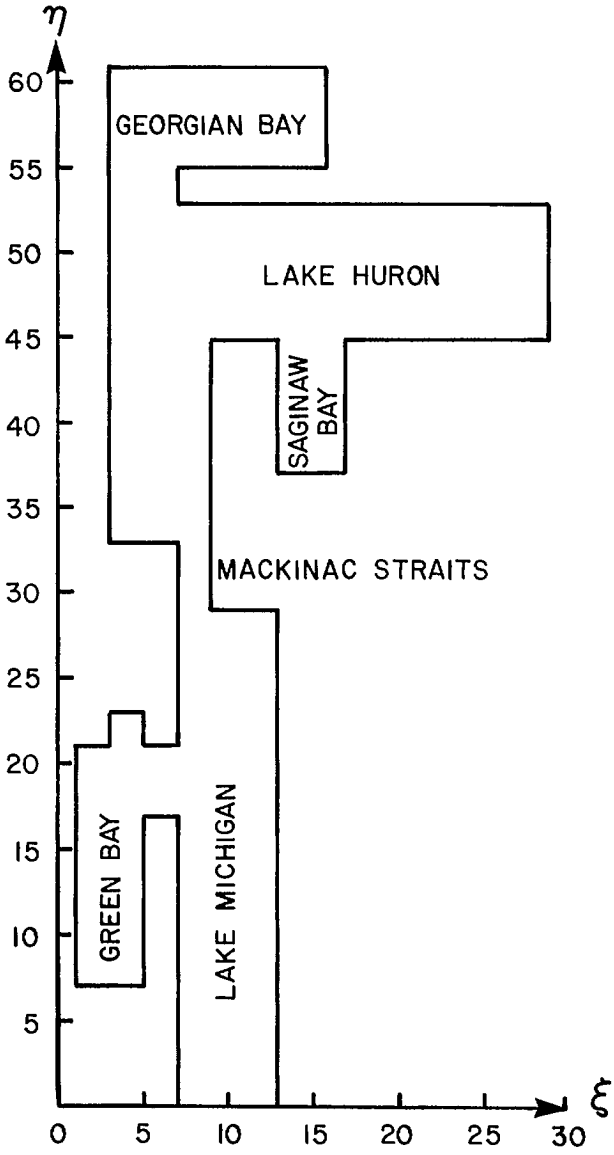

FIG. 2.16. Basins of lakes Michigan and Huron as arranged on the (ξ, η) plane.

$$\gamma \frac{\partial V}{\partial z} = V \text{ at } z = -1 \tag{2.402}$$

where $V = D(u + iv)$, ν is the vertical eddy viscosity, $T = (\tau_x + i\tau_y)/\rho$, and γ is a constant slip parameter.

The nonorthogonal curvilinear grid shown in Fig. 2.15b is constructed freehand using hydrographic charts of the water bodies. The advantage of such a grid is that the boundary

of the water body always falls on a coordinate line and the grid points are closely spaced in narrow and shallow areas. A rectangular area is designated for each major part of the basin (Fig. 2.16) such that a one-to-one correspondence exists between each point on the curvilinear grid and a point on a square grid covering the rectangle. The length to width ratio of the rectangle is then determined by the number of rows of points to the number of columns required to resolve the subregions and the entrances to the other regions. The finite-difference scheme used by Birchfield and Murty (1974) necessitates that the number of rows and columns in the rectangle be odd. When this procedure is used for all the major regions of the basin, the total basin consists of a series of interconnected rectangles.

Then, one can develop a table consisting of the cartesian coordinates (x, y) of the curvilinear grid on the hydrographic chart and each corresponding coordinate (ξ, η) on the rectangle. Thus, in essence, one has developed an empirical, nonconformal mapping of the (x, y) plane onto the (ξ, η) plane. For a one-to-one mapping one can write the following:

$$\xi = f_1(x, y)$$

$$\eta = f_2(x, y)$$

Then, eq. 2.145−2.147 can be written as follows, after defining some new coefficients (see Birchfield and Murty 1974 for details):

$$\text{(2.403)} \quad \frac{\partial M}{\partial t} = gD\left(A_2 \frac{\partial f_1}{\partial y} - A_1 \frac{\partial f_1}{\partial x}\right)\frac{\partial h}{\partial \xi} + gD\left(A_2 \frac{\partial f_2}{\partial y} - A_2 \frac{\partial f_2}{\partial x}\right)\frac{\partial h}{\partial \eta} - C_1 M + C_2 N + B_1 \tau_{S_x} - B_2 \tau_{S_y}$$

$$\text{(2.404)} \quad \frac{\partial N}{\partial t} = gD\left(A_2 \frac{\partial f_1}{\partial x} + A_1 \frac{\partial f_1}{\partial y}\right)\frac{\partial h}{\partial \xi} - gD\left(A_2 \frac{\partial f_2}{\partial x} + A_1 \frac{\partial f_2}{\partial y}\right)\frac{\partial h}{\partial \eta} - C_2 M - C_1 N + B_1 \tau_{S_y} + B_2 \tau_{S_x}$$

$$\text{(2.405)} \quad \frac{\partial h}{\partial t} = -\frac{\partial f_1}{\partial x}\frac{\partial M}{\partial \xi} - \frac{\partial f_2}{\partial x}\frac{\partial M}{\partial \eta} - \frac{\partial f_1}{\partial y}\frac{\partial N}{\partial \xi} - \frac{\partial f_2}{\partial y}\frac{\partial N}{\partial \eta}$$

Note that these equations are no more difficult than the original equations. Whereas in the original equations the coefficients depend only on the depth D, in these equations they depend also on the derivatives of the mapping function. Since the curvilinear coordinates are not orthogonal, there is no particular advantage in resolving the motion into components along the local (ξ, η) axis. Also note that, here, the map scale variations have not been taken into consideration.

For purposes of numerical integration, it is convenient to rotate the (ξ, η) axis by 45°. Making use of two Richardson lattices, central space-differences, and forward-time differences, the equations are integrated in time.

Reid et al. (1977) developed a transformed stretched coordinate system to calculate storm surges on a continental shelf. The principle underlying this scheme is to find a transformation involving mapping relations to keep the orthogonality and to make sure that the new independent variables, ξ and η, are continuous monotonic functions of the original independent variables, x and y. Further, the transformation must map the coastline and seaward boundaries as isolines of the curvilinear coordinate, η.

A point (x, y) on the z-plane will be transformed to (ξ, η) in a rectangular region on the ζ-plane and will satisfy the above conditions provided the mapping relation is conformal:

$$\zeta = \xi + i\eta = F(x + iy) \tag{2.406}$$

or conversely,

$$z = x + iy = G(\xi + i\eta) \tag{2.407}$$

where F and G are single-valued real functions. The function $G(\zeta)$ may be represented by a truncated Fourier series as

$$G(\zeta) = P_0 + Q_0\zeta + \sum_{n=1}^{N} [P_n \cos(n\zeta) + Q_n \sin(n\zeta)] \tag{2.408}$$

Here, the coefficients P_n and Q_n are complex constants.

The real and imaginary parts of eq. 2.408 give x and y in terms of ξ and η, respectively. The coefficients are determind in such a way that for constant $\eta = \beta$, the corresponding x and y as a function of ξ will map the coastline under consideration. Another constraint will be the representation of the seaward boundary (for example, the 200-m depth contour) as $\eta = -\beta$.

The coefficients P_n and Q_n can be evaluated by iteration using a least-square principle (Reid and Vastano 1966):

$$\begin{aligned} P_n &= A_n + iB_n \\ Q_n &= C_n + iD_n \end{aligned} \tag{2.409}$$

where A_n, B_n, C_n, and D_n with $n = 1, 2, \ldots, N$ are real constants. Then eq. 2.408 gives

$$\begin{aligned} x = A_0 + C_0\xi - D_0\eta &+ \sum_{n=1}^{N} [A_n \cosh(\eta n) - D_n \sinh(\eta n)] \cos(n\xi) \\ &+ \sum_{n=1}^{N} [B_n \sinh(\eta n) + C_n \cosh(\eta n)] \sin(\eta\xi) \end{aligned} \tag{2.410}$$

and

$$\begin{aligned} y = B_0 + C_0\eta + D_0\xi &+ \sum_{n=1}^{N} [B_n \cosh(\eta n) + C_n \sinh(\eta n)] \cos(n\xi) \\ &+ \sum_{n=1}^{N} [D_n \cosh(\eta n) - A_n \sinh(\eta n)] \sin(n\xi) \end{aligned} \tag{2.411}$$

Here, the range of ξ is $-\pi$ to $+\pi$.

The curves can be represented in the following parametric manner.

Seaward:

$$\begin{aligned} x &= x_S(\xi, -\beta) \\ y &= y_S(\xi, -\beta) \end{aligned} \tag{2.412}$$

Coastline:

$$\begin{aligned} x &= x_C(\xi, +\beta) \\ y &= y_C(\xi, +\beta) \end{aligned} \tag{2.413}$$

where

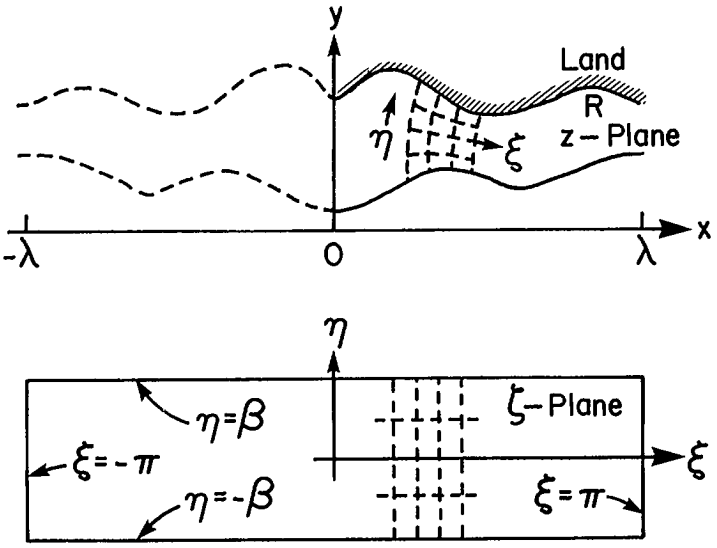

FIG. 2.17. Coast curves and seaward boundary to be mapped from (x, y) space to straightline boundaries in (ξ, η) space. (Reid et al. 1977a)

$$x_S(\xi, -\beta) = A_0 + C_0\xi + D_0\beta + \sum_{n=1}^{N} [C_n \cosh(n\beta) - B_n \sinh(n\beta)] \sin(n\xi) + \sum_{n=1}^{N} [A_n \cosh(n\beta) + D_n \sinh(n\beta)] \cos(n\xi) \tag{2.414}$$

$$y_S(\xi, -\beta) = B_0 - C_0\beta + D_0\xi + \sum_{n=1}^{N} [B_n \cosh(n\beta) - C_n \sinh(n\beta)] \cos(n\xi) + \sum_{n=1}^{N} [A_n \sinh(n\beta) + D_n \cosh(n\beta)] \sin(n\xi) \tag{2.415}$$

$$x_C(\xi, \beta) = A_0 + C_0\xi - D_0\beta + \sum_{n=1}^{N} [B_n \sinh(n\beta) + C_n \cosh(n\beta)] \sin(n\xi) + \sum_{n=1}^{N} [A_n \cosh(n\beta) - D_n \sinh(n\beta)] \cos(n\xi) \tag{2.416}$$

$$y_C(\xi, \beta) = B_0 + C_0\beta + D_0\xi + \sum_{n=1}^{N} [B_n \cosh(n\beta) + C_n \sinh(n\beta)] \cos(n\xi) + \sum_{n=1}^{N} [D_n \cosh(n\beta) - A_n \sinh(n\beta)] \sin(n\xi) \tag{2.417}$$

Note that $x_S(\xi, -B)$ and $x_C(\xi, +\beta)$ represent a periodic range of 2π and this corresponds to the distance 2λ in Fig. 2.17. This implies that $C_0 = \pi/\lambda$ and $A_n = D_n = 0$; $n = 0, 1, 2, \ldots, N$, and B_0 is determined as the mean distance between the coast and seaward boundary curves. Note that β must be determined along with the coefficients in eq. 2.414–2.417 using a curve-fitting scheme. However, the range of ξ and the scale factor C_0 are free parameters.

The coefficients and β must be determined for a given N such that eq. 2.414–2.417 give an accurate approximation to the curves X_S, Y_S, X_C, and Y_C in a least-squares sense. Note that these curves represent the coastline and seaward boundary as a function of the arc length. One must begin with an initial approximation of arc length in terms of ξ for each curve and use an iteration technique to minimize the error function, E:

$$(2.418) \quad E = \frac{1}{2\pi} \int_{-\pi}^{\pi} [(Y_S - y_S)^2 + (X_S - x_S)^2 + (Y_C - y_C)^2 + (X_C - x_C)^2] \, d\xi$$

For economy of computation, one would like to have more grid points in regions of specific interest and fewer grid points elsewhere. To be able to do this, one can stretch the orthogonal curvilinear grid system in both the shoreward and longshore directions. A curvilinear grid in the (x, y) space, which follows from the transformation, is shown in Fig. 2.18a. The corresponding grid in the (ξ, η) space is shown in Fig. 2.18b. From this grid, we would like to transform to another grid with uniform grid increments. To be able to do this, a transformation is made to an (S^*, T^*) space in two steps.

The relation

$$(2.419) \quad S^* = S^*[S_p(\xi)]$$

is used to generate a uniform ΔS^* spacing. Here, S_p is the arc length distance along the transform-generated coast. The relation in eq. 2.419 is generated by a choice of ΔS^* that gives the necessary longshore resolution. In the shoreward direction, the travel time, T^*, for a long wave to cover the distance between the seaward to shoreward boundary along a ξ line can be divided into a desired (from the point of view of resolution) number of increments. This can be written as

$$(2.420) \quad T^* = T^*[S_\eta(\eta)]$$

where S_η is the distance along the ξ line and

$$(2.421) \quad T^* = \int_{S_\eta(\eta)} dS/\sqrt{gD}$$

Here, D is the local water depth. Thus, choices of ΔS^* and ΔT^* generate the (S^*, T^*) grid shown in Fig. 2.18c. The shoreline and seaward boundaries are defined by constant values of T^*, whereas constant values of S^* identify the lateral boundaries.

Let Q be the volume transport per unit width, τ the wind stress, σ the bottom stress, h the perturbation of the water level relative to its undisturbed position, and h_B the hydrostatic elevation corresponding to atmospheric pressure anomaly. Let F be a scale factor of the curvilinear coordinate system given by

$$(2.422) \quad F = \left[\left(\frac{\partial x}{\partial \xi} \right)^2 + \left(\frac{\partial y}{\partial \xi} \right)^2 \right]^{1/2}$$

Let μ and ν be scale factors representing the transformation to the (S^*, T^*) system:

$$(2.423) \quad \mu = \frac{\partial \xi}{\partial S_p} \frac{\partial S_p}{\partial S^*}, \qquad \nu = \frac{\partial \eta}{\partial S_\eta} \frac{\partial S_\eta}{\partial T^*}$$

Then, the vertically integrated equations in the (S^*, T^*) system are

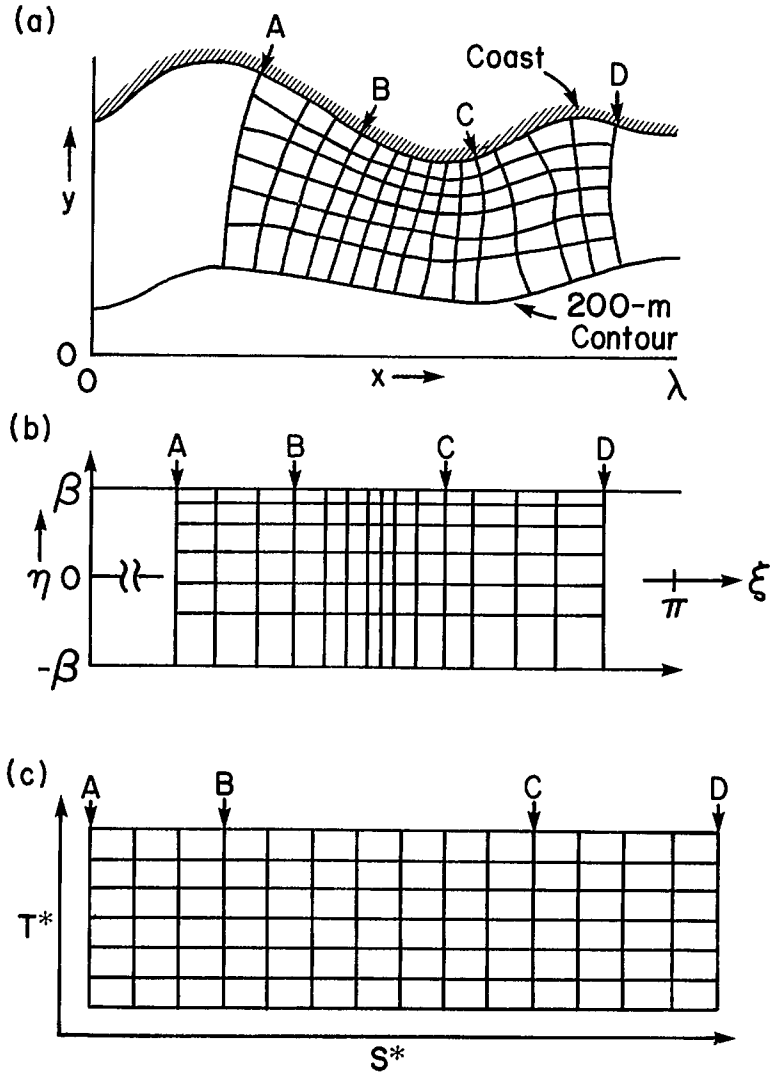

FIG. 2.18. (a) (x, y) space to be mapped by the transformation equations given in the text; (b) transformed system represented in the (ξ, η) space; (c) (ξ, η) space transformed to (S^*, T^*) space. (Reid et al. 1977a)

$$\frac{\partial Q_{S^*}}{\partial t} - fQ_{T^*} + \frac{gD}{F\mu}\frac{\partial}{\partial S^*}(h - h_B) = \tau_{S^*} - \sigma_{S^*} \tag{2.424}$$

$$\frac{\partial Q_{T^*}}{\partial t} + fQ_{S^*} + \frac{gD}{F\nu}\frac{\partial}{\partial T^*}(h - h_B) = \tau_{T^*} - \sigma_{T^*} \tag{2.425}$$

$$\frac{\partial h}{\partial t} + \frac{1}{F^2}\left[\frac{1}{\mu}\frac{\partial}{\partial S^*}(FQ_{S^*}) + \frac{1}{\nu}\frac{\partial}{\partial T^*}(FQ_{T^*})\right] = 0 \tag{2.426}$$

The wind stress, τ, is determined from

$$\tau = \frac{\rho_a C_D W_{10}^2}{\rho_w} \tag{2.427}$$

where ρ_a and ρ_w are air and water densities, respectively, and C_D is a nondimensional drag coefficient such that

$$\frac{\rho_a C_D}{\rho_w} = K = \begin{cases} K_1 \text{ for } W_{10} < 7 \text{ m}\cdot\text{s}^{-1} \\ K_1 + \left(1 - \frac{7}{W_{10}}\right)^2 K_2 \text{ for } W_{10} \geq 7 \text{ m}\cdot\text{s}^{-1} \end{cases} \tag{2.428}$$

where $K_1 = 1.1 \times 10^{-6}$ and $K_2 = 2.5 \times 10^{-6}$ and W_{10} is the wind speed at a height of 10 m above the ground. The bottom stress terms are written as

$$\begin{aligned} \sigma_{S^*} &= \frac{K_0 Q Q_{S^*}}{D^2} \\ \sigma_{T^*} &= \frac{K_0 Q Q_{T^*}}{D^2} \end{aligned} \tag{2.429}$$

where K_0 is a dimensionless drag coefficient and is taken as 2.5×10^{-3}. The surface stress (wind stress) components are written as

$$\begin{aligned} \tau_S^* &= \tau_x \cos\theta + \tau_y \sin\theta \\ \tau_{T^*} &= -\tau_x \sin\theta + \tau_y \cos\theta \end{aligned} \tag{2.430}$$

where

$$\theta = \tan^{-1}\left(\frac{\partial y/\partial \xi}{\partial x/\partial \xi}\right) \tag{2.431}$$

The wind stress components τ_x and τ_y are assumed to be known.

At the lateral boundaries, the gradient of the volume transport in the S^* direction must vanish:

$$\frac{\partial Q_{S^*}}{\partial S^*} = 0 \tag{2.432}$$

On the seaward boundary, the water level is taken as the hydrostatic equivalent of the atmospheric pressure anomaly:

$$h = h_B \tag{2.433}$$

Note that Jelesnianski (1965) used the same condition. At the shoreline boundary the assumption is that (infinitely high wall) there is no transport in the shoreward direction:

$$Q_{T^*} = 0 \tag{2.434}$$

For the numerical integration of eq. 2.424–2.426, an explicit, central-difference, leapfrog scheme (Alvarez 1973) was used. In this scheme, Q_{S^*} and Q_{T^*} are specified at the same location (and time) but h is staggered in space and time from these. This scheme was tested by Reid et al. (1977) by simulating the surge on the coast of the Gulf of Mexico due to Hurricane Carla.

Jelesnianski (1976) used a sheared coordinate system for application to gently curved

coastlines. This method is applicable for coastlines without bays, inlets, capes, etc. He stated:

> . . . a mildly curved coastline is shifted or sheared onto a straight base line. A surface plane, truncated from the ocean shelf and containing the curved coast as a boundary, is fitted with a curved, nonorthogonal grid. The plane with curved boundaries is then transformed via a sheared coordinate system onto an image rectangle. In the transformed system, the computational grid is cartesian, orthogonal, equally spaced and the coast lies exactly on and not across a grid line.

Butler (1979) used a stretched coordinate system for studying hurricane surges in Galveston Bay. The scheme is somewhat similar to that of Wanstrath (1976). Hamilton (1978), in his study of storm surges in the Thames Estuary, used a somewhat different approach; i.e. he wrote the equations in conformal coordinates.

The equations of motion in conformal coordinates for long waves (nondispersive) are

$$\frac{\partial u}{\partial t} - fv + \frac{\partial J}{\partial \xi}\left(\frac{1}{2}u^2 + \frac{1}{2}v^2\right) + Ju\frac{\partial u}{\partial \xi} + Jv\frac{\partial u}{\partial \zeta} + g\frac{\partial h}{\partial \xi} = \tau^{(\xi)}(\rho J^{-1/2})^{-1} \tag{2.435}$$

$$\frac{\partial v}{\partial t} + fu + \frac{\partial J}{\partial \zeta}\left(\frac{1}{2}u^2 + \frac{1}{2}v^2\right) + Ju\frac{\partial v}{\partial \xi} + Jv\frac{\partial v}{\partial \zeta} + g\frac{\partial h}{\partial \zeta} = \tau^{(\zeta)}(\rho J^{-1/2})^{-1} \tag{2.436}$$

$$\frac{\partial h}{\partial t} + J\frac{\partial}{\partial \xi}(D + h)u + J\frac{\partial}{\partial \zeta}(D + h)v = S(\xi, \zeta, t) \tag{2.437}$$

where an arbitrary conformal mapping,

$$\xi + i\zeta = w(\phi + i\psi) \tag{2.438}$$

will produce the coordinates ξ and ζ and the metric

$$J(\xi, \zeta) = \frac{d\xi\, d\zeta}{dA} = R^2 \operatorname{sech}^2 \mu\left[\left(\frac{\partial \mu}{\partial \xi}\right)^2 + \left(\frac{\partial \mu}{\partial \zeta}\right)^2\right]^{-1} \tag{2.439}$$

Here, R is the radius of the earth, ϕ is the east longitude, θ is the north latitude, and μ is the Mercator coordinate given by

$$\tanh \mu = \sin \theta \tag{2.440}$$

and J is the ratio of an elemental area $d\xi\, d\zeta$ to the actual area dA. Note that

$$\begin{aligned} u &= \frac{1}{J}\frac{\partial \xi}{\partial t} \\ v &= \frac{1}{J}\frac{\partial \zeta}{\partial t} \end{aligned} \tag{2.441}$$

and h is the free surface height, D is the water depth, $\tau^{(\xi)}$ and $\tau^{(\zeta)}$ are the stress components, and S is a source term. The velocities u and v in the (ξ, ζ) system are related to the actual velocities U and V through

$$\begin{aligned} u &= UJ^{-1/2} \\ v &= VJ^{-1/2} \end{aligned} \tag{2.442}$$

Chapter 3

Other Numerical Solutions

In Chapter 2, exclusively two-dimensional (vertically integrated) numerical finite-difference models were considered. In this chapter, other numerical models will be discussed beginning with three-dimensional finite-difference models (with and without stratification) and then the so-called two-and-a-half-dimensional models (which are basically similar to vertically integrated two-dimensional models, as considered in Chapter 2, but include an additional computation to determine the vertical distribution of the horizontal velocity components). The two-and-a-half-dimensional models were developed for a better treatment of the bottom stress.

Next, the so-called one-and-a-half-dimensional models will be briefly discussed in which the y variations (in the transverse direction) are ignored and the computations are performed in the $x-z$ plane. Then, the logical step would be a discussion of the one-dimensional models, which are basically similar to the vertically integrated forms of the two-dimensional models, except that the transverse velocity and the variations in the transverse direction are ignored (note that in the one-and-a-half-dimensional models, there is no vertical integration). Next will follow a consideration of combinations of two-dimensional and one-dimensional models such as done for the North Sea, the Strait of Georgia, and the Bay of Bengal in which a two-dimensional model for the sea or bay is coupled with a one-dimensional model for a river or estuary. The chapter will conclude with a discussion of the finite-element methods and irregular-grid finite-difference methods.

It should be noted that there are still several other forms of solutions for the storm surge problem. In Chapters 2 and 3, attention is paid exclusively to numerical solutions. In Chapter 4, these other forms will be considered: analytical, empirical, graphical, statistical, hydraulic, laboratory experiments, hybrid (i.e. combination of hydraulic and numerical) methods, and electric analog techniques.

3.1 Three-Dimensional Models

In this section, three-dimensional models with and without stratification will be considered. For the vertical motion associated with storm surges, influence of stratification is not important, but for an accurate determination of the horizontal motion, inclusion of stratification is useful. There is considerable literature on three-dimensional models under the rigid lid approximation for the free surface. Since this approximation assumes that the surface cannot move up and down, models using this approximation are not relevant for the vertical motion associated with storm surges, although they may still yield reasonably accurate information on the horizontal motion.

Backhaus (1978) considered a three-layer model for the calculation of tides in the German Bight, ignoring stratification. Basically, he wrote the vertically integrated forms of the equations of motion and continuity for each layer. These layers are dynamically coupled through the interfacial shear stresses and the barotropic pressure gradient.

Simons (1980) showed how stratification can be introduced into the classical Ekman problem: first through the horizontal pressure gradients, which have a baroclinic component when stratification is included, and second through the vertical eddy viscosity, which is much less in the stratified case than in the homogeneous case. Abbot et al. (1976)

developed a time-dependent two-layer model for storm surges in the Baltic Sea and the North Sea.

Geisler (1970) studied the steady-state linear response of a two-layer ocean to a moving hurricane, whereas Galt (1971) considered the time-dependent nonlinear response. Krauss (1978) considered the response of a stratified ocean to traveling mesoscale weather systems such as meteorological fronts and squall lines. Kuo and Ichiye (1977) dealt with the problem of the response of a barotropic ocean to a moving hurricane. However, these studies are for the deep ocean and are not particularly relevant for the storm surge problem.

In a series of reports, the Rand Corporation (for example, see Liu and Leendertse 1979) developed sophisticated three-dimensional models and applied these to various water bodies. A detailed consideration will follow of a three-dimensional model developed by Simons (1973) for application to Lake Ontario. In this model, Simons treats the water body as a completely closed system (which of course is justified for Lake Ontario); for bays and gulfs with openings, the model must be modified.

Under the assumption of incompressibility the continuity equation is

$$\frac{\partial u}{\partial x} + \frac{\partial v}{\partial y} + \frac{\partial w}{\partial z} = 0 \tag{3.1}$$

where u and v are the horizontal velocity components along the horizontal axes x and y and w is the velocity along the vertical coordinate z. Let $D(x, y)$ be the water depth in the undisturbed state and let $h(x, y, t)$ be the free surface deviation from its equilibrium position. The vertical integration of eq. 3.1 gives

$$\frac{\partial}{\partial x}\int_{-D}^{h} u\,dz + \frac{\partial}{\partial y}\int_{-D}^{h} v\,dz + \frac{\partial h}{\partial t} = 0 \tag{3.2}$$

The hydrostatic relation

$$\frac{\partial P}{\partial z} = -\rho g \tag{3.3}$$

can be vertically integrated to give the internal pressure distribution.

$$P = P_S + \rho_0 g(h - z) + \int_z^h \sigma\,dz \tag{3.4}$$

where P is the pressure, P_S is the atmospheric pressure at the water surface, ρ is the density of water, ρ_0 is the value of ρ at the temperature of maximum density, g is gravity, and σ is a density anomaly given by

$$\sigma = \frac{\rho - \rho_0}{g} \tag{3.5}$$

The density anomaly may be related to temperature and pressure by an equation of state. Usually, the pressure effect can be neglected and one can write

$$\sigma = -\epsilon\theta^2 \tag{3.6}$$

where ϵ is a constant and

$$\theta \equiv T - T_0 \tag{3.7}$$

Here, T is the temperature and T_0 is its value at maximum density.

Following Simons (1973), define a barotropic pressure function ψ and a baroclinic pressure field ϕ such that

$$\begin{aligned} \psi &\equiv P_s + \rho_0 g h \\ \phi &\equiv \int_z^h \sigma dz \end{aligned} \tag{3.8}$$

Note that the ϕ field is z dependent but that the ψ field is not. Also note that ψ is only a part of the total barotropic pressure field which increases linearly with depth.

Next, Simons defines two operators $\mathcal{L}$ and δ which respectively represent the advection by large-scale motions and diffusion by subgrid scale processes. Let Φ be any scalar field and let α, β, and γ be the components of the diffusive flux of this scalar along x-, y-, and z-axes. Then:

$$\begin{aligned} \mathcal{L}(\Phi) &= \frac{\partial \Phi}{\partial t} + \frac{\partial}{\partial x}(u\Phi) + \frac{\partial}{\partial y}(v\Phi) + \frac{\partial}{\partial z}(w\Phi) \\ \delta(\Phi) &= -\frac{\partial \alpha}{\partial x}(\Phi) - \frac{\partial \beta}{\partial y}(\Phi) - \frac{\partial \gamma}{\partial z}(\Phi) \end{aligned} \tag{3.9}$$

With this notation the equations of horizontal motion can be written in the following form:

$$\begin{aligned} \mathcal{L}(u) &= fv - \frac{\partial}{\partial x}\left(\frac{\psi + \phi}{\rho_0}\right) + \delta(u) \\ \mathcal{L}(v) &= -fu - \frac{\partial}{\partial y}\left(\frac{\psi + \phi}{\rho_0}\right) + \delta(v) \end{aligned} \tag{3.10}$$

The thermal energy equation can be written as

$$\mathcal{L}(\theta) = \delta(\theta) \tag{3.11}$$

Let A and ν respectively be the eddy viscosities in the horizontal and vertical directions. Then:

$$\begin{aligned} \alpha(u) &= -A\frac{\partial u}{\partial x} \qquad \alpha(v) = -A\frac{\partial v}{\partial x} \\ \beta(u) &= -A\frac{\partial u}{\partial y} \qquad \beta(v) = -A\frac{\partial v}{\partial y} \\ \gamma(u) &= -A\frac{\partial u}{\partial z} \qquad \gamma(v) = -A\frac{\partial v}{\partial z} \end{aligned} \tag{3.12}$$

From eq. 3.10 and 3.12 one can see that the horizontal diffusion will be in the form of a Laplacian operator. In the numerical model, this term represents the subgrid scale diffusion. The vertical flux component will be in the form of stresses between the various layers and represents the momentum transfer downward from the surface.

Similarly, for the thermal energy one can write

$$\begin{aligned} \alpha(\theta) &= -A_0\frac{\partial \theta}{\partial x} \\ \beta(\theta) &= -A_0\frac{\partial \theta}{\partial y} \\ \gamma(\theta) &= -\kappa\frac{\partial \theta}{\partial z} \end{aligned} \tag{3.13}$$

where A_0 and κ are respectively the horizontal and vertical eddy diffusivities. The parameter κ depends on the static stability $\partial\sigma/\partial z$. During unstable situations this can assume very large values and the convective overturning can be simulated. That is, during numerical integration, if any static instability occurs, then instantaneous adjustment is permitted to remove the instability.

The following boundary conditions are relevant.
At the surface, $z = h$:

$$w = u\frac{\partial h}{\partial x} + v\frac{\partial h}{\partial y} + \frac{\partial h}{\partial t} \tag{3.14}$$

At the bottom, $z = -D$:

$$w = -u\frac{\partial D}{\partial x} - v\frac{\partial D}{\partial y} \tag{3.15}$$

These conditions mean that the water particles follow the motion of the boundary under consideration.

At the surface $z = h$, the wind stress condition can be written as

$$\begin{aligned} \tau_{S_x} &= -\rho_0\left[\gamma(u) - \alpha(u)\frac{\partial h}{\partial x} - \beta(u)\frac{\partial h}{\partial y}\right] \\ \tau_{S_y} &= -\rho_0\left[\gamma(v) - \alpha(v)\frac{\partial h}{\partial x} - \beta(v)\frac{\partial h}{\partial y}\right] \end{aligned} \tag{3.16}$$

The conditions at the bottom $z = -D$ (i.e. bottom stress) are

$$\begin{aligned} \tau_{B_x} &= -\rho_0\left[\gamma(u) + \alpha(u)\frac{\partial D}{\partial x} + \beta(u)\frac{\partial D}{\partial y}\right] \\ \tau_{B_y} &= -\rho_0\left[\gamma(v) + \alpha(v)\frac{\partial D}{\partial x} + \beta(v)\frac{\partial D}{\partial y}\right] \end{aligned} \tag{3.17}$$

Let q_S be the downward surface flux of heat. Then, the thermal conditions are the following.
At the surface, $z = h$:

$$q_S = -\left[\gamma(\theta) - \alpha(\theta)\frac{\partial h}{\partial x} - \beta(\theta)\frac{\partial h}{\partial y}\right] \tag{3.18}$$

At the bottom, $z = -D$:

$$0 = \gamma(\theta) + \alpha(\theta)\frac{\partial D}{\partial x} + \beta(\theta)\frac{\partial D}{\partial y} \tag{3.19}$$

For the layered model, the equations of motion and continuity are vertically integrated in each layer. With reference to Fig. 3.1 when the interfaces between the layers intersect the bottom, the number of layers will be a function of x and y and could also be a function of t. However, it is convenient to assume that the total number of layers is the same throughout the water body, and this can be done by allowing the interface to coincide with the bottom beyond their intersection. Thus, in principle, each layer extends over the whole surface area of the water body.

Let the number of layers be k and let H_k with $k = 1, 2, \ldots, k - 1$ be the distance between the interface and the equilibrium free surface ($z = 0$). The nature of the interfaces

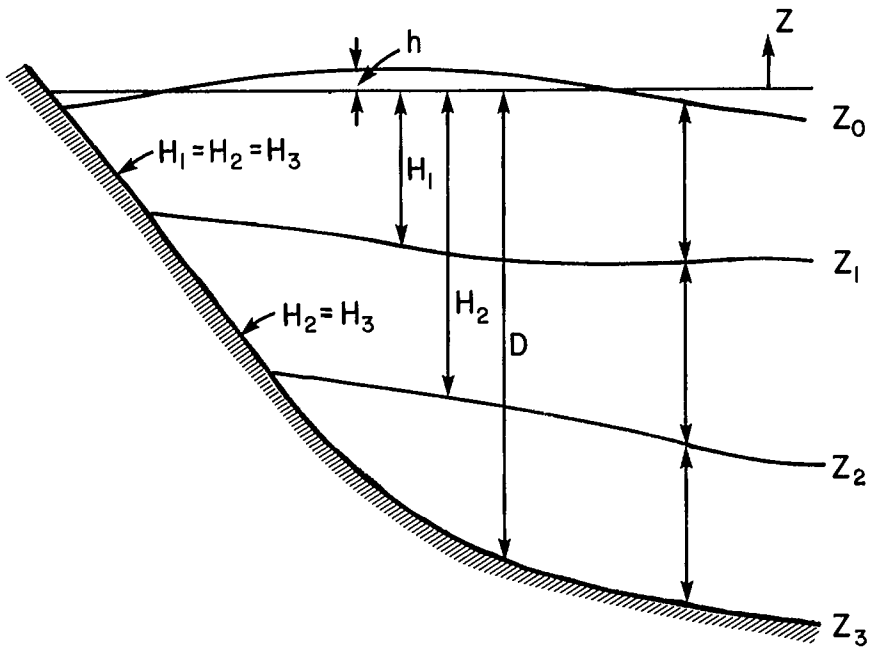

FIG. 3.1. Vertical configuration of a three-dimensional model. (Simons 1973)

could be any of the following three: $H_k = H_k(x, y, t)$, i.e. the layers are separated by moving material surfaces; $H_k = H_k(x, y)$, i.e. the layers are separated by rigid permeable interfaces; H_k is constant, i.e. the layers are separated by rigid levels.

Thus, one can denote the surface and the interfaces by

$$z = z_k(x, y, t), \qquad k = 0, 1, 2, \ldots, K \tag{3.20}$$

Then:

$$\begin{aligned} &\text{Free surface: } z_0 = h(x, y, t) \\ &\text{Interfaces: } z_k = -H_k(x, y, t), \qquad k = 1, 2, \ldots, K-1 \\ &\text{Bottom: } z_k = -D(x, y) \end{aligned} \tag{3.21}$$

Note that for certain regions of the water body, some of the interfaces may coincide with the bottom.

The principal dependent variables are the thickness, transports, and heat content in each layer. The following notation is introduced:

$$\begin{aligned} &\text{Layer thickness: } d_{k-1/2} \equiv z_{k-1} - z_k \\ &\text{Layer transports: } (M, N)_{k-1/2} \equiv \int_{z_k}^{z_{k-1}} (u, v)\, dz \\ &\text{Layer heat content: } T_{k-1/2} \equiv \int_{z_k}^{z_{k-1}} \theta\, dz \end{aligned} \tag{3.22}$$

As can be seen from Fig. 3.1, an integer subscript denotes a variable evaluated at an

interface whereas a half-integer subscript refers to a layer.

To be able to generalize the model to a multilayer situation, Simons introduced a vertical velocity ω_k relative to a surface z_k as

$$\omega_k \equiv w_k - u_k \frac{\partial z_k}{\partial x} - v_k \frac{\partial z_k}{\partial y} - \frac{\partial z_k}{\partial t} \tag{3.23}$$

Let χ denote the diffusive flux through a surface z_k:

$$\chi(\Phi)_k \equiv \gamma(\Phi)_k - \alpha(\Phi)_k \frac{\partial z_k}{\partial x} - \beta(\Phi)_k \frac{\partial z_k}{\partial y}, \qquad k = 0, 1, \ldots, K \tag{3.24}$$

If the scalar Φ denotes momentum and temperature, then eq. 3.24 represents the stresses and the heat fluxes between layers, which are denoted in Fig. 3.1 by τ and q.

Corresponding to eq. 3.9 one must define advection and diffusion operators for each layer:

$$\begin{aligned} L(\Phi)_{k-1/2} &\equiv \int_{z_k}^{z_{k-1}} \mathcal{L}(\Phi)\, dz \\ \Delta(\Phi)_{k-1/2} &\equiv \int_{z_k}^{z_{k-1}} \delta(\Phi)\, dz \end{aligned} \tag{3.25}$$

Integrate eq. 3.9 with respect to z over each layer and interchange differentiation and integration and use eq. 3.23 and 3.24 to give

$$L(\Phi)_{k-1/2} \equiv \frac{\partial}{\partial t} \int_{z_k}^{z_{k-1}} \Phi\, dz + \frac{\partial}{\partial x} \int_{z_k}^{z_{k-1}} u\Phi\, dz + \frac{\partial}{\partial y} \int_{z_k}^{z_{k-1}} v\Phi\, dz + (\omega\Phi)_{k-1} - (\omega\Phi)_k \tag{3.26}$$

and

$$\Delta(\Phi)_{k-1/2} \equiv -\frac{\partial}{\partial x} \int_{z_k}^{z_{k-1}} \alpha(\Phi)\, dz - \frac{\partial}{\partial y} \int_{z_k}^{z_{k-1}} \beta(\Phi)\, dz - \chi(\Phi)_{k-1} + \chi(\Phi)_k \tag{3.27}$$

Next, for the layered variables given by eq. 3.22 one must derive the equations of motion and continuity. From eq. 3.22 and 3.23 the continuity equation becomes

$$\frac{\partial d_{k-1/2}}{\partial t} + \frac{\partial}{\partial x} M_{k-1/2} + \frac{\partial}{\partial y} N_{k-1/2} + \omega_{k-1} - \omega_k = 0 \tag{3.28}$$

Using eq. 3.26 this equation can be written as

$$L(1)_{k-1/2} = 0 \tag{3.29}$$

Using this equation one can either compute the displacement $\partial z_k/\partial t$ of a material surface or the apparent vertical motion, ω_k, through a rigid interface. The computation could start at the bottom and proceed upward with the following conditions being applied.

Bottom (rigid, impermeable), $z_k(x, y)$:	$\omega_k = \dfrac{\partial z_k}{\partial t} = 0$
Rigid interface (permeable), $z_k(x, y)$:	$\dfrac{\partial z_k}{\partial t} = 0$
Material interface (impermeable), $z_k(x, y, t)$:	$\omega_k = 0$
Free surface (impermeable): $z_0(x, y, t)$:	$\omega_0 = 0$

(3.30)

Note that these conditions are written using eq. 3.14 and 3.15.

The equations of motion (3.10) integrated over z in each layer become

$$(3.31)\quad L(M)_{k-1/2} = fN_{k-1/2} - \frac{d_{k-1/2}}{\rho_0}\frac{\partial \psi}{\partial x} - \int_{z_k}^{z_{k-1}} \frac{\partial}{\partial x}\left(\frac{\phi}{\rho_0}\right) dz + \Delta(M)_{k-1/2}$$

and

$$(3.32)\quad LN_{k-1/2} = -fM_{k-1/2} - \frac{d_{k-1/2}}{\rho_0}\frac{\partial \psi}{\partial y} - \int_{z_k}^{z_{k-1}} \frac{\partial}{\partial y}\left(\frac{\phi}{\rho_0}\right) dz + \Delta(N)_{k-1/2}$$

From eq. 3.11 the thermal energy equation becomes

$$(3.33)\quad L(\theta)_{k-1/2} = \Delta(\theta)_{k-1/2}$$

For convenience, define

$$z_{k-1/2} \equiv \frac{1}{2}(z_{k-1} + z_k)$$

$$(3.34)\quad S_{k-1/2} \equiv \int_{z_k}^{z_{k-1}} \sigma\, dz$$

$$\phi_{k-1/2} \equiv \int_{z_{k-1/2}}^{h} \sigma\, dz$$

The baroclinic pressure field defined by eq. 3.8 can be assumed to vary linearly with height in each layer. Then, differentiating ϕ with respect to x and y and integrating with respect to z gives

$$(3.35)\quad \int_{z_k}^{z_{k-1}} \nabla\phi\, dz = d_{k-1/2}\nabla\phi_{k-1/2} + S_{k-1/2}\nabla z_{k-1/2}$$

The first term on the right is the gradient of the baroclinic pressure evaluated at the midpoint of the layer. The second term is a correction for the variable thicknesses of the layers.

For numerical integration purposes, although we now have a closed set of equations, these must be expressed in terms of the primary dependent variables defined in eq. 3.22. The product terms can be approximated as follows:

$$(3.36)\quad \int_{z_k}^{z_{k-1}} u\theta\, dz = \left(\frac{MT}{d}\right)_{k-1/2}$$

From eq. 3.6 and 3.34 the layer density can be defined as

$$(3.37)\quad S_{k-1/2} = -\epsilon\left(\frac{T^2}{d}\right)_{k-1/2}$$

Then, from eq. 3.26 the advection of temperature is given by

$$(3.38)\quad L(\theta)_{k-1/2} = \frac{\partial T_{k-1/2}}{\partial t} + \frac{\partial}{\partial x}\left(\frac{MT}{d}\right)_{k-1/2} + \frac{\partial}{\partial y}\left(\frac{NT}{d}\right)_{k-1/2} + (\omega\theta)_{k-1} - (\omega\theta)_k$$

The nonlinear inertial terms also can be approximated in the same manner. The interpolation schemes to calculate the temperature and horizontal velocity fields at the inter-

faces will be governed by energy considerations. For the details of this as well as for the formulation of the horizontal diffusion, temperature fluxes, and interfacial stresses, see Simons (1973).

The scheme for the numerical integration is as follows. Initially, the temperature field, positions of all the interfaces and surface, and the horizontal transport components are prescribed. Then, the barotropic pressure gradient is given by eq. 3.8 and the baroclinic pressure gradient is obtained from eq. 3.34, 3.35, and 3.37. The vertical motion at rigid interfaces can be calculated from eq. 3.28. Then, the time stepping of the primary variables is determined by eq. 3.28, 3.31, and 3.32. Note that the numerical scheme in time and space for the layered model is the same as for the homogeneous model. Simons (1973) showed through energy considerations that inclusion of the nonlinear advective terms does not lead to any instability as long as the finite-difference schemes are conservative (Lilly 1965; Arakawa 1966; Bryan 1966).

3.2 Two-and-a-Half-Dimensional Models and Improved Treatment of Bottom Stress

A two-and-a-half-dimensional model is a combination of a two-dimensional vertically integrated model and a locally one-dimensional Ekman model. These models serve to determine the vertical variation of the horizontal current and also permit a better treatment of the bottom stress. In Chapter 2 it was shown that the vertical integration of the terms $\nu\partial^2 u/\partial z^2$ and $\nu\partial^2 v/\partial z^2$, where ν is the vertical eddy viscosity and u and v are the x and y components of the velocity, leads to $\tau_{S_x} - \tau_{B_x}$ in the x-momentum equation and to $\tau_{S_y} - \tau_{B_y}$ in the y-momentum equation. Here, τ_S is the surface wind stress and τ_B is the bottom stress. In numerical models of storm surges, since the vertically integrated forms of the equations are usually used, rather than prescribing ν one can deal directly with τ_S and τ_B. The wind stress is prescribed either from observations or hypothetically, whereas the bottom stress is parameterized through an empirical drag coefficient. In Chapter 2, three versions of such a parameterization (linear, quasilinear, and nonlinear) were discussed.

In the classical Ekman theory (1905, 1923) one deals directly with the terms $\nu\partial^2 u/\partial z^2$ and $\nu\partial^2 v/\partial z^2$ rather than with their vertically integrated forms. Also, the classical Ekman theory was developed for the steady state only, although later authors extended it to the transient state. The steady-state equations of motion used in the classical Ekman theory are as follows:

$$\begin{aligned} \nu\left(\frac{\partial^2 u}{\partial z^2}\right) + fv &= fv_g \\ \nu\left(\frac{\partial^2 v}{\partial z^2}\right) - fu &= -fu_g \end{aligned} \tag{3.39}$$

where f is the Coriolis parameter and u_g and v_g are components of the geostrophic current, defined by

$$\begin{aligned} u_g &= -\frac{1}{\rho f}\frac{\partial P}{\partial y} \\ v_g &= +\frac{1}{\rho f}\frac{\partial P}{\partial x} \end{aligned} \tag{3.40}$$

where ρ is the density of water and P is pressure.

With reference to an origin taken at the undisturbed water surface, with the vertical coordinate z positive upward, the boundary conditions are the following:
At the surface, $z = 0$:

$$(3.41) \qquad \nu\left(\frac{\partial u}{\partial z}\right) = \frac{\tau_{S_x}}{\rho}, \qquad \nu\left(\frac{\partial v}{\partial z}\right) = \frac{\tau_{S_y}}{\rho}$$

At the bottom, $z = -D$, the no-slip condition is

$$(3.42) \qquad u = v = 0$$

The solutions of eq. 3.39 under these boundary conditions are (Simons 1980)

$$(3.43) \qquad \begin{aligned} u &= \left(1 - \frac{\alpha}{C}\right)u_g - \frac{\beta}{C}v_g + \frac{1}{\Delta\rho f}\left[\frac{(\gamma + \epsilon)}{C}\tau_{S_x} + \frac{(\gamma - \epsilon)}{C}\tau_{S_y}\right] \\ v &= \left(1 - \frac{\alpha}{C}\right)v_g + \frac{\beta}{C}u_g + \frac{1}{\Delta\rho f}\left[\frac{(\gamma + \epsilon)}{C}\tau_{S_y} - \frac{(\gamma - \epsilon)}{C}\tau_{S_x}\right] \end{aligned}$$

where C is a nondimensional parameter defined by

$$(3.44) \qquad C \equiv \cosh(2\delta) + \cos(2\delta)$$

and

$$(3.45) \qquad \delta = \frac{D}{\Delta}$$

$$(3.46) \qquad \Delta = \sqrt{\frac{2\nu}{f}} = \text{Ekman depth}$$

In eq. 3.43 the parameters α, β, γ, and ϵ are all functions of z and are defined as follows:

$$(3.47) \qquad \begin{aligned} \alpha &\equiv \cosh(\delta + \zeta)\cos(\delta - \zeta) + \cosh(\delta - \zeta)\cos(\delta + \zeta) \\ \beta &\equiv \sinh(\delta + \zeta)\sin(\delta - \zeta) + \sinh(\delta - \zeta)\sin(\delta + \zeta) \\ \gamma &\equiv \sinh(2\delta + \zeta)\cos(\zeta) + \sinh(\zeta)\cos(2\delta + \zeta) \\ \epsilon &\equiv \cosh(2\delta + \zeta)\sin(\zeta) + \cosh(\zeta)\sin(2\delta + \zeta) \end{aligned}$$

where

$$(3.48) \qquad \zeta \equiv \frac{z}{\Delta}$$

For great water depths (i.e. small Ekman numbers), $\delta \to \infty$ and eq. 3.47 reduces to

$$(3.49) \qquad \begin{aligned} \frac{\alpha}{C} &\sim e^{-\zeta'}\cos\zeta' \\ \frac{\beta}{C} &\sim e^{-\zeta'}\sin\zeta' \\ \frac{\gamma}{C} &\sim e^{\zeta}\cos\zeta \\ \frac{\epsilon}{C} &\sim e^{\zeta}\sin\zeta \end{aligned}$$

where

$$\zeta' = \zeta + \delta \tag{3.50}$$

Thus, in deep water, the solutions for u and v are a linear combination of (a) the geostrophic current, (b) a bottom current, and (c) a surface drift current. Of these, the first is uniform in the vertical direction, the second decreases exponentially starting at the bottom, and the third decreases rapidly with depth starting at the top. The surface drift current satisfies the upper boundary condition whereas the geostrophic current, together with the bottom current, satisfies the lower boundary condition. One important result is that, at the surface, the drift current is directed 45° to the right of the wind stress in the Northern Hemisphere.

The x and y components of the volume transport and the components of the bottom stress can be written as follows:

$$\begin{aligned} M &= \int_{-D}^{0} u\,dz = D[(1-B)u_g - Av_g] + \frac{1}{\rho f}[E\tau_{S_x} + (1-F)\tau_{S_y}] \\ N &= \int_{-D}^{0} v\,dz = D[(1-B)v_g + Au_g] + \frac{1}{\rho f}[E\tau_{S_y} - (1-F)\tau_{S_x}] \end{aligned} \tag{3.51}$$

and

$$\begin{aligned} \tau_{B_x} &= \rho f D(Au_g - Bv_g) + F\tau_{S_x} + E\tau_{S_y} \\ \tau_{B_y} &= \rho f D(Av_g + Bu_g) + F\tau_{S_y} - E\tau_{S_x} \end{aligned} \tag{3.52}$$

where the dimensionless constants A, B, E, and F are defined by

$$\begin{aligned} A &\equiv \frac{\sinh(2\delta) - \sin(2\delta)}{2\delta C} \\ B &\equiv \frac{\sinh(2\delta) + \sin(2\delta)}{2\delta C} \\ E &\equiv \frac{2\sinh(\delta)\sin(\delta)}{C} \\ F &\equiv \frac{2\cosh(\delta)\cos(\delta)}{C} \end{aligned} \tag{3.53}$$

For great water depths, $\delta \to \infty$

$$A \sim \frac{1}{2\delta},\quad B \sim \frac{1}{2\delta},\quad E \sim 0,\quad F \sim 0 \tag{3.54}$$

Hence, in deep water

$$\begin{aligned} M &= \left(D - \frac{\Delta}{2}\right)u_g - \frac{\Delta}{2}v_g + \frac{1}{\rho f}\tau_{S_y} \\ N &= \left(D - \frac{\Delta}{2}\right)v_g + \frac{\Delta}{2}u_g - \frac{1}{\rho f}\tau_{S_x} \end{aligned} \tag{3.55}$$

and

$$\tau_{B_x} = \frac{1}{2\rho f \Delta}(u_g - v_g)$$
$$\tau_{B_y} = \frac{1}{2\rho f \Delta}(u_g + v_g) \tag{3.56}$$

It can be seen that in the deepwater case, the bottom stress is directed 45° to the left of the geostrophic current (or 45° to the right of the pressure gradient force) and the surface drift transport is directed 90° to the right of the wind stress.

In the shallow-water limit, eq. 3.51 and 3.52 reduce to

$$M = \frac{D^2}{\rho\nu}\left(\frac{\tau_{S_x}}{2} - \frac{D}{3}\frac{\partial P}{\partial x}\right)$$
$$N = \frac{D^2}{\rho\nu}\left(\frac{\tau_{S_y}}{2} - \frac{D}{3}\frac{\partial P}{\partial y}\right) \tag{3.57}$$

and

$$\tau_{B_x} = -D\left(\frac{\partial P}{\partial x}\right) + \tau_{S_x}$$
$$\tau_{B_y} = -D\left(\frac{\partial P}{\partial y}\right) + \tau_{S_y} \tag{3.58}$$

At times the no-slip condition at the bottom given by eq. 3.42 could be restrictive. In its place, one can use a more flexible statement that the velocity and stress be parallel at the bottom, i.e.:

$$V_b = S\left(\frac{\partial V}{\partial z}\right)_b \tag{3.59}$$

where S is a slip parameter, V is a vector denoting the current, and subscript b denotes bottom. When $S = 0$, the no-slip condition results, and when $S = \infty$, the stress is zero. In a model in which the vertical eddy viscosity, ν, is held constant, it is necessary to use eq. 3.59 so that the drastic decrease of ν as the bottom approaches can be taken into account.

Fjeldstad (1930) and Hidaka (1933) extended the theory to the transient state. In the steady-state case of the Ekman problem, one can express the vertically integrated transport in terms of the local surface gradient and wind stress and then solve for the horizontal motion using the lateral boundary conditions and the continuity equation. However, in the time-dependent case, the equation for the surface elevation in terms of wind stress is an integrodifferential equation (Welander 1957) and is not easy to solve. Approximate solutions to the time-dependent problem are given by Nomitsu (1934) and Platzman (1963).

Welander (1957), making use of the Ekman theory, showed that the bottom stress can be determined from the local time histories of the wind stress and the surface slope through the use of a convolution integral. He extended the Ekman theory to the shallow case. The linearized equations of motion with the neglect of horizontal friction are as follows:

$$\frac{\partial u}{\partial t} - fv = -g\frac{\partial h}{\partial x} + \nu\frac{\partial^2 u}{\partial z^2}$$
$$\frac{\partial v}{\partial t} + fu = -g\frac{\partial h}{\partial y} + \nu\frac{\partial^2 v}{\partial z^2} \tag{3.60}$$

where the coefficient of vertical eddy viscosity, ν, is assumed to be constant. The boundary conditions are

$$
\begin{aligned}
&\nu\left(\frac{\partial u}{\partial z}\right)_{z=0} = \tau_{S_x} \\
&u|_{z=-D} = 0 \\
&\nu\left(\frac{\partial v}{\partial z}\right)_{z=0} = \tau_{S_y} \\
&v|_{z=-D} = 0
\end{aligned}
\tag{3.61}
$$

Ekman (1905) determined the current structure from these equations for prescribed wind stress components τ_{S_x} and τ_{S_y} and surface slopes $\partial h/\partial x$ and $\partial h/\partial y$. Ekman (1923) assumed that the depth of frictional influence, d, which is given by

$$
d = \pi\sqrt{\frac{2\nu}{f}} \tag{3.62}
$$

is small compared with the water depth, D.

For convenience, following Welander (1957), write

$$
\begin{aligned}
&w = u + iv \\
&\frac{\partial h}{\partial n} = \frac{\partial h}{\partial x} + i\frac{\partial h}{\partial y} \\
&\tau_S = \tau_{S_x} + i\tau_{S_y}
\end{aligned}
\tag{3.63}
$$

The boundary conditions (eq. 3.61) then become

$$
\begin{aligned}
&\nu\left(\frac{\partial w}{\partial z}\right)_{z=0} = \tau_S \\
&w|_{z=-D} = 0
\end{aligned}
\tag{3.64}
$$

Let $w_a(z, t)$ and $w_b(z, t)$ respectively represent the current generated as a result of a suddenly imposed wind stress of unit magnitude and a suddenly imposed surface slope of unit magnitude. For the first case, the equation of motion and the boundary conditions can be written as

$$
\begin{aligned}
&\frac{\partial w}{\partial t} + ifw = \nu\frac{\partial^2 w}{\partial z^2} \\
&\nu\left(\frac{\partial w}{\partial z}\right)_{z=0} = 1 \\
&w|_{z=-D} = 0 \\
&w|_{t=0} = 0
\end{aligned}
\tag{3.65}
$$

For the second case (i.e. suddenly imposed surface slope):

$$\frac{\partial w}{\partial t} + ifw = -g + \nu \frac{\partial^2 w}{\partial z^2}$$

$$\nu\left(\frac{\partial w}{\partial z}\right)_{z=0} = 0$$

(3.66)

$$w|_{z=-D} = 0$$

$$w|_{t=0} = 0$$

Following Fjeldstad (1930) and Hidaka (1933), the general solution of eq. 3.65 and 3.66 are as follows:

$$w_a = -\frac{1}{\pi^2}\frac{D}{\nu}\left(\frac{d}{D}\right)^2 \sum_{n=0}^{\infty} \frac{1}{(\mu_n^2 + i)} \cos\left(\frac{2n+1}{2}\right)\frac{\pi z}{D} e^{-(\mu_n^2 + i)if} + \bar{w}_a \tag{3.67}$$

and

$$w_b = -\frac{\sqrt{2}}{\pi}\frac{g}{f}\frac{d}{D} \sum_{n=0}^{\infty} \frac{(-1)^n}{(\mu_n^2 + i)} \cos\left(\frac{2n+1}{2}\right)\frac{\pi z}{D} e^{-(\mu_n^2 + i)if} + \bar{w}_b \tag{3.68}$$

where

$$\mu_n \equiv \frac{1}{2\sqrt{2}}(2n+1)\frac{D}{d} \tag{3.69}$$

and $\bar{w}_a$ and $\bar{w}_b$ are the steady-state solutions.

The combined response to an impulsively introduced wind stress $\Delta\tau_S$ and a surface slope $\Delta\partial h/\partial n$ is

$$w = \Delta\tau_S w_a(z, t) + \Delta\frac{\partial h}{\partial n} w_b(z, t)$$

since

$$\Delta\tau_S = \frac{\partial \tau_S}{\partial t}\Delta t \text{ and } \Delta\frac{\partial h}{\partial n} = \frac{\partial^2 h}{\partial t \partial n}\Delta t$$

and adding all the contributions from such differential step-forcing from wind stress and surface slope for all time $\alpha < \tau$ gives

$$w = \int_0^{\infty}\left[\frac{\partial \tau_S}{\partial t}(t-\alpha)w_a(z, \alpha) + \frac{\partial^2 h}{\partial t \partial n}(t-\alpha)w_b(z, \alpha)\right] d\alpha \tag{3.70}$$

It is assumed here that initially, τ_S and $\partial h/\partial n$ are zero.

From eq. 3.70 after integration by parts

$$w = \int_0^{\infty}\left[\tau_S(t-\alpha)\frac{\partial w_a}{\partial t}(z, \alpha) + \frac{\partial h}{\partial n}(t-\alpha)\frac{\partial w_b}{\partial t}(z, \alpha)\right] d\alpha \tag{3.71}$$

If eq. 3.71 is integrated with respect to z and substituted for w_a and w_b from eq. 3.67 and 3.68:

$$w = \frac{4}{\pi}\int_0^{\infty}\tau_S(t-\alpha)\sum_{n=0}^{\infty}\frac{(-1)^n}{(2n+1)} e^{-(\mu_n^2+i)\alpha f}\, d\alpha$$

$$-\frac{8}{\pi^2} gD \int_0^{\infty}\frac{\partial h}{\partial n}(t-\alpha)\sum_{n=0}^{\infty}\frac{1}{(2n+1)} e^{-(\mu_n^2+i)\alpha f}\, d\alpha \tag{3.72}$$

The continuity equation can be written as

$$\frac{\partial h}{\partial t} = -\text{div } w \tag{3.73}$$

Substituting eq. 3.72 into eq. 3.73 gives one integrodifferential equation, which is a prediction equation for h. The interesting point is that the right side of this equation contains terms representing the time histories of the wind stress and surface slope.

Jelesnianski (1970) used a convolution integral of the local time histories of the wind stress and surface slope for a study of storm surges on the Atlantic coast of the United States. It was seen earlier that the transient Ekman problem consists of a drift current due to wind stress and a gradient current due to the slope of the surface. The vector velocity, V, is given by Simons (1980) as

$$V = \frac{2}{\rho D} \sum_{n=1}^{\infty} \cos(\alpha_n z) \int_0^t \left[\tau_S(t - t') + \frac{(-1)^n}{\alpha_n} \nabla P(t - t') e^{-\theta_n t'} \alpha t' \right. \tag{3.74}$$

where

$$\begin{aligned} \alpha_n &\equiv \left(n - \frac{1}{2}\right)\frac{\pi}{D} \\ \theta_n &\equiv if + \nu\alpha_n^2 \end{aligned} \tag{3.75}$$

Note that to derive the integrodifferential equation of Welander (1957), one can integrate eq. 3.74 with respect to z and substitute the transport components into the vertically integrated form of the continuity equation. The bottom stress, τ_B, can be obtained from the relation

$$\frac{\tau_B}{\rho} = \nu \frac{\partial V}{\partial z} \text{ at } z = -D \tag{3.76}$$

where V is given by eq. 3.74. Jelesnianski defined the following Kernel functions (K_τ and K_P):

$$\begin{aligned} K_\tau(t) &\equiv \sum_{n=1}^{\infty} (-1)^n \alpha_n e^{-\nu\alpha_n^2 t} \\ K_P(t) &\equiv \sum_{n=1}^{\infty} e^{-\nu\alpha_n^2 t} \end{aligned} \tag{3.77}$$

Equations 3.74, 3.76, and 3.77 give

$$\tau_B = -\frac{2\nu}{D} \int_0^t [K_\tau(t')\tau_S(t - t') + K_P(t')\nabla P(t - t')] e^{-ift'} \, dt' \tag{3.78}$$

Since the terms in the series decay exponentially, the first few terms are sufficient to evaluate K_τ and K_P. Jelesnianski gave a recurrence relation for eq. 3.78.

Gedney and Lick (1972) used a technique similar to that of Welander (1957) and Jelesnianski (1970) for circulation in the Gulf of Mexico. In all of these studies a constant value was assumed for the vertical eddy viscosity, ν.

Weatherly (1977) showed from observations in the North Sea that there is overwhelming evidence for the existence of a logarithmic boundary layer at the bottom. Also for the North Sea, Bowden (1965) and Ronday (1976) showed that the vertical eddy viscosity increases with height near the bottom and then flattens out in the upper layers, following a parabolic curve.

Nihoul (1977) used a variable eddy viscosity. He made series expansions of the modified Ekman variables in eigenfunctions of the vertical turbulent diffusity and sought analytical solutions to the Ekman equations in terms of wind stress, vertically averaged current, and the surface elevation. Near amphidromic points (locations in a water body where the vertical range of the tide is zero) where the nonlinear advection terms are important he used an iteration procedure.

Following Nihoul (1977), a two-and-a-half-dimensional model will be developed beginning with the equations of motion and continuity in a Cartesian coordinate system, neglecting horizontal friction but including the advective terms:

$$\frac{\partial u}{\partial t} + \underset{\sim}{V}\nabla u - fv = -\frac{\partial}{\partial x}\left(\frac{P_a}{\rho} + gh\right) + \frac{\partial}{\partial z}\left(\nu\frac{\partial u}{\partial z}\right) \tag{3.79}$$

$$\frac{\partial v}{\partial t} + \underset{\sim}{V}\nabla v + fu = -\frac{\partial}{\partial y}\left(\frac{P_a}{\rho} + gh\right) + \frac{\partial}{\partial z}\left(\nu\frac{\partial v}{\partial z}\right) \tag{3.80}$$

$$\underset{\sim}{\nabla}\underset{\sim}{V} = 0 \tag{3.81}$$

where $\underset{\sim}{V} = (u, v, w)$ is the velocity vector and $\underset{\sim}{\nabla}$ is the three-dimensional operator. The origin is taken at the undisturbed level so that the free surface is denoted by $z = h$ and the bottom by $z = -D$.

Introduce a new independent variable ξ to replace the vertical coordinate z such that

$$\xi \equiv \frac{z + D}{H} \tag{3.82}$$

where

$$H \equiv D + h \tag{3.83}$$

Note that $0 \leq \xi \leq 1$. This change of variable is convenient in the determination of eigenfunctions of the vertical eddy viscosity parameter.

According to Nihoul (1977), ξ should, strictly speaking, vary from a very small value $\xi_0 = z_0/H$ to 1 where z_0 is the so-called Rugosity length (z_0 is the distance above the bottom where the velocity is set to zero, $z_0 \sim 10^{-3}$ m). Although $\xi_0 \ll 1$, it cannot be taken as zero because the linear variation of the vertical eddy viscosity, ν, near the bottom leads to a logarithmic velocity profile that is singular at $\xi = 0$. The lower limit of ξ can be taken as zero so long as it does not create a singularity.

The first two terms on the left side of eq. 3.79 and 3.80 become, after the change of variable,

$$\frac{\partial V_i}{\partial t} + A_i + B_i + S_i, \qquad i = 1, 2 \tag{3.84}$$

where

$$A_i = u\frac{\partial V_i}{\partial x} + v\frac{\partial V_i}{\partial y}, \qquad i = 1, 2 \tag{3.85}$$

$$B_i = \frac{1}{H}\frac{\partial V_i}{\partial \xi}(1 - \xi)\left(u\frac{\partial D}{\partial x} + v\frac{\partial D}{\partial y} + w\right), \qquad i = 1, 2 \tag{3.86}$$

$$S_i = \frac{1}{H}\frac{\partial V_i}{\partial \xi}\xi\left[(u_S - u)\frac{\partial h}{\partial x} + (v_S - v)\frac{\partial h}{\partial y} - (w_S - w)\right], \qquad i = 1, 2 \tag{3.87}$$

Here, subscript S denotes the surface; in writing the above relations, use was made of the relation

$$\frac{\partial h}{\partial t} + u_S \frac{\partial h}{\partial x} + v_S \frac{\partial h}{\partial y} = w_S \text{ at } z = h \tag{3.88}$$

Nihoul (1977) pointed out that without some knowledge of the vertical profile of the velocity field, the orders of magnitude of the terms A, B, and S cannot be estimated. Although it is somewhat theoretically unsatisfactory (Nihoul 1975) near the bottom, since it reproduces the observations reasonably well, Nihoul (1977) used the so-called van Veen (1938) profile:

$$\underset{\sim}{V} = \underset{\sim}{V}_S \xi^{0.2} \tag{3.89}$$

The terms B_1 and B_2 from eq. 3.86 have maximum values near the bottom and vanish at the surface. For long waves, one may consider a frequency ω (i.e. angular velocity of the earth's rotation) and a typical wave length c/ω where $c = \sqrt{gh}$. Noting that $\omega \sim f \sim 10^{-4}$, for a grid of 10-km size, the B terms are comparable with the time derivative terms near the bottom where the streamlines may follow the bathymetry approximately. It is expected that

$$u \frac{\partial D}{\partial x} + v \frac{\partial D}{\partial y} + w \sim 0 \text{ at the bottom} \tag{3.90}$$

Thus, for a 10-km grid, the B terms will be ignored at the bottom, since the three terms together cancel to zero. However, for a smaller grid the B terms may be important near the bottom.

The A and S terms are generally negligible compared with the time derivative terms. The ratio of A to S is V/c where V is the horizontal velocity. Compared with the B terms, the S terms vary more evenly over the water depth. Near amphidromic points, the A term may not be smaller than the time derivative terms. In fact, it may be an order of magnitude greater. Hence, near amphidromic points, one must retain the nonlinear advective terms (Nihoul 1975; Nihoul and Ronday 1975).

The last terms on the right side of eq. 3.79 and 3.80 become, with the introduction of ξ,

$$\frac{1}{H^2} \frac{\partial}{\partial \xi} \left(\nu \frac{\partial V_i}{\partial \xi} \right), \qquad i = 1, 2$$

Bowden (1965) argued from observational evidence that the vertical eddy viscosity, ν, can be expressed as the product of a function of t, x, and y and a function of ξ, i.e.:

$$\frac{\nu}{H^2} = \sigma(t, x, y)\lambda(\xi) \tag{3.91}$$

When the nonlinear terms are ignored, eq. 3.79 and 3.80 become, in the present notation,

$$\frac{\partial u}{\partial t} - fv = -\frac{\partial}{\partial x}\left(\frac{P_a}{\rho} + gh\right) + \sigma \frac{\partial}{\partial \xi}\left(\lambda \frac{\partial u}{\partial \xi}\right) \tag{3.92}$$

and

$$\frac{\partial v}{\partial t} + fu = -\frac{\partial}{\partial y}\left(\frac{P_a}{\rho} + gh\right) + \sigma \frac{\partial}{\partial \xi}\left(\lambda \frac{\partial v}{\partial \xi}\right) \tag{3.93}$$

These equations are valid everywhere except near localized areas (e.g. amphidromic points) where the discarded nonlinear terms become important. In the case where the nonlinear terms are important, one can treat them as driving forces and initiate an iteration process.

Next, consider a locally one-dimensional model of the variation of the horizontal current in the vertical direction. Let

$$V = u + iv \tag{3.94}$$

and

$$\tau = \nu \frac{\partial V}{\partial z} = \sigma H \lambda \frac{\partial V}{\partial \xi} \tag{3.95}$$

Let

$$\phi = -\frac{\partial}{\partial x}\left(\frac{P_a}{\rho} + gh\right) - i\frac{\partial}{\partial y}\left(\frac{P_a}{\rho} + gh\right) \tag{3.96}$$

Then eq. 3.92 and 3.93 can be combined into a single equation:

$$\frac{\partial V}{\partial t} + ifV = \Phi + \sigma \frac{\partial}{\partial \xi}\left(\lambda \frac{\partial V}{\partial \xi}\right) \tag{3.97}$$

where the forcing function, Φ, is a function of t, x, and y.

Thus, although the vertical dependence cannot be seen, one must treat V as a function of ξ, t, x, and y. For any given location (x, y) eq. 3.97 gives a locally one-dimensional model for determining the vertical variation of V as a function of t.

The depth-averaged velocity $\bar{V}$ is given by

$$\frac{\partial \bar{V}}{\partial t} + if\bar{V} = \Phi + \frac{(\tau_S - \tau_B)}{H} \tag{3.98}$$

The deviation $\hat{V} \equiv V - \bar{V}$ is expressed by

$$\frac{\partial \hat{V}}{\partial t} + if\hat{V} = \sigma\left[\frac{\partial}{\partial \xi}\left(\lambda \frac{\partial \hat{V}}{\partial \xi}\right) - \frac{(\tau_S - \tau_B)}{\sigma H}\right] \tag{3.99}$$

The vertical variation of the eddy viscosity, ν, may differ from case to case; however, its asymptotic form for small ξ is

$$\nu = \mathrm{K}|\tau_B|^{1/2}(z + D) \tag{3.100}$$

where K may be taken to be the Von Karman constant of the classical turbulent boundary layer theory. From eq. 3.91 and 3.100 it can be seen that $\sigma H \sim \mathrm{K}|\tau_B|^{1/2}$. According to Nihoul (1977) there is no loss of generality in giving a value of unity to the proportionality constant. Thus

$$\sigma H = \mathrm{K}|\tau_B|^{1/2} \tag{3.101}$$

Also note that $\lambda(\xi) \sim \xi$ for small values of ξ.

Define new variables W and Y through

$$\hat{V} = We^{-ift} + \frac{\tau_S}{\sigma H} S(\xi) + \frac{\tau_B}{\sigma H} b(\xi) \tag{3.102}$$

and

$$(3.103)\quad Y = \int_0^t \sigma(E)\, dE$$

where E denotes a dummy variable. Also define

$$(3.104)\quad S(\xi) = \int_{\xi_0}^{\xi} \frac{\eta}{\lambda(\eta)}\, d\eta$$

and

$$(3.105)\quad b(\xi) = \int_{\xi_0}^{\xi} \frac{1-\eta}{\lambda(\eta)}\, d\eta$$

where η is another dummy variable.
Define

$$(3.106)\quad \theta_2 = \frac{e^{if_1}}{\sigma}\left(\frac{\partial}{\partial t} + if\right)\left(\frac{\tau_\alpha}{\sigma H}\right) = \frac{\partial}{\partial Y}\left(e^{if_1}\frac{\tau_\alpha}{\sigma H}\right), \qquad \alpha = S, b$$

Then, eq. 3.99 becomes

$$(3.107)\quad \frac{\partial W}{\partial Y} + \theta_S S(\xi) + \theta_b b(\xi) = \frac{\partial}{\partial \xi}\left(\lambda \frac{\partial w}{\partial \xi}\right)$$

The boundary conditions are

$$(3.108)\quad \lambda \frac{\partial W}{\partial \xi} = 0 \text{ at } \xi = 0,\ 1$$

If one knows the vertical profile of ν, then S and b can be determined as functions of ξ. Then, from eq. 3.107 the vertical profile of the velocity can be determined in terms of σ, H, θ_S, and θ_b. Note that for any given point (x, y), these are functions of t and thus of Y.

Nihoul (1977) gives the following relation between $\hat{V}$, τ_S, τ_B, and $\bar{V}$:

$$(3.109)\quad \hat{V} = \frac{\tau_S}{\sigma H}[S(\xi) - \bar{S}] + \frac{\tau_B}{\sigma H}[b(\xi) - \bar{b}] - \frac{1}{\sigma}\frac{\partial}{\partial t}\left[\frac{e^{if_1}}{\sigma H}\left(\frac{S_1\tau_S + b_1\tau_B}{\alpha_1}\right)\right] f_1(\xi) e^{-if_1 t}$$

Since the total velocity must vanish at the bottom

$$(3.110)\quad \hat{V} = -\bar{V} \text{ at } \xi = \xi_0$$

The bottom stress can be parameterized in terms of depth-averaged velocity and wind stress and this bottom stress then can be used in the vertically integrated two-dimensional model. The two-dimensional model gives the depth-averaged velocity, h, and hence τ_B and σ. These can be substituted into eq. 3.109 to give the vertical profile of the velocity. The mean (in the vertical) velocity field calculated from the two-dimensional (broken line) and the two-and-a-half-dimensional (solid line) models is compared in Fig. 3.2.

Heaps (1973, 1974, 1975) developed two-and-a-half-dimensional models for calculation of storm surges and tides. He expanded the horizontal components of the velocity in terms of a set of eigenfunctions through the depth and reduced the problem somewhat similar to the traditional two-dimensional problem so that similar finite-difference tech-

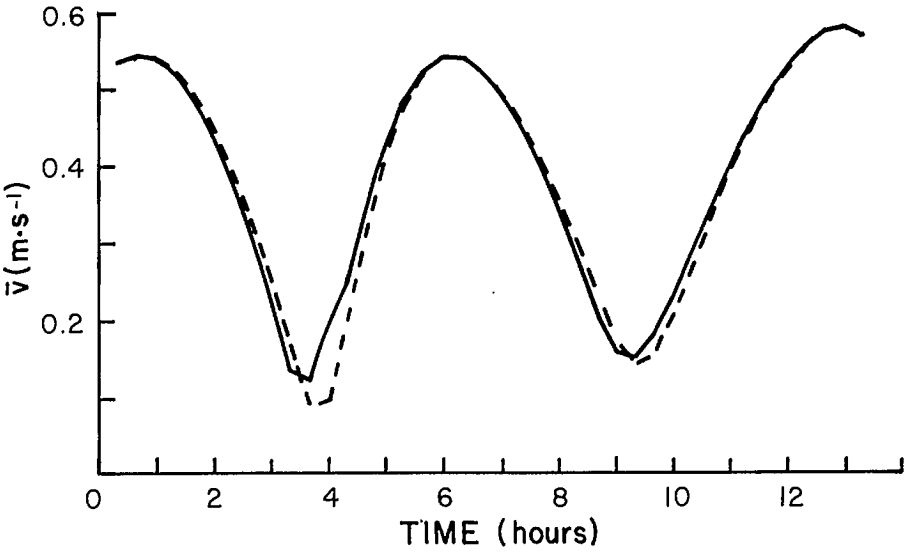

FIG. 3.2. Comparison between the mean velocity computed by the depth-integrated two-dimensional model (broken line) and the locally one-dimensional depth-dependent model subject to the condition of zero velocity at the bottom (solid line). (Nihoul 1977)

niques could be used for numerical integration. He began with the following forms of the equations of motion and continuity:

$$\frac{\partial u}{\partial t} - fv = -g\frac{\partial}{\partial x}(h - h') + \frac{\partial}{\partial z}\left(\nu\frac{\partial u}{\partial z}\right) \tag{3.111}$$

$$\frac{\partial v}{\partial t} + fu = -g\frac{\partial}{\partial y}(h - h') + \frac{\partial}{\partial z}\left(\nu\frac{\partial v}{\partial z}\right) \tag{3.112}$$

$$\frac{\partial h}{\partial t} + \frac{\partial}{\partial x}\int_0^D u\,dz + \frac{\partial}{\partial y}\int_0^D v\,dz = 0 \tag{3.113}$$

Here, h' is a parameter that could be interpreted as the elevation of the sea surface if the water was at every instant in hydrostatic equilibrium under the tide-generating forces, with the atmospheric pressure, P_a, and the other symbols as previously defined. One can write

$$\frac{\partial h'}{\partial x} = \frac{\partial \bar{h}}{\partial x} - \frac{1}{\rho g}\frac{\partial P_a}{\partial x} \tag{3.114}$$

$$\frac{\partial h'}{\partial y} = \frac{\partial \bar{h}}{\partial y} - \frac{1}{\rho g}\frac{\partial P_a}{\partial y} \tag{3.115}$$

where $\bar{h}$ is the equilibrium tide.
At the surface, $z = 0$ (due to the linear approximation $z = h$ is replaced by $z = 0$):

$$\begin{aligned} -\rho\left(\nu\frac{\partial u}{\partial z}\right)_0 &= \tau_{S_x} \\ -\rho\left(\nu\frac{\partial v}{\partial z}\right)_0 &= \tau_{S_y} \end{aligned} \tag{3.116}$$

At the bottom, $z = D$:

$$\begin{aligned} -\rho\left(\nu\frac{\partial u}{\partial z}\right) &= \tau_{B_x} \\ -\rho\left(\nu\frac{\partial v}{\partial z}\right) &= \tau_{B_y} \end{aligned} \tag{3.117}$$

Using a linear form for the bottom friction:

$$\begin{aligned} \tau_{B_x} &= K\rho u D \\ \tau_{B_y} &= K\rho v D \end{aligned} \tag{3.118}$$

In the above equations, τ_{S_x} and τ_{S_y} are the x and y components of the wind stress, τ_{B_x} and τ_{B_y} are the x and y components of the bottom stress, and ρ is the density of water. The initial conditions are

$$u = v = h = 0 \text{ at } t = 0 \tag{3.119}$$

Along closed boundaries, the normal horizontal flow must vanish:

$$u \cos\psi + v \sin\psi = 0 \tag{3.120}$$

where ψ is the inclination of the normal to the x-axis, directed away from the sea. At any position, E, on an open boundary, a shape function of current through the depth might be assumed with either the time variation of h given by

$$h = h_E(t) \tag{3.121}$$

or a radiation condition postulated by which energy is transmitted only outwards across the boundary, in the form of a simple progressive wave, according to the relation

$$\bar{u} \cos\psi + \bar{v} \sin\psi = \frac{ch}{D} \tag{3.122}$$

where

$$c = \sqrt{gD} \tag{3.123}$$

Let $F(z)$ be a differentiable (but unknown) function of z within the range $0 \leq z \leq D$ for a given location (x, y). Multiply eq. 3.111 by $F(z)$ and integrate with respect to z from $z = 0$ to $z = D$:

$$\frac{\partial u}{\partial t} - fv = -ga\frac{\partial}{\partial x}(h - h') + \frac{1}{D}\int_0^D F(z)\frac{\partial}{\partial z}\left(\nu\frac{\partial u}{\partial z}\right) dz \tag{3.124}$$

where

$$u \equiv \frac{1}{D}\int_0^D F(z)u\, dz \tag{3.125}$$

$$v \equiv \frac{1}{D}\int_0^D F(z)v\, dz \tag{3.126}$$

and

$$a \equiv \frac{1}{D}\int_0^D F(z)\, dz \tag{3.127}$$

From eq. 3.111, 3.112, and 3.124, after some algebra, one can write

$$\frac{\partial \boldsymbol{u}}{\partial t} + \lambda \boldsymbol{u} - f\boldsymbol{v} = -g_a \frac{\partial}{\partial x}(h - h') + \frac{\tau_{S_x}}{\rho D} \tag{3.128}$$

$$\frac{\partial \boldsymbol{v}}{\partial t} + \lambda \boldsymbol{v} + f\boldsymbol{u} = -g_a \frac{\partial}{\partial y}(h - h') + \frac{\tau_{S_y}}{\rho D} \tag{3.129}$$

where λ is defined such that

$$\begin{aligned} &\frac{d}{dz}[\nu F'(z)] = -\lambda F(z) \\ &F' = \frac{dF}{dz} \end{aligned} \tag{3.130}$$

For eq. 3.128 and 3.129 to be satisfied, only certain combinations of λ and F are possible, i.e.

$$\begin{aligned} &\lambda = \lambda_r \\ &F = F_r(z) \\ &r = 1, 2, 3, \ldots, \infty \end{aligned} \tag{3.131}$$

These are eigenvalues (in ascending order) associated with the differential equation 3.130 when it is solved subject to the following conditions:

$$F'(0) = 0 \tag{3.132}$$

$$\nu D F'(D) + K F(D) = 0 \tag{3.133}$$

$$F(0) = 1 \tag{3.134}$$

From eq. 3.125–3.127 define

$$\boldsymbol{u}_r = \frac{1}{D}\int_0^D F_r(z) u \, dz \tag{3.135}$$

$$\boldsymbol{v}_r = \frac{1}{D}\int_0^D F_r(z) v \, dz \tag{3.136}$$

$$a_r = \frac{1}{D}\int_0^D F_r(z) \, dz \tag{3.137}$$

Then from eq. 3.128 and 3.129

$$\frac{\partial \boldsymbol{u}_r}{\partial t} + \lambda_r \boldsymbol{u}_r - f\boldsymbol{v}_r = -g a_r \frac{\partial}{\partial x}(h - h') + \frac{\tau_{S_x}}{\rho D}, \qquad r = 1, 2, 3, \ldots, \infty \tag{3.138}$$

$$\frac{\partial \boldsymbol{v}_r}{\partial t} + \lambda_r \boldsymbol{v}_r + f\boldsymbol{u}_r = -g a_r \frac{\partial}{\partial y}(h - h') + \frac{\tau_{S_y}}{\rho D}, \qquad r = 1, 2, 3, \ldots, \infty \tag{3.139}$$

Let

$$\begin{aligned} u &= \sum_{r=1}^{\infty} A_r F_r(z) \\ v &= \sum_{r=1}^{\infty} B_r F_r(z) \end{aligned} \tag{3.140}$$

where A_r and B_r are independent of z. From eq. 3.130, 3.132, and 3.133:

$$\int_0^D F_r(z)\,F_S(z)\,dz = 0 \text{ for } r \neq S \tag{3.141}$$

and

$$\int_0^D F_r^2(z)\,dz = I_r(D) - I_r(0) \tag{3.142}$$

where

$$I_r(z) = \nu\left(F'\frac{\partial F}{\partial \lambda} - F\frac{\partial F'}{\partial \lambda}\right)_{\lambda=\lambda_r} \tag{3.143}$$

Then from eq. 3.140−3.142:

$$\begin{aligned} u &= \sum_{r=1}^{\infty} \phi_r u_r F_r(z) \\ v &= \sum_{r=1}^{\infty} \phi_r v_r F_r(z) \end{aligned} \tag{3.144}$$

where

$$\phi_r = \frac{D}{I_r(D) - I_r(0)} \tag{3.145}$$

From eq. 3.144 and 3.113:

$$\frac{\partial h}{\partial t} + \sum_{r=1}^{\infty}\left[\frac{\partial}{\partial x}(Da_r\phi_r u_r) + \frac{\partial}{\partial y}(Da_r\phi_r v_r)\right] = 0 \tag{3.146}$$

The final set of equations are eq. 3.138, 3.139, and 3.146 for the three dependent variables u_r, v_r, and h. Once u_r and v_r are determined by numerical integration, the horizontal velocity components, u and v, at any depth can be determined from eq. 3.144. Thus, this model enables one to determine the horizontal currents as the sum of a series of vertical modes of progressively increasing order.

Clarke (1974) modified the above procedure by removing the bottom stress from the vertical eigenfunction expansion; he applied the bottom stress externally on each vertical column of fluid. The only advantage of this technique appears to be that, whereas Heaps is forced to use a linear form for the bottom stress, Clarke can express the bottom stress as an arbitrary (not necessarily linear) function of the horizontal velocity. Davies and Furnes (1980) modified Heap's method further by allowing eddy viscosity to be an arbitrary function of space and time. Davies (1980) also used a coupled two-dimensional and two-and-a-half-dimensional model.

3.3 One-and-a-Half-Dimensional Models

In one-and-a-half-dimensional models, one horizontal coordinate and the vertical coordinate are the independent variables, along with time (i.e. the system is x, z, t). The models are referred to as one-and-a-half-dimensional because the x direction is properly treated whereas the z direction is approximately included. One-and-a-half-dimensional models are mostly used in estuarine circulation studies and are not popular with storm surge studies. Nevertheless, some typical models of this type will be briefly considered.

Although salinity intrusion into estuaries is not particularly relevant to storm surges, it will be included to show the versatility of the $x-z$ models.[4]

Hamilton (1975, 1976) developed several different models of the (x, z, t) type. In his 1975 paper, application was made to the Rotterdam watersay. In his 1976 paper, he discussed a semi-implicit method that permits longer time steps. In both papers, unlike in layered models, variables are treated as continuous in the vertical direction. His treatment is mainly applicable to narrow estuaries, because no attention was paid to the lateral direction (models by other authors using lateral averaging will be considered later).

For a narrow water body with rectangular cross-section, the governing equations under the Boussinesq approximation are the following.
Continuity:

$$(3.147)\quad \frac{\partial h}{\partial t} + \frac{1}{b}\frac{\partial}{\partial x}\left(b\int_{-h}^{D} u\,dz\right) = 0$$

$$(3.148)\quad \frac{\partial}{\partial x}(bu) + b\frac{\partial w}{\partial z} = 0$$

Salt conservation:

$$(3.149)\quad \frac{\partial S}{\partial t} + u\frac{\partial S}{\partial x} + w\frac{\partial S}{\partial z} - \frac{\partial}{\partial z}\left(K_z\frac{\partial S}{\partial z}\right) - \frac{1}{b}\frac{\partial}{\partial x}\left(bK_x\frac{\partial S}{\partial x}\right) = 0$$

Momentum conservation:

$$(3.150)\quad \frac{\partial u}{\partial t} + u\frac{\partial u}{\partial x} + w\frac{\partial u}{\partial z} = \underline{-ag(z+h)\frac{\partial S}{\partial x} - g\frac{\partial h}{\partial x}} + \frac{\partial}{\partial z}\left(\nu\frac{\partial u}{\partial z}\right)$$

where x is the horizontal coordinate pointing towards the sea, z is the vertical coordinate pointing downwards, D is the undisturbed water depth, h is the free surface perturbation, b is the channel width ($b = b(x)$), u and w are the velocity components in the x and z directions, respectively, S is salinity, K_x and K_z are the horizontal and vertical eddy diffusivities, respectively, and ν is a coefficient of vertical eddy viscosity. An equation of state can be written as

$$(3.151)\quad \rho = \rho_0(1 + aS)$$

where ρ_0 is the density of freshwater and $a = 7.8 \times 10^{-4}$ (from σ_t tables). For an estuary of length L, the following boundary conditions can be used (assuming that all the freshwater flows in at the head):

$$(3.152)\quad S(x, z, t) = 0 \text{ at } x = 0$$

$$(3.153)\quad u(x, z, t) = \frac{q}{(D+h)b} \text{ at } x = 0, z, t$$

where q is the river flow. At the mouth ($x = L$) the tide as well as the salinity are prescribed:

$$(3.154)\quad h(x, t) = A(t) \text{ at } x = L$$

[4]On the coasts of India and Bangladesh, salinity intrusion into estuaries and rivers and flooding of farmland by salt water due to storm surges has detrimental effects on crops in the subsequent years.

(3.155) $S(x, z, t) = S_0$ at $x = L$

For a semidiurnal tide

$$A(t) = -A_0 \cos(\sigma t)$$
$$\sigma = \frac{2\pi}{T} \quad (3.156)$$

where A_0 is the tidal amplitude and T is the tidal period (12.42 h for M_2). Further boundary conditions are as follows.
No salt flux at the bottom and the water surface:

(3.157) $K_z \frac{\partial S}{\partial z} = 0$ at $z = D$ and $-h$

The wind stress at the surface will be ignored (this can be introduced quite easily):

(3.158) $\nu \frac{\partial u}{\partial z} = 0$ at $z = -h$

A quadratic form for the bottom stress will be used:

(3.159) $-\nu \frac{\partial u}{\partial z} = K|u_\Delta|u_\Delta$ at $z = D$

where $K \sim 0.0025$ and

(3.160) $z = h - \Delta$

Here, the bottom stress is expressed in terms of the velocity at a distance Δ above the bottom ($\Delta \sim 1$ m).

The following approximation is made in writing the underlined terms in eq. 3.150 using the hydrostatic approximation. Actually, we have

(3.161) $\frac{\partial P}{\partial x} = g(z + h)\frac{\partial \bar{\rho}}{\partial x} + g\bar{\rho}\frac{\partial h}{\partial x}$

where P is the pressure and $\bar{\rho}$ is the average density of a water column stretching from $z = -h$ to D. Hence

(3.162) $\bar{\rho}(x, t) = \frac{1}{(z + h)} \int_{-h}^{z} \rho(x, z, t)\, dz$

The approximation made here is to replace $\bar{\rho}$ by ρ in eq. 3.161 and use 3.151 putting $\rho/\rho_0 \sim 1$. This approximation (which introduces only a slight error) will simplify the numerical integration of eq. 3.162. The grid and the finite-difference scheme used were similar to those of Heaps (1969).

Hamilton (1976) extended the earlier model to permit the free surface to move vertically through the grid points. He also introduced a semi-implicit scheme for use with larger time steps. Special attention was paid to the seaward boundary condition. Blumberg (1976) used lateral averaging, thus simplifying the formulation, and expressed the vertical eddy diffusivity in terms of a Richardson number. Application was made to the Potomac Estuary on the east coast of the United States. Wang and Kravitz (1980) gave the following equations for a laterally averaged estuary model.

Continuity:

$$(3.163)\quad \frac{\partial}{\partial x}(uB) + \frac{\partial}{\partial z}(wB) = 0$$

$$(3.164)\quad \frac{\partial}{\partial t}(B_0 h) + \frac{\partial}{\partial x}\int_{-D}^{h}(uB)\,dz = 0$$

Momentum:

$$(3.165)\quad \frac{\partial}{\partial t}(uB) + \frac{\partial}{\partial x}(uuB) + \frac{\partial}{\partial z}(uwB) - \frac{\partial}{\partial x}\left(B\nu_x\frac{\partial u}{\partial x}\right) - \frac{\partial}{\partial z}\left(B\nu_z\frac{\partial u}{\partial z}\right) + Ku|u|\left|\frac{\partial B}{\partial z}\right| + \frac{gB}{\rho_0}\frac{\partial}{\partial x}\int_z^0 \rho\,dz' = 0$$

Salt conservation:

$$(3.166)\quad \frac{\partial}{\partial t}(SB) + \frac{\partial}{\partial x}(SuB) + \frac{\partial}{\partial z}(SwB) - \frac{\partial}{\partial x}\left(BK_x\frac{\partial S}{\partial x}\right) - \frac{\partial}{\partial z}\left(BK_z\frac{\partial S}{\partial z}\right) = 0$$

Equation of state:

$$(3.167)\quad \rho = \rho_0(\alpha + \beta S)$$

Here, u and w are the velocity components in the x and z directions, B is the width of the estuary, h is the surface deviation from equilibrium, $D(x)$ is the water depth in the undisturbed state, S is the salinity, K_x and ν_x are the longitudinal diffusivity and viscosity, K_z and ν_z are the vertical diffusivity and viscosity, and K is the boundary friction coefficient. The boundary conditions are

$$(3.168)\quad K_z\frac{\partial S}{\partial z} = 0 \text{ at } z = h \text{ and } z = -D$$

$$(3.169)\quad \nu_z\frac{\partial u}{\partial z} = \text{prescribed wind stress at } z = h$$

$$(3.170)\quad \nu_z\frac{\partial u}{\partial z} = Ku|u| \text{ at } z = -D$$

At the estuary head, the horizontal salt flux is set to zero and the inflow condition is specified.

These above equations can be solved by standard explicit finite-difference techniques on a staggered grid. The diffusion and friction terms are lagged one time step for stability. The Euler backward scheme is used at every 10 time steps to eliminate the time splitting due to the use of the leapfrog scheme.

To save computer time, a semi-implicit formulation is also attempted. Integrating eq. 3.165 from the bottom to the top gives

$$(3.171)\quad \frac{\partial}{\partial t}\int_{-D}^{h} uB\,dz + g\frac{\partial h}{\partial x}\int_{-D}^{h} B\,dz = \text{remaining terms}$$

If the right side of eq. 3.171 is zero, equations eq. 3.164 and 3.171 are the traditional shallow-water wave equations governing the fastest gravity waves. Equation 3.164 and the left side of 3.171 will be approximated implicitly, whereas the right side of eq. 3.171 will be treated explicitly, i.e.

$$(3.172)\quad B_0\delta_t h_n + \frac{1}{2}(\delta_x M_{n+1} + \delta_x M_n) = 0$$

(3.173) $$\delta_t M_n + \left(g \int_{-D}^{h} B\, dz\right)\frac{1}{2}\left(\delta_x h_{n+1} + \delta_x h_n\right) = (\text{right side of eq. } 3.171)_n$$

where δ_t and δ_x are centered difference operators in time and space and M is the total transport. The subscript n denotes variables calculated at time step n. Equations 3.172 and 3.173 can be simplified to a system of equations for h_{n+1} knowing the values at time step n. The Gaussian elimination method is used to solve these equations.

There is no stability criterion for the implicit method. However, it was found that, whereas it reproduces the circulation well, it gives somewhat lower values to the amplitude of storm surges. On the other hand, the explicit method reproduces the storm surges well but must be governed by the following stability criteria.

C−F−L criterion for stability:

(3.174) $$\Delta t \leq \frac{\Delta x}{(gD_{\max})^{1/2}}$$

Diffusion criteria (for circulation):

(3.175) $$\Delta t \leq \frac{1}{4}\frac{(\Delta z)^2}{K_z} \text{ and } \Delta t \leq \frac{1}{4}\frac{(\Delta z)^2}{\nu_z}$$

For other versions of one-and-a-half-dimensional models see Blumberg (1976) and Elliott (1976).

3.4 One-Dimensional Models

One could obtain a one-dimensional (x, t) model by putting $v = 0$ and $\partial/\partial y = 0$ in the two-dimensional vertically integrated model. However, the one-dimensional models are usually more rigorously derived. There are literally dozens of one-dimensional models available; here, one typical one-dimensional storm surge model will be discussed. In this era of ever increasing computer storage capacities, one-dimensional models have lost some of their earlier appeal. Nevertheless, for narrow and elongated water bodies, these models may yield useful and reasonably accurate results because two-dimensional models might be impractical for narrow water bodies.

As a typical one-dimensional storm surge model, the model of Svansson and Szaron (1975) is used which was applied to the Baltic Sea. With reference to Fig. 3.3, the water body under consideration must be divided into sections that are perpendicular to the local axis of the channel. It is assumed that the water moves only in a longitudinal (i.e. x) direction. Then, the vertically integrated horizontal equations of motion become

(3.176) $$\frac{\partial M}{\partial t} + \frac{M}{(A + bh)}\frac{\partial M}{\partial x} = -g(A + bh)\frac{\partial h}{\partial x} - (A + bh)\frac{\partial P_a}{\partial x} + g(A + bh)\frac{\partial \bar{h}}{\partial x} + b\tau_{S_x} - b\tau_{B_x}$$

and

(3.177) $$fM = -g(A + bh)\frac{\partial h}{\partial y} - (A + bh)\frac{\partial P_a}{\partial y} + b\tau_{S_y}$$

The continuity equation assumes the following form:

(3.178) $$\frac{\partial h}{\partial t} = -\frac{1}{b}\frac{\partial M}{\partial x}$$

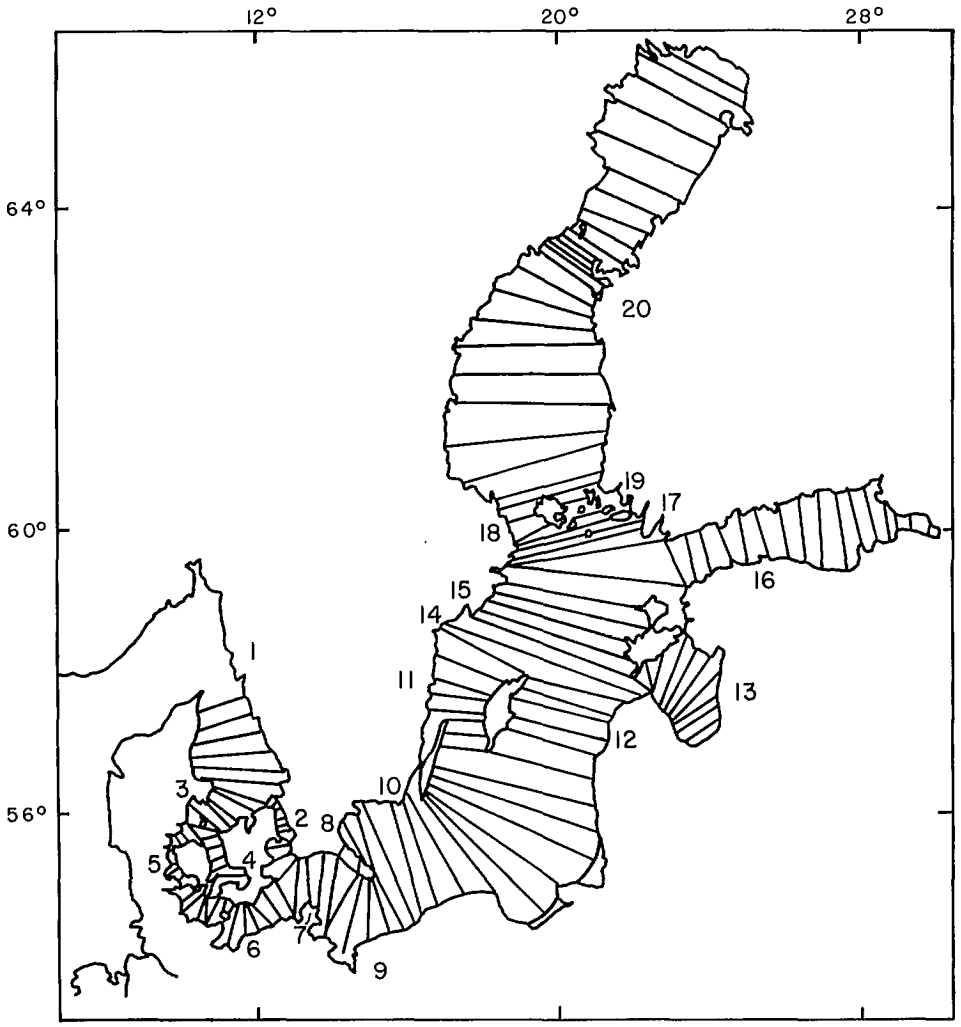

FIG. 3.3. One-dimensional numerical model of the Baltic Sea. The numbers refer to the various channels. (Svansson and Szaron 1975)

In several one-dimensional models, traditionally there is only one momentum equation (in the longitudinal direction x) and the continuity equation. Here, the momentum equation in the transverse direction is partly retained for the following reasons: (a) to provide the boundary conditions at the junction of two branches and (b) to compare the computed water level with the observed level on one side of the narrow water body.

In the above set of equations, M is the transport in the longitudinal direction, A is the cross-sectional area of a given section, b is its width, h is the variation of the level, $\bar{h}$ is the equilibrium tide (which is generally not important), f is the Coriolis parameter, P_a is the atmospheric pressure, g is gravity, τ_S is the wind stress, τ_B is the bottom stress, and y is the transverse direction.

The above authors defined the bottom stress term as follows:

$$\tau_{B_x} = \frac{R' M|M|}{(A + bh)^2}$$
$$\tau_{B_y} = 0 \tag{3.179}$$

where R' is a friction coefficient whose value is in the range of 0.003–0.015. The following boundary conditions were used. At the first section in channel 1, the average of the observed sea level at Goteborg and Frederikshaun was used. At the closed ends of the Gulfs of Finland, Riga, and Bothnia, M was taken to be zero. At branching sections the following two conditions were prescribed: (a) continuity of M and (b) equality of h except for a correction determined from eq. 3.177.

For the numerical integration, Fischer's (1959) scheme was used, i.e. central-differences in x and forward-differences in t. The finite-difference forms of eq. 3.176–3.179 are as follows:

$$M_{j,n+1} = M_{j,n} - \frac{\Delta t M_{j,n}}{(A_j + b_j h_j)} \frac{(M_{j+1,n} - M_{j-1,n})}{\Delta x_{j-1} + \Delta x_j} - \frac{g \Delta t (A_j + b_j h_j)(h_{j+1,n} - h_{j-1,n})}{(\Delta x_{j-1} + \Delta x_j)} - \Delta t (A_j + b_j h_j) \left(\frac{\Delta P_a}{\Delta x_j}\right)_{n+1/2} + g \Delta t (A_j + b_j h_j) \frac{(\bar{h}_{j+1,n+1/2} - \bar{h}_{j-1,n+1/2})}{(\Delta x_{j-1} + \Delta x_j)} + \Delta t\, b_j\, \tau_{S_{xj,n+1/2}} - \frac{\Delta t b_j R' M_{j,n}|M_{j,n}|}{(A_j + b_j h_j)^2} \tag{3.180}$$

$$h_{j,n+1} = h_{j,n} - \frac{\Delta t (M_{j+1,n+1} - M_{j-1,n+1})}{\left[\frac{(b_{j-1} + b_j)}{2} \Delta x_{j-1} + \frac{(b_j + b_{j+1})}{2} \Delta x_j\right]} \tag{3.181}$$

$$\Delta h_{j,n+1} = \frac{b_j}{2g(A_j + b_j h_j)} \left[b_j \tau_{S_{yj,n+1}} - f_j M_{j,n+1} - (A_j + b_j h_j) \left(\frac{\Delta P_a}{\Delta y_j}\right)_{n+1}\right] \tag{3.182}$$

For the linearized case, the stability criterion is

$$\Delta t < \frac{2\Delta x}{\sqrt{gH}} \tag{3.183}$$

The authors found it necessary to use smoothing when the nonlinear terms are included (as in the present situation). The following procedure was used for the smoothing. In eq. 3.180, rather than

$$M_{j,n+1} = M_{j,n} + \Delta t\,(\ldots)$$

the following smoothed form is used:

$$M_{j,n+1} = \alpha M_{j,n} + \frac{(1 - \alpha)}{2} (M_{j+1,n} + M_{j-1,n}) + \Delta t\,(\ldots)$$

where α is the smoothing coefficient.

The following steps can be used for the numerical integration.

1) At time step $n = 0$, specify $M_{j,0}$ *and* $h_{j,0}$.
2) Using eq. 3.180, solve $M_{j,1}$ for $j = 1, 2, \ldots, (N-1)$, i.e. for all the internal sections in each canal.
3. In canals 2, 4, 5, 6, 8, 9, 11, 12, 18, and 19 use backward-differences to solve $M_{N,1}$:

$$M_{N,1} = \frac{-\Delta t M_{N,0}}{(A_N + b_N h_N)} \frac{(M_{N,0} - M_{N-1,0})}{\Delta x_{N-1}} - g\Delta t (A_N + b_N h_N) \frac{(h_{N,0} - h_{N-1,0})}{\Delta x_{N-1}}$$

$$- \Delta t (A_N + b_N h_N) \left(\frac{\Delta P_a}{\Delta x_N}\right)_{1/2} + g\Delta t (A_N + b_N h_N) + \frac{(\bar{h}_{N_{1/2}} - \bar{h}_{(N-1)_{1/2}})}{\Delta x_{N-1}}$$

$$+ \Delta t\, b_N (\tau_{S_{tN}})_{1/2} - \frac{\Delta t\, b_N M_{N,0} |M_{N,0}|}{(A_N + b_N h_N)^2}$$

   Similarly, use forward-differences to solve $M_{0,1}$ in canals 1, 2, 3, 4, 5, 8, 9, 11, 12, 13, 15, 16, 17, 18, and 19.
4) In the remaining sections (except channel 13, section 10; channel 16, section 16; and channel 20, section 25, which are boundary conditions) the condition of continuity of transport is used to determine the M_1's in the branching points.
5) Using eq. 3.181 determine $h_{j,1}$ for $j = 1,2, \ldots, (N-1)$.
6) Use backward-differences again to solve $h_{N,1}$ in canals 1, 3, 7, 10, 13, 14, 15, 16, 17, and 20:

$$h_{N,1} = h_{N,0} - \Delta t \frac{(M_{N,1} - M_{N-1,1})}{\left(\frac{b_{N-1} + b_N}{2}\right) \Delta x_{N-1}}$$

   Then use forward-differences to calculate $h_{0,1}$ in canals 6, 7, 10, 14, and 20.
7) Equation 3.177 must be used to determine the water level in certain branching points: 1:*N*, 3:*N*, 6:0, 7:0, 7:*N*, 10:0, 10:*N*, 14:0, 14:*N*, 15:*N*, 17:*N*, 20:0.

This completes the integration for step $n = 1$. The same steps must be repeated for $n = 2, 3, \ldots$

Next, a model that paid special attention to islands in the water body will be considered. Prandle and Crookshank (1972, 1974) developed a one-dimensional model for tidal propagation in the St. Lawrence Estuary. The sections are shown in a schematic form in Fig. 3.4. In this diagram, in the middle portion, the two networks on either side of the main axis together represent the Orleans Island near Quebec City. The length of each section lies in the range of 2–12 mi (3.2–19.2 km) and is determined by using the stability criterion:

$$(3.184) \quad \frac{\Delta x}{\Delta t} \geq U + C$$

where U is the velocity in the x direction and $C = \sqrt{gH}$ where H is the average water depth in that section.

First, the estuary was divided lengthwise into sections. Then the cross-section at the center of each reach was drawn, and the area of cross-section A for each elevation was determined. At the corresponding elevations, the surface area, S, for each reach was

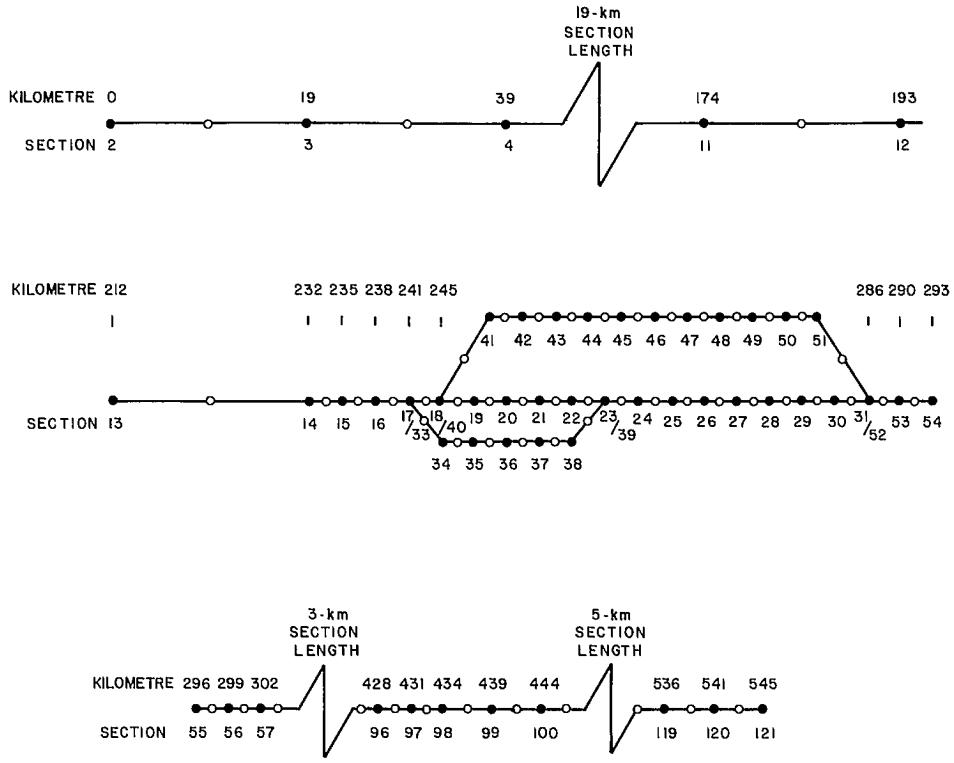

FIG. 3.4. Section length and rotation for a one-dimensional model of the St. Lawrence Estuary in Canada. (Prandle and Crookshank 1972)

measured. Note that one must use the hydrographic charts for this and interpolate between high and low water.

To obtain the surface width, B, one must divide S by the reach length, Δx. In the bottom friction term (to be discussed later) there is a hydraulic radius R equal to A/P where P is the wetted perimeter. Since it is difficult to determine P, Prandle and Crookshank (1972) used the hydraulic mean depth, M (equal to A/B), in place of R.

Further difficulties arise when one uses cross-sectional average values. Prandle and Crookshank divided the estuary into conveying and storage sections (Fig. 3.5) with the understanding that the storage sections do not contribute to any momentum along the channel. This division can be accomplished by using the formula

$$(3.185) \quad A = A_1 + A_2 \sqrt{\frac{D_2}{D_1}}$$

where A_1, A_2, D_1, and D_2 are shown in Fig. 3.5. This division is not exact because the ratio D_2/D_1 depends on the state of the tide.

The grid scheme used in the numerical integration is shown in Fig. 3.6. A staggered grid with central finite-differences in x is used. The equation of motion in the longitudinal x direction is

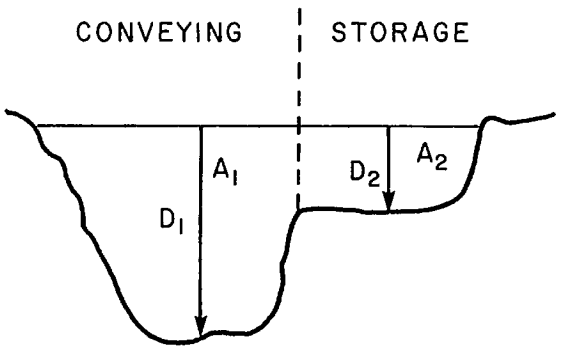

FIG. 3.5. Division of the channel into conveying and storage sections. (Prandle and Crookshank 1972)

$$(3.186)\quad \frac{\partial U}{\partial t} + U\frac{\partial U}{\partial x} + g\frac{\partial H}{\partial x} + F + Q_T\frac{U}{A} = 0$$

where U is the velocity in the x direction, F is the bottom friction, and Q is the discharge ($Q = UA$) where A is the area of cross-section and Q_T is the discharge of freshwater from the tributaries into the estuary per unit length. The continuity equation is

$$(3.187)\quad \frac{\partial Q}{\partial x} + B\frac{\partial H}{\partial t} - Q_T = 0$$

where B is the width of the channel.

The Chezy formulation for the friction term is

$$(3.188)\quad F = \frac{gU|U|}{C^2R}$$

where C is the Chezy friction factor (R as previously defined).

In eq. 3.186 wind stress is not included. However, it can be easily added without causing any problems. The finite-difference form of eq. 3.186 is

$$(3.189)\quad \frac{U\left(x+\frac{1}{2}, t+\frac{1}{2}\right) - U\left(x+\frac{1}{2}, t-\frac{1}{2}\right)}{\Delta t} + \left[U\left(x+\frac{1}{2}, t+\frac{1}{2}\right) + U\left(x+\frac{1}{2}, t-\frac{1}{2}\right)\right]\left[U\left(x+\frac{3}{2}, t-\frac{1}{2}\right) - U\left(x-\frac{1}{2}, t+\frac{1}{2}\right)\right] + \frac{g[H(x+1, t) - H(x, t)]}{\Delta x} + \frac{gKU\left(x+\frac{1}{2}, t+\frac{1}{2}\right)\left|U\left(x+\frac{1}{2}, t-\frac{1}{2}\right)\right|}{R\left(x+\frac{1}{2}, t\right)} = 0$$

where

$$K = \frac{1}{C^2}$$

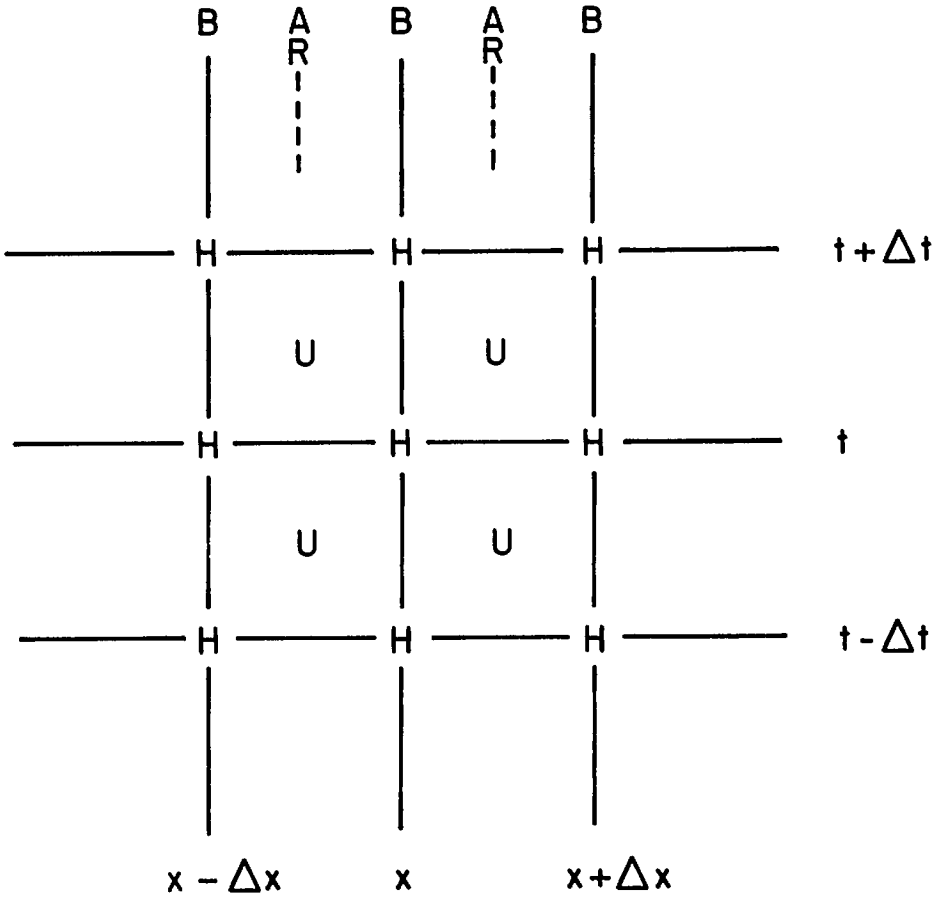

FIG. 3.6. Staggered grid used in the one-dimensional model for the St. Lawrence Estuary. (Prandle and Crookshank 1972)

Note that Δx and K are functions of x (although not written as such in eq. 3.189). Here, $H(x + \frac{1}{2}, t)$ is the average of $H(x, t)$ and $H(x + 1, t)$.

The continuity eq. 3.187 centered at $(x, t + \frac{1}{2})$ can be written as

$$\frac{\left[U\left(x+\frac{1}{2},t+\frac{1}{2}\right)A\left(x+\frac{1}{2},t+\frac{1}{2}\right)-U\left(x-\frac{1}{2},t+\frac{1}{2}\right)A\left(x-\frac{1}{2},t+\frac{1}{2}\right)-Q_T(x)\right]}{\Delta x} + B\left(x,t+\frac{1}{2}\right)\frac{[H(x,t+1)-H(x,t)]}{\Delta t}=0 \tag{3.190}$$

Equations 3.189 and 3.190 can be rearranged to provide expressions for $U(x + \frac{1}{2}, t + \frac{1}{2})$ and $H(x, t + 1)$.

At a junction, eq. 3.189 and 3.190 must be modified. In eq. 3.189, it is the convective term $U(\partial U/\partial x)$ that must be modified. Since its contribution may not be very

significant, Prandle and Crookshank (1972) simply ignored this term immediately adjacent to junctions and boundaries rather than complicating the equations.

Initially, the water was assumed to be at rest. The seaward boundary condition is the specification of tidal elevation at Pointe au Pere. (For storm surge calculation the wind stress must also be specified.) The landward boundary condition at Montreal involves the specification of the river discharge.

Next, consider computational stability problems for one-dimensional models. Leendertse (1967) proposed an implicit finite-difference scheme for long-wave problems in two dimensions. He performed a stability analysis for a simplified form of the finite-difference equations (Weare (1967a) refers to this as scheme I) and showed that the system is unconditionally stable except for a weak constraint arising from the Coriolis terms. Weare (1967a) showed that there is an instability due to the imperfect time centering of the nonlinear terms.

Leendertse (1970) gave a modified version of the original scheme (referred to by Weare as scheme II) which exhibits a similar but even stronger instability. At times, this instability can be controlled through the friction term. This instability occurs even in one-dimensional (in space) systems, and for simplicity, only the one-dimensional case will be considered. The following discussion is based on Weare (1967a) and gives a comprehensive view of the stability problems associated with one-dimensional models (the same principles apply to two- and three-dimensional models).

The continuity equation and the equation of motion are

$$\frac{\partial h}{\partial t} + \frac{\partial}{\partial x}(uH) = 0 \tag{3.191}$$

and

$$\frac{\partial u}{\partial t} + u\frac{\partial u}{\partial x} = -g\frac{\partial h}{\partial x} - \frac{g}{C^2}\frac{u|u|}{H} \tag{3.192}$$

where x is the coordinate along the axis of the water body, h is the deviation of the free surface from its equilibrium position, D is the water depth in the undisturbed state (i.e. bed level), and

$$H = D + h \tag{3.193}$$

Note that u is the depth-averaged velocity and C is a Chezy friction coefficient.

In scheme I, the parameters h and u are defined at each time step on a staggered grid. Scheme I consists of an explicit step from $(t - \frac{1}{2})\,\Delta t$ to $t\Delta t$ and an implicit step from $t\Delta t$ to $(t + \frac{1}{2})\,\Delta t$ for both eq. 3.191 and 3.192. The finite-difference forms in the explicit step are as follows:

$$\frac{(h_{j,0} - \bar{h}_j)}{(\Delta t/2)} + \frac{(\bar{H}_{j+1}\bar{u}_{j+1}) - (\bar{H}_{j-1}\bar{u}_{j-1})}{\Delta x} = 0 \tag{3.194}$$

and

$$\frac{(u_{j+1,0} - \bar{u}_{j+1})}{(\Delta t/2)} + u_{j+1,0}\frac{(\bar{u}_{j+3} - \bar{u}_{j-1})}{2\Delta x} + \frac{g}{\Delta x}(\bar{h}_{j+2} - \bar{h}_j) = -\frac{g}{C^2}\bar{u}_{j+1}\frac{|\bar{u}_{j+1}|}{\bar{H}_{j+1}} \tag{3.195}$$

In the implicit step:

$$\frac{(h_j^+ - h_{j,0})}{(\Delta t/2)} + \frac{(H_{j+1,0}u_{j+1}^+) - (H_{j-1,0}u_{j-1}^+)}{\Delta x} = 0 \tag{3.196}$$

and

$$(3.197)\quad \frac{(u^+_{j+1} - u_{j+1,0})}{(\Delta t/2)} + u^+_{j+1}\frac{(u_{j+3,0} - u_{j-1,0})}{2\Delta x} + \frac{g}{\Delta x}(h^+_{j+2} - h^+_j) = -\frac{g}{C^2}u^+_{j+1}\frac{|u_{j+1,0}|}{H_{j+1,0}}$$

where

$$(3.198)\quad \bar{H}_{j+1} \equiv \frac{1}{2}(\bar{h}_{j+2} + \bar{h}_j) - h_{j+1}$$

Note that eq. 3.194 and 3.195 can be solved directly for h_0 and u_0. However, eq. 3.196 and 3.197 must be solved simultaneously for h^+ and u^+.

In scheme II the above explicit and implicit equations are combined into a single step implicit equation of the Crank–Nicolson type. In this scheme eq. 3.194 and 3.196 still hold for h. On the other hand, for u, the intermediate step u_0 is eliminated. Then, the combined equation for u is

$$(3.199)\quad \frac{(u^+_{j+1} - \bar{u}_{j+1})}{\Delta t} + \bar{u}_{j+1}\frac{(\bar{u}_{j+3} - \bar{u}_{j-1})}{2\Delta x} + \frac{g}{2\Delta x}(h^+_{j+2} + \bar{h}_{j+2} - h^+_j - \bar{h}_j) = -\frac{g}{C^2}\frac{(u^+_{j+1} + \bar{u}_{j+1})}{2}\frac{|\bar{u}_{j+1}|}{H_{j+1,0}}$$

One cannot perform a stability analysis of the full equations 3.194–3.199 because of the presence of nonlinear terms. The usual approach with linear equations is to determine the growth of an individual Fourier component in the solution. Since nonlinear terms give rise to interactions, one should not consider the propagation of individual components. However, in the case of the shallow-water equations, the nonlinear interactions are generally weak. Then, one can obtain some idea of the stability by considering a quasi-linear system. The following set of equations are obtained from the original set 3.194–3.198 by dropping the friction terms, assuming that the depth, D, is uniform, and ignoring the nonlinear advective terms in the velocity equations:

$$(3.200)\quad \frac{(h_{j,0} - \bar{h}_j)}{(\Delta t/2)} + \frac{D}{\Delta x}(\bar{u}_{j+1} - \bar{u}_{j-1}) = 0$$

$$(3.201)\quad \frac{(u_{j+1,0} - \bar{u}_{j+1})}{(\Delta t/2)} + \frac{g}{\Delta x}(\bar{h}_{j+2} - \bar{h}_j) = 0$$

$$(3.202)\quad \frac{(h^+_j - h_{j,0})}{(\Delta t/2)} + \frac{D}{\Delta x}(u^+_{j+1} - u^+_{j-1}) = 0$$

$$(3.203)\quad \frac{(u^+_{j+1} - u_{j+1,0})}{(\Delta t/2)} + \frac{g}{\Delta x}(h^+_{j+2} - h^+_j) = 0$$

These equations can be combined to eliminate h_0 and u_0. Then it is similar to a Crank–Nicolson implicit scheme. As is shown by Leendertse (1967), this scheme is unconditionally stable.

Actually, it is not necessary to omit the nonlinear terms completely. Let the solutions for the water level be $z + h$ and for the velocity field be $V + u$ where z and V vary slowly

with x and t, and h and u are error terms. Then, by definition, $h \ll z$ and $u \ll V$.

Substitute $z + h$ and $V + u$ into eq. 3.194–3.197, then to first order in the error terms:

$$(3.204)\quad \frac{(h_{i,0} - \bar{h}_i)}{(\Delta t/2)} + \frac{H}{\Delta x}(\bar{u}_{j+1} - \bar{u}_{j-1}) + \frac{V}{2\Delta x}(\bar{h}_{j+2} - \bar{h}_{j-2}) = 0$$

$$(3.205)\quad \frac{(u_{j+1,0} - \bar{u}_{j+1})}{(\Delta t/2)} + \frac{g}{\Delta x}(\bar{h}_{j+2} - \bar{h}_j) + \frac{V}{2\Delta x}(\bar{u}_{j+3} - \bar{u}_{j-1}) = 0$$

$$(3.206)\quad \frac{(h_j^+ - h_{j,0})}{(\Delta t/2)} + \frac{H}{\Delta x}(u_{j+1}^+ - u_{j-1}^+) + \frac{V}{2\Delta x}(h_{j+2,0} - h_{j-2,0}) = 0$$

$$(3.207)\quad \frac{(u_{j+1}^+ - u_{j+1,0})}{(\Delta t/2)} + \frac{g}{\Delta x}(h_{j+2}^+ - h_j^+) + \frac{V}{2\Delta x}(u_{j+3,0} - u_{j-1,0}) = 0$$

where

$$H = z + D$$

Equations 3.204–3.207 determine the propagation of the error terms h and u in x and t. For simplicity, define the following linear operators:

$$(3.208)\quad \hat{d}h_{j+1} \equiv \frac{\Delta t}{2\Delta x}(h_{j+2} - h_j)$$

and

$$(3.209)\quad \hat{S}uj \equiv \frac{(u_{j+1} + u_{j-1})}{2}$$

Define a column vector:

$$(3.210)\quad V = \begin{vmatrix} h \\ u \end{vmatrix}$$

and define the following four matrix operators:

$$(3.211)\quad \hat{A}_1 = \begin{vmatrix} 1 & 0 \\ 0 & 1 \end{vmatrix}$$

$$(3.212)\quad \hat{B}_1 = \begin{vmatrix} 1 - V\hat{d}\hat{S} & -H\hat{d} \\ -g\hat{d} & 1 - V\hat{d}\hat{S} \end{vmatrix}$$

$$(3.213)\quad \hat{A}_2 = \begin{vmatrix} 1 & g\hat{d} \\ g\hat{d} & 1 \end{vmatrix}$$

$$\hat{B}_2 = \begin{vmatrix} 1 - V\hat{d}\hat{S} & 0 \\ 0 & 1 - V\hat{d}\hat{S} \end{vmatrix}$$

Equations 3.204 and 3.205 together can be written as

(3.214) $\hat{A}_1 V^0 = \hat{B}_1 V^-$

Equations 3.189 and 3.190 together can be written as

(3.215) $\hat{A}_2 V^+ = \hat{B}_2 V^0$

Considering the propagation of a single Fourier component of wave number σ, let the errors in water level and velocity field be of the form

$$\begin{aligned} h &= h_0 e^{i\sigma x} \\ u &= u_0 e^{i\sigma x} \end{aligned} \tag{3.216}$$

Here, amplitudes h_0 and u_0 are functions of time and σ. Define

(3.217) $\theta \equiv \frac{1}{2} \sigma \Delta x$

The influence of the linear operators $\hat{d}$ and $\hat{S}$ on h can be written as

(3.218) $\hat{d}h = \frac{\Delta t}{2\Delta x} 2ih \sin \theta$

and

(3.219) $\hat{S}h = h \cos \theta$

Let λ denote the amplification factor in the two-step process given by eq. 3.198 and 3.199, i.e.

(3.220) $h_0(t + \Delta t) = \lambda h_0(t)$

The factor λ is the roots of the characteristic equation obtained by eliminating the intermediate step V^0 in eq. 3.214 and 3.215, i.e.

(3.221) $|A_1^{-1} B_1 - \lambda B_2^{-1} A_2| = 0$

Define

$$\begin{aligned} \nu' &\equiv \nu \sin \theta \cos \theta \\ \mu' &\equiv \mu \sin \theta \end{aligned} \tag{3.222}$$

where

(3.223) $\nu \equiv \frac{\Delta t}{\Delta x} V$

and

(3.224) $\mu \equiv \frac{\Delta t}{\Delta x} \sqrt{gH}$

Since eq. 3.221 is quadratic in λ, the roots can be written as

(3.225) $\lambda = (1 - i\nu')(1 - i\nu' \pm i\mu')(1 \pm i\mu')^{-1}$

The two roots of this equation correspond to propagation in the $+x$ and $-x$ directions. For propagation in the same direction as V (the mean flow) it can be seen from eq. 3.225 that

$$(3.226)\quad |\lambda|^2 = (1 + \nu'^2)\left\{1 + \left[\frac{2\nu'\mu' + \nu'^2}{(1 + \mu'^2)}\right]\right\}$$

Thus

$$(3.227)\quad |\lambda|^2 > 1$$

Hence, for this scheme I, the calculation will always be unstable, and this instability is due to the presence of the nonlinear terms (which generate the ν terms).

When $\nu \to 0$, the situation considered by Leendertse (1967) is arrived at. Then, the amplification factor is given by

$$(3.228)\quad \lambda \to \lambda_0 = \frac{1 \pm i\mu'}{1 \pm i\mu'} = 1$$

Thus, the scheme is stable because $|\lambda_0|^2 = 1$ for all θ (i.e. all wavelengths).

Weare (1967a) studied this instability through a numerical experiment. A basin of 20-km length was used and the undisturbed water depth was taken as 10 m. Initially, a wave with an amplitude of 1 m was assumed and Δx and Δt were chosen to be 2 km and 100 s. First, the linearized equations 3.200–3.203 were used and the total energy was calculated. The scheme was found to be stable. Then, the nonlinear terms are included (but not the frictional terms), and using eq. 3.194–3.197 the total energy is again calculated as a function of time. The scheme was found to be unstable. Later, situations will be considered in which this instability is weak enough to be controlled by frictional terms.

One can proceed as above for the stability analysis of scheme II which leads to the following characteristic equation:

$$(3.229)\quad \lambda^2(1 + \mu'^2) - \lambda[(1 - i\nu')^2 + (1 - 2i\nu') - \mu'^2(2 - i\nu')] + [(1 - i\nu')(1 - 2i\nu') + \mu'^2](1 - i\nu') = 0$$

When $\nu \to 0$, $\lambda \to \lambda_0$ as in eq. 3.228. Even without solving eq. 3.229 it can be shown that scheme II is unstable (with the nonlinear terms present). For this scheme to be stable $|\lambda_1|$ and $|\lambda_2|$ must be less than or equal to 1. Hence, for stability $|\lambda_1 \lambda_2| \leq 1$. Here, λ_1 and λ_2 denote the roots of eq. 3.213. From eq. 3.229 one can write

$$(3.230)\quad \lambda_1\lambda_2 = \frac{1 - i\nu'}{1 + \mu'^2}[(1 - i\nu')(1 - 2i\nu') + \mu'^2]$$

It can be seen that $|\lambda_1\lambda_2| \leq 1$ only when $\nu \to 0$. Hence, scheme II is unstable.

One can obtain some idea of the relative strength of the instabilities by comparing the magnitude of the amplification factors in schemes I and II. For situations in which $|V| \ll \sqrt{gH}$, i.e. when $\nu \ll \mu$, one can expand λ in a series of ν as follows:

$$(3.231)\quad \lambda = \lambda_0 + \nu\lambda_1 + \theta(\nu^2)$$

Substitute eq. 3.231 into eq. 3.229 to give for scheme II

$$(3.232)\quad |\lambda|^2 = 1 \pm 3\frac{\nu'\mu'}{(1 + \mu'^2)} + \theta(\nu^2)$$

Hence, scheme II is more unstable, which is easy to understand because the time centering of the nonlinear terms is poorer in scheme II. The numerical experiment confirms this result.

Thus, for a given V and H, the strength of the instability depends on μ and ν, i.e.

on the values of Δx and Δt. One can expect that frictional terms will damp to a certain extent the instability due to the nonlinear terms. Since a stability analysis with the inclusion of the nonlinear and frictional terms is difficult, a simpler set of equations corresponding to the fully time-centered Crank–Nicolson approximation for the linearized equations 3.200–3.203 will be studied:

$$(3.233)\quad \frac{(h_j^+ - h_j^-)}{\Delta t} + \frac{H}{2\Delta x}(u_{j+1}^+ + u_{j+1}^- - u_{j-1}^+ - u_{j-1}^-) = 0$$

$$(3.234)\quad \frac{(u_{j+1}^+ - u_{j+1}^-)}{\Delta t} + \frac{g}{2\Delta x}(h_{j+2}^+ + h_{j+2}^- - h_j^+ - h_j^-) = -\frac{g}{C^2 H}(u_{j+1}^+|u_{j+1}^+| + u_{j+1}^-|u_{j+1}^-|)$$

The amplification factor for these difference equations satisfies the following characteristic equation:

$$(3.235)\quad (\lambda + 1)^2 \mu'^2 + 2K(\lambda + 1)(\lambda - 1) + (\lambda - 1)^2 = 0$$

where

$$(3.236)\quad K = \frac{1}{2}\frac{gV}{C^2 H}\Delta t$$

The roots of this are

$$(3.237)\quad \frac{\lambda - 1}{\lambda + 1} = -K \pm (K^2 - \mu'^2)^{1/2}$$

In the overall stability of a finite-difference scheme, it is the shortwave components that are the most important. Since generally $K < 1$, the frictional damping due to shortwave components is (as for schemes I and II)

$$(3.238)\quad |\lambda|^2 = 1 - \frac{4K}{(1 + \mu'^2)}$$

A comparison of eq. 3.238 with eq. 3.231 shows that the overall stability condition can be written as

$$(3.239)\quad \gamma\mu < \text{constant}$$

where

$$(3.240)\quad \gamma \equiv \frac{C^2 H}{g\Delta x} \text{ and } \mu \equiv \frac{\Delta t}{\Delta x}\sqrt{gH}$$

The nondimensional parameter γ is a measure of the frictional effect whereas the parameter μ is a measure of the accuracy of the finite-difference scheme. When an explicit scheme is used, $\mu < 1$ and is limited by the C–F–L stability criterion. For an implicit scheme, although in theory there is no such restriction, in practice there is a restriction based on the accuracy of the scheme (there is also a lower limit on Δx).

The following numerical experiment verifies the result of eq. 3.239. A one-dimensional basin of 9.5-km length with a uniform undisturbed water depth of 10 m was taken. The boundary conditions are $u = 0$ at $x = 0$ and $h = \cos(\omega t)$ at $x = 9.5$ km. The period $T = 2\pi/\omega$ is taken as $25\Delta t$. The initial conditions are $u = 0$ and $h = 1$ m

everywhere. With $C^2 = 4000\ \mathrm{m \cdot s^{-2}}$ and $\Delta t = 200$ s, four tests were conducted using scheme I. In these four tests, Δx was taken as 1000, 500, 250, and 125 m. The corresponding values of γ were 4, 8, 16, and 32 and the values for μ were 2, 4, 8, and 16. The first two tests were stable, whereas the finer grid calculations proved to be unstable.

In this test, at the velocity point adjacent to the open boundary, $u\,\partial u/\partial x$ was set equal to zero (Leendertse 1967). The numerical experiment used to test scheme II showed for which combinations of γ and μ scheme II was stable and for which combinations it was unstable.

3.5 Combination of Two-Dimensional and One-Dimensional Models

In dealing with storm surge problems in real water bodies, situations are often faced in which the surge is generated in a bay or gulf and is amplified (or dissipated) as it propagates into an estuary, inlet, or river. It is impractical to use a two-dimensional model for the whole system because the river or estuary is too narrow. On the other hand, a one-dimensional model for the whole system is unrealistic because it cannot represent accurately the topography of the bay or gulf and the influence of the transverse motions. For situations such as this, one must use a two-dimensional model (for the bay or gulf) that runs concurrently with a one-dimensional model for the river. Two such models will be considered: one for the North Sea and Thames River and the other for the Bay of Bengal and one of its estuaries.

Prandle (1974, 1975) developed a dynamically coupled two-part model to calculate the propagation of tides and storm surges in the southern part of the North Sea and the Thames River. A two-dimensional model for that part of the North Sea south of 53°20′ latitude and that part of the English Channel east of the Greenwich meridian is interfaced with a one-dimensional model for the Thames River.

Both models are vertically integrated. The model developed by Prandle (1974, 1975) is somewhat similar to that of Banks (1974) for the same area. First, consider the one-dimensional model. The continuity equation is

$$S\frac{\partial h}{\partial t} + \frac{\partial Q}{\partial x}\Delta x - Q_T = 0 \tag{3.241}$$

where S is the surface area between adjacent sections, h is the elevation of the water surface above a fixed horizontal datum, x is the axis along the river (positive towards upstream), Q is the total flow in the longitudinal direction, Δx is the section length, and Q_T is the water discharge from the tributaries.

The equation of motion is

$$\frac{\partial u}{\partial t} + u\frac{\partial u}{\partial x} + g\frac{\partial h}{\partial x} + \frac{g u|u|}{C^2 M} = 0 \tag{3.242}$$

where u is the velocity in the x direction (average value over a cross-section), M is the hydraulic depth, and C is a Chezy coefficient.

Equation 3.241 can be written at (j, n) as follows:

$$\frac{S_j(h_{j,n+1/2} - h_{j,n-1/2})}{\Delta t} + A_{j+1/2}\,u_{j+1/2,n} - A_{j-1/2}\,u_{j-1/2,n} - Q_{T_j} = 0 \tag{3.243}$$

where A is the area of cross-section.

To calculate A and S, the following interpolations are made.

For $A_{j-1/2}$:

$$h_{j-1/2,n} = \frac{1}{2}(h_{j,n-1/2} + h_{j-1,n+1/2})$$

For $A_{j+1/2}$:

$$h_{j+1/2,n} = \frac{1}{2}(h_{j,n+1/2} + h_{j+1,n-1/2})$$

For S_j:

$$h_{j,n} = \frac{1}{2}(h_{j,n+1/2} + h_{j,n-1/2})$$

It can be seen for the calculation of $A_{j+1/2}$ and S_j that $h_{j,n+1/2}$ must be known. Hence, eq. 3.243 must be solved by iteration. Beginning with an initial value of $h_{j,n-1/2}$, in practice four iterations appeared to be sufficient. Equation 3.242 is solved at $(j + 1/2, n + 1/2)$ and the following expression can be written for $u_{j+1/2,n+1}$:

$$\text{(3.244)} \quad \frac{(u_{j+1/2,n+1} - u_{j+1/2,n})}{\Delta t} + \frac{g(h_{j+1,n+1/2} - h_{j,n+1/2})}{\Delta x_j} + \frac{g u_{j+1/2,n+1}|u_{j+1/2,n}|}{(C^2_{j+1/2} M_{j+1/2})} = 0$$

Equations 3.243 and 3.244 must be solved for the two dependent variables (water level and velocity). The stability condition is

$$\text{(3.245)} \quad \frac{\Delta x}{\Delta t} \geq u + C$$

The equations for the two-dimensional model are as follows:

$$\text{(3.246)} \quad \frac{\partial u}{\partial t} + g\frac{\partial h}{\partial x} + \frac{1}{\rho}\frac{\partial P}{\partial x} + \tau_{S_x} + \frac{g u|(u^2 + v^2)^{1/2}|}{C^2 D} - fv = 0$$

$$\text{(3.247)} \quad \frac{\partial v}{\partial t} + g\frac{\partial h}{\partial y} + \frac{1}{\rho}\frac{\partial P}{\partial y} + \tau_{S_y} + \frac{g v|(u^2 + v^2)^{1/2}|}{C^2 D} - fu = 0$$

$$\text{(3.248)} \quad \frac{\partial h}{\partial t} + \frac{\partial u}{\partial x}(h + D) + \frac{\partial v}{\partial y}(h + D) = 0$$

where u and v are the depth-averaged velocities along the x and y directions, D is the depth of the bed below the same horizontal datum, P is the atmospheric pressure, ρ is the density of water, τ_{S_x} and τ_{S_y} are the wind stress components in the x and y directions, and f is the Coriolis parameter.

Using a central finite-difference staggered grid, eq. 3.246 is centered at $(x, y + \Delta y/2, n + 1/2)$ to give an expression for $u_{x,y+1/2,n+1}$. Let j and k denote the indices for x and y. Then

$$\text{(3.249)} \quad \frac{(u_{j,k+1/2,n+1} - u_{j,k+1/2,n})}{\Delta t} + g\frac{(h_{j+1/2,k+1/2,n+1/2} - h_{j-1/2,k+1/2,n+1/2})}{\Delta x} + \frac{(P_{j+1/2,k+1/2,n+1/2} - P_{j-1/2,k+1/2,n+1/2})}{\rho \Delta x} + \tau_{S_{y,k+1/2}} + \frac{g u_{j,k+1/2,n+1}|(u^2_{j,k+1/2,n} + v^2_{\text{Bar}})^{1/2}|}{C^2_{j,k+1/2} DE} - f_{k+1/2} v_{\text{Bar}} = 0$$

where

$$v_{\text{Bar}} = \frac{(v_{j-1/2,k,n+1} + v_{j-1/2,k+1,n+1} + v_{j+1/2,k,n} + v_{j+1/2,k+1,n})}{4}$$

and

$$DE = D_{j,k+1/2} + \frac{(h_{j+1/2,k+1/2,n+1/2} + h_{j-1/2,k+1/2,n+1/2})}{2}$$

Equation 3.247 is centered at $(x + \Delta x/2, t + \Delta t/2)$, which gives an expression for $v_{j+1/2,k,n+1}$:

$$(3.250)\quad \frac{(v_{j+1/2,k,n+1} - v_{j+1/2,k,n})}{\Delta t} + \frac{g(h_{j+1/2,k+1/2,n+1/2} - h_{j+1/2,k-1/2,n+1/2})}{\Delta y} + \frac{(P_{j+1/2,k+1/2,n+1/2} - P_{j+1/2,k-1/2,n+1/2})}{\rho \Delta y} + \tau_{S_{v_{j+1/2,k}}} + \frac{g v_{j+1/2,k,n+1} |(v^2_{j+1/2,k,n} + u^2_{\text{Bar}})^{1/2}|}{C^2_{j+1/2} DE} - f_k u_{\text{Bar}} = 0$$

where

$$u_{\text{Bar}} = \frac{(u_{j,k+1/2,n+1} + u_{j,k-1/2,n+1} + u_{j+1,k-1/2,n} + u_{j+1,k-1/2,n})}{4}$$

and

$$DE = H_{j+1/2,k} + \frac{(h_{j+1/2,k+1/2,n+1/2} + h_{j+1/2,k-1/2,n+1/2})}{2}$$

Equation 3.248 is centered at $(x + \Delta x/2, y + \Delta y/2, t + \Delta t/2)$ and gives an expression for $h_{j+1/2,k+1/2,n+3/2}$:

$$(3.251)\quad \frac{(h_{j+1/2,k+1/2,n+3/2} - h_{j+1/2,k+1/2,n+1/2})}{\Delta t} + \frac{(u_{j+1,k+1/2,n+1} DE1 - u_{j,k+1/2,n+1} DE2)}{\Delta x} + \frac{(v_{j+1/2,k+1,n+1} DE3 - v_{j+1/2,k,n+1} DE4)}{\Delta y} = 0$$

where

$$DE1 = H_{j+1,k+1/2} + \frac{(h_{j+1/2,k+1/2,n+3/2} + h_{j+3/2,k+1/2,n+1/2})}{2}$$

$$DE2 = H_{j,k+1/2} + \frac{(h_{j+1/2,k+1/2,n+1/2} + h_{j-1/2,k+1/2,n+3/2})}{2}$$

$$DE3 = H_{j+1/2,k+1} + \frac{(h_{j+1/2,k+1/2,n+3/2} + h_{j+1/2,k+3/2,n+1/2})}{2}$$

$$DE4 = H_{j+1/2,k} + \frac{(h_{j+1/2,k+1/2,n+1/2} + h_{j+1/2,k-1/2,n+3/2})}{2}$$

Initial conditions are specified for values of h at $t - \Delta t/2$ and values of u and v at

time t. For correct interfacing of the one- and two-dimensional models, the mass and momentum transfer across the interface must be correctly represented. The downstream boundary condition for the Thames River is denoted as the volume transport to or from the adjacent boundary of the North Sea model. This ensures correct transfer of mass. To represent correctly the transfer of momentum, the volume transfer is calculated in terms of the water level on either side of the common boundary. From the continuity equation for the one-dimensional model:

$$(3.252) \quad \frac{S_2(h_{2,n+1/2} - h_{2,n-1/2})}{\Delta t} + A_2 u_{2,n} - Q_1 = 0$$

where Q_1 is the volume of water transported across the interface and is given by

$$(3.253) \quad Q_1 = -u_{7,18,n}\left[D_{7,18} + \frac{1}{2}(h_{2,n+1/2} + h_{7,18,n-1/2})\right]\Delta y$$

where (7, 18) is the interface point. The negative sign corrects for opposing direction of axes in the one- and two-dimensional models.

The equation of motion in the x direction for the two-dimensional scheme is used to obtain an expression for the velocity at the interface:

$$(3.254) \quad \frac{(u_{7,18,n+1} - u_{7,18,n})}{\Delta t} + \frac{g(h_{7,18,n+1/2} - h_B)}{\Delta x} + \text{other terms} = 0$$

where $h_B = h_{6,18,n+1/2}$ for an interior grid point if located 10′ west of $h_{7,18}$. The one-dimensional model is so chosen such that the location of the first tidal elevation in the Thames River is at a location 10′ west of $h_{7,18}$. Hence, one can simply use

$$(h_B = h_{2,n+1/2})$$

For inclusion of tidal flats, the following scheme was used in which the boundary grid squares are modified. A triangular-edged prismatic section is added to the landward side of the grid. The velocity $u_{j,k}$ across this grid is set to zero, which of course is not strictly correct. The continuity equation for the boundary grid gives

$$(3.255) \quad \frac{\partial h}{\partial t} + \frac{\tan\theta}{2\Delta x}\frac{\partial}{\partial t}(h + A)^2 + \frac{\partial}{\partial x}u(h + D) + \frac{\partial}{\partial y}v(h + D) = 0$$

where D is the water depth in the undisturbed state and h is the height of the water surface at the center of the square. The parameters A and θ define the slope of the prismatic section.

The first two terms in eq. 3.338 can be reduced to $\partial h/\partial t\,[1 + (\tan\theta/\Delta x)(h + A)]$. Equation 3.254 is then solved in the same manner as eq. 3.250.

The value of h in the term $1 + [\tan\theta\,(h + A)]/\Delta x$ is given an approximate value of $h_{j,k}$ of the previous time step. Then, eq. 3.254 is solved through iteration. The magnitudes of the parameter A were set equal to the maximum tidal amplitude at the locations under consideration. The values of θ were calculated so that the horizontal movement of the land–water boundary in the model is equivalent to the distance between high and low water levels. Note that the same scheme can be used to provide a smooth transition between successive grid points when grid squares are added or subtracted (which is an alternate but more complicated scheme).

Next, a model for the Bay of Bengal will be considered. Johns and Ali (1980) developed a two-dimensional model for the Bay coupled to a one-dimensional model for the Ganges–Brahmaputra–Meghna river system. The geographical area and the grid

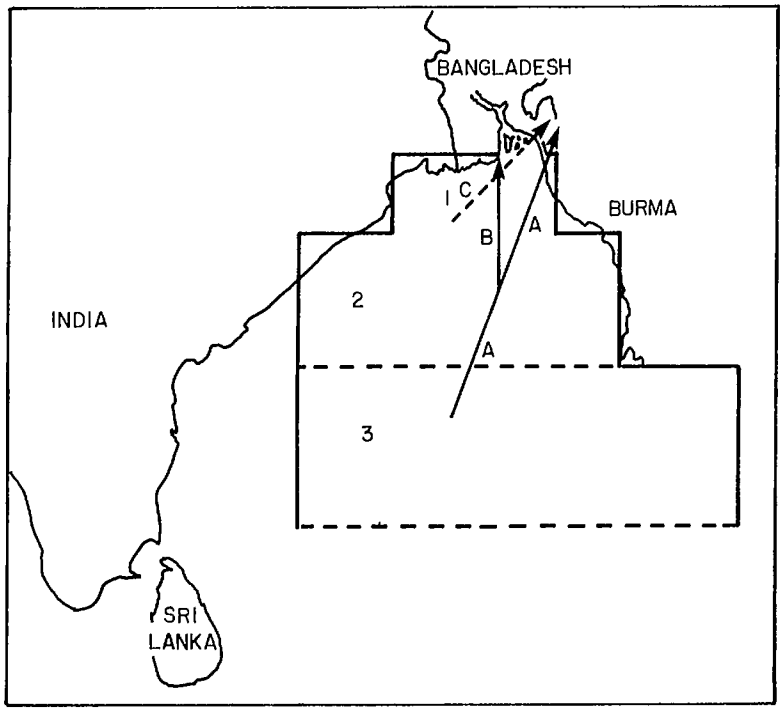

FIG. 3.7. Grid system used in the Bay of Bengal model. (Johns and Ali 1980)

limits for the two models are shown in Fig. 3.7. Uniform depth was assumed in region 3, and in regions 2 and 1, depth decreases towards the lateral boundaries and equals 10 m along the coastline. The depths in rivers 1, 2, and 3 are taken as 8, 7, and 7 m, respectively, and they were all assumed to be uniform. The model is nonlinear so that tide–surge interaction could be studied. Region 3 has a coarse grid with $\Delta x = \Delta y =$ 72 km, and regions 1 and 2 have a fine mesh with $\Delta x = \Delta y = 18$ km. Also in the rivers, $\Delta y = 18$ km.

For the two-dimensional model, the equations of motion are, in the flux form,

$$(3.256)\quad \frac{\partial}{\partial t}[(h+D)u] + \frac{\partial}{\partial x}[(h+D)u^2] + \frac{\partial}{\partial y}[(h+D)uv] - f(h+D)v = -g(h+D)\frac{\partial h}{\partial x} + \frac{\tau_{s_x}}{\rho} - Ku(u^2+v^2)^{1/2}$$

and

$$(3.257)\quad \frac{\partial}{\partial t}[(h+D)v] + \frac{\partial}{\partial x}[(h+D)uv] + \frac{\partial}{\partial y}[(h+D)v^2] + f(h+D)u = -g(h+D)\frac{\partial h}{\partial y} + \frac{\tau_{s_y}}{\rho} - Kv(u^2+v^2)^{1/2}$$

In these equations, D is the water depth, h is the free surface elevation, and K is a bottom friction coefficient. The continuity equation is

$$(3.258)\quad \frac{\partial h}{\partial t} + \frac{\partial}{\partial x}[(h + D)u] + \frac{\partial}{\partial y}[(h + D)v] = 0$$

For the one-dimensional model, let $b(y)$ be the breadth of the river at location y. The continuity equation is

$$(3.259)\quad b\frac{\partial h}{\partial t} + \frac{\partial}{\partial y}[b(h + D)v] = 0$$

The equation of motion along the axis of the river is

$$(3.260)\quad \frac{\partial}{\partial t}[b(h + D)v] + \frac{\partial}{\partial y}[b(h + D)v^2] = -gb(h + D)\frac{\partial h}{\partial y} - Kbv|v|$$

The matching of the two-dimensional model to the one-dimensional model is done as follows. Let B be the breadth of region 1 at section PQ where it joins river 1. Continuity of water level elevation requires that

$$(3.261)\quad h_{\text{river}} = \frac{1}{B}\int_{PQ} h_{\text{sea}}\, dx$$

Continuity of volume flux implies that

$$(3.262)\quad B[(h + D)v]_{\text{river}} = \int_{PQ} [(h + D)v]_{\text{sea}}\, dx$$

Equations 3.259 and 3.260 are solved knowing the water level elevation from region 1 of the Bay model (i.e. two-dimensional model) in river 1. Motion is communicated from river 1 to rivers 2 and 3.

At the open boundary of region 3 in the two-dimensional model, the tidal elevation is prescribed as follows:

$$(3.263)\quad h = \sum_s a_s \sin(\sigma_s t + \gamma_s)$$

where, a_s, σ_s, and γ_s are the amplitude, frequency, and phase, respectively, of the relevant tidal constituents. The numerical integration is performed on a staggered grid.

3.6 Finite-Element and Irregular-Grid Finite-Difference Models

This section will be concerned mainly with the finite-element approach to storm surges and tides and will later deal with some irregular-grid finite-difference techniques which combine the best features of both the finite-element and the finite-difference methods. Compared with the finite-difference methods, the finite-element methods are more recent (they began to appear in the literature in the middle 1960's) but they are better suited for representing the topography realistically than are regular-grid finite-difference techniques.

Following Wang and Connor (1975a), the literature on finite-element methods will be briefly reviewed. Unlike in the finite-difference method, in the finite-element method the variables satisfying the governing equations and boundary conditions are approximated by piecewise polynomials. The main advantage of the finite-element method is the highly flexible grid so that real water bodies can be modeled more realistically.

Wang and Connor (1975a) distinguished between the finite-element method and the

discrete-element method as follows. The discrete-element method makes use of both the finite-difference and finite-element methods. In the discrete-element method, rather than using differential equations for the infinitesimal element, one can perform all the balances on the computational discrete element which can have an arbitrary shape. However, one generally uses square, rectangular, or triangular elements. In an element the variation of any given parameter is represented by discrete nodal values. Usually, these nodes are located at the center of the sides of the elements. To satisfy conservation, the discrete equations must approximate the differential equations as the control volume is reduced to zero. This may be difficult to prove for odd-shaped elements. Simon-Tov (1974) and Eraslan (1974) gave some examples of the discrete-element method. Wang and Connor (1975a) pointed out that one drawback of the discrete-element method is that if one wants to refine the grid at one point, e.g. (x_0, y_0), then one must have the same value of Δx for all the elements along the line $y = x_0$ and the same value of Δy for all elements along the line $x = y_0$. However, this is not a serious shortcoming because either an interpolation technique or trapezoidally shaped elements can be developed to get around this problem.

According to Wang and Connor (1975a) the finite-element method was first used in 1956 in aeronautics. Until the late 1960's its use was mainly confined to solid and structural mechanics (Zienkewicz 1971). In the early stages the success of the finite-element method depended on the existence of a variational statement of the problem. However, Finlayson and Scriven (1965) showed that Galerkin's method can be derived from the method of weighted residuals and there is no need for a variational statement.

Consider the differential equation

$$Lu = f_0 \tag{3.264}$$

where L is a differential operator, u is an exact solution, and f_0 is the inhomogeneous term. Define the residual R as

$$R = L\hat{u} - f_0 \tag{3.265}$$

where $\hat{u}$ is an approximate solution. Application of a weighting function w to the residual and summation over the complete domain Ω gives

$$WR = \int_\Omega Rwd\omega = \int_\Omega (L\hat{u} - f_0)w\, d\omega \tag{3.266}$$

where WR is the weighted residual. The finite-element solution is based on the condition that the weighted residual should vanish.

For some applications of the finite-element method to circulation in shallow water bodies, see Gallagher et al. (1973), who calculated the steady wind driven circulation in shallow lakes under the rigid lid approximation. Taylor and Davis (1972) used a fourth-order predictor–corrector method for the time integration. They compared the trapezoidal rule and the finite elements in time. Grotkop (1973) studied the same problem using linear finite elements in space and time. According to Wang and Connor (1975a) this method is less accurate than the trapezoidal rule. Consider the equation

$$\underset{\sim}{M}\,\dot{\underset{\sim}{x}} = \underset{\sim}{F} \tag{3.267}$$

where the tilde denotes a matrix quantity. Applying the linear finite elements in time to this equation gives the following recurrence relation:

$$\underset{\sim}{M}\,\underset{\sim}{x}_{n+1} = \underset{\sim}{M}\,\underset{\sim}{x}_n + \Delta t\left(\frac{1}{3}F_n + \frac{2}{3}F_{n+1}\right) \tag{3.268}$$

On the other hand, the trapezoidal rule can be written as

$$(3.269)\quad \underline{M}\,\underline{x}_{n+1} = \underline{M}\,\underline{x}_n + \frac{\Delta t}{2}(F_n + F_{n+1})$$

Note that the trapezoidal form is centered around time $n + 1/2$ and is better than the skewed form (eq. 3.268). Taylor and Davis (1972) made use of a cubic expansion in time based on trial runs. It should be noted that the predictor–corrector method and the cubic finite-element method give more accurate results than the trapezoidal rule; however, they require much more computational effort. Because of asymmetric matrices, even the trapezoidal rule is not very efficient.

Norton et al. (1973) used the Newton–Ralphson method to include the nonlinear terms. Wang and Connor (1975a, 1975b) gave some new concepts which helped to solve troublesome details encountered in earlier studies. The boundary condition of nonzero slip in the tangential velocity field is conceptually difficult to apply when curved land boundaries are approximated by triangular elements. At the break points of the model boundary, the nonzero tangential velocity component gives rise to flow across the adjoining segments. Then, to satisfy the continuity equation at the break points, one is forced to equate both velocity components to zero. Norton et al. (1973) suggested that one should keep as few break points as possible and at these points both the velocity components must be prescribed equal to zero. Once one is forced to do this, the flexibility of the finite-element grid is sacrificed; also, near the break points one must use a fine grid. This will necessitate the use of long and narrow triangles (distorted elements). Wang and Connor (1975a) resolved this problem by a proper definition of a normal direction at the break points, and this permits a nonzero tangential component of the velocity without reducing the number of break points.

For a detailed derivation of the equations involved in the finite-element method see Wang and Connor (1975a). They solved several simple problems to enable comparison with analytical solutions. Finally, they applied the technique to a study of tides in the Massachusetts Bay. Wang and Connor (1975a) also formulated a two-layer model (for other details see Connor and Wang (1973) and Wang and Connor (1975b)).

Weare (1976a) compared the computational expenses for the shallow-water problems using finite-difference and finite-element methods and concluded that, at present, finite-element methods are less economical due to the use of band algorithms. However, the situation is changing now. Gray and Pinder (1976) made a comprehensive comparison of finite-difference and finite-element methods and showed that the finite-element representation of the differential equations is essentially a spatial average of standard finite-difference equations written for each mode of the grid.

Kleinstreuer and Holdeman (1980) developed an interactive triangular finite-element mesh generator for water bodies of arbitrary geometry. Niemeyer (1979a) applied a finite-element technique to study tidal flow in certain water bodies in Hawaii. Orlob (1972) used triangular grids for studying circulation in the San Francisco Bay area, but he wrote the equations in finite-difference form. Fix (1975) used a finite-element model to study the circulation in a limited area of the midocean.

Grotkop (1973) used a finite-element technique for studying long waves in the North Sea. Cheng (1972a, 1974), Cheng et al. (1976), Cheng and Tung (1970), Gallagher et al. (1973), Gallagher and Chan (1973), and Huebner (1974) applied finite-element techniques to study wind-driven circulation in lakes. Other relevant works are those of Cheng (1978), Walters and Cheng (1980a, 1980b), Jamart and Winter (1979), Mei and Chen (1975),

Reichard and Celikol (1978), Hauguel (1978), Le Provost (1978), Leimkuhler et al. (1975), and Taylor and Hood (1973).

Jamart and Winter (1978) used the finite-element approach to study tidal propagation. One of their important assumptions is periodic motion. Because of this assumption, this model cannot be used to study storm surges (which are not periodic). Kawahara et al. (1977) used a mixed approach of the finite-element method and perturbation method, again with the assumption of periodic motion. Thacker (1977) studied the normal modes in a circular basin using an irregular-grid finite-difference model (this will be considered in detail below). Wang (1977) criticized Thacker's work and pointed out that Thacker's model is unstable and inaccurate.

Mei and Chen (1975) introduced a hybrid-element method for water-wave problems in infinite fluid domain. They introduced artificial boundaries and thus divided the fluid into a finite-element region in the neighborhood of infinity or of singular points. In the finite-element region, polynomial interpolating functions are used to approximately represent the unknown functions. In the super-element region, infinite series solutions are used. Numerical computations involve only integrals in a finite domain and the inversion of a banded symmetric matrix. Examples of shallow-water waves in a harbor are included.

Houston (1978) used a finite-element numerical model to study the interaction of tsunamis with the Hawaiian Islands. This model solves the generalized Helmholtz equation:

$$\nabla[D(x, y)\,\nabla\phi(x, y)] + \frac{\omega^2}{g}\,\phi(x, y) = 0$$

where $\phi(x, y)$ is the velocity potential, ω is the angular frequency, and $D(x, y)$ is the water depth. This equation is not relevant for storm surge studies, at least in its present simple form.

Finite-Element Models for Tides and Storm Surges

Brebbia and Partridge (1976) studied the tides and storm surges in the North Sea using two finite-element models. In both the models they used six-noded triangular elements. One model made use of an implicit integration scheme with curved sides, and the other utilized an explicit integration scheme. The models are vertically integrated and include tides, wind stress, atmospheric pressure gradients, bottom friction, Coriolis force, and advection terms.

Following Brebbia and Partridge (1976), a Cartesian coordinate system, with the origin at the equilibrium water level and the z-axis pointing upwards, is used. Let $D(x, y)$ be the deviation of the free surface from its equilibrium position. The horizontal momentum equations can be written in the following form:

$$\begin{aligned} &\frac{\partial u}{\partial t} + u\frac{\partial u}{\partial x} + v\frac{\partial u}{\partial y} = B_x \\ &\frac{\partial v}{\partial t} + u\frac{\partial v}{\partial x} + v\frac{\partial v}{\partial y} = B_y \end{aligned} \tag{3.270}$$

$$\begin{aligned} B_x &= fv - g\frac{\partial h}{\partial x} - \frac{\partial}{\partial x}\left(\frac{P_a}{\rho}\right) + \frac{1}{\rho}\tau_{S_x} - \frac{1}{\rho}\tau_{B_x} \\ B_y &= fu - g\frac{\partial h}{\partial y} - \frac{\partial}{\partial y}\left(\frac{P_a}{\rho}\right) + \frac{1}{\rho}\tau_{S_y} - \frac{1}{\rho}\tau_{B_y} \end{aligned} \tag{3.271}$$

where u and v are the x and y components of the velocity field averaged in the vertical direction.

The following expressions can be written for the surface stress, τ_S, and the bottom stress, τ_B.

$$\tau_{S_i} = \frac{\gamma}{\rho}\frac{W_i}{H^2}(W_x^2 + W_y^2)^{1/2}, \qquad i = x \text{ or } y$$

(3.272)

$$\tau_{B_i} = -\frac{g}{C^2}\rho\frac{V_i}{H}(u^2 + v^2)^{1/2}, \qquad i = 1, 2$$

If $i = 1$, $V_i = u$; if $i = 2$, $V_i = v$. Here, C is a Chezy coefficient, W_x and W_y are the x and y components of the wind, and γ is a parameter related to the atmospheric density, ρ_a($\gamma = \rho_a \cdot$ constant). Finally, $H = D + h$.

The vertically integrated form of the continuity equation is

$$\frac{\partial H}{\partial t} + \frac{\partial}{\partial x}(Hu) + \frac{\partial}{\partial y}(Hv) = 0 \tag{3.273}$$

At closed boundaries, the velocity component perpendicular to the boundary is set to zero, while the tangential component is nonzero. At open boundaries, either the normal component of the velocity or the water level is prescribed.

To develop the finite-element model, the two momentum equations (3.270) and the continuity equation (3.273) together with the influx type boundary conditions must be written in the following weighted residual manner:

$$\iint \left(\frac{\partial u}{\partial t} + u\frac{\partial u}{\partial x} - B_x\right)\delta u dA = 0$$

$$\iint \left(\frac{\partial v}{\partial t} + u\frac{\partial v}{\partial x} + v\frac{\partial v}{\partial y} - B_y\right)\delta v dA = 0 \tag{3.274}$$

$$\iint \left[\frac{\partial H}{\partial t} + \frac{\partial}{\partial x}(Hu) + \frac{\partial}{\partial y}(Hv)\right]\delta H dA = \int (HV_n - H\bar{V}_n)\,\delta H dS = \int H\bar{V}_n\,\delta H dS$$

where n denotes the normal and V_n denotes the normal component of the velocity. It will be assumed that over an element, the same interpolation applies for the unknowns u, v, and H. Thus

$$\begin{aligned} u &= \phi u^n \\ v &= \phi v^n \\ H &= \phi H^n \end{aligned} \tag{3.275}$$

where ϕ is the interpolation function and u^n, v^n, and H^n are the nodal values of u, v, and H.

A six-nodal triangular finite-element grid was used. These elements were referred to as "isoparametric" by Brebbia and Partridge (1976). The advantage of using curved elements is the suppression of the spurious forces generated on the boundaries by straight line segments joining at an angle (Connor and Brebbia 1976).

From eq. 3.274 and 3.275

$$M\frac{\partial u^n}{\partial t} + Ku^n - fMv^n + G_x H^n + F_x = 0$$

(3.276) $$M\frac{\partial v^n}{\partial t} + Kv^n - fMu^n + G_y H^n + F_y = 0$$

$$M\frac{\partial H^n}{\partial t} + C_x u^n - C_y v^n + F_H = 0$$

with the following definitions (superscript T denotes the transpose):

$$K = \int \frac{\partial}{\partial x}(\phi^T\phi)u dA + \int \frac{\partial}{\partial y}(\phi^T\phi)v dA + \frac{g}{C^2}\int \frac{\phi^T(u^2+v^2)^{1/2}}{H}\phi dA$$

$$G_x = g\int \frac{\partial}{\partial x}(\phi^T\phi)dA$$

$$G_y = g\int \frac{\partial}{\partial y}(\phi^T\phi)dA$$

$$M = \int \phi^T\phi\, dA$$

$$F_x = \int \phi^T \frac{\partial}{\partial x}\left(\frac{P_a}{\rho}\right)dA + \frac{\gamma}{\rho}\int \phi^T \frac{W_x}{H}(W_x^2 + W_y^2)^{1/2}\, dA$$

$$F_y = \int \phi^T \frac{\partial}{\partial y}\left(\frac{P_a}{\rho}\right)dA + \frac{\gamma}{\rho}\int \phi^T \frac{W_y}{H}(W_x^2 + W_y^2)^{1/2}\, dA$$

$$C_x = \int \frac{\partial}{\partial x}(\phi^T) H\phi dA$$

$$C_y = \int \frac{\partial}{\partial y}(\phi^T) H\phi dA$$

$$F_H = \int H\bar{V}_n\, \phi^T\, dA$$

(3.277)
$$\begin{bmatrix} M & \cdot & \cdot \\ \cdot & M & \cdot \\ \cdot & \cdot & M \end{bmatrix} \begin{Bmatrix} \frac{\partial u^n}{\partial t} \\ \frac{\partial v^n}{\partial t} \\ \frac{\partial H^n}{\partial t} \end{Bmatrix} + \begin{bmatrix} K & -fM & G_x \\ fM & K & G_y \\ -C_x & -C_y & 0 \end{bmatrix} \begin{Bmatrix} u^n \\ v^n \\ H^n \end{Bmatrix} + \begin{Bmatrix} F_x \\ F_y \\ F_H \end{Bmatrix} = \begin{Bmatrix} 0 \\ 0 \\ 0 \end{Bmatrix}$$

or in the abbreviated form

(3.278) $$M\dot{Q} + KQ = F$$

Then, all such elements must be assembled and the boundary conditions applied.

Two different time integration procedures were used. The first one is an implicit scheme involving the tapezoidal rule. Assume

$$\dot{Q} = \frac{Q_T - Q_0}{\Delta t}$$

(3.279) $$Q = \frac{Q_T + Q_0}{2}$$

$$F = \frac{F_0 + F_t}{2}$$

Then, eq. 3.278 becomes

(3.280) $$\left(\frac{2}{\Delta t} M + K\right) Q_t = (F_0 + F_t) + \left(\frac{2M}{\Delta t} - K\right) Q_0$$

This can be written in the abbreviated form as

(3.281) $$K^* Q_t = F^*$$

Then, the recurrence relationship is given by

(3.282) $$Q_t = (K^*)^{-1} F^*$$

The K^* matrix which must be inverted will generally be a large asymmetrical banded matrix of size approximately three times the number of nodes by six times the element band width (i.e. the maximum difference between element nodal point numbers plus one). The explicit time integration used here follows the fourth-order Runge–Kutta method.

Hamblin (1976) used finite-element techniques to study seiches, circulation, and storm surges in Lake Winnipeg. His paper will be considered in some detail below. With reference to a Cartesian coordinate system (x, y) directed towards east and north, respectively, for a homogeneous fluid, under the hydrostatic approximation, with the neglect of the nonlinear terms and assuming a uniform value for the Coriolis parameter f:

$$\frac{\partial u}{\partial t} - fv + g \frac{\partial h}{\partial x} = 0$$

(3.283) $$\frac{\partial v}{\partial t} + fu + g \frac{\partial h}{\partial y} = 0$$

$$\frac{\partial h}{\partial t} + \frac{\partial}{\partial x}(Du) + \frac{\partial}{\partial y}(Dv) = 0$$

where u and v are the vertically averaged horizontal velocity components in the x and y directions, $D(x, y)$ is the water depth, and $h(x, y, t)$ is the deviation of the water level from its equilibrium position.

In studying seiches, since concern is with periodic motion, the explicit time dependence can be eliminated by using an exponential time factor. Then, the modified set of equations in 3.283 can be written using an elliptical operator (self-adjoint) for all boundary conditions (except when energy radiates through the openings). A variational formulation of the problem may be made and a numerical solution can be sought. For this, multiply the first equation of 3.283 by u^* (u^* is the complex conjugate of u) and add this to the product of the second equation of 3.283 with v^*. Then, use the continuity equation, integrate over the volume of the lake, and use Green's theorem to give the total kinetic and potential energy in the lake:

$$(3.284)\quad I(h) = \int_A\int \left\{hh^* + \frac{gD}{(f^2 - \sigma^2)}\left[\frac{f}{i\sigma}\left(\frac{\partial h}{\partial y}\frac{\partial h^*}{\partial x} - \frac{\partial h}{\partial x}\frac{\partial h^*}{\partial y}\right) + \left(\frac{\partial h}{\partial x}\frac{\partial h^*}{\partial x} + \frac{\partial h}{\partial y}\frac{\partial h^*}{\partial y}\right)\right]\right\} dx\, dy$$

where $i = \sqrt{-1}$ and σ is the frequency of oscillation (i.e. seiche).

In deriving this equation, it is assumed that any of the following three boundary conditions can be used, noting that all of them permit zero energy flux across the boundaries: (a) vanishing depth at the shoreline and finite values of h and its gradients, (b) finite depth at the shoreline and zero velocity normal to the shoreline, and (c) finite depth and nonzero normal current but zero value of h across the boundary. Hamblin (1976) took zero depths at the coastline.

It can be shown that the function that minimizes eq. 3.284 will be the solution of eq. 3.283. The parameters h and h^* are expanded in a series of trial functions ψ_i and weighting coefficients q_i':

$$h = \sum_i q_i' \psi_1 \text{ and } h^* = \sum_i q_i'^* \psi_i$$

Substituting into eq. 3.284 gives

$$(3.285)\quad I(q'q'^*) = q'^{*T}\sigma^3[L]\,q' + q'^{*T}\sigma[M]q' + q'^*[N]q'$$

Here, $[L]$, $[M]$, and $[N]$ are Hermitian matrices, q' is the vector of unknown coefficients, and q'^{*T} is the transpose of q'^*.

To determine the minimum of the approximating function:

$$\frac{\partial I}{\partial q'^*} = 0$$

which gives from eq. 3.285

$$(3.286)\quad \sigma^3[L]z + \sigma[M]z + [N]z = 0$$

where z is the vector of weights minimizing I. The calculation of the approximating function proceeds as follows.

Lake Winnipeg is subdivided into triangular elements (Fig. 3.8a) giving a total of 144 elements. In the interior, the sides of the elements are straight lines, whereas at the coast they are curved. In locations where detail is not important, a coarser grid has been used. The trial function is chosen such that the weighting coefficients become the free surface displacements, h, at the vertices and the three midedge points (left side of Fig. 3.8b). Six points are required to determine the six coefficients of the second-order polynomial in x and y. The quadratic surface determined in this manner is continuous across the edges between the triangles, but the gradients may not be continuous.

Next, the depth D is expanded using an identical polynomial expression, in which the weighting coefficients become the specified depths at the six nodes of the triangle. If one expresses the Lagrangian interpolation functions in terms of the local triangular coordinates (rather than the global x and y coordinates), all the integrations in eq. 3.284 can be performed analytically for the interior elements. The matrices $[L]$, $[M]$, and $[N]$ are formed by summing the contributions from each element I. Owing to the symmetry of the variational formulation, the computer storage requirements and the number of integrations required are halved.

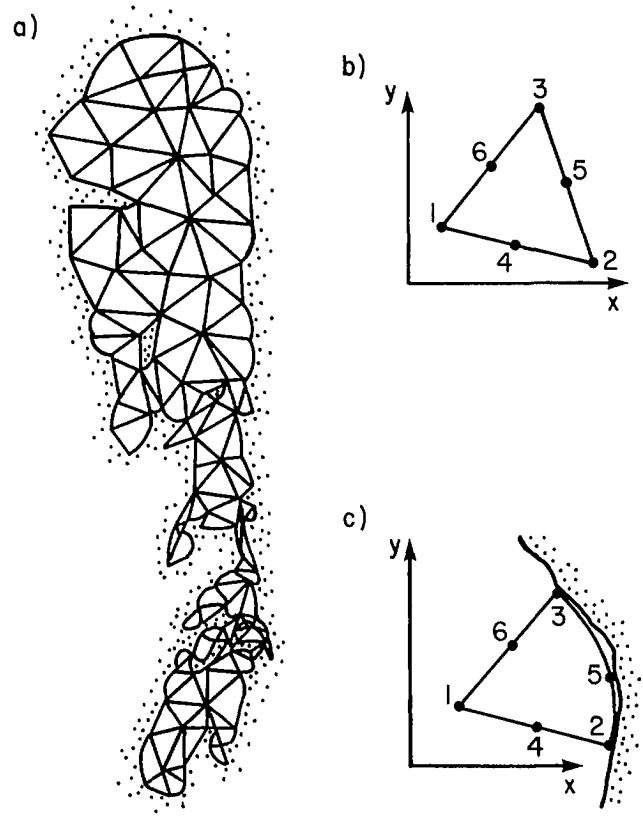

FIG. 3.8. (a) Triangular finite-element grid for Lake Winnipeg (144 elements); (b) a typical triangular element in the interior of the lake (the six nodes defining the element are numbered); (c) element adjacent to a boundary. (Hamblin 1976)

In general, the side of a triangle along the coastline will not coincide with the boundary (right side of Fig. 3.8b) and one must transform the curved shoreline into a straight line by means of a coordinate transformation. Define a coordinate system such that

$$x = x(p, q)$$

$$y = y(p, q)$$

Then, a boundary integration of the form

$$\iint \psi_i(x, y)\, \psi_j(x, y)\, h_K\, dxdy$$

becomes

$$\iint \psi_i[x(p, q), y(p, q)\psi_j]\, [x(p, q), y(p, q)]\, h_K J(p, q)\, dpdq$$

where J is the Jacobian of the coordinate transformation:

$$J = \frac{\partial x}{\partial p}\frac{\partial y}{\partial q} - \frac{\partial x}{\partial q}\frac{\partial y}{\partial p}$$

For the boundary elements, numerical integration is necessary (unlike analytical integration for interior elements).

Next, Hamblin (1976) considered the problem of steady wind driven circulation and setup in Lake Winnipeg, while retaining the vertical friction term. The relevant equations are

$$-fv = -g\left(\frac{\partial h}{\partial x}\right) + \nu\left(\frac{\partial^2 u}{\partial z^2}\right)$$

$$fu = -g\left(\frac{\partial h}{\partial y}\right) + \nu\left(\frac{\partial^2 v}{\partial z^2}\right) \tag{3.287}$$

$$\frac{\partial u}{\partial x} + \frac{\partial v}{\partial y} + \frac{\partial w}{\partial z} = 0$$

where ν is the vertical eddy viscosity and w is the vertical component of the velocity (here, u and v are not vertically averaged).

The boundary conditions are the following:

$$\nu\left(\frac{\partial u}{\partial z}\right)_{z=0} = \frac{\tau_{S_x}}{\rho} \quad \text{and} \quad \nu\left(\frac{\partial v}{\partial z}\right)_{z=0} = \frac{\tau_{S_y}}{\rho} \tag{3.288}$$

where τ_{S_x} and τ_{S_y} are the wind stress components at the surface and

$$u|_{z=-D} = 0 \quad \text{and} \quad v|_{z=-D} = 0 \tag{3.289}$$

In the vertically integrated form the continuity equation is

$$\frac{\partial U}{\partial x} + \frac{\partial V}{\partial y} = 0 \tag{3.290}$$

where

$$(U, V) = \int_{-D}^{0} (u, v)\, dz$$

is the horizontal transport vector. At the lateral boundaries the normal transport is taken as zero.

Making use of the Galerkin method, Hamblin (1976) developed a technique which enables one to determine the free surface and transport variables with a single solution of the equations, which is applicable for multiple-connected regions. The variational formulation used earlier is not applicable because the self-adjointness condition is not satisfied owing to the presence of the surface wind stress terms. Hence, a somewhat weaker formulation, namely the Galerkin method, is used. In this method, a stationary point (rather than a minimum) of an expression related to the function will be determined.

Multiply eq. 3.290 by a weighting function $W(x, t)$ and integrate over the area of the whole lake to give

$$\int W\left(\frac{\partial U}{\partial x} + \frac{\partial V}{\partial y}\right) dxdy = 0 \tag{3.291}$$

Using Galerkin's method, W must be chosen such that eq. 3.290 is satisfied at all the

nodes. As above, expand the variables U, V, and h in a series of trial functions ψ_i and weighting coefficients q_i':

$$h = \sum_i q_i' \psi_i$$

Partial integration of eq. 3.291 gives

$$\oint_{\text{Boundary}} W(\vec{V}\,\vec{dn}) - \iint \left(U\frac{\partial W}{\partial x} + V\frac{\partial W}{\partial y}\right) dxdy = 0$$

Note that the line integral is zero in the case where there is no river input or outflow. Using eq. 3.289 one can eliminate U and V and write

$$(3.292)\quad \iint gD\left(E\frac{\partial h}{\partial x} - F\frac{\partial h}{\partial y}\right)\frac{\partial W}{\partial x}\,dxdy + \iint gD\left(F\frac{\partial h}{\partial x} + E\frac{\partial h}{\partial y}\right)\frac{\partial W}{\partial y}\,dxdy$$

$$= -\iint [C\tau_{S_x} - D\tau_{S_y}]\frac{\partial W}{\rho\partial x}\,dxdy - \iint (A\tau_{S_y} + C\tau_{S_y})\frac{\partial W}{\rho\partial x}\,dxdy$$

(For details on the parameters C, A, E, and F, see Welander (1957). In this section, Welander's parameter D has been replaced with A.)

For evaluating eq. 3.292, the parameters D, C, A, E, F, τ_{S_x}, and τ_{S_y} are expanded in a series of the same trial functions, i.e.:

$$\tau_{S_x} = \sum_i^6 \tau_{S_{x_i}} \psi_i$$

Then, eq. 3.292 gives a system of six equations for each element:

$$(3.293)\quad \sum_{j=1}^{6} \iint gD\left(E\frac{\partial \psi_j}{\partial x} - F\frac{\partial \psi_j}{\partial y}\right)\frac{\partial \psi_i}{\partial x}\,dxdy + \iint gD\left(F\frac{\partial \psi_j}{\partial x} + E\frac{\partial \psi_j}{\partial y}\right)\frac{\partial \psi_i}{\partial y}\,dxdy$$

$$= -\iint (C\tau_{S_x} - A\tau_{S_y})\frac{\partial \psi_i}{\rho\partial x}\,dxdy - \iint (A\tau_{S_x} + C\tau_{S_y})\frac{\partial \psi_i}{\rho\partial x}h_j\,dxdy \text{ for } i = 1 \text{ to } 6$$

For the whole water body, the equations are obtained by successive integrations of each element and by adding all these, which assumes continuity of h_i at each node. The matrix

$$[M]\,h = B$$

is solved by Gaussian elimination.

Finally, Hamblin (1976) considered storm surges in Lake Winnipeg by beginning with the following time-dependent equations:

$$(3.294)\quad \begin{aligned} &\frac{\partial u}{\partial t} - fv + g\frac{\partial h}{\partial x} = \frac{\tau_{S_x}}{D\rho} - \frac{\tau_{B_x}}{D\rho} \\ &\frac{\partial v}{\partial t} - fu + g\frac{\partial h}{\partial y} = \frac{\tau_{S_y}}{D\rho} - \frac{\tau_{B_y}}{D\rho} \\ &\frac{\partial h}{\partial t} + \frac{\partial}{\partial x}(Du) + \frac{\partial}{\partial y}(Dv) = 0 \end{aligned}$$

where τ_B is the bottom stress.

Hamblin used a semianalytic technique (spectral method) in which the time variable is treated analytically and the space variables are treated numerically. Equations 3.294 can be written in the finite-element method as

$$\frac{dQ}{dt} = [M]Q + T(t) \tag{3.295}$$

where the vector Q consists of the individual components of the current and h, the vector T consists of the wind stress components at each node, and the matrix $[M]$ consists of coefficients which include f, g, D, and the bottom friction.

For the initial condition, $Q(0)$, the general solution of eq. 3.295 can be written as

$$Q(t) = [X(t)]\,Q(0) + \int_0^t [X(t - t')]\,T(t')\,dt' \tag{3.296}$$

where

$$[X(t)] = [C]\begin{bmatrix} e^{\sigma_1 t} & & \\ & \ddots & \\ & & e^{\sigma_n t} \end{bmatrix}[C]^{-1}$$

Here, σ are the eigenvalues and $[C]$ is the matrix of eigenvectors of

$$\{[M] - \sigma[I]\}\{C_i\} = 0$$

If the water body is initially at rest, $Q(0) = 0$ and a suddenly imposed wind stress can be written as $T(t) = K$. Integration of eq. 3.296 gives

$$Q(t) = -[C]\begin{bmatrix} \frac{1}{\sigma_1} & & \\ & \ddots & \\ & & \frac{1}{\sigma_n} \end{bmatrix}[C]^{-1}K + [C]\begin{bmatrix} \frac{e^{\sigma_1 t}}{\sigma_1} & & \\ & \ddots & \\ & & \frac{e^{\sigma_n t}}{\sigma_n} \end{bmatrix}[C]^{-1}K \tag{3.297}$$

The first term in this equation can be shown to be $[M]^{-1}K$, which is the solution to the steady-state problem

$$[M]Q = K$$

The second term is a weighted sum of the free modes of oscillation of the discrete problem of order n:

$$\sum_i^n W_i\{C_i\}e^{\sigma_i t}$$

The transient response of the lake interpreted in this manner shows the connection between the general time-dependent problem and the steady-state seiche problems considered earlier.

Let the vector of the free surface displacements be denoted by S and let the eigenvectors, C_i, consist only of h; then, eq. 3.297 can be approximated:

$$h(t) \sim S + \sum_i^{n'} W_i\{C_i\}e^{\sigma_i t}$$

where the limit n' is a subset of the total n eigenvectors of $[M]$. Since the water body is at rest initially, $h(0) = 0$. Then

$$[C]W = S$$

noting that the imaginary part of S is zero. Since initially, u and v are zero, then

$$\left.\frac{\partial h}{\partial t}\right|_{t=0} = 0 \quad \text{and} \quad \left.\frac{\partial^2 h}{\partial t^2}\right|_{t=0} = 0$$

Hence,

$$[C]\sigma W = 0 \quad \text{and} \quad [C]\sigma^2 W = 0$$

From these equations the weighting coefficients may be determined by minimizing the square of the free surface deviation, h, at each node in the water body.

After obtaining the step function response, h may be calculated for a general time history of wind forcing using the convolution integral. The unit impulse response can be obtained by differentiation of the step function response. The free surface displacement, h, can be calculated by convoluting the wind input, $T(t)$, with h_{imp}

$$h(t) = \int_0^t h_{\text{imp}}\,(t - t')\,T(t')\,dt'$$

In the discrete form, this can be written as

$$h_K = \Delta t \sum_{i=0}^{j} h^i_{\text{imp}}\,T_{K-i}$$

Recent Developments

Platzman (1979) paid particular attention to proper treatment of the multiconnected regions in finite-element models and applied these concepts to a study of the normal modes of the world ocean. Platzman (1981) discussed the response characteristics of finite-element tidal models.

Lynch and Gray (1980b) developed a variable size triangular-grid finite-element model in which the boundary is permitted to deform. This technique is especially suitable for simulating the penetration of storm surges over land. Certain details of their earlier works leading to this model are contained in Gray and Lynch (1977, 1979), Lynch (1980), and Lynch and Gray (1978a, 1979, 1980a). Here, mainly the moving boundary model will be considered.

Lynch and Gray (1980b) used the Galerkin finite-element approach (for fixed boundaries) with certain modifications to the moving boundary problem. First, consider the fixed boundary problem. In their notation, the problem may be stated as

$$Lu = f \tag{3.298}$$

where L is a differential operator with derivatives in space and time, $u(X, t)$ is the unknown function, $f(X, t)$ is the known forcing function, X is the set of independent space variables, and t is time. One can use an approximate solution $\hat{u}(x, t)$ as

$$u \sim \hat{u} = \sum_{j=1}^{N} u_j(t)\,\phi_j(X) \tag{3.299}$$

where $\phi_j(X)$ are known basis functions.

Substituting eq. 3.299 into eq. 3.298 produces a nonzero residual $r(X, t)$:

$$L\hat{u} - f \equiv r(X, t) \tag{3.300}$$

The basic requirement in the Galerkin procedure is that the residual must be orthogonal to each of the basis functions ϕ_i, i.e.:

$$\langle r(X, t), \phi_i \rangle = 0 \qquad i = 1, \ldots, N \tag{3.301}$$

where angle brackets denote the inner product. It can be seen that eq. 3.301 forms a set of ordinary differential equations for the functions $u_j(t)$.

For the moving boundary problem, the following modifications must be made to this procedure. The basis function ϕ_j now becomes an implicit function of time because its value at any point depends on the location of the nodes (of a grid which is deforming):

$$\phi_j = \phi_j[X, X_b(t)] = \phi_j(X, t) \tag{3.302}$$

where the node coordinates are denoted by $X_b(t)$. In eq. 3.301, the integration domain of the inner product changes in time. Thus, the equations become nonstationary and nonlinear, as can be seen, for example, from the fact that the mass matrix, $\langle \phi_j, \phi_i \rangle$, which multiplies the time derivative terms, duj/dt, changes with time.

Next, an additional relation must be added for the node motion:

$$\frac{d}{dt} X_b(t) = V_b(t) \tag{3.303}$$

where V_b is the velocity of node b. Generally, for the interior nodes $V_b = 0$ and for the boundary nodes $V_b = v_b$ where V_b is the velocity of the node and v_b is the fluid velocity at node b. Finally, eq. 3.299 must be replaced with

$$\hat{u}(X, t) = \sum_{j=1}^{N} u_j(t)\, \phi_j(X, t) \tag{3.304}$$

where $u_j(t)$ is the value of $\hat{u}$ at node j (i.e. at the moving joint, $X_j(t)$).

The time derivatives of $\hat{u}(X, t)$ will have, as expected, additional terms (underlined) not contained in a fixed boundary model:

$$\frac{\partial \hat{u}}{\partial t} = \sum_{j=1}^{N} \frac{du_j}{dt} \phi_j + \underline{\sum_{j=1}^{N} u_j \frac{\partial \phi_j}{\partial t}} \tag{3.305}$$

and

$$\frac{\partial^2 \hat{u}}{\partial t^2} = \sum_{j=1}^{N} \frac{d^2 u_j}{dt^2} \phi_j + 2 \sum_{j=1}^{N} \frac{du_j}{dt} \frac{\partial \phi_j}{\partial t} + \sum_{j=1}^{N} u_j \frac{\partial^2 \phi_j}{\partial t^2} \tag{3.306}$$

Since the spatial domain is changing with time, the terms $\partial \phi_j / \partial t$ and $\partial^2 \phi_j / \partial t^2$ must be defined throughout the domain. Since these terms depend exclusively on the node locations $X_b(t)$ and their derivatives, in principle one can write expressions for $\partial \phi_j / \partial t$ and $\partial^2 \phi_j / \partial t^2$. However, since this is a tedious procedure, Lynch and Gray (1980b) developed an alternate procedure, which is applicable to any isoparametric element. For any two-dimensional isoparametric element, let x and y represent the global coordinates and ξ and η represent the local coordinates. It is convenient to transform this element from the global domain (in which it may have an irregular shape) to the local domain in which it will always have the shape of a square (in the (ξ, η) domain the basis functions depend only on ξ and η). Since the (ξ, η) space does not deform, a basis function $\phi_i(\xi, \eta)$ at a location (ξ_0, η_0) will not change with time. The corresponding location to (ξ_0, η_0) in the (x, y) domain, however, may change with time and it depends on the isoparametric transformation:

$$X(t) = \sum_{i=1}^{M} X_i(t)\, \phi_i(\xi, \eta)$$

From this, at a given point (ξ, η):

$$(3.307)\quad \frac{dX}{dt} = \sum_{i=1}^{M} \frac{dX_i}{dt}\,\phi_i(\xi, \eta) = \sum_{i=1}^{M} V_i(t)\,\phi_i(\xi, \eta) = V^e$$

where V^e is the elemental velocity (i.e. the velocity with which the element is moving). In a reference frame which is moving with the elemental velocity, there is no change in ϕ_i, and one can write

$$(3.308)\quad \frac{d\phi_i}{dt} = \frac{\partial \phi_i}{\partial t} + V^e\,\nabla\phi_i = 0$$

Similarly, one can write

$$(3.309)\quad \frac{\partial^2 \phi_i}{\partial t^2} = -\left[\sum_{j=1}^{N} \frac{dV_j}{dt}\,\phi_j\right] \nabla\phi_i + 2V^e(\nabla V^e)\,\nabla\phi_i + V^e(\nabla\nabla\phi_i)V^e$$

Lynch and Gray (1979) showed that, for the shallow-water problem, rather than using the continuity equation in its ordinary form, a computationally superior way is to use the following wave equation, which can be derived from the momentum and continuity equations:

$$(3.310)\quad \frac{\partial^2 H}{\partial t^2} + \tau\frac{\partial H}{\partial t} = \nabla(gH\nabla\zeta) + HV\nabla\tau + \nabla\left[\nabla(HVV) + fXHV - W\right]$$

This has to be integrated in time together with the horizontal momentum equation

$$(3.311)\quad \frac{\partial V}{\partial t} = -V\nabla V - fXV - g\nabla\zeta - \tau V + \frac{W}{H}$$

where $H(X, t)$ is the total depth, $\zeta(X, t)$ is the free surface perturbation, $h(X)$ is the equilibrium water depth, $V(X, t)$ is the horizontal velocity vector (vertically averaged), f is the Coriolis parameter, g is gravity, and $W(X, t)$ is the wind stress. The bottom stress is written as

$$(3.312)\quad \tau V(X, t) = \frac{g|V|V}{C^2 H}$$

where $C(X, t)$ is the Chezy coefficient.

The boundary condition is

$$(3.313)\quad \begin{aligned} &H = 0 \text{ on } X = X_0 + \int_0^t V\,dt \\ &V = v \end{aligned}$$

where $X(t)$ is the location of the boundary at time t, X_0 is the initial position of the boundary, V is the velocity of the boundary, and v is the velocity of the fluid.

Solutions of eq. 3.310 and 3.311 can be written in the finite-element form as follows:

$$(3.314)\quad \begin{aligned} H(X, t) &\sim \sum_{j=1}^{N} H_j(t)\,\phi_j(X, t) \\ V(X, t) &\sim \sum_{j=1}^{N} V_j(t)\,\phi_j(X, t) \\ \tau(X, t) &\sim \sum_{j=1}^{N} \tau_j(t)\,\phi_j(X, t) \end{aligned}$$

Substituting eq. 3.314 into eq. 3.310 and 3.111 and equating the weighted residuals to zero gives the following set of ordinary differential equations:

$$(3.315)\quad \sum_{j=1}^{N} \left(\frac{d^2 H_j}{dt^2} \langle \phi_j, \phi_i \rangle + 2 \frac{dH_j}{dt} \left\langle \frac{\partial \phi_j}{\partial t}, \phi_i \right\rangle + H_j \left\langle \frac{\partial^2 \phi_j}{\partial t^2}, \phi_i \right\rangle \right.$$
$$\left. + \frac{dH_j}{dt} \langle \tau \phi_j, \phi_i \rangle + H_j \left\langle \tau \frac{\partial \phi_j}{\partial t}, \phi_i \right\rangle \right) = \langle R_W, \phi_i \rangle$$

and

$$(3.316)\quad \sum_{j=1}^{N} \left(\frac{dV_j}{dt} \langle \phi_j, \phi_i \rangle + V_j \left\langle \frac{\partial \phi_j}{\partial t}, \phi_i \right\rangle \right) = \langle R_M, \phi_i \rangle, \qquad i = 1, \ldots, N$$

Here, $R_W(X, t)$ and $R_M(X, t)$ are the right sides of eq. 3.310 and 3.311, respectively.

For the time derivative terms, a standard three-level finite-difference scheme has been used. For a stationary grid and one-dimensional case the C–F–L stability criterion reduces to

$$(3.317)\quad gH \left(\frac{\Delta t}{\Delta x} \right)^2 \leq \frac{1}{3}$$

The boundary condition $V = v$ (i.e. fluid velocity equals the velocity of boundary movement) may lead to significant shearing of the boundary elements. To avoid this, Lynch and Gray (1980b) satisfied the mass conservation by requiring that

$$(3.318)\quad H = 0 \text{ or } X = X_0 + \int_0^t V \, dt, \qquad (V - v)n = 0$$

where n is a unit vector normal to the boundary. Rather than attempting to satisfy this relation at every boundary grid point, one can satisfy it in an average sense by requiring that

$$(3.319)\quad \int_S (V - v) n \, dS = 0$$

where S is the moving boundary. Using the finite-element solution forms for V and v:

$$(3.320)\quad V \sim \sum_i V_i \phi_i, \qquad v \sim \sum_i v_i \phi_i$$

Substituting eq. 3.320 into 3.319 gives

$$(3.321)\quad \sum_i \int_S (V_i - v_i) \, n \, \phi_i \, dS = 0$$

To obtain an expression for the local nodal normal direction, it is required that each term of eq. 3.321 be zero, i.e.:

$$(3.322)\quad (V_i - v_i) \int_S n \, \phi_i \, dS = 0$$

From this one can define the nodal normal direction, n_i, as follows:

$$(3.323) \quad n_i \equiv \int_S n\,\phi_i\,dS \Big/ \left| \int_S n\,\phi_i\,dS \right|$$

where node i represents the junction of two moving segments of the boundary. Using the divergence theorem:

$$(3.324) \quad \int_S n\,\phi_i\,dS = \iint_A \nabla\,\phi_i\,dA$$

where A is the total domain. The moving boundary condition becomes, finally,

$$(3.325) \quad \begin{aligned} &H_i = 0 \text{ on } X_i = X_{i,0} + \int_0^t V_i\,dt, \qquad (V_i - v_i)\,n_i = 0 \\ &V_i\,\lambda_i = 0 \end{aligned}$$

where i represents all moving boundary nodes. Here, λ_i is the tangential direction at node i. The second relation in eq. 3.325 is invoked to reduce element shearing.

A typical time step proceeds as follows.

1) Using eq. 3.323 and based on the existing grid, the nodal normal directions are determined.
2) The nodal velocities at the boundary are determined using eq. 3.325. The locations of the nodes are calculated from the following finite-difference form of the first relation in eq. 3.325:

$$(3.326) \quad X_{i,t+\Delta t} \sim X_{i,t-\Delta t} + 2\Delta t\,V_{i,t}$$

3) The term dV_i/dt (which is required to evaluate $\partial^2\phi_j/\partial t^2$) is calculated from

$$(3.327) \quad \frac{dV_i}{dt} = \frac{d^2X_i}{dt^2} \sim \frac{X_{i,t+\Delta t} - 2X_{i,t} + X_{i,t-\Delta t}}{(\Delta t)^2}$$

4) From eq. 3.315 and 3.316 H_i and V_i are calculated at $t + \Delta t$. Then, the steps are repeated by beginning with the determination of the new nodal normals.

Irregular-Grid Finite-Difference Models

Although, strictly speaking, this topic should have been included in Chapter 2 under the two-dimensional finite-difference models, it is deliberately deferred until now to point out that irregular-grid finite-difference techniques have many similarities with finite-element models, the first similarity being that both techniques can make use of identical grids. There appears to be a controversy about the relative merits of the finite-element and finite-difference methods. For example, Lam (1977) suggested that the finite-element method is superior whereas Thacker (1978a, 1978b) suggested the reverse. It appears that both techniques, as applied to the storm surge problems, are constantly being improved and an objective comparison cannot be made at present.

In both the finite-element and finite-difference methods, one of the most important steps is the construction of the grid. Usually, in most of the models, the grid consists of irregular sized and shaped triangular elements. Thacker (1980a) reviewed the presently available techniques of automating (using the computer) the construction of these grids; references within (a total of 80) show that there is a well-advanced literature on this topic. Following Thacker et al. (1980), a technique for automatic construction of irregular triangular grids for storm surge models will be considered in detail. Such a model was

applied by these authors to Lake Okeechobee in Florida and also to Mobile Bay in Alabama (Thacker 1978c). An equilateral triangular grid is superimposed on the region of the water body to be modeled. The segments of the curved coastline are then approximated by the nearest sides of the triangle, and this process results in a zigzag grid (i.e. a grid composed of triangular elements with the boundary being straight line segments and not curved lines). A curvilinear grid is then developed from the zigzag grid by simultaneously solving a set of equations for the coordinates of the points on the curvilinear grid. To be able to do this, Thacker et al. (1980) made use of the analogy with springs under tension.

The springs are supposed to be infinitesimal in length (when unstretched) and all interior springs are assumed to have the same strength, whereas the boundary springs are stronger by a factor r. The coordinates of the interior grid points are given by

$$X_K = \frac{1}{N_K} \sum_{i=1}^{N_K} X_{n_i(K)}$$
$$Y_K = \frac{1}{N_K} \sum_{i=1}^{N_K} X_{n_i(K)} \tag{3.328}$$

Here, K is the index of the interior point and $n_i(K)$ are the indices of its N_K neighbors (note that usually, $N_K = 5$, 6, or 7). For the boundary points the equations are as follows:

$$X_K = \sum_{i=1}^{N_K} \phi_{n_i(K)} \left(X_{n_i(K)} \cos^2 \theta_{b(K)} + Y_{n_i(K)} \cos \theta_{b(K)} \sin \theta_{b(K)}\right) + X_{b(K)} \sin^2 \theta_{b(K)} - Y_{b(K)} \cos \theta_{b(K)} \sin \theta_{b(K)}$$
$$Y_K = \sum_{i=1}^{N_K} \phi_{n_i(K)} \left(X_{n_i(K)} \cos \theta_{b(K)} \sin \theta_{b(K)} + Y_{n_i(K)} \sin^2 \theta_{b(K)}\right) - X_{b(K)} \cos \theta_{b(K)} \sin \theta_{b(K)} + Y_{b(K)} \cos^2 \theta_{b(K)} \tag{3.329}$$

Note that the factors $\phi_{n_i(K)}$ account for the different strengths of boundary and interior springs.

$$\phi_{n_i(K)} = \frac{1}{(2r + N_K - 2)} \text{ (for an interior point)}$$
$$\phi_{n_i(K)} = \frac{r}{(2r + N_K - 2)} \text{ (for a boundary point)} \tag{3.330}$$

Making use of some iterative technique, these above equations can be solved.

The next step is the determination of the depth at each grid point. The depth at any given grid point is determined by linearly interpolating the depths D_a, D_b, and D_c from the three closest neighboring points:

$$D = \Phi_a D_a + \Phi_b D_b + \Phi_c D_c \tag{3.331}$$

where

$$\Phi_a = \frac{(X - X_b)(Y - Y_c) - (X - X_c)(Y - Y_b)}{(X_a - X_b)(Y_a - Y_c) - (X_a - X_c)(Y_a - Y_b)} \tag{3.332}$$

Similar relations can be written for Φ_b and Φ_c. Note that the denominator in eq. 3.332 corresponds to twice the area of the triangle with vertices a, b, and c.

Once the depths are determined at each grid point, they are checked for smoothness as follows:

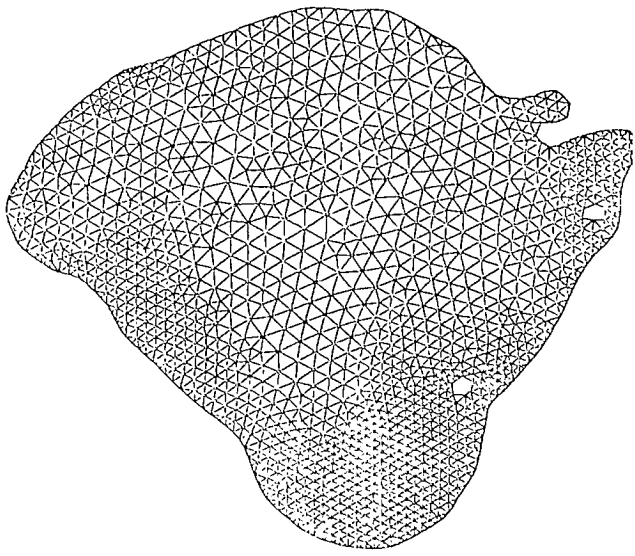

FIG. 3.9. Irregular triangular grid for Lake Okeechobee, U.S.A. (Thacker et al. 1980)

$$(3.333)\quad S_K = \frac{\frac{1}{6}\sum_{i=1}^{6}(D_{n_i(K)} - D_K)}{D_K}$$

It can be seen that the smaller the term S_K the smoother is the bathymetry. For a grid system consisting of only equilateral triangular elements, the relationship

$$|S_K| < \frac{\pi^2}{12}$$

means that the depth pattern has no Fourier components with wavelengths shorter than two grid increments. The condition $S_K = 0$ signifies that the Laplace equation is exactly satisfied. Although, in principle, this condition provides the smoothest possible bathymetry, it is too stringent a condition for practical purposes (since when this condition is satisfied, it means that the interior depths are solely determined by the boundary depths).

The criterion for the suitability of the grid size to the bathymetry is that the ratio, R_K, of the polygonal area, A_K, of each element to its local depth, D_K, be the same for each element. When this condition is satisfied, the time taken by a long wave to travel between successive elements is the same anywhere in the waterbody. Again, in practice, a uniform value of R_K throughout the basin is difficult to achieve, and one must use a more relaxed condition:

$$(3.334)\quad \alpha R_{\max} < R_K < R_{\max}$$

for all interior points K and $0 < \alpha < 1$.

Contour lines of $\alpha R_{\max}$ can be drawn so that the elements outside these contour lines are compatible with the depth field and those inside are too closely spaced. In a systematic manner, some of these closely spaced elements may be combined to obtain a coarser grid. A grid obtained in this manner for Lake Okeechobee in Florida is shown in Fig. 3.9. This same technique was applied by this author for the Bay of Bengal, to the Dixon entrance–Hecate Strait–Queen Charlotte Sound near the west coast of Canada, and the Arctic Ocean coast of Canada.

Chapter 4

Different Approaches to the Storm Surge Problems

In Chapter 2 the storm surge equations were formulated and two-dimensional finite-difference solutions were discussed. In Chapter 3, three-dimensional, two-and-a-half-dimensional, one-and-a-half-dimensional, and one-dimensional finite-difference solutions as well as finite-element solutions were considered. In this chapter, other approaches to the storm surge problems will be considered and the following techniques discussed: analytical, empirical, graphical, statistical, electric analog, laboratory experiments, hydraulic models, and hybrid models (i.e. combination of hydraulic and numerical models).

4.1 Analytical Methods

Analytic methods were popular before the computer era but, at present, these methods are little used in storm surge studies, except possibly for a quick and approximate study of some practical problem. Nevertheless, these methods will be considered not only for the sake of completeness and historical interest, but also because they provide insight into the physics of the problems. Since analytical solutions can only be obtained mainly for water bodies with rather simple geometries, hypothetical water bodies with rectangular and other regular shapes will be the focus of attention.

There is a vast literature on this topic in Japanese and Russian and some in Spanish. Not knowing these languages and not having any translation facilities for his use, the writer is forced to ignore this literature. Surprisingly, there is little North American literature on this topic and the main source is western European literature. There are several interesting analytical works dealing with the interaction between storm surges and tides (this will be discussed in Chapter 5). In this section, the simple (in concept) analytical models that were used in studying storm surges mainly in the North Sea and surrounding region will be discussed.

Proudman (1954b) studied storm surges in a closed rectangular basin and in a rectangular gulf (i.e. a partially open basin) with the aim of application to the North Sea. His study showed that wind stress is much more important than atmospheric pressure gradients in space and time. Proudman also showed that the equations of motion used in the vertically integrated form are quite satisfactory for storm surge studies. Before proceeding with a detailed discussion of this paper, reference is made to some other useful papers dealing with analytical models. These are Kivisild (1954), Schönfeld (1955), Langhaar (1951), Birchfield and Hickie (1977), and Lynch and Gray (1978a, 1978b).

Storm Surges in a Closed Rectangular Basin

To keep the mathematical problem tractable, Proudman (1954b) assumed uniform depth and homogeneity of the water column, ignored the nonlinear advective terms and the Coriolis force, but retained friction. Let the ends of the basin be denoted by $x = 0$ and $x = \pi/\chi$ and let D be the uniform depth of the basin. Let u denote the horizontal component of the current, t is time, g is gravity, ρ is the density of water, and h is the deviation of the water level from its equilibrium position. At $t = 0$ it is assumed that a wind field and a spatially nonuniform atmospheric pressure field are suddenly imposed on the basin at its surface $z = 0$ (z is the vertical coordinate) and then the forcing function is held

constant. The imposed wind stress can be written as

$$(4.1) \qquad \frac{\tau_S}{\rho} = \nu \frac{\partial u}{\partial z} = gDW \sin(\chi x)$$

where τ_S is the friction per unit area of the wind on the sea surface and ν is a coefficient of eddy viscosity assumed constant and uniform. The atmospheric pressure field, P_a, at the sea surface can be written as

$$(4.2) \qquad P_a = \text{constant} + \frac{g\rho}{\chi} P \cos(\chi x)$$

In eq. 4.1 and 4.2, W and P are constants. Define

$$(4.3) \qquad \alpha \equiv \frac{\nu^2}{gD^5\chi^2}$$

Note that parameter α was later referred to by Platzman (1963) as the Proudman number (see Chapter 2).

The water elevation, h, due to the wind stress and atmospheric pressure gradient is given by, subject to the boundary condition $u = 0$ at $z = -D$,

$$(4.4) \qquad h = -\frac{\cos(\chi x)}{\chi}\left(P + \frac{3}{2}W + \sum_S C_S e^{-\lambda_S Nt/D^2}\right)$$

where λ_S is a root of

$$(\tan \lambda^{1/2}) = \lambda^{1/2} + \alpha\lambda^{5/2}$$

with

$$(4.5) \qquad C_S = \frac{2P\alpha + 2W\left[\dfrac{\sec(\lambda_S^{1/2}) - 1}{\lambda_S^2}\right]}{\left[\dfrac{\tan(\lambda_S^{1/2})}{\lambda_S}\right]^2 - 5\alpha}$$

Note that if the water level disturbance is due to atmospheric pressure only, then $W = 0$. Proudman and Doodson (1924) numerically evaluated h from eq. 4.4 for the case $W = 0$ and $\alpha = 0.0615$; their solution was

$$(4.6) \qquad h = H \cos(\chi x)\left[1 - 1.062e^{-1.272Nt/D^2} \cos\left(3.435\frac{Nt}{D^2} - 19.2°\right) + 0.003e^{-22Nt/D^2} + \ldots\right]$$

with

$$(4.7) \qquad H \equiv -\frac{P}{\chi}$$

If the storm surge is produced by wind only, then $P = 0$ and

$$(4.8) \qquad h = H \cos(\chi x)\left[1 - 1.075e^{-1.272Nt/D^2} \cos\left(3.435\frac{Nt}{D^2} - 22.8°\right) - 0.009e^{-22Nt/D^2} + \ldots\right]$$

with

$$H \equiv -\frac{3}{2}\frac{W}{\chi} \tag{4.9}$$

Both solutions 4.6 and 4.8 tend to

$$h \to H \cos(\chi x) \text{ as } t \to \infty \tag{4.10}$$

although H is different in both cases.

Thus, in the steady state, which is asymptotically reached as $t \to \infty$, the form of the solution for h is the same whether the surge is produced by wind or atmospheric pressure. However, there is one important difference. In the case of pressure-generated stationary water level, there are no horizontal currents, whereas for the wind case, there are currents in the direction of the wind near the surface and in the opposite direction near the bottom, although the depth-mean value of the currents is zero.

In eq. 4.6 and 4.8 the numerical coefficients are so close that one may use eq. 4.6 whether the water level disturbance is generated by pressure field or wind field. One may intuitively feel that, even when the currents do not follow the (artificial) law assumed above, but are nonzero near the bottom, the above relations might be valid even for the case of a variable eddy viscosity. These ideas will be incorporated in the following treatment. The equation of motion is

$$\frac{\partial u}{\partial t} = -g\frac{\partial h}{\partial x} - \frac{1}{\rho}\frac{\partial P_a}{\partial x} + \frac{1}{\rho}\frac{\partial F}{\partial z} \tag{4.11}$$

The continuity equation is

$$D\frac{\partial \bar{u}}{\partial x} + \frac{\partial h}{\partial t} = 0 \tag{4.12}$$

where $\bar{u}$ is the depth-mean value of u. Integrate eq. 4.11 with respect to z and then divide by D to give

$$\frac{\partial \bar{u}}{\partial t} = -g\frac{\partial h}{\partial x} - \frac{1}{\rho}\frac{\partial P_a}{\partial x} + \frac{1}{\rho D}(\tau_S - \tau_B) \tag{4.13}$$

where τ_B is the bottom friction. The following form is assumed for the bottom friction

$$\tau_B = 2K\rho D\bar{u} \tag{4.14}$$

where K is a bottom friction coefficient.

From eq. 4.1, 4.2, 4.13, and 4.14:

$$-\frac{1}{\rho}\frac{\partial P_a}{\partial x} + \frac{\tau_S}{\rho D} = g(P + W)\sin(\chi x) \tag{4.15}$$

Hence, in the stationary state

$$h = -(P + W)\frac{\cos(\chi x)}{\chi} \tag{4.16}$$

From eq. 4.4 the solution is

$$h = -\left(P + \frac{3}{2}W\right)\frac{\cos(\chi x)}{\chi} \tag{4.17}$$

The difference between eq. 4.16 and 4.17 is the factor $\frac{3}{2}$ multiplying W in the latter

equation. According to Proudman (1954b) the true value lies between 1 and $\frac{3}{2}$.

From eq. 4.15, on writing

$$-\frac{1}{\rho}\frac{\partial P_a}{\partial x} + \frac{\tau_S}{\rho D} = -\chi g H \sin(\chi x) \tag{4.18}$$

the equation of motion 4.13 becomes

$$\frac{\partial \bar{u}}{\partial t} + 2K\bar{u} + g\frac{\partial h}{\partial x} = -\chi g \sin(\chi x) \tag{4.19}$$

With the initial condition $h = 0$ and $\bar{u} = 0$ at $t = 0$, the solution of eq. 4.19 and 4.12 is

$$h = H \cos(\chi x)\left\{1 - e^{-kt}\left[\cos(\sigma t) + \frac{K}{\sigma}\sin(\sigma t)\right]\right\} \tag{4.20}$$

where

$$\sigma^2 \equiv \chi^2 C^2 - K^2 \tag{4.21}$$

Equation 4.20 can also be written as

$$h = H \cos(\chi x)[1 - e^{-kt} \sec\gamma \cos(\sigma t - \gamma)] \tag{4.22}$$

where

$$\begin{aligned} \sigma &\equiv \chi C \cos\gamma \\ K &\equiv \chi C \sin\gamma \end{aligned} \tag{4.23}$$

To enable comparison of eq. 4.6 with eq. 4.22, take

$$\begin{aligned} \sigma' &= 3.435\frac{\nu}{D^2} \\ K' &= 1.272\frac{\nu}{D^2} \end{aligned} \tag{4.24}$$

Then, using eq. 4.3 and for the same value of α as above:

$$\begin{aligned} \sigma &= 0.9444\chi C \\ K &= 0.3289\chi C \end{aligned} \tag{4.25}$$

The close agreement of σ to σ', K to K', and $\sec\gamma(=1.058)$ to 1.062 (in eq. 4.6) suggests that eq. 4.22 may be used instead of eq. 4.6. That is, eq. 4.20 may be used approximately for the generation of a steady state in which

$$h = H \cos(\chi x) \tag{4.26}$$

whether the forcing function be wind or pressure or both acting together.

Next, the decay of the storm surge once the steady state (eq. 4.26) is reached will be examined by assuming that the wind is suddenly stopped and the atmospheric pressure gradient forcing is removed. Assuming $t = 0$ as the time at which the decay begins, then, for subsequent times

$$h = H \cos(\chi x) e^{-K't}\left[\cos(\sigma t) + \frac{K}{\sigma}\sin(\sigma t)\right] \tag{4.27}$$

where σ is given by eq. 4.21.

For the case $K < \chi C$ the solutions are given by eq. 4.20 and 4.21. For $K > \chi C$ the corresponding solutions are obtained from eq. 4.12 and 4.19 as

$$h = H \cos(\chi x)\left\{1 - e^{-KT}\left[\cosh(\sigma_1 t) + \frac{K}{\sigma_1}\sinh(\sigma_1 t)\right]\right\} \tag{4.28}$$

where

$$\sigma_1^2 \equiv K^{2\cdot} - \chi^2 C^2 \tag{4.29}$$

STORM SURGES IN A RECTANGULAR GULF OF INFINITE LENGTH

Consider a rectangular gulf of inifinite length closed at the end $x = 0$. At $t = 0$, it is assumed that h and u are zero everywhere in the gulf. The wind and the atmospheric pressure are suddenly imposed at $t = 0$ and then maintained constant. Suppose that the water level in the gulf tends to a steady state in which the water level is given by

$$h = F(x) \text{ for } 0 \leq x < \infty \tag{4.30}$$

where F is a function such that the integral 4.32 below converges for all x. Using the Fourier integral representation:

$$F(x) = \int_0^\infty H(\chi)\cos(\chi x)\,dx \tag{4.31}$$

where

$$H(\chi) = \frac{2}{\pi}\int_0^\infty F(\chi)\cos(\chi x)\,dx \tag{4.32}$$

By superposition of an infinite number of infinitesimal motions of the type given by eq. 4.1, 4.20, and 4.28:

$$h = \int_0^{k/c} H(\chi)\cos(\chi x)\left\{1 - e^{-Kt}\left[\cosh(\sigma_1 t) + \frac{K}{\sigma_1}\sinh(\sigma_1 t)\right]\right\} d\chi + \int_{K/c}^\infty H(\chi)\cos(\chi x)\left\{1 - e^{-Kt}\left[\cos(\sigma t) + \frac{K}{\sigma}\sin(\sigma t)\right]\right\} d\chi \tag{4.33}$$

where σ and σ_1 are given by eq. 4.21 and 4.29. Thus, h is given by eq. 4.33 in the process of generating the steady state given by eq. 4.30.

Next, consider the decay of the storm surge, once the forcing functions are removed, say at $t = 0$. Then

$$h = e^{-Kt}\int_0^{K/c} H(\chi)\cos(\chi x)\left[\cosh(\sigma_1 t) + \frac{K}{\sigma_1}\sinh(\sigma_1 t)\right] d\chi + e^{-Kt}\int_{K/c}^\infty H(\chi)\cos(\chi x)\left[\cos(\sigma t) + \frac{K}{\sigma}\sin(\sigma t)\right] d\chi \tag{4.34}$$

For small values of bottom friction coefficient K, eq. 4.33 becomes

$$h = F(x) - \frac{1}{2}e^{-Kt}[F(x + ct) + F(x - ct)] + \frac{K}{c}\int_{x-ct}^{x+ct} F(\xi)\,d\xi \tag{4.35}$$

An approximate solution for the equation of motion and continuity of free motion in a channel is given by

$$h = e^{-Kt}\left[f'(x + ct) + \frac{K}{c}f(x + ct)\right] \tag{4.36}$$

and

$$\bar{u} = -\frac{c}{D}e^{-Kt}f'(x + ct) \tag{4.37}$$

where f' is the derivative of f provided that $K^2f(x + ct)/c^2f''(x + ct)$ may be neglected. Here, f'' is the second derivative of f with respect to x. Note that the sign of c in eq. 4.37 may be reversed.

In the stationary state, let the perturbation h be only within a distance a from the closed end of the gulf. Then

$$F(x) = 0 \text{ for } x \geq a$$

Then for $ct + x > a$ from eq. 4.35

$$h = F(x) - \frac{1}{2}e^{-Kt}\left[F(x - ct) + \frac{K}{c}\int_{x-ct}^{a} F(\xi)\,d\xi\right] \tag{4.38}$$

This represents damped waves progressing away from the closed end of the gulf. For $ct - x > a$, the solution is

$$h = F(x) - \frac{K}{c}e^{-Kt}\int_{0}^{a} F(\xi)\,d\xi \tag{4.39}$$

For $x = 0$, for all values of t:

$$h = F(0) - e^{-Kt}\left[F(ct) + \frac{K}{c}\int_{0}^{ct} F(\xi)\,d\xi\right] \tag{4.40}$$

To the same degree of approximation as in eq. 4.36 and 4. 37, other solutions of the equation of motion and continuity for free motion in a channel are

$$\begin{aligned} h &= e^{-Kt}f'(x + ct) \\ \bar{u} &= -\frac{c}{D}e^{-Kt}\left[f'(x + ct) - \frac{K}{c}f(x + ct)\right] \end{aligned} \tag{4.41}$$

$$h = e^{Kx/c}\left[f'(x + ct) + \frac{K}{c}f(x + ct)\right]$$

$$\bar{u} = -\frac{c}{D}e^{kx/c}f'(x + ct) \tag{4.42}$$

$$\begin{aligned} h &= e^{Kx/c}f'(x + ct) \\ \bar{u} &= -\frac{c}{K}e^{Kx/c}\left[f'(x + ct) - \frac{K}{c}f(x + ct)\right] \end{aligned} \tag{4.43}$$

The sign of c may be reversed in each case.

If eq. 4.43 is treated as a surge approaching the closed end of the gulf, then the reflected surge is given by

$$\begin{aligned} h &= e^{-Kx/c}f'(ct - x) \\ \bar{u} &= \frac{c}{D}e^{-Kx/c}\left[f'(ct - x) - \frac{K}{c}f(ct - x)\right] \end{aligned} \tag{4.44}$$

Adequacy of the Depth-Averaged Equations

Proudman (1954a) considered the question of adequacy of the depth-averaged equations for storm surge studies. Following Charnock and Crease (1957), one can write the depth-averaged equations as follows (compare these with the vertically integrated linearized storm surge equations for the transport field in section 2.1):

$$\frac{\partial U}{\partial t} - fV = -g\frac{\partial h}{\partial x} - \frac{1}{D}\frac{\partial P_a}{\partial x} + \frac{1}{\rho D}(\tau_{S_x} - \tau_{B_x}) \tag{4.45}$$

$$\frac{\partial V}{\partial t} + fU = -g\frac{\partial h}{\partial y} - \frac{1}{\rho D}\frac{\partial P_a}{\partial y} + \frac{1}{\rho D}(\tau_{S_y} - \tau_{B_y}) \tag{4.46}$$

$$\frac{\partial U}{\partial x} + \frac{\partial V}{\partial y} = -\frac{1}{D}\frac{\partial h}{\partial t} \tag{4.47}$$

Here, U and V are the depth-averaged velocities (not transport) in the x and y directions, f is the Coriolis parameter, h is the water level perturbation, τ_S is the wind stress, τ_B is the bottom stress, P_a is the atmospheric pressure, and D is the uniform water depth.

Suppose motion is considered in the $x-z$ plane only and variations in the y direction are ignored. The non-depth-averaged equation of motion in the x direction, after ignoring the earth's rotation, is

$$\frac{\partial U}{\partial t} = -g\frac{\partial h}{\partial x} - \frac{1}{\rho}\frac{\partial P_a}{\partial x} + \frac{\partial}{\partial z}\left(K\frac{\partial u}{\partial z}\right) \tag{4.48}$$

where u is the velocity in the x direction. The continuity equation is

$$\frac{\partial}{\partial x}\int_{-D}^{h} u\,dz + \frac{\partial h}{\partial t} = 0 \tag{4.49}$$

From eq. 4.48 and 4.49:

$$\left(\frac{\partial^2}{\partial x^2} - \frac{1}{gD}\frac{\partial^2}{\partial t^2}\right)h = -\frac{1}{\rho}\frac{\partial^2 P_a}{\partial x^2} + \frac{K}{D}\left(\frac{\partial u}{\partial z}\right)_{z=h} - \frac{K}{D}\left(\frac{\partial u}{\partial z}\right)_{z=-D} \tag{4.50}$$

This is essentially a nonaveraged equation because $u = u(x, z, t)$ must be prescribed from eq. 4.48 and 4.49 and the following boundary conditions:

$$u = 0 \text{ for } x = 0,\ x = l, \text{ and } z = -D \tag{4.51}$$

Also, one must prescribe the stress at the surface, i.e. the term $K/D(\partial u/\partial z)_{z=-h}$ in eq. 4.50 must be prescribed. The depth-averaged equations are given by eq. 4.45, 4.46, and 4.47. From the one-dimensional forms of these, the equation for h is

$$\left(\frac{\partial^2}{\partial x^2} - \frac{1}{gD}\frac{\partial^2}{\partial t^2}\right)h = -\frac{1}{\rho}\frac{\partial^2 P_a}{\partial x^2} + \frac{1}{\rho D}(\tau_x)_{z=h} - \frac{1}{\rho D}(\tau_x)_{z=-D} \tag{4.52}$$

For the boundary conditions:

$$\frac{K}{D}\left(\frac{\partial u}{\partial z}\right)_{z=h} = \frac{1}{\rho D}(\tau_x)_{z=h}$$

Thus, eq. 4.50 and 4.52 differ only in their bottom stress terms. Thus, insofar as the computation of h is concerned, the adequacy of using the depth-averaged equations depends entirely on the assumptions made regarding the form of the bottom stress. This

statement concerning the averaged and nonaveraged equations is quite general and holds even if K is not constant in eq. 4.48 and 4.49 and the motion occurs under different boundary conditions.

Influence of the Nature of the Forcing Function on the Storm Surge

Haurwitz (1951) considered the relevance of the time required to generate maximum storm surge amplitudes and he also included variable wind velocity in his studies of storm surges on a lake with application to Lake Okeechobee in Florida. Following Crease (1955) and Holland (1969, 1970), the influence of the rate of growth of the storm on the maximum amplitude of the surge, as well as on the time of occurrence of this maximum amplitude, will be considered. The vertically averaged (not integrated) equations of motion and continuity are given by eq. 4.45–4.47.

To keep the mathematical problem tractable, the simplest topography will be considered, namely an infinite rotating sea. Crease (1955) showed that in the nonrotating case, a forcing function acting over a semi-infinite plane will lead to an ever increasing surface elevation. However, rotation will lead to a dispersion of the waves and will produce a steady elevation after a long period of time. Again, for simplicity, the bottom stress and variations in the y direction are ignored. Then, eq. 4.45–4.47 become

$$\frac{\partial U}{\partial t} - fV = -g\frac{\partial h}{\partial x} - \frac{1}{\rho}\frac{\partial P_a}{\partial x} + \frac{1}{\rho D}\tau_{S_x} \tag{4.53}$$

$$\frac{\partial V}{\partial t} + fU = 0 \tag{4.54}$$

$$\frac{\partial U}{\partial x} = -\frac{1}{D}\frac{\partial h}{\partial t} \tag{4.55}$$

Define

$$E(x, t) = \frac{1}{\rho g}\left(\frac{\partial P_a}{\partial x} - \frac{\tau_{S_x}}{D}\right) \tag{4.56}$$

Eliminate U and V from eq. 4.53 and 4.54 and substitute in eq. 4.55 to give

$$\left[\frac{\partial^2}{\partial t^2} - \frac{1}{gD}\left(\frac{\partial^2}{\partial t^2} + f^2\right)\right]\frac{\partial h}{\partial t} = -\frac{\partial^2 E}{\partial x \partial t} \tag{4.57}$$

Integration of this with respect to t gives:

$$\left[\frac{\partial^2}{\partial t^2} - \frac{1}{gD}\left(\frac{\partial^2}{\partial t^2} + f^2\right)\right]h = -\frac{\partial E}{\partial x} \tag{4.58}$$

The constant of integration can be taken as zero if at some time h, $\partial^2 h/\partial t^2$, and $\partial E/\partial x$ are all zero. The initial conditions are $h = \partial h/\partial t = 0$ and $E =$ constant for $t \leq 0$.

Take the Laplace Transform of $h(x, t)$ and $E(x, t)$ to give

$$\bar{h}(x, S) = \int_0^\infty h(x, t) \exp(tS)\, dt \tag{4.59}$$

$$\bar{E}(x, S) = \int_0^\infty E(x, t) \exp(tS)\, dt \tag{4.60}$$

Making use of the initial conditions, the equation for $\bar{h}$ becomes

$$\left[\frac{\partial^2}{\partial x^2} - \frac{1}{gD}(S^2 + f^2)\right]\bar{h} = -\frac{\partial \bar{E}}{\partial x}$$

Define

$$\psi^2 \equiv \frac{(S^2 + f^2)}{gD} \quad \text{and} \quad L^2 \equiv \frac{\partial^2}{\partial x^2}$$

Then the above equation becomes

$$(4.61) \qquad (L^2 - \psi^2)\bar{h} = -\frac{\partial \bar{E}}{\partial x}$$

The particular integral becomes

$$\bar{h} = \frac{1}{2\psi}\left[\frac{1}{(L + \psi)} - \frac{1}{(L - \psi)}\right]\frac{\partial \bar{E}}{\partial x}$$

or

$$(4.62) \qquad \bar{h} = \frac{1}{2\psi}\left[\exp(-\psi x)\int_{a_0}^{x} \exp(\psi x_0)\frac{\partial \bar{E}}{\partial x_0}(x_0, S_0)\,dx_0 - \exp\int_{b_0}^{x} \exp(-\psi x_0)\frac{\partial \bar{E}}{\partial x_0}(x_0, S)\,dx_0\right.$$

The constants a_0 and b_0 must be evaluated simultaneously with the constants A and B, which are determined by the complimentary function

$$(4.63) \qquad \bar{h} = A \exp(\psi x) + B \exp(-\psi x)$$

Thus, the total solution for $\bar{h}$ is

$$(4.64) \qquad \bar{h} = A \exp(\psi x) + B \exp(-\psi x) + \frac{1}{2\psi}\left[\exp(-\psi x)\int_{a_0}^{x} \exp(\psi x_0)\frac{\partial \bar{E}}{\partial x_0}\mathrm{d}x_0 - \exp\int_{b_0}^{x} \exp(-\psi x_0)\frac{\partial \bar{E}}{\partial x_0}\,dx_0\right]$$

The choice $a_0 = -\infty$ and $b_0 = \infty$ will ensure the convergence of the two integrals in eq. 4.64. The condition $h = 0$ at $t = 0$ gives $\bar{h} = 0$ for $S = \infty$, i.e. $\bar{h} = 0$ for $\psi = \infty$. The condition that $\bar{h}$ must be finite for both positive and negative values of x for large $|x|$ leads to $A = B = 0$. Define

$$(4.65) \qquad F(S) \equiv \frac{\exp(-Q\sqrt{S^2 + R^2})}{\sqrt{S^2 + R^2}}$$

whose inverse Laplace Transform is

$$(4.66) \qquad F(t) = J_0(R\sqrt{t^2 - Q^2})H(t - Q)$$

where J_0 is the Bessel function of order zero and H is the Heaveside step function. Making use of the convolution rule and noting that $\partial E/\partial x_0$ is the value of $\partial E/\partial x$ at x_0 and t_0:

$$(4.67)\quad h = \frac{\sqrt{gD}}{2}\int_{-\infty}^{x} dx_0 \int_0^t J_0\left\{f\left[(t-t_0)^2 - \frac{(x-x_0)^2}{gD}\right]^{1/2}\right\} H\left[(t-t_0) - \frac{(x-x_0)}{\sqrt{gD}}\right]\frac{\partial E}{\partial x_0}\,dt_0 - \frac{\sqrt{gD}}{2}\int_{\infty}^{x} dx_0 \int_0^t J_0\left\{f\left[(t-t_0)^2 - \frac{(x-x_0)^2}{gD}\right]^{1/2}\right\} \times H\left[(t-t_0) - \frac{(x_0-x)}{\sqrt{gD}}\right]\frac{\partial E}{\partial x_0}\,dt_0$$

A simple adjustment of the limits of integration and the step functions gives

$$(4.68)\quad h = \frac{\sqrt{gD}}{2}\int_0^t dt_0 \int_{-\infty}^{\infty} \frac{\partial E}{\partial x_0} J_0\left\{f\left[(t-t_0)^2 - \frac{(x-x_0)^2}{gD}\right]^{1/2}\right\} \times H\left[(t-t_0) - \frac{|x-x_0|}{\sqrt{gD}}\right] dx_0$$

From eq. 4.53–4.55, equations for U and V can be written:

$$(4.69)\quad \left[\frac{\partial^2}{\partial t^2} - \frac{1}{gD}\left(\frac{\partial^2}{\partial t^2} + f^2\right)\right]U = \frac{1}{D}\frac{\partial E}{\partial t}$$

$$(4.70)\quad \left[\frac{\partial^2}{\partial x^2} - \frac{1}{gD}\left(\frac{\partial^2}{\partial t^2} + f^2\right)\right]V = -\frac{f}{D}E$$

Using the same procedure as above, the solutions for U and V can be written as

$$(4.71)\quad U = -\frac{1}{2}\sqrt{\frac{g}{D}}\int_0^t dt_0 \int_{-\infty}^{\infty} \frac{\partial E}{\partial t_0} J_0\left\{f\left[(t-t_0)^2 - \frac{(x-x_0)^2}{gD}\right]^{1/2}\right\} \times H\left[(t-t_0) - \frac{|x-x_0|}{\sqrt{gD}}\right] dx_0$$

and

$$(4.72)\quad V = \frac{f}{2}\sqrt{\frac{g}{D}}\int_0^t dt_0 \int_{-\infty}^{\infty} E J_0\left\{f\left[(t-t_0)^2 - \frac{(x-x_0)^2}{gD}\right]^{1/2}\right\} \times H\left[(t-t_0) - \frac{|x-x_0|}{\sqrt{gD}}\right] dx_0$$

To understand the nature of these solutions, following Crease (1955), assume the following form for the generating function:

$$(4.73)\quad E(x, t) = A\,H(t)\delta(-x)$$

Using this in eq. 4.68 and integrating with respect to x:

$$(4.74)\quad h = \frac{A}{2}\sqrt{gD}\int_0^{t_0} H(t_0)\,J_0\left\{f\left[(t-t_0)^2 - \frac{x^2}{gD}\right]^{1/2}\right\} H\left[(t-t_0) - \frac{|x|}{\sqrt{gD}}\right] dt_0$$

Define

$$(4.75)\quad \begin{aligned} t - t_0 &\equiv \tau \\ f\tau &\equiv \beta \\ ft &\equiv b \\ \frac{fx}{\sqrt{gD}} &\equiv a \end{aligned}$$

The nondimensional form of eq. 4.74 after incorporating the step function into the integration limit is

$$(4.76) \quad \frac{2f}{A\sqrt{gD}}h = \int_{|a|}^{b} J_0[(\beta^2 - a^2)^{1/2}]\, d\beta$$

This equation is valid for all values of a and is symmetric about $a = 0$. The upper limit of integration could be replaced by $\max|a|$, which is the maximum distance a disturbance could travel in time t. Here, the maximum group velocity is $\sqrt{gD}$.

From eq. 4.71 and 4.72:

$$(4.77) \quad U = \frac{Ag}{2f}\int_{a}^{\infty} J_0[(b^2 - \alpha^2)^{1/2}]H(b - |\alpha|)\, d\alpha$$

and

$$(4.78) \quad V = -\frac{Ag}{2f}\int_{0}^{b} d\beta \int_{a}^{\infty} J_0[(\beta^2 - \alpha^2)^{1/2}]H(\beta - |\alpha|)\, d\alpha$$

For $a > 0$, eq. 4.77 becomes

$$U = \frac{Ag}{2f}H(b - a)\int_{a}^{b} J_0[(b^2 - \alpha^2)^{1/2}]\, d\alpha$$

On splitting this integral into two parts and simplifying:

$$(4.79) \quad U = \frac{Ag}{2f}H(b - a)\left\{\sin b - \int_{0}^{a} J_0[(b^2 - \alpha^2)^{1/2}]\, d\alpha\right\}$$

Thus, finally for $a > 0$, U is given by eq. 4.79 and V is given by

$$(4.80) \quad V = -\frac{Ag}{2f}\left\{1 - \cos b - \int_{0}^{a} d\alpha \int_{\alpha}^{b} J_0[(\beta^2 - \alpha^2)^{1/2}]\, d\beta\, H(b - a)\right\}$$

For $a < 0$, two situations arise: $b > |a|$ and $b < |a|$. In the former case:

$$(4.81) \quad U = \frac{Ag}{2f}\left\{2 \sin b - H(b - |a|)\int_{-b}^{a} J_0[(b^2 - \alpha^2)^{1/2}]\, d\alpha\right\}$$

and

$$(4.82) \quad V = -\frac{Ag}{2f}\left\{1 - \cos b + \int_{0}^{|\alpha|} d\alpha \int_{\alpha}^{b} J_0[(\beta^2 - \alpha^2)]\, d\beta\right\}$$

For the second case:

$$(4.83) \quad U = \frac{Ag}{2f}2 \sin b = \frac{Ag}{f}\sin b$$

$$(4.84) \quad V = -\frac{2Ag}{2f}(1 - \cos b) = -\frac{Ag}{f}(1 - \cos b)$$

Note that the time taken for a surge to travel a distance x with the maximum group velocity is given by $b = a$. This is the minimum time the surge can take to travel a distance x.

At $t = 0$, assume that a force is impulsively applied over one-half of an infinite ocean (i.e. $-\infty < x < 0$) in the x direction. As a result of this, some motion is created in the same direction in the region over which the force is acting. Because of this motion, a

transverse velocity field develops, which balances the effects due to rotation.

Note that the generating force has a discontinuity at $x = 0$, which propagates with a maximum velocity of $\sqrt{gD}$. Before this discontinuity can reach a point (i.e. $b < |a|$) there can be no motion at this point if this point lies outside the generating area (i.e. $a > 0$). If it lies inside the generating area (i.e. $a < 0$), then, inertial motion (horizontal motion without accompanying water level changes) occurs. Hence, in either case there is no change in the water level until the discontinuity at $x = 0$ reaches this point. When this happens, $b \geq |a|$ and there will be a positive h.

When the earth's rotation is not included, the above system should lead to an infinite surface elevation, and all wavelengths travel with velocity $\sqrt{gD}$ (i.e. no dispersion). On the other hand, in the rotating case, dispersion allows a steady-state elevation to be reached as $t \rightarrow \infty$ because the pressure gradient force from the steady slope is balanced by the transverse velocity.

Until now, it has been assumed that the generating force is impulsively applied. However, in reality, the generating force takes a finite time to build up to its maximum value. To allow for this finite growth period, the generating function given by eq. 4.73 will be rewritten as follows:

$$E = AH(-x)H(t) \tanh(\epsilon t) \tag{4.85}$$

Using the same procedure as above and defining

$$\epsilon_0 \equiv \frac{\epsilon}{f} \tag{4.86}$$

the solution for the water level becomes

$$h = \frac{A\sqrt{gD}}{2f} \int_{|a|}^{b} \tanh[\epsilon_0(b - \beta)] J_0[(\beta^2 - a^2)^{1/2}] \, d\beta \tag{4.87}$$

Comparison of eq. 4.76 and 4.87 shows that the only difference is the factor $\tanh[\epsilon_0(b - \beta)]$ in the latter case.

For practical convenience, Holland (1969) defined the growth period as the time interval during which the generating force achieves 90% of its maximum value. The surge (in dimensionless form) against time (also in dimensionless form) for two different growth periods, i.e. 0.5 and 10 h, is shown in Fig. 4.1. It can be seen that (1) the maximum amplitude of the surge decreases as the growth period increases and (2) as the growth period increases, the maximum surge occurs at increasingly later times. The first result may partly explain why intensive and small-scale pressure systems such as squall lines in which the growth period is small can generate large-amplitude surges. However, in water bodies where tides are significant, the maximum water level deviation (tide plus surge) need not be the greatest for the shortest growth period. This is due to the second result above, i.e. as the growth period changes, the time of occurrence of the maximum surge also changes. It may just happen that the surge due to a moderate growth period may occur at the same time as the high tide, in which case the total water level deviation may be greater.

Holland also considered a finite generating width. He also referred to Proudman's (1929) work in which Proudman showed that there will be resonance if the disturbance creating the surge is not stationary but moves with velocity $\sqrt{gD}$. For example, Crease (1955) took the forcing function as

$$E(x, t) = -AH(t)H(V_0 t - x) \tag{4.88}$$

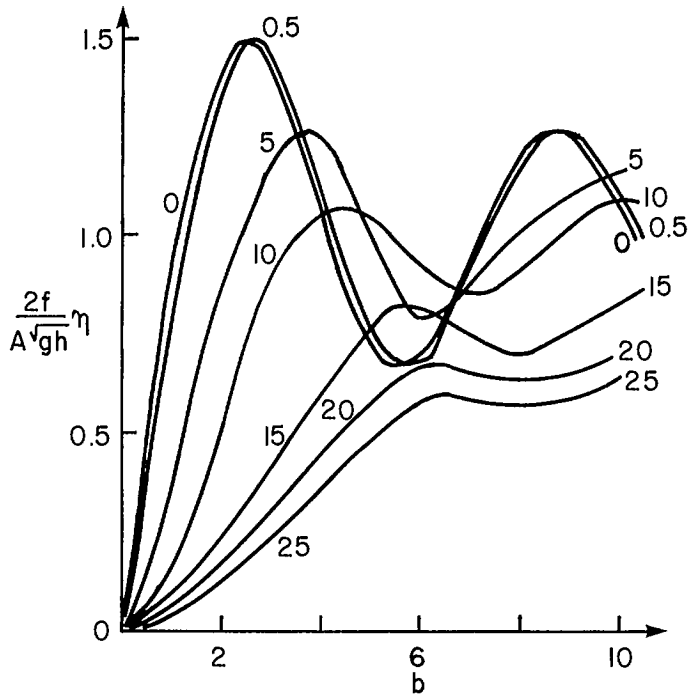

FIG. 4.1. Dimensionless storm surge (ordinate) versus dimensionless time (abcissa) for several growth rates of the storm.

This force is applied beginning at $t = 0$ over the region $-\infty < x < V_0 t$. This means the discontinuity in the force at the edge of the generating area is moving with velocity V_0.

The elevation at the leading edge (i.e. at $x = \sqrt{gD}t$ or $a = b$) is

$$\frac{2f}{A\sqrt{gD}}h = \frac{1}{2}\lim_{b\to a}\left(\frac{b+a}{b-a}\right)^{1/2} J_1(b^2 - a^2)^{1/2} = b \tag{4.89}$$

Hence, h grows indefinitely at the leading edge, and this leads to a discontinuity. The surface slope at the leading edge is given by

$$\frac{2f}{A\sqrt{gD}}\frac{\partial h}{\partial a} = \frac{1}{2} - \frac{a^2}{4}$$

In Chapter 5, resonance effects due to traveling atmospheric disturbances will be discussed in detail.

STORM SURGES ON A CONTINENTAL SHELF

Lauwerier (1957a, 1957b) calculated the storm surges on a continental shelf using analytic models. He included the Coriolis force as well as bottom friction and considered several time-dependent but uniform wind stress fields. Kajiura (1959) also studied similar problems. Ichiye (1962) studied storm surges due to a model hurricane which moves onto a continental shelf of uniform depth and uniform width. Several authors studied ana-

lytically the water level changes due to wind fields in infinite and semi-infinite water bodies (Lauwerier 1955; Crease 1956; Takegami 1936; Miyazaki 1957, 1956; Kajiura 1956; Ichiye 1949; Nomitsu and Takegami 1934; Nomitsu 1934, 1935; Goldsborough 1952; Jeffreys 1923; Hidaka 1953).

In the discussion below, a simple analytical study of storm surges on a continental shelf, following Heaps (1965), will be presented. A shelf of uniform depth and uniform width, terminating in a long straight coast on one side and bounded by an infinitely deep ocean on the other side, will be considered. The origin of a Cartesian coordinate system (x, y, z) is taken at the undisturbed level of the water surface with x pointing towards the ocean and z pointing downward. Let l and D be the length of the shelf and the depth of water on the shelf, respectively.

In the vertically averaged eq. 4.45−4.47, using eq. 4.14 for the bottom stress and ignoring y dependence, one can rewrite the equations of motion and continuity. Heaps used this set of equations to study the following cases: (1) the response of the water level on the continental shelf to a prescribed time variation in the water level at the oceanic edge, i.e. a surge generated in the ocean and propagating onto the shelf, (2) surges generated on the shelf by wind, (3) surges due to a stationary wind field impulsively applied over part of the shelf, and (4) surges due to a traveling wind field.

Essentially the same method of solution is used for these four cases. Here, only the first case will be considered. For this case

$$\tau_{S_x} = \tau_{S_y} = 0 \text{ and } \frac{\partial P_a}{\partial x} = 0 \tag{4.90}$$

and

$$h = F(t) \text{ at } x = l$$

(i.e. prescribed). Initially

$$u = v = h = 0 \text{ at } t = 0 \tag{4.91}$$

Then, the equations of motion and continuity reduce to the following after taking the Laplace Transform:

$$(S + 2K)\bar{u} - f\bar{v} = -g\frac{d\bar{h}}{dx} \tag{4.92}$$

$$(S + 2K)\bar{v} + f\bar{u} = 0 \tag{4.93}$$

$$\frac{d\bar{u}}{dx} + \frac{S}{D}\bar{h} = 0 \tag{4.94}$$

where the upper bar denotes Laplace Transform defined by

$$\bar{R}(x, S) = \int_0^\infty e^{-St} R(x, t)\, dt \tag{4.95}$$

where $\bar{R}$ is the Laplace Transform of R, and S is a dummy variable.

Eliminating $\bar{v}$ and $\bar{h}$ from eq. 4.92−4.94 gives

$$\frac{d^2\bar{u}}{dx^2} = \alpha^2\bar{u} \tag{4.96}$$

where

$$(4.97) \quad \alpha^2 \equiv \frac{S[(S + 2K)^2 + f^2]}{(S + 2K)gD}$$

Solving eq. 4.96 for $\bar{u}$ and then using eq. 4.92–4.94 to solve for $\bar{v}$ and $\bar{h}$:

$$(4.98) \quad \bar{u} = A \cosh(\alpha x) + B \sinh(\alpha x)$$

$$(4.99) \quad \bar{v} = -\left\{\frac{f}{(S + 2K)}[A \cosh(\alpha x) + B \sinh(\alpha x)]\right\}$$

$$(4.100) \quad \bar{h} = -\left(\frac{\alpha D}{S}\right)[A \sinh(\alpha x) + B \cosh(\alpha x)]$$

The condition of zero normal flow at the coast is given by

$$(4.101) \quad u = 0 \text{ and } \bar{u} = 0 \text{ at } x = 0$$

The condition of prescribed h at the ocean edge is

$$(4.102) \quad \bar{h} = \bar{F}(S) \text{ at } x = l$$

From eq. 4.98 to 4.102 the constants A and B can be determined and the solutions become

$$(4.103) \quad \bar{h} = \bar{F}(S)\frac{\cosh(\alpha x)}{\cosh(\alpha l)}$$

$$(4.104) \quad \bar{u} = -\frac{S\bar{F}(S)}{D\alpha}\frac{\sinh(\alpha x)}{\cosh(\alpha l)}$$

$$(4.105) \quad \bar{v} = \frac{FS\bar{F}(S)}{D\alpha(S + 2K)}\frac{\sinh(\alpha x)}{\cosh(\alpha l)}$$

Inverting the Laplace Transforms:

$$(4.106) \quad h = \frac{1}{2\pi i}\int_{\gamma_1 - i\infty}^{\gamma_1 + i\infty} \bar{F}(S)\frac{\cosh(\alpha x)}{\cosh(\alpha l)} e^{St}\, dS$$

$$(4.107) \quad u = -\frac{1}{2\pi i}\int_{\gamma_1 - i\infty}^{\gamma_1 + i\infty} \frac{S\bar{F}(S)}{D\alpha}\frac{\sinh(\alpha x)}{\cosh(\alpha l)} e^{St}\, dS$$

$$(4.108) \quad v = \frac{1}{2\pi i}\int_{\gamma_1 - i\infty}^{\gamma_1 + i\infty} \frac{FS\bar{F}(S)}{D\alpha(S + 2K)}\frac{\sinh(\alpha x)}{\cosh(\alpha l)} e^{St}\, dS$$

Note that in each of the integrals, γ_1 is real and positive and is greater than the real parts of all the singularities of the integrand.

Flather (1976b) extended this work and considered an idealized shelf connected to an ocean of uniform depth and width. McIntyre (1979) used the models of Heaps (1965) and Flather (1976b) to study storm surges on the west coast of the United Kingdom. Simons (1980) reviewed some of the analytical solution studies on storm surges. Røed (1979) developed an analytical model to include the effects of stratification.

Using analytical techniques, Miyazaki (1952) studied the storm surges due to traveling atmospheric disturbances. Galt (1971) studied storm surges on a continental shelf assuming the water column to be homogeneous in density. Geisler (1970) included stratification and studied the linear response of a two-layer deep ocean to a moving

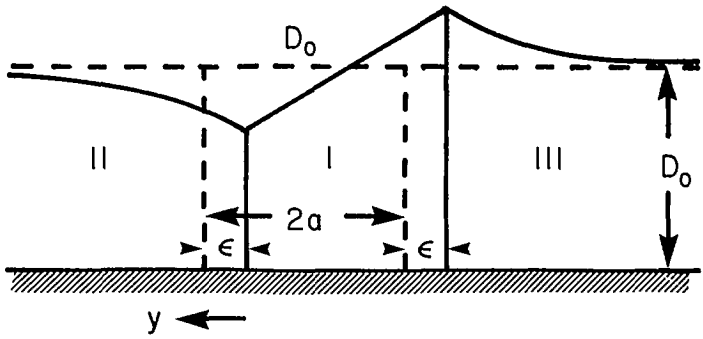

FIG. 4.2. Schematic representation of the adjustment process for the homogeneous case. (Rossby 1937)

hurricane. In his model the forcing function is a localized radially symmetric pattern of positive wind stress curl and negative pressure anomaly. In the steady state, there is an internal wake in the lee of the storm when the speed of movement of the storm is greater than the speed of the baroclinic long waves. The duration of the wind stress determines the amplitude of the wake. Since the scale of the hurricane is much larger than the baroclinic radius of deformation, the angle of the wedge-shaped wake is small. After the dispersion of the wake, a geostrophically balanced baroclinic ridge remains along the track of the hurricane.

THE ROSSBY ADJUSTMENT PROBLEM AND THE ULTRASHALLOW WATER STORM SURGES

The classical adjustment problem first formulated by Rossby (1937, 1938) will be briefly discussed followed by its relevance to the so-called ultrashallow water storm surges. Rossby examined the mechanism by which initially unbalanced fields of mass and momentum adjust to a final state of geostrophic balance. At present, this problem is referred to as the Rossby (geostrophic) adjustment problem. This problem will be summarized following Blumen (1972).

Rossby (1938) considered a homogeneous ocean of uniform depth (Fig. 4.2) and of inifinite lateral extent. At $t = 0$, a certain amount of momentum is imparted to the fluid in a region of width $2a$. Rossby showed that in the steady state there will be a slope of the free surface (rising to the right in the Northern Hemisphere) which is balanced by the Coriolis force. There will be a geostrophic current in the strip $2a$ (in Fig. 4.2, the current is directed into the paper), and outside this strip on either side there will be counter currents. Also note that by the time the adjustment is completed, the current system has shifted to the right side by an amount ϵ. In the final state, the balance of forces is given by

$$(4.109) \quad f_0 U_g = -g \frac{dD}{dy}$$

where f_0 is the Coriolis parameter, assumed to be uniform, U_g is the geostrophic velocity (positive into the paper in Fig. 4.2), g is gravity, D is the variable depth, and y is the coordinate pointing towards the north.

Rossby also showed that the sum of the kinetic and potential energies in the final state is less than the kinetic energy of the initial state. The difference in energy goes into

inertia–gravity waves which propagate outside from the strip of width $2a$. Cahn (1945) studied the transient aspects of the adjustment problem and considered the linearized version of the initial value problem, and based on these results, he offered an explanation for the nonlinear process of adjustment towards a geostrophic state. Note that the inclusion of the nonlinear terms is essential for obtaining the shift mentioned above.

Mihaljan (1963) gave an exact solution to the adjustment problem. Some notable later works on this and related topics are those of Bolin (1953), Charney (1955), Veronis (1956), Veronis and Stommel (1956), Blumen (1967), Geisler and Dickinson (1972), Kibel (1955), Matsumoto (1961), Øakland (1970), and Røed and O'Brien (1981). Obukhov (1949) distinguished between the process of adjustment to a geostrophic state from the evolution of the geostrophic flow pattern; these two time scales, i.e. a shorter adaptation time and a longer evolution time, have great significance in storm surges in very shallow water (ultrashallow water) as will be shown later.

Consider a Cartesian coordinate system (x, y) pointing towards east and north, respectively. The equations for horizontal motion and continuity can be written as follows:

$$\frac{\partial u^*}{\partial t} + u^* \frac{\partial u^*}{\partial x} + v^* \frac{\partial u^*}{\partial y} - fv^* = -\frac{\partial}{\partial x}(gh^*) \tag{4.110}$$

$$\frac{\partial v^*}{\partial t} + u^* \frac{\partial v^*}{\partial x} + v^* \frac{\partial v^*}{\partial y} + fu^* = -\frac{\partial}{\partial y}(gh^*) \tag{4.111}$$

$$\frac{\partial h^*}{\partial t} + \frac{\partial}{\partial x}(u^*h^*) + \frac{\partial}{\partial y}(v^*h^*) = 0 \tag{4.112}$$

Here, u^* and v^* are the velocities in the x and y directions and an asterisk denotes a dimensional quantity (note that the asterisk has not been used for x, y, f, g, and t, although they are dimensional). Also

$$h^* = D_0\left(1 + \frac{h}{D_0}\right) \tag{4.113}$$

where h is the deviation of the free surface from its equilibrium position and D_0 is the undisturbed uniform depth. The hydrostatic approximation has been made and the Coriolis parameter, f, is treated as uniform (f_0).

Obukhov (1949) suggested that the characteristic time scale, T, for adjustment is $T \sim f_0^{-1}$ whereas the characteristic time scale for evolution (which is a slower process) is $\tau \sim LU_0^{-1}$ where L is a characteristic horizontal scale and U_0 is a characteristic horizontal velocity. The ratio of these two time scales is the Rossby number, R_0:

$$R_0 = \frac{T}{\tau} = \frac{U_0}{f_0 L} \tag{4.114}$$

Ordinarily, the Rossby number is interpreted as the ratio of the acceleration term to the Coriolis term.

Next, the following dimensionless variables are introduced:

$$\begin{aligned} u' &\equiv \frac{u^*}{U_0}, \qquad x' \equiv \frac{x}{L}, \qquad t' \equiv tf_0 \\ v' &\equiv \frac{v^*}{U_0}, \qquad y' \equiv \frac{y}{L}, \qquad \frac{gh}{gD_0} = \left(\frac{f_0 U_0 L)}{gD_0}\right)p' = \left(\frac{L}{\lambda}\right)^2 R_0 p' \end{aligned} \tag{4.115}$$

where λ is the Rossby radius of deformation, given by

$$\lambda \equiv \frac{\sqrt{gD_0}}{f_0} \tag{4.116}$$

Equation 4.110–4.112 become, after using eq. 4.115 and 4.116 and dropping the primes for convenience:

$$\frac{\partial u}{\partial t} + R_0\left(u\frac{\partial u}{\partial x} + v\frac{\partial u}{\partial y}\right) - v = -\frac{\partial p}{\partial x} \tag{4.117}$$

$$\frac{\partial v}{\partial t} + R_0\left(u\frac{\partial v}{\partial x} + v\frac{\partial v}{\partial y}\right) + u = -\frac{\partial p}{\partial y} \tag{4.118}$$

$$\frac{\partial p}{\partial t} + R_0\left(u\frac{\partial p}{\partial x} + v\frac{\partial p}{\partial y}\right) + \left(\frac{L}{\lambda}\right)^2\left[1 + \left(\frac{L}{\lambda}\right)^2 R_0 p\right]\left(\frac{\partial u}{\partial x} + \frac{\partial v}{\partial y}\right) = 0 \tag{4.119}$$

where p is defined in eq. 4.115.

Following the multiple time scale technique developed by Cole (1968), define a "fast time"

$$T = t[1 + O(R_0^2)] \tag{4.120}$$

and a "slow time"

$$\tau = R_0 t \tag{4.121}$$

Thus

$$\frac{\partial}{\partial t} = \frac{\partial}{\partial T} + R_0\frac{\partial}{\partial \tau} + O(R_0^2) \tag{4.122}$$

Assume the following expansions:

$$\begin{aligned} u &= \sum_{n=0}^{\infty} R_0^n u_n \\ v &= \sum_{n=0}^{\infty} R_0^n v_n \\ p &= \sum_{n=0}^{\infty} R_0^n p_n \end{aligned} \tag{4.123}$$

Substituting eq. 4.121 and 4.122 into eq. 4.116–4.118 gives two sets of equations. Zero order:

$$\begin{aligned} &\frac{\partial u}{\partial T} - v_0 + \frac{\partial p_0}{\partial x} = 0 \\ &\frac{\partial v_0}{\partial T} + u_0 + \frac{\partial p_0}{\partial y} = 0 \\ &\frac{\partial p_0}{\partial T} + \left(\frac{L}{\lambda}\right)^{-2}\left(\frac{\partial u_0}{\partial x} + \frac{\partial v_0}{\partial y}\right) = 0 \end{aligned} \tag{4.124}$$

First order:

$$\frac{\partial u_1}{\partial T} - v_1 + \frac{\partial p_1}{\partial x} = -\left[\frac{\partial u_0}{\partial \tau} + u_0\frac{\partial u_0}{\partial x} + v_0\frac{\partial u_0}{\partial y}\right]$$

$$\frac{\partial v_1}{\partial T} + u_1 + \frac{\partial p_1}{\partial y} = -\left[\frac{\partial v_0}{\partial \tau} + u_0\frac{\partial v_0}{\partial x} + v_0\frac{\partial v_0}{\partial y}\right] \tag{4.125}$$

$$\frac{\partial p_1}{\partial T} + \left(\frac{L}{\lambda}\right)^{-2}\left(\frac{\partial u_1}{\partial x} + \frac{\partial v_1}{\partial y}\right) = -\left[\frac{\partial p_0}{\partial \tau} + u_0\frac{\partial p_0}{\partial x} + v_0\frac{\partial p_0}{\partial y} + p_0\left(\frac{\partial u_0}{\partial x} + \frac{\partial v_0}{\partial y}\right)\right]$$

From the first two equations of 4.124, eliminate p_0 by cross-differentiation and use in the third equation to give

$$\frac{\partial}{\partial T}\left[\frac{\partial v_0}{\partial x} - \frac{\partial u_0}{\partial y} - \left(\frac{L}{\lambda}\right)^2 p_0\right] = 0 \tag{4.126}$$

The statement of the conservation of potential vorticity is

$$\frac{d}{dt}\left[\frac{\left(\frac{\partial v^*}{\partial x} - \frac{\partial u^*}{\partial y} + f\right)}{h^*}\right] = 0 \tag{4.127}$$

However, the expression

$$\Omega_0 \equiv \frac{\partial v_0}{\partial x} - \frac{\partial u_0}{\partial y} - \left(\frac{L}{\lambda}\right)^2 p_0 \tag{4.128}$$

appearing in eq. 4.126 is not necessarily independent of time, because integration gives

$$\Omega_0 = \Omega_0(x, y, \tau) \tag{4.129}$$

Any solution of the zero-order equations in 4.124 that satisfies $\partial/\partial T = 0$ is the nondivergent geostrophic solution

$$V = K \times \nabla P \tag{4.130}$$

where K is the unit vector in the vertical direction pointing upward. Then the zero-order variables can be written as

$$\begin{aligned} u_0 &= U(x, y, \tau) + u(x, y, T, \tau) \\ v_0 &= V(x, y, \tau) + v(x, y, T, \tau) \\ p_0 &= P(x, y, \tau) + p(x, y, T, \tau) \\ \Omega_0 &= \Omega(x, y, \tau) + \omega(x, y, T, \tau) \end{aligned} \tag{4.131}$$

where u, v, p, and ω are the nongeostrophic (ageostrophic) solutions.

From eq. 4.129–4.131:

$$\left[\Delta - \left(\frac{L}{\lambda}\right)^2\right]P = \Omega(x, y, \tau) \tag{4.132}$$

and

$$\omega \equiv \frac{\partial v}{\partial x} - \frac{\partial u}{\partial y} - \left(\frac{L}{\lambda}\right)^2 p = 0 \tag{4.133}$$

where

$$\Delta \equiv \frac{\partial^2}{\partial x^2} + \frac{\partial^2}{\partial y^2}$$

From the first-order equations in 4.125:

$$(4.134) \quad \frac{\partial \Omega_1}{\partial t} = -\left[\frac{\partial \Omega_0}{\partial \tau} + u_0 \frac{\partial \Omega_0}{\partial x} + v_0 \frac{\partial \Omega_0}{\partial y} + \left(\frac{\partial u_0}{\partial x} + \frac{\partial v_0}{\partial y}\right)\Omega_0\right]$$

where

$$(4.135) \quad \Omega_1 \equiv \frac{\partial v_1}{\partial x} - \frac{\partial u_1}{\partial y} - \left(\frac{L}{\lambda}\right)^2 p_1$$

From eq. 4.130–4.134:

$$(4.136) \quad \frac{\partial \Omega_1}{\partial T} + \frac{\partial}{\partial x}(u\Omega) + \frac{\partial}{\partial y}(v\Omega) = -\left[\frac{\partial \Omega}{\partial \tau} + U\frac{\partial \Omega}{\partial x} + V\frac{\partial \Omega}{\partial y}\right]$$

Note that one can determine the nongeostrophic solutions from the zero-order system.

Obukhov (1949) gave the following general solutions for u:

$$(4.137) \quad u = Aq_A(x, y, T) + Bq_B(x, y, T)$$

where q_A and q_B are independent solutions of the zero-order equations and A and B can be arbitrary functions of τ. One can write a similar solution for v. From eq. 4.132, 4.136, and 4.137:

$$(4.138) \quad \frac{\partial}{\partial T}[\Omega_1 + \text{function}(\tau)\ \text{function}(x, y, T)] = -\left[\frac{\partial \Omega}{\partial \tau} + U\frac{\partial \Omega}{\partial x} + V\frac{\partial \Omega}{\partial y}\right]$$

The secular terms on the right side of eq. 4.138 are functions of τ only. Hence, for the expansion 4.123 to be uniformly valid to the slow time τ, one must set

$$(4.139) \quad \frac{\partial \Omega}{\partial \tau} + U\frac{\partial \Omega}{\partial x} + V\frac{\partial \Omega}{\partial y} = 0$$

Hence, the total solution of the zero-order system consists of a slowly varying geostrophic part, determined independently from eq. 4.137, and a nongeostrophic wave solution 4.135, which is modulated by a slowly varying amplitude whose time scale is the same as that of the geostrophic solution.

Tseng-Hao and Shih-Zao (1975) applied the concepts of geostrophic adjustment and geostrophic evolution to storm surges. They divided the theory of storm surges into two parts: (a) ordinary shallow-water theory of storm surges and (b) ultrashallow-water theory of storm surges. For an ultrashallow sea such as the Pohai Sea, the adaptation time is of the order of several days. According to these authors, for the ordinary shallow-water storm surges the time derivative terms are as important as the other terms and one cannot conveniently make any distinction between the adaptation time and the evolution time. For the ultrashallow-water surges, the time derivative terms are at least an order of magnitude smaller than the other terms. Hence, there is a quasibalance among the rest of the terms and if this state is disturbed by atmospheric forcing, it will be restored vigorously.

The Normal Mode Approach

The work of Haurwitz (1951) was referred to earlier in which he mentioned that the duration of the development of the storm surge must depend on the sieche type motion

(normal modes). In Chapter 5 the normal mode problems will be studied in some detail. Here, following Schwab (1975), a method of calculating storm surges using the normal mode approach will be discussed.

In the equations of motion, if all the inhomogeneous terms are omitted, the solutions of the homogeneous system are the normal modes, and there is, in principle, an infinite spectrum of these modes. However, when the system is forced (such as happens in the storm surge case when the forcing is from the atmosphere), the particular solutions of the inhomogeneous equations can be determined by an expansion in terms of the normal modes with time-dependent coefficients. Reid (1958) used this procedure to calculate the edge waves on the shelf. The advantage of using the normal mode approach is that the expansion automatically satisfies the space dependence. Each expansion coefficient satisfies a first-order inhomogeneous ordinary differential equation in time and these equations can be solved by numerical techniques. Since this is an uncoupled system, no expensive matrix inversion techniques are required. Although the normal mode approach is, in principle, very elegant and efficient, this approach is rarely used in storm surge studies, probably because the method has not lived up to its expectations, especially when applied to real water bodies with irregular coastlines, depth variations, and openings. Rao (1974) used this technique for certain idealized situations.

Following Schwab (1975), the equations for horizontal motion can be written in the following vector form:

$$\frac{\partial M}{\partial t} - f[M] = -gD\nabla h + \tau \tag{4.140}$$

where M is the horizontal transport vector and is defined as

$$M \equiv \int_{-D}^{h} V\, dz$$

where V is the horizontal velocity vector, ∇ is the horizontal gradient operator, $\tau(x, y, t)$ is the prescribed forcing function, and $[\,]$ is an operator that denotes rotation of a vector 90° clockwise in the horizontal plane (the other variables have been previously defined). The continuity equation is

$$\frac{\partial h}{\partial t} + \nabla M = 0 \tag{4.141}$$

The boundary condition is

$$M \cdot n = DV \cdot n = 0 \tag{4.142}$$

where n is a vector normal to the shoreline. The normal modes represent the solutions of eq. 4.140–4.142 when $\tau = 0$.

Following Rao and Schwab (1974), the transport vector M will be expressed as the sum of a nondivergent part and an irrotational part:

$$M = M^{\phi} + M^{\psi} \tag{4.143}$$

where

$$\begin{aligned} M^{\phi} &\equiv D\nabla\phi \\ M^{\psi} &\equiv -[\nabla\psi] \end{aligned} \tag{4.144}$$

Here, ϕ and ψ represent, respectively, the velocity potential and the stream function for

the transport field. We have the following properties:

$$\begin{aligned} &\nabla\cdot[D^{-1}M^{\phi}] = 0 \\ &\nabla\cdot M^{\psi} = 0 \end{aligned} \tag{4.145}$$

Equation 4.143 is valid as long as M is independent of depth (because it is vertically integrated) and the boundary conditions are adiabatic.

The boundary condition 4.142 becomes

$$\begin{aligned} &M^{\phi}\cdot n = 0 \\ &M^{\psi}\cdot n = 0 \end{aligned} \tag{4.146}$$

or in terms of ϕ and ψ this becomes

$$\begin{aligned} &D\frac{\partial\phi}{\partial n} = 0 \\ &\psi = 0 \end{aligned} \tag{4.147}$$

on the shoreline.

The divergence of the transport field and the vorticity of the velocity field can be written as follows:

$$\begin{aligned} &\nabla\cdot D\nabla\phi = -\nabla\cdot M \\ &\nabla\cdot D\nabla\psi = \nabla\cdot[D^{-1}M] \end{aligned} \tag{4.148}$$

The parameters ϕ and ψ will be expressed in terms of the spectra of the elliptic operators in eq. 4.148. That is, the following characteristic value problems are considered:

$$\begin{aligned} &\nabla\cdot D\nabla\phi_{\alpha} = -\lambda_{\alpha}\phi_{\alpha} \\ &D\frac{\partial\phi_{\alpha}}{\partial n} = 0 \end{aligned} \tag{4.149}$$

on the boundary, and

$$\begin{aligned} &\nabla\cdot D^{-1}\nabla\psi_{\alpha} = -\mu_{\alpha}\psi_{\alpha} \\ &\psi_{\alpha} = 0 \end{aligned} \tag{4.150}$$

on the boundary. The subscript α refers to the number of the spectral components. The systems 4.149 and 4.150 are self-adjoint under the more stringent boundary condition

$$D^{-1}\psi_{\alpha} = 0$$

Thus, the characteristic values λ_{α} and μ_{α} are real, and the related eigenfunctions ϕ_{α} and ψ_{α} give rise separately to an internally orthogonal set. The orthogonality condition is

$$\begin{aligned} &\int D^{-1}M_{\alpha}^{\phi}M_{\beta}^{\phi}\,dA = \lambda_{\alpha}\int\phi_{\alpha}\phi_{\beta}\,dA = gA\delta_{\alpha\beta} \\ &\int D^{-1}M_{\alpha}^{\psi}M_{\beta}^{\psi}\,dA = \mu_{\alpha}\int\psi_{\alpha}\psi_{\beta}\,dA = gA\delta_{\alpha\beta} \end{aligned} \tag{4.151}$$

where δ is the Kronecker delta and A is the surface area of the water body.

From eq. 4.144:

$$\begin{aligned} &M_{\alpha}^{\phi} = -D\nabla\phi_{\alpha} \\ &M_{\alpha}^{\psi} = -[\nabla\psi_{\alpha}] \end{aligned} \tag{4.152}$$

To represent M^{ϕ} and M^{ψ} define the following nondimensional expansion coefficients:

$$
\begin{aligned}
P_{\alpha} &= \frac{1}{gA}\int D^{-1}M_{\alpha}^{\phi}M^{\phi}\,dA = \frac{1}{gA}\int D^{-1}M_{\alpha}^{\phi}\,dA \\
Q_{\alpha} &= \frac{1}{gA}\int D^{-1}M_{\alpha}^{\psi}M^{\psi}\,dA = \frac{1}{gA}\int D^{-1}M_{\alpha}^{\psi}\,dA
\end{aligned}
\tag{4.153}
$$

Then

$$
\begin{aligned}
M^{\phi} &= \sum_{\alpha} P_{\alpha}M_{\alpha}^{\phi} \\
M^{\psi} &= \sum_{\alpha} Q_{\alpha}M_{\alpha}^{\psi}
\end{aligned}
\tag{4.154}
$$

Because of eq. 4.151, the right sides in 4.154 represent the left side in a least square sense if the summation in 4.154 covers the complete spectra of eq. 4.149 and 4.150.

From eq. 4.141 it is evident that the divergent part of M determines h. Thus

$$h_{\alpha} = g^{-1}\lambda_{\alpha}^{1/2}\phi_{\alpha} \tag{4.155}$$

Then, the orthogonality relation is

$$\int h_{\alpha}h_{\beta}\,dA = A\delta_{\alpha\beta} \tag{4.156}$$

Then, h can be expanded:

$$h = \sum_{\alpha} R_{\alpha}h_{\alpha} \tag{4.157}$$

where

$$R_{\alpha} \equiv \frac{1}{A}\int h_{\alpha}h\,d\mathrm{A} \tag{4.158}$$

Define

$$
\begin{aligned}
A_{\alpha\beta} &\equiv \{M_{\alpha}^{\phi}, [M_{\beta}^{\phi}]\} \\
B_{\alpha\beta} &\equiv \{M_{\alpha}^{\phi}, [M_{\beta}^{\psi}]\} \\
C_{\alpha\beta} &\equiv \{M_{\alpha}^{\psi}, [M_{\beta}^{\phi}]\} \\
E_{\alpha\beta} &\equiv \{M_{\alpha}^{\psi}, [M_{\beta}^{\psi}]\}
\end{aligned}
\tag{4.159}
$$

The notation $\{\boldsymbol{A}, \boldsymbol{B}\}$ represents the inner product

$$\{\boldsymbol{A}, \boldsymbol{B}\} = \frac{1}{gA}\int fD^{-1}\boldsymbol{A}\cdot\boldsymbol{B}\,dA$$

From eq. 4.159 it can be seen that

$$
\begin{aligned}
A_{\alpha\beta} &= -A_{\beta\alpha} \\
B_{\alpha\beta} &= -C_{\beta\alpha} \\
E_{\alpha\beta} &= -E_{\beta\alpha}
\end{aligned}
\tag{4.160}
$$

Substituting eq. 4.154 and 4.157 into eq. 4.140 and 4.141 and taking $\tau = 0$ and then using the orthogonality conditions 4.153 and 4.156 gives the following spectral prediction equations:

$$
\begin{aligned}
&\frac{dP_\alpha}{dt} - \sum_\beta A_{\alpha\beta}P_\beta - \sum_\beta B_{\alpha\beta}Q_\beta - \nu_\alpha R_\alpha = 0 \\
&\frac{dQ_\alpha}{dt} - \sum_\beta C_{\alpha\beta}P_\beta - \sum_\beta E_{\alpha\beta}Q_\beta = 0 \\
&\frac{dR_\alpha}{dt} + \nu_\alpha P_\alpha = 0
\end{aligned} \tag{4.161}
$$

Define the following column vectors and matrices:

$$
\begin{aligned}
&\bar{P} \equiv \text{col}\,(P_\alpha), \qquad \bar{Q} \equiv \text{col}\,(Q_\alpha) \\
&\bar{R} \equiv \text{col}\,(R_\alpha), \qquad \bar{S} \equiv \begin{pmatrix} \bar{P} \\ \bar{Q} \\ \bar{R} \end{pmatrix}
\end{aligned} \tag{4.162}
$$

and the following matrices:

$$
\begin{aligned}
&A \equiv |A_{ij}|, \qquad C \equiv |C_{ij}| \\
&B \equiv |B_{ij}|, \qquad E \equiv |E_{ij}| \\
&\langle \nu \rangle \equiv \text{diagonal}\,\langle \nu_\alpha \rangle
\end{aligned} \tag{4.163}
$$

Then, eq. 4.161 can be written in the matrix form

$$
\frac{d\bar{S}}{dt} + a\bar{S} = 0 \tag{4.164}
$$

where a is a square matrix defined by

$$
a = \begin{vmatrix} -A & -B & -\langle \nu \rangle \\ -C & -D & 0 \\ \langle \nu \rangle & 0 & 0 \end{vmatrix} \tag{4.165}
$$

Making use of the property that the time dependence of $\bar{S}$ is given by $e^{i\sigma t}$ where σ is the frequency of oscillation, eq. 4.164 becomes

$$
\begin{aligned}
&i\sigma\bar{S} + a\bar{S} = 0 \text{ or} \\
&(\sigma \boldsymbol{I} - ia)\bar{S} = 0
\end{aligned} \tag{4.166}
$$

where $\boldsymbol{I}$ is the identity matrix. The eigenvalue problem 4.166 can be solved for the characteristic (real) values of σ and the eigenvectors $\bar{S}$. Once the eigenvectors are known, using eq. 4.152, 4.154, and 4.157, the M and h fields can be derived.

Note that here, only gravity modes have been considered, which are also referred to as oscillations of the first class (OFC). In Chapter 5, OFC and oscillations of the second class (OSC) will be discussed briefly. For a real water body with irregular geometry, the characteristic value problem (eq. 4.419, 4.150, and 4.166) must be solved numerically. Analogous to the tidal problem one can construct cotidal lines and corange lines. To be able to do this, write

$$
h = \text{Real} \sum_\alpha R_\alpha h_\alpha e^{i\sigma t} = A(x, y) \cos\,[\sigma t - \theta(x, y)] \tag{4.167}
$$

The isolines of $A(x, y)$ give the cotidal diagram, and the isolines of $\theta(x, y)$ represent the corange lines.

Let the solutions of M and h with $\tau = 0$ (i.e. the free solutions) be M_F and h_F, respectively. These can be expressed as

$$\begin{aligned} M_F &= M_{j\alpha}(x, y)e^{i\sigma_\alpha t} \\ h_F &= h_{j\alpha}(x, y)e^{i\sigma_{j\alpha} t} \end{aligned} \tag{4.168}$$

The space-dependent normal mode functions can be found from eq. 4.154 and 4.157. Here, α is a subscript to order the normal modes and j can take a value of either 1 or 2 to represent the normal mode or its complex conjugate. Note that the complex functions satisfy the normal mode equations

$$\begin{aligned} i\sigma_{j\alpha} M_{j\alpha} - f[M_{j\alpha}] &= -gD\nabla h_{j\alpha} \\ i\sigma_{j\alpha} h_{j\alpha} + \nabla M_{j\alpha} &= 0 \end{aligned} \tag{4.169}$$

These functions are orthogonal (in a general Hilbert sense).

Let $M^*_{K\beta}$ and $h^*_{K\beta}$ be the complex conjugates of the normal mode functions for $\sigma_{K\beta}$. The conjugate equations for eq. 4.169 are

$$\begin{aligned} -i\sigma^*_{K\beta} M^*_{K\beta} - f[M^*_{K\beta}] &= -gD\nabla h^*_{K\beta} \\ -i\sigma^*_{K\beta} h^*_{K\beta} + \nabla M^*_{K\beta} &= 0 \end{aligned} \tag{4.170}$$

The orthogonality condition is

$$\int \left(\frac{M_{j\alpha} M_{K\beta}}{gD} + h_{j\alpha} h^*_{K\beta} \right) dA = X_{j\alpha} \delta_{jK} \delta_{\alpha\beta} \tag{4.171}$$

where $X_{j\alpha}$ is the normalization for the normal mode associated with $\sigma_{j\alpha}$. The solution of the forced problem (i.e. $\tau \neq 0$) can be expressed as

$$\begin{aligned} M(x, y, t) &= \sum_{j=1}^{2} \sum_{\alpha} A_{j\alpha}(t) M_{j\alpha}(x, y) \\ h(x, y, t) &= \sum_{j=1}^{2} \sum_{\alpha} A_{j\alpha}(t) h_{j\alpha}(x, y) \end{aligned} \tag{4.172}$$

Here, $A_{j\alpha}$ represents the complex time-dependent amplitude factor for the normal mode with frequency $\sigma_{j\alpha}$.

Substituting eq. 4.172 into eq. 4.140 and 4.141 gives

$$\begin{aligned} &\sum_{j=1}^{2} \sum_{\alpha} \frac{dA_{j\alpha}}{dt} M_{j\alpha} + f \sum_{j=1}^{2} \sum_{\alpha} A_{j\alpha}[M_{j\alpha}] = -gD \sum_{j=1}^{2} \sum_{\alpha} A_{j\alpha} h_{j\alpha} + \tau \\ &\sum_{j=1}^{2} \sum_{\alpha} \frac{dA_{j\alpha}}{dt} h_{j\alpha} + \sum_{j=1}^{2} \sum_{\alpha} A_{j\alpha} \nabla M_{j\alpha} = 0 \end{aligned} \tag{4.173}$$

Multiply the first equation of 4.173 by $M^*_{K\beta}$, the second equation by $h^*_{K\beta}$, the first equation of 4.170 by $M/(gD)$, and the second equation by h (here, M and h are given by eq. 4.172) and add these and integrate over the area of the water body and use the orthogonality condition 4.171 to give

$$(4.174)\quad X_{j\alpha}\left(\frac{dA_{j\alpha}}{dt} + i\sigma_{j\alpha}A_{j\alpha}\right) = \int \frac{\tau M_{j\alpha}^*}{gD}\, dA$$

or

$$(4.175)\quad \frac{dA_{j\alpha}}{dt} + i\sigma_{j\alpha}A_{j\alpha} = \frac{1}{X_{j\alpha}} \int \frac{\tau M_{j\alpha}^*}{gD}\, dA$$

Since τ is a known quantity, the equation for $A_{j\alpha}(t)$ is an ordinary inhomogeneous differential equation of the first order.

Formally, the solution of eq. 4.175 can be written as

$$(4.176)\quad A_{j\alpha}(t) = \int_0^t B_{j\alpha}(\tau) e^{i\sigma_{j\alpha}(\tau - t)}\, d\tau$$

where

$$(4.177)\quad B_{j\alpha} = \frac{1}{X_{j\alpha}} \int \frac{\tau M_{j\alpha}^*}{gD}\, dA$$

In real situations the integrand on the right side of eq. 4.177 will not be a simple analytical function of time, and one must use numerical integration. Schwab (1975) used the following finite-difference scheme:

$$(4.178)\quad \frac{1}{\Delta t}[A_{j\alpha}(t + \Delta t) - A_{j\alpha}(t)] + \frac{i}{2}[A_{j\alpha}(t + \Delta t) + A_{j\alpha}(t)] = \frac{1}{2}[B_{j\alpha}(t + \Delta t) + B_{j\alpha}(t)]$$

This can be rearranged to give

$$(4.179)\quad A_{j\alpha}(t + \Delta t) = \left(\frac{2 - i\sigma_{j\alpha}\Delta t}{2 + i\sigma_{j\alpha}\Delta t}\right) A_{j\alpha}(t) + \left(\frac{\Delta t}{2 + i\sigma_{j\alpha}\Delta t}\right)[B_{j\alpha}(t + \Delta t) + B_{j\alpha}(t)]$$

According to Kurihara (1965a, 1965b) this scheme is unconditionally stable for any Δt. However, if Δt is greater than one-sixth of the period of the fastest wave in the system, phase errors will then occur.

The integration procedure is as follows. Once the normal modes are determined, from eq. 4.171 the normalization factors $X_{j\alpha}$ can be calculated. Since τ is given for all time, the $B_{j\alpha}$ values that enter eq. 4.179 can be detemined from eq. 4.177. Since the earlier mode calculation also gives the normal mode frequencies, $\sigma_{j\alpha}$, the time-dependent expansion coefficients can be determined from eq. 4.179. Then, at each time step, the M and h fields can be determined from eq. 4.173. Schwab (1975) claimed that although the numerical integration involved appears to be a considerable effort, the ability to limit the range of the index α in eq. 4.179 makes this approach more efficient than the ordinary finite-difference techniques.

4.2 Empirical Methods

Empirical methods are those techniques that are derived from simple analytical theories and experience and that are usable more or less directly for practical situations. In the empirical storm surge techniques, the contributions and reviews by two authors, namely R. Silvester and C. L. Bretschneider, are considered here. Hence, one subsection

will be devoted to the works of each of these authors; other works will be considered in a third subsection.

THE WORK OF SILVESTER

In stretches of open coast or in bays where actual measurements of storm surge amplitudes are not available, one might have to determine the amplitude in the deeper part of the ocean (or sea) and trace the long wave shorewards. From analytical theories, relationships are available for the propagation of waves across channel transitions with either variable depth or width and with friction included in channels of uniform depth.

Silvester (1969) developed a method that enables one to derive multiplicative factors for calculating the surge amplitude farther inshore. The friction coefficients are assumed based on wave Reynolds number and bed roughness factor. Following Dean (1964), Silvester first considered the solutions for the frictionless case. Let H be the wave height, b the width, and d the depth, and let subscripts 1 and 2 denote the deepwater side and the shallow-water side of the transition, respectively. An amplification ratio. H_2/H_1, can be computed for ratios d_1/d_2 and $(b_1/b_2)^2$. Define

$$Z_A \equiv \frac{4\pi d^{1/2}}{g^{1/2}TS_V} \quad \text{(for depth variations)} \tag{4.180}$$

and

$$Z_B \equiv \frac{\pi b_1}{g^{1/2}d^{1/2}TS_H} \quad \text{(for width variations)} \tag{4.181}$$

The notation is defined in Fig. 4.3. Using this figure, one can write these factors as follows:

$$Z_A = \frac{4\pi L}{\lambda} \text{ and } Z_B = \frac{2\pi L}{\lambda}$$

where L is also defined in the figure. Here, λ is the wavelength, and its value in the frictionless case is

$$\lambda_0 = T\sqrt{gd}$$

where T is the wave period.

Consider the following four limiting cases.

(i) $Z_A = 0$ (i.e. $L = 0$) gives rise to an abrupt step:

$$\frac{H_2}{H_1} = \frac{2\sqrt{d_1}}{(\sqrt{d_1} + \sqrt{d_2})}$$

Hence, as $d_2 \to 0$, $H_2/H_1 \to 2$.

(ii) $Z_A = \infty$ (i.e. $L = \infty$) gives rise to an infinitely long channel:

$$\frac{H_2}{H_1} = \left(\frac{d_1}{d_2}\right)^{1/4}$$

for shallow-water situation (i.e. $C = \sqrt{gD}$). Hence, as $d_2 \to 0$, $H_2/H_1 \to \infty$ (note that here the effect of friction and breaking waves is not considered).

(iii) $Z_B = 0$ (i.e. $L = 0$) leads to an abrupt reduction in width:

$$\frac{H_2}{H_1} = \frac{2b_1}{(b_1 + b_2)}$$

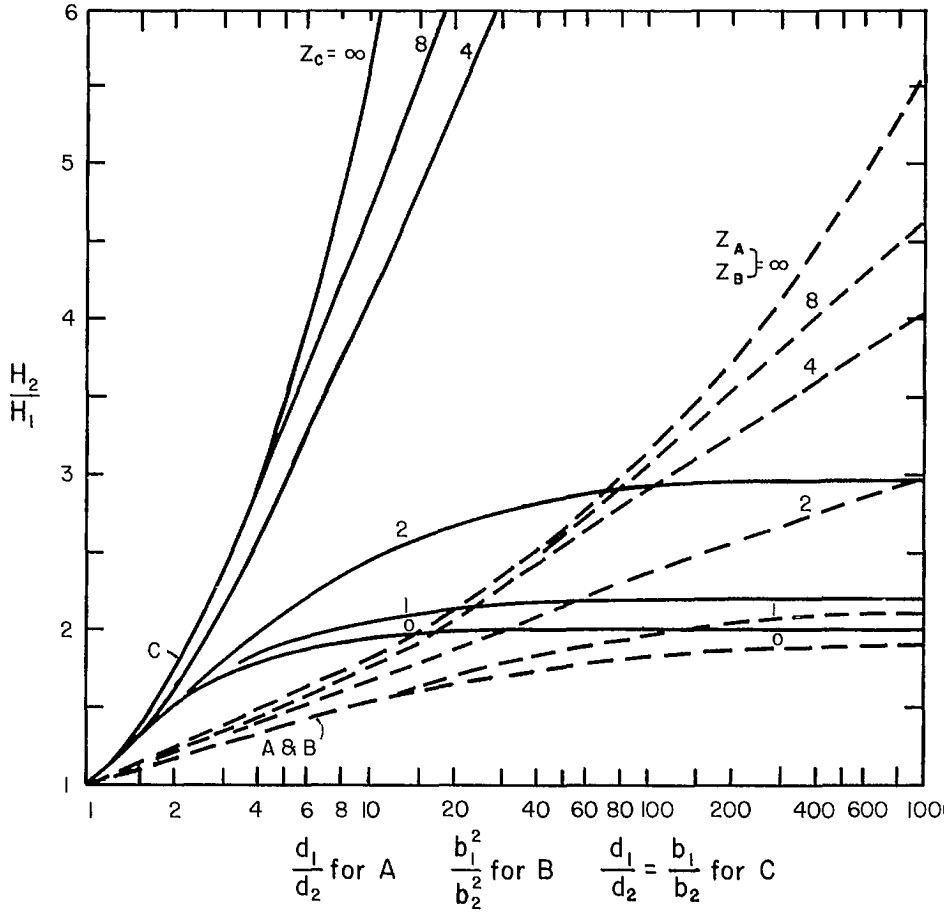

FIG. 4.3. Wave amplification in a channel transition without the inclusion of friction. (Silvester 1969)

Hence, as $b_2 \to 0$, $H_2/H_1 \to 2$.

(iv) $Z_B = \infty$ (i.e. $L = \infty$) leads to an infinitely long channel:

$$\frac{H_2}{H_1} = \left(\frac{b_1}{b_2}\right)^{1/2}$$

for shallow-water conditions. Hence, as $b_2 \to 0$, $H_2/H_1 \to \infty$. From Fig. 4.3 one can determine the wave amplification, H_2/H_1, for varying depths and widths.

Next, Silvester used the work of Jonsson (1965, 1966) to include the modifications due to friction. Using pipe flow as an analogy, Jonsson gave a $f_W - R_W$ diagram for long waves. Here, f_W is a wave friction factor and R_W is a wave Reynolds number defined as

$$R_W \equiv \frac{U_{\max} x_{\max}}{\nu}$$

where $U_{\max}$ is the maximum water particle velocity, x_{max} is the maximum deviation of the water particles from their mean position, and ν is the kinematic viscosity of seawater.

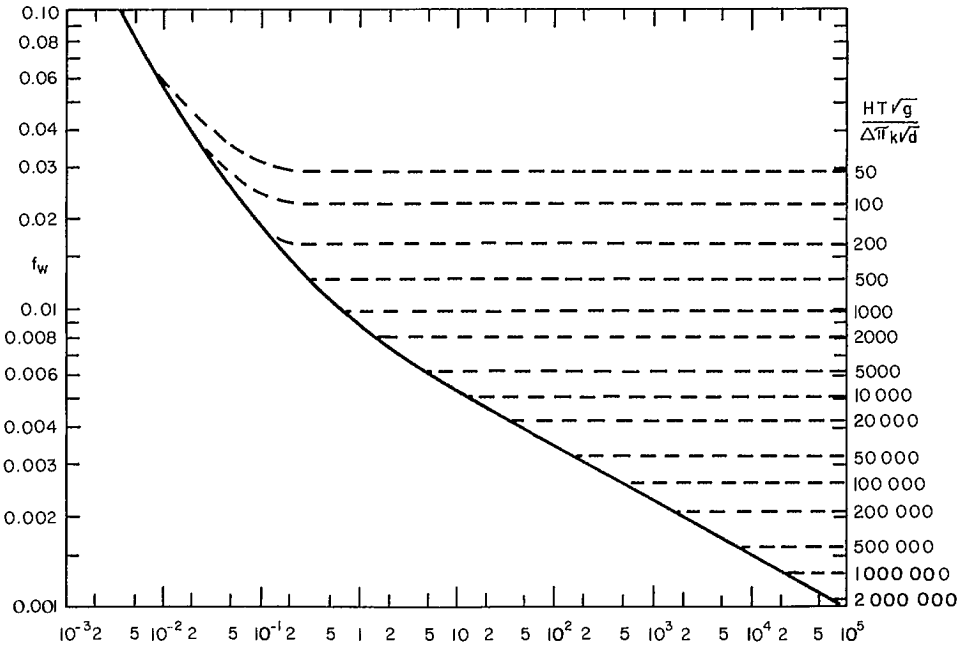

FIG. 4.4. Wave friction factor f_w for waves for the case $2\pi dT^2/g \leq 0.01$. See text for an explanation of the symbols. (Silvester 1969)

In Fig. 4.4 the abcissa is R_W whereas the ordinate is $\tau_{0_{max}}$ where

$$\tau_{0_{max}} \equiv f_W \frac{1}{2} \rho U_{max}^2$$

For shallow-water conditions, making use of the linear theory, one can write

$$(4.182) \quad R_W = \frac{H^2 T}{d}\left(\frac{g}{8\pi\nu}\right)$$

Note that Silvester takes $\nu = 11 \times 10^{-6}$ ft·s^{-1} (10^{-6} m·s^{-1}).

For the bed roughness factor, Jonsson used x_{max}/K where K is the Nikuradse sand roughness on a smooth surface. Silvester wrote

$$(4.183) \quad \frac{x_{max}}{K} = \frac{HTg^{1/2}}{4\pi K d^{1/2}}$$

This is shown in Fig. 4.4. Kajiura (1964) showed that for large values of d/K the friction factor varies only with the right side of eq. 4.183. In Fig. 4.4 for values of H^2/T greater than 10^5, the smooth bed curve can be extrapolated by using

$$(4.184) \quad f_W = \frac{0.075}{(R_W)^{0.19}} \text{ or } \frac{0.0084}{(H^2T/d)^{0.19}}$$

Next, Silvester made use of the work of Ippen and Harleman (1966) who studied a damped long wave traveling through a canal of infinite length (so that no reflections occur). Silvester considers the continental shelf as a combination of discrete sections, each

of uniform depth. Using the wave height for the frictionless case, a wave attenuation factor M can be derived:

$$(4.185)\quad M = \frac{f_w U_{\max}}{3\pi g d} = \frac{fH}{6\pi g^{1/2} d^{3/2}}$$

This can also be written as

$$(4.186)\quad M = \frac{2\pi}{Tg}\tan 2\alpha = \frac{2\pi}{Tg}\left[\frac{2\tan\alpha}{(1-\tan^2\alpha)}\right]$$

where

$$\tan\alpha \equiv \frac{\mu\lambda}{2\pi}$$

and μ is a parameter. Here, it is assumed that μ and λ are uniform over the section of constant or slightly varying width. From above:

$$(4.187)\quad \frac{f_w H T\sqrt{gd}}{d^2} = \frac{f_w H \lambda_0}{d^2} = 24\pi^2\left[\frac{\mu\lambda/2\pi}{1-(\mu\lambda/2\pi)^2}\right]$$

For the frictionless case, the wavelength is λ_0 and $C = \sqrt{gd}$:

$$(4.188)\quad \left(\frac{2\pi}{\lambda_0}\right)^2 = \left(\frac{2\pi}{\lambda}\right)^2 - \mu^2 \text{ or } \left(\frac{\mu\lambda}{2\pi}\right)^2 = 1 - \left(\frac{\lambda}{\lambda_0}\right)^2$$

Substituting eq. 4.188 into 4.187 gives

$$(4.189)\quad \frac{f_w H T\sqrt{gd}}{d^2} = 24\pi^2\left[\frac{1-(\lambda/\lambda_0)^2}{(\lambda/\lambda_0)^2}\right]$$

Silvester (1969) included a graph of solutions to this equation for a range of values of λ/λ_0.

The wave attenuation depends on λ/λ_0 and the ratio of the distance traveled to the wavelength. Let H_x be the wave height at a distance from the entrance of the channel section. Then

$$(4.190)\quad \frac{H_x}{H} = e^{-\mu x}$$

or

$$(4.191)\quad \frac{H_x}{H} = e^{-2\pi x/\lambda_0}\sqrt{\left(\frac{\lambda}{\lambda_0}\right)^2 - 1}$$

where

$$\lambda_0 = T\sqrt{gd}$$

Silvester included a diagram of the graph of eq. 4.191 for a range of λ/λ_0 and $x/(T\sqrt{gd})$.

Silvester (1971) considered an enclosed body of water such as a rectangular lake. Let d be the (uniform) depth of the lake, U_{10} the wind speed 10 m above the water surface, L the length of the lake (or wind fetch), and S the surge amplitude at the downwind end. Then

$$(4.192)\quad \frac{S}{d} = \frac{K_{10} U_{10}^2 L}{2gd^2}$$

where $K_{10} = 3.3 \times 10^{-6}$ (wind drag coefficient). Note that this equation is dimensionless. For nonrectangular shapes, S/d must be multiplied by a form factor N.

For storm surges on the continental shelf, Silvester assumed a uniform variation from a depth d_1 at the shelf edge to d_2 near the coast. Let L be the width of the shelf and F the fetch length. The depth ratio d_2/d_1 can be expressed in terms of L/x where x is the distance inland where the plane of the bed meets the mean water level. For extratropical cyclones, $F > L$ generally; however, we must take $F = L$, since only the portion of the fetch over the shallow zone is effective in producing the surge. On the other hand, for tropical cyclones, usually $F < L$. Let V be the speed of movement of the wind field; if $V = 0$, the wind field is referred to as a static wind field.

For the static wind field case, the surge S is given by Bretschneider (1966a) as

$$(4.193) \quad \frac{S}{d_1} = \frac{KU^2L}{gd_1^2\left(1 - \frac{d_1}{d_2}\right)} \ln\left(\frac{d_1}{d_2}\right)$$

For tropical cyclones a triangular wind field is more relevant. Reid (1956) expressed the surge amplitude as

$$(4.194) \quad \frac{S}{d_1} = \frac{KU_{\max}^2 L}{gd_1^2}\left[\frac{1.12}{1 + \sqrt{\frac{d_2}{d_1}}} \left(\frac{d_1}{d_2}\right)^{1/4}\right]$$

Silvester graphed this relation.

When a wind field is moving across the shelf towards the shore, the forward part of the surge wave system is being reflected as the later waves are still approaching the shore, Reid (1956) considered the interaction between these two wave systems and included graphs for the ratio, R, of the maximum surge, $S_{\max}$, to that of static storm situations. Silvester gave the following formula for the surge, S_a, due to reduction in the atmospheric pressure:

$$(4.195) \quad S_a = (1013 - P_c)\, 0.033$$

where S_a is the surge amplitude in feet and P_c is the pressure at the storm cente in millibars. This relation is also known as the inverse barometer effect and, as usually expressed, indicates that a decrease of 1 mb in the atmospheric pressure gives rise to an increase of 1 cm in the water level.

The Work of Bretschneider

Bretschneider (1966a) gave the following convenient classification (Table 4.1) of water bodies for engineering design purposes with respect to storm surges. Consider a rectangular channel of uniform depth and let the wind blow with a constant speed along the channel axis. Under steady-state conditions the following equations may be written (Hellstrom 1941; Langhaar 1951; Keulegan 1951, 1952).

Slope of the water surface:

$$(4.196) \quad \frac{dS}{dx} = \frac{\tau_S + \tau_b}{\rho g(h + S)}$$

TABLE 4.1. A convenient classification of water bodies for developing empirical relations for engineering design problems. (Bretschneider 1966a)

A. Enclosed lakes and reservoirs
   1. Rectangular channel, constant depth
   2. Regular in shape
   3. Somewhat irregular in shape
   4. Very irregular in shape

B. Off coast or on continental shelf
   1. Bottom of constant depth
   2. Bottom of constant slope
   3. Slightly irregular bottom profile
   4. Irregular bottom profile

C. Coastline
   1. Smooth coastline
   2. Coastline somewhat irregular
   3. Jagged coastline

D. Behind coastline
   1. Low natural barriers
   2. Medium-high natural barriers
   3. High natural barriers

E. Open bays and estuaries
   1. Entrance backed by long estuaries and with tidal flow moving freely past entrance
   2. Entrance backed by short estuary and with tidal flow moving freely past entrance
   3. Entrance obstructed sufficiently to prevent free movement of tidal flow past entrance

Conservation of volume for nonlinear exposed bottom:

$$(4.197) \quad \int_0^l (h + S)dx = lh$$

Conservation of volume for exposed bottom:

$$(4.198) \quad \int_{x_0}^l (h + S) = lh$$

Here, S is the surge amplitude, x is the horizontal distance, τ_S is the wind stress, h is the water depth, l is the channel length, x_0 is the length of the exposed bottom (when applicable), and τ_b is the bottom stress.

Based on studies in Lake Okeechobee, Saville (1953, 1961) wrote

$$\frac{\tau_S}{\rho g} = 3.0 \times 10^{-6} U^2/g \text{ and } \tau_b/\tau_S \sim 0.1$$

Then, eq. 4.196 can be written as

$$(4.199) \quad \frac{dS}{dx} = \frac{KU^2}{g(h + S)}$$

where $K = 3.3 \times 10^{-6}$ and U is the wind speed. It is quite possible that the wind stress is proportional to U^m where $m \neq 2$ (see Chapter 6). With reference to Fig. 4.5, for exposed bottom, the constant of integration in eq. 4.196 is x_0, and the setup between $x = 0$ and $x = x_0$ is $S = -h$. For the case of a nonexposed bottom, $x_0 = 0$ and eq. 4.197 can be used

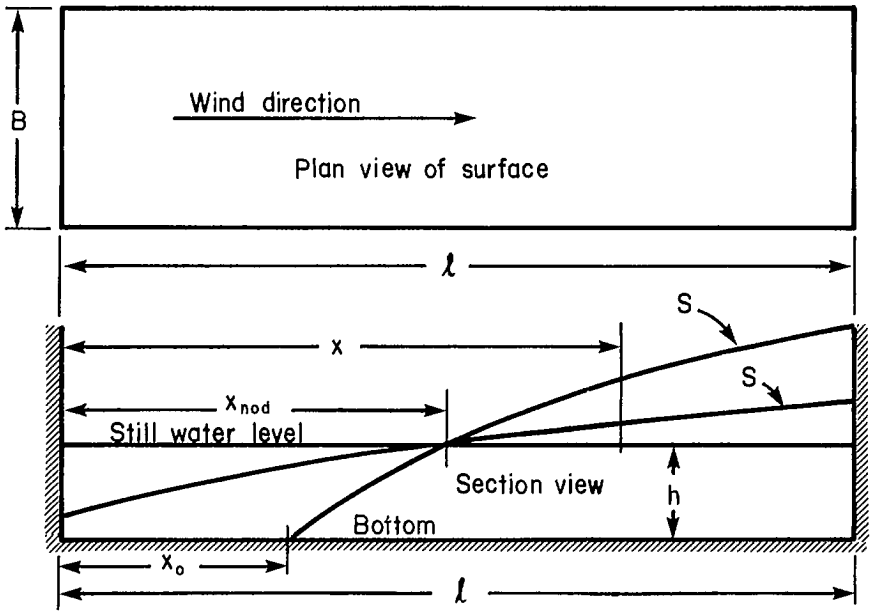

FIG. 4.5. Schematic representation of a rectangular channel of uniform depth for storm surge calculations. (Bretschneider 1966b)

to evaluate the constant of integration in eq. 4.196. For finite values of U, h, and l the nodal point (i.e. $S = 0$ at $x = x_{nod}$) is given by

$$\frac{x_{nod}}{l} = 1 - \left(\frac{S_{max}^2 + 2S_{max}h}{2KU^2L}\right) \tag{4.200}$$

where $S = S_{max}$ at $x = l$. Solutions of the above equations are given in Tables 5.2 and 5.3 of Bretschneider (1966) for the cases of nonexposed and exposed bottoms, respectively (not included here).

Next consider an enclosed lake of regular shape. Essentially the same equations as above can be used, as a first approximation, if the depth is replaced by the average depth $\bar{h}$. To obtain the next level of approximation the lake can be divided into several segments, and then eq. 4.196–4.199 can be solved numerically. Since this will involve trial and error, the process can be made efficient by incorporating the second-order term into the equations.

With reference to Fig. 4.6, the incremental rise, ΔS_i, of the water level over the ith section can be written as

$$\Delta S_i = h_T\left[\sqrt{\frac{2NKU^2\Delta x}{g(h_T)^2} + 1} - 1\right] \tag{4.201}$$

where Δx is the length of the section. The total water depth, h_T, in the ith section (excluding incremental ΔS_i rise over that section) is given by

$$h_T = \bar{h}_i + \sum_{i=1}^{M-1} \Delta S_i \tag{4.202}$$

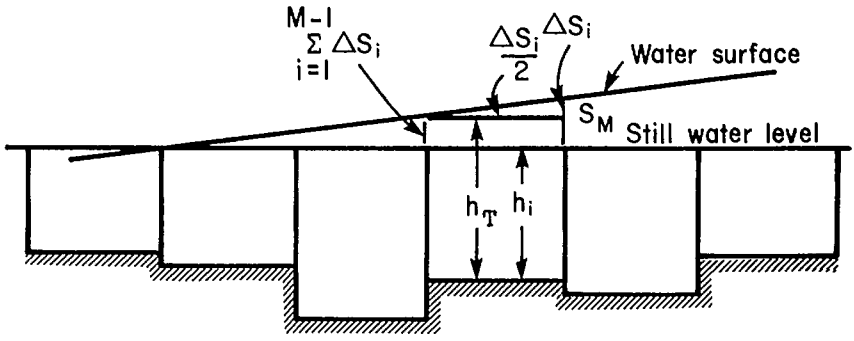

FIG. 4.6. Schematic diagram for empirical formula for wind setup calculations. (Bretschneider 1966b)

where $\bar{h}_i$ is the average still water depth in the ith section. In eq. 4.201 the parameter N is the planform factor. The surge is given by

$$(4.203) \quad S_M = \sum_{i=1}^{M} \Delta S_i$$

The wind stress effect can be written as

$$(4.204) \quad \frac{KU^2L}{gh^2} = \sum_{i=1}^{M} \left[\frac{KU^2\Delta x}{g(h_i)^2}\right]$$

To begin the computation, one must know a first approximation for the nodal point, and Tables 5.2 and 5.3 of Bretschneider (1966) can be used. The convention is such that ΔS_i is positive from the nodal point to the downwind end of the lake and negative towards the upwind end of the lake. The continuity relation is

$$(4.205) \quad \sum_{i=1}^{M} B_i S_i \Delta x = 0$$

where B_i is the width of the ith section.

Essentially the same procedure can be used for enclosed lakes of slightly irregular shape. Bretschneider (1966) selected Lake Okeechobee (Florida) and Lake Ponchartrain (Louisiana) as examples of lakes of slightly irregular shape, and for lakes of very irregular shape he chose Fork Peck Reservoir (Montana), Lake Texoma (Texas), and Lake Mead (Colorado River). He suggested that the irregular lakes may be subdivided into several more or less regular-shaped lakes in certain situations. In some other situations, statistical techniques (correlating storm surges with the winds) may be appropriate. The writer feels that for irregular bodies of water, numerical models are preferable.

Until now it has been assumed that the wind blows either parallel to the lake or perpendicular to the lake. It is more likely that winds blow at an angle to the lake. In this case, in eq. 4.201 or 4.204, $U^2/\Delta x$ can be replaced with $UU_x\Delta x$ and solving for ΔS_x (here, U_x is the wind speed in the x direction) which is the setup in the x direction and repeating the calculation by replacing $U^2\Delta x$ with $UU_y\Delta y$ and solving for ΔS_y. Then one can determine two nodal lines x_{nod}/l and y_{nod}/l. The point of intersection of these two lines is the nodal center. At this point one can begin the computation using eq. 4.202 and noting that $\Delta S_i = \Delta S_x + \Delta S_y$.

Next, Bretschneider (1966) considered a continental shelf of uniform depth and wind

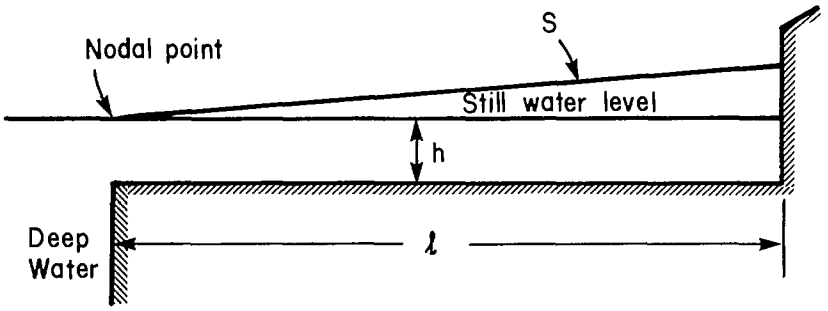

FIG. 4.7. Schematic representation of a continental shelf of uniform depth. (Bretschneider 1966b)

blowing perpendicular to the coast. With reference to Fig. 4.7 the solution of eq. 4.196 is

$$(4.206) \quad S = \frac{KU^2x}{g(h + S/2)}$$

This being a quadratic equation for S, the positive root is given by

$$(4.207) \quad S = h\left(\sqrt{\frac{2KU^2x}{gh^2} + 1} - 1\right)$$

It may be noted that eq. 4.207 and 4.201 are similar and would be identical if eq. 4.201 were used as a one-step formula.

For the case of a shelf of uniform slope (Fig. 4.8), the maximum surge due to a wind field moving perpendicular to the coast with a triangular wind stress distribution such as that due to a hurricane is given by

$$(4.208) \quad S_{max} = K\frac{T_1}{c_1}\left(\frac{h_1}{h_0}\right)^{1/4} U_{max}^2 Z$$

where, as above, the wind stress coefficient has a numerical value of 3.0×10^{-6}, h_1 is the depth at the edge of the shelf, h_0 is the depth near the coast where S_{max} applies, l is the length of the shelf, U_{max} is the maximum wind speed, and Z is the response factor. Other relations are $c_1 = \sqrt{gh_1}$, $c_0 = \sqrt{gh_0}$, $\bar{c} = \frac{1}{2}(c_1 + c_2)$, and $T_l = l/\bar{c}$. In shallow areas (i.e. when h_0 is small) in eq. 4.208 one may replace h_0 with $h_0 + S$.

For steady-state storm surge calculation over a continental shelf of uniform slope (see Fig. 4.8) one can write

$$(4.209) \quad h = h_1 - m_1 x$$

where m_1 is the bottom slope and the integration proceeds from $x_1 = 0$ at h_1 to x at h. In eq. 4.199 the term S in the denominator on the right side can be written approximately:

$$(4.210) \quad S = m_2 x$$

where the second-order term, m_2, is the mean waterslope and is assumed to be constant in the region of integration. The solution of eq. 4.199 is

$$(4.211) \quad S = \frac{KU^2}{g(m - m_2)} \ln\left(\frac{h_1}{h_1 - (m_1 - m_2)x}\right)$$

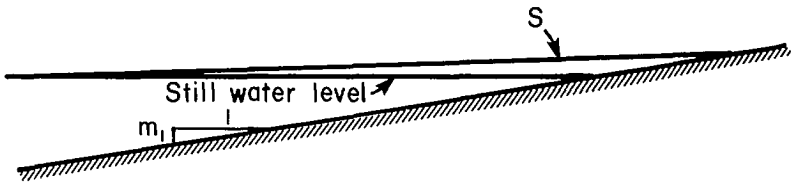

FIG. 4.8. Schematic representation of a continental shelf with a uniformly sloping bottom. (Bretschneider 1966b)

Using eq. 4.209 and 4.210, eq. 4.211 becomes

$$(4.212)\quad S = \frac{KU^2x}{g(h_1 - h - S)} \ln\left(\frac{h_1}{h + S}\right)$$

Note that for the case of uniform depth, $h_1 = h$, eq. 4.212 reduces to eq. 4.206.

In an approximate manner, eq. 4.212 can be modified for variable wind speed and direction if U^2 is replaced by

$$(4.213)\quad U_e^2 = \frac{1}{l}\int_{x_2}^{x_1} |U| U_x dx$$

This can be achieved through computing cross-sections of wind field or stress diagrams and using that portion giving maximum value of the integral of eq. 4.213 over length l where $l = x_1 - x_2$.

It will be seen in section 4.3 that the component of the wind stress parallel to the coast gives rise to the so-called bathystrophic storm surge. Based on the work of Freeman et al. (1957), Bretschneider (1966a, 1966b) wrote

$$(4.214)\quad \frac{dS}{dx} = \frac{KUU_x}{g(h + S)} + \frac{fF_y}{g(h + S)}$$

Here, U is the absolute value of the wind speed, U_x is the component perpendicular to the bottom contours, f is the Coriolis parameter, and F_y is the flux parallel to the depth contours and is given by

$$(4.215)\quad F_y = \int_0^{(h+S)} v dz$$

where v is the current parallel to the depth contours. The following equation holds for F_y:

$$(4.216)\quad \frac{\Delta F_y}{\Delta t} = KUU_y - \frac{\mathcal{H}}{(h + S)^{7/3}} F_y^2$$

where U_y is the component of wind speed parallel to the bottom contours, $K = 3.0 \times 10^{-6}$, and $\mathcal{H}$ lies between 10^{-2} and 10^{-3}.

If the wind speed is constant during some time interval, the solution of eq. 4.216 is

$$(4.217)\quad F_y(2) = \sqrt{\frac{KUU_y(h + S)^{7/3}}{\mathcal{H}}} \tanh\left[\sqrt{\frac{K\mathcal{H}UU_y}{(h + S)^{7/3}}}(t_2 - t_1) + \tan^{-1}\frac{F_y(1)}{\sqrt{\frac{KUU_y(d + S)^{7/3}}{\mathcal{H}}}}\right]$$

Here, $F_y(1)$ and $F_y(2)$ refer to F_y at times t_1 and t_2, respectively.

For a uniformly sloping bottom to a (straight) coastline the surge S at the coast ($h = 0$) becomes (from eq. 4.208)

$$(4.218) \quad S = \frac{KU^2x}{g(h_1 - S)} \ln \frac{h}{S}$$

The bottom slope usually increases rapidly near the coast; hence, eq. 4.218 can overestimate the surge. A better technique is to use eq. 4.212 to a depth h, prior to the sudden increase in bottom slope, and then use either eq. 4.212 or the numerical equation to solve for ΔS in the remaining region.

Bretschneider gave greater emphasis to the planform factor mentioned above in his later work (Bretschneider 1975). In certain enclosed bodies of water such as lakes, the varying depth and width can be approximately taken into account by utilizing the planform factor N. Equation 4.199 then becomes

$$(4.219) \quad \frac{dS}{dX} = N(X) \frac{KU^2}{g(h + S)}$$

where $N(X)$ is the planform factor and is a function of distance down the channel, varying depth, and varying width of the channel. At the downwind end of the channel, $X = L$, the planform factor $N(X) = N$.

For an enclosed lake and assuming linearity, the setup (surge) at the downwind side is equal to the draw at the upwind side and S is small compared with h. Hence, in the denominator of eq. 4.219, S can be ignored compared with h. Then, this equation can be written as follows:

$$(4.220) \quad S = N \frac{KU^2}{2gh}$$

In deriving mathematical expressions for $N(X)$ it is convenient to consider the following three subcases for an enclosed lake: (a) constant depth, variable width, (b) constant width, variable depth, and (c) a combination of a and b. For the first case either an exponential change or a trapezoidal change may be considered. For simplicity, consider an enclosed channel with exponential width variation:

$$(4.221) \quad B = B_0 \exp(-2\alpha X)$$

where B is the width of the channel at distance X measured from B_0, which is the width at the beginning of the channel, L is the length of the channel, and α is a constant to be determined.

Integration of eq. 4.199 with respect to X gives

$$(4.222) \quad S = \frac{KU^2L}{2g(h + S/2)} + C = \frac{NKU^2L}{2g(h + S/2)}$$

where C is the constant of integration. To determine this, note that

$$(4.223) \quad \int_0^L B(h + S)\, dX = A_S(h + S)$$

where A_S is the surface area, $A_S(h + S)$ being the volume of water in the channel. Noting that

$$(4.224) \quad B = B_0 \exp\left(-2\alpha \frac{X}{L}\right)$$

and

$$A_S = \int_0^L B\, dX \tag{4.225}$$

we obtain

$$A_S = \frac{B_0 L}{2\alpha}[1 - \exp(-2\alpha)] \tag{4.226}$$

Hence, the planform factor is given by

$$N(X) = 2\left\{1 + \frac{1 - 2\alpha\left(\frac{X}{L}\right)\exp\left[-\frac{2\alpha X}{L}\right] - \exp\left[-\frac{2\alpha X}{L}\right]}{2\alpha[\exp(-2\alpha) - 1]}\right\} \tag{4.227}$$

where

$$\alpha \equiv B_0/B_L$$

Generally speaking, one must select B_0 by trial and error so that the exponential change in width is satisfied. Bretschneider's (1975) Fig. 23 shows N as a function of B_0/B_L. Note that when $\alpha = 0$, we have a rectangular channel of constant depth and width, and $N = 1$.

Next, consider a trapezoidal channel for which

$$B = B_0 - \beta X \tag{4.228}$$

where

$$\beta \equiv \frac{B_0 - B_L}{L}$$

For this case, it can be shown that the planform factor is given by

$$N = \frac{2}{3}\left(\frac{2B_0 + B_L}{B_0 + B_L}\right) \tag{4.229}$$

Next, consider a bottom sloping upward in the direction of the wind. To simplify the problem, assume trapezoidal variation both in the depth and in the width. This slope is usually referred to as the prismoidal planform.

Write

$$B = B_0 - \beta X \tag{4.230}$$

$$h = h_0 - mX \tag{4.231}$$

where m is the bottom slope and β is the slope of convergence of the sides. The surface area of the water is given by

$$A_x = \int_0^L B\, dX \tag{4.232}$$

and the volume of water in the channel is given by

$$V = \int_0^L Bh\, dX \tag{4.233}$$

The planform factor can be shown to be given by

$$(4.234)\quad N = 2\left[\frac{1}{2} - \frac{7}{12}m + \frac{1}{6}m^2 - \frac{9}{320}m^3 + \frac{7}{160}m^4 - \beta\left(\frac{1}{12} + \frac{1}{120}m^2 + \frac{1}{2120}m^4\right)\right]$$

For a trapezoidal channel of constant depth, $m = 0$, and eq. 4.234 reduces to

$$(4.235)\quad N = 1 - \frac{1}{6}\beta$$

When both m and β are zero (i.e. rectangular channel of constant depth and width), then $N = 1$. Note that until now, N has been derived on the assumption that $S \ll h$. But when the winds are stronger and the surges are significant, a second approximation may be obtained by replacing h with $h + S/2$.

Next, Bretschneider (1975) considered surges over the continental shelf. Under the bathystrophic approximation (see section 4.3) the equations of motion and continuity can be written as

$$(4.236)\quad \frac{dQ}{dt} = KUU_y - KD^{-1/3}\left(\frac{Q}{D}\right)^2$$

$$(4.237)\quad \frac{dS}{dX} = \frac{1}{gD}(KUU_x + fQ)$$

$$(4.238)\quad \frac{\partial S}{\partial t} - \frac{\partial Q}{\partial y} = 0$$

where Q is the transport in the direction perpendicular to the shore (i.e. x), S is the surge (feet), y is the direction parallel to the coast, f is the Coriolis parameter, D is the water depth (feet), U is the wind speed, U_y is the component of the wind speed parallel to the coast (feet per second), and K is a wind stress coefficient. Integration of eq. 4.236 between the limits Q_0 and Q_1 for times t_0 and t_1 gives

$$(4.239)\quad Q_1 = \left(\frac{KUU_yD^{7/3}}{\mathcal{H}}\right)\tanh\left[\left(\frac{K\mathcal{H}UU_y}{D^{7/3}}\right)^{1/2}\Delta t + \tanh^{-1}Q_0\left(\frac{\mathcal{H}}{KUU_yD^{7/3}}\right)^{1/2}\right]$$

If it is assumed that $Q_0 = 0$ at $t_0 = 0$, then

$$(4.240)\quad Q = \left(\frac{KUU_yD^{7/3}}{\mathcal{H}}\right)^{1/2}\tanh\left(\frac{K\mathcal{H}UU_y}{D^{7/3}}\right)^{1/2}\Delta t$$

The mean current parallel to the coast is given by

$$(4.241)\quad \bar{V} = \frac{Q}{D}$$

Hence

$$(4.242)\quad \frac{\bar{V}}{U} = D^{1/6}\left(\frac{K}{\mathcal{H}\sin\theta}\right)^{1/2}\left[\tanh\frac{Ut}{D}\left(\frac{K\mathcal{H}\sin\theta}{D^{1/3}}\right)^{1/2}\right]$$

From eq. 4.237 and 4.242:

$$(4.243)\quad \frac{dS}{dx} = \frac{KU^2\cos\theta}{g(D+S)} + \frac{fU}{g}\left(\frac{K}{\mathcal{H}}\sin\theta\right)^{1/2}(D+S)^{1/6} \times \tanh\left[\frac{Ut}{(D+S)}\left(\frac{K\mathcal{H}\sin\theta}{(D+S)^{1/3}}\right)^{1/2}\right]$$

Here, $\mathcal{K}$ is between 10^{-2} and 10^{-3} and θ is the angle at which the wind is blowing towards the coastline. To obtain the steady state, the tanh term is set at unity.

For the case of a constant bottom slope:

$$D + S = D_0 - mx \tag{4.244}$$

where D_0 is the break-off end of the slope at the edge of the continental shelf, m is the slope of the continental shelf, and x is measured shoreward from $X = X_0 = 0$ where $D = D_0$. The solution of eq. 4.243 for the steady state becomes

$$S = \frac{KU^2 \cos\theta}{gm} \ln \frac{D_0}{(D_0 - mx)} + \frac{6}{7} \frac{fU}{gm} \left(\frac{K}{\mathcal{K}} \sin\theta\right)^{1/2} [D_0^{7/6} - (D_0 - mx)^{7/6}] \tag{4.245}$$

From eq. 4.244 and 4.245:

$$S = S_x + S_y$$

where

$$S_x = \frac{KU^2 X \cos\theta}{g[D_0 - (D + S)]} \ln \frac{D_0}{(D + S)} \tag{4.246}$$

$$S_y = \frac{6}{7} \frac{fUX}{g} \left(\frac{K}{\mathcal{K}} \sin\theta\right)^{1/2} \left[\frac{D_0^{7/6} - (D + S)^{7/6}}{D_0 - (D + S)}\right] \tag{4.247}$$

At the coastline, $D = D_c$ and $X = F$, the fetch length. Hence, eq. 4.246 becomes

$$S_x = \frac{KU^2 F \cos\theta}{g[D_0 - (D_c + S)]} \ln \frac{D_0}{(D_c + S)} \tag{4.248}$$

For small values of $D_c + S$, eq. 4.247 becomes

$$S_y = \frac{6}{7} \frac{fUF}{g} \left(\frac{K}{\mathcal{K}} \sin\theta\right)^{1/2} D_0^{1/6} \tag{4.249}$$

Here, D_c includes the astronomical tide. For the technique of choosing D_c, D_0, and F, see Bretschneider (1975).

Some Miscellaneous Works

Rao and Mazumdar (1966) expressed the storm surge S as

$$S = B + P + X + F \tag{4.250}$$

where B is the static rise due to atmospheric pressure deficiency towards the center of the storm, P is the rise due to piling up of the water against the coast by offshore winds, X is the height of crests of individual waves (wind-generated waves) superimposed on the general rise of the water level, and F is the effect of forerunners.

Of these, P and X are the most important. These authors combined the effects of B, P, and X and gave the following formula for the surge:

$$S = \frac{5}{3} \times 4.8 \times 10^{-9} \overline{W^2} \sum_{d_1 \cdot \Delta D_1}^{d_n \cdot \Delta D_n} \frac{\Delta D}{D} + \frac{5}{3} \frac{\Delta P_a}{g} \times 10^{-3} \tag{4.251}$$

where W is the sustained speed of the onshore component of the wind, ΔD is the horizontal length of a section, d is the depth of the water column, and ΔP_a is the pressure deficiency (in millibars) at the point under consideration.

Murty and Polavarapu (1975) expressed the surge S as a combination of S_1 (inverse barometric effect), S_2 (due to the component of wind stress perpendicular to the bottom contours), and S_3 (bathystrophic storm surge):

$$(4.252) \quad S_1 = 1.14\Delta P_0(1 - e^{-R/r})$$

where ΔP_0 is the reduction in atmospheric pressure in inches of mercury, R is the radius of the maximum winds, r is the radial distance from the storm center to the point of interest, and the factor 1.14 converts inches of mercury to feet. For the second component:

$$(4.253) \quad S_2 = \sum_{1}^{N-1} \Delta S_i$$

where ΔS_i is the rise in water level in an increment of distance N (in units of grid increments) along the profile due to wind action. In general:

$$(4.254) \quad \Delta S_i = d_t \sqrt{\frac{2KUU_x(\Delta x + 1)}{g(d_t)^2}} - 1$$

where d_t is the total water depth at the point under consideration, including the rise from all previous sections but excluding S_i for the section under consideration, K is a stress parameter equal to 3.0×10^{-6}, U is the absolute wind speed, U_x is the component of the wind speed in the profile direction, and Δx is the increment of horizontal distance along the profile.

Bolduc (1974) used empirical techniques to simulate storm surges at Point Petre on Lake Ontario. Hamblin and Budgell (1973) used empirical techniques to calculate storm surges in Lake St. Clair (which connects the Detroit River with the St. Clair River). Armstrong (1962) also used empirical techniques to simulate storm surges on the west coast of Canada. These three papers will be considered in some detail in section 7.1.

Barrientos and Jelesnianski (1976) and Jelesnianski and Barrientos (1975) used empirical techniques to compute storm surges on the east coast of the United States due to hurricanes and extratropical storms. Donn (1958) used empirical techniques for predicting storm surges at six locations on the northeast coast of the United States. Wilson (1959) did a comprehensive study of storm surges in New York due to hurricanes, using empirical techniques. Kajiura (1959) made a thorough study of certain aspects of storm surges on the east coast of the United States. These papers will be treated in some detail in section 7.2.

4.3 Graphical Techniques

Reid (1956) appears to be among the first to use a graphical technique (method of characteristics) for calculating storm surges. By ignoring Coriolis force and bottom friction and using one-dimensional hydrodynamic equations, he evaluated the changes in the water level at the shore of a sloping shelf due to a wind field moving directly on shore. It should be noted that the graphical method's appeal was mainly in the precomputer era. However, for engineering and practical purposes and quick and approximate estimates, the graphical methods, along with empirical and statistical methods, have a useful role to play in storm surge studies.

Method of Wave Derivatives

The method of characteristics (e.g. see Freeman 1951), as is commonly understood,

is used when there are two independent variables. Freeman and Baer (1957) developed a technique that can be used with three independent variables (e.g. the two horizontal coordinates x and y and time t); they referred to this technique as "the method of wave derivatives." With the neglect of bottom friction, the equations of motion and continuity are

$$\frac{\partial u}{\partial t} + u\frac{\partial u}{\partial x} + v\frac{\partial u}{\partial y} + c\frac{\partial}{\partial x}(2c) = fv + \frac{\tau_{S_x}}{\rho h} \tag{4.255}$$

$$\frac{\partial v}{\partial t} + u\frac{\partial v}{\partial x} + v\frac{\partial v}{\partial y} + c\frac{\partial}{\partial y}(2c) = -fu + \frac{\tau_{S_y}}{\rho h} \tag{4.256}$$

$$\frac{\partial}{\partial t}(2c) + u\frac{\partial}{\partial x}(2c) + v\frac{\partial}{\partial y}(2c) + c\frac{\partial u}{\partial x} + c\frac{\partial v}{\partial y} = 0 \tag{4.257}$$

where $c = \sqrt{gh}$ (h is the water depth, assumed to be uniform).

Equations 4.255–4.257 are combined in four different ways, i.e. [1] ± [2] ± [3]. Here, the notation [ ] represents the left side of the corresponding equation. This operation yields four equations. To both sides of these four equations, add and subtract $(\partial v/\partial x + \partial u/\partial y)$. Let the resulting four equations be A, B. C, and D. Then, the following four operators again result in the following four equations ([A + B], [C + D], [A + C], and [B + D]):

$$\frac{D_1A_1}{dt} + \frac{D_2A_2}{dt} = 2fv + \frac{2\tau_{S_x}}{\rho h} \tag{4.258}$$

$$\frac{D_3A_3}{dt} + \frac{D_4A_4}{dt} = 2fv + \frac{2\tau_{S_x}}{\rho h} \tag{4.259}$$

$$\frac{D_1A_1}{dt} + \frac{D_3A_3}{dt} = 2fv - 2u + \frac{2\tau_{S_x}}{\rho h} + \frac{2\tau_{S_y}}{\rho h} \tag{4.260}$$

$$\frac{D_2A_2}{dt} + \frac{D_4A_4}{dt} = 2fv + 2fu + \frac{2\tau_{S_x}}{\rho h} - \frac{2\tau_{S_y}}{\rho h} \tag{4.261}$$

where

$$\begin{aligned}
\frac{D_1}{dt} &\equiv \frac{\partial}{\partial t} + (u + c)\frac{\partial}{\partial x} + (v + c)\frac{\partial}{\partial y} \\
\frac{D_2}{dt} &\equiv \frac{\partial}{\partial t} + (u + c)\frac{\partial}{\partial x} + (v - c)\frac{\partial}{\partial y} \\
\frac{D_3}{dt} &\equiv \frac{\partial}{\partial t} + (u - c)\frac{\partial}{\partial x} + (v - c)\frac{\partial}{\partial y} \\
\frac{D_4}{dt} &\equiv \frac{\partial}{\partial t} + (u - c)\frac{\partial}{\partial x} + (v + c)\frac{\partial}{\partial y}
\end{aligned} \tag{4.262}$$

and

$$\begin{aligned}
A_1 &\equiv u + v + 2c \\
A_2 &\equiv u - v + 2c \\
A_3 &\equiv u + v - 2c \\
A_4 &\equiv u - v - 2c
\end{aligned} \tag{4.263}$$

In eq. 4.258–4.261, temporarily set f and τ_{S_x} to zero. Then, the resulting equations are relatively easy to solve graphically. The equation

$$\frac{D_1A_1}{dt} + \frac{D_2A_2}{dt} = 0 \tag{4.264}$$

means if we move along vector V_1 (with components $u + c$ and $v + c$) and measure A_1, and along vector V_2 (with components $u + c$, $v - c$) and measure A_2, the sum of the changes in A_1 and A_2 measured in this manner do not change.

When f and τ_{S_x} are not zero, in eq. 4.258 multiply and divide the right side by $\partial A_1/\partial x$ to give

$$\frac{D_1A_1}{dt} + \frac{D_2A_2}{dt} = \left[\frac{2\left(fv + \frac{\tau_{S_x}}{\rho h}\right)}{\left(\frac{\partial A_1}{\partial x}\right)}\right]\left(\frac{\partial A_1}{\partial x}\right)$$

Define the following operator:

$$\frac{D_1'}{dt} \equiv \frac{\partial}{\partial t} + \left[(u + c) - \frac{2\left(fv + \frac{\tau_{S_x}}{\rho h}\right)}{\left(\frac{\partial A_1}{\partial x}\right)}\right]\frac{\partial}{\partial x} + (v + c)\frac{\partial}{\partial y} \tag{4.265}$$

Then, eq. 4.258 can be written as

$$\frac{D_1'A_1}{dt} + \frac{D_2A_2}{dt} = 0 \tag{4.266}$$

Equation 4.266 can be treated exactly as eq. 4.264 except that vector V_1 involves $\partial A_1/\partial x$. Thus, eq. 4.258–4.261 become, in addition to eq. 4.266,

$$\frac{D_3A_3}{dt} + \frac{D_4'A_4}{dt} = 0 \tag{4.267}$$

$$\frac{D_4''A_1}{dt} + \frac{D_3A_3}{dt} = 0 \tag{4.268}$$

$$\frac{D_2A_2}{dt} + \frac{D_4''A_4}{dt} = 0 \tag{4.269}$$

where

$$\frac{D_4'}{dt} \equiv \frac{\partial}{\partial t} + \left[(u - c) - \frac{2\left(fv + \frac{\tau_{S_x}}{\rho h}\right)}{\frac{\partial A_4}{\partial x}}\right]\frac{\partial}{\partial x} + (v + c)\frac{\partial}{\partial y} \tag{4.270}$$

$$\frac{D_1''}{dt} \equiv \frac{\partial}{\partial t} + \left[(u + c) - \frac{\left(2fv + \frac{\tau_{S_x}}{\rho h}\right)}{\left(\frac{\partial A_1}{\partial x}\right)} - \frac{\left(-2fu + \frac{\tau_{S_y}}{\rho h}\right)}{\left(\frac{\partial A_1}{\partial x}\right)}\right] + (v + c)\frac{\partial}{\partial y} \tag{4.271}$$

$$(4.272)\quad \frac{D_4''}{dt} \equiv \frac{\partial}{\partial t} + \left[(u - c) - \frac{\left(2fv + \frac{2\tau_{S_x}}{\rho h}\right)}{\left(\frac{\partial A_4}{\partial x}\right)} + \frac{\left(-2fu + \frac{2\tau_{S_y}}{\rho h}\right)}{\left(\frac{\partial A_4}{\partial x}\right)} \right] \frac{\partial}{\partial x} + (v + c)\frac{\partial}{\partial y}$$

A knowledge of u, v, and c at a given time enables determination of A_1 to A_4 at that time. The above equations can then be used to calculate $A_1 + A_2$, $A_3 + A_4$, $A_1 + A_3$, and $A_2 + A_4$ at a later time. But the situation is not straightforward because of the following reason. From the following set of equations

$$A_1 + A_2 = K_1$$
$$A_3 + A_4 = K_2$$
$$A_1 + A_3 = K_3$$
$$A_2 + A_4 = K_4$$

one cannot determine A_1 to A_4 because the equations are not linearly independent. Since the aim is to determine u, v, and c, one can write from eq. 4.263

$$(4.273)\quad u = \frac{(A_1 + A_3) + (A_2 + A_4)}{4}$$

$$(4.274)\quad v = \frac{(A_1 + A_3) - (A_2 + A_4)}{4}$$

$$(4.275)\quad 2c = \frac{(A_1 + A_2) - (A_3 + A_4)}{4}$$

Then

$$(4.276)\quad \begin{aligned} A_1 &= \frac{(A_1 + A_3)}{2} + \left[\frac{(A_1 + A_2) - (A_3 + A_4)}{4}\right] \\ A_2 &= \frac{(A_2 + A_4)}{2} + \left[\frac{(A_1 + A_2) - (A_3 + A_4)}{4}\right] \\ A_3 &= \frac{(A_1 + A_3)}{2} - \left[\frac{(A_1 + A_2) - (A_3 + A_4)}{4}\right] \\ A_4 &= \frac{(A_2 + A_4)}{2} - \left[\frac{(A_1 + A_2) - (A_3 + A_4)}{4}\right] \end{aligned}$$

Once the terms such as $A_1 + A_2$, etc., are determined, using graphical addition and subtraction one can determine $2c$ first and then A_1 to A_4. Freeman and Baer (1957) used this method to determine the u and v fields associated with the spread of a mound of water placed in a basin of uniform depth.

The Bathystrophic Storm Surge

Freeman et al. (1957) introduced the concept of "bathystrophic storm tide" as the surge that results from winds blowing parallel to the coastline; they showed that this is a very important component of the storm surge. The calculation of the bathystrophic storm surge is somewhat simpler than the traditional two-dimensional surge computations.

Bretschneider (1966b) mentioned that there are at least two well-documented cases of bathystrophic storm surge (i.e. winds blowing parallel to the coast causing extreme surges): Hurricane Carla during September 9–12, 1961, in the Gulf of Mexico and the Ash Wednesday storm on the east coast of the United States during March 5–6, 1962. Pararas-Carayannis (1975) used a bathystrophic approach to study storm surges on the east coast of the United States due to hurricanes. This will be considered in some detail in section 7.2.

To formulate the bathystrophic storm surge, Freeman et al. (1957) began with the assumption that on an open coastline with regular depth contours there is no sustained transport towards the shore across the depth contours. The justification used is that if there were such a sustained transport, then much larger land areas than are usually observed should be inundated. These authors mathematically justify this assumption in their appendix. To give a numerical example, they stated that a 20-knot (37 $km \cdot h^{-1}$) wind blowing toward the shore for a period of 10 h, *if uncompensated*, would create a surge of 6-ft (1.8 m) amplitude which would penetrate 60 mi (96 km) inland. This result follows from the simple relation:

$$\frac{\partial F_x}{\partial t} = \frac{\tau_{S_x}}{\rho}$$

where F_x is the flux normal to the depth contours, t is time, τ_{S_x} is the x component of the wind stress (i.e. the component perpendicular to the coast), and ρ is the water density. A similar result holds for offshore flow. Freeman et al. (1957) defined the "compensating sustained current" as the bathystrophic flow. (This concept is somewhat analogous to geostrophic flow in the atmosphere.)

The second assumption made is that divergence of the velocity field does not bring about significant changes in the water level. In justification of this, they mentioned that a mound of water placed on a sea surface with a sloping bottom will be dissipated in a much shorter time than its potential buildup. Basically, these authors have assumed that a small amount of cross-contour transport develops to compensate for the divergence in the bathystrophic current and the continuity equation need not be considered.

A third assumption is that the water level changes in a direction parallel to the shore (i.e. the y direction) are insignificant. A fourth and final assumption is that space derivatives of the current speed are negligible compared with the Coriolis term. These four assumptions can be mathematically expressed as follows:

$$|F_x| \ll |F_y| \tag{4.277}$$

$$\left|\frac{\partial F_y}{\partial y}\right| \ll \left|\frac{\partial \eta}{\partial t}\right| \tag{4.278}$$

$$\left|gh\frac{\partial \eta}{\partial y}\right| \ll \left|\frac{\tau_{S_y}}{\rho}\right| \tag{4.279}$$

$$\frac{\partial u}{\partial x}, \quad \frac{\partial u}{\partial y}, \quad \frac{\partial v}{\partial x}, \quad \frac{\partial v}{\partial y} \ll f \tag{4.280}$$

Here,

$$F_x = \int_{-h}^{\eta} u dz$$

$$F_y = \int_{-h}^{\eta} v dz$$

where u and v are the current speeds in the x (x is positive towards the shore) and y directions, h is the mean low water depth, η is the deviation of the water level from the mean low water depth, and τ_{S_x} and τ_{S_y} are the wind stress components in the x and y directions.

Vertical integration of the equations of motion and use of eq. 3.426 gives

$$\frac{\partial F_x}{\partial t} = -gh\frac{\partial \eta}{\partial x} + fF_y + \frac{\tau_{S_x}}{\rho} - \frac{\tau_{B_x}}{\rho} \tag{4.281}$$

$$\frac{\partial F_y}{\partial t} = -gh\frac{\partial \eta}{\partial y} - fF_x + \frac{\tau_{S_y}}{\rho} - \frac{\tau_{B_y}}{\rho} \tag{4.282}$$

where τ_B is the bottom stress. Using eq. 4.277 and 4.278, these reduce to

$$gh\frac{\partial \eta}{\partial x} = fF_y + \frac{\tau_{S_x}}{\rho} - \frac{\tau_{B_x}}{\rho} \tag{4.283}$$

$$\frac{\partial F_y}{\partial t} = \frac{\tau_{S_y}}{\rho} - \frac{\tau_{B_y}}{\rho} \tag{4.284}$$

Using eq. 4.277 and using Manning's form, the bottom friction can be written as (Linsley et al. 1949)

$$\begin{aligned} \frac{\tau_{B_x}}{\rho} &= 0 \\ \frac{\tau_{B_y}}{\rho} &= \frac{K}{h^{7/3}}F_y^2 \end{aligned} \tag{4.285}$$

where K is a bottom friction parameter.

Hence, the two prediction equations for the two unknowns η and F_y from eq. 4.283–4.285 are

$$\frac{\partial F_y}{\partial t} = \frac{\tau_{S_y}}{\rho} - \frac{K}{h^{7/3}}F_y^2 \tag{4.286}$$

$$gh\frac{\partial \eta}{\partial x} = fF_y + \frac{\tau_{S_x}}{\rho} \tag{4.287}$$

Using eq. 4.286, F_y can be calculated at a given time step, and then using eq. 4.287, η can be determined by beginning at the deep water where η is assumed to be zero. Freeman et al. (1957) suggested that on a time scale of several hours and over 25–50 mi (40–80 km) of open coastline, the bathystrophic storm surge is a good approximation to the total storm surge.

Solutions for Lakes and Bays with Uniform and Variable Depth

The energy imparted by a moving atmospheric disturbance to a water body depends on the degree of resonant coupling that is possible when the speed of movement of the atmospheric disturbance is approximately equal to that of the free gravity waves in the water body. Chrystal (1908) considered an atmospheric pressure jumpline moving with constant speed and intensity over infinite and semi-infinite water bodies, and he also looked into the question of resonance. Takegami (1938) studied the influence of initial conditions in the case of a pressure jump moving from the open sea towards the coast.

If the horizontal scale of the atmospheric disturbance is smaller than the horizontal scale of the water body, the water body can be considered semi-infinite. On the other hand,

if the scale of the water body is comparable with or smaller than the scale of the atmospheric disturbance, then one must consider the reflection of the gravity waves at the lateral boundaries of the water body. In connection with the study of a surge on Lake Michigan, Harris (1957a) gave a solution for the case of a finite canal valid for a short interval of time.

Rao (1967) studied the water level oscillations in a lake due to an atmospheric disturbance passing over the lake. He ignored the influence of the earth's rotation (his study is aimed at Lake Erie, which is a narrow elongated lake) and bottom friction (somewhat justified as long as interest focuses on the initial transient motion).

Following Rao, consider a lake of uniform depth h, uniform width, and uniform density ρ. Take the origin of a Cartesian coordinate system at the undisturbed level of the lake surface and z-axis upward, y-axis along the width, and x-axis along the length of the lake. The lake has rigid boundaries at $x = 0$ and $x = L$. In the one-dimensional case the vertically integrated equation of motion and continuity are, after ignoring the nonlinear terms and using the hydrostatic relation,

$$\frac{\partial M}{\partial t} = -c^2 \frac{\partial \eta}{\partial x} + R \tag{4.288}$$

$$\frac{\partial \eta}{\partial t} = -\frac{\partial M}{\partial x} \tag{4.289}$$

where

$$M = \int_{-h}^{0} u\,dz$$

u being the velocity component in the x direction. The external force R is expressed as

$$R = \frac{\tau}{\rho}$$

where τ is the surface wind stress. In the above equations η is the deviation of the water level from its equilibrium position and $c^2 = gh$ (c is the speed of free long gravity waves in the lake). Ignoring rotation gives a nondispersive system and all the gravity waves propagate with the same speed. The boundary conditions are

$$M = 0 \text{ at } x = 0 \text{ and } x = L \tag{4.290}$$

Initially, the lake is at rest, i.e. $M = 0$ and $\eta = 0$ at $t = 0$.

Rao defined the setup as the difference in the water levels at $x = L$ and $x = 0$. Equations 4.288 and 4.289 are solved for a prescribed R as a function of x and t. For convenience, define the following dimensionless parameters:

$$\begin{aligned} \frac{x}{L} &\equiv x^* \\ \frac{ct}{L} &\equiv t^* \\ \frac{c^2\eta}{R_0 L} &\equiv \eta^* \\ \frac{cM}{R_0 L} &\equiv M^* \\ \frac{R}{R_0} &\equiv R^* \end{aligned} \tag{4.291}$$

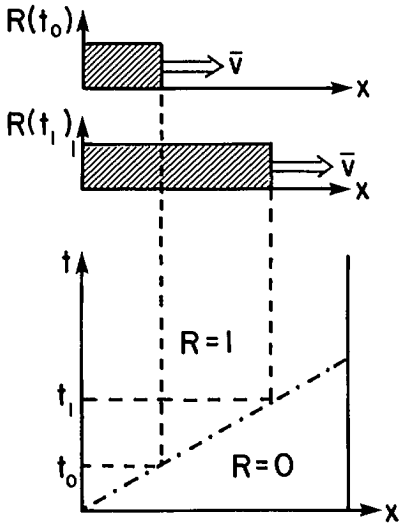

FIG. 4.9. Schematic in the (x, t) plane of a semi-infinite wind-stress band moving across a lake of uniform depth. The dashed–dotted line shows the position of the leading edge of the stress band. (Rao 1967)

where R_0 is a scale value of the wind stress.

Substituting eq. 4.291 in eq. 4.288 and 4.289 and then adding and subtracting eq. 4.289 in eq. 4.288 gives (omitting the asterisk for convenience)

$$\frac{\partial}{\partial t}(M \pm \eta) \pm \frac{\partial}{\partial x}(M \pm \eta) = R \tag{4.292}$$

Essentially, this states that

$$\frac{d}{dt}(M \pm \eta) = R \text{ for } \frac{dx}{dt} = \pm 1 \tag{4.293}$$

For a lake of uniform depth, the positive and negative characteristics are straight lines given by $x = \pm t +$ constant.

Following Rao (1967), consider the case of a semi-infinite stress band moving with a speed V (nondimensionalized by $\sqrt{gh}$), as shown in Fig. 4.9. For this case:

$$\begin{aligned} R &= 0 \text{ for } t \leq \frac{x}{V} \\ R &= 1 \text{ for } t \geq \frac{x}{V} \end{aligned} \tag{4.294}$$

The top part of Fig. 4.9 shows two successive positions of the stress band and the bottom parts show R in the $x-t$ plane. For details on the integration of eq. 4.293 using the method of characteristics, see Rao (1967) who considered the two cases $V > 1$ (atmospheric disturbances traveling faster than $\sqrt{gh}$) and $V < 1$.

The case of a finite-stress band can be studied by the superposition (this is permissible in the linear case studied here) of a positive stress band and a negative stress band of the

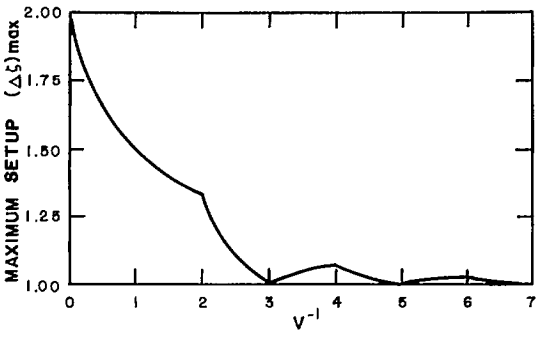

FIG. 4.10. Maximum setup (ordinate) versus V^{-1} for a semi-infinite stress band. (Rao 1967)

same intensity (as the positive stress band), both moving with the same speed and in the same direction but with their jumps separated by a finite distance. The formulae for the setup in the case of the negative stress band are the same as the formulae for the positive stress band, except that the sign of the setup must be reversed and $t - T$ substituted where t appears (here, T is the dimensionless time interval between transits of the front and rear of the stress band at a fixed point). Hence, one can write

$$R = 0 \text{ for } t \leq \frac{x}{V} \text{ and } t \geq \frac{x}{V} + T$$

$$R = 1 \text{ for } \frac{x'}{V} \leq t \leq \frac{x}{V} + T \tag{4.295}$$

Again, see Rao (1967) for a detailed form of the solutions. The interesting results obtained from this study can be summarized as follows. With reference to Fig. 4.10 for a given V, the maximum setup for all time and all band widths is achieved for a semi-infinite stress band. If $V = 1$ the maximum is reached for all band widths $a > 1$ (i.e. for all stress band widths greater than the lake length). For $V > 1$, the maximum is reached for all band widths $a > V$. The most important result is that for all t, all a, and all V, the maximum setup is achieved for the case of an instantaneous semi-infinite stress band. In the case of the semi-infinite stress band the maximum setup decreases from its dimensionless upper limit of 2 at $1/V = 0$ to a lower limit of 1 at $1/V = 3$, after which the response curve shows a sawtooth type behavior (see Fig. 4.10) and the setup reaches a value of 1 asymptotically as $1/V \rightarrow \infty$.

To study the response in the case of finite band widths, one must consider two cases: $a > 1$ and $a < 1$. For the case $a < 1$, the maximum setup for all t and all V is achieved at $V = 1$, which shows the importance of resonant coupling. For the case $a > 1$, the maximum setup is achieved for $a/V = 1$ ($a/V = 1$ means that the time taken by the stress band to pass a fixed point in the lake is the same as the time taken by a free gravity wave to cross the lake). In the case of a pressure jump (i.e. stress band of zero width) due to resonant coupling, a setup of magnitude 1 is produced at $V = 1$ and the setup is 0 for all other V. The setup for different transit times is shown in Fig. 4.11.

Rao (1967) also solved the response of the fundamental mode (his appendix A) and showed for the semi-infinite case that the maximum setup of 1.62 occurs at $1/V = 0$ and decreases to 0.81 as $1/V$ increases from 0 to 3; after this, the setup shows essentially the same features as the total response, but with a smoother variation.

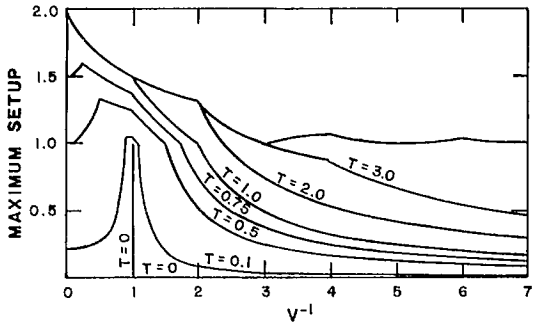

FIG. 4.11. Maximum setup versus V^{-1} for various transit times T. (Rao 1967)

Irish and Platzman (1962) performed a statistical study of storm surges on Lake Erie and conlcuded that resonant coupling is not important. Rao (1967) explained this apparent disagreement between these results and his results by pointing out that statistical evidence for resonance requires a classification based on band width. Since Irish and Platzman did not sort out their data according to band width, they did not find significant support for resonant coupling.

Platzman (1963) found in a numerical calculation of storm surges on Lake Erie that the fundamental mode is quite well developed in some cases and quenched in others. Rao (1969) examined this by calculating the residual energy in the fundamental mode (residual energy is the energy left after the passage of the atmospheric disturbance). Rao showed in his appendix B that there are certain adverse combinations of width and propagation speed of the stress band that quench the fundamental mode by extracting a major part of the energy supplied to the lake during the passage of the disturbance over the lake.

Rao (1969) extended his earlier study to the case of a bay (in the case of a bay, only one lateral boundary is closed). In the case of the lake the boundary condition at both the lateral boundaries is zero volume transport whereas in the case of the bay, at the closed end a zero volume transport is invoked and at the open end the water level fluctuation is prescribed as zero.

Next, a lake with variable depth is considered. Murty (1971) used the method of characteristics to study the case of a lake with a depth discontinuity. The formulation and the method of solution are similar to that of Rao (1967). For a lake of length L and uniform density ρ, let the left boundary be $x = 0$, the depth discontinuity at $x = L/2$, and the right boundary at $x = L$. The vertically integrated forms of the equations of motion and continuity in the areas to the left side of the depth discontinuity (subscript 1) and the right side of the discontinuity (subscript 2) are

$$\frac{\partial M_{1,2}}{\partial t} = -gD_{1,2}\frac{\partial h_{1,2}}{\partial x} + R \tag{4.296}$$

$$\frac{\partial h_{1,2}}{\partial t} = -\frac{\partial M_{1,2}}{\partial x} \tag{4.297}$$

where

$$M_{1,2} \equiv \int_{-D_{1,2}}^{h_{1,2}} u_{1,2}\,dz$$

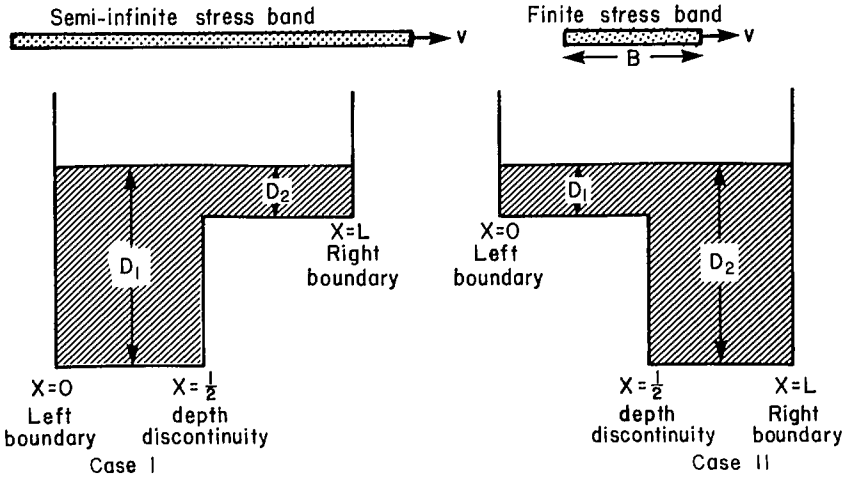

FIG. 4.12. Semi-infinite stress band moving over deeper to shallower water and a finite stress band moving over shallower to deeper water.

Here, M is the volume transport through a vertical section and u is the velocity component along the length of the lake; $R = \tau/\rho$, τ is the wind stress, and ρ is water density. The boundary conditions are

$$\begin{aligned} M_1 &= 0 \text{ at } x = 0 \\ M_2 &= 0 \text{ at } x = L \end{aligned} \tag{4.298}$$

At the depth discontinuity, continuity of M and h is invoked:

$$\begin{aligned} M_1 &= M_2 \\ &\text{at } x = \frac{L}{2} \\ h_1 &= h_2 \end{aligned} \tag{4.299}$$

Let $c_{1,2}$ represent the speeds of long gravity waves in regions 1 and 2. Then

$$c_{1,2}^2 = gD_{1,2} \tag{4.300}$$

Addition and subtraction of eq. 4.296 and 4.297 and using eq. 4.300 gives

$$\frac{d}{dt}(M_{1,2} \pm c_{1,2}h_{1,2}) = R \text{ for } \frac{dx}{dt} = \pm c_{1,2} \tag{4.301}$$

This means the quantity $M_{1,2} \pm c_{1,2}h_{1,2}$ is constant along the characteristics $dx/dt = \pm c_{1,2}$. Since both regions of the lake have uniform depths individually, the characteristics in both regions are straight lines with slopes c_1 and c_2.

The calculations were performed both for semi-infinite and finite stress bands traveling over deep to shallow (case I) and shallow to deep (case II) water. The left side of Fig. 4.12 shows an atmospheric disturbance of the semi-infinite stress band type moving from left to right with a constant speed V for case I. The right side shows a finite stress band for case II.

Murty (1971) performed the calculations for various combinations of parameters such as band width, V, c_1, and c_2. The water levels at the left and right boundaries for cases I

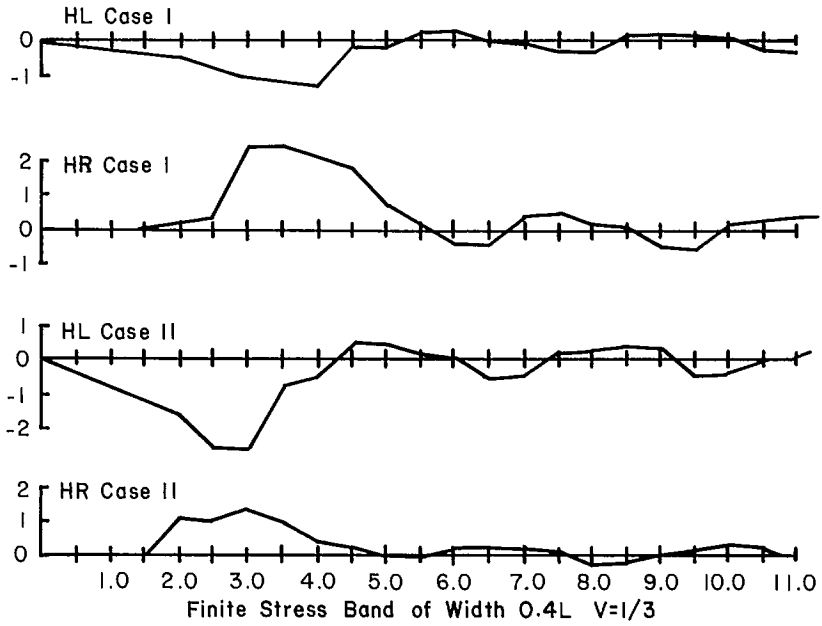

FIG. 4.13. Variation of water level at left and right boundaries for cases I and II for a finite stress band of width $0.4L$.

and II for a finite stress band of width $0.4\,L$ are shown in Fig. 4.13. The important results follow. For semi-infinite stress bands the water level at the left side is predominantly negative whereas it is positive on the right side and it becomes both positive and negative for finite band widths. The results for the case of a depth discontinuity differ from that without the discontinuity in that, whereas for the latter case the setup becomes periodic some time after the disturbance crosses the lake, this does not happen in the former case. Dingle and Young (1965) also used the method of characteristics to simulate storm surges in an idealized lake due to a moving squall line.

4.4 Statistical Techniques

In this section, statistical techniques for storm surge prediction for real time purposes will be considered. Those statistical techniques dealing with probability, theory of extremes, etc., will be discussed in Chapter 7. Harris (1962) appears to be among the first who suggested the relevance of statistical methods for storm surge prediction. He ascribed the superiority of statistical methods over dynamical methods to the nonrequirement in the former case of interpolation of input data in space and time, which is needed in the latter case. He also showed that one can derive a regression equation that can contain the same information as a numerical solution of the linearized storm surge equations.

Welander (1956, 1957) introduced the so-called "admittance method" (in his 1961 paper, he referred to it as the "influence method") for storm surge calculations. At each location where a storm surge prediction is needed, one must calculate an influence or admittance function. Either theoretical considerations or analysis of historical data can be

used to detemine this function. Hamblin (1978) also made use of the influence method in a calculation of storm surges on Lake St. Clair.

If the initial conditions lose their influence after some time interval, which is short compared with the time interval of the development of the surge, the solution of the linearized storm surge equations can be written as

$$(4.302) \quad \eta(x_0, y_0, t) = \sum a_{i,j,k}(x_0, y_0) F_{j,k}(t - i\Delta t)$$

where η is the storm surge amplitude at location (x_0, y_0) at time t, Δt is the time step, i is the number of time steps between the time of observation and time t, j is an index referring to the observation station, k is an index that denotes the nature of the observation, $F_{j,k}(t - i\Delta t)$ is a meteorological factor of type k from station j at time $t - i\Delta t$, and $a_{i,j,k}(x_0, y_0)$ are coefficients that depend on x_0, y_0, i, j, k, and η. Note that eq. 4.302 contains all the information about η inherent in the linear storm surge equations as well as the available meteorological data. As mentioned above, the values of a can be determined from theoretical considerations and the assumptions required for numerical solutions of the equations, or by evaluation of existing data.

In deriving statistically the regression equations, one requirement is that the observation stations be fixed and the same time lag pattern be used. However, these stations need not be equally spaced, nor must they be real stations (for example, they could be grid points on a chart).

Wilson (1960) studied storm surges in New York Bay resulting from two hurricanes and two extratropical cyclones and, using multivariate analysis, developed a model with nine regression coefficients. Four constants must be subjectively determined to make the regression analysis possible. Harris (1961) made some improvements to Wilson's model.

Storm Surge Forecasting on Lake Erie

Significant storm surges occur more often at Buffalo (at the eastern end of Lake Erie) than at any other location in the United States (Harris and Angelo 1963), probably because Buffalo is situated on the shallowest of the Great Lakes and in the path of traveling cyclones, and the local topography is conducive to significant storm surge generation. Irish and Platzman (1962) originally introduced the term "setup" to define the difference in the water level between Buffalo and Toledo (located at the western end of Lake Erie). This concept is supported by the fact that positive surges at Buffalo are almost always accompanied by negative surges at Toledo.

Harris and Angelo (1963) used hourly wind and pressure observations from six weather stations around Lake Erie, namely Toledo, Sandusky, Cleveland, Erie, Buffalo, and Clear Creek, and hourly lake level observations at two stations, namely Toledo and Buffalo; to derive the coefficients in eq. 4.302 they used linear as well as quadratic wind stress laws but the differences were insignificant.

Richardson and Pore (1969) discussed two methods for predicting surges at Buffalo and Toledo. The first method is for manual use at a weather forecast office and the second method is for use at a center where numerical weather forecasts are available in real time as input. However, both methods were developed using regression techniques and calibrated with dependent data and tested with independent data. The major axis of Lake Erie is along west–southwest – east–northeast, a direction in which significant winds can develop and be sustained. Irish and Platzman (1962) showed that the wind stress is mainly responsible for creating surges on Lake Erie and atmospheric pressure gradients are of secondary importance. (Platzman 1967 developed a simplified one-dimensional model for

operational storm surge forecasting.)

Richardson and Pore (1969) used the same input data as Harris and Angelo (1963), i.e. 19 dependent storms and 11 independent storms during the period 1940–59. However, their studies differed: whereas Harris and Angelo represented the pressure and wind fields over the lake by observed winds at several stations surrounding the lake, Richardson and Pore used a grid of sea level pressures. This is an improvement because this scheme is not affected (at least directly) by closing off some weather stations. Richardson and Pore (1972) extended their earlier study of 1969 using more data.

Richardson (1972) discussed the evaluation of Lake Erie storm surge forecasts for the period 1971–72 using regression equations. Pore et al. (1975), based on data from 1940 to 1972, deduced that the observed water level at Buffalo exceeded the monthly mean level by at least 1.4 m on an average of once a year and the water level at Toledo was depressed by the same amount with the same frequency. Schwab (1978) developed an operational forecasting model using the impulse response method. This model has the following features: two dimensionality of the lake and the wind field; resolves the wind and water level changes on an hourly basis (so that the peak surge may not be missed); the surge can be predicted at any point on the shoreline of the lake. In this model, forecast winds (e.g. Feit and Barrientos 1974) were used instead of sea level pressure.

Schwab began with a linear dynamical model and determined the response functions at several water level stations for three different types of forcing, namely lake average forcing, interpolated two-dimensional forcing, and forcing at Great Lakes wind forecast points. For a total of 15 episodes studied, inclusion of the atmospheric stability in determining the drag coefficient improved the prediction.

Richardson and Schwab (1979) compared storm surge forecasts for Lake Erie made from the statistical model of Richardson and Pore (1969) and the dynamical model of Schwab (1978) and concluded that the dynamical method yields better predictions at Buffalo than the statistical method. However, at Toledo the improvement using the dynamical method is slight.

For the statistical model, water level deviations from the monthly mean at Buffalo and Toledo were correlated with analyzed 6-h sea level pressure with the National Meteorological Center's (NMC) (Shuman and Hovermale 1968) primitive equation model (Fig. 4.14). Using a screening correlation program (Miller 1958) the best predictors were found for the storm surge. The regression equations have the form

$$h_k = A_0 + \sum_{j=1}^{n} A_j P_j \tag{4.303}$$

where h_k is the storm surge at time k, A_0 is a constant, A_j is the regression coefficient, P_j is the sea level pressure at a NMC grid point with a lag time of 0, 1, 2, 3, 4, or 5 h, and n is the number of predictors. In 1973 the regression equations were updated using atmospheric pressure as well as storm surge data for the period 1940–71. Six equations were developed for Buffalo whereas for Toledo, only three equations were derived (because water level data for Toledo were available only during even hours); observed pressures at NMC grid points 2, 3, 7, 8, 12, and 13 (Fig. 4.14) were used as predictors with a lag time of 0, 1, 2, 3, 4, or 5 h.

In the dynamical model (Schwab 1978), impulse response functions were used to calculate the storm surge height. The storm surge is represented as the weighted sum of forcing terms during some period before the specified time, i.e.

$$h_k = \sum_{j=1}^{m} \sum_{j=1}^{n} \vec{G}_{ij} \vec{\tau}_{i,k-j} \tag{4.304}$$

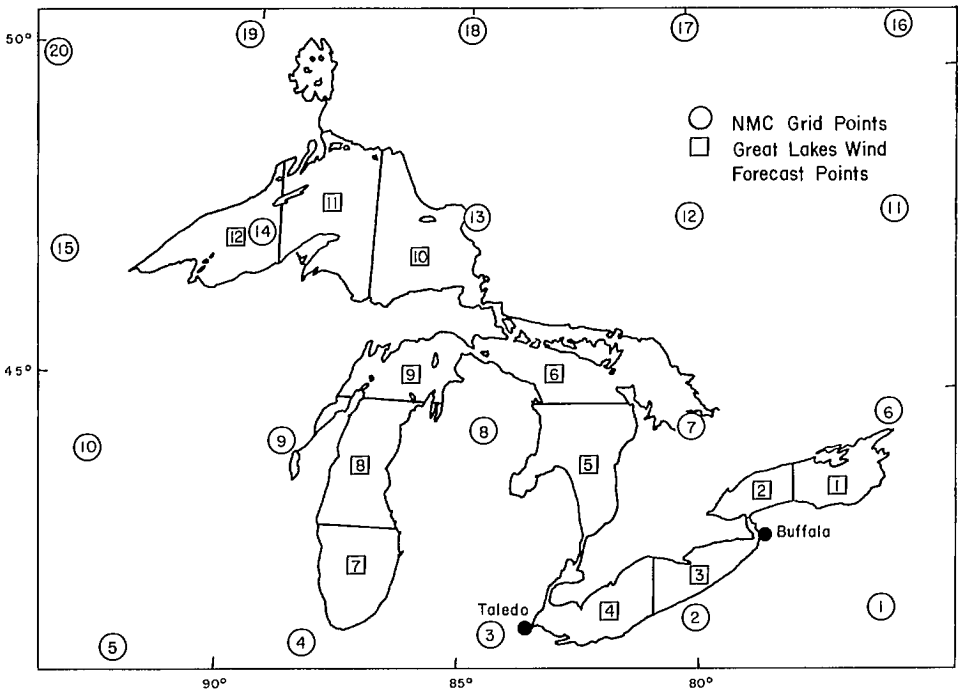

FIG. 4.14. Location of National Meteorological Center (NMC) primitive equation model grid points surrounding the Great Lakes and the Great Lakes wind forecast points. (Feit and Barrientos 1974)

where h_k is the storm surge at time k, $\vec{G}_{ij}$ is the water level response at time j due to an impulse from forcing at station i, $\vec{\tau}_{i,k-j}$ is the forcing function at station i and time $k-j$, m is the number of forcing stations, and n is the length of the response function. The forcing function is calculated as

$$\vec{\tau}_{ij} = C|\vec{V}_{ij}|V_{ij} \tag{4.305}$$

where $\vec{V}_{ij}$ is the wind vector at station i and time j and C is a dimensionless constant.

The response functions $\vec{G}_{ij}$ were calculated by means of a linear finite-difference numerical model of Lake Erie (Schwab 1978). To include hourly changes in the forcing function, the response functions are recorded as hourly values. The observed and forecasted storm surges at Buffalo using the dynamical and statistical methods are compared in Fig. 4.15. It can be seen that the dynamical method provided better prediction. Similar results for Toledo are shown in Fig. 4.16. In this case, the dynamical method is only slightly superior. In Fig. 4.17, comparison is made between observed storm surge and predicted storm surge using the dynamic method only for Buffalo and Toledo. As can be seen, the perdictions are quite reasonable.

STORM SURGE PREDICTION IN OTHER GREAT LAKES

Here, storm surge prediction in the other Great Lakes and connecting waters will be briefly considered. On Lake Ontario, one area of storm surge generation is Point Petre (Bolduc 1974). Although Point Petre is not located at the end of Lake Ontario, the storm surge here is greater than at any other location on this lake. For example, on January 25,

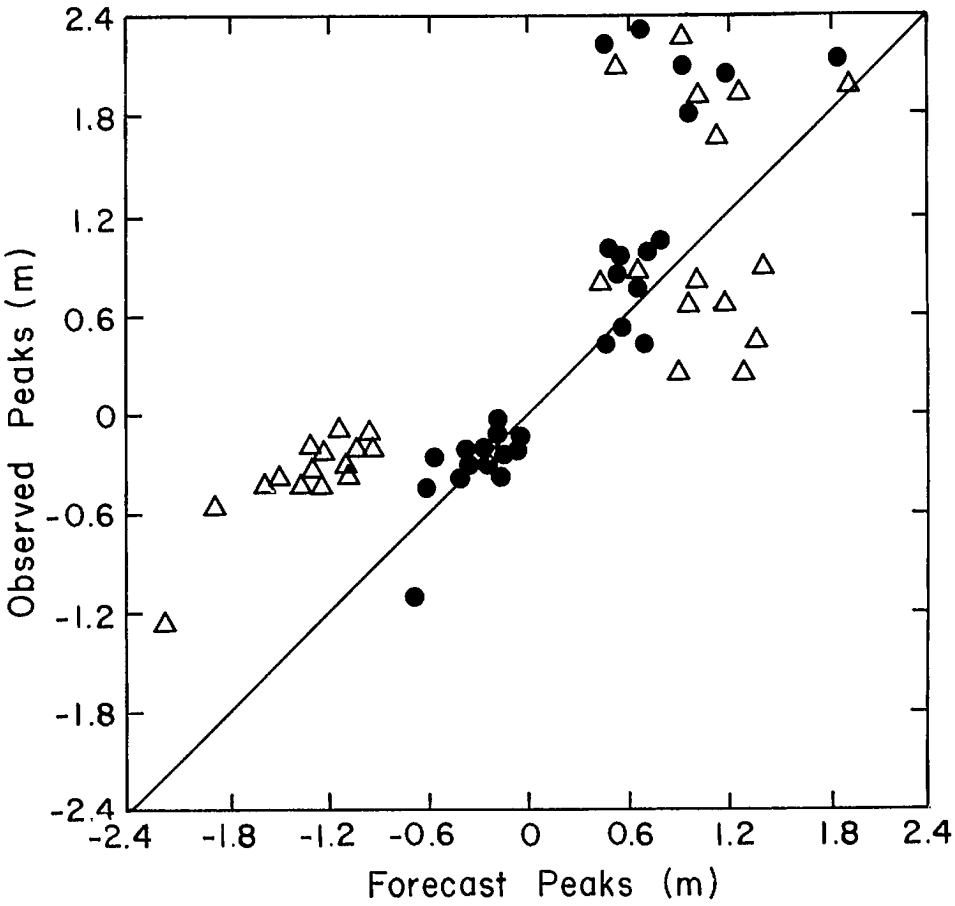

FIG. 4.15. Comparison of observed and computed peak storm surges at Buffalo, NY. ●, dynamical method; △, statistical method. (Richardson and Schwab 1979)

1972, the surge at Point Petre was 1 m whereas at Burlington (at the western end of the lake) the surge was only 27 cm and at Kingston (at the eastern end of the lake) the surge was 46 cm. Bolduc (1974) developed prediction formulae for storm surges at Point Petre, making use of the water level and wind measurements.

Hamblin and Budgell (1973) developed prediction equations for storm surges on Lake St. Clair. One important feature in this work is the inclusion of atmospheric thermal stability.

Venkatesh (1974) developed statistical regression models for storm surge prediction at several stations in Lakes Ontario, Erie, Huron (including Georgian Bay), and St. Clair. He mentioned that storm surges are not important in Lake Superior. Using data for the period 1961–73, regression relations in terms of sea level pressures and air–water temperature differences with lag times of 0–6 h have been developed for Lakes Ontario, Erie, Huron, and Georgian Bay, whereas for Lake St. Clair, the sea level pressures were replaced by local winds.

The grid points shown in Fig. 4.18 (also see Table 4.2) are the same as in the

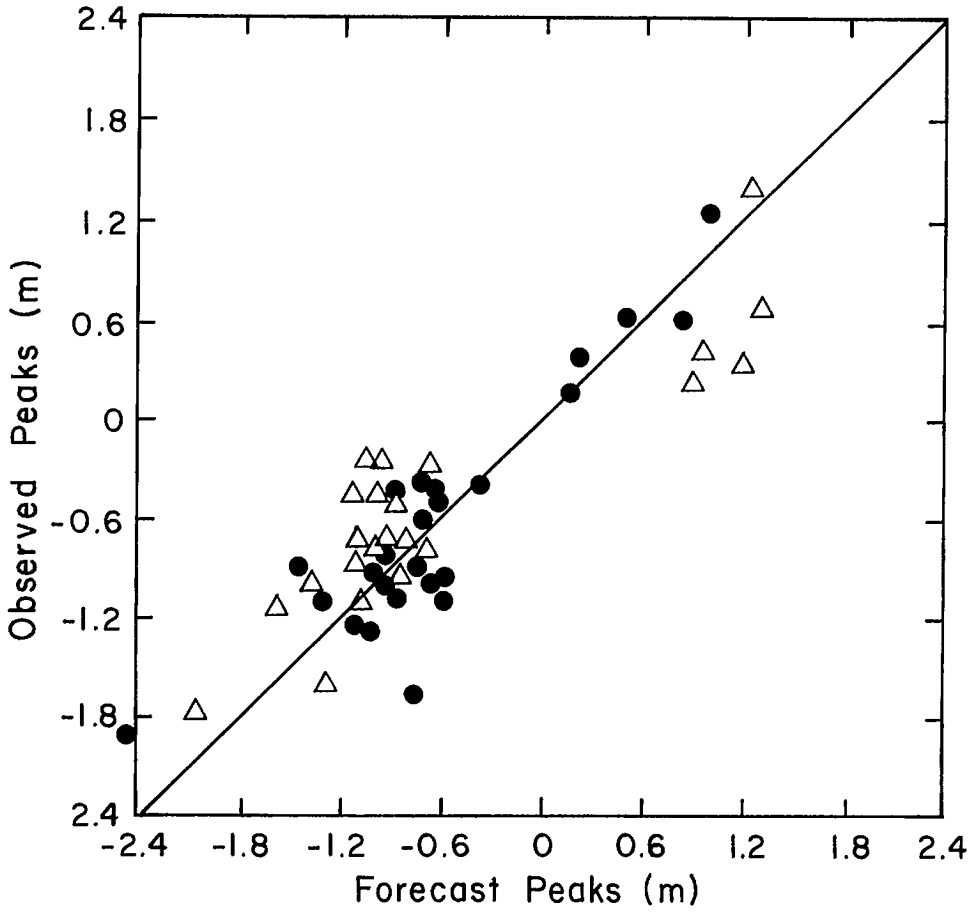

FIG. 4.16. Comparison of observed and computed peak storm surges at Toledo, OH. ●, dynamical method; △, statistical method. (Richardson and Schwab 1979)

Canadian Meteorological Center's numerical weather forecast models so that the sea level pressures forecast can be directly used. For Lake Erie grid points 1, 2, 3, 4, 6, and 7 are used, for Lakes Huron and Georgian Bay grid points 3, 4, 6, 7, 9, and 10 are used, and for Lake Ontario grid points 4, 5, 7, 8, 10, and 11 are used. The input data were divided into two parts, namely dependent and independent storms (Table 4.3). The data from the dependent storms have been used in developing the regression relations and the data from the independent storms are used to verify the models. The portion of the variance in the storm surges accounted for by the statistical method is between 55 and 75%. The model compares best with observed data for Lake St. Clair. The standard error of the estimate for all the lakes except Erie is between 0.2 and 0.3 ft (0.06–0.09 m) whereas for Lake Erie it is about 0.6 ft (0.18 m).

The following equation gives the storm surge S at Belle River on Lake St. Clair:

$$S = 0.0189 + 0.0007511V^2 - 0.0000446(T_A - T_W)_0V^2 + 0.0000149(T_A - T_W)_{-1}V^2 \tag{4.306}$$

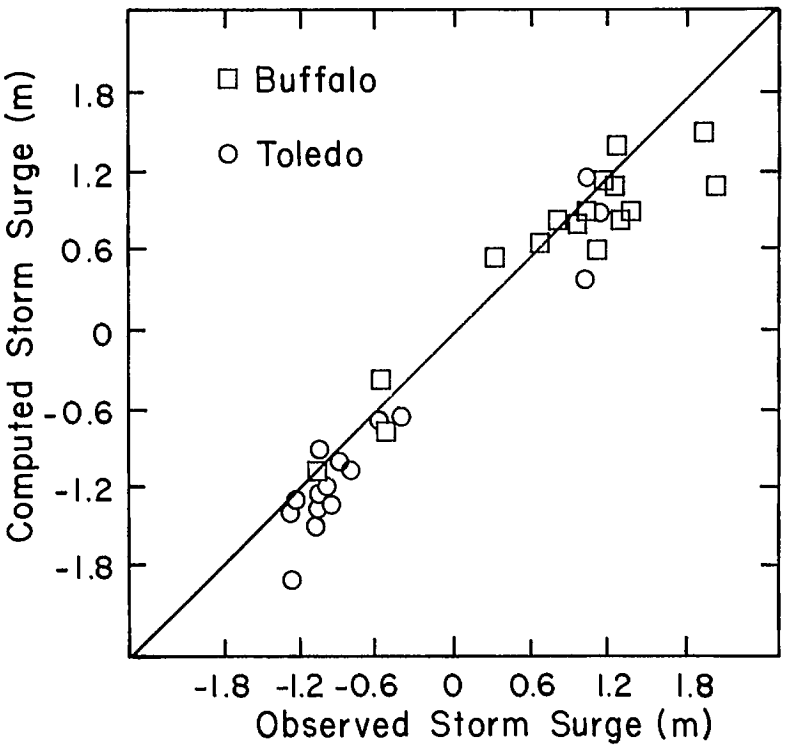

FIG. 4.17. Observed and computed (using dynamical method) peak surges at Buffalo (□) and Toledo (○). (Richardson and Schwab 1979)

TABLE 4.2. Stations for determining sea level pressure at each of the grid points of Fig. 4.18 (A, airport). (Venkatesh 1974)

Grid point	Station name	Station code	Grid point	Station name	Station code
1	Lexington	LEX	7	Wiarton (A)	YVV
	Cincinnati	CVG		Mount Forest	WMN
	Huntington	HTS		Muskoka (A)	YQA
2	Roanoke	ROA	8	Trenton	YTR
	Beckley	BKW		Ottawa Int. (A)	YOW
	Elkins	EKN		Massena	MSS
3	Fort Wayne	FWA	9	White River	YWR
	Toledo	TOL		Sault Ste. Marie	YAM
	Columbus	CMH		Timmins	YTS
4	Youngstown	YNG	10	Earlton (A)	YXR
	Erie	ERI	11	Val d'Or (A)	YVO
	Bradford	BFD		Roberval (A)	YRJ
5	Wilkes Barre	AVP		Ottawa Int. (A)	YOW
6	Houghton Lake	HTL			
	Oscada	OSC			
	Saulte Ste. Marie	SSM			

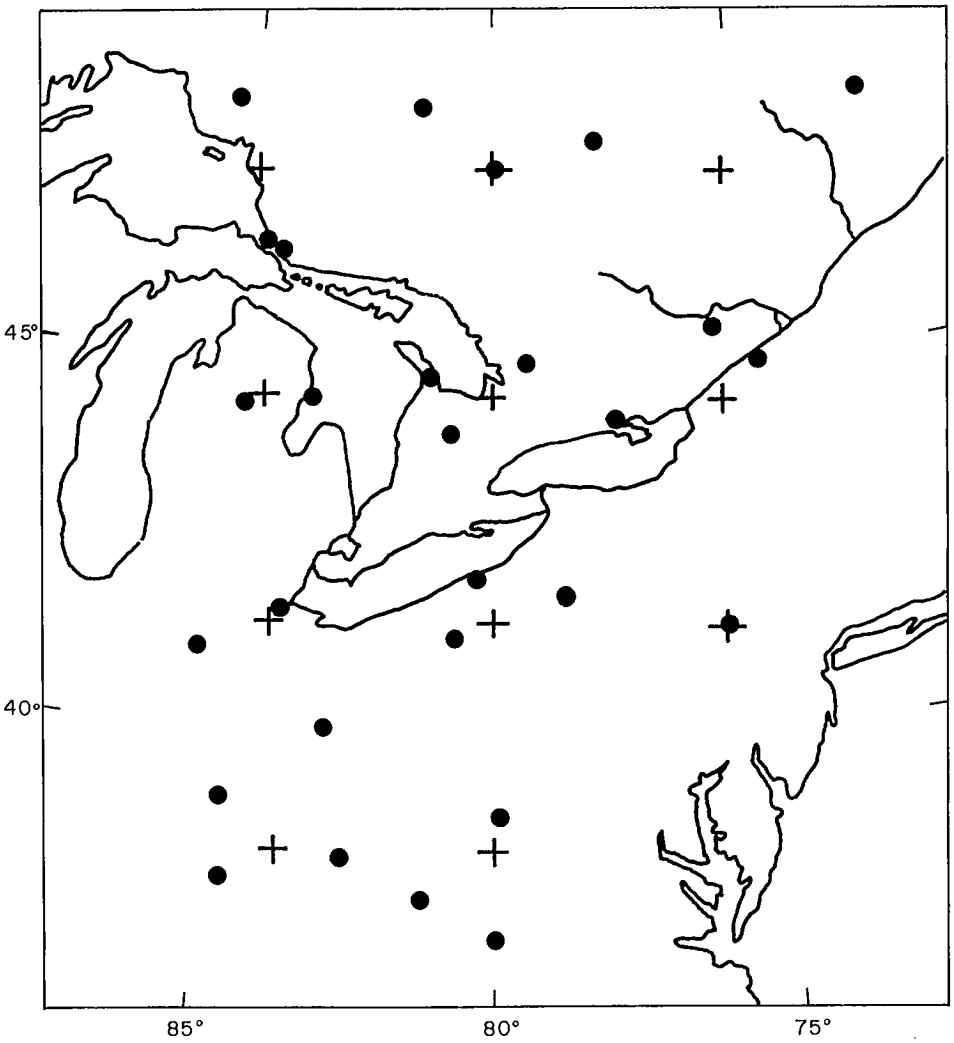

FIG. 4.18. Locations of grid points (+) and observing stations (●) for the Great Lakes area. (Venkatesh 1974)

TABLE 4.3. Number of dependent and independent storms by location for stations on Lake St. Clair, Lake Ontario, Georgian Bay, and Lake Huron. (Venkatesh 1974)

Location	No. of dependent storms	No. of independent storms
Belle River	24	6
Burlington	13	8
Collingwood	21	6
Point Edward	29	5
Port Colborne	26	9
Kingsville	14	9

where S is the surge in feet from mean water level, V^2 is the component of effective wind speed in the north–south direction, and $(T_a - T_W)_0$ and $(T_a - T_W)_{-1}$ are the air–water temperature differences at 0- and 1-h lag times, respectively. As an example, the storm surge equations at Collingwood on Georgian Bay are listed below. Prediction equations for other locations on the Great Lakes are given in Venkatesh (1974):

$$
\begin{aligned}
S_0 &= 10.903050 + 0.01097P_{(4,-6)} - 0.03517P_{(10,-6)} - 0.02183P_{(3,0)} \\
&\quad + 0.04691P_{(6,0)} - 0.01164P_{(10,0)} - 0.004680(T_a - T_W)_0 \\
S_1 &= 9.890630 + 0.01580P_{(4,-6)} - 0.02339P_{(9,-6)} - 0.01110P_{(10,-6)} \\
&\quad - 0.003700(T_A - T_W)_{-6} - 0.02271P_{(3,0)} + 0.06267P_{(6,0)} - 0.02559P_{(7,0)} \\
&\quad + 0.0548P_{(9,0)} - 0.02093P_{(0,0)} - 0.001740(T_A - T_W)_0 \\
S_2 &= 8.069170 - 0.01213P_{(5,-6)} + 0.03338P_{(7,-6)} - 0.01754P_{(9,-6)} \\
&\quad - 0.01323P_{(10,-6)} - 0.01314P_{(3,0)} + 0.05873P_{(6,0)} - 0.03047P_{(7,0)} \\
&\quad + 0.02644P_{(9,0)} - 0.04000P_{(10,0)} - 0.004320(T_A - T_W)_0 \\
S_3 &= 8.389940 + 0.02566P_{(7,-6)} - 0.02229P_{(9,-6)} - 0.00598P_{(10,-6)} \\
&\quad + 0.0117P_{(3,0)} + 0.05529P_{(6,0)} - 0.03541P_{(7,0)} + 0.02561P_{(9,0)} \\
&\quad - 0.03940P_{(10,0)} - 0.005040(T_A - T_W)_0 \\
S_4 &= 9.677820 - 0.01089P_{(3,-6)} + 0.03688P_{(7,-6)} - 0.01901P_{(10,-6)} \\
&\quad + 0.06540P_{(6,0)} - 0.05273P_{(7,0)} - 0.02922P_{(10,0)} - 0.003790(T_A - T_W)_0 \\
S_5 &= 9.393110 - 0.02087P_{(3,-6)} + 0.04418P_{(7,-6)} - 0.02025P_{(9,-6)} \\
&\quad - 0.0128P_{(10,-6)} + 0.01087P_{(3,0)} + 0.05780P_{(6,0)} - 0.0566P_{(7,0)} \\
&\quad + 0.01208P_{(9,0)} - 0.02615P_{(10,0)} - 0.004380(T_A - T_W)_0
\end{aligned}
\tag{4.307}
$$

where S = surge (feet), with the subscript representing the number of hours after the time of the pressure forecast, $P_{(N,T)}$ = pressure (millibars) at grid point number N (see Fig. 4.18) and lag time T (hours), and $(T_A - T_W)$ = air–water temperature difference at the water level station at lag time T (hours).

Time Series Modeling

The time series modeling approach of Box and Jenkins (1970) has also been used in storm surge studies (Budgell and El-Shaarawi 1979) for Lake St. Clair. The input data are hourly water level measurements at Belle River and hourly wind stress values estimated from meteorological observations at Windsor Airport. The calculation of wind stress included the influence of atmospheric stability, as suggested by Hamblin (1978). The drag coefficient was made to depend on the atmospheric stability, as given by McClure (1970), and on the wind speed, as suggested by Smith and Banke (1975). The following discussion is based on Budgell and El-Shaarawi (1979).

One can regard the storm surge as the output of a dynamic system under the influence of a set of physical parameters; here, these parameters are the x and y components of the wind stress. Let the input data, which is assumed to consist of N observations taken at equal time intervals, be written as

$$(\eta_1, \tau_{x_1}, \tau_{y_1}), \quad (\eta_2, \tau_{x_2}, \tau_{y_2}) \ldots (\eta_t, \tau_{x_t}, \tau_{y_t}), \quad (\eta_N, \tau_{x_N}, \tau_{y_N})$$

where η_t, τ_{x_t}, and τ_{y_t} are, respectively, the observed water level and the x and y components of the wind stress at time $t (t = 1, 2, \ldots, N)$.

The model of Box and Jenkins (1970) consists of two major parts. In the first part is the discrete transfer function model:

$$\eta_t - \delta_1\eta_{t-1} - \ldots - \delta_r\eta_{t-r} = \omega_0\tau_{x,t-b_1} + \omega_1\tau_{x,t-b_1-1} + \ldots + \omega_S\tau_{x,t-b_1-s} + \lambda_0\tau_{y,t-b_2} + \lambda_1\tau_{y,t-b_2-1} \tag{4.308}$$

for $t = 1, 2, \ldots, N$. Here, b_1, b_2, $\delta_i (i = 1, 2, \ldots, r)$, $\omega_j (j = 1, 2, \ldots, s)$, and $\lambda_k (k = 1, 2, \ldots, V)$ are unknown constants that must be determined.

Let B denote a backward shift operator such that

$$B^m\eta_t = \eta_{t-m}$$

Then, eq. 4.308 becomes

$$\delta(B)\eta_t = \omega(B)B^{b_1}\tau_{xt} + \lambda(B)B^{b_2}\tau_{y_t} \tag{4.309}$$

where

$$\begin{aligned} \delta(B) &= 1 - \delta_1 B - \delta_2 B^2 - \ldots - \delta_r B^r \\ \omega(B) &= \omega_0 + \omega_1 B + \ldots + \omega_s B^s \\ \lambda(b) &= \lambda_0 + \lambda_1 B + \ldots + \lambda_V B^V \end{aligned} \tag{4.310}$$

Equation 4.309 can be rearranged to read

$$\eta_t = \delta^{-1}(B)\omega(B)B^{b_1}\tau_{xt} + \delta^{-1}(B)\lambda(B)B^{b_2}\tau_y(t) \tag{4.311}$$

The second part of the present model deals with a correction for the noise that affects the output. Let N_t denote the resulting error in the transfer function. The joint transfer function and noise model is

$$\eta_t = \delta^{-1}(B)\omega(B)B^{b_1}\tau_{x_t} + \delta^{-1}(B)\lambda(B)B^{b_2}\tau_{y_t} + N_t \tag{4.312}$$

The idea is to fit the observed data to eq. 4.312.

Budgell and El-Shaarawi (1979) did this following a technique from Haugh and Box (1977). They outlined the following steps: (1) fit an univariate Box and Jenkins model to each of the three series η_t, τ_{xt}, τ_{yt}; (2) estimate the residual for each univariate model; (3) fit a Box and Jenkins transfer function to the residuals, taking the residual of the η_t series as the dependent variable and the residuals of the τ_{xt} and τ_{yt} series as the independent variables; (4) substitute the expressions for the η_t, τ_{xt}, and τ_{yt} residuals obtained in step 1 into the transfer function obtained in step 3 to obtain a transfer function in terms of the variables η_t, τ_{xt}, and τ_{yt}; (5) check the adequacy of the fit and rectify the fit models if necessary.

The details of the univariate model and the transfer function model are provided by Budgell and El-Shaarawi (1979), who studied the storm surge episode of July 10–14, 1964, on Lake St. Clair using a time series of 91 hourly observations for η_t, τ_{xt}, and τ_{yt}. It was found that the autocorrelation function for these does not attenuate quickly, which suggests nonstationarity. The original time series is then modified by taking the first differences. The resulting autocorrelation and partial autocorrelation functions then are small. This means, taking the first differences generated, a more or less stationary time series.

The observed storm surge and the surge computed from this model for the July 1964 episode are compared in Fig. 4.19. The model was also tested on another 18 storm surge

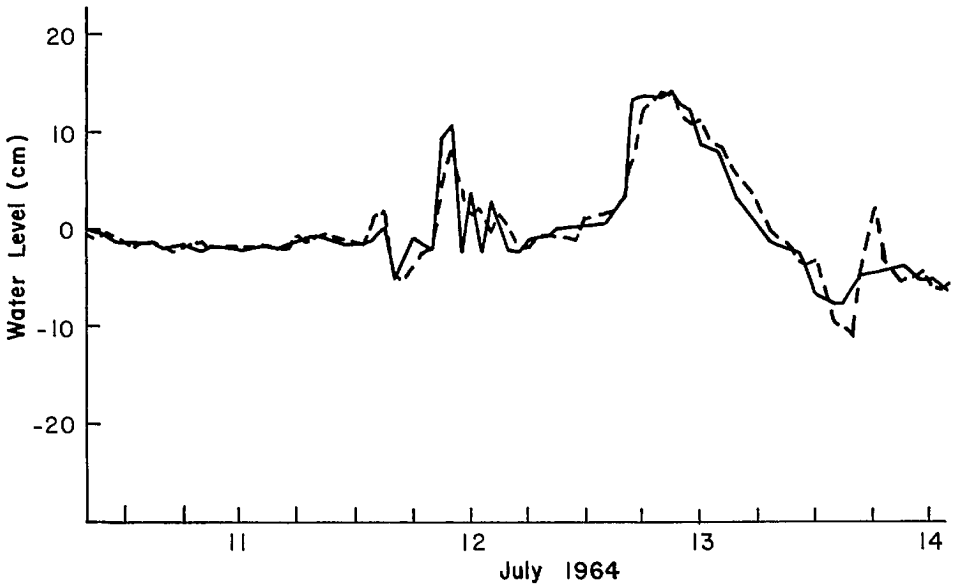

FIG. 4.19. One-step-ahead predictions (broken line) and observed (solid line) water levels (for dependent storm) for Lake St. Clair in North America. (Budgell and El-Shaarawi 1978)

episodes. The model reproduced about 72% of the total variation in the water level, and the residual variance was 16.6 cm^2. The observed and computed surge for this episode and the largest storm surge, in this water body, are compared in Fig. 4.20.

Tronson and Noye (1973) developed statistically a regression model, a numerical model, and also an autoregressive moving average (ARMA) model for storm surges at Port Adelaide on the eastern shore of St. Vincent's Gulf in the southern part of Australia. The general form of the ARMA model is

$$(4.313) \quad S_t = \sum_{k}^{K} \gamma_k S_{t+k} + \sum_{l}^{L} \alpha_l P_{t+l} + \sum_{m}^{M} \beta_m W_{t+m} + \sum_{n}^{N} \lambda_n E_{t+n}$$

where S_t, P_t, W_t, and E_t are the water level residual, atmospheric pressure, northwest wind stress, and northeast wind stress, respectively, at time t and the coefficients γ, α, β, and λ are to be determined. The summations extend over sets of K, L, M, and N integers, which depend on the variables considered.

Although, regression analysis gives large variances, since it is simple for practical purposes, it has been used to obtain the following fomula for the storm surge:

$$(4.314) \quad S_t = 1.81P_{t-5} + 3.70W_{t-2} + 0.91E_{t-1}$$

where $L = M = N = 1$ and $l = -5$, $m = -2$, and $n = 1$ in eq. 4.313. Note that $t = -5$ means a lag of 5 h. Equation 4.314 accounts for only 70% of the variance. Using autoregression gives a better relation:

$$(4.315) \quad S_t = 0.83S_{t-1} + 0.36P_{t-5} + 0.77W_{t-2}$$

where $k = -1$, $l = -5$, $m = -2$, and $n = -1$.

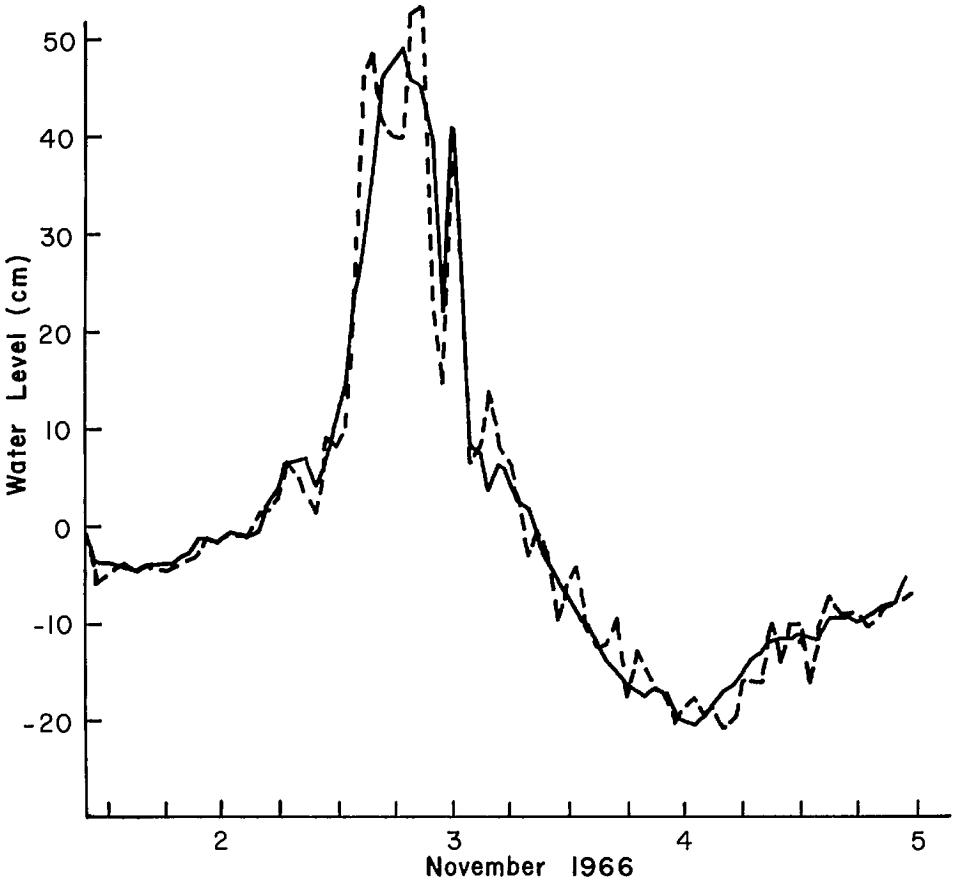

FIG. 4.20. One-step-ahead predictions (broken line) and observed (solid line) water levels (for independent storm) for Lake St. Clair in North America. (Budgell and El-Shaarawi 1978)

4.5 Electronic Analog Models

There are two approaches for storm surge calculation and prediction that have great potential but have not been made use of fully. These are hydraulic models and electronic analog models. Electronic analog models will be dealt with in this section (hydraulic models will be discussed in the next section). Significant work on these models has been done by Ishiguro (1963, 1968, 1972, 1976a, 1976b). The following discussion is based on the excellent review paper by Ishiguro (1972). Some other important works on this topic are those of Smith (1962), Blackford (1966), and Makarov and Menzin (1970).

Here, no distinction is made between electric and electronic analogs but they are referred to under the general title "electronic analog models". Ishiguro (1972) defined an electronic analog as an electronic system that is in some respects analogous to another system, so that the phenomena in the second system may be simulated. Electronic analogs can be classified from different points of view: principles of analogy, mode of operation

(i.e. steady or transient), linearity or nonlinearity, dimensions (one, two, or three), type of apparatus used, and type of application. The factor that causes the major differences among various models is whether it simulates a steady state or transient motion.

Ishiguro (1972a, 1972b) pointed to the analogy between an electric circuit and a hydrodynamic system as follows: (1) an external force creates water currents in the hydrodynamic system whereas an electromotive force generates electric currents in an electric network; (2) an electric current through an electric impedance produces a voltage across it, whereas water flow over a dynamic impedance produces a water level difference across the impedance; (3) in the hydrodynamic system, there is continuity of water currents and in the electrical system there is continuity of electric currents in the network; (4) time is relevant in both systems; however, a scale factor is needed to relate both time units.

Systems where there is a direct analogy in the above manner are called direct analogs. In direct analogs it is not necessary to express a phenomenon mathematically. However, in indirect analogs such a mathematical expression is necessary. A hydrodynamic phenomenon first must be expressed mathematically in the indirect analog and then solved using an electric analog computer. Discussion here will be confined to direct analogs.

Direct Analogs

According to Ishiguro (1972a), one-, two-, and three-dimensional hydrodynamic motions can be simulated electronically because the dynamics in both systems can be expressed through a Laplacian equation. In the electronic analog, one can either use a discrete network or a distributed network. Whereas the former type is better in principle, the latter type is more practical. In the discrete type, the space increments must be sufficiently small so that the scale of the motion to be simulated can be properly represented. This problem is akin to the grid resolution problem in numerical finite-difference models.

To express the quantitative relationships between the variables in the hydrodynamic system and in the electronic system, the following scale factors were chosen by Ishiguro (1972):

$$t = K_t t_e \tag{4.316}$$

$$\Phi_e = K_e e \tag{4.317}$$

$$\Phi_i = K_i i \tag{4.318}$$

In the hydrodynamic system, t is time and Φ_e and Φ_i are two dependent variables (e.g. water level and transport). In the electronic system, t_e is time and l and i are two variables (e.g. voltage and current). If Φ_e is taken as the water level displacement, ζ, and Φ_i is taken as the volume transport, W, of water, then

$$\zeta = K_e e \tag{4.319}$$

$$W = K_i i \tag{4.320}$$

Scale factors for other variables can be derived from combinations of these three parameters K_t, K_e, and K_i. The reason this system was chosen is its simplicity, since voltage and current can be measured easily.

One-Dimensional Time-Dependent Analogs for Long Waves

Ishiguro (1972a) stated that, in principle, there is no difference between one- and

two-dimensional analogs, except that one of the horizontal components is treated as zero in the one-dimensional system. Ignoring the Coriolis force, but including the nonlinear terms, the equation of motion in the x direction and the continuity equation can be written as

$$-\frac{\partial \zeta}{\partial x} = \frac{1}{g}\frac{\partial u}{\partial t} + \frac{1}{g}u\frac{\partial u}{\partial x} + \frac{K_c|u|u}{g(h+\zeta)} \tag{4.321}$$

$$-\frac{\partial \zeta}{\partial t} = \frac{1}{b}\frac{\partial}{\partial x}[ub(h+\zeta)] \tag{4.322}$$

where A is the area of cross section when the water level is at its mean position, b is the width, ζ is the water level deviation, u is the depth-averaged velocity, and K_c is the bottom friction coefficient and is written as

$$K_c = gC_c^{-2} \tag{4.323}$$

where C_c is a Chézy coefficient and

$$h = \frac{A}{b} \tag{4.324}$$

The volume transport Q is

$$Q = h'bu \tag{4.325}$$

where

$$h' = h + \zeta \tag{4.326}$$

Equations 4.321 and 4.322 can be written as

$$-\frac{\partial \zeta}{\partial x} = \frac{1}{gh'b}\frac{\partial Q}{\partial t} + \frac{Q}{gh'b}\frac{\partial}{\partial x}\left(\frac{Q}{h'b}\right)\frac{|Q|Q}{C_c^2 h'^3 b^2} \tag{4.327}$$

$$-\frac{\partial \zeta}{\partial t} = \frac{1}{b}\frac{\partial Q}{\partial x} \tag{4.328}$$

The finite-difference forms of these two equations are

$$-\frac{\Delta \zeta}{\Delta x} = \frac{1}{g}\frac{\partial}{\partial t}\left(\frac{Q_0}{h_0' b_0}\right) + \frac{Q_0}{g(h_0' b_0)^3 \Delta x}(h_0' b_0 \Delta Q - Q_0 b_0 \Delta h' - Q_0 h_0 \Delta b) + \frac{|Q_0|Q_0}{C_c^2 h_0'^3 b_0^2} \tag{4.329}$$

and

$$-\frac{\partial \zeta_0}{\partial t} = \frac{1}{b}\frac{\Delta Q}{\Delta x} \tag{4.330}$$

Subscript 0 denotes that the variable is at the center of a section of length Δx.

An analog representation of eq. 4.329 and 4.330 is shown schematically in Fig. 4.21a. The system consists of two voltage generators G_1 and G_2, an element G_3, which differentiates i or integrates e, a voltage sampling circuit V_s, and a current sampling circuit C_s. Each of the voltage generators generates a voltage of $\frac{1}{2}f_e(e_0, i_0)$. With reference to the notation of Fig. 4.21a:

$$-\Delta e = f_e(e_0, i_0) \tag{4.331}$$

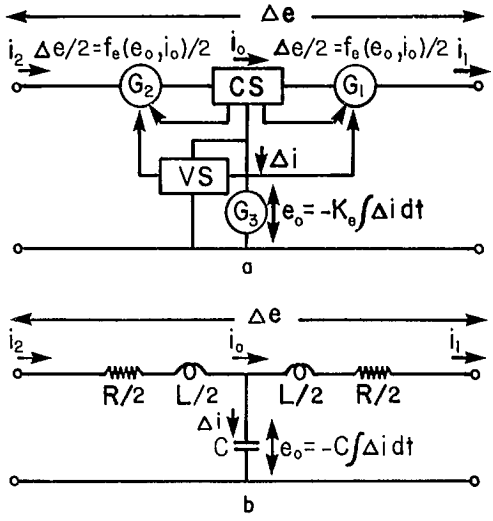

FIG. 4.21. (a) Principle of one-dimensional nonsteady nonlinear analogue; (b) example of one-dimensional nonsteady linear LCR analogue. (Ishiguro 1972a)

$$(4.332) \quad -\frac{\partial e_0}{\partial t} = \frac{1}{K_e}\Delta i$$

where

$$(4.333) \quad i_0 = \frac{i_1 + i_2}{2} \text{ and } \Delta i = \frac{i_2 - i_1}{2}$$

where K_e is a coefficient.

Figure 4.21b represents the network in the absence of nonlinear terms. In this case, the components are all passive only. Then eq. 4.331 becomes

$$(4.334) \quad -\Delta e = L\left(\frac{\partial i_0}{\partial t}\right) + Ri_0$$

From eq. 4.316, 4.319, and 4.320:

$$(4.335) \quad L = \frac{K_i}{K_e K_t}\frac{\Delta x}{b_0}\frac{1}{gh_0'}$$

$$(4.336) \quad R = \frac{K_i}{K_e}\frac{\Delta x}{b_0}\frac{r_b}{gh_0'^2}$$

$$(4.337) \quad C = \frac{K_e}{K_i K_t}\Delta x b_0$$

where the linear bottom friction coefficient is represented by r_b.

Next, the inclusion of the nonlinear terms will be considered. First, consider the nonlinear bottom friction term, which is the last term on the right side of eq. 4.327. Equating this term alone to the term on the left side of this equation gives

$$(4.338) \quad |Q|Q = -\frac{\partial \zeta}{\partial x} C_c^2 h'^3 b^2$$

If the analog is so constructed that

$$\begin{aligned} Q &\sim i \\ \zeta &\sim e_\zeta \\ h' &\sim e_h \end{aligned} \tag{4.339}$$

then the electric resistance element should have a characteristic

$$i^2 = -K_F e_\zeta e_h^3 b^2 \tag{4.340}$$

where K_F is a coefficient. The following five types of electronic elements have been developed to include the nonlinear bottom friction: two-diode circuit, two-triode circuit, thermocouple circuit, single-transistor circuit, and two-transistor circuit.

Time-dependent one-dimensional analogs have been constructed for the following water bodies: tidal river Lek in Holland (van Veen 1947a, 1947b, 1947c; northern part of the Dutch Delta (Schönfeld and Verhagen 1959; Schönfeld and Stroband 1961), California delta tidal system (Glover et al. 1953; Harder and Nelson 1966), proposed sea level Panama Canal (Harder and Masch 1961), tidal river Hooghly (Bandopadhyay and Mazumdar 1969a, 1969b, 1970), and Nagasaki Bay (Ishiguro 1950; Ishiguro and Fujiki 1954, 1955). This list is not meant to be exhaustive and there must be several other models available. Observed storm surges in Nagasaki Bay are compared with those determined from an electronic analog model in Fig. 4.22.

Two-Dimensional Time-Dependent Analogs for Long Waves

As pointed out earlier, in principle, there is no difference between one- and two-dimensional analogs, except that in the latter case, provision must be made to include the Coriolis force. The finite-difference forms of the linearized version of the relevant equations are (here the x and y derivatives are in the difference form, except for the ζ term, and the t derivative is in the continuous form):

$$-\Delta x \frac{\partial \zeta}{\partial x} = \frac{1}{gh}\left(\frac{\Delta x}{\Delta y}\right)\frac{\partial W_x}{\partial t} - \frac{\Omega W_y}{gh} + \frac{\Delta x \tau_{b_x}}{\rho g h} - \frac{\Delta x \tau_{a_x}}{\rho g h} + \frac{\Delta x}{\rho g}\frac{\partial P}{\partial x} + \frac{\Delta x}{g} X \tag{4.341}$$

$$-\Delta y \frac{\partial \zeta}{\partial y} = \frac{1}{gh}\left(\frac{\Delta y}{\Delta x}\right)\frac{\partial W_y}{\partial t} + \frac{\Omega W_x}{gh} + \frac{\Delta y \tau_{b_y}}{\rho g h} - \frac{\Delta y \tau_{a_y}}{\rho g h} + \frac{\Delta y}{\rho g}\frac{\partial P}{\partial y} + \frac{\Delta y}{g} Y = 0 \tag{4.342}$$

$$-\frac{\partial \zeta}{\partial t} = \frac{1}{\Delta y}\frac{\partial W_x}{\partial x} + \frac{1}{\Delta x}\frac{\partial W_y}{\partial y} \tag{4.343}$$

where

$$W_x = \int_{-h}^{0} \int_{-\frac{\Delta y}{2}}^{\frac{\Delta y}{2}} u\,dz\,dy \tag{4.344}$$

and

$$W_y \equiv \int_{-h}^{0} \int_{-\frac{\Delta x}{2}}^{\frac{\Delta x}{2}} v\,dz\,dy \tag{4.345}$$

and $\Omega \equiv 2\omega \sin\theta$ is the Coriolis parameter, θ being the latitude.

In the above equations, τ_{a_x} and τ_{a_y} are the x and y components of the wind stress, τ_{b_x} and τ_{b_y} are the components of the bottom stress, P is the atmospheric pressure, X and Y

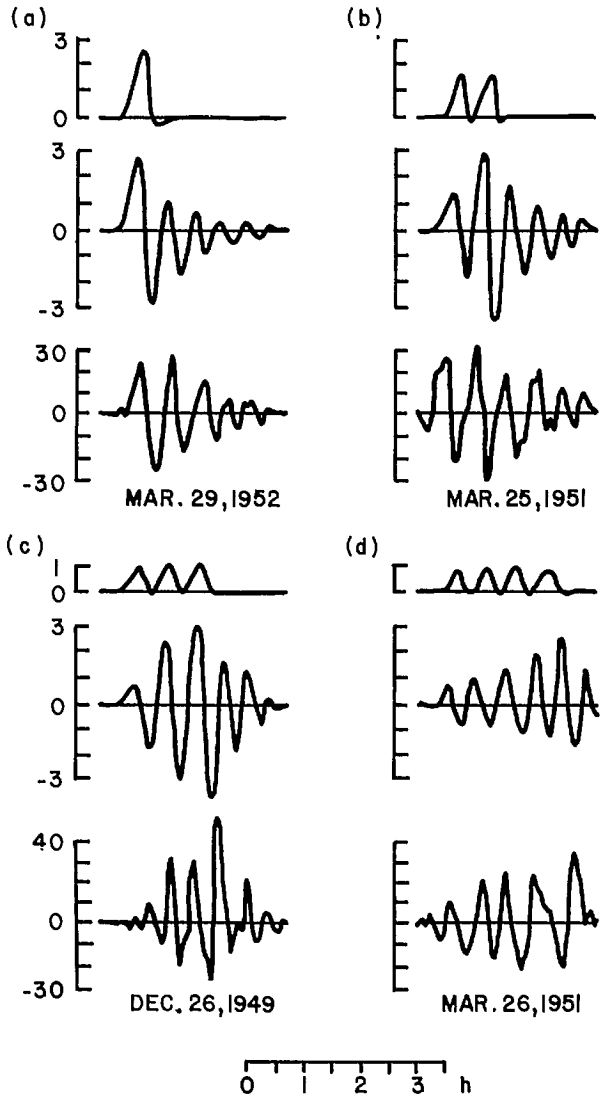

FIG. 4.22. Storm surge of (a) March 19, 1952, (b) March 25, 1951, (c) December 26, 1949, and (d) March 26, 1951. Top: simulated disturbance at the entrance to Nagasaki Bay; middle: simulated surge at the head of the bay; bottom: observed surge at the head of the bay. (Ishiguro 1972a)

are external forces, ρ is the density of water, ζ is the deviation of the water level from its equilibrium position, and u and v are the currents in the x and y directions, respectively. The quantities W_x and W_y are the components of the volume transport.

The electric analog circuit consists of four horizontal arms and one vertical arm connecting the center to earth. Each one of these four arms is made up of a current-differentiating (or voltage-integrating) element, a resistive element, and two voltage

generators, one for representing the Coriolis force and the other for all the external forces. There is a current-integrating (voltage-differentiating) element, a capacitor can be used as a current-integrating element, and a linear resistor serves as a resistive element.

The technique of introducing Coriolis force in the analog was developed by Ishiguro (1956, 1962). Two-dimensional time-dependent models have been developed for rectangular basins and V-shaped bays by Ishiguro (1959), and the latter is applied to Lough Neaugh in Northern Ireland. Scholer (1960) developed a model for Port Kembla Harbor in Australia. Makarov (1963) developed models to represent the semidiurnal tides in the North Sea and White Sea. Makarov and Menzin (1965) studied a channel connected to a rectangular bay.

Joy (1965, 1966) developed a model for the Chesapeake Bay. Joy (1966) constructed a model for Cabrillo Marina in Los Angeles. Makarov and Menzin (1967) studied the normal modes of a rectangular basin, as well as the North Sea. The northern boundary of the North Sea was kept open in the model. The agreement between observed periods and those determined from the model was within 2.5%.

Ishiguro (1976a, 1976b) developed several models for the North Sea to study tides and storm surges. Some of his results will be discussed in section 7.3. Prandle (1980) made use of the analogy to AC circuit theory in modeling the influence of tidal barriers on the tides in the North Sea, and he placed particular emphasis on the open boundary problem.

4.6 Instrumentation, Laboratory Experiments, and Hydraulic Models

In the laboratory modeling of storm surges, similar to the laboratory modeling of any other physical phenomenon, one must consider the question of similitude. This will be done following Nakamura et al. (1964). It will be useful for the present discussion to rewrite the storm surge equations in a slightly different form:

$$\frac{\partial u}{\partial t} + u\frac{\partial u}{\partial x} + v\frac{\partial u}{\partial y} = 2\Omega v \sin\phi - g\frac{\partial}{\partial x}\left(\frac{P}{\rho g} + \eta\right) + \frac{1}{\rho}\frac{\partial \tau_x}{\partial z} \tag{4.346}$$

$$\frac{\partial v}{\partial t} + u\frac{\partial v}{\partial x} + v\frac{\partial v}{\partial y} = -2\Omega u \sin\phi - g\frac{\partial}{\partial y}\left(\frac{P}{\rho g} + \eta\right) + \frac{1}{\rho}\frac{\partial \tau_y}{\partial z} \tag{4.347}$$

$$\frac{\partial h}{\partial t} = -\int_0^h \left(\frac{\partial u}{\partial x} + \frac{\partial v}{\partial y}\right) dz \tag{4.348}$$

where u and v are the velocity components in the x and y directions, ϕ is the latitude, Ω is the angular velocity of the earth's rotation, g is gravity, P is pressure, ρ is the density of water, η is the deviation of the water surface from its equilibrium position, h is the water depth, and τ_x and τ_y are the components of the shear stress.

Let u', v', and w' be the components of the fluctuation velocity and let ϵ_x and ϵ_y be the coefficients of eddy viscosity in the x and y directions. Then

$$\begin{aligned} \tau_x &= -\rho\overline{u'w'} = \epsilon_x \frac{\partial u}{\partial z} \\ \tau_y &= -\rho\overline{v'w'} = \epsilon_y \frac{\partial v}{\partial z} \end{aligned} \tag{4.349}$$

Define

$$\alpha_x \equiv \int_0^h \left(\frac{u}{U}\right)^2 \frac{dz}{h}$$

$$\alpha_y \equiv \int_0^h \left(\frac{v}{V}\right)^2 \frac{dz}{h} \tag{4.350}$$

$$\beta_x \equiv \beta_y \equiv \int_0^h \frac{u}{U}\,\frac{v}{V}\,\frac{dz}{h}$$

where U and V are the vertically averaged values of u and v, respectively.

Using eq. 4.349 and 4.350 in eq. 4.346–4.348 and using subscript r to denote the ratio between nature and model, it can be shown that the following parameters must be equal to unity:

$$\alpha_{x_r} = \alpha_{y_r} = \beta_{x_r} = \beta_{y_r} = \left(2\Omega \frac{L'}{V'} \sin\phi\right)_r = \left(\frac{gD'}{V'^2}\right)_r = \left(\frac{\tau' L'}{\rho V'^2 D'}\right)_r = 1 \tag{4.351}$$

where L' denotes the scale of the horizontal dimension, V' the scale of the horizontal velocity, D' the scale of the vertical dimension, and τ' the scale of the stress. It can be shown (Nakamura et al. 1964) that

$$(\alpha_{x_r}, \alpha_{y_r}, \beta_{x_r}, \beta_{y_r}) \sim 0(1) \tag{4.352}$$

Since gravity is the same both in nature and the model, the condition on gravity requires that

$$\left(\frac{D'}{V'^2}\right)_r = 1 \text{ or } V'_r - \sqrt{D'_r} \tag{4.353}$$

Since $V'_r = L'_r/T'_r$, from eq. 4.353, the scale ratio for the time factor is

$$T'_r = \frac{L'_r}{\sqrt{D'_r}} \tag{4.354}$$

From eq. 4.351 and 4.353, for the stress term:

$$\frac{\tau'_r L'_r}{\rho_r D'_r} = 1 \text{ or}$$

$$\tau'_r = \frac{\rho_r D'_r}{L'_r} \tag{4.355}$$

From eq. 4.349 and 4.355 the scale ratio for the eddy viscosity is

$$\epsilon'_r = \frac{\rho_r D'^{5/2}_r}{L'_r} \tag{4.356}$$

In terms of a roughness coefficient, n', eq. 4.355 becomes

$$n'_r = \frac{\tau'^{1/2}_r}{\rho'^{1/2}_r D'^{3/2}_r} \tag{4.357}$$

The Coriolis term in eq. 4.351 requires that

$$\left(\frac{2\Omega L'}{V'} \sin\phi\right)_r = 1$$

If the latitude, ϕ, is chosen such that $2\Omega \sin\phi \sim 1$, then this condition simply becomes

$$(4.358) \quad \frac{L_r'}{V_r'} = 1$$

Note that conditions 4.353 and 4.358 are mutually incompatible, and the conclusion is that the condition on the Coriolis term is difficult to satisfy.

However, Nakamura et al. (1964) satisfied the condition on the Coriolis force in an approximate manner by requiring that

$$(4.359) \quad \Omega_m = \left(\frac{D_r'^{1/2}}{L_r'} - \frac{\sin \phi_m}{\sin \phi_p}\right) \Omega_p \sin \phi_p$$

where subscripts m and r denote model and nature, respectively. Nakamura et al. (1964) performed laboratory experiments on storm surges in Ise Bay, Japan. In these experiments, the following scale ratios were used for the horizontal and vertical dimensions:

$$L_r' = \frac{1}{1000} \text{ and } D_r' = \frac{1}{65}$$

From the above relationships, the scale ratios for the other parameters will be

Time $= T_r' = 1/124$
Wind stress $= \tau_r' = 1/435$
Eddy viscosity $= \epsilon_r' = 1/34.1$
Bottom roughness $= n_r' = 1.91/1$
Coriolis force $= \Omega_m = 5.06 \times 10^{-3}$
Horizontal velocity $= V_r' = 1/8.06$

In the literature, one can find references to several hydraulic models for studying tides. Early examples of tidal models are for the Sagami Bay by Okada and Miyoshi (1933, 1935) and for various harbors by Carr (1952); a recent example is the tidal model for the Seto Inland Sea by Higuchi et al. (1978). The storm surge hydraulic models to be discussed in the next section are also capable of simulating tides and, indeed, generally, these models are first calibrated against known tidal regimes.

Abraham (1961) modeled storm surges due to hurricanes, especially taking into account their resonance amplification. Redfield and Miller (1955), making use of observations during hurricanes, showed that the magnitude of the storm surge in the open deep sea is approximately equal to the static water displacement (i.e. the change in sea level due to change in the barometric pressure). Abraham (1961) invoked the resonance amplification concept to account for storm surge displacements. In his study, he modeled the following three surges: (1) the Lake Michigan surge of June 26, 1954, (2) the Lake Erie surge of May 5, 1952, and (3) the United States east coast surge of August 30 and 31, 1954.

In his model study, Abraham (1961) simulated a moving low pressure area (i.e. a hurricane) by towing a suction fan over the surface. The wind pattern in the hurricane was not included in this simulation. Based on this study, the following was deduced: a time duration of about 1 h is adequate for the development of the maximum surge.

Hydraulic Models of Storm Surges

Tickner (1961) studied the transient aspects of storm surge development in shallow water using a laboratory wave tank. One of the important results of this study is that the

water surface setup will overshoot its steady-state value by a factor of two. For deepwater cases, this factor is slightly greater than two, and for shallower water it is slightly less than two. Another important result is that the surface current reaches a steady state in a short time and achieves a value of about 1/30 of the average wind velocity for a Reynolds number $\geq 2 \times 10^{-3}$.

The experiments were performed in a tank 18.3 m long, 0.3 m wide, and 0.39 m deep. The wind was generated by a blower mounted at one end of the channel. Piezometers located at five different positions were used to measure the water depth and the pressure in the channel, with reference to atmospheric pressure.

Brogdon (1969) discussed the effects of proposed barriers on storm surges generated by hurricanes in Galveston Bay. Fairchild (1956) discussed a model study of wave setup at Narragansett Pier in Rhode Island. Simmons (1964) made a thorough study of the protection of Narragansett Bay from storm surges through a scheme of barriers. Certain details of this model will be considered, following McAleer (1964).

Storm surges generated by hurricanes on the Atlantic coast of the United States have amplitudes as great as 4.3 m. In the 1938 storm surge, 110 people died; but because of better warning the loss of life was only 10 in a 1954 surge. In addition to storm surges, wind waves of amplitudes up to 7.6 m were recorded near the entrance of the bay. Maximum sustained winds up to 121 $km \cdot h^{-1}$ and gusts up to 201 $km \cdot h^{-1}$ were noted. Minimum pressures of 964.8 mb were recorded.

In the hydraulic model for Narragansett Bay, the barriers (for storm surge protection) studied were of the rockfill type with large ungated navigation openings at the three entrances of the bay. The model tests showed that, by suitably locating the barriers, the surge amplitudes could be reduced up to 1.8–2.1 m. The simulated effect of the barriers on the 1938 storm surge levels is shown in Fig. 4.23. In the absence of the barriers, most of the increase of 3.3 m in the mean sea level took place within 2 h in the bay, and the total duration of the surge was 6–8 h. When barriers are present, since the bay opening is reduced to about a fourth of its original area, the rate of rise of the water level is lower and the surge levels are also lower. Although the normal tidal range is not significantly affected by the barriers, the phase of the tide in the bay will lag behind the ocean tide by about 15 min when barriers are present.

Allen et al. (1955) used a hydraulic model to simulate the storm surge of February 1, 1953, in the Thames Estuary. The model was 24.4 m long and the following scale relationships were used: horizontal (linear) scale, 1/3000; vertical (linear) scale, 1/120; vertical exaggeration, 25; time scale, 1/273.8; velocity scale, 1/10.95; discharge scale, $1/(3.943 \times 10^6)$. In the model, the tides were generated by an electronically controlled pneumatic displacer. The displacer is made up of an inverted box located across the seaward end of the model and opens only below the lowest low-water level on the side towards the upstream direction. At the top of the displacer there is an exhaust fan, which creates a reduced air pressure above the water surface. The displacer is connected to the atmosphere through a pipe in which there is a butterfly valve. By controlling the angular opening of this valve, any type of tidal motion may be created. Obviously, this type of tide generator is more sophisticated than the usual plunger type. To provide for adequate bottom roughness, a wire mesh was placed at the bottom. After reproducing the normal tides and the 1953 storm surge, experiments were carried out on the effect of a barrier on the flooding levels. Allen et al. (1954) used the term "barrage" to refer to a structure that would consist of a number of gates suspended between piers above the water level, the central spans being wider than those at the sides and their gates being suspended higher above the water to provide a passage for shipping. The gates would be lowered to act as

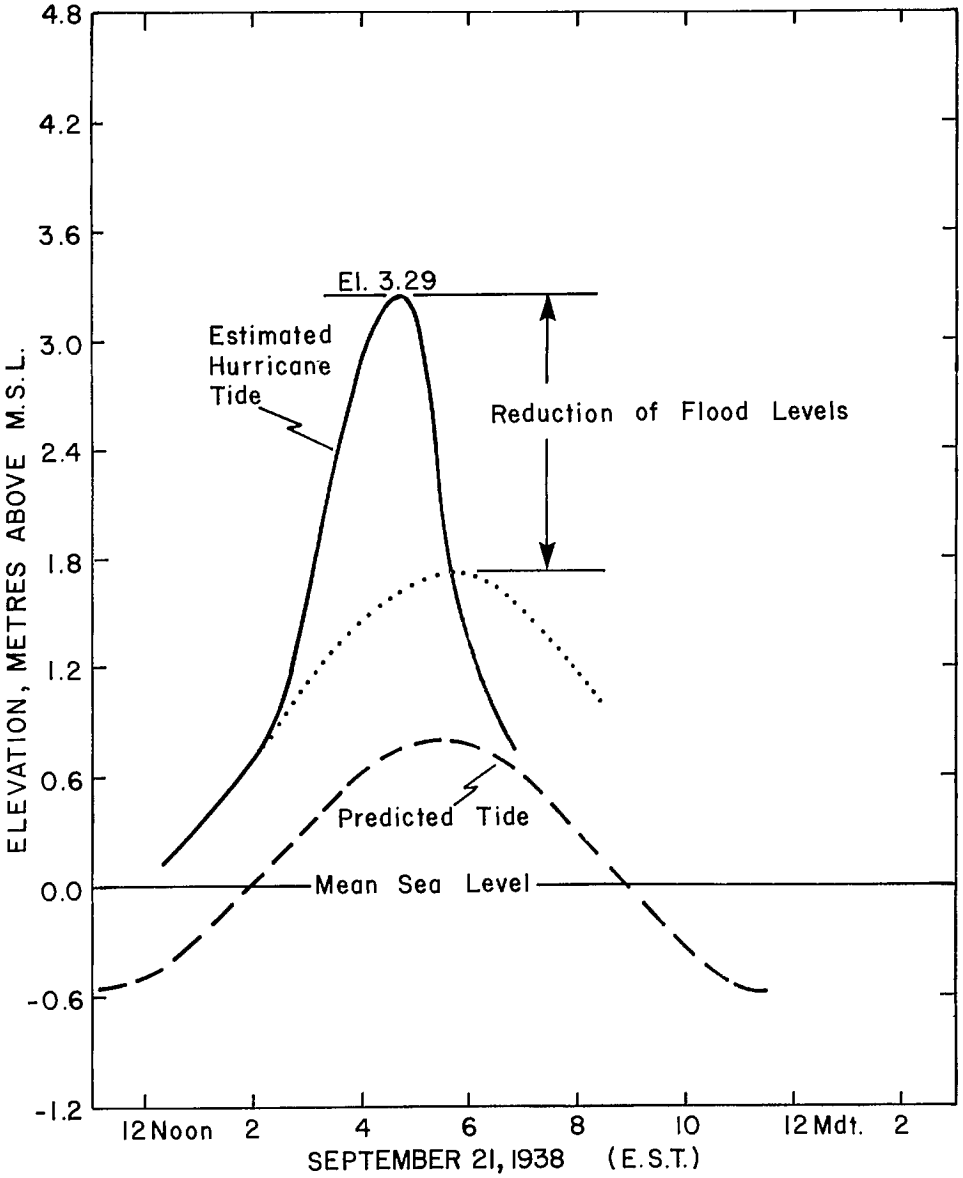

FIG. 4.23. Effect of barriers on storm surges at Newport, Narragansett Bay, RI. (McAleer 1964)

a barrage only when a dangerous surge was predicted. Ordinarily, this structure provides almost no obstruction to the tidal flow.

In the tests, this barrage was located 30.6 km downstream of the London Bridge, and the simulations showed that the flooding risk to London is reduced, whereas there is a slight tendency toward an increase of water levels on the downstream side of the barrage.

Hayami et al. (1955) modeled storm surges in the rivers and canals around Osaka

City. They paid particular attention to the correct simulation of the bottom friction. They wrote the one-dimensional equation of motion and continuity in the following form:

$$\frac{\partial U}{\partial t} + U\frac{\partial U}{\partial x} = -\frac{\lambda}{2R}U^2 + g\left(i - \frac{\partial h}{\partial x}\right) \tag{4.360}$$

$$\frac{\partial A}{\partial t} + \frac{\partial}{\partial x}(AU) = 0 \tag{4.361}$$

where A is the cross-sectional area, i is the slope of the channel bed, R is the hydraulic mean depth, h is the water depth, λ is the coefficient of friction, g is gravity, and U is the average velocity in the x direction. Let subscripts 1 and 2 denote nature and the model, respectively.

From similitude considerations:

$$\frac{U_2}{U_1}\frac{t_1}{t_2} = \left(\frac{U_2}{U_1}\right)^2\frac{x_1}{x_2} = \frac{\lambda_2}{\lambda_1}\frac{R_1}{R_2}\left(\frac{U_2}{U_1}\right)^2 = \frac{h_2}{h_1}\frac{x_1}{x_2} \tag{4.362}$$

$$\frac{A_2}{A_1}\frac{t_1}{t_2} = \frac{U_2}{U_1}\frac{A_2}{A_1}\frac{x_1}{x_2} \tag{4.363}$$

From eq. 4.362 and 4.363 the following relations can be written:

$$\begin{aligned} &\frac{\lambda_2}{\lambda_1} = \frac{R_2}{R_1}\frac{x_1}{x_2} \\ &\frac{t_2}{t_1} = \frac{x_2}{x_1}\left(\frac{h_2}{h_1}\right)^{-1/2} \end{aligned} \tag{4.364}$$

The relationship for the friction is given by the first equation of 4.364 and the time scale is given by the second equation of 4.364 (the time relationship indicates that the Froude number must be the same in nature and the model).

A resistance low for turbulent flow in a channel can be written as

$$\sqrt{\frac{2}{\lambda}} = A_r + \frac{1}{\chi}\ln\frac{R}{K} + \delta \tag{4.365}$$

where A_r is a constant whose value depends on the roughness, χ is a mixing length, K is a roughness height (in the bed), and δ is a correction factor for the nonuniformity of the free surface and the shearing stress.

From eq. 4.365 and 4.363:

$$\frac{A_{r_1} + \frac{1}{\chi_1}\ln\frac{R_1}{K_1} + \delta_1}{A_{r_2} + \frac{1}{\chi_2}\ln\frac{R_2}{K_2} + \delta_2} = \left(\frac{R_2}{R_1}\right)^{1/2}\left(\frac{x_1}{x_2}\right)^{1/2}$$

This becomes, after assuming $\chi_1 = \chi_2 = \chi$ and $A_{r_1} = A_{r_2} = A_{r_0}$,

$$\frac{K_{s_2}}{R_2} = q\left(\frac{K_{s_1}}{R_1}\right)^P \tag{4.366}$$

where

$$P \equiv \left(\frac{R_2}{R_1}\right)^{-1/2}\left(\frac{x_1}{x_2}\right)^{-1/2} \tag{4.367}$$

(4.368) $q \equiv \exp \chi [A_{r_0}(1 - P) + (\delta_2 - P\delta_1)]$

and K_s is the equivalent sand roughness.

The value of K_{s_1} can be determined from Manning's formula:

(4.369) $n^2 = \lambda \frac{R^{1/3}}{2g}$

From eq. 4.369 and 4.365:

(4.370) $\frac{K_s}{R} = \exp \chi (A_{r_0} + \delta - g^{-1/2} R^{1/6} n^{-1})$

The following values were used: $n = 0.03$, $A_{r_0} = 6.0$, $\chi = 0.4$.

For a channel of rectangular geometry, Keulegan (1938) wrote

(4.371) $\delta = \frac{B}{\chi} = \frac{1}{\chi}\left[\ln\left(1 + \frac{2h}{B}\right) - \frac{h}{B}\right]$

where h is the water depth and B is the width of the channel. Using eq. 4.366–4.368, K_{s_2} (bottom friction in the model) can be determined.

Murota (1963) simulated the effect of breakwaters on storm surges in Osaka Bay. His results indicate that the water levels might actually increase due to the presence of breakwaters, and increased seiche motion is invoked as the main reason.

Models for Wind and Bottom Stress

In this section, hydraulic and laboratory models for storm surges, in which special emphasis was given to the wind stress and bottom friction terms, will be considered. Hellstrom (1941), Francis (1951), and Keulegan (1951) performed laboratory experiments on surface slope due to wind stress. Although Hellstrom (1941), Haurwitz (1951), and Keulegan (1951) studied theoretically the slope of the free surface in a confined body of water acted upon by a uniform steady wind, they did not include the inertial terms in their treatment. van Dorn (1953) measured the surface slope and wind stress in an 800-ft (244 m) model yacht pond. Following van Dorn, the physical forces that govern the slope of the free surface will be examined.

With reference to Fig. 4.24, taking the x-axis in the direction of the wind and taking the origin of the vertical coordinate z at the bottom of the water body, which is assumed to be homogeneous, the vertically integrated form of the vertical momentum equation becomes, after neglecting the pressure gradient and Coriolis terms,

(4.372) $\frac{\partial}{\partial t}\int_0^{H+h} u dz + \frac{\partial}{\partial x}\int_0^{H+h} u^2 dz = -g(H + h)\frac{\partial h}{\partial x} + \frac{(\tau_s + \tau_b)}{\rho}$

where H is the water depth in the undisturbed state, h is the deviation of the water surface from its equilibrium level, ρ is the water density, u is the velocity component in the x direction, and τ_s and τ_b are the horizontal stresses at the surface and bottom, respectively. Basically, eq. 4.372 is a statement of the momentum budget for a column of water of unit area extending from the surface to the bottom.

Assuming steady state will suppress the first term in eq. 4.372. Since the free surface height h was measured at the end of the tank, it is convenient to average the remaining terms over the length L of the pond to give

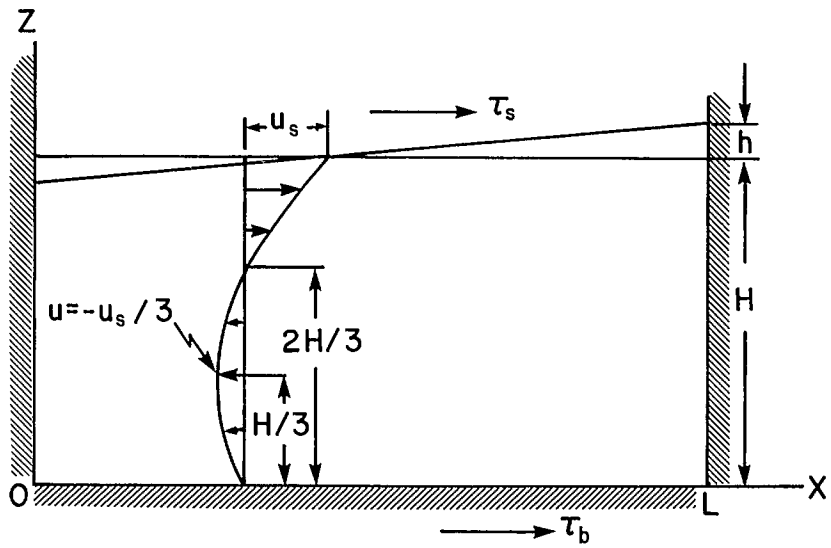

FIG. 4.24. Longitudinal section of a rectangular channel to show the slope of the free surface under the action of the wind stress τ_s. The velocity distribution within the water for laminar flow is also shown. (van Dorn 1953)

$$(4.373)\quad \frac{1}{L}\int_0^L \frac{\partial}{\partial x}\int_0^{H+h} u^2 dz dx = -\frac{g}{L}\int_0^L (H+h)\frac{\partial h}{\delta x}dx + \frac{1}{\rho L}\int_0^L (\tau_s + \tau_b)dx$$

Actually, L is 220 m and is slightly less than the length l of the pond, which is 240 m. If the bottom profile is symmetric, then eq. 4.373 will hold provided the two points at which h is measured are at an equal distance from the respective end.

With these considerations, the advection term vanishes, and if $H \gg h$ and if H is uniform (in the case of H varying with x, H should be treated as the mean depth), then eq. 4.373 becomes

$$(4.374)\quad 0 = \frac{gH}{L}(h_0 - h_L) + (\bar{\tau}_s + \bar{\tau}_b)$$

where the bar denotes average value over the length L. In the discussion below, for convenience, the bar will be omitted. On defining the setup S as the difference in h between the two ends of the pond, the average surface slope S/L is related to the surface stress τ_s through

$$(4.375)\quad \frac{S}{L} = \frac{n\tau_s}{\rho g h}$$

where n is defined through

$$(4.376)\quad n - 1 \equiv \frac{\tau_b}{\tau_s}$$

For laminar flow:

$$(4.377)\quad \tau = \mu\frac{\partial u}{\partial z}$$

where μ is the dynamic viscosity of water.

Using this value of τ in the nonintegrated form of the equation for horizontal motion, and after ignoring the time-dependent term and inertial term, Keulegan (1951) showed that

$$\frac{d^2u}{dz^2} = \frac{g}{\nu}\frac{dh}{dx} \tag{4.378}$$

where ν is the kinematic viscosity of water. Based on the condition that the net flow through any cross section be zero, this relation can be integrated directly to give

$$\frac{dh}{dx} = \frac{6\nu u_s}{gH^2} \tag{4.379}$$

and

$$\tau_s = -2\tau_b = \frac{4\mu u_s}{H} \tag{4.380}$$

where u_s is the value of u at the surface. From eq. 4.376 and 4.380

$$n = \frac{3}{2} \tag{4.381}$$

The horizontal velocity distribution in the vertical direction is given by

$$u = u_s\left[3\left(\frac{z}{H}\right)^2 - 2\left(\frac{z}{H}\right)\right] \tag{4.382}$$

This relation is plotted in Fig. 4.24.

Note that the circulation consists of a current at the surface in the wind direction and this current extends to one-third depth. Below this current, there is a current in the opposite direction and this has a minimum value $u = u_s/3$ at two-thirds depth. Also note that the bottom stress is half of the surface stress. These results are for laminar motion only. For turbulent flow, one cannot simply relate τ_s and τ_b. Hellstrom (1941), making use of the Boussinesq theory of turbulence and also using an analogy to open channel flow, deduced that n lies between 1.0 and 1.5. van Dorn (1953) assumed n to be unity. In his experiments van Dorn found that the bottom stress was less than one tenth of the surface stress.

Keulegan (1951) suggested that the total setup results from two factors: (a) the frictional drag on the water surface, which exists at all wind speeds, and (b) an additional drag due to the presence of wind waves at the surface. This drag exists only if the wind velocity exceeds a critical value V_c referred to as the "formula velocity." This partition of the setup can be expressed as follows:

$$\begin{aligned} S_1 &= aV^2 \\ S_2 &= b(V - c)^2 \end{aligned} \tag{4.383}$$

where S_1 and S_2 are the setups due to surface drag and waves, respectively. Note that

$$\begin{aligned} S &= S_1 \text{ for } V \leq V_c \\ S_1 &+ S_2 \text{ for } V > V_c \end{aligned} \tag{4.384}$$

Using dimensional considerations, Keulegan (1951) proposed the following forms for a and b:

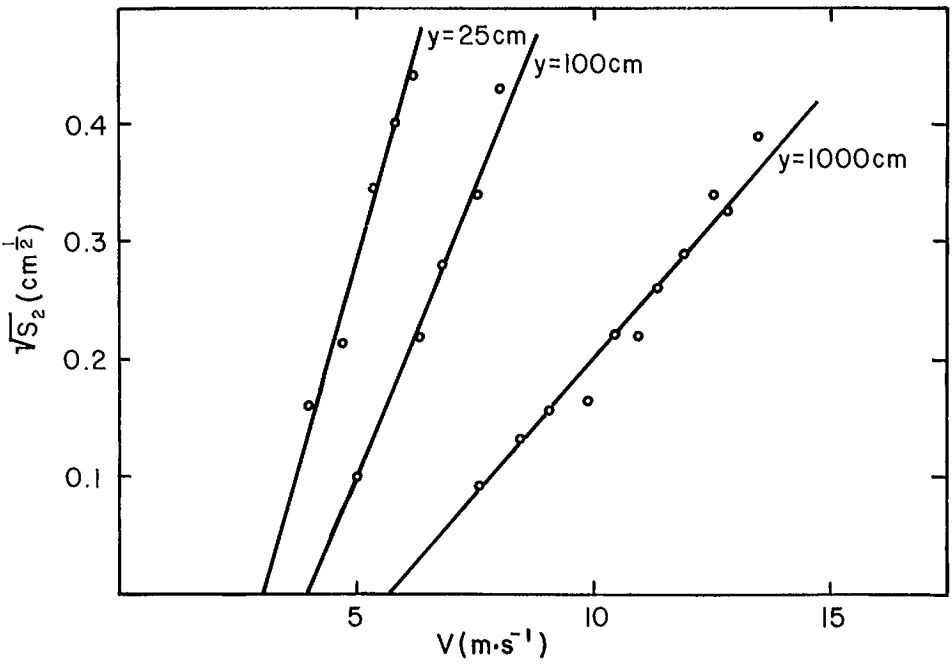

FIG. 4.25. Square root of the additional setup S_2 due to waves as a function of the wind speed for three different anemometer heights. (van Dorn 1953)

$$a = \frac{AL}{gH}$$
$$b = \frac{BL}{gH}\sqrt{\frac{H}{L}} \tag{4.385}$$

where A and B are nondimensional constants for any given set of wind measurements.

Instead of eq. 4.385, van Dorn (1953) proposed the following:

$$a = \frac{L}{gH}\alpha^2$$
$$b = \frac{L}{gH}\beta^2 \tag{4.386}$$

where α is determined from the slope of the straight line that gives the best fit to the observed data with detergent used at the surface (to suppress waves) and making use of the first formulae in eq. 4.383 and 4.386. In Fig. 4.25 the square root of S_2 is plotted against wind speed for three different anemometer elevations (25, 100, and 1000 cm). The intercepts at $S_2 = 0$ were taken to be the values of V_c, and the slope is the value of β.

The values of α, β, and V_c deduced for different anemometer elevations are listed in Table 4.4. The values obtained by Keulegan (1951) are also shown. The setup as a function of the wind at 10 m elevation is shown in Fig. 4.26. In calculating the setup, entries from Table 4.4 were used.

For $V \leq V_c$, from eq. 4.383 and 4.375:

TABLE 4.4. Comparison of three empirical parameters for the model yacht pond and the laboratory channel. (van Dorn 1953)

Anemometer elevation (cm)	$\alpha \times 10^3$	$\beta \times 10^3$	V_c (m·s^{-1})
25	2.1	4.6	3.1
100	1.7	3.2	4.0
1000	1.1	1.5	5.6
Keulegan	1.8	3.7[a]	3.9[a]

[a]Average for five water depths.

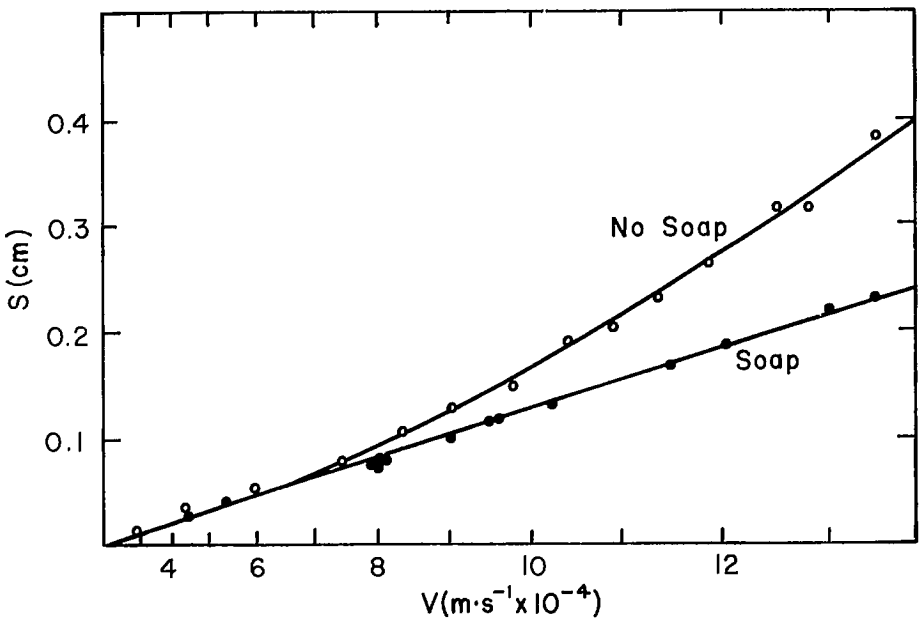

FIG. 4.26. Setup as a function of the square of the wind speed at 10 m of elevation. (van Dorn 1953)

(4.387) $\tau_s = \rho\alpha^2 V^2$

Taylor (1916) expressed the surface stress in terms of a resistance coefficient γ^2:

(4.388) $\tau_s = \gamma^2 \rho_a V^2$

where ρ_a is air density. Thus

(4.389) $\gamma^2 = \frac{\rho}{\rho_a}\alpha^2$

For $V \geq V_c$:

(4.390) $\tau_s = \rho\alpha^2 V^2 + \rho\beta^2 (V - V_c)^2$

Since α and β depend only on the anemometer height at which the wind is measured, to a first approximation, the wind stress appears to be independent of the fetch and thus

independent of the size of the waves.

Sibul and Johnson (1957) mentioned that all the modeling studies on wind tides prior to their work were done with smooth bottom. These authors paid particular attention to the bottom roughness, and they used three different types of bottom roughness: (a) smooth bottom, (b) rough bottom, and (c) rough bottom with strips of cheesecloth in the channel to imitate the effect of vegetation (such as in Lake Okeechobee). For steady state, the momentum balance per unit width can be expressed as

$$(4.391) \quad \frac{\gamma}{2}[(z_s + dz_s)^2 - z_s^2] = (\tau_s + \tau_b)dx$$

The water surface is given by (after ignoring higher order terms)

$$(4.392) \quad \frac{dz_s}{dx} = \frac{(\tau_s + \tau_b)}{\gamma z_s}$$

where γ is unit weight of water, z_s is the distance from the bottom to the mean level, and τ_s and τ_b are the surface and bottom stress, respectively. Following Keulegan (1951):

$$(4.393) \quad \tau_b = \tau_s(\lambda - 1)$$

where λ is a coefficient that depends on turbulence in the flow.

From eq. 4.392 and 4.393:

$$(4.394) \quad \frac{dz_s}{dx} = \lambda \frac{\tau_s}{\gamma z_s}$$

This is a relation that is used by several authors in modeling storm surges. For example, Hellstrom (1941) integrated eq. 4.394 to give

$$(4.395) \quad z_s^2 = \frac{2\lambda\tau_s}{\gamma}(x + C_1)$$

This means that the water surface is parabolic in shape and may be written in (ζ_s, ξ) coordinates as follows:

$$(4.396) \quad \zeta_s^2 = \frac{2\lambda\tau_s}{\gamma}\xi$$

For details in determining the constant C_1, see Sibul and Johnson (1957). The surge amplitude h can be determined from

$$(4.397) \quad h = \sqrt{\frac{2\lambda\tau_s}{\gamma}(x + C_1)} - d$$

When the water depth is much greater than the surge, Hellstrom (1941) writes

$$(4.398) \quad h = \frac{\lambda}{\gamma}\frac{\tau_s}{d}\left(x - \frac{F}{2}\right)$$

The water level at the windward side ($x = 0$) is

$$(4.399) \quad h_{x=0} = -\frac{\lambda}{2}\frac{\tau_s}{\gamma}\frac{F}{d}$$

and at the leeward shore ($x = F$) is

$$(4.400) \quad h_{x=F} = \frac{\lambda}{2} \frac{\tau_s}{\gamma} \frac{F}{d}$$

where F is the fetch (i.e. the distance from the leeward still water shoreline to the point at which the water level is measured).

Langhaar (1951) defined the statical tide as the surge due to a persistent wind and the dynamical tide as due to seiche action. For small surges and when the bottom is not exposed, the surge is given at the leeward shore by

$$(4.401) \quad h_{x=F} = \frac{\tau_s F}{2\gamma d}$$

This is identical to eq. 4.400 provided $\lambda = 1$. For the case in which a part of the windward bottom is exposed, the total water level is given by

$$(4.402) \quad S' = 3\sqrt{\frac{3\tau_s F d}{\gamma}}$$

Based on actual data, this was modified for the surge:

$$(4.403) \quad h'_{x=F'} = 3\sqrt{\frac{3.373\tau_s F d N}{\gamma}} - d$$

The planiform factor is $N = 1$ for uniform width (of the water body), $N < 1$ for diverging cases, and $N > 1$ for converging situations.

The so-called Zuider Zee formula (Thijsse 1938) is

$$(4.404) \quad S = \frac{U^2 F}{800 d}$$

where S is the difference between windward and leeward water surface elevations (feet), U is the wind velocity (miles per hour), F is the fetch (miles), and d is the water depth (feet). A slightly modified form of this is

$$(4.405) \quad h = \frac{U^2 F}{1400 d} \cos A$$

where h is the water level (feet) above the undisturbed level and A is the angle between the wind and the axis of the surge. Saville (1952) gave

$$(4.406) \quad S = \frac{K\lambda \rho_a U^2 F}{\rho g d} \cos A$$

where S is the difference between the water levels at the windward and leeward sides, ρ_a is air density, ρ is water density, $K \sim 0.003$, and A is the angle between the wind direction and the fetch. Equation 4.406 is referred to as the Beach Erosion Board formula.

The experiments performed at the U.S. Beach Erosion Board (Sibul 1955; Sibul and Johnson 1957) were done in a channel 18.3 m long, 0.3 m wide, and 0.4 m deep. The wind was generated by a blower mounted at one end of the channel. The water depth and the pressure were measured using piezometers. By using parallel wire resistance elements connected to brush recorders, the wave heights and periods were measured at four locations.

Experiments were performed using the following bottom roughness. For the smooth-bottom case, the original bottom was painted with white oxide primer paint (for this case the Manning coefficient $n = 0.0116$). For the rough-bottom case, the smooth-painted

bottom was covered with a 7/8-in. expanded metal lath. For this case, $n = 0.0207$. In a third set of experiments, a combination of the rough bottom and cheesecloth in the channel was placed at the bottom. The top of each piece of the cloth was made to float with the help of a thin strip of balsawood. The buoyancy of the cloth was adjusted to be at a minimum so that it could follow the current in much the same way as blades of grass submerged in water.

The experimental data were compared with the data computed from the relationships above. Keulegan's (1951) relationship fits the data for not too shallow water. For shallow water, Langhaar's (1951) formula agrees better with observations. The modified Zuider Zee formula underestimates the surge for the deepwater cases. Reid (1957b) showed that the traditional quadratic bottom stress law is not appropriate when significant wind stress exists on the water surface, and he derived a more appropriate formula for the bottom stress taking the effect of the wind stress into account. This will be considered in Chapter 6.

Tickner (1957) studied, using a laboratory channel, the effect of bottom roughness by using strips of common window screen. The simulations showed that when the water depth was slightly greater than the thickness of the roughness elements, the surge amplitudes were about twice those for the smooth-bottom case. However, when the water depth was about half the thickness of the roughness elements the surge heights were about 0.08 of those for the smooth-bottom case. For cases in which the ratio of the undisturbed water depth to the roughness height is greater than 4, the surge heights are independent of the height of the roughness elements.

Tickner (1961) also modeled the effect of sloping bottoms and reefs at the bottom. He showed that when reefs are present, the surge heights are about twice the value for the smooth-bottom case for a solid reef and somewhat less in the case of a reef with an opening in it.

Two recent examples are considered. Tang et al. (1978) simulated wind-induced flow phenomena in a laboratory tank. The wind stress coefficients were found to be well scaled by the Froude number (Wu 1969)

$$\frac{1}{\sqrt{C_y}} = \frac{1}{K} \ln \left(\frac{1}{0.0112 C_y F_r^2} \right) \tag{4.407}$$

where C_y is the wind stress coefficient defined through

$$C_y \equiv \frac{\tau_0}{\rho_a U_y^2} \tag{4.408}$$

Here, F_r is the Froude number defined as

$$F_r = \frac{U_y}{\sqrt{gy}} \tag{4.409}$$

where τ_0 is the wind stress, K is Karman's constant, U_y is the wind velocity at height y, ρ_a is air density, and g is gravity.

In these experiments, the bottom stress also was measured as a function of the wind friction velocity and was compared with the wind stress. The average bottom stress increases slightly as the wind friction velocity increases. It can also be seen that the bottom friction increases remarkably as the water depth increases. The ratio of the wind stress to the bottom stress varied from 5 to 0.08 depending on the wind friction velocity and the water depth.

DeVries and Amorocho (1980) performed field tests on a 9.7-km stretch of the

California Aquaduct near Patterson, California, with a view to measuring wind setups in large open channels. They pointed out that whereas considerable data exist on wind setups in lakes and semienclosed seas, there are little data for open channels.

Wind setup in channels can be locally important: e.g. (a) irrigation canals in Australia, (b) St. Lucie canal in Florida (large storm surges were recorded in this canal following hurricane occurrences), (c) canals and fjords on the coast of Jutland in Denmark (storm surges from the North Sea propagate into these canals), and (d) several canals in the western part of the United States.

In the field tests of DeVries and Amorocho (1980), the wind shear was determined by (a) measuring the wind velocity profiles above the water, (2) theoretical calculation, or (3) measuring the Reynolds stresses in the wind stream. The results of this study showed that the general relationship between wind shear and wind speed for the open sea is also applicable to open channels.

Storm Surge Instrumentation

In most storm surge studies, storm surge data are obtained as the residuals that are calculated by subtracting the predicted astronomical tide from the recorded water levels. Briand (1980) systematically examined storm surge data for a period of 11 yr in Canadian waters, and he found that the residuals, although more or less satisfactory in a majority of cases, show unrealistic results in certain cases (these unrealistic results appear as persistent and large positive or negative surges). Part of the difficulty can be traced to an improper removal of the tide from the total record. In those water bodies where the tide–surge interaction is significant, a linear addition of tide and surge is not appropriate. This problem will be considered in detail in Chapter 5.

Besides the difficulty in calculating the residues, there are some fundamental problems associated with the recording of the water level itself. Lennon (1971) remarked that since most of the tide gauges usually are located in harbors, coastal regions, and estuaries, these sites have a maximum noise from the point of view of long-wave phenomena, the noise being due to wind waves, seiches, variations of temperature and salinity, and freshwater discharge. Also, as pointed out by Lennon (1971), the basic instrumentation, which has not changed much in several decades, consists of a stilling well and a recorder; both of these have serious shortcomings. The main problem is filtering out the wind waves while leaving the long-wave motion unaffected as far as possible. This is accomplished by using a vertical tube connected to the open water through an orifice or pipe. However, the filter may be influenced by clogging due to weeds, trash, marine growth, and siltation.

The stilling well can be thought of as a pressure device in which equilibrium is sought between pressures imposed at the orifice by the water inside and outside of the well. There may be density variations in the water in the stilling well. Turbulence outside the well could also have serious consequences. Besides the problems with stilling wells, the recording of the water level itself is another difficult task. The problems are more serious for analog gauges. Problems in the pen carriage drive, nonconstant tension in the float suspension, etc., are also present. Most of the instruments show a lag in response to water level changes but this is not a serious problem for long waves.

At present, digital tide gauges with electronic wave filters are being developed and used, although most of the tide gauge installations are still of the old type. For theoretical studies on the response of the stilling well, see Shipley (1963) and Noye (1968). Braddock (1980) gave a most thorough discussion of the response of a conventional tide gauge to long waves such as tsunamis. Muir (1978) discussed the Bernoulli effects on pressure-

activated water level gauges. Other important works are those of Noye (1974a, 1974b, 1974c) and Braddock (1977). One of the interesting results obtained by Braddock is that the tide well is basically a linear device for periods greater than about 10^3-10^6 s (tides and storm surges fall into this category) and behaves in a nonlinear fashion for periods less than this (tsunamis fall into this category).

Finally, the use of vertical pendulums in storm surge observations will be considered. Zschau an Kümpel (1979) argued that the additional mass of water in a storm surge influences tilt measurements inland from the water body, similar to the manner in which marine tides influence earth tidal measurements. Two effects occur: the first is a tilt of the local vertical and the second is a tilt of the crustal surface.

Three vertical pendulums were used near the German Bight of the North Sea to measure tilt due to nine storm surges during the period November–December 1973. The measured tilts can precede the surges by as much as 12 h.

4.7 Hybrid Models

Holz (1977) and Funke and Crookshank (1979) appear to have introduced the concepts of hybrid modeling in tidal estuarine problems. In a hybrid model, long-wave propagation in a coastal water body is simulated by dynamically coupling a hydraulic model representing a portion of the water body to a numerical model of the remaining portion of the water body, so that both models can be run jointly at the same time. For example, the water level at the junction (of the numerical and hydraulic models) can be measured in real time in the hydraulic model and fed into the numerical model. Then, the flow can be computed numerically and the flow at the junction of the models can be used as a boundary condition to the hyraulic model. In this manner, one can construct the hydraulic model to represent the area of immediate interest and the numerical model to cover a larger area so that boundary conditions can be provided.

Funke and Crookshank (1979) developed a hybrid model for the St. Lawrence Estuary whereas Prandle et al. (1980) developed a hybrid model for the Bay of Fundy. In the St. Lawrence Estuary case, the numerical model used was one dimensional, whereas for the Bay of Funday a two-dimensional model was used. Since the concepts are similar, and since the one-dimensional model is simpler, certain details of the St. Lawrence Estuary model will be considered.

The hybrid model of the St. Lawrence Estuary, in which a hydraulic (physical) model and a numerical model are run simultaneously and interactively by exchanging information at their mutual interface, is shown in Fig. 4.27. The original hydraulic model of the St. Lawrence Estuary, which was partially dismantled (due to space requirements for other projects), represents the reach from Pointe-au-Père to Montreal. The dismantled portion is from Neuville to Montreal. A one-dimensional numerical model was developed for this dismantled portion and was dynamically coupled to the remaining part of the hydraulic model. Thus, the hybrid model simulates the tidal motion in the estuary from Pointe-au-Père to Montreal. Thus, out of a total stretch of 550 km in the hybrid model, a 330-km stretch is simulated by the physical model and the remaining 220-km stretch is simulated by the numerical model.

At the downstream end of the hybrid model (i.e. Pointe-au-Père), the water depth is about 300 m and the width of the estuary is about 47 km. At the interface of the two models (i.e. Neuville), the depth is about 15–20 m and the width is about 3 km. The tidal range at Pointe-au-Père varies from 1.5 to 4.5 m with a maximum discharge of about 2×10^6 $m^3 \cdot s^{-1}$. Near Quebec City the tidal range varies from 3.5 to 6.0 m. At Neuville, the tidal

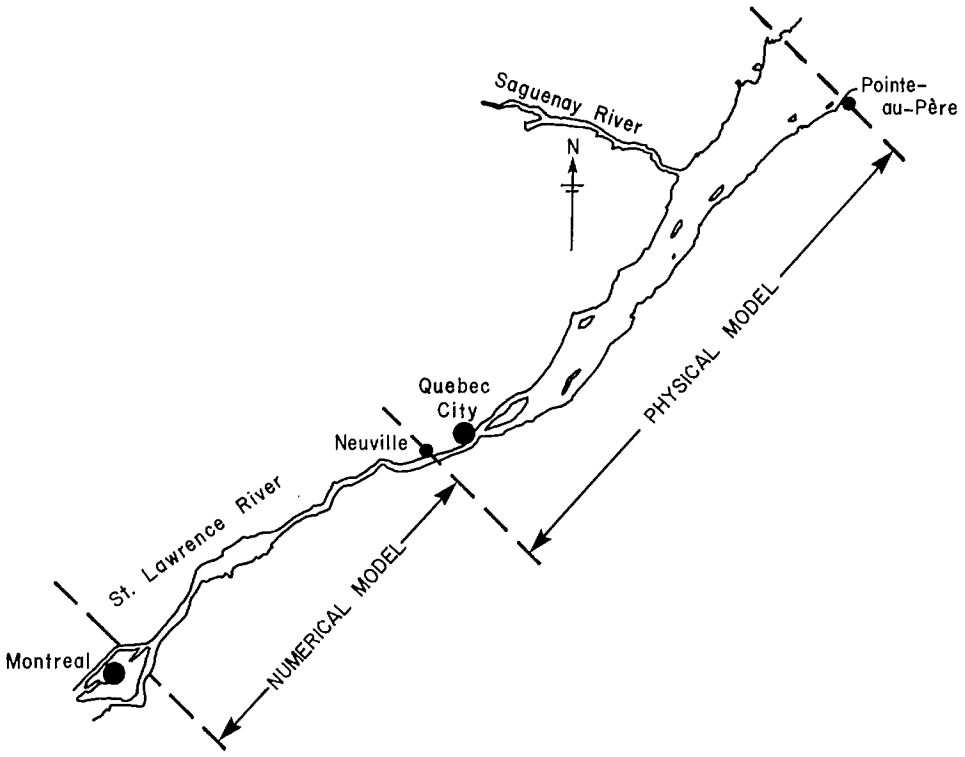

FIG. 4.27. Scheme of a hybrid model for the St. Lawrence Estuary in Canada. (Funke and Crookshank 1979)

range is about 3−5 m with a maximum discharge of about 28 000 $m^3 \cdot s^{-1}$. At Montreal, there are no diurnal or semidiurnal tides, but the average discharge is about 7000 $m^3 \cdot s^{-1}$ (all the numbers given above are for the natural state).

The total length of the physical model is 165 m and its horizontal and vertical scales are 1:2000 and 1:120, respectively. Funke and Crookshank (1978, p. 2857) stated that the downstream boundary is 23.5 m wide and is connected to a bidirectional variable pitch impeller pump with a capacity of 1 $m^3 \cdot s^{-1}$. Computer control at this point follows a known vertical tide. The upstream boundary is discharge controlled by means of a fixed inflow into a 4 × 4 m tidal basin and a variable outflow from this basin over a sharp-edged 3-m horizontal weir operating under computer control. The difference between basin inflow and outflow is the model discharge, which is bidirectional and of the order of 0.02 $m^3 \cdot s^{-1}$.

The diurnal vertical tide and the pump control curve at the downstream boundary are harmonic recompositions of the Fourier coefficients for the specified tide and the control curve. One can generate 14-d tidal cycles, including wind setups.

In the numerical model, one-dimensional explicit finite-difference solutions to the shallow-water wave equations are obtained for a 220-km stretch consisting of 58 sections whose grid sizes vary from 3.2 to 4.8 km. The boundary conditions to this model are provided as a constant discharge at Montreal and a variable water elevation at Neuville obtained by locating a water level gauge at Neuville in the hydraulic model. The output of the numerical model is a value for the discharge at Neuville, which is fed into the control

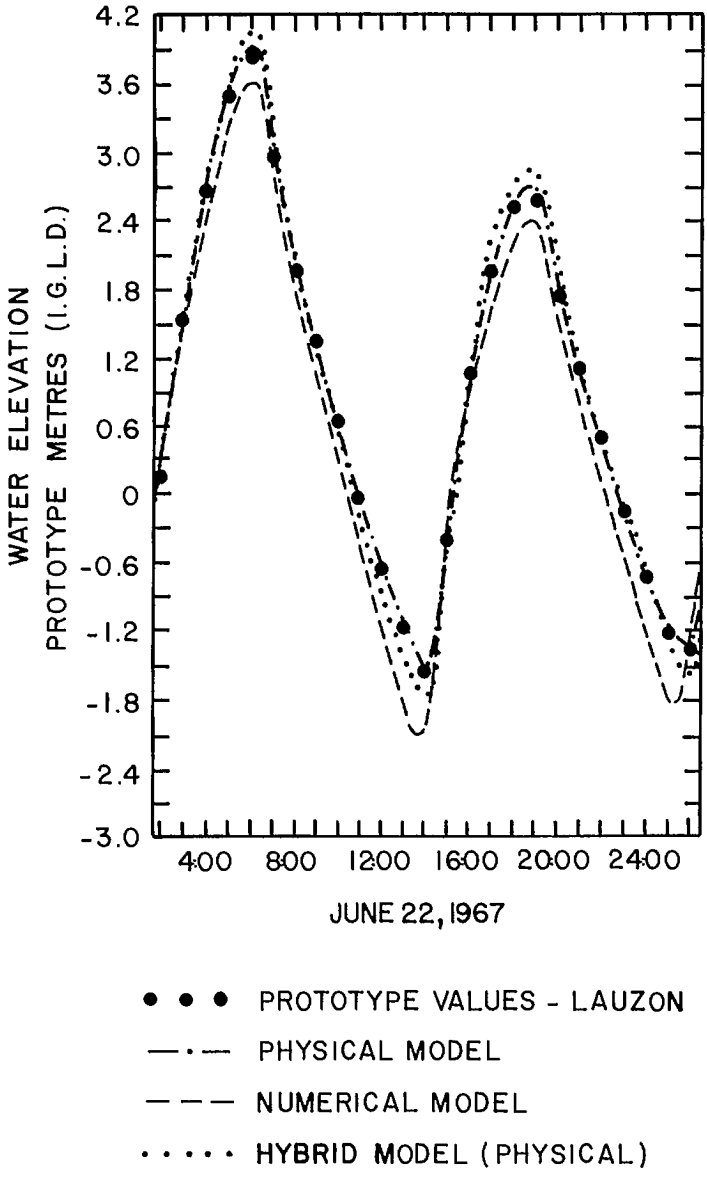

FIG. 4.28. Comparison of the water level at Lauzon, Que., obtained from the various models. (Funke and Crookshank 1979)

computer, for providing the discharge value at the downstream boundary.

Since the time domain of the hybrid model is determined by the hydraulic model, the time domain of the numerical model must be synchronized. The simulated results at Lauzon obtained from various models are compared in Fig. 4.28. It can be seen that the hybrid model reproduces the tide quite satisfactorily.

Chapter 5

Special Hydrodynamic Problems

In this chapter the following topics will be discussed: the phenomenon of resonance, which plays an important role in the coastal effects of storm surges; edge waves, a knowledge of which is needed in interpreting certain storm surge records; tides in the oceans and in certain selected coastal water bodies; the interaction between storm surges and tides and between storm surges and wind waves, which are different because wind waves are short-period waves whereas tides and storm surges are long-period waves; the influence of an ice layer and stratification on storm surges.

5.1 Resonance, Edge Waves

The topic of resonance, although relevant to storm surges, is so vast that it cannot be considered in detail here. Reference is made to Proudman (1953), Defant (1961), Murty (1977), and Leblond and Mysak (1978). For acoustical analogy and electrical analogy to the resonance phenomenon, see Raichlen (1966) and Miles (1974), respectively.

Any water body, such as a lake, inlet, bay, gulf, or a continental shelf, has natural modes of oscillation whose periods are determined by the geometry of the water body and the water depth. A knowledge of the natural modes of the water body is quite important in determining whether a given storm surge will be amplified or not and in determining the detailed characteristics of the surge in a particular water body for a given forcing.

For convenience, this section will be divided into three subsections: in the first subsection the theory of seiches will be described in some detail; in the second subsection the Helmholtz mode will be considered; in the final subsection the correct boundary conditions at the open part of the water body will be discussed.

The Theory of Seiches

The following discussion is based on Wilson (1972). The word "seiche" is believed to be derived from the Latin word "siccus," meaning dry or exposed, and has been used for several centuries to describe water level oscillations in Lake Geneva. The first mention of such a motion in Lake Constance (Switzerland) was made by Schulthaiss (1549, in Wilson 1972), and de Duillier (1730, in Wilson 1972), recorded such an oscillation. Vaucher (1803, in Wilson 1972) noted that similar motion occurred in many other lakes and he attributed this motion to meteorological causes. In the Great Lakes of North America the seiche motion was mentioned by Fra Marquette (1673), Baron Hontan (1689), Charlevoix (1721), and Dearborn (1829) (all in Wilson 1972). Major Whiting (1829, in Wilson 1972) attributed atmospheric pressure variations and wind as the causes of this motion.

Probably the first scientific study of seiches was that of Forel (1892), and Chrystal (1905) was probably the first to put forth a hydrodynamic theory of seiches. Important contributions to the theory of seiches were reviewed by Harris (1908), Lamb (1945), Proudman (1953), Defant (1961), Wilson (1972), and Miles (1974).

Merian (1828) gave a theory for free oscillations of water in a rectangular basin of length L and uniform depth h, the period T being given by

$$T = \frac{2L}{\sqrt{gh}} \tag{5.1}$$

where g is gravity. Forel (1892) applied this formula to seiches in lakes. For real lakes with variable depth, he chose an average value of h to replace the variable depths. Lagrange (1781) showed that the velocity c of a long wave is given by

$$c \sim \sqrt{gh} \tag{5.2}$$

From eq. 5.1 and 5.2

$$T = \frac{2L}{c} = \frac{\lambda}{c} \tag{5.3}$$

where λ is the wavelength of the oscillation (assuming it is in the form of a wave). Thus, the length of the wave is twice that of the water body (or basin). Forel explained this apparent paradox as being due to the superposition of two long waves whose length is twice that of the basin and traveling in opposite directions.

In the following, an attempt will be made to visualize a seiche as a special type of standing wave. For this, consider two progressive waves traveling in opposite directions in water of uniform depth. At every quarter period the crests and troughs are either in phase or out of phase. At half-wavelength intervals ($x = \lambda/4, 3\lambda/4, 5\lambda/4, \ldots$) surface elevation is continuously zero with time. Such points are called nodes and the points intermediate to these are the antinodes. This type of standing wave can also result if a progressive wave is reflected (without dissipation) at a vertical wall. Then, there will be an antinode of amplitude $2A$ (A being the amplitude of the progressive wave) at the wall and a first node at $x = \lambda/4$ from the wall.

A seiche is a special case of a standing wave that would result from interposing a second vertical barrier at any of the points $x = \lambda/2, 3\lambda/2, 2\lambda, \ldots$. The standing wave or seiche exists due to repeated reflections (assuming no dissipation) from the two vertical walls, where it would have its antinodes. On the other hand, if the second vertical barrier were inserted at any point other than a multiple of $\lambda/2$, the standing wave would become an irregular motion of the water surface. Thus, one can think of a seiche as a standing wave that is commensurate with the basin length L.

The seiche is uninodal for $L = \lambda/2$, binodal for $L = \lambda$, trinodal for $L = 3\lambda/2, \ldots$, n-nodal for $L = n\lambda/2$. Hence, from eq. 5.3, the period T_n of the nth mode of oscillation in a rectangular basin of length L and uniform depth h is

$$T_n = \frac{2L}{n\sqrt{gh}} \tag{5.4}$$

This is a generalization of the Merian formula and is valid for one-dimensional oscillation (no transverse motions). Note that at the nodes the motion is purely horizontal and at the antinodes it is purely vertical. The higher nodal (binodal, trinodal, etc.) seiches that may occur simultaneously with the fundamental mode (i.e. uninodal oscillation) are higher harmonics of the fundamental.

From eq. 5.4:

$$\frac{T_n}{T_1} = 1, \frac{1}{2}, \frac{1}{3}, \ldots, \frac{1}{n}, \quad n = 1, 2, \ldots, n$$

However, for irregular water bodies with variable depth (unlike in the case of a narrow rectangular basin of uniform depth), such a simple relation as above need not exist. Another point worth remembering is that neither the use of an average depth $\bar{h}$ nor a better version of this, as done by du Boys (see Defant 1961)

$$T_n \sim \frac{2}{n} \int_0^L \frac{dx}{[gh(x)]^{1/2}} \tag{5.5}$$

improves the Merian formula significantly.

Next, the concept of regarding seiches as a combination of free and forced oscillations will be developed. Any natural system, when displaced from its equilibrium position, will try to regain its equilibrium position (due to a restoring force) and will exhibit free oscillations once the disturbing force is removed. The nature of these oscillations depends on the system alone, the influence of the disturbing force being restricted to setting the initial amplitude of the oscillation. After some time, the free oscillations will gradually dissipate. In a water body or basin, the seiche is a type of free oscillation of the water, the restoring force being gravity. However, in nature the seiches could be of a forced nature because the disturbing force, instead of being instantaneous, can act over some period of time.

The equation of motion for a linear vibrating mass spring system subject to a displacement X due to a disturbing force $F(t)$ is, in the canonical form,

$$\ddot{X} + 2\beta\omega\dot{X} + \omega^2 X = \frac{F(t)}{m} \tag{5.6}$$

where β is a nondimensional damping coefficient, m is the mass of the vibrating body, ω is the angular frequency, and $m\omega^2$ is a spring constant for the restoring force. The solution of eq. 5.6 can be visualized as the combination of a free and forced part of a transient and steady-state part. To obtain the solution for the free oscillation, put $F(t) = 0$. Then

$$X_0 = e^{-\beta\omega t}[a \sin(\gamma t) + b \cos(\gamma t)] \tag{5.7}$$

where a and b are amplitudes of the motion determined by the initial conditions. The natural frequency γ of the system is

$$\gamma = \omega(1 - \beta^2)^{1/2} \tag{5.8}$$

and the natural period T is given by

$$T = \frac{2\pi}{\gamma} \tag{5.9}$$

The frictional damping, which is given by β, makes the free oscillations decay at a rate such that the amplitude decreases in one cycle by $e^{-\delta}$ where δ is the logarithmic decrement and is given by

$$\delta = \beta\omega T \tag{5.10}$$

For the forced solution, one must use eq. 5.6 in complete form and take a periodic disturbing force as follows:

$$(5.11) \qquad \frac{F(t)}{m} = F \cos(\sigma t + \epsilon)$$

where ϵ is an arbitrary phase angle. Then

$$(5.12) \qquad X_f = \frac{F\mu}{\omega^2} \cos(\sigma t + \epsilon - \alpha)$$

where

$$(5.13) \qquad \mu = \left\{\left[1 - \left(\frac{\sigma}{\omega}\right)^2\right]^2 + \left[2\beta\left(\frac{\sigma}{\omega}\right)\right]^2\right\}^{-1/2}$$

$$(5.14) \qquad \tan \alpha = \frac{2\beta\left(\frac{\sigma}{\omega}\right)}{1 - \left(\frac{\sigma}{\omega}\right)^2}$$

Here, μ is the dynamic amplification of the oscillation and α is a phase angle by which the forced oscillation lags the disturbing force. Thus, the total solution is

$$(5.15) \qquad X = X_0 + X_f$$

Here, X_0 decays with time whereas X_f persists as long as the disturbing force is applied. One can deduce that

$$(5.16) \qquad \mu = \frac{X_{\max}}{\left(\frac{F}{\omega}\right)^2} = \frac{X_{\max}}{X_i}$$

where X_i is the amplitude of the input displacement.

Ordinarily, one shows μ and α as ordinates versus σ/ω as abcissa. If the damping coefficient $\beta < \frac{1}{2}$, then from eq. 5.8 the natural freuency γ of the system is approximately given by ω. Hence, the ratio σ/ω in eq. 5.13 and 5.14 is effectively the ratio of the forced to the natural frequency. The dynamic amplification μ approaches its peak value when $\sigma/\omega \sim 1$. When this happens, resonance occurs and the amplitude of motion will be several times greater than the amplitude of the disturbing force.

For small frequency ratios $\sigma/\omega \ll 1$, the magnification is small, $\mu \sim 1$, and the motion follows the excitation (i.e. $\alpha \rightarrow 0$). For $\sigma/\omega \gg 1$, the resulting motion is much smaller than that of the exciting force; then, $\mu \rightarrow 0$ and the motion tends to become out of phase (i.e. $\alpha \rightarrow 180°$). Hence, the degree of resonance is determined by the damping factor 2β. Miles and Munk (1961) defined the degree of resonance through the factor Q, which is the maximum value of the dynamic amplification μ. From eq. 5.13 if $\sigma/\omega \sim 1$ (as occurs at resonance)

$$(5.17) \qquad \mu_{\max} \equiv Q \equiv \frac{1}{2\beta}$$

In the frequency range $(1 - \beta) < \sigma/\omega < (1 + \beta)$, if the damping factor 2β is small, the power amplification μ^2 has a value greater than $Q^2/2$. Hence, the frequency band width (over which the power amplification exceeds half its maximum value Q^2) is $1/Q$.

Thus, the sharper is the resonance, the narrower will be the spectral energy peak. This can be quantitatively expressed by stating that near resonance

$$\frac{Q^2}{\mu^2} \sim 1 + 4Q^2\left(1 - \frac{\sigma}{\omega}\right)^2 \tag{5.18}$$

The following results can be easily deduced from the above relations. For low Q conditions (i.e. heavy dissipation), a large rate of absorption of energy from the disturbing force to the oscillating system is necessary whereas for high Q (small damping) only a small energy absorption rate is sufficient for resonance. Miles and Munk (1961) showed that for a water body with a rather regular topography, low damping prevails; hence, the response is of the high Q type. Hence, a relatively small amount of energy (from, e.g. atmospheric pressure gradients) at the correct frequency can excite strong resonance. However, if the topography is irregular, damping is heavy and a low Q situation prevails.

Next, some theoretical aspects of free and forced seiches will be considered. With reference to a Cartesian coordinate system (x, y), let q_x and q_y be the components of the transport, η is the water level deviation from its equilibrium position, h is the water depth, P_a is the atmospheric pressure, τ_{s_x} and τ_{s_y} are the wind stress components, and K_x and K_y are the bottom friction coefficients. The equations of motion are

$$\frac{\partial q_x}{\partial t} + K_x q_x + g(h + \eta)\frac{\partial \eta}{\partial x} = F_{s_x} \tag{5.19}$$

$$\frac{\partial q_y}{\partial t} + K_y q_y + g(h + \eta)\frac{\partial \eta}{\partial y} = F_{s_y} \tag{5.20}$$

where

$$\begin{aligned} F_{s_x} &\equiv \frac{\tau_{s_x}}{\rho} + \frac{(h + \eta)}{\rho}\frac{\partial P_a}{\partial x} \\ F_{s_y} &\equiv \frac{\tau_{s_y}}{\rho} + \frac{(h + \eta)}{\rho}\frac{\partial P_a}{\partial y} \end{aligned} \tag{5.21}$$

Here the Coriolis terms are omitted, which, however, will be important for large lakes and bays.

For simplicity it will be assumed that $\partial/\partial y = 0$ and $v = 0$. Then, the equation of motion 5.19 reduces to

$$\frac{\partial q}{\partial t} + Kq + g(h + \eta)\frac{\partial \eta}{\partial x} = F_S(x, t) \tag{5.22}$$

where subscript x on q is omitted. The continuity equation is

$$\frac{\partial \eta}{\partial t} + \frac{\partial q}{\partial x} = 0 \tag{5.23}$$

Equations 5.22 and 5.23 can be transformed into two hyperbolic equations in the dependent variables q and η:

$$\frac{\partial^2 \eta}{\partial t^2} + K\frac{\partial \eta}{\partial t} - g\frac{\partial}{\partial x}\left[(h + \eta)\frac{\partial \eta}{\partial x}\right] = -\frac{\partial F_S}{\partial x} \tag{5.24}$$

$$\frac{\partial^2 q}{\partial t^2} + K\frac{\partial q}{\partial t} - g(h + \eta)\frac{\partial^2 q}{\partial x^2} = \frac{\partial F_S}{\partial t} \tag{5.25}$$

The solutions of eq. 5.24 and 5.25 with the right-hand sides set to zero give the solutions for the free oscillation, whereas the solutions for the complete equations are the forced oscillations.

In a rectangular basin of length L and uniform depth h, in which a free oscillation is generated by equating the disturbing force F_S to zero, eq. 5.2, 5.24, and 5.25 give

$$\frac{\partial^2 \eta}{\partial t^2} + K\frac{\partial \eta}{\partial t} - c^2\frac{\partial^2 \eta}{\partial x^2} = 0 \tag{5.26}$$

$$\frac{\partial^2 q}{\partial t^2} + K\frac{\partial q}{\partial t} - c^2\frac{\partial^2 q}{\partial x^2} = 0 \tag{5.27}$$

Since these equations have the same form in η and q, one can use the method of separation of variables to solve them:

$$\eta(\text{or } q) = X(x)T(t) \tag{5.28}$$

The solution can be shown to be

$$\eta(\text{or } q) = e^{-Kt/2}[A\cos(kx) + B\sin(kx)][C\cos(\gamma t) + D\sin(\gamma t)] \tag{5.29}$$

where the angular frequency γ of the free oscillation is given by

$$\gamma = \omega\left(1 - \frac{k}{2\omega}\right)^{1/2} \tag{5.30}$$

The wave number k and the angular frequency ω are related through

$$\omega = kc \tag{5.31}$$

in which either k or ω must be determined.

To determine the constants of integration A, B, C, D, the following boundary conditions must be used. At the ends of the basin, $x = 0, L$ transport q must be zero for all time. Thus

$$\begin{aligned} q &= B'e^{-Kt/2}\sin(kx)\sin(\gamma t + \epsilon) \\ \sin(kL) &= 0 \end{aligned} \tag{5.32}$$

where B' is a constant to be determined and ϵ is a phase angle. From the continuity equation and taking a as the amplitude of free oscillation:

$$\begin{aligned} \eta &\sim ae^{-Kt/2}\cos(kx)\cos(\gamma t + \epsilon) \\ q &\sim \frac{a\gamma}{k}e^{-Kt/2}\sin(kx)\sin(\gamma t + \epsilon) \end{aligned} \tag{5.33}$$

The wave number k can be determined from the second equation of 5.32 to give

$$kL = n\pi, \quad n = 1, 2, 3, \ldots \tag{5.34}$$

Then, one can determine γ and ω from eq. 5.30 and 5.31. Since eq. 5.31 represents a standing wave whose amplitude is a at $t = 0$ and decays exponentially with time, this oscillation is similar to the mechanical system discussed earlier. Thus

$$k = 2\beta\omega \tag{5.35}$$

Next, the disturbing force will be explicitly introduced. Since the role of edge waves in storm surges and resonant coupling to the atmosphere will be considered later in this

section, this disturbing force will be prescribed as an atmospheric pressure pulse moving with a uniform velocity V over the water body along the length of the water body. Note that in Chapter 4 solutions to essentially a similar problem using the method of characteristics were discussed. The atmospheric pulse is assumed to be sinusoidal with a pulse length $2l$. The amplitude of the pulse is the pressure gradient $(\partial P_a/\partial x)_{\max}$ or simply ΔP.

The external force F_S in eq. 5.22 can then be written using the Fourier series representation as follows:

$$F_S = -\frac{4}{\pi}\frac{\Delta P}{\rho}\frac{hl}{L}\sum_{r=1}^{\infty}\left[1-\left(\frac{rl}{L}\right)^2\right]^{-1}\sin(k_r l)\sin(k_r x)\cos(k_r V t) \tag{5.36}$$

where

$$k_r = \frac{r\pi}{L}, \qquad r = 1, 2, 3, \ldots$$

The right-hand sides of eq. 5.24 and 5.25 then become

$$\begin{aligned} -\frac{\partial F_S}{\partial x} &= 4\frac{\Delta P}{\rho}\frac{hl}{L^2}\sum_{r=1}^{\infty} r\left[1-\left(\frac{rl}{L}\right)^2\right]^{-1}\sin(k_r l)\sin(k_r x)\cos(k_r V t) \\ \frac{\partial F_S}{\partial t} &= 4\frac{\Delta P}{\rho}\frac{hl}{L^2}\sum_{r=1}^{\infty}\left[1-\left(\frac{rl}{L}\right)^2\right]^{-1}\sin(k_r l)\sin(k_r x)\sin(k_r V t) \end{aligned} \tag{5.37}$$

Wilson (1972) simplified the problem by considering only a general rth term in these Fourier summations and obtained solutions to eq. 5.24 and 5.25 by a trial of possible solutions:

$$\begin{aligned} \eta_r &= M_r(t)\cos(k_r x) \\ q_r &= N_r(t)\sin(k_r x) \end{aligned} \tag{5.38}$$

where $M_r(t)$ and $N_r(t)$ must be determined, and the complete solutions can be written as

$$\begin{aligned} \eta &= \sum_{r=1}^{\infty}\eta_r \\ q &= \sum_{r=1}^{\infty} q_r \end{aligned} \tag{5.39}$$

Substituting eq. 5.38 into eq. 5.24 and 5.25 gives

$$\begin{aligned} \frac{\partial M_r}{\partial t} + K\frac{\partial M_r}{\partial t} + \left(\frac{r\pi c}{L}\right)^2 M_r &= P_r\cos(k_r V t) \\ \frac{\partial N_r}{\partial t} + K\frac{\partial N_r}{\partial t} + \left(\frac{r\pi c}{L}\right)^2 N_r &= P_r V\sin(k_r V t) \end{aligned} \tag{5.40}$$

where

$$P_r = 4\frac{\Delta P}{\rho}\frac{h}{L}\left\{\frac{rl}{L}\left[1-\left(\frac{rl}{L}\right)^2\right]^{-1}\right\}\sin(k_r l) \tag{5.41}$$

This system is analogous to the mechanical system discussed earlier. To be able to exploit the analogy, define

$$\omega_r \doteq \frac{r\pi c}{L} = k_r c$$

$$\sigma_r = \frac{r\pi V}{L} = k_r V$$

(5.42)

$$k_r = \frac{r\pi}{L}$$

$$2\beta\omega_r = K$$

By analogy to the mechanical system, the forced oscillations M_r and N_r can be written as

(5.43) $$M_r = \frac{P_r\mu}{\omega_r^2}\cos(\sigma_r t - \alpha)$$

(5.44) $$N_r = \frac{P_r\mu V}{\omega_r^2}\sin(\sigma_r t - \alpha)$$

where

$$\mu = \left\{\left[1 - \left(\frac{V}{c}\right)^2\right]^2 + \left[2\beta\left(\frac{V}{c}\right)\right]^2\right\}^{-1/2}$$

(5.45)

$$\tan\alpha = \frac{2\beta\left(\frac{V}{c}\right)}{\left[1 - \left(\frac{V}{c}\right)^2\right]}$$

From eq. 5.38 and 5.41–5.44, the contributions from the rth terms to the forced oscillations can be written (using subscript f to denote forced motion) as

(5.46) $$(\eta_f)_r = R\phi_r\mu\cos(k_r x)\cos(\sigma_r t - \alpha)$$

(5.47) $$(q_f)_r = RV\phi_r\sin(k_r x)\sin(\sigma_r t - \alpha)$$

where

$$R = \frac{4}{\pi^2}\frac{L\Delta P}{\rho g}$$

(5.48) $$\phi_r = \frac{\psi_r \sin\pi\psi_r}{r^2(1 - \psi_r^2)}$$

$$\psi_r = \frac{rl}{L}$$

Here, the quantity ϕ_r is an excitation amplification factor that varies according to the relative size l/L of the pressure pulse (in the rth mode) with reference to the basin length. The relationship between l/L and ϕ_r is shown in Fig. 5.1. It can be seen that when $l/L = 1.125$, the forced oscillation reaches the maximum possible amplitude, and mostly the fundamental mode is generated (i.e. $r = 1$). For $l/L = 0.563$, the second mode $r = 2$ has its maximum amplitude, although its amplitude will be less than that of the fundamental mode. The smaller the value of l/L, the greater is the tendency for a large number of harmonic oscillations with small amplitudes to be generated. Each harmonic will have a maximum amplitude for a certain value of l/L.

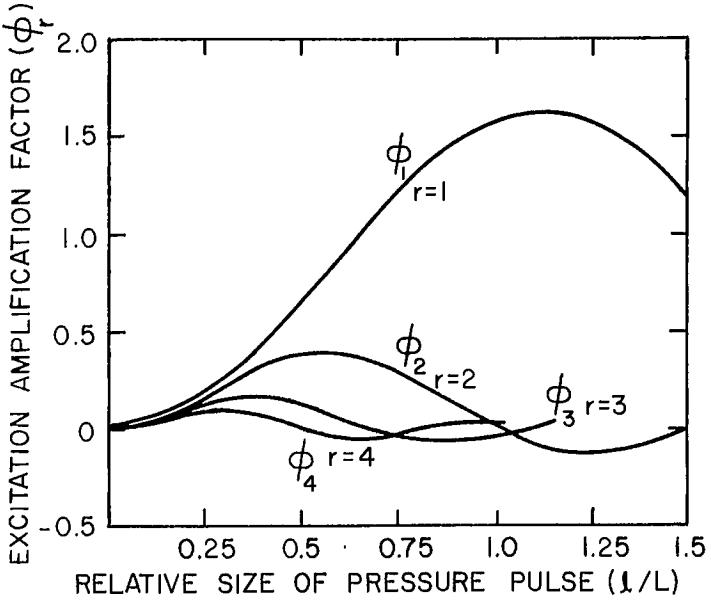

FIG. 5.1. Excitation amplification factor ϕ_r as a function of the relative size of pressure pulse l/L for several harmonic modes ($r = 1, 2, 3, 4$). (Wilson 1972)

The free oscillations generated by the pressure pulse are

$$(\eta_0)_r = a_r \exp(-\beta\omega_r t) \cos(k_r x) \cos(\gamma_r t + \epsilon)$$
$$(q_0)_r = \frac{a_r \gamma_r \exp(-\beta\omega_r t)}{k_r} \sin(k_r x) \sin(\gamma_r t + \epsilon) \tag{5.49}$$

Here the amplitude a_r and the phase angle ϵ must be determined.

The total solutions can be written as follows:

$$\eta_r = (\eta_f)_r + (\eta_0)_r$$
$$q_r = (q_f)_r + (q_0)_r \tag{5.50}$$

The amplitude a_r and the phase angle ϵ can be determined from the following two initial conditions (i.e. before the pressure pulse starts to move over the water body):

$$\eta_r = 0 \text{ and } q_r = 0 \text{ at } t = -\frac{L}{V} \tag{5.51}$$

From eq. 5.46, 5.47, and 5.49–5.51, $(a_r)_0$ and ϵ_0 can be determined from the following simultaneous equations:

$$R\phi_r \mu \cos(k_r l + \alpha) + (a_r)_0 \exp\left[\beta\left(\frac{c}{V}\right)k_r l\right] \cos\left[\left(\frac{\gamma_r l}{V}\right) - \epsilon_0\right] = 0$$
$$R\phi_r \mu V \sin(k_r l + \alpha) + (a_r)_0 \left(\frac{\gamma_r}{k_r}\right) \exp\left[\beta\left(\frac{c}{V}\right)k_r l\right] \sin\left[\left(\frac{\gamma_r l}{V}\right) - \epsilon_0\right] = 0 \tag{5.52}$$

where subscript 0 denotes the beginning of the fetch.

The solutions for $(a_r)_0$ and ϵ_0 obtained from eq. 5.52 are relevant as long as the pressure pulse is over the water surface. During this stage there are free and forced oscillations. However, from the instant the pulse passes over the far end of the basin, i.e. $t = (L + l)/V$, only free oscillations occur. Thus

$$\eta_r = \eta_0 \text{ and } q_r = q_0 \text{ at } t = \frac{L + l}{V} \tag{5.53}$$

The free oscillations at the end of the fetch will be denoted by subscript L. Hence, during this free oscillation stage, $(a_r)_L$ and ϵ_L can be determined from the following two simultaneous equations:

$$R\phi_r\mu \cos [k_r(L + l) - \alpha] + (a_r)_0 \exp \left[-\beta\left(\frac{c}{V}\right)k_r(L + l)\right] \times \cos \left[\frac{\gamma_r(L + l)}{V} + \epsilon_0\right] = (a_r)_L \exp \left[-\beta\left(\frac{c}{V}\right)k_r(L + l)\right] \cos \left[\frac{\gamma_r(L + l)}{V} + \epsilon\right] \tag{5.54}$$

and

$$R\phi_r\mu V \sin [k_r(L + l) - \alpha] + (a_r)_0\left(\frac{\gamma_r}{k_r}\right) \exp \left[-\beta\left(\frac{c}{V}\right)k_r(L + l)\right] \times \sin \left[\frac{\gamma_r(L + l)}{V} + \epsilon_0\right] = (a_r)_L\left(\frac{\gamma_r}{k_r}\right) \exp \left[-\beta\left(\frac{c}{V}\right)k_r(L + l)\right] \times \sin \left[\frac{\gamma_r(L + l)}{V} + \epsilon_L\right] \tag{5.55}$$

When the speed V with which the pressure pulse moves is about the same as the velocity c with which a long gravity wave moves in the water body, then resonance occurs. That is, when $V/c \sim 1$, eq. 5.45 gives

$$\begin{aligned} \mu &\sim \frac{1}{2\beta} \\ \alpha &\sim 90^\circ \end{aligned} \tag{5.56}$$

Then from eq. 5.52:

$$\begin{aligned} (a_r)_0 &= \frac{R\phi_r}{2\beta \exp (\beta k_r l)} \\ \epsilon_0 &= 90^\circ \end{aligned} \tag{5.57}$$

Then from eq. 5.46, 5.47, 5.50, and 5.52:

$$\begin{aligned} \eta_r &= \frac{R\phi_r}{2\beta}\left\{1 - \exp \left[-\beta\omega_r\left(t + \frac{l}{V}\right)\right]\right\} \cos (k_r x) \sin (\omega_r t) \\ q_r &= \frac{R\phi_r(gh)^{1/2}}{2\beta}\left\{1 - \exp \left[-\beta\omega_r\left(t + \frac{l}{V}\right)\right]\right\} \sin (k_r x) \cos (\omega_r t) \end{aligned} \tag{5.58}$$

during the interval $-l/V < t < (L + l)/V$.

For this resonant case, the free oscillations after the pulse completes its traverse over the water body are given by the right sides of eq. 5.54 and 5.55. The parameters $(a_r)_L$ and

ϵ_L have the following solutions:

$$(a_r)_L = \frac{R\phi_r}{2\beta} \frac{\{1 - \exp[-\beta k_r(L + l)]\}}{\exp[-\beta k_r(L + l)]}$$
$$\epsilon_L = 90° \tag{5.59}$$

For $t > (L + l)/V$, the water body exhibits damped oscillations, which are given by

$$\eta_r = \frac{R\phi_r}{2\beta}\{1 - \exp[-\beta k_r(L + 2l)]\} \exp\left\{-\beta\omega_r\left[t - \frac{(L + l)}{V}\right]\right\} \times \cos(k_r x) \sin(\omega_r t)$$
$$q_r = -\frac{R\phi_r(gh)^{1/2}}{2\beta}\{1 - \exp[-\beta k_r(L + 2l)]\} \exp\left\{-\beta\omega_r\left[t - \frac{(L + l)}{V}\right]\right\} \times \sin(k_r x) \cos(\omega_r t) \tag{5.60}$$

for $t > (L + l)/V$.

Wilson (1972) evaluated the above solutions for the following two sizes of the pressure pulse: (1) $l/L = 1.125$ for which $\phi_1 = 1.62$ is a maximum for the fundamental mode oscillation ($r = 1$) and (2) $l/L = 0.563$ for which $\phi_1 = 0.80$ is a maximum for $r = 1$ and $\phi_2 = 0.40$ is a maximum for $r = 2$ in the second harmonic.

In case 1, only the fundamental mode $r = 1$ is important and in case 2 the fundamental mode $r = 1$ and the second harmonic $r = 2$ are important (Fig. 5.1).

The relationship between the dimensionless time Vt/L as abcissa versus amplitude of oscillation (in units of R) as ordinate is shown in Fig. 5.2 (for a definition of R see eq. 5.48). In this calculation β was taken as 0.0075. The resonance condition is $V = c = \sqrt{gh}$. The results for cases 1 and 2 can be summarized as follows. Case 1 dealt with a larger pressure pulse, which took a longer time to cross the water body, and case 2 dealt with a smaller pulse and a shorter duration to cross the water body. For case 1 type forcing, a strong uninodal oscillation is excited, which reaches its maximum amplitude a short time after the pulse traverses the water body. This uninodal seiche decays as the logarithmic decremental law of eq. 5.10. For case 2 type forcing, a strong binodal oscillation also appears, and at times this augments the uninodal seiche. However, this binodal oscillation disappears faster, and after some time only the uninodal oscillation remains.

From the foregoing the following conclusions can be stated concerning excitation of seiches by pressure pulses.

1) When the speed of movement V of the pressure pulse agrees with the phase velocity c of a free wave in the water body, resonance occurs and the dynamic amplification μ, defined as $\mu = 1/2\beta$, can have large values. In Fig. 5.2, $\beta = 0.075$; thus, $\mu = 6.7$.

2) The size of the pressure pulse $2l$ relative to the distance L it traverses over the water body determines the response factor ϕ_r. In Fig. 5.1, for the fundamental mode, ϕ_r can contribute an amplification factor of 1.62 when $l/L \sim 1$.

3) When the size of the pulse is not optimal for the maximum response of the water body, higher seiche modes also appear.

Next, the magnitude of the pressure anomaly required to produce a seiche or surge of the amplitudes that occur in natural water bodies is considered:

$$P_0 = \frac{2l}{\pi}\Delta P \tag{5.61}$$

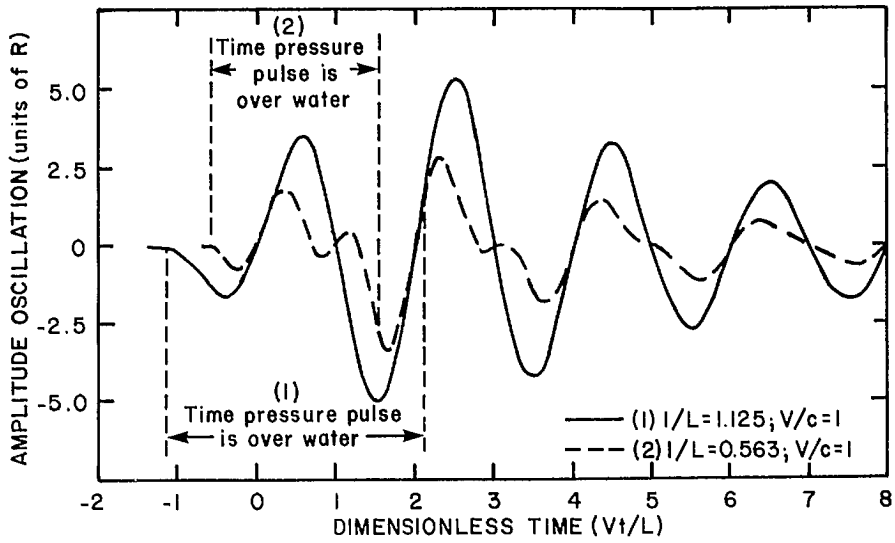

FIG. 5.2. Free and forced seiches induced by a traveling pressure pulse in a rectangular basin of uniform depth (at $x = 0$). (Wilson 1972)

where

P_0 = pressure anomaly

(5.62) ΔP = maximum pressure gradient

$$P_0 = \frac{\rho' g H}{12}$$

where ρ' is the density of mercury and H is the pressure anomaly in terms of inches of mercury.

From eq. 5.48, 5.61, and 5.62:

$$(5.63) \quad H = 6\pi \frac{\rho}{\rho'} \frac{l}{L} R$$

Taking $\rho'/\rho = 13.6$ and $l/L \sim 1$, then

$$(5.64) \quad H = 1.39R$$

Here, H is in inches and R is in feet. In Fig. 5.2, the maximum amplitude of the seiche for $l/L \sim 1$ is roughly $5R$. If $\eta \sim 1$ ft (0.305 m) (i.e. $5R = 1$ ft or $R = 0.2$ ft), from eq. 5.64 the pressure anomaly required to produce this disturbance is 0.28 inches of mercury (10 mb). Note that the inverse barometer effect requires $H = 1$ in. for $\eta = 1$ ft.

Next, some actual cases will be considered in which moving pressure fronts excited seiches. Proudman (1953) was probably among the first to invoke resonant coupling between a squall line and the gravity waves in the water on the coast of the United Kingdom to account for certain water level disturbances. However, in the hydrodynamic context, Lamb (1945) recognized such a possibility and discussed the role of the dynamic magnification μ (see eq. 5.45 and assume that the damping coefficient β is zero).

TABLE 5.1. Seiches in typical lakes: observed modes of oscillation. (Wilson 1972)

Lake	Location	Fundamental mode T_1(min)	Period ratios (T_n/T_1) for higher modes at n				
			2	3	4	5	6
Geneva	Switzerland	74.0	0.480				
Constance	German–Swiss border	55.8	0.700	0.503			
Garda	Italy	42.9	0.666	0.507	0.348	0.281	0.230
Loch Earn	Scotland	14.5	0.557	0.414	0.275	0.244	0.198
Loch Treig	Scotland	9.2	0.560				
Loch Neagh	Ireland	96.0	0.718	0.468			
Ontario	U.S.A., Canada	289.0					
Erie	U.S.A., Canada	858.0	0.632	0.499	0.292	(0.262)	
Michigan–Huron	U.S.A., Canada	2700.0					
Michigan	U.S.A.	543.0	0.578	0.411	0.344	0.278	0.222
Superior	U.S.A., Canada	480.0					
Tanganyika	Africa	4.5	0.511	0.378			
Chiemsee	S. Bavaria, Germany	41.0					
Vättern	Sweden	179.0	0.542				
Königsee	Germany	10.6					
Yamanaka	Japan	15.6	0.677	0.350			
Chiuzenji	Japan	7.7					
Baikal	USSR	278.2					
Sea of Aral	USSR	1368.0					
Sea of Azov	USSR	1470.0	0.603	0.522			
George	Australia	131.0					
Baltic Sea–Gulf of Finland	Europe	1636.0					

EXAMPLES OF SEICHES GENERATED BY ATMOSPHERIC DISTURBANCES

1) Weather front over the Gulf of Mexico, March 17–19, 1952. A weather front traveled eastward across the northern coastline of the Gulf of Mexico followed by large oscillations at several locations. At the mouth of the Mississippi River in Southwest Pass, at Burrwood a large surge occurred. The weather front traveled with a speed V greater than 26 $mi \cdot h^{-1}$ (41.5 $km \cdot h^{-1}$) across this delta. According to Wilson (1972), resonant air–water coupling occurred between Southwest Pass and the main Louisiana coastline. Wilson (1957b) suggested that the fundamental mode and the second mode with periods of 3.5 and 1.8 h are present in the Burrwood marigram. The existence of a low-amplitude third mode probably accounts for the sharpness of the first wave. From the decay of the fundamental and the first harmonic it was deduced that $\beta = 0.075$. Wilson (1972) deduced, using the equations discussed earlier, that the theoretically expected amplitude of the fundamental should be 0.58 ft and the second and third modes together should be 0.35 ft. The marigrams support this conjecture.

2) Squall line over Lake Michigan, June 26, 1954. This case will be discussed in detail later.

3) Storm surge resurgence off the coast of New York, August 30–September 1, 1954. Hurricane Carol generated a surge along the east coast of the United States. A train of long-period surges were also produced with periods of the order of 7 h. This activity, mainly between Atlantic City and New York, was identified as edge waves by Munk et al. (1956).

TABLE 5.2. Coastal seiches in typical gulfs, bays, and harbors: observed modes of oscillation. (Wilson 1972)

Gulf, bay, or harbor	Location	Observed periods of oscillation (approximate) (min) for fundamental higher modes					
St. John Harbor	Bay of Fundy, Canada	74	42				
Narragansett Bay	Rhode Island	44	46				
Vermillion Bay	Louisiana	180	120				
Galveston Bay	Texas	75					
San Pedro Bay	Los Angeles, CA	72–84	60–65	44–45	35–40	28–35	24–27
San Francisco Bay	California	116	47	34–41	24–27	17–19	
Monterey Bay	California	60–66	36–38	28–32	22–24	16–20	10–15
Hilo Bay	Hawaii	20–25	10	7			
Guanica	Puerto Rico Caribbean	45					
Lerwick	Scotland	28–30					
Port of Leixoes	Near Porto, Portugal	20–25	13–15	3–5			
Bay of Naples	Italy	48	17–18				
Gulf of Venice–Gulf of Trieste	North Adriatic Sea	210–240	60	40	10	5	
Euripus, Gulf of Talanta	Greece between Is. Euboe and mainland	105	60				
Algiers	Algeria, North Africa	20–26					
Casablanca	Morocco, North Africa	35–40	18–20				
Table Bay, Capetown	South Africa	58–62	38–43	25–30	18–21	14–17	10–11
Algoa Bay, Port Elizabeth	South Africa	69–75	57	42–52	35	20–25	16–17
Tamatave	Madagascar (Malagasy Republic)	15	8–10	1–2			
Tuticorin, Gulf of Mannar	India–Ceylon	180					
Bay of Hakodate	Hokkaido, Japan	45–57	21–24				
Bay of Aomori	Honshu, Japan	295	103	23–26			
Bay of Ofunato	Honshu, Japan	41–44	36–39	12–17	5–6		
Bay of Nagasaki	Kyushu, Japan	69–72	54	44–45	40	32–38	22–25
Wellington	New Zealand	28	?	?			
Lyttleton	New Zealand	156	?	?			

4) Seiches and barometric fluctuations, Loch Earn, Scotland. A classic study of this problem was done by Chrystal (1906). He showed that wind alone cannot account for the seiches, and atmospheric pressure gradients should also be considered.

5) Pressure pulse over San Francisco Bay, November 21, 1910. Marmer (1926) studied the small seiches produced.

6) Eastward moving pressure fronts generate seiches in the Gulf of Venice and the Gulf of Trieste. Invoking resonant air–water coupling, Greco et al. (1957) accounted for several of the seiches produced.

7) Seiches in Table Bay, Cape Town, South Africa. See Wilson (1972) for details.

8) Atlantic Ocean Islands. Cartwright (1960), Donn et al. (1954), and Donn and McGuinness (1959) discussed seiches at Lerwick in the Shetland Islands and at St. George's Harbour (Bermuda).

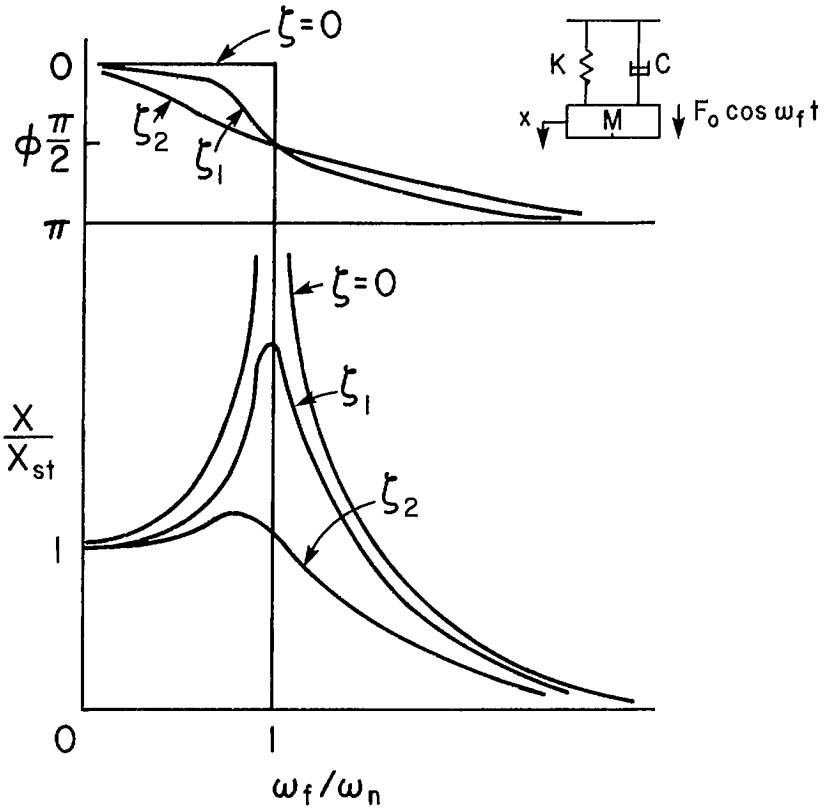

FIG. 5.3. Resonance characteristics of a system with a single degree of freedom. (Raichlen 1966)

The periods of seiches in selected lakes are listed in Table 5.1 and the periods of seiches in selected gulfs, bays, and harbors are listed in Table 5.2.

HELMHOLTZ MODE

Following mechanical and acoustical analogy, the so-called Helmholtz mode will be defined and then a hydrodynamic explanation invoked. With reference to Fig. 5.3, the equation of motion for the mechanical system shown can be written as (Raichlen 1966):

$$M\ddot{x} + c\dot{x} + kx = F_0 \cos(\omega_f t) \tag{5.65}$$

where M is the mass of the oscillating body, c is a linear damping coefficient, k is a spring constant, and ω_f is a (circular) forcing frequency; dots denote differentiation with respect to t.

The following steady-state solution can be assumed:

$$x = X \cos(\omega_f t - \phi) \tag{5.66}$$

where X is the maximum displacement and ϕ is a phase angle between the input and output functions. The parameters X and ϕ can be made nondimensional as follows:

$$(5.67) \qquad \frac{X}{X_{st}} = \frac{1}{\left\{\left[1 - \left(\frac{\omega_f}{\omega_n}\right)^2\right]^2 + \left(2\zeta\frac{\omega_f}{\omega_n}\right)^2\right\}^{1/2}}$$

$$(5.68) \qquad \tan\phi = \frac{2\zeta\omega_f/\omega_n}{1 - \left(\frac{\omega_f}{\omega_n}\right)^2}$$

where

$$X_{st} \equiv \frac{F_0}{k}$$

$$(5.69) \qquad \omega_n \equiv \left(\frac{k}{M}\right)^{1/2}$$

$$\zeta \equiv \frac{c}{2M\omega_n}$$

Figure 5.3 represents graphically eq. 5.67 and 5.68. First, consider the behavior of X/X_{st}. For the case of small frictional dissipation, when the frequency is approximately equal to the undamped natural frequency of the system, the forcing function X_{st} is greatly amplified. As the damping ζ gets bigger, the difference between the resonant frequency and ω_n increases. For low values of the frequency ratio, the amplitudes of the input and the output are approximately equal. However, for frequencies considerably above the resonant frequency, the response decreases substantially and the maximum displacement of the mass approaches zero. If the damping is zero, eq. 5.67 gives infinite amplitude at resonance. However, this result, which is obtained from the linear theory, must be modified at great amplitudes to include the influence of the nonlinear effects.

Next, consider the behavior of the phase angle with respect to the forcing frequency. For low values of the frequency ratio, the forcing function is mainly in phase with the output displacement, and at high values they are 180° out of phase. At resonance the phase angle becomes 90°, and hence, the force $F_0 \cos(\omega_f t)$ is in phase with the velocity $\dot{x}$. Thus, when the mass is going through its zero-displacement position, a maximum force is impressed upon the system.

The number of degrees of freedom of a system is the number of independent coordinates that are required to describe the motion of the system. Raichlen (1966) cited the vibration of a clamped circular membrane as an example of a system possessing infinite degrees of freedom, whereas the spring–mass–dashpot system considered here is an example of a system with a single degree of freedom.

In acoustics, an example of a single degree of freedom system is the so-called Helmholtz resonator, which consists of a cavity of volume V connected to a tube of length l and area of cross-section A. The equation of motion for this system is:

$$(5.70) \qquad M\ddot{x} + r_a\dot{x} + \frac{x}{B} = P\cos(\omega_f t)$$

where x is the volume displacement, c is the wave velocity, r_a is the radiation loss coefficient, and

$$M \equiv \frac{\rho l}{A}$$

(5.71)

$$B \equiv \frac{V}{\rho c^2}$$

The natural frequency of the Helmholtz resonator is given by

$$\omega_n \equiv c\sqrt{\frac{A}{lV}} \tag{5.72}$$

Since eq. 5.70 and 5.65 are similar, it can be seen that when the frequency is equal to ω_n, the ratio of the volume displacement to the applied pressure will be ∞ when r_a is zero. Also, the ratio of the volume displacement to the applied pressure varies, as shown in Fig. 5.3.

Next, consider the Helmholtz mode in the context of hydrodynamics (Miles (1971) used the term "Helmholtz mode," Platzman (1972) used "co-oscillating mode," and Lee and Raichlen (1972) referred to it as the "pumping mode"). Basically, Helmholtz resonance represents the balance between the kinetic energy of water flowing in through a narrow connecting channel and the potential energy from the rise in the mean water level within the harbor (Freeman et al. 1974). It is an additional gravitational mode of a substantially longer period than the fundamental free oscillation, as can be seen below.

To conceptualize the Helmholtz mode, Platzman (1972) presented the following argument. Suppose that at the mouth of a rectangular bay an adjustable barrier exists and that this barrier is gradually moved from the two sides of the bay to the center, completely closing off the bay. The open modes with periods initially of the form $2T/(2n - 1)$, $n = 1, 2, 3, \ldots$, will be transformed continuously into the closed mode periods of T/n, $n = 0, 1, 2, \ldots$. It is obvious that the fundamental mode for the open bay transforms into the zeroth mode for the closed basin, and as the barrier closes, this period approaches ∞. For small openings, the period of the Helmholtz mode is less than ∞ but greater than the period for a completely open bay. Platzman (1972) showed that rotation changes the period of the Helmholtz mode by, at most, 3%.

In section 7.1, how the Helmholtz mode in Goderich Harbor (Lake Huron) contributed to an amplified storm surge will be considered in detail. The classic theory for the Helmholtz mode can be applied only to a single channel harbor. Freeman et al. (1974) extended this to a harbor (or basin) with multiple channels (or openings). The dissipative forces (due to the eddy viscosity of the fluid and to the energy radiated from the mouth) are ignored. These forces affect the amplification factor at resonance and will shift the resonant frequency slightly. The solution developed by Freeman et al. (1974) for the frequency ω_0 is

$$\omega_0 = \sqrt{\frac{g}{A}} \sum_{i=1}^{n} \left(\frac{S_i}{L_i}\right)^{1/2} \text{rad} \cdot \text{s}^{-1} \tag{5.73}$$

where g is gravity, A is the surface area of the harbor, S_i is the cross-sectional area of the ith channel, and L_i is the length of the ith channel.

Miles and Munk (1961) introduced the so-called harbor paradox in which they showed that narrowing of a harbor mouth (relative to the other dimensions) diminishes the protection from seiching. For a quantitative estimation of this in terms of the sharpness or Q at resonance, the reader is referred to their paper. Miles and Lee (1975) used equivalent electric circuit analysis to study this problem. Garrett (1970) showed that the harbor

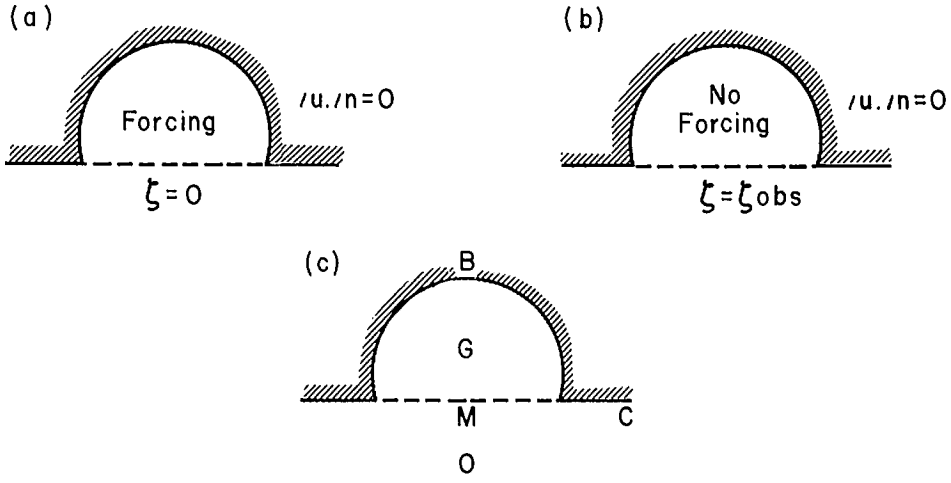

FIG. 5.4. Defant's (1961) distinction between independent and cooscillating tides. (a) Independent tide; (b) cooscillating tide; (c) gulf G with mouth M and coastline B set into the coastline C of ocean O. (Garrett 1975)

paradox, as originally postulated by Miles and Munk (1961), only holds for the Helmholtz mode.

OPEN BOUNDARY CONDITIONS

Garrett (1975) considered the problem of the proper boundary conditions to be used when calculating the co-oscillating tide between an ocean and a gulf. He also showed that the traditional method (e.g. see Defant 1961) is incorrect. The traditional method of separating the co-oscillating and independent tides in a gulf is illustrated in Fig. 5.4. The independent tide is due to the direct action of the astronomical forces on the gulf and is obtained as the solution of the tidal equations, including the tide-generating forces with the boundary conditions of zero normal velocity over the gulf's boundary and with the elevation at the gulf's mouth equal to the observed tide.

With reference to an ocean and gulf, as shown in Fig. 5.4, the equations of motion and continuity can be written as

$$\frac{\partial \hat{u}}{\partial t} + f \times \hat{u} + g\nabla(\hat{\zeta} - \hat{\zeta}_e) + \hat{F} = 0 \tag{5.74}$$

$$\frac{\partial \hat{\zeta}}{\partial t} + \nabla\cdot(h\hat{u}) = 0 \tag{5.75}$$

Here, $\hat{u}(x, t)$ is the current and $\hat{\zeta}(x, t)$ is the water level deviation. The depth h and the Coriolis parameter f can vary with x, and $\hat{F} = \lambda(x)\hat{u}$ is a linear bottom stress law. Let $\hat{\zeta}_e$ be the potential or equilibrium tide; then, $g\nabla\hat{\zeta}_e$ is the tide-generating force. On the coastlines B and C of the gulf and ocean (Fig. 5.4) the normal velocity $\hat{u}\cdot n = 0$. Also, the normal mass flux $h\hat{u}\cdot n$ and elevation $\hat{\zeta}$ must be continuous across the mouth M of the gulf. Assume periodic solutions of the following form:

$$\begin{aligned} \hat{u} &= R_e\hat{u}(x)e^{i\omega t} \\ \hat{\zeta} &= R_e\zeta(x)e^{i\omega t} \end{aligned} \tag{5.76}$$

The periodic forcing is represented by

(5.77) $\hat{\zeta}_e = R_e \zeta_e(x) e^{i\omega t}$

Then, from eq. 5.74–5.77:

(5.78) $i\omega \boldsymbol{u} + f \times \boldsymbol{u} + g\nabla(\zeta - \zeta_e) + \lambda \boldsymbol{u} = 0$

(5.79) $i\omega\zeta + \nabla \cdot (h\boldsymbol{u}) = 0$

Next, the solutions for $\boldsymbol{u}$ and ζ will be split into two parts: $\boldsymbol{u}^{(1)}$, $\zeta^{(1)}$ and $\boldsymbol{u}^{(2)}$, $\zeta^{(2)}$. Let subscripts G and O represent gulf and ocean, respectively. The solutions to eq. 5.78 and 5.79 with the boundary condition $\boldsymbol{u}^{(1)} \cdot \boldsymbol{n} = 0$ on M, B, and C are $\boldsymbol{u}^{(1)}$ and $\zeta^{(1)}$. These solutions (with subscripts G and O) refer to the tide that would be generated in the gulf and ocean when they are assumed to be separated by a thin rigid wall. Here, $\boldsymbol{n}$ is the outward pointing normal to the gulf, and let S be the distance measured along M. The solutions of eq. 5.78 and 5.79 without the forcing term $g\nabla\zeta_e$ and with the boundary conditions $\boldsymbol{u}^{(2)} \cdot \boldsymbol{n} = 0$ on B and C and $h\boldsymbol{u}^{(2)} \cdot \boldsymbol{n} = F(S)$ on M are $\boldsymbol{u}^{(2)}$ and $\zeta^{(2)}$. Here, $F(S)$ is a function to be determined; since $h\boldsymbol{u} \cdot \boldsymbol{n}$ is continuous, this function is the same for the gulf and the ocean.

The total solution of eq. 5.78 and 5.79 is given, then, by $\boldsymbol{u}^{(1)} + \boldsymbol{u}^{(2)}$ and $\zeta^{(1)} + \zeta^{(2)}$. The condition that the elevation is continuous across the mouth of the gulf can be written as

(5.80) $\zeta_G^{(1)} + \zeta_G^{(2)} = \zeta_O^{(1)} + \zeta_O^{(2)}$ on M

Note that $\zeta_G^{(1)}$ and $\zeta_O^{(1)}$ are determined entirely from the geometry and the tide-generating force but $\zeta_G^{(2)}$ and $\zeta_O^{(2)}$ are dependent on the flux $F(S)$ on M.

The next problem is the determination of $F(S)$. For this, assume that $h\boldsymbol{u}^{(2)} \cdot \boldsymbol{n} = \delta(S - \sigma)$ produces water levels $\zeta_G(S) = K_G(S, \sigma)$ and $\zeta_O(S) = -K_O(s, \sigma)$ on the gulf side and ocean side of the mouth, $\delta(S)$ being the Dirac delta function. Then eq. 5.80 becomes an integral equation for the current $F(\sigma)$:

$$\zeta_G^{(1)}(S) + \int_M K_G(S, \sigma) + F(\sigma) d\sigma = \zeta_O^{(1)}(S) - \int_M K_O(S, \sigma) F(\sigma) d\sigma$$

Write

$$F(\sigma) = F_G(\sigma) + F_O(\sigma)$$

where

(5.81) $$\int_M [K_O(S, \sigma) + K_G(S, \sigma)] F_G(\sigma) d\sigma = -\zeta_G^{(1)}(S)$$

(5.82) $$\int_M [K_O(S, \sigma) + K_G(S, \sigma)] F_O(\sigma) d\sigma = \zeta_O^{(1)}(S)$$

The mass flux $F(\sigma)$ produces a response $\boldsymbol{u}^{(2)}$ and $\zeta^{(2)}$. For the water level write

(5.83) $\zeta_G^{(2)}(x) = \zeta_{GG}^{(2)}(x) + \zeta_{GO}^{(2)}(x)$

where $\zeta_{GG}^{(2)}$ is the elevation produced in the gulf due to mass flux $F_G(S)$ at the mouth and $\zeta_{GO}^{(2)}$ is due to $F_O(S)$.

Garrett (1975) developed the formal solutions using the impedance approach. These solutions will not be discussed here. To summarize, the tidal response in the gulf can be

interpreted as follows, in terms of the forcing functions. (1) Direct astronomical forcing produces separate responses in the gulf and the ocean, when it is assumed that the mouth of the gulf is closed. (2) The water levels for the gulf and the ocean will be different at the mouth of the gulf. To balance this difference, a mass flux $F(S)$ is needed, and this is obtained as the solution of eq. 5.81. (3) This mass flux $F(S)$ produces a response over the gulf and the ocean.

In terms of the response, the tide in the gulf can be assumed to be made up of the following parts: (i) response $\zeta_G^{(1)}$ of the closed gulf to direct forcing, (ii) response $\zeta_{GG}^{(2)}$ of the gulf associated with the mass flux $F_G(S)$ in the mouth required to balance $\zeta_G^{(1)}(S)$, and (iii) response $\zeta_{GO}^{(2)}$ of the gulf associated with the mass flux in the mouth required to balance $\zeta_O^{(1)}(S)$.

Although Garrett's work is of interest, like many other analytical works, it is not easy to use in practical situations. More comprehensible and amenable to practical application is the paper by Heaps (1975), which will be considered in detail below. Heaps applied his results to resonant oscillations between Lake Michigan and Green Bay. Observations showed that long-wave disturbances in Lake Michigan acting at the mouth of Green Bay set up resonant co-oscillations in Green Bay with periods of 9.0 and 12.4 h. Heaps attributed these to the fundamental mode of Lake Michigan and the M_2 tide, respectively. The period of the fundamental mode of Green Bay is 10.8 h and since this lies between 9.0 and 12.4 h, conditions for near-resonance exist in Green Bay.

Let ζ be the actual (observed) water level at the mouth of Green Bay and let a portion of it, namely $\hat{\zeta}$, be attributed to disturbances from Lake Michigan. Then $\zeta - \hat{\zeta}$ is due to the response of Green Bay. Here, the assumption is made that the presence of Green Bay has no effect on $\hat{\zeta}$. One can visualize two distinct cases here. In the first case, the water level is prescribed at the mouth of Green Bay (i.e. assume a node at the mouth as is traditionally done) and its resonance periods are calculated. In the second case, the total system is considered, i.e. Lake Michigan together with Green Bay, and the resonance periods of the total system are considered. The periods calculated for both cases will agree only when each mode of the total system has a node at the mouth (a node is a location where the vertical water level deviation from the equilibrium position is zero).

Observations show that the period of the fundamental mode of Green Bay (connected freely with Lake Michigan) is 10.8 h. Numerical models for the period of the fundamental mode of Green Bay (assuming a node at the mouth) gave a period of 9.75 h. These results will now be interpreted from a mathematical point of view.

The equation of motion and continuity equation for free oscillations in a narrow rectangular gulf of length l and uniform depth h are, after ignoring the friction and nonlinear terms,

$$\frac{\partial u}{\partial t} = -g\frac{\partial \zeta}{\partial x} \tag{5.84}$$

$$h\frac{\partial u}{\partial x} = -\frac{\partial \zeta}{\partial t} \tag{5.85}$$

The condition of perfect reflection at the head requires

$$u = 0 \text{ at } x = 0 \tag{5.86}$$

The solutions for the rth mode of free oscillation can be written as

$$u = U(x)e^{i\sigma_r t}$$
(5.87)
$$\zeta = Z(x)e^{i\sigma_r t}$$

where

(5.88) $$Z \equiv H \cos(\alpha_r \xi)$$

(5.89) $$U \equiv -\left(\frac{ig}{c}\right) H \sin(\alpha_r \xi)$$

(5.90) $$\alpha_r \equiv \frac{\sigma_r l}{c}$$

(5.91) $$c \equiv \sqrt{gh}$$

(5.92) $$\xi \equiv \frac{x}{l}$$

The period of the rth mode is given by $2\pi/\sigma_r$. Here, H is a constant that denotes the amplitude of ζ at the closed end.

Taking the real parts in eq. 5.87 and 5.89, it can be seen that high water occurs at $x = 0$ at $t = 0$. From eq. 5.88 and 5.89:

(5.93) $$\frac{\zeta}{u} = \frac{ihB_r}{c} \text{ at } x = l$$

with

(5.94) $$B_r = \cot \alpha_r$$

Here, B_r is proportional to the impedance of the gulf evaluated at σ_r. From eq. 5.93 it can be seen that equating B_r to zero is the same as

(5.95) $$\zeta = 0 \text{ at } x = l$$

(i.e. there is a node at the mouth). From eq. 5.94 the frequencies $\sigma_r (r = 1, 2, 3, \ldots)$ are given by $\cot \alpha_r = 0$. Thus

(5.96) $$\alpha_r = (2r - 1)\frac{\pi}{2}$$

From this

(5.97) $$\sigma_r = (2r - 1)\frac{\pi c}{2l}$$

The periods are given by

(5.98) $$T_r = \frac{2\pi}{\sigma_r} = \frac{4l}{c}\frac{1}{(2r - 1)}$$

There is no a priori reason to assume that the free oscillations of Green Bay have a node at the mouth. Thus, in general, B_r is not zero. Assume that it is positive. Then from eq. 5.93 it can be seen that ζ leads u by a quarter period at $x = l$, and from eq. 5.94:

(5.99) $$\alpha_r = (2r - 1)\frac{\pi}{2} - \tan^{-1} B_r$$

Then

$$(5.100)\quad \sigma_r = (2r-1)\frac{\pi c}{2l} - \frac{c}{l}\,tan^{-1}\,B_r$$

or

$$(5.101)\quad T_r = \frac{4l/c}{2r - 1 - \frac{2}{\pi}\tan^{-1} B_r}$$

These results tend to the earlier ones if $B_r \rightarrow 0$.

Comparison of eq. 5.98 and 5.101 shows that the periods T_r are greater when B_r is positive. In other words, when a node is assumed at the mouth, the periods of free oscillation are smaller than those when a node is not assumed at the mouth. For Green Bay the corresponding periods for the fundamental mode are 9.75 and 10.8 h, respectively. For the Bay of Fundy, for example, the corresponding periods are 9.05 and 13.3 h.

Thus, the condition 5.93 incorporates the influence of Lake Michigan on Green Bay. Here, one assumption that was made is that B_r is real (which is a necessary condition for free oscillations). Complex B_r represents damped oscillations, the damping agent being the external water body (Lake Michigan in this example).

Heaps (1975) also considered the forced response of a gulf from the outer sea and showed that the surface elevation at the mouth may be equated to the elevation of the incident wave only when $B_r = 0$. Since, in general, $B_r \neq 0$, prescribing the water level at the mouth cannot represent a totally external input, since such a prescribed water level contains a contribution from the gulf's response.

Numerical Models for Resonance Calculations

Murty (1977) discussed numerical methods for resonance calculations in complex one-dimensional systems, such as coastal inlets and rivers, and semianalytic techniques for two-dimensional systems, such as bays and gulfs. The discussion below will be confined to numerical techniques for two-dimensional systems. First, smaller water bodies such as harbors will be considered where the earth's rotational effects are not significant. Then, how to include rotation will be considered. Finally, certain examples will be given.

Typical examples of resonance calculations in two-dimensional basins (assuming a node at the mouth) without including the effects of rotation are given in Loomis (1970, 1972, 1973). In this technique, one begins with the linear shallow-water wave equation:

$$(5.102)\quad \nabla\cdot(h\nabla\phi) = \frac{1}{g}\frac{\partial^2\phi}{\partial t^2}$$

where ϕ is the velocity potential and $h(x, y)$ is the water depth. The boundary of the water body is taken in a general way so that two types of boundaries can exist:

$$(5.103)\quad \frac{\partial\phi}{\partial n} = 0 \text{ on } B_1$$

and

$$(5.104)\quad \phi = 0 \text{ on } B_2$$

Substituting

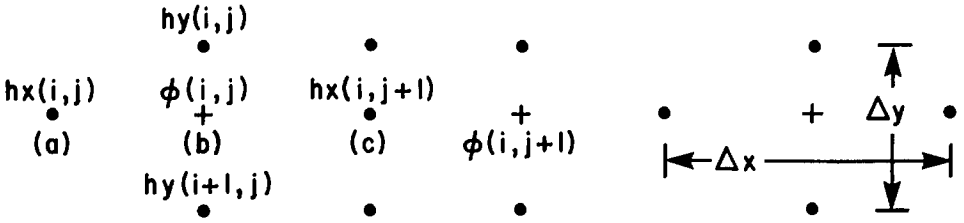

FIG. 5.5. Spatial relations of $hx(i, j)$, $hy(i\,j)$, and $\phi(i, j)$. (Loomis 1973)

(5.105) $\phi(x, y, t) = e^{i\omega t}\phi_1(x, y)$

into eq. 5.102 gives

(5.106) $\nabla\cdot(h\nabla\phi_1)e^{i\omega t} = -\dfrac{\omega^2}{g}e^{i\omega t}$

For convenience, omit the subscript on ϕ_1, divide by $e^{i\omega t}$, and define $\lambda \equiv \omega^2/g$ to give

(5.107) $\nabla\cdot(h\nabla\phi) = \lambda\phi$

Note that a value λ for which there is a nonzero solution $\phi(x, y)$ is an eigenvalue and the corresponding $\phi(x, y)$ is an eigenfunction. The grid is shown in Fig. 5.5. Note that the bathymetric specifications $hx(i, j)$ and $hy(i, j)$ are somewhat unconventional. In writing the finite-difference from of eq. 5.107, the following form is used:

$$(5.108)\quad \frac{\partial}{\partial x}\left(h\frac{\partial\phi}{\partial x}\right) = \frac{1}{\Delta x}\left\{hx(i, j+1)\left[\frac{\phi(i, j+1) - \phi(i, j)}{\Delta x}\right] - hx(i, j)\left[\frac{\phi(i, j) - \phi(i, j-1)}{\Delta x}\right]\right\}$$

The first square-bracketed term on the right-hand side is a differencing centered at point c of Fig. 5.5, and the second square-bracketed term is centered at point a so that the entire right-hand side is centered at point b. Similar arguments can be used for the y derivative. In this scheme

$$(5.109)\quad h\frac{\partial\phi}{\partial x} = hx(i, j)\left[\frac{\phi(i, j) - \phi(i, j-1)}{\Delta x}\right]$$

is centered at point a. The boundary condition $\partial\phi/\partial x = 0$ at point a can be affected by taking $hx(i, j) = 0$ at a so that eq. 5.109 is zero. Hence, at each point where $hx(i, j) = 0$ and/or $hy(i, j) = 0$, eq. 5.109 or a similar relation for $h\partial\phi/\partial y$ will be zero so that on the boundaries of the water body, equating h to zero gives the same difference equations as though $\partial\phi/\partial x$ and/or $\partial\phi/\partial y$ were set to zero. This arrangement takes care of the B_1-type boundaries. Boundaries of B_2 type where $\phi(i, j) = 0$ are handled differently.

The finite-difference form of eq. 5.107 is

$$(5.110)\quad \frac{hx(i, j+1)}{(\Delta x)^2}\phi(i, j+1) + \frac{hx(i, j)}{(\Delta x)^2}\phi(i, j-1) + \frac{hy(i+1, j)}{(\Delta x)^2}\phi(i+1, j) + \frac{hy(i, j)}{(\Delta y)^2}\phi(i-1, j) - \left[\frac{hx(i, j+1) + hx(i, j)}{(\Delta x)^2} + \frac{hy(i+1, j) + hy(i, j)}{(\Delta y)^2}\right]\phi_{i,j} = \lambda\phi_{i,j}$$

This can be rearranged in the form

$$(5.111)\quad a_{ij}(i, j+1)\phi(i, j+1) + a_{i,j}(i, j-1)\phi(i, j-1) + a_{i,j}(i+1, j)\phi(i+1, j) + a_{i,j}(i-1, j)\phi(i-1, j) + a_{i,j}(i, j)\phi(i, j) = \lambda\phi(i, j)$$

Let $\vec{\phi}$ represent a vector with components $\phi(i, j)$ and let A represent the matrix of coefficients. Then eq. 5.111 becomes

$$(5.112)\quad A\vec{\phi} = \lambda\vec{\phi}$$

Although eq. 5.111 gives the impression of double-indexing for ϕ and four indices for A, a single index $I(i, j) = 1, 2, \ldots, n$ can be defined so that a single distinct integer could be assigned to each (i, j) using capital letters for the new indices. Thus, if $(i, j) \leftrightarrow I$ and $(i, j+1) \leftrightarrow J$, then

$$(5.113)\quad a_{i,j}(i, j+1) = a_{IJ}$$

which will be the coefficient of Φ_J in the Ith equation. The coefficient of Φ_I in the Jth equation will be a_{JI}. It can be shown that

$$a_{IJ} = a_{JI}$$

so that A is symmetric, which can be deduced from eq. 5.110.

To take care of a boundary condition of the type $\Phi_J = 0$ one can assign to those boundary grid points an index $J > n$ so that when the $n \times n$ matrix A is constructed, those A_{IJ} values will lie outside the matrix, which in essence makes

$$\Phi_J = 0$$

Since A is symmetric, the eigenvalues of eq. 5.112 will be real. Thus, the solutions are $\lambda_1, \vec{\phi}_1; \lambda_2\vec{\phi}_2; \ldots; \lambda n, \vec{\phi}_n$ and the normal mode frequencies are given by

$$(5.114)\quad f_i = \frac{\omega_i}{2\pi} = \frac{\sqrt{-g\lambda i}}{2\pi}, \qquad i = 1, 2, \ldots, n$$

The vectors $\vec{\phi}_i$, $i = 1, 2, \ldots, n$, describe the envelope of the normal mode.

Next, numerical models for resonance calculations when the Coriolis terms are included will be considered. To this author's knowledge, such calculations were originally made by Platzman (1972), and some modifications and alternate techniques were suggested by Hamblin (1972) and Rao (1974). Here, the so-called "resonance-iteration" method introduced by Platzman will be briefly discussed.

The equations of motion and continuity for an inviscid, homogeneous fluid are in the vector form

$$(5.115)\quad \frac{\partial V}{\partial t} = -g\nabla(\zeta - \bar{\zeta}) - 2\boldsymbol{\Omega}XV$$

$$(5.116)\quad \frac{\partial \zeta}{\partial t} = -\nabla \cdot hV$$

where h is the fluid depth, g is gravity, ζ is the deviation of the water level from its equilibrium level, V is the horizontal velocity of the fluid, ∇ is the horizontal gradient operator, and $\boldsymbol{\Omega}$ is the vertical part of the earth's rotation vector (i.e. it is equal to the earth's rotation speed multiplied by the sine of latitude multiplied by the vertical unit vector). In the above equation, $g\nabla\bar{\zeta}$ is the tidal force.

For convenience, a matrix column $a \equiv (\zeta, V)$ is defined. Then eq. 5.115 and 5.116 become

$$\frac{\partial a}{\partial t} = i\mathcal{L}(a - \bar{a})$$

(5.117)

$$\mathcal{L} \equiv i\begin{bmatrix} 0 & \nabla h \\ g\nabla & 2\boldsymbol{\Omega}X \end{bmatrix}$$

where

$$\bar{a} \equiv (\bar{\zeta}, 0)$$

The boundary conditions considered here are of the adiabatic type, i.e. normal component of

(5.118) $hV = 0$

or

(5.119) $\zeta = 0$

These boundary conditions do not permit flux of energy into or out of the region at any time. Condition 5.118 applies to solid boundaries and condition 5.119 is used for the openings.

The properties of the operator $\mathcal{L}$ are determined by the scalar product of two arbitrary vectors a' and a:

(5.120) $\{a', a\} = \int (g\zeta'\zeta + hV'V)dS = 0$

where dS is an area element and the integration is carried out around the boundary. It can be shown that the system 5.117–5.119 is self-adjoint and hence, the eigenvalues of $\mathcal{L}$ are real. If these eigenvalues are denoted by σ and the corresponding eigenvectors by $A \equiv (z, V)$, then

(5.121) $\mathcal{L}A = \sigma A$

Then $Ae^{i\sigma t}$ is a normal mode solution of eq. 5.118 with $\bar{a} = 0$.

Noting that $\mathcal{L}$ is purely imaginary, real representation of the normal mode with frequency $|\sigma|$ is

$$Ae^{i\sigma t} \pm A^*e^{-i\sigma t}$$

where A^* is the complex conjugate of A.

The scalar product of A^* with each side of eq. 5.121 gives the primitive Rayleigh quotient:

(5.122) $$\sigma = \frac{\{A^*, \mathcal{L}A\}}{\{A^*, A\}}$$

The numerator and denominator are

$$\{A^*, \mathcal{L}A\} = i \int [gz^*\nabla \cdot hV + hV^* \cdot (g\nabla z + 2\boldsymbol{\Omega}XV)]dS$$

$$\{A^*, A\} = \int (g|z|^2 + h|V|^2)dS$$

In using eq. 5.122 in estimating σ from the approximation to $A \equiv (z, V)$, one can take in principle any z and V that satisfies the boundary conditions. Other constraints are the

kinematic and dynamic parts of eq. 5.121, which are, respectively,

$$\sigma z = i\nabla \cdot hV \tag{5.123}$$

$$(\sigma - 2\Omega iX)V = ig\nabla z \tag{5.124}$$

The parameter z can be explicitly expressed in terms of V in the kinematic part; the dynamic part can be manipulated to express V explicitly in terms of z:

$$\begin{aligned} \sigma V &= iFg\nabla z \\ F &= \left(1 - \frac{4\Omega^2}{\sigma^2}\right)^{-1}\left[1 + \left(\frac{2\Omega i}{\sigma}\right)X\right] \end{aligned} \tag{5.125}$$

The operator $\sigma - 2\Omega iX$ is nonsingular except for the trivial case when σ and Ω are zero. Hence, in the operator F, the latitudes (if any) where $4\Omega^2 = \sigma^2$ are only apparent singularities.

Irish and Platzman (1972) pointed out that three alternatives are possible for the use of the Rayleigh quotient. (1) The kinematic and dynamic constraints are not used. Then the relevant operator is $\mathcal{L}$ in eq. 5.117. The normal mode frequencies σ are identical to the eigenvalues of this operator and hence are equal to the stationary values of the corresponding Rayleigh quotient 5.122. (2) The dynamic constraint is imposed and the velocities are eliminated in the traditional way. Then the relevant operator is the second-order Laplacian tidal operator and its spectrum is parametrically dependent on σ. Then the Rayleigh quotient becomes a variational statement, which can be solved explicitly for σ only for the case of uniform depth. (3) The kinematic constraint is imposed. Again, the relevant operator is of second order with a spectrum parametrically dependent on σ. In this case, the Rayleigh quotient becomes an explicit equation quadratic in σ with coefficients that are homogeneous quadratic functions of the particle velocities or displacements. Platzman (1972) used the Richardson lattice for space discretization and a leapfrog scheme for time discretization. Murty and Taylor (1975) computed two-dimensional free oscillations of Georgian Bay (on Lake Huron), Green Bay (on Lake Michigan), and Chedabucto Bay (in Nova Scotia). However, the method used here is not as elegant as that of Platzman (1972) but is more straightforward and can be used only when the frequencies of the gravitational modes and those of the rotational modes are well separated.

The free oscillations (normal modes) of any water body can be conveniently classified into gravitational and rotational modes. The gravitational modes owe their existence to disturbances of the mass field, whereas the rotational modes primarily depend on deformations of the potential vorticity (Platzman 1974). A spectrum of gravitational modes would exist in the absence of Coriolis force, and similarly, a spectrum of rotational modes would exist in the absence of gravity. Gravitational modes cluster at the short-period end of the spectrum and rotational modes cluster at the long-period end.

Identification of a given mode (whether it is of gravitational or rotational type) can be made on the basis of several factors (Platzman 1975). The distribution of the periods provides some basis for identification. As the typical length of the disturbances (that excites these modes) increases, the period of a rotational mode will decrease and the period of a gravitational mode will increase. Since the length scale of the water body is an upper limit of the length scale of the disturbance, there is a limiting minimum value for the rotational mode periods and a limiting maximum value for the gravitational mode periods.

Murty and Taylor (1975) used the time-dependent two-dimensional equations of motion and continuity and solved them numerically. For the basic condition for calculating the free oscillations, they invoked the standard (but not strictly correct) condition of zero

surface elevation at the mouth. The free oscillations were excited by applying a wind stress for some length of time over the bay. The resonant frequencies were abstracted from the numerical model output by spectrally analyzing the computed water level at selected locations in the bay. One disadvantage of this technique is that all the modes may not systematically be identified. However, the results for Green Bay and Georgian Bay agree with the results of other calculations. Tronson (1975) calculated the normal modes of the South Australian Gulf System.

Heath (1975) calculated the normal modes of Lake Wakatipu in New Zealand. One very interesting feature is that the most energetic mode is not the fundamental but the second one. Quoting from Heath (1975, p. 235):

> One reason generally given for most of the seiche energy in a lake being in the fundamental mode is that this mode has the longest wavelength and is therefore less affected by scattering than the higher order modes. It can be shown by Fourier decomposition of the initial shape of the lake level that in a unidirectional lake most of the seiche energy might also be expected to be initially in the fundamental mode. However, further examination of this method of generation indicates that this dog-leg shaped lake might respond like three uni-directional lakes acting separately with the elevation distribution of the fundamental mode in the two meridional legs being similar to that of the second mode in the entire lake.

Kelvin Waves, Sverdrup Waves, and Poincaré Waves

There are classes of normal mode solutions with special properties that have been referred to as Kelvin waves, Sverdrup waves, and Poincaré waves. These wave types have been frequently invoked to explain the tidal phenomena in water bodies. For an excellent review on this topic, see Platzman (1971). Other relevant works are Defant (1961), Proudman (1953), Voyt (1974), and Leblond and Mysak (1978). Simons (1980) has given a rather concise summary, and this discussion will essentially follow his line of argument.

Earlier, the gravitational and rotational modes were introduced, also referred to as oscillations of the first class (OFC) and oscillations of the second class (OSC). It was also pointed out that OFC are motions with large divergence, whereas OSC are essentially nondivergent. For introducing the concepts of different types of wave motion mentioned here, discussion begins with the linearized version of the vertically integrated equations, and these will be applied to a rectangular basin of uniform depth:

$$\begin{aligned} \frac{\partial U}{\partial t} - fV &= -c^2 \frac{\partial \eta}{\partial x} \\ \frac{\partial V}{\partial t} + fU &= -c^2 \frac{\partial \eta}{\partial y} \\ \frac{\partial \eta}{\partial t} + \frac{\partial U}{\partial x} + \frac{\partial V}{\partial y} &= 0 \end{aligned} \tag{5.126}$$

where U and V are the x and y components of the volume transport, η is the deviation of the water level from its equilibrium position, f is the Coriolis parameter, and $c^2 = gD$ where D is the unform water depth.

Assuming a time factor $e^{i\sigma t}$ where σ is the frequency and eliminating U and V from eq. 5.126 gives the wave equation

$$(\sigma^2 - f^2)\eta + c^2 \nabla^2 \eta = 0 \tag{5.127}$$

The boundary condition of zero normal transport to a boundary can be stated as

$$(5.128)\quad f\frac{\partial \eta}{\partial S} + i\sigma\frac{\partial \eta}{\partial n} = 0$$

where S and n are the coordinates along and perpendicular, respectively, to the wall. Equation 5.127 can be satisfied by

$$\exp\left[i(kx + ly)\right]$$

where the frequency σ is given by

$$(5.129)\quad \sigma^2 = f^2 + c^2(k^2 + l^2)$$

For the nonrotating case, the condition 5.128 is easily satisfied by standing waves with wave numers $k = m\pi/L$ and $l = n\pi/B$ where m and n are integers and L and B are the length and breadth of the basin, respectively. However, in the rotating case, because of the complicated nature of the boundary condition 5.128 it is difficult to determine the normal modes. However, even in the rotating case, for an infinitely long channel, there are some elementary wave solutions that do satisfy the boundary conditions.

In eq. 5.126, if $V = 0$, then the solutions to the resulting equations are

$$\eta = \eta_0 e^{-fy/c} e^{ik(x-ct)}$$

$$(5.130)\quad U = -\frac{c^2}{f}\frac{\partial \eta}{\partial y}$$

$$V = 0$$

The wave speed is the same for the nonrotating and the rotating cases, but in the latter, the wave amplitude decreases exponentially from right to left for an observer looking in the direction of wave propagation. The rate of decrease of the amplitude from right to left is proportional to c/f, the Rossby radius of deformation. These waves are known as Kelvin waves.

Another elementary solution can be obtained by setting $\partial/\partial x$ and $\partial/\partial y$ to zero. This will result in inertial oscillations with frequency f (note that η is zero for these and there is only horizontal motion). If only the gradients in one horizontal direction are ignored, e.g. $\partial/\partial x = 0$, then the solutions are

$$(5.131)\quad \begin{aligned} \eta &= \eta_0 e^{i(ly-\sigma t)} \\ \sigma &= f^2 + c^2 l^2 \end{aligned}$$

These waves are referred to as Sverdrup waves and have horizontal crests. For a straight shore parallel to the x-axis, two Sverdrup waves traveling in opposite directions may be combined to form a standing wave that satisfies the boundary condition 5.128. Thus, standing Sverdrup waves with wave numbers $l = n\pi/\beta$ are the normal modes of an infinitely long rotating channel.

The more general solutions of eq. 5.127 are known as Poincaré waves. One can combine pairs of progressive Poincaré waves into standing waves that display cellular patterns. For an infinite channel, in analogy with Sverdrup waves, Poincaré waves can be made to satisfy the boundary conditions by properly choosing the transverse wave numbers.

At a transverse barrier in the channel, none of these waves could be made to satisfy the boundary condition 5.128. Hence, the analytical determination of the normal modes

of a rotating rectangular bay is more difficult, and it is convenient to resort to numerical techniques.

Edge Waves and Their Role in Storm Surges

The literature on the topic of edge waves has grown enormously in recent times, and the reader is referred to Leblond and Mysak (1978) and Murty (1977) for a review. Here, edge waves will be considered strictly for the role they play in storm surges; discussion will not deal with the general phenomenon of edge waves.

Stokes (1847) obtained solutions for wave motion over a sloping beach, these solutions being different from the traditional wave pattern on beaches. In these new solutions, the crests are perpendicular to the coast, but they travel in a direction parallel to the coast and their amplitudes decrease drastically from the shore seaward, and at a distance of one wavelength from the beach, their amplitudes are negligible. Lamb (1945) called them edge waves. Ursell (1952) showed that the Stokes solution is the gravest of an infinite number of possible modes of edge waves. For the nth mode (which has n extrema in elevation between the coast and the sea), the velocity c and the length L are given by

$$c = \frac{gT \sin (2n + 1)\beta}{2\pi} \tag{5.132}$$

$$L = \frac{gT^2 \sin (2n + 1)\beta}{2\pi} \tag{5.133}$$

where T is the period of the edge wave, g is gravity, and β is the slope of the beach.

Munk et al. (1956) detected edge waves in the recorded water levels at Scripps Pier. On January 6, 1954, at 03:35 (GMT) an unusual gust was recorded at Scripps Pier. Atmospheric pressure abruptly increased by 2 mb and wind speed rose from 3 to 14 $mi \cdot h^{-1}$ ($4.8-22$ $km \cdot h^{-1}$). This was followed by pressure and wind oscillations of an 8-min period. These authors detected periods corresponding to edge waves (with modal number $n = 1$) in the recorded water level at Scripps and at Oceanside, which is 38 km distant.

On August 31, 1954, Hurricane Carol crossed Atlantic City. Munk et al. (1956) computed the edge wave modes at Atlantic City and Sandy Hook and compared the calculated periods with observed periods (as shown in Table 5.3). The observed surges at Atlantic City and Sandy Hook are shown in Fig. 5.6. In Table 5.3 the calculated and observed periods for three other storms are also shown. It can be seen from the table that the observed periods agree well with the computed periods. The main result is that the edge wave periods are largely due to the gently sloping bottom. The longest edge wave period is associated with the fastest hurricane.

Munk et al. (1956) also computed the edge wave modes for Osaka Bay, Japan, over which a storm passed on August 29, 1953. The bottom slope in Osaka Bay is about 15 times greater than that of the New Jersey coast. Hence, the periods of edge waves in Osaka Bay should be about 1/15 those on the New Jersey coast, and this result is supported by observations.

Greenspan (1970) did a theoretical study of edge waves in an exponentially stratified fluid. He showed that the first mode is completely insensitive to the density field. Stratification modifies the range of existence of higher modes.

On June 26, 1954, a squall line passed over the southern part of Lake Michigan and caused a surge on the Chicago water front. Several people were killed. This was explained by resonant coupling between the squall line and the resulting gravity waves generated in

TABLE 5.3. Periods and durations of edge waves generated by four hurricanes. (Munk et al. 1956)

Hurricane	Velocity U ($km \cdot h^{-1}$)	Track length Y (km)	Travel time D (h)	Wave period T (h)				Duration (h)		
				Computed		Observed			Observed	
				$\sin\beta = 5 \times 10^{-4}$	$\sin\beta = 4.2 \times 10^{-4}$	Atlantic City	Sandy Hook	Computed	Atlantic City	Sandy Hook
Aug. 30–Sept. 1 (Carol)	59–63	1000	24	5.8–6.1	6.9–7.2	5.5	7.0	16–24	20	26
Sept. 11–12, 1954 (Edna)	59	981	24	5.8	6.9	6.0	7.0	17–24	23	?
Sept. 14–15, 1944	61	666	12	6.0	7.1	5.6	7.2	11–12	23	30
Sept. 21–22, 1938	74	666	9	7.3	8.6	—	8.0	9	—	16

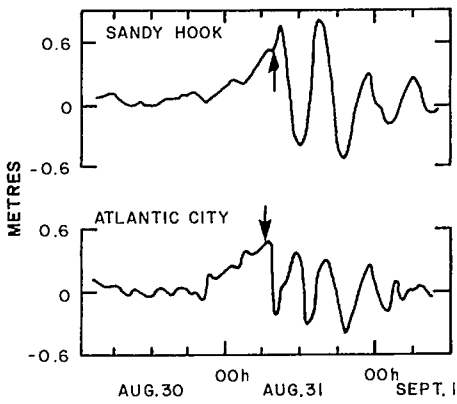

FIG. 5.6. Storm surges at Sandy Hook and Atlantic City, New Jersey, during Hurricane Carol of August 30–September 1, 1954. Arrows indicate the time of passage of the storm center. (Munk et al. 1956)

TABLE 5.4. Time of occurrence and pressure change for the squall line of July 6, 1954, in the United States. (Donn and Ewing 1956)

Station name	Station code	State	Time (CST) of occurrence of pressure change	Magnitude of pressure change (mb)
Fargo	FAR	North Dakota	06:50	2.03
St. Cloud	STC	Minnesota	08:39	3.05
Minneapolis	MSP	Minnesota	09:54	2.37
Green Bay	GRB	Wisconsin	11:00	1.36
Traverse City	TVC	Michigan	12:30	0.68
Madison	MSN	Wisconsin	13:02	2.71
Milwaukee	MKE	Wisconsin	13:24	2.03
Muskegon	MKG	Michigan	14:00	1.36
Chicago	CHI	Illinois	15:30	3.39
Battle Creek	BTL	Michigan	15:30	1.36
South Bend	SBN	Indiana	15:55	2.03

the lake (Donn and Ewing 1956). A resurgence (i.e. reflection of the waves from the eastern shore of the lake) explains its unexpected arrival at Chicago some 2 h after the squall line had passed.

On July 6–7, 1954, another squall line crossed Lake Michigan from north to south with an average speed of 50 $mi \cdot h^{-1}$ (80.5 $km \cdot h^{-1}$). Long-period waves were recorded at several locations following this squall line. Donn and Ewing (1956) invoked edge waves to account for these water level disturbances. The time of arrival of the squall line and the magnitude of the pressure change at several stations are listed in Table 5.4, and the travel time curves of the squall line are shown in Fig. 5.7. The abbreviations for the stations shown in this diagram are the same as in Table 5.4. The water level records from Waukegan, Wilson Avenue (Chicago), Calumet Harbor (Chicago), and Ludington (see Fig. 5.8) were used.

The pertinent meteorological and water level data at these four stations are summarized in Table 5.5. It can be seen from Fig. 5.8 that the depth increases more or less

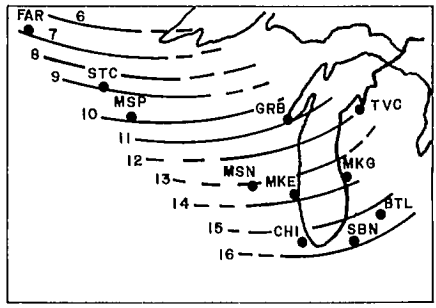

FIG. 5.7. Travel time curves (isochrones) of the squall line on July 6, 1954, over Lake Michigan and surroundings. Numbers represent hours Central Standard Time. FAR, Fargo, North Dakota; STC, St. Cloud, Minnesota; MSP, Minneapolis, Minnesota; GRB, Green Bay, Wisconsin; TVC, Traverse City, Michigan; MSN, Madison, Wisconsin; MKE, Milwaukee, Wisconsin; MKG, Muskegon, Michigan; CHI, Chicago, Illinois; BTL, Battle Creek, Michigan; SBN, South Bend, Indiana. (Donn and Ewing 1956)

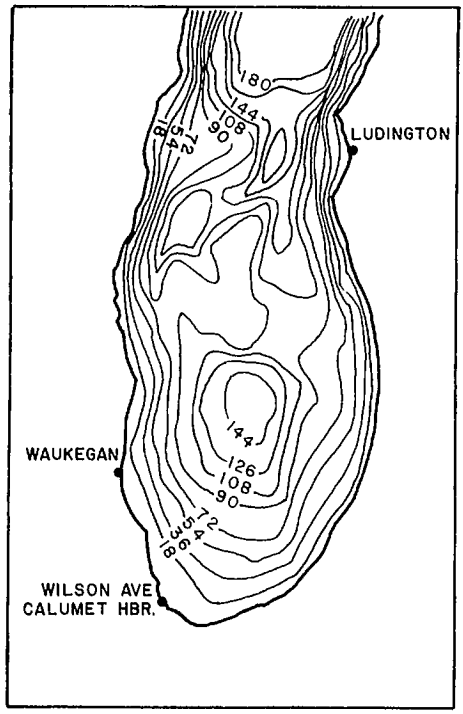

FIG. 5.8. Bottom topography of the southern port of Lake Michigan and the water level stations used in the study. (Donn and Ewing 1956)

uniformly with distance from the shore. The distance (i.e. $\lambda/2\pi$) at which the edge wave amplitude should be negligible is about 16 mi (25.6 km). Starting just north of Chicago to up to 50 mi (80.5 km) north of Waukegan, the bottom slope was determined to the 300-ft (91.4 m) contour at six different locations. These values (i.e. of $\sin\beta$) were 0.0016, 0.0021, 0.0024, 0.0035, 0.0034, and 0.0029. For the phase velocity c of the edge wave a value of 72.5 $ft \cdot s^{-1}$ (22 $m \cdot s^{-1}$) was used. This gives from eq. 5.132 (for $n = 1$) a period of 103 min. From Table 5.5 the average period is 109 min. Thus, the calculated period of edge waves agrees with the observed period.

Calculations gave values of 50 $mi \cdot h^{-1}$ (80.4 $km \cdot h^{-1}$) and 61 $mi \cdot h^{-1}$ (98 $km \cdot h^{-1}$), respectively, for the edge wave velocity in the northern and southern parts of Lake Michigan. Since the speed of travel of the squall line was 50 $mi \cdot h^{-1}$ (80.4 $km \cdot h^{-1}$), resonance transfer of energy occurred from the squall line to the gravity waves in the water. At Ludington, the bottom topography precludes generation of edge waves. Hence, just after the passage of the squall line (at 1:00 p.m.) the amplitudes of the water waves were small. However, at 8:00 p.m. much larger waves appeared at Ludington. This was explained as due to the reflected larger waves from other areas traveling towards Ludington.

The observed duration of the water level disturbance in the Chicago–Waukegan area is estimated to be about 29 h. About 20 h of this record at Calumet Harbor is shown in Fig. 5.9. The theoretical estimate of 18 h for the edge wave duration is somewhat smaller. The period of the edge waves was close to that of the seiche period in the southern part

TABLE 5.5. Arrival time of pressure jump and first wave of surge and wave periods and duration of the water level disturbance at four stations in Lake Michigan associated with the squall line of July 6, 1954. (Donn and Ewing 1956)

Station	Pressure jump arrival time (CST)	Time of arrival of first wave of surge (CST)	Period (min)[a]		Duration of wave disturbance (h)
			Long-period waves	Short-period waves	
Waukegan (Illinois)	~15:00	15:00	110–120	20	29
Wilson Ave. (Chicago)	15:30	15:30	97–100	18–20	29
Calumet Harbor (Chicago)	15:30	15:30	115	20	—[b]
Ludington (Michigan)	~13:00	20:00–22:00	84	—	—[b]

[a]Not to be confused with wind waves whose periods are of the order of a few seconds.
[b]Record incomplete.

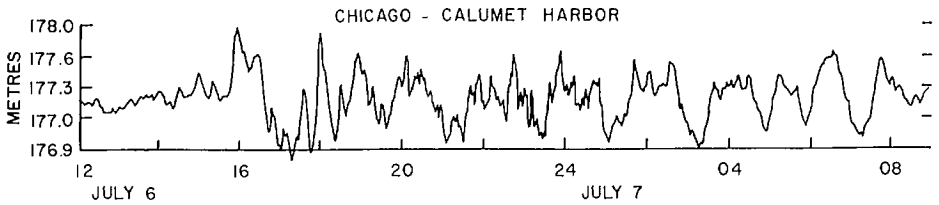

FIG. 5.9. Water level disturbance at Chicago's Calumet Harbor during July 6–7, 1954. (Donn and Ewing 1956)

of Lake Michigan; hence, seiche activity is expected and observed water levels confirm this.

Earlier, reference was made to the storm surge in Lake Michigan due to a squall line on June 26, 1954 (six persons were killed in Chicago). Platzman (1958a) studied this surge using a time-dependent two-dimensional numerical model. The travel time curves of this squall line are shown in Fig. 5.10. The lake level, wind, and atmospheric pressure at the Wilson Avenue crib in Chicago are shown in Fig. 5.11.

Platzman made five computations, i.e. using five different speeds of propagation for the squall line. These were 42, 48, 54, 60, and 66 knots (1 knot = 1.85 km·h^{-1}). In each of these five computations he took the direction of propagation of the squall line as northwest to southeast, the width of the squall line as 10 nautical miles (18.5 km), and the magnitude of the pressure rise as 4 mb. The observed and computed results are compared in Table 5.6. In interpreting these results, it should be noted that the computations include atmospheric pressure gradient as a forcing term, but not wind stress. (Also, the Coriolis terms were ignored, although this omission may not be significant.)

Platzman (1958) summarized the results at the Wilson Avenue crib as follows.

1) The computed amplitude of the main (reflected) surge is approximately one-half the observed amplitude, but the inclusion of wind stress probably will remove this discrepancy.

2) The computed phases between significant events (Table 5.6) are in good agreement with the observations.

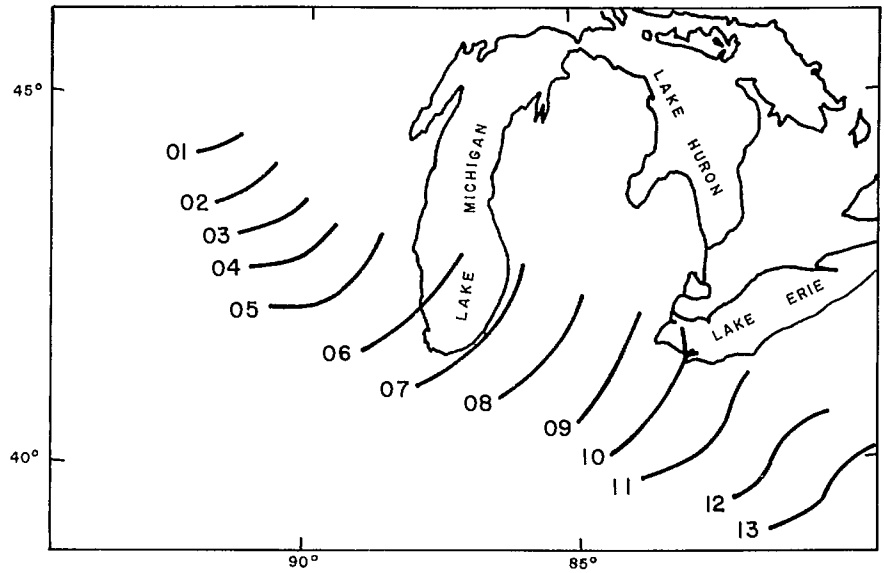

FIG. 5.10. Isochrones of the pressure jumpline of June 26, 1954, over Lake Michigan and surroundings. Numbers represent hours Central Standard Time. (Platzman 1958a)

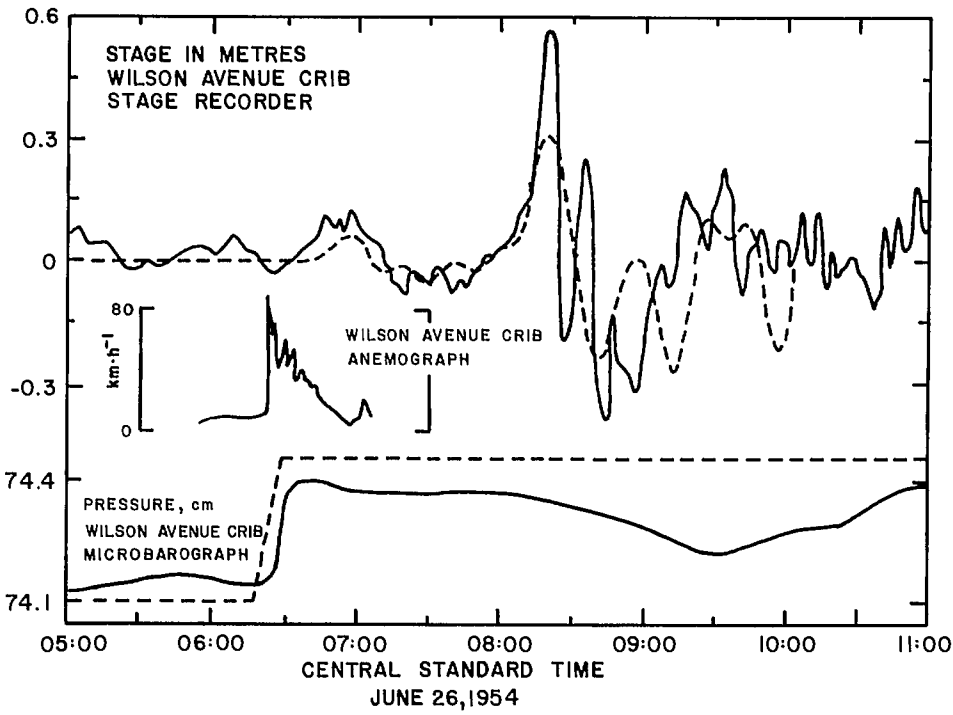

FIG. 5.11. Lake level, wind, and atmospheric pressure records at Wilson Avenue crib on June 26, 1954. The broken curve of lake level shows the results of numerical computation for a squall line speed of 100 $km \cdot h^{-1}$; the broken curve of pressure gives the corresponding pressure increase assumed in the calculation. (Platzman 1958a)

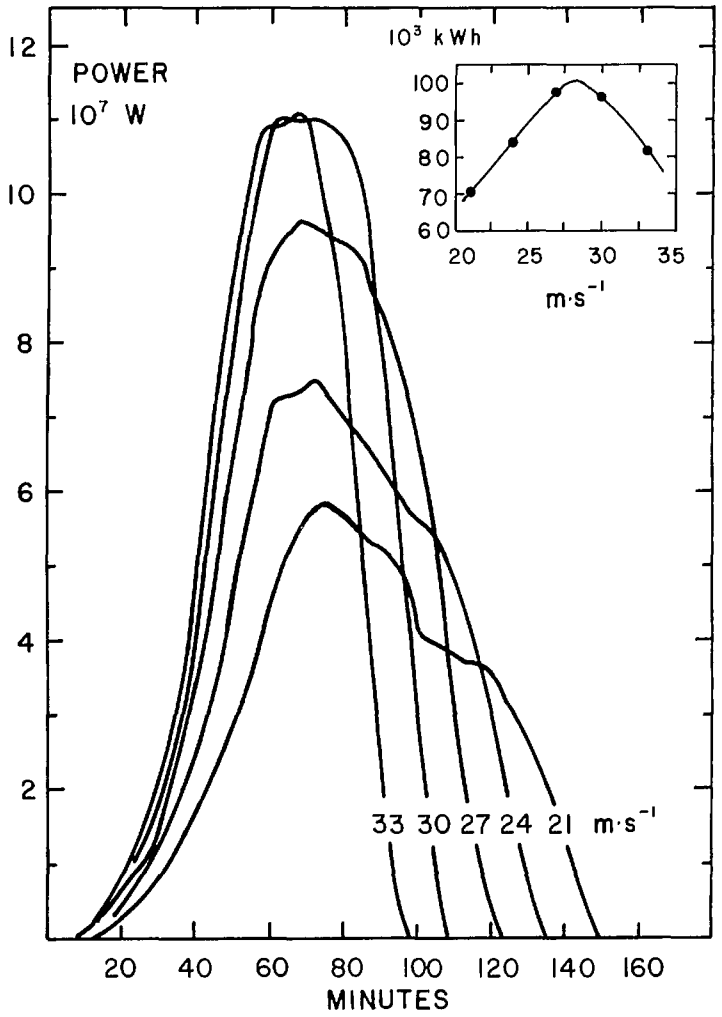

FIG. 5.12. The power transmitted by the atmosphere to the lake as a function of time for each of the five computed cases. Inset shows the total energy absorbed by the lake as a function of squall line speed. (Platzman 1958a)

3) The structure of the tail of the reflected surge (and probably also the primary surge) is not in agreement with the observed structure, probably because the resolving power of the grid is inadequate for this purpose.
4) The background fluctuations of lake level that arise from normal meteorological disturbances must be computed if one attempts to obtain better agreement.

The power transmitted by the atmosphere to the lake as a function of time for the five cases computed is shown in Fig. 5.12. Platzman also discussed the three phases involved in this surge's propagation (see Fig. 9 of Platzman 1958). Phase I (t = 0–100 min) includes the formative stage of the surge and ends when reflection sets in on the southeastern shore of the lake. In this interval the developing surge advances into still water as

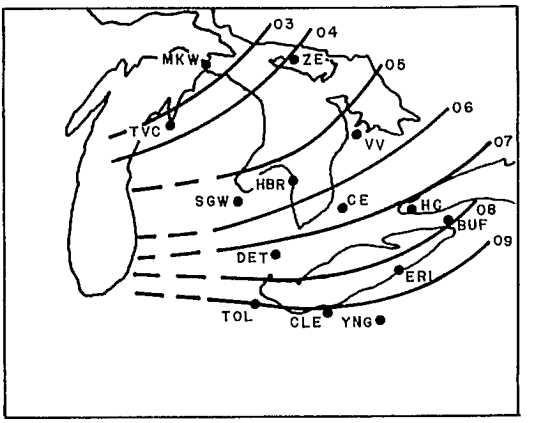

FIG. 5.13. Isochrones of the squall line of May 5, 1952. Numbers represent hours Central Standard Time. MKW, Mackinaw City, Michigan; TVC, Traverse City, Michigan; SGW, Saginaw, Michigan; HBR, Harbor Beach, Michigan; TOL, Toledo, Ohio; YNG, Youngstown, Ohio; ZE, Gore Bay, Ontario; HC, Hamilton, Ontario; V V, Wiarton, Ontario; ERI, Erie, Pennsylvania; DET, Detroit, Michigan; CLE, Cleveland, Ohio; CE, Centralia, Ontario; BUF, Buffalo, New York. (Donn 1959)

a solitary wave (of elevation) and leaves in its wake a broad area of slightly lower water levels. As the wave advances into depths greater than 260 ft (79 m) or more, the wave speed exceeds the squall line speed (54 knots (100 $km \cdot h^{-1}$)) and the central portion of the surge moves ahead of the squall line and the surge assumes a slightly convex shape.

Phase II lasted from 100 to 180 min. It began with reflection at the southeastern shore followed by a wave of depression. During this interval the surge contracted and moved southwest to the Chicago water front. Phase III lasted from 180 to 300 min. It began with reflection at the southwestern shore and a standing wave appeared in the southernmost portion of the lake. It should be noted that the highest water levels in the Chicago area were not produced in phase I but by the reflected surge that formed in phase II and arrived from the northeast about 85 min after the first wave.

Freeman and Murty (1972) and Murty and Freeman (1973) discussed a squall line generated surge on Lake Huron. This will be discussed in section 7.1. Donn (1959) studied the storm surges in Lakes Huron and Erie due to a squall line on May 5, 1952. The travel time curves of the squall line are shown in Fig. 5.13. The pressure and wind data are summarized in Tables 5.7 and 5.8, respectively. Water level data are used from MacKinaw City and Harbor Beach (both on Lake Huron) and from Cleveland and Buffalo (both on Lake Erie). Donn showed that either long gravity waves or edge waves were generated depending on the local topography and the orientation of the squall line track. Significant seiches were excited when the periods of either the gravity waves or the edge waves were close to the natural modes of oscillation of the whole lake or distinctive parts of the lake.

Greenspan (1956) developed an analytical theory for the transient aspects of the steady-state problem of Munk et al. (1956) and applied it to edge wave generation by hurricanes on the east coast of the United States. It was assumed that edge waves generated here in this fashion had amplitudes η of the order of 3 ft (0.9 m), a wavelength λ of the

TABLE 5.6. Computed and observed time intervals between significant events associated with the squall line of June 26, 1954, in the United States. Columns: 1, speed of squall line ($km \cdot h^{-1}$); 2, duration of pressure jump (min); 3, time interval between first surge at Michigan City and second surge at Wilson Avenue Crib (Chicago) (min); 4, time interval between first and second surges at Wilson Avenue Crib (min); 5, time interval between arrival of pressure jump and occurrence of and second surge at Wilson Avenue Crib (min); 6, time interval between second surge and first one following depression at Wilson Avenue Crib (min). (Platzman 1958a)

1	2	3	4	5	6
		Computed			
78	14.3	55	85	109	35
89	12.5	63	85	114	25
100	11.1	66	85	118	20
111	10.0	68	85	120	17
122	9.1	67	85	121	18
		Observed			
	5	68	88	113	6

TABLE 5.7. Atmospheric pressure data at several stations in the United States and Canada for the squall line of May 5, 1952 (NA, not available). (Donn 1959)

Location	Station code	Time (EST) of arrival of pressure jump line	Magnitude of pressure jump (mb)
Buffalo, NY	BUF	08:00	4.06
Centralia, Ont.	CE	06:30	5.08
Cleveland, OH	CLE	09:28	2.71
Detroit, MI	DET	07:38	2.37
Erie, PA	ERI	08:00	3.39
Harbor Beach, MI	HBR	05:20	NA
Mackinaw City, MI	MKW	02:36	NA
Saginaw, MI	SGW	05:40	2.03
Toledo, OH	TOL	09:40	0.68
Traverse City, MI	TVC	03:45	0.68
Youngstown, OH	YNG	09:30	3.39
Gore Bay, Ont.	ZE	04:30	3.39
Hamilton, Ont.	HE	07:30	NA
Wiarton, Ont.	VV	05'15	4.74

order of 200 mi (322 km), and a period of about 6 h. These scales permit the use of the linear shallow-water theory.

The equations of motion and continuity are in the usual notation:

$$\frac{\partial u}{\partial t} = -\frac{1}{\rho}\frac{\partial P}{\partial x}$$
$$\frac{\partial v}{\partial t} = -\frac{1}{\rho}\frac{\partial P}{\partial y} \tag{5.134}$$

TABLE 5.8. Wind data at several stations in the United States and Canada for the squall line of May 5, 1952. (Donn 1959)

Station	Wind data
Buffalo, NY	On arrival of pressure jump, weak winds shifted from east to north
Cleveland, OH	On arrival of pressure jump, winds at 32 km·h^{-1} from northeast shifted to 48 km·h^{-1} from southeast
Detroit, MI	On arrival of pressure jump, winds at 40 km·h^{-1} from southeast shifted to 63 km·h^{-1} from northeast
Erie, PA	Winds of 35 km·h^{-1} from the north. On arrival of pressure jump, winds shifted to southeast
Mackinaw City, MI	Winds of 58 km·h^{-1} shifted at 02:36 (EST)
South Bend, IN	Winds of 29 km·h^{-1} from northwest. On arrival of jump, wind shifted to northeast to north–northeast
Toledo, OH	On arrival of jump, wind shifted from south to north (19–24 km·h^{-1})
Tranverse City, MI	On arrival of jump, wind shifted from southeast to east (32–40 km·h^{-1})
Youngstown, OH	On arrival of jump, wind shifted from north to southeast (48–56 km·h^{-1})
Centralia, Ont.	On arrival of jump, wind shifted from south–southwest to north–northeast
Gore Bay, Ont.	Wind shifted from east to north (16–41 km·h^{-1})
Hamilton, Ont.	Wind from northeast at 16 km·h^{-1}
Wiarton, Ont.	Wind speed increased from 5 to 27 km·h^{-1} and shifted from northeast to north–northeast

$$\frac{\partial \eta}{\partial t} = -\frac{\partial}{\partial x}(uh) - \frac{\partial}{\partial y}(vh) \tag{5.135}$$

where $P(x, y, z, t) = P(x, y, 0, t) + g\rho(\eta - z)$ and $P(x, y, 0, t)$ is the applied surface pressure. Eliminating u and v from above gives

$$\nabla\cdot(h\nabla\eta) - \frac{1}{g}\frac{\partial^2\eta}{\partial t^2} = -\frac{1}{\rho g}(h\nabla^2 P + \nabla h\cdot\nabla P) \tag{5.136}$$

Define a potential ϕ such that

$$u = \frac{\partial\phi}{\partial x}, \qquad v = \frac{\partial\phi}{\partial y}$$

Eliminating η gives

$$\nabla\cdot(h\nabla\phi) - \frac{1}{g}\frac{\partial^2\phi}{\partial t^2} = \frac{1}{\rho g}\frac{\partial P}{\partial t} \tag{5.137}$$

and the wave height is given by

$$\eta = \frac{P}{\rho g} - \frac{1}{g}\frac{\partial\phi}{\partial t} \tag{5.138}$$

Assume that the coastline is straight and assume a linear depth profile perpendicular

to the shore, i.e. $h = \alpha y$. The average slope over the first 120 mi (193 km) was chosen for α. Thus, with $h = \alpha y$, eq. 5.136 becomes

$$(5.139)\quad y\nabla^2\eta + \frac{\partial\eta}{\partial t} - \frac{1}{\alpha g}\frac{\partial^2\eta}{\partial t^2} = -q_1(x, y, t)$$

$$= -\frac{1}{\rho g}\left(\frac{\partial P}{\partial y} + y\nabla^2 P\right)$$

Equation 5.137 becomes

$$(5.140)\quad y\nabla^2\phi + \frac{\partial\phi}{\partial t} - \frac{1}{\alpha g}\frac{\partial^2\phi}{\partial t^2} = -q_2(x, y, t)$$

$$= \frac{1}{\rho g\alpha}\frac{\partial P}{\partial t}$$

Since $P(x, y, t) = 0$ for $t < 0$, the boundary conditions are

$$\eta(x, y, 0) = 0$$

$$\frac{\partial\eta}{\partial t}(x, y, 0) = 0$$

$$\eta(x, y, t) \to 0 \text{ as } |x| \to \infty \text{ for all positive } y \text{ and for all } x \text{ as } y \to \infty$$

Note that except for the forcing function, eq. 5.139 and 5.140 are similar. Hence, eq. 5.139 can be solved for η and then η replaced by ϕ and q_1 replaced by q_2. Making use of Fourier and Laplace transforms and expanding in Laguerre polynomials, Greenspan (1956) solved eq. 5.139.

For application to the cases considered by Munk et al. (1956), Greenspan (1956) assumed that

$$(5.141)\quad P(x, y, t) = \frac{P_0 a(y + a)}{(x - Ut)^2 + (y + a)^2}H(t)$$

where U is the velocity with which the hurricane moves parallel to the coast, a is the half pressure radius, and $H(t)$ is the Heaviside function. From eq. 5.139 the forcing function is

$$q_1(x, y, t) = \frac{P_0 a}{\rho g}\frac{(x + Ut)^2 - (y + a)^2}{[(x - Ut)^2 + (y + a)^2]^2}$$

Greenspan (1956) showed that the pressure distribution assumed here can excite only the fundamental edge wave mode because in the solution, only the first Laguerre polynomial appears.

The solution for the water level is written as

$$(5.142)\quad \eta(x, y, t) = -\frac{\gamma}{2\pi}(\mathrm{I} + \mathrm{II} + \mathrm{III})$$

where

$$(5.143)\quad \gamma \equiv -\frac{\alpha\pi P_0 a}{\rho}$$

and I, II, and III are integrals (see eq. 31 of Greenspan 1956). Integral I represents the

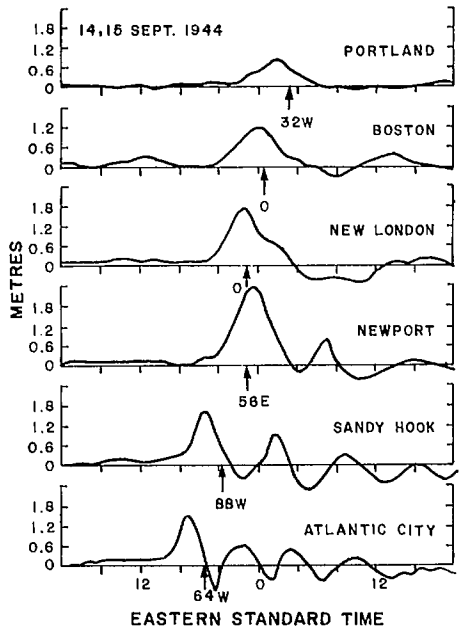

FIG. 5.14. Storm surge of September 14–15, 1944, along the east coast of the United States. Arrows indicate the time of nearest approach of the hurricane's center, distance in kilometres, and direction of tide gauge from the storm track. (Groen and Groves 1961)

quasi-steady-state solution of Munk et al. (1956). Greenspan (1956) showed that integral III is equal to the complex conjugate of II. Hence

$$\eta = -\frac{\gamma}{2\pi}(\mathrm{I} + 2Re\mathrm{II}) \tag{5.144}$$

where Re stands for "the real part of."

The asymptotic solution of the wave height of the resurgence phenomenon is

$$\eta_w \sim \begin{cases} 0 \text{ for } x > Ut \\ \dfrac{2\pi P_0 a k_0}{\rho g} \exp\left[-k_0(y + a)\right] \sin k_0(x - Ut) \text{ for } \dfrac{1}{2}Ut < x < Ut \\ 0 \text{ for } x < \dfrac{1}{2}Ut \end{cases} \tag{5.145}$$

The computed and observed edge wave periods and durations for four hurricanes are compared in Table 5.3.

Redfield and Miller (1957) divided hurricane-produced surges into three parts: the forerunner, the hurricane surge, and resurgences. The forerunner is a slow and gradual change in the water level, commencing several hours before the arrival of the storm. There appears to be good coherence between the records at nearby stations in this stage, and one must consider winds over a more extended region than the hurricane proper. Facing the coast from the ocean, if the hurricane moves to the right along the coast, the forerunner

usually is a rise in the water level and if the hurricane moves to the left, the forerunner consists of a decrease in the water level.

The hurricane surge is a sharp rise in the water level that occurs at about the time the hurricane center passes over the station. The duration of this stage usually does not exceed 2.5−5 h. In this stage, the coherence between neighboring stations is not good. This means that the strong winds in the hurricane proper are responsible for the water level oscillations. In the Northern Hemisphere, the highest water levels occur to the right of the hurricane track.

The resurgences (see the Atlantic City record in Fig. 5.14), being unexpected (since the storm has passed), could be dangerous. These were attributed by Munk et al. (1956) to a wake of waves in the trail of the hurricane, and these have periods of free edge waves. Kajiura (1959) mentioned that even at stations close by (i.e. separated only by one wavelength) the periods could be considerably different. He attributed the resurgences to a free onshore−offshore standing wave on the shelf.

Webb (1976) considered resonance problems of long gravity waves on the continental shelf. He began with a simple model of a rectangular continental shelf at the end of a canal. It is assumed that a Kelvin wave propagates along the canal, which is partly absorbed and partly reflected by the continental shelf. The depth of the canal is of the same order as that of the deep oceans and the shelf parameters are taken to represent the Patagonian Shelf off Argentina. The simple analytical model showed that usually most of the incident wave energy is reflected by the edge of the shelf. However, at the dominant shelf resonance frequencies, more than 95% of the energy is absorbed by the shelf.

Myers (1970) cited an example of extremely strong edge waves at Brown's Bank off the east coast of the United States, and he provided a good review of the theory of edge waves. A significant advance in the theory of edge waves occurred with the publication of a paper by Longuet-Higgins (1967) on long-wave trapping around Macquarie Island. To understand the relation between trapped modes and edge waves, begin with the equations of motion and continuity:

$$\begin{aligned} &\frac{\partial u}{\partial t} = -\frac{1}{\rho g}\frac{\partial P}{\partial x} = -\frac{\partial \zeta}{\partial x} \\ &\frac{\partial v}{\partial t} = -\frac{1}{\rho g}\frac{\partial P}{\partial y} = -\frac{\partial \zeta}{\partial y} \\ &\frac{\partial \zeta}{\partial t} + \frac{\partial}{\partial x}(hu) + \frac{\partial}{\partial y}(hv) = 0 \end{aligned} \tag{5.146}$$

in the standard notation. The equations can be made dimensionless by dividing the horizontal length scale by L and the vertical length scale by the water depth h. Taking the origin at the undisturbed level, the bottom is given by $z = -h(x, y)$. From eq. 5.146 eliminate u and v to give

$$\left(\nabla^2 - \frac{1}{h}\frac{\partial^2}{\partial t^2}\right)\zeta + \frac{1}{h}(\nabla h)(\nabla \zeta) = 0 \tag{5.147}$$

Basically, eq. 5.147 is a wave equation, and the propagation velocity is given by the traditional $c = \sqrt{gh}$ where $h(x, y)$ is the local water depth. Since the propagation velocity is proportional to the water depth, the wave crests and troughs swing towards the shallows during propagation. Hence, it is possible that waves propagating towards the ocean may turn around and propagate towards the coast. One may think of a hypothetical barrier in the ocean beyond which the waves cannot travel towards the ocean. These waves, which

have been turned back, would be partly reflected and the process repeats itself. Thus, resonance is possible even on an open coast and also around islands.

Consider plane waves near a straight coast. Take the x-axis perpendicular to the coast and positive away from the coast and the y-axis along the coast. Taking $h = h(x)$ gives for the water level

$$\zeta(x, y, t) = A(x) \exp(imy - i\omega t) \tag{5.148}$$

From eq. 5.147

$$\frac{d}{dx}\left(h\frac{dA}{dx}\right) + (\omega^2 - m^2 h)A = 0 \tag{5.149}$$

The nature of the solution of eq. 5.149 depends on the sign of the coefficient

$$\omega^2 - m^2 h = q(x)$$

Let h_∞ be the depth as $x \to \infty$. Then, positive number pairs (ω, m) exist such that $q(x) > 0$ near the coast and $q(x) < 0$ far from the coast. These pairs satisfy the relation

$$0 < \frac{\omega^2}{m^2} < h_\infty \tag{5.150}$$

The waves described by any of these numbered pairs are periodic in y but oscillatory in x only near the coast. Away from the shore they are exponentially damped. This transition from oscillatory to exponential behavior occurs at the caustic $x = x_c$ defined by

$$q(x_c) = \omega^2 - m^2 h(x_c) = 0$$

This is the mathematical representation of the hypothetical barrier.

Waves that are restricted to only a portion of the shelf are termed "trapped waves," and edge waves are an example of trapped waves. On the other hand, there are pairs (ω, m) such that $(\omega/m)^2 > h_\infty$ and the solutions correspond to wave forms 5.148. These waves are reflections from the coast of plane waves incident from ∞. It can be seen that on open coasts (unlike in bays and gulfs), trapping is essential for resonance to occur. However, the existence of trapped waves does not necessarily imply resonance (e.g. shelf waves are trapped waves but are not always resonant).

5.2 Tidal Regimes in the Oceans and Coastal Water Bodies

This section will begin with a description of the tides in the global oceans. Although storm surges are not important in the oceans, but achieve significant amplitudes only in the coastal areas, nevertheless some understanding of the tides in the oceans is necessary because the coastal seas usually are not large enough to generate their own tides and the observed tides in these coastal water bodies are usually the result of co-oscillation with the neighboring ocean.

For a discussion of the theory of tides and analysis of tidal data the reader is referred to Defant (1961), Godin (1972), and Leblond and Mysak (1978). It is well known that the oceanic tides arise mainly from the attractions of the moon and sun. Although the moon is a much smaller body than the sun, it exerts a stronger influence in generating oceanic tides because of its proximity to the earth. The most important of the semidiurnal and diurnal tidal constituents that are needed in representing an observed tidal record are listed in Table 5.9.

TABLE 5.9. Tidal constituents usually required for determining the tide at a given location. Note that this is only a small part of a rather lengthy list, most of which is generally irrelevant for storm surge–tide interaction purposes.

Nature of constituent	Symbol for constituent	Frequency (degrees·h^{-1})	Period (h)
Semidiurnal	M_2	28.98	12.42
Semidiurnal	N_2	28.44	12.66
Semidiurnal	S_2	30.00	12.00
Semidiurnal	K_2	30.08	11.97
Diurnal	O_1	13.94	25.82
Diurnal	K_1	15.04	23.94
Diurnal	P_1	14.96	24.06

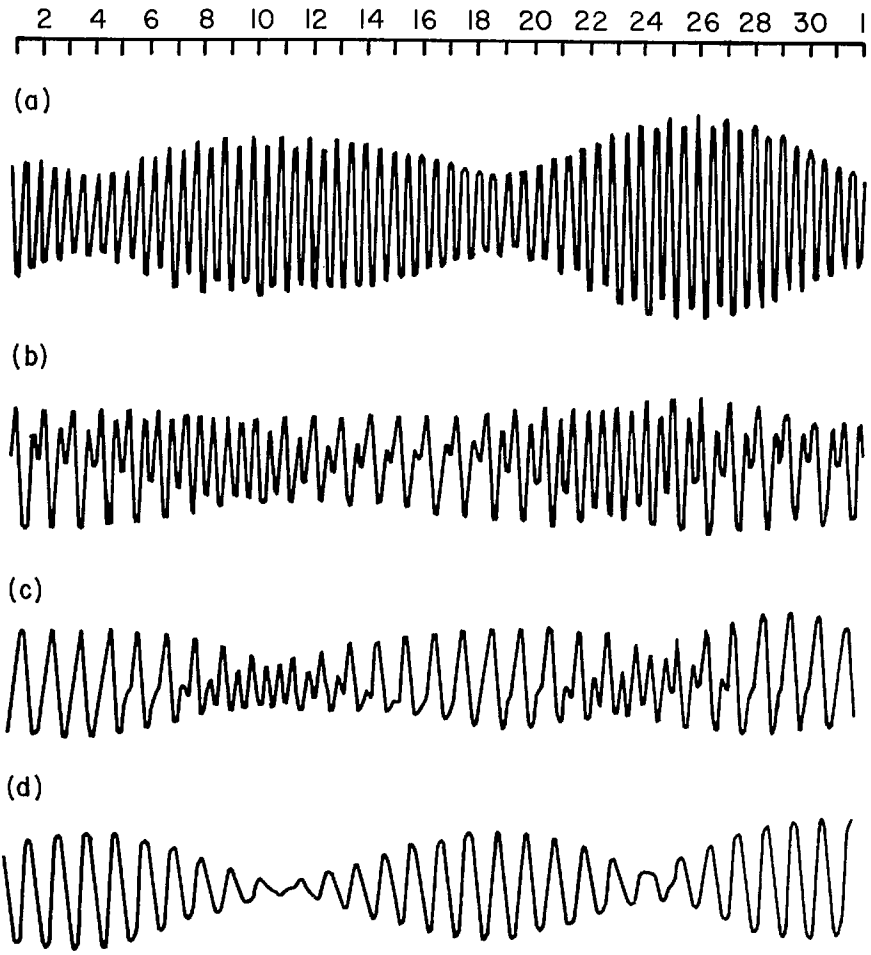

FIG. 5.15. Schematic representation of a 1-mo-long tidal record. (a) Semidiurnal; (b) mixed, mainly semidiurnal; (c) mixed, mainly diurnal; (d) diurnal.

FIG. 5.16. Tides in Canadian waters classified according to the following scheme: 1, semidiurnal; 2, mixed, mainly semidiurnal; 3, mixed, mainly diurnal; 4, diurnal. (Dohler 1967b)

Following Godin (1980a, 1980b), the vertical component $z(t)$ of the tide is as follows:

$$(5.151) \quad z(t) = z_0 + \sum_{j=1}^{n} A_j \cos(\sigma_j t - a_j)$$

where z_0 is a constant that denotes the reference level, which is chosen such that the observed water level rarely, if ever, falls below z_0, and the other term on the right is a summation of n constituents of amplitude A_j, frequency σ_j, and phase a_j where j varies from 1 to n. Note that the frequencies σ_j of the constituents are the same for any tidal record (for the same constituent); however, the amplitude and phase of the constituent might vary from one tidal station to another. Through a harmonic analysis of the observed tidal record, one can determine the amplitudes and phases of the various tidal constituents. In principle, the total number of constituents could be as high as 500, but rarely must one use more than a dozen or so of the important constituents in representing a tidal record.

In practical tidal studies, it was found convenient to classify the tides into the following four types: semidiurnal, mixed—mainly semidiurnal, mixed—mainly diurnal, and diurnal. A tide is referred to as semidiurnal if there are two high waters and two low

waters daily of roughly the same amplitude (Fig. 5.15a). Mixed tides of the mainly semidiurnal type have two high waters and two low waters with the amplitudes being unequal (Fig. 5.15b). Mixed tides of the mainly diurnal type are said to exist if at times there is only one high water and one low water per day and at other times there are two large inequalities (Fig. 5.15c). For diurnal tides, there is one high water and one low water per day (Fig. 5.15d). Canadian waters are classified according to this scheme in Fig. 5.16.

A cotidal chart is a convenient way of presenting tidal information for each tidal constituent separately. Two sets of lines exist on a cotidal chart. Corange (coamplitude) lines represent contours of the range (amplitude) of the constituent, whereas cophase lines represent the contours of equal phase (usually with reference to Greenwich, expressed in degrees per hour). Amphidromic points, which appear for certain constituents in water bodies, are the locations where the range (amplitude) of the particular constituent is zero. Thus, it is basically a node for the vertical motion, the nodal line becoming just a point either due to the presence of transverse motion or due to the influence of the earth's rotation (George 1980). In a water body, one tidal constituent may have an amphidromic point, whereas another constituent may have more than one or no amphidromic points. Similarly, a given constituent may have an amphidromic point in one water body but may have more than one or no amphidromic points in another water body.

Tides in the Oceans

The tidal regimes in the world oceans are usually described through cotidal charts, which show lines of simultaneous occurrence of high water in various regions. Whewell (1833) appears to have produced the first cotidal chart for the semidiurnal tides in the global oceans. These charts are not very accurate because they are produced by simply interpolating from the coastal data. The next charts to appear were those of Harris (1904). This work also suffered many drawbacks, notable ones being neglect of the earth's rotation and not giving absolute values of amplitudes of the tides. Sterneck (1920) produced charts for the semidiurnal tides, mainly based on interpolation of observed data. Dietrich (1944a, 1944b) gave charts for the constituents M_2, S_2, K_1, and O_1. Villain (1952) gave a chart for the M_2 tide in the global oceans. Defant (1961) appears to be among the first to have produced a cotidal chart based on a numerical model. Since then, dozens of numerically produced cotidal charts for various water bodies on the globe have appeared in the literature.

Proudman (1944) studied the distribution of the M_2 tide in a section of the Atlantic Ocean between 35°S and 45°N including the effects of the earth's rotation but ignoring coastal energy dissipation. He prescribed arbitrary values for the current and water level along the 35°S latitude as boundary conditions. The motion he considered consisted of an independent tide due to the tidal potential and four free oscillations in the form of northward and southward propagating Kelvin and Poincaré waves. Linear combinations of these have been made to agree with observed M_2 at different coastal locations.

Accad and Pekeris (1978) studied M_2 and S_2 tidal regimes in the global oceans by solving the Laplace tidal equations, based on a knowledge of the tidal potential alone. There are about 1300 tidal stations in the open ocean at which the tide is measured by recording the pressure with an instrument located at the bottom. The topography of the global ocean model is made up of 2° arcs of latitude and longitude on a Mercator projection. It was assumed that tidal dissipation occurred only at the coast where a portion of the incident tidal energy is assumed to be absorbed.

To understand the influence of sharp corners introduced in the numerical model by approximating the continuous coastline with arcs of latitude and longitude, a model with

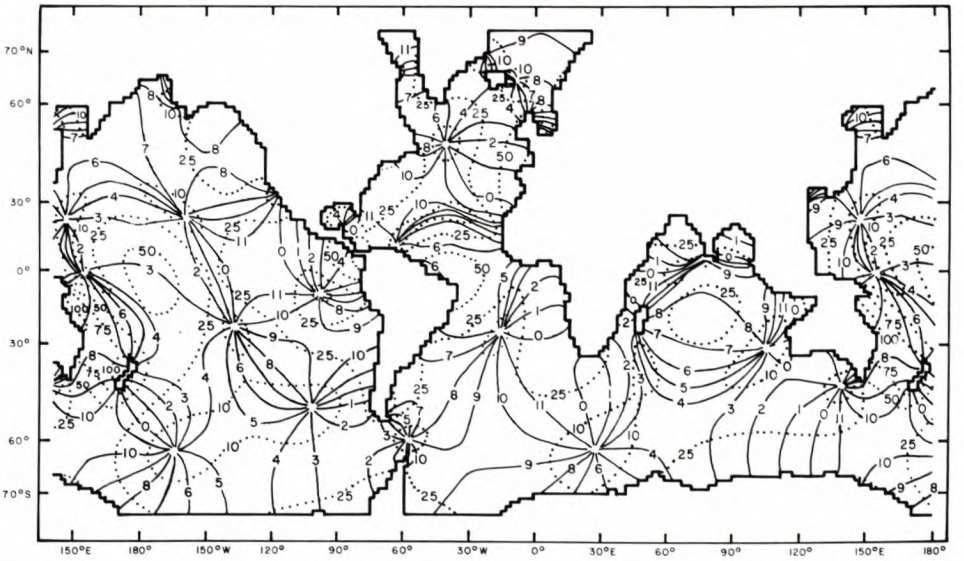

FIG. 5.17. Distribution of the M_2 tide in the global oceans. Solid lines show phases in Greenwich hours and dotted lines show tidal range in centimetres. (Accad and Pekeris 1978)

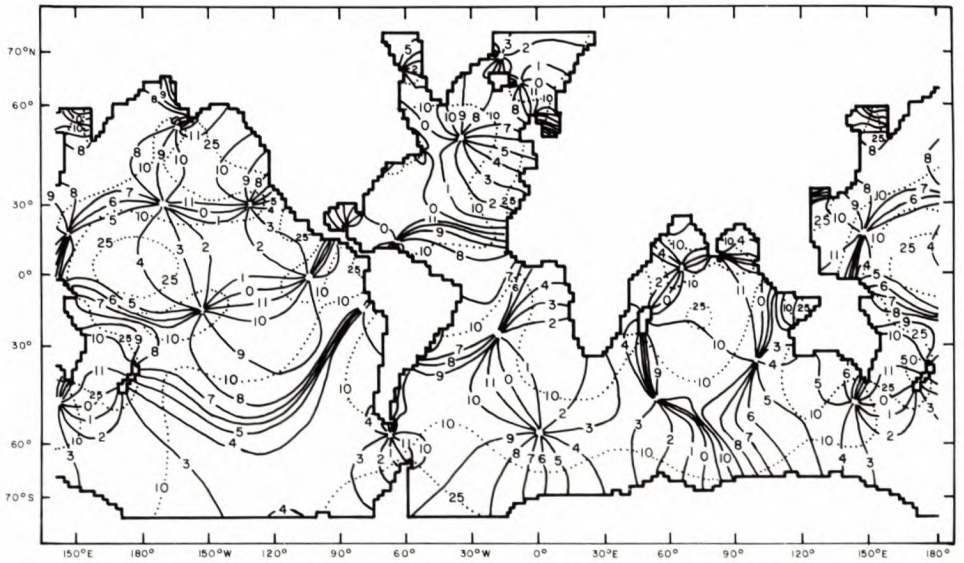

FIG. 5.18. Distribution of the S_2 tide in the global oceans. Solid lines show phases in Greenwich hours and dotted lines show tidal range in centimetres. (Accad and Pekeris 1978)

a smooth coastline was also run. The influence of the sharp corners appears to be insignificant in the results. The M_2 and S_2 tidal regimes in the global oceans, as computed by Accad and Pekeris (1978), are shown in Fig. 5.17 and 5.18, respectively. Observed and calculated tides at selected island stations in the various oceans are compared in Table 5.10.

TABLE 5.10. Comparison of observed and computed M_2 tidal amplitudes and phases at island stations in the oceans. (Accad and Pekeris 1978)

Station	Region	Amplitude (cm)		Phase lag (h)	
		Observed	Computed	Observed	Computed
North Atlantic Ocean					
Flores Island	Azores	39	34	2.0	1.8
Santa Maria Island	Azores	51	48	2.0	2.1
Funchal	Madeira	72	71	1.5	1.8
Tenerife	Canary Island	69	70	1.0	1.3
Santo Antao	Cape Verde Island	30	21	8.7	9.2
Eleuretha Island	Bahama Island	32	20	0.7	11.7
St. George's Island	Bermuda	37	24	0.0	11.5
South Atlantic Ocean					
Ascension Island		33	27	5.9	6.0
Fenando de Noronha		79	70	6.9	7.0
St. Helena Island		32	27	2.7	2.4
Isla Trinidade		33	33	7.0	6.8
Tristan da Cunha		23	25	0.4	0.3
Stanley Harbour	Falkland Island	45	31	9.1	9.1
Elsehul	South Georgia	27	22	9.0	9.1
Scotia Bay	South Orkney Island	46	30	8.7	8.8
Indian Ocean					
Port Victoria	Seychelles Island	40	35	0.4	0.4
Port Louis	Mauritius	13	43	8.9	8.9
Addu Atoll		29	36	8.4	8.5
Port Refuge	Cocos Island	27	31	10.4	9.5
St. Paul Island		38	36	7.7	8.0
Port-aux-Français	Kerguelen	51	16	6.5	6.8
North Pacific Ocean					
Pagan Island	Marianas Island	17	2	9.8	4.1
Kusail Island	Caroline Island	42	49	4.3	3.3
Port Rhin	Marshall Island	57	55	4.4	3.6
Midway Island		11	6	3.0	4.2
Johnston Island		27	23	3.5	3.0
Honolulu	Hawaiian Islands	16	16	2.1	0.1
Kahului	Hawaiian Islands	18	18	0.4	0.1
Hilo	Hawaiian Islands	21	20	1.0	0.3
South Pacific Ocean					
Lord Howe Island	Tasman Sea	59	33	10.1	9.0
Paagoumene Bay	New Caledonia	45	47	9.0	8.3
Vila Harbour	New Hebrides	34	34	6.9	7.3
Kingston	Norfolk Island	57	79	8.8	8.3
Nukualofa	Tonga Island	52	45	6.4	5.9
Funafuti	Ellice Island	57	50	5.1	4.5
Aitutaki	Cook Island	17	32	7.0	5.6
Hanga Piko	Easter Island	21	12	0.5	10.0
Caleta Aeolian	Galapagos Island	72	49	8.2	7.3
Cambier Island	Polynesian Archipelago	27	12	11.6	9.0
Ahe		12	4	2.9	4.1
Nukuhiva		47	21	1.2	0.6

Schwiderski (1978a, 1978b, 1979, 1980a, 1980b, 1980c) studied global ocean tides by introducing several novel features in his numerical models. First, he derived the ocean tidal equations in continuous as well as discrete forms. In these equations, the Boussinesq linear eddy dissipation law is used and the eddy viscosity is made to depend on the lateral mesh area (which is derived from the grid size and the local water depth). The bottom friction coefficient also depends on the mesh area. In addition to the tidal potential, secondary factors such as the influence of the oceanic and terrestrial tides on the tidal potential are included. Zahel (1973) studied the diurnal K_1 tide in the world oceans.

Harris (1911) appears to be among the first to give a cotidal chart for the Arctic Ocean. He showed that the tide entering from the Atlantic Ocean takes about 20 h to cross the Arctic Ocean. Following the observations taken during the Maud expedition, Defant (1924) and Fjeldstad (1929a, 1929b) showed that the tide wave takes only 12 h (instead of 20 h) to cross the Arctic Ocean. Goldsbrough (1913) developed an analytical model for the tides in the Arctic Ocean. His study, which was limited to the region between 60 and 75°30′N, showed that the semidiurnal tides in the Arctic Ocean are very small. Goldsborough concluded that the independent tide in the Arctic Ocean is insignificant and the observed tide is a co-oscillation with the Atlantic Ocean tide.

Defant (1924) used a one-dimensional numerical model for the combined Atlantic and Arctic oceans and showed that for the M_2 tide in the Arctic Ocean there is an amphidromic point north of Canada. Nekrasov (1962) used Defant's method for the Greenland Sea and the Norwegian Sea. Dvorkin et al. (1972) used a two-dimensional numerical model with a grid spacing of 1°. Actually, Zahel's model is for the global oceans and includes the Arctic Ocean also. Kowalik and Untersteiner (1978) developed a two-dimensional numerical model with a grid size of 75 km for the Arctic Ocean. One novel feature of this model is the manner in which these authors avoid the difficulty associated with the integration in a spherical polar coordinate system near the pole (the North Pole in this case). Kowalik and Bich Hung (1977) used a stereographic polar coordinate system by means of a scale factor m, and this was adapted by Kowalik and Untersteiner (1978).

Take the origin at the North Pole and let x and y be coordinates along 0 and 90°E longitudes. Let M and N be the transport components along the x- and y-axes and η be the free surface elevation. Then the equations of motion and continuity are

$$\frac{\partial M}{\partial t} - m^2 A \nabla^2 M + \frac{k}{H^2} M|\boldsymbol{M}| - fN + mgH\frac{\partial \eta}{\partial x} = F_x \tag{5.152}$$

$$\frac{\partial N}{\partial t} - m^2 A \nabla^2 N + \frac{k}{H^2} N|\boldsymbol{M}| + fM + mgH\frac{\partial \eta}{\partial y} = F_y \tag{5.153}$$

$$\frac{\partial \eta}{\partial t} + m\frac{\partial M}{\partial x} + m\frac{\partial N}{\partial y} = 0 \tag{5.154}$$

Here, A is the horizontal eddy viscosity (taken as 10^9 cm$^2\cdot$s^{-1}), k is a bottom friction coefficient (3×10^{-3}), f is the Coriolis parameter, $\boldsymbol{M} = (M, N)$, $H(x, y)$ is the water depth, and F_x and F_y are the components of the tidal potential (taken to be zero). The gravity g is determined from

$$g = 978.05\ (1 + 0.0053 \sin^2 \phi)\ \text{cm}\cdot\text{s}^{-2} \tag{5.155}$$

where ϕ is the latitude (of a given grid point). The scale factor m relates the surface elements δS on a stereographic map to those on a sphere as follows:

$$m = \frac{\delta S_{\max}}{\delta S_{\text{sphere}}} = \frac{1 + \sin \phi_0}{1 + \sin \phi} \tag{5.156}$$

where ϕ_0 is the latitude through which a parallel plane of the stereographic projection passes. Near the pole, m is unity.

At the closed boundary

$$M = N = 0 \tag{5.157}$$

and at the open boundary

$$\eta = \eta(t) \tag{5.158}$$

is prescribed.

Conservation of mass is assured by requiring that the integral taken over one tidal period T_p along the open boundary be zero:

$$\int_0^{T_p} \int_0^L (M \cos \alpha + N \sin \alpha) dt dS = 0 \tag{5.159}$$

where α is the angle between the perpendicular direction to the open boundary and the x-axis and L is the length of the open boundary.

A staggered grid in space (Hansen 1962) and a leapfrog scheme in time are used. The stability criterion is

$$\Delta t \leq \frac{\Delta}{m\sqrt{2gH}} \tag{5.160}$$

where Δ is the grid size (taken as 75 km). However, in practice the following stability criterion is more appropriate (Phillips 1959):

$$\Delta t \leq \frac{R + 2m^2 \frac{A}{\Delta^2}}{2f^2} \tag{5.161}$$

where R is related to r, H, M, and N (see Kowalik and Untersteiner 1978).

Topography plays a major role in the Arctic Ocean tidal model because the depth varies from 5.1 to 0 km. The north Siberian Shelf is the widest continental shelf on the globe and hence, lateral friction is also important. One might expect that at a critical latitude (where the tidal and inertial periods agree with each other), resonance occurs. However, Flattery (1967) showed that this does not happen. Kagan (1968) showed that the almost permanent ice cover in the Arctic Ocean has negligible effect on the tide. For a general discussion of the influence of an ice layer on long waves, see Murty and Polavarapu (1979).

The cotidal and corange lines for the M_2 tide in the Arctic Ocean are shown in Fig. 5.19A and 5.19B, respectively. These cotidal and corange maps agree with those of the U.S. Navy Hydrographic Office (Anonymous 1958) and those of Zahel (1977). There is an amphidromic point at latitude 81°30′N and longitude 133°W. This is in the deep water of the Canadian Basin off Prince Patrick Island. The M_2 tide from the Atlantic Ocean mainly enters through the Greenland Sea. At Spitsbergen its amplitude is about 40 cm and during its propagation northwards decreases to about 2 cm near the East Siberian and Chukchi seas. In the region of the East Siberian Shelf, Chukchi Sea, and Beaufort Sea, the cotidal lines are somewhat parallel to the depth contours. At the entrance to the East Siberian Sea the amplitude is 10−15 cm falling to 2−3 cm near the coast.

Another branch of the Atlantic Ocean tide enters the Arctic Ocean between Spitsbergen and Norway. This causes higher amplitudes in the southern part of the Barents Sea and in the White Sea and begins to dissipate towards Novaya Zemlya. The model of

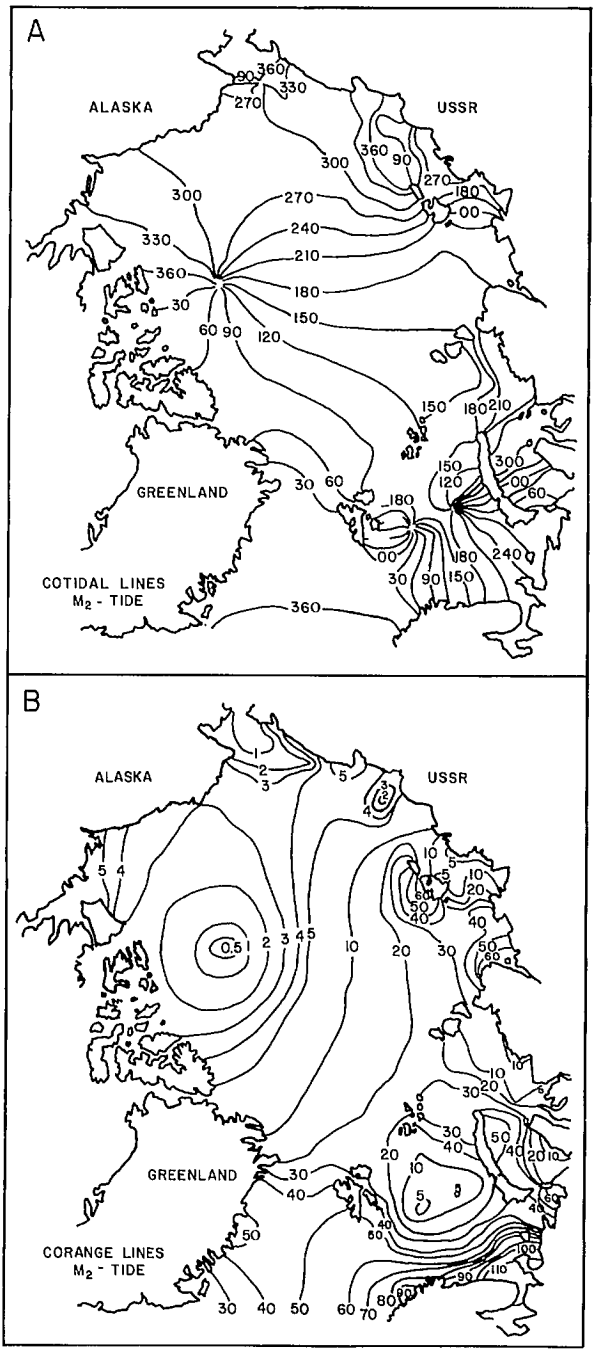

FIG. 5.19. (a) Cotidal lines for M_2 in the Arctic Ocean. Phase angles (with reference to Greenwich) are in degrees. (b) Corange lines (centimetres) of M_2 in the Arctic Ocean. (Kowalik and Untersteiner 1978)

Kowalik and Untersteiner (1978) did not reproduce the tide in the area of the White Sea, western part of the Barents Sea, and around Novaya Zemlya.

Platzman (1975, 1979) calculated the normal modes of the Atlantic and Indian oceans, including their topography and the effect of the earth's rotation in a finite-element framework and paying particular attention to the effects of multiple connectivity due to the presence of islands. Tidal regimes can then be developed using the results of the normal modes. Several authors (e.g. Fairbairn 1954) used the so-called Proudman tidal theorem to calculate the tides in the oceans or in small water bodies. This theorem permits one to determine the tidal regime across the open boundary of a water body, knowing the tides around its shore. However, Foreman et al. (1980) showed that the mathematical problem is ill-posed, and attempts to use the theorem numerically have failed.

Thacker (1979) simulated tidal motion on a sphere using a geodesic finite-difference method. This method permits variable resolution of the grid, and the use of a three-dimensional Cartesian coordinate system, rather than a two-dimensional curvilinear surface coordinate system, makes computations on irregular surfaces somewhat easier. Clarke and Battisti (1980) considered the influence of the continental shelf on coastal tides. Their coastal boundary layer theory suggests that semidiurnal tides will be amplified on wide continental shelves in middle and low latitudes, but diurnal tides will not be amplified. Observations bear out these theoretical results.

Tides in Canadian Waters

In this subsection, the tidal regimes in various Canadian water bodies will be considered in some detail. In the next subsection, the tidal regimes in certain selected water bodies on the globe will be considered.

The second greatest tidal range in Canada, and probably in the world (the greatest tidal range occurs in Ungava Bay, which joins the Hudson Strait in Canada), occurs in the Bay of Fundy in which the tidal range is greater than 40 ft (12.2 m). Along the Atlantic coast of Canada from Cape Race to Cape Ray (Newfoundland), across to Glace Bay (Nova Scotia), and along the shores of Nova Scotia and New Brunswick, the tide is semidiurnal (Dohler 1967a). From Placentia Bay (Newfoundland) to Shelbourne (Nova Scotia), high water occurs almost at the same time. The tidal range (i.e. difference between high- and low-water heights) here is usually less than 6 ft (1.83 m). However, near the southern tip of Nova Scotia, the tidal range as well as the time of occurrence of high water varies significantly over short distances.

Along the east coast of Newfoundland and along the Labrador coast south of Cartwright, the tide is mainly semidiurnal. North of Cartwright the tide becomes increasingly semidiurnal, and at the northernmost point of Labrador (at Cape Chidley) the tide is entirely semidiurnal. The tidal range here is about 0.9 m but it increases towards the Davis Strait.

The tide that propagates through the Cabot and Belle Isle straits into the Gulf of St. Lawrence is also mainly semidiurnal, expect between Cape Tormentine and Richibucto (New Brunswick) and also near Savage Harbor (Prince Edward Island) where the tide is dominated by diurnal constituents. At the southern end of Magdalen Islands and near Crossman Point (New Brunswick) the tide is diurnal. The tidal range in the Gulf of St. Lawrence is less than 2.4 m.

The tide in the Gulf of St. Lawrence (which is a co-oscillating tide with the Atlantic Ocean) propagates through the St. Lawrence Estuary and River to Lake St. Peter (a distance of 644 km from Sept-Îles). It takes the crest of the tide 1 h (counting from

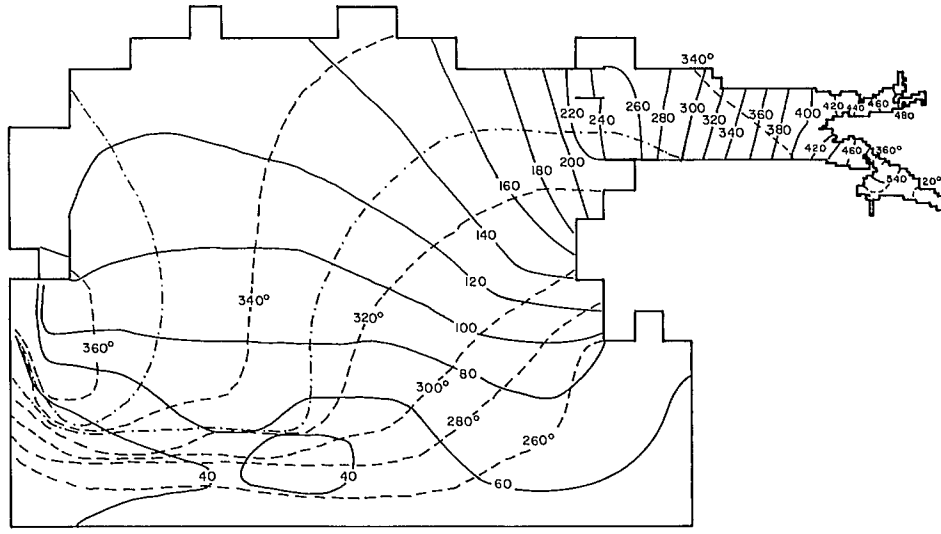

FIG. 5.20. Computed tidal regime for the M_2 constituent in the Bay of Fundy and the Gulf of Maine. Solid lines show the amplitude (centimetres) and broken lines show the phase (degrees). (Greenberg 1975)

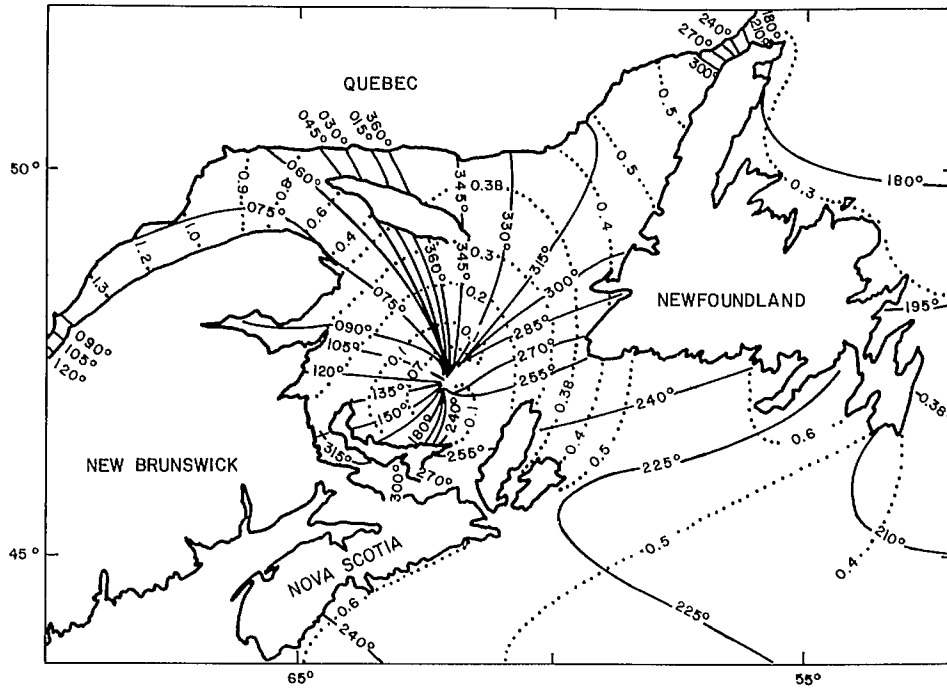

FIG. 5.21. Distribution of the M_2 tide in the Gulf of St. Lawrence, Canada. Amplitudes are in centimetres and phases are in degrees. (Farquharson 1970)

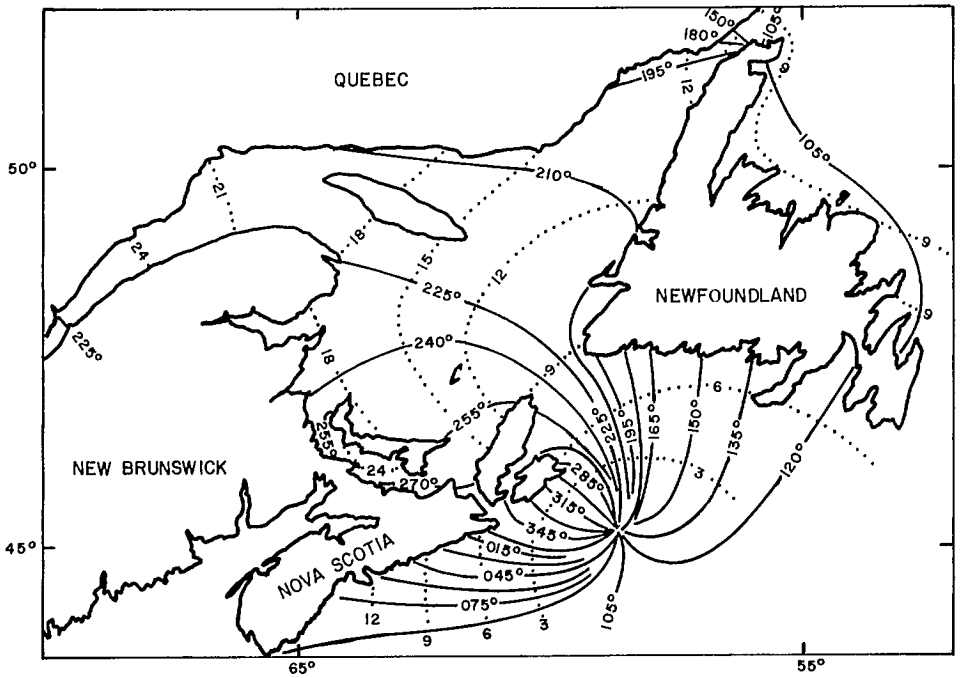

FIG. 5.22. Distribution of the K_1 tide in the Gulf of St. Lawrence, Canada. Amplitudes are in centimetres and phases are in degrees. (Farquharson 1970)

Sept-Îles) to travel to the mouth of the Saguenay River, 5 h to Quebec City, and 10 h to Lake St. Peter. The range of the tide increases from about 2.1 m at Sept-Îles to about 4.3 m at Quebec City and decreases to about 0.3 m in Lake St. Peter. Upstream of Lake St. Peter, a semidiurnal tide with a range of 0.15 m is present. A very small tidal range of 0.03 m can be seen in the Great Lakes.

In the Hudson Strait, Hudson Bay, and Foxe Basin, the tide is mainly semidiurnal, except in a small region between Povungnituk and Port Harrison and also at Hall Beach. Here, large diurnal variations take place. Beginning at the mouth of the Hudson Strait, along the north shore the tidal range increases from 5.5 m to about 9.1 m (at Ashe Inlet) and decreases again to 4.9 m at Schooner Harbor. Along the southern shore of Hudson Strait, the tidal range increases rapidly and the average range is about 12.2 m in the Leaf Basin. At the mouth of Hudson Bay the tidal range is about 1.8 m and increases to about 3.7 m near the western shore and decreases gradually along the southern and eastern shores to about 0.3 m at Port Harrison. At the head of James Bay, frequent large storm surges obscure the tidal effect (Dohler 1967a).

From the Labrador Sea, the tidal range increases northward into Davis Strait and decreases again towards Baffin Bay. Halfway along the Baffin Island coast, the tidal range is almost zero. From here, it increases towards Smith Sound and Lancaster Sound. In Davis Strait, high water occurs almost simultaneously everywhere. However, in Baffin Bay, high water at the northern end occurs at the same time as low water at the southern end. In Smith Sound, the tidal range is about 3.1 m and in Lancaster Sound (at Resolute) the average range is about 1.2 m. In the inlets leading off from Lancaster Sound, the mean range is about 1.8 m. In the western Arctic, west of Barrow Strait, the tidal range is very small.

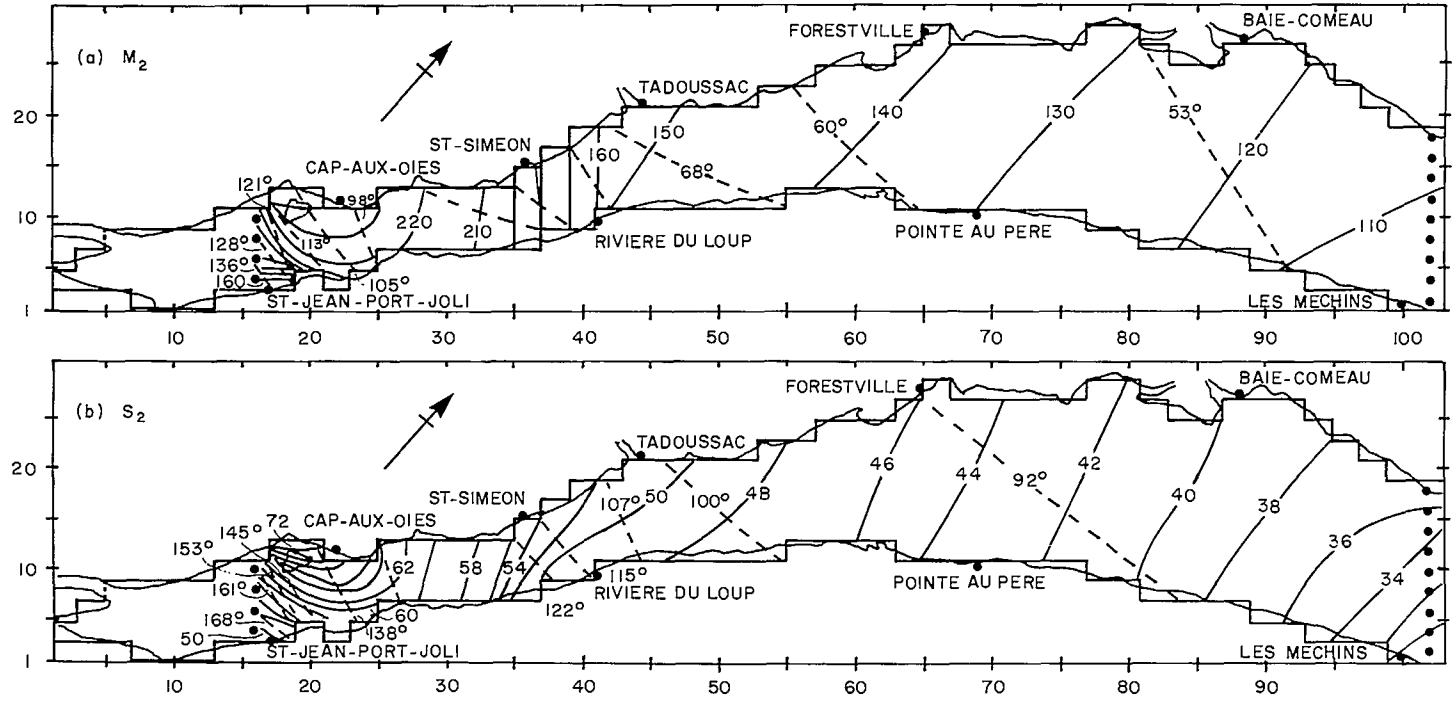

FIG. 5.23. (a) M_2 tide and (b) S_2 tide in the St. Lawrence Estuary, Canada. Amplitudes are in centimetres and phases are in degrees. (Levesque 1977)

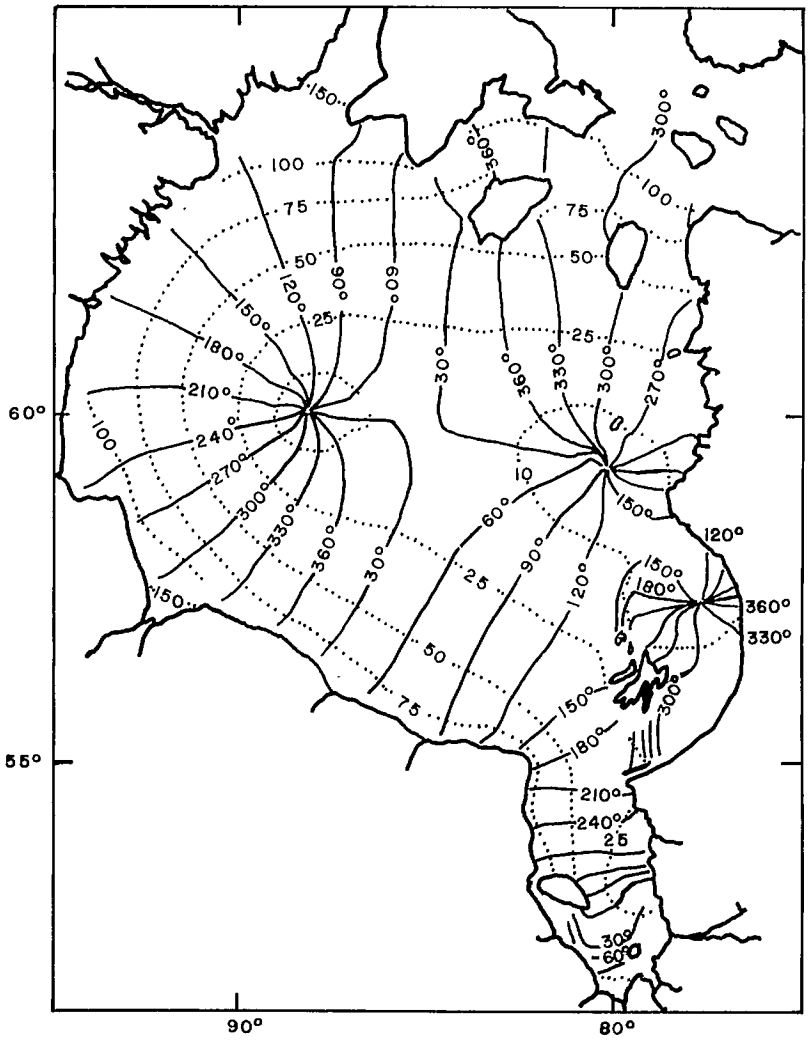

FIG. 5.24. M_2 tide in Hudson Bay. Amplitudes are in centimetres and phases are in degrees.

Tides on the west coast of Canada will not be considered because significant storm surges do not occur here (except possibly in the Hecate Strait and Queen Charlotte Sound). For more details on tides in eastern Canadian water bodies, see Yuen (1967), Greenberg (1975, 1979), Garrett and Greenberg (1977), DeWolfe (1979), Farquharson (1970), Levesque (1977), Dohler (1967a), Easton (1972), Godin (1965a, 1965b, 1966a, 1966b, 1974), and Freeman and Murty (1976). Godin (1980a) produced cotidal charts for all Canadian waters.

One of the important water bodies in western Canada that is relevant for storm surge studies is the Beaufort Sea. Henry and Foreman (1977) studied the tides in this water body using a two-dimensional numerical model. The tidal regimes in Canadian water bodies in which storm surges are significant are shown in Fig. 5.20–5.27.

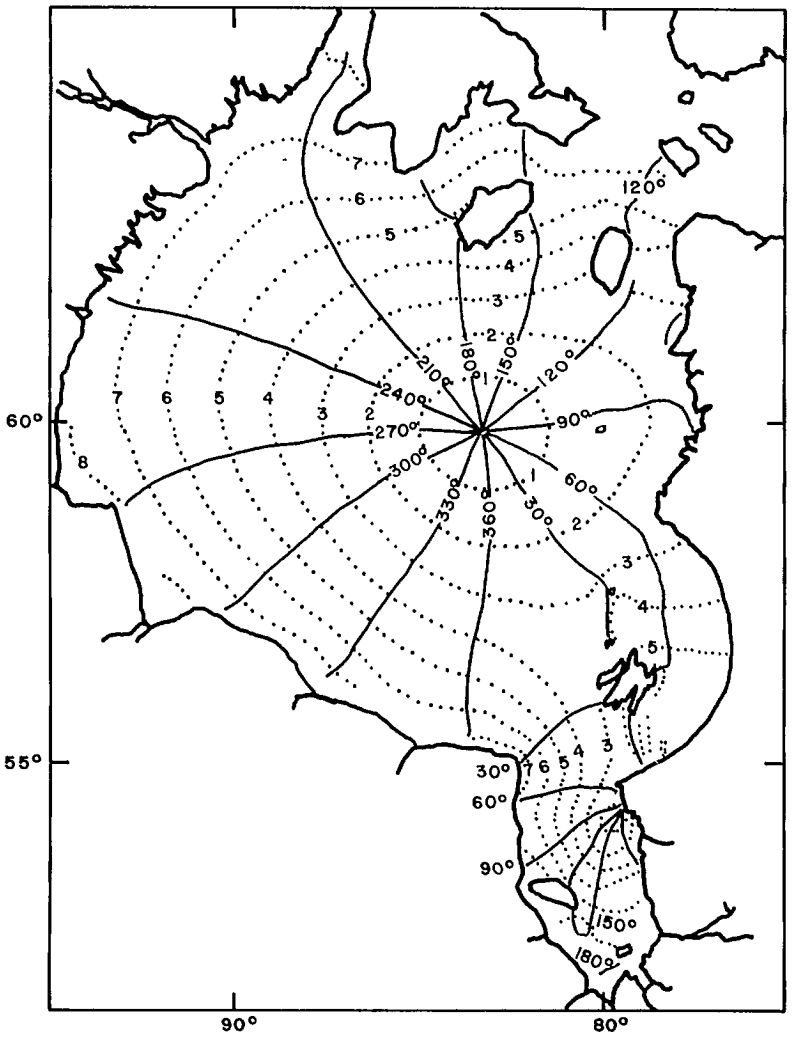

FIG. 5.25. K_1 tide in Hudson Bay. Amplitudes are in centimetres and phases are in degrees.

TIDES IN SELECTED WATER BODIES ON THE GLOBE

The M_2 tidal regime in the North Sea is shown in Fig. 5.28. Three amphidromic points can be seen. The cotidal chart for M_2 in the Baltic Sea is shown in Fig. 5.29. Again, one can see three amphidromic points. In Fig. 5.30 is shown the M_2 tidal regime in the Adriatic Sea, which has only one amphidromic point. The Black Sea also shows only one amphidromic point (Fig. 5.31). Tidal regimes are also illustrated for the Persian Gulf (Fig. 5.32), Indonesian Archipelago (Fig. 5.33), Eastern China Sea (Fig. 5.34), and the Sea of Okhotsk (Fig. 5.35). The M_2 and K_1 tidal regimes in the Gulf of Mexico are shown in Fig. 5.36 and 5.37, respectively. The K_2 tidal regimes in the Arabian Sea and the Bay of Bengal

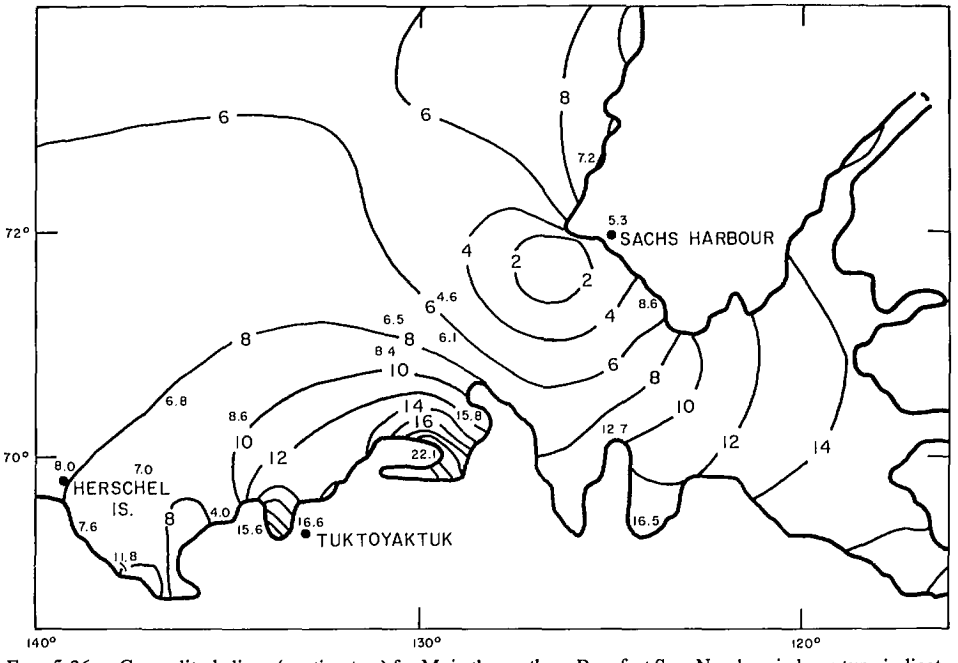

FIG. 5.26. Coamplitude lines (centimetres) for M_2 in the southern Beaufort Sea. Numbers in large type indicate computed values and those in small type denote observed values. (Henry and Foreman 1977)

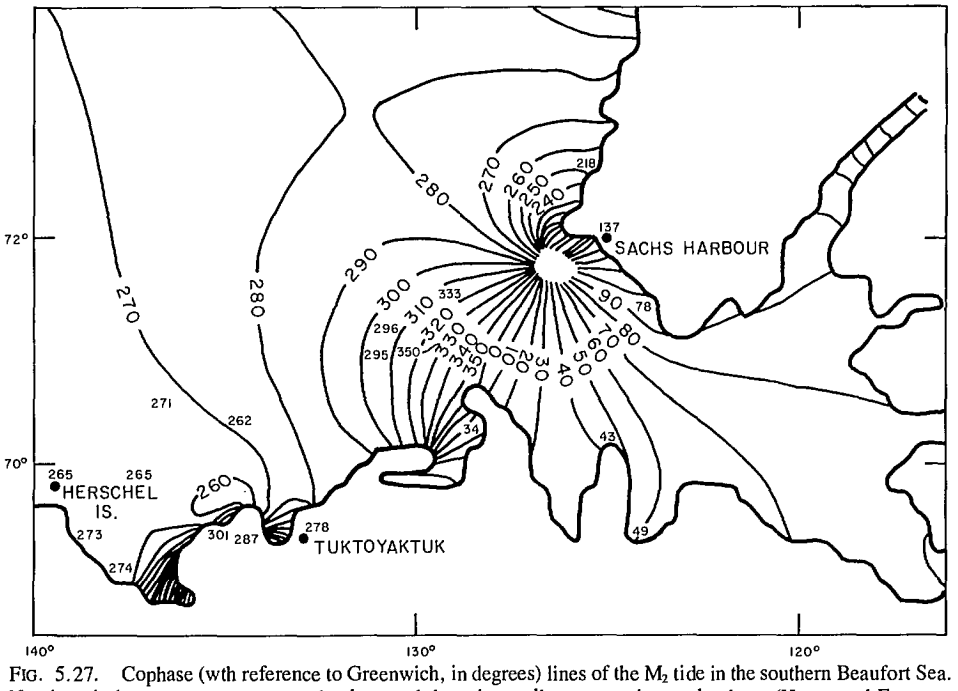

FIG. 5.27. Cophase (wth reference to Greenwich, in degrees) lines of the M_2 tide in the southern Beaufort Sea. Numbers in large type are computed values and those in small type are observed values. (Henry and Foreman 1977)

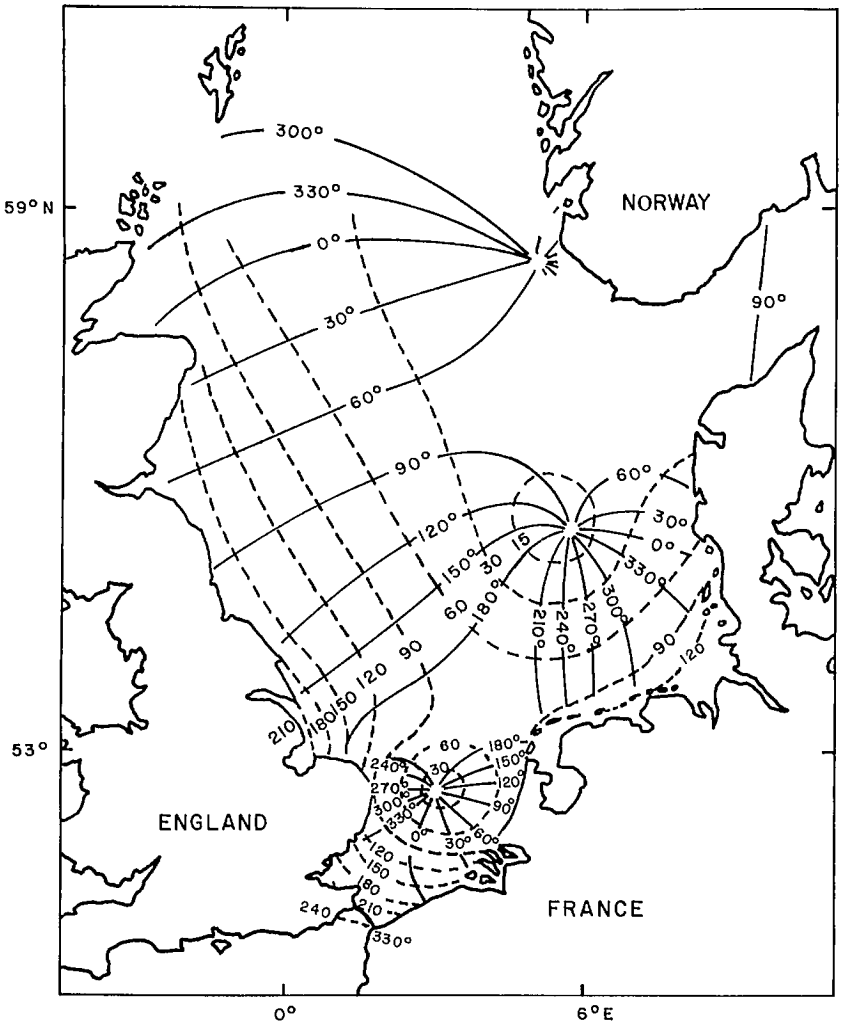

FIG. 5.28. Cophase (degrees, solid lines) and corange (centimetres, broken lines) of the M_2 tide in the North Sea. (Defant 1961)

are illustrated in Fig. 5.38. The M_2 tidal regime in the northern part of the Bay of Bengal is shown in Fig. 5.39 and 5.40.

5.3 Interaction Between Storm Surges and Tides

The traditional method of subtracting the astronomical tide from the observed water level and treating the residue as storm surge assumes that tide and surge are linearly additive and that there is no nonlinear interaction. However, observations show that there are situations in which there is an interaction (i.e. tide influencing the propagation of the surge and vice versa), especially in shallow areas. This interaction phenomenon, although probably present in other water bodies as well, appears to be quite pronounced in the

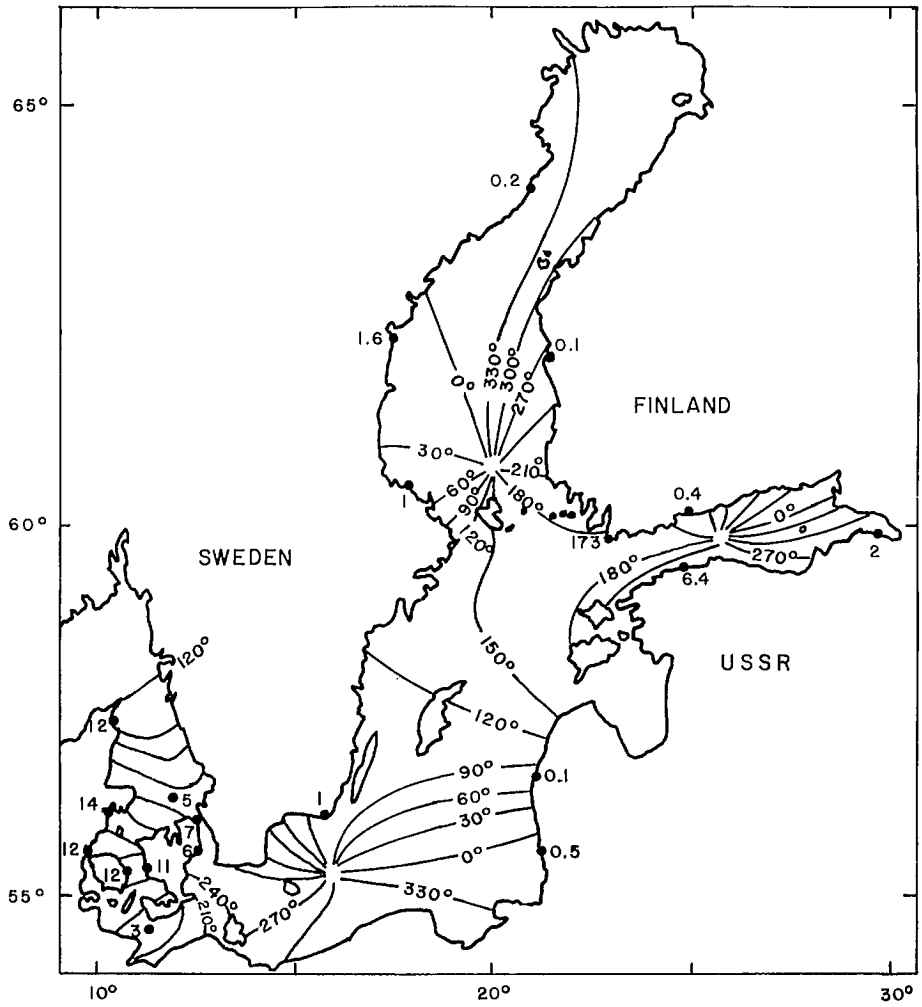

FIG. 5.29. Cophase lines (degrees) for the M_2 tide in the Kattegat and Baltic seas. The observed amplitudes (centimetres) are also shown. (Defant 1961)

Thames Estuary of the North Sea. In a series of papers, Proudman (1955a, 1955b, 1957, 1958) studied this problem analytically, and his work will be considered at some length.

ANALYTICAL THEORIES

Observations in the North Sea and Thames Estuary show that maximum surges (both positive and negative) occur nearer the time of tidal low water than the time of tidal high water. Proudman (1955a) explained this observation through an analytical theory in which it was assumed that the surge and tide are generated in the North Sea and then propagate into the estuary. Ignoring the earth's rotation, computations have been made for uniform as well as variable width of the estuary.

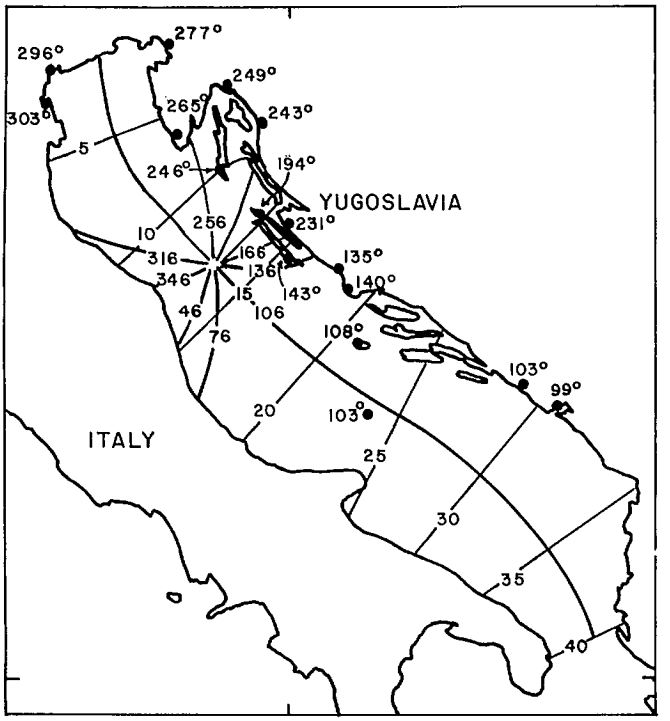

FIG. 5.30. M_2 tide in the Adriatic Sea. Numbers at stations represent the phases (degrees). Transverse lines correspond to the sections used for the computation. (Defant 1961)

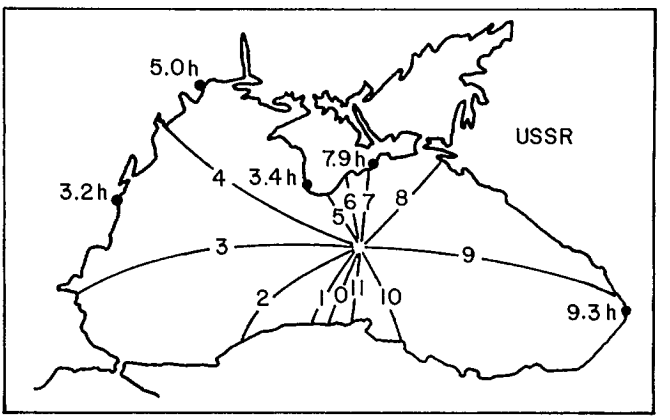

FIG. 5.31. Amphidromy of the semidiurnal tide in the Black Sea. (Defant 1961)

Before giving a summary of the mathematical analysis of Proudman, the important results from his theory will be stated. For this purpose the following terms in the equations of motion are identified: $(K|u|u)/h$ is the friction term, $\partial u/\partial x$ is the convective term, and $\partial/\partial x(\zeta u)$ is the shallow-water term. The important results are as follows.

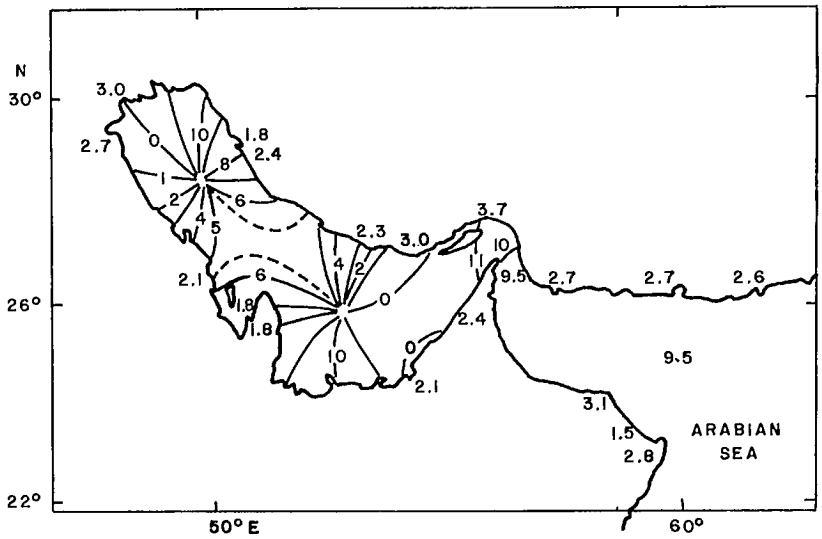

FIG. 5.32. Phase (lunar hours) and amplitude (centimetres) of the spring tides in the Persian Gulf derived from observations. (Defant 1961)

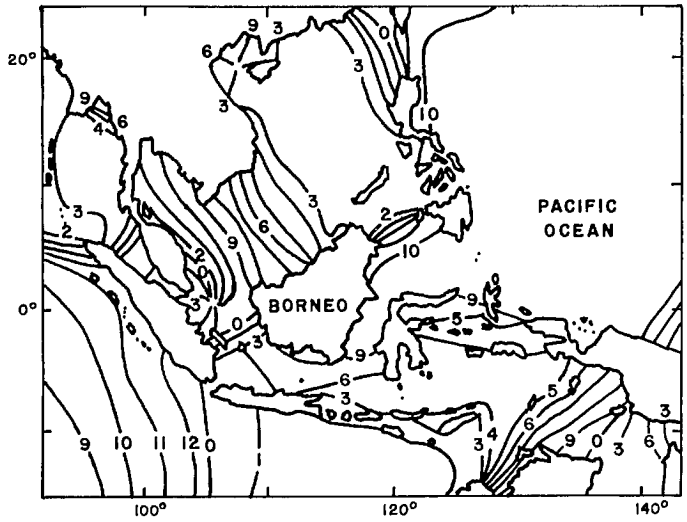

FIG. 5.33. Cotidal lines of M_2 in the Indonesian Archipelago (with reference to the upper culmination of the moon in Greenwich). (Defant 1961)

1) For the case of a progressive wave in an estuary of uniform width, friction has no influence on the times of high and low waters. The shallow-water term makes the high water occur earlier and the low water occur later than otherwise. Also, for a given meteorological situation, the height of the surge in the estuary whose maximum occurs near the time of tidal low water tends to be greater than the surge height whose maximum occurs nearer the time of tidal high water.

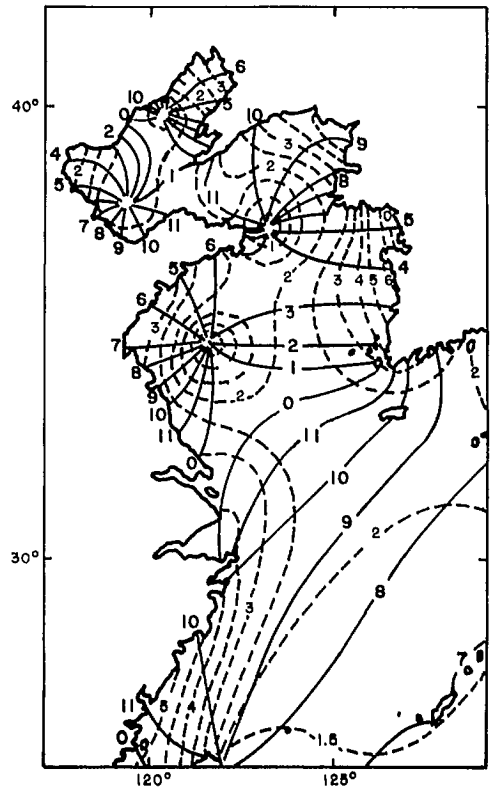

FIG. 5.34. Cotidal lines of M_2 and range of the semi-diurnal tide in the East China Sea. Phases are with reference to 135°E; corange $2(M_2 + S_2)$ in metres. (Defant 1961)

2) For a progressive wave in an estuary of variable width, the contraction of the estuary influences the shallow-water term and the friction term. However, the direct effect of the variable width is to make high waters higher and low waters lower than they would be in an estuary of uniform cross-section. The friction term makes high water lower and low water higher whereas the shallow-water term makes high water occur earlier and low water occur later than otherwise.

3) For the case of a standing wave in an estuary of uniform cross-section, both the friction and the shallow-water terms make the time of high water occur later than otherwise. Regarding the amplitude of the surge, friction could either increase it or decrease it depending on the nature of the variation of the surge with time. For example, if the surge curve rises to its maximum value at a greater rate than it decreases from the maximum, the friction term will tend to decrease the surge height.

It should be noted that these above results apply only for a short distance down the length of the estuary, the distance being measured from the junction of the estuary with the open sea. Also, the analysis applies only for small values of tide and surge amplitudes. In his second paper, Proudman (1955b) ignored the nonlinear inertial (i.e. convective) terms but removed the restriction on the distance from the open sea and also on the amplitudes of the tide and surge. The important results from this paper are the following.

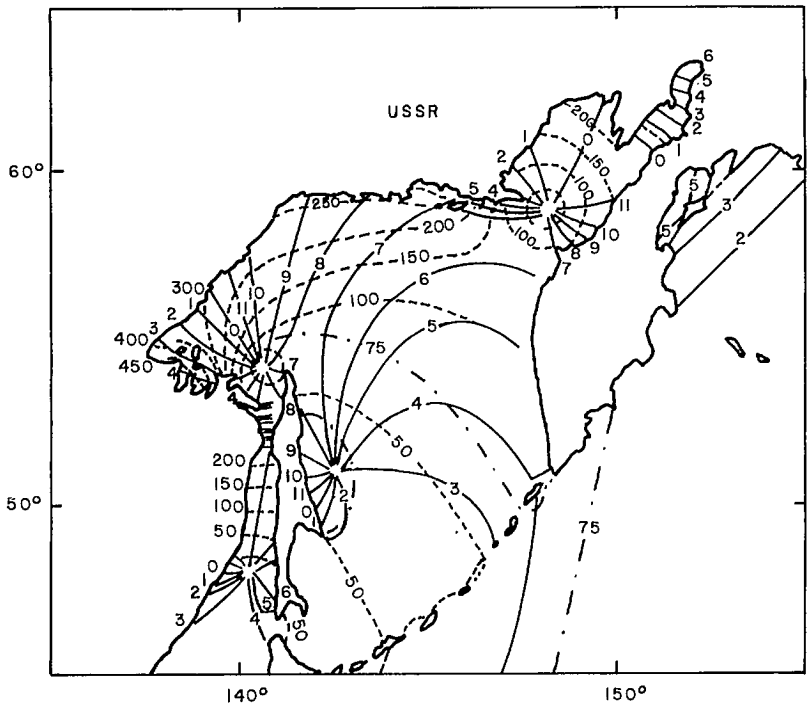

FIG. 5.35. Cotidal lines of M_2 and range $2(M_2 + S_2)$ in metres for the Sea of Okhotsk. Phases are with reference to 135°E. (Defant 1961)

For a progressive wave, the surge amplitude is greater at the time of low water than at the time of high water, and this is attributed to the friction term. In his third paper, Proudman (1957) showed that for the case of a standing wave, the shallow-water term will make the surge height greater at the time of tidal high water.

The mathematical development, following Proudman 1955b, leading to the result that for the case of a progressive wave, friction makes the surge height greater at the time of tidal low water than at the time of tidal high water will be considered. For a one-dimensional system, the equations of motion and continuity are

$$(5.162) \quad \frac{\partial u}{\partial t} = -g\frac{\partial \zeta}{\partial x} - \frac{K}{h}|u|u$$

$$(5.163) \quad \frac{\partial}{\partial x}(Au) + b\frac{\partial \zeta}{\partial t} = 0$$

where u is the current averaged over a cross-section in the x direction, t is time, g is gravity, ζ is the deviation of the water level from the average level, K is a friction coefficient (0.0025), A is the area of vertical cross-section up to the level of the average water height, and b is the estuary width at the level where A is considered, and

$$(5.164) \quad h = \frac{A}{b}$$

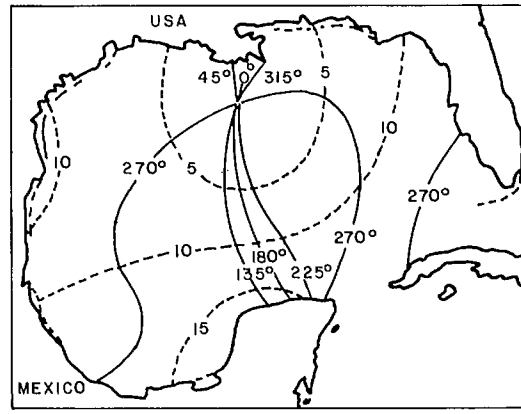

FIG. 5.36. Cotidal lines and amplitudes of the M_2 tide in the Gulf of Mexico. (Defant 1961)

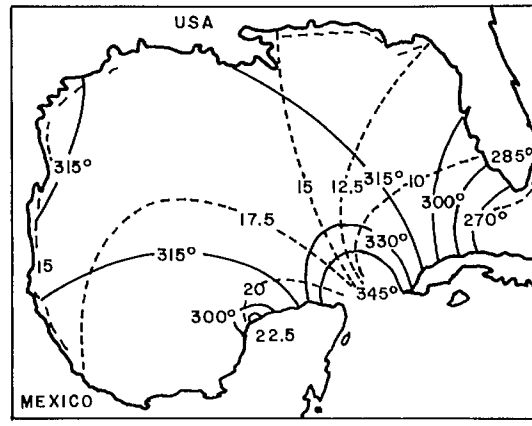

FIG. 5.37. Cotidal lines and amplitudes of the K_1 tide in the Gulf of Mexico. Solid lines are phases with reference to 89.9°W; broken lines are amplitudes (centimetres). (Defant 1961)

Define

$$c \equiv \sqrt{gh} \tag{5.165}$$

Assume that the tide and the surge are generated in the open ocean and travel into the estuary. Let $x = 0$ be the mouth of the estuary and let $F(t)$ be the form of ζ at $x = 0$. Define a contraction coefficient P and a friction function q:

$$P \equiv \sqrt{\frac{b_0 c_0}{bc}}$$

$$q \equiv \frac{K}{4bh^2P}\frac{u}{|u|} \tag{5.166}$$

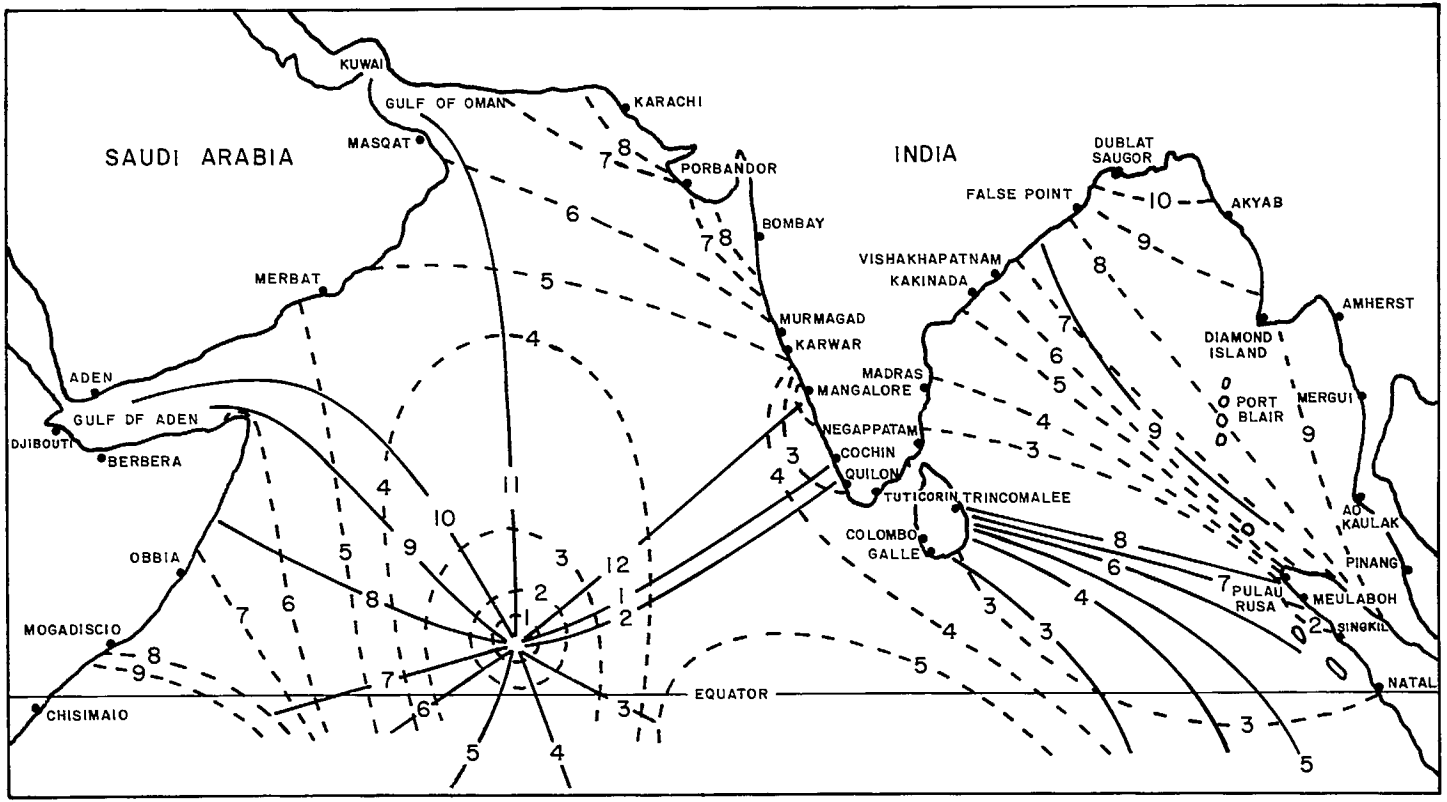

FIG. 5.38. Cotidal and corange lines for the constituent K_2. Numbers on solid lines are the time (hours) of high water that are half of the period, the time origin being the standard meridian. Numbers on broken lines are the amplitudes (centimetres). (Fairbairn 1954)

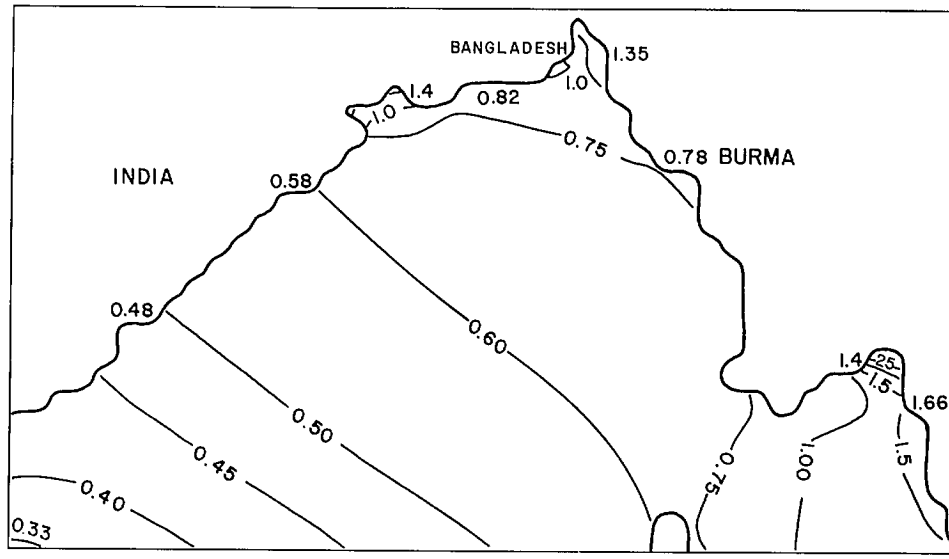

FIG. 5.39. M_2 tidal amplitudes (metres) in the northern part of the Bay of Bengal.

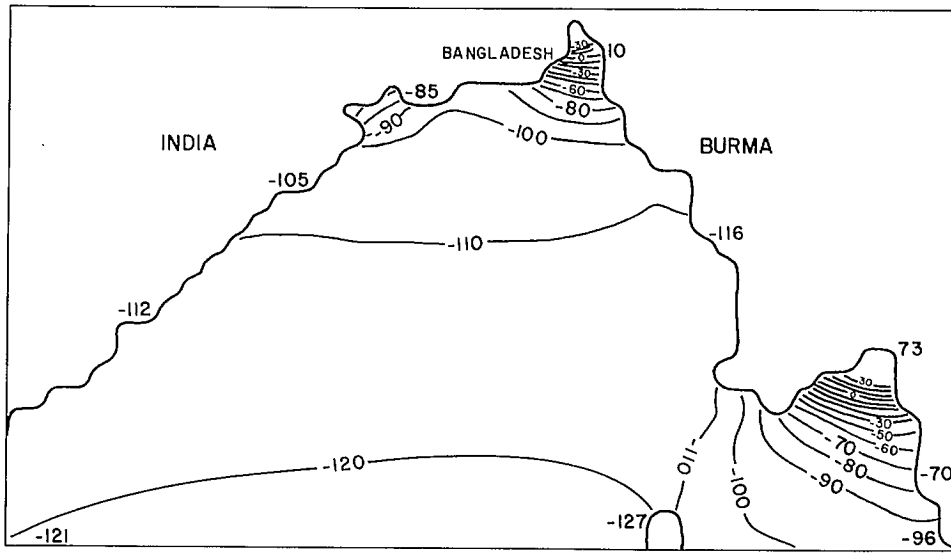

FIG. 5.40. M_2 phases (degrees) in the northern part of the Bay of Bengal.

Also define

$$V \equiv PAu$$

$$\theta \equiv \int_0^x \frac{dx'}{c(x')} \tag{5.167}$$

$$\frac{1}{H} \equiv \frac{K}{2} \int_0^x \frac{P}{h^2}\, dx'$$

where prime denotes variables of integration. Note that for an estuary of uniform cross-section, h is uniform and $P = 1$; then

$$H = \frac{2k^2}{Kx}$$

and this situation is considered in Proudman (1955a). For convenience, also define

$$\begin{aligned} \xi &\equiv \theta + t \\ \eta &\equiv \theta - t \end{aligned} \tag{5.168}$$

Proudman restricted his study by making the following assumptions: (1) $d^2P/d\theta^2$ is negligible; (2) only those distributions of the current are permitted, in which there is entirely either flood or ebb but not a combination of both between the estuary mouth and the cross-section under consideration. From eq. 5.166:

$$q = \pm \frac{K}{4bh^2P} \tag{5.169}$$

the positive sign being used for the flood and the negative sign for the ebb.

Use of eq. 5.166 and 5.167 transforms eq. 5.162 and 5.163 to

$$\frac{\partial}{\partial\theta}(Au) + \frac{b_0c_0}{P^2}\frac{\partial\zeta}{\partial t} = 0 \tag{5.170}$$

and

$$\frac{\partial}{\partial t}(Au) + \frac{b_0c_0}{P^2}\frac{\partial\zeta}{\partial\theta} = -Kb|u|u \tag{5.171}$$

Eliminate ζ in eq. 5.170 and 5.171, use eq. 5.166, ignore $\partial^2P/\partial\theta^2$, and use eq. 5.168 to give

$$\frac{\partial^2V}{\partial\xi\partial\eta} = q\left(\frac{\partial}{\partial\xi} - \frac{\partial}{\partial\eta}\right)V^2 \tag{5.172}$$

For small values of η, the solution of eq. 5.172 can be written as

$$V = \phi(\xi + \eta, \eta) + \int_0^\eta \psi(\xi + \eta, \eta')\, d\eta' \tag{5.173}$$

After neglecting some integrals, which are small, eq. 5.172 can be written as

$$\frac{\partial^2\phi}{\partial\xi^2} + \frac{\partial^2\phi}{\partial\xi\partial\eta} + \frac{\partial\psi}{\partial\xi} + q\frac{\partial^2\phi^2}{\partial\eta^2} + 2q\phi\psi = 0 \tag{5.174}$$

Proudman represented eq. 5.174 in two parts as

$$\frac{\partial^2\phi}{\partial\xi\partial\eta} + \frac{\partial}{\partial\eta}(q\phi^2) = 0 \tag{5.175}$$

and

$$\frac{\partial^2\phi}{\partial\xi^2} + \frac{\partial\psi}{\partial\xi} - \frac{\partial q}{\partial\xi}\phi^2 + 2q\phi\psi = 0 \tag{5.176}$$

After some algebra, the expression for the water level ζ can be written as

$$(5.177)\quad \frac{b_0 c_0 \zeta}{P} = \phi + \int_0^{\eta} \left(\psi - 2q\phi^2 - \frac{1}{P}\frac{dP}{d\theta}\phi\right) d\eta'$$

For the case of a progressive wave, at the estuary mouth ($x = 0$):

$$\theta = 0,\ \xi + \eta = 0,\ P = 1$$

and

$$\phi = U,\ \psi = U^2(Y + 2q)$$

where U and Y are defined through

$$(5.178)\quad -\frac{1}{\phi} + \int_{-\eta}^{\xi} q\, d\xi' = -\frac{1}{U(\eta)}$$

and

$$(5.179)\quad Y = 2\int_{-\eta}^{\xi} q^2\phi\, d\xi' - 2q + \frac{\psi}{\phi^2}$$

From

$$(5.180)\quad b_0 c_0 \zeta = U + \int_0^{\eta} \left[YU^2 - \left(\frac{dP}{d\theta}\right)_0 U\right] d\eta'$$

Assuming the following forms:

$$(5.181)\quad Y = \left(\frac{dP}{d\theta}\right)_0 \frac{1}{U}$$

$$U = b_0 c_0 F(\eta)$$

and $\zeta = F(-t)$ at the mouth of the estuary gives

$$(5.182)\quad \phi = \frac{U}{1 + 2U\int_0^{\theta} q\, d\theta'}$$

from

$$(5.183)\quad \frac{b_0 c_0}{P}\zeta = \phi + \int_0^{\eta} \left\{\phi^2\left[\left(\frac{dP}{d\theta}\right)_0 \frac{1}{U} - 4\int_0^{\theta} q^2\phi\, d\theta'\right] - \frac{1}{P}\frac{dP}{d\theta}\phi\right\} d\eta'$$

Finally, from eq. 5.167, 5.181, 5.182, and 5.183:

$$(5.184)\quad \frac{\zeta}{P} = \frac{F}{\left(1 \pm \frac{F}{H}\right)} + \int_0^{\eta} \left\{\frac{1}{\left(1 \pm \frac{F}{H}\right)^2}\left[\left(c\frac{dP}{dx}\right)_0 F - \frac{1}{4}K^2F^3\int_0^{x} \frac{cP^2 dx'}{h^4\left(1 \pm \frac{F}{H}\right)}\right]\right.$$

$$\left. - \frac{c}{P}\frac{dP}{dx}\frac{F}{\left(1 \pm \frac{F}{H}\right)}\right\} d\eta'$$

Next, following Proudman, the origin of time is chosen so that high water occurs at the cross-section at x for $t = \theta$ (i.e. $\eta = 0$). Since for a flood current the positive sign in eq. 5.184 must be taken, the height of the high water is given by

$$(5.185) \quad \frac{PF(0)}{\left[1 + \frac{F(0)}{H}\right]}$$

Denoting by $T(-t)$ and $S(-t)$ the tide and surge heights at the estuary mouth and writing

$$F(\eta) = T(\eta) + S(\eta)$$

and using eq. 5.185, the height of the high water is given by

$$(5.186) \quad \frac{PT(0) + PS(0)}{1 + \left[\frac{T(0) + S(0)}{H}\right]}$$

The predicted astronomical tide at the same location and time is given by

$$(5.187) \quad \frac{PT(0)}{\left[1 + \frac{T(0)}{H}\right]}$$

For the same h, the height of the surge at the time of high water is given by eq. 5.186 and 5.187 and is

$$(5.188) \quad \frac{PS(0)}{\left[1 + \frac{T(0)}{H}\right]\left[1 + \frac{T(0) + S(0)}{H}\right]}$$

Note that, provided $T(0)$ and $S(0)$ are positive, then for a given $S(0)$, the surge height given by eq. 5.188 decreases as $T(0)$ increases.

Next, the low water situation will be considered. For this write

$$F(\eta) = -T(\eta) + S(\eta)$$

and assume that low water occurs at the cross-section x for $t = 0$.

For an ebb current between the estuary mouth and the cross-section at x, the height of the low water is given by

$$(5.189) \quad \frac{-P'T(0) + P'S(0)}{1 - \left[\frac{-T(0) + S(0)}{H'}\right]}$$

where P' and H' denote the values of P and H at low water. The predicted tide at the same location and time is

$$(5.190) \quad \frac{-P'T(0)}{1 + \frac{T(0)}{H'}}$$

Then the surge height at low water is given by

$$(5.191)\quad \frac{P'S(0)}{\left[1+\frac{T(0)}{H'}\right]\left[1+\frac{T(0)-S(0)}{H'}\right]}$$

Since a lowering of the water level increases the degree of contraction of the estuary, then $P' > P$. Thus, for a given $T(0)$ and $S(0)$ the surge height at low water (given by eq. 5.191) will be greater than the surge height at high water (given by eq. 5.188) provided

$$P'\left\{1+\frac{T(0)}{H}\right\}\left\{1+\frac{[T(0)+S(0)]}{H}\right\} > P\left\{1+\frac{T(0)}{H'}\right\}\left\{1+\frac{[T(0)-S(0)]}{H'}\right\}$$

In other words, the surge height at low water will be greater than the surge height at high water provided the following condition is satisfied:

$$(5.192)\quad \frac{S(0)}{T(0)} > \frac{2\left(\frac{P}{H'}-\frac{P'}{H}\right)+T(0)\left(\frac{P}{H'^2}-\frac{P'}{H^2}\right)}{\left(\frac{P}{H'}+\frac{P'}{H}\right)+T}$$

Proudman (1957) considered a standing wave, as opposed to a progressive wave in his two earlier papers (1955a, 1955b), and showed that for a short estuary (for the definition of a short estuary see eq. 7.1 and 7.2) the amplitude of the surge is lower at tidal high water. Thus, the result for the standing wave case is exactly opposite to that for the progressive wave case. The result in the standing wave case is attributed to the shallow-water terms whereas the opposite result in the progressive wave case is accounted for by the friction terms.

Proudman (1958) considered an idealized situation of an infinitely long estuary of uniform cross-section when a permanent current independent of the tide and surge is present. In this analysis, friction was ignored. Proudman pointed out that his results are similar to those of McCowan (1894). The important result is that the heights of high and low water at any place up the estuary are the same as at the mouth and that a bore will always form. The exact location of formation of the bore depends on the amplitude and form of the oscillation at the estuary mouth.

Wolf (1978) extended Proudman's work by considering two-plane progressive waves traveling together in a semi-infinite channel of uniform cross-section. She evaluated the influence of the various nonlinear terms. The nature of this work is similar to that of Proudman in the sense that these are one-dimensional models and the influence of the earth's rotation is ignored.

Wolf (1978) wrote the one-dimensional nonlinear equations of motion and continuity as

$$(5.193)\quad \frac{\partial u}{\partial t}+u\frac{\partial u}{\partial x}+g\frac{\partial \zeta}{\partial x}+\frac{K|u|u}{h}=0$$

and

$$(5.194)\quad \frac{\partial \zeta}{\partial t}+h\frac{\partial u}{\partial x}+\frac{\partial}{\partial x}(\zeta u)=0$$

where u denotes the velocity in the x direction, h is the water depth, ζ is the water level,

and K is a friction coefficient. Let the solutions for ζ and u for the first-order part of these equations be denoted by subscript 1 and for the second-order part by subscript 2.

Let $c = \sqrt{gh}$ be the phase speed of the wave and let F be an arbitrary function of $t - x/c$. Then the first-order solution can be written as

$$\frac{\zeta_1}{h} = F\left(t - \frac{x}{c}\right) = \frac{u_1}{c} \tag{5.195}$$

Writing

$$\begin{aligned} \zeta &= \zeta_1 + \zeta_2 \\ u &= u_1 + u_2 \end{aligned} \tag{5.196}$$

and substituting eq. 5.196 into 5.193 and 5.194 gives

$$\frac{\partial^2 u_2}{\partial t^2} - c^2 \frac{\partial^2 u_2}{\partial x^2} = g \frac{\partial^2}{\partial x^2}(\zeta_1 u_1) - \frac{\partial^2}{2\partial x \partial t}(u_1^2) - \frac{K}{h} \frac{\partial}{\partial t}(|u_1|u_1|) \tag{5.197}$$

and

$$h \frac{\partial u_2}{\partial x} + \frac{\partial \zeta_2}{\partial t} = -\frac{\partial}{\partial x}(\zeta_1 u_1) \tag{5.198}$$

Using eq. 5.195, eq. 5.197 and 5.198 must be solved for u_2 and ζ_2 using the following boundary conditions:

$$\left.\begin{aligned} u_2 &= 0 \\ \zeta_2 &= 0 \end{aligned}\right\} \text{ at } x = 0 \text{ for all } t \tag{5.199}$$

By these conditions, the possibility of nonlinear effects at the channel mouth is suppressed. The initial condition is

$$\zeta_2 = 0 \text{ at } t = 0 \text{ for all } x \tag{5.200}$$

i.e. initially everywhere there is no nonlinear part in the water level.

For convenience, Wolf (1978) made the same transformation as per Proudman (1957):

$$\begin{aligned} \xi &\equiv t + \frac{x}{c} \\ \eta &\equiv t - \frac{x}{c} \end{aligned} \tag{5.201}$$

or

$$\begin{aligned} x &= c\left(\frac{\xi - \eta}{2}\right) \\ t &= \left(\frac{\xi + \eta}{2}\right) \end{aligned} \tag{5.202}$$

The solution of eq. 5.197 can be shown to be, after some algebra,

$$(5.203)\quad \frac{u_2}{c} = \frac{3x}{4c}\left[F^2\left(t-\frac{x}{c}\right)\right] - \frac{F^2}{8}\left(t-\frac{x}{c}\right) + \frac{F^2}{8}\left(t+\frac{x}{c}\right) - \frac{kx}{2h}\left|F\left(t-\frac{x}{c}\right)\right| \times F\left(t-\frac{x}{c}\right) + \frac{Kc}{4h}\int_{t-x}^{t+x}|F(\theta)|F(\theta)d\theta$$

where θ is a variable for integration. The solution of eq. 5.198 is

$$(5.204)\quad \frac{\zeta_2}{h} = \frac{F^2}{8}\left(t-\frac{x}{c}\right) - \frac{F^2}{8}\left(t+\frac{x}{c}\right) + \frac{3x}{4c}\left[F^2\left(t-\frac{x}{c}\right)\right]' - \frac{Kx}{2h}\left|F\left(t-\frac{x}{c}\right)\right|F\left(t-\frac{x}{c}\right) - \frac{F^2}{8}\left(-\frac{x}{c}\right) + \frac{F^2}{8}\left(\frac{x}{c}\right) - \frac{3x}{4c}\left[F^2\left(-\frac{x}{c}\right)\right] + \frac{Kx}{2h}\left|F\left(-\frac{x}{c}\right)\right|F\left(-\frac{x}{c}\right) + \frac{Kc}{4h}\int_{-x/c}^{x/c}|F(\theta)|F(\theta)d\theta - \frac{Kc}{4h}\int_{t-x/c}^{t+x/c}|F(\theta)|F(\theta)d\theta$$

where prime denotes differentiation with respect to ξ.

Since u_1 and ζ_1 are known from eq. 5.195 and from eq. 5.203 and 5. 204, the total solutions can be written as

$$(5.205)\quad \frac{u}{c} = F\left(t-\frac{x}{c}\right) + \frac{3x}{4c}\left[F^2\left(t-\frac{x}{c}\right)\right]' - \frac{F^2}{8}\left(t-\frac{x}{c}\right) + \frac{F^2}{8}\left(t+\frac{x}{c}\right) - \frac{Kx}{2h}\left|F\left(t-\frac{x}{c}\right)\right|F\left(t-\frac{x}{c}\right) + \frac{Kc}{4h}\int_{t-x/c}^{t+x/c}|F(\theta)|F(\theta)d\theta$$

and

$$(5.206)\quad \frac{\zeta}{h} = F\left(t-\frac{x}{c}\right) + \frac{F^2}{8}\left(t-\frac{x}{c}\right) - \frac{F^2}{8}\left(t+\frac{x}{c}\right) + \frac{3x}{4c}\left[F^2\left(t-\frac{x}{c}\right)\right]' - \frac{Kx}{2h}\left|F\left(t-\frac{x}{c}\right)\right|F\left(t-\frac{x}{c}\right) - \frac{F^2}{8}\left(-\frac{x}{c}\right) + \frac{F^2}{8}\left(\frac{x}{c}\right) - \frac{3x}{4c}\left[F^2\left(-\frac{x}{c}\right)\right]' + \frac{Kx}{2h}\left|F\left(-\frac{x}{c}\right)\right|F\left(-\frac{x}{c}\right) + \frac{Kc}{4h}\int_{-x/c}^{x/c}|F(\theta)|F(\theta)d\theta - \frac{Kc}{4h}\int_{t-x/c}^{t+x/c}|F(\theta)|F(\theta)d\theta$$

The second-order solutions were given by eq. 5.203 and 5.204. Next, the contributions from the quadratic friction term $K|u|u/h$, the convective term $\partial u/\partial x$, and the shallow-water term $\partial/\partial x(\zeta u)$ will be determined separately solving the following second-order equations (but using the same boundary and initial conditions as above):

$$(5.207)\quad \frac{\partial^2 u_2}{\partial t^2} - c^2\frac{\partial^2 u_2}{\partial x^2} = -\frac{K}{h}\frac{\partial}{\partial t}(|u_1|u)$$

and

$$(5.208)\quad h\frac{\partial u_2}{\partial x}+\frac{\partial \zeta_2}{\partial t}=0$$

The solution for the set of eq. 5.207 and 5.208 is

$$(5.209)\quad \left(\frac{\zeta_2}{h}\right)_{\substack{\text{quadratic}\\ \text{friction}}}=\frac{Kc}{4h}\int_{-x/c}^{x/c}|F(\theta)|F(\theta)d\theta-\frac{Kc}{4h}\int_{t-x/c}^{t+x/c}|F(\theta)|F(\theta)d\theta$$
$$+\frac{Kx}{2h}\left|F\left(-\frac{x}{c}\right)\right|F\left(-\frac{x}{c}\right)-\frac{Kx}{2h}\left|F\left(t-\frac{x}{c}\right)\right|F\left(t-\frac{x}{c}\right)$$

Next, solve the following set:

$$(5.210)\quad \frac{\partial^2 u_2}{\partial t^2}-c^2\frac{\partial^2 u_2}{\partial x^2}=-\frac{1}{2}\frac{\partial^2}{\partial x\partial t}(u_1^2)-\frac{K}{h}\frac{\partial}{\partial t}(|u_1|u)$$

and

$$(5.211)\quad h\frac{\partial u_2}{\partial x}+\frac{\partial \zeta_2}{\partial t}=0$$

This results in

$$(5.212)\quad \frac{\zeta_2}{h}=-\frac{F^2}{8}\left(t-\frac{x}{c}\right)-\frac{F^2}{8}\left(t+\frac{x}{c}\right)+\frac{F^2}{8}\left(-\frac{x}{c}\right)-\frac{F^2}{8}\left(\frac{x}{c}\right)$$
$$+\frac{x}{4c}\left[F^2\left(t-\frac{x}{c}\right)\right]'-\frac{x}{4c}\left[F^2\left(-\frac{x}{c}\right)\right]'-\frac{Kx}{2h}\left|F\left(t-\frac{x}{c}\right)\right|F\left(t-\frac{x}{c}\right)$$
$$+\frac{Kx}{2h}\left|F\left(-\frac{x}{c}\right)\right|F\left(-\frac{x}{c}\right)+\frac{Kc}{4h}\int_{-x/c}^{x/c}|F(\theta)|F(\theta)d\theta$$
$$-\frac{Kc}{4h}\int_{t-x/c}^{t+x/c}|F(\theta)|F(\theta)d\theta$$

Note that eq. 5.209 gives the contribution from the quadratic friction term to the second-order solution. To obtain the contribution from the convective term, the difference between eq. 5.212 and 5.209 must be taken, which gives

$$(5.213)\quad \left(\frac{\zeta_2}{h}\right)_{\text{convective}}=-\frac{F^2}{8}\left(t-\frac{x}{c}\right)+\frac{F^2}{8}\left(t+\frac{x}{c}\right)+\frac{x}{4c}\left[F^2\left(t-\frac{x}{c}\right)\right]'$$
$$+\frac{F^2}{8}\left(-\frac{x}{c}\right)-\frac{F^2}{8}\left(\frac{x}{c}\right)-\frac{x}{4c}\left[F^2\left(-\frac{x}{c}\right)\right]'$$

The contribution from the shallow-water term is the difference between eq. 5.204 and 5.212, which becomes

$$(5.214)\quad \left(\frac{\zeta_2}{h}\right)_{\substack{\text{shallow}\\ \text{water}}}=\frac{F^2}{4}\left(t-\frac{x}{c}\right)-\frac{F^2}{4}\left(t+\frac{x}{c}\right)+\frac{F^2}{4}\left(\frac{x}{c}\right)-\frac{F^2}{4}\left(-\frac{x}{c}\right)$$
$$+\frac{x}{2c}\left[F^2\left(t-\frac{x}{c}\right)\right]'-\frac{x}{2c}\left[F^2\left(-\frac{x}{c}\right)\right]'$$

Next, consider the interaction between the surge and the tide. Let $S(t-x/c)$ denote the first-order surge, $T(t-x/c)$ the first-order tide, and ζ_{T+S} the total water level at time t and at distance x from the open end of the channel. Substituting

$$(5.215)\quad F\left(t-\frac{x}{c}\right)=S\left(t-\frac{x}{c}\right)+T\left(t-\frac{x}{c}\right)$$

into eq. 5.206 gives an expression for ζ_{T+S}. The solution ζ_T for the tide alone can be obtained by setting $F(t-x/c)=T(t-x/c)$ in eq. 5.206. The residual water level ζ_R is then given by

$$(5.216)\quad \zeta_R=\zeta_{T+S}-\zeta_T$$

The same procedure can be used to derive separately the influence of the quadratic friction term, the shallow-water term, and the convective term.

The interaction between tide and surge, denoted by ζ_I, is given by

$$(5.217)\quad \zeta_I=\zeta_R-\zeta_S=\zeta_{T+S}-\zeta_T-\zeta_S$$

noting that ζ_S can be determined from eq. 5.206 by setting $F(t-x/c)=S(t-x/c)$. The reader is referred to Wolf (1978) for details of the expression for ζ_I. These expressions were used by Wolf to study the interaction between tide and surge on the east coast of the United Kingdom. This will be discussed in Chapter 6 when the North Sea surges are considered. However, some important results of general interest will be stated here: the shallow-water and convective terms are responsible for an increase in residuals on rising tide whereas the quadratic friction causes a decrease in residuals on high tide.

Wolf defined two different measures for the degree of interaction. The first one is called the mean absolute interaction or real interaction, which is defined as the mean of all values of the absolute difference between each residual and the corresponding surge obtained when the tide is absent (given by ζ_I). The second measure is termed the observed interaction, and this can be applied to observations when ζ_I is not available. The observed interaction is defined as the standard deviation of the mean absolute residual height at each tidal phase with respect to tidal phase.

Computations were made for the magnitude of both types of interactions for a channel of depth $h=40$ m, a tidal amplitude $A_T=1.0$ m, and surge amplitudes $A_S=0.4$, 0.6, 0.8, and 1.0 m. It was found that the contributions from the convective term and the shallow-water term to both the real and observed interactions are about the same whereas the contribution from the quadratic friction is about twice in the real interaction than in the observed interaction. This difference in behavior could probably be attributed to the fact that whereas the shallow-water and convective terms tend to redistribute the energy with respect to tidal phase, the quadratic friction term actually removes energy from the surge.

Among the three terms, the largest contribution comes from the quadratic friction term. Roughly, it can be said that the contribution from the convective term is about 14%, the contribution from the shallow-water term is about 29%, and the remaining contribution is from the quadratic friction term. The magnitude of the interaction appears to increase with increasing surge amplitude as well as with increasing distance from the mouth of the estuary.

Empirical Methods

Rossiter (1959a) presented a method for extracting storm surges from tidal records. This method was developed in the precomputer days when tide-predicting machines were in use. Hence, Rossiter's method is of historical interest only. Earlier, the work of Proudman (1955a, 1955b, 1957, 1958) was considered in which he developed analytical theories to study the interaction between tide and surge in the North Sea and Thames

TABLE 5.11. Number of occasions when surge heights at Southend exceeded given values for four states of tide: high water (H), low water (L), rising tide (R), falling tide (F). (Rossiter 1961)

State of tide	Surge height (m)														
	0.0	0.15	0.30	0.46	0.61	0.76	0.91	1.07	1.22	1.37	1.52	1.68	1.83	1.98	2.13
								Positive surges							
H	633	368	186	91	44	23	15	5	2	2	1	1	1		
F	594	339	168	66	36	22	11	5							
L	539	306	161	90	55	31	15	9	2	2	1				
R	579	378	255	156	94	58	39	17	10	7	1				
								Negative surges							
H	425	230	113	62	38	23	15	10	6	3	3	2	1	1	
F	464	233	131	77	41	18	12	7	5						
L	519	274	129	72	30	20	8	3	1						
R	479	301	172	99	60	39	23	17	12	6	4	1	1	1	1
								All surges							
H	1058	598	299	153	82	46	30	15	8	5	4	3	2	1	
F	1058	572	299	143	79	40	23	12	5						
L	1058	580	290	162	85	51	23	12	3	2	1				
R	1058	679	427	255	154	97	62	34	22	13	5	1	1	1	1

TABLE 5.12. Number of occasions when surge heights exceeded given values for four states of tide: high water (H), low water (L), half-tide rising (R), and falling (F). (Keers 1968)

State of tide	Surge height (m)													
	0.0	0.15	0.30	0.46	0.61	0.76	0.91	1.07	1.22	1.37	1.52	1.68	1.83	1.98
							Aberdeen							
H	301	177	80	21	4									
F	296	166	79	27	5	2								
L	303	196	98	35	7	3								
R	296	181	102	38	11	2	1							
							Tyne							
H	343	237	105	48	15	2								
F	328	234	130	61	26	6	2							
L	349	254	136	54	16	8	3	1						
R	341	237	154	82	34	12	4	1						
							Immingham							
H	291	209	116	62	26	11	3	1						
F	267	160	93	51	23	10	3	1						
L	309	224	149	92	37	14	11	5	3					
R	310	252	182	125	69	34	18	8	2					
							Lowestoft							
H	379	289	221	137	82	37	13	7	2	2	1			
F	374	298	212	148	104	47	18	10	4	2	1			
L	366	296	230	152	93	50	19	11	7	4	1	1		
R	373	298	234	172	104	59	27	14	8	4	1			
							Harwich							
H	300	227	137	79	40	14	8	4						
F	278	195	121	85	40	17	10	6	3					
L	295	240	181	115	67	35	21	12	4	3	2	1		
R	290	240	199	142	88	49	26	13	7	3	2	2	1	
							Southend							
H	321	214	113	56	26	11	5	1						
F	280	183	115	70	41	24	11	5						
L	325	251	175	106	50	31	16	12	6	3	2	1	1	
R	309	264	212	169	124	86	52	29	15	8	6	5	4	2

Estuary. However, it was Rossiter (1959b, 1961) who looked specifically at this problem using real data, and he attributed the interaction to the fact that the surge changes the phase of the tide and vice versa. For this to be possible the tide must have the nature of a progressive wave, which according to Rossiter is the situation in the Thames Estuary.

Discussion will begin with the 1961 paper of Rossiter. Attention was given to this interaction problem because positive surges at the time of high water in the region of Lowestoft and Harwich and propagating southwards with the tide seldom were as great as was originally expected. Earlier, Doodson (1956) attempted to explain the interaction, treating the tide as a continuous oscillation with a period of 12 h and the surge as a transient oscillation with a period of about 24 h. The geometry used by Doodson is rather simple: a uniform gulf of depth 128 ft (39 m) and length 105 mi (169 km). No appreciable interaction was noticed and this is attributed by Rossiter (1961) to the fact that Doodson

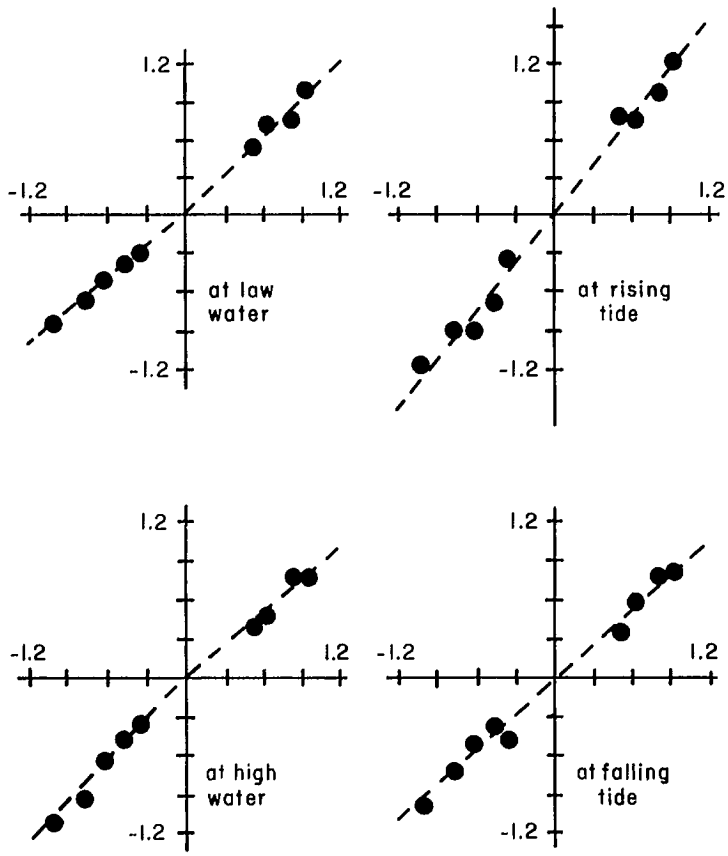

FIG. 5.41. Values of surge height (metres) at Southend, U.K. (ordinate), at four stages of tide relative to surge height averaged over the tidal cycle (abcissa). (Rossiter 1961)

used a mean depth that was too large.

Rossiter (1961) inferred the interaction in the observed data through the following technique. From the mouth of the Thames Estuary, Southend is located at about 7 mi (11.3 km) up the estuary and Richmond Lock (at the head of the tidal portion of the river) is at a distance of 68 mi (109.5 km). It is assumed that the water level at Southend is typical of the estuary. For the period 1928–38, the hourly surge heights for all significant surge episodes were tabulated (both positive and negative surges were considered). Each of these hourly surge heights was identified to be associated with one of the four stages of the tide: high water (H), low water (L), rising tide (R), and falling tide (F). The number of surge heights exceeding given values for these four states of the tide is listed in Table 5.11.

It can be seen from Table 5.12 that there is a tendency for the surges to be greatest on the rising tide and no particular preference among the other three stages. Doodson (1929) noted this earlier, although the data used by him were much less. Rossiter (1961) used the χ^2 test to prove that the result (i.e. tendency of surges to be greatest on the rising tide) is statistically significant. Next, Rossiter attempted to quantify this qualitative result by listing the surge height in units of a tidal cycle and grouping according to the mean

residual in each cycle. In Fig. 5.41 the mean residuals for each of the four states of tide are plotted on the ordinate and the mean residual for the complete tidal cycle is plotted on the abscissa. If one assumes linearity over the range considered, one can infer that the surges are about one quarter greater on the rising tide compared with the other three stages.

Before offering an explanation for the interaction, Rossiter (1961) disagreed with some of the earlier explanations by Doodson (1929). Doodson suggested that the interaction is typical of the North Sea and occurs at other locations also. But Rossiter (1961), after examining the residuals at Aberdeen, Tynemouth, Immingham, and Lowestoft, concluded that there is no significant interaction at any of these locations and the result noted at Southend is due to local effects. Doodson (1929) suggested a second possibility: water level gradients generated by wind are inversely proportional to the water depth. According to Tomezac (1952a, 1952b) this effect is indeed important in the estuaries in Germany. However, Rossiter ruled this out for the Thames Estuary and concluded that the interaction occurs while the surge and tide propagate together from the open sea into the estuary.

To verify the possibility of interaction while the tide and surge travel together, Rossiter (1961) used a one-dimensional numerical model following Hansen (1956) and Otter and Day (1960). These calculations showed that a positive surge can accelerate the propagation of the tide and a negative surge can retard the tide. Two simple reasons can be seen why a positive surge can accelerate the tide. First, since the speed of propagation of the tide is proportional to the square root of the water depth, on a positive surge the tide can travel faster. Second, since the bottom friction is inversely proportional to the water depth, on a positive surge there is less bottom friction and the tide can travel faster. Rossiter and Lennon (1965) suggested that a positive surge hastens the tide due to increased rate of travel and also due to decreased effect of bottom friction. These effects combine to produce a forward phase shift of the tide, which distorts the surge heights.

However, this may be too simple an explanation. Also, the above explanation assumes that the tide is a progressive wave. Rossiter (1961) argued that the earlier held opinion that the tide in the Thames is a standing wave is based on the assumption that the estuary has uniform cross-section. However, Otter and Day (1960) showed that an estuary of exponential cross-section would more likely give rise to a progressive wave.

The next paper of an empirical nature to be considered is that of Keers (1968) who considered the tide–surge interaction problem on the east coast of the United Kingdom and not just for the Thames Estuary. His main conclusion was that for locations under the influence of the same amphidromic system, the degree of interaction is highly correlated with the tidal range. But the correlation of the degree of interaction with surge height is considerably less.

The significance of the tide–surge interaction as they travel together southward along the east coast of the United Kingdom is shown in Fig. 5.42. Whereas there is reasonable correlation between the surge at Lowestoft and the northerly component of the geostrophic wind, the surge at Southend is dominated by nonlinear shallow-water effects. The main effect of the interaction is the frequent occurrence of large surge heights on rising tide and the fact that at the time of high water fewer large surge heights occur (Table 5.12). Note that for the case of no interaction there would be an equal number of surge heights at each of the four stages of the tide. Thus, the standard deviation of the differences from 25% for the four states of the tide is a measure of the interaction between the surge and the tide.

Keers studied the degree of interaction by considering the distribution of the 100 largest surge heights at each location (see Table 5.13). For these six locations, the average of these 100 surge heights, averaged over the four stages of the tide, is given in the third

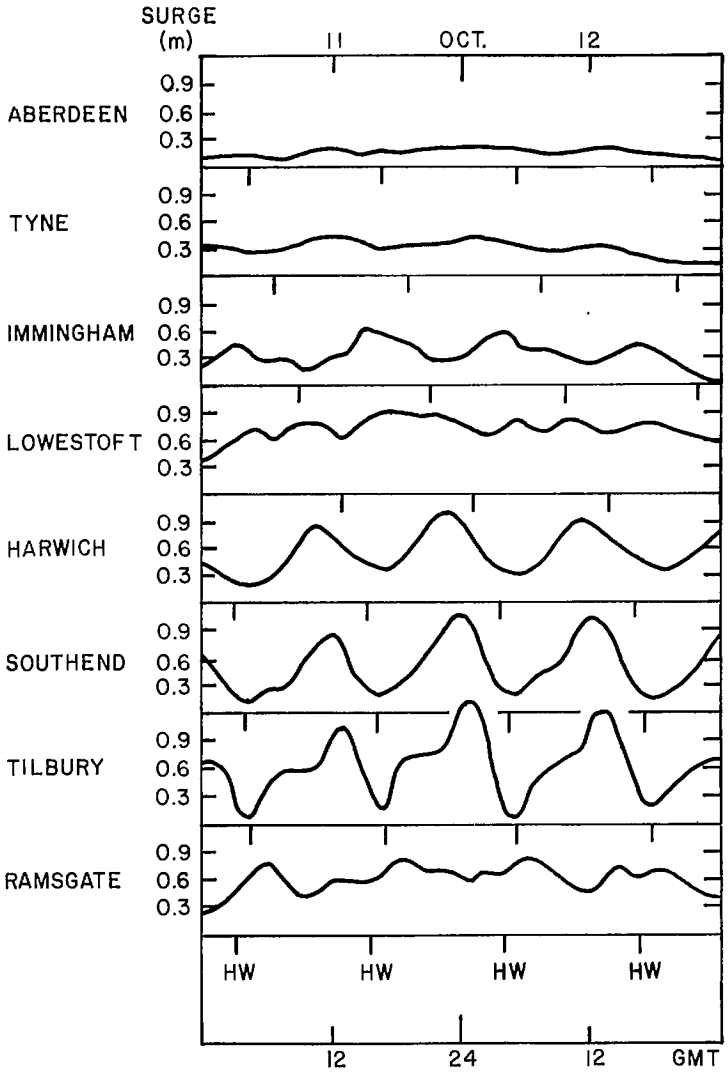

FIG. 5.42. Storm surges at eight locations in the United Kingdom during October 11–12, 1960. HW, time of high water. (Keers 1968)

column of Table 5.13. It can be seen that as the tide and surge propagate together, the interaction increases from Aberdeen to Immingham, with a marked discontinuity between Immingham and Lowestoft, followed by an even greater increase of interaction with distance traveled. These two distinct regimes of interaction are related to the two amphidromic systems in the North Sea. There is strong correlation between the degree of interaction and the mean range of the spring tide (the later quantity is listed in the second column of Table 5.13). The factors that determine the degree of interaction appear to be range of the tide, depth of the sea, bottom friction, surge height, coastline geometry, and the duration the tide and surge traveled together.

TABLE 5.13. Distribution of the 100 largest surge heights at six locations on the east coast of the United Kingdom. The numerals indicate the number of times the surge occurred at the time of rising, low, falling, or high tide. (Keers 1968)

Location	Tidal range (m)	Average surge height (m)	Rising tide	Low tide	Falling tide	High tide
Aberdeen	3.62	0.61	32	28	22	18
Tyne	4.30	0.73	38	18	28	16
Immingham	6.22	0.91	47	22	15	16
Lowestoft	1.95	1.13	33	26	23	18
Harwich	3.63	1.07	43	30	15	12
Southend	5.30	1.13	60	20	14	6

TABLE 5.14. Number of occasions when the negative surges exceeded given heights at Southend during the period 1928–38. (Rossiter 1971)

	Given height (m)				
Stage of tide	2.13	1.83	1.52	1.22	0.91
Rising	1	1	4	12	23
High		1	3	6	15
Falling				5	12
Low water				1	8

Keers (1968) used the following technique to examine quantitatively the interaction problem. Let $t = 0$ refer to the time of tidal high water and let η be the surge height at time t. Let η^* represent a hypothetical linear surge. Then

$$(5.218) \quad \eta(t) = \sum_{n=0}^{4} A_n(t)\eta^*(t - 3n) + \sum_{n=0}^{4} B_n(t, h)\eta^*(t - 3n)$$

Here, $A_n(t)$, $n = 0, 1, \ldots, 4$, are nondimensional constants for a given value of t and $B_n(t, h)$, $n = 0, 1, \ldots, 4$, are arbitrary functions of time and tidal height h.

Keers (1968) assumed that the degree of interaction at any given location is independent of the range of the tide. For Southend he also assumed that the hypothetical linear surge is given by the observed surge η_L at Lowestoft (however, there is a 3-h time duration for the tide and surge to travel between Lowestoft and Southend). Also, ignoring meteorological forcing, eq. 5.218 becomes

$$(5.219) \quad \eta(t) = \sum_{n=0}^{4} A_n(t)\eta_{L,t-3(n+1)} + c$$

where c is a constant. Using the method of least squares one can then find the nondimensional regression coefficients $A_n(t)$ in eq. 5.219 for any given time relative to the time of tidal high water at Southend. Keers (1968) pointed out that in contrast with the theoretical prediction by Proudman (1955a, 1955b), including the range of the tide at Southend on the right-hand side of eq. 5.219 made matters worse.

Heaps (1967) remarked that as long as the nonlinear terms in the equations of motion are retained, the interaction between tide and surge can be simulated with reasonable

accuracy. Rossiter (1971) briefly examined the interaction between tides and negative surges, which can be seen from Table 5.14, which lists the number of occasions when the negative surges at Southend exceeded prescribed amplitudes during the period 1928–38. Note that the characteristics of the surge–tide interaction are not necessarily the same for negative surges as for positive surges.

Numerical Models for the Tide–Surge Interaction

Banks (1974) appears to be among the first to use a two-dimensional numerical model to study tide–surge interaction in the North Sea. She showed that in the southern part of the North Sea, the major part of the interaction is between the M_2 tide and the surge. Prandle and Wolf (1978a) studied the interaction between tide and surge in the Thames Estuary through a one-dimensional model and used a so-called parallel model approach (i.e. to run a tidal model with surge interaction term and to run a surge model with tide interaction term). Here the parallel model approach for the two-dimensional case, as developed by Prandle and Wolf (1978), will be described.

In a right-handed Cartesian coordinate system, with x towards east and y towards north, the equations of motion and continuity in depth-averaged velocities u and v and free surface height η are

$$\frac{\partial U}{\partial t} + \frac{\partial}{\partial x}\left(\frac{U^2}{H}\right) + \frac{\partial}{\partial y}\left(\frac{UV}{H}\right) + gH\frac{\partial \eta}{\partial x} + Ku(u^2 + v^2)^{1/2} - fV = 0 \tag{5.220}$$

$$\frac{\partial V}{\partial t} + \frac{\partial}{\partial x}\left(\frac{UV}{H}\right) + \frac{\partial}{\partial y}\left(\frac{V^2}{H}\right) + gH\frac{\partial \eta}{\partial y} + Kv(u^2 + v^2)^{1/2} + fU = 0 \tag{5.221}$$

$$\frac{\partial \eta}{\partial t} + \frac{\partial U}{\partial x} + \frac{\partial V}{\partial y} = 0 \tag{5.222}$$

where

$$\begin{aligned} H &\equiv D + \eta \\ U &\equiv uH \\ V &\equiv vh \end{aligned} \tag{5.223}$$

Here, D is the water depth in the undisturbed state, U and V are the volume transport components, and K is a friction coefficient.

At this stage Prandle and Wolf made an assumption that could be satisfactory from a practical point for the southern North Sea; but nevertheless, theoretically the assumption is not satisfactory. They assumed that the interaction between tide and surge is contained only in the quadratic friction term and the contribution of the nonlinear convective terms to the interaction is insignificant.

The basic idea of the parallel model approach is that at every location and at every time step, the transports and surface elevation in the tidal model denoted respectively by U_T, V_T, and η_T and the corresponding parameters in the surge model, U_S, V_S, and η_S, satisfy the following relationships:

$$
\begin{aligned}
U_C &= U_T + U_S \\
V_C &= V_T + V_S \\
\eta_C &= \eta_T + \eta_S \\
u_C &= u_T + u_S \\
v_C &= v_T + v_S
\end{aligned} \tag{5.224}
$$

Here, subscript C denotes the values obtained from a model in which the tide and surge are combined.

Substitute eq. 5.224 into 5.220–5.222 to give

$$
\frac{\partial}{\partial t}(U_T + U_S) + (D + \eta_S + \eta_T)g\frac{\partial}{\partial x}(\eta_S + \eta_T) + K(u_S + u_T)[(u_S + u_T)^2 + (v_S + v_T)^2]^{1/2} - f(V_T + V_S) = 0 \tag{5.225}
$$

$$
\frac{\partial}{\partial t}(V_T + V_S) + (D + \eta_S + \eta_T)g\frac{\partial}{\partial y}(\eta_S + \eta_T) + K(v_S + v_T) \times [(u_S + u_T)^2 + (v_S + v_T)^2]^{1/2} + f(U_S + U_T) = 0 \tag{5.226}
$$

$$
\frac{\partial}{\partial t}(\eta_T + \eta_S) + \frac{\partial}{\partial x}(U_T + U_S) + \frac{\partial}{\partial y}(V_T + V_S) = 0 \tag{5.227}
$$

At open boundaries the water level elevation $\eta_0(t)$ must be prescribed. Thus, in the parallel models, the open boundary condition is

$$
\eta_{0,C} = \eta_{0,T} + \eta_{0,S} \tag{5.228}
$$

Another major assumption (no satisfactory justification) is that eq. 5.225, 5.226, and 5.227 can be separated into two parts as follows.

For the tide:

$$
\frac{\partial}{\partial t}U_T + (D + \underline{\eta_S} + \eta_T)g\frac{\partial}{\partial x}\eta_T + Ku_T[(\underline{u_S} + u_T)^2 + (\underline{v_S} + v_T)^2]^{1/2} - fV_T = 0 \tag{5.229}
$$

$$
\frac{\partial}{\partial t}V_T + (D + \underline{\eta_S} + \eta_T)g\frac{\partial}{\partial y}\eta_T + Kv_T[(\underline{u_S} + u_T)^2 + (\underline{v_S} + v_T)^2]^{1/2} + fU_T = 0 \tag{5.230}
$$

$$
\frac{\partial}{\partial t}\eta_T + \frac{\partial}{\partial x}U_T + \frac{\partial}{\partial y}V_T = 0 \tag{5.231}
$$

with the boundary condition

$$
\eta_0 = \eta_{0,T} \tag{5.232}
$$

For the surge:

$$
\frac{\partial}{\partial t}U_S + (D + \eta_S + \underline{\eta_T})g\frac{\partial}{\partial x}\eta_S + Ku_S[(u_S + \underline{u_T})^2 + (v_S + \underline{v_T})^2]^{1/2} - fV_S = 0 \tag{5.233}
$$

$$
\frac{\partial}{\partial t}V_S + (D + \eta_S + \underline{\eta_T})g\frac{\partial}{\partial y}\eta_S + Kv_S[(u_S + \underline{u_T})^2 + (v_S + \underline{v_T})^2]^{1/2} + fU_S = 0 \tag{5.234}
$$

$$
\frac{\partial}{\partial t}\eta_S + \frac{\partial}{\partial x}U_S + \frac{\partial}{\partial y}V_S = 0 \tag{5.235}
$$

with the boundary condition

(5.236) $\eta_0 = \eta_{0,S}$

In running the tidal model with eq. 5.229−5.232 the surge parameters η_S, U_S, and V_S, which appear in eq. 5.229 and 5.230, are evaluated from the simultaneous operation of the surge model, whereas in running the surge model with equations 5.233−5.236 the tidal parameters η_T, U_T, and V_T, which appear in eq. 5.233 and 5.234, are obtained from the concurrently running tidal model.

In the above equations (i.e. 5.229, 5.230, 5.233, and 5.234), the terms underlined represent the interaction terms. In eq. 5.229 and 5.230, the interaction terms involving η_S are called the shallow-water terms and the other interaction terms are referred to as the quadratic friction terms. This is also the case for eq. 5.233 and 5.234.

Next, a paper by Das et al. (1974) will be briefly considered in which interaction of tide and surge in the Bay of Bengal was studied through a two-dimensional numerical model. A destructive storm surge occurred in the Bay of Bengal on November 12−13, 1970, and the casualties were over 200 000 people (more details of this will be given in Chapter 7.) At Chittagong Harbor (located 60 km to the south of the landfall of the storm) the observed surge was 1.5 m whereas the surge predicted by the numerical model was 3.2 m. Das et al. (1974) at the outset attributed the difference between the observed and predicted surge to a faulty tide gauge and interaction between tide and surge.

Their detailed calculations showed that a linear superposition of surge and tide, as was done by Flierl and Robinson (1972), overestimated the observed water level (Flierl and Robinson gave a value of 8.7 m for the peak surge in the Bay of Bengal whereas the observed value was between 6 and 9 m). The model of Das et al. (1974) in which tide and surge were included in the computations (not linear superposition) predicted a value of 5 m. However, the tide−surge interaction in their model could not account for the 2-h time difference between the observed and computed time of occurrence of maximum elevation. Murty and El-Sabh (1981) studied tide−surge interaction in the St. Lawrence Estuary. This will be considered in section 7.1.

Miscellaneous Techniques for Tide−Surge Interaction

Garcia and Houston (1974) described a method to study the interaction between tide and tsunami. Interestingly, they attributed this method to a personal communication from R. O. Reid in which it appears that the technique was originally developed to study the interaction between tide and surge. Following Garcia and Houston (1974), this technique for tide−tsunami interaction will be briefly considered with the understanding that a similar technique can be applied to tide−surge interaction. Since the period of tsunami waves at the coast (0−2 h) is less than the tidal period, the variation in the tidal level is assumed to be negligible between the times of arrival of the initial and maximum tsunami wave.

Let z be the runup at a given time above local mean sea level, $P_S(z)$ the cumulative probability distribution for runup at a given site being equal to or exceeding z due only to the maximum wave of the tsunami, $P_\beta(z)$ the probability of the runup at the same location being equal to or exceeding z due only to the astronomical tide (tidal runup here means the tidal level), and $P(z)$ the cumulative probability distribution for runup at a given site being equal to or exceeding z due to the maximum wave of the tsunami and the tide. Following Chandrasekhar (1942), one can write

$$(5.237)\quad P(z) = \int_{-\infty}^{\infty} f_\beta(\lambda) P_S(z - \lambda) d\lambda$$

where

$$(5.238)\quad f_\beta(z) = -\frac{dP_\beta(z)}{dz}$$

Here, $f_\beta(z)$ is the probability density for the tide.

If one excludes the situation that two different tsunamis arrive simultaneously at a given location, one can write

$$(5.239)\quad P_S(z) = \sum_{n=1}^{N} P_{S_n}(z)$$

for N independent source regions, and $P_{S_n}(z)$ is the cumulative probability distribution for runup at a given site being equal to or exceeding z due to tsunamis from source region n.

The next step is to express these probabilities by an exponential function:

$$(5.240)\quad P_{S_n}(z) = A_n e^{-\alpha_n z}$$

and

$$(5.241)\quad P_S(z) = \sum_{n=1}^{N} A_n e^{-\alpha_n z} \text{ for } N \text{ sites}$$

Let $P_\beta(z)$ be approximated by a Gaussian distribution. Then

$$(5.242)\quad f_\beta(z) = \frac{1}{\sigma\sqrt{2\pi}} e^{-z^2/2\sigma^2}$$

in which the variance σ^2 is given by

$$\sigma^2 = \sum_{m=1}^{\infty} C_m^2$$

Hence, C_m is the mth tidal constituent. Substituting eq. 5.241 and 5.242 into eq. 5.237 and integrating gives

$$(5.243)\quad P(z) = \sum_{n=1}^{N} A_n e^{-(\alpha_n z + (\alpha_n^2 \sigma^2/2))}$$

For two different source regions the sum of the two exponential terms in eq. 5.241 can be represented by a single exponential:

$$(5.244)\quad P_S(z) = \sum_{n=1}^{2} A_n e^{-\alpha_n z} = A e^{-\alpha z}$$

Hence

$$P(z) = A e^{-\alpha(z - (\alpha\sigma^2/2))}$$

or

$$(5.245)\quad P(z) = A e^{-\alpha z'}$$

where

$$(5.246)\quad z' \equiv z - \frac{\alpha\sigma^2}{2}$$

Hence, the influence of the astronomical tide is to create a $P(z)$ identical to $P_S(z)$ except for a shift of z by an amount $\alpha\sigma^2/2$. Knowing the tidal constants for any given location one can determine the variance σ.

Myers (1970) presented a joint probability method of tide frequency analysis in which storm surges are combined with the tide in a random manner rather than adding the maximum surge to the high tide. This analysis was applied to the coast of New Jersey, and some of the results will be dealt with in Chapter 7.

Cartwright (1968) proposed a rather unconventional method of studying the interaction between tides and surges and applied this technique to the North Sea. The tide at any given location is represented as a weakly nonlinear response to the gravitation and radiation potential of the sun and moon. The functions chosen to describe the meteorological forcing are the first six coefficients of a special Taylor expansion of the atmospheric pressure field. (Note that a linear wind stress is implied through the pressure gradients.) Cartwright used a 3-yr data record covering the period 1959–61. Thus, his approach differs form the traditional one in that whereas in the traditional approach storm surges are regarded as isolated events, Cartwright treats them as continuous events (although at certain times their amplitudes are greater than at other times).

Finally, the role of the so-called perigean spring tides and the interaction with storm surges will be considered, and in this discussion an important monograph by Wood (1978) serves as the source. From Wood (1978, p. XXVII) perigean spring tides and proxigean spring tides are defined:

> Tides are caused by the gravitational attractions of the moon and sun acting upon the oceans and major water bodies of the earth. Two times during each month, at new moon (conjunction) and full moon (opposition), the earth, moon and sun come into direct alignment in celestial longitude and, in the combination of their gravitational forces, enhanced tide-raising forces result. Tides produced at these times are called spring tides. Since the lunar orbit is elliptical in shape, once each revolution the moon also attains its closest monthly approach to the earth, a position known as perigee.
>
> Oridinarily, the passage of the moon through perigee and the alignment of moon, earth, and sun at new moon or full moon (either position being called syzygy) do not take place at the same time. Commensurable relationships between the lengths of the synodic and anomalistic months do, however, make this possible. On the relatively infrequent occasions when these two phenomena occur within 1½ days of each other, the resultant astronomical configuration is described as perigree–syzygy, and the tides of increased daily range thus generated are termed perigean spring tides, or simply, perigee springs.
>
> Whenever such alignments between perigee and syzygy occur within a few hours or less of each other, augmented dynamic influences act to increase sensibly the eccentricity of the lunar orbit, the lunar parallax, and hence also the orbital velocity of the moon itself. Such solar-induced perturbations also reduce the moon's perigee distance in each case by an amount which is greater the closer is the coincidence of alignment between these two astronomical positions, but which also fluctuates with other factors throughout the years. The tide-raising force varies inversely as the cube of the distance between the earth and moon (or sun). On certain occasions, lunar passage through perigee involves a particularly close approach of the moon to the earth. To distinguish these cases of unusually close perigee, the new term "proxigee" has been devised, and the associated tides of proportionately increased amplitude and range are designated as 'proxigean spring tides.'

Evidence presented by Wood (1978) indicates that the appreciably enhanced influences on the tides produced at the time of proxigee–syzygy are revealed, not so much in increasing the height of the tide (usually a maximum increase of about 0.5–1 ft

(0.15−0.3 m) above mean high water springs) but in accelerating the rate at which these augmented high waters are reached. This accelerated growth rate in the height of the tides, together with an increased horizontal current movement, creates a sea−air interface situation particularly susceptible to the coupling action of surface winds. Although the perigean spring tides do not, of themselves, constitute a major flooding threat to coastlines, friction between strong, persistent, onshore winds and the sea surface can raise the astronomically produced tide level to cause extensive flooding of the coast in lowland regions.

In addition, at the times of perigee−syzygy (proxigee−syzygy), various dynamic influences combine to lengthen the tidal day, increasing the period within which the enhanced tide-raising forces, effective for some few days on either side of the perigee−syzygy alignment, can exert their maximized effects. Actual instances of coastal flooding associated with perigean spring tides and storm surges (occurring together) will be considered in Chapter 7.

5.4 Interaction Between Storm Surges and Wind Waves

One of the areas of storm surge research that is grossly neglected is that of the interaction between storm surges and wind waves. In some sense, this problem is similar to the interaction between storm surges and tides; however, important differences exist. Both storm surges and tides have periods of the order of hours whereas wind-generated waves (or simply, wind waves) have periods of the order of a few seconds. Thus, in the present case the interaction is between waves of grossly differing periods (and wavelengths). The influence of wind waves on storm surges can be visualized in at least two different ways. One is to create an extra drag on the water surface and thus increase the wind stress (this aspect will be covered in Chapter 6). The other influence is an extra setup (i.e. change of water level) due to the presence of wind waves. In this section, this second aspect will be discussed.

Harris (1967) considered the influence of wind waves and rainfall on storm surges because, as he put it, since the storm surge results from high winds, it is usually accompanied by breaking waves and heavy rainfall. For his mathematical analysis the x-momentum equation can be written as

$$\rho\left(\frac{\partial u}{\partial t} - fv + u\frac{\partial u}{\partial x} + v\frac{\partial u}{\partial y} + w\frac{\partial u}{\partial z}\right) = \frac{\partial}{\partial x}T_{xx} + \frac{\partial}{\partial y}T_{yx} + \frac{\partial}{\partial z}T_{zx} \tag{5.247}$$

where u, v, and w are the velocity components in the x, y, and z directions, respectively, f is the Coriolis parameter, and ρ is water density. Also

$$T_{xx} = \mu\frac{\partial u}{\partial x} - P$$

$$T_{yx} = \mu\frac{\partial u}{\partial y} \tag{5.248}$$

$$T_{zx} = \mu\frac{\partial u}{\partial z}$$

where μ is the coefficient of molecular viscosity and P is the pressure. The continuity equation is

$$\frac{\partial u}{\partial x} + \frac{\partial v}{\partial y} + \frac{\partial w}{\partial z} = 0 \tag{5.249}$$

For convenience in treating the nonlinear terms, the momentum equation is rewritten as

$$\rho\left[\frac{\partial u}{\partial t} - fv + \frac{\partial}{\partial x}(u^2) + \frac{\partial}{\partial y}(uv) + \frac{\partial}{\partial z}(uw)\right] = \frac{\partial}{\partial x}T_{xx} + \frac{\partial}{\partial y}T_{yx} + \frac{\partial}{\partial z}T_{zx} \tag{5.250}$$

Let a bar denote the average flow and a prime denote the perturbation. Then

$$\begin{aligned} u &= \bar{u} + u' \\ v &= \bar{v} + v' \\ \rho &= \bar{\rho} + \bar{\rho}_w + \rho' \\ w &= \bar{w} + w' \\ P &= \bar{P} + P' + \bar{P}_w \\ \eta &= \bar{\eta} + \eta' \end{aligned} \tag{5.251}$$

where η is the height of the free surface, $\bar{P}$ is the mean pressure not including the effect of surface waves, and $\bar{P}_w$ is the mean dynamic pressure due to wave action. By definition, an averaged quantity is unchanged by repeated averaging, and the average of a perturbation quantity is zero. However, the average of the product of two perturbed quantities need not be zero.

Substituting eq. 5.248 and 5.251 into eq. 5.250, dividing by ρ, and averaging all terms gives

$$\begin{aligned} \frac{1}{\bar{\rho}}\frac{\partial \bar{P}}{\partial x} = {} & \nu\frac{\partial^2 \bar{u}}{\partial z^2} - \frac{\partial}{\partial z}\overline{u'w'} - \frac{\partial \bar{u}}{\partial t} + f\bar{v} - \frac{\partial}{\partial x}\bar{u}^2 - \frac{\partial}{\partial y}\overline{uv} - \frac{\partial}{\partial z}\overline{uw} \\ & + \nu\frac{\partial^2 \bar{u}}{\partial x^2} - \frac{\partial}{\partial x}(u')^2 + \nu\frac{\partial^2 \bar{u}}{\partial y^2} - \frac{\partial}{\partial y}\overline{u'v'} - \frac{1}{\bar{P}}\frac{\partial \bar{P}_w}{\partial x} + \frac{1}{\bar{\rho}}\frac{\bar{\rho}'}{\bar{\rho}}\frac{\partial P'}{\partial x} \end{aligned} \tag{5.252}$$

In eq. 5.252, $\overline{(\rho'/\rho')^2}$ is neglected compared with unity.

The perturbed quantities consist of three different types of small-scale phenomena: turbulence, waves, and unresolvable features by the grid. In this scale analysis, Harris (1967) ignored the third type. Generally, the influence of turbulence on the mean flow is treated by redefining the stress tensor as follows:

$$\begin{aligned} T_{xx} + P &= \mu\frac{\partial \bar{u}}{\partial x} - \overline{(u')^2} \\ T_{yx} &= \mu\frac{\partial \bar{u}}{\partial y} - \overline{u'v'} \\ T_{zx} &= \mu\frac{\partial \bar{u}}{\partial z} - \overline{u'w'} \end{aligned} \tag{5.253}$$

These could be also written as

$$\begin{aligned} T_{xx} + P &= A_1\frac{\partial \bar{u}}{\partial x} \\ T_{yx} &= A_2\frac{\partial \bar{u}}{\partial y} \\ T_{zx} &= A_3\frac{\partial \bar{u}}{\partial z} \end{aligned} \tag{5.254}$$

Thus, the A's will consist of quantities such as μ, $\overline{(u')^2}$, $\overline{u'v'}$, and $\overline{u'w'}$.

Next, eq. 5.253 is used to represent the effects of viscosity and turbulence, and the prime notation is used only for the influence of surface waves. Equation 5.252 becomes

$$(5.255)\quad \frac{1}{\bar{\rho}}\frac{\partial \bar{P}}{\partial x} = \frac{\partial}{\partial z}T_{zx} - \frac{\partial \bar{u}}{\partial t} + f\bar{v} - \frac{\partial}{\partial x}\overline{u^2} - \frac{\partial}{\partial y}\bar{u}\bar{v} - \frac{\partial}{\partial z}\bar{u}\bar{w} + \frac{\partial}{\partial x}(T_{xx} + \bar{P})$$

$$+\frac{\partial}{\partial y}T_{yx} - \frac{\partial}{\partial x}\overline{(u')^2} - \frac{\partial}{\partial y}\overline{u'v'} - \frac{\partial}{\partial z}\overline{u'w'} - \frac{1}{\bar{\rho}}\frac{\partial \bar{P}_w}{\partial x} + \frac{1}{\bar{\rho}}\overline{\frac{\rho'}{\bar{\rho}}\frac{\partial P'}{\partial x}}$$

Although for the short waves (wind waves) the vertical acceleration term is important, and since this is being treated separately here, one may use the hydrostatic equation for $\bar{P}$. Thus

$$(5.256)\quad \frac{\partial \bar{P}}{\partial x} = g\rho(\bar{h})\frac{\partial \bar{h}}{\partial x} + g\int_z^{\bar{h}}\frac{\partial \bar{\rho}}{\partial x}\,dz$$

Substituting eq. 5.256 into 5.255 and then integrating from the bottom to the free surface and rearranging the terms gives the following expression for the mean slope of the water surface (see the appendix in Harris 1967):

$$(5.257)\quad \frac{\partial \bar{h}}{\partial x} = \underset{\text{(I)}}{1}\ \underset{\text{(II)}}{\frac{1}{g\bar{\rho}(\bar{h})}\frac{\partial P_a}{\partial x}} + \underset{\text{(III)}}{\frac{1}{gD(1 + (\bar{h}/D))}}\left\{\underset{\text{(IV)}}{\frac{\bar{\rho}}{\bar{\rho}(\bar{h})}}\underset{\text{(V)}}{[T_{zx}(\bar{h}) - T_{zx}(-D)]} - \underset{\text{(VI)}}{\frac{\partial U}{\partial t}}\right.$$

$$\left. + \underset{\text{(VII)}}{fV} - \underset{\text{(VIII)}}{\left[\underset{\text{(IX)}}{\frac{\partial}{\partial x}\frac{U^2}{(D + h)}} + \underset{\text{(IX)}}{\frac{\partial}{\partial y}\frac{UV}{(D + h)}}\right]}\right\} + R$$

where

$$(5.258)\quad R = \underset{\text{(III)}}{\frac{1}{gD(1 + (\bar{h}/D))}}\left\{-\underset{\text{(X)}}{\frac{\partial}{\partial x}\int_{-D}^{\bar{h}}\hat{u}^2 dz} - \underset{\text{(X)}}{\frac{\partial}{\partial y}\int_{-D}^{\bar{h}}\hat{u}\hat{v}\,dz} - \underset{\text{(XI)}}{\int_{-D}^{\bar{h}}\frac{g}{\bar{\rho}}\int_z^{\bar{h}}\frac{\partial \rho}{\partial x}\,dz}\right.$$

$$+ \underset{\text{(XII)}}{\int_{-D}^{\bar{h}}\left[\frac{\partial}{\partial x}(T_{xx} + \bar{P}) + \frac{\partial}{\partial y}T_{xx}\right]dz} + \underset{\text{(XIII)}}{\int_{-D}^{\bar{h}} - D\overline{\frac{1}{\rho}\frac{\rho'}{\bar{\rho}}\frac{\partial P'}{\partial x}}\,dz}$$

$$\left. - \underset{\text{(XIV)}}{\int_{-D}^{\bar{h}}\left[\frac{\partial}{\partial x}\overline{(u')^2} + \frac{\partial}{\partial y}\overline{u'v'} + \frac{\partial}{\partial z} + \frac{\partial}{\partial z}\overline{u'w'} + \frac{1}{\bar{\rho}}\frac{\partial \bar{P}_w}{\partial x}\right]dz}\right\}$$

In eq. 5.257 and 5.258 the terms indicated by roman numerals have the following significance: I, water surface slope term; II, atmospheric pressure gradient term; III, depth term; IV, stratification term; V, wind stress term; VI, bottom friction term; VII, acceleration term; VIII, Coriolis term; IX, vertically averaged inertial terms; X, vertical shear inertial terms; XI, density gradient term; XII, eddy viscosity term; XIII, density perturbation term; XIV, wave setup term.

The continuity equation can be written as

$$\frac{\partial h}{\partial t} + \frac{\partial U}{\partial x} + \frac{\partial V}{\partial y} = 0 \tag{5.259}$$

In the above equations $\bar{P}$ is the mean atmospheric pressure at the sea surface. Also

$$\begin{aligned} U &= \int_{-D}^{\bar{h}} \bar{u} dz \\ V &= \int_{-D}^{\bar{h}} \bar{v} dz \end{aligned} \tag{5.260}$$

$$\begin{aligned} \hat{u} &= \bar{u}(z) - \frac{U}{(D + \bar{h})} \\ \hat{v} &= \bar{v}(z) - \frac{V}{(D + \bar{h})} \end{aligned} \tag{5.261}$$

$$\begin{aligned} \bar{\rho} &= \bar{\bar{\rho}} + \hat{\rho}(z) \\ \bar{\bar{\rho}} &= \frac{1}{(D + \bar{h})} \int_{-D}^{\bar{h}} \bar{\rho}(z) dz \end{aligned} \tag{5.262}$$

Note that in eq. 5.257 and 5.258, the following terms are normally included in storm surge numerical models: water surface slope term, atmospheric pressure gradient term, wind stress term, bottom friction term, acceleration term, Coriolis term. It can be seen that the atmospheric pressure gradient term is independent of the water depth, whereas the wind stress term is inversely proportional to the total depth. The two sources that can impart energy to the water are atmospheric pressure gradient force and wind stress, whereas energy is dissipated by bottom friction. The other terms merely redistribute the energy between potential and kinetic forms.

The relative importance of the various terms in the above equations will be considered. The terms whose importance is obvious (such as the surface slope term, atmospheric pressure gradient term, wind stress term, bottom friction term, acceleration term, Coriolis term) will not be considered. If the flow is not restricted by boundaries, the inertial terms are not significant. If the x-axis is taken parallel to the flow, then as long as the velocity decreases in the flow direction, the inertial terms make a positive contribution to the slope. For example, if the flow is towards the head of a water body, then $\bar{u}^2$ must be zero at the head. Thus, the conversion of kinetic energy to potential energy will create, at the head, water levels higher than computed using a linear theory. Harris (1967) cited a practical example. Hydraulic model studies of Ise Bay, Japan, showed greater storm surge heights than predicted from a linearized numerical model (Nakamura et al. 1964).

Equation 5.258 includes terms for which data are not usually available (density gradients, vertical shear of the mean current, effects of subgrid scale phenomena). One can expect the inertial terms that depend on the vertical profile of the mean current to be related to the transport terms. In some studies, these terms are approximately taken into account by multiplying the transport terms by a factor slightly different from unity. Usually these terms will be insignificant unless the topography causes abnormal variations of the vertical

profile of the mean current within a short distance. The eddy viscosity term could be simplified to

$$(5.263)\quad \int_{-D}^{\bar{h}} \left[\frac{\partial}{\partial x}(T_{xx} + \bar{P}) + \frac{\partial}{\partial y} T_{yx}\right] dz = \frac{\partial}{\partial x} A_4 \frac{\partial U}{\partial x} + \frac{\partial}{\partial y} A_5 \frac{\partial U}{\partial y}$$

where A_4 and A_5 could be determined from observations such that computational results agree with observations. Ordinarily one assumes that

$$A_4 = A_5 = \text{constant}$$

although, strictly speaking, they are functions of space and time.

Next, the main aspect of this section will be considered, namely the influence of wind waves on storm surges. To simplify the problem, Harris (1967) took the x-axis in the direction of wave travel so that the v' term vanishes. Using Wiegel (1964), Harris (1967) wrote the nonlinear solutions of the progressive wave equations, noting that the interactions between wind waves and surges will be nonlinear:

$$\begin{aligned}
&\eta' \sim AZ_1(z) \cos k(x - ct) + A^2 Z_2(z) \cos 2k(x - ct)\\
&u' \sim AZ_3(z) \cos k(x - ct) + A^2 Z_4(z) \cos 2k(x - ct)\\
&w' \sim AZ_5(z) \sin k(x - ct) + A^2 Z_6(z) \sin 2k(x - ct)\\
&P' - \rho g z \sim AZ_7(z) \cos k(x - ct) + A^2[Z_8(z) \cos 2k(x - ct) + Z_9(z)]
\end{aligned} \qquad (5.264)$$

Here, A is the amplitude of the wave and it is a slowly varying function of x such that

$$\frac{\partial A}{\partial x} \ll kA$$

Although A may vary from deep water to the shore in a significant manner, its variation over one wavelength may be negligible. For convenience, one may choose Z_1 and Z_2 such that both assume values of unity at $z = 0$. The imposed boundary conditions and the flow structure determine the exact form of Z. For the following discussion the exact forms are irrelevant.

Substituting eq. 5.264 into 5.258 gives for the wave set term

$$(5.265)\quad \int_{-D}^{\bar{h}} \left[\frac{\partial}{\partial x}\overline{(u')^2} + \frac{\partial}{\partial z}\overline{u'w'} + \frac{1}{\rho}\frac{\partial \bar{P}_w}{\partial x}\right] dz = -\int_{-D}^{\bar{h}} \frac{\partial}{\partial x} A^2 \frac{1}{2}[A_3^2 + Z_9] dz$$

$$= -B\frac{\partial}{\partial y} A^2$$

where

$$B = \int_{-D}^{\bar{h}} \left[\frac{1}{2} Z_3^2 + Z_9\right] dz$$

where Z_3 and Z_9 are implied from eq. 5.264.

When the wind waves approach shallow water, their amplitude decreases until the depth to wavelength ratio reduces to about 0.16 (at this stage the wave amplitude is about 91% of the deepwater value). As the wave moves farther into shallow water, its amplitude increases rapidly until it breaks. After breaking, the wave amplitude decreases very rapidly until the wave disappears on the beach. Hence, the influence of the waves is to decrease the water level (due to the surge) on the seaward side of the breaker zone and to increase

TABLE 5.15. Characteristics of some selected hurricanes in the Gulf of Mexico. A wave energy index can be calculated as the product of the radius of maximum winds and the difference between the ambient and central pressures. (Wilson 1958)

Date	Location	Ambient pressure (mb)	Central pressure (mb)	Radius of max. winds (km)
Sept. 8, 1900	Galveston, TX	1008.5	936.0	56
Aug. 16, 1915	Velasco, TX	1001.4	952.9	85
Sept. 29, 1915	New Orleans, LA	1020.7	943.8	122
Aug. 18, 1916	Santa Gertrudis, TX	1042.0	948.2	179
Sept. 9, 1919	Dry Tortugas, FL	1006.8	929.2	64
Sept. 14, 1919	Corpus Christi, TX	1000.3	970.2	124
June 22, 1921	Houston, TX	1016.9	961.1	52
Aug. 13, 1932	East Columbia, TX	1019.6	942.4	51
Sept. 5, 1933	Brownsville, TX	1024.0	948.9	123
Sept. 17, 1947	Hillsboro, FL	1010.2	940.1	38
Sept. 19, 1947	New Orleans, LA	1005.8	968.8	55
Oct. 9, 1949	Freeport, TX	1020.3	978.0	65

the surface slope between the breaker zone and the beach. For studies on the effect of wind waves on sea level, see Longuet-Higgins and Stewart (1962, 1963, 1964) and Saville (1961). To summarize, Harris (1967) regarded the contribution of wind waves to the storm surge as a conversion of the momentum carried by the waves to a gradient in the hydrostatic pressure due to the surge. Thus, the kinetic energy of wave motion is converted into the potential energy of an increased sea level.

There have been other studies, either more rigorous or less rigorous than the treatment of Harris (1967). For example, Rao and Mazumdar (1966) simply added the height of crests of individual waves to the storm surge. Fortak (1962) gave a more rigorous (than Harris's) derivation of the influence of wind waves on storm surges.

SOME INFORMATION ON WIND WAVES

Although it is not intended to discuss wind waves (which are a major topic in oceanography, and several excellent works on this topic are available, e.g. Kinsman 1965), nevertheless a few remarks will be made.

Wilson (1958) studied the statistics of hurricane-generated wind waves in the Gulf of Mexico using a 50-yr data record (1900–49). The tracks of most of the hurricanes listed in Table 5.15 are shown in Fig. 5.43. This study showed the relative vulnerability to hurricane waves at several locations as follows (in decreasing order): Gilchrist (Texas), Burrwood (Mississippi), Brownsville (Texas), Apalachicola (Florida), and Tampa (Florida).

At least once in 2 yr the wave heights at Burrwood are as great as those at Gilchrist (about 19 ft or 5.8 m) and once in 5 yr they are about 30 ft (9.1 m). Brownsville and Apalachicola have roughly the same vulnerability. Tampa is quite well protected from hurricane-generated wind waves because of its location relative to hurricane tracks.

Forristall (1978) analyzed a 116-h-long record of wind waves in the Gulf of Mexico. These waves were generated by hurricanes, the tracks of which are shown in Fig. 5.44. His study showed that the Rayleigh distribution overpredicts the heights of the higher waves in the record. A statistical study based on 1000 cases revealed that the highest wave is only 0.907 times the height predicted by the Rayleigh distribution.

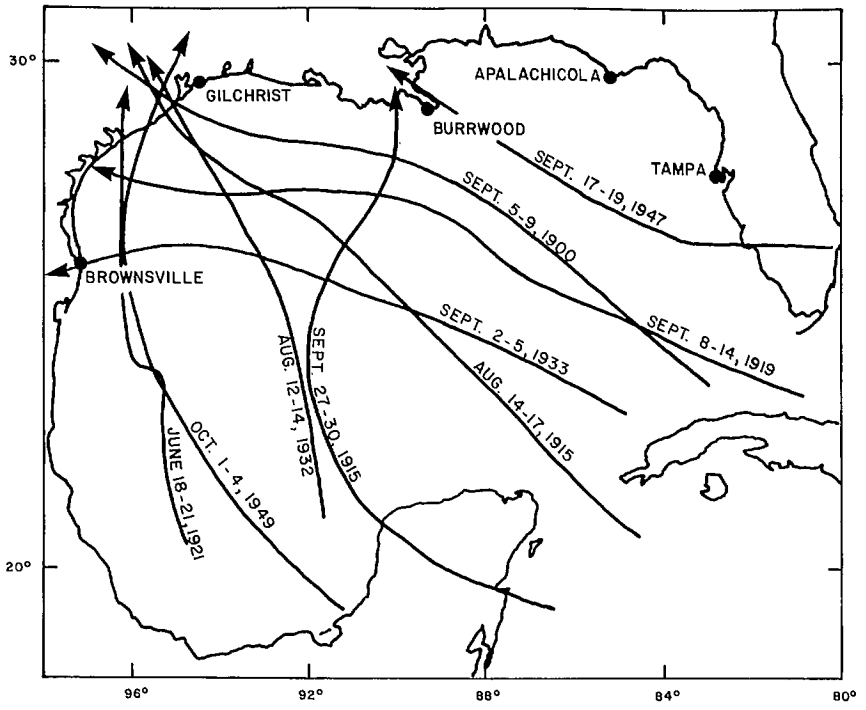

FIG. 5.43. Tracks of selected hurricanes over the Gulf of Mexico during 1900–49. (Wilson 1958)

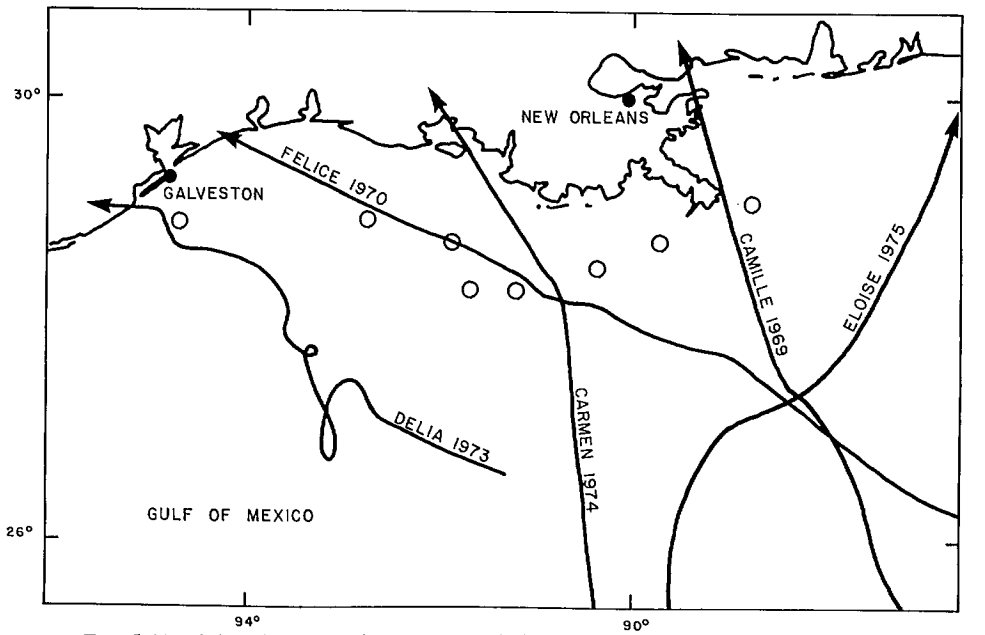

FIG. 5.44. Selected storm tracks over the Gulf of Mexico during 1969–75.(Forristall 1978)

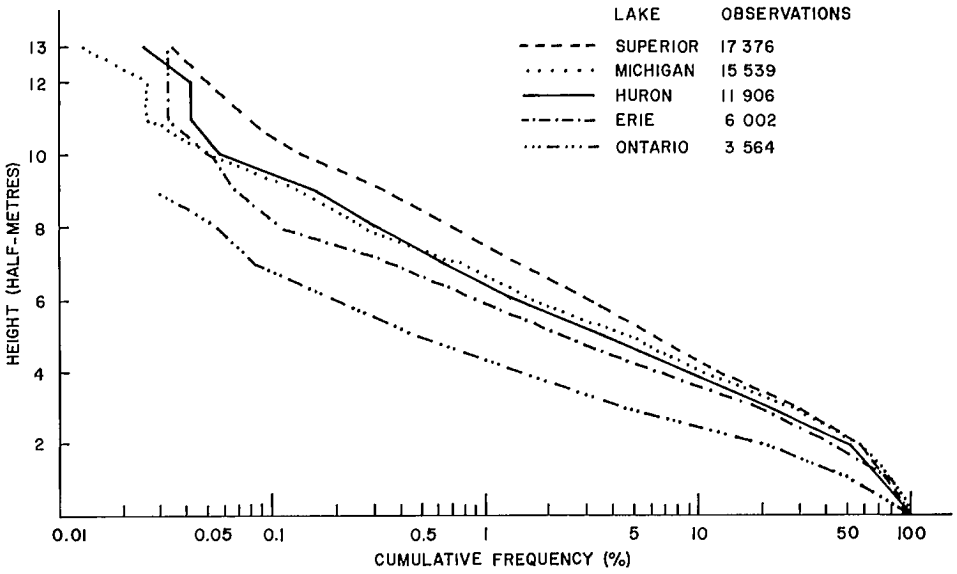

FIG. 5.45. Cumulative frequency on logarithmic scale of wave heights observed in the Great Lakes. (Pore et al. 1971)

In the Great Lakes of North America, since the astronomical tides are not significant, the interaction between storm surges and wind waves assumes special importance. Pore et al. (1971) made a wave climate study of the Great Lakes using a 10-yr data record for the period 1960–69. Their results are summarized in Fig. 5.45. It can be seen that in Lake Superior the wind waves have the highest amplitudes and in Lake Ontario the lowest. Lakes Michigan and Huron exhibited very similar behavior, and Lake Erie is somewhat similar to Lakes Michigan and Huron.

Krauss (1972), making use of the concept of radiation stress, argued that, whereas the mean surface elevation is depressed in the wave-breaking zone, shoreward of the breakers the wave setup can be as high as 20% of the incident wave height. Durning (1971) described a method of predicting maximum wind wave heights from historical data. Cardone et al. (1977) described an experiment to predict wind waves due to hurricanes, and this method was applied to Hurricanes Belle of 1976 and Anita of 1977. King and Shemdin (1978) described radar observations of hurricane wave directions. Long (1979) summarized the techniques of forecasting wind waves following hurricanes.

Rabe and Brand (1977) described numerical techniques for calculating wind waves due to tropical cyclones, and Sobey (1978) discussed wind wave frequencies in a tropical cyclone region. Fox and Davis (1979) described computer models for wind wave calculation. One example of a region not affected by violent tropical storms is the coast of Brazil. The wave climate in such a region is described by Homsi (1978). Other useful references on wind waves are Phillips (1978), Bretschneider and Rocheleau (1979), Niemeyer (1979a, 1979b), Büsching (1979), and a U.S. Navy Hydrographic Office publication (Anonymous 1966).

5.5 Influence of Ice and Stratification on Storm Surges

This section will begin with a brief discussion of the ice cover in certain North

TABLE 5.16. Dates of freeze-over and breakup for certain locations in Canadian waters. (Based on Allen and Cudbird 1971)

Station	Water body	Beginning of freeze-over	Complete freeze-over	Beginning of breakup	Complete breakup
Resolute	Resolute Bay	Sept. 21	Sept. 27	July 18	Aug. 7
Tuktoyaktuk	Kugmalitt Bay	Sept. 26	Oct. 2	June 4	June 22
Clifton Point	Amundsen Gulf	—	—	June 23	July 15
Clinton Point	Amundsen Gulf	Oct. 24	Nov. 15	June 3	June 30
Cape Parry	Amundsen Gulf	Oct. 6	Nov. 2	June 7	Aug. 14
Bray Island	Foxe Basin	—	—	June 20	July 31
Hall Beach	Foxe Basin	Oct. 11	Nov. 2	June 24	July 28
Rowley Island	(Miller Bay)	Oct. 11	Nov. 10	June 27	July 11
Coral Harbor	Hudson Bay	Oct. 7	Oct. 28	June 29	July 13
Churchill (NW of Churchill airport)	Hudson Bay	Nov. 1	Nov. 20	June 8	July 10
Poste-de-la-Baleine	Hudson Bay	Dec. 4	Dec. 28	May 19	June 21
Cape Hopes Advance	Hudson Strait	Nov. 14	Nov. 20	May 23	—
Broughton Island	Davis Strait	Oct. 20	Nov. 3	June 18	Sept. 29
Cape Hooper	(Home Bay)	Nov. 13	Dec. 2	June 27	Aug. 17
Resolution Island	Davis Strait	—	—	June 23	July 22
Daniels Harbor	Gulf of St. Lawrence	Dec. 1	Dec. 18	Apr. 28	May 3
Summerside	Gulf of St. Lawrence (Malpeque Bay)	Dec. 23	Dec. 31	Apr. 14	Apr. 26
Corner Brook	Humber Arm	—	Dec. 10	—	—
Mont-Joli	St. Lawrence River	Dec. 16	—	—	Apr. 5
Montreal	St. Lawrence River	Dec. 13	Dec. 27	Mar. 28	Apr. 11
Quebec City	St. Lawrence River	Dec. 7	—	—	Apr. 17
Rivière-du-Loup	St. Lawrence River	Nov. 24	Dec. 15	Mar. 21	Apr. 15

TABLE 5.17. Percentage of ice cover in the Canadian Archipelago and nearby waters by month. One hundred percent refers to the situation when the water body is totally frozen at the surface. (Sater et al. 1971)

Water body	J	F	M	A	M	J	J	A	S	O	N	D
Beaufort Sea	97	97	97	97	97	91	94	63	63	89	97	97
Canadian Archipelago	97	97	97	97	96	95	93	79	84	93	97	97
Davis Strait–Baffin Bay	97	97	97	96	93	87	68	34	16	75	87	94
Central Polar Ocean	99	99	99	99	99	99	97	97	96	97	99	99

American water bodies (mainly Canadian) followed with a general discussion of the influence of ice cover on storm surges. This section will end with a consideration of the effect of stratification on storm surges.

ICE REGIMES IN WATER BODIES

The atmospheric Environment Service of the Department of Environment (Federal Government of Canada) provides ice prediction services for Canadian waters. For details on ice regimes and related information, their reports should be consulted. Wittman and Burkhart (1973) provided a review of the forecast services available for North American Arctic waters.

Allen and Cudbird (1971) listed the freeze-up and breakup dates of Canadian water

bodies. For further information on freeze-up and breakup, see Catchpole and Moodie (1974) and Williams (1965). Some pertinent information about freeze-up and breakup dates for selected locations in Canadian waters is listed in Table 5.16. This table has been prepared based on data up to 1970 (Allen and Cudbird 1971).

Sater et al. (1971) summarized (Table 5.17) the percentage of ice cover by month in certain water bodies. Berry et al. (1975), Cooper (1975), Markham (1974), and Ramseier et al. (1974) discussed the ice conditions in the Beaufort Sea. Murty and Barber (1973) discussed ice transport in Hudson Bay making use of the results from a box model. The ice conditions in Baffin Bay for certain dates are shown in Fig. 5.46. Keen (1977) discussed the response of Baffin Bay ice conditions to changes in atmospheric circulation patterns.

Matheson (1967) related the ice conditions in the Gulf of St. Lawrence to meteorological situations. The ice conditions in the Gulf of St. Lawrence on different dates are shown in Fig. 5.47. Murty and Smith (1973) used a box model to study the transport of ice in the Gulf of St. Lawrence. Bugden (1976) developed sophisticated numerical models to study the modification of ice and its movement in the Gulf of St. Lawrence. For ice conditions in the St. Lawrence River and Seaway, see Anonymous (1974). The maximum ice cover in the Great Lakes during February 1977 (Remus 1979) is shown in Fig. 5.48 and ice conditions in the Great Lakes are summarized in Table 5.18. Wake and Rumer (1979) discussed mathematical modeling of Lake Erie ice regimes.

Kagan (1967a, 1967b) used numerical models to study the influence of tides on ice cover and vice versa. He showed that tides will introduce cracks (somewhat similar to wind-produced cracks) and zones of convergence and divergence in the ice cover. His study, which was applied to the Okhotsk Sea, produced results in agreement with observations. Various empirical and analytical relations were developed to predict ice cover using concepts of degree days, ice potential, etc. For details of these techniques see Zubov (1943), Brown (1954), Bilello (1964), Fertuk et al. (1971), and Assel (1976).

Influence of Ice Cover on Storm Surges

Einarsson (1972) appears to be among the first to have explicitly stated that the influence of an ice layer on long waves might be different from that on wind waves. It has been fairly well established that wind waves suffer attenuation in the presence of ice (Dean 1969; Defant 1961; Robin 1963; Wadhams 1972, 1973). Sverdrup (1926) considered the influence of an ice layer on tides in the North Siberian Shelf and showed that the amplitude of the tide might be somewhat smaller when ice is present and also that the propagation of the tide wave may be somewhat retarded.

Zubov (1943) studied the influence of ice cover on tides in the Kamenka and Pya rivers (which empty into the White Sea) and found that the tidal range decreases and the high and low waters are retarded. Laktionov (1960) developed empirical relations for determining the changes in the amplitude and phase of the tide during ice cover. Influence of ice cover on tides in the Canadian Arctic has been examined by Henry and Foreman (1977) and Godin (1977).

Godin and Barber (1980) showed that in some parts of the Canadian Arctic, ice cover has an influence on the tides. They speculated that Hudson Bay and Amundsen Gulf have resonance frequencies close to the tidal frequency and this resonance frequency is altered when ice is present. One interesting result is that, whereas the amplitude of the tide decreases when ice is present, the phase is not necessarily retarded (in some cases high and low waters occur earlier when ice is present). Godin (1980b) extended this study.

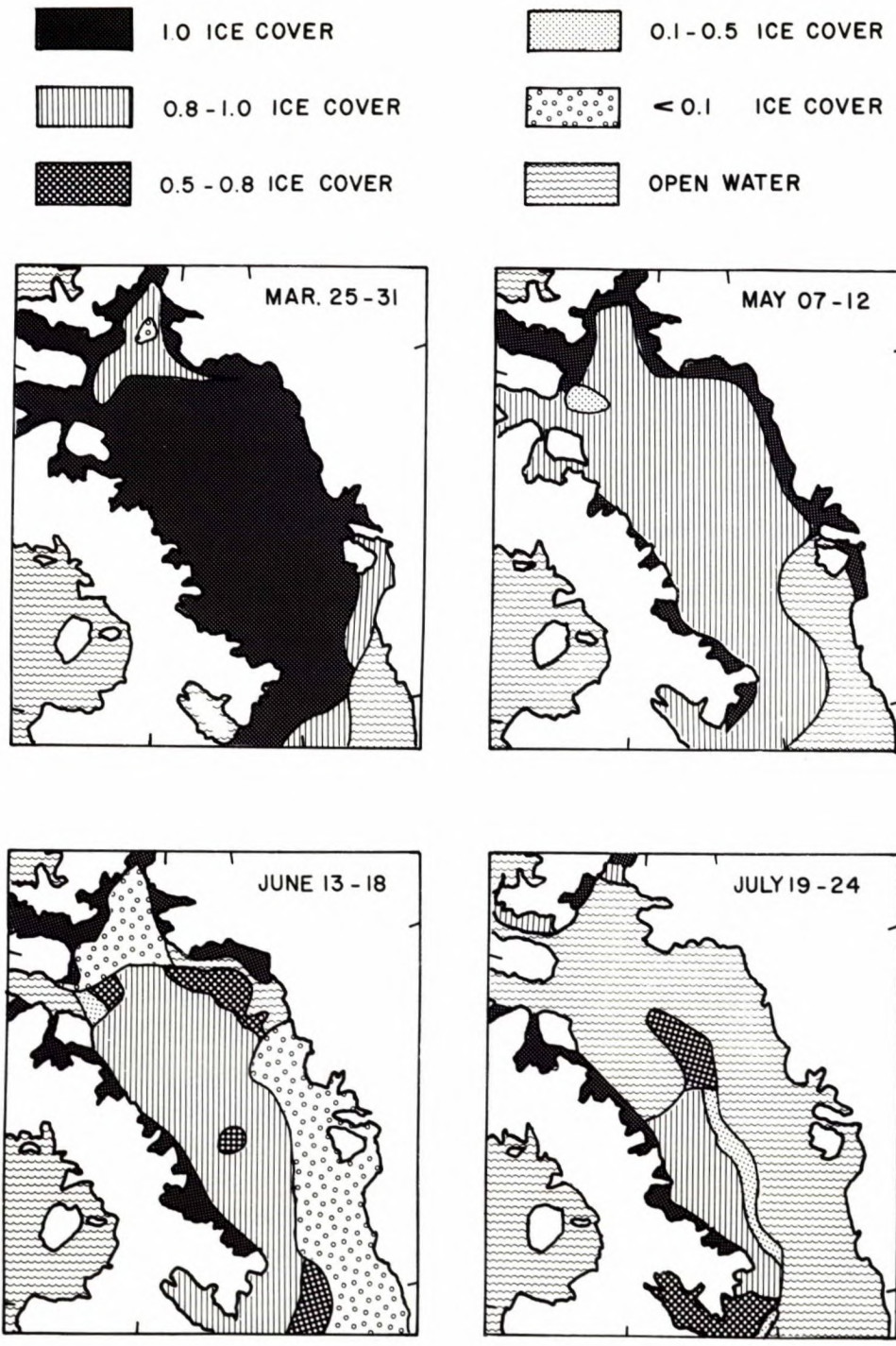
1.0 ICE COVER
0.8 - 1.0 ICE COVER
0.5 - 0.8 ICE COVER
0.1 - 0.5 ICE COVER
< 0.1 ICE COVER
OPEN WATER
MAR. 25 - 31
MAY 07 - 12
JUNE 13 - 18
JULY 19 - 24

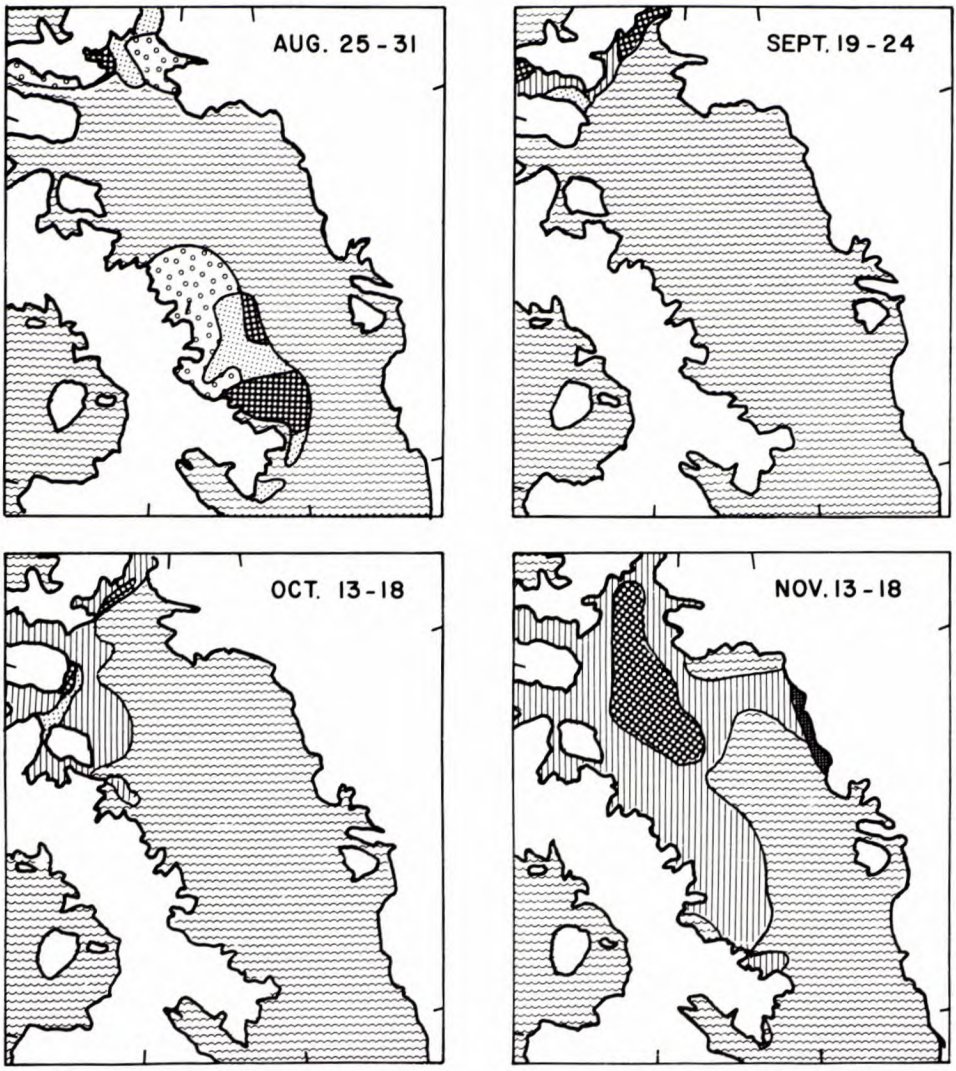

FIG. 5.46. Surface ice cover for Baffin Bay. (Anonymous 1956)

Kagan (1967a, 1967b) studied the influence of ice cover on tides in the Okhotsk Sea. Sheng and Lick (1972) developed a numerical model to calculate wind-driven currents in a partially ice-covered lake. Liland (1975) studied surges in ice-covered channels. Henry (1975) compared storm surges in the southern Beaufort Sea in summer and winter and concluded that the effectiveness with which wind can generate a surge is greatly reduced when there is a fairly complete ice cover.

Lisitzin (1974) discussed the influence of an ice layer on storm surge amplitudes in the Baltic Sea. She showed that the storm surge amplitudes are smaller when ice is present, and thus her results are in agreement with the classical concepts. Lisitzin (1974) used the following formula to compute the slope $\partial h/\partial x$ of the water surface:

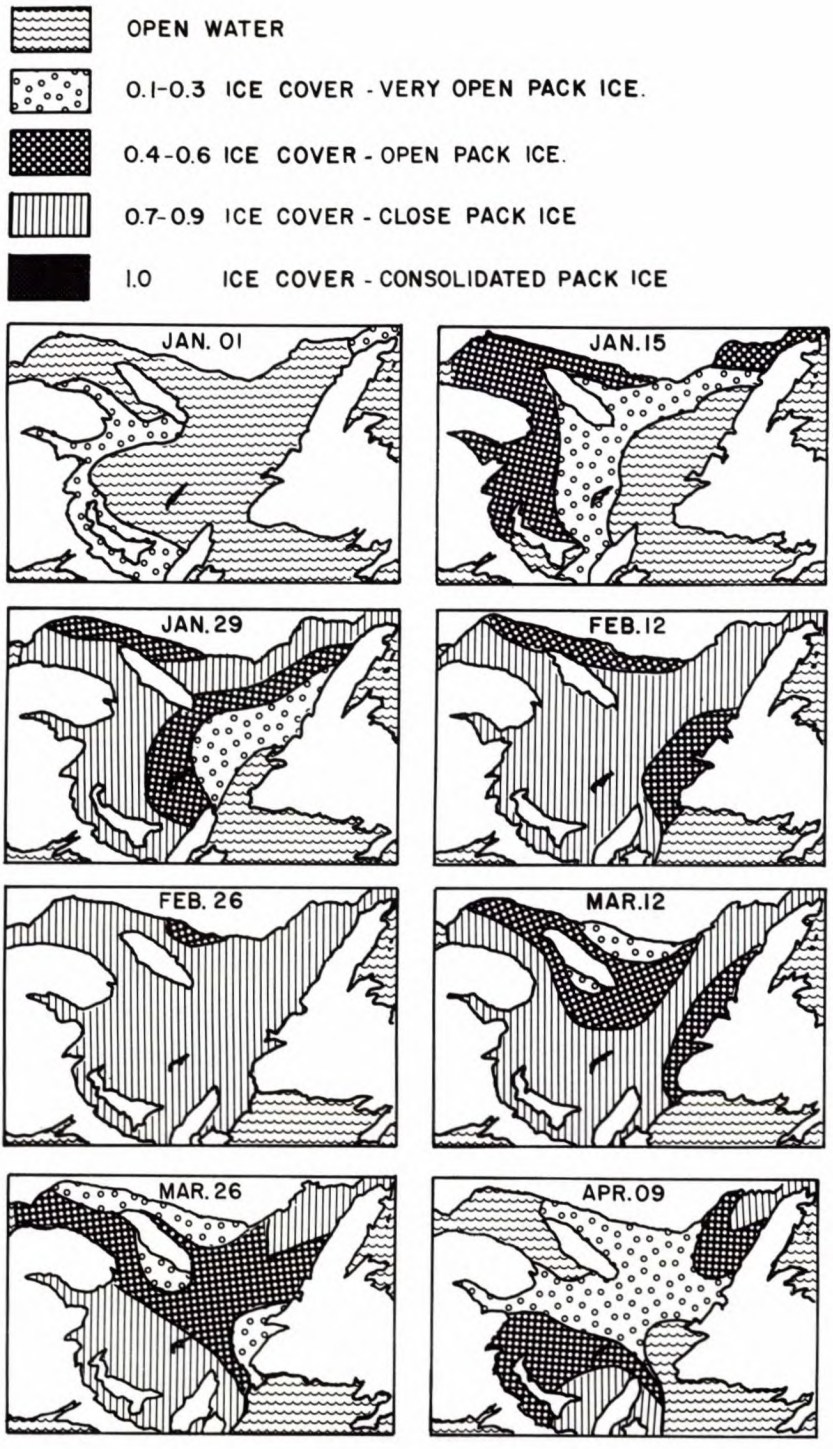
OPEN WATER
0.1-0.3 ICE COVER - VERY OPEN PACK ICE.
0.4-0.6 ICE COVER - OPEN PACK ICE.
0.7-0.9 ICE COVER - CLOSE PACK ICE
1.0 ICE COVER - CONSOLIDATED PACK ICE
JAN. 01
JAN.15
JAN.29
FEB.12
FEB. 26
MAR.12
MAR.26
APR.09

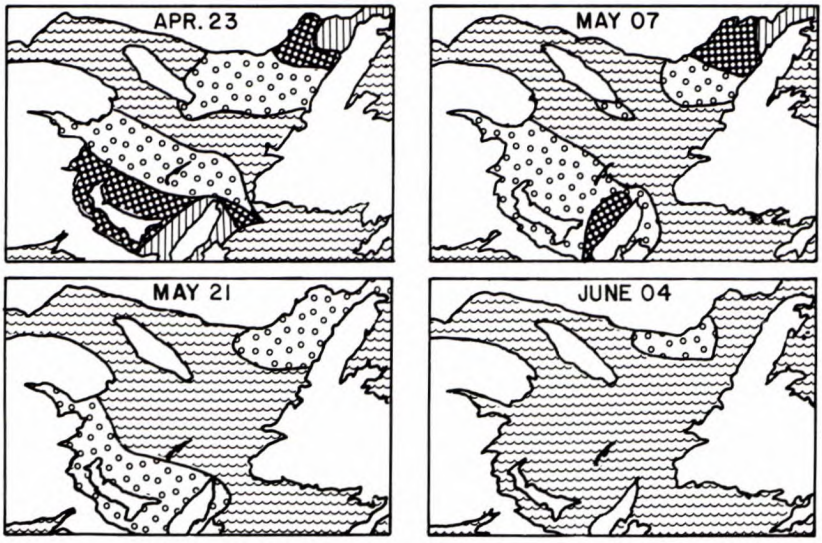

FIG. 5.47. Five-year mean ice concentration in the Gulf of St. Lawrence. (Matheson 1967)

$$(5.266) \quad \frac{\partial h}{\partial x} = \frac{F\tau}{g\rho H}$$

where h is the deviation of the free surface from its equilibrium position, x is the horizontal coordinate in the direction of the wind, g is gravity, ρ is the density of water, H is the average depth of the water body, and τ is the wind stress. The factor F depends on the water depth and the frictional conditions at the bottom of the water body, and it varies from 1 to 1.5 (for deep water, $F \sim 1$).

Let W denote the wind velocity at the anemometer level. The following relation is used to express the wind stress in terms of the wind:

$$(5.267) \quad \tau = k\rho_a W^2$$

where ρ_a is the density of air and k is a drag coefficient that depends on the roughness of the water surface. Taking $k = 2.4 \times 10^{-3}$, $\rho_a \sim 1.3 \times 10^{-3}$ g·cm^{-3}, $\rho \sim 1.0$ g·cm^{-3}, $g \sim 980$ cm·s^{-2}, and $F \sim 1$ in eq. 5.266 gives

$$(5.268) \quad \frac{\partial h}{\partial x} = \frac{3.2 \times 10^{-9}}{H} W^2$$

where W is expressed in centimetres per second. Lisitzin (1974), however, found the following formula to be more practical than eq. 5.268:

$$(5.269) \quad \Delta H = \frac{\alpha W^2}{H}$$

where ΔH denotes the increase in sea level (centimetres) for a distance of 100 km in the direction of the wind. In eq. 5.269, if W is expressed in metres per second and H in metres, then $\alpha \sim 3.2$. The value of α depends on the density of air (which depends on air temperature and atmospheric pressure) and may vary by 10%.

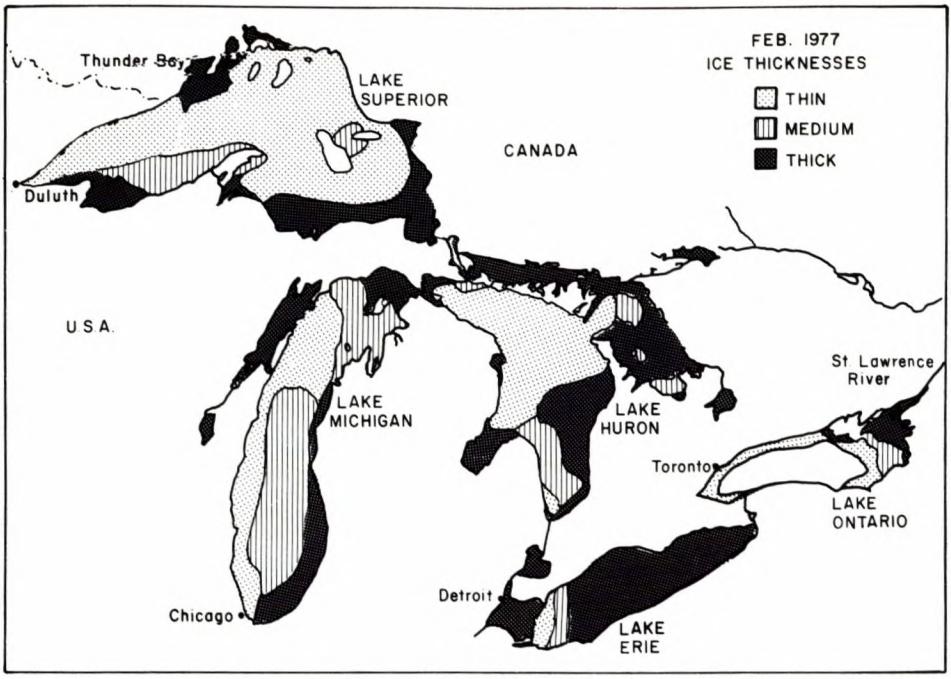

FIG. 5.48. Maximum ice cover in February 1977 in the Great Lakes. (Remus 1979)

TABLE 5.18. Dates of ice cover events during a normal winter and the percentage of ice-covered lake surface during mild, normal, and severe winters for each of the Great Lakes. (Rondy 1969)

Ice events during a normal winter	Lake Superior	Lake Michigan	Lake Huron	Lake Erie	Lake Ontario
Early ice cover	Jan. 20–30	Jan. 25–Feb. 5	Jan. 25–Feb. 5	Jan. 15–25	Jan. 25–Feb. 5
Midseason ice cover	Feb. 25–Mar. 5	Feb. 20–28	Feb. 25–Mar. 5	Feb. 1–10	Feb. 15–25
Maximum ice cover	Mar. 25–Apr. 5	Mar. 15–25	Mar. 20–30	Feb. 20–28	Mar. 10–20
Early decay period	Apr. 1–10	Mar. 20–30	Mar. 25–Apr. 5	Feb. 25–Mar. 5	Mar. 15–25
% maximum lake surface ice covered					
Mild winter	40	10	40	50	8
Normal winter	60	40	60	95	15
Severe winter	95	80	80	100	25

Lisitzin (1974) recognized that, when fast ice is present, although the wind stress might be the same as in the open sea, the drag coefficients may be different because the roughness of the ice surface and water is different. Also, according to her, when the sea is completely covered by fast ice, the wind stress will be transferred to the coasts through the pressure exerted by the ice cover, and no effects will be transferred to the water below

the ice cover. Then water can pile up only as a result of the atmospheric pressure gradients and not wind stress.

Lisitzin (1974) selected two stations: Kemi (in the northern part of Bothnian Bay) and Vaasa (in the southern part). The principal axis of this bay is the south–southwest and north–northeast direction. From wind data over a 15-yr period (1928–42), a number of cases were selected in which the wind speed was equal to or greater than 14 $m \cdot s^{-1}$, and the wind direction was between south and west. In this manner one can make certain that the piling up of water is accentuated and the relative effects of the other factors influencing the storm surge are minimized. Finally, 40 cases were selected and the coefficient α was estimated from eq. 5.269 based on the water level data at Kemi and Vaasa. The results showed that the average value of α for the ice-free period was 3.0 and it was considerably less when ice was present.

Murty and Polavarapu (1979) examined the problem of the influence of ice cover on storm surge amplitudes in the Gulf of St. Lawrence and the St. Lawrence Estuary in eastern Canada. The following three sets of stations were selected: (1) Pointe-au-Père and Bai-Comeau, separated by the St. Lawrence Estuary, (2) Harrington Harbor and Lark Harbor, separated by the Gulf of St. Lawrence, and (3) Charlottetown and Pictou, separated by the Northumberland Strait. All the storm surge data for these stations for a period of 11 yr (1965–75) were examined to select at least one case for each month with similar meteorological characteristics. Sometimes, this was not possible (e.g. for the Pointe-au-Père–Baie-Comeau case, no satisfactory storm could be selected for the month of July). The calculations were performed in a manner essentially similar to that of Lisitzin (1974). For the Harrington Harbor–Lark Harbor case, the surges show greater amplitudes during the ice-free period. The results for Pointe-au-Père–Baie-Comeau show that the storm surge amplitudes do not significantly change between ice-free and ice cover periods. The results for Charlottetown–Pictou show greater storm surge amplitudes when ice is present. Although this disagrees with Lisitzin's result, since the data are not extensive enough, this result must be interpreted with caution. If indeed this result is correct, one explanation may be that the resonance amplification may be somehow greater during the ice cover period.

Murty et al. (1981) extended the study of Murty and Polavarapu (1979) in several respects. First, the water bodies considered in this study were the Bay of Fundy and part of the Atlantic Coast, in addition to the Gulf of St. Lawrence and the St. Lawrence Estuary. Second, a distinction was made between positive and negative surges, and this distinction is justified by the results, which show somewhat different influences of ice cover on positive and negative surge amplitudes. Third, in addition to the hourly residues, mean monthly residues were also examined for the influence of ice on them.

For the storm surge amplitude study on the Atlantic Coast, Bay of Fundy, and Gulf of St. Lawrence, the following stations were used: North Sidney, Port-aux-Basques, Pictou, Charlottetown, Harrington Harbor, Lark Harbor, and Sept-Îles. Statistical analysis of the storm surge data showed that the highest positive surges of amplitudes of about 3.0 m occurred only during the months of May–August and December, when no or little ice was present. The highest negative surges occurred during January and February, when ice was present. Murty and Holloway (1983) showed that ice cover dissipates positive surges more strongly than negative surges. The results of Henry (1975) for the southern Beaufort Sea confirm this hypothesis (see Fig. 7.26).

For the study on the St. Lawrence Estuary, the following stations were selected: Ste-Anne-des-Monts, Baie-Comeau, Pointe-au-Père, Tadoussac, Rivière-du-Loup, St-Joseph-de-la-Rive, and St-Jean-Port-Joli. In the St. Lawrence Estuary, highest positive

TABLE 5.19. Occurrence of maximum storm surge amplitudes in eastern Canadian waters during the period 1965–75.

Station	Water body	Year	Month
St. John, N.B.	Bay of Fundy	1975	December
Port-aux-Basques	Atlantic coast	1975	May, June
Pointe-du-Chêne	Gulf of St. Lawrence	1972	January
Rivière-au-Renard	Gulf of St. Lawrence	1975	August
Sept-Îles	Gulf of St. Lawrence	1975	June
Baie-Comeau	St. Lawrence Estuary	1975	August
Pointe-au-Père	St. Lawrence Estuary	1975	September
St. Joseph-de-la-Rive	St. Lawrence Estuary	1975	September
Rivière-du-Loup	St. Lawrence Estuary	1975	June, August
Quebec	St. Lawrence Estuary	1972	December
		1975	August
Tadoussac	St. Lawrence Estuary	1975	December
		1975	August, October, December

surges occurred during June, August, September, October, and December and extreme negative surges occurred during December and February. Also in the St. Lawrence Estuary, the duration of the postitive surges is shorter on the north shore and the duration of the negative surges is shorter on the south shore.

The above remarks pertain to hourly values of the storm surges, which are calculated as the residue after subtracting the hourly values of the predicted astronomical tides from the observed hourly water level values. However, when the monthly residues were examined, the results were somewhat different. In the Gulf of St. Lawrence, the extreme positive values usually occurred during October, December, and January, whereas the extreme negative surges occurred during June–September. The months in which maximum surges occurred during the 11-yr period of this study are listed in Table 5.19.

INFLUENCE OF STRATIFICATION ON STORM SURGES

Røed (1979) studied the storm surges along a straight coast in a continuously stratified sea of uniform depth. He used an analytical model and applied it to a part of the Norwegian coast. Following Røed, consider a continuously stratified sea with the origin of a Cartesian coordinate system at the undisturbed level of the free surface. The system rotates with an angular velocity $\frac{1}{2}f$ about the verical z-axis. The bottom is given by $z = -H(x, y)$ and the free surface is given by $z = \eta_S(x, y, t)$; initially, $\eta_S = 0$. The coastline is parallel to the x-axis, and the y-axis points towards the sea. It is assumed that there are no horizontal variations in density so that in the equilibrium state, the density field $\rho(z)$ and the pressure field vary with z only. Other assumptions are the hydrostatic approximation and linearization.

Using the method of normal modes (Lighthill 1969a, 1969b) the horizontal and vertical variations can be separated. To do this, expand the variables as follows:

$$(5.270)\quad V(x, y, z, t) = \sum_{n=0}^{\infty} V_n(x, y, t)\hat{\eta}_n'(z)$$

$$(5.271)\quad \eta(x, y, z, t) = \sum_{n=0}^{\infty} \eta_n(x, y, t)\hat{\eta}_n(z)$$

and

$$(5.272)\quad P(x, y, z, t) = P_S(x, y, t) + \rho_S \sum_{n=0}^{\infty} P_n(x, y, t)\hat{\eta}_n'(z)$$

where V is the horizontal velocity vector, η is the displacement of the isopycnals from their equilibrium position, P is the perturbation pressure, and P_S is the surface pressure anomaly. The eigenfunctions $\hat{\eta}_n(z)$ are solutions of the following eigenvalue problem:

$$(5.273)\quad \hat{\eta}_n'' + \frac{N^2(z)}{c_n^2}\hat{\eta}_n = 0 \text{ for } -H < z < 0$$

$$(5.274)\quad \hat{\eta}_n' - \frac{g}{c_n^2}\hat{\eta}_n = 0 \text{ at } z = 0$$

$$(5.275)\quad \hat{\eta}_n = 0 \text{ at } z = -H$$

where

$$(5.276)\quad P_n = c_n^2\eta_n$$

c_n being the eigenvalue and $N^2(z)$ the Brunt–Väisälä frequency given by

$$(5.277)\quad N^2 = -\frac{g}{\rho_S}\frac{d\rho}{dz}$$

Here, g is gravity and ρ_S is the value of the equilibrium density at the surface.

The eigenfunctions (which are orthogonal) can be normalized through

$$(5.278)\quad \int_{-H}^{0} |\eta_n'(z)|^2 dz = H$$

Then the modal equations can be written as (Gill and Clarke 1974)

$$(5.279)\quad \frac{\partial V_n}{\partial t} + fkXV_n = -c_n^2\nabla\eta_n + \boldsymbol{\tau}_n$$

$$(5.280)\quad \nabla V_n + \frac{\partial \eta_n}{\partial t} = 0$$

where the forcing function $\boldsymbol{\tau}_n$ is given by

$$(5.281)\quad \boldsymbol{\tau}_n = -\frac{\hat{\eta}_n(0)}{\rho_S H}\nabla P_S + \frac{1}{\rho_S H}\int_{-H}^{0} \frac{\partial \boldsymbol{\tau}}{\partial z}\hat{\eta}_n'(z)dz$$

Here, $\boldsymbol{\tau}$ is the tangential stress due to turbulence acting between horizontal planes whose value $\boldsymbol{\tau}_S$ at the surface is the wind stress.

The boundary conditions are the following. At the coast

$$(5.282)\quad V_n = 0 \text{ at } y = 0$$

Far away from the coast, the displacements must be bounded, i.e.

$$(5.283)\quad |\eta_n| < \infty \text{ for } y \to \infty$$

Initially

$$(5.284)\quad \eta_n = 0 \text{ and } V_n = 0 \text{ for } t = 0$$

To determine the influence of stratification on storm surges, comparison is made with the homogeneous model of Gjevik and Røed (1976) and the same pressure and wind stress distribution as used by them were also used in the stratified model. A traveling storm with no pressure fluctuations but with the following forcing was considered:

$$\begin{aligned} \tau_S &= \rho_S e^{-k(x-u_0 t)^2 i} \\ P_S &= \text{constant} \end{aligned} \tag{5.285}$$

The tangential stress $\tau(z)$ can be written as

$$\tau(z) = \rho_S \tau(z) e^{-k(x-u_0 t)^2 i} \tag{5.286}$$

with

$$\tau(0) = \tau_S$$

where u is the speed of movement of the storm and $1/\sqrt{k}$ expresses the horizontal extent of the storm.

Using eq. 5.281, the forcing function τ_n can be written as

$$\tau_n = \tau_n e^{-k(x-u_0 t) i} \tag{5.287}$$

with

$$\tau_n = \frac{1}{H} \int_{-h}^{0} \frac{\partial \tau}{\partial z} \hat{\eta}_n'(z) dz \tag{5.288}$$

If the horizontal extent $k^{-1/2}$ of the wind field is equal to or greater than the barotropic radius of deformation c_0/f, then the solution of eq. 5.279 and 5.280 in terms of displacement η_n of each mode at the coast can be written approximately as

$$\eta_n = \frac{1}{2} \frac{\tau_n}{c_n^2} \sqrt{\frac{\pi}{k}} \frac{c_n}{(c_n - u_0)} [\operatorname{erf} \sqrt{k}(x - u_0 t) - \operatorname{erf} \sqrt{k}\,(x - c_n t)] \text{ for } y = 0 \tag{5.289}$$

In the appendix of Røed (1979) it was shown that if $\sqrt{k}\, c_0/f \leq 1$ then $\sqrt{k}\, c_n/f \ll 1$ for $n > 1$.

The following representative data are used for the west coast of Norway: mixed layer thickness $h_1 = 10$ m and thickness of pycnocline layer $h_2 - h_1 = 40$ m. In this layer, the density increases linearly with depth from the surface value $\rho_S = 1.0252$ g·cm^{-3} to a value $\rho_b = 1.0275$ g·cm^{-3}. In a deep bottom layer, the density is assumed to be uniform at 1.0275 g·cm^{-3}.

The following three different forms were used for the tangential stress $\tau(z)$: (1) a stress that decreases linearly from its surface value to zero at the bottom of the mixed layer, (2) a stress that decreases linearly from its surface value to zero at the bottom of the pycnocline layer, and (3) a stress that is uniform and equal to the surface value throughout the mixed layer and decays linearly to zero at the bottom of the pycnocline layer. These three models can be expressed as

$$\tau(z) = \tau_S \begin{cases} 1 + \gamma \dfrac{z}{h_1}, & -h_1 \leq z \leq 0 \\ (1 - \gamma) \dfrac{(z + h_2)}{(h_2 - h_1)}, & -h_2 < z < -h_1 \\ 0 & -H \leq z \leq -h_2 \end{cases} \tag{5.290}$$

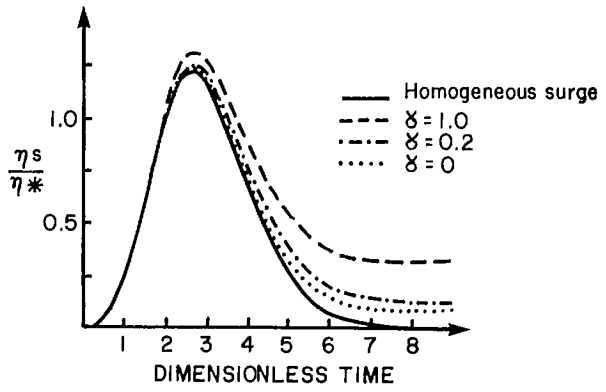

FIG. 5.49. Effect of stratification of the water body on the storm surge. Abcissa, dimensionless time; ordinate, dimensionless surge amplitude. The solid curve shows the homogeneous case and the three broken curves show the influence of stratification for the three different parameterizations of the tangential stress. (Røed 1979)

Models 1, 2, and 3 correspond to $\gamma = 1$, $\gamma = h_2/h_1$ ($=0.2$ in this study), and $\gamma = 0$, respectively.

From eq. 5.288 and 5.290 it can be shown that

$$\tau_n = \tau_S \frac{c_n^2}{gH} \frac{S_n(\gamma)}{\hat{\eta}_n(0)} \tag{5.291}$$

with

$$S_n(\gamma) = \frac{g\hat{\eta}_n(0)}{c_n^2}\left\{\gamma\hat{\eta}_n'(0) + \frac{(1+\gamma)}{(h_2 - h_1)}[\hat{\eta}_n(-h_1) - \hat{\eta}_n(-h_2)]\right\} \tag{5.292}$$

From eq. 5.276 and 5.289 the storm surge at the coast is given by

$$\eta = \frac{1}{2}\frac{\tau_S}{gH}\sqrt{\frac{\pi}{k}}\sum_{n=0}^{\infty}\frac{c_n S_n(\gamma)\hat{\eta}_n(z)}{(c_n - u_0)\hat{\eta}_n(0)}[\text{erf}\sqrt{k}\,(x - u_0 t) - \text{erf}\sqrt{k}\,(x - c_n t)] \tag{5.293}$$

It was shown in the appendix of Røed(1979) that $c_n S_n(\gamma)/(c_n - u_0)$ decays as n^{-3} where $\hat{\eta}(z)/\hat{\eta}(0)$ grows as n^2 unless $z = 0$. Hence, the storm surge at the coast can be reasonably well approximated by truncation of the series after six to seven terms.

The effect of stratification on the storm surge for the three different tangential stress formulations is shown in Fig. 5.49. It can be seen that stratification has little influence on storm surge. The above analysis is for the case with no bottom friction. Obviously, inclusion of bottom friction will reduce the amplitude of the surge. Next, a two-layer model for storm surges (and tides), after Heaps (1981) and applied by Heaps and Jones (1981) to the Irish Sea, will be briefly discussed. In this model, although stratification is not included, the vertical eddy viscosity is given different values in the top and bottom layers. The results of these models will be considered in section 7.3.

Chapter 6

Meteorological Problems

This chapter will discuss the dynamics of extratropical cyclones and tropical cyclones and the meteorological problems associated with these cyclones in the Pacific, Atlantic, and Indian oceans, as well as in other smaller water bodies. The problems associated with obtaining wind stress data for synoptic scale and mesoscale weather systems will be examined in detail.

6.1 Extratropical Cyclones

The treatment in this section follows closely Petterssen (1956a, 1956b). Fitz-Roy (1863) appears to be among the first to propose a model of an extratropical cyclone as originating on the boundary between two different air masses (e.g. a warm and moist air mass originating in subtropical latitudes and a colder and drier air mass originating in the polar regions). Some later authors who recognized that discontinuities in temperature, moisture content, and speed of motion were essential for cyclone development were Blasius (1875), Helmholtz (1888, 1889), Margules (1905), and Shaw (1921).

Bjerknes (1919) proposed the first dynamical model for cyclones and agreed with Margules (1905) that the kinetic energy of the cyclones comes from the potential energy due to the juxtaposition of warm and cold air masses and a decrease of the potential energy follows the development of a cyclone. According to Bjerknes the cold air forms a wedge under the warm air, with a slope of separation of about 1:100, and the cyclonic disturbances travel along the frontal surface similar to waves traveling along a discontinuity.

The life cycle of a cyclone has several stages. In the initial stage, a small amplitude wave forms on a more or less straight quasi-stationary front. The currents on either side of the front could be in the same direction or in opposite directions. In the second stage, the warm air rises to higher levels over the warm front and the cold front wedges in under the warm air. In the third stage, the warm air sectors become progressively narrower and the cold front tends to overtake the warm front. At this stage the cyclone has reached the occlusion stage.

It is customary to refer to cyclone families, rather than individual cyclones (Fitz-Roy 1863). Usually there would be two to four or five cyclones in a series, one following the other and all moving in a general southwest to northeast direction. Bjerknes and Solberg (1921, 1922) accounted for cyclone families as wave disturbances on the polar front. In a family of four cyclones, typically the first one would be old and occluded, the second would be somewhat younger, the third would be a young wave cyclone, and the fourth would be a nascent cyclone wave. On the average, a cyclone family takes 5–6 d to pass a given location. The occurrence of cyclone families is a regular phenomenon over the North Atlantic and western Europe (because of regular major polar outbreaks from the Greenland–Labrador area) and not as regular over North America and central Eurasia.

Usually, cyclone formation begins near sea level and develops to higher levels in the atmosphere as the occlusion develops. Once a complete occlusion occurs, generally a closed cyclonic circulation can be found in the middle and upper troposphere (located over the cold rear of the occluded sea level cyclone). Sometimes, the depression in the pressure field aloft may merge with the semipermanent low over the polar region. When this

happens, a high-level trough can be noticed in the rear of the occluded sea level cyclone. Thus, these upper level troughs represent the vertical extension of the cyclones. However, sometimes (particularly during winter), cyclone development may begin at the higher levels and at other times simultaneously with the lower level development. One refers to these more or less independent developments aloft (middle and upper troposphere) as "cutoff cyclones."

Next, the thermal structure of cyclones will be briefly examined. At sea level there is no definite thermal pattern and irregularities occur because of the diurnal variations, cloud cover, etc. However, at higher levels the temperature distribution is simpler (but the frontal structures aloft are not as sharp as at sea level).

The thermal structure at the 500-mb level for a 1-d-old cyclone is shown in Fig. 6.1. This diagram is for typical winter conditions. Note the zone of demarcation between the Arctic air and the warmer polar air. In the summer, usually the Arctic air is absent at the upper levels and the temperatures everywhere are greater than shown here. In this diagram, note the uniformity of the temperatue aloft on the equatorial side of the sea level front (this uniformity is due to the fact that the air is not involved in any significant vertical motion). It is convenient to represent the thermal structure of cyclones by the thickness of any layer bounded by two isobaric surfaces (it can be shown that the thickness of a layer between two isobaric surfaces is proportional to the average temperature of the layer).

Sources and Sinks of Vorticity

In determining the movement of weather systems, the thermodynamic influences due to geographically bound heat and cold sources and the mechanical influences due to mountain ranges must be taken into account. The rate of change (following the motion) of the potential temperature represents the strength of the thermal source. Petterssen (1956) showed that

$$(6.1) \qquad \nabla \cdot (QV) = F - \frac{\partial Q}{\partial \theta} \dot{\theta}$$

where Q is the component of absolute vorticity normal to the surface of constant potential temperature, V is the velocity vector, and the dot over θ denotes differentiation with respect to time. The term on the left side of eq. 6.1 is the export per unit time of vorticity through the boundaries of a unit area in a surface of constant potential temperature. Such an export is determined by the vorticity of the frictional force F and the strength $\dot{\theta}$ of the thermal source.

It can be seen from eq. 6.1 that the influence of a thermal source varies accordingly as the vorticity increases or decreases in the direction of increasing potential temperature. Noting that in the mean state, the slope of a θ surface is of the order of 10^{-3} and since θ increases with height, the signs of $\partial Q/\partial \theta$ and $\partial Q/\partial z$ will be the same. Hence, a cold source will make a positive contribution if the absolute vorticity increases with height (a heat source makes a positive contribution if the absolute vorticity decreases with height). These concepts will now be applied to the polar regions, the midlatitude belt, and the intertropical belt.

As shown in Fig. 6.2, consider an idealized circular continent (or region of ice) centered at the pole and surrounded by water of significantly greater temperature. As shown in Fig. 6.2A, the surfaces of constant potential temperature form domes over the

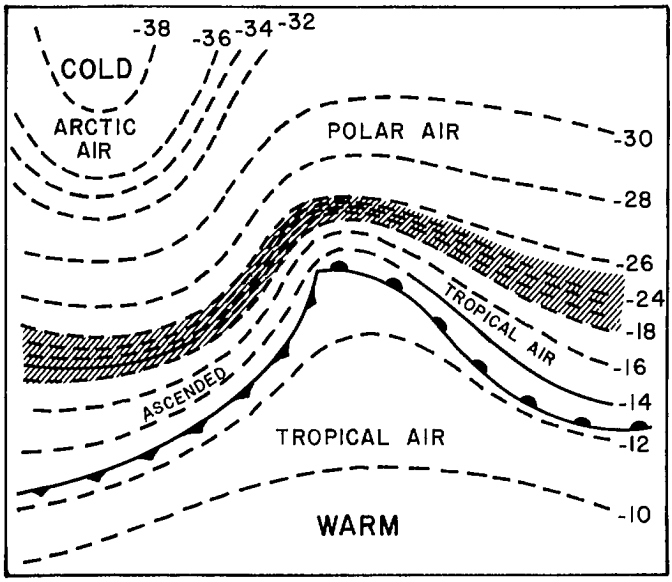

FIG. 6.1. Schematic representation of the isotherms at the 500-mb level associated with a wave cyclone. The front at sea level is represented by conventional symbols (◓, warm front; ▼, cold front) and the frontal zone at the 500-mb level is represented by a hatched ribbon. An Arctic frontal zone farther to the north is also indicated. The temperatures (degrees celcius) represent typical winter conditions. (Petterssen 1956)

cold continent. Note the great concentration of isotherms along the coast during the winter season (which this diagram represents).

An air mass moving into the Arctic in the winter season is cooled (partly through heat loss to the underlying surface and partly through radiation), i.e. $\dot{\theta}$ is negative. Since the surroundings of the polar region are warmer, the horizontal pressure gradient must increase with height. If it is assumed that the geostrophic relation is valid (i.e. the pressure force is balanced by the Coriolis force), then the relative as well as the absolute vorticity must increase with height. Since θ also increases with height, eq. 6.1 shows that the thermal component of the vorticity source must be positive.

To evaluate the frictional component, note that the average pressure distribution and the vorticity of the motion in the Arctic at low levels are anticyclonic (i.e. clockwise in the Northern Hemisphere). Since friction acts against the motion, the vorticity of the frictional force must be cyclonic, i.e. F is positive in eq. 6.1. Hence, both the thermal and the frictional forces are a positive vorticity source in the Arctic. One can visualize from eq. 6.1 that the absolute vorticity thus created is exported towards the surrounding warmer waters along θ surfaces (see Fig. 6.2). Since the Coriolis parameter decreases in this direction, in the region of the maximum concentration of isotherms, an even larger export of relative cyclonic vorticity takes place. Since the pressure force must mainly balance the Coriolis force, a low pressure area must exist along the Arctic coasts. The configuration shown in Fig. 6.2B usually appears in the Antarctic, since the distribution of land and oceans is not symmetric. The northern parts of North America and Eurasia act as cold

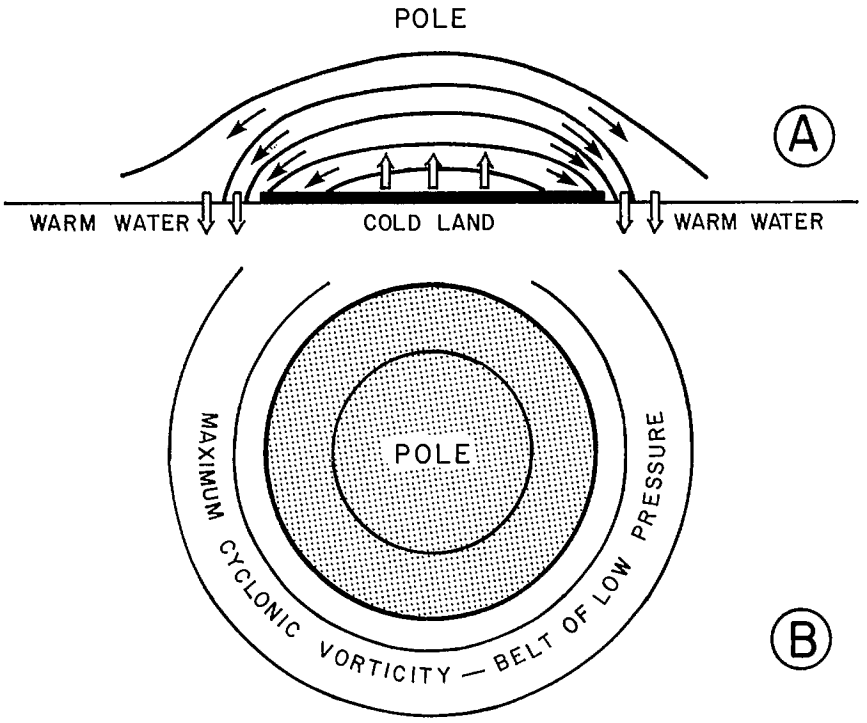

FIG. 6.2. (a) Schematic representation of surfaces of constant potential temperature (θ-surfaces) over a cold continent. Single-shafted arrows indicate the vorticity export. Double-shafted arrows indicate transfer of vorticity to and from the earth's surface. (b) Resulting pressure field at sea level. (Petterssen 1956)

sources in winter, and cyclonic vorticity is exported zonally as well as meridionally towards the North Atlantic and North Pacific. Hence, cyclonic activity occurs over the northern parts of these oceans (Fig. 6.3). One should also expect maxima of cyclonic activity over nonfrozen water bodies surrounded by land. Examples are the Great Lakes of North America, the warm bays on the edge of Arctic ice fields, the Black Sea, the Caspian Sea, the Mediterranean Sea, and the Baltic Sea. Observations bear out this situation for the winter months.

During summer, in the northern regions, the continents are warm and the principal temperature differences are found along the northern coasts and along the boundaries between cold and warm ocean currents in higher latitudes. In this case, vorticity is mainly exported from oceans to the continents and from cold to warm ocean currents. Hence, low pressure areas will develop over the northern parts of the continents.

Next, consider the midlatitude belt. There are several problems in trying to use the vorticity transfer concepts in this region. (1) Nothing definite can be prescribed about the thermal sources. For example, the northern part of the North Atlantic Ocean is an intense heat source for air masses traveling from the Arctic, whereas it is a weak cold source for air masses propagating from the subtropical regions. Another example is the Eurasian continent, which is a cold source (in winter) for air masses coming from the Atlantic

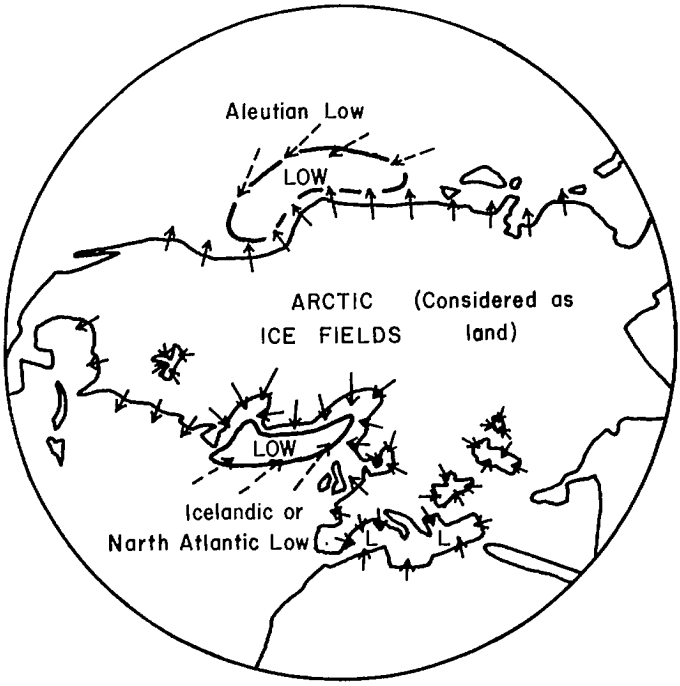

FIG. 6.3. Schematic representation of the vorticity export from cold land to warmer water. Broken arrows indicate northward drift of cyclones. (Petterssen 1956)

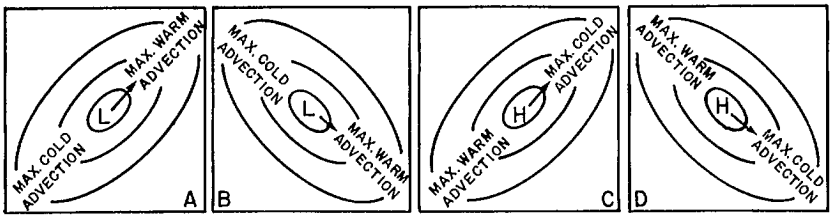

FIG. 6.4. Meridional movement of cyclones and anticyclones. (Petterssen 1956)

whereas it is neutral to air masses traveling from the Arctic. Hence, in the midlatitude belt the thermal sources are not absolute but can be identified relative to the moving cyclones and anticyclones. (2) The latent heat liberation must be considered and this also must be defined with reference to the mobile systems. (3) The two main assumptions in deriving eq. 6.1 (namely stationariness of Q and θ and no correlation between the variables) are not satisfied.

Note that cyclones and anticyclones in this region mainly move along the gradient of the Laplacian of the thermal advection. In an idealized case, as shown in Fig. 6.4, cyclones move in the direction from cold to warm advection. Thus, cyclones of the type in Fig. 6.4A will move poleward, whereas those of the type in Fig. 6.4B will move toward the equator. In the Northern Hemisphere, the principal frontal zones are so oriented that

cyclones will mainly be of the type in Fig. 6.4A. Cyclones of the type in Fig. 6.4B occur mainly in winter on a trailing front that extends from the Canadian west coast to the Great Lakes (these so-called "Alberta lows" usually travel southeast or east–southeast). Also, cyclones of the type in Fig. 6.4B occur on any frontal zone with an unusual orientation.

In the intertropical belt, there is a high degree of stationariness and eq. 6.1 holds accurately. Both the frictional and the thermal components of the vorticity source are positive in the tradewind belt and, hence, absolute vorticity must be exported from this zone. The following are the vorticity sinks: (1) the doldrums are a frictional sink of vorticity, (2) the monsoon systems are the thermal lows over the southern continents, and (3) vorticity is exported near the western edges of the subtropical anticyclones and delivered to the westerlies.

Next, the influence of the mountains on the vorticity transfer will be examined. In midlatitudes, the horizontal vorticity vector Q will be directed towards north and if mountain chains are oriented in a north–south direction (e.g. the Rockies), then the gradient of the vertical velocity ∇w_n will be mainly zonal and the vectors q_H and $\nabla\omega$ will be almost perpendicular to each other (here, subscript H denotes horizontal and ω denotes the vertical velocity with reference to pressure as a vertical coordinate). The vorticity equation can be written as

$$\frac{\partial Q}{\partial t} = -V\cdot\nabla Q - DQ - w_n\frac{\partial Q}{\partial n} \tag{6.2}$$

where Q is the component of absolute vorticity normal to the surface, q is the vorticity vector tangent to the surface, and n measures the length along the normal. This equation can be rewritten as

$$\frac{\partial Q}{\partial t} = -\nabla_3\cdot(QV) + Q\frac{\partial w_n}{\partial n} \tag{6.3}$$

where V is the three-dimensional wind vector and ∇_3 is the three-dimensional operator. In this equation, $\partial Q/\partial t$ is the accumulation per unit time of absolute vorticity in a unit area of a surface of constant potential temperature. The term $-\nabla_3\cdot(QV)$ represents the import per unit time of Q into a unit volume of unit cross-section in the same surface. The term $Q\partial w_n/\partial n$ is the intensity of the vorticity source, which is determined mainly by the amount of stretching or shrinking perpendicular to the surfaces of constant potential temperature. A significant upper level trough travels over a mountain chain; the leeward side will act as a vorticity source and the windward side will act as a sink.

Cyclone Patterns

The patterns of cyclogenesis during winter will be examined first. In the North Pacific Ocean a zonal pattern exists around 30–35°N. Also, over the continents, large maxima of cyclogenesis occur in the lee of great mountain chains. These patterns are not sensitive to seasonal variations. Three pronounced maxima are associated with the Rockies: Sierra Nevada, Colorado, and Alberta regions. Similar maxima can be located to the east of the Appalachian Mountains, the Scandinavian mountains, and also in East Asia.

If the frequency of cyclone centers is examined, the influence of mountain ranges can be seen even more. Examples are the leeward side of the Colorado and Alberta ranges. The cyclones that develop here are mostly of short duration, whereas those that develop in the lee of the Appalachians and the mountains in East Asia are of longer duration and they also move faster. All major unfrozen inland water bodies show maxima of cyclone

centers during winter. In the Mediterranean Sea, there is a maximum on both sides of the Italian Peninsula. Other examples are the Great Lakes, the Black Sea, the Caspian Sea, the Aral Sea, and the Baltic Sea. Hudson Bay, which freezes over by early December, does not show a pronounced maximum similar to the Great Lakes.

Warm water bodies surrounded by colder land masses also show pronounced cyclogenesis. Examples are (1) the Gulf of Alaska in winter, (2) Baffin Bay and Davis Strait in winter, as well as in summer, (3) Denmark Strait, mostly in the winter, and (4) the Barents Sea in winter.

One can account for the large cyclone frequency over the northern portions of the North Atlantic and North Pacific oceans due to local thermal sources as well as due to the poleward flux of cyclones from the midlatitude belt.

In the subtropics, during summer, cyclogenesis occurs over large areas. Examples are the regions south of California and West Africa.

Next, two terms are introduced: "blocking" and "index cycle." In the midlatitudes, the cyclones travel towards the east. Superimposed on this zonal motion is a meridional motion. The thermal wind in the middle troposphere to some extent guides the movement of the cyclones. Sometimes, when a warm cutoff high forms in the middle and upper troposphere, cyclones at sea level are steered either to the south or to the north of these highs. This phenomenon is referred to as the "blocking" of the sea level cyclones and occurs predominantly off the west coasts of Europe and North America. The blocking is more common in the Atlantic Ocean than in the Pacific Ocean and is highest in April and least during August to September.

The general circulation of the atmosphere not only undergoes an annual variation but also undergoes irregular quasi-cyclic changes with periods ranging from 3 to 8 wk. The intensity of the zonal circulation is expressed by the average pressure difference between two latitude circles. Ordinarily, the latitudes chosen are 35 and 55°N; the average sea level pressure difference between the latitude circles is referred to as the "zonal index."

Bradbury (1954) studied the frequency of cyclones during high and low index situations during the period 1900–39. She found that during summer, the cyclone frequency is greater in high latitudes during high index periods and in low latitudes during low index periods. The differences are not as pronounced in winter. During winter, large areas of high cyclone frequency occur during high index periods (a) over the North Pacific Ocean north of 50°N, (b) over the North Atlantic Ocean north of 50°N and to the east of 45°W, and (c) along the southern coast of the United States. During low index periods in winter, high cyclone frequency occurs (a) over the central part of the North Pacific Ocean to the south of 45°N, (b) over the western part of the North Atlantic Ocean, and (c) over the Mediterranean Sea.

Instability Theories of Cyclone Formation

Margules (1905) speculated that the potential energy associated with horizontal temperature gradients provides the kinetic energy of cyclones. Solberg (1936) showed that frontal cyclones will grow as a result of the inherent instability of the polar front (similar to the growth of a wave at a discontinuity). Charney (1947), Eady (1949), Berson (1949), and Fjortoft (1950) have shown that the baroclinicity of the zonal current may lead to instability in which the kinetic energy of the growing perturbations is derived from the potential and internal energies due to horizontal thermal gradients. Kuo (1949) and Fjortoft (1950) showed that certain categories of horizontal velocity patterns across a zonal current will lead to instability.

It has generally been observed that cyclones develop within a period of 1−3 d. In this short time scale, it is customary to assume that the motion is adiabatic and frictionless. Another assumption is that even during growth, the energy of an unstable zonal current is conserved. Let K, P, and E denote the kinetic, potential, and internal energies, respectively. Hence, according to the above assumptions:

(6.4) $K + P + E = \text{constant}$

The kinetic energy per unit mass can be expressed as

$$\frac{1}{2}V^2 = \frac{1}{2}\bar{V}^2 + \bar{V}\cdot V' + \frac{1}{2}V'^2$$

where $\bar{V}$ is the averaged velocity of the undisturbed current and V' is a deviation from this value. The kinetic energy K can be determined by integration over the total mass. During this integration, the second term on the right side of the above equation disappears. Hence

(6.5) $K = K_m + K_d$

where K_m and K_d are the integrated forms of the first and third terms, respectively, and these are referred to as the kinetic energy of the mean current and the kinetic energy of the perturbation. Equation 6.5 may be rewritten as

(6.6) $K_d + K_m + P + E = \text{constant}$

Since K_d represents the average intensity of all the disturbances, for the growth of these, K_d must increase with time. This means that K_d can increase only at the expense of one of the three sources K_m, P, or E or from combinations of these.

Next, the potential energy of a column of air of unit cross-section is given by

$$P = \int_0^\infty gz\rho dz$$

Using the hydrostatic equation $dp = -g\rho dz$ and integrating by parts:

$$p = \int_0^{p_0} z d\rho = [zp]_{p=p_0} - [zp]_{p=0} - \int_0^{p_0} p\frac{\partial z}{\partial p}dp$$

where p_0 is the pressure at the bottom of the air column. In this equation, on the right side the first term becomes zero at $z = 0$ (bottom of the air column) and the second term vanishes because $pz \to 0$ as $p \to 0$. The third term becomes, after noting $\alpha = 1/\rho$ where α is the specific volume,

$$p = \int_0^\infty pdz = \int_0^\infty p\alpha\rho dz$$

The equation of state is

$$\alpha P = RT$$

where R is the gas constant and T is the temperature. Using this, the above equation becomes

(6.7) $$P = R\int_0^\infty T\rho dz$$

The internal energy of the air column may be written as

$$E = C_v \int_0^\infty T\rho dz \tag{6.8}$$

where C_v is the specific heat of air at constant volume. Hence

$$\frac{P}{E} = \frac{R}{C_v} \sim 0.4 \tag{6.9}$$

Thus, it can be seen that the potential and internal energies of a column of air (from the sea level to the top of the atmosphere) will change proportionately to each other. For this reason, the potential and internal energies in eq. 6.6 should not be treated as two different energy sources; hence, only two energy sources exist for the perturbations to amplify: (1) the kinetic energy K_m of the mean motion and (2) the sum of the potential and internal energies $P + E$.

The perturbations of the basic zonal current may grow through three different types of instability. The first one is the so-called linear current instability. The energy for the perturbations is derived from the kinetic energy of the basic current. This instability mechanism is similar to the hydrodynamic instability of a linear flow of a homogeneous and incompressible fluid between two parallel walls. The second type of instability is referred to as baroclinic instability. In this case, the potential and internal energies of the basic baroclinic current supply the energy for the growth of the disturbances. The third type of instability is referred to as Solberg–Holland instability. Solberg (1936) considered a system that initially consists of two barotropic layers separated by a sloping frontal surface in the east–west direction. Both layers are assumed to move towards the east, with the warmer (southern) layer moving faster. He found that waves with lengths less than a few kilometres and also those with lengths between 1000 and 3000 km will amplify and waves with lengths in the remaining range will dissipate. The growth of the waves with lengths shorter than a few kilometres is similar to the classical Helmholtz instability problem, and these short waves are of no relevance to the cyclone problem. A sharp discontinuity is essential for their generation. The growth of waves with lengths of 1000–3000 km can account for the growth of cyclone disturbances.

It can be shown that each of these barotropic layers can give rise to stable wave motion. The wave motion in each layer can be tuned so that each can grow as a result of a resonance effect. In this type of instability the disturbances derive energy from the kinetic energy of the mean motion whereas the potential and internal energies are sink terms.

The Development Equation

Bjerknes (1937) expressed the cyclogenesis problem in terms of an instability of the frontal surface. On the other hand, Sutcliffe (1947) formulated the same problem in terms of vertical velocity and divergence, and this approach is more suitable from a synoptic meteorology point of view whereas Bjerknes' approach is a problem in dynamic meteorology.

In synoptic meteorology for forecasting purposes, emphasis is given to vertical velocity and divergence. Adiabatic cooling due to upward motion mainly determines the rates of condensation and precipitation, whereas divergence in the atmosphere is very important for the development of cyclones. However, the magnitudes of vertical velocity and divergence in the atmosphere are small, as will be seen below.

In a coordinate system in which the pressure field p is the vertical coordinate, the vertical velocity ω can be expressed as

$$\omega = \frac{dp}{dt} \tag{6.10}$$

In this coordinate system, the continuity equation can be written as

$$D = -\frac{\partial \omega}{\partial p} \tag{6.11}$$

where D is the divergence (which is determined by the variation of the vertical velocity in the vertical direction). Thus, if the motion is entirely horizontal, the divergence would be zero and the absolute vorticity of each air parcel would be conserved. Scale considerations show that divergence in excess of $10^{-4} \cdot s^{-1}$ occurs in tornadoes and possibly in tropical storms during periods of rapid development. Divergence of up to $4 \times 10^{-5} \cdot s^{-1}$ can be found in upper air troughs and values up to $2 \times 10^{-5} \cdot s^{-1}$ can be seen in rapidly developing and fast-moving sea level cyclones.

Next, the concept of Dines compensation will be introduced. Let the average divergence in an air column stretching between two isobaric surfaces be denoted by $\bar{D}$. Integration of the continuity equation 6.11 gives

$$\bar{D}(p_1 - p_0) = -(\omega_1 - \omega_0) \tag{6.12}$$

where subscripts 0 and 1 refer to the lower and upper levels, respectively. If the two levels considered are the sea level and the top of the atmosphere, then $p_1 = 0$, $\omega_1 = 0$, and eq. 6.12 becomes

$$\bar{D} = -\frac{\omega_0}{1000} \tag{6.13}$$

taking $p_0 \sim 1000$ mb. The air parcel at sea level is restricted to horizontal motion, then ω_0 is small and has the same order of magnitude as the local pressure change $\partial p_0 / \partial t$. Thus, taking a local pressure change as high as 10 mb in 3 h, the mean divergence of the air column will be less then $10^{-6} \cdot s^{-1}$. Hence, the average divergence of an air column stretching from sea level to the top of the atmosphere will be at least an order of magnitude smaller than the typical values for traveling cyclones. Hence, it follows that the divergence must change its sign at least once in the air column so that its average value is small. Dines (1912, 1929) suggested that boxes of convergence and divergence alternate in the atmosphere so that the net divergence almost vanishes. This concept is referred to as "Dines compensation." Sutcliffe (1947) made use of this concept in his formulation of the so-called development equation in which he takes the amount of convergence as an indication of the rate of development.

Let C be the velocity of the cyclone movement and $\delta Q / \delta t$ be the local rate of change of vorticity at a point whose position with reference to the moving cyclone is the same. Then

$$\frac{\delta Q}{\delta t} = \frac{\partial Q}{\partial t} + C \cdot \nabla Q \tag{6.14}$$

The vorticity equation can be written as

$$\dot{Q} = \frac{\partial Q}{\partial t} + V \cdot \nabla Q = \frac{\delta Q}{\delta t} + (V - C) \cdot \nabla Q = -DQ \tag{6.15}$$

It can be seen that a portion of the divergence goes into the intensification of the vorticity system at the rate $\delta Q / \delta t$ whereas the rest goes into advecting the vorticity with the velocity $V - C$ relative to the moving system. From geostrophic considerations, the

vorticity tendency may be expressed as (which relates observed height changes to vorticity tendency)

$$(6.16) \quad \frac{\partial Q}{\partial t} = \frac{g}{f}\nabla^2 \frac{\partial z}{\partial t}$$

where z is the height of an isobaric surface and f is the Coriolis parameter. If it is assumed that the density is horizontally uniform:

$$(6.17) \quad \frac{\partial Q}{\partial t} = \frac{\alpha}{f}\nabla^2 \frac{\partial p}{\partial t}$$

where α is the specific volume. From earlier discussion, it has been seen that there is at least one level in the atmosphere where the divergence vanishes. At this level, the vorticity equation 6.15 reduces to

$$(6.18) \quad \frac{\partial Q}{\partial t} + V \cdot \nabla Q = -\omega \frac{\partial Q}{\partial p} \text{ at } D = 0$$

where V is the horizontal wind.

Let V_0 denote the wind field at 1000 mb and V_T be the thermal wind between 1000 mb and the level of nondivergence. Then

$$(6.19a) \quad V = V_0 + V_T$$

The absolute vorticity at the level of nondivergence is

$$(6.19b) \quad Q = Q_0 + Q_T$$

where Q_T is the vorticity of the thermal wind.

The following can also be written:

$$\frac{\partial Q}{\partial p} = \frac{\partial q_T}{\partial p}$$

since $D = 0$ at the level of nondivergence:

$$D_0 = -D_T$$

Hence, the divergence at sea level (or at 1000 mb) is equal to the convergence of the thermal wind. From eq. 6.18

$$(6.20) \quad \dot{Q}_0 = -D_0 Q_0 = -\frac{\partial q_T}{\partial t} - V \cdot \nabla q_T - V_T \cdot \nabla Q_0 - \omega \frac{\partial q_T}{\partial p}$$

Here, the dot denotes the derivative with respect to time, and terms without a subscript refer to the level of nondivergence.

Since thermal wind is a measure of the baroclinicity in the atmosphere, it can be seen that vorticity can neither be created nor destroyed at sea level, for a barotropic state. However, baroclinicity (although a necessary condition) is not a sufficient condition for development because the terms on the right side of eq. 6.20 may be in balance. The value of the so-called development equation 6.20 lies in the fact that it shows that the rate of production of vorticity and divergence at sea level can be determined solely from the conditions existing below the level of nondivergence. Hence, it is important to know where the level of nondivergence exists.

It can be shown that the last term on the right side of eq. 6.20 makes only a small

contribution; hence, this will be ignored. Also, using eq. 6.19 and noting that

$$\dot{Q}_0 = \frac{\partial Q_0}{\partial t} + V_0 \cdot \nabla Q_0$$

eq. 6.20 reduces to

$$\frac{\partial Q_0}{\partial t} = -V \cdot \nabla Q - \frac{\partial q_T}{\partial t} \tag{6.21}$$

where V and Q refer to the level of nondivergence. Let A_q and A_T denote the vorticity advection at the level of nondivergence and the thickness advection from 1000 mb to the level of nondivergence, respectively.

Sutcliffe (1947) found a convenient expression for $\partial q_T/\partial t$ as follows. Let the adiabatic and the actual lapse rates in terms of height be denoted by γ_a and γ, respectively, and let Γ_a and Γ be the corresponding parameters in terms of pressure. From the hydrostatic relation

$$-\delta p = \rho g \delta z \tag{6.22}$$

the following can be written:

$$\Gamma_a = \frac{1}{\rho g}\gamma_a \text{ and } \Gamma = \frac{1}{\rho g}\gamma \tag{6.23}$$

The first law of thermodynamics may be written as

$$\frac{\partial T}{\partial t} = -V \cdot \nabla T + (\Gamma_a - \Gamma)\omega + \frac{1}{C_p}\frac{dW}{dt} \tag{6.24}$$

where C_p is the specific heat of air at constant pressure, $-V \cdot \nabla T$ is the horizontal advection of temperature, and dW/dt is the heat (other than latent heat) supplied or extracted from a unit mass of air in unit time. It can be seen from eq. 6.24 that the temperature tendency (i.e. local rate of change of temperature) is made up of three contributions: (1) the horizontal advection, (2) the adiabatic change, and (3) the changes due to nonadiabatic heating or cooling.

Integration of eq. 6.24 with respect to log p from 1000 mb to the level of nondivergence gives an expression for the thickness tendency:

$$\frac{\partial q_T}{\partial t} = \frac{R}{f}\nabla^2\left\{\frac{g}{R}A_T + \log\left(\frac{p_0}{p}\right)\left[\overline{\omega(\Gamma_a - \Gamma)} + \frac{1}{C_p}\overline{\frac{dW}{dt}}\right]\right\} \tag{6.25}$$

where R is the gas constant and the bar denotes mean values through the layer. For convenience define

$$\begin{aligned} \log\left(\frac{p_0}{p}\right)\overline{\omega(\Gamma_a - \Gamma)} &= S \\ \log\left(\frac{p_0}{p}\right)\frac{1}{C_p}\overline{\frac{dW}{dt}} &= H \end{aligned} \tag{6.26}$$

Then, eq. 6.25 becomes

$$\frac{\partial q_T}{\partial t} = \frac{R}{f}\nabla^2\left(\frac{g}{R}A_T + S + H\right) \tag{6.27}$$

Equation 6.21 becomes

$$(6.28)\quad \frac{\partial Q_0}{\partial t} = A_Q - \frac{R}{f}\nabla^2\left(\frac{g}{R}A_T + S + H\right)$$

$$= A_Q - \frac{g}{f}\nabla^2 A_T - \frac{R}{f}\nabla^2 S - \frac{R}{f}\nabla^2 H$$

Equation 6.20 becomes

$$(6.29)\quad \dot{Q}_0 = -Q_0 D_0 = A_Q + V_0 \cdot \nabla Q_0 - \frac{R}{f}\nabla^2\left(\frac{g}{R}A_T + S + H\right)$$

Since $V_0 \cdot \nabla Q_0$ makes only a small contribution, it can be seen that at sea level the vorticity production $\dot{Q}_0$ and the vorticity tendency $\partial Q_0/\partial t$ are about the same.

It can be seen from eq. 6.28 that the development at sea level is due to the imbalance between the vorticity advection at the level of nondivergence and the Laplacian of the thermal components A_T, S, and H. From synoptic weather charts one can routinely calculate the vorticity advection and thickness advection. However, the contributions from adiabatic and nonadiabatic temperature changes require special treatment.

In eq. 6.28 if the atmosphere were at rest relative to the earth, the terms A_Q, A_T, and S would be zero. Then this equation becomes

$$\frac{\partial q_0}{\partial t} = -\frac{R}{f}\nabla^2 H$$

Since it is assumed that the atmosphere is at rest, relative vorticity is created only due to thermal sources (heat sources create cyclonic vorticity and cold sources generate anticyclonic vorticity). Examples of weather systems generated in this manner are monsoons, land and sea breezes, mountain and valley winds, etc.

Earlier it was seen that geographical distribution of thermal sources could lead to development. In the case of a water body surrounded by colder land, H in eq. 6.23 will be positive and $\nabla^2 H$ will be negative, and this makes a positive contribution to the vorticity tendency. For the case of cold land surrounded by warmer water, $H < 0$ and $\nabla^2 H < 0$ and a negative contribution is made. It is not so much the amount of heating or cooling that matters, but it is the pattern or the Laplacian of the thermal process that is relevant.

Geographically fixed thermal sources are mainly important only locally and they cannot influence cyclone development over long durations. A more important source is the nonadiabatic heating or cooling associated with the movement of an air mass over a nonuniform surface. The heat loss or gain during such a motion is distributed through deep layers in the atmosphere by eddy exchange. Since the nonadiabatic thermal pattern is somewhat in tune with the mobile systems, it is more effective for development. These nonadiabatic influences will make a positive contribution to cyclone development in situations where an air mass moves from a colder to a warmer surface. Examples of cyclone development and intensification due to nonadiabatic influences can be found over the Great Lakes in winter and in cyclones entering the North Atlantic from North America.

In eq. 6.28, the term containing A_T denotes the thickness advection. Again, it is the Laplacian of the advection that is important. Noting that thermal advection has a positive maximum ahead of a developed cyclone and a negative minimum in the rear, one can see that the Laplacian of the advection will make a positive contribution ahead and a negative contribution in the rear of a cyclone, and the contribution at the center of the cyclone is minimal. Basically, the thickness advection creates an asymmetry in the development

process so that positive vorticity production occurs in the area of maximum warm advection and negative vorticity production occurs in the region of maximum cold advection. Noting that the center of the cyclone moves in the direction of increasing vorticity tendency, it can be seen that the main contribution of the thickness advection is to the movement of the cyclone.

The thermal and thickness advections are usually opposed by the nonadiabatic effects due to the underlying surface. In eq. 6.28 the thermal terms S and H are usually difficult to determine from synoptic charts. Means (1954) used the following equation to calculate the vorticity changes associated with cyclones:

$$\frac{\partial Q_0}{\partial t} = A_Q - \frac{g}{f}\nabla^2 A_T \tag{6.30}$$

This equation gave patterns of $\partial Q_0/\partial t$ that more or less agree with observed patterns but the actual values were overestimated by a factor of 2 to 4. According to Petterssen (1956), this exaggeration reflects the circumstance that the effect of thermal advection is normally opposed by the effects of adiabatic and nonadiabatic temperature changes.

Note that the thermal advection is mainly determined by the circulatory motion around cyclones. In the first stages of cyclone development when the front wave is forming, the thermal advection is rather small. Hence, initially some other mechanism produces thermal advection. Once the temperature field is distorted due to the circulatory motion around cyclones, further contributions are made from $(g/f)\nabla^2 A_T$ and the system is self-developing.

Next, the vorticity advection (vorticity advection is positive when the wind blows from high towards low values of vorticity) is briefly considered. Petterssen (1956) noted that the vast majority of cyclogenesis at sea level occurs when the area of positive vorticity advection ahead of an advancing trough becomes superimposed upon a quasi-stationary or slowly moving front along which the thermal advection is discontinuous. One of the most reliable indicators of sea level cyclogenesis is this overtaking by an upper trough (with positive vorticity advection ahead of it) of a frontal system in the lower troposphere. Usually, a steepening and intensification of the frontal zone occurs after this overtaking.

To derive an expression for the vorticity advection, write for the absolute vorticity:

$$Q = VK_S - \frac{\partial V}{\partial n} + f$$

The vorticity advection A_Q is

$$A_Q = -V\frac{\partial Q}{\partial S}$$

where S is the length along the streamlines or contours. Note that the shear and the Coriolis parameter do not change much along the streamlines. Hence, one can write

$$A_Q = -V\left(V\frac{\partial K_S}{\partial S} + K_S\frac{\partial V}{\partial S}\right) \tag{6.31}$$

The term $\partial V/\partial S$, which denotes confluence, may be replaced with VK_n where K_n is the orthogonal curvature (note that K_n is positive or negative depending on whether the streamlines converge or diverge in the downwind direction). Thus

$$(6.32) \quad A_Q = -V^2\left(\frac{\partial K_S}{\partial S} + K_S K_n\right)$$

Thus, the vorticity advection is proportional to the square of the wind speed. Hence, in the jet stream, one could expect very large vorticity advection (provided the streamline structure is suitable).

In Fig. 6.5A the streamlines are sinusoidal and parallel. Hence, $\partial K_S/\partial n$ is negative downwind from the trough (positive upwind from the trough) and maxima (in a numerical sense) occur at the inflection points. In this case, K_n is uniformly small and the vorticity advection is insignificant. In Fig. 6.5B and 6.5C the influence of confluence and diffluence of the streamlines on the vorticity advection is shown. There is a tendency for the vorticity advection to be located near troughs and wedges with confluence entrance and diffluence exit (Petterssen 1956).

Some Examples of Cyclone Development

Reitan (1974) summarized the frequencies of cyclones and cyclogenesis for North America. Danard and Ellenton (1980) examined the physical influences on the cyclogenesis on the east coast of North America making use of an eight-level primitive equation model. This model includes sensible and latent heat from the ocean surface, parameterized convective and large-scale precipitation and release of latent heat, surface frictional drag, and orography. The study was applied to several intensive storms, which included the storm of January 20, 1977, which produced a Canadian all-time record low sea level pressure of 940.2 mb at St. Anthony, Nfld., and the slow moving storm of February 6–8, 1978, which dumped 90 cm of snow on the New England states and the Maritime provinces. One of the important results of this study is that input of heat and water vapor from the ocean surface did not contribute significantly during the deepening of the low. However, these fluxes produced an initial vertical distribution of temperature and moisture that helped subsequent development.

Danard (1971) examined the roles played by long-wave radiation and surface friction in the cyclone development process. Danard and Rao (1972) examined the role of the Great Lakes on winter cyclones.

Brand and Guard (1979) studied the evolution of extratropical storms from tropical cyclones. According to these authors, a tropical cyclone is identified as becoming extratropical when it loses its tropical nature (i.e. northward displacement from the tropics as well as the conversion of the cyclone's primary energy source from latent heat release to baroclinic processes). The movement of recurved tropical cyclones is difficult to predict. According to Burroughs and Brand (1973), errors as high as 30% could occur. Even when the recurved tropical cyclone becomes somewhat weaker, if it becomes an extratropical cyclone, it could still be important. For typhoons to the east of China, during the period 1971–75, the average value of the maximum wind when the cyclones became extratropical was 28 $m \cdot s^{-1}$. In September 1974, Typhoon Agnes became extratropical at 34°N and at that time the maximum wind speed was 51 $m \cdot s^{-1}$.

According to Sekioka (1970, 1972a, 1972b) and Matano and Sekioka (1971a, 1971b), this transformation of tropical cyclones to extratropical cyclones can occur at least in two ways: (1) a tropical cylone meets an already existing front causing a new extratropical cyclone to form and grow on the front and (2) a preexisting extratropical cyclone merges with a tropical cyclone and usurps the tropical vortex.

Angell et al. (1969) detected a quasi-biennial (period of about 28 mo) variation in the

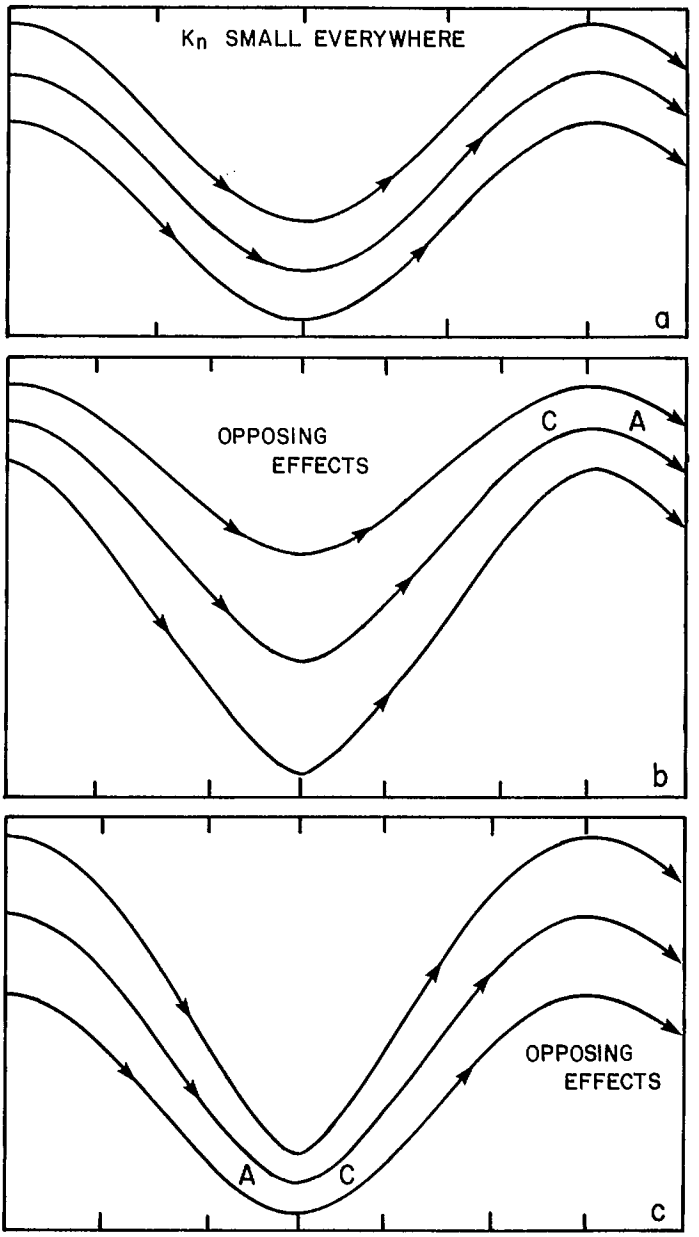

FIG. 6.5. Schematic representation of the streamline curvature (K_s) and the orthogonal curvature (K_n). In sinusoidal waves (a) the vorticity advection is generally small with numerical maxima at the inflexions. In waves with confluence and diffluence (b and c) the vorticity advection is highly concentrated in the vicinity of troughs and wedges with confluent entrance regions. The areas favorable for cyclone development at sea level are indicated by C and those favorable for anticyclone development by A. (Petterssen 1956)

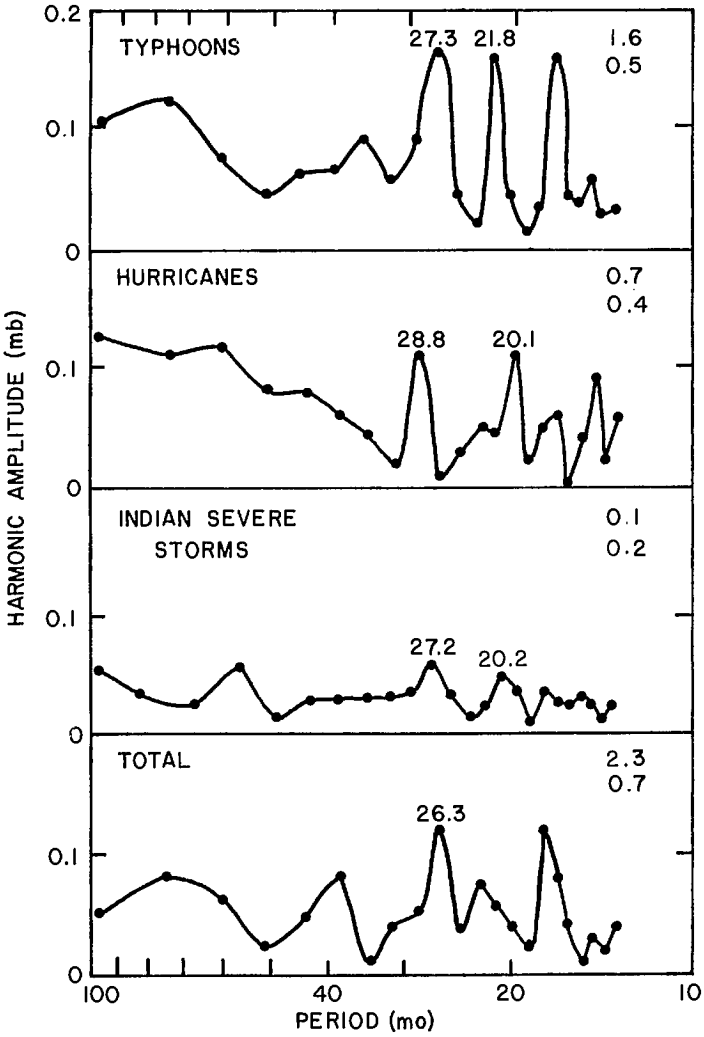

FIG. 6.6. Harmonic amplitude of the mean monthly frequency of North Pacific typhoons, North Atlantic hurricanes, severe storms (winds greater than 25 $m \cdot s^{-1}$) in the vicinity of India, and the total of all three. Numbers above the peaks indicate the dominant quasibiennial periods of oscillation (months). The two numbers in the upper right-hand corner represent the harmonic amplitudes of the annual (upper number) and semiannual (lower number) oscillations in surface pressure at the station. (Angell et al. 1969)

centers of action such as the Icelandic and Aleutian low pressure centers. They related the frequency of hurricanes and typhoons to this quasi-biennial activity. Mean monthly surface pressures at stations with long data records were subjected to harmonic analysis. The following important results emerged.

Quasi-biennial variations in the surface pressure occur near the North Atlantic and North Pacific subtropical highs and subpolar lows, with amplitudes up to 0.4 mb. The quasi-biennial variations in latitude and longitude of the subtropical highs are about 1°.

The Atlantic high moves in a northwest–southeast direction. Hurricanes in the North Atlantic, typhoons in the North Pacific, and severe storms in the vicinity of India show a quasi-biennial variation in frequency (Fig. 6.6).

It is possible that the relatively large annual oscillation may contaminate the harmonic analysis for the quasi-biennial band. For this reason Angell et al. (1969) also performed an alternate analysis. In the so-called even-minus-odd-year difference method, the number of hurricanes or typhoons in the odd-numbered years is subtracted, year by year, from the number in the even-numbered years, and these first differences are smoothed through determination of a 3-yr running average. The results agree reasonably with observations.

Explosive Cyclogenesis

Bergeron (cited in Sanders and Gyakum 1980) coined the phrase "meteorological bomb" to refer to explosive cyclogenesis, i.e. deepening of an extratropical low pressure system in which the central pressure decreases by at least 24 mb in 24 h. According to Sanders and Gyakum (1980), Bergeron's work referred to the area of Bergen in Norway, at latitude 60°N. A geostrophically equivalent deepening rate for any latitude ϕ is obtained by multiplying 24 mb $\cdot$ 24 h^{-1} by $\sin \phi / \sin 60°$. This critical rate is denoted as 1 Bergeron and varies from 12 mb $\cdot$ 24 h^{-1} at 25°N to 28 mb $\cdot$ 24 h^{-1} at the pole.

Sanders and Gyakum (1980) performed a comprehensive study of the explosive cyclogenesis problem. Their data were for the period of September 1976 to May 1979 in the Northern Hemisphere. They deduced that this phenomenon is mainly maritime and occurs in the cold season usually about 400 nautical miles (741 km) downstream from a mobile 500-mb trough, within or poleward of the maximum westerlies, and within or ahead of the planetary scale trough.

A more detailed study for the 1978–79 season by the same authors showed that explosive deepening occurs over a wide range of sea surface temperatures but mainly in the vicinity of strongest gradients. The forecasts of the National Meteorological Center (United States) appear to underestimate the deepening rates.

This study excluded most of Europe, North Africa, Asia, and the Mediterranean Sea where this phenomenon is either totally absent or rare, according to Sanders and Gyakum (1980). Holliday and Thompson (1979) found similar deepening rates, as discussed above, in rapidly intensifying typhoons.

Hammond (1980) examined the same phenomenon in the Northeast Pacific Ocean with emphasis on the cyclones that were of relevance to the west coast of Canada. For the 1979–80 season he found several cases that qualify as meteorological bombs. He also deduced that the Canadian Meteorological Center's forecasts underestimate the deepening rates. The cases selected from Hammond's work for a more detailed study by Murty et al. (1983), who extended this study to include several more seasons (1954–77), are listed in Table 6.1. Explosive cyclogenesis in the northeastern part of the Pacific Ocean occurred predominantly during October to March. The number of cases of explosive cyclogenesis by 5° squares during the period 1954–77 is shown in Fig. 6.7.

6.2 Tropical Cyclones

In this section, the formation and structure of tropical cyclones and the various stages in their life cycle will be considered followed with a discussion of the various models being used to forecast their intensity and movement.

TABLE 6.1. Number of explosively developing extratropical cyclones in the Northeast Pacific Ocean that eventually were relevant for the west coast of Canada, during the period 1955–77.

Year	Jan.	Feb.	Mar.	Apr.	May	June	July	Aug.	Sept.	Oct.	Nov.	Dec.
1955	4	0	0	1	2	0	0	1	0	1	1	1
1956	1	0	2	2	0	0	0	0	0	2	1	2
1957	1	0	1	0	1	0	0	0	0	0	2	2
1958	0	2	2	1	0	0	0	0	1	2	2	0
1959	1	0	1	2	0	0	0	0	1	1	3	5
1960	3	3	1	3	2	0	0	0	0	2	3	4
1961	3	2	5	0	0	0	0	0	9	0	3	2
1962	1	3	1	2	0	0	0	0	1	6	5	4
1963	0	1	1	0	1	6	0	0	0	5	7	1
1964	3	2	2	3	1	1	1	2	0	6	0	2
1965	0	1	1	2	2	2	0	0	1	6	1	0
1966	4	1	2	0	0	0	0	0	4	5	1	2
1967	3	3	0	0	1	0	0	0	1	4	2	3
1968	1	0	3	0	0	1	1	0	3	6	3	1
1969	0	2	0	1	0	1	0	0	0	2	6	4
1970	3	1	0	2	0	0	2	0	1	3	2	3
1971	0	3	3	2	3	0	0	0	3	0	1	1
1972	2	2	0	1	0	0	0	0	0	3	2	2
1973	1	3	3	0	1	1	0	0	0	2	1	3
1974	2	2	0	1	0	0	0	0	0	1	2	2
1975	3	0	2	4	1	0	0	0	0	4	4	3
1976	3	1	4	2	1	0	0	0	2	3	3	3
1977	4	3	2	3	0	0	1	0	0	3	0	1

FORMATION AND STRUCTURE OF TROPICAL CYCLONES

The main source of material for this subsection is Gray (1978a, 1978b, 1978c, 1978d). Annually over the globe there are about 80 tropical cyclones with maximum sustained wind speeds of 20–25 $m \cdot s^{-1}$. The areas of the generation of tropical cyclones over a 20-yr period are shown in Fig. 6.8. About one half to two thirds of these cyclones reach hurricane strength (i.e. maximum sustained wind speeds greater than 33 $m \cdot s^{-1}$). Over the globe, the percentage change in the number of tropical cyclones over a recent 20-yr period (1958–77) varied from +23 to −13, with an average of 8 (Table 6.2). The ratio of the number of tropical cyclones in the Northern Hemisphere to those in the Southern Hemisphere varied from 1.5 to 4.0.

Month by month occurrences of tropical cyclones for the same 20-yr period for the Northern and Southern Hemispheres are shown separately in Tables 6.3 and 6.4, respectively. The data for the various ocean basins, which are identified in Fig. 6.8, are shown in Table 6.5.

About 80% of the tropical cyclones occur in the belt between 20°N and 20°S. The rest occur poleward of 20° latitude, but mainly in the Northern Hemisphere. Annually, about two thirds of all tropical cyclones occur in the Northern Hemisphere; similarly, about two thirds occur in the Eastern Hemisphere (as opposed to the Western Hemisphere). Most of the tropical cyclones form in the latitudinal belt 5–15°, and rarely do they form within 4–5° from the equator. In the Southern Hemisphere, tropical cyclones do not form poleward of 22°, whereas in the Northern Hemisphere they form at latitudes up to 36°.

Considering longitude, there are three favored locations for the formation of tropical cyclones: 90°E, 140°E, and 105°W. The western part of the North Pacific Ocean accounts for about one third of all tropical cyclones. Generally, summer is the favored season for

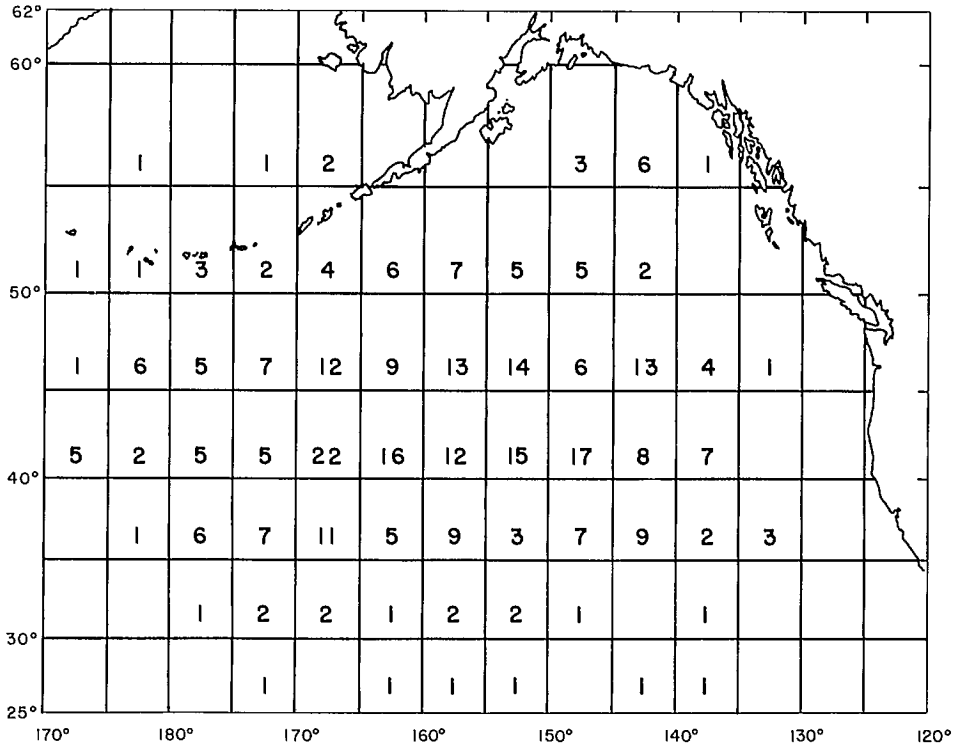

FIG. 6.7. Number of explosive cyclones originating in 5° × 5° squares during 1954–77.

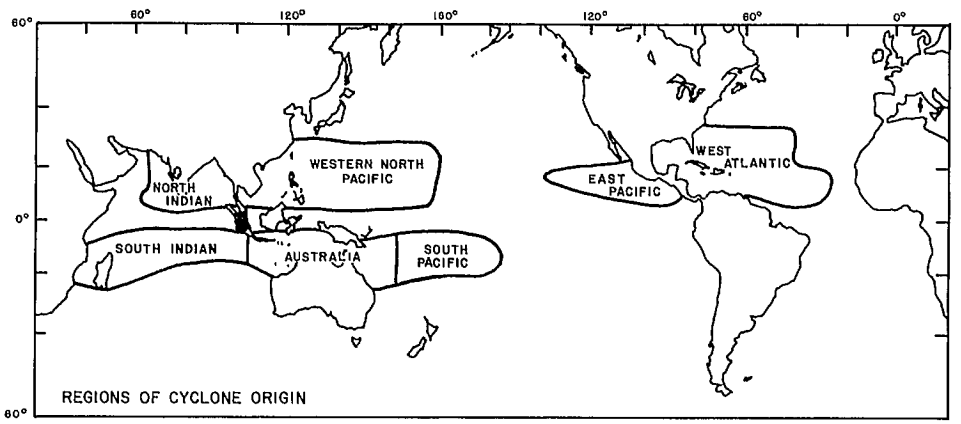

FIG. 6.8. Ocean basins for which tropical cyclone frequency is given in Table 6.5. (Gray 1978a)

tropical cyclone formation, but they do occur in other seasons, especially in the western part of the North Pacific Ocean.

In the North Indian Ocean, there are two seasons of cyclone formation in the 5–15° latitude belt: a major period in the autumn associated with the retreat of the southwest

TABLE 6.2. Tropical cyclone statistics for the period 1958–77. NH, Northern Hemisphere; SH, Southern Hemisphere. (Gray 1978a)

Year		No. of cylones			% deviation from 20-yr average	Ratio (NH:SH)
NH	SH	NH	SH	Total		
1958	1958–59	52	25	77	−3	2.1
1959	1959–60	48	21	69	−13	2.3
1960	1960–61	48	22	70	−12	2.2
1961	1961–62	58	23	81	+2	2.5
1962	1962–63	50	30	80	+1	1.7
1963	1963–64	49	23	72	−9	2.1
1964	1964–65	65	19	84	+6	3.4
1965	1965–66	56	22	78	−1	2.5
1966	1966–67	64	16	78	−1	4.0
1967	1967–68	63	28	91	+15	2.2
1968	1968–69	61	23	84	+6	2.6
1969	1969–70	49	23	72	−9	2.1
1970	1970–71	56	26	82	+4	2.1
1971	1971–72	70	27	97	+23	2.6
1972	1972–73	54	35	91	+15	1.5
1973	1973–74	46	28	74	−6	1.6
1974	1974–75	55	19	75	−5	2.9
1975	1975–76	47	29	76	−4	1.6
1976	1976–77	55	30	85	+7	1.8
1977	1977–78	47	20	67	−15	2.3
Total		1093	489	1583		
Average		54.6	24.5	79.1	±8	2.3

TABLE 6.3. Frequency of Northern Hemisphere tropical cyclone genesis by year and month. (Gray 1978a)

Year	Jan.	Feb.	Mar.	Apr.	May	June	July	Aug.	Sept.	Oct.	Nov.	Dec.	Total
1958	1	0	0	0	2	5	10	9	11	9	4	1	52
1959	0	0	0	1	2	6	7	11	9	8	2	2	48
1960	0	0	0	1	3	7	6	14	6	8	2	1	48
1961	1	1	1	1	4	5	10	5	14	9	6	1	58
1962	0	1	0	1	3	2	7	11	11	7	4	3	50
1963	0	0	0	1	3	5	6	5	14	11	0	4	49
1964	0	0	0	0	3	4	11	15	12	8	10	2	65
1965	2	2	1	1	4	8	8	8	12	3	4	3	56
1966	0	0	0	2	2	3	9	13	20	5	7	3	64
1967	2	1	1	1	2	4	10	12	12	13	3	2	63
1968	0	0	0	1	2	5	7	17	11	11	6	1	61
1969	1	0	1	1	1	0	7	13	10	9	4	2	49
1970	0	1	0	0	4	6	11	10	9	8	7	0	56
1971	1	0	1	3	7	3	15	11	15	9	4	1	70
1972	1	0	0	1	4	2	9	12	12	6	4	3	54
1973	0	0	0	0	0	5	12	8	8	7	5	1	46
1974	1	0	0	2	4	6	5	14	13	6	4	0	55
1975	2	0	0	0	2	3	6	11	9	8	6	0	47
1976	1	1	0	3	2	7	9	15	10	4	0	3	55
1977	0	0	1	0	3	4	8	4	13	9	4	1	47
Total	13	7	6	20	57	90	173	218	231	158	86	34	1093
Average	0.7	0.3	0.3	1.0	2.9	4.5	8.6	10.9	11.5	7.9	4.3	1.7	54.6

TABLE 6.4. Frequency of Southern Hemisphere tropical cyclone genesis by year and month. (Gray 1978a)

Year	Oct.	Nov.	Dec.	Jan.	Feb.	Mar.	Apr.	May	Total
1958–59	1	1	3	5	7	6	2	0	25
1959–60	0	1	4	3	2	7	4	0	21
1960–61	0	1	1	9	7	4	0	0	22
1961–62	0	1	4	6	8	2	2	0	23
1962–63	1	0	4	6	9	5	2	3	30
1963–64	0	1	3	7	3	7	1	1	23
1964–65	0	2	5	4	5	3	0	0	19
1965–66	0	0	3	7	6	6	0	0	22
1966–67	0	1	3	5	1	3	2	1	16
1967–68	0	2	4	8	7	3	4	0	28
1968–69	1	1	3	7	8	2	1	0	23
1969–70	0	1	0	5	6	7	3	1	23
1970–71	1	3	6	4	7	4	1	0	26
1971–72	0	1	6	3	10	3	2	2	27
1972–73	1	3	4	10	6	7	3	1	35
1973–74	1	3	5	7	4	6	2	0	28
1974–75	0	0	2	6	2	5	4	0	19
1975–76	0	4	4	8	5	4	3	1	29
1976–77	1	0	4	8	9	5	3	0	30
1977–78	0	3	4	3	4	4	2	0	20
Total	7	29	72	121	117	93	41	10	489
Average	0.4	1.5	3.6	6.1	5.9	4.7	2.1	0.5	24.5

TABLE 6.5. Yearly variation of tropical cyclones by ocean basins. SH, Southern Hemisphere; NW Atl., Northwest Atlantic Ocean; NE Pac., Northeast Pacific Ocean; NW Pac., Northwest Pacific Ocean; S. Pac., South Pacific Ocean; Aust., Australia; N. Ind., North Indian Ocean; S. Ind., South Indian Ocean. (Gray 1978a)

Year	SH	NW Atl.	NE Pac.	NW Pac.	N. Ind.	S. Ind.	Aust.	S. Pac.	Total
1958	1958–59	12	13	22	5	11	11	7	81
1959	1959–60	11	13	18	6	6	13	2	69
1960	1960–61	6	10	28	4	6	8	8	70
1961	1961–62	11	12	29	6	12	7	4	81
1962	1962–63	6	9	30	5	8	17	3	78
1963	1963–64	9	9	25	6	9	7	7	72
1964	1964–65	13	6	39	7	6	9	4	84
1965	1965–66	5	11	34	6	12	7	4	79
1966	1966–67	11	13	31	9	5	5	6	80
1967	1967–68	8	14	35	6	11	9	8	91
1968	1968–69	7	20	27	7	8	7	8	84
1969	1969–70	14	10	19	6	10	7	6	72
1970	1970–71	8	18	23	7	11	12	3	82
1971	1971–72	14	16	34	6	7	14	6	97
1972	1972–73	4	14	28	6	13	12	10	88
1973	1973–74	7	12	21	6	4	16	8	74
1974	1974–75	8	17	23	7	6	10	3	74
1975	1975–76	8	16	17	6	8	16	5	76
1976	1976–77	8	18	24	5	9	12	9	85
1977	1977–78	6	17	19	5	6	7	7	67
Total		176	268	526	121	168	206	118	1583
Average		8.8	13.4	26.3	6.4	8.4	10.3	5.9	79.1

monsoon and a minor period in the spring associated with the onset of the monsoon. Note that the Southeast Pacific Ocean and the South Atlantic Ocean are not regions of tropical cyclones. The seasonal location of the intertropical convergence zone (ITCZ) is a favored region for tropical cyclogenesis.

According to Gray (1978a, 1978b, 1978c, 1978d), tropical cylones tend to cluster in time as well as in space. Within a period of 1−2 wk there may be as many as 5−15 tropical cyclones over the globe and then a lull for several weeks. During such active periods there may be as many as two to six times as many cyclones than in the less active periods. Gray (1978a, 1978b, 1978c, 1978d) attributed this to the influence of the larger scale general circulation of the tropical atmosphere with time scales of 10−20 d.

About 80−85% of the tropical cyclones originate in or near the poleward side of the ITCZ or the doldrum trough. The remainder occur in the tradewinds at some distance from the ITCZ but usually in conjunction with an upper tropospheric trough to their northwest.

There are some anomalous warm core systems belonging to the class of subtropical or semitropical cyclones accounting for about 3−5% of the tropical cyclones. These originate in the subtropics inside baroclinic regions where stagnant frontal zones exist to the east of the westerly troughs aloft (e.g. Northwest Atlantic and Northwest Pacific oceans). These mixed type of tropical midlatitude cyclones usually do not generate intense cyclones.

Since tropical cyclones spend most of their lifespan over the warm waters of the tropical oceans, traditional data sources are not dense enough. Aircraft data have contributed significantly. However, for an accurate vertical structure determination, Rawinsonde data are the most pertinent. Since enough synoptic Rawinsonde data are not available, it is necessary to combine the data of different periods for similar weather systems.

According to Gray (1978a, 1978b, 1978c, 1978d) the seasonal tropical cyclone frequency can be related to the following six climatological genesis parameters: (1) low level relative vorticity, ζ_r, (2) Coriolis parameter, f, (3) the inverse of the vertical shear S_z of the horizontal wind between the lower and upper troposphere, $1/S_z$, (4) ocean thermal energy, sea temperature excess above 26°C to a depth of 60 m, E, (5) vertical gradient of θ_e between the surface and 500 mb, $\partial\theta_e/\partial p$, where θ_e is the equivalent potential temperature of air, and (6) midtroposphere relative humidity, RH.

The rationale for selecting these parameters is the following. The first parameter is selected because, all things being equal, seasonal cyclone frequency should be related to the magnitude of the seasonal lower tropospheric relative vorticity. The Coriolis parameter is relevant because cyclones do not appear to form within 4−5° of the equator. Cyclogenesis does not occur near the equator because wind accelerations are small due to weak pressure gradients whereas frictional dissipation is as large as at any other latitude. The third parameter is relevant because tropical cyclones form when there is minimum vertical shear of the horizontal wind between the lower and upper troposphere.

The fourth parameter becomes relevant when recognizing that tropical cyclones can have considerable influence on the temperature of the water body over which they travel. The feedback effect of the altered ocean temperature influences the cyclone. It appears that the inner region of the average-sized hurricane (0−240 km) can consume up to 4000 $\text{cal}\cdot\text{cm}^{-2}\cdot\text{d}^{-1}$ from the ocean's sensible and latent heat energy (for details see Leipper and Jensen 1971; Leipper and Volgenau 1972; Hefferman 1972; Perlroth 1967, 1969). On the other hand, Malkus and Riehl (1960) put this value at 3100 $\text{cal}\cdot\text{cm}^{-2}\cdot\text{d}^{-1}$. According to Frank (1977b), for Pacific typhoons for the inner 80 km, the consumption rate is around 1470 $\text{cal}\cdot\text{cm}^{-2}\cdot\text{d}^{-1}$. If a typhoon crosses the track of another typhoon, the second one may

weaken sometimes because of the lowered sea surface temperature due to the upwelling caused by the first typhoon (Brand 1971).

The hurricane or typhoon can influence the ocean temperatures down to a depth of 60 m. Leipper and Jensen (1971) and Leipper and Volgenau (1972) defined an ocean thermal energy potential (for cyclogenesis) E (calories per square centimetre) as the ocean thermal energy above 26°C down to a depth of 60 m, i.e.

$$E = \int \rho_w C_w (T - 26)\, dz \tag{6.33}$$

where the integral is from the surface down to a depth of 60 m (or to where $T = 26°C$). Here, ρ_w is the density of seawater, T is the ocean temperature (degrees Celsius), and C_w is the specific heat of water.

The importance of the fifth parameter is obvious when it is considered that cyclones do not form unless the lower and upper tropospheric flow patterns are well coupled. The primary mechanism for this coupling is the cumulonimbus convection. Hence, cyclogenesis should depend on the seasonally averaged moist buoyancy potential (i.e. the seasonal magnitude of the difference in the equivalent potential temperature θ_e between the boundary layer and the middle troposphere). The importance of the sixth parameter can be seen from the observations that tropical cyclones form in areas where seasonal middle level humidity values are high. In other words, when the humidity is high, deep cumulus convection occurs leading to better coupling in the vertical.

Based on these considerations, Gray (1978a, 1978b, 1978c, 1978d) defined a "seasonal genesis parameter" (SGP) as follows:

(6.34) SGP = vorticity parameter × Coriolis parameter × vertical shear parameter × ocean energy parameter × moist stability parameter × humidity parameter

Here, vorticity parameter = $\zeta_r + 5$ where ζ_r is in units of $10^{-6} \cdot s^{-1}$, Coriolis parameter = f, vertical shear parameter = $1/(S_z + 3)$ where $S_z = |\partial V/\partial p|$ is in units of metres per second per 750 mb and V is the wind vector, ocean energy parameter = E is defined by eq. 6.33 and is in units of 10^{-5} cal·cm^{-2}, moist stability parameter = $\partial\theta_e/\partial p + 5$ where $\partial\theta_e/\partial p$ is in K·500 mb^{-1}, and humidity parameter = $(\overline{RH} - 40)/30$ where $\overline{RH}$ is the mean relative humidity between 500 and 700 mb but is zero for $\overline{RH} \leq 40$ and for $\overline{RH} \geq 70$. Note that in the above expressions, arbitrary units are added to enable daily values to be used instead of seasonal values.

Another interpretation of SGP is as follows:

(6.35) SGP = dynamic potential × thermal potential

where dynamic potential = $f(\zeta_r + 5)[1/(S_z + 3)]$ and thermal potential = $E(\partial\theta_e/\partial p + 5)(\overline{RH})$. The thermal potential might be thought of as potential for cumulonimbus convection. The dynamic potential is in units of 10^{-11} s^{-2} (m·s^{-1})/750 mb and the thermal potential is in units of 10^{-5} cal·cm^{-2}·K·500 mb^{-1}. The SGP is in units of 1.5×10^{-8} cal·K·s^{-1}·cm^{-3}. Gray (1978a, 1978b, 1978c, 1978d) reported that there is very close agreement between the predicted (from SGP) and the observed cyclogenesis frequencies.

Life Cycle of a Tropical Cyclone

Riehl (1979) summarized the life cycle of tropical cyclones. For storms with the

strength of hurricanes, the duration from their birth to the time of landfall or recurvature into middle latitudes is usually about 6 d. The life cycle of a tropical cyclone may be considered to be made up of the following four stages: formative stage, immature stage, mature stage, and terminal stage.

Tropical cyclones form in the vicinity of preexisting weather systems. The deepening can occupy several days or may occur explosively in as short a time as 12 h. In the formative stage, winds are usually less than hurricane force (i.e. 1-min sustained winds are less than 74 $mi \cdot h^{-1}$ (119 $km \cdot h^{-1}$)). Strongest winds occur in the quadrant that is to the east of the center and poleward. Surface pressure usually drops to 1000 mb.

Several of these incipient cyclones never deepen enough to become hurricanes. In those cases that do deepen, the lowest pressure rapidly decreases to less than 1000 mb. Winds with speeds of up to 74 $mi \cdot h^{-1}$ occur in a tight band around the center (and not just in one quadrant). The disorganized squalls of the formative stage change into narrow and organized bands of clouds spiraling inward. In this immature stage only a small area is involved in the intense inner core (30- to 50-km radius) although there may be a large outer core.

In the mature stage, the surface pressure at the center stops decreasing and the maximum wind speeds do not increase further. However, the area of intense circulation expands (up to 300-km radius in certain cases). The symmetry of the immature stage is destroyed and strong winds and bad weather preferentially occur to the right of the center looking downstream in the direction of movement of the cyclone. Some storms with a central low pressure as low as 950 mb could still be only 100–200 km in radius. Riehl (1979) estimated that for a storm with an average surface pressure of 1000 mb, the total weight of air and water involved in the circulation is about 3×10^{11} to 1×10^{12} t (3.05×10^{14} to 1.016×10^{15} kg). However, another storm with a radius of 1000 km but with the same average surface pressure of 1000 mb will have a weight of about 5×10^{12} to 3×10^{13} t (5.8×10^{15} to 3.05×10^{16} kg). By comparison, in an ordinary midlatitude cyclone, the weight involved is about 5×10^{12} to 1×10^{13} t (5.8×10^{15} to 1.016×10^{16} kg).

When the tropical cyclone hits land, usually its core size decreases and sometimes the storm dissipates within 1–2 d. Storms can dissipate even over the ocean if they travel over cold ocean currents (e.g. Northeast Pacific Ocean). Many cyclones recurve (both over land and ocean) into the westerlies and travel towards northeast or east (in the Northern Hemisphere).

Some Characteristics of Tropical Cyclones

Riehl (1979) offered the following classification of tropical cyclones. (A) Tropical depression: at most, winds barely acquire gale force in one quadrant. (B) Tropical storm: winds acquire gale force but less than hurricane force of 64 knots (119 $km \cdot h^{-1}$ or 74 $mi \cdot h^{-1}$). (C) Minimal hurricane: winds above 64 knots only in one quadrant. (D) Moderate hurricane: winds of 80–90 knots (148–167 $km \cdot h^{-1}$) around the center, with the maximum wind being around 100 knots (185 $km \cdot h^{-1}$) or more. (E) Severe hurricane: maximum winds up to 200 knots (370 $km \cdot h^{-1}$).

Tropical cyclone intensity classification is not uniformly used in the various meteorological services for the various regions of the globe. For example, in the western part of the Pacific Ocean, unless the maximum winds are about 150 knots (278 $km \cdot h^{-1}$), a typhoon will not be considered severe.

Riehl (1979) mentioned that the word "hurricane" means "big wind" in the Taino

language. In the Pacific Ocean, tropical cyclones are referred to as "typhoons," as "willy-willy" in Australia, and "baguio" in the Philippines.

Next, some characteristics of tropical cyclones will be briefly examined with respect to their surface pressure, winds, and thermal structure. Since ordinarily, surface pressure varies only by about 3 mb (0.3%) in the tropics whereas pressure varies 5–10% below average sea level pressure during tropical cyclones, a useful tool for analysis is the sea level isobar field. Gradients of 0.5–2 mb·km^{-1} can occur.

When the tropical cyclone is over an ocean, the increase of wind with height usually occurs in the first 100 m. Above that it increases slowly to about the 300-m level where the winds probably attain maximum values. For Hurricane Eloise of 1977 the wind speed at the 100-m level was 20 m·s^{-1}; from 200 to 500 m it was 22 m·s^{-1}. Then it decreased to 14 m·s^{-1} at 1200 m. Usually, the wind at 50 m is about three quarters the geostropic wind speed (Riehl 1979).

In hurricanes, in the inner 80-km core, winds up to 45 m·s^{-1} can occur. Winds are greater on the right side because here the carrying current and the circulation are in the same direction whereas to the left they oppose each other. One of the safest ways to identify tropical cyclones is to look for this asymmetry in the surface wind field. For convenience, one may think of the following four quadrants around the center: right front, right rear, left front, and left rear. Inward spiraling of streamlines is pronounced in the rear quadrants. Here, the radial component of the motion is strongest.

Riehl (1979) gave the following relationship between pressure and wind fields in a tropical cyclone (this was derived empirically based on 28 yr of Pacific typhoon data):

$$V_m = 3.35(1010 - p_c)^{0.644} \tag{6.36}$$

where V_m is the maximum wind (metres per second) and p_c is the central pressure (millibars).

The theory of vortex flows shows that in the center of every revolving vortex, there is a singular point. In a tropical cyclone this center is referred to as the eye, near which the circulation is weak. At the edge of the eye, strong precipitation abruptly stops and the sky may clear at least partly. The diameter of the eye in a mature hurricane ranges from 30 to 50 km and probably twice this value in a severe typhoon. The eye need not be circular and sometimes it is diffuse and has a double structure.

Riehl (1979) mentioned that one of the earliest controversies about tropical cyclones concerned their vertical extent. Estimates varied from 3 to 10 km or greater. According to Haurwitz (1935) the tropical cyclone extends through the troposphere, and high level observations substantiated this idea. However, a surprising result revealed from Rawinsonde data was that the circulation at higher levels is opposite to that at lower levels. This changeover level is at about 300 mb.

As expected, the air inside a tropical cyclone is less dense than its surroundings. For Hurricane Daisy of 1958 near Florida, in the mature stage, the surface pressure in the eye was 950 mb and the maximum wind was 50 m·s^{-1}. Hurricane Daisy is considered to be a hurricane of moderate intensity, and even in this case more than half the temperature gradient needed for its existence was internally generated. Riehl (1979) maintained that this is the main reason why intense hurricanes occur rarely. In contrast, in extratropical cyclones, the cyclone grows at the expense of the potential energy in a preexisting temperature field, which becomes pronounced. On the other hand, in a tropical cyclone, the cyclone itself must generate most of the required temperature gradient.

Riehl (1979) suggested that a hurricane may be regarded as a rankine vortex with a velocity profile defined by v_0/r = constant in the inner core of maximum winds and

$v_\theta r$ = constant in the outer core. Here, r is the radial coordinate and v_θ is the azimuthal velocity. The outer core can be defined as

(6.37) $$v_\theta r^x = \text{constant}, \qquad 0.4 \le x \le 0.6$$

In the outer core, with increasing distance from the center, v_θ tends to zero.

Momentum and Energy Budgets for Tropical Cyclones

Following Riehl (1979), the energy and momentum budgets for hurricanes will be considered. In polar coordinates, the equations of horizontal motion with the neglect of lateral friction are

(6.38)
$$\frac{dv_\theta}{dt} + \frac{v_\theta v_r}{r} + f v_r = -\frac{1}{\rho}\frac{\partial p}{r\partial\theta} + \frac{1}{\rho}\frac{\partial \tau_{\theta z}}{\partial z}$$
$$\frac{dv_r}{dt} - \frac{v_\theta^2}{r} - f v_\theta = -\frac{1}{\rho}\frac{\partial p}{\partial r} + \frac{1}{\rho}\frac{\tau_{rz}}{\partial z}$$

Here, v_r and v_θ are the radial and azimuthal velocities, respectively. After certain algebra involving these two equations, it can be shown that

(6.39) $$\frac{d}{dt}\left(v_\theta r + \frac{fr^2}{2}\right) - \frac{r^2}{2}\frac{df}{dt} = -\frac{1}{\rho}\frac{\partial p}{\partial\theta} + \frac{r}{\rho}\frac{\partial \tau_{\theta z}}{\partial z}$$

The component of the earth's angular momentum (per unit mass) about the vertical axis of the tropical cyclone is

(6.40) $$\Omega = v_\theta r + \frac{fr^2}{2} = \text{constant}$$

For symmetrical storms, eq. 6.40 is a good representation in the upper troposphere. If eq. 6.39 is integrated over the entire volume in the storm, by definition the pressure term will disappear, but the frictional term will not because of transfer of momentum from the atmosphere to the ocean. To compute the momentum budget, integrate eq. 6.37 over the volume of the storm to obtain expressions for the transport F_Ω (radial) at any radius and F_Ω (vertical) between two radii. These are

(6.41) $$F_\Omega(\text{radial}) = -\frac{2\pi r^2}{g}\left[\int_{p_2}^{p_1} \overline{v_\theta}\,\overline{v_r}\,dp + \int_{p_2}^{p_1} \overline{v_\theta' v_r'}\,dp + \frac{fr}{2}\int_{p_2}^{p_1} \overline{v_r}\,dp\right]$$

(6.42) $$F_\Omega(\text{vertical}) = -\frac{2\pi}{g}\left[\int_{r_1}^{r_2} \tilde{v}_\theta \tilde{\omega} r^2 dr + \int_{r_1}^{r_2} \tilde{v}_\theta^* \omega^* r^2 dr + \frac{f}{2}\int_{r_1}^{r_2} \tilde{\omega} r^3 dr\right]$$

where

$$\omega \equiv dp/dt$$

The surface transport to the ocean is given by

(6.43) $$E_\Omega(\text{surface}) = 2\pi \int_{r_1}^{r_2} \tau_{0.0} r^2 dr$$

where $\tau_{0.0}$ is the stress at the ship's deck level (or anemometer level).

In eq. 6.41 the first term represents the transport by the mean ageostrophic circulation $\bar{v}_r$, the second term denotes the deviation from symmetry when one goes round the

TABLE 6.6. Transports through 1° radius (10^{12} kJ·s^{-1}) showing the radial energy balance in two different hurricanes. (Riehl 1979)

Parameter	Hurricane Daisy (1960)	Hurricane Helene (1951)
Net latent heat inflow	+34.1	+31.9
Flux of latent and sensible heat from the sea	+3.4	+6.2
Import of kinetic energy	+0.4	+0.2
Total energy source	37.9	38.3
Less net export of $(CpT + gz)$	−36.9	−37.4
Balance for radiation cooling	1.0	0.9

perimeter, and the third term is the influence due to the earth's rotation, assuming the Coriolis parameter to be constant.

One can regard the atmosphere, and particularly a tropical cyclone, in the present situation as a thermal engine for which the efficiency (of converting heat to mechanical energy) is defined as the ratio of the mechanical energy produced to the heat released. For an average hurricane, the kinetic energy produced was estimated by Riehl (1979) as 15×10^{18} ergs·s^{-1} or 0.36×10^{12} kW-h·d^{-1} (1 erg = 0.1 μJ, 1 kW-h = 3.6 MJ). The latent heat released was 13.3×10^{12} kW-h·d^{-1}. Thus, the efficiency ϵ is 3%. This is very low but is somewhat higher than for extratropical cyclones and the general circulation of the atmosphere. Hence, weather systems and the atmosphere are very inefficient heat engines. This low value of efficiency for the tropical cyclones indicates that the mechanism for energy release is in the central area with local oceanic heat source and not in the advection of large masses of water vapor into the system from outside.

The balance of radial energy for Hurricanes Helen of 1951 and Daisy of 1960 is shown in Table 6.6. Concerning oceanic input of energy, Gray (1978a) provided the following analysis. In the tropical cyclone, moist static energy h can increase or decrease through latent and sensible heat exchange with the ocean E_S through radiation R and through horizontal transport through the boundaries $\nabla \cdot Vh$. One can write for this energy balance

$$\frac{\partial h}{\partial t} = E_S + R - \nabla \cdot Vh \tag{6.44}$$

where

$$h = gz + C_pT + Lq \tag{6.45}$$

Note that all these terms have been integrated through the thickness of the troposphere.

For the inner 4° radius of tropical storms, $E_S + R$ is slightly positive for weak disturbances, but for hurricanes it is highly positive because strong input of energy takes place from the ocean. The vertical circulations in a tropical cyclone will act as an energy sink dissipating the system and the main energy source is the ocean. For this reason, many tropical systems weaken or dissipate once they are not traveling over the ocean.

Modeling of Hurricane Formation and Intensification

According to Gray (1978a, 1978b) little effort has gone into numerically modeling tropical cyclogenesis. Ooyama (1964), Charney and Eliassen (1964), Ogura (1964), Kuo (1965), and several later authors modeled the intensification of hurricanes. The low level

TABLE 6.7. Comparison of observed western Pacific disturbances with regard to their average maximum tangential wind, 900-mb tangential wind, and relative vorticity. (Zehr 1976)

Weather system	Radius of maximum tangential wind about the disturbance (km)	Average 900-mb tangential wind about disturbance center at radius of maximum wind ($m \cdot s^{-1}$)	Mean relative vorticity inside the radius of maximum tangential wind ($10^{-6} \cdot s^{-1}$)
Typical tropical disturbance (summer)	~400	1.6	8
Average tropical disturbance (all seasons)	~500	2.5	10
Precyclone disturbance in early intensificaiton stage	~400	5.3	26
Intensifying cyclone	~200	10.1	107
Mean assumed initial vortex of modelers[a]	172	12.2	142

[a]Based on the numerical models listed in Table 6.8 excluding Carrier (1971) model.

TABLE 6.8. Some numerical modeling papers on tropical cyclone intensification and their assumed initial lower tropospheric cyclone strength. (Gray 1978a)

Modelers	Assumed initial maximum wind velocity ($m \cdot s^{-1}$) and radius (km) of maximum wind		Vortex vorticity inside the radius of maximum winds ($10^{-6} \cdot s^{-1}$)	Type of vortex
Kuo (1965)	10	141	142	Symmetrical
Yamasaki (1968)	4.7	100	94	Symmetrical
Ooyama (1969)	10	50	400	Symmetrical
Miller (1969)	10	200	100	Real vortex
Rosenthal (1970)	7	250	56	Symmetrical
Sundqvist (1970a, 1970b)	15	200	150	Symmetrical
Carrier (1971)	21	50	840	Symmetrical
Anthes et al. (1971a, 1971b)	18	240	150	Asymmetrical
Anthes (1972)	18	240	150	Asymmetrical
Mathur (1972)	15	200	150	Asymmetrical
Harrison (1973)	~10	~120[a]	~170	Asymmetrical
Kurihara and Tuleya (1974)	12	200	120	Symmetrical
Ceselski (1974)	17	~100–150	~200	Real vortex
Kurihara and Tuleya (1974)	12	200	120	Symmetrical
Anthes (1977)	18	240	150	Symmetrical
Rosenthal (1978)	7.2	220	65	Symmetrical

NOTE: Typical precyclone cloud cluster vorticity is 10×10^{-6} to $15 \times 10^{-6} \cdot s^{-1}$.
[a]Estimated from initial height field.

winds for different classes of tropical disturbances, as deduced from Rawinsonde composite studies, are shown in Table 6.7. These winds are much smaller than the initial cyclone strength assumed by numerical modelers, as summarized in Table 6.8. According to Gray (1978a, 1978b, 1978c, 1978d) the transformation of a disturbance to a cyclone has yet to be realistically modeled.

Gray (1978a, 1978b, 1978c, 1978d) classified the disturbance stages and gave estimates of central pressure and maximum sustained surface winds. These are shown in Table 6.9. Even in a stage 6 cyclone (i.e. typhoon) approximately 50% of the mass inflow at 4°

TABLE 6.9. Tropical disturbance classification stages and surface pressure and wind estimates at these various stages; two classes of nonintensifying disturbance and six stages of disturbance-to-cyclone intensification are shown. (Gray 1978a)

Disturbance classification	Stage	Estimated minimum sea level pressure (mb)	Estimate of maximum sustained surface winds ($m \cdot s^{-1}$)
General class of nondeveloping disturbances	0	1008	8
Nondeveloping disturbances of summer in cyclone genesis region	00	1008	8
Initial cluster	1	1007	8
Pretyphoon cluster	2	1005	10
Genesis	3	1003	12
Intensifying	4	1000	18
Tropical storm (980–1000 mb)	5	990	25
Typhoon (950–980 mb)	6	965	40

radius takes place above the 900-mb layer. Hence, there is significantly more mass inflow than can be accounted for by boundary layer processes. In fact, mass convergence could occur in a layer as high as 400 mb.

Ooyama (1964) and Charney and Eliasen (1964) introduced the concept of "conditional instability of the second kind" (CISK). This theory can account for the processes in the inner core region of already developed cyclones but may be deficient as a general theory. Regarding the use of this theory and numerical modeling of cyclonegenesis, Gray (1978a, p. 189) stated that the numerical models avoided the most important question, i.e. how the deep tropical cyclone (from which integrations are made) itself has formed. Also, in the numerical models, unrealistically great cyclone strengths and vertical dimensions are assumed, and they have not incorporated the eddy processes in the large outer radius. For a recent review on numerical models for hurricanes, see Baer (1979). Presently available hurricane models and their features are summarized in Table 6.10.

MOVEMENT OF TROPICAL CYCLONES: PREDICTION AND MODELING

Several different techniques are being used for predicting the tracks of tropical cyclones: empirical, statistical, and dynamical. Empirical techniques will be considered first. According to Hebert (1979), these may be further classified into three categories: (a) persistence and climatology, (b) synoptic, and (c) satellite. These techniques can be used for prediction of the hurricane track for 12–24 h in advance. Any extrapolation beyond 24 h will result in large errors, except possibly in the deep easterlies of the tropics.

In the persistence technique, one simply extrapolates linearly the last track, assuming uniform speed and no change of direction. One can use a higher order persistence forecast by allowing for variation of speed of movement and direction of the hurricane in the past 12–24 h. The simplicity of this technique is its chief advantage. It is obvious that errors could occur if the persistence assumption does not hold.

In a climatological forecast one makes use of the knowledge of the temporal and spatial frequency of past hurricanes in given grid areas (e.g. 2.5° latitude–longitude squares and time scales up to 5 d). This method works well when the frequency of occurrence is great. It fails with increasing latitude (due to recurvature) as well as for

TABLE 6.10. List of hurricane models. PE, primitive equations; BAL, balance equation; PBL, planetary boundary layer. Serial Nos.: 1, Kasahara 1961; 2, Rosenthal 1964; 3, Charney and Eliassen 1964; 4, Ogura 1964; 5, Kuo 1965; 6, Yamasaki 1968; 7, Ooyama 1969; 8, Sundqvist 1970a; 9, Sundqvist 1970b; 10, Rosenthal 1970; 11, Yamasaki 1977; 12, Anthes 1977; 13, Rosenthal 1978; 14, Anthes 1972; 15, Miller et al. 1972; 16, Harrison 1973; 17, Kurihara and Tuleya 1974; 18, Mathur 1974; 19, Madala and Paiesek 1975; 20, Ley and Elsberry 1976; 21, Jones 1977. (Baer 1979)

Serial No.	System	Convective parameterization	Moisture prediction	Vertical structure	Grid	Additional features
			Symmetric models			
1	PE	No	No	50-mb levels	Regular	
2	PE	No	No	550-mb levels	Coarse	
3	BAL	Yes	No			Linear solution
4	BAL	Yes	No	2 levels	Fine	
5	BAL	Yes	Yes	2 levels	Variable	
6	PE	Yes	No	13 layers	Expanding	
7	BAL	Yes	No	Incompressible layers	Fine	
8, 9	BAL	Yes	Yes	100-mb levels	Regular	
10	PE	Yes	Yes	7 levels	Regular–fine	
11	PE and nonhydrostatic	No	Yes	25 layers variable	Ultrafine	
12	PE	Yes	Yes	4 layers σ-coordinates	Variable coarse	
13	PE	No	Yes and liquid water prediction	12 layers σ-coordinates	Expanding	
			Three-dimensional models			
14	PE	Yes	Yes	3 levels	Staggered	
15	PE	Yes	Yes	6 layers	Coarse	Real initial conditions
16	PE	No	No	3 layers	Nested	Simulated forcing
17	PE	Yes	Yes	11 layers	Variable	
18	PE	Yes	Yes	3 layers and PBL	Nested	Real initial conditions
19	PE	Yes	No	3 layers	Expanding	β-plane
20	PE	No	No	3 levels	Multinested	Real initial conditions
21	PE	Yes	Yes	3 levels	Multinested, moving	

untypical situations. Other times when it fails is when a bimodal structure is present.

In the persistence plus climatology forecasts (Bell 1962; Aoki 1979) one uses the formula $np + mC$ where p and C represent the persistence and climatology, respectively, and n and m are weighting factors. Usually, $n = m = 0.5$ is used. Amadore (1972) gave different weightings to get latitude and longitude components separately for the tropical cyclones east of the Philippines. However, according to Hebert (1979), similar attempts for the South China Sea region did not significantly improve the results.

In the synoptic technique, the main assumption is that the air mass in which the tropical cyclone is embedded is homogeneous. In the surface geostrophic steering method, the zonal (east–west) and the meridional (north–south) components of the hurricane movement are determined by estimating (from the synoptic charts) the pressure gradient (millibars per degree of latitude) across the storm. Since the surrounding air mass is not uniform, one must apply a correction to the pressure gradient to account for the non-homogeneity. The main advantage of this technique lies in the fact that almost all forecast centers have surface pressure analysis charts.

In the control point method (Chin 1970), which has been in use for several years at the Hong Kong Observatory, one makes use of the observed high correlation between the wind direction at certain locations in the midtroposphere and the direction of movement of the tropical cyclone. The disadvantage is that in areas of sparse data, midtropospheric analyses might be difficult to make.

In predicting the movement of cyclones, one should also consider the so-called Fujiwhara effect (Fujiwhara 1921) in which two vortices close to each other will rotate about a common point located on the line joining their centers.

Next, satellite techniques, which are playing an ever increasing role in the prediction of the tracks of cyclones, will be considered. The basic principle is to relate past changes in cloud features to future changes in the direction of motion.

Fett and Brand (1975) used six identifiable cloud patterns and extrapolated the rotation of one or more of these patterns during the previous 24 h to calculate the change in the motion direction for the next 24 h. In making this extrapolation, an analogy of the relationship of the turning of a tropical cyclone to its hyperbolic point was used.

The method that is occasionally used in the Australian Bureau of Meteorology was developed by Lajoie and Nicholls (1974). From available satellite pictures, they identify certain cloud features and based on these, extrapolation is made for the next 12 h regarding the change of direction of motion of the cyclone. The two main principles involved are as follows: tropical cyclones frequently move in the direction of the line connecting their centers to the most developed cumulonimbus cluster at or near the downstream end (i.e. in a cyclonic direction of the inflow current) of the outer cloud band and tropical cyclones usually do not move towards a cumulonimbus-free sector.

The advantage of the satellite techniques is that they can be used in regions where conventional data are sparse. The disadvantages are difficulty in obtaining good satellite pictures and the subjectivity involved in interpreting them. Nevertheless, certain simple concepts are useful in the prediction of the tracks. For example, Ramage (1973) noted the extent of cloudiness along the track of a tropical cyclone. In Japan, substantial observations exist to show that the successive positions of the spiral cloud band correlate well with the movement of recurving typhoons.

Cyclones moving towards the west sometimes recurve towards northeast after interaction with upper air troughs in the westerlies. Chan (1978), based on a study of recurring typhoons in the western part of the North Pacific Ocean, suggested that the following two parameters, which can be determined from satellite imagery, can be used to estimate the

recurvature: D/d, where D is the diameter of the central dense overcast of the topical cyclone and d is the average width of the cloud band associated with the interacting trough, and θ, which is the angle between the axis of the cloud band and the latitude of the tropical cyclone center. If $30° \leq \theta \leq 40°$ and $D/d < 1.5$, then it is highly probable that a tropical cyclone will recurve.

Statistical Techniques of Track Prediction

Following Neumann (1979), statistical models will be discussed. These are broadly divided into two categories: models based on analogs and models based on regression equations. Regression equation models can be further classified into (i) models using predictors based on climatology and persistence, (ii) models that include, but are not limited to, predictors derived from observed synoptic data, and (iii) models that include, but are not limited to, predictors derived from numerically forecasted data. Models of type (i) are referred to as simulated analog, models of type (ii) are referred to as classical models (or statistico-synoptic), and models of type (iii) are called statistical–dynamical models.

Neumann (1969) developed an operational model for predicting the movement of hurricanes using analog methods. This model was extended by Hope and Neumann (1969, 1970) for a 72-h prediction based at the National Hurricane Center in Miami. This model is known by its acronym HURRAN (for hurricane analog) and has been in use since the 1969 hurricane season.

The basic principle involved in these models is the recognition of the fact that temporal and spatial analyses of tracks reveal repetitiveness and close association with identifiable synoptic patterns. Hodge and McKay (1970) developed an analog prediction model for the North Pacific typhoons. This model, referred to as TYFOON, was modified by Jarrell and Somervell (1970) and has been in operation since August 1970 at the Fleet Numerical Weather Center/Joint Typhoon Warning Center in Guam. Simpson (1971) attributed the moderate success of models HURRAN and TYFOON to the presentation of the predictions in terms of probability ellipses, which provide significant diagnostic information. Other similar models were those of Gupta and Datta (1971) and Sikka and Suryanarayana (1972) for the North Indian Ocean, Jarrell and Wagoner (1973) for the North Pacific, Brand et al. (1974) for the Southwest Indian Ocean, Jarrell et al. (1975) for the northeastern Pacific, Brand and Blelloch (1976) for the southwestern Pacific and Australia, Annette (1976) for Australia (the CYCLOGUE model), Neumann and Randrianarison (1976) for the Malagasy Republic, and Chen et al. (1977) for China (an adaptation of HURRAN).

The advantage of the analog method is that it is usually the first available forecast for the tracks. Its disadvantage is that it works well only for typical situations. Next, the regression methods will be considered. Riehl (1956) gave the first objective technique for predicting the movement of tropical cyclones. In this method, known as the Riehl–Haggard technique, one makes use of the steering principle, namely that the tropical cylone's movement speed is proportional to the speed of the vertically integrated flow surrounding the vortex. The 500-mb level was used for approximating this flow. This technique was originally used for the Atlantic hurricanes. Wang (1954, 1956, 1960) developed regression equations for typhoon motion over 24 h based on predictors at the 700-mb level. Miller and Moore (1960) used the 700-mb level for the Atlantic hurricanes. Arakawa (1963) and Tse (1966) developed models for the Pacific Ocean and Kumar and Prasad (1973) developed models for the North Indian Ocean.

Veigas et al. (1959) used stepwise screening regression methods and used predictors

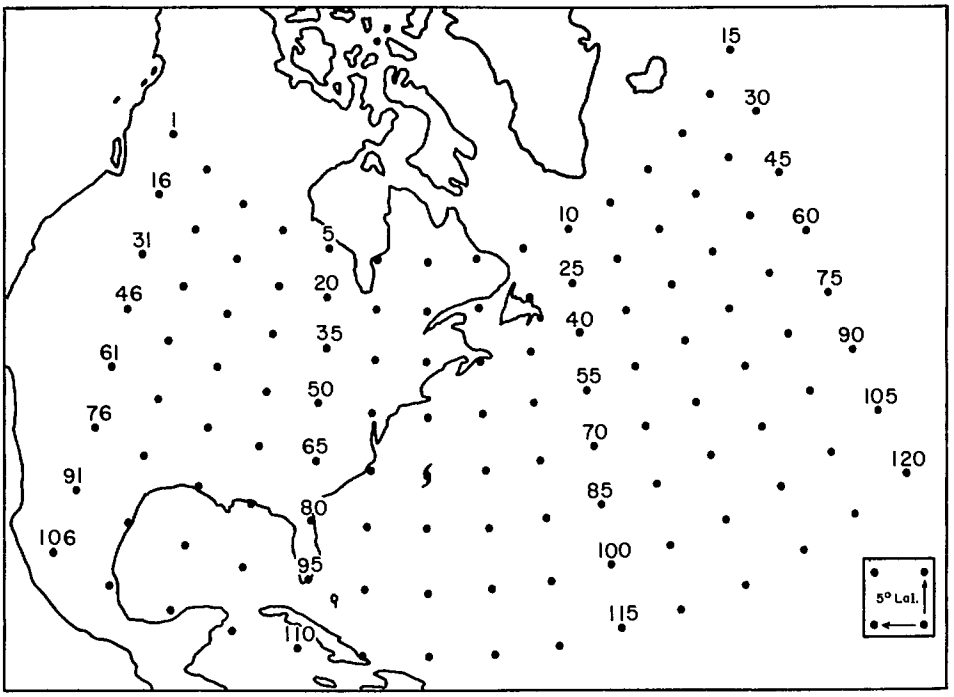

FIG. 6.9. Locations of the 8 × 15 grid for a hurricane centered at 35°N, 70°W with a grid spacing of 556 km. The grid moves with the storm. (Neumann 1979)

from a larger area rather than using a small area in the vicinity of the storm. This original model, known as T-59, was modified to T-60 by Veigas (1961, 1962). These models are not very sensitive to the initial analyses near the storm, and they are operationally used in Hong Kong (Chin 1976).

Miller and Chase (1966) combined the best features of the Riehl–Haggard method and the Miller–Moore method into a single model. This National Hurricane Center model (NHC64) uses predictors from the 700- and 500-mb levels and provides forecasts up to 72 h. Also, this model uses the objective forecasts of the National Meteorological Center for the 1000-, 700-, and 500-mb levels and removes the drudgery of hand analyses. Miller et al. (1968) revised the NHC64 model into NHC67, which is presently in operation at the National Hurricane Center in Miami. Other models that deserve mention are CLIPER (for climate and persistence) for the Atlantic by Neumann (1972), a model for the South Indian Ocean by Neumann and Randrianarison (1976), a model for the North Indian Ocean by Neumann and Mandal (1978), and a model for the eastern North Pacific by Neumann and Leftwich (1977).

The NHC72 model incorporates the best features of the analog and regression models (Neumann et al. 1972). The NHC67 and NHC72 models did not work well for untypical Atlantic hurricanes in the early 1970's. Hence, statistical–dynamical models (which use the output of a numerical mode as input to a statistical model) were developed (e.g. Veigas 1966). Neumann and Lawrence (1975) developed the NHC73 model using predictors from the 24-, 36-, and 48-h 500-mb geopotential height field forecasts. Other models are HATRACK (Renard 1968) and MOHATT (Renard et al. 1973).

The synoptic data predictors that are used for these models are generally screened from a great number of predictors given by storm-centered moving grids. A grid that has been used for Atlantic hurricanes is shown in Fig. 6.9.

Dynamical Methods for Predicting Hurricane Movement

Following Pelissier (1979), the numerical models that were developed for predicting hurricane motion will be considered. The numerical modeling effort has been slow until the 1970's principally because tropical storms mainly occur over the data-sparse areas of the tropical oceans, and it is difficult to provide the initial state of the atmosphere. From a grid resolution point, the scale of the intense part of the tropical cyclone is small compared with the synoptic weather disturbances. Generally, prediction of the tracks of tropical cyclones is more successful than prediction of the intensification because the movement of the storm is mainly related to the steering current in which the storm is embedded.

Sanders and Burpee (1968) originally developed a barotropic model, referred to as SANBAR, which was modified by Pike (1972). In this model the tropical cyclone track is predicted based on the track of minimum stream function and maximum vorticity centers. On a Mercator projection using a grid size of 1.5° and extending from the equator to 55°N and from 36.5°W to 123.5°W and using a time step of 30 min, forecasts are made up to 72 h in advance. The initial observations are averaged over the 1000- to 100-mb layer.

After specifying the initial winds, the nondivergent part of the wind field is calculated through a relaxation of the stream function ψ in the interior of the grid using the relation

$$\nabla^2\psi = \frac{\partial v}{\partial x} - \frac{\partial u}{\partial y} + \frac{u \tan (\text{latitude})}{R_E} \tag{6.46}$$

where u and v are the eastward and northward components, respectively, of the hurricane motion and R_E is the radius of the earth. One must specify the component of the wind parallel to the boundaries. Then, using the barotropic vorticity equation

$$(\nabla^2 - M)\frac{\partial \psi}{\partial t} = J(f + \nabla^2\psi, \psi) \tag{6.47}$$

one can determine ψ where J is the Jacobian, ∇^2 is the horizontal Laplacian, and M is the Helmholtz coefficient.

One can identify the storm center with a local minimum in ψ or a maximum in $\nabla^2\psi$ (or as an average between these two positions). Usually, the storm is replaced by an idealized circularly symmetric vortex defined by

$$v_\theta = 0.72 v_{\max} \left\{ \sin \left[\pi \left(\frac{r}{r_m} \right) \right]^{\left(\frac{\ln 0.5}{\ln r_e / r_m} \right)} \right\}^{1.5} \tag{6.48}$$

where v_θ is the symmetric tangential wind field.

The Japan Meteorological Agency developed a balanced barotropic model for typhoon track prediction northward of 20°N using a 51 × 15 grid with a mesh length of 381 km at 60°N. At least three types of systematic errors appear: forecast positions for low latitude storms are occasionally poor due to a westward bias in the predicted tracks, the predicted speed of movement is usually smaller than observed values, and the predicted recurvature is usually less than the observed recurvature.

In this model the initial stream function ψ is determined from the geopotential by

TABLE 6.11. Frequency distribution of direction using the balanced barotropic model. The angular intervals listed are the ranges of absolute differences between predicted and observed directions of displacement. Data listed under 24- and 48-h forecast periods are the number of typhoons that exhibited these directional deviations. (Pelissier 1979)

Angular interval (degrees)	24-h forecast period	48-h forecast period
0–5	10	8
6–10	12	7
11–20	13	9
21–30	5	10
31–45	7	3
45	7	7

TABLE 6.12. Same as Table 6.11, except this is for eastward moving typhoons. (Pelissier 1979)

Angular interval (degrees)	24-h forecast period	48-h forecast period
0–5	11	15
6–10	14	8
11–20	16	10
21–30	10	4
31–45	5	8
45	3	5

TABLE 6.13. Errors in predicted speed of movement relative to recurvature point. Overrun No. indicates number of typhoons that moved slower than the forecast. R, actual typhoon displacement; F, prediction by the balanced barotropic model. (Pelissier 1979)

	24-h forecast period			48-h forecast period		
Typhoon position	Total No.	Overrun No.	$\frac{\lvert R-F\rvert}{R}$	Total No.	Overrun No.	$\frac{\lvert R-F\rvert}{R}$
Before recurvature	42	16	0.406	38	14	0.341
Near recurvature	45	13	0.334	34	12	0.498
After recurvature	20	0	0.340	9	0	0.379
Total (mean)	107	29	(0.381)	81	26	(0.401)

solving the balance equation

$$\nabla\cdot(f\nabla\psi) + 2\left(\frac{\partial^2\psi}{\partial x^2}\frac{\partial^2\psi}{\partial y^2} - \frac{\partial^2\psi}{\partial x\partial y}\right) = \nabla^2\psi \tag{6.49}$$

where ϕ is the geopotential and f is the Coriolis parameter. Using Arakawa's (1966) finite-difference schemes, the equation is integrated in time. Based on the data at 00:00 and 12:00 GMT, forecasts are issued for 48 h in advance, twice daily.

The frequency distribution of direction errors for westward moving typhoons is shown in Table 6.11. In this table, the first row contains the ranges of absolute differences between observed and predicted directions of displacements. One can see that there is no

directional bias in the forecast. The frequency distribution of the direction errors for eastward moving typhoons is shown in Table 6.12. The errors in the forecast speed of the the hurricane are classified in Table 6.13 according to the location relative to the point of recurvature. The term "overrun" means the number of typhoons that moved slower than predicted. Usually, this happens before recurvature but never afterwards.

A primitive equation model is considered next. The Fleet Numerical Weather Center (FNWC) at Monterey, CA, and the Joint Typhoon Warning Center (JTWC) at Guam use a primitive equation model referred to as the coarse mesh grid model (CMG), which is a simplified version of a more elaborate triple-nested grid model (Hinsman 1977). The primitive equations are expressed in the pressure coordinates as follows:

$$\frac{\partial u}{\partial t} = -L(u) + fv - M\frac{\partial \phi}{\partial x} + \frac{\partial \tau_{xx}}{\partial x} + \frac{\partial \tau_{yx}}{\partial y} \tag{6.50}$$

$$\frac{\partial v}{\partial t} = -L(v) - fu - M\frac{\partial \phi}{\partial y} + \frac{\partial \tau_{xy}}{\partial x} + \frac{\partial \tau_{yy}}{\partial y} \tag{6.51}$$

$$\frac{\partial \theta}{\partial t} = -L(\theta) \tag{6.52}$$

$$\frac{\partial \phi_{1000}}{\partial t} = -L(\phi_{1000}) \tag{6.53}$$

$$\frac{\partial w}{\partial p} = -M^2\left[\frac{\partial}{\partial x}\left(\frac{u}{M}\right) + \frac{\partial}{\partial y}\left(\frac{v}{M}\right)\right] \tag{6.54}$$

$$\frac{\partial \phi}{\partial p} = \phi C_p \frac{\partial}{\partial p}\left(\frac{p}{1000}\right)^{R/C_p} \tag{6.55}$$

where

$$L(S) = M^2\left[\frac{\partial}{\partial x}\left(\frac{u_S}{M}\right) + \frac{\partial}{\partial y}\left(\frac{v_S}{M}\right)\right] + \frac{\partial}{\partial p}(w_S) \tag{6.56}$$

The region of computation is like a channel with cyclic boundary conditions in the east and west and free-slip conditions on the north and south walls. In the vertical there are three layers. A movable grid is placed over the tropical cyclone so that initially the storm is in the lower central portion of the grid, which covers a span of 56° of longitude and 48° of latitude, with a mesh interval of 2°. An objective analysis of the flow fields at the 850-, 700-, and 200-mb levels, as well as the temperature at the 850-mb level, serve as input. Using a time step of 10 min, the model is integrated in time. The errors in the predicted track for the western and eastern Pacific are shown separately and together in Table 6.14. The errors are in kilometres and the numbers in parentheses are the cases studied.

At the National Meteorological Center, a multilevel nested grid model was developed (Hovermale and Livezey 1978). This is referred to as the moving fine mesh (MFM) model. This model appears to be unique in the sense that a nested high-resolution grid centered over the tropical cyclone moves during the numerical integration through a coarse outer grid. The error analysis for the forecasts based on this model is given in Table 6.15 and comparison is made with the errors from other models. For a review of the forecast errors using barotropic models, see Sanders et al. (1978). Hope and Neumann (1978) provided a survey of tropical cyclone models available worldwide. Elsberry (1979) summarized the three-dimensional models that are available for hurricane track prediction. In his survey

TABLE 6.14. Average forecast errors (km) for 1976 for the U.S. Navy primitive equation tropical cyclone prediction model (CMG). Number of cases in parentheses. (Pelissier 1979)

Area	24-h forecast period	48-h forecast period	72-h forecast period
Western Pacific	287 (65)	480 (57)	693 (43)
Eastern Pacific	263 (18)	387 (15)	724 (15)
Both together	283 (81)	461 (72)	702 (58)

TABLE 6.15. Mean vector errors (km) of the MFM, official forecasts, and other operational objective techniques based on statistical, climatological, and persistence methods (homogeneous sample) for Hurricane Belle of August 7–8, 1976. MFM, movable fine mesh; NHC, National Hurricane Center; NHC-67, National Hurricane Center's 1967 model. For a description of SANBAR and CLIPER, see text. (Hovermale and Livezey 1978)

Forecast period (h)	MFM	Official	NHC-67	NHC-72	NHC-73	SANBAR	CLIPER
12	124	87	67	72	67	86	76
24	213	185	200	226	152	228	204
36	215	—	241	365	270	426	454
48	280	404	311	507	369	644	748

TABLE 6.16. Characteristics of several baroclinic models being applied for prediction of tropical cyclone motion based on operational data. NMC, National Meteorological Center (U.S.A.); MFM, movable fine mesh; FNWC, Fleet Numerical Weather Center (Monterey, CA); TCM, tropical cyclone model; NRL, Naval Research Laboratory; NEPRF, Naval Environmental Prediction Research Facility; PSU, Pennsylvania State University; NPS, Naval Post Graduate School (Monterey, CA); JMA, Japan Meteorological Agency; MNG, multiple-nested grid. (Elsberry 1979)

Agency-model	Vertical coordinate	No. of layers	Grid size (km)	No. of points	Relocatable grid	Lateral boundary conditions[a]
NMC-MFM	σ	10	60	50×50	Yes	OW
FNWC-TCM	p	3	205	32×24	No	OW
NRL-NEPRF	σ	5	60	51×51	No	OW
PSU-NPS	σ	5	120	40×40	No	OW
JMA-MNG	σ	3	291	31×31	No	OW
			145	31×31	Yes	TW
			73	31×31	Yes	TW
			36	31×31	Yes	TW

[a]OW, one-way interaction; TW, two-way interaction.

he omitted the barotropic models. Since it is almost certain that all future forecasts will be made with baroclinic models, these three-dimensional models will be briefly reviewed.

The features of some of the baroclinic models presently available are listed in Table 6.16. These models (except the FNWC–TCM) are capable of resolving the inner structure of the tropical cyclone. Although a 60-km grid such as that used by the NMC and NRL–NEPRF models can resolve the primary interaction between the vortex and the steering current, to predict intensification the inner core of the typhoon must be resolved. Since it is impractical to cover the whole region of the typhoon with a fine grid, one can

TABLE 6.17. Track error (km) statistics at 24 and 48 h for selected 1977 typhoons for official (JTWC), NMC-MFM, and FNWC-TCM. JTWC, Joint Typhoon Warning Center, Guam. (Elsberry 1979)

	Official		NMC-MFM		FNWC-TCM	
Typhoon	24 h	48 h	24 h	48 h	24 h	48 h
Vera-1	178	107	294	289	106	111
Ivy	226	472	109	248	—	—
Dinah-1	181	778	356	559	152	285
Thelma	159	707	96	148	146	574
Jean	126	578	339	441	—	—
Dinah-2	206	437	56	385	250	270
Babe	583	—	282	885	437	—
Dinah-3	204	693	115	324	52	350
Vera-2	300	444	254	181	143	52
Gilda	243	407	183	580	100	376
Babe	191	782	217	198	196	726
Homogeneous	250	544	206	333	176	343
Sample (N)	9	8				

use a nested grid, the fine grid having a resolution of 10 km. Also, this inner grid must be moved with the storm. At present, the JMA model has these capabilities, although the inner grid size is 36 km.

Two types of boundary conditions are presently used in these models. In the one-way (OW) type, no feedback is allowed from the tropical cyclone to the hemispherical model. Note that the JMA nested grid model has a two-way (TW) interaction boundary condition for the inner grids. The statistics at 24 and 48 h for selected 1977 typhoons for official (JTWC), NMC−MFM, and FNWC−TCM models are shown in Table 6.17.

One important data source should be mentioned. The National Climatic Center's (Ashville, NC) magnetic tape deck 993 contains 12-h tropical storm movements for all ocean basins (Crutcher et al. 1978) for the period 1886−1975, and this file is continually being updated. Crutcher (1971a, 1971b) and Crutcher and Quinlan (1971) used the bivariate normal elliptical distribution as a model for the statistics of the distributions of hurricane movements. Crutcher et al. (1978) deduced tropical storm accelerations based on the data contained in this vast file.

FORECASTING TROPICAL CYCLONE RECURVATURE

Most of the forecast errors associated with storm track prediction occur when the cyclones turn (or recurve). Chan et al. (1980) studied tropical cyclones in the West Indies area for the period 1961−77 using compositing. These studies indicated that through an observation of certain parameters around a tropical cyclone (e.g. wind rotation, vertical wind shear between 200 and 900 mb, or a gradient of tropospheric mean temperature), better forecasts for 24−36 h ahead can be made. The basis for this statement is the fact that significant differences exist in the large-scale wind fields at 200-, 500-, and 900-mb levels for left-turning, straight-moving, and right-turning cyclones.

This study was limited to those cyclones west of 55°W and with maximum sustained winds of at least 18 $m \cdot s^{-1}$. Three categories are defined as follows (Fig. 6.10):

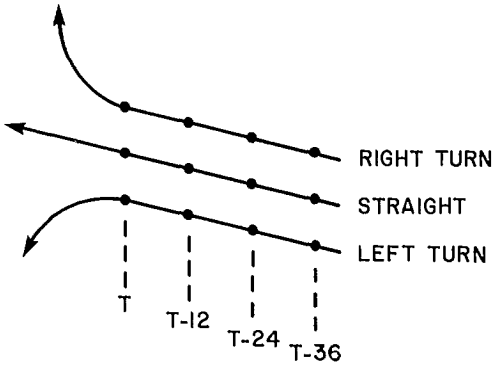

FIG. 6.10. Idealized picture of the three turn classes of tropical cyclones and of the time periods (hours) prior to the turn. (Chan et al. 1980)

TABLE 6.18. Average 24-h official tropical cyclone track forecast errors (km) issued by the National Hurricane Center, Miami. T, time when the storm begins to turn. (Chan et al. 1980)

Turn classification	$T-24$	T	$T+24$
Left turn (10 cases)	235	289	206
Straight (23 cases)	148	169	196
Right turn (22 cases)	178	324	239
Special right turn (16 cases)	148	417	245

TABLE 6.19. Directional deviation (degrees) of the mean 24-h forecast position made at turn time from the mean verifying position and the mean extrapolated track. A positive number means the forecast position is to the right of the verifying position of the extrapolated track. (Chan et al. 1980)

Turn classification	From mean extrapolated track	From mean verifying position
Left turn	21	50
Straight	9	11
Right turn	2	−38

$$\begin{aligned} &\text{Left-turning:} && D(T+12)-D(T) < -20^\circ \\ (6.57)\quad &\text{Straight-moving:} && -10^\circ < D(T+12)-D(T-12) \\ &\text{Right-turning:} && D(T+12)-D(T) > 20^\circ \end{aligned}$$

where D is the direction of movement of the storm at a standard time T (00:00 or 12:00 GMT). A total of 16 left-turning, 33 straight-moving, and 28 right-turning storms were selected for this study.

The 24-h forecasts given by the National Hurricane Center were analyzed for each case at three time periods: (a) 24 h before turn time, i.e. $T-24$, (b) at turn time T, and (c) 24 h after turn time, i.e. $T+24$. The forecast errors are listed in Table 6.18. The

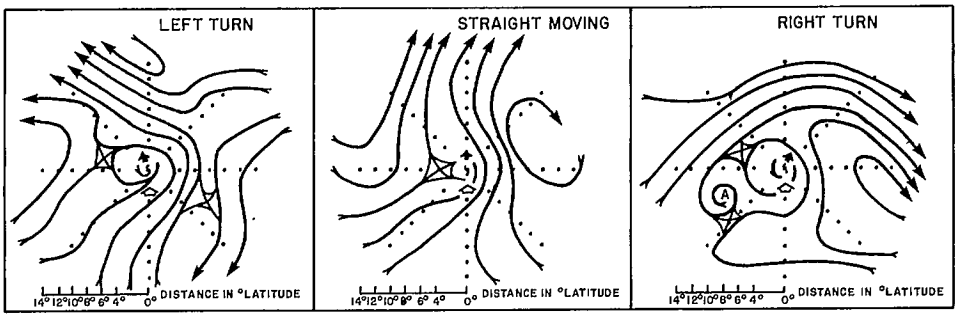

FIG. 6.11. Streamlines (500 mb) for the three turn cases shown in Fig. 6.10, at turn time. Open arrows indicate the instantaneous direction of storm motion. Solid arrows indicate the movement of the storm during the next 12 h. (Chan et al. 1980)

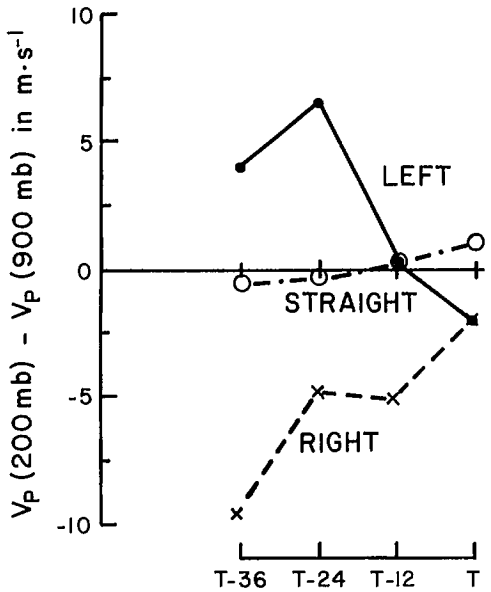

FIG. 6.12. Vertical wind shear for different time periods. The ordinate is the value of the average vertical wind shear within 7–11° radius from the storm centre in octants 1 and 5. (Chan et al. 1980)

special right-turn class is for those cases with an error greater than 350 km. The average directional deviation of the forecast locations from the verified locations and the extrapolated tracks are given in Table 6.19.

The basis for this study is the recognition of the fact that midtropospheric wind patterns have a strong influence on tropical cyclone motion. According to George and Gray (1977), 500 mb is the best steering level for direction of movement and 700 mb is the best level for the speed of movement of the storm. For refining the prediction, flow fields at 900-, 700-, 500-, and 200-mb levels were used. The streamline field at the 500-mb level for the three classes of cyclones is shown in Fig. 6.11.

The vertical wind shear for these three classes is shown in Fig. 6.12. Here, V_P represents the wind component parallel to the track and V_N is the wind component perpendicular to the track. It can be seen from this diagram that usually the shear (i.e. V_P at 200 mb minus V_P at 900 mb) is greater than 5 $m \cdot s^{-1}$ for left-turning tropical cyclones, is in the range of -5 to 5 $m \cdot s^{-1}$ for straight-moving storms, and is less than -5 $m \cdot s^{-1}$ for right-turning cyclones.

Sometimes it may not be possible to derive satellite winds at the 900- and 200-mb levels because of extensive cloud cover. In these situations, the satellite sounder (which can measure tropospheric difference) could be used. Generally, for left-turning storms the mean tropospheric temperature is lower to the left front of the storm. For straight-moving storms a weak temperature gradient shows across the front of the storm. Right-moving storms indicate a relatively cold troposphere to the right front of the storm.

Project Stormfury

Project Stormfury is a scientific program aimed at studying the structure and dynamics of tropical cyclones and the possibility of modifying them, e.g. through cloud-seeding experiments (Sheets and LaSeur 1978). The project formally began in 1962, although some initial seeding experiments were done in 1961. These experiments are designed to effect a reduction in the maximum wind speeds in cyclones through changing the location of the energy released near the cyclone's center. It is well known that the source of energy for a tropical cyclone is the latent heat released during convective overturning of the atmosphere. The active convective area in which updrafts of 10–20 $m \cdot s^{-1}$ occur is less than 1% of the area of the hurricane. Hence, one must modify only a small area of the hurricane to change its characteristics. The dynamics of the modification through seeding is explained by Sheets and LaSeur (1978, p. 281) as follows:

> Injection of silver iodide particles into the upper portion of these clouds causes the droplets to freeze, releasing the latent heat of fusion. This additional heat causes that portion of the cloud to be warmer and thereafter lighter than the surrounding air and thus triggers an increase in the ascending flow. As the air rises, it expands and cools, and water vapor condenses or sublimates, releasing considerably more latent heat. The result is that the seeded cloud grows to the outflow level, providing a new convective conduit that intercepts the inflowing low level air. The result is that a new eyewall is formed at a greater distance from the storm center than the initial eyewall.

The tests on Hurricane Debbie of 1969 showed that winds could be reduced by 15–30%. For experiments on typhoon modification, see World Meteorological Organization (1975) report No. 408.

Naming Hurricanes

In the July 1978 issue of the Journal NOAA (which is a publication of the U.S. National Oceanic and Atmospheric Administration), an interesting article appeared on the practice of naming hurricanes. Part of this article was extracted from a book by Tannehill (1950) and some recent information was added. Here, a brief summary of this article is given.

In the United States during the nineteenth century and the first half of the twentieth century, there were occasions when a hurricane was named after a region, town, person, or saint. But most were unnamed.

Towards the end of the nineteenth century, an Australian meteorologist, Clement Wragge, began naming hurricanes using female names. However, he restricted female

TABLE 6.20. Official list of hurricane names originating in the Atlantic Ocean for the seasons of 1979–83. (Anonymous 1978a)

1978	1980	1981	1982	1983
Ana	Allen	Arlene	Alberto	Alicia
Bob	Bonnie	Bret	Beryl	Barry
Claudette	Charley	Carla	Chris	Chantal
David	Danielle	Dennis	Debby	Dean
Elena	Earl	Emily	Ernesto	Erin
Frederic	Frances	Floyd	Florence	Felix
Gloria	Georges	Gert	Gilbert	Gabrielle
Henri	Hermine	Harvey	Helene	Hugo
Isabel	Ivan	Irene	Isaac	Iris
Juan	Jeanne	Jose	Joan	Jerry
Kate	Karl	Katrina	Keith	Karen
Larry	Lisa	Lenny	Leslie	Luis
Mindy	Mitch	Maria	Michael	Marilyn
Nicolas	Nicole	Nate	Nadine	Noel
Odette	Otto	Ophelia	Oscar	Opal
Peter	Paula	Philippe	Patty	Pablo
Rose	Richard	Rita	Rafael	Roxanne
Sam	Shary	Stan	Sandy	Sebastien
Teresa	Tomas	Tammy	Tony	Tanya
Victor	Virginie	Vince	Valerie	Van
Wanda	Walter	Wilma	William	Wendy

names to those storms that arrived in Australia from the tropics. Those storms that did not originate in the tropics were named after politicians whom he disliked.

Since the early part of the twentieth century, Pacific typhoons were also named after females. Pan American Airways pilots began using female names for hurricanes in 1938. In September 1950 three hurricanes occurred almost simultaneously (one north of Bermuda, the second north of Puerto Rico, and the third in the Gulf of Mexico). To avoid confusion, these were identified by alphabetical letters. In 1951 the agencies involved in weather communication decided to use the following list: Able, Baker, Charlie, Dog, Easy, Fox, George, How, Item, Jig, King, Love, Mike, Nan, Oboe, Peter, Queen, Roger, Sugar, Tare, Uncle, Victor, William, X ray, Yoke, Zebra.

However, in 1952 a new international list was suggested as follows: Alpha, Bravo, Coca, Delta, Echo, Foxtrot, Golf, Hotel, India, Juliet, Kilo, Lima, Metro, Nectar, Oscar, Papa, Quebec, Romeo, Sierra, Tango, Union, Victor, Whiskey, Extra, Yankee, Zulu. To avoid confusion, the United States agencies began using female names for hurricanes in the Atlantic, Caribbean Sea, and the Gulf of Mexico. For the 1953 season the list was Alice, Barbara, Carol, Dolly, Edna, Florence, Gilda, Hazel, Irene, Jill, Katherine, Lucy, Mabel, Norma, Orpha, Patsy, Queen, Rachel, Susie, Tina, Una, Vicky, Wallis. Although there was some criticism occasionally from the press and the public, this practice of using female names (however, the list is changing every year) continued until the 1970's.

In 1971 the U.S. National Weather Service prepared a semipermanent list of 10 sets of hurricanes (to be used over a decade and then repeated), still with female names only. Names beginning with Q, U, X, Y, and Z were eliminated because of a scarcity of such names. Beginning in 1977, under the auspices of the World Meteorological Organization, new lists were composed. In these lists, female and male names alternate. These lists for the Atlantic hurricanes and the eastern Pacific storms are shown in Tables 6.20 and 6.21, respectively.

TABLE 6.21. Official list of tropical storm names in the eastern part of the Pacific Ocean for the seasons of 1978–81. (Anonymous 1978a)

1978	1979	1980	1981
Aletta	Andres	Agatha	Adrian
Bud	Blanca	Blas	Beatriz
Carlotta	Carlos	Celia	Calvin
Daniel	Dolores	Darby	Dora
Emilia	Enrique	Estelle	Eugene
Fico	Fefa	Frank	Fernanda
Gilma	Guillermo	Georgette	Greg
Hector	Hilda	Howard	Hilary
Iva	Ignacio	Isis	Irwin
John	Jimena	Javier	Jova
Kristy	Kevin	Kay	Knut
Lane	Linda	Lester	Lidia
Mirian	Marty	Madeline	Max
Norman	Nora	Newton	Norma
Olivia	Olaf	Orlene	Otis
Paul	Pauline	Paine	Pilar
Rosa	Rick	Roslyn	Ramon
Sergio	Sandra	Seymour	Selma
Tara	Terry	Tina	Todd
Vicente	Vivian	Virgil	Veronica
Willa	Waldo	Winifred	Wiley

TABLE 6.22. Monthly average number of storms per year for each major ocean basin. T, tropical storms only; H, hurricanes only. For the North Indian Ocean, replace the term hurricane with cyclone (winds $\geq$ 89 km·h^{-1}). —, zero. (Crutcher and Quayle 1974)

	North Atlantic		Eastern North Pacific		Western North Pacific		Southwest Pacific and Australian area		Southwest Indian Ocean		North Indian Ocean	
Month	T	H	T	H	T	H	T	H	T	H	T	H
Jan.	—	—	—	—	0.2	0.3	2.7	0.7	2.0	1.3	0.1	—
Feb.	—	—	—	—	0.3	0.2	2.8	1.1	2.2	1.1	—	—
Mar.	—	—	—	—	0.3	0.2	2.4	1.3	1.7	0.8	—	—
Apr.	—	—	—	—	0.2	0.7	1.3	0.3	0.6	0.4	0.1	0.1
May	0.1	—	—	0.3	0.4	0.9	0.3	—	0.2	—	0.3	0.5
June	0.4	0.3	1.5	0.6	0.5	1.2	0.2	—	—	—	0.5	0.2
July	0.3	0.4	2.8	0.9	1.2	2.7	—	0.1	—	—	0.5	0.1
Aug.	1.0	1.5	2.3	2.0	1.8	4.0	—	0.1	—	—	0.4	—
Sept.	1.5	2.7	2.3	1.8	1.5	4.1	—	—	—	—	0.4	0.1
Oct.	1.2	1.3	1.2	1.0	1.0	3.3	0.1	—	0.3	—	0.6	0.4
Nov.	0.4	0.3	0.3	—	0.8	2.1	0.4	0.3	0.3	—	0.5	0.6
Dec.	—	—	—	—	0.6	0.7	1.5	0.5	0.8	0.5	0.3	0.2

6.3 Cyclones of the Pacific Ocean

Most of the damage from storm surges on the coast of the Pacific Ocean results from tropical storms. Hence, these will be emphasized in this section. The extratropical cyclones that occasionally generate storm surges along the Pacific coast will be treated in

other sections (while dealing with storm surges in the United States, Canada, Australia, etc.). Note that a storm surge is a rare event on the Pacific coasts of Canada and the United States (with the exception of Alaska); along these coasts, wind waves and swell are of primary importance.

Earlier it was mentioned that tropical cyclones form over all the tropical oceans except in the South Atlantic and in the South Pacific east of 140°W. The highest frequency of tropical cyclones occurs in the western Pacific, although maximum damage has occurred on the coasts surrounding the Bay of Bengal. Indeed one may say that tropical cyclones and their associated storm surges together are probably the most devastating natural phenomena, even more so than earthquakes.

The number of tropical storms and hurricanes (i.e. tropical storms with sustained winds equal to or greater than 48 knots (89 $km \cdot h^{-1}$) are listed by month for various ocean basins in Table 6.22. It can be seen that the maximum frequency is in the western part of the North Pacific Ocean during the months of August and September. The preferred tropical cyclone tracks over the globe are shown in Fig. 6.13. Again, it can be seen that the tracks in the Pacific Ocean and Indian Ocean have more fine structure than those in the Atlantic Ocean. Contours of the speed of movement of tropical storms for various ocean basins are shown in Fig. 6.14. Maximum values of 35 knots (65 $km \cdot h^{-1}$) occur in the western North Pacific, with maximum values of 30 knots (56 $km \cdot h^{-1}$) in the Atlantic, and with maximum values of 27.5 (51 $km \cdot h^{-1}$) in the eastern edge of the South Indian Ocean. In the following subsections, certain characteristics of tropical cyclones in the eastern North Pacific, central North Pacific, and western North Pacific will be detailed.

Characteristics of Tropical Cyclones in the Eastern North Pacific

This discussion will be based on the tropical cyclone seasons of 1976, 1977, and 1978 (Gunther 1977, 1978, 1979). For the 1976 season, tropical cyclone activity began on June 1 and ended on October 29. The season was average in the sense that there were eight hurricanes, six tropical storms, and four tropical depressions. The 1977 season began on May 25 and ended on October 23. Thus, the length of the 1977 season was 152 d whereas in 1976 it was 150 d. The total number of tropical storms in 1977 was 17 compared with 18 in 1976. However, in 1977 only 47% of the storms reached hurricane intensity. Note that the number of tropical cyclones reaching storm or hurricane intensity in 1977 was 47% less than the average for the period 1966–76. For the 1976 season, the highest sustained wind speed was 125 knots (231 $km \cdot h^{-1}$) whereas for the 1977 season it was 90 knots (167 $km \cdot h^{-1}$).

In 1978, the season began on May 30 and ended on October 20, with a duration of 144 d. Although the 1978 season was 8 d shorter than the 1977 season, there was an increase of 24% in cyclone activity. The number of cyclones reaching storm or hurricane intensity was 86% in 1978 compared with 47% in 1977. The highest sustained wind speed in the 1978 season was 120 knots (222 $km \cdot h^{-1}$).

The first tropical cyclone to hit southern California since 1939 was Hurricane Kathleen in 1976. In the 1977 season, Hurricane Doreen struck again and in the 1978 season Hurricane Norman reached the coast. Though none of these three hurricanes caused any storm surge activity on the California coast, the heavy rains associated with these caused extensive damage.

During the hurricane season bulletins are issued four times per day from the Eastern Pacific Hurricane Center in San Francisco. The number of eastern North Pacific tropical storms reaching hurricane intensity is given in Table 6.23. The tracks of Hurricanes

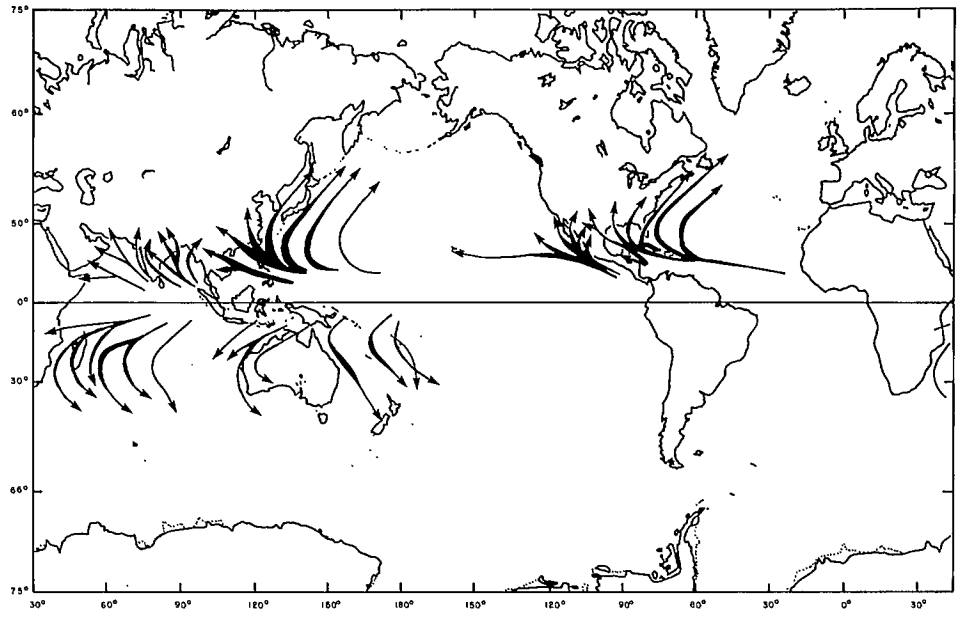

FIG. 6.13. Preferred annual tropical cyclone paths. Arrow widths are proportional to storm frequencies along indicated paths. (Crutcher and Quayle 1974)

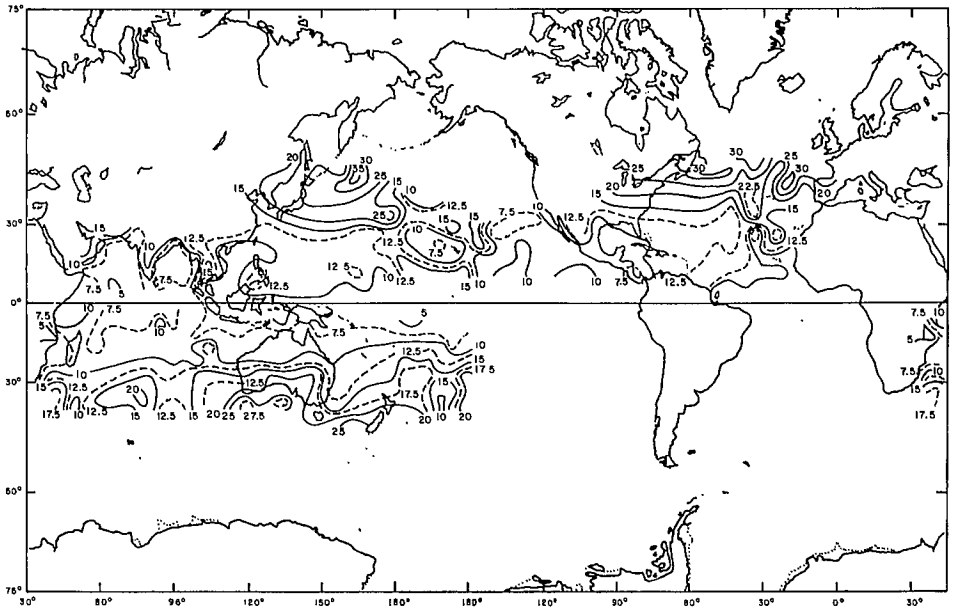

FIG. 6.14. Average (for annual data) speeds (knots) of storm movement (1 knot = 1.852 km·h^{-1}). (Crutcher and Quayle 1974)

TABLE 6.23. Number of eastern North Pacific tropical storms reaching hurricane intensity by month and year. Cyclones are ascribed to the month in which they began. (Gunther 1979)

Year	May	June	July	Aug.	Sept.	Oct.	Nov.	Total
1966	0	1	0	4	2	0	0	7
1967	0	1	0	2	1	2	0	6
1968	0	0	0	3	2	1	0	6
1969	0	0	1	1	1	1	0	4
1970	1	0	1	1	0	1	0	4
1971	1	1	5	2	2	1	0	12
1972	1	0	0	6	1	0	0	8
1973	0	1	3	0	2	1	0	7
1974	0	2	2	4	2	1	0	11
1975	0	1	2	3	1	1	0	8
1976	0	2	1	2	3	0	0	8
1977	0	0	1	1	1	1	0	4
1978	1	2	3	4	1	1	0	12
Total	4	11	19	33	19	11	0	97
Average	0.3	0.8	1.5	2.5	1.5	0.8	0.0	7.5

Kathleen of September 1976 and Doreen of August 1977 are shown in Fig. 6.15. All the tropical cyclones during 1977 did not reach land, as they were dissipated over the ocean. Hence, the damage in the 1977 season was less than in the 1976 season (during this season, several hurricanes moved onshore). In the 1978 season, only three cyclones moved onshore. Hurricane statistics prior to 1966 were not used in this study because satellite coverage was not adequate prior to 1966 and some hurricanes might have been missed.

The forecast error for the 1977 season is shown in Table 6.24. These are based on various computer models available at the National Hurricane Center in Miami. In this table, EPHC stands for the Eastern Pacific Hurricane Center, CLIPER is a simulated analog model, EPHC77 is a statistical synoptic model, EPHANALOG is an analog model, and SANBAR is a barotropic model. Of these four computer models, EPHC77 gave the best results, and these were subjectively improved by the EPHC forecasters.

TROPICAL CYCLONES OF THE CENTRAL NORTH PACIFIC

For forecast purposes, the central North Pacific is defined as the region between 140°W to the international dateline and from the equator to 35°N (see Fig. 6.16). The forecasts for this region are issued by the Central Pacific Hurricane Center in Honolulu. The 1978 season began on June 24 and ended on October 24; this was the season of greatest tropical cyclone activity since weather records were kept (Shaw 1979). A total of 13 tropical cyclones either originated here or passed through this area during this season. Hurricane Fico of July 17 was an exceptional case in the sense that it maintained hurricane intensity for as long as 17 d and its track involved a total length of about 5000 mi (8000 km). Even on July 31, its effect was felt at Cold Bay in the Aleutians.

Another hurricane of this season, Susan, of October 18 was one of the two most intense hurricanes (in the central Pacific) on record with maximum sustained winds of 120 knots (222 $km \cdot h^{-1}$). The other intense hurricane occurred on August 1972 and was referred to as Celeste. Hurricane Susan presented several interesting features. First of all, it began rather late in the season when the forecasters thought the hurricane season was over. After arriving 220 mi (354 km) southeast of the big island of Hawaii, it abruptly

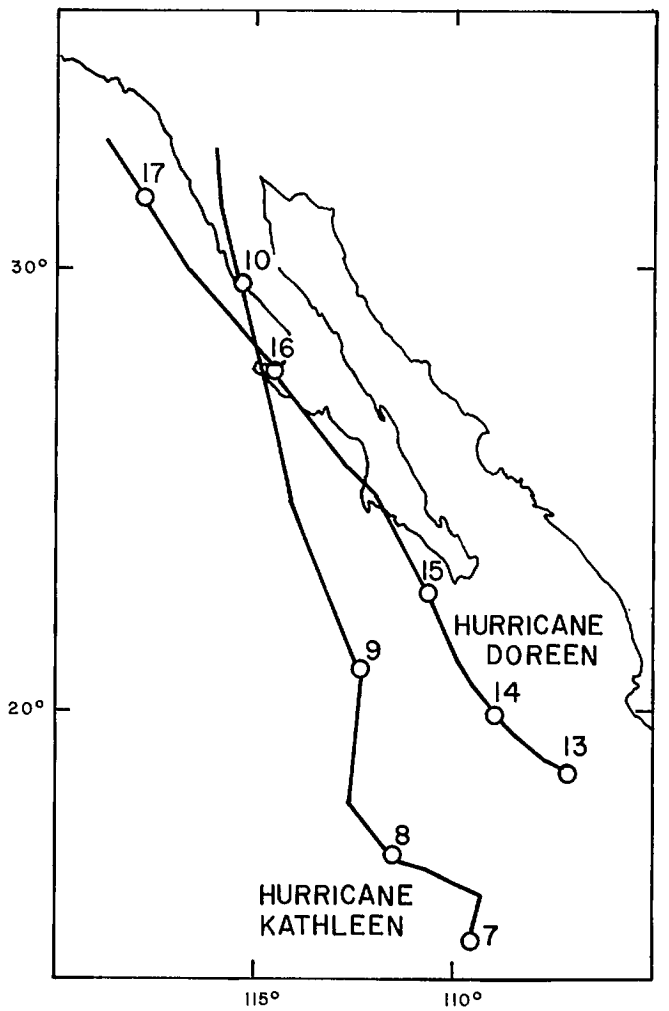

FIG. 6.15. Tracks of Hurricanes Kathleen of September 1976 and Doreen of August 1977 near Baja California. (Gunther 1978)

TABLE 6.24. Average forecast errors (km) in tropical cyclone movement using different models. Data in columns 2 to 6 show the average error (km). Value in parentheses shows the number of cases. EPHC, Eastern Pacific Hurricane Center; EPANALOG, Eastern Pacific analog model. (For a description of these models, see the text.) (Gunther 1978)

Forecast period (h)	EPHC forecasters	EPANALOG	EPHC-77	CLIPER	SANBAR
24	113 (126)	104 (141)	96 (129)	104 (129)	22 (137)
48	44 (239)	56 (265)	50 (255)	56 (255)	15 (271)
72	13 (284)	22 (365)	19 (292)	22 (378)	6 (508)

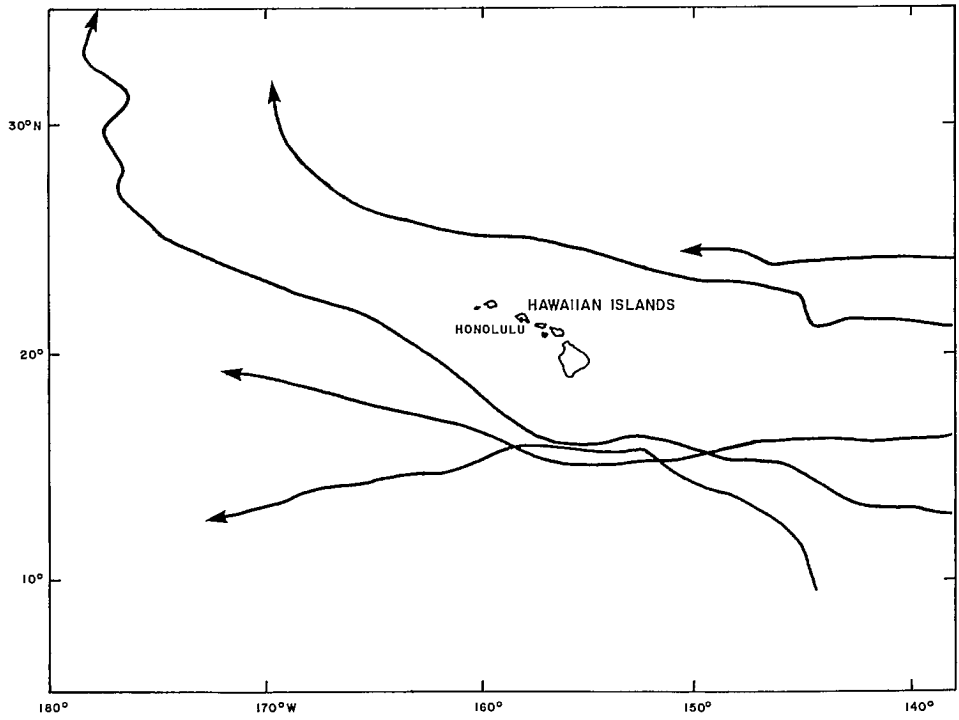

FIG. 6.16. Typical tracks of tropical cyclones in the central part of the North Pacific Ocean. (Shaw 1979)

turned southwestward and dissipated rapidly. The central pressure rose more than 50 mb in 24 h.

Hurricane Gilma of July 22 was also somewhat unusual in the sense that it covered an area as large as 3×10^5 mi^2 (7.8×10^5 km^2). Hurricanes for the 1978 season in the central Pacific are summarized in Table 6.25.

TYPHOONS OF THE WESTERN NORTH PACIFIC

The Joint Typhoon Warning Center for the western North Pacific was set up at Guam in 1959. The frequency of typhoons by month and year is listed in Table 6.26 and the western North Pacific tropical cyclones for the season of 1977 are listed in Table 6.27. The 1977 season began on March 23 and ended in January 1978. The 1978 season officially began on January 8 and ended on November 30. It can be seen that in the western North Pacific, typhoons can and do occur at any time of the year. In this respect this ocean basin is different from the central North Pacific, eastern North Pacific, and North Atlantic Ocean basins where the tropical cyclone season does not span the full year.

The seasons of 1977 and 1978 (Joint Typhoon Warning Center 1978, 1979) will be compared. The season of 1977 had the lowest number of tropical cyclones since 1959. Of a total of 21, 2 dissipated as depressions, 8 peaked out as tropical storms, and the remaining 11 matured into hurricanes. The monsoon systems of the Indian subcontinent and Southeast Asia appear to have some influence on the tropical cyclones in the western North Pacific. During the 1977 season there were only 12 multiple storm days (a multiple

TABLE 6.25. Central North Pacific tropical cyclone data for 1978. All data pertain to the period during which the storms were in the Central North Pacific only. H, hurricane; TS, tropical storm; TD, tropical depression; ET, extratropical cyclone; —, information not available. (Shaw 1979)

Name of storm	Date	Maximum class	Maximum sustained wind ($km \cdot h^{-1}$)	Lowest pressure (mb)	Total hours observed
Bud	June 24–26	Vortex	—	—	48
Carlotta	June 26–July 3	Vortex	—	—	168
Daniel	July 3–11	Vortex	—	—	192
Fico	July 17–28	Hurricane	185	955	225(H) 15(TS) 36(ET)
Gilma	July 22–27	Vortex	—	—	144
Hector	July 31–Aug. 2	Vortex	—	—	60
TD-10	Aug. 6–9	TD	56	—	84
Iva	Aug. 19–21	Vortex	—	—	54
John	Aug. 23–30	Hurricane	167	965	48(H) 72(TS) 48(TD)
Kristy	Aug. 26–28	TS	93	—	18(TS) 45(TD)
Lane	Aug. 20–23	TS	93	—	66(TS) 27(TD)
Miriam	Aug. 27–Sept. 2	TS	102	—	72(TS) 6(TD)
Susan	Oct. 18–24	Hurricane	222	945–954	81(H) 30(TS) 24(TD)

TABLE 6.26. Frequency of typhoons in the western North Pacific. (Joint Typhoon Warning Center 1978)

Year	Jan.	Feb.	Mar.	Apr.	May	June	July	Aug.	Sept.	Oct.	Nov.	Dec.	Total
1954–58 (average)	0.4	0.1	0.3	0.4	0.7	1.1	2.0	2.9	3.2	2.4	2.0	0.9	16.3
1959	0	0	0	1	0	0	1	5	3	3	2	1	20
1960	0	0	0	1	0	2	2	8	0	4	1	1	19
1961	0	0	1	0	2	1	3	3	5	3	1	1	20
1962	0	0	0	1	2	0	5	7	2	4	3	0	24
1963	0	0	0	1	1	2	3	3	3	4	0	2	19
1964	0	0	0	0	2	2	6	3	5	3	4	1	26
1965	1	0	0	1	2	2	4	3	5	2	1	0	21
1966	0	0	0	1	2	1	3	6	4	2	0	1	20
1967	0	0	1	1	0	1	3	4	4	3	3	0	20
1968	0	0	0	1	1	1	1	4	3	5	4	0	20
1969	1	0	0	1	0	0	2	3	2	3	1	0	13
1970	0	1	0	0	0	1	0	4	2	3	1	0	12
1971	0	0	0	3	1	2	6	3	5	3	1	0	24
1972	1	0	0	0	1	1	4	4	3	4	2	2	22
1973	0	0	0	0	0	0	4	2	2	4	0	0	12
1974	0	0	0	0	1	2	1	2	3	4	2	0	15
1975	1	0	0	0	0	0	1	3	4	3	2	0	14
1976	1	0	0	1	2	2	3	0	4	1	0	0	14
1977	0	0	0	0	0	0	3	0	2	3	2	1	11
1959–77 (average)	0.3	0.1	0.1	0.7	0.9	1.1	2.8	3.6	3.2	3.2	1.6	0.5	18.3

TABLE 6.27. Tropical cyclones in the western North Pacific for the season of 1977. TY, typhoon; TS, tropical storm; STY, supertyphoon. (Joint Typhoon Warming Center 1978)

Name of typhoon	Period of warning	Intensity	Maximum surface wind ($km \cdot h^{-1}$)	Minimum observed sea level pressure (mb)
Patsy	Mar. 23–31	TS	93	981
Ruth	June 14–17	TS	111	980
Sarah	July 16–21	TY	139	970
Thelma	July 21–26	TY	157	957
Vera	July 28–Aug. 1	TY	204	926
Wanda	July 31–Aug. 4	TS	83	986
Amy	Aug. 20–23	TS	74	990
Babe	Sept. 2–10	STY	241	906
Carla	Sept. 3–5	TS	65	994
Dinah	Sept. 14–23	TY	139	964
Emma	Sept. 15–20	TS	111	966
Freda	Sept. 23–25	TS	102	997
Gilda	Oct. 3–10	TY	130	968
Harriet	Oct. 16–20	TS	102	984
Ivy	Oct. 21–27	TY	167	945
Jean	Oct. 28–31, Nov. 2–3	TY	120	972
Kim	Nov. 6–17	TY	232	916
Lucy	Nov. 28–Dec. 7	TY	213	919
Mary	Dec. 20–Jan. 3	TY	185	947

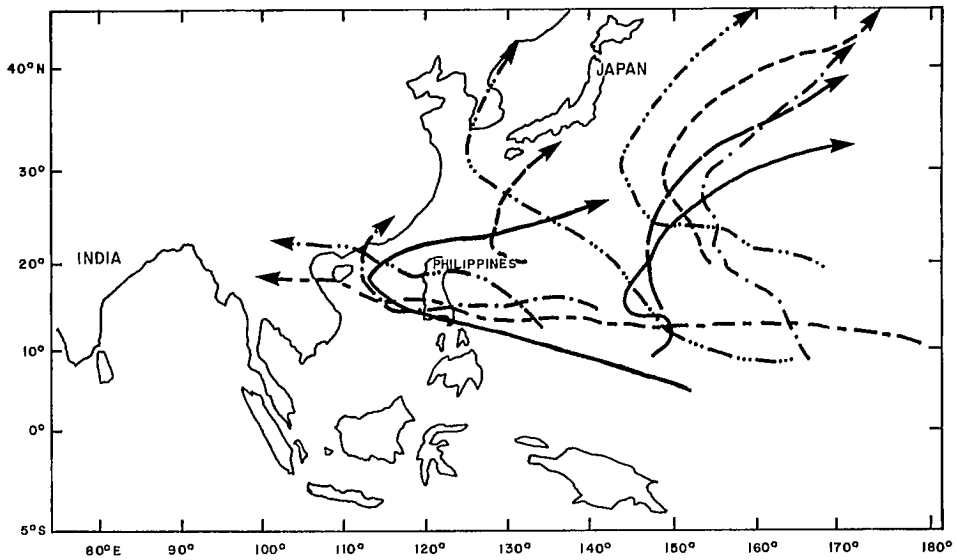

FIG. 6.17. Typical tracks of tropical cyclones in the western North Pacific. (Joint Typhoon Warning Center 1977, 1978)

storm day is one during which there is more than one tropical cyclone in the region). In 1970 and 1975, at certain times there were three or more tropical cyclones simultaneously. Storms with long durations could occur. Typhoon Kim of November 6, 1977, spanned

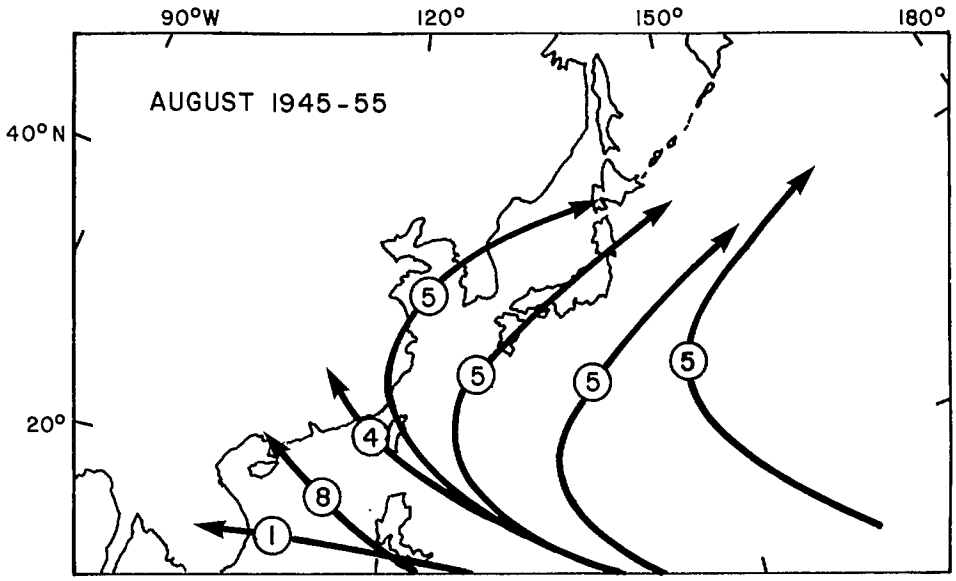

FIG. 6.18. Mean typhoon tracks and frequency (over an 11-yr period) for August in the western North Pacific. (Jamison 1956)

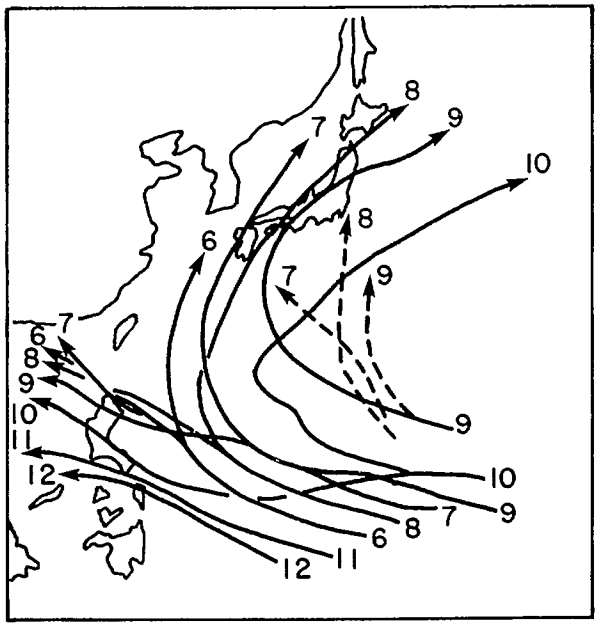

FIG. 6.19. Monthly mean tracks of tropical cyclones in the western North Pacific. Numbers refer to the months. (Aoki 1979)

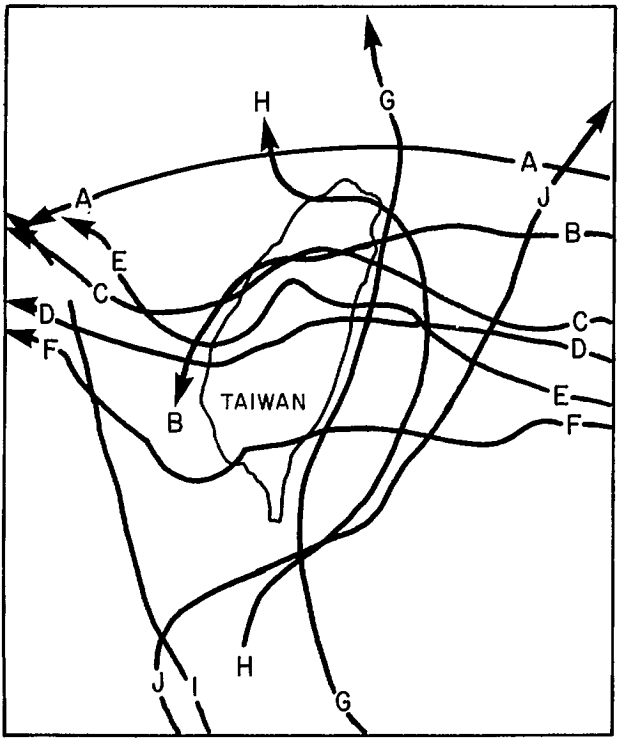

FIG. 6.20. Typical tracks of typhoons around Taiwan. A, Trix, 1960; B, Agnes, 1960; C, Pamela, 1961; D, Nora, 1967; E, Nina, 1975; F, Betty, 1975; G, Dinah, 1965; H, Wendy, 1974; I, Nora, 1973; J, Judy, 1953. (Chu et al. 1978)

12 d. In this season, Typhoon Babe was classified as a supertyphoon.

One important feature of the typhoons in the western North Pacific is that they could have rather erratic tracks and loops (usually the loops occur when the steering currents are weak). The 1978 season had about an average number of tropical cyclones. However, there were several surprises. Ten storms and typhoons had erratic tracks. Typhoon Carmen was almost stationary for 3 d. Typhoon Faye's track had a large anticyclonic loop and then it deepened explosively (surface central pressure decreased by 18 mb in just 6 h). Typhoon Trix was the most ill-behaved of all. Storms Hester and Phyllis attained speeds of movement of 40 and 50 knots (74 and 93 $km \cdot h^{-1}$), respectively, after recurvature in their extratropical transition. Typhoons Virginia and Mamie were so compact in size (but not in intensity) that they were called midget typhoons. Typhoon Virginia traveled farthest north (to 42°N) still behaving like a tropical cyclone. Supertyphoon Rita covered an amazing distance of 4142 mi (6669 km) and is second only to Typhoon Sarah of 1976, which traveled 4499 mi (8000 km). Some typical tracks of typhoons in the western North Pacific are shown in Fig. 6.17.

TROPICAL CYCLONE TRACKS NEAR JAPAN, TAIWAN, AND THE PHILIPPINES

Jamison (1956) described the average tracks of typhoons in this region for the month of August based on 11 yr of data (1945–55). These tracks are illustrated in Fig. 6.18.

TABLE 6.28. List of typhoons around Taiwan during 1953–75. (Chu et al. 1978)

Name of typhoon	Date	Maximum wind speed ($km \cdot h^{-1}$)	Name of typhoon	Date	Maximum wind speed ($km \cdot h^{-1}$)
Judy	June 1953	74–111	Gilda	Nov. 1967	148–185
Kit	July 1953	204	Elsie	Sept. 1969	194
Thelma	Apr. 1956	157	Betty	Aug. 1972	157–222
Trix	Aug. 1960	204–222	Joan	Aug. 1973	56–83
Agnes	Aug. 1960	74–102	Nora	Oct. 1973	111–176
Pamela	Sept. 1961	222–278	Jean	July 1974	93
Sally	Sept. 1961	130	Wendy	Sept. 1974	93
Wendy	July 1963	185–250	Nina	Aug. 1975	250
Dinah	June 1965	74–241	Betty	Sept. 1975	157–167
Nora	Aug. 1967	111–120	Elsie	Oct. 1975	222–259

During this period there were a total of 43 typhoons, of which 15 had rather erratic tracks (not shown here). The number along each track is the number of typhoons that occurred during this 11-yr period. Note that the lowest frequency is for the track that crosses Vietnam and the highest is for the Philippines area and continuing toward the Gulf of Tonkin. The number of tropical cyclones that traveled over Korea and Japan during this period was five.

The average tracks for several months based on the data for 1940–69 (Aoki 1979) are shown in Fig. 6.19. The numerals correspond to the month.

The tracks of some selected typhoons in the vicinity of Taiwan during the period 1953–75 (Chu et al. 1978) are shown in Fig. 6.20. Noting that Taiwan is an island with a central mountain range with heights exceeding 3000 m, one can expect these mountains to influence the typhoon tracks. In Fig. 6.20, the deflecting effect of the mountain range can be seen. For a steering current in the east–west direction, the track veers to the north when it approaches the island. After it crosses over or around the mountains, it turns toward the south. After it leaves the island, the track is similar to the original track (before encountering the island).

On the other hand, for a typhoon moving from south towards north, the track first veers towards the east and then moves more or less parallel to the mountain ranges (which are generally in the north–south direction), and again it resumes its original track (see tracks G–I in Fig. 6.20; track G especially is appropriate). Some details of these typhoons around Taiwan are given in Table 6.28.

EXPLOSIVELY DEVELOPING TROPICAL CYCLONES AND SUPERTYPHOONS IN THE PACIFIC

Clark (1978a, 1978b), using satellite imagery, studied rapidly developing tropical cyclones in the northeastern Pacific Ocean during the period 1973–76. In his analysis, he made use of the so-called T number (Dvorak 1975a, 1975b).[5] During this 4-yr period, of a total of 62 cyclones, 12 underwent a rapid development. The tracks of these rapidly developing tropical cyclones fall within a small area near Mexico (Fig. 6.21). Clark (1978a, 1978b) cited persistent atmospheric conditions as contributing to the existence of

[5]The T number is based on the maximum wind speed. For example, T1 corresponds to 25 knots, T2 to 30 knots, T3 to 45 knots, T4 to 65 knots, etc., with T8 corresponding to 170 knots (1 knot = 1.852 $km \cdot h^{-1}$).

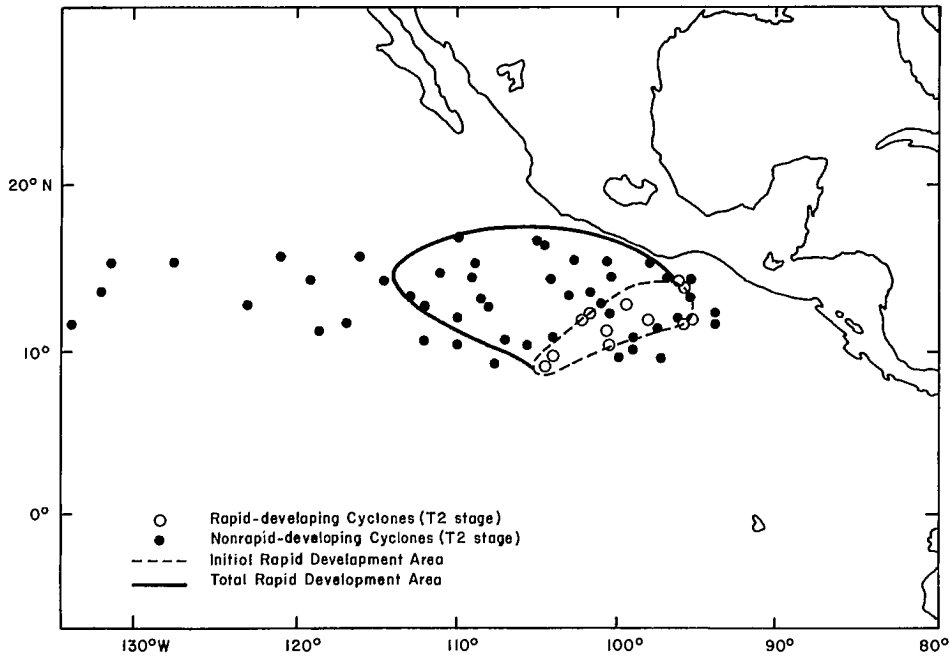

FIG. 6.21. Area of development of eastern North Pacific tropical cyclones, 1973–76 (Clark 1978b)

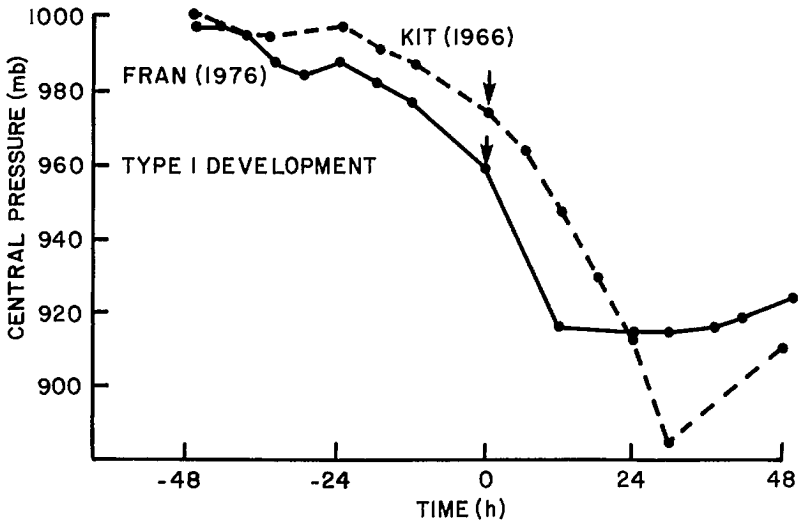

FIG. 6.22. History of central pressure readings for typhoons typical of type I development (Hurricanes Kit of June 1966 and Fran of September 1976). Arrow indicates onset of rapid deepening ($\geq$1.75 mb·h^{-1}). (Holliday and Thompson 1979)

a relatively small area of rapid development.

Holliday and Thompson (1979) made a study of rapidly deepening typhoons in the western part of the North Pacific Ocean using data from the period 1956–76. Their

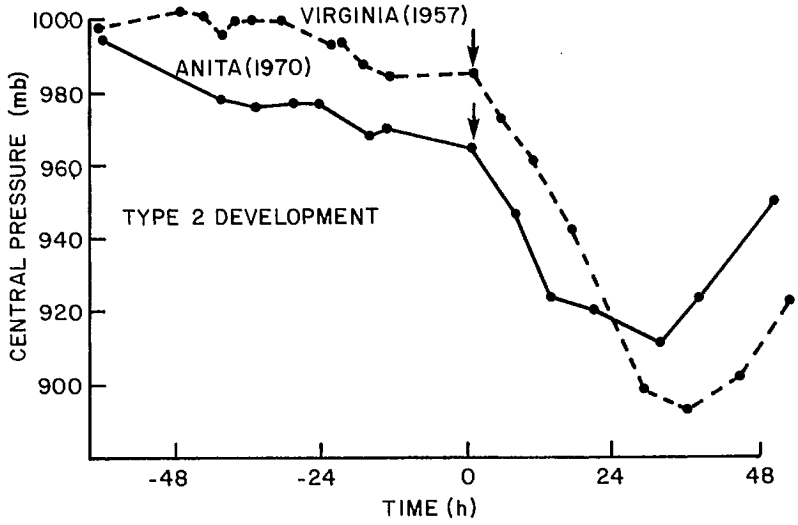

FIG. 6.23. History of central pressure readings for typhoons of type 2 development (Hurricanes Virginia of June 1957 and Anita of August 1970). Arrow indicates onset of rapid deepening (≥ 1.75 mb·h^{-1}). (Holliday and Thompson 1979)

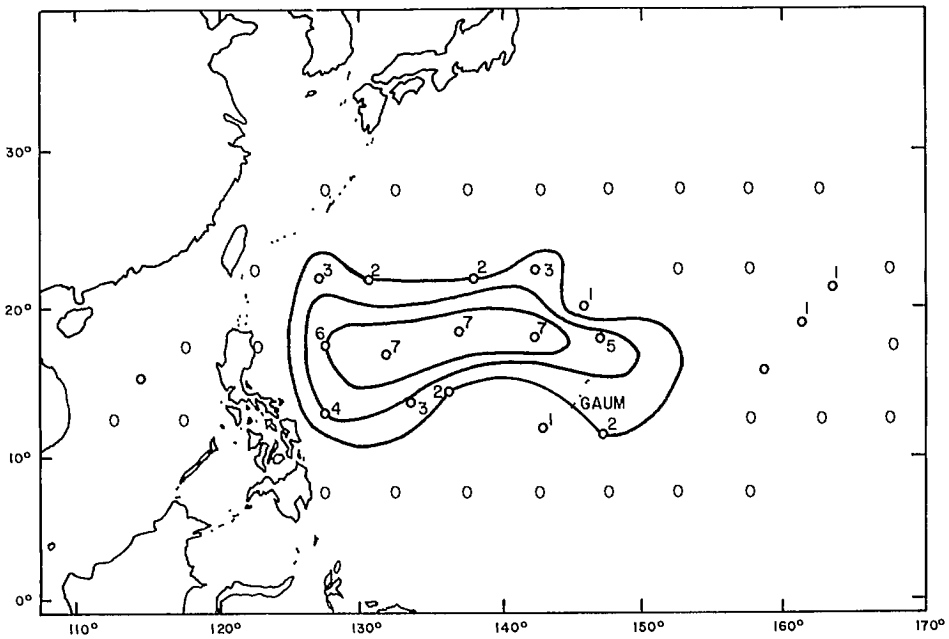

FIG. 6.24. Areas where typhoons intensified rapidly during summer and early fall (June 20–October 16). Numbers represent occurrences during 1956–76. (Holliday and Thompson 1979)

definition of rapid deepening is a fall in the central surface pressure by at least 42 mb in 24 h. In a total of 79 cases, rapid deepening (i.e. over an interval of 18 h with the steepest fall in the first 6 h) produced surface central pressures of 920 mb or less. For a tropical

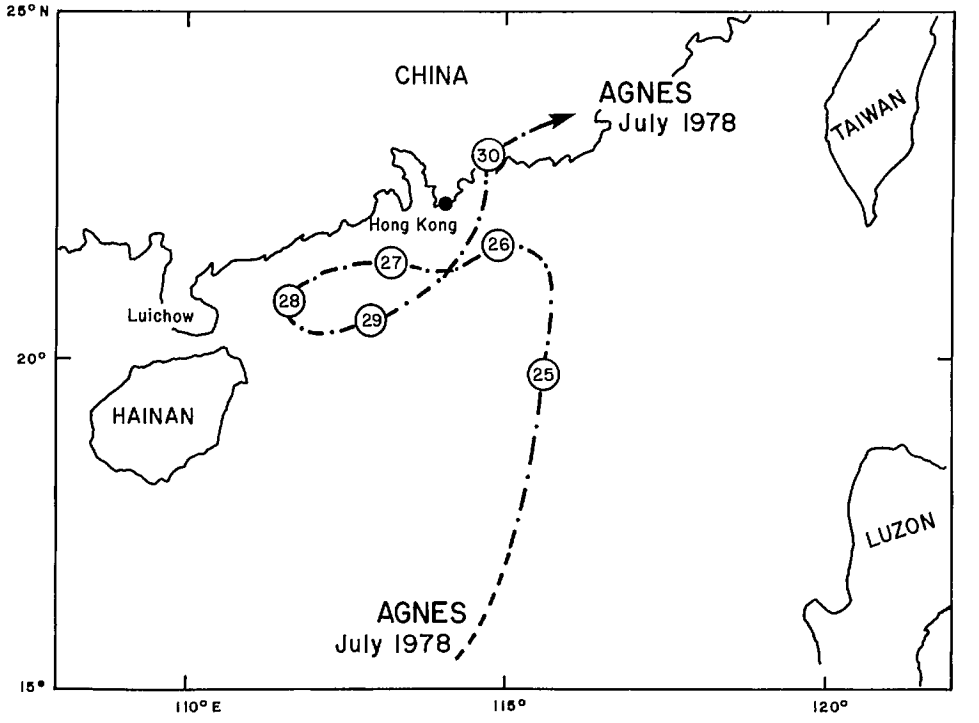

FIG. 6.25. Track of severe tropical storm Agnes from its formation on July 24, 1978, to its passage across the coast on July 30, 1978. (Bell 1979)

cylone to mature into a typhoon, the underlying ocean temperature (up to a depth of 30 m) must be at least 28°C. This is a necessary condition for rapid deepening but not a sufficient condition.

Two basic types of deepening were noticed. In type 1 (Fig. 6.22) the central pressure falls at a moderate rate (≥ 0.8 mb·h^{-1}) at least over a period of 12–24 h. This is accompanied by accelerated development (≥ 1.75 mb·h^{-1}). This behavior for Typhoons Kit of 1966 and Fran of 1976 is shown in Fig. 6.22. In type 2 behavior, initially there is slower development (<0.8 mb·h^{-1}) suddenly followed by explosive deepening (≥ 1.75 mb·h^{-1}). This is shown for Typhoons Virginia of 1957 and Anita of 1970 in Fig. 6.23. In the 79 case studies, 36% exhibited type 1 behavior and the remainder showed type 2 behavior.

About 36% of the rapid deepening occurred during daytime and 64% occurred during nighttime. Sheets (1969) suggested that this may be related to the differences in the atmospheric stability during day and night. However, Sheets' (1969) study of hurricanes and Frank's (1978) study of typhoons on diurnal variations showed little evidence for diurnal changes except in the temperature field and other parameters in the upper troposphere and stratosphere.

The time interval between the weak circulation stage to the commencement of rapid deepening varied from 72 to 172 h. The time interval between the tropical storm stage to the onset of rapid deepening varied from 12 to 108 h. The interval between the time of

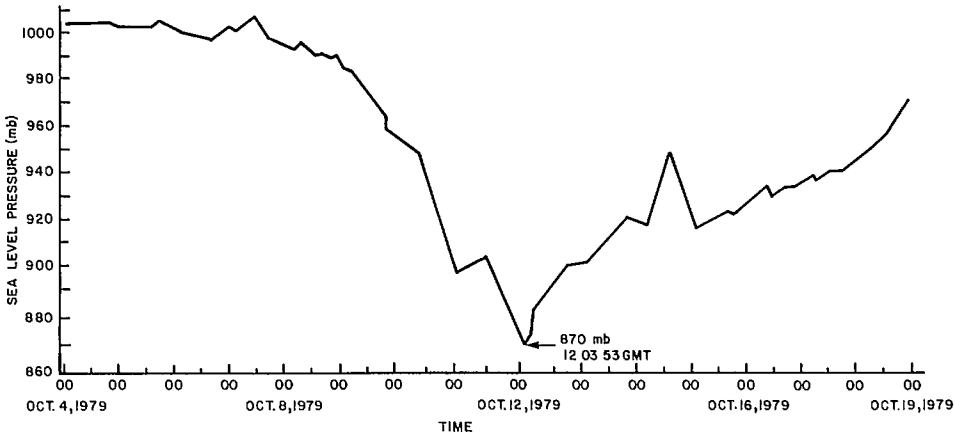

FIG. 6.26. Central pressure trace for Supertyphoon Tip of October 1979. (Dunnavan and Diercks 1980)

TABLE 6.29. Some features of selected ports as possible safe havens in case of typhoon occurrence.

Port	Wind waves	Storm surges	Remarks
Apra Harbor (Guam)	Maximum heights up to 6.5 m	Maximum heights up to 6 m	Not safe
Hong Kong	Greater than 10 m	Greater than 2 m	Not safe
Kaohsiung (Taiwan)	Negligible	Negligible	Due to shoaling outside the harbor, strong currents exist; not safe
Yokosuka (Tokyo Bay)	Negligible	Negligible	Safe
Manila	More than 3 m	—	Not safe
Pusan	Up to 4 m	1.5–2 m	Not safe

reaching typhoon stage and initiation of rapid deepening varied from 0 to 72 h.

At the time of initiation of rapid deepening the eye diameters ranged from 29 to 37 km (average 33 km). Twelve hours after initiation of rapid deepening, the mean diameter of the eye decreased to 30 km, and 24 h after rapid deepening commencement, the average diameter was 26 km. Most of the rapid deepening occurred during the period July–November, with maximum activity in August and September. The area where rapid development began is shown in Fig. 6.24. The numerals show the number of cases during 1956–76.

Next, two interesting typhoons will be considered: Agnes of July 1978 and Tip of October 1979. The track of Typhoon Agnes is shown in Fig. 6.25. Because of the loop in the track, according to Bell (1979) it is the only tropical storm on record that caused gale signals to be hoisted twice at Hong Kong. Another unusual feature was that the so-called Fujiwara effect occurred between Typhoons Agnes and Wendy, although they were separated by 1000 mi (1600 km). Another interesting feature from a public information point of view was that the American spacecraft *Apollo* ran into this with 60-knot (111 km·h^{-1}) winds and 25-ft (8 m) waves when it splashed down into the Pacific Ocean.

Supertyphoon Tip developed in the western part of the North Pacific Ocean in early October 1979. This had at least two unique features: it holds the world record for the

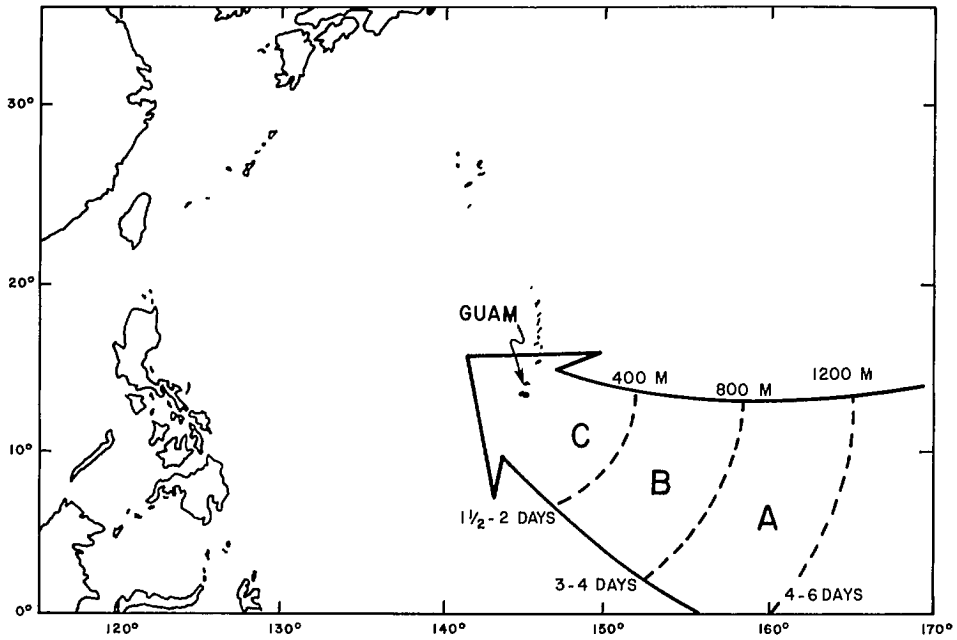

FIG. 6.27. Tropical cyclone threat axis for Guam. Distance and approach times are measured from Guam based on an 8- to 12-knot speed of movement (1 knot = 1.852 km·h^{-1}; 1 nautical mile (M) = 1.852 km). (Brand et al. 1977b)

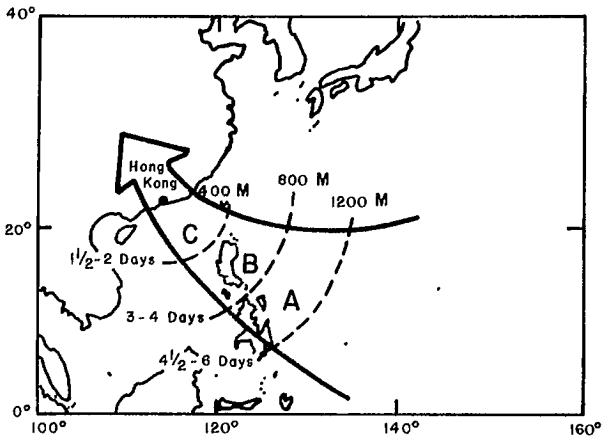

FIG. 6.28. Tropical cyclone threat axis for Hong Kong (1 nautical mile (M) = 1.852 km). (Brand et al. 1977a)

lowest minimum sea level pressure (870 mb) ever measured in a tropical cyclone (see Fig. 6.26) and it possessed the largest surface circulation pattern ever observed for a tropical cyclone (about 2200 km in diameter). Finally, this was transformed into an extratropical cyclone around October 18, 1979. Although it caused great destruction in Japan, the destruction was minimal for its size because the maximum intensity was reached

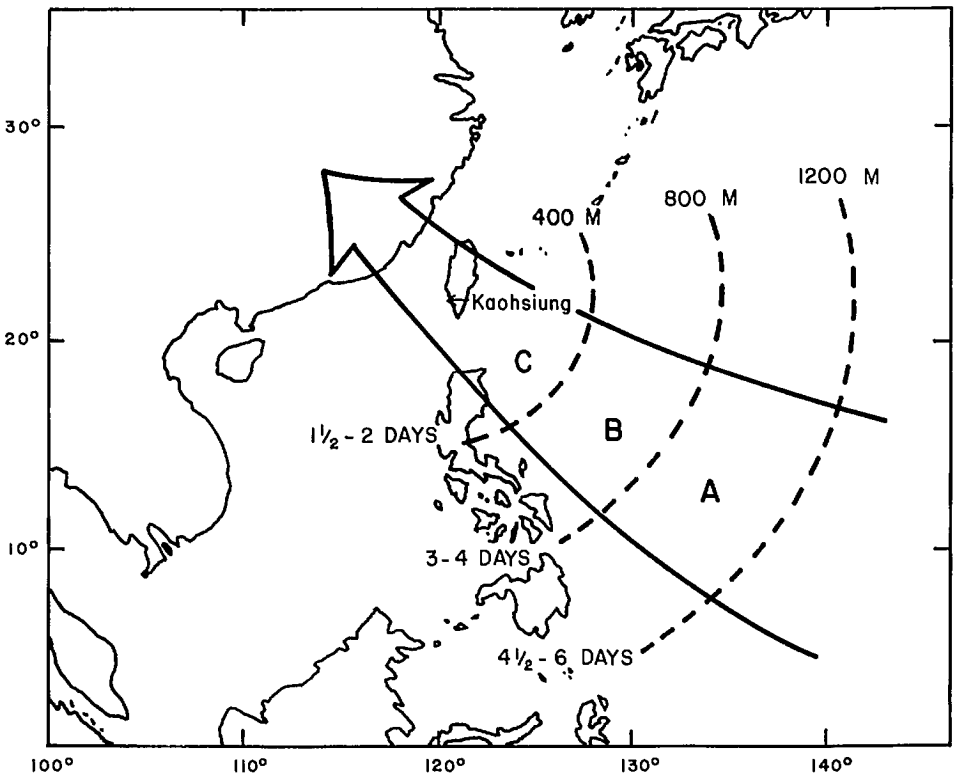

FIG. 6.29. Tropical cyclone threat axis to Kaohsiung, Taiwan (1 nautical mile (M) = 1.852 km). (Brand et al. 1978a)

while the system was still far away from inhabited areas. Dunnavan and Diercks (1980) referred to it as the most significant tropical cyclone of this century.

EXAMINATION OF SOME SELECTED PORTS AS TYPHOON HAVENS

Brand and Blelloch (1976) published a book entitled *Typhoon Havens Handbook for the Western Pacific and Indian Oceans*, and the journal *Mariners Weather Log* published a series of articles in which various harbors were examined as to their safety for ships during a tropical cyclone. Here, the ports of Guam, Manila, Kaohsiung (Taiwan), Hong Kong, Tokyo Bay, and Pusan will be briefly examined. The features of these ports are summarized in Table 6.29 and the threat axes to these various ports are shown in Fig. 6.27–6.34. Note that for the port of Yokosuka (Tokyo Bay), the threat axis changes from month to month, as can be seen from Fig. 6.31 and 6.32 for the months of June and July. A similar situation exists for Pusan. For details on typhoon havens, see Brand et al. (1977a, 1977b, 1978a, 1978b, 1979, 1980).

6.4 Cyclones of the Atlantic Ocean

Extratropical cyclones that affect North America are born in the western parts of the

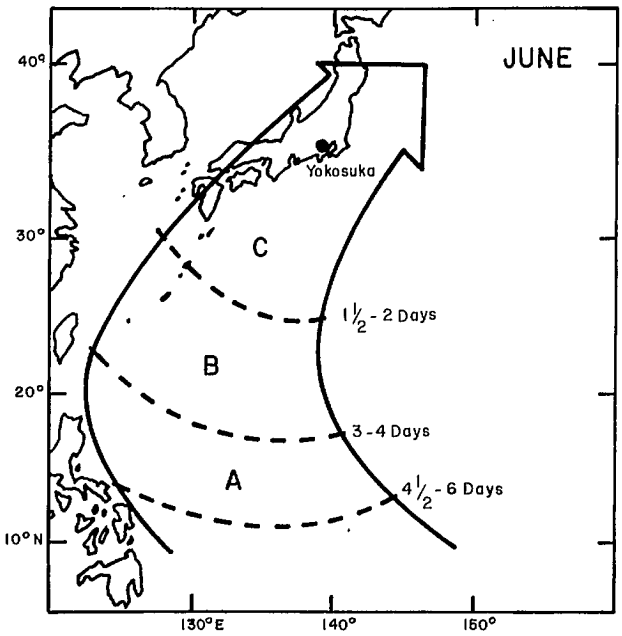

FIG. 6.30. Tropical cyclone threat axis for Yokosuka (June). (Brand et al. 1978b)

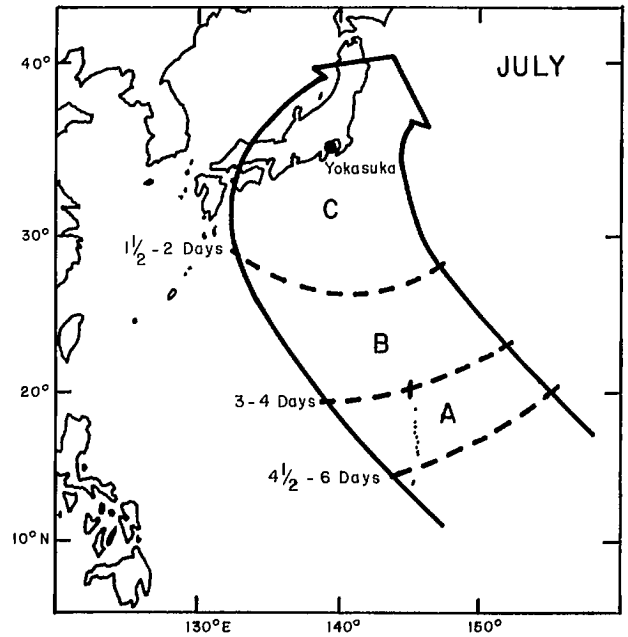

FIG. 6.31. Tropical cyclone threat axis for Yokosuka (July). (Brand et al. 1978b)

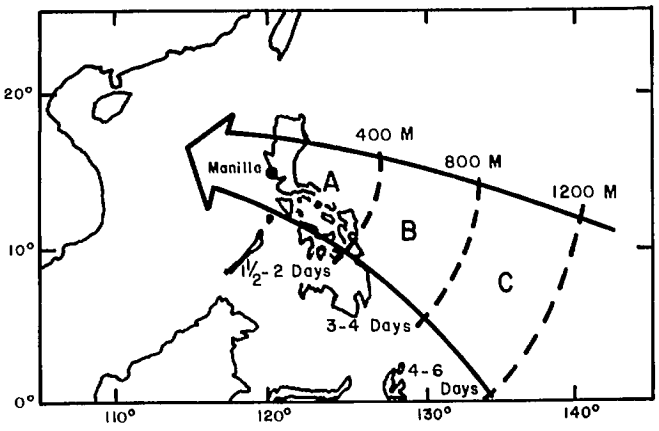

FIG. 6.32. Tropical cyclone threat axis for Manila (1 nautical mile (M) = 1.852 km). (Brand et al. 1979)

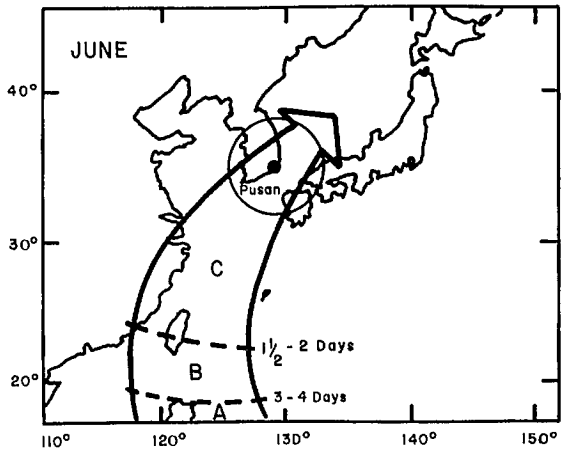

FIG. 6.33. Typhoon threat axis for Pusan, Korea (June). (Brand et al. 1980)

continent or in the Pacific Ocean and travel generally towards east (also east–northeast and northeast). Extratropical cyclones originating in the Atlantic generally do not affect North America but will travel towards Europe. These will be considered in a later section. Here, basically, tropical cyclones originating in the Atlantic that affect mainly the North American continent will be considered.

Neumann et al. (1978) gave detailed tracks and statistics of the tropical cyclones of the North Atlantic Ocean for the period 1871–1977. It was mentioned earlier that two large tropical ocean basins do not give rise to tropical cyclones. These are the South Atlantic and the eastern part of the South Pacific oceans. During this 107-yr period, at least 850 tropical cyclones (storms as well as hurricanes) occurred in the North Atlantic. These form over the warm tropical and subtropical waters, and about a week or 10 d later usually dissipate over the cold waters of the North Atlantic or sometimes evolve into extratropical cyclones.

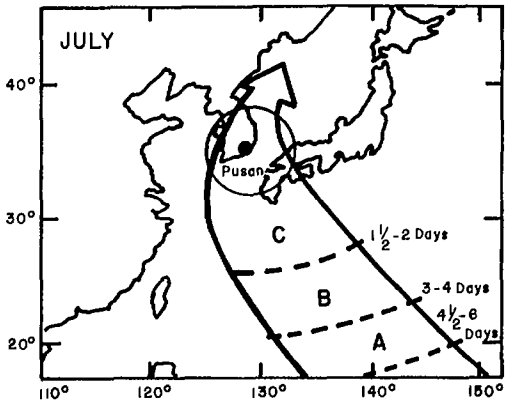

FIG. 6.34. Typhoon threat axis for Pusan (July). (Brand et al. 1980)

These storms are listed by month in Table 6.30 for each of these years. Those that eventually became hurricanes are listed in Table 6.31. The distribution of the observed duration of hurricanes is given in Fig. 6.35. The cumulative percentage frequency distribution of beginning and ending dates of Atlantic tropical cyclone seasons from 1886 to 1977 is given in Fig. 6.36. Dates shown are of the first and last recorded positions with at least tropical storm intensity. The annual distribution of the 257 Atlantic tropical storms and hurricanes together (open bars) and the 140 hurricanes only (solid bars) that either crossed or passed near the United States coastline (from Texas to Maine) during the period 1899–1977 is given in Fig. 6.37. Note that the average annual number of such storms plus hurricanes is 3.3, whereas that for hurricanes is 1.8. The 9-d moving averages of the number of tropical storms and hurricanes together and hurricanes separately are shown in Fig. 6.38.

Frank (1978) studied the geographical distribution of the generation areas and other characteristics of these Atlantic storms for the period 1968–77. During this 10-yr period, a total of 1044 systems appeared. Of these, 58% originated near Dakar (Africa). Of the approximately 100 tropical weather systems developing in each hurricane season (June 1–November 30) about 25% become depressions and about 10% become storms.

COMPUTERIZED TROPICAL CYCLONE CLIMATOLOGY

Neumann and Hill (1976) described the computerized tropical cyclone climatological data at the National Hurricane Center in Miami. The tracks of the 680 recorded Atlantic tropical cyclones for the period 1886–1969 were plotted. Later, this number increased to 743 tracks up to the end of the 1975 hurricane season. Most of these data are based on ship reports, and in later years these data were supplemented by aircraft reconnaissance and satellite data. The storm track data are maintained at the National Climatic Center in Asheville, NC. Based on these computerized data, three examples were prepared (Fig. 6.39–6.41). Neumann and Cry (1978) discussed the revised Atlantic tropical cyclone climatology.

TABLE 6.30. Number of recorded Atlantic tropical cyclones (excluding depressions and after 1967, including subtropical cyclones) that reached at least tropical storm intensity in the specified month, 1871–1977. (Neumann et al. 1978)

Year	Jan.	Feb.	Mar.	Apr.	May	June	July	Aug.	Sept.	Oct.	Nov.	Dec.	Total
1871						2		2	2				6
1872							1	1	2	1			5
1873								1	3				5
1874							1	1	4	1			7
1875									3	1			4
1876									2	1			3
1877								1	4	2	1		8
1878							1	1	3	4	1		10
1879								3	1	3	1		8
1880						1		4	2	2			9
1881								4	1	1			6
1882									2	1			3
1883								2	1	1			4
1884									2	1			3
1885								3	4	1			8
1886						3	1	2	2	2			10
1887					1		2	2	3	6	1	2	17
1888						1	1	2	2	1	2		9
1889					1	1		1	5	1			9
1890							1						1
1891							1	2	3	4	1		11
1892						1		1	4	3			9
1893						1	1	5	3	1	1		12
1894								2	1	3			6
1895								2	1	3			6
1896							1	1	2	2			6
1897								1	2	2			5
1898								2	5	2			9
1898							1	2	1	2			6
1900								1	3	3			7
1901						1	2	2	3	2			10
1902						2			1	1	1		5
1903							1	1	4	2	1		9
1904						1			1	3			5
1905									3	2			5

TABLE 6.30. (*Continued*)

Year	Jan.	Feb.	Mar.	Apr.	May	June	July	Aug.	Sept.	Oct.	Nov.	Dec.	Total
1906						2		1	3	4	1		11
1907							1		2	1			4
1908			1				1	1	3	2			8
1909						2	2	2	2	1	1		10
1910								1	2	1			4
1911								2	1	1			4
1912						1	1		1	2	1		6
1913						1		1	1	1			4
1914									1				1
1915							1	3	1				5
1916						1	2	3	4	3	1		14
1917								2	1				3
1918								3	2				5
1919							1		1		1		3
1920									4				4
1921						1			3	2			6
1922						1			1	2			4
1923								1	1	5			7
1924						1		2	2	2	1		8
1925									1		1		2
1926							2	1	5	2	1		11
1927								1	3	3			7
1928								2	3	1			6
1929						1			1	1			3
1930								2					2
1931						1	1	2	3	1	1		9
1932					1			3	3	3	1		11
1933					1	1	3	7	5	3	1		21
1934					1	1	1	2	2	3	1		11
1935								3	1	2			6
1936						3	2	6	4	1			16
1937							1	2	6				9
1938								3	1	3	1		8
1939						1		1	1	2			5
1940					1			3	2	2			8

TABLE 6.30. (*Concluded*)

Year	Jan.	Feb.	Mar.	Apr.	May	June	July	Aug.	Sept.	Oct.	Nov.	Dec.	Total
1941									4	2			6
1942								3	3	3	1		10
1943							1	2	4	3			10
1944							3	2	4	2			11
1945						1	1	4	3	2			11
1946						1	1	1	1	2			6
1947							1	2	3	3			9
1948					1		1	2	3	1	1		9
1949								3	7	2	1		13
1950								4	3	6			13
1951					1			3	3	3			10
1952		1						2	2	2			7
1953					1			3	4	4	1	1	14
1954						1	1	2	4	1	1	1	11
1955							1	4	5	2			12
1956						1	1	1	4		1		8
1957						2		1	4	1			8
1958						1		4	4	1			10
1959					1	2	2	1	3	2			11
1960						1	2	2	2				7
1961							1		6	2	2		11
1962									2	1	2		5
1963								2	5	2			9
1964						1	1	3	5	1	1		12
1965						1		2	2	1			6
1966						1	4	1	4		1		11
1967								1	4	3			8
1968						3		1	3	1			8
1969							1	5	6	5	1		18
1970					1		1	3	3	2			10
1971							1	4	6	1	1		13
1972					1	1		2	2		1		7
1973							2	2	2	2			8
1974						1	1	4	4	1			11
1975						1	1	2	3	1		1	9
1976					1		1	5	2	1			10
1977								1	3	2			6

TABLE 6.31. Number of storms listed in Table 6.30 that eventually became hurricanes. (Neumann et al. 1978)

Year	Jan.	Feb.	Mar.	Apr.	May	June	July	Aug.	Sept.	Oct.	Nov.	Dec.	Total
1871													
1872													
1873													
1874													
1875													
1876													
1877													
1878													
1879													
1880													
1881													
1882													
1883													
1884													
1885													
1886						2	1	2	2	1			8
1887							1	2	3	2	1	1	10
1888						1		2		1	1		5
1889					1			1	3				5
1890								1					1
1891							1	2	3	2			8
1892								1	2	1			4
1893						1	1	5	3				10
1894								1	1	3			5
1895								1		1			2
1896							1	1	2	2			6
1897								1	1				2
1898								2	2				4
1899							1	2	1	1			5
1900								1	2				3
1901							1	2					3
1902						1			1	1			3
1903							1	1	3	2	1		8
1904									1	1			2
1905										1			1
1906						1		1	2	2			6

TABLE 6.31. (*Continued*)

Year	Jan.	Feb.	Mar.	Apr.	May	June	July	Aug.	Sept.	Oct.	Nov.	Dec.	Total
1907													0
1908			1				1		2	1			5
1909							1	1	1	1			4
1910									2	1			3
1911								2	1				3
1912									1	2	1		4
1913						1		1	1				3
1914													0
1915								3	1				4
1916						1	2	3	2	2	1		11
1917								1	1				2
1918								2	1				3
1919									1				1
1920									4				4
1921						1			2	1			4
1922									1	1			2
1923								1	1	1			3
1924								2	1	1	1		5
1925											1		1
1926							2	1	4	1			8
1927								1	3				4
1928								2	1	1			4
1929						1			1	1			3
1930								2					2
1931									2				2
1932								3	1	1	1		6
1933						1	1	3	3	1			9
1934						1	1	1	1	1	1		6
1935								2	1	2			5
1936						1	1	3	2				7
1937									3				3
1938								2	1				3
1939								1		2			3
1940								3	1				4
1941									3	1			4
1942								3			1		4

TABLE 6.31. (*Concluded*)

Year	Jan.	Feb.	Mar.	Apr.	May	June	July	Aug.	Sept.	Oct.	Nov.	Dec.	Total
1943							1	1	2	1			5
1944							2	1	3	1			7
1945						1		1	1	2			5
1946							1		1	1			3
1947								2	1	2			5
1948								1	3	1	1		6
1949								2	4	1			7
1950								4	3	4			11
1951					1			2	2	3			8
1952								2	2	2			6
1953								2	3	1			6
1954						1		2	3	1		1	8
1955								3	5	1			9
1956							1	1	1		1		4
1957						1			2				3
1958								3	3	1			7
1959						1	2		3	1			7
1960							1	2	1				4
1961							1		5	1	1		8
1962								1		2			3
1963								2	4	1			7
1964								1	4	1			6
1965								2	1	1			4
1966						1	3	1	1		1		7
1967								1	3	2			6
1968						2		1	1	1			5
1969								4	4	3	1		12
1970					1			1	1	2			5
1971								2	4				6
1972						1		1	1				3
1973							1	1	1	1			4
1974								2	2				4
1975							1	2	3				6
1976								4	1	1			6
1977								1	3	1			5

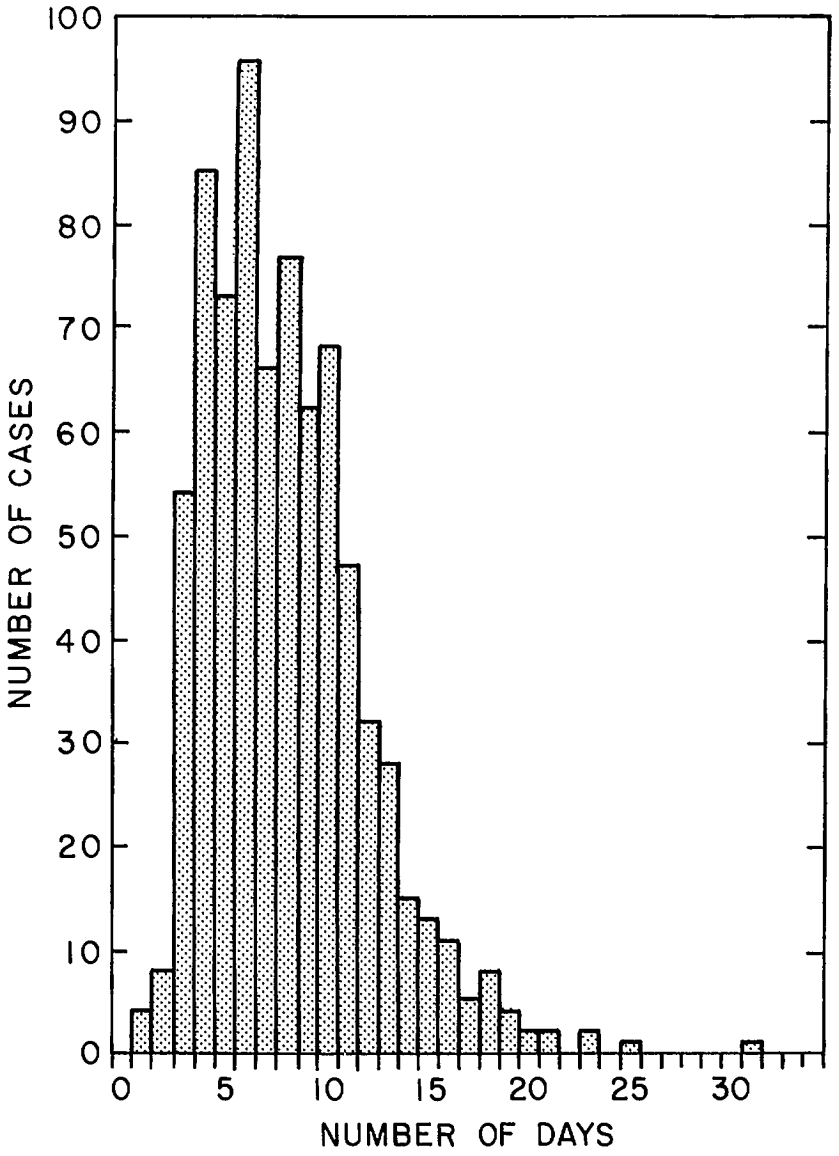

FIG. 6.35. Distribution of observed duration of Atlantic tropical cyclones, 1886–1977. (Neumann et al. 1979)

NORTH ATLANTIC TROPICAL CYCLONE SEASONS FOR THE YEARS 1976–79

To examine the variations from one season to the next, the hurricane seasons of 1976, 1977, 1978, and 1979 were selected. During the 1976 season, there were eight named tropical cyclones of which six became hurricanes. This was an average season (the annual average for the past 30 yr being nine storms including six hurricanes). However, there

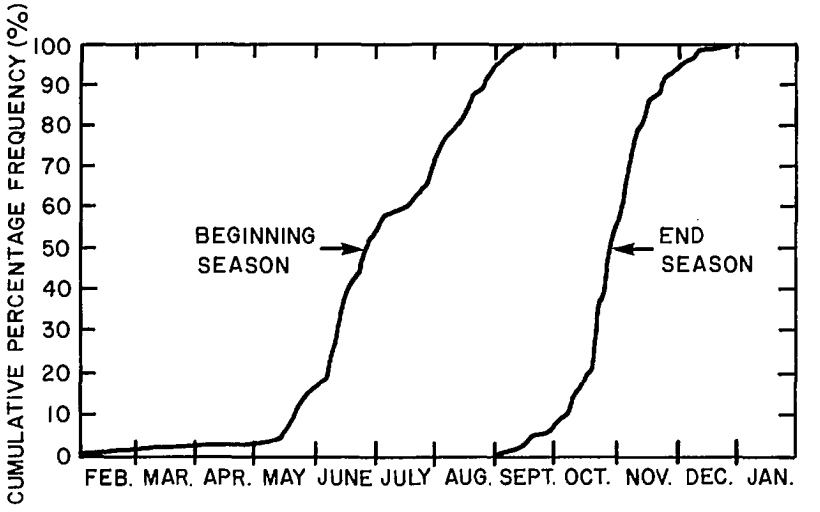

FIG. 6.36. Cumulative percentage frequency distribution of beginning and ending dates of Atlantic tropical cyclone season, 1886–1977. (Neumann et al. 1978)

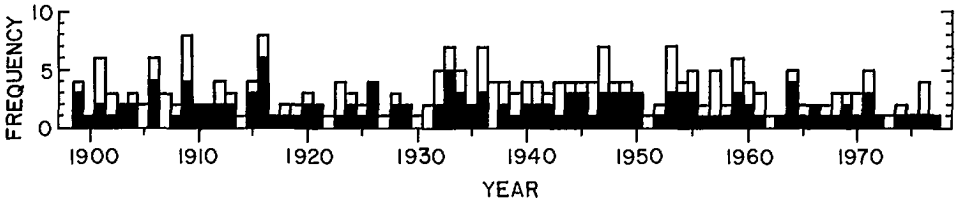

FIG. 6.37. Annual distribution of the 257 tropical storms and hurricanes together (open bars) and the 140 hurricanes only (solid bars) that have crossed or passed immediately adjacent to the United States coast (from Texas to Maine) during 1899–1977. (Neumann et al. 1978)

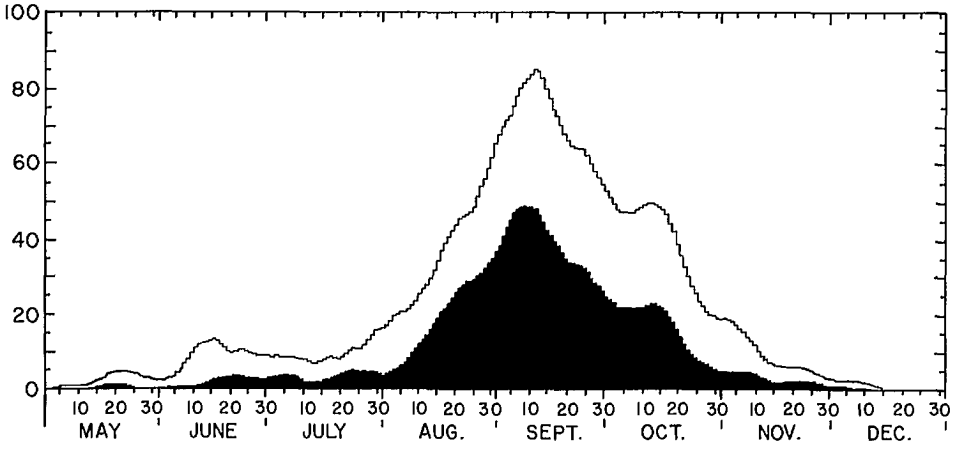

FIG. 6.38. Number of tropical storms and hurricanes together (open line) and hurricanes only (solid line) for 9-d averages from May 1 to December 30 based on data for 1886–1977 for the Atlantic Ocean. (Neumann et al. 1978)

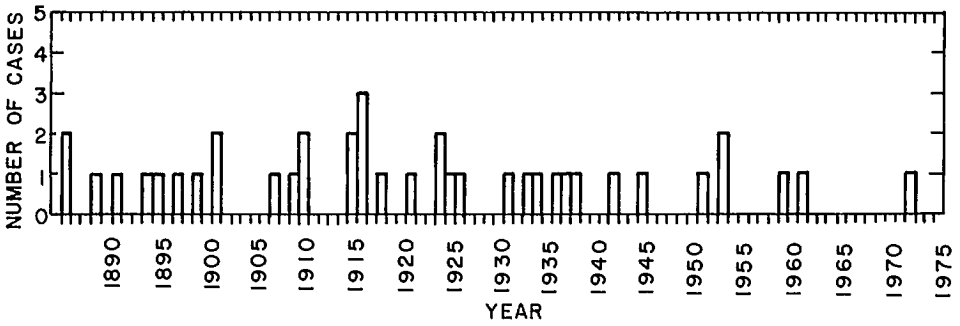

FIG. 6.39. Tropical storms and hurricanes that passed through the Yucatan Channel on their way from the Caribbean Sea to the Gulf of Mexico. (Neumann and Hill 1976)

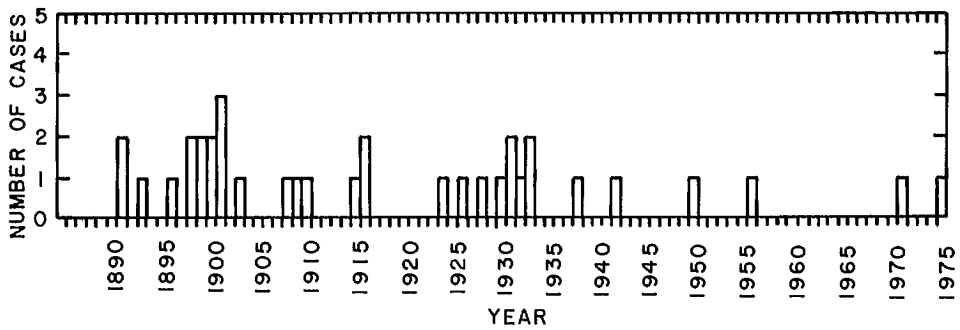

FIG. 6.40. Tropical storms and hurricanes that passed within 100 km of Puerto Rico. (Neumann and Hill 1976)

were two unusual features of the 1976 season. First, no storm crossed either the Caribbean Sea or the Gulf of Mexico. In the twentieth century, this has happened only once before, during 1962 (Lawrence 1977). Another unusual feature is associated with the tracks of Hurricanes Emmy and Frances. They recurved towards the east at very low latitudes. According to Lawrence (1977) this southern latitude of recurvature so early in the season is unprecedented. Hurricane Belle of August 6–10, 1976, generated storm surges along the east coast of the United States (mainly in the New York–New England area).

The season of 1977 is considered as rather inactive. In this season there were six named storms of which five became hurricanes (Lawrence 1978). The number of hurricane days during this season was 9 compared with the long-term average of 29. Also, the hurricane season began quite late (on August 29 with Hurricane Anita). The season ended with Hurricane Frieda on October 18, rather early. This interval of 51 d is less than half the long-term average of 110 d.

Another interesting feature of the 1977 season is that none of the storms originated east of 60°W. In the 30 yr prior to this, only once did this happen (in 1972). Hurricane Anita showed a central pressure of 926 mb, which is the fourth lowest ever recorded in the Gulf of Mexico. Also, Hurricane Anita has been ranked (Lawrence 1978a, 1978b) as the fourth most intense storm in the Gulf of Mexico behind the 1935 Labor Day storm in the Florida Keys (892 mb), Camille in 1969 (905 mb), and Beulah in 1967 (923 mb). During the 1977 season the only named storm to directly hit the United States was Hurricane Babe, which made a landfall along the Louisiana coast on September 5.

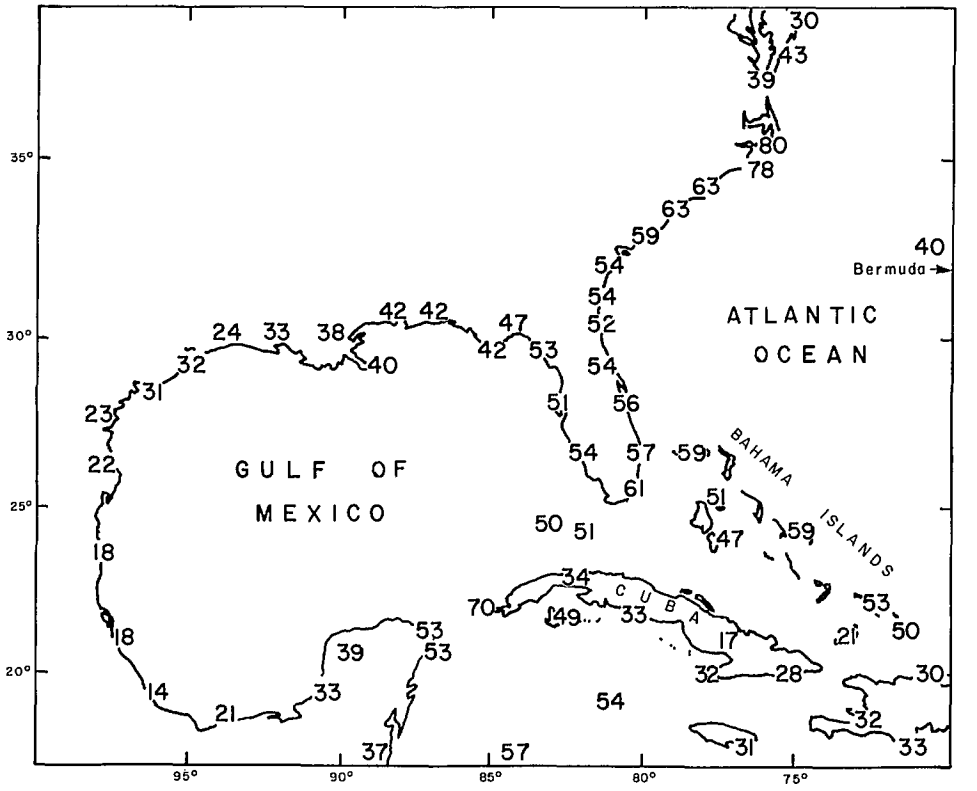

FIG. 6.41. Number of tropical cyclones during the period 1886–1969 (including depressions) that passed within 100 km of the locations shown. (Neumann and Hill 1976)

The 1978 season had 11 named tropical cyclones of which 5 became hurricanes. The only unusual feature of this season was the short duration of the individual cyclones (Lawrence 1979a, 1979b). The total number of hurricane hours (i.e. each hour the storm has wind speeds greater than 63 knots (117 km·h^{-1})) for this season was 307 compared with the long-term average of 620. Hurricane Debra of August 26–29 generated storm surges along the Louisiana coast.

The following are the highlights of the 1979 season (Hebert 1980; Frank and Clark 1980). Hurricane David (i.e. the winds and the storm surge) killed 56 in Dominica and more than 2000 in the Dominican Republic. It also rendered 60 000 of the 80 000 residents of Dominica homeless. About 200 000 people were made homeless in the Dominican Republic, and the damage there exceeded U.S.$1 billion. Hurricane Frederic caused an estimated damage of $2.3 billion in the United States, making it the costliest hurricane in United States history. Hurricane Claudette produced a 42-in. (1.1 m) rainfall in 24 h in Alvin, TX, which is a United States record for rainfall in a 24-h period. In 1979, the total damage resulting from tropical cyclones in the United States exceeded $3 billion, another record.

In the 1979 season there were eight named storms of which five became hurricanes. Hebert (1980, p. 973) stated:

> After 13 consecutive years without a hurricane, the Lesser Antilles, Puerto Rico, the

Virgin Islands and the Florida east coast were seriously affected by hurricanes. The Mobile, Alabama–Pascagoula, Mississippi area had its most intense hurricane of this century. Frederic was the first hurricane to strike Mobile directly since 1932. David was the first hurricane to strike the Cape Canaveral area directly since 1926. David was the most intense hurricane of the season, and probably of this century, in the eastern Caribbean Sea area. It was the strongest hurricane at Dominica since 1834 and at Santo Domingo (Dominican Republic) since 1930.

Storm surges were generated on the United States east coast by both Hurricanes David and Frederic. However, the surges due to Frederic were greater (up to 5 m at Gulf State Park, AL).

Some Comparisons of the Tropical Cyclone Activity in the Atlantic and Pacific Oceans

Nunez and Gray (1978) and Gray (1978c) compared some meteorological parameters associated with Atlantic hurricanes and Pacific typhoons, and their findings are summarized in Table 6.32.

6.5 Cyclones of the Indian Ocean

There are no extratropical cyclones in the North Indian Ocean. The extratropical cyclones of the South Indian Ocean are not very relevant for storm surge studies and, in any case, these will be briefly considered in section 7.4. In this section will be considered mainly the tropical cyclones of the South and North Indian oceans with emphasis on the Bay of Bengal and to a lesser extent on the Arabian Sea. However, while discussing tropical cyclones, another type of cyclone (which is neither tropical nor extratropical) referred to as a subtropical cyclone will be considered.

Subtropical Cyclones

Simpson (1952) referred to the upper level cutoff lows, which frequently develop over the eastern part of the North Pacific Ocean during winter, north of Hawaii (locally referred to as Kona storms and which occasionally cause heavy flooding in Hawaii), as subtropical cyclones. These appear to be preceded by the injection of cold air aloft through the mechanism of large-amplitude troughs in the polar westerlies (Palmén 1949). Ramage (1962) suggested that subtropical cyclones indeed are direct energy-creating systems. This answers the question of how a cold upper cyclone can persist and intensify and even occasionally extend to the surface after being cut off from a fresh supply of cold air when condensation and precipitation should inevitably weaken the thermal and pressure gradients of the system.

Based on a study of two subtropical cyclones near Hawaii, Ramage (1962) gave the following results. About 500 km from the center and beyond, the upward motion is weak and resembles that of a relatively warm-cored weak tropical cyclone circulation. In the downward branch (beyond 500 km from the center) gentle downward motion extends to the subsidence inversion level. In the surface layer beneath the subsidence inversion, a regime that bears some resemblance to the trade winds exists. Local regions of wind maxima and corresponding zones of convergence and divergence occur. The eye diameter could be as large as 200 km. Although a subtropical cyclone somewhat resembles a large-amplitude trough in the polar westerlies associated with a surface low, the sub-

TABLE 6.32. Comparison of Atlantic hurricanes and Pacific typhoons.

Parameter	Atlantic hurricanes (West Indies)	Pacific typhoons
Temperature anomaly. This is determined as follows. A mean temperature is calculated by averaging the temperature values at 9 and 15° to the east and west of the position of the cyclone. Deviation from this mean temperature is the anomaly	Warm core throughout most of the troposphere. Warmest temperature at about 300 mb. The anomaly is +4°C for the hurricane (at 300 mb) Cold core in the upper troposphere and lower stratosphere. This region occurs at a lower level than for typhoons and its radial extent is greater	Warm core throughout most of the troposphere. Warmest temperature at about 250 mb. The anomaly is +7°C for the typhoon (at 250 mb). Cold core in the upper troposphere and lower stratosphere
Relative humidity	About 10% less than for typhoons at equivalent radii and heights Boundary layer relative humidity is about 15% lower than for the West Pacific	Moister inner core with relative humidities greater than 90% up to 400 mb whereas in the hurricane, such a high relative humidity cannot be found higher than at 575 mb
Radial winds	Maximum inflow at 950 mb with a wind of 8 $m \cdot s^{-1}$. At 150 mb there are two outflow jets: northeast and southwest. The northeast jet is about four times stronger	Maximum inflow at 950 mb with a wind of 6 $m \cdot s^{-1}$. At 150 mb there are two outflow jets: northeast and southwest. The southwest jet is somewhat greater
Tangential wind	Maximum cyclonic flow is at the top of the frictional boundary layer at 850 mb The tangential wind is smaller than in typhoons The anticyclonic maximum occurs at 150 mb Generally the hurricane size is smaller than a typhoon's Vertical shear between 950 and 150 mb is 10–15 $m \cdot s^{-1}$	Maximum cyclonic flow is at the top of the frictional boundary layer at 850 mb The anticyclonic maximum occurs at 150 mb. The anticyclonic circulation is relevant also in determining the weather associated with the typhoon Vertical shear between 950 and 150 mb is 15–20 $m \cdot s^{-1}$
Inflow angle	The boundary layer inflow angle decreases from quadrant to quadrant in the following order: right, front, back, left	The boundary layer inflow angle decreases in the following order: front, right, left, back
Steering current concept for predicting tracks	Applies	Applies West Pacific typhoons move more to the left of the mean current than do West Atlantic hurricanes

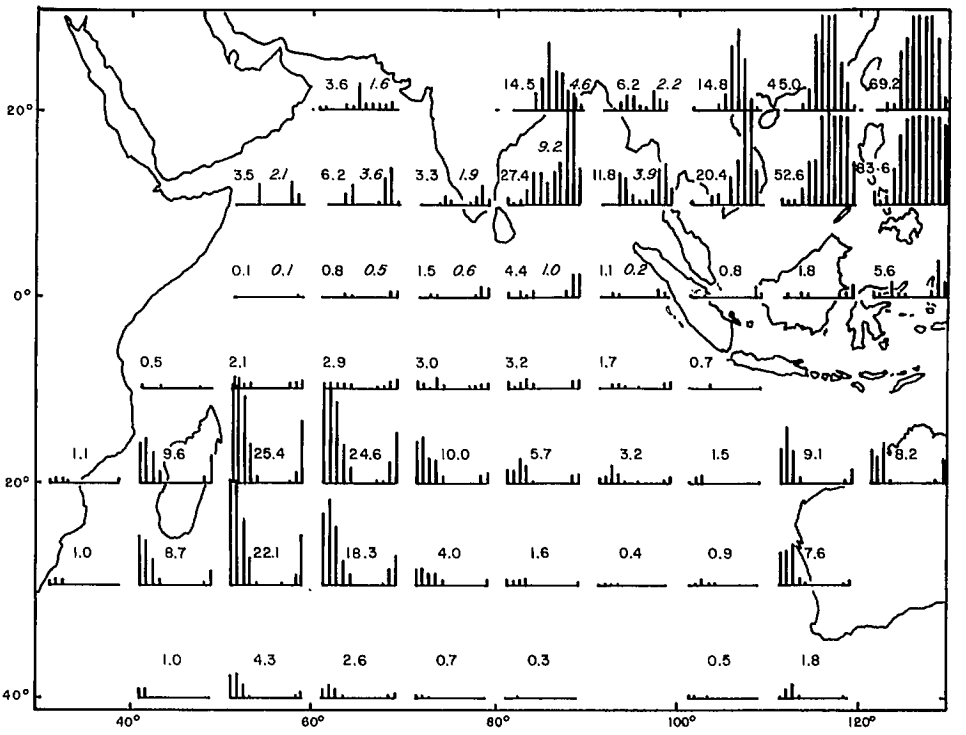

FIG. 6.42. Frequency of tropical cyclones in the Indian Ocean (average numbers of occurrences per 10 yr for each 10° square by months). Roman-type numbers indicate average 10-yr totals over the northern Indian Ocean. The unblackened segments of the histograms and the italicized numbers given corresponding information for severe tropical storms. (Ramage 1971)

tropical cyclone is more symmetric and its field of motion, clouds, and weather are quite different.

Subtropical cyclones occur in the Atlantic as well as in the Indian Ocean (in addition to those in the Pacific). In connection with the meteorological program of the International Indian Ocean Expedition (IIOE) during the 1960's, Ramage (1971) mentioned the existence of a subtropical cyclone over the Bay of Bengal in June 1963. In July 1963 another subtropical cyclone was detected over the northeastern part of the Arabian Sea.

Miller and Keshavamurthy (1968) developed a model for the subtropical cyclone using composited data. Subtropical cyclones develop predominantly near heat troughs and in the areas dominated by trade winds. Whereas in the eastern part of the North Pacific, the subtropical cyclones persist for weeks without weakening, in the Arabian area, they dissipate, probably as a result of ventilation of the cyclone by drier air.

In the Bay of Bengal and Arabian Sea areas, storm surges occur usually during the postmonsoon (September–December) and the premonsoon (April–May) months. Hence, subtropical cyclones are not very relevant for storm surge studies.

TROPICAL CYCLONES OF THE INDIAN OCEAN

Tropical cyclones develop in all parts of the Indian Ocean. This is in contrast with

TABLE 6.33. Tropical cyclones of the South Indian Ocean for the 1975–76 season. H, hurricane; T, tropical storm. (DeAngelis 1977a)

No.	Name	Intensity	Date	Maximum wind ($km \cdot h^{-1}$)[a]	Lowest pressure (mb)[a]
1	Audrey	T	Nov. 17–29	96	995
2	Barbara	H	Dec. 3–19	157	980
3	Clotilde	H	Jan. 7–20	250	980
4	Danae	H	Jan. 12–29	250	955
5	Gladys	T	Mar. 27–Apr. 10	111	998
6	Heliotrope	T	Apr. 3–12	83	1000

[a]Estimated.

TABLE 6.34. Tropical cyclones of the South Indian Ocean during the 1976–77 season. H, hurricane; T, tropical storm. (De Angelis 1978d)

No.	Name	Intensity	Date	Maximum wind ($km \cdot h^{-1}$)[a]	Lowest pressure (mb)[a]
1	Agathe	T	Oct. 3–13	102	995
2	Brigitta	T	Nov. 6–Dec. 1	83	1000
3	Clarence	H	Jan. 5–16	204	960
4	Domitile	T	Jan. 18–23	102	992
5	Emilie	H	Jan. 26–Feb. 5	176	980
6	Fifi	H	Jan. 29–Feb. 10	148	985
7	Gilda	T	Feb. 3–9	83	1000
8	Io (Jack)	H	Feb. 15–Mar. 2	250	935
9	Hervea	H	Feb. 17–Mar. 3	185	970

[a]Estimated.

the Atlantic and Pacific oceans. There are no tropical cyclones in the South Atlantic and eastern part of the South Pacific. The average number of tropical cyclones during a 10-yr period for each 10° square by months is shown in Fig. 6.42. It can be seen that the highest frequencies occur north of Indonesia (not counting the Philippines area). In the Bay of Bengal and to the region east of the Malagasy Republic (Madagascar) high frequencies also occur. However, one difference is that whereas in the Bay of Bengal the highest frequencies are during September–December, in the region east of the Malagasy Republic (i.e. the western part of the South Indian Ocean) and in the region west of the west coast of Australia (i.e. the eastern part of the South Indian Ocean) the high frequencies occur during January–March.

TROPICAL CYCLONES OF THE SOUTH INDIAN OCEAN

Certain features of the tropical cyclones of the South Indian Ocean for the seasons 1975–76 and 1976–77 are summarized in Tables 6.33 and 6.34, respectively. In the 1975–76 season there were a total of six tropical cyclones of which three reached hurricane strength. In the 1976–77 season, of a total of nine cyclones, five became hurricanes. The tropical cyclones for the period 1965–77 are summarized by month for various ocean basins in Table 6.35. Note that in terms of frequency, the North Indian Ocean has the lowest and the South Indian Ocean has the second lowest. However, this

TABLE 6.35. Tropical cyclones in various ocean basins during the period 1965–77. Numbers in parentheses indicate tropical cyclones that reached hurricane intensity (i.e. winds ≥ 119 km·h^{-1}). (DeAngelis 1979a)

Month	North Atlantic	Eastern North Pacific	Western North Pacific	North Indian	South Indian	Australia–South Pacific	Total	Average
Jan.	0(0)	0(0)	9(5)	2(1)	29(17)	52(20)	92(43)	7.1(3.3)
Feb.	0(0)	0(0)	4(1)	0(0)	30(16)	41(16)	75(33)	5.8(2.5)
Mar.	0(0)	0(0)	6(1)	0(0)	15(5)	39(18)	60(24)	4.6(1.8)
Apr.	0(0)	0(0)	11(9)	4(2)	6(1)	18(6)	39(18)	3.0(1.4)
May	3(1)	5(3)	14(10)	14(5)	3(0)	4(3)	42(22)	3.3(1.7)
June	8(4)	24(9)	20(13)	5(1)	0(0)	0(0)	59(27)	4.4(2.1)
July	13(7)	41(16)	60(35)	2(0)	1(0)	2(0)	119(58)	9.2(4.5)
Aug.	32(22)	53(31)	67(38)	2(1)	0(0)	0(0)	154(92)	11.8(7.1)
Sept.	44(26)	41(20)	63(43)	11(4)	1(0)	0(0)	160(93)	12.3(7.2)
Oct.	20(12)	20(10)	50(40)	16(7)	5(3)	4(1)	115(73)	8.8(5.6)
Nov.	4(2)	4(0)	34(19)	19(8)	5(2)	18(7)	84(38)	6.5(2.9)
Dec.	1(0)	0(0)	11(4)	11(4)	21(6)	33(15)	77(29)	5.9(2.2)
Total	125(74)	188(89)	349(218)	86(33)	116(50)	211(86)	1075(550)	
Average	9.6(5.7)	14.5(6.8)	26.8(16.8)	6.6(2.5)	8.9(3.8)	16.2(6.6)	82.7(42.3)	
Percent hurricanes	59	47	63	38	43	41		

TABLE 6.36. Cornparison of the ratings of western Pacific and Indian Ocean ports evaluated as typhoon havens (also see Table 6.29 for details on certain ports). (Brand 1978)

Port	Region	Rating
Apra Harbor	Guam	Poor
Kaohsiung	Taiwan	Poor
Chilung (Keelung)	Taiwan	Poor
Hong Kong Harbor	Hong Kong	Poor
Yokosuka	Japan	Good
Nunazu operating area	Japan	Poor
Iwakuni	Japan	Marginal (but has easily accessible anchorages close by that are good)
Kure	Japan	Good
Saskebo	Japan	Good (except for carriers)
Kagoshima	Japan	Poor
Buckner Bay (Okinawa)	Japan	Poor
Naha (Okinawa)	Japan	Poor
Subic Bay	Philippines	Marginal to poor
Manila	Philippines	Poor
Cebu	Philippines	Poor
Inchon	Korea	Poor (unless shelter is available in the tidal basin, then it would be considered a good haven)
Pusan	Korea	Poor
Chinhae	Korea	Marginal (but has easily accessible anchorages nearby that are considered good)
Colombo	Sri Lanka	Good
Karachi	Pakistan	Marginal
Auckland	New Zealand	Good to marginal
Freemantle	Australia	Marginal (unless shelter is available in Cockburn Sound or the inner harbor, then it would be considered good)
Diego Garcia Harbor	Diego Garcia	Poor

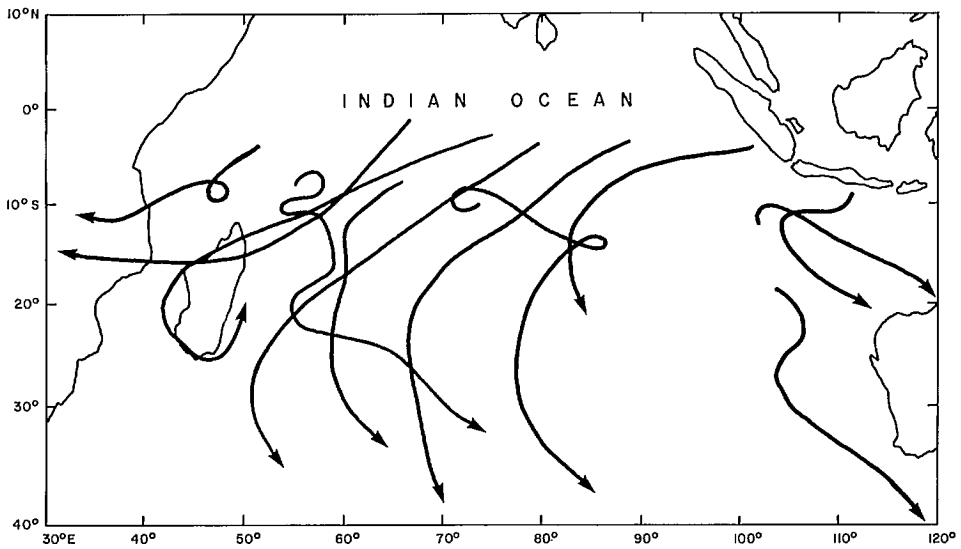

FIG. 6.43. Typical tropical cyclone tracks in the South Indian Ocean between the Malagasy Republic and the west coast of Australia.

FIG. 6.44. Typical tropical cyclone tracks near the west coast of Australia.

may be misleading when one considers the damage due to tropical cyclones (and storm surges generated by them). More than 60% of the deaths and almost 40% of the damage due to tropical cyclones occur on lands bordering the Bay of Bengal, which is only a small part of the North Indian Ocean.

Considered earlier were typhoon waves among harbors located around the Pacific Ocean. Some Indian Ocean harbors as well as some Pacific Ocean harbors (for comparison) are listed in Table 6.36. Among the Indian Ocean harbors, only Colombo is listed as "good" and Karachi as "marginal" (Brand 1978).

Some typical tropical cyclone tracks in the region between the Malagasy Republic and the west coast of Australia are illustrated in Fig. 6.43 and typical tracks near the west coast of Australia in Fig. 6.44. For comparison, tropical cyclone tracks near the east coast of Australia and those affecting New Zealand are shown in Fig. 6.45 and 6.46, respectively.

Australia is the only continent that is affected by tropical cyclones on both the east and west coasts. Certain features of the tropical cyclones of Australia are described in Tables 6.37–6.39. The average tropical cyclone frequencies for the west and east coasts of Australia for the months of December and January are given in Fig. 6.47 and 6.48,

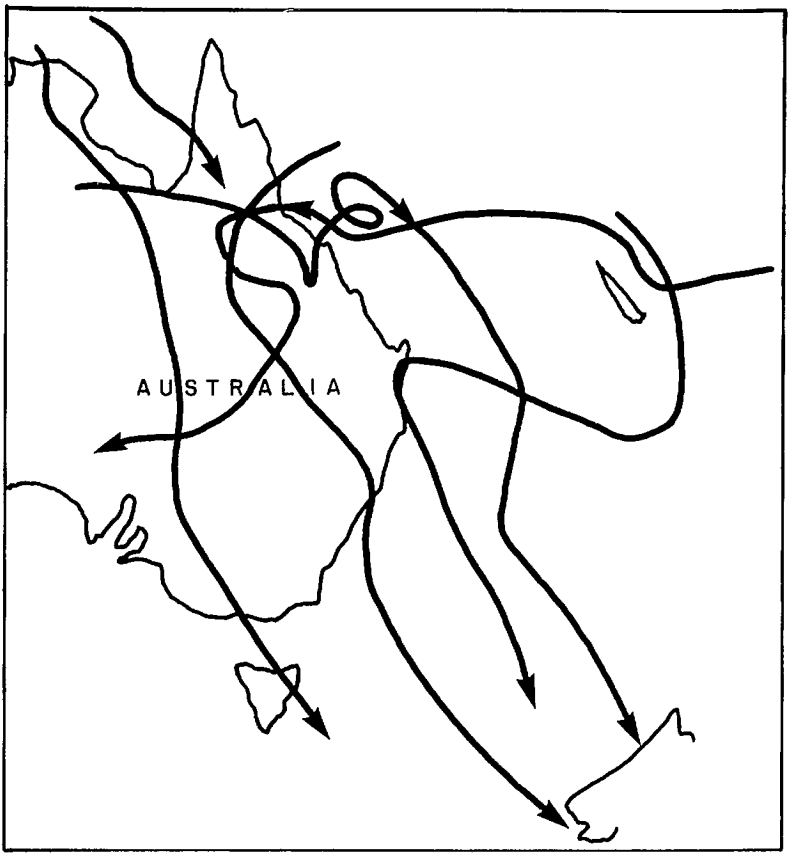

FIG. 6.45. Typical tropical cyclone tracks near the east coast of Australia.

respectively. The frequency of cyclone days in Australia is given in Fig. 6.49 and the cyclone frequency change (i.e. trend) during the period 1905–55 is shown in Fig. 6.50.

TROPICAL CYCLONES OF THE NORTH INDIAN OCEAN

James Cappar in India suggested in 1801 (also William Dunbar in the United States in the same year) that there is a vortex in the center of a tropical cyclone (Ludlam 1963). However, it was Henry Piddington who, in 1851, coined the word "cyclone" from the Greek word "kyklon" meaning coil of snake to describe the rotary motion. Piddington was the president of the Marine Courts at Calcutta, India, and in 1851 he published a sailor's handbook in which he stated some laws for tropical storms. During 1839–58 he published a series of articles on the structure and movement of tropical storms (Rao 1968). Other notable early workers on this topic were Blanford (1883), Chambers (1882 to 1885, cited in Rao 1968), Dallas (1891a, 1891b), and Eliot (1900). Basically, all these studies were based on surface data only.

Koteswaram and Gasper (1956), using compositing data for 31 storms, gave detailed surface structure of tropical storms in the North Indian Ocean. In these studies, essentially

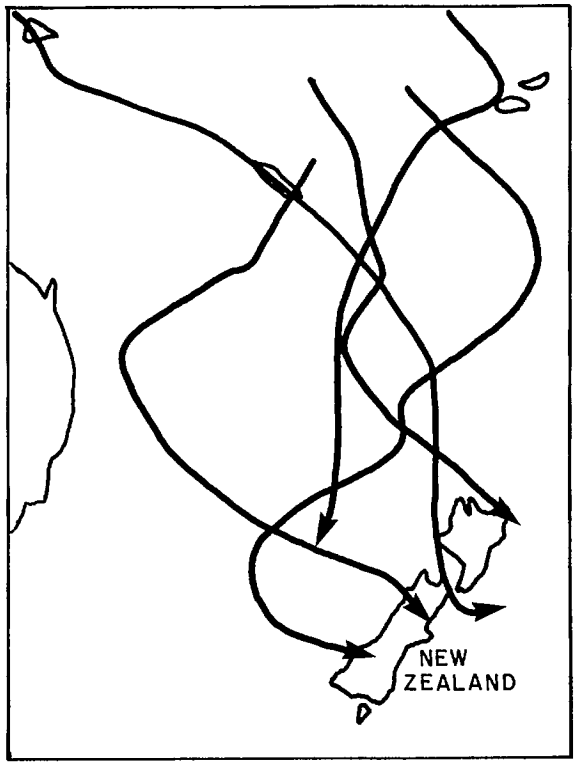

FIG. 6.46. Typical tropical cyclone tracks near New Zealand.

the following nomenclature was used: depression (wind speed between 18 and 33 knots), moderate storm (wind speed between 34 and 47 knots), and severe storm (wind speed greater than 47 knots) (1 knot = 1.852 $km \cdot h^{-1}$).

Cyclones that affect the Indian subcontinent basically develop out of perturbations originating in the intertropical convergence zone (Rao 1968). Since this zone exhibits seasonal variations in intensity and latitudinal position, it is natural to expect similar changes in the cyclones. During the summer period, the ITCZ lies mostly over land and severe cyclones capable of generating destructive storm surges do not form. However, depressions giving heavy precipitation occur regularly and frequently.

During spring and fall, the belt between 10 and 15°N gives rise to several depressions, some of which mature into storms and some even into severe storms. Usually, these move towards the northwest and strike the Andhrapradesh coast of India. However, some of them recurve over the Bay of Bengal and hit the northern coast of the bay (the west Bengal state of India and the coast of Bangladesh). During autumn, the storms take a more southerly course and strike the peninsular part of India. Some of these storms recurve and strike the north coast of the bay (the Sunderban coast). Some cross the peninsula and redevelop over the Arabian Sea and travel west–northwest and strike the Arabian Sea coast of the subcontinent. Usually, there are no storms during winter. On the rare occasion when they occur, they could be extremely violent.

The tropical cyclones of the North Indian Ocean are usually less frequent and less

TABLE 6.37. Percentage frequency and types of tropical cyclone tracks for the west coast of Australia. (Brunt and Hogan 1956)

Type of path	Dec.	Jan.	Feb.	Mar.	Apr.	Season
Parabolic	4	5	12	8	2	31
More or less straight	6	16	12	13	1	48
Reverse curvature	1	1	6	0	0	8
Cusp	0	3	2	5	1	11
Doubling of track	0	2	0	0	0	2
Total						100

TABLE 6.38. Percentage frequency and types of tropical cyclone tracks for the east coast of Australia. (Brunt and Hogan 1956)

Type of path	Dec.	Jan.	Feb.	Mar.	Apr.	Season
Parabolic	2	6	14	15	2	39
More or less straight	2	11	8	11	5	37
Reverse curvature	1	8	0	1	2	12
Cusp	0	2	7	1	0	10
Doubling of track	1	0	0	0	1	2
Total						100

TABLE 6.39. Probability of cyclones endangering coastal sections in Australia. (Brunt and Hogan 1956)

Section of coast	Dec.	Jan.	Feb.	Mar.	Apr.
Hamlin Pool–Roebourne	0.05	0.18	0.21	0.18	0
Roebourne–Broome	0.10	0.24	0.18	0.13	0.03
Broome–Wyndham	0.10	0.26	0.08	0.13	0.03
Wyndham–Darwin	0.03	0.03	0.05	0.03	0
Darwin–Melville Bay	0.08	0.03	0.03	0.03	0.03
N.T. Gulf coast	0.02	0.14	0.08	0.08	0
Queensland Gulf coast	0.02	0.22	0	0	0
Thursday Island–Cooktown	0.04	0.04	0.04	0.08	0.04
Cooktown–Townsville	0	0.12	0.28	0.12	0.04
Townsville–Rockhampton	0.04	0.08	0.12	0.16	0.06
Rockhampton–N.S.W. border	0	0.06	0.16	0.16	0.06

intense than the hurricanes of the Atlantic Ocean or the typhoons of the Pacific Ocean (Rao 1968). Also, their life span is shorter, i.e. 2–3 d compared with 6 d or more elsewhere. This shorter life span (even for recurving storms) is basically due to the relatively short track over the waters compared with other ocean basins. This, of course, does not mean that the destruction of life and damage to property are less. Two of the lowest central pressures recorded in these storms are 919.4 mb (False Point Cyclone of September 1885) and 959.7 mb (the Nellore Cyclone of November 1927).

The severe storms have winds up to or more than 100 knots (185 $km \cdot h^{-1}$). However, their areal extent is quite small. The highest wind speed of 120 $mi \cdot h^{-1}$ (193 $km \cdot h^{-1}$) was recorded in the Midnapore Cyclone of 1942 (the estimated maximum wind speed for this was 140 $m \cdot h^{-1}$ (224 $km \cdot h^{-1}$)). During the 1964 Rameswaram Cyclone, the maximum estimated winds over Sri Lanka were up to 150 knots (278 $km \cdot h^{-1}$).

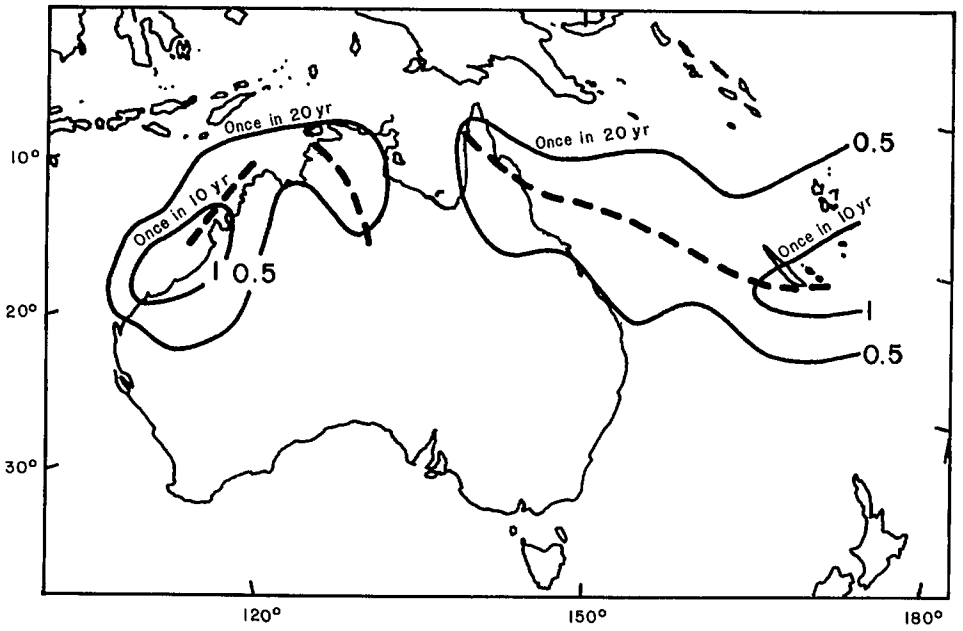

FIG. 6.47. Average frequency of tropical cyclones crossing 5° latitude–longitude squares per 10 yr in December. Heavier broken lines indicate the axes of maximum values. (Brunt and Hogan 1956)

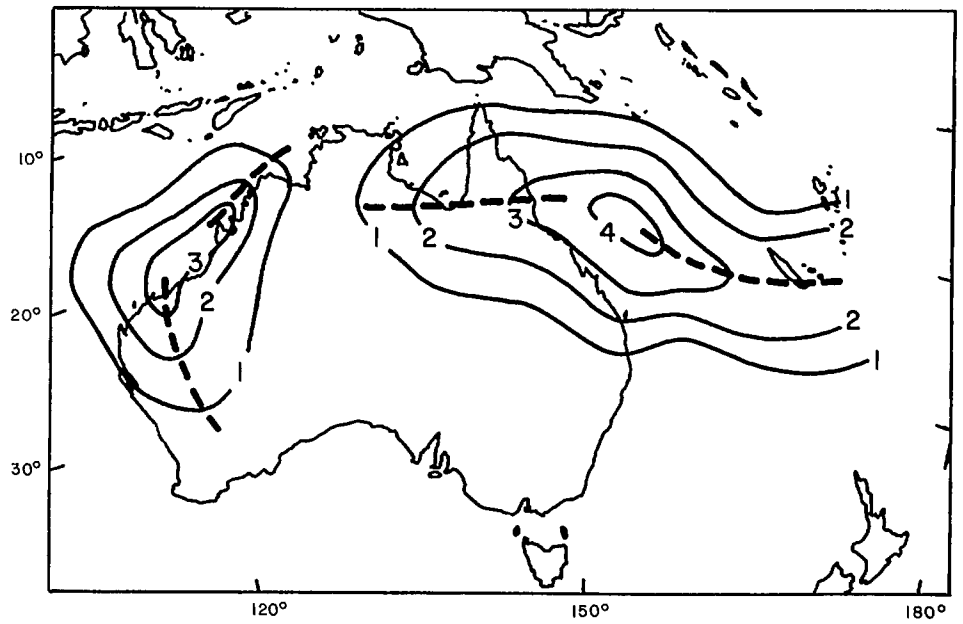

FIG. 6.48. Average frequency of tropical cyclones crossing 5° latitude–longitude squares per 10 yr in January. Heavier broken lines indicate the axes of maximim values. (Brunt and Hogan 1956)

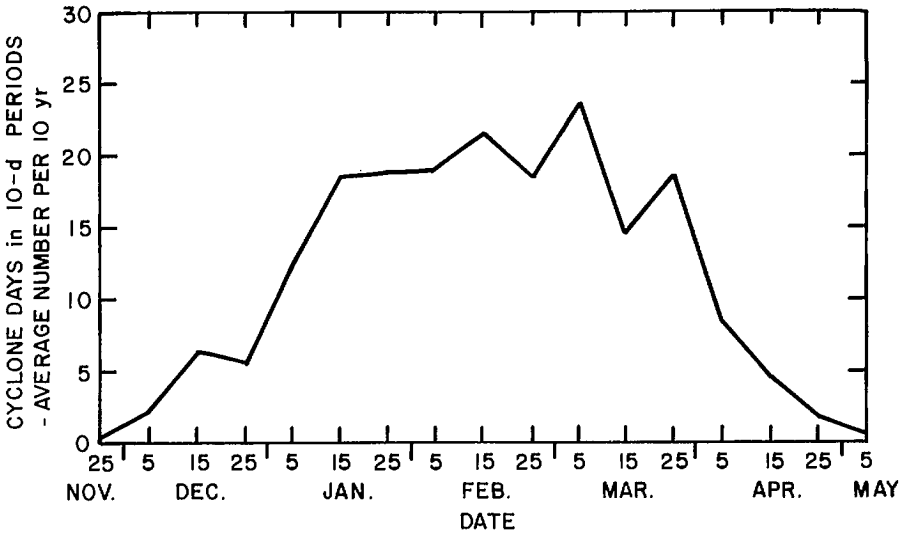

FIG. 6.49. Frequency of cyclone days in Australia. (Brunt and Hogan 1956)

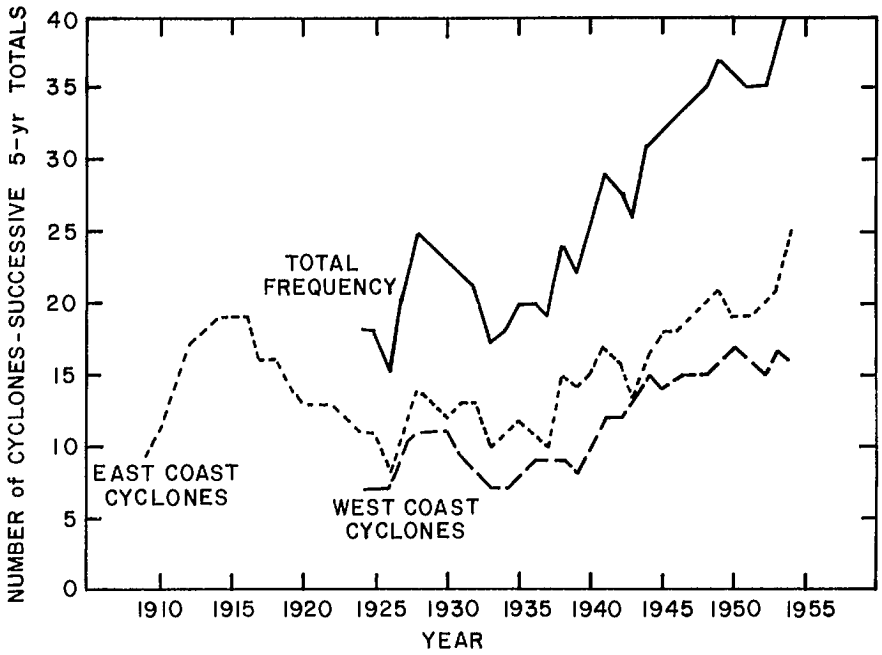

FIG. 6.50. Frequency of tropical cyclones in and around Australia (successive 5-yr totals). (Brunt and Hogan 1956)

Another interesting feature of these storms is the difference in the location of the maximum winds. For the premonsoon storms (April–May) the sector of strongest winds is usually in the southeast or east, whereas for the postmonsoon storms

TABLE 6.40. Number of cyclonic disturbances that originated over the Bay of Bengal and the Arabian Sea in different months for the period 1891–1960. Note that "storms" includes "severe storms" also, whereas "cyclonic disturbances" includes storms and severe storms in addition to cyclonic disturbances. (Rao 1968)

	Cyclonic disturbances	Storms	Severe storms
Jan.	13	4	1
Feb.	3	1	1
Mar.	5	4	2
Apr.	26	18	7
May	56	28	18
June	93	34	4
July	132	38	7
Aug.	145	25	1
Sept.	151	27	8
Oct.	132	53	19
Nov.	102	56	23
Dec.	52	26	9
Year	910	314	100

(October–December), it is to the north of the center (Rao 1968). Mowla (1968) compared the cyclogenesis in the Bay of Bengal and the Arabian Sea.

After the Second World War, using radiosonde data, the upper structure of these storms was studied, and several articles appeared in the *Indian Journal of Meteorology and Geophysics* (now called *Mausam*), especially on the tracks of cyclonic disturbances in various months with emphasis on the recurvature. These studies revealed that the areas of generation and the tracks in every month are closely related to the anticyclonic cell in the upper troposphere at a 10- to 12-km height. However, variations in the tracks could occur due to changes in the general circulation produced by troughs in the midlatitude westerlies.

Frequencies of Cyclonic Storms in the Bay of Bengal

The number of cyclonic disturbances over the Bay of Bengal for each month during the period 1891–1960 is given in Table 6.40. Raghavendra (1973) performed a statistical analysis of the number of tropical storms and depressions in the Bay of Bengal for the period 1890–1969 (for a more recent study, see Mooley 1980b). The average annual number of storms and depressions is 13. The monsoon season accounts for 56% of these and the postmonsoon season accounts for 31%. The highest number (20 storms) occurred in 1927. The frequency distribution of storms and depressions of monsoon and post-monsoon seasons is normal and that of the annual season is almost normal with slight kurtosis. The decade of 1920–29 had the highest mean and the decade of 1950–59 the lowest mean for the annual and monsoon seasons, thus indicating a cycle of 60 yr.

Sadler and Gidley (1973) gave tracks of the storms in the North Indian Ocean. Chakravorthy (1956) discussed the dimensions of the eye of the Bay of Bengal storms. He found that the eye diameter varied from 7 to 20 mi (11.5–32 km).

Mooley (1980a, 1980b) studied the severe cyclonic storms of the Bay of Bengal for the period 1877–1977. He found that during the period 1965–77, a higher percentage (than the average) of storms intensified into severe storms and a higher percentage of

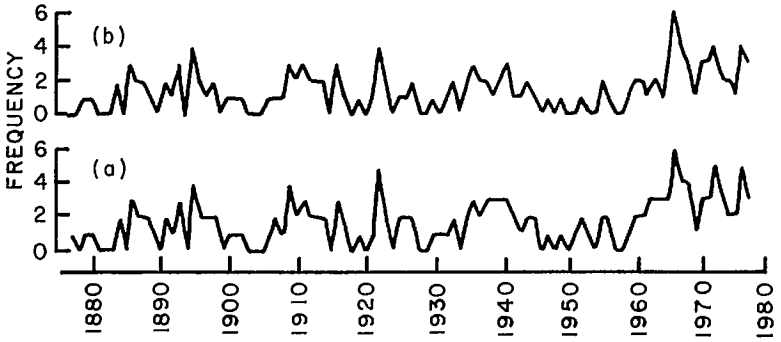

FIG. 6.51. Annual frequency of severe cyclonic storms that over the period 1877–1977 (a) formed over the Bay of Bengal and (b) struck the coast. (Mooley 1980)

TABLE 6.41. Mean and variance of the number of severe storms forming over the Bay of Bengal, and the number of severe storms striking the coast in a year. (Mooley 1980)

	Severe storms forming over the Bay of Bengal		Severe storms striking the coast	
Period	Mean	Variance	Mean	Variance
1891–1964	1.50	1.420	1.22	1.087
1877–1964	1.42	1.374	1.16	1.091
1877–1977	1.67	1.910	1.40	1.530
1965–77	3.38	1.923	3.00	1.833

TABLE 6.42. Number of cyclonic storms that formed over the Bay of Bengal, number that intensified into severe storms over the bay, and number that struck the coast as severe storms in different 13-yr periods. (Mooley 1980)

Period	Number of storms that formed	Number of storms that intensified into severe storms	Number of severe storms that struck the coast	Efficiency of intensification of storms into severe storms over the bay	Ratio of severe storms that struck the coast to storms that struck the coast
1877–89	49	13	12	0.26	0.31
1890–1902	56	19	18	0.34	0.36
1903–15	64	19	17	0.30	0.30
1916–28	61	19	16	0.31	0.36
1929–41	70	24	19	0.34	0.39
1942–54	46	13	8	0.28	0.28
1952–64	45	21	13	0.47	0.43
1965–77	70	44	39	0.63	0.66
1886–98	74	24	23	0.32	0.35
1924–36	74	16	13	0.22	0.25
1932–44	71	27	22	0.38	0.47

storms made landfall. Generally, the formation and landfall of these severe storms are random events and are consistent with the Poisson stochastic process.

For this study, a severe cyclonic storm is defined as one with winds greater than or

TABLE 6.43. Frequency of cyclonic storms that formed over the Bay of Bengal, frequency of storms that intensified into severe storms, efficiency of intensification of storms, and frequency of severe storms that crossed the coast in different months. Data presented are for the whole period 1877–1977 (not annual average). (Mooley 1980)

	Jan.	Feb.	Mar.	Apr.	May	June	July	Aug.	Sept.	Oct.	Nov.	Dec.	Annual
Frequency of storms	5	0	5	21	48	43	48	30	42	77	91	43	453
Frequency of storms that intensified into severe storms	2	0	3	9	32	6	8	3	14	30	44	18	169
Efficiency of intensification				0.43	0.67	0.14	0.17	0.10	0.33	0.39	0.49	0.42	0.37
Frequency of severe storms that crossed the coast	1	0	2	6	29	6	8	3	12	28	35	11	141

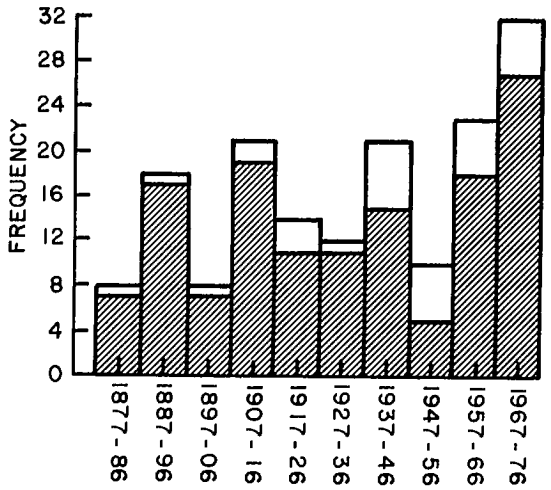

FIG. 6.52. Frequency of severe cyclonic storms that formed over the Bay of Bengal (entire rectangles) and struck the coast (hatched rectangles) in 10-yr periods during 1877–1976. (Mooley 1980)

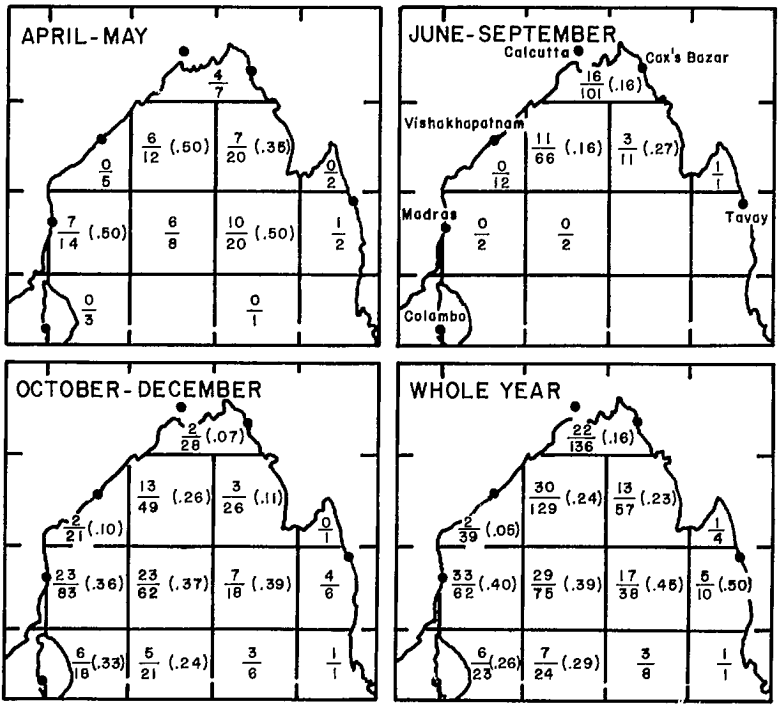

FIG. 6.53. Number of storms located (denominator), number of storms intensified into severe storms (numerator), and the efficiency of intensification (in parentheses) in the different sectors of the Bay of Bengal for the period 1877–1977. (Mooley 1980)

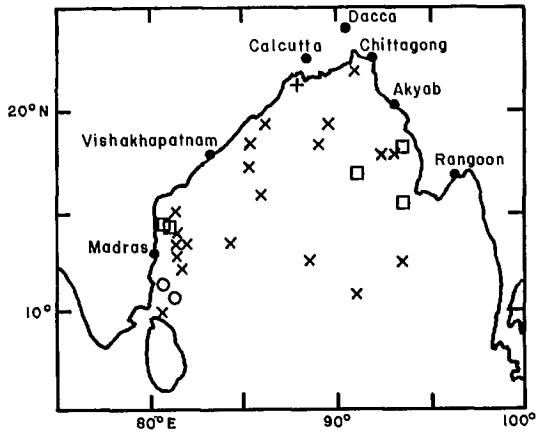

FIG. 6.54. Locations of severe storms just prior to their weakening into storms and depressions over the Bay of Bengal during the period 1877–1977. ○, January–March; □, April and May; +, June–September; ×, October–December. (Mooley 1980)

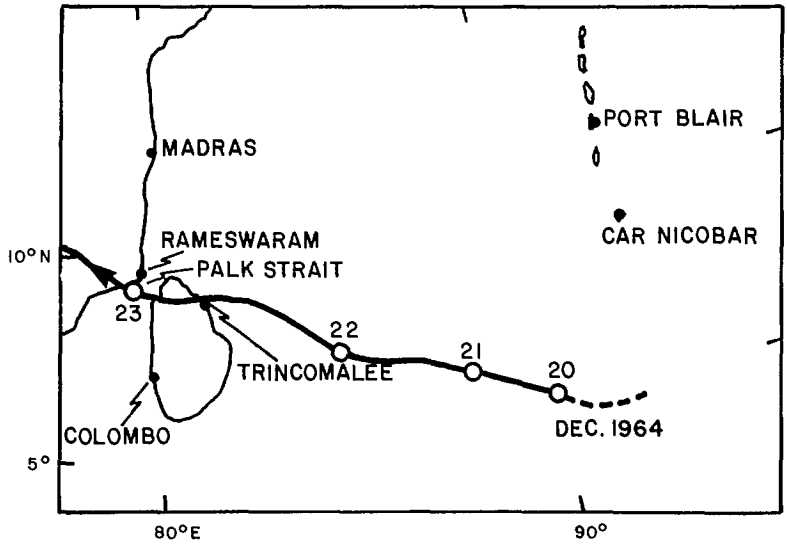

FIG. 6.55. Track of the severe storm of December 1964 over Sri Lanka. (Rao 1968)

equal to 48 knots (89 km·h^{-1}). Severe storms can form in any part of the Bay of Bengal, in any month, and can strike any section of the coast. However, they do not usually form during January–March and they do not strike the Tenasserim coast.

The annual frequency of severe cyclones that formed over the Bay of Bengal and those that struck the coast is shown in Fig. 6.51. The mean and variance of the number of severe storms forming over the Bay and those striking the coast are listed in Table 6.41. Further details are provided in Tables 6.42 and 6.43. The frequency of severe cyclonic storms that formed over the Bay of Bengal and those that struck the coast, for each 10-yr

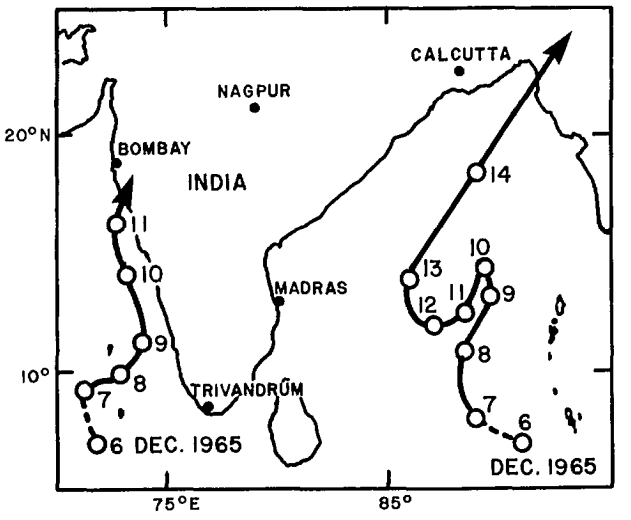

FIG. 6.56. Tracks of a storm pair in the Bay of Bengal (December 7–15, 1965) and Arabian Sea (December 7–12, 1965). (Swaminathan 1966)

TABLE 6.44. Details of storm pairs in the Bay of Bengal and the Arabian Sea during the period 1891–1960. Date indicated refers to the original date of the storm. In each pair, the top row is for the Bay of Bengal and the bottom row for the Arabian Sea. (Swaminathan 1969)

	Origin	
Date	Latitude (°N)	Longitude (°E)
Nov. 1, 1981	8.0	74.5
Nov. 1, 1891	9.5	98.5
Oct. 25, 1912	15.0	72.5
Oct. 28, 1912	8.5	89.0
Apr. 18, 1922	9.0	68.5
Apr. 19, 1922	9.5	93.0
May 31, 1927	11.5	71.0
May 31, 1927	17.5	91.5
Nov. 3, 1936	9.5	75.0
Nov. 4, 1936	9.0	88.0

period, is given in Fig. 6.52. The efficiency of intensification (i.e. a cyclonic storm maturing into a severe storm) for different areas in the Bay of Bengal, for the periods April–May, June–September, October–December, and the whole year, is shown in Fig. 6.53. The locations of severe storms just prior to their weakening into storms or depressions are illustrated in Fig. 6.54.

CASE STUDIES OF CYCLONIC STORMS IN THE BAY OF BENGAL DURING THE PERIOD 1964–78

The Rameswaram Cyclone of December 1964 was one of the most severe storms of the North Indian Ocean (Rao 1968). It was unique in several respects. First, the in-

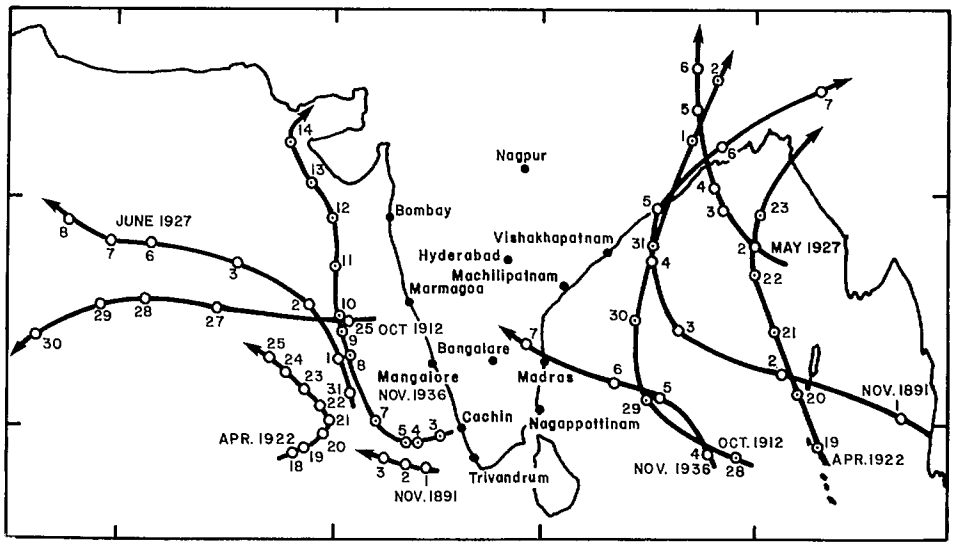

FIG. 6.57. Tracks of storm pairs in the Bay of Bengal and the Arabian Sea during 1891–1960. (Swaminathan 1966)

tensification occurred at a rather low latitude (6.5°N). Probably, it is the only severe storm that moved across the Palk Strait (see Fig. 6.55) during an 80-yr period ending with 1964. Another feature was that the size (but not the intensity) of the storm was small (the closed isobaric field extended only 3° in latitude from the storm center) and the strong winds were confined to a region 100–150 km from the center. During the severe storm stage, the inner ring of hurricane winds was only 40 km in width (Rao 1968). Estimated maximum wind speed was 175 knots (324 km·h^{-1}), probably the highest ever in India and Sri Lanka. The eye passed over Rameswaram (India) between 01:30 and 02:30 GMT on December 23, 1964. Another unusual feature was that the diameter of the eye was only 6–7 km (this is the smallest eye diameter reported for a severe storm in the Indian area). This compares well with the smallest eye diameter reported for Atlantic hurricanes, which was 4 mi (6.5 km) for a hurricane occurring on July 27, 1936, and which struck the coast of southern Florida (Dunn and Miller 1960).

The upper air structure showed that this storm extended to 400 mb in the vertical. Storm surges occurred over the islands of Mannar (Sri Lanka) and Rameswaram (India) (these will be discussed in section 7.4) with great loss of life and damage of property.

The 1965 season also presented some interesting features. The storm of December 1965 in the Bay of Bengal showed an unusual track (Fig. 6.56). Storm surges were generated on the coast of Bangladesh and heavy casualties followed. Not only was the track unusual, but the duration of the storm was 9 d compared with the usual 1–3 d. During a 70-yr period, about 77% of the storms in the Bay of Bengal lasted only 1–4 d, 17% lasted for 5–6 d, and only 7% (i.e. three storms) lasted for 7 d. The average duration for the Bay of Bengal storms is 3.5 d (compared with the average life span of global tropical cyclones, which is 6.5 d according to Riehl 1954). Another unusual feature was that this storm hit Bangladesh and Burma in December. Note that in the 70-yr period only 13 storms did this. A final unusual feature was the simultaneous presence of another storm in the Arabian Sea (see Fig. 6.56). Only five times before has a similar situation existed

(i.e. storms in the Bay of Bengal and the Arabian Sea at the same time). These cases are listed in Table 6.44 and their tracks are illustrated in Fig. 6.57.

The 1966 season produced the maximum number of storms in the postmonsoon season in almost a century (Raman et al. 1967). Between the last week of September and mid-December 1966 there were as many as seven cyclonic storms and one depression. In the month of November alone, there were four storms. Comparison was made between the general circulation for this high-activity season and that for the low-activity seasons (e.g. 1954 and 1959). The following deductions were made by Raman et al. (1967).

The thermodynamical conditions necessary for the development of cyclone storms, as discussed by Palmén (1955), are found in all the postmonsoon months. However, additional conditions must be satisfied. One of the reasons for the high cyclone activity in the 1966 season was the continued northward position of the equatorial trough. Even though the low latitude wind fields in 1959 and 1966 were similar, the absence of northward horizontal shear in the wind field of 1959 inhibited the development.

The required minimum energy for development is available at the air–sea interface during all postmonsoon months. However, for maturity into severe storms, the zones of maximum evaporation should also take place in preferred areas. During the 1966 season, the atmosphere gained the maximum heat over the southwest and west central parts of the Bay of Bengal. Generally, only in this region do all disturbances mature into cyclonic storms. On the other hand, in November 1954, maximum evaporation took place over the southwest part of the bay, south of 10°N. Finally, the origin, intensification, and movement of cyclonic storms coincide with the zones of convergence of the total energy that is available in the atmosphere.

The 1967 season produced at least two storm surges. A storm during May 16–18 with winds up to 87 knots (161 $km \cdot h^{-1}$) at Rangoon caused great destruction. The *Mariner's Weather Log* (1967, Vol. II, No. 4, p. 206) reported that the storm surge inundated whole villages and more than 100 000 persons were left homeless after the storm destroyed 800 villages. At least 100 people were reported dead or missing. On October 10, another cyclone made landfall near Calcutta and at least 200 000 people were left homeless (50 dead and 300 missing).

During the 1968 and 1969 seasons nothing significant happened. One of the most destructive ever storm surges struck the coast of Bangladesh on November 13, 1970, and killed at least 200 000 people. This storm surge has been singled out for a detailed study in section 7.4.

Towards the end of October 1971, a severe storm struck the Orissa coast of India near Paradeep. About 10 000 people and 50 000 cattle perished in the 2- to 6-m storm surges and 800 000 houses were destroyed (Das et al. 1972). Nothing unusual happened in the 1972 and 1973 seasons. The 1974 season had very low activity. Again, nothing unusual happened in the 1975 and 1976 seasons.

However, the 1977 season was an especially bad one. On November 19, a cyclone hit the coast of Andhrapradesh (India) and produced storm surges greater than 5 m in amplitude. The path of this storm is shown in Fig. 6.58a (track A). Between November 21 and 22, another Bay of Bengal originated storm struck the west coast of India (Fig. 6.58a, track B). This storm also caused great damage. On October 28, a storm originating in the Bay of Bengal struck the coast of Arabia between November 4 and 5 (Fig. 6.58b, track C).

Winchester (1979) provided the following details about the Andhra coast storm of November 19. The storm made a landfall near the mouth of the Krishna River with a speed of 12 $mi \cdot h^{-1}$ (19.5 $km \cdot h^{-1}$) with wind speeds of 75 $mi \cdot h^{-1}$ (121 $km \cdot h^{-1}$) and gusting

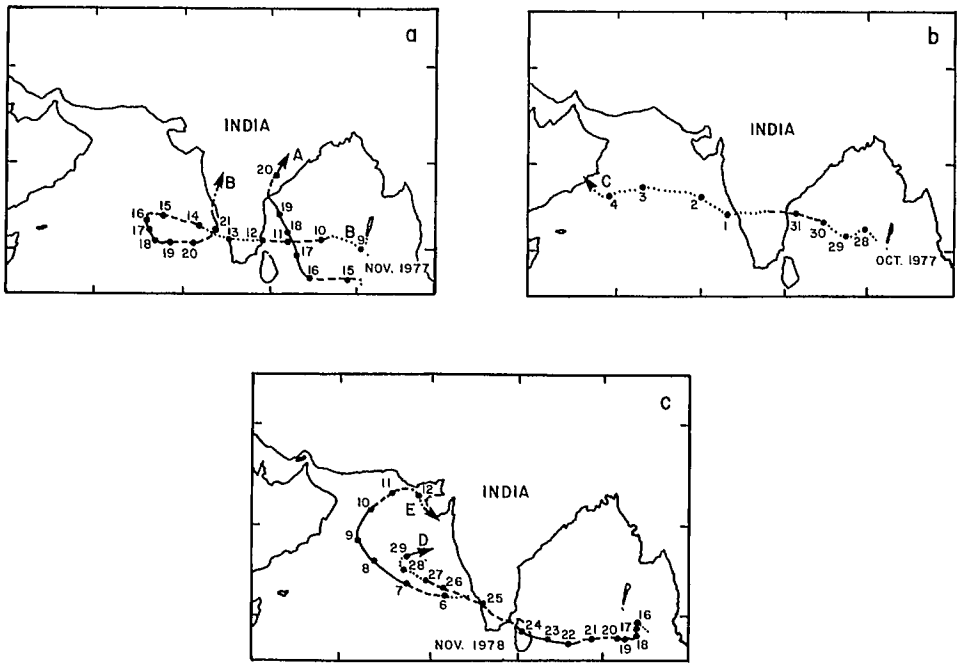

FIG. 6.58. (a) Track A: storm of November 1977 that caused great damage to the Andhra Pradesh Coast of India; track B: storm of November 1977 that did moderate damage to the west coast of India. (b) Track C: storm originating in the Bay of Bengal on October 28, 1977, that struck the coast of Arabia. (c) Track D: storm of November 1978 that did great damage on the east coast of Srilankas; track E: storm of November 1978 originating in the Arabian Sea and striking the Gujarat coast of India. (De Angelis 1978a, 1978b, 1978c, 1978d)

to 120 mi $\cdot$ h^{-1} (193 km $\cdot$ h^{-1}). The storm surge was 5 m in amplitude and penetrated at least 10 mi (16 km) inland with a speed of about 10 mi $\cdot$ h^{-1} (16 km $\cdot$ h^{-1}) over a coastal stretch of 35 mi (56 km). The high water due to the surge remained for about 10 h. The cyclone and the storm surge together totally damaged an area of about 7500 mi^2 (19 5000 km^2). At least 20 000 people died and 2 million people were left homeless (DeAngelis 1978a, 1978b, 1978c, 1978d).

There was no significant storm surge activity in India during 1978. However, Sri Lanka experienced a very devastating storm surge during this year (damage of $50 million). On November 21, 1978, a tropical storm generated near the Nicobar Islands matured to hurricane strength and on November 23 it struck the east coast of Sri Lanka (Fig. 6.58c, track D). The resulting storm surge together with the cyclone and the resulting landslides that occurred killed 373 people and destroyed 80 000 houses. Wind gusts up to 204 km $\cdot$ h^{-1} occurred. The storm surge inundated rice fields up to 8 km inland. The storm then moved to India over the Gulf of Mannar where it killed 10 people (DeAngelis 1979a, 1979b, 1979c).

One humorous sidelight of this cyclone was that 160 convicts escaped when the roof blew off the jail in Batticaba (Sri Lanka). The fact that not everybody is inconvenienced by a natural disaster such as a storm surge can be seen from the fact that, invariably, after the disaster looters descend upon the scene and help themselves. These are also good times for black marketeers and food hoarders, especially in the developing countries.

TABLE 6.45. Storms and depressions in the Bay of Bengal, 1945–54. A, total number; B, number that recurved. Storms and depressions that recurved on land or while in the Arabian Sea have been excluded. (Chakravorthy and Basu 1956)

Type	Jan.	Feb.	Mar.	Apr.	May	June	July	Aug.	Sept.	Oct.	Nov.	Dec.
A	5	1	1	5	6	11	18	19	19	18	12	11
B	2	0	0	1	1	0	0	0	0	5	1	4

TABLE 6.46. Pressure decrease (mb) before recurvature of cyclones over the Bay of Bengal. For NE quadrant the representative station is Akyab (except for entry two for which the station is Cox's Bazar). For the SE and SW quadrants the representative stations are Port Blair and Madras, respectively. For the NW quadrant, the station is Gopalpur (except for entry one for which the station is Visakhapatnam). Note that in the cases listed, the recurvature occurred at 08:30 (on the dates shown) Indian Standard Time. (Chakravorthy and Basu 1956)

	Point of recurvature		Pressure decrease (mb) 12–24 h before recurvature in various quadrants			
Date of recurvature	Latitude (°N)	Longitude (°E)	NE	SE	SW	NW
Oct. 23, 1947	16.5	89.5	4	8	2	2
Dec. 10, 1951	17.5	88.5	3	1	3	5
Nov. 9, 1952	17.5	88.5	2	2	2	6

When this author visited his native village in Andhrapradesh, India, in 1978 (1 yr after the disastrous storm surge of November 1977), tales of how village officers confiscated the emergency relief funds (provided by the federal government of India as well as by several international agencies) for their own use were mentioned to him. Although this author is not an expert on sociological aspects, his early background in developing countries convinced him that there is much truth to these tales. He was given to understand by the villagers that corruption is minimal to nonexistent with federal (central) government officers (due to the higher calibre of the federal civil service and also due to various built-in checks against corruption), and that corruption increases by an order of magnitude with the provincial (state) government officers, then by another order of magnitude with the district (county) level of government, and to absolute and total corruption at the municipal (city, town, village) level. This author would like to recommend to the international agencies who provide emergency relief funds to any developing country that only the federal government officials be involved in the handling of the relief operations.

PREDICTING THE TRACKS OF CYCLONIC STORMS IN THE BAY OF BENGAL

Chakravorthy and Basu (1956), making use of the data for the period 1945–54, studied the recurvature of storms in the Bay of Bengal. The total number of storms by month for this period, as well as those that recurved, is listed in Table 6.45 and the pressure changes associated with the recurving storms are given in Table 6.46. The spatial distribution of the occurrence of storms and depressions in the Bay of Bengal and that of the recurving storms during the period 1945–54 are given in Fig. 6.59 and some tracks of these recurving storms are illustrated in Fig. 6.60.

Other important features associated with recurving storms in the Bay of Bengal are

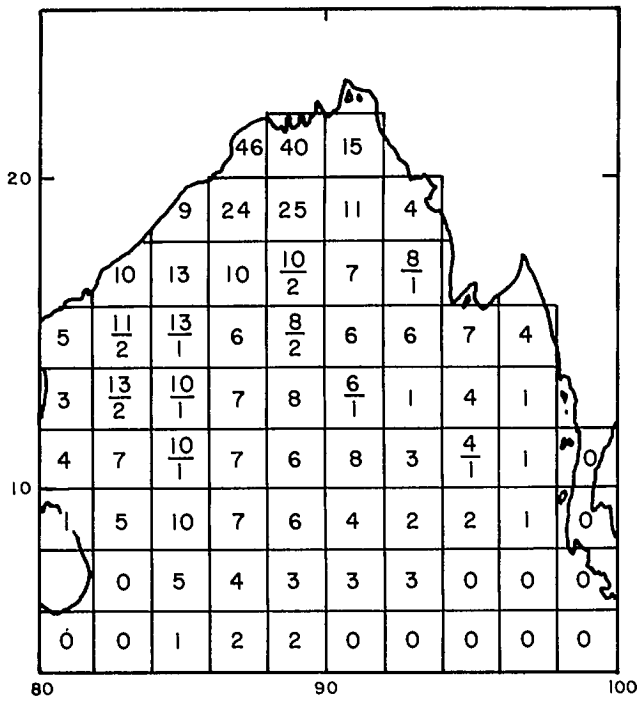

FIG. 6.59. Spatial distribution of the occurrence of storms and depressions in the Bay of Bengal and that of recurving storms during the years 1945–54. Lower numbers indicate recurving storms and upper numbers indicate total number of storms. Where there are no recurving storms, only the upper number is given. (Chakravorthy and Basu 1956)

the following. About 12–18 h before recurvature, the active front turns from west or northwest to north or northeast with an associated turning of the significant precipitation belt and cloud field from west or northwest to north or northeast. About 80% of the recurved storms showed this feature. Another feature was a retardation in the movement before recurvature (i.e. from an average of 18 km · h^{-1} before curvature to 8 km · h^{-1} about 12–18 h before recurvature). Usually, the recurvature occurs between 10 and 18°N. If there is any significant anticyclone in the upper air over Burma and surroundings, this anticyclone will probably shift eastward or southeastward before recurvature of the cyclone over the bay. Also, before recurvature the upper amospheric structure changes in such a manner that the average steering force will be directed progressively towards the east (i.e. westerlies at about 3000-m height will strengthen before recurvature).

According to Datta (1969) the movement of the storms in the Bay of Bengal for the month of May can be deduced by dividing the bay into three regions with different characteristics, as shown in Table 6.47. Bansal and Datta (1974) used a statistical approach for forecasting the movement of cyclonic storms in the Bay of Bengal. Regression equations were derived separately for the premonsoon season (April to early June) and the postmonsoon season (late September to early December). Using a total of 33 predictors, equations were developed for computing ahead the central pressure and the position of the storm.

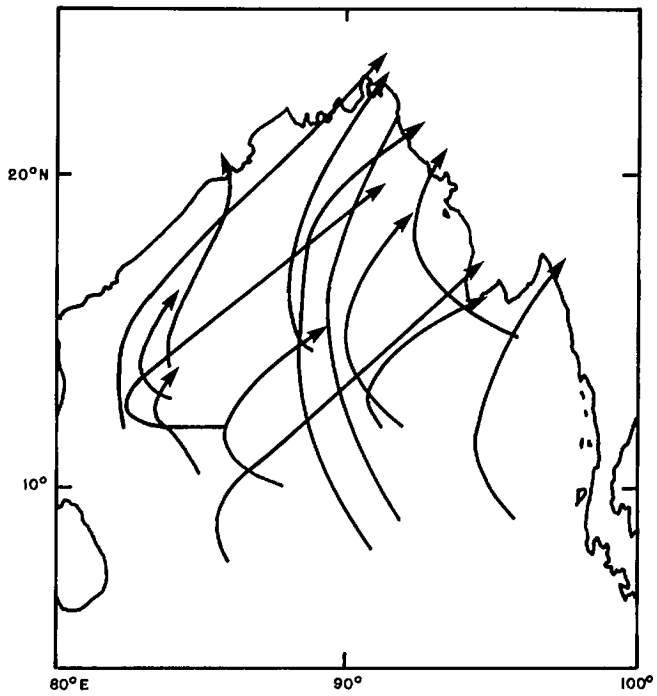

FIG. 6.60. Tracks of some of the recurring storms in the Bay of Bengal during the period 1945–54. (Chakravorthy and Basu 1956)

TABLE 6.47. Movement of cyclonic storms in the Bay of Bengal in the month of May.

Region	Storm movement
East of 95°E	No westerly component of motion
South of 12°N between 89 and 84°E	No westerly component of motion
West of 84°E	Mostly towards the west
In the area bordered by 13 and 17°N and 95 and 91°E	Mostly towards the west
South of 13°N between 95 and 89°E	Mostly towards the west
Remaining areas of the Bay	Predominantly northerly

Choudhury (1978) made use of the theory of images (in hydrodynamics) to calculate the tracks of cyclonic storms in the Bay of Bengal. He assumed the cyclone to be a cylindrical vortex and considered the motion of this vortex with reference to two land-masses perpendicular to each other (see Fig. 6.61). He wrote a complex potential:

$$W = \phi + i\psi \tag{6.58}$$

where ϕ and ψ are the velocity potential and stream function, respectively. Note that both ϕ and ψ satisfy the Laplace equation:

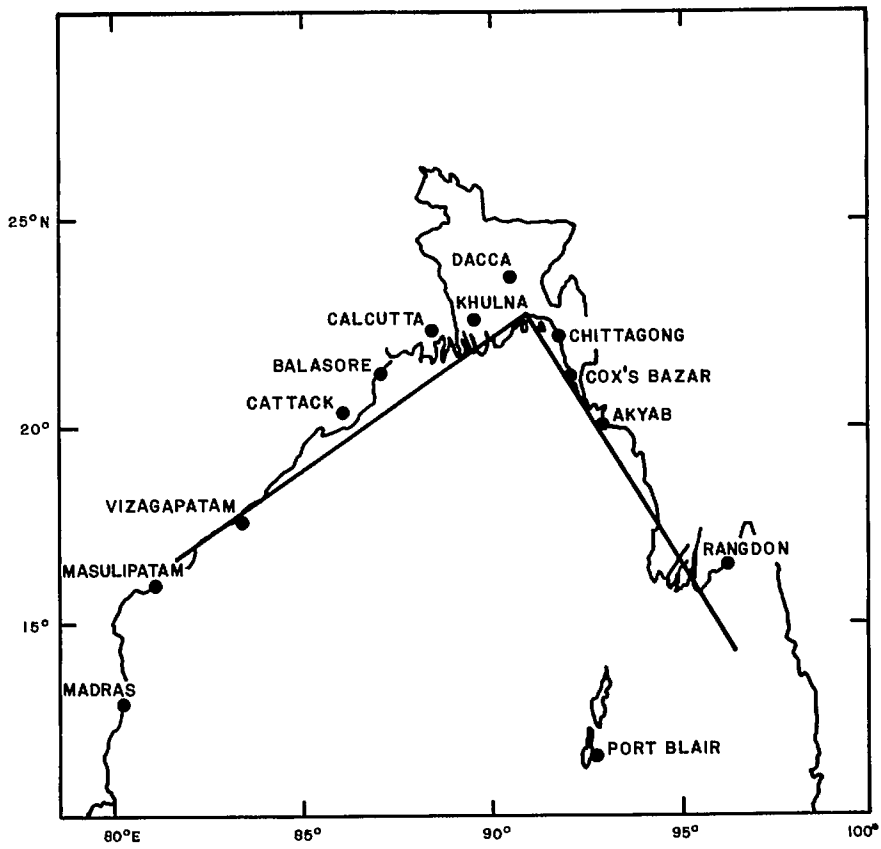

FIG. 6.61. Theoretical model in which it was assumed that the Bay of Bengal is bounded by almost two perpendicular boundaries intersecting at the Meghna Estuary of Bangladesh. (Choudhury 1978)

$$\begin{aligned} \nabla^2\phi &= 0 \\ \nabla^2\psi &= 0 \end{aligned} \tag{6.59}$$

In polar coordinates one can write the radial and azimuthal velocity components as follows:

$$\begin{aligned} q_r &= -\frac{d\phi}{dr} = -\frac{1}{r}\frac{d\psi}{d\theta} \\ q_\theta &= -\frac{1}{r}\frac{d\phi}{d\theta} = \frac{d\psi}{dr} \end{aligned} \tag{6.60}$$

where r and θ are the radial and azimuthal coordinates, respectively. Let a be the radius of the cyclone vortex. Inside the vortex, the vorticity is assumed to be constant (equal to ω) and outside the vortex, the vorticity is assumed to be zero. Then, the velocity distributions inside ($r < a$) and outside ($r > a$) the vortex are given by

$$V = \frac{1}{2}\omega r \text{ for } r < a$$

(6.61)

$$V = \frac{1}{2}\frac{\omega a^2}{r} \text{ for } r > a$$

The complex potential for a vortex of strength μ ($\mu = {}^1/_2\,\omega a^2$) is

(6.62) $$W = i\mu \log (z - z_0)$$

where z_0 is the position of the vortex. The existence of the orthogonal plane boundaries will create a system of three images. The complex potential for this system of a vortex and three images is

(6.63) $$W' = i\mu \log (z^2 - z_0^2) - i\mu \log (z^2 - \bar{z}_0^2)$$

where $\bar{z}_0$ is the complex conjugate of z_0. Since the vortex has no effect on itself, excluding this, the complex potential can be written as

(6.64) $$W = i\mu \log (z^2 - z_0^2) - i\mu \log (z^2 - \bar{z}_0^2)) - i\mu \log (z - z_0)$$

$$= i\mu \log (z + z_0) - i\mu \log (z^2 - \bar{z}_0^2)$$

The velocity components of the real vortex are

(6.65) $$q_r = \frac{\mu}{R}\frac{\cos 2\theta}{\sin 2\theta}$$

(6.66) $$q'_\theta = -\frac{\mu}{2r}$$

An introduction of an azimuthal wind μ/r will lead to

(6.67) $$q_\theta = -\frac{\mu}{2r} + \frac{\mu}{r} = \frac{\mu}{2r}$$

Division of eq. 6.65 by eq. 6.67 and integration leads to

(6.68) $$r = K \sin 2\theta$$

where K is the constant of integration. Note that eq. 6.68 is the equation for a rose petal with four loops (Fig. 6.62). This means, in the idealized model, a rose petal is the trajectory of a tropical cyclone when the land boundaries are two orthogonal planes and the origin is the point of landfall.

Choudhury (1978) used this simple idealized model to compute the trajectories of certain cyclones and storms in the Bay of Bengal. In general, the differences between predicted and observed tracks are less than 20%. The actual calculations are performed as follows. From the initial motion of the cyclone, after at least two observations, the radius of curvature ρ of the track and the velocity V of motion can be written as

(6.69) $$\rho = \frac{K(1 + 3\cos^2 2\theta)^{3/2}}{\sin^2 2\theta + 8}$$

(6.70) $$V = \frac{\mu(1 + 3\cos^2 2\theta)^{1/2}}{2K \sin^2 2\theta}$$

The parameter μ is determined from satellite pictures. Then, θ can be determined from

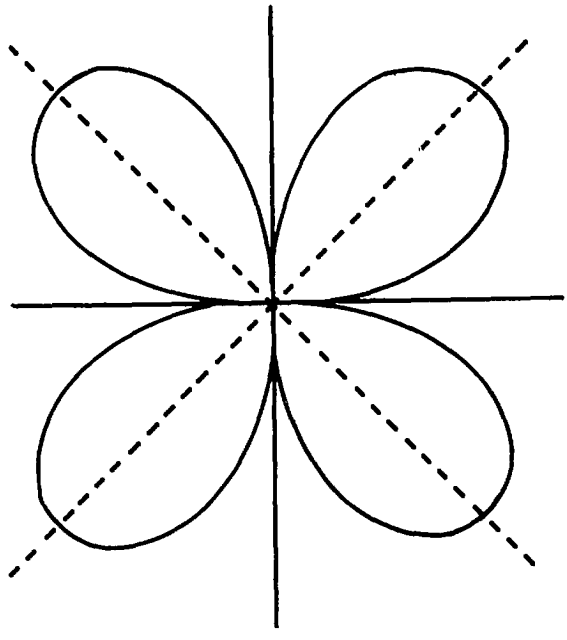

FIG. 6.62. A rose petal with four loops (Choudhury 1978)

eq. 6.69 and 6.70. Since $\tan \phi = \frac{1}{2} \tan 2\theta$ (where ϕ is the angle the radial vector makes with the tangent) the point of landfall (origin) can be determined. From eq. 6.69 and 6.70, K can also be determined and hence the curve for the rose petal (eq. 6.68) can be traced. As more and more observations are available, the trajectory can be modified. According to Choudhury (1978), after 1 d of observations, a prediction of the trajectory (and landfall) can be made 2–3 d ahead. The travel time of the storm is given by

$$T = \frac{K^2}{\mu}\left(\theta - \frac{\sin 4\theta}{4}\right) \tag{6.71}$$

Hence, one can calculate the time of landfall also.

The observed track of the November 1970 cyclone and the predicted track positions are shown in Fig. 6.63. Also shown are the positions of landfall based on two, three, and four observations. The errors in the time of landfall for these positions are +9, +23, and 0 h, respectively.

Choudhury (1978) also explained why a cyclone accelerates as it approaches land, and he also suggested that this theory can be generalized to angles other than 90° between the two coasts. For an angle π/n, where n is an integer, the formula for the cyclone track is

$$r = K \sin (n\theta) \tag{6.72}$$

Note that for $n = 1$ (straight coast), the trajectory is a circle. This means, for a straight coast, that the probability of landfall at a given location is less than the case for two coasts meeting at an angle. According to Choudhury (1978), this explains why several cyclones make a landfall on the coast of Bangladesh, even though the length of the coast is only a few hundred kilometres. Although this model seems to give reasonably good results for

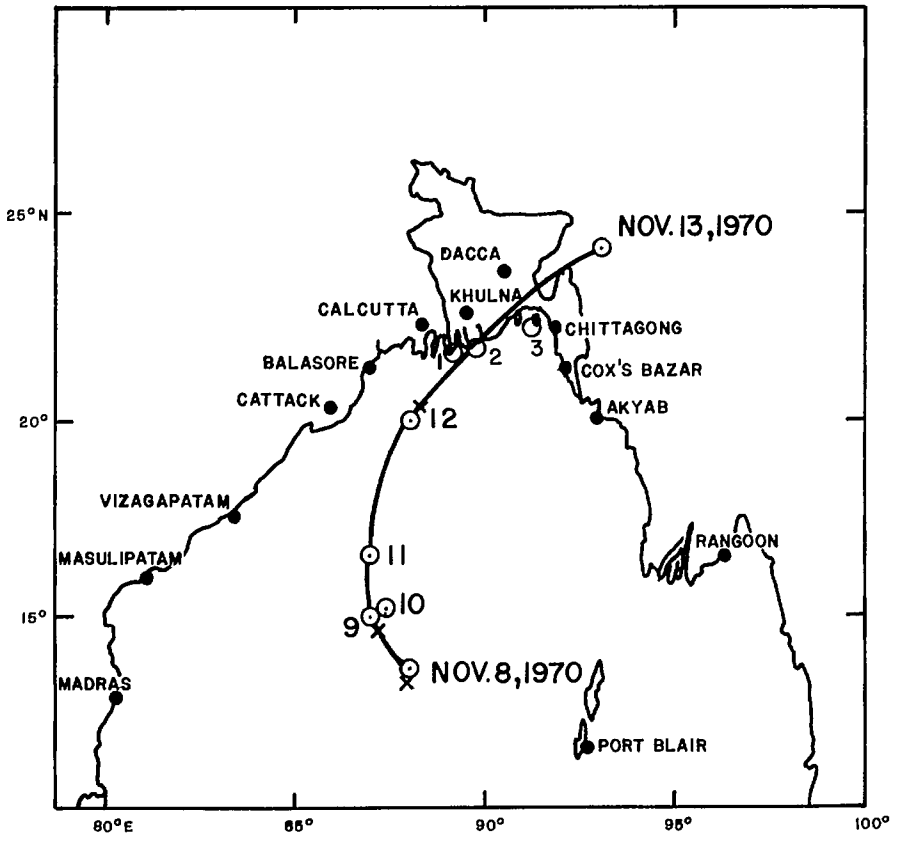

FIG. 6.63. Track of the November 1970 cyclone. The circles represent the observed points and the crosses represent the fitted points for the rose petal. Predicted landfall points 1, 2, and 3 represent the predictions made respectively on November 9, 10, and 11. (Choudhury 1978)

the track, the prediction of the landfall positions is not accurate enough for storm surge purposes.

CYCLONIC STORMS IN THE ARABIAN SEA

Compared with the Bay of Bengal, the storms of the Arabian Sea are less frequent, generally less intense, and the accompanying storm surges are usually less destructive. The statistics by month for the period 1891–1960 are given in Table 6.48.

Pedgley (1969) mentioned that cyclones develop preferentially over the southeastern quadrant of the Arabian Sea and move in a west to northwest direction towards Arabia. However, sometimes they recurve to the north or northeast towards northwestern India and Pakistan (Fig. 6.64). About one storm in three passes over the western part of the Arabian Sea and strikes the coast of the Arabian peninsula.

The frequency of cyclonic storms for the period 1891–1967 is given in Table 6.49. About one cyclonic storm in 3 yr strikes the coast and about half of these that strike have cyclone strength. Usually the cyclones make landfall near Salalah and they show a

TABLE 6.48. Data on the cyclonic storms of the Arabian Sea during the period 1891–1960. (Rao 1968)

Type of storm	Jan.	Feb.	Mar.	Apr.	May	June	July	Aug.	Sept.	Oct.	Nov.	Dec.	Year
Total number of cyclonic disturbances	6	0	1	7	20	30	11	2	10	36	36	8	165
Total number that intensified into storms	2	0	0	5	13	13	3	1	4	17	21	3	82
Total number that intensified into severe storms	0	—	—	4	11	8	0	0	1	7	16	1	48

TABLE 6.49. Number of occurrences of cyclones (Beaufort ≥12) and cyclonic storms (BF ≥8) over the whole Arabian Sea during the period 1890–1950 and number of occurrences along the Arabian coast during the period 1891–1967. For the Beaufort wind scale, see Table 6.67. (Pedgley 1969)

	Jan.	Feb.	Mar.	Apr.	May	June	July	Aug.	Sept.	Oct.	Nov.	Dec.	Year
Cyclones and cyclonic storms over the whole Arabian Sea	1	0	0	4	10	11	2	1	4	15	12	3	63
Cyclones and cyclonic storms along the coast of Arabia	0	0	0	0	8	5	1	0	0	7	6	1	28
Cyclones along the coast of Arabia	0	0	0	0	6	2	0	0	0	2	2	1	13

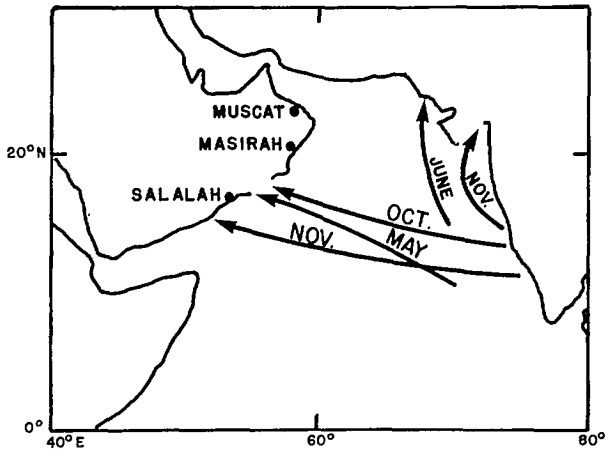

FIG. 6.64. Common tracks of Arabian Sea cyclones. (Pedgley 1969)

TABLE 6.50. Cyclones near the coast of the Arabian peninsula during 1943–1967. (Pedgley 1969)

Date of approach or crossing the coast	Nature of the cyclone
June 6, 1946	Decaying before approaching Masirah from east–southeast
October 1, 1948	Decaying before approaching coast between Masirah and Ra's al Hadd from east
October 25, 1948	Cyclonic storm crossed Salalah, approaching from southeast
May 24, 1959	Severe cyclone crossed Salalah, approaching from east–southeast
October 18, 1959	Severe cyclone crossed near Ras Madraka, approaching from east
May 18, 1960	Severe cyclone crossed coast at Ras Fartak
November 23, 1960	Cyclonic storm approached entrance to Gulf of Aden from east
May 30, 1962	Decaying before crossing coast at Ras Madraka
May 26, 1963	Severe cyclone, passed just south of Salalah, approaching from east–southeast and then turning towards west–southwest
November 13, 1966	Severe cyclone with a track similar to that of May 1963

tendency to turn to the left at a distance of a few hundred kilometres from the coast. The 10 cyclones that hit the Arabian coast during 1943–67 are listed in Table 6.50.

The following pressure distribution

$$p = 1008 - 1.64(v_r r) \tag{6.73}$$

appears to fit the central pressure of the Arabian Sea cyclones. Here, p is the central pressure (millibars) and v_r is the radial wind speed in knots at a distance from the center of r degrees latitude (Krueger 1959). The maximum wind speed v_m can be estimated from Myers (1957):

$$v_m = K\sqrt{p' - p} \tag{6.74}$$

where p' is the surrounding pressure and K is a constant (equal to 11). For example, taking $p = 960$ mb and $p' = 1010$ mb gives $v_m = 80$ knots (148 km·h^{-1}).

Although most of the Arabian Sea cyclones originate locally, some (6 of the 28

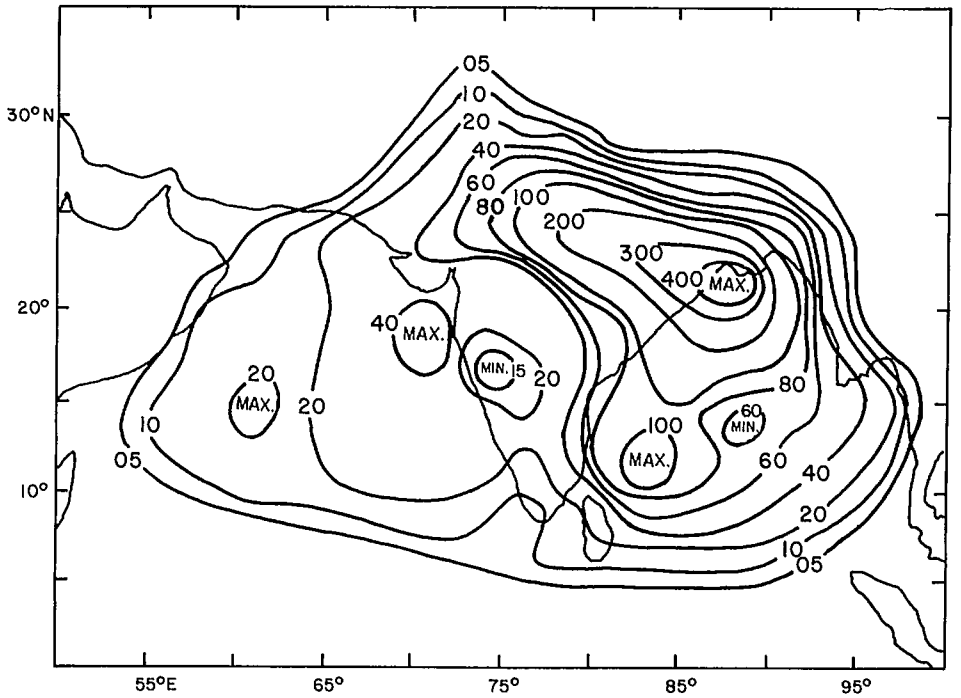

FIG. 6.65. Contours of a number of tropical cylones (including depressions) passing through 2.5° latitude–longitude squares for the period 1877–1974. (Neumann and Mandal 1978)

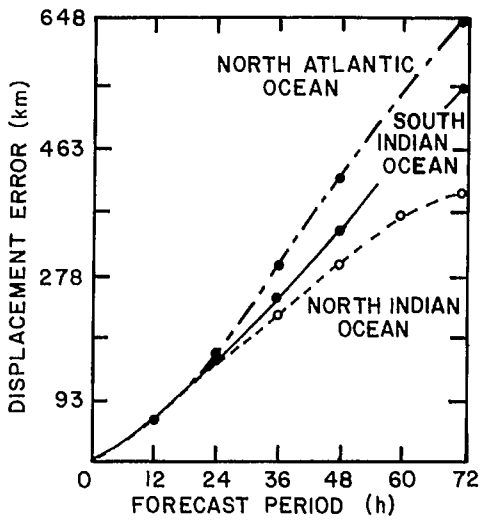

FIG. 6.66. Forecast errors in the tracks of tropical cyclones for three different ocean basins. (Neumann and Mandal 1978)

mentioned in Table 6.49) originated in the Bay of Bengal. Usually, cyclones with this distant origin occur towards the end of the cyclone season (i.e. towards November). Occasionally, the Arabian Sea cyclones cross the Gulf of Aden and even rarely the Gulf of Oman.

One difference between the cyclones of the Arabian Sea and the Bay of Bengal is that, whereas in the Bay of Bengal more cyclones occur in the postmonsoon season (September to December) than in the premonsoon season (April to May), in the Arabian Sea they are about equally distributed between the two cyclone seasons (i.e. May to June and October to November). Most of these originate over the southeastern Arabian Sea and move towards west–northwest. However, a few originate in the Bay of Bengal and cross southern India before emerging over the Arabian Sea.

Neumann and Mandal (1978) used statistical techniques to predict the storm movement over the Arabian Sea and the Bay of Bengal. The number of tropical cyclones (including depressions) passing through 2.5° latitude–longitude squares for the period 1877–1974 is given in Fig. 6.65. It can be seen that maximum values of up to 400 cyclones and depressions occurred near the coasts of West Bengal (India) and Bangladesh in the Bay of Bengal. By comparison, in the Arabian Sea, the maximum number is only 40 and it occurs near the Maharashtra–Gujarat coast of India.

The errors of prediction of the tracks of tropical cyclones for the North Indian Ocean, South Indian Ocean, and North Atlantic Ocean using similar models are compared in Fig. 6.66. It is interesting to note that the least errors occurred in the North Indian Ocean and maximal errors occurred in the North Atlantic Ocean.

6.6 Wind Stress and Atmospheric Pressure Gradients

Earlier it was mentioned that the main forcing functions for the generation of storm surges are the wind stress on the water surface and the atmospheric pressure gradient forces, whereas bottom stress is the chief retarding force. The exchange of momentum and energy at the surface of the ocean, which is also the lower boundary of the atmospheric boundary layer, will be considered. Since the ocean surface is not rigid, kinetic energy can be transferred to the ocean by tangential stresses (from the atmosphere), which produce accelerations parallel to the surface, and by normal pressure forces that could create time-dependent motions of the surface (Krauss 1967). Krauss wrote the following equation, which describes the approximate kinetic energy balance for the atmosphere and ocean (either whole or for an enclosed part) averaged over a suitably long time interval:

$$\int \rho g w dV - \int \theta dV = - \int U \tau dS - \int \rho v_n dS \tag{6.75}$$

where ρ is the density of air, g is gravity, w is the vertical velocity, V is the volume, θ is the dissipation per unit volume, U is the average wind velocity, τ is the stress, S is an element of unit area of the sea surface, and v_n is the velocity of the boundary normal to itself.

In eq. 6.75, the two terms on the left side give the volume integrals of the potential energy conversion and dissipation. The first term on the right side gives the work done by the stress τ along the surface S (note that this is zero if $U = 0$ at the surface) and the second term on the right side is the work associated with the vector deformation v_n of the boundary. The question of interest is how energy can be transferred from the atmosphere to the ocean so that transient motions such as storm surges can be generated. The reason for asking this question is that it can be shown that viscous friction at the air–water interface is not large enough to account for the energy of wind-driven ocean currents and

for exciting inertial oscillations (Krauss 1967). Thus, momentum and energy must be transferred from the wind to the ocean by processes other than viscous shear at the interface. It will be shown below that short-period wind waves predominantly provide such a mechanism.

Air–Sea Momentum Exchange

Taylor (1916) appears to have been the first to suggest the following relation:

$$\tau = \rho\gamma^2 W^2 \tag{6.76}$$

where ρ is the density of air, τ is the tangential stress at the water surface, W is the wind speed at 15 m above the sea surface, and γ is a dimensionless parameter (referred to as a drag coefficient). Close to a rough plane wall, Prandtl (1932) wrote

$$\gamma^2 = \frac{0.0302}{\left(\log \dfrac{1500 + z_0}{z_0}\right)^2} \tag{6.77}$$

where z_0 (centiemtres) is referred to as the roughness length. Using empirical data, Wüst (1920) and Rossby and Montgomery (1935) showed that eq. 6.77 holds near a water surface. According to Rossby (1936), γ^2 is independent of the wind speed for moderate and strong winds and is equal to 2.6×10^{-3}.

Ekman (1905, 1923) and Palmén and Lauria (1938) also calculated γ^2 from observed water level oscillations due to atmospheric storms and they deduced a value similar to Rossby's. However, Neumann (1948) wrote a different form for the stress as follows:

$$\tau = 0.09\rho W^{3/2} \tag{6.78}$$

where the stress is in dynes per square centimetre. In this relation, γ^2 (which is implicit) is not constant and varies with wind speed proportional to $W^{-1/2}$. Sverdrup and Munk (1947) mentioned that one must also include the effect of waves. Krauss (1967) gave an elegant discussion of the basic formulas involving drag coefficients, roughness lengths, etc.

Miyazaki (1951a) formulated the wind stress problem by assuming an eddy-generating layer in the air–sea boundary. In his theory, two parameters appear that depend on the tangential stress and the wind waves. The functional forms of these parameters are obtained for stationary motions with large Reynolds numbers. According to Miyazaki (1951a) his formulation is valid for wind speeds greater than 6–7 $\mathrm{m \cdot s^{-1}}$.

Miyazaki (1951a) wrote

$$u = \frac{u^*}{\chi}\left(\log z - \log \frac{h}{2} + \frac{\beta h \tau^{1/2}}{\lambda^{4/3}}\right) \tag{6.79}$$

where u is the wind velocity, z is the height measured from the equilibrium position of the sea surface, u^* is a functional velocity (equal to $\sqrt{\tau/\rho_w}$ where τ is the tangential stress and ρ_w is the density of water), χ is the universal turbulence constant (equal to 0.4), h is the wave height, λ is the wavelength, and β is a constant.

Miyazaki (1951b) extended his earlier study and gave the following modified formula:

$$u = \frac{u^*}{\chi}\left[\log z - 3.218 - \log \frac{\tau}{\rho_w} + 1.382 \left(\frac{\tau}{\rho_w}\right)^{1.6}\right] \tag{6.80}$$

He suggested that this formula agrees with Rossby's formula in the wind speed range of $5-25\ m \cdot s^{-1}$. Below this speed, the water surface is hydrodynamically smooth and both formulas break down. Above $25\ m \cdot s^{-1}$ Rossby's formula gives stress values smaller than Miyazaki's. There is another difference also: in Miyazaki's formula, γ^2 is not constant; it has a maximum value of 2.68×10^{-3} at a wind speed of about $15\ m \cdot s^{-1}$.

Stewart (1961, 1974) considered the question of transfer of momentum from the atmosphere to the water and stated that a very large fraction of the momentum transfer is in the form of wave generation. Baines (1974) showed that when the wind wave spectrum in shallow water is approximately independent of wind speed due to the combined effects of white capping and bottom friction, then the wave-induced drag coefficient has a maximum value when the wind speed is twice the maximum wave speed, and as the wind speed increases further, the drag coefficient slowly decreases.

Simons (1978) made the important point that numerical models for hindcasting storm surges usually require drag coefficients (for wind stress) as high as 3×10^{-3} whereas observations appear to indicate a value about half of this. Donelan (1979) resolved this problem by suggesting that the form stress (due to wave drag) is large if the sea state is not in equilibrium with the wind (i.e. during the initial stages of a storm when the waves are developing). However, once the wave field has adjusted to the wind, the drag coefficient decreases.

The stress produced by wind blowing over a water body consists partly of skin friction and partly of form drag. Taylor and Gent (1978) showed the dependence of the drag coefficient on certain wave parameters such as steepness and wave age. Donelan (1979) showed through observational data that the drag coefficient is mostly dependent on inverse wave age and wave height and can be approximated well by a simple model involving the form drag τ_f and the skin drag τ_s.

Of the form drag τ_f, a portion τ_w adds or subtracts momentum directly from the gravity wave spectrum. The remaining part τ_c generates changes in the currents. Of the momentum flux τ_w, a portion τ_η produces a net growth or decay of the wave momentum. The remaining part τ_d is lost from the wave field by viscous dissipation and white capping. Hence, the total drag τ between air and water is

$$\tau = \tau_s + \tau_\eta + \tau_d + \tau_c \tag{6.81}$$

where

$$\tau_w \equiv \tau_\eta + \tau_d$$

and

$$\tau_f \equiv \tau_w + \tau_c$$

The problem here is to determine the wave field and wind stress, given the wind at a 10-m height. For predicting the wave field, τ_η must be known and for the determination of the wind stress, $\tau - \tau_\eta$ must be known. Donelan (1979) stated "to the hydrodynamic modeller, to whom wind waves are a sub-grid scale process, the appropriate wind stress is not the total τ, but the total less that which is carried away by the waves τ_η. If, as we believe, the waves significantly affect the drag coefficient and the local surface stress is depleted by the growth and advection of the wave field, then the prediction of the surface stress depends rather critically on a knowledge of the wave field."

Donelan's (1979) model differs somewhat from those of Hasselman et al. (1976), Gelci and Devillaz (1970), Barnett (1968), and Pierson et al. (1966). In contrast with an energy transport equation used by these authors, Donelan (1979) used a local momentum

balance equation. Using this model, he computed wind stress over Lake Ontario for storm episodes, and the wind stress values agree closely with what numerical modelers would need for hindcasting storm surges.

Wind Stress and Drag Coefficients

Early measurements of wind stress usually focused on the climatological values, i.e. average values for season (or year) for large areas. Priestley (1951) gave wind stress values for each 5° latitude zone from 55°N to 55°S for each season for the different oceans. Although studies of this type are useful for other problems, these averaged wind stress values are of little relevance for storm surge work.

Garratt (1977) reviewed the drag coefficients over the oceans from all available literature. Based on this paper, the literature will be briefly reviewed and certain terms will be defined before summarizing the drag coefficients. Earlier, reference was made to Taylor's (1916) velocity square law involving the dimensionless coefficient of skin friction. Based on measurements over land, Taylor (1915) gave values of 2×10^{-3} to 3×10^{-3} for this coefficient. Sutcliffe (1936) gave values of 4×10^{-3} to 7×10^{-3} for land and 0.4×10^{-3} for water.

Deacon (1957) established that, over land, the square law generally holds, except for low wind speeds. It is not clear whether it applies to a water surface. Deardorff (1972) represented the drag coefficient C_D through the aerodynamic roughess length z_0. In the atmospheric constant flux layer above a horizontally homogeneous surface, the local surface stress can be written in terms of the surface wind $V(z)$ at height z as

$$\tau_0 = \rho C_D V^2(z) \tag{6.82}$$

where ρ is the density of air and C_D is related to the aerodynamic roughness length z_0 and the stability parameter ζ:

$$\zeta = \frac{z}{L}$$

where L is the Monin-Obukhov length. Thus

$$C_D = \frac{C_{D_N}}{\left[1 - \frac{1}{K}(C_{D_N})^{1/2}\psi(\zeta)\right]^2} \tag{6.83}$$

where

$$C_{D_N} = \frac{K^2}{\left(\ln \frac{z}{z_0}\right)^2} \tag{6.84}$$

where K is the von Karman constant and

$$\psi(\zeta) = \int_{\zeta_0}^{\zeta} \frac{1 - \Phi(\zeta')}{\zeta'} d\zeta'$$

A knowledge of the dimensionless wind gradient $\Phi(\zeta)$ allows one to determine C_D/C_{D_N} as a function of ζ (or a bulk Richardson number) and z/z_0.

In numerical models, usually the stress is related to a large-scale wind $\hat{V}$ such as the surface geostrophic wind V_G. The stress is expressed as

(6.85) $$\tau_0 = \rho C_G \hat{V}^2$$

where C_G is the geostrophic drag coefficient when $\hat{V} = V_G$. Generally, C_G will depend on the surface Rossby number

$$R_0 = \frac{V_G}{fz_0} \text{ or } \frac{l}{z_0}$$

where l is a height scale. It also depends on the boundary layer stability:

$$\mu = -\frac{K\mu_*}{fL}$$

and the baroclinicity

$$S = \frac{\partial V_G}{\partial z}$$

Thus

(6.86) $$\ln R_0 = A(\mu, S) - \ln C_G^{1/2} + KC_G^{-1/2} \cos \alpha_0$$

where

$$\alpha_0 = \sin^{-1}\left[\frac{B(\mu, S)C_G^{1/2}}{K}\right]$$

is the angle between the surface wind and the wind vector $\hat{V}$; the similarity functions A and B must be determined from observations.

Charnock (1955) showed that

(6.87) $$\frac{z_0 g}{u_*^2} = \text{constant} = \alpha$$

This formula was later modified by Charnock and Ellison (1967) to include effects of viscosity, surface tension, and water density. Kitaigorodskii (1968) and Kitaigorodskii and Zaslavskii (1974) included the effects of fetch and wind duration and wrote

(6.88) $$\frac{z_0 g}{u_*^2} = f\left(\frac{C_0}{u_*}\right)$$

where C_0 is the phase velocity of the dominant wave and C_0/u_* is the wave age.

Observations of surface stress over water bodies by various authors (see Garratt 1977 for details) and the deduced values of C_{D_N} were summarized by Garratt (1977). Based on these he suggested that

(6.89) $$C_{D_N} = 0.51 \times V^{0.46} \times 10^{-3}$$

or in another form

(6.90) $$C_{D_N} = (0.75 + 0.067V) \times 10^{-3}$$

where V is the wind speed in metres per second at a 10-m height.

It is well known that wind stress depends on the stability of the atmospheric surface layer. In earlier observations of drag coefficients, little attention was paid to atmospheric stability conditions. Hence, for comparison with earlier data, several later investigators also made measurements under neutral stability conditions. Wu (1980) summarized the

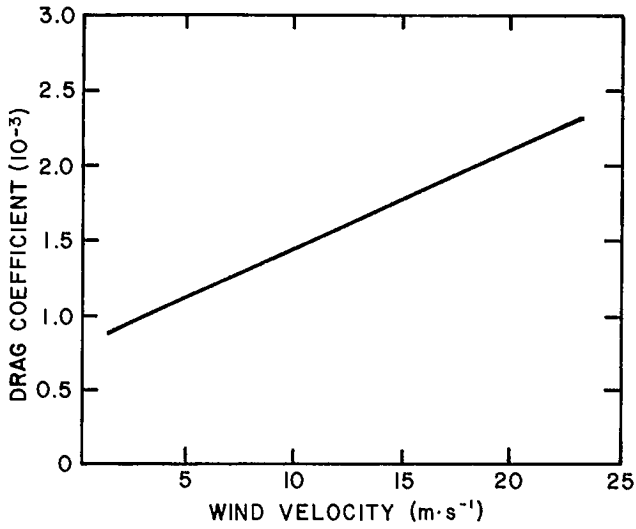

FIG. 6.67. Variation of drag coefficient with wind velocity. (Wu 1980)

wind stress coefficients over the sea surface for neutral conditions. He presented a scaling law for wind stress coefficients; the coefficient increases with wind velocity (see Fig. 6.67) and decreases with fetch.

Smith (1980) considered the question of wind stress over the ocean for strong winds (i.e. gale force). He also showed that the drag coefficient increases gradually with increasing wind speed.

The approach by Donelan (1979) of dividing the total drag into a form drag and a skin drag was discussed earlier. Plate and Wengefeld (1979) used a similar approach but wrote the equations somewhat differently. The work done by the air on the water is divided into two parts: one part produces the energy change of the mean water motion and the other part maintains the wave pattern. The energy balance equation for the first part can be written as

$$\frac{dE_W}{dt} = \frac{dE_{k_W}}{dt} + \frac{dE_{p_W}}{dt} - D_W + \frac{dW_W}{dt} = 0 \tag{6.91}$$

where the subscript W refers to water, E_k, E_p, and E are the means (in time) of the kinetic, potential, and total energies, respectively, W_W is the work done on the water body, and D_W is the mean energy dissipation inside the water column.

The second part that maintains the waves against energy loss due to radiation and dissipation can be written as

$$\frac{dE_0}{dt} = \frac{dE_{k_0}}{dt} + \frac{dE_{p_0}}{dt} - D_0 + \frac{dW_0}{dt} = 0 \tag{6.92}$$

where subscript 0 stands for the wave field and W_0 is the work done to maintain the wave field.

The total work done by the air on the water surface is $W_W + W_0$. However, it is not clear how this partitioning can be specified. Under the assumption that the mean flow does not vary in x, the flux of vertical momentum at a height δ is constant and is equal to τ_∞

TABLE 6.51. Values of the coefficients a, b, c, and d in eq. 6.95 as a function of fetch and water depth. (Hamblin 1979)

		Fetch (km)		
Depth (m)	Coeff.	1	10	100
5	a	0.100	0.850	0.830
	b	0.150	0.190	0.190
	c	−0.068	−0.091	−0.110
	d	−0.390	−0.280	−0.260
20	a	1.100	0.670	0.440
	b	0.150	0.180	0.200
	c	−0.068	−0.094	−0.140
	d	−0.380	−0.170	0.220
100	a	1.100	0.630	0.320
	b	0.150	0.170	0.170
	c	−0.067	−0.092	−0.130
	d	−0.370	−0.140	0.340

(for example). Closer to the surface, a part of the momentum flux is transferred downward through shear stresses, which gives rise to a surface shear stress τ_D. The remaining part τ_∞ is converted (through the changes in the curvature of the streamlines) into a pressure pattern and this creates a form drag given by an average stress τ_F through

$$\tau_F = \frac{1}{\lambda} \int_{\eta_{max}}^{\eta_{max}} (p_u - p_d) dy \tag{6.93}$$

The work done by the air on the water can be written as

$$\frac{dW}{dt} = \tau_F C + \tau_0 u_S \tag{6.94}$$

This can be solved only if τ_0 and τ_F are known. However, only τ_∞ is known, which is given by

$$\tau_\infty = \tau_F + \tau_0$$

P. F. Hamblin (1979, Canada Center for Inland Waters, Burlington, Ont., unpublished data) considered the problem of wind stress on small enclosed lakes (Lake St. Clair in North America). He gave a convenient formula for practical computations of the drag coefficient:

$$C_D \times 10^3 = a + bU + C\Delta\theta + d\frac{\Delta\theta}{U^2} \tag{6.95}$$

where C_D is the drag coefficient (referred to a 10-m height), U is the wind speed, and $\Delta\theta$ is the air−water temperature difference. He tabulated the values of the coefficients a, b, c, and d for a range of fetch and water depth (Table 6.51). His results are shown (Fig. 6.68) for the neutral case for a wind speed of 10 $m \cdot s^{-1}$. Gerritsen (1962) showed through laboratory experiments the role of wind waves in wind stress.

WIND AND PRESSURE FIELDS IN TROPICAL CYCLONES

Storm surges are generated by tropical as well as extratropical cyclones. From the

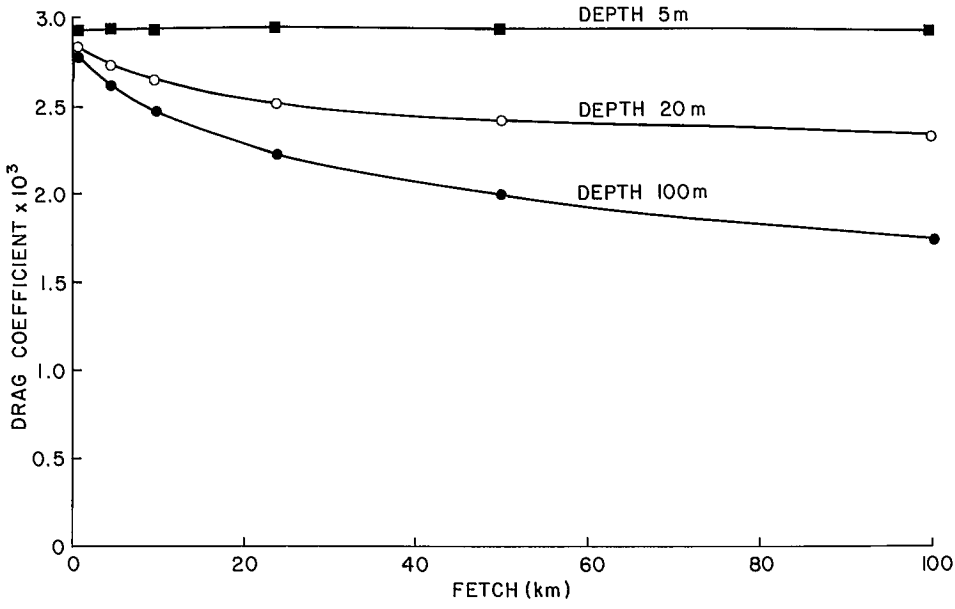

FIG. 6.68. Drag coefficient for three different water depths as a function of the fetch. (Hamblin 1979a)

point of view of damage to life and property, tropical cyclone generated storm surges are more important. This is one reason why special attention will be paid to the meteorological forcing terms for storm surges generated by tropical cyclones. The other reason is that, because of the shape and nature of tropical cyclones, certain convenient (if not always correct) analytical forms for the wind and pressure fields are used. On the other hand, for extratropical cyclones, no such simple analytical forms are commonly used and for these, traditionally, the pressure gradients and wind stresses are derived using interpolation techniques from surface weather charts and related data. Thus, the meteorological problems associated with extratropical cyclones will be considered, not as a special problem, but in various examples later.

The maximum sustained surface wind in a tropical cyclone can be determined as a function of the local maximum pressure gradient and the radius of maximum winds (Atkinson and Holliday 1977). From aircraft and satellite data, the radius of maximum winds can be determined reasonably accurately, but it is difficult to determine the local maximum pressure gradient. For the various ocean basins and seas, empirical relationships between the local minimum pressure and maximum winds were developed based on observed data. Holliday (1969) summarized these relationships for the North Atlantic.

Takahashi (1939) gave the following form of the cyclostrophic wind equation for the western part of the North Pacific:

$$V_m = K(p_n - p_c)^{0.5} \tag{6.96}$$

where V_m is the maximum speed (knots) of the surface wind, p_n is the environmental pressure (millibars), p_c is the central pressure (millibars), and K is a constant. For the western North Pacific, he took $K = 13.4$ and $p_n = 1010$ mb. Later, Takahashi (1952) suggested that $K = 11.5$ is more appropriate for higher latitudes.

Making use of aircraft reconnaissance data on central pressure and maximum winds,

McKnown et al. (1952) gave the following relation:

$$(6.97) \quad V_m = \left(20 - \frac{\theta}{5}\right)(1010 - p_c)^{0.5}$$

where θ is the latitude in degrees.

Making use of 700 mb height field observations, Fortner (1958) replaced p_c with 700 mb height h_7 (metres) and wrote

$$(6.98) \quad V_m = \left(20 - \frac{\theta}{5}\right)\left(372 - \frac{h_7}{8.54}\right)^{0.5}$$

Note that eq. 6.98 is in the C.G.S. system. Further modifications were suggested by Wacholz (1961) and Seay (1964). The Joint Typhoon Warning Center uses the following relationship:

$$(6.99) \quad V_m = \left(19 - \frac{\theta}{5}\right)\left(364 - \frac{h_7}{8.54}\right)^{0.5}$$

The general feeling was that this equation overestimated the surface wind by 23.4 knots on the average. For wind speeds greater than 45 knots, a modified form was used.

Atkinson and Holliday (1977) used 28 yr of data collected at coastal and island stations in the western North Pacific. Recognizing that there are problems in measuring and interpreting sustained wind speeds at the surface, they made use of only recorded peak gusts. These peak gust values were reduced to a standard anemometer level of 10 m using a power law relationship and then converted to 1 min of sustained wind speeds making use of gust factors representative of an overwater environment. They gave the following relationship:

$$(6.100) \quad V_m = 6.7(1010 - p_c)^{0.644}$$

where p_c is the minimum sea level pressure (millibars) and V_m is the maximum sustained (1 min) wind speed (knots). This equation gives maximum wind speeds that are significantly lower than given in earlier studies.

Holland (1980) used an analytic model to relate the wind and pressure fields in a hurricane. Earlier analytic models included the modified Rankine vortex (Depperman 1947) and the negative exponential model (Schloemer 1954). Holland modified Schloemer's model in the following manner.

The pressure field was first normalized to eliminate variations due to different central and ambient pressures through the following parameter:

$$(6.101) \quad \frac{p - p_c}{p_n - p_c}$$

where p is the pressure at radius r, p_c is the central pressure, and p_n is the ambient pressure (at infinite radius in theory but, in practice, the position of the first anticyclonically curved isobar). A plot of this parameter 6.101 against the radial distance from the center gives a curve that looks like a rectangular hyperbola and may be approximated by

$$(6.102) \quad r^B \ln\left[\frac{(p_n - p_c)}{(p - p_c)}\right] = A$$

where A and B are scaling parameters. Taking the antilogarithm of eq. 6.102 and rearranging gives

$$(6.103)\quad p = p_c + (p_n + p_c)\exp\left(-\frac{A}{r^B}\right)$$

Making use of the gradient wind relation, the wind profile can be expressed as

$$(6.104)\quad V_g = \left[AB(p_n - p_c)\exp\frac{\left(\frac{-A}{r^B}\right)}{\rho r^B} + \frac{r^2 f^2}{4}\right]^{1/2} - \frac{rf}{2}$$

where V_g is the gradient wind at radius r, f is the Coriolis parameter, and ρ is the density of air (1.15 kg·m^{-3}).

In the area of maximum wind speed, the pressure gradient and centrifugal forces are dominant and the Coriolis force can be ignored. Thus, for the cyclostrophic equilibrium one can write

$$(6.105)\quad V_c = \left[AB(p_n - p_c)\frac{\exp\left(-\frac{A}{r^B}\right)}{\rho r^B}\right]^{1/2}$$

The radius of maximum winds, R_{MW} or R_w, is obtained by equating dV_c/dr to zero to give

$$(6.106)\quad R_w = A^{1/B}$$

Thus, R_w is determined only by the scaling parameters A and B and is not dependent on the central and ambient pressures. To obtain the maximum wind speed, V_m, eq. 6.106 is substituted into eq. 6.105 to give

$$(6.107)\quad V_m = C(p_n - p_c)^{1/2}$$

with

$$(6.108)\quad C \equiv \left(\frac{B}{\rho e}\right)^{1/2}$$

where e is the base of natural logarithms. Note that eq. 6.107 with an empirically determined C (instead of eq. 6.108 for C) was used by Takahashi (1939), Myers (1954), Kraft (1961), and Atkinson and Holliday (1977).

From the above relations it can be seen that the maximum wind speed is independent of the radius of maximum winds but it depends on the shape of the pressure profile through B. From eq. 6.103, the radius R_p of maximum pressure gradient is given by

$$(6.109)\quad R_p = \left[\frac{AB}{B+1}\right]^{1/B}$$

From eq. 6.106 and 6.109

$$(6.110)\quad \frac{R_p}{R_w} = \left(\frac{B}{B+1}\right)^{1/B}$$

Based on observed data, a lower limit for B is found to be 1.0 and an upper band is 3.0 and a representative value was found to be 2.5. Then, from eq. 6.106, one can determine A by using the observed R_w values.

Equating B to 1 underestimates the maximum wind speeds for most hurricanes. The maximum wind speeds at various central pressures for tropical cyclones in the Northwest Pacific are listed in Table 6.52. Schloemer (1954) suggested that eq. 6.103 and 6.104 with $A = R_w$ and $B = 1$ can be used universally. The errors of the Schloemer's (1954) formula

TABLE 6.52. A comparison of maximum wind speeds at various central pressures for Northwest Pacific tropical cyclones. D, from Dvorak (1975a); AH, from Atkinson and Holliday (1977); S, from Schloemer (1954). (Holland 1980)

	Maximum wind speed ($m \cdot s^{-1}$)		
Central pressure (mb)	D (1-min surface wind)	AH (1-min surface wind)	S (1-min gradient wind)
981	33	30	30
973	40	35	34
964	46	41	38
954	53	46	42
942	59	52	47
929	69	58	51
915	72	65	55
900	80	71	59
884	88	78	63

TABLE 6.53. Mean absolute errors and maximum errors resulting from applying Schloemer's (1954) model and eq. 6.103 to nine hurricanes. (Holland 1980)

	Schloemer 1954		eq. 6.103	
Radius (km)	Mean absolute error (mb)	Maximum error (mb)	Mean absolute error (mb)	Maximum error (mb)
5	3	13	3	11
10	5	19	3	6
20	5	23	2	8
30	6	26	1	5
40	7	28	1	3
60	8	26	1	3
100	7	18	1	2
150	6	13	1	4
200	6	13	1	3

and the one suggested by Holland (1980) are compared in Table 6.53. It can be seen that the modified method of Holland is superior.

Depperman (1947) suggested that a hurricane could be thought of as a Rankine vortex:

(6.111) $Vr^{-1} = \text{constant}$

inside the radius of maximum winds and as

(6.112) $Vr = \text{constant}$

outside this radius. Thus, the hurricane is assumed to be a solid rotating body inside this radius, and outside this radius it conserves relative angular momentum. Since the air inside the boundary layer loses angular momentum by frictional dissipation, eq. 6.112 should be modified to give

TABLE 6.54. Relationship among the various parameters as determined from satellite imagery. CI, current intensity; MSW, maximum sustained wind speed ($km \cdot h^{-1}$); MSLP, minimum sea level pressure (mb). (Dvorak 1973)

		MSLP				MSLP	
CI	MSW	Atlantic	Pacific	CI	MSW	Atlantic	Pacific
1.5	46	1010	1004	5.0	157	970	964
2.0	56	1007	1001	5.5	180	960	954
2.5	65	1003	997	6.0	204	948	942
3.0	74	998	992	6.5	226	934	928
3.5	93	993	987	7.0	250	920	914
4.0	111	988	982	7.5	278	906	900
4.5	133	979	973	8.0	315	891	885

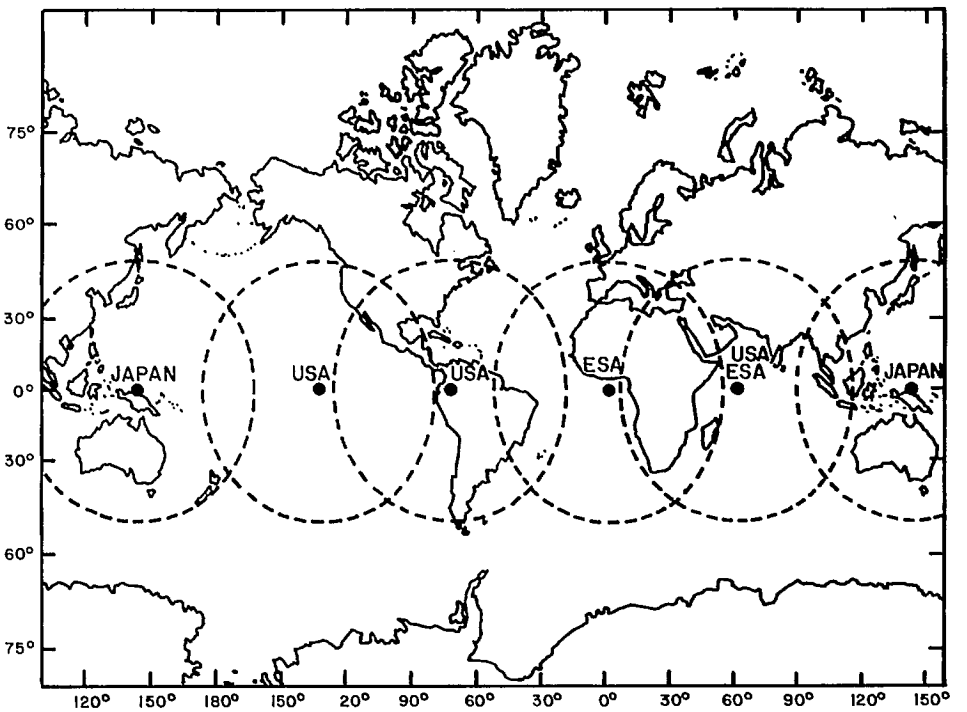

FIG. 6.69. Coverage by the five geostationary satellites. Note that the circle at the right extreme is a repeat of the circle at the left extreme. The circles show the extent of the areas where good wind estimates can be made. Satisfactory cloud images can be received from substantially larger areas. (Houghton 1978)

$$(6.113) \quad Vr^x = D$$

where x is less than unity and D is a constant. Observations indicate that x usually lies between 0.4 and 0.6 (Hughes 1952; Riehl 1954, 1963; Gray and Shea 1973). Although the Rankine vortex approach can give a good fit to the wind profile in a hurricane, it requires a very accurate estimate of the radius of maximum winds (which is difficult), and this is one of the disadvantages of this method as compared with Holland's (1980) technique.

Dvorak (1973, 1975a, 1975b) pioneered the techniques of estimating the intensity of tropical cyclones based on satellite imagery. He defined a T number (which ranges from 1 to 8) as the description of a tropical disturbance in terms of cloud characteristics visible in satellite data, and the T number can be determined by systematically merging the satellite imagery data with a model of tropical cyclone development. However, the T number is not used for intensity estimates because the wind speed may be different (for the same T number) for developing and weakening storms.

However, a current intensity number (CI) is used for relating the present (current) intensity of the cyclone to the maximum sustained wind speed (MWS) and the minimum sea level pressure (MSLP) of the storm. This relationship determined empirically for data for the Atlantic hurricanes and Pacific typhoons is listed in Table 6.54. The detailed procedures of determining the T number and CI number can be found in Dvorak (1973).

Dvorak and Wright (1978) discussed the technique of using enhanced infrared satellite data for determining the intensity of tropical cyclones. Gentry et al. (1978) used satellite-measured equivalent blackbody temperatures, T_{BB}, of cloud tops around a hurricane to obtain estimates of the storm's intensity and to predict future changes. Rodgers et al. (1978) discussed the technique of using short-interval satellite imagery to determine winds for tropical cyclones. Gray (1978a, 1978b, 1978c, 1978d, 1979) discussed the techniques of determining tropical cyclone intensity through upper tropospheric aircraft reconnaissance. Baynton (1979) suggested that Doppler radars will provide good estimates of the wind field.

Geostationary satellites also could provide useful data (Houghton 1978). The coverage of the tropics provided by the five geostationary satellites is shown in Fig. 6.69. A U.S. geostationary satellite is presently helping to track Atlantic hurricanes within ± 17 nautical miles and determining the wind speeds with an error of about 10 knots (E.O.S. Vol. 61, No. 29, July 15, 1980).

Suomi (1969) and Fujita et al. (1969) described techniques for determining winds from cloud pictures provided by geostationary satellites. Basically, cumulus clouds at the 900-mb level and cirrus clouds at the 200-mb level are used. According to Fujita et al. (1975) there could be errors of up to $\pm 40\%$ in the estimated winds. According to Suchman and Martin (1976) errors of up to 2 $m \cdot s^{-1}$ at the cirrus cloud level and 1.3 $m \cdot s^{-1}$ at the cumulus cloud level could occur in the wind field. However, Hubert (1976) and Davis et al. (1976) found greater errors than reported by Suchman and Martin (1976). Gaby and Poteat (1973) gave the climatology of low-level winds from satellite images.

6.7 Meteorological Problems Associated with Storm Surges in Canada

Storm surges are generated in Canada by extratropical storms and occasionally by a hurricane that has transformed into an extratropical storm. In eastern Canada, storm surges occur in the Great Lakes, St. Lawrence Estuary, Gulf of St. Lawrence, Bay of Fundy, and along the Atlantic coast. Storm surges also occur in Hudson Bay, James Bay, Lake Winnipeg, Beaufort Sea, Hecate Strait, and Queen Charlotte Sound. The main storm surge season is autumn and early winter, and occasionally, storm surges could occur in summer and in late winter. Since all the surge-producing storms are extratropical in origin, the calculation of the meteorological forcing terms from the weather charts is straightforward (it does not necessarily mean the values are accurate). For convenience, Alaska will be discussed in this section along with western Canada. Similarly, the Great Lakes will be

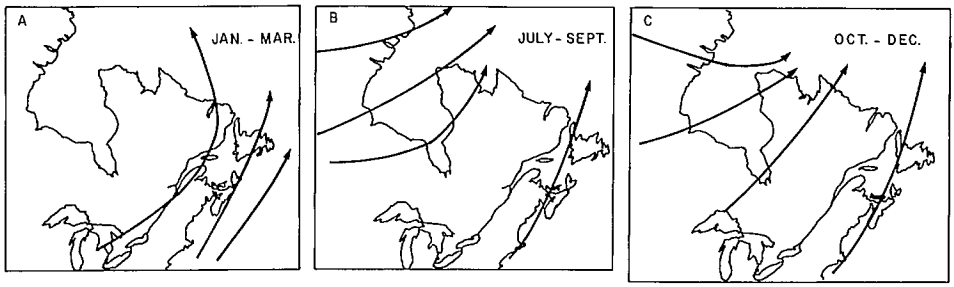

FIG. 6.70. Tracks of intense storms over eastern Canada (A) January–March, (B) July–September, and (C) October–December. (Archibald 1945)

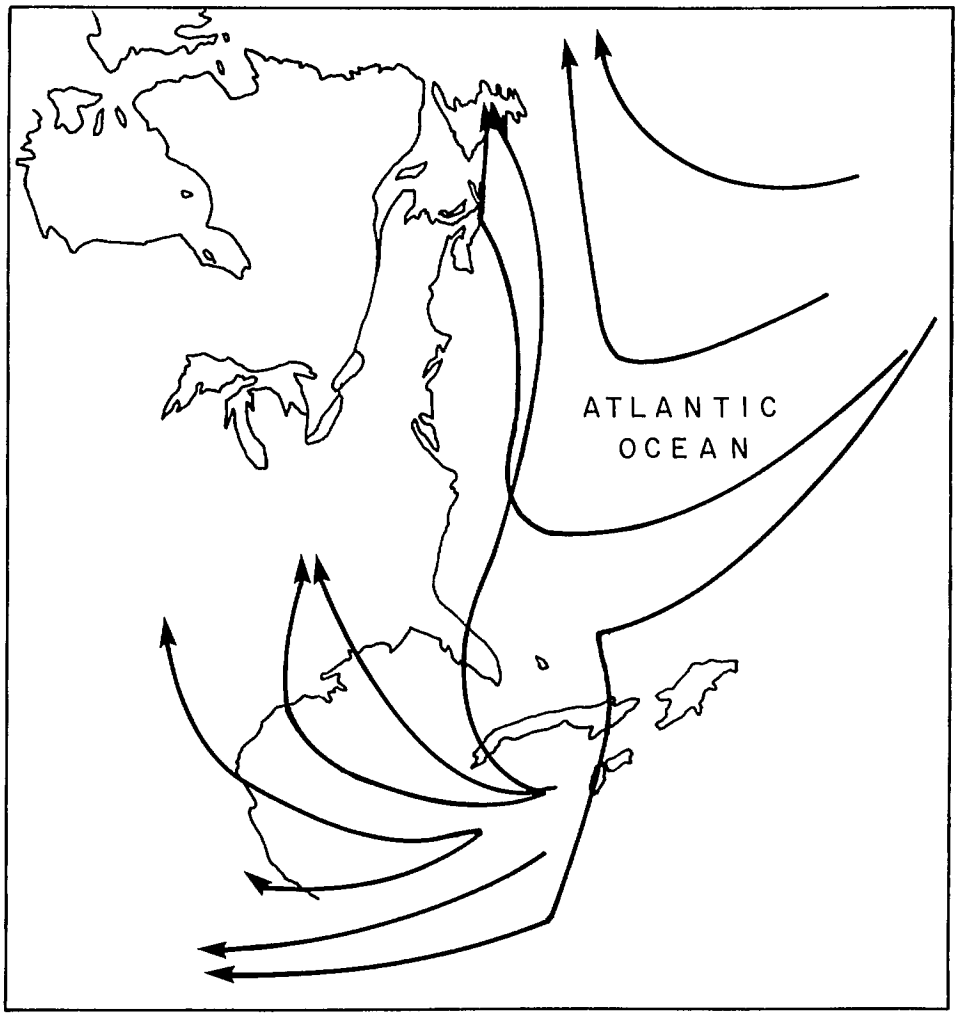

FIG. 6.71. Tracks of storms of tropical origin along the east coast of North America. (Archibald 1945)

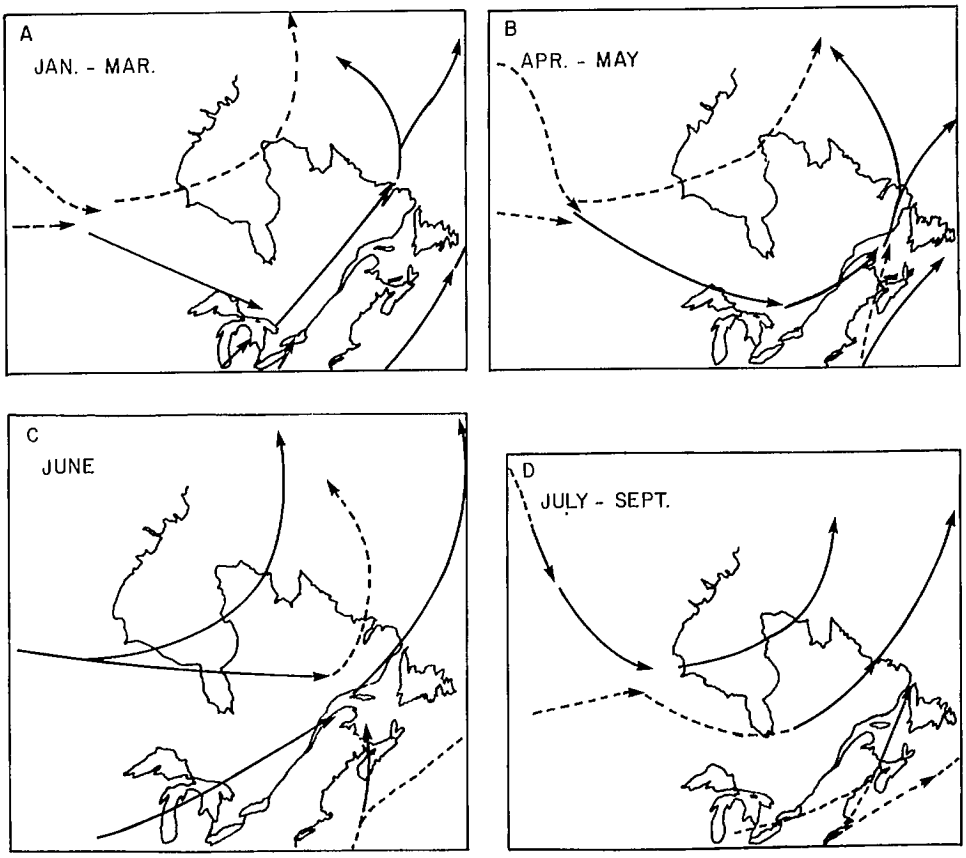

FIG. 6.72. Storm tracks over Hudson Bay and surroundings (A) January–March, (B) April and May, (C) June, and (D) July–September. (Archibald 1945)

treated in this section. However, meteorological problems associated with mesoscale systems such as squall lines will be deferred to section 6.11.

Principal tracks of intense storms (based on the data for the period 1963–67) are shown in Fig. 6.70A for January to March, in Fig. 6.70B for July and August, and in Fig. 6.70C for October to December. The tracks of storms of tropical origin are shown in Fig. 6.71, and the tracks of storms for the Hudson Bay region for different months are shown in Fig. 6.72A–6.72D. However, occasionally, rather irregular tracks can occur. In Fig. 6.73 are shown the tracks for four storms in 1969 over Hudson Bay. While the track for the November storm is not unusual, the tracks for the other three storms show forward–backward movements of the storm center, which could be the result of improper observations or could be real on certain occasions.

The corridors for the tracks of intense and ordinary storms in the northwestern part of Canada are shown in Fig. 6.74. The surface weather map for the Alaska area during a storm on October 3, 1963, is given in Fig. 6.75A. The distribution of the computed wind stress field is illustrated in Fig. 6.75B and the variation of the computed wind stress with time near Barrow, Alaska, is shown in Fig. 6.75C.

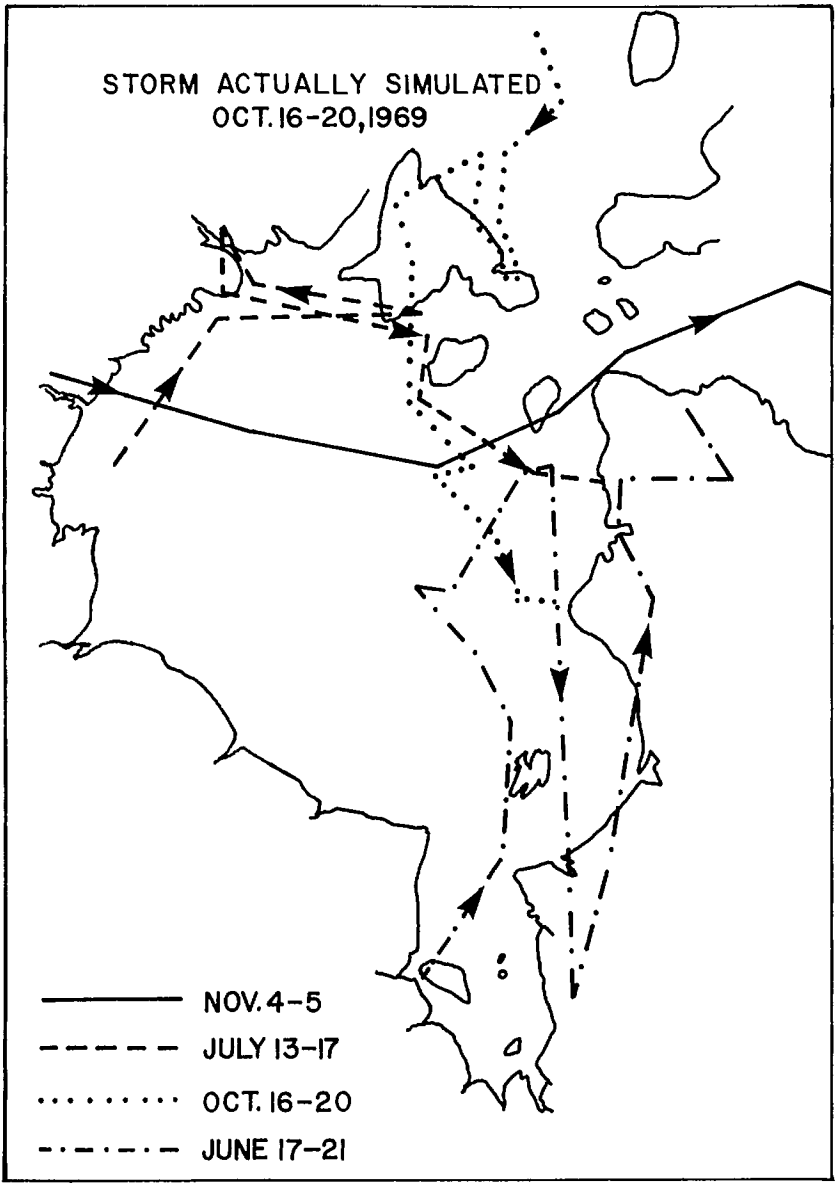

FIG. 6.73. Selected storm tracks over Hudson Bay for the year 1969.

METEOROLOGICAL PROBLEMS IN THE GREAT LAKES

Barrientos (1970) discussed objective methods for predicting winds over Lakes Erie and Ontario. Making use of 1000-mb geostrophic wind and sea level pressure forecasts issued routinely for eight stations surrounding these lakes, as well as marine observations

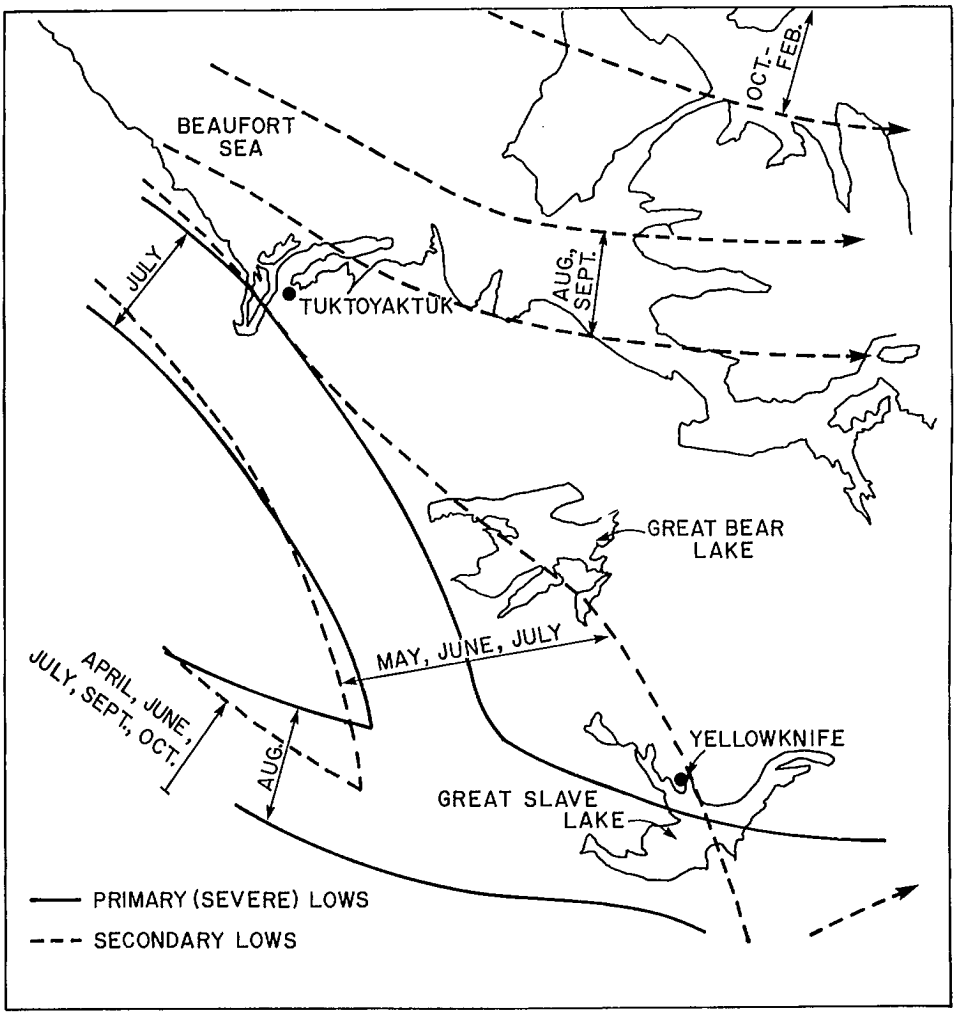

FIG. 6.74. Corridors of primary and secondary lows over the northwest part of Canada. (Burns 1973)

from anemometer-equipped vessels, two sets of regression equations were derived for predicting wind speed.

Venkatesh and Danard (1976) used a one-level primitive equation model for computing the mesoscale influences of orography, friction, and heating on surface winds. They included the influence of atmospheric stability and land–water temperature contrast. Estoque and Gross (1979) discussed diurnal wind variations over Lake Ontario, as deduced from Rawinsonde data at six stations.

Resio and Vincent (1977) estimated winds over the Great Lakes knowing winds over adjacent land. Feit and Pore (1978) discussed objective wind forecasting for all of the Great Lakes using a technique developed by Feit and Barrientos (1974). The predictors are the various forecast parameters computed by the National Meteorological Center's primitive equation (PE) model. The 12 locations at which wind forecasts are made at 6-h

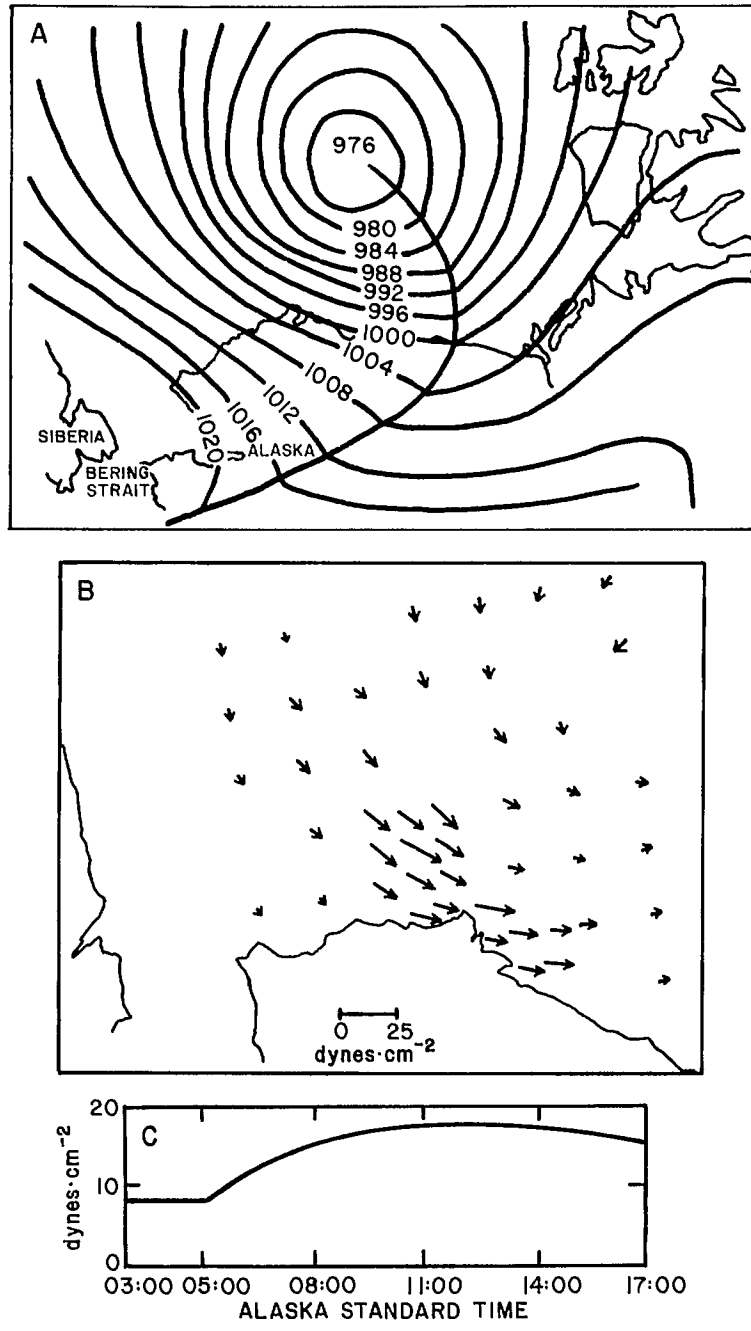

FIG. 6.75. (A) Simplified surface weather chart for October 3, 1963, at 11:00 (Alaska Standard Time); (B) computed wind stress field for 11:00–14:00; (C) variation of wind stress with time at Barrow, Alaska (1 dyne = 10 N). (Schafer 1966)

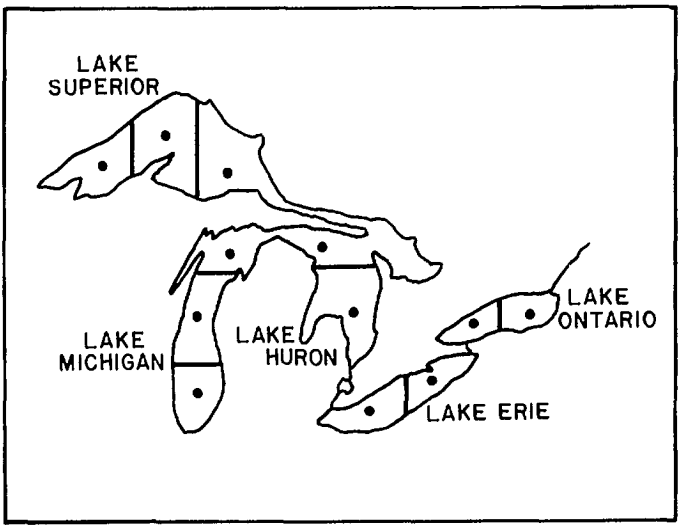

FIG. 6.76. Twelve locations in the Great Lakes where winds are routinely predicted by the U.S. National Weather Service. (Feit and Pore 1978)

intervals, 36 h in advance, are shown in Fig. 6.76. Mean absolute error in wind speed is 5–8 knots (2.6–4.1 $m \cdot s^{-1}$) and mean absolute error in wind direction is about 20° for short-term forecasts (6–12 h) and about 70° for long-term forecasts (30–36 h).

Keulegan (1953) took a somewhat different approach. He derived the wind stress and the roughness parameter for Lake Erie using water level data for a 50-yr period. In other words, he used the observed storm surge data to estimate the wind stress. He defined an effective lake wind velocity as the wind velocity that would be needed to produce the observed storm surge, assuming that the wind blows with this effective velocity along the lake axis. Recently, Schwab (1982) used a similar but more sophisticated inverse technique.

Keulegan (1953) used the following relationship to deduce the wind stress from the storm surge:

$$(6.114) \quad \frac{(\tau_S + \tau_0)}{\rho g H_0} \frac{L}{H_0} = 0.867 \frac{\Delta H}{H_0} - 0.134 \left(\frac{\Delta H}{H_0}\right)^2$$

where τ_S is the wind stress, τ_0 is the bottom stress, ρ is the density of water, g is gravity, H_0 is the average water depth, ΔH is the storm surge (feet), and L is the length of the lake (feet). The bottom stress τ_0 was related to the surface wind stress through

$$(6.115) \quad \tau_0 = n\tau_S$$

Then, eq. 6.114 becomes

$$(6.116) \quad \tau_S = \frac{1}{(1+n)} \left[0.867 \frac{\Delta H}{H_0} - 0.134 \left(\frac{\Delta H}{H_0}\right)^2\right] \frac{H_0}{L} \rho g H_0$$

Write

$$(6.117) \quad \tau_S = \gamma \rho_a V^2$$

TABLE 6.55. Relationship between observed storm surges (in the United States) and drag coefficients of wind. (Modified from Keulegan 1953)

Date of storm surge	Observed storm surge (m)	Observed wind speed ($km \cdot h^{-1}$)	Drag coefficient $\gamma \times 10^3$
Nov. 21, 1900	4.00	81.3	2.13
Oct. 20, 1905	2.04	5.05	2.87
Oct. 20, 1906	2.97	61.6	2.78
Jan. 20, 1907	3.67	77.4	2.17
Dec. 7, 1909	3.20	64.5	2.73
Dec. 31, 1911	2.90	62.6	2.63
Jan, 31, 1914	2.42	55.8	2.76
Dec. 9, 1917	3.10	69.5	2.23
Dec. 9, 1917	1.39	53.3	1.78
Dec. 10, 1917	2.32	55.2	2.71
Dec. 18, 1921	3.75	72.6	2.52
Dec. 8, 1927	4.04	76.3	2.44
Dec. 9, 1927	1.26	43.8	2.35
Dec. 9, 1927	1.05	42.0	2.15
Dec. 9, 1927	0.53	35.6	1.53
Apr. 1, 1929	4.06	82.6	2.88
Jan. 22, 1939	2.87	62.4	2.64
Sept. 25, 1941	2.76	57.5	2.96
Jan. 2, 1942	3.82	65.0	3.22
Jan. 3, 1942	0.73	31.4	2.68
Nov. 22, 1946	2.55	55.0	2.99
Mar. 25, 1947	2.54	57.5	2.77

where ρ_a is the density of air, V is the wind speed (feet per second), and the drag coefficient γ is given by

$$(6.118) \quad \gamma = \frac{0.867}{(1+n)}\left[1 - 0.16\frac{\Delta H}{H_0}\right]\frac{\Delta H}{H_0}\frac{\rho}{\rho_a}\frac{gH_0}{V^2}$$

The 22 storms during the period 1900–47 on Lake Erie, the observed wind speed, the observed storm surge (during westerly winds), and the calculated value of γ from eq. 6.118 are listed in Table 6.55.

Hunt (1959) discussed the relationship between the parameter α defined as

$$(6.119) \quad \alpha \equiv \frac{\tau_S + \tau_B}{\tau_S}$$

and D/K where D is the water depth, K is the bottom roughness coefficient, and τ_S and τ_B are the wind and bottom stresses. The relationship for Lake Erie is shown in Fig. 6.77. Hunt (1959) also gave diagrams showing the variation with time in fall and spring of the ratio U_W/U_L at Cleveland on Lake Erie (Fig. 6.78). Here, U_W and U_L are the overwater and overland wind speeds. The reason for examining this ratio is to account for atmospheric stability. The ratio U_W/U_L at four stations on Lake Erie for stable, adiabatic, and unstable atmospheric conditions is given in Table 6.56. The overwater wind speeds on Lake Erie at 21:00 on November 8, 1957, are shown in Fig. 6.79.

Irish and Platzman (1961) discussed the meteorological conditions associated with extreme storm surges on Lake Erie. The monthly frequency distribution of severe storms

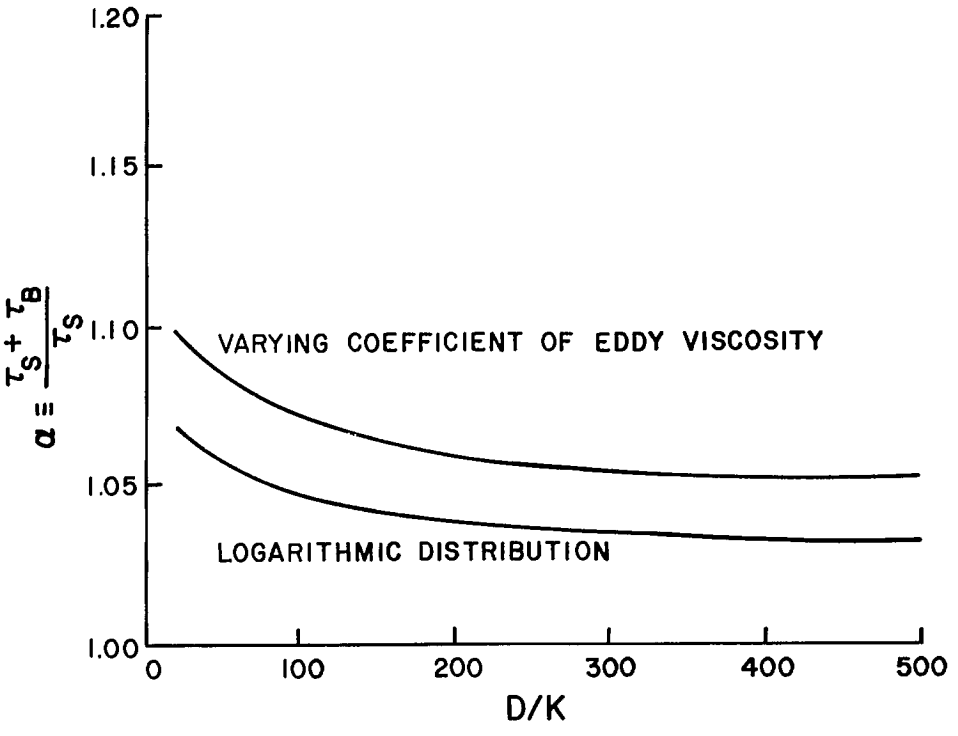

FIG. 6.77. Variation of α versus D/K (D = water depth, K = bottom roughness parameter, τ_S = wind stress, and τ_B = bottom stress). The relationship is shown for two different distributions of bottom stress. (Hunt 1959)

on the Great Lakes, as given by these authors for the period 1876–1900, are given in Fig. 6.80. It can be seen that maximum frequency occurs during October to December, November being the month of greatest frequency.

Platzman (1965b) showed that over Lake Erie, there is a distinct diurnal constituent of the longitudinal component of the wind square vector, with maximum in the direction Toledo to Buffalo shortly after noontime. This variation is due to the usual convective oscillation of the atmospheric boundary layer. The amplitude of this variation is about 10 $m^2 \cdot s^{-2}$.

Schwab (1978) used the impulse response method to simulate storm surges on Lake Erie. For inclusion of spatial dependence in the wind field, he used a weighting factor W_i in the interpolation of winds from different stations, similar to that used by Platzman (1963):

$$\tau(x, y, t) = \sum_{i=1}^{m} W_i(x, y)\tau_i(t)$$
$$\sum_{i=1} W_i(x, y) = 1 \tag{6.120}$$

where W_i is proportional to the inverse square of the distance from station i.

Schwab (1978) converted the observed wind speeds S_L at the coastal stations into overlake wind speeds S_W through

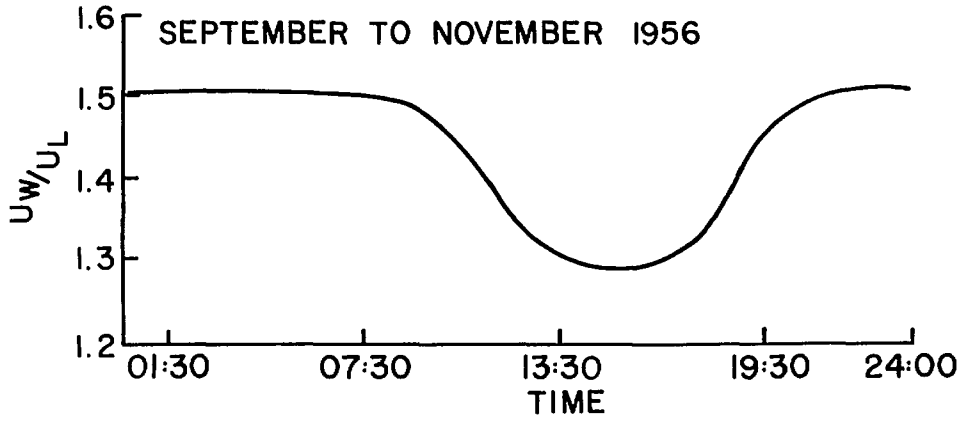

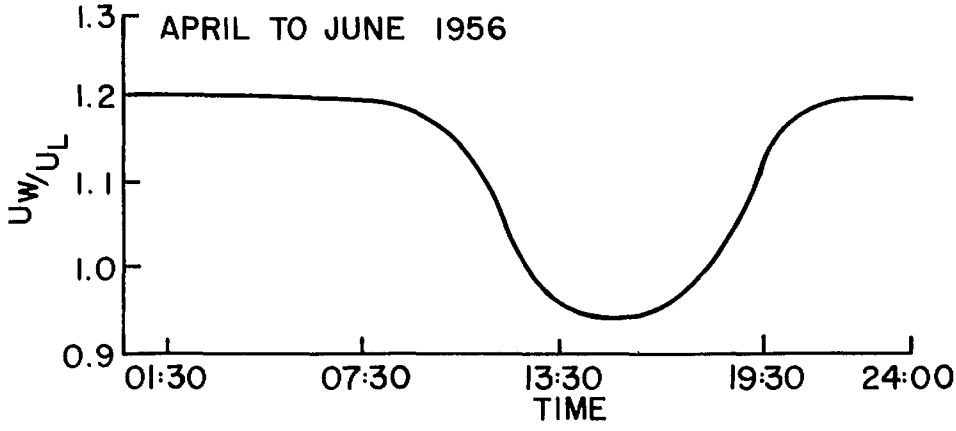

FIG. 6.78. Daily variation in U_W/U_L for southwesterly winds by season at Cleveland, Ohio, during 1956. (Hunt 1959)

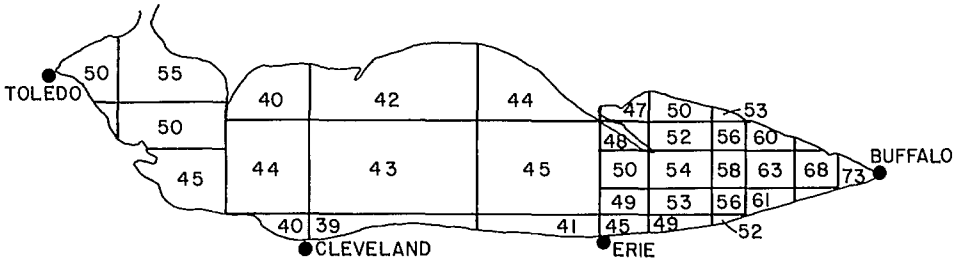

FIG. 6.79. Overwater wind speeds (feet per second) in Lake Erie (1 ft = 0.3048 m). (Hunt 1959)

TABLE 6.56. U_W/U_L for four Lake Erie sectors according to temperature (°C) classification. U_W, overwater wind; U_L, overland (shore station) wind; T_A, air temperature; T_W, water temperature. Data are the values of the ratio U_W/U_L for the three following states of the atmosphere: $T_A - T_W \leq 22.2$°C, unstable; $T_A - T_W = -21.7$ to 13.9°C, adiabatic; $T_A - T_W \geq -13.3$°C, stable. (Hunt 1959)

Sector	Unstable	Adiabatic	Stable
Toledo	1.95	1.59	1.13
Cleveland	1.48	1.37	1.00
Erie	2.35	2.03	1.00
Buffalo	1.59	1.13	0.90

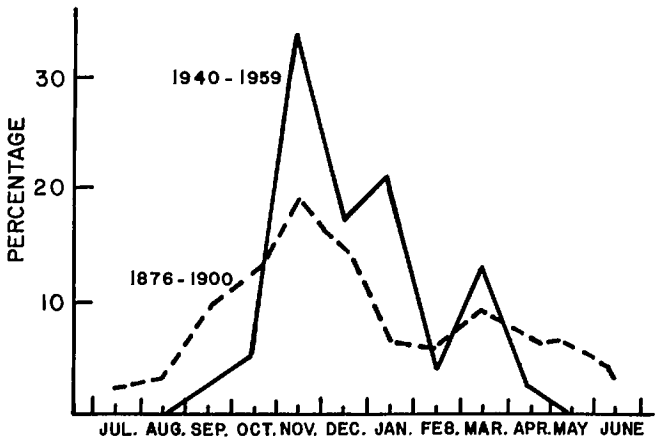

FIG. 6.80. Monthly frequency distribution of severe storms on the Great Lakes for the period 1940–59 (solid line) and for the period 1876–1900 (broken line). (Irish and Platzman 1961)

$$\frac{S_W}{S_L} = \psi(S_L)\phi(T_a - T_w) \tag{6.121}$$

where T_a and T_w are the air and water temperatures, respectively, and

$$\psi = 1.2 + \frac{1.9}{S_L} \tag{6.122}$$

$$\phi = 1.0 - \left(\frac{T_a - T_w}{1900}\right)^{1/3} \tag{6.123}$$

These relations are given by Resio and Vincent (1977) based on boundary layer theory. In eq. 6.122, S_L is expressed in metres per second. The vector surface stress is taken proportional to the product of wind speed and vector wind U, i.e.

$$\frac{\tau_i}{\rho_a} = C_d|U_i|U_i \tag{6.124}$$

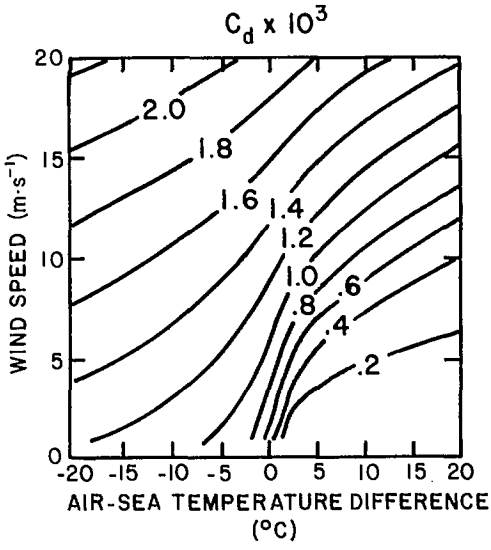

FIG. 6.81. Drag coefficient C_d as a function of air–water temperature difference and wind speed at a 10-m height. (Schwab 1978)

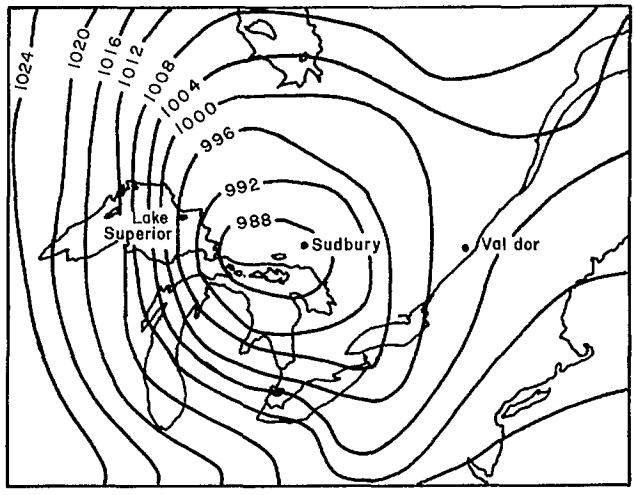

FIG. 6.82. Simplified surface weather chart at 01:00 (Eastern Standard Time) on April 6, 1979. The pressure field is in millibars. (Hamblin 1979b)

The air density ρ_a is taken as 1.25×10^{-3} g·cm^{-3}. The drag coefficient C_d as a function of $(T_a - T_w)$ and wind speed (at a 10-m height) is shown in Fig. 6.81.

Hamblin (1979) numerically simulated the storm surge of April 6, 1979, which produced a record setup of 4.5 m on Lake Erie. The surface isobaric field for this storm is shown in Fig. 6.82 and the time variation of the wind stress at four stations is given in Fig. 6.83. Hamblin (1979) mentioned that the computed drag coefficients varied from

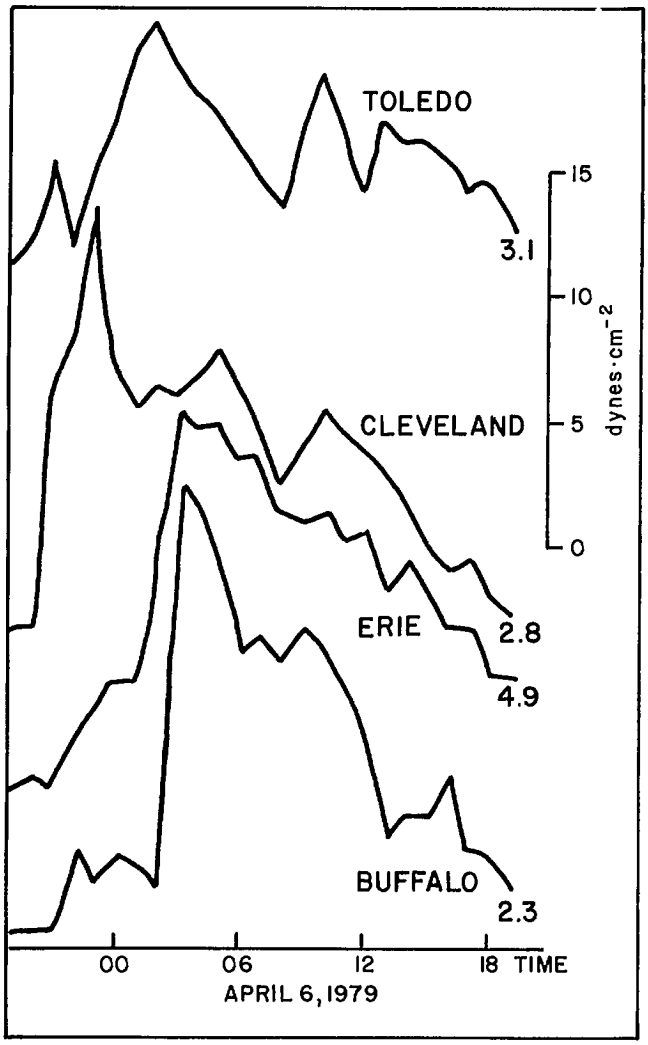

FIG. 6.83. Time history of wind stress at four locations on Lake Erie. (Hamblin 1979b)

0.9×10^{-3} to 3.5×10^{-3} during the duration of the storm.

Simons (1975) determined the effective wind stress over Lakes Erie and Ontario from long-term numerical water level simulations. He showed that the effective wind stress over water is greater than indicated by atmospheric boundary layer measurements over Lake Ontario; the theoretically derived drag coefficient appears to be about 1.85×10^{-3}. Over Lake Erie, the drag coefficient is about the same magnitude in spring and early summer, but increases to about 2.5×10^{-3} during the stormy autumn season. These results confirm Donelan's (1975) study of the interaction between wind waves and the atmospheric boundary layer, whose primary result was that the drag coefficient increases significantly if the wave field is not completely adjusted to the wind field. Usually, boundary layer

observations are made during steady winds (when no storms are present) and, hence, such measurements are not representative of drag coefficient during stormy periods.

6.8 Meteorological Problems Associated with Storm Surges in the United States

Extratropical (and Tropical) Cyclones

Frequencies of cyclones over North America were determined for the period 1899–1939 by Petterssen (1950) and Klein (1957). This period characterized a gradually increasing Northern Hemisphere temperature (and predominant zonal flow). Cyclone frequency studies were made for the period 1951–70 (Reitan 1974). During this period, the temperature in the Northern Hemisphere gradually decreased (more frequent meridional flow occurred). The year 1950 appears to be the boundary between these two epochs.

Reitan (1974) used a grid with an area of 550 000 km^2 whereas Klein (1957) used a grid with an area of 230 000 km^2 and Petterssen (1950) used a grid of 100 000 km^2. In the studies of Petterssen and Klein, a cyclonic event was counted whenever the cyclone center was within the area at a specific time (12:30 GMT). Reitan (1974) counted a cyclonic event if the track of the cyclone passed through a grid area. The grid system used for the total area of the study (Reitan 1979) is shown in Fig. 6.84. The continental United States approximately covers the area occupied by rows D–G and columns 4–10.

The number of cyclonic events by year for the period 1951–70 for the entire grid as well as for the continental United States is listed in Table 6.57. The frequencies are given separately for January, April, July, and October. Some important differences occurred between the results for the post-1950 data and the pre-1950 data. During the pre-1950 period, the January cyclogenesis maximum occurred in the prairie provinces of Canada with a secondary maximum in Colorado, whereas for the post-1950 period, the primary maximum was in Colorado with a secondary maximum in Alberta. In the pre-1950 period the Gulf of Alaska and the coast of the State of Washington were areas of cyclogenesis, whereas this was not true in the post-1950 period. Also, a maximum of cyclogenesis off the southwest coast of Greenland in the early period was not found in recent data (Reitan 1974). Similar differences exist during the other months.

Reitan (1979) extended his earlier study (Reitan 1974) to cover the period 1949–76. This study showed a general trend for a decrease in the number of cyclonic events in recent years. Zishka and Smith (1980) studied the climatology of cyclones over North America and surrounding area for the period 1950–77. Generally speaking, cyclones are more frequent, more intense, and have tracks far more southerly in January than in July. Predominant cyclogenesis occurs along the east coast of the United States and in the lee of the Rockies. The cyclone frequency has indeed decreased during the post-1950 period.

In these studies, latitude-dependent area normalization has been used (e.g. O'Connor 1964; Taljaard 1967; Reitan 1974, 1979). Hayden (1981a, 1981b) pointed out that latitude-dependent area adjustments, made after the data extraction is completed, introduce a latitude-dependent bias in the frequency patterns. For example, south of the reference latitude, area normalization adjusts the frequency downward and forces it to represent an area smaller than the one from which the original data were extracted. This artificially decreases the frequency of the cyclones (or whatever parameter being tabulated). On the other hand, north of the reference latitude, the frequency is artificially increased. To correct this situation, Hayden (1981a, 1981b) recommended the use of the so-called "practical equal area grid" as developed by Ballenzweig (1959).

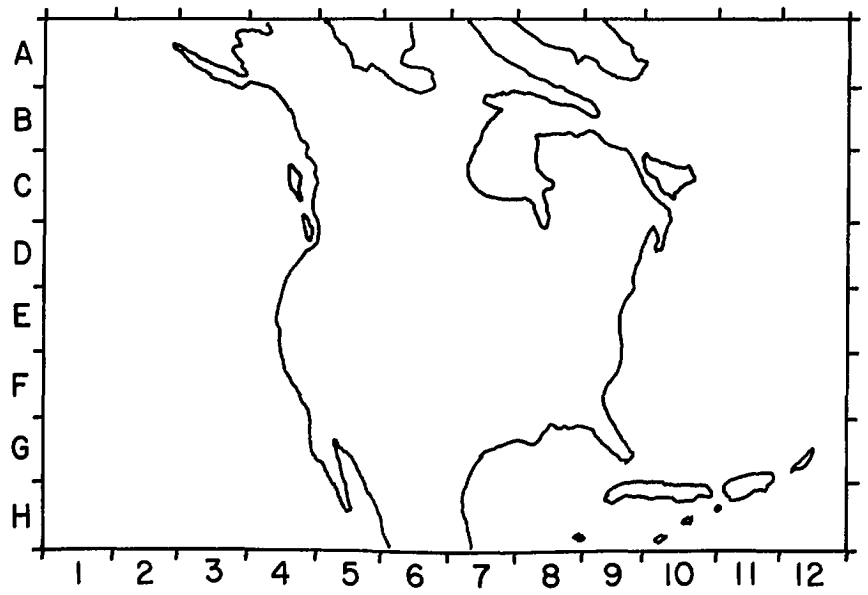

FIG. 6.84. Grid system used for counting cyclone frequencies. (Reitan 1979)

Hayden (1981a) performed a principal component analysis on extratropical cyclone data for the Atlantic coast of the United States and surrounding area (shown in Fig. 6.85 for the period 1885–1978). He stated (p. 162):

> ... principal component analysis provides a description of the major modes of variability in the data set. Typically, each component is identified with some property of the data field. The analysis also provides an index which measures the importance of each component within each year. Finally, the analysis provides an estimate of the total percent of variance in the data set which can be explained on the basis of each component.
>
> The objective of the analysis is to isolate characteristic, recurrent, and independent modes of covariance among variables into a new set of independent variables. Basically, the analysis transforms a set of intercorrelated variables into a new coordinate system in which the axes are linear combinations of the original variables and are mutually orthogonal. To prevent those grid cells with high mean cyclone frequencies (high latitudes) from dominating the total variance and consequently from dominating the eigen vector forms, the correlation matrix was used rather than the covariance matrix.

The area shown in Fig. 6.85 was divided into 74 rectangles (2.5° latitude by 5° longitude). The first principal component showed that, since the beginning of the twentieth century, the frequency of cyclones over the marine areas has increased whereas the frequency decreased over the continental areas. This trend peaked in the 1960's. The second principal component was identified as a cyclogenesis function for the east coast of the United States. This showed an increased cyclogenesis starting at the beginning of the twentieth century with a maximum in the 1950's. The third and fourth components explain the geographic variations in cyclogenesis in the Gulf coast and Great Lakes regions. The average cyclone frequencies over the eastern United States for the period 1885–1978 are

TABLE 6.57. Cyclone event frequency for four typical months for the grid shown in Fig. 6.84 and for the coterminus United States (i.e. rows D–C and columns 4–9 of Fig. 6.84). (Reitan 1979)

	Entire grid				Coterminous United States			
Year	Jan.	Apr.	July	Oct.	Jan.	Apr.	July	Oct.
1949	220	260	117	179	63	87	20	33
1950	242	134	111	228	83	52	36	66
1951	259	225	190	311	107	78	53	96
1952	397	262	185	265	125	67	30	32
1953	276	269	200	261	97	93	31	55
1954	385	253	217	201	135	73	85	50
1955	274	202	154	226	103	64	28	49
1956	242	282	185	198	77	80	45	50
1957	254	177	148	168	69	61	32	16
1958	270	186	159	218	80	66	34	34
1959	222	210	258	207	75	59	32	59
1960	313	248	190	235	97	76	41	56
1961	279	249	188	266	71	84	43	65
1962	360	202	219	264	119	55	52	69
1963	261	237	166	210	68	79	40	31
1964	299	193	132	256	110	44	25	57
1965	332	193	177	197	122	51	44	34
1966	182	226	150	187	46	54	30	33
1967	322	242	100	205	111	93	13	62
1968	200	232	139	248	60	70	24	78
1969	171	236	128	197	54	69	25	62
1970	244	187	163	216	50	76	33	36
1971	244	230	176	228	78	73	42	59
1972	233	210	126	210	66	62	32	48
1973	289	204	99	165	76	64	16	42
1974	223	229	158	206	79	63	38	34
1975	277	170	140	182	86	49	23	50
1976	184	201	175	206	52	49	32	44
Total	7455	6148	4447	6138	2359	1871	979	1400
Average	266	220	159	219	84	67	35	50

also shown in Fig. 6.85.

Usually, one uses the Norwegian cyclone model to explain extratropical cyclogenesis. Reed (1979) pointed out that it is not always necessary for the cyclone to originate as a wave perturbation on a polar front separating tropical and polar air masses. An alternate mechanism is the formation of cyclones in polar air streams behind or poleward of the polar front, as sometimes happens in winter over the oceans.

Cyclones that form in this manner are relatively small in size. One interesting feature is that, in their mature stage, these cyclones exhibit a comma-shaped pattern. A surface low pressure center may not always be easily identifiable. When it exists, such a low pressure center is situated beneath the head of the comma. Also, under the trailing edge of the comma tail, there is almost always a surface trough of low pressure. Thus, cyclones of this type somewhat resemble large frontal cyclones.

WIND STRESS AND PRESSURE IN EXTRATROPICAL CYCLONES OVER THE UNITED STATES

Tancreto (1958) used the significant wave (wind waves) height as an indication of the intensity of the storm. An extratropical cyclone generated storm surge during March 1962

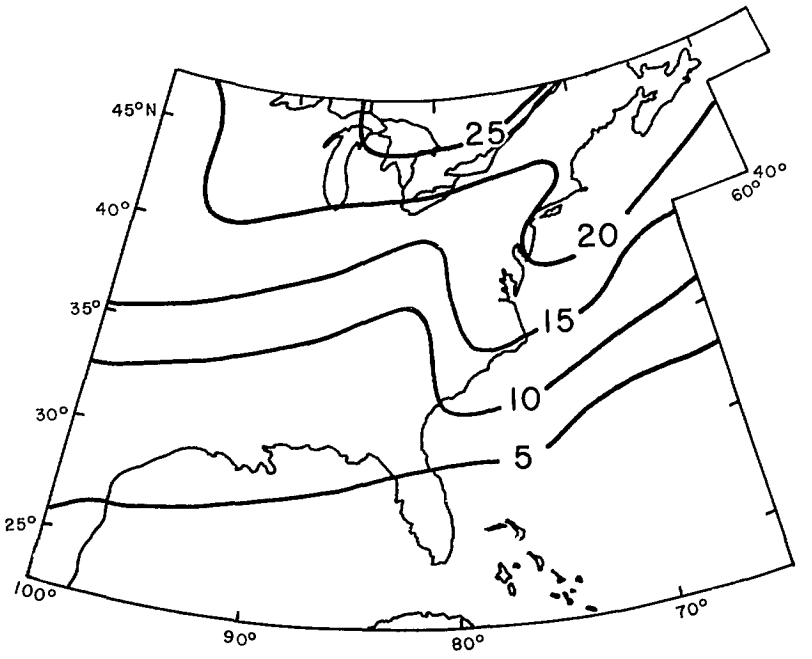

FIG. 6.85. Average annual frequency of extratropical cyclones over the eastern part of the United States. (Hayden 1981a)

caused tremendous damage in Atlantic City (New Jersey). The surge was so severe it bisected a steel pier (Pore 1964). Extratropical cyclone generated storm surges are not rare on this part of the east coast of the United States (e.g. February 1958).

Hustead (1955) related the 2-h northeast wind movement at Norfolk (Virginia) to the storm surge. Miller (1957) made use of geostrophic winds and showed that maximum surges are associated with east–northeast winds. There is a lag of 12 h between the wind and the surge.

Pore (1964) studied 18 storm surges during the period 1956–61. For these 18 storms, there was a total of 1910 hourly observations available. Most of these storms passed over the southeastern United States and then moved offshore over the Atlantic Ocean. Maximum wind speeds varied from 22 to 50 knots (41–93 $km \cdot h^{-1}$). Three meteorological forcing terms were considered separately: (a) onshore component of the wind stress (which produces a setup), (b) alongshore component of the wind stress (which generates alongshore currents, which then are deflected to the right by the Coriolis force, and this creates an upward slope of the water surface toward the right), and (c) atmospheric pressure (inverse barometer effect).

An interesting result of this study is that the storm surge at Atlantic City is strongly dependent on the alongshore component of the wind. There appears to be little difference between the results obtained using linear wind stress and quadratic wind stress.

Pore (1965) studied extratropical cyclone generated storm surges in Chesapeake Bay. There were 11 storms during the period March 1954 to March 1961. The storms that passed to the north of Chesapeake Bay and caused a cold front (or a frontal system) to move across the bay were called type A storms. The storms that approached the bay from the south were referred to as type B storms. Type A storms usually generate significant

surges at Baltimore (in the northern part of Chesapeake Bay) but not at Hampton Roads (in the southern part). On the other hand, type B storms could generate significant surges at both locations.

Wang (1979) examined the response of the water level in Chesapeake Bay to the time scale of atmospheric forcing. For time scales longer than 7 d, the water levels in the bay were driven nonlocally by the coastal water levels. For periods between 4 and 7 d, the water level in the bay was driven both by the coastal sea level as well as the lateral component of the wind. For time scales of 1–3 d, the water level in the bay was driven by the longitudinal component of the wind.

Wasserman and Gilhousen (1976) examined the meteorological factors involved in beach erosion due to storms and storm surges. Severe erosion occurs under the following conditions: (1) an angle between 0 and 20° between the predominant wind direction and the orientation of the Long Island coastline (for the New Jersey coast this range is 20–40°), (2) a setup period in excess of 18 h during which the coastal winds are within 20° of the predominant wind direction, (3) at no time during this setup period the wind direction upstream (up to 550 km) varies by more than 20° from the coastal wind direction, and (4) during at least a portion of the setup period, the upwind surface pressure gradient is at least 4 mb·200 km^{-1}.

Saunders (1977) computed seasonal averages of wind stress over the eastern continental shelf of North America making use of about 1 million ship observations for the period 1941–72. He assumed a drag coefficient that increases with the wind speed from 1.0×10^{-3} at 5 $m \cdot s^{-1}$ wind speed to 2.3×10^{-3} at 25 $m \cdot s^{-1}$. Atmospheric stratification was found to have little effect. The stress is strongest in winter (1–15 dynes·cm^{-2}) and weakest in fall (0.25–0.5 dynes·cm^{-2}). In summer the stress is directed towards the northeast whereas in the other three seasons it is directed south and east. The wind stress generally increases with increasing latitude, but local maxima are found over the Gulf of Maine and the Gulf of St. Lawrence. Saunders (1977) attributed the local maxima and minima to cyclonic activity.

Hurricanes Affecting the United States

The term "hurricane" comes from the Spanish word "huracon," which probably originated from Maya and Carib Indian usage meaning evil spirit, storm god, or devil. A hurricane is an intense tropical storm with wind speeds in excess of 74 mi·h^{-1} (64 knots or 33 $m \cdot s^{-1}$). In the twentieth century, hurricanes originating in the Atlantic Ocean, Caribbean Sea, and the Gulf of Mexico caused about 45 000 deaths (13 000 in the United States). About 90% of the deaths were due to drowning in the storm surge. In the twentieth century, damage in the United States resulting from hurricanes exceeded $12 billion.

There appears to be no definite periodic cycle for hurricanes. During the 1940's Florida took the brunt, during the 1950's the east coast of the United States was mostly affected, and during the 1960's and 1970's most damage occurred along the coast of the Gulf of Mexico. There is some indication in the early 1980's that the same trend as in the 1940's and 1950's may occur (Owen 1980b).

In the North Atlantic Ocean, from June through November, some 100 disturbances develop every year. Of these, about five to six intensify into hurricanes. About 70% of these storms originate near the west coast of Africa and are referred to as Cape Verde storms. Locations were shown earlier (Fig. 1.14) at which Atlantic tropical storms reached hurricane intensity during the period 1901–63.

TABLE 6.58. The Saffir–Simpson hurricane damage potential scale. (Simpson and Riehl 1981)

Scale No.	Central pressure (mb)	Wind speed ($km \cdot h^{-1}$)	Storm surge amplitude (m)	Damage
1	≥980	119–153	1.22–1.52	Minimal
2	965–979	155–177	1.83–2.44	Moderate
3	945–964	179–209	2.74–3.66	Extensive
4	920–944	211–249	3.96–5.49	Extreme
5	<920	>2.49	>5.49	Catastrophic

In the 1960's there was a great improvement in forecasting tropical cyclones. However, this rapid progress did not continue into the 1970's although computer and satellite technology improved (Chang 1981). The lack of substantial progress has been attributed to the imprecise knowledge of the initial conditions for the numerical models. According to Hovermale and Livezey (1978), for a 36- to 48-h forecast, the error in the track prediction over the oceans (where data is scarce) is three times the error at coastal stations. Not everybody agrees with this evaluation. The EOS Bulletin (Vol. 61, No. 28, July 15, 1980, p. 538) mentioned that a NOAA satellite that is 22 300 mi (35 680 km) out in space is locating Atlantic Ocean hurricanes with an average accuracy of about 17 nautical miles and is pinpointing their intensity within an average of 10 knots. For a recent summary of the status of operational prediction of tropical cyclone motion over the North Atlantic Ocean, see Neumann and Pelissier (1981a). These authors concluded that none of the seven models (five statistical and two dynamical) that are in use at the National Hurricane Center in Miami can be singled out as superior to the others in every respect. One disappointing aspect is that one cannot combine the good points from all these models into a single model.

Hurricanes are classified according to the Saffir–Simpson scale (named after Herbert Saffir, a consulting engineer, and Dr. R. H. Simpson, former director of the National Hurricane Center in Miami), which is an intensity scale based on the central pressure, wind speed, amplitude of the storm surge, and the resulting damage. This scale is illustrated in abbreviated form in Table 6.58. More details about this scale can be found in Simpson and Riehl (1981). Note that in the twentieth century, only three storms affecting the United States are given the highest rank (5) on this scale. These are the Labour Day storm of 1935, Hurricane Camille of 1969, and Hurricane Allen of 1980.

HURRICANE STATISTICS FOR THE UNITED STATES

Some of the most disastrous hurricanes of the twentieth century in the United States and the damage are listed in Table 1.1. Bruun et al. (1962) gave a list of major hurricanes affecting Florida during the period 1900–60. In this table there are 40 entries. The inverted barometer effect could be quite significant in the generation of storm surges here. For each inch (of mercury) of reduction of the central pressure of the hurricane (1 in. = 2.54 cm) the corresponding hydrostatic water head is 14 in. (Bretschneider 1967). For the storm of September 2, 1935, at Lower Matecumbe Key in Florida, the lowest central pressure was 26.35 in.Hg (892.3 mb). Taking the normal sea level pressure as 29.92 in.Hg (1013.2 mb) gives a 4.1-ft (1.3 m) rise in water level. Similar inverted barometer effects could be noticed in typhoons, also. For the typhoon of August 18, 1927, the central pressure some 460 mi (740 km) east of Luzon (Philippines) was 26.18 in. (886.6 mb)

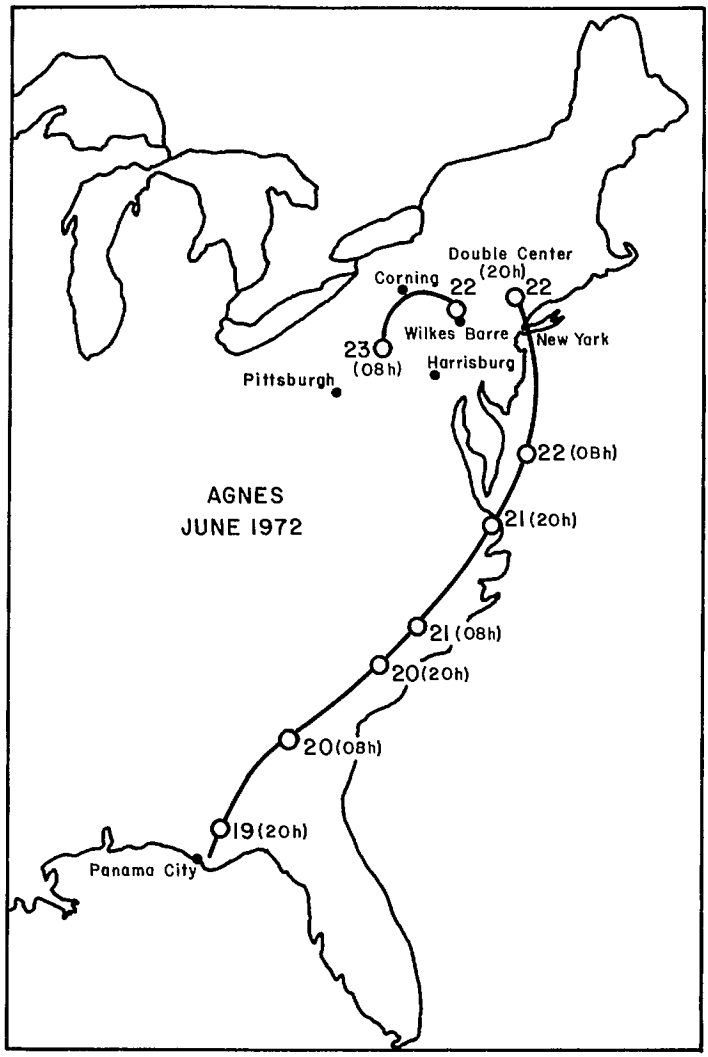

FIG. 6.86. Track of Hurricane Agnes of June 1972.

giving rise to a surge amplitude of 4.3 ft (1.31 m).

Friedman (1975) gave a list of hurricane-generated storm surges, deaths, and damage along the Gulf of Mexico coast and the southern part of the east coast of the United States. For the period 1873–1973 there were 90 entries in this table. Price (1956) discussed the hurricanes that affected the Texas coast from Galveston to Rio Grande. During the period 1830–1950, a total of 54 hurricanes were noted.

Simpson and Riehl (1981) discussed tornadoes generated by hurricanes. The damage potential from these tornadoes is much smaller than that from the hurricane itself. Hurricane tornadoes occur to varying degrees along the Gulf of Mexico coast, in Florida, and along the southern part of the east coast of the United States. They stated (p. 218):

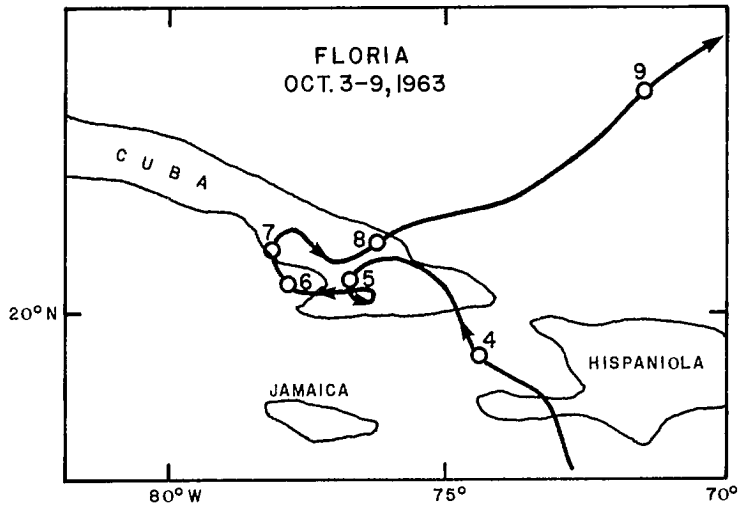

FIG. 6.87. Example of an unusual track of a hurricane (Hurricane Flora of October 1963). Numbers indicate the dates. (Simpson and Riehl 1981)

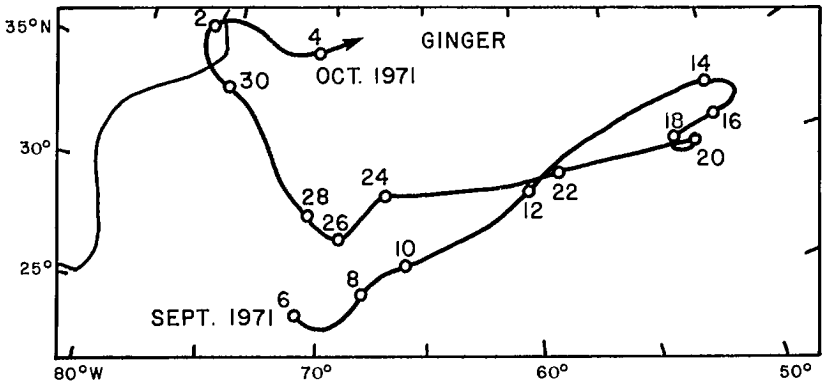

FIG. 6.88. Another example of an unusual hurricane track (Hurricane Ginger of October 1971). Numbers indicate the dates. (Simpson and Riehl 1981)

> Hurricane tornadoes develop in the spiral rain bands, mostly in the right-front quadrant outside the areas of sustained hurricane or gale force winds.... Although some hurricanes produce families of tornadoes, the individual event is a small, rope-type vortex similar to a water spout. It has a short path length, maximum wind speeds are usually less than 50 meters per second, and pressure drops in the funnels are believed to be more than about 20 mb.

As pointed out earlier, hurricanes usually travel from east toward west or northwest with a possible recurvature towards northeast or east. However, sometimes they could have a predominantly northward motion. The track of Hurricane Agnes of June 1972 is shown in Fig. 6.86. An interesting feature of this hurricane is that during June 22–23, 1972, it exhibited a double center. Two rather unusual tracks of hurricanes (Hurricane Flora of October 1963 and Hurricane Ginger of September 1971) are illustrated in Fig. 6.87 and 6.88, respectively.

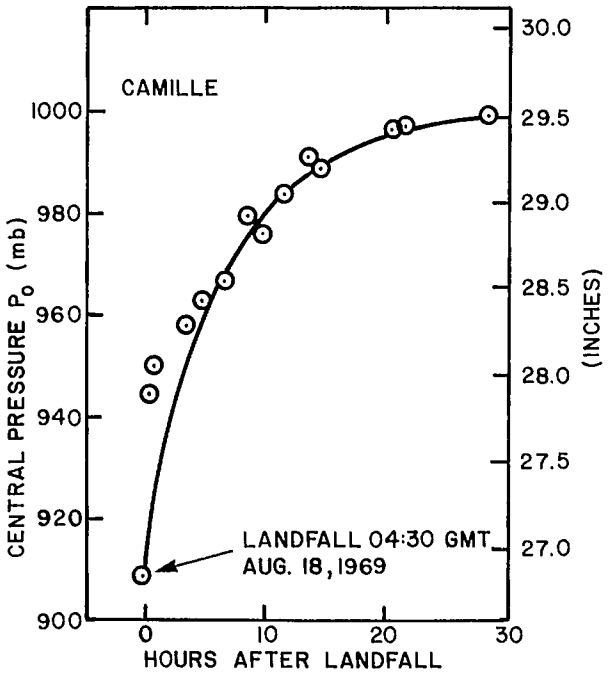

FIG. 6.89. Increase of central pressure P_0 with time for Hurricane Camille (August 1969) after she crossed the Mississippi coast. (Schwerdt 1978)

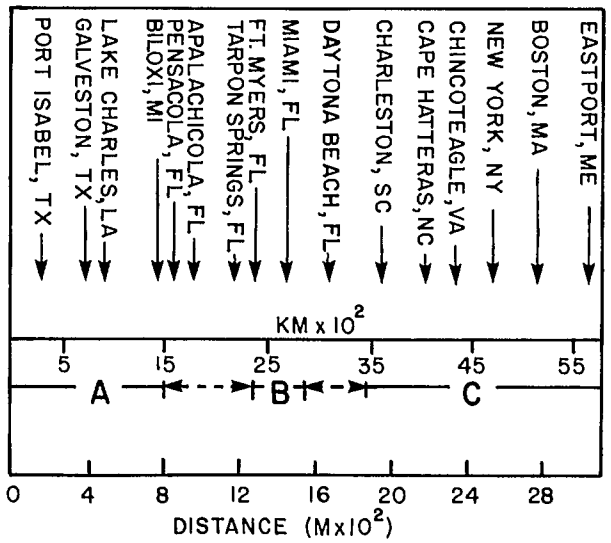

FIG. 6.90. Coastal regions of applicability for adjustment factor curves in Fig. 6.91 for wind speed (1 nautical mile (M) = 1.852 km). (Schwerdt 1978)

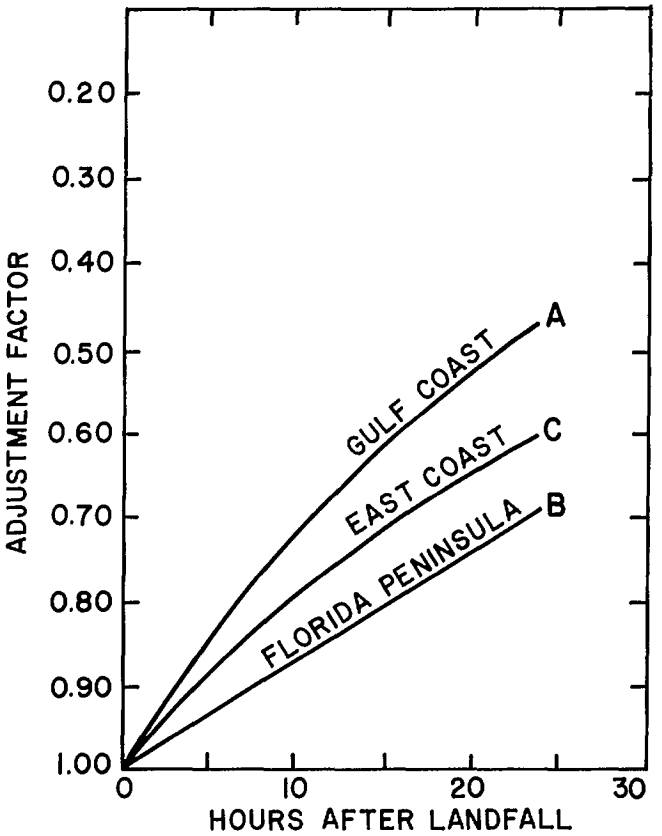

FIG. 6.91. Smoothed adjustment factor curves for reducing hurricane wind speeds when the center is over land. (Schwerdt 1978)

Baynton (1979) argued that the present hurricane detection radars on the United States coast are outdated and he suggested deployment of Doppler radars, which will provide, in real time, colored displays of the wind field in a hurricane.

HURRICANE MOVEMENT OVER OCEAN AND LAND

Earlier, it was seen that hurricanes are born primarily over oceanic areas and they weaken when they travel over the continents. A numerical model simulation by Chang and Madala (1980) showed that hurricanes appear to move into areas of higher sea surface temperature (SST) if the SST gradient is perpendicular to the mean ambient flow vector (MAFV). An area of warmer SST located to the right of MAFV is more favorable for hurricane intensification than an area situated to the left.

Schwerdt (1978) studied the reduction of the wind field when a hurricane moves from the ocean to over land. Once a hurricane crosses the coast from the ocean to the land its central pressure starts increasing and the wind fields start decreasing, and this so-called filling process is most pronounced in the inner portion of the hurricane.

According to Palmén and Newton (1969), filling occurs because the heat flux from

the land is negligible, which causes a reduction of the excess temperature of the hurricane core. Consequently, the kinetic energy decreases. Bergeron (1954) showed that a reduction in the equivalent potential temperature of the ascending air in the core leads to the filling process. Miller (1963) showed that surface friction plays a minor role in the filling process.

The increase of central pressure of Hurricane Camille (August 1969) after she crossed the Mississippi coast from the ocean is shown in Fig. 6.89. Similar increases have been noted for other hurricanes. However, there is little change in the peripheral pressure of a hurricane after it crosses over to land. Schwerdt (1978) classified the hurricanes affecting the east and Gulf of Mexico coasts of the United States (as shown in Fig. 6.90). Category C extends to the Canadian border and category A extends to the Mexican border.

The adjustment factor curves for reducing hurricane wind speeds when the center is over the land are shown in Fig. 6.91. The following equation holds for the curves for categories A and C:

$$W_l = W_c e^{(\alpha t + \beta t^2)} \tag{6.125}$$

where W_l is the maximum frictionless overland wind speed at some specific time after landfall, W_c is the maximum overwater wind speed at the time of landfall, t is time, and α and β are coefficients. For category A (i.e. for the hurricanes landfalling on the Gulf coast from Mississippi westward and up to the Mexican border), Schwerdt (1978) gave

$$\alpha = -0.035$$

$$\beta = 0.00013$$

For category C (i.e. the east coast of the United States north of Savannah, Georgia, up to the Canadian border)

$$\alpha = -0.026$$

$$\beta = 0.00018$$

For category B (i.e. Florida coast south of 27°N) the relationship is

$$W_l = W_c(1.0 - 0.013t) \tag{6.126}$$

Hurricanes of category B showed a somewhat different behavior from those of A and C. Whereas in categories A and C, intense hurricanes have greater filling rates, in category B, intense hurricanes tend to fill slowly. For other related works on storm modifications, see Jelesnianski and Taylor (1973), Jelesnianski and Barrientos (1975), and Simpson and Riehl (1981). Some characteristics of landfall hurricanes in the United States are listed in Table 6.59.

Hurricane Wind and Pressure Field Relationships

On a large-scale weather chart, the surface pressure field of a hurricane looks almost circular (see Fig. 6.92). The streamlines for the surface flow of a hurricane are shown in Fig. 6.93. One can see the spiraling inflow. The isotachs of wind speed at the surface for an intense hurricane are shown in Fig. 6.94. The radial profiles of wind speed for a tropical storm, a minimal hurricane, a moderate hurricane, and a maximum (intense) hurricane are illustrated in Fig. 6.95. The tangential wind speed (averaged around the hurricane) is plotted logarithmically against the radius for Hurricane Anita of September 1977 (Fig.

TABLE 6.59. Characteristics of landfall hurricanes that brought a sustained hurricane force wind to a 160-km strike area on the central Texas coast during the period 1900–78. (Ho et al. 1975)

Date	Minimum pressure, P_0 (mb)	Radius of maximum winds, R (km)	Approach speed, C (km·h^{-1})
Sept. 9, 1900	936	22.5	18.5
July 21, 1909	959	30.6	22.2
Aug. 17, 1915	949	46.7	20.4
June 22, 1921	954	27.4	20.4
June 28, 1929	969	20.9	27.8
Aug. 14, 1932	942	19.3	27.8
Sept. 23, 1941	959	33.8	24.1
Aug. 30, 1942	951	29.0	25.9
Aug. 27, 1945	968	29.0	7.4
Oct. 4, 1949	963	32.2	20.4
Sept. 11, 1961	931	32.2	11.1

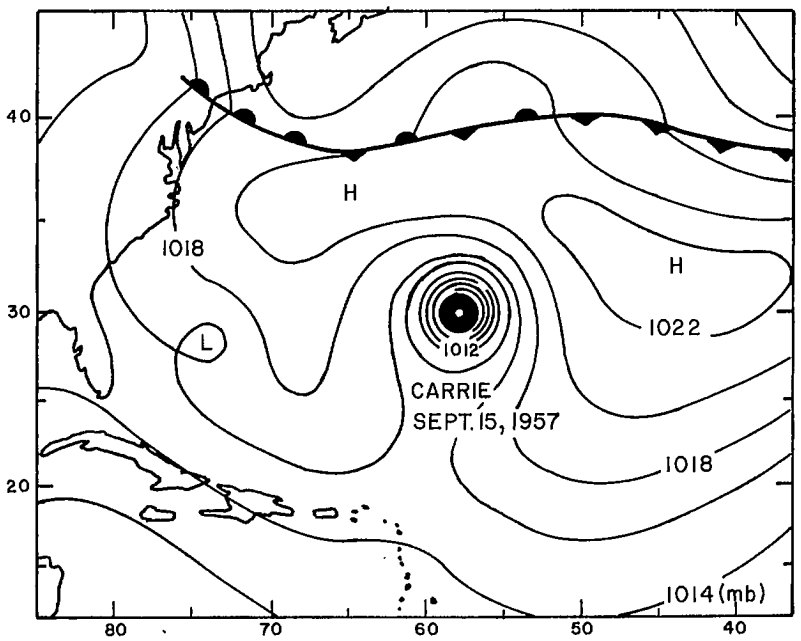

FIG. 6.92. Surface weather chart on September 15, 1957, showing Hurricane Carrie. (Simpson and Riehl 1981)

6.96). The central pressure versus maximum sustained wind speed for Atlantic hurricanes is shown in Fig. 6.97.

Simpson and Riehl (1981) defined the habitation layer as the lowest 500 m of the atmosphere. They considered the balance of forces in this layer at a coastal station as a hurricane approaches the station. The centrifugal force C_e and the Coriolis force C_0 are directed outwards, whereas the pressure gradient force P_g and the frictional force F_s are

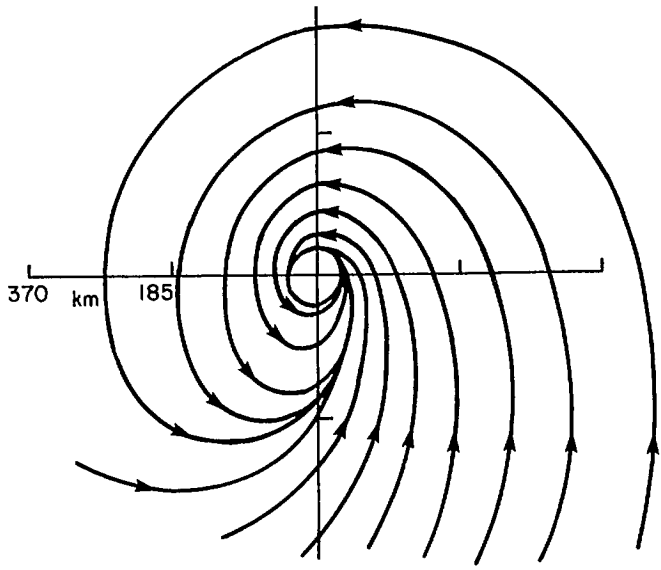

FIG. 6.93. Streamlines showing the circulation in a hurricane. (Simpson and Riehl 1981)

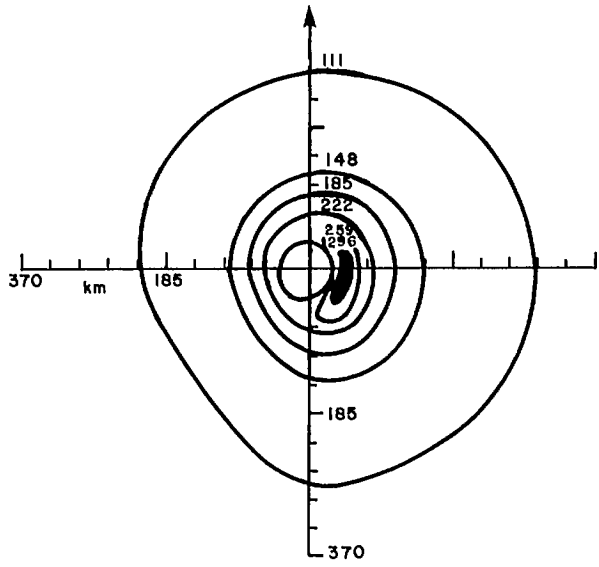

FIG. 6.94. Isotachs of surface wind speed (knots) in an intense hurricane. Black area shows the region of strongest winds (to the right of the eye) (1 knot = 1.852 km·h^{-1}). (Simpson and Riehl 1981)

directed inward (perpendicular to the streamline). This leads to an acceleration of the tangential wind component as the air spirals inward.

In a hurricane, mainly the tangential (rotational) component of the wind increases

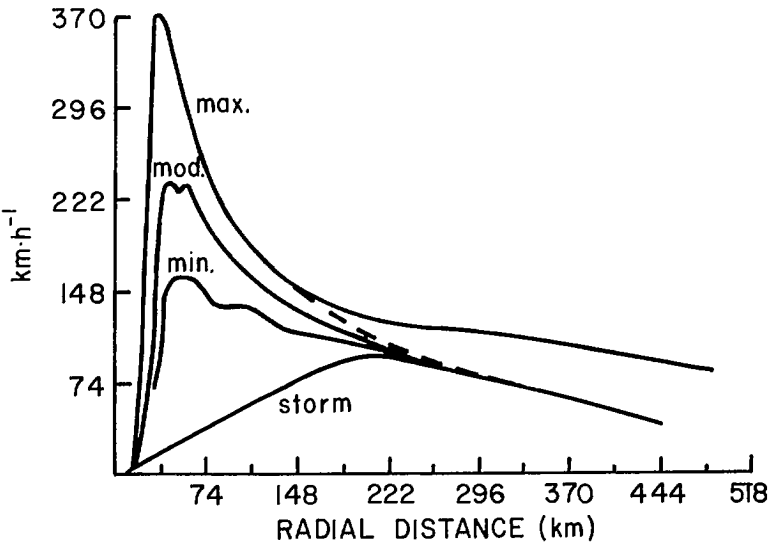

FIG. 6.95. Model of radial profiles of wind speed for three hurricane intensities and for a tropical storm. (Simpson and Riehl 1981)

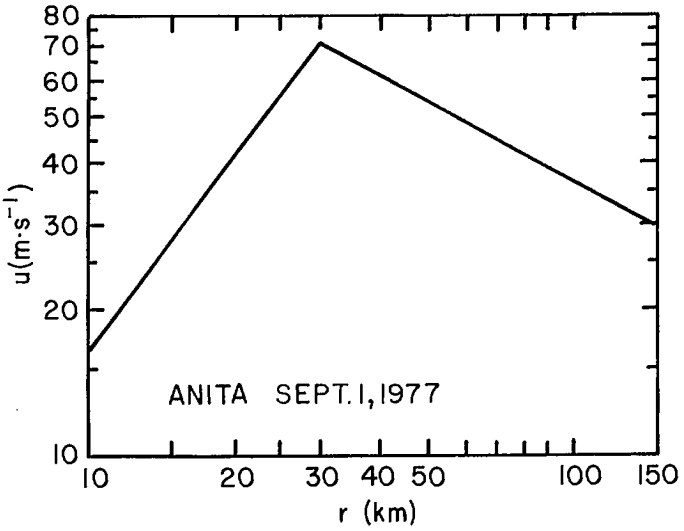

FIG. 6.96. Tangential wind speed (u) averaged around Hurricane Anita (September 1, 1977) and plotted logarithmically against the radius (r). (Simpson and Riehl 1981)

from the periphery of the vortex to the ring of maximum winds (RMW). According to Simpson and Riehl (1981) this ring has a radius of less than 35 km:

$$u = V \cos \beta \tag{6.127}$$

where V is the wind speed and β is the angle made by the streamlines with the isobars.

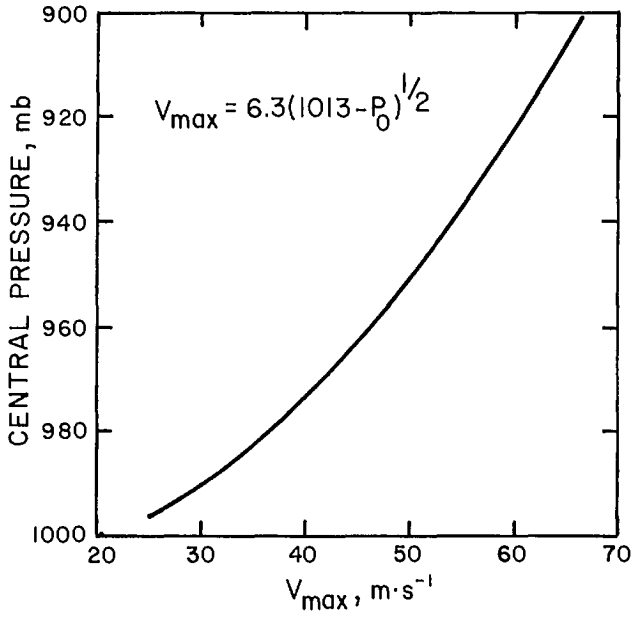

FIG. 6.97. Maximum sustained wind speed versus central pressure for Atlantic hurricanes. (Simpson and Riehl 1981)

Neglecting losses due to friction, the angular momentum Ω per unit mass supplied by the surroundings to the hurricane vortex is

$$\Omega = ur + \frac{fr^2}{2} \tag{6.128}$$

where f is the Coriolis parameter, r is the radial distance from the observation point to the center of the vortex, and u is the tangential wind speed. The first term on the right side of eq. 6.128 gives the angular momentum relative to the surface of the earth whereas the second term represents the angular momentum due to the earth's rotation.

From eq. 6.127 and 6.128

$$u = \frac{\Omega}{r} - \frac{fr}{2} \tag{6.129}$$

As the angular momentum is transported inside, the average value of u increases as can be seen from eq. 6.129 (ignoring frictional effects). The maximum value of u occurs for cyclostrophic balance (i.e. when the pressure gradient force balances the centrifugal plus Coriolis forces) and when β of eq. 6.127 tends to zero.

In principle, the increase of u with decreasing r would create centrifugal forces that would far exceed the pressure gradient forces, and the air should spiral outward towards higher pressure. However, surface friction reduces the value of Ω steadily and this outward spiraling tendency is offset. Hence, surface friction plays a dual role. First of all, it permits a crossing angle between the streamlines and isobars so that air from the surroundings is drawn towards the vortex center by pressure gradient forces. Second, it reduces the imported angular momentum so that the centrifugal forces cannot dominate the pressure gradient forces and a radius of maximum winds can develop near the center. In this ring,

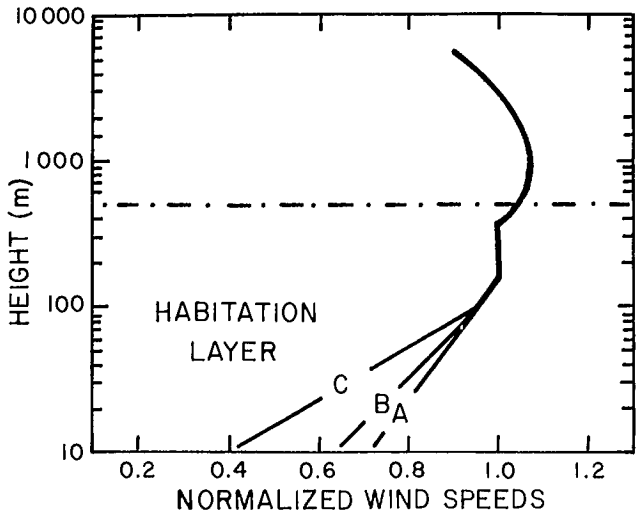

FIG. 6.98. Model of wind speed variation with height in tropical cyclones. Speeds are normalized with reference to wind speeds measured by aircraft in the 150- to 300-m layer. A, over water; B, over land; C, profile for 1/7-power law. (Bates 1977)

as the air (drawn from the surroundings) ascends, a convective eye wall is created, and this leads to the central warm core that maintains surface pressure gradients. Of course, friction also is responsible for the creation of gusts in the wind field.

From the edge of the radius of maximum winds to the center of the eye, wind decreases monotonically to almost zero. The point of zero wind speed is (theoretically) displaced to the left of the track of lowest pressure at a distance that is proportional to the speed with which the vortex moves.

Usually, the combined Rankine vortex model is used to model the average horizontal wind structure in a hurricane. The area inside the RMW is in solid rotation, i.e. u/r is constant. Outside the RMW the wind speed decreases exponentially as

$$(6.130) \quad u = \frac{\text{constant}}{r^x}$$

For a Rankine vortex, $x = 1$. However, for a hurricane, $0.4 < x < 0.8$.

Above the first few hundred metres, the strongest winds of a hurricane do not vary much up to 4–5 km of height. The wind speed variation with height in tropical cyclones is shown in Fig. 6.98.

The international standard for sustained winds is the average speed for a 10-min period. In the United States the sustained wind is a 1-min average. For extreme winds in the United States the unit of measurement is the fastest mile (the highest speed at which 1 mi of wind passes the anemometer).

Wilson (1958) considered hurricane wind and pressure fields, particularly with reference to application for computing wind waves. His period of study was 1900–49 (the hurricanes studied are listed in Table 5.16). Let R be the radius of maximum winds and let p_0 and p_n be the minimum central pressure and the ambient pressure, respectively, at a great distance from the eye. Then, let

(6.131) $\Delta p \equiv p_n - p_0$

and

(6.132) $E \equiv (\Delta p)R$

Here, E is referred to as the wave energy index (Reid 1955).

Myers (1954) gave the following formula for determining the rate of change of pressure p with radial distance r from the hurricane center:

(6.133) $$\frac{dp}{dr} = (\Delta p)\frac{R}{r^2}e^{-R/r}$$

Integration of eq. 6.133 gives

(6.134) $p = p_0 + (p_n - p_0)e^{-R/r}$

To determine the surface wind field from the surface pressure field, the cyclonic gradient flow equation for a moving cyclone (Holmboe 1945) was used:

(6.135) $$K_{hs}U^2 + \left(2\omega \sin \phi + \frac{\partial \psi}{\partial t}\right)U - \frac{1}{\rho}\frac{\partial p}{\partial r} = 0$$

where K_{hs} is the horizontal curvature of the streamlines, U is the horizontal wind velocity above the friction layer, ω is the angular velocity of the earth's rotation, ϕ is the latitude of the point under consideration, ψ is the horizontal angle of the wind vector (positive counterclockwise from the eastwest direction, say), ρ is air density, p is the pressure, and r is the radial distance to the point from the center of the hurricane.

If V is the speed of movement of the hurricane, then

(6.136) $$\frac{U^2}{r} + \frac{UV}{r}\sin\theta + 2\omega U \sin\phi = \frac{1}{\rho}\frac{\partial p}{\partial r}$$

where θ is the angle at the point under consideration. For large radial distances, eq. 6.136 reduces to the geostrophic wind relation

(6.137) $$U = U_g = \frac{1}{2\rho \sin \phi}\frac{\partial p}{\partial r}$$

However, close to the center of the hurricane, one must use the complete equation 6.136. Its solution for U will be designated by U_G and is referred to as the gradient wind:

(6.138) $U_G = U_c(\sqrt{\gamma^2 + 1} - \gamma)$

where the cyclostrophic wind U_c is defined by

(6.139) $$U_c = \sqrt{\frac{r}{\rho}\frac{\partial p}{\partial r}}$$

and the parameter γ is given by

(6.140) $$\gamma \equiv \frac{1}{2}\left(\frac{V \sin \theta}{U_c} + \frac{U_c}{U_G}\right)$$

Gilman and Myers (1958) gave the profiles of pressure variation from the center to a distance of 140 nautical miles (259 km) for five hurricanes (Fig. 6.99). Gradients up to 70 mb in 140 nautical miles have occurred. They also gave correction factors for the wind

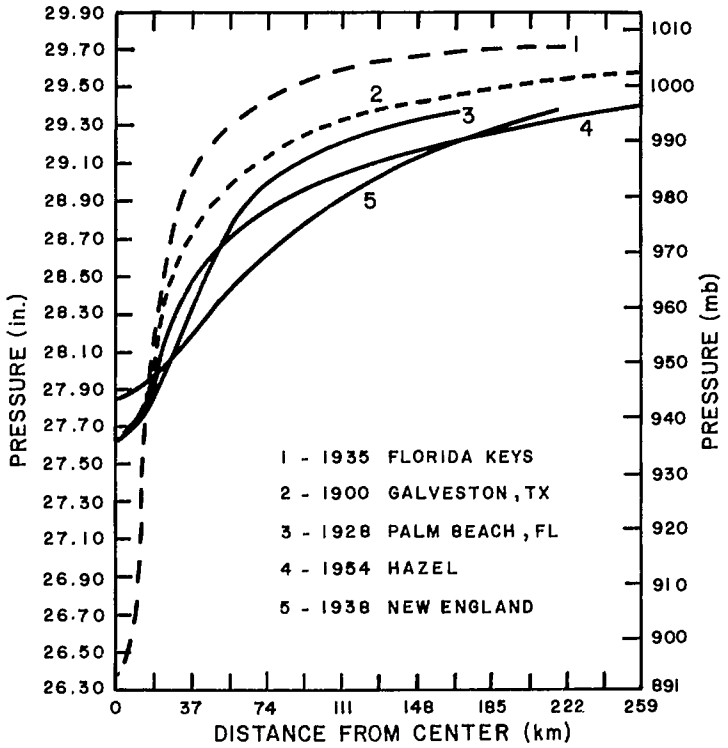

FIG. 6.99. Pressure profiles for five selected hurricanes affecting the east coast of the United States. (Gilman and Myers 1958)

fields for filling hurricanes. Taylor (1980) gave a plot of central pressure depression against the square of the wind speed for five different speeds of hurricane movement (Fig. 6.100). Ross (1979) compared computed and observed wind wave heights based on wind and pressure fields for five selected hurricanes (Table 6.60).

In the U.S. National Weather Service and in the U.S. Army Corps of Engineers, the ideas about Probable Maximum Hurricane (PMH) and Standard Project Hurricane (SPH) originated in the 1950's (e.g. Graham and Nunn 1959). The PMH is defined as a hypothetical hurricane having that combination of values of meteorological parameters that will make it the most severe that can probably occur at a particular coastal location. The SPH is defined as a hypothetical hurricane with the most severe combination of values of hurricane parameters reasonably characteristic of a specified geographic location, thus excluding extremely rare combinations (Schwerdt 1976; Mogolesko 1976).

In determing PMH and SPH, the following meteorological parameters of the hurricane are used: central pressure p_0, peripheral pressure p_W, radius R of maximum winds, forward speed T of movement, and direction θ of movement. From p_0, p_W, R, and T the maximum gradient wind V_{gx} and the maximum winds V_x over water at distance R at a height of 10 m are given by

$$(6.141) \quad V_{gx} = K(p_W - p_0)^{1/2} - \frac{Rf}{2}$$

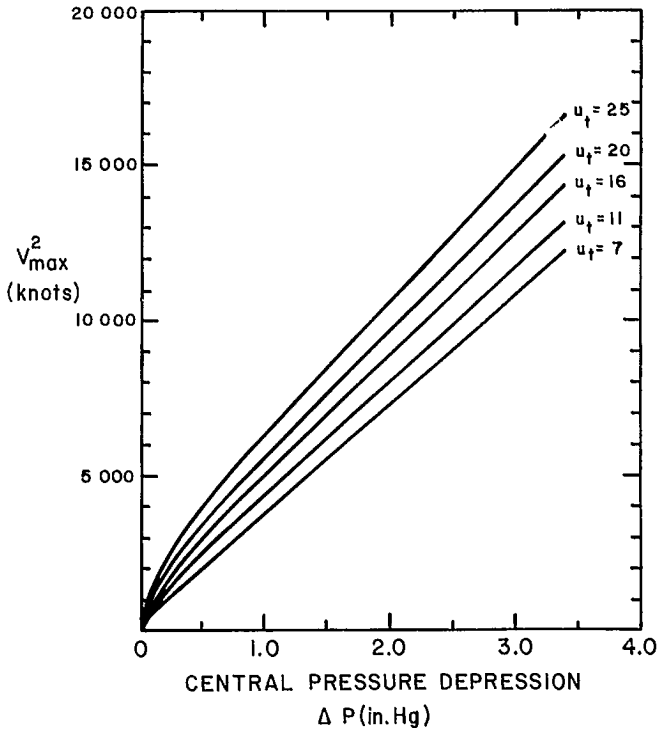

FIG. 6.100. Central pressure depression ΔP (inches of mercury) versus square of maximum wind speed (knots^2) for five different speeds (u_f) of movement of hurricane (knots) (1 in.Hg = 1013.3 mb; 1 knot = 1.852 km·h^{-1}). (Taylor 1980)

TABLE 6.60. Characteristics of selected hurricanes and computed and observed significant wave heights. ΔP, difference between the peripheral pressure and the central pressure of the hurricane (mb); V_f, forward velocity of the hurricane (km·h^{-1}); R, radius of maximum winds (km); U, wind velocity at a height of 10 m (m·s^{-1}); H, significant wave height (m). (Ross 1979)

				U		Wave height	
Hurricane	ΔP	R	V_f	Observed	Calculated	Observed	Calculated
Anita	41	37.0	7.4	34.0	29.9	6.5	6.7
Ava	100	27.8	22.2	—	48.3	—	13.3
Belle	58	22.2	24.1	33.0	37.8	7.8	8.5
Camille	105	27.8	22.2	51.7	49.4	13.5	13.6
Eloise	41	27.8	27.8	35.8	32.8	8.7	7.2

where K is a constant that depends on the density of air and f is the Coriolis parameter (latitudinal dependency permitted) and

$$(6.142) \quad V_x = 0.9V_{gx} + \frac{Rr}{(R^2 + r^2)}T = 0.9V_{gx} + \frac{T}{2}$$

where r is the distance from the hurricane center.

Jelesnianski (1965) computed storm surges due to hurricanes on a continental shelf. He assumed the storm to be circular and symmetric with maximum winds V_R at a distance R from the center. Then, in general, he took the wind speed V at any distance r as follows:

$$V = \begin{cases} V_R\left(\frac{r}{R}\right)^{3/2} & \text{for } 0 \leq r \leq R \\ V_R\left(\frac{R}{r}\right)^{1/2} & \text{for } r \geq R \end{cases} \tag{6.143}$$

For a tropical storm of August 1949 the observed wind field compared quite well with that computed from eq. 6.143.

A quadratic law was assumed for the wind stress:

$$\begin{aligned} \tau &= K|V|V \\ K &= \frac{k\rho_a}{\rho} \end{aligned} \tag{6.144}$$

where k is a stress factor, ρ_a is the density of the air, and ρ is the density of water. Jelesnianski (1965) referred to the angle made by the wind with the isobars as the "ingress angle," which is a function of space and time. Let ϕ and θ be the ingress angle and the polar angle, respectively (see Fig. 17 of Jelesnianski 1965). Then, the x and y components of the wind stress are

$$\begin{aligned} \tau_x &= -KV^2 \sin(\theta + \phi) \\ \tau_y &= KV^2 \cos(\theta + \phi) \end{aligned} \tag{6.145}$$

From eq. 6.143–6.145

$$\begin{aligned} &\tau_x = KV_R^2 \frac{r^2}{R^3} A \quad \text{and} \quad \tau_y = KV_R^2 \frac{r^2}{R^3} B \quad \text{for } 0 \leq r \leq R \\ &\tau_x = KV_R^2 \frac{R}{r^2} A \quad \text{and} \quad \tau_y = KR_r^2 \frac{R}{r^2} B \quad \text{for } r \geq R \end{aligned} \tag{6.146}$$

where

$$\begin{aligned} A &\equiv -y \cos\phi - x \sin\phi \\ B &\equiv x \cos\phi - y \sin\phi \end{aligned}$$

Jelesnianski (1965) added an additional wind velocity V_{S_M} to include the effect of movement of the storm. This velocity V_{S_M} is determined from

$$V_{S_M} = \begin{cases} \frac{r}{R+r}(U_{S_i} + V_{S_j}) & \text{for } 0 \leq r \leq R \\ \frac{R}{R+r}(U_{S_i} + V_{S_j}) & \text{for } r \geq R \end{cases} \tag{6.147}$$

where i and j are unit vectors along the x- and y-axes and U_S and V_S are the x and y components of motion of the hurricane. Finally, the surface wind can be written as

$$V^* = V + V_{S_M} \tag{6.148}$$

To obtain the wind stress, replace V in eq. 6.144 with V^*. The wind velocity corrected for the ingress angle ϕ is

$$V = \begin{cases} V_R \left(\frac{r}{R}\right)^{3/2} \frac{1}{r}(Ai + Bj) & \text{for } 0 \leq r \leq R \\ V_R \left(\frac{R}{r}\right)^{1/2} \frac{1}{r}(Ai + Bj) & \text{for } r \geq R \end{cases} \tag{6.149}$$

The final forms of the wind stress components are obtained by substituting eq. 6.147 and 6.149 into eq. 6.148.

To allow for the growth of the meteorological forcing terms in time, the wind stress was multiplied by the following time factors:

$$F(t) = \begin{cases} 0 \text{ for } t \leq 0 \\ \frac{1}{2}\left(1 - \cos \frac{\pi t}{T}\right) \text{ for } 0 \leq t \leq T \\ 1 \text{ for } t \geq T \end{cases} \tag{6.150}$$

where T is the growth time.

Jelesnianski (1965) included approximately the effect of surface friction on the pressure gradient and wrote

$$p_\infty - p_0 = \frac{4}{3}\rho_a \left(\frac{V_R}{\gamma}\right) \tag{6.151}$$

where p_∞ is the ambient pressure, p_0 is the central pressure, ρ_a is the air density, V_R is the maximum wind (at radius R), and γ is given by

$$\gamma \equiv 2V_R \sqrt{\frac{\rho_a}{3(p_\infty - p_0)}} \tag{6.152}$$

Jelesnianski (1967) computed storm surges on the east coast of the United States originating from hurricanes, with particular application to surges at Atlantic City. He gave a nomogram incorporating the storm parameters such as the maximum wind speed, pressure drop, radius of maximum winds, and the inflow angle (Fig. 6.101). Wanstrath (1977a, 1977b) made use of Jelesnianski's (1965) model for the wind field in his curvilinear grid storm surge model.

Wilson (1959) computed storm surges in New York Bay originating from hurricanes. He used the following form for the wind stress:

$$\tau_S = \rho_a(A + BU + CU^2) \tag{6.153}$$

where ρ_a is the density of air, U is the wind speed, and A, B, and C are constants. He gave a table summarizing the drag coefficients C (for various wind speeds) from 30 different speeds during the period 1905–59. Noble and Hendrickson (1974) gave the following values:

$$A = 1.0 \times 10^{-3} \text{ to } 1.1 \times 10^{-3}$$

$$B = 1.2 \times 10^{-3} \text{ to } 1.8 \times 10^{-3}$$

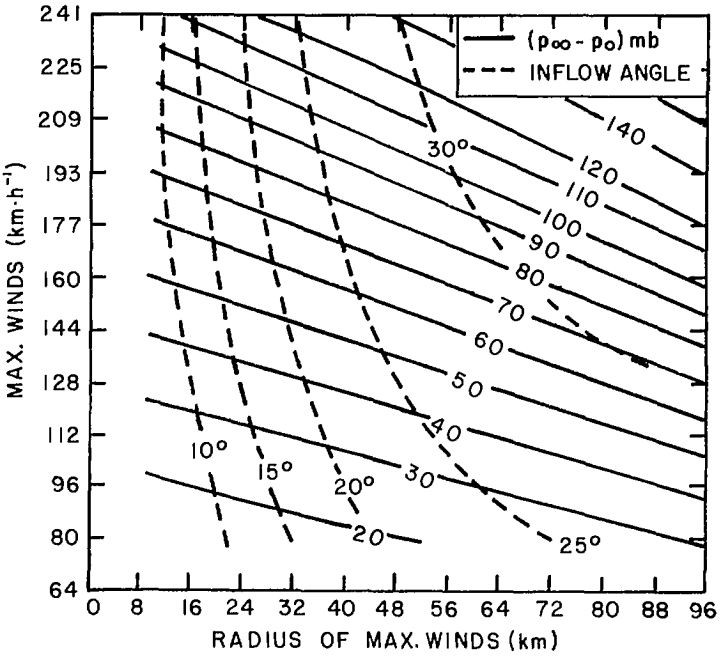

FIG. 6.101. Nomogram relating three model storm parameters: stationary storm maximum wind, radius of maximum winds, and pressure drop. The inflow angle occurs 161 km from the storm centre, which is assumed to be at 30°N. (Jelesnianski 1965)

Pagenkopf and Pearce (1975) used a formulation somewhat similar to that of Wilson (1959). They wrote for the surface pressure field

$$p_\eta = p_0 + \Delta p e^{-R_{\max}/r} \tag{6.154}$$

and the gradient wind U_G is taken as

$$U_G = U_C(\sqrt{\gamma^2 + 1} - \gamma) \tag{6.155}$$

where the cyclostrophic wind U_C is written as

$$U_C = \sqrt{\frac{\Delta p}{\rho_a}\frac{R_{\max}}{r} - e^{R_{\max}/r}} \tag{6.156}$$

with

$$\gamma \equiv \frac{1}{2}\left(\frac{V'}{U_C} + \frac{U_C}{U_G}\right) \tag{6.157}$$

where

$$V' = V_f \sin\theta$$

V_f being the forward velocity of the storm.

Finally, they wrote for the wind speed U at 10 m of height

TABLE 6.61. Deflection angles (i.e. the angle between the true wind direction and a tangent to a circle whose center is the storm center) for the standard project hurricane (SPH) and the probable maximum hurricane (PMH). (Pagenkopf and Pearce 1975)

Radius	Deflection angle (degrees) for SPH	PMH
Center to region of maximum winds, R_{max}	20	0–10
R_{max} to $1.2R_{max}$	20–25	10–25
$1.2R_{max}$ and beyond to outer limit of hurricane	25	25

$$(6.158)\quad U = \frac{r}{2}\left(-2\Omega(\sin\phi)(0.865) - V_f \sin(\theta+\beta) + \left\{\left[\frac{V_f}{r}\sin(\theta+\beta) + 2\Omega(\sin\phi)\right] + \frac{\Delta p}{\rho_a}\frac{R_{max}}{r}e^{-R_{max}/r}\right\}^{1/2} 0.865\right)$$

where the angles θ and β are shown in Fig. 3.8 of Pagenkopf and Pearce (1975). The factor 0.865 is a reduction factor to allow for surface friction. Here, ϕ is the latitude and Ω is the angular velocity of the earth's rotation.

For the wind stress itself, these authors wrote

$$\tau_x = \rho K|U|U_x$$
$$\tau_y = \rho K|U|U_y$$

where

$$U = \sqrt{U_x^2 + U_y^2}$$

and

$$(6.159)\quad K = \begin{cases} K_1 \text{ for } U < U_{cr} \\ K_1 + K_2\left(1 - \dfrac{U_{cr}}{U}\right)^2 \text{ for } U \geq U_{cr} \end{cases}$$

where

$$K_1 = 1.1 \times 10^{-6} \text{ to } 1.2 \times 10^{-6}$$
$$K_2 = 1.8 \times 10^{-6} \text{ to } 2.5 \times 10^{-6}$$
$$U_{cr} = 13\text{–}14 \text{ knots } (22\text{–}23.6 \text{ ft}\cdot\text{s}^{-1} \text{ or } 24.1\text{–}25.9 \text{ km}\cdot\text{h}^{-1})$$

where cr = critical.

Pagenkopf and Pearce (1975) also made use of the SPH and PMH in their formulation. The deflection angles used by them are summarized in Table 6.61. Pearce (1972) also made use of a similar formulation (i.e. to that of Wilson 1957b) in his calculation of the storm surges due to Hurricane Camille of August 1969. Other storm surge studies in which some simple analytical forms for the meteorological factors in the hurricane are used are Sethuraman (1979) and Overland and Myers (1976).

Overland (1975) used the wind speed profile of the SPLASH model in his computation of storm surges in Apalachicola Bay, Florida. The maximum wind speed at a distance r from the hurricane center is given by

$$(6.160)\quad W_S(r) = \frac{2RrW_{S_{max}}}{R^2 + r^2}$$

where $W_{S_{max}}$ is the maximum wind speed and R is the radius of maximum winds. The following form was prescribed for the inflow angle:

$$(6.161)\quad \phi = \begin{cases} 0.2856\left(\frac{r}{R}\right)^3 \exp\left(-\frac{r}{R}\right) & \text{for } r < 4.4R \\ 0.2967 & \text{for } r > 4.4R \end{cases}$$

The surface pressure gradient was given the following form:

$$(6.162)\quad \frac{\partial p_a}{\partial r} = (p_\infty - p_0)\frac{R}{r^2}\exp\left(-\frac{R}{r}\right)$$

where p_∞ is the ambient surface pressure. The effect of the storm movement on the wind is taken into account by writing

$$(6.163)\quad \vec{W} = \vec{W}_S(r) + \frac{Rr\vec{V}_F}{R^2 + r^2}$$

where $\vec{V}_F$ is the forward speed of the hurricane and $\vec{W}$ is the composite wind velocity at any given location.

Patterson (1972) gave the following form for the wind field in a hurricane:

$$(6.164)\quad V = (A + B\rho + C\rho^2 + D\rho^3 + E\rho^4) \times \left\{0.865\left[73(\Delta p)^{1/2} - 0.575Rf\right] + \frac{V_f}{2}\right\} - \frac{V_f}{2}(1 - \cos\theta)$$

where r is the distance from the center (to the location where the wind speed V is needed) divided by the radius R of maximum winds, V_f is the forward speed of the storm, θ is the angle from the storm track, Δp is the barometric depression, and A, B, C, D, and E are empirical constants.

Tetra Tech. Inc. (1978) used the following form for the radial distribution of maximum winds (Collins and Viehman 1971):

$$(6.165)\quad V_{max}r = \begin{cases} \frac{\bar{V}_{max}}{C_1 r^k}\log_{10}\frac{R}{C_2 r^m} & \text{for } r > R \\ 1.5\bar{V}_{max}\left(\frac{r}{R} - \frac{1}{3}\right) & \text{for } R \geq r > \frac{R}{3} \\ 0 & \text{for } \frac{R}{3} \geq r \end{cases}$$

where $\bar{V}_{max}$ is the maximum wind speed in the hurricane and R is the distance from the center at which $\bar{V}_{max}$ occurs. The empirical constants k, C_1, C_2, and m have the following values: $k = -0.15128$, $C_1 = 3.354$, $C_2 = 1.265 \times 10^{-3}$, and $m = 1.607$. Here, the pressure field is in inches of mercury, R is in nautical miles, and the speed is in knots.

The maximum wind speed $\bar{V}_{max}$ is

$$(6.166)\quad \bar{V}_{max} = C[63.364(p_\infty - p_0)^{1/2} - 0.5fR] + V_f$$

where p_0 is the central pressure, p_∞ is the ambient pressure, and f is the Coriolis parameter. Observations show that $C = 0.885$ along the Gulf of Mexico and the Atlantic coasts (for the Florida peninsula, $C = 0.865$). Introducing azimuthal dependence of the wind field

$$V(r, \theta) = V_{\max}(r)\left[1 - \frac{0.5V_f(1 - \cos\theta)}{\bar{V}_{max}}\right] \tag{6.167}$$

Yeh and Chou (1979) used the following form for the wind stress:

$$\tau = \rho_a K W^2 \tag{6.168}$$

where the wind shear stress coefficient K is given the following values:

$$K = \begin{cases} 1.25 \times 10^{-6} \text{ for } W \leq W_1 \\ 1.25 \times 10^{-6} + 1.75 \times 10^{-6} \sin\dfrac{\pi}{2}\dfrac{(W - W_1)}{(W_2 - W_1)} \text{ for } W_1 < W < W_2 \\ 3.0 \times 10^{-6} \text{ for } W \geq W_2 \end{cases} \tag{6.169}$$

METEOROLOGICAL FORCING TERMS FOR ENCLOSED LAKES AND OTHER SMALLER SCALE WATER BODIES

Meteorological problems associated with storm surges in the Great Lakes were considered in section 7.1. Here, Lake Okeechobee in Florida will be used as an example of an enclosed lake. Schloemer (1954) examined the wind fields over Lake Okeechobee due to hurricanes. Some typical hurricane tracks that influence this lake are shown in Fig. 6.102. The dates of some important hurricanes during the period 1925–50 are listed in Table 6.62 together with the radius of maximum winds and the maximum wind speed and the pressure field. Ten different pressure profile formulas that were used by Schloemer (1954) are listed in Table 6.63. The data of Table 6.62 appear to fit the second equation of Table 6.63.

The average deflection angle appears to be uniform in the outer portion of the storm, and it decreased rapidly near the radius of maximum winds. The most common deflection angle was 35°. The hurricanes near Lake Okeechobee appear to move with a speed of about 16 $km \cdot h^{-1}$ prior to and during recurvature but much faster after recurvature. However, the maximum winds appear to occur before recurvature. Hurricane winds over Lake Okeechobee for a synthesized storm at 0, 1, and 2 h are shown in Fig. 6.103. Notice the changes in pattern that could occur even in a 1-h time interval.

Myers (1954) studied hurricanes in and near Lake Okeechobee for the period 1900–49. His table has 73 entries. For each case the central pressure, ambient pressure, maximum wind speed, and radius of maximum winds were listed. The wind field pattern for the hurricane of August 26–27, 1949, is illustrated in Fig. 6.104. In this diagram the following wind speeds are shown as a function of distance from the center: calculated cyclostrophic wind speed V_c, calculated gradient wind speed V_g, gust speeds over water V_{pW}, gust speeds off-land V_{pl}, 10-min average overwater wind speed V_0, 10-min average off-water wind speed V_W, and 10-min average off-land wind speed V_l. For details of the definitions of these winds see Myers (1954).

6.9 Meteorological Problems Associated with Storm Surges in Europe

Cyclones causing storm surges in the waters in and around Europe are mainly of the

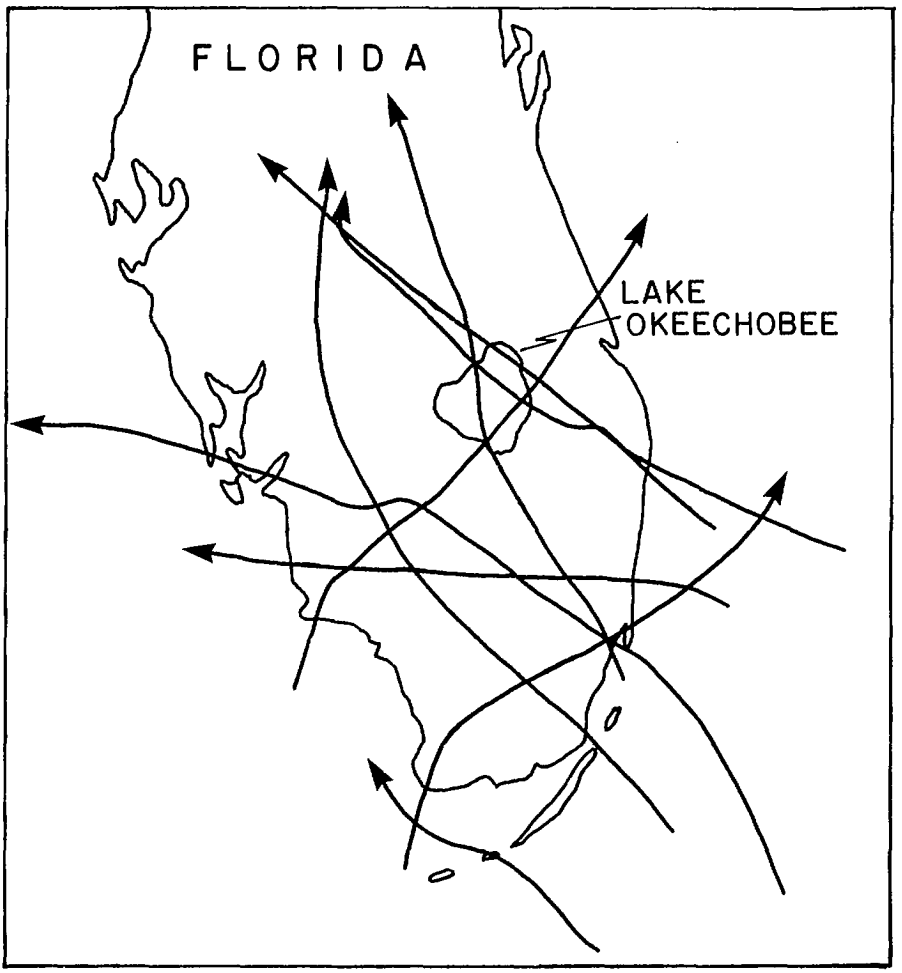

FIG. 6.102. Typical hurricane tracks over and near Lake Okeechobee, Florida. (Schloemer 1954)

TABLE 6.62. Hurricane data for Lake Okeechobee, Florida. (Based on Schloemer 1954)

Date of hurricane	Central pressure, P_0 (mb)	Ambient pressure, P_∞ (mb)	Maximum wind speed ($km \cdot h^{-1}$)	Radius of maximum winds (km)
Sept. 18, 1926	960	1009	199	28
Sept. 16–17, 1928	955	1015	185	43
Sept. 2–3, 1935	977	1008	163	27
Sept. 15–16, 1945	962	1010	185	24
Sept. 17, 1947	940	1010	180	37
Sept. 21–22, 1948	946	1012	140	30
Oct. 5, 1948	892	1010	142	51
Aug. 26–27, 1949	929	1006	140	37
Oct. 17–18, 1950	935	1005	117	21

TABLE 6.63. Ten different forms used to approximate $(P - P_0)/(P_\infty - P_0)$ in a hurricane. Here, P is the pressure at a distance r from the center, P_0 is the central pressure, and P_∞ is the ambient pressure. Parameters n, i, and j must be determined empirically. (Schloemer 1954)

(1)	$1 - e^{-nri}$	(6)	$\frac{2}{\pi} \arctan \frac{1}{nr^i}$
(2)	$e^{-n/ri}$	(7)	$\frac{2}{\pi} \operatorname{arc\,cot} \frac{1}{nr^i}$
(3)	$\frac{1}{1 + \frac{1}{nr^i}}$	(8)	$\frac{2}{\pi} \operatorname{arc\,sec} (1 + nr^i)$
(4)	$\frac{1}{\left(1 + \frac{1}{nr}\right)^j}$	(9)	$\frac{2}{\pi} \operatorname{arc\,cosec} \left(1 + \frac{1}{nr^i}\right)$
(5)	$\frac{1}{\left(1 + \frac{1}{nr^i}\right)^j}$	(10)	$\tanh nr^i$

extratropical type and the meteorological problems associated with these storms are somewhat simpler than those due to tropical cyclones. Most of the storm surges in Europe occur in the North Sea; other areas where surges occasionally occur are the Irish Sea, Adriatic Sea, Ligurian Sea, the coast of Portugal, the Baltic Sea, and the coasts of Norway and Sweden.

Early Storm Surges in the North Sea, Including the Thames Estuary

For convenience all surges that have occurred up to 1950 will be referred to here as "early surges." Doodson (1929) classified the storm surges in the Thames Estuary (based on tidal records at Southend and Dunbar) into three classes: class A, surges exceeding 6 ft (1.83 m); class B, surges in the range of 4–6 ft (1.22–1.83 m); class C, surges in the range of 2–4 ft (0.61–1.22 m). He classified the meteorological situations leading to these surges: type I, a cyclonic depression forms west of Scotland and travels to the Baltic, the winds veering from southwest to northwest or north; type II, a cyclonic depression travels over the Flemish Bight; type III, the winds are steady for a long time, the isobars running almost parallel to one another in a northwest direction over very large areas, with steady northwest winds; type IV, the southwesterly type corresponding roughly with type III but with steady southwest winds. Most of the major storm surges in the Thames Estuary are associated with type I meteorological situations.

Doodson (1929) and Dines (1929) listed the storm surges in the Thames Estuary during the period 1912–28. Table 6.64 is prepared based on these data. The surface isobaric patterns at two different times for the storm of December 30–31, 1921, are shown in Fig. 6.105.

One interesting aspect of the meteorological forcing terms is that whereas in most storm surge calculations, priority is given to the wind stress terms, in the early storm surge studies on the Thames Estuary, more importance is given to the atmospheric pressure gradient terms. Doodson (1929) expressed the surge as follows:

$$(6.170) \quad \zeta - \bar{\zeta} = K(B - \bar{B}) + \lambda(E - \bar{E}) + \mu(N - \bar{N})$$

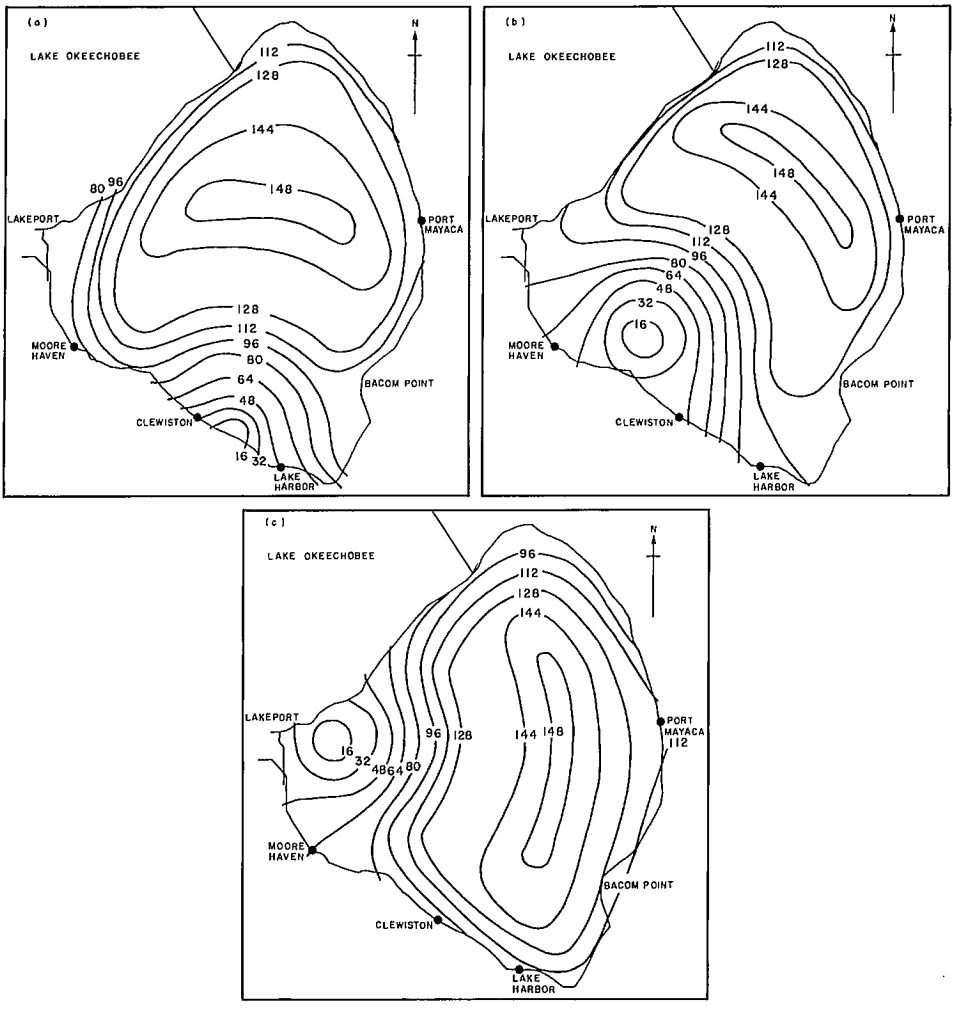

FIG. 6.103. Wind field (kilometres per hour) for a synthesized hurricane over Lake Okeechobee at (a) 0 h, (b) 1 h, and (c) 2 h after a specified zero time. (Schloemer 1954)

where ζ is the storm surge, B is the atmospheric pressure at a location P, E is the excess of pressure 500 km east of P over the pressure 500 km west of P, and N is the excess of pressure 500 km north of P over the pressure 500 km south of P. In eq. 6.170, $\bar{\zeta}$, $\bar{B}$, $\bar{E}$, and $\bar{N}$ are the arithmetic means of ζ, B, E, and N over a time interval considered. The constants K, λ, and μ are such that if B, E, and N are measured in millibars, then ζ is in centimetres.

Let z be the mean value of ζ from 25 (or more) hourly heights symmetrically arranged in time and let M be the number of observations used in evaluating the constants in eq. 6.170. This equation can be rewritten as

$$(6.171)\quad \zeta - \bar{\zeta} = K(B - \bar{B}) + G\sqrt{\lambda^2 + \mu^2}\cos(\psi - \epsilon) - \text{constant}$$

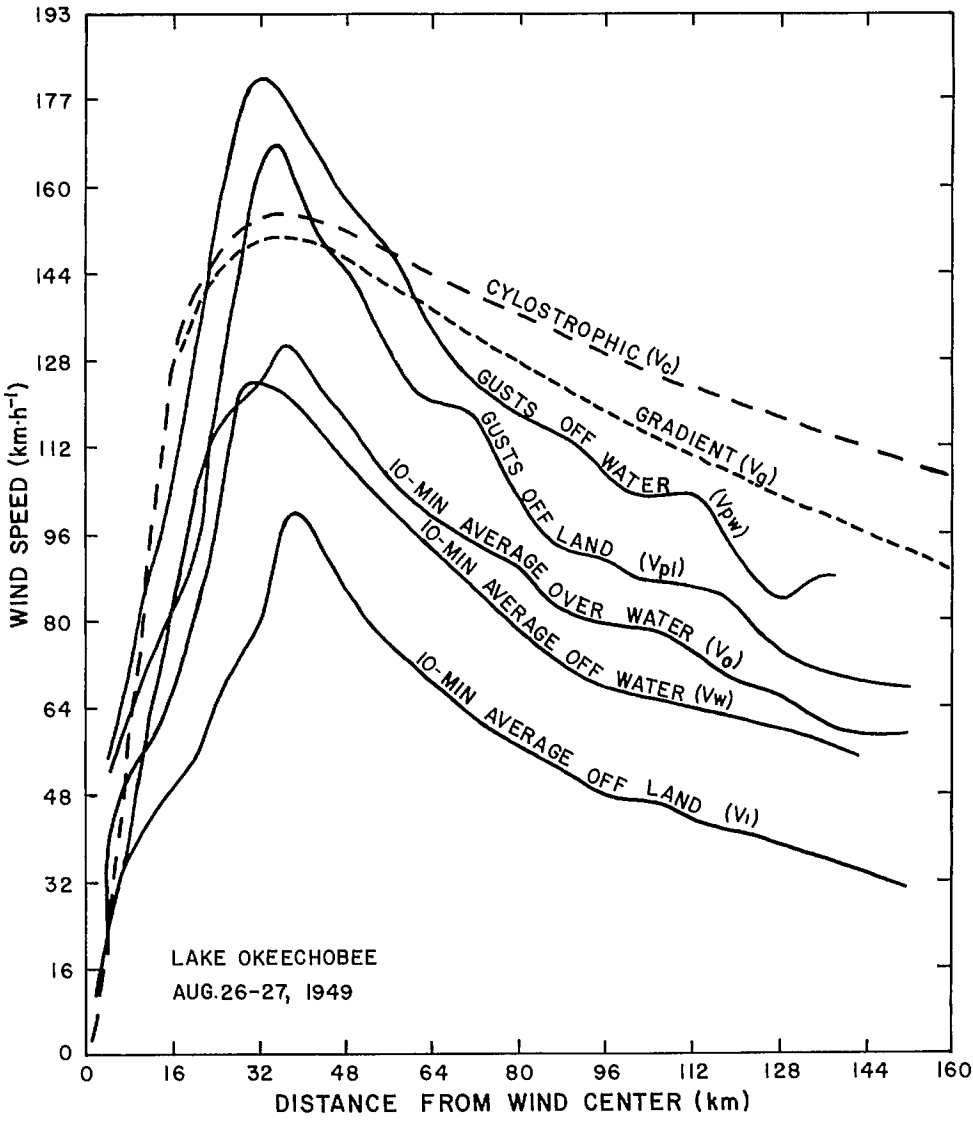

FIG. 6.104. Wind speed profiles over Lake Okeechobee for the hurricane of August 26–27, 1949. (Myers 1954)

where ψ is the direction of maximum pressure gradient, G is the atmospheric pressure gradient over a distance of 1000 km in the direction of ψ, and

$$(6.172) \quad \epsilon = \tan^{-1}\left(\frac{\mu}{\lambda}\right)$$

The "constant" in eq. 6.171 is the average value of the second term on the right side. Maximum surge occurs when (assumption) $\psi = \epsilon$. Taking the direction from which the

wind blows as 70° behind the direction of maximum pressure gradient, the most effective wind (to generate a storm surge) blows from the direction $\epsilon - 70°$. Doodson (1929) tabulated the values of B, E, and N, etc., for the storm of January 6–7, 1928.

Corkan (1948) used somewhat similar methods to study the following three storm surges: January 1–3, 1928, November 10–13, 1929, and November 30–December 2, 1936. He expressed the difference in the storm surges at Southend and Dunbar in terms of the square of the pressure gradients at two points, A and B (located in the North Sea). He wrote

$$(6.173) \quad R_S - R_D = \alpha N|N| + \beta E|E| + \gamma n|n| + \delta e|e|$$

where R_S is the surge at Southend after correction for the effect of local pressure assuming a static law and R_D is the observed disturbance at Dunbar after correction for the effect of local pressure assuming a static law, 6–10 h earlier. The parameters N and E are the north and east gradients of pressure at point A and n and e are the north and east gradients at point B, 6–10 h earlier, and α, β, γ, and δ are constants. Doodson (1947) also used similar methods to study not only the three surges studied by Corkan (1948) but also three other surges: January 6–7, 1928, October 17–21, 1935, and February 10–13, 1938.

Corkan (1950) studied the storm surge of January 8, 1949. The surge was caused by a deep depression that developed rather rapidly near the west coast of Scotland and traveled rapidly eastward. The passage of the center of the storm across the North Sea was accompanied by a quick veering of the winds in the rear of the storm from southwest to northwest and north. The disturbance at Southend was computed making use of the pressure gradients at points A, C, and D (Fig. 6.106) and the surge at Dunbar 9 h earlier (this is to allow for water level disturbances originating outside the North Sea). Corkan (1950) wrote

$$(6.174) \quad 10(R_S - R_D) = 0.33N|N| - 0.55E|E| - 0.75n|n| - 0.95e|e|$$

where R_S is the observed surge (feet) at Southend after correction for the local pressure effect (assuming a static law), R_D is the observed surge 9 h earlier at Dunbar (feet) after a similar correction, N and E are the north and east pressure gradients at point A (Fig. 6.106), and n and e are the average of the north and east pressure gradients at points C and D (Fig. 6.106) 6 h earlier. The pressure gradients are taken as the difference in the pressure (millibars) at the ends of the straight lines shown in Fig. 6.106. Note that eq. 6.174 is a slightly modified version of eq. 6.173.

The Storm Surge of January 31–February 1, 1953

The storm surge in the North Sea during January 31–February 1, 1953, caused extensive flooding and damage on the east coast of the United Kingdom and killed 307 people (Steers 1954). However, there have been earlier instances in which even more damage and deaths occurred. Peters (1954) mentioned that a series of surges occurred during the period 1086–99 and a surge in the year 1099 killed 100 000 people. During the twelfth century, there were more surges. Another period of great surges was 1218–23. Other periods when the death toll exceeded 100 000 were in the years 1421 and 1446. Great surges also occurred (though the death toll was much smaller) on November 15, 1875, January 2, 1877, January 18, 1881, and November 29, 1897. After this period, the next comparable surge occurred in 1928 and then in 1953.

TABLE 6.64. Storm surges in the Thames Estuary during 1912–1928. A, surges >1.83 m; B, surges of 1.22–1.83 m; C, surges of 0.61–1.22 m; T, water level exceeded the Trinity high water mark.

Date	Class of surge	Type of meteorological situation	Remarks
Nov. 11–12, 1912	B		
Nov. 27, 1912	A		
Dec. 4, 1912	B		
Dec. 10–19, 1912	A/B		
Jan. 25, 1913	C/T		
Feb. 8, 1913	B		
Feb. 28–Mar. 7, 1913	B		
Mar. 18–19, 1913	A/B		
Mar. 22, 1913	BT		
Mar. 24, 1913	BT		
Apr. 16–17, 1913	B		
Dec. 13–14, 1913	B		
Dec. 26, 1913	B		
Jan. 7–8, 1914	A/B		
Sept. 28–29, 1914	A		
Nov. 11–13, 1914	A		
Dec. 26–30, 1914	A/B		
Feb. 17, 1915	A		
Oct. 25, 1915	B		
Dec. 9, 1915	BT		
Dec. 27–28, 1915	B		
Jan. 2–4, 1916	B		
Jan. 8, 1916	B/CT		
Jan. 13–16, 1916	A		NW winds 121–161 km·h^{-1}
Feb. 5, 1916	AT		
Feb. 14–16, 1916	A/B		
Oct. 14–15, 1916	B		
Aug. 3, 1917	B		
Oct. 25–26, 1917	B		
Oct. 30, 1917	B		
Nov. 25–26, 1917	A		Winds 113 km·h^{-1}
Dec. 2–3, 1917	A		Winds 113–161 km·h^{-1}
Dec. 17, 1917	CT	III	
Jan. 11, 1918	B		
Jan. 15, 1918	B	I?	
Jan. 16, 1918	BT	I?	
Feb. 26, 1918	B		
Dec. 24–26, 1918	A	I	
Feb. 18, 1919	CT		
May 2, 1919	CT		
Dec. 19, 1919	A	I	
Jan. 11, 1920	B	I	
Feb. 13–14, 1920	A/B	I	W winds 97 km·h^{-1} to NW 129 km·h^{-1}
Feb. 27–28, 1920	B	IV	
Dec. 4, 1920	A	I	NNW to NE winds 129 km
Jan. 19, 1921	A	I	W to WNW winds 81–113 km·h^{-1}
Mar. 2–3, 1921	A/B	I	
Oct. 23–24, 1921	A	I	
Nov. 1, 1921	AT	I	NW winds 97 km·h^{-1}
Nov. 6–7, 1921	B	I/III	
Dec. 18, 1921	AT	III	NW winds 129 km·h^{-1}
Dec. 20, 1921	B		

TABLE 6.64. (*Concluded*)

Date	Class of surge	Type of meteorological situation	Remarks
Dec. 24, 1921	B	I	
Dec. 25, 1921	B		
Dec. 31, 1921	AT	I	NNW winds 161 km·h^{-1}
Jan. 4, 1922	A	III	N winds 129 km·h^{-1}
Sept. 16–20, 1922	B	I	
Nov. 1, 1922	A/B	IV	
Nov. 10, 1922	B	?	
Dec. 6, 1922	B	I	
Dec. 25, 1922	?		
Apr. 25, 1923	B	IV?	
Aug. 20, 1923	B	II/IV	
Dec. 27–28, 1924	BT	IV	
Jan. 1–2, 1925	A	IV	
Jan. 14–15, 1925	B	IV?	
Jan. 29–30, 1925	A/B	?	W winds 97 km·h^{-1}
Nov. 25–27, 1925	A	I/III	N winds 113 km·h^{-1}
Dec. 23–24, 1925	A/B	I/II	
Mar. 5–11, 1926	A	I	NNW winds 65 km·h^{-1}
Oct. 9–10, 1926	A	I	NNW winds 97–129 km·h^{-1}
Oct. 25, 1926	B	II	
Nov. 5, 1926	A/B	IV	
Nov. 13, 1926	A	IV	
Dec. 18–20, 1926	B	I	
Jan. 28–29, 1927	A	?	
Oct. 3, 1927	B	I	
Oct. 29, 1927	B	IV	
Dec. 26, 1927	A/BT	?	
Jan. 6–7, 1928	AT	I	N winds 129 km·h^{-1}

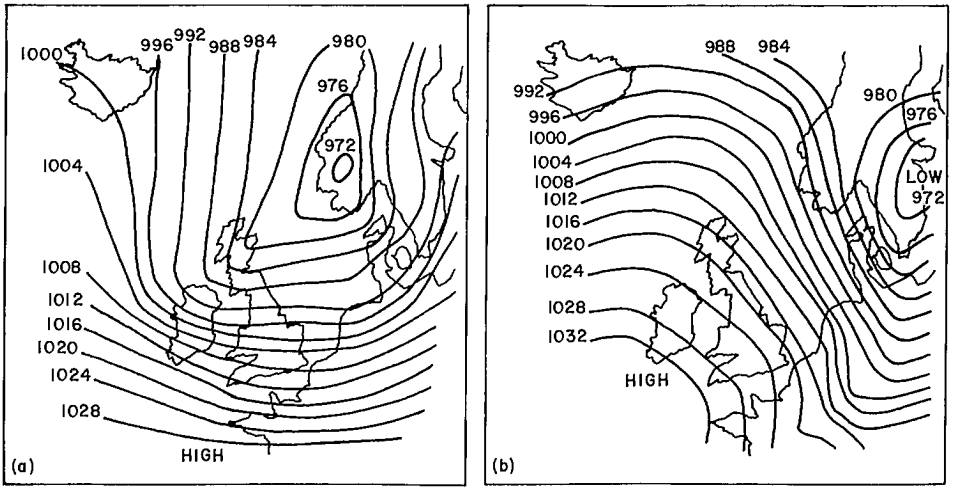

FIG. 6.105. (a) Surface pressure field (millibars) on December 30, 1921, at 6 p.m. (local time) over the North Sea and surroundings; (b) surface pressure field on December 31, 1921, at 7 p.m. (Dines 1929)

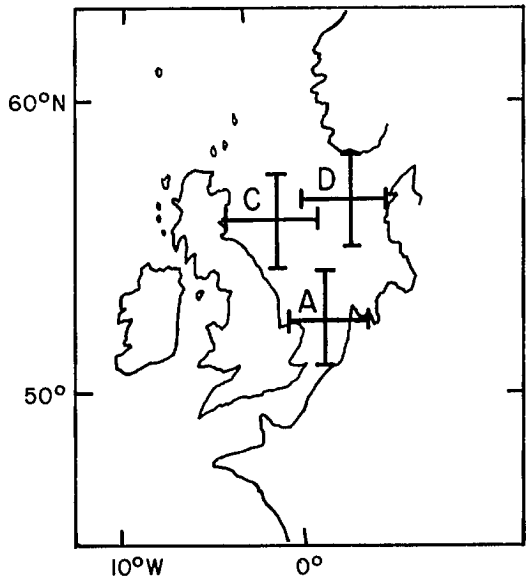

FIG. 6.106. Locations (A, C, and D) in the North Sea where pressure gradients are evaluated. (Corkan 1950)

The track of the storm and the central pressure is illustrated in Fig. 6.107. For details on the meteorological conditions, see Hay and Laing (1954). Rossiter (1954) studied this storm surge and also used the same pressure points (Fig. 6.106) and the same method as Doodson (1924, 1929) and Corkan (1948, 1950).

STORM SURGES IN THE NORTH SEA DURING 1954–78

Two storms in December 1954, one on the 21st and the other on the 24th, produced storm surges in the North Sea. However, since it was not the springtime tides, the damage was minimal. These surges, generated 3 d apart, produced interesting resonance effects in the water levels in the North Sea (Weenink 1956). This will be considered in section 7.3. Murray and Marshall (1955) gave some details of the meteorological situation of these two cases. These storms orginated over the waters off the southeast coast of Greenland after a deep depression from eastern Canada struck the west coast of Greenland.

Timmerman (1975) showed that storm surges can be generated in the North Sea not only by westerly winds over the continental shelf but also by atmospheric pressure gradients near the area of transition from deep to shallow water. He mentioned that this effect is usually disregarded in storm surge calculations. For the storm surge of February 16, 1962, the atmospheric pressure gradient effect was very significant. Hansen (1966) and Heaps (1969) studied this storm surge.

Koopman (1963) studied the surge of October 16–17, 1963. In this case, atmospheric pressure gradients were also a significant factor. The storm that generated the surge on December 10, 1965, was similar (type III) to that of January 6, 1928. An example of a type IV storm is the one that generated the surge of February 25, 1958 (Keers 1968). Other important storm surge dates are September 28, 1969 (Hunt 1972), December 11–15, 1972, and January 29, 1974. In the two latter cases, atmospheric pressure

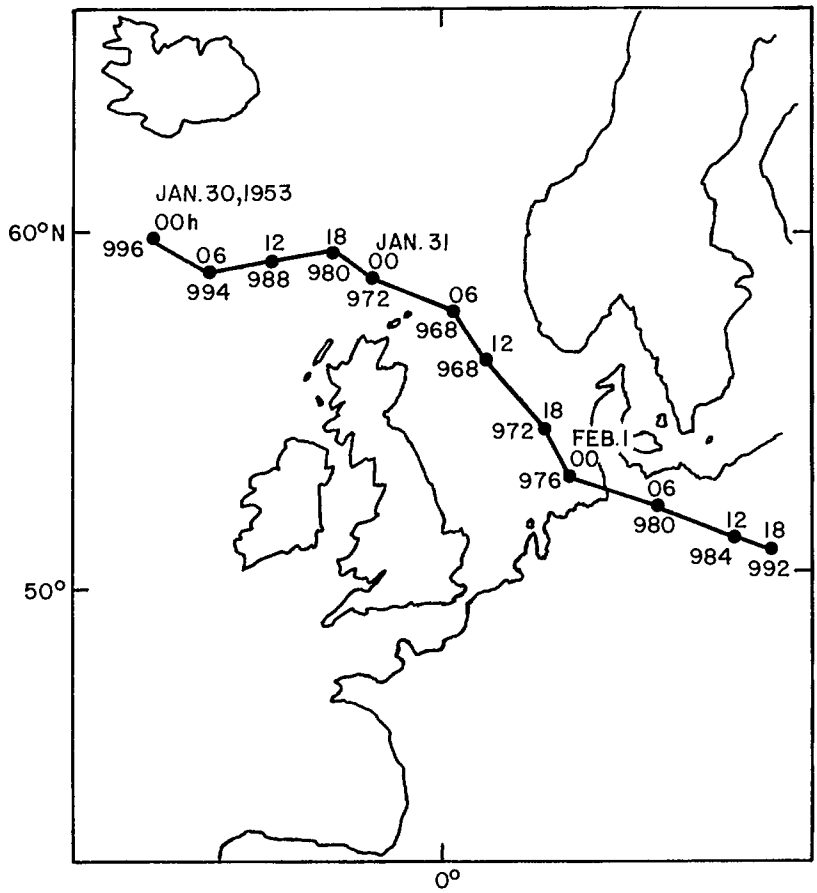

FIG. 6.107. Track of the storm of January 30–February 1, 1953 (pressure field in millibars).

gradients were important (Timmerman 1975).

Davies and Flather (1977) developed numerical models to study the storm surge of April 1–6, 1973. A coarse grid covered the whole northwestern European continental shelf and a fine grid covered only the North Sea. They determined the wind field from the geopotential height field extracted from 12-h weather charts for a period of 36 h. From the forecast data at 7 and 19 h, the geopotential height H of the 1000-mb level was used. The sea surface pressure p is calculated from

$$p = 1000 + \rho_a g H \tag{6.175}$$

where ρ_a is the air density and g is gravity. From the pressure gradients the geostrophic wind was determined. The surface wind w is determined from the geostrophic wind $\hat{w}$ using the empirical relationship of Hasse and Wagner (1971):

$$w = A\hat{w} + B \tag{6.176}$$

where $A = 0.56$ and B has a range of values depending on atmospheric stability. The above formula is valid when w and $\hat{w}$ are in metres per second. Flather and Davies (1975, 1976)

used the above formula with $B = 2.4\ \mathrm{m \cdot s^{-1}}$. This gave reasonable results for the storm surge of March 26–30, 1972, but gave unsatisfactory results for the surge of April 1–6, 1973.

Hasse (1974a, 1974b) expressed A and B in terms of air–sea temperature differences. He also related the angular deviation δ between the surface and geostrophic wind fields to the air–sea temperature differences. Hasse (1974b) gave an average value for δ as 17.2° whereas Dunn-Christensen (1971) used a value of 18° in their calculation of the surge of February 1967. Flather (1976b) obtained better results for the surge of April 1–6, 1976, when he used a value of 20° (compared with the results for $\delta = 0°$).

Timmerman (1975) and Dunn-Christensen (1975) used a value of δ that depended on air–sea temperature differences. Hence, their value of δ varied in space and time. Davies and Flather (1977) used $A = 0.56$, $B = 2.4\ \mathrm{m \cdot s^{-1}}$, and $\delta = 20°$ for the surge of April 1–6, 1973. The wind stress at the sea surface was assumed to be in the same direction as the wind and it was computed using a quadratic law with the following values for the drag coefficient, C_D (Heaps 1965):

$$(6.177)\quad C_D \times 10^3 = \begin{cases} 0.565 & \text{for } w \leq 5 \\ -0.12 + 0.137w & \text{for } 5 < w \leq 19.22 \\ 2.513 & \text{for } w > 19.22 \end{cases}$$

where the surface wind speed w is in metres per second.

There was a series of storm surges in the North Sea during the period November 4–December 18, 1973. Davies and Flather (1978) simulated these numerically, again using a coarse model for the whole shelf and a fine model for the North Sea alone. The meteorological input data were obtained in a manner similar to their earlier study (Davies and Flather 1977). Flather and Davies (1978) simulated the storm surge of January 2–4, 1976. In this study the meteorlogical input data were prepared in a somewhat different manner.

The basic meteorological data were extracted from the forecasts of the 10-level Bushby–Timpson model (Benwell et al. 1971), which gives the data on a rectangular array of grid points on a stereographic projection. The following relationships exist between the dimensionless Cartesian coordinates (x, y) of the atmospheric prediction model and the coordinates of the ocean model:

$$(6.178)\quad \begin{aligned} x &= \frac{2R}{S} \tan\left(\frac{\pi}{4} - \frac{\phi}{2}\right) \sin(\chi + 35°) \\ y &= -\frac{2R}{S} \tan\left(\frac{\pi}{4} - \frac{\phi}{2}\right) \cos(\chi + 35°) \end{aligned}$$

where R is the earth's radius, S is the grid size at the pole (~100 km), χ is east longitude, and ϕ is latitude. The atmospheric pressure at the sea surface is computed from eq. 6.175. Then, the longitudinal and latitudinal pressure gradients can be written as

$$(6.179)\quad \begin{aligned} P &= \frac{1}{R \cos\phi} \frac{\partial}{\partial \chi} P_a = \frac{(1 + \alpha^2)}{2\alpha R}\left(-y \frac{\partial P_a}{\partial x} + x \frac{\partial P_a}{\partial y}\right) \\ Q &= \frac{1}{R} \frac{\partial}{\partial \phi} P_a = -\frac{(1 + \alpha^2)}{2\alpha R}\left(x \frac{\partial P_a}{\partial x} + y \frac{\partial P_a}{\partial y}\right) \end{aligned}$$

where

$$\alpha^2 \equiv \frac{S^2(x^2 + y^2)}{4R^2} \tag{6.180}$$

The eastward and northward components of the geostrophic wind are

$$\hat{w}_\chi = -\left[\frac{(1 + \alpha^2)}{(1 - \alpha^2)}\right]\frac{Q}{2\omega\rho_a}$$
$$\hat{w}_\phi = \left[\frac{(1 + \alpha^2)}{(1 - \alpha^2)}\right]\frac{P}{2\omega\rho_a} \tag{6.181}$$

where ω is the angular velocity of the earth's rotation. A linear relationship was assumed between the geostrophic wind $\hat{w}$ and the surface wind w:

$$w_\chi = (\hat{w}_\chi \cos\delta - \hat{w}_\phi \sin\delta)(A\hat{w} + B)/\hat{w}$$
$$w_\phi = (\hat{w}_\chi \sin\delta + \hat{w}_\phi \cos\delta)(A\hat{w} + B)\hat{w} \tag{6.182}$$

where δ is the angular deviation between the geostrophic and surface winds and a and b are empirical constants, as in the earlier model of Davies and Flather (1977).

Fischer (1979) developed a combined atmosphere–ocean model to simulate the storm surge of January 3, 1976, in the North Sea. The atmospheric model has a grid size of 1.4° latitude and 2.8° longitude and has eight levels in the vertical. The ocean model has a 22-km grid. The surface wind calculated from the atmospheric model was used to determine the wind stress τ_0 in the following manner:

$$|\tau_0| = \rho_a C_D \gamma^2 |v_0| v_0 \tag{6.183}$$

where v_0 is the wind at the anemometer level, C_D is the drag coefficient, $\gamma = 1$ (when observed winds were used) and $\gamma = 1.55$ (when predicted winds were used), and ρ_a is the density of air. Wind at the anemometer level is

$$|v_0| = 0.54 - 0.012\Delta\theta|v_{g0}| + 1.68 - 0.015\Delta\theta \tag{6.184}$$

where the cross-isobar angle is 8° for an unstable atmosphere and 213° for the very stable case and θ is the potential temperature. The drag coefficient is

$$C_D = (1.18 + 0.016|v_{g0}|) \times 10^{-3} \tag{6.185}$$

where v_{g0} is in metres per second. Here, subscript 0 denotes the water surface.

The storm surge of January 11–12, 1978 (Townsend 1979), was the worst on record after the January 1953 surge in the North Sea. This surge was simulated successfully by using empirical methods (Townsend 1979).

Modeling of North Sea Storm Surges

The models of Davies and Flather (1977, 1978) and Flather and Davies (1978) were briefly mentioned. Here, the meteorological aspects of to the models will be briefly considered. Useful reviews were prepared by Welander (1961) and Groen and Groves (1962). Weenink and Groen (1958a, 1958b) introduced a so-called "apparent windstress" as follows. They assumed that the wind stress τ_S is related to the gradient wind V_r through

$$V = l \times 0.75V_r = lV_1 \tag{6.186}$$

where

$$V_1 = 0.75V_r$$

The wind stress τ_S is related to the surface wind V through

(6.187) $\tau_S = KV^2$

Thus

(6.188) $\tau_S = Kl^2V_1^2 = f_SV_1^2$

where

(6.189) $f_S = Kl^2$

The factor f_S should depend on the wind direction α. Hence

(6.190) $\tau_S = f_S(\alpha)V_1^2$

Welander (1957) showed that if one uses a constant vertical eddy viscosity and permits the current to be zero at the bottom, then inconsistencies occur. In addition, the bottom stress would have a value equal to half the wind stress. According to Weenink and Groen (1958) the bottom stress should be no more than a tenth of the wind stress.

Bowden (1953a, 1953b) showed that in a shallow sea with strong tidal currents, there is an additional bottom stress τ_b due to the drift current. This additional stress is proportional to the velocity above the bottom boundary layer. An approximate value of this current is

(6.191) $U_m = \dfrac{Q}{D}$

where Q is the volume transport and D is the water depth. Since the bottom stress does not go to zero when Q vanishes one can write the linear expression

(6.192) $\tau_b = \tau_0 - \dfrac{r\rho Q}{D}$

where r is a friction factor to be determined empirically, ρ is the density of water, and

(6.193) $\tau_0 = m\tau_S$

where m is about 0.1.

The total stress can be written from eq. 6.187, 6.192, and 6.193:

(6.194) $$\begin{aligned}\tau_b + \tau_S &= (1 + m)\tau_S - \frac{r\rho Q}{D} \\ &= (1 + m)f_S(\alpha)|V_1|V_1 - \frac{r\rho Q}{D} \\ &= \tau_{S_A} + \tau_{b_A}\end{aligned}$$

where the apparent wind stress τ_{S_A} is

(6.195) $\tau_{S_A} = f(\alpha)|V_1|V_1 = (1 + m)f_S(\alpha)|V_1|V_1$

and the apparent bottom stress τ_{b_A} is

(6.196) $\tau_{b_A} = -\dfrac{r\rho Q}{D}$

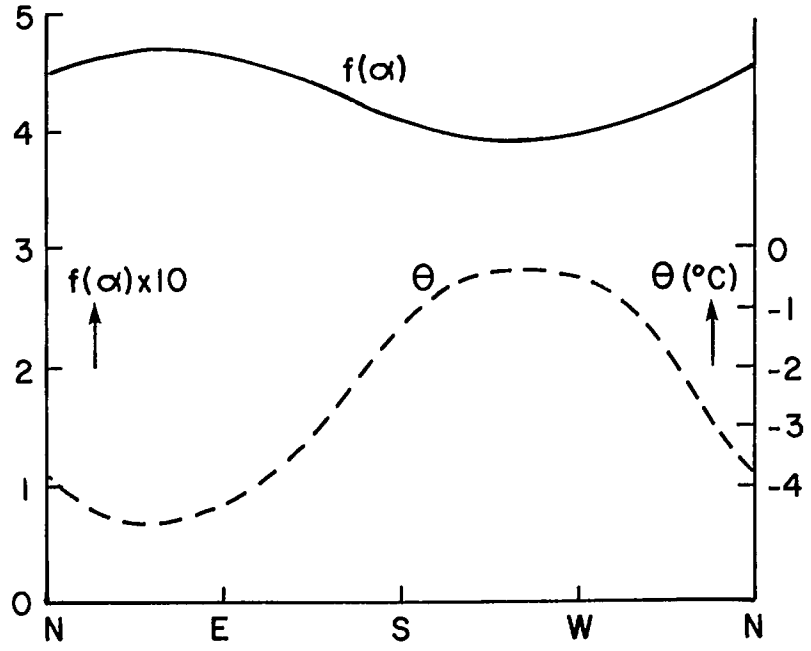

FIG. 6.108. Wind stress factor $f(\alpha)$ for the southern part of the North Sea during the storm surge season of November–February (solid line). Broken line shows the difference θ between the air temperature and the sea surface temperature. The abcissa is wind direction α. (Weenink and Groen 1958b)

A plot of the wind stress factor $f(\alpha)$ for the southern part of the North Sea during the storm surge season (November through February) is shown in Fig. 6.108.

The electronic analog models of Ishiguro (1976a, 1976b) for the North Sea have been referred to as well as the two-dimensional (in spherical polar coordinates) model of Heaps (1969). This model and the model of Banks (1974) have been discussed elsewhere in this book. Other North Sea models developed for storm surge prediction were those of Flather and Davies (1976) and Flather (1979).

The Belgian real-time storm surge model for the North Sea was described by Adam (1979). In this model the wind stress was written as

$$\tau_S = (1 + m)\frac{\rho_a}{\rho_w}\frac{C_D}{H}W|W| \tag{6.197}$$

where $m \sim 0.1$, W is the wind velocity, and the drag coefficient C_D is given the following values:

$$C_D = \begin{cases} 1.26 \times 10^{-3} \text{ for } |W| \leq 10 \text{ m}\cdot\text{s}^{-1} \\ 2.4 \times 10^{-3} \text{ for } |W| > 10 \text{ m}\cdot\text{s}^{-1} \end{cases} \tag{6.198}$$

Adam (1979) mentioned that the use of eq. 6.177 in place of eq. 6.198 did not make much improvement.

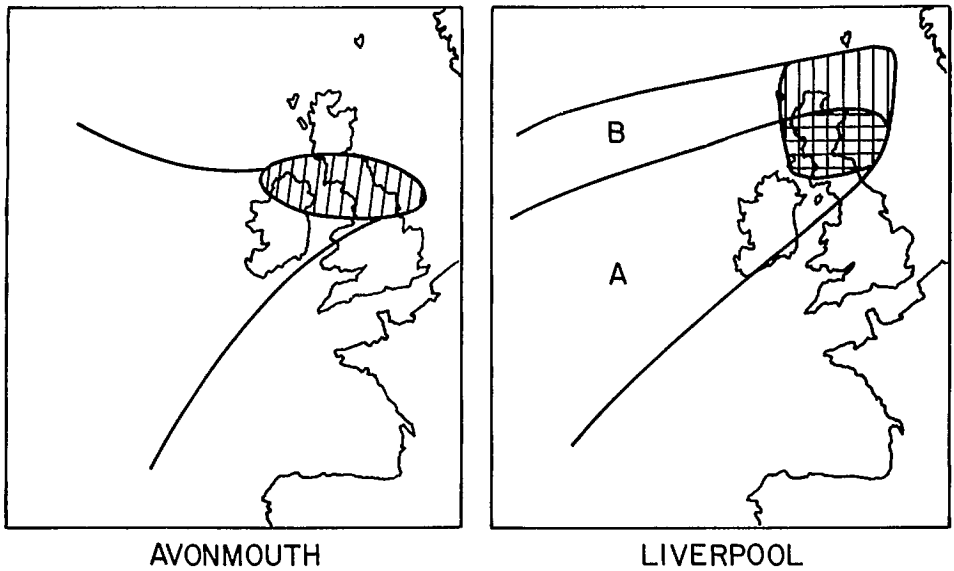

FIG. 6.109. Envelope of the depression tracks that cause large storm surges at Avonmouth and Liverpool. For Avonmouth the hatched area shows the region in which the storm centers of the depressions lie when major surges occur at Avonmouth. For Liverpool the envelope is divided into a southern section (A) and a northern section (B). The cross-hatched and single-hatched areas are, respectively, associated with zones A and B. (Lennon 1963)

STORM SURGES IN THE IRISH SEA

Storm surge studies for the Irish Sea are fewer than those for the North Sea, although large surges occur in the Irish Sea. Lennon (1963) examined the meteorological situations associated with large surges at Avonmouth and Liverpool. He suggested that the speed with which the depression moves is quite relevant for surge amplification due to resonance, and he defined a dynamic factor to express this:

$$\text{(6.199)} \quad \text{Dynamic factor} = \frac{1}{\left(1 - \frac{V^2}{gh}\right)}$$

where V is the speed of movement of the depression, h is the average depth of water, and g is gravity.

Lennon (1963) examined the period of 1920–55 and arrived at seven major surges; i.e. in all these cases, the surge at Avonmouth exceeded 6 ft (1.8 m) and at Liverpool the surge exceeded 4.9 ft (1.5 m). Even the smallest (in size) of the depressions producing these surges has a diameter of 400 mi (645 km).

Based on the tracks of these depressions, one can delineate corriders of dangerous zones for Avonmouth and Liverpool, which are shown in Fig. 6.109. The hatched areas shows the positions of the depression centers at the times of maximum surges. The meteorological character of these depressions is summarized in Tables 6.65 and 6.66.

In Fig. 6.109 the Avonmouth approach zone is simpler compared with the Liverpool approach zone, which is divided into a southern section (section A) and a northern section (section B). Depressions whose tracks lie in zone A produce maximum surges when their

TABLE 6.65. Some details of the depressions that caused large storm surges at Avonmouth. (Lennon 1963)

Date	Speed of movement ($km \cdot h^{-1}$)	Location of depression center at time of maximum surge	Radius of depression (km)	Pressure gradient (mb) over 463 km
Jan. 12, 1930	87	Irish Sea	241	24
Sept. 17, 1935	74	Irish Sea	333	32
Jan. 9, 1936	78	Ireland	296	34
Nov. 23, 1938	65	South Scotland	389	26
Mar. 16, 1947	72	North England	333	26
Apr. 23, 1947	74	North Ireland	370	28
Nov. 30, 1954	59	East England	333	38

TABLE 6.66. Some details of the depressions that caused large storm surges at Liverpool, U.K. (Lennon 1963)

Date	Speed of movement ($km \cdot h^{-1}$)	Location of depression center at time of maximum surge	Radius of depression (km)	Pressure gradient (mb) over 463 km
Jan. 9, 1936	78	Ireland	296	34
Oct. 27, 1936	69	North of Scotland	278	32
Nov. 23, 1938	65	North England	389	26
Jan. 25, 1944	65	West Scotland	482	23
Dec. 2, 1946	70	Off West Scotland	333	23
Apr. 23, 1947	74	North Ireland	370	28
Nov. 30, 1954	59	East Ireland	296	34

centers lie in the cross-hatched area. Depressions in approach zone B produce maximum surges when their centers lie in the single-hatched area. The timing of the maximum surges is not as accurate in zone B as in zone A. If the track is such that it crosses from zone A to B before arriving at the hatched areas, then the surges produced are not large. An example of such a case is the surge of January 31–February 1, 1957, which produced a surge of 3.0 ft (less than 1 m) at Liverpool. However, a storm on February 4, 1957, produced a much greater surge.

Based on this study, Lennon (1963) suggested that a major storm surge occurs on the west coast of the British Isles, provided the following meteorological situations occur together: (1) a deep depression approaches in zone A or B, (2) the speed of movement is of the order of 40 knots (74 $km \cdot h^{-1}$) (giving a dynamic factor of 2 for this area), (3) the depression can be represented by an independent and approximately concentric system of isobars to a radius of 150–200 nautical miles (278–370 km), and (4) the pressure gradient in the right rear quadrant must be about 30 mb in 250 nautical miles (463 km).

Cresswell (1928) discussed the storm surges in the Irish Sea at Holyhead, Preston, Fleetwood, and Belfast due to a storm on October 28–29, 1927. The first three stations are on the east side of the Irish Sea and Belfast is on the west side. The surge height was smallest at Belfast (3 ft 2 in. or 66 cm) and largest at Preston (10 ft 2 in. or 310 cm).

Heaps (1965, 1967) studied storm surges in the Irish Sea. Heaps and Jones (1975) used a two-and-a-half-dimensional model (they called it a three-dimensional model) of the Irish Sea to simulate storm surges for the period January 10–18, 1965. The first storm surge of this period was associated with a storm of January 13–14. A deep depression

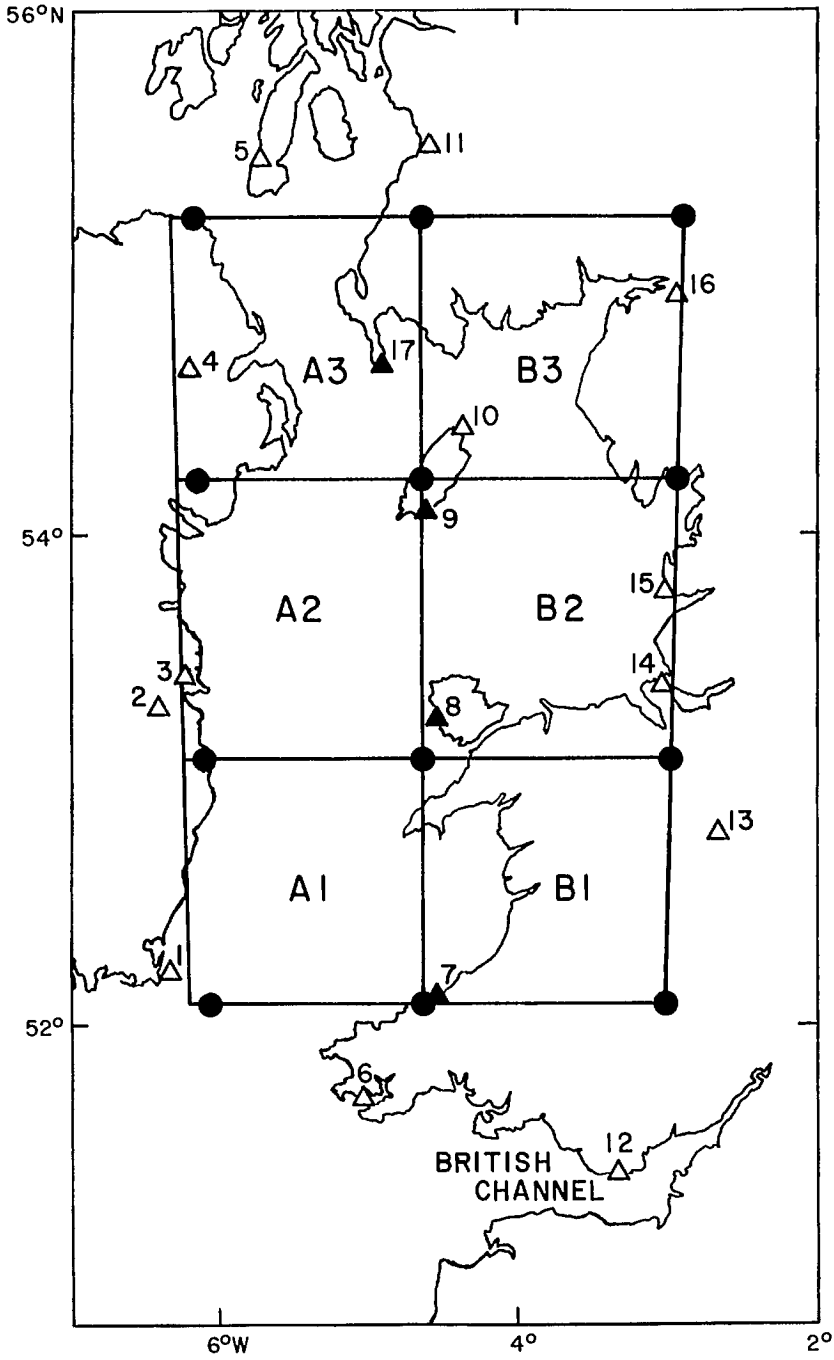

FIG. 6.110. Irish Sea model with six subareas for determining atmospheric pressure gradients and wind stress. (Heaps and Jones 1975)

moved from the Atlantic with a speed of about 35 knots (65 km·h^{-1}) on a track (towards the east) lying to the north of Ireland. Fronts from this depression swept across the Irish Sea and winds veered from south to west. The second storm (January 16–18) was associated with a large slow-moving depression to the north of Scotland.

The following meteorological forcing terms were included in the numerical model: atmospheric pressure gradients over the water surface determined at 3-h intervals from pressure records and wind stress determined at 3-h intervals from geostrophic winds, or alternatively, at 6-h intervals from measured surface winds.

The six rectangular subareas of the Irish Sea and surroundings (regions A1, A2, A3, B1, B2, and B3) are shown in Fig. 6.110. From observations of atmospheric pressure, $p_{i,j}$ values were extrapolated for each grid point at each time step. The 16 meteorological stations whose pressure data are used are also shown. Heaps and Jones (1975) wrote the following for subarea A2

$$\frac{\partial p}{\partial x} = \frac{1}{2}\frac{(p_{22} - p_{12} + p_{23} - p_{13})}{7\Delta x} \tag{6.200}$$

$$\frac{\partial p}{\partial y} = \frac{1}{2}\frac{(p_{13} - p_{12} + p_{23} - p_{22})}{9\Delta y} \tag{6.201}$$

where $\Delta x = \Delta y = 7.5$ nautical miles (13.8 km).

For each subarea, the following empirical formulae were used to determine the surface wind V from the geostrophic wind V_G:

$$V = 0.56V_G + 2.4 \tag{6.202}$$

$$\theta = \theta_G - 22 \tag{6.203}$$

where θ and θ_G are the angular veering from the south (degrees) of the surface and geostrophic winds, respectively. Finally, the wind stress τ_S was determined from

$$\tau_S = 12.5C_D V^2 \tag{6.204}$$

Equation 6.177 is used for C_D.

An alternate procedure to determine the meteorological forcing terms was to use the measured surface winds (and not the calculated geostrophic winds) to determine the wind stress. The anemometer locations are also shown in Fig. 6.110. Based on both approaches it was deduced that

$$\begin{aligned} V &= \beta V_G \\ \theta &= \theta_G - 22 \end{aligned} \tag{6.205}$$

with

$$\beta = \begin{cases} 0.75 \text{ for } V_G \leq 10 \\ \dfrac{(640 - 7V_G)}{760} \text{ for } 10 \leq V_G \leq 48 \\ 0.4 \text{ for } V_G \geq 48 \end{cases} \tag{6.206}$$

where V_G is in metres per second.

Heaps and Jones (1979) simulated the storm surges of January 1976 and November 1977 in the Irish Sea using a model similar to that of Heaps and Jones (1975) but with improvements. Based on this and other studies, it can be concluded that major storm

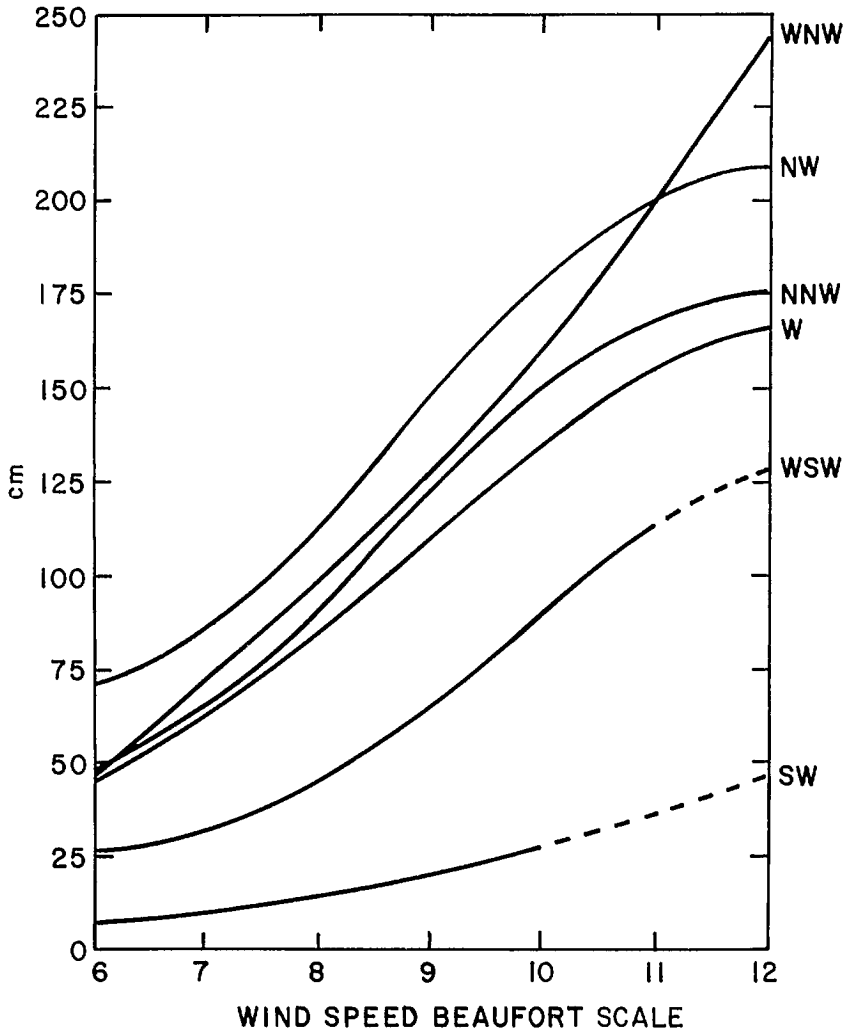

FIG. 6.111. Storm surge versus wind speed (see Table 6.67 for the Beaufort Scale) at Hook of Holland. These results were summarized by Schalkwijk based on earlier studies by a Netherlands Government committee. (Schalkwijk 1947)

surges in the Irish Sea are associated with the secondary depressions from the Atlantic that move towards the east and cross the British Isles with a speed of about 40 knots (74 $km \cdot h^{-1}$). Heaps (1965) showed that the Celtic Sea area (south of Ireland) is a major region of generation of storm surges.

SURGES IN THE GERMAN BIGHT AND ON THE COAST OF THE NETHERLANDS

Schalkwijk (1947) gave a comprehensive analysis of storm surges on the coast of the Netherlands until 1940 and the following discussion is based on his paper. He mentioned

TABLE 6.67. International and Bleck equivalents of the Beaufort Scale. (Schalkwijk 1947)

Degrees Beaufort	International equivalent of wind speed ($m \cdot s^{-1}$)	Bleck equivalent of wind speed ($m \cdot s^{-1}$)	Degrees Beaufort	International equivalent of wind speed ($m \cdot s^{-1}$)	Bleck equivalent of wind speed ($m \cdot s^{-1}$)
1	1.1	1.8	7	13.8	17.4
2	2.5	4.4	8	16.7	20.0
3	4.3	7.0	9	19.9	22.6
4	6.3	9.6	10	23.3	25.2
5	8.6	12.2	11	27.1	27.8
6	11.1	14.8	12	>29.0	>29.0

TABLE 6.68. Values of deviation angle ψ (degrees), wind speed V ($m \cdot s^{-1}$), and surge η (cm) for the storm surges on the Netherlands coast. (Schalwijk 1947)

Date	Hour	ψ	V	η
Jan. 19, 1921	1	50	20.8	155
Jan. 19, 1921	7	58	19.0	134
Jan. 19, 1921	13	64	16.7	99
Jan. 19, 1921	18	55	14.6	70
Nov. 25, 1928	18	53	17.4	115
Nov. 26, 1928	1	59	20.1	172
Nov. 26, 1928	7	61	19.3	142
Nov. 26, 1928	13	60	17.0	105
Nov. 26, 1928	18	59	15.0	86
Nov. 27, 1928	1	55	13.0	74
Nov. 27, 1928	7	54	12.1	71
Nov. 27, 1928	13	58	12.3	71
Jan. 17, 1931	7	40	18.9	133
Jan. 17, 1931	13	51	18.4	139
Jan. 18, 1931	18	47	12.5	45
Oct. 30, 1935	13	50	14.3	71
Oct. 20, 1935	18	50	12.4	44
Oct. 20, 1936	18	46	11.0	54
Dec. 1, 1936	1	43	18.3	141
Dec. 1, 1936	7	44	18.2	176
Dec. 2, 1936	18	47	13.6	71
Jan. 30, 1938	1	42	17.7	119

that very destructive storm surges occurred on the following dates: November 18, 1421, November 1, 1570, December 25, 1717, November 14, 1775, February 4, 1825, and January 13–14, 1916. In the storm surge of 1421, at least 10 000 people died.

The destructive storm surge of 1916 caused the Netherlands government to start a storm surge warning service. Ortt (1978) expressed the surge height on the Netherlands coast through

$$\eta = KR + R_b(76 - p) \tag{6.207}$$

where η is the storm surge (centimetres), K is a factor representing the influence of the strength of the wind, R is a factor representing the wind direction, R_b is a factor representing the effect of atmospheric pressure, and p is the atmospheric pressure (centimetres of mercury).

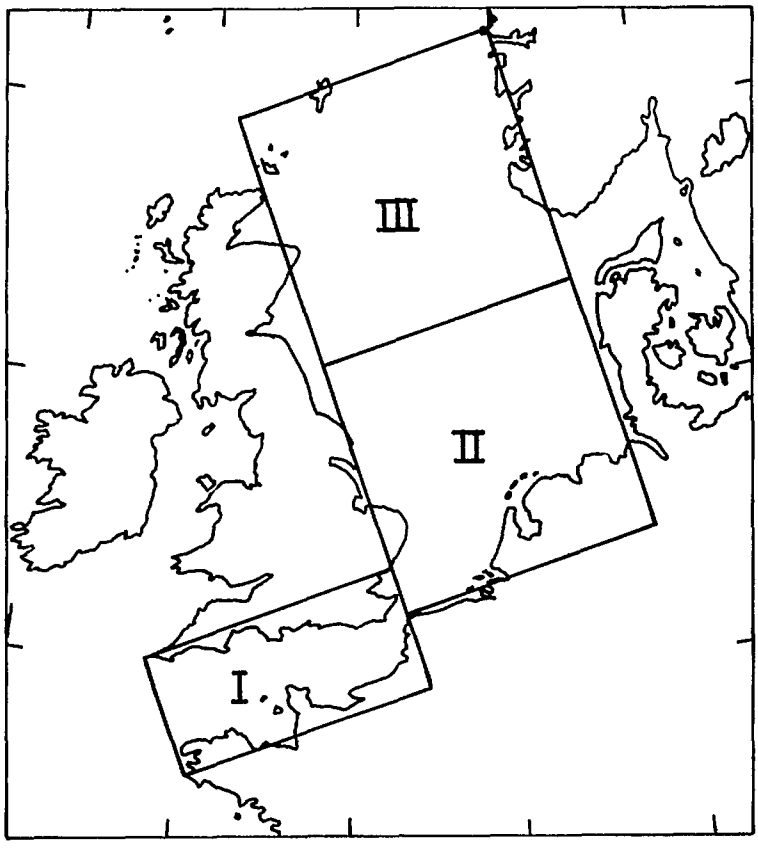

FIG. 6.112. Three sections of the North Sea for which the storm surge study was made. (Schalkwijk 1947)

For the Netherlands coast

$$K = 0.14V^2 \tag{6.208}$$

where V is the wind velocity. Schwalkwijk (1947) gave tables of R and R_b for various wind directions. Ortt (1897) showed that large surges are produced by west to west–northwest winds and the smallest surges are produced by east to east–southeast winds and, in general, there is a lag of about 6 h between the wind and the surge.

Gallé (1915) calculated the storm surge residues from the total water level (after subtracting the tide) every hour in contrast with earlier works of every 6 h. However, he ignored the effect of atmospheric pressure gradient in his study of 42 storm surges.

The committee (Rotterdamsche Waterweg) established by the Netherlands government in 1920 studied 19 storm surges for the period 1887–1917. They related the surges to the wind but ignored time lag and atmospheric pressure gradients. The results of this study are shown in Fig. 6.111 (the Beaufort scale is explained in Table 6.67). One interesting result is that the winds over the southern part of the North Sea are more relevant than the local winds in generating these surges.

Mazuré (1937) wrote the following for a closed channel:

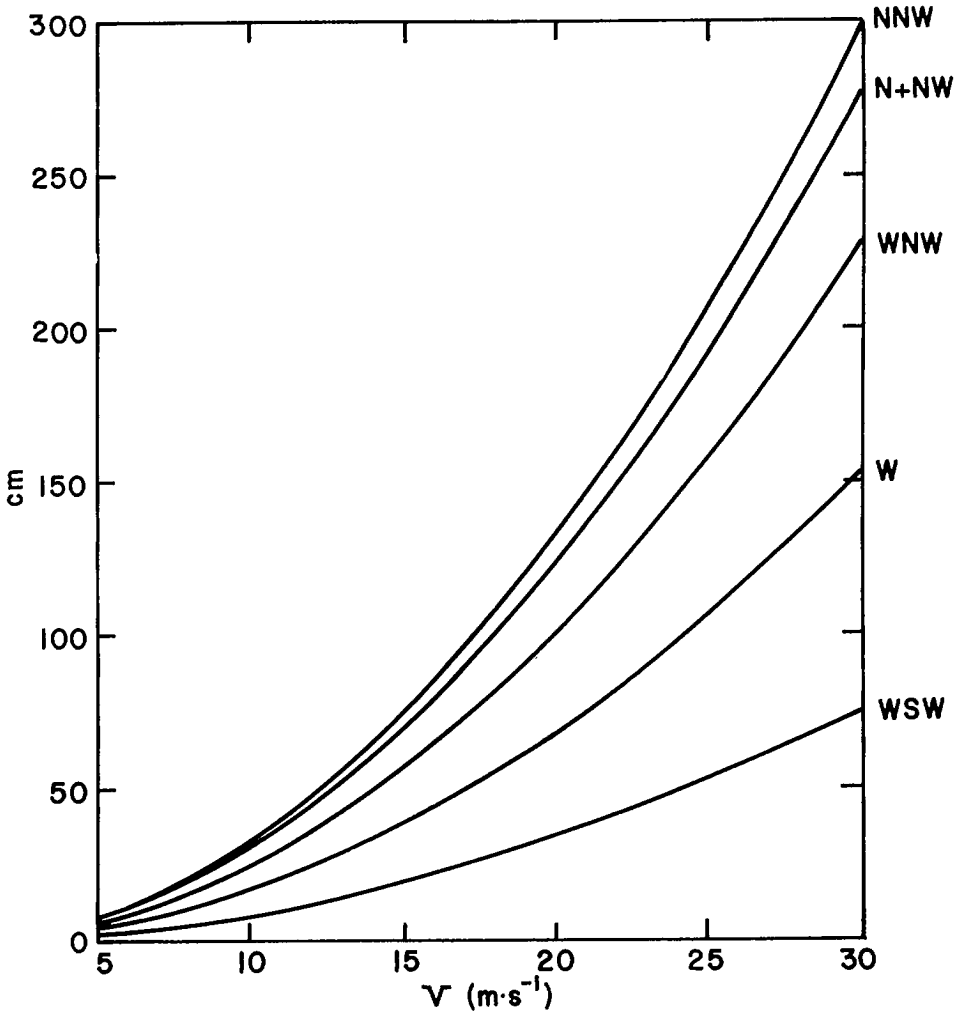

FIG. 6.113. Storm surge versus wind speed for section I of Fig. 6.112. (Schalkwijk 1947)

$$\eta = \frac{aV^2L\cos\psi}{H} \tag{6.209}$$

where $a = 0.0036$, V is the wind velocity (metres per second), η is the surge (centimetres), H is the water depth (metres), L is the channel length (kilometres), and ψ is the angle between the wind direction and the channel axis. Colding (1880, 1881) used a slightly different formula:

$$\eta = \frac{0.048LV^2\cos^2\psi}{H} \tag{6.210}$$

This formula was successfully used to hindcast the storm surges of November 12–14, 1872, on the Danish coast and in the Baltic Sea.

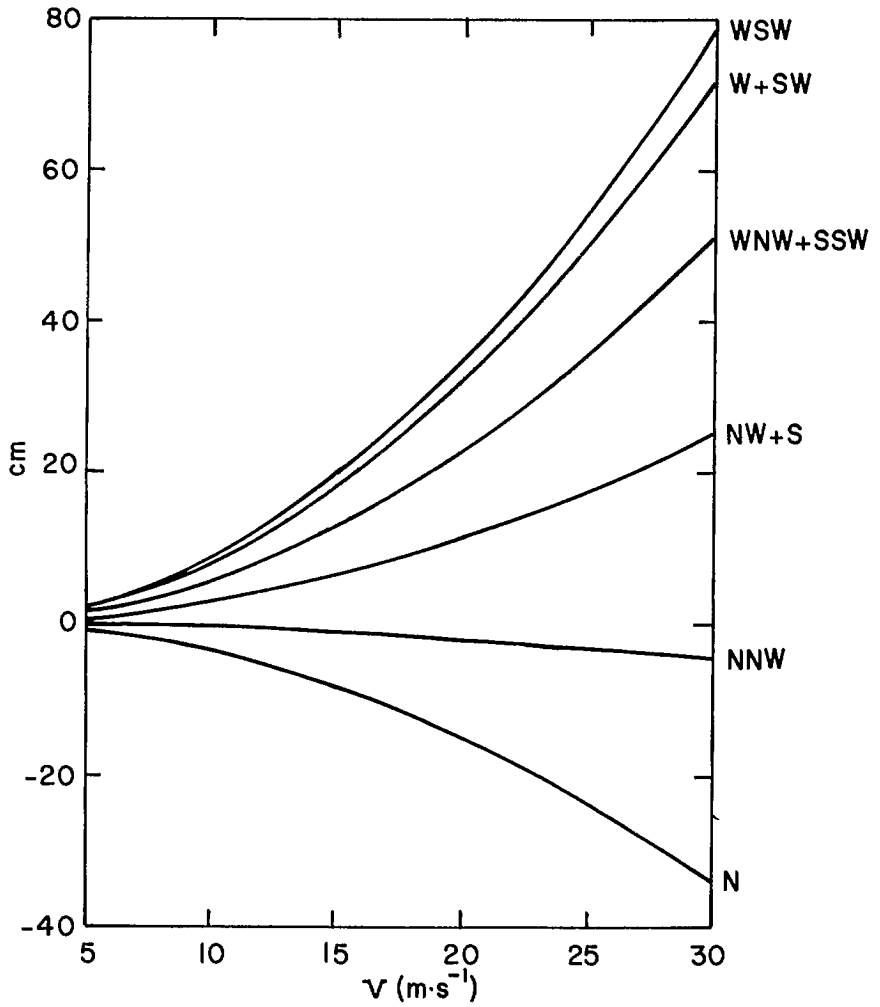

FIG. 6.114. Storm surge versus wind speed for section II of Fig. 6.112. (Schalkwijk 1947)

Palmén (1932) used eq. 6.209 for the Baltic Sea with $a = 0.032$. He found that the direction of the water level slope deviated by 3° to the right of the wind during the surge of October 3–7, 1936. Witting (1908) obtained values of 1–5° deviation.

Based on these studies, the following results can be deduced for the Netherlands coast. The time lag between the wind and surge is 3–6 h. If one includes the water level oscillations, the duration of the surge is about 2 d. The most effective wind direction in generating surges is northwest. The relationship between the surge and atmospheric pressure gradient is related to the structure and movement of the pressure field. The surge in the southern part of the North Sea is closely related to the average wind over the whole North Sea. Along the Netherlands coast, the variations in the surge south of Helder are not significant.

Schalkwijk (1947) developed an analytical theory applicable to an enclosed sea, a

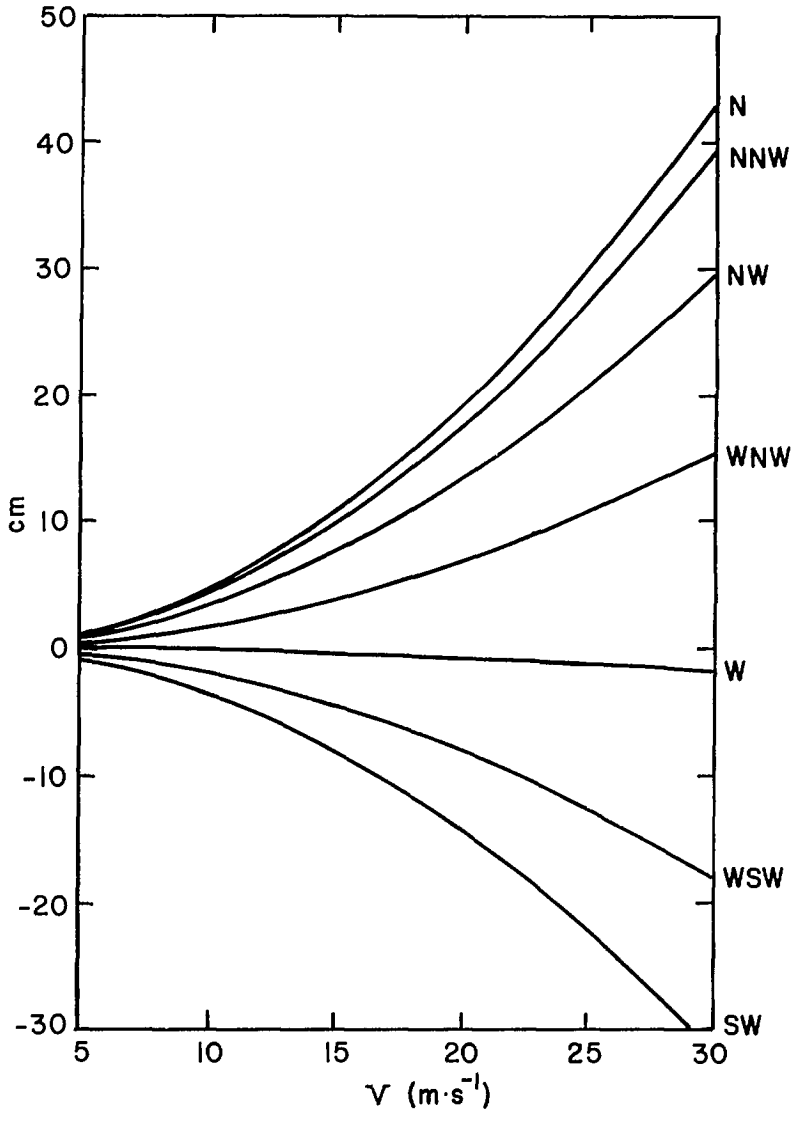

FIG. 6.115. Storm surge versus wind speed for section III of Fig. 6.112. (Schalkwijk 1947)

partly open sea, a bay of uniform depth, and a bay of variable depth. He included the influence of the Dover Strait and inhomogeneities and time variations in the wind field. He selected 14 surges for the period 1920–40. These cases with factors ψ, V, and η (from eq. 6.209) are listed in Table 6.68 (in this table, 22 cases appear because some cases are broken down into separate events).

Schalkwijk's 1947 study showed that the average deviation of the wind from the isobars is 8°, which is somewhat smaller than the values given by other authors, which ranged from 13 to 20°. He also found that on the rising part of the curve the time lag between wind and surge is 2.2 h whereas on the falling part of the curve the lag is 2.8 h.

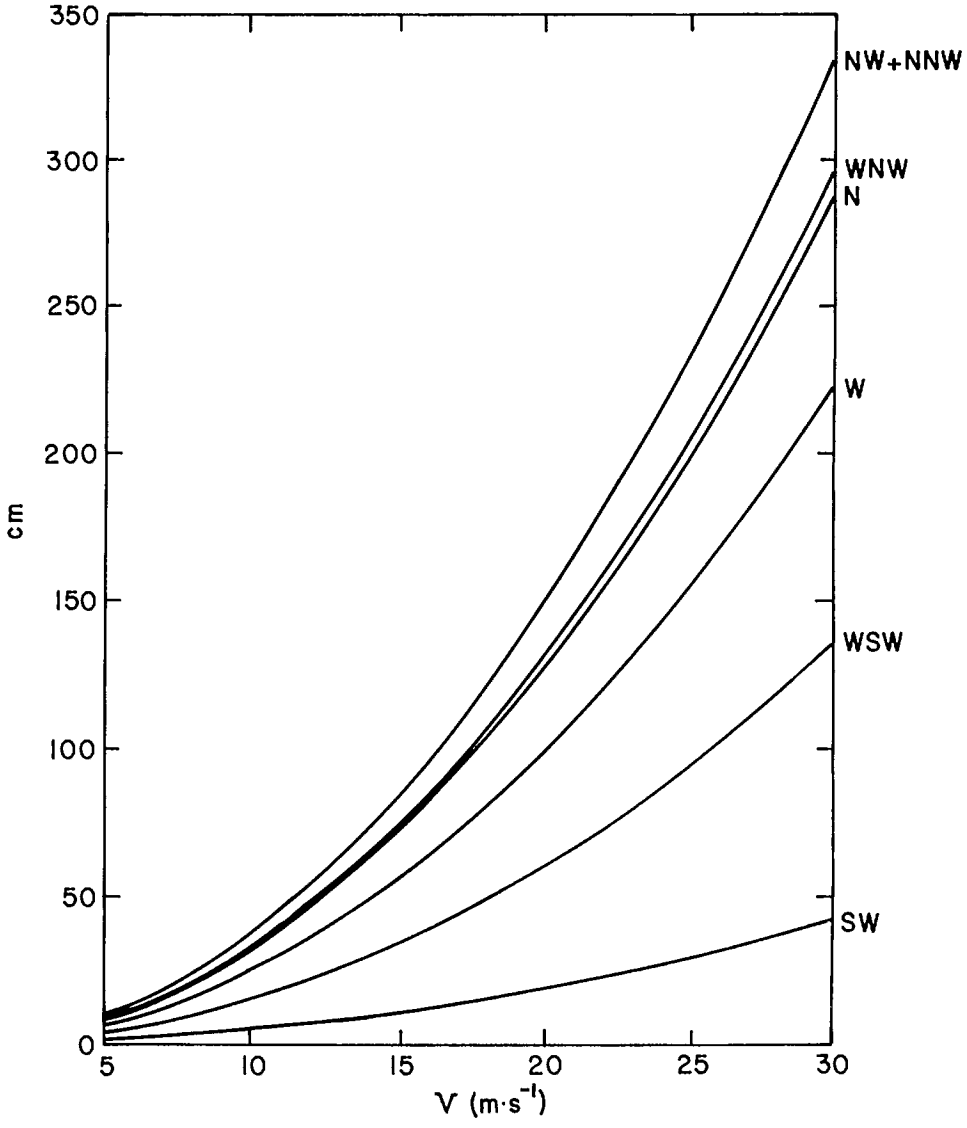

FIG. 6.116. Storm surge versus wind speed for the whole of the North Sea based on Schalkwijk's results. (Schalkwijk 1947)

The three separate regions of the North Sea for which this study is made are shown in Fig. 6.112. The results for sections I, II, and III are summarized in Fig. 6.113, 6.114, and 6.115, respectively. The results for the whole North Sea are shown in Fig. 6.116. Comparison of Fig. 6.111 and 6.116 shows that differences exist between the results of Schalkwijk's (1947) study and the Netherlands government committee's earlier study.

Schalkwijk also examined the surges in the East Scheldt Estuary. The relevant parameters for various surges are listed in Table 6.69 and the results for this case are summarized in Fig. 6.117.

TABLE 6.69. Values of wind velocity V ($m \cdot s^{-1}$), deviation angle ψ (degrees), and surge η (cm) for the storm surges in the East Scheldt Estuary. (Schalkwijk 1947)

Date	V	ψ	η	Date	V	ψ	η
Jan. 17, 1921	11.5	−85	6	Feb. 17, 1935	9.0	−10	11
Jan. 18, 1921	14.0	−45	16	Oct. 19, 1935	16.0	−55	12
Jan. 18, 1921	20.0	0	30	Oct. 20, 1935	12.5	30	16
Jan. 19, 1921	18.5	25	26	Sept. 8, 1936	18.0	−5	32
Nov. 5, 1921	15.5	5	23	Oct. 16, 1936	13.0	20	4
Nov. 6, 1921	22.0	30	26	Oct. 17, 1936	13.0	−10	12
Nov. 25, 1925	16.0	40	35	Oct. 18, 1936	15.0	30	13
Nov. 26, 1925	4.0	90	2	Oct. 19, 1936	13.0	20	18
Nov. 27, 1925	14.0	30	22	Oct. 20, 1936	12.0	65	20
Mar. 9, 1926	13.0	−30	20	Oct. 26, 1936	11.5	−60	−8
Mar. 10, 1926	20.5	35	29	Oct. 27, 1936	20.0	0	33
Oct. 9, 1926	17.0	−25	7	Oct. 28, 1936	15.0	35	1
Oct. 10, 1926	20.0	15	25	Nov. 30, 1936	11.0	−5	−7
Oct. 10, 1926	9.0	−20	3	Dec. 1, 1936	16.5	35	12
Oct. 11, 1926	12.0	−55	−3	Dec. 2, 1936	12.0	20	22
Oct. 12, 1926	7.0	−30	5	Dec. 4, 1936	11.0	−10	14
Oct. 13, 1926	12.0	−20	4	Dec. 5, 1936	10.0	−70	4
Dec. 20, 1926	17.5	90	40	Dec. 6, 1936	15.0	−5	22
Dec. 21, 1926	7.0	40	−1	Dec. 7, 1936	11.0	80	−6
Nov. 23, 1928	8.0	−65	9	Feb. 19, 1937	9.0	20	0
Nov. 24, 1928	18.5	0	43	Jan. 28, 1938	16.0	20	17
Nov. 25, 1928	16.0	−20	24	Jan. 29, 1938	17.0	−50	−9
Nov. 26, 1928	17.0	30	21	Jan. 30, 1938	22.0	20	57
Jan. 13, 1930	12.5	−25	−4	Jan. 31, 1938	15.0	60	30
Aug. 14, 1930	16.0	15	24	Feb. 1, 1938	10.0	−50	1
Aug. 15, 1930	15.0	20	23	Feb. 2, 1938	15.0	−30	15
Aug. 16, 1930	7.0	20	5	Apr. 3, 1938	11.0	20	8
Nov. 10, 1930	13.5	25	6	Apr. 4, 1938	17.0	45	18
Nov. 11, 1930	16.0	50	1	May 30, 1938	9.0	10	7
Nov. 12, 1930	11.0	0	8	May 31, 1938	19.0	−10	35
Nov. 22, 1930	13.0	−60	25	Oct. 3, 1938	8.5	−70	−16
Nov. 23, 1930	21.0	50	50	Oct. 4, 1938	16.5	−55	−6
Nov. 23, 1930	16.0	10	35	Oct. 5, 1938	22.0	−20	33
Jan. 17, 1931	19.0	25	53	Apr. 22, 1939	18.0	−65	−17
Jan. 18, 1931	14.0	30	22	Apr. 23, 1939	12.0	20	12
Feb. 16, 1935	19.0	−25	29				

Wemelsfelder (1954) mentioned that the meteorological conditions associated with the storm of February 1, 1953, are quite different from the traditional storm tracks that emerge over Scotland and disappear over Norway or Denmark. In this 1953 case, the storm track crossed the North Sea from Scotland to Hamburg. The Netherlands coast is very vulnerable (from a storm surge point of view) to this type of track. Detailed meteorological data about this storm are presented by Sneyers (1953).

Reference has already been made to the work of Hasse (1974a) in relating the surface wind to the geostrophic wind in the German Bight. Christiansen and Siefert (1979) developed a simple scheme for storm surge prediction in the German Bight, making use of actual (not predicted) wind direction and speed from a reference station and tide data from two locations. A total of 100 storm surges that occurred in the period 1930–78 were examined to develop the following relation:

$$H_B = 1.2H_A + \Delta V + \Delta R - 80 \text{ cm} \quad (6.211)$$

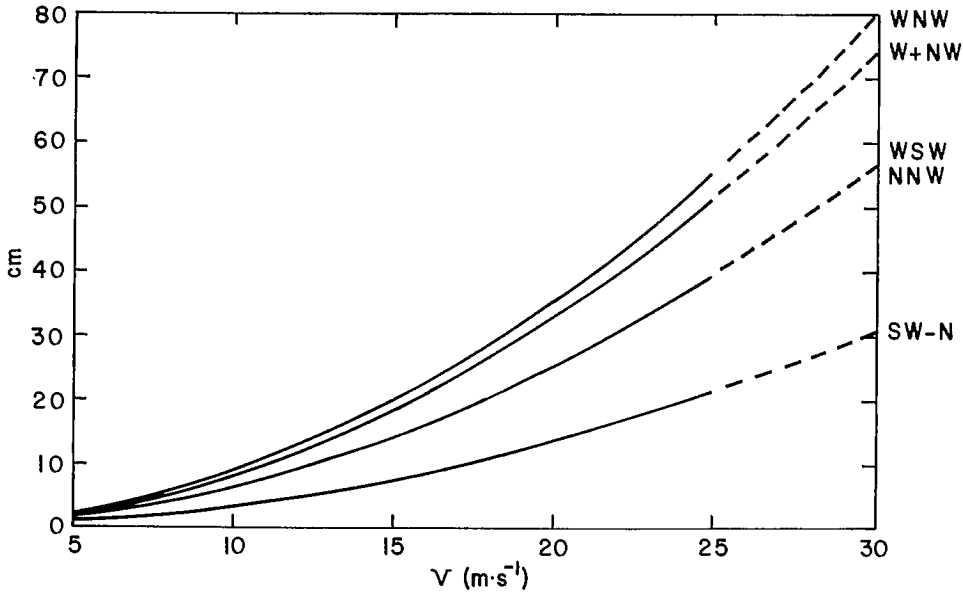

FIG. 6.117. Storm surge versus wind speed for the East Scheldt Estuary. (Schalkwijk 1947)

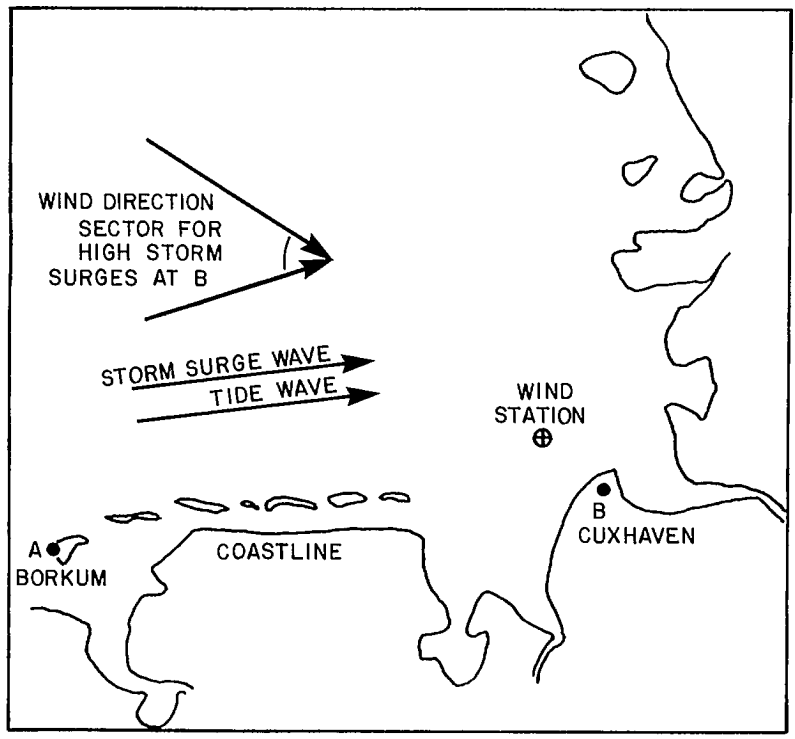

FIG. 6.118. Geography of the German Bight. (Christiansen and Siefert 1979)

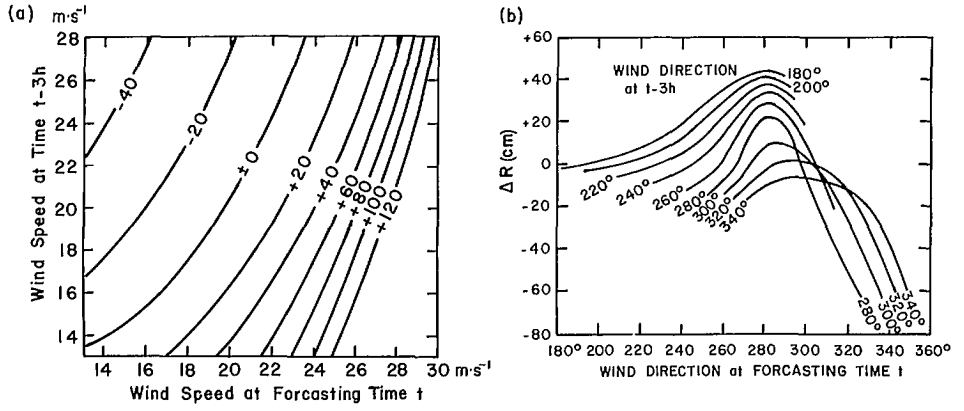

FIG. 6.119. (a) ΔV (centimetres) as a function of wind speed at t and at $t - 3$ h (see eq. 6.210); (b) ΔR (centimetres) as a function of wind direction at t and at $t - 3$ h. (Christiansen and Siefert 1979)

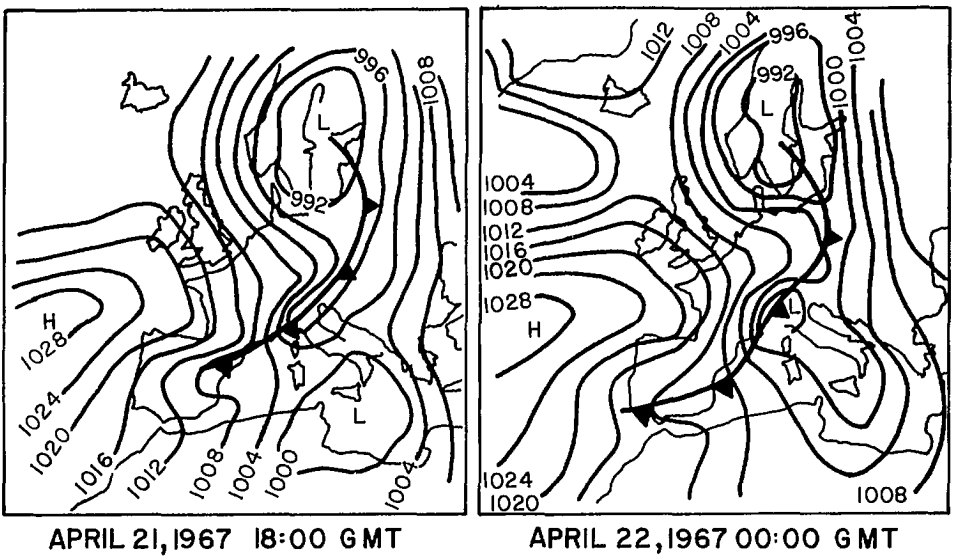

FIG. 6.120. Surface weather charts associated with the depression at the western end of the Alps that caused a storm surge at Venice during April 21–22, 1967. (Tomasin and Frasetto 1979)

where H_A and H_B are the surges at locations A and B in Fig. 6.118 and ΔV and ΔR are the contributions from wind speed and direction for the surge buildup. Using this formula, surges at Cuxhaven can be predicted knowing the surge at Borkum and measured wind speed some 3 h earlier. The relationship of wind speeds at time $t - 3$ h and time t, giving the values of ΔV in centimetres, is shown in Fig. 6.119a. The relationship of wind directions at $t - 3$ h and at time t, giving the values of ΔR in centimetres, is shown in Fig. 6.119b.

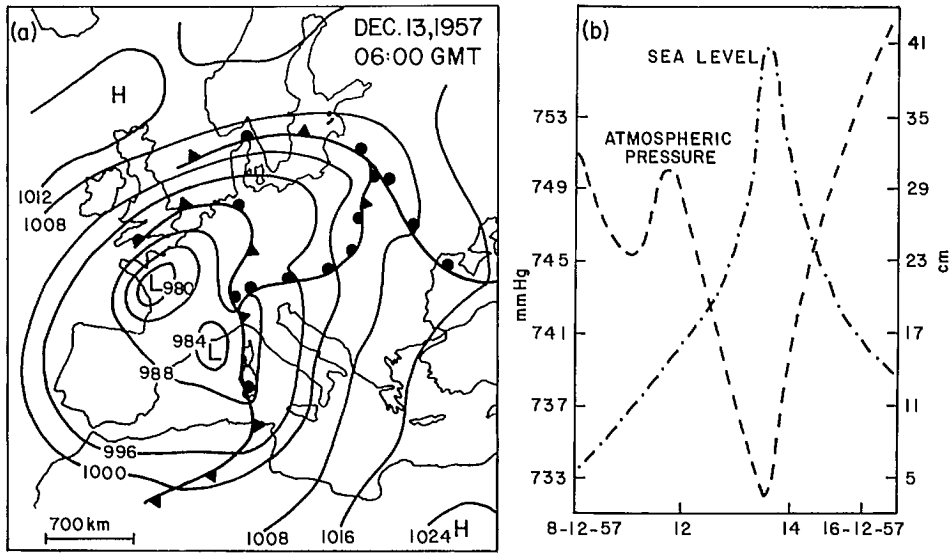

FIG. 6.121. (a) Surface weather chart showing frontal systems associated with a deep low traveling over the Ligurian Sea on December 13, 1957; (b) records of atmospheric pressure and sea level at Genoa during December 8–16, 1957. (Basano and Papa 1978)

METEOROLOGICAL CONDITIONS ASSOCIATED WITH STORM SURGES IN OTHER PARTS OF EUROPE

The city of Venice lies in a lagoon off the Adriatic Sea and less than 1 m above the mean sea level. Hence, storm surges with amplitudes less than even 1 m cause serious flooding problems in Venice. To add to the problem, the openings between the sea and the lagoon are more extensive now (due to dredging) than before, which allows the storm surge from the sea to travel unimpeded. In addition, in the twentieth century the city subsided by 20 cm.

Storm surges occur quite frequently in this area (Tomasin and Frasetto 1979), for example, in the years 1966, 1967, and 1972. The storm surge season lasts from November to February and occasionally to April. The first two normal modes of the Adriatic Sea have periods quite close to the diurnal and semidiurnal tides. The tidal range is 25–80 cm, the tide being forced from the Mediterranean Sea. There appears to be no interaction between the tide and the surge.

The Ligurian Sea is a region of cyclogenesis. Depressions from the Atlantic reaching this sea are intensified here and then travel eastwards. Southeast winds appear to generate the greatest surges in the Venice area. The surface weather charts at two times for the surge of April 21–22, 1967, are shown in Fig. 6.120. Note the depression at the western end of the Alps.

Storm surges occur on the northern part of the Atlantic coast of Portugal. Morais and Abecasis (1975) discussed the storm surge that occurred on Leixoes during January 16–17, 1973. The tidal range in this area is about 3.8 m, and wind waves up to 13 m in height occur here. The storm lasted about 24 h at Leixoes, which is unusually long for this region.

van Hamme (1979) studied the cyclogenesis in the Ligurian Sea. Basano and Papa

(1978) showed that an oscillation of the Ligurian Sea with a period of 3.66 h is conspicuous when large surges occur in this sea. Even when no surges are present, this oscillation can occur when frontal systems cross this sea from west to east. This is somewhat like the inverse barometer effect and is shown in Fig. 6.121b. The frontal system is shown in Fig. 6.121a.

Earlier in this book it was mentioned that the early studies on seiches in Lake Geneva might be considered as one of the serious beginning points for studies on storm surges. Although storm surges in this lake are not important, nevertheless, important aerodynamic drag measurements are made here. Graf and Prost (1979) summarized the data and suggested drag coefficients for various ranges of wind speed.

Bergesten (1955) discussed the water levels and winds on the coast of Sweden. He mentioned that surges with amplitudes up to 2 m occur on the Baltic coast. In the southern part of the Baltic, northerly winds raise the water level whereas southerly winds reduce it.

Gjevik and Røed (1974) discussed the storm surges along the west coast of Norway. Severe surges occur at Grip and Ona islands. Southwesterly winds appear to create large surges on the coast between 62 and 66°N. Largest surges occur when the winds are initially southwesterly; after the surge is developed, the winds become westerly. The surges on the coast from Stad to Bodø are mainly generated by the wind stress, the contribution from the atmospheric pressure gradient being smaller.

Gjevik and Røed (1974) studied especially three storm surges: (1) November 2, 1971, (2) December 30, 1972, and (3) December 31, 1972. The second and third are typical surges that frequently occur along the coast between 62 and 68°N. The first one is exceptional because the peak surge coincided with the peak tide along the coast between Sula and Sandnessjøen.

The surface weather chart at 21:00 GMT on November 2, 1971, is shown in Fig. 6.122. A low pressure system (central pressure 965 mb) crossed the Norwegian Sea in a northeasterly direction and crossed the coast at Lofoten. The strong southwesterly wind field associated with this low pressure system caused wind speeds greater than 35 $m \cdot s^{-1}$ (70 knots) at Nordøyan. The maximum surge occurred between 64 and 66°N. The surges at Hammerfest and Tromsö, however, are probably due to the atmospheric pressure gradient (and not due to wind stress) because these two stations are located to the north of the wind field associated with this system.

Gjevik and Røed (1974) presented detailed surface weather charts for the three surge cases considered here. They showed that the meteorological situation was somewhat similar for cases 1 and 3. The peak of the wind field moved with an average speed of about 25 $m \cdot s^{-1}$. These authors used the following values of drag coefficients for different wind speeds:

$$C_D = \begin{cases} 2.5 \times 10^{-3} \text{ for } 25 m \cdot s^{-1} \\ 3.0 \times 10^{-3} \text{ for } 30 \text{ } m \cdot s^{-1} \\ 3.5 \times 10^{-3} \text{ for } 35 \text{ } m \cdot s^{-1} \end{cases}$$

In the analytical model for the surges on the Norwegian coast, these authors considered surge development due to a wind field moving along the coast. The following forms are assumed for the wind stress components and the pressure field:

$$\begin{aligned} \tau_{S_x} &= \rho T_{0x} F(x, t) e^{-\alpha y} \\ \tau_{S_y} &= \rho T_{0y} G(x, t) e^{-\beta y} \\ P_0 &= \text{constant} \end{aligned} \tag{6.212}$$

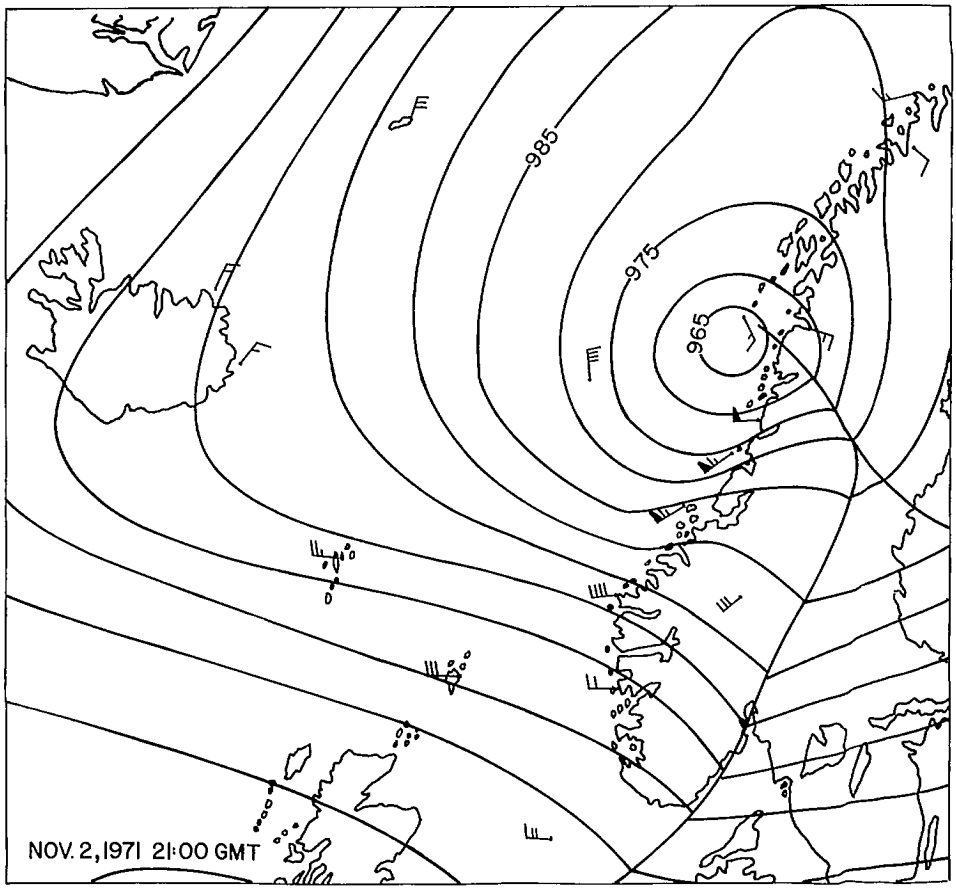

FIG. 6.122. Surface weather chart at 21:00 GMT on November 2, 1971. (Gjevik and Røed 1974)

for $t \geq 0$, where T_{0x}, T_{0y}, α, and β are constants and F and G are functions of x and t only. Here, ρ is the water density and the horizontal coordinate y is directed perpendicular to the coast. The following forms are prescribed for F and G:

$$F = e^{-K(x-u_0 t)^2}$$
$$G = e^{-Kx^2} h(t) \tag{6.213}$$

where $h(t)$ is a function of time and $0 \leq h(t) \leq 1$.

In the nondimensionalization of the equations of motion and continuity, the following two parameters appear:

$$R \equiv \frac{f}{C_0} x \tag{6.214}$$

$$\nu \equiv \frac{u_0}{C_0} \tag{6.215}$$

where R is a dimensionless wind fetch (i.e. distance between the initial position of the

wind maximum and the observation point, f is the Coriolis parameter, and $C_0 = \sqrt{gH}$, H being the average depth of the water body. Note that for $f = 1.32 \times 10^{-4} \cdot s^{-1}$ and $C_0 = 50\ m \cdot s^{-1}$, $R = 1$ gives a fetch of 380 km. Gjevik and Røed (1974) suggested that for the west coast of Norway, $R < 5$. The parameter ν expresses the travel speed of the wind field. Except in very shallow areas, this is less than unity.

Two other dimensionless parameters appear:

$$P \equiv \frac{C_0}{f}\sqrt{K} \tag{6.216}$$

$$B \equiv \frac{\alpha C_0}{f} \tag{6.217}$$

The parameter P is a Rossby number defined through a characteristic horizontal length scale of the wind field. Note that small values of P correspond to large wind fields. For the Norwegian coast, P is of order unity. Parameter B is a measure of the extent of the wind field perpendicular to the coast. Large values of B signify wind fields near the coast only. For the Norwegian coast, the contribution to the surge from the component of the wind stress normal to the coast is negligible compared with the component parallel to the coast.

6.10 Meteorological Problems Associated with Storm Surges Elsewhere than in Canada, the United States, and Europe

Northwest Pacific Ocean

Lappo and Rozhdestvenskiy (1977, 1979) studied the energy transferred to the ocean from a typhoon via the storm surge. They referred to the storm surge as meteorological ocean tides. In their calculations they ignored the influence of the wind but included the effect of the atmospheric pressure. When the cyclone is stationary, the energy transferred to the ocean is equal to the potential energy associated with the change in the sea level. For a moving cyclone, however, there is an additional transfer of kinetic energy.

Lappo and Rozhdestvenskiy (1977) formulated this problem along the lines of the classical quasi-stationary Proudman problem (Proudman 1929). For a plane pressure disturbance, with a pressure deficit of 40 mb, a cross-sectional diameter of the cyclone of 10^3 km, and the distance traveled as 5×10^3 km, these authors gave the following values for an average cyclone (Joules):

Total energy of cyclone $= E_1 = 5 \times 10^{17}$ to 8×10^{17}

Kinetic energy $= E_2 = 5 \times 10^{16}$ to 8×10^{16}

Mechanical energy imparted to the ocean (ignoring wind stress) $= E_l = 5 \times 10^{15}$

Potential energy of the storm surge created $= E_0 = 10^{15}$

Lappo and Rozhdestvenskiy (1979) considered moving disturbances with spatial scales of 100–1000 km and with time scales of ten to hundreds of hours, moving with an average speed of about $10\ m \cdot s^{-1}$. Proudman (1929) showed that for a long symmetric wave in the ocean traveling in a field of constant atmospheric pressure gradient, the forces will be unequal on its sloping parts. The horizontal component of the difference in forces

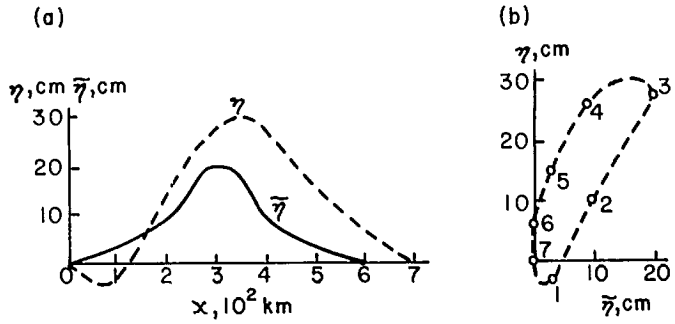

FIG. 6.123. (a) Storm surge η and static level $\bar{\eta}$ as a function of x; (b) plot of η versus $\bar{\eta}$. Numbered circles represent the values of the spatial parameter of the ηP_a loop (in hundreds of kilometres) that correspond to Fig. 6.123a. (Lappo and Rozhdestvenskiy 1979)

causes the waves to accelerate or decelerate. For a plane wave, this horizontal component F becomes

$$(6.218) \quad F = \int_{-\lambda}^{\lambda} p_a \frac{\partial \eta}{\partial x}\, dx$$

where p_a is the atmospheric pressure, η is the deviation of the water level from its equilibrium position, x is the direction along which the depression is traveling, and 2λ is the dimension of the area where $\partial p_a/\partial x \neq 0$. Let

$$(6.219) \quad \bar{\eta} \equiv -\frac{\Delta p_a}{\rho g}$$

where Δp_a is the pressure deficit in the depression, ρ is the water density (assumed to be uniform), and g is gravity.

The distribution of the actual water level η and the static water level $\bar{\eta}$ as a function of x is shown in Fig. 6.123a. A plot of η versus $\bar{\eta}$ is given in Fig. 6.123b. The graph is in the form of a curve, actually a closed loop, which was referred to as a ηp_a hysteresis loop by Lappo and Rozhdestvenskiy (1979). If the water level deviations lag behind the atmospheric pressure changes, then the loop is traversed in a counterclockwise sense with increasing x. The area S of the loop is

$$(6.220) \quad S = \oint \eta p_a dp_a$$

or

$$(6.221) \quad S = \int_{-\lambda}^{\lambda} \eta(x) \frac{\partial p_a}{\partial x}\, dx$$

If the depression is traveling in a straight line with a uniform velocity U, then it can be shown that the area of the spatial $\eta(x)p_a(x)$ loop is equal to the $\eta(t)p_a(t)$ loop, i.e.

$$(6.222) \quad \int_{-\Delta t}^{\Delta t} \eta(x - Ut) \frac{\partial p_a}{\partial t}(x - Ut)dt = \int_{-U\Delta t}^{U\Delta t} \eta(x_1) U \frac{\partial p_a}{\partial x_1}(x_1) \frac{dx_1}{U}$$

$$= \int_{-\lambda}^{\lambda} \eta(x_1) \frac{\partial p_a}{\partial x_1}(x_1) dx_1$$

In this situation, time $t = x/U$ is the parameter that varies around the loop.

Observations of traveling depressions (and the associated sea level variations) near the Kurile Islands and Japan showed that the loops can be of different shapes and sizes.

The loops with the largest areas are caused by depressions crossing the coast in a perpendicular direction. The areas of these loops are 10−100 times greater than the areas of the loops associated with pressure systems traveling parallel to the coast. Note that if there is no phase lag between the atmospheric pressure change and the change in the sea level, then the loop degenerates into a straight line. In the Kurile Islands region, the phase shift for storm surges traveling perpendicular to the shore is about 24°, whereas for surges traveling parallel to the shore, the value is about 14°. This phase shift, ϕ, varies with the time scale of the loop and attains a maximum at 10−18 h. Short-period (5−7 h) loops correspond to nondeforming storm surges.

Australia and New Zealand

Although storm surges are not a serious problem in Australia and New Zealand, they do occur and cause damage. In Australia, the areas particularly susceptible to storm surges are the central north coast of eastern Queensland and parts of the Gulf of Carpentaria. Hopley and Harvey (1979) studied the storm surges all along the coast of Australia. The cyclones in this study are listed in Table 6.70. Cyclones affect the northern parts of the east and west coasts of Australia, as well as its north coast. The frequency of cyclones (capable of generating storm surges) varies from 0.4 to 2.8 per year. Lowest central pressures occur on the east and west coasts between 20 and 25°S. The central pressures on the west coast are usually 3−4 mb lower than those on the coast of Queensland. Central pressures drop gradually towards the north but more drastically towards the south.

Intense cyclones with central pressures less than 960 mb occur on the central part of the west coast (Northwest Cape to Port Hedland), the region between Princess Charlotte Bay and Mackay on the Queensland coast. However, in the Gulf of Carpentaria, central pressures less than 960 mb rarely occur.

Cyclones in the Australian region usually travel with speeds between 6 and 11 knots although sometimes with a speed as high as 35 knots (particularly on the Queensland coast between 25 and 30°S). They travel with low speeds over the Gulf of Carpentaria and off Arnhemland (Coleman 1972). The variabiility in the meteorological parameters associated with cyclones in the Australian region, based on data for 1960−72, is shown in Table 10.3 of Hopley and Harvey (1979). This variability was determined for the following three parameters: (a) variability in the direction of movement by measuring the difference between the point on the coast for which the cyclone was heading 24 h prior to landfall and the observed landfall location, (b) variability in pressure by comparing changes in the pressure field during the 24 h prior to landfall, and (c) variability in the speed of movement by comparing the average speed in the 24 h prior to landfall with the mean speed in the previous 24 h.

Nelson (1975) listed 30 severe tropical cyclones in the Australian region during the period 1880−1970 that generated storm surges with amplitudes of at least 0.5 m along the north coast of Australia. One of the lowest central pressures ever recorded, a storm on March 5, 1899, that traveled over Bathurst Bay and struck Barrow Point on the Queensland coast, was 914 mb. The storm and the storm surge together killed 300 people and the surge penetrated 5 km inland (Whittingham 1958).

In the 1970's two storm surges did considerable damage in Australia. Cyclone Althea of December 24, 1971, made a landfall to the north of Townsville on the Queensland

TABLE 6.70. Cyclones in and around Australia. (Hopley and Harvey 1979)

Name	Date of landfall or nearest point to coast	Tidal station closest to cyclone	Lowest central pressure (mb)	Highest record of surge at any station (m)	Remarks
Adeline	Jan. 28, 1973	Centre Island	990	0.52	
Agnes	Mar. 6, 1956	Townsville	961	1.4	
Althea	Dec. 24, 1971	Townsville	952	2.85	3.6 m at Toolakea
Bridget	Jan. 27, 1969	Lucinda	1002	0.34	
Emily	Apr. 2, 1972	Gladstone	920	1.78	Filled rapidly before crossing
Eva	Dec. 4, 1970	Broome	970	0.16	1.2- to 1.5-m surge reported at Broome (Met. Bur. 1973)
Gertie	Feb. 16, 1971	Lucinda	983	0.52	
Glynis	Feb. 6, 1970	Perth	970	1.01	Surge incorrectly reported as 4.1 m above normal at Carnarvon (Met. Bur. 1973). Record tides elsewhere
Ida	Feb. 16, 1971	Mourilyan	980	0.37	
Ingrid	Feb. 16, 1970	Carnarvon	970	1.32	Surge incorrectly reported as 2.3 m above normal at Carnarvon (Met. Bur. 1973)
Joan	Dec. 7, 1975	Port Hedland	~992	1.52	Port Hedland recorder malfunction during rising surge
Leah	Feb. 28, 1973	Milner Bay	990	0.45	
Madge	Mar. 4, 1973	Milner Bay	990	0.42	Affected east coast and Gulf
Pam	Feb. 6, 1974	Kirra	~930	0.4	Came within 450 km of Queensland but very large cyclone
Sheila–Sophie	Feb. 3, 1971	Port Hedland	970	1.8	
Tracy	Dec. 24, 1974	Darwin	940	1.6	2.0-m surge reported to north of city
Una	Dec. 19, 1973	Townsville	988	0.72	
Wanda	Jan. 25, 1974	Noosa	990	0.6	Associated with Brisbane floods
Zoe	Mar. 13, 1974	Broadwater	975	0.56	

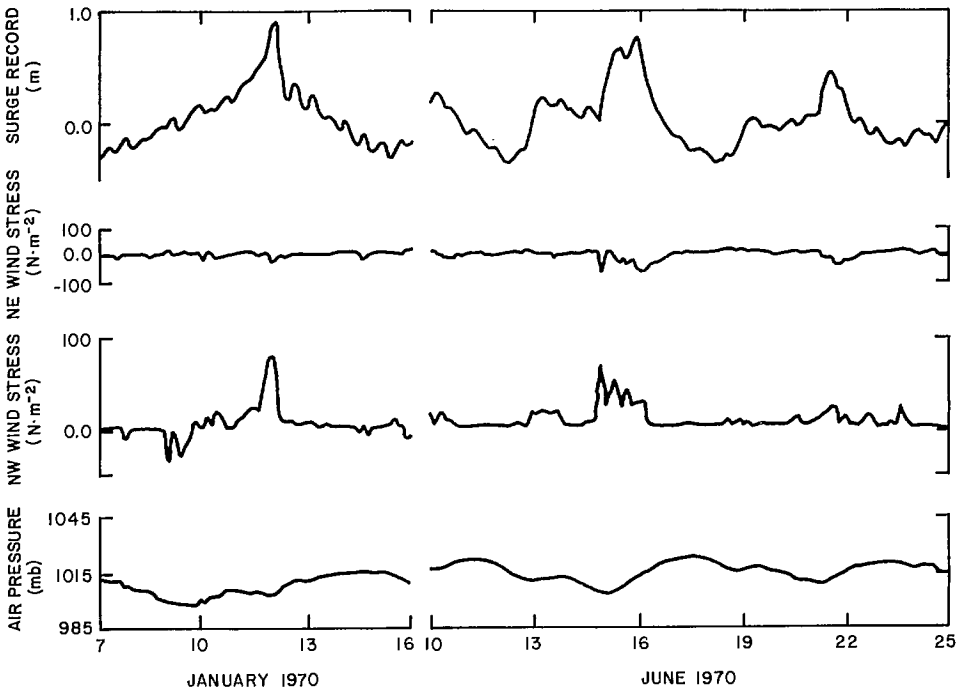

FIG. 6.124. Storm surges, atmospheric pressure, and wind stress at Adelaide, Australia. (Tronson and Noye 1973)

coast. Winds up to 196 $km \cdot h^{-1}$ and lowest central pressure of 971.5 mb generated a maximum surge of about 2.7 m at Townsville. Cyclone Tracy of December 25, 1974, hit Darwin; a central pressure of 955 mb and winds up to 200 $km \cdot h^{-1}$ generated a maximum surge of about 1.6 m.

Tronson and Noye (1973) developed statistical models to predict storm surges on the coast near Adelaide in South Australia. The storm surges in this region are particularly sensitive to the wind direction. On April 12, 1948, steady winds from the southwest with a speed of 90 $km \cdot h^{-1}$ caused a surge of about 1.2 m. On June 28, 1972, a surge with the same amplitude was generated by winds from the northwest, with a speed of about 45 $km \cdot h^{-1}$. Surges with amplitudes of up to 4 m can occur at Adelaide, e.g. on May 12, 1960, and June 28, 1972. The atmospheric pressure field, the wind stress, and the surges at Adelaide for two cases (January 7–16 and June 10–25, 1970) are shown in Fig. 6.124.

Heath (1979) discussed the storm surges on the coasts of New Zealand. Storm surge amplitudes on the coasts of New Zealand are rather small and are usually less than 1 m (Agnew 1966; Gilmour 1963; Pickrill 1972). Even though the amplitudes may be small, they could cause severe erosion, especially on the west coast of the North Island, in the Bay of Plenty, and on the east coast of the North Island, north of Auckland.

Heath (1979) studied the following three surges: April 9–11, 1968, on the east coast of the North Island, July 30–August 1, 1975, on the east coast of the South Island, and September 11–14, 1976, on the west coast of the North Island. The surface weather chart for the third case is given in Fig. 6.125.

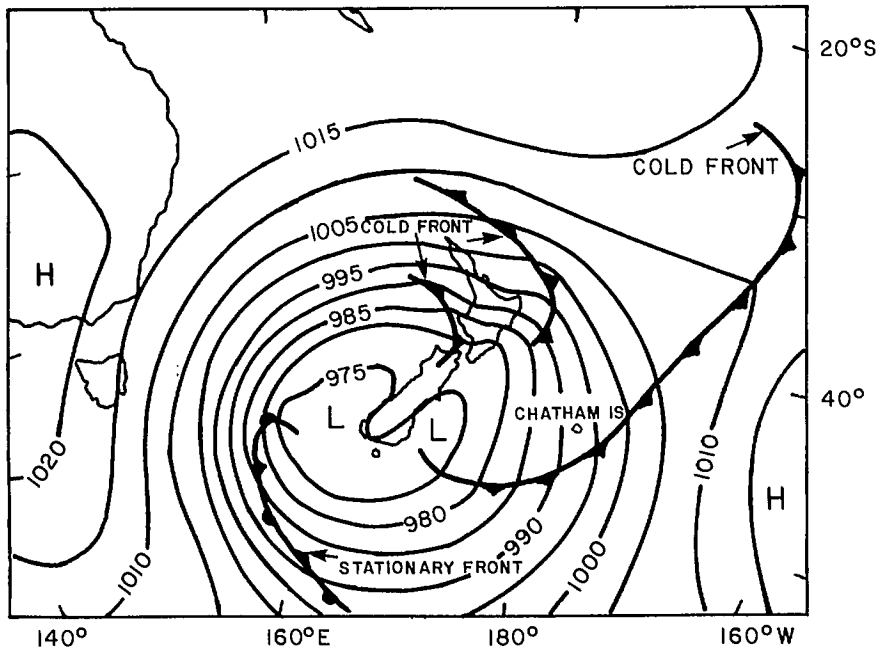

FIG. 6.125. Simplified surface weather chart at 0 h (New Zealand Standard Time) on September 13, 1976. (Heath 1979)

JAPAN

During the period 1900–53, at least 60 major storm surges occurred in Japan (Wadati and Hirono 1954). The dates and locations of the surges are listed in their Table 1. The locations where major surges have occurred are shown in Fig. 6.126. The tracks of some of the typhoons that generated surges in Tokyo Bay are illustrated in Fig. 6.127.

Storm surges occur frequently in Ariake Sea, the Seto Inland Sea, Osaka Bay, Tokyo Bay, Suruga Bay, and Toyama Bay. The first four of these are shallow water bodies; only Toyama Bay is situated on the northwest side of the country. Most of the shallow water bodies in Japan are situated on the southern coastline with their mouths towards southwest. Wadati and Hirono (1954) listed the pressure fields, wind speeds and directions, damage, and the number of people killed during major surges in these bays.

For early (i.e. precomputer days) investigations of storm surges in and around Japan, see Terada and Yamaguti (1928), Yamaguti (1929), Kawabata and Fujito (1951), Honsyû (1932), and Unoki (1959). Terada (1912) and Nakano (1949) investigated the secondary undulations associated with storm surges in Japan. Rabe and Brand (1980) studied the extreme sea states associated with typhoons.

Miyazaki (1975) studied the characteristics of storm surges along the coast of Japan. Some of the major surges (that exceeded 2 m) during the period 1900–73 are listed in Table 6.71. The damage associated with some selected surges is listed in Table 6.72.

There were 15 major surges in Kobe harbor during the period 1926–54. The surge of September 21, 1934, had a peak value of 3.5 m (Miyazaki 1975). These surges and pertinent meteorological data are listed in Table 1 of Miyazaki (1975). Nomitsu (1935) studied the surges in Lake Biwa due to the Muroto typhoon of September 21, 1934. Ogura

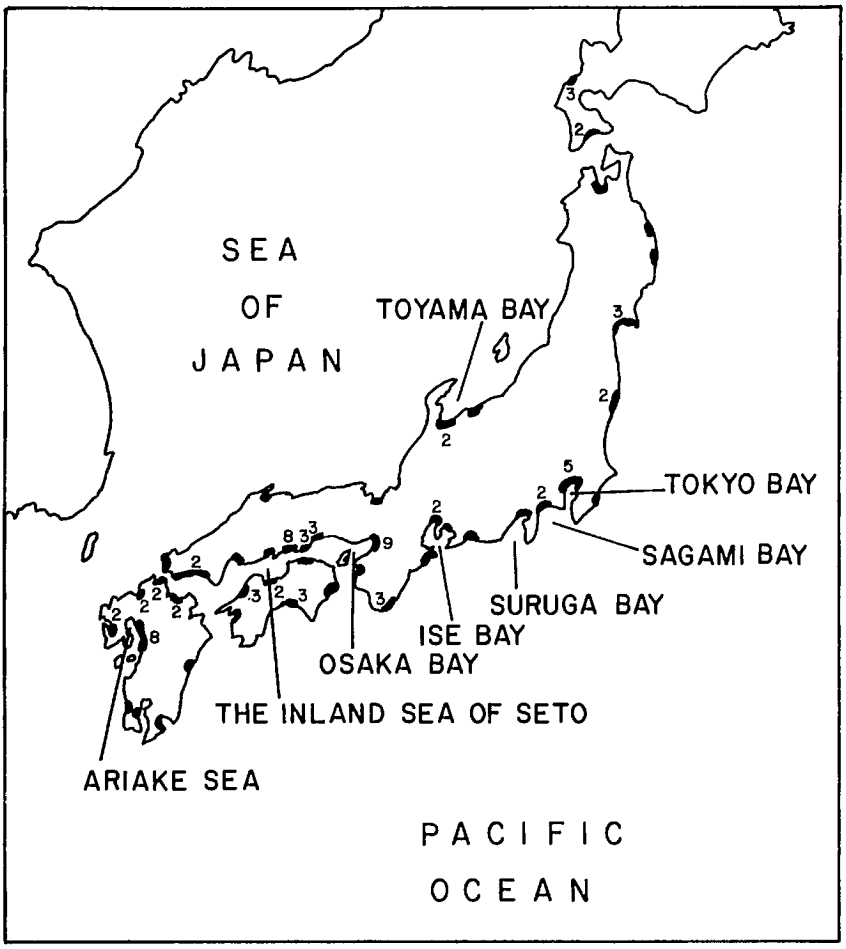

FIG. 6.126. Locations on the coast of Japan where storm surges occurred during 1900–53 (numerals indicate number of occurrences). Blackened coastal areas without numerals had one occurrence. (Wadati and Hirono 1954)

(1925) studied the surges around the Tisima or Kurile Islands. Terada (1939) used an analtyical model to study the storm surges in Osaka Bay due to the Muroto typhoon.

In Japanese storm surges, the contribution from the atmospheric pressure gradients was at most 15%. In the numerical model of Isozaki (1970a, 1970b, 1970c) the following pressure field distributions were specified:

$$p(r) = p(\infty) - \frac{\Delta p}{\left[1 + \left(\frac{r}{r_0}\right)^2\right]^{1/2}} \tag{6.223}$$

or

$$p(r) = 1010 - \frac{\Delta p}{\left(1 + \frac{r}{r_0}\right)^2} \tag{6.224}$$

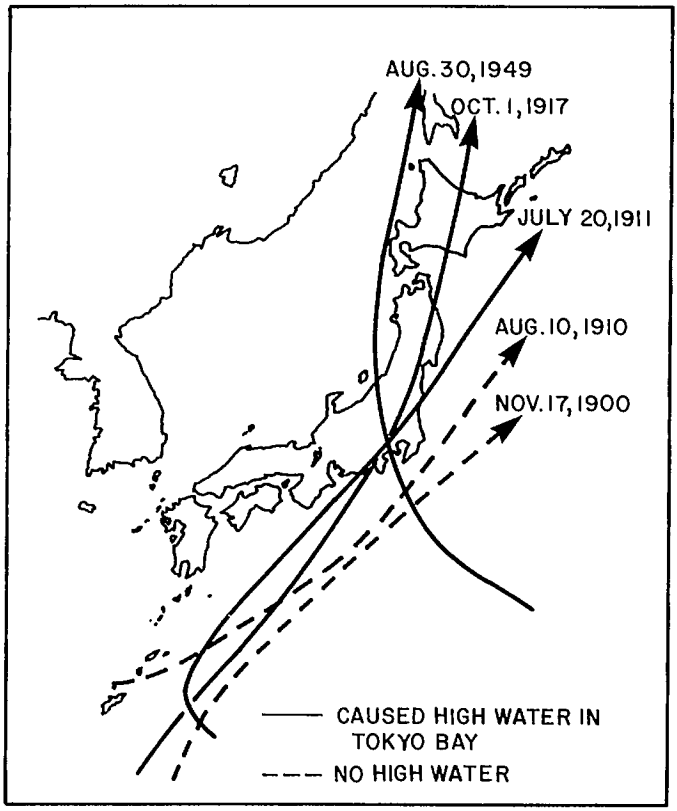

FIG. 6.127. Tracks of typhoons that passed near Tokyo Bay. (Wadati and Hirono 1954)

TABLE 6.71. Storm surges in Japan during the period 1900–73 with maximum amplitudes in excess of 2 m. Highest level includes surge and tide. (Miyazaki 1975)

				Meteorological extreme values		
Date	Affected area	Peak surge (m)	Highest level (m)	Central pressure (mb)	Wind ($m \cdot s^{-1}$)	Location
Oct. 1, 1917	Tokyo Bay	2.3	3.1	950.4	SSE 40.0	Tokyo
July 18, 1930	Ariake Sea	2.5	—	954.6	ENE 30.6	Tomie
Sept. 21, 1934	Osaka Bay	3.1	3.2	954.3	S 48.4	Osaka
Sept. 1, 1938	Tokyo Bay	2.2	—	978.6	S 31.0	Tokyo
Sept. 3, 1950	Osaka Bay	2.1	2.5	964.3	NE 33.4	Kobe
Aug. 17, 1956	Ariake Sea	2.4	4.2	968.4	SE 27.0	Saga
Sept. 26, 1959	Ise Bay	3.4	3.9	958.5	SSE 37.0	Nagoya
Sept. 16, 1961	Osaka Bay	2.5	2.9	937.3	SSE 33.3	Osaka
Sept. 25, 1964	Osaka Bay	2.1	2.6	983.5	S 27.1	Sumoto
Sept. 10, 1965	Osaka Bay	2.2	—	966.0	SSE 38.8	Sumoto
Aug. 21, 1970	Tosa Bay	2.4	3.1	962.3	SW 35.8	Ashizuri

TABLE 6.72. Severe damage caused by storm surges in Japan during the period 1900–73. (Miyazaki 1975)

Date	Affected area	Highest sea level (m)	Peak surge (m)	Lives lost	Houses destroyed or swept away
Oct. 1, 1917	Tokyo Bay	3.0	2.1	1324	60 175
Sept. 13, 1927	Ariake Sea	3.8	0.9	439	2 211
Sept. 21, 1934	Osaka Bay	3.1	2.9	3036	92 323
Aug. 27, 1942	Inland Sea	3.3	1.7	1158	102 374
Sept. 17, 1945	South Kyushu	2.6	1.6	3121	115 984
Sept. 3, 1950	Osaka Bay	2.7	2.4	534	120 923
Oct. 14, 1951	South Kyushu	2.8	1.0	943	72 648
Sept. 27, 1959	Ise Bay	3.9	3.4	5098	156 676
Sept. 16, 1961	Osaka Bay	3.0	2.5	200	54 782

where $p(r)$ and $p(\infty)$ are the sea level pressures at radial distance r and at the periphery of the typhoon, respectively, r_0 is the radius of maximum winds, and Δp is the pressure drop. Equation 6.224 gives a more rapid decrease of pressure with r but uses a constant value of 1010 mb at the typhoon periphery. The cyclostrophic wind corresponding to eq. 6.224 is

$$V^2 = 4V_m^2\left[\frac{\mu^2}{(1+\mu^2)^2}\right] \tag{6.225}$$

where $\mu \equiv r/r_0$ and V_m is the maximum wind at r_0. The maximum wind and the pressure drop are related through

$$V_m = C(V_m)^{1/2} \tag{6.226}$$

where C is a constant.

In other studies, the Jelesnianski (1972) model is used:

$$v(r) = V(r_0)\frac{2r_0}{r_0^2 + r^2} \tag{6.227}$$

where, again, r_0 is the radius of maximum winds. Myers and Malkin (1961) determined the angle of inflow for a stationary storm using the equations of motion. The angle varies from 0 at the center of the storm to about 30° at a radial distance of about $3r_0$ (where r_0 is the radius of maximum winds) and is roughly constant after that. Usually, within the region up to r_0, the wind field computed from the pressure field (i.e. cyclostrophic or gradient winds) is reasonably correct. Outside r_0, the angle of inflow (i.e. the angle of the wind vector across circular isobars) must be considered.

Takahashi (1939) used the following form:

$$p(r) = p(\infty) - \frac{\Delta p}{\left(1 + \frac{r}{r_0}\right)} \tag{6.228}$$

This formula underestimates the pressure field at the center. Kawahara et al. (1980) used a finite-element model for storm surge propagation in Suragawa Bay. They used eq. 6.223 to specify the pressure field.

In China, storm surges mainly occur on the southeastern coast. In the 1970's, the biggest storm surge in China occurred at Shantou on August 2, 1979. The peak surge was over 2 m. In the dynamic models for surge prediction used in China (Jin-Chuan and Guang 1979), Myers' (1954) formula (similar to eq. 6.134) is used:

$$\Delta p = \Delta p_0(1 - e^{-R/r}) \tag{6.229}$$

where

$$\Delta p_0 = p_\infty - p_C \text{ and } \Delta p = p_\infty - p \tag{6.230}$$

where p_C is the central pressure, p_∞ is the peripheral pressure, p is the pressure at any point at distance r from the center, and R is the radius of maximum winds.

The tangential component of the wind field is expressed as

$$V_0 = \begin{cases} V_{\max}\dfrac{r}{R}\cos\alpha & \text{for } r \le R \\ V_{\max}\dfrac{R}{r}\cos\alpha & \text{for } r > R \end{cases} \tag{6.231}$$

The radial component of the wind field is written as

$$V_r = \begin{cases} -V_{\max}\dfrac{r}{R}\sin\alpha & \text{for } r \le R \\ -V_{\max}\dfrac{R}{r}\sin\alpha & \text{for } r > R \end{cases} \tag{6.232}$$

where α is the angle measured inward between the wind direction and the isobars. In the surge computations for the Chinese coast, α was taken as 30°.

The tangential and radial components of the wind stress are computed from:

$$\begin{aligned} \tau_0 &= K\rho_a|V|V_0 \\ \tau_r &= K\rho_a|V|V_r \end{aligned} \tag{6.233}$$

where $K = 2.5 \times 10^{-3}$ and $\rho_a = 1.2 \times 10^{-3}$ g·cm^{-3}.

Storm surges are quite frequent in Hong Kong. About three to four occur per year in Hong Kong Harbor (World Meteorological Organization 1978). A total of 35 surges with amplitudes varying from 0.2 to 1.8 m occurred in Hong Kong during 1954–64 (Cheng 1967). One of the important surges was caused by Typhoon Wanda in September 1962. The surge was 1.8 m at Hong Kong and 3.2 m at Taipo (farther inland in a narrow channel).

Chan and Walker (1979) mentioned that two of the most disastrous surges in Hong Kong occurred on September 2, 1937, and September 1, 1962, in the Tolo Harbor region. Watts (1959) concluded that pronounced surges occur in Hong Kong when the center of a westward moving storm passes over Hong Kong within several tens of kilometres to the south.

If the storm track lies to the west of Hong Kong, the wind field at Hong Kong will be strong (east–northeast to east–southeast) and a major surge could be generated. On the other hand, if the track is to the east of Hong Kong, the winds will be weak (west–northwest to west–southwest) and surges, if generated, will be small. Most of the

storms that affect Hong Kong originate in the Philippine Sea. A few, however, develop in the South China Sea, and in this case, the above criterion (track to the east or west of Hong Kong) does not apply. Also, those storms that make a landfall at Hong Kong usually are associated with weak local winds and would not generate significant surges. The major surges at Hong Kong are associated with storms that make a landfall within 60 nautical miles (111 km) either to the north or south of Hong Kong.

Based on storm surge data at North Point, the storm surges are classified into three categories by Chan and Walker (1979): type O refers to storms whose centers lie within a 60 nautical mile radius of Hong Kong, type W for storms whose centers are outside the 60 nautical mile radius and which travel to the west of Hong Kong over the land, and type E for storms with centers outside the radius and traveling over the land to the east of Hong Kong. For these three categories, the average values of the peak surges are 2.49 ± 0.25, 1.71 ± 0.13, and 1.31 ± 0.18 ft (1 ft = 0.3048 m).

For type O storms, the following empirical relation was deduced:

$$s = 0.102\,(1009.1 - p) \tag{6.234}$$

where s is the peak surge (feet) and p is the local minimum hourly sea level pressure (millibars). Note that in this relation, the local minimum hourly mean sea level pressure is used to represent the central pressure of the storm when it landfalls near Hong Kong. For type O storms, the coefficient of correlation between the central pressure and the peak surge was -0.89. For type W and E storms the correlation was poor.

Again, for type O storms, the correlation coefficient between the peak surge s and the maximum hourly mean wind speed W_{60} was 0.84 and the following regression equation was derived:

$$s = 0.088 W_{60} - 0.75 \tag{6.235}$$

The local wind field appears to have more influence on the type W and E storm surges than type O. For type W, maximum surges are associated with winds from east–northeast, east, or east–southeast. The following relation has been empirically deduced for type W storm surges:

$$s_W = 0.00217\, W_{60}^2 + 0.43 \tag{6.236}$$

The correlation coefficient between s_W and W_{60}^2 was 0.88. No correlation could be found for type E storm surges.

Lau (1980a, 1980b) adapted the SPLASH (Jelesnianski 1972, 1974) model to predict storm surges in Hong Kong. Using 57 hypothetical storms, peak surge heights at various locations along the South China coast near Hong Kong were determined. In these calculations, a standard storm is chosen with the following six parameters: (a) a central pressure of 973 mb at nearest approach, (b) a movement on bearing 300° at nearest approach, (c) a speed of 10 knots at nearest approach, (d) a radius of maximum winds of 26 nautical miles at nearest approach, (e) a nearest approach of 26 nautical miles, and (f) landfalling to the west of Hong Kong. This standard storm will generate on an open coast a surge (using the SPLASH program) of 1.92 m at North Point.

Bay of Bengal

In principle, the entire coast of the Bay of Bengal from Sri Lanka to Thailand is vulnerable to storm surges, although in practice, storm surges occur only on certain stretches. Storm surges are not frequent in Sri Lanka; however, in 1978 a major surge

TABLE 6.73. Storm surges on the coasts of Tamilnadu and Andhra Pradesh in Southeast India during 1964–77. (Modified from DeAngelis 1978a)

Date	Minimum estimated central pressure (mb)	Maximum estimated wind speed ($km \cdot h^{-1}$)	Point of landfall	Remarks
Dec. 17–24, 1964	970	120	South of Tondi	Storm surge amplitude at Dhanushkodi about 5 m, 500 people died
Dec. 4–8, 1967	988	130	Near Nagapattinam	Major storm surge, 7 people died
Nov. 4–9, 1969	970	176	Between Masulipatnam and Kakinada	Storm surges at Visakhapatnam and and Koringa, 200 people died
Sept. 7–14, 1972	957	204	Near Baruva	Storm surges of 1–3 m between Baruva and Chandbali
Nov. 15–23, 1972	983	148	South of Nellore	Minor storm surge
Nov. 14–20, 1977	919	250	Chirala	Surges up to 6 m near Divi. At least 10 000 people died. Surges occurred on a coastal stretch 80 km long and penetrated 8–15 km inland

TABLE 6.74. Relationship between T number, maximum wind speed, and pressure drop in a cyclone. (Dvorak 1975a; Mishra and Gupta 1976)

T	Maximum wind speed ($km \cdot h^{-1}$)	Pressure drop (mb)	T	Maximum wind speed ($km \cdot h^{-1}$)	Pressure drop (mb)
1	46	—	5	167	40
1.5	46	—	5.5	189	52
2	56	—	6	213	66
2.5	65	6	6.5	235	80
3	83	10	7	259	97
3.5	102	15	7.5	287	119
4	120	21	8	315	143
4.5	143	29			

occurred that caused great devastation. Most of the storms developing in the Andaman Sea travel towards northwest and strike the coast of Tamilnadu or Andhrapradesh (southeast part of India), rather than travel towards the west and strike the coast of Sri Lanka. Certain storms have a more northerly component in their motion and these can landfall on the coast of Orissa. Those that recurve can hit the coasts of West Bengal, Bangladesh, and Burma.

On the coasts of Tamilnadu and Andhrapradesh, at least six storm surges occurred during the period 1964–77. These are listed in Table 6.73 along with the minimum central pressure and maximum wind speed. There appears to be some controversy regarding the intensity of the November 1977 cyclone (last entry in Table 6.73). Pant et al. (1980) suggested that the minimum central pressure was 943 mb and the maximum wind speed was 125 knots (231 $km \cdot h^{-1}$). This cyclone intensified from T6 to T7 between November 17 and 19 (see Table 6.74 for the classification of T numbers in terms of pressure drop and wind speed). Ghosh (1980) suggested that the lowest pressure was 919 mb and not 943 mb. In intensity, this cyclone was comparable with that of the 1927 cyclone. However, the 1927 cyclone generated a surge smaller than the 1977 cyclone (in the storm surge of 1927, 300 people died compared with at least 10 000 in the 1977 surge). The 1927 cyclone made a landfall near Nellore where the topography was much steeper and hence the surge was smaller. Another cyclone that had a pressure drop in excess of 90 mb occurred in 1885 (Eliot 1890).

At Visakhapatnam, on the east coast of India, the maximum (positive or negative) surge appears to occur usually about a day after the winds attain their maximum intensity. The amplitude of the surge depends more on the wind direction than on the wind speed (Ramanadham and Varadarajulu 1965). The storm surges at Visakhapatnam are usually associated with three types of storm tracks: (a) storms originating to the south of Visakhapatnam and recurving near the east coast of India and making a landfall at the Chittagong–Arakan coast, (b) storms originating to the south of Visakhapatnam and crossing the coast between Masulipatnam and Visakhapatnam, and (c) storms that develop in the northern part of the Bay of Bengal and cross the coast near the head of the Bay. Storms of the first two types produce positive surges and storms of the third type produce negative surges at Visakhapatnam. The maximum amplitudes of the surges are usually between 40 and 50 cm.

The observed winds appear to have a linear relationship with the gradient wind calculated from the following formula:

$$(6.237) \quad V_g = \left[\frac{R}{\rho}\frac{\partial p}{\partial r} + (\omega R \sin \phi)^2\right]^{1/2} - \omega R \sin \phi$$

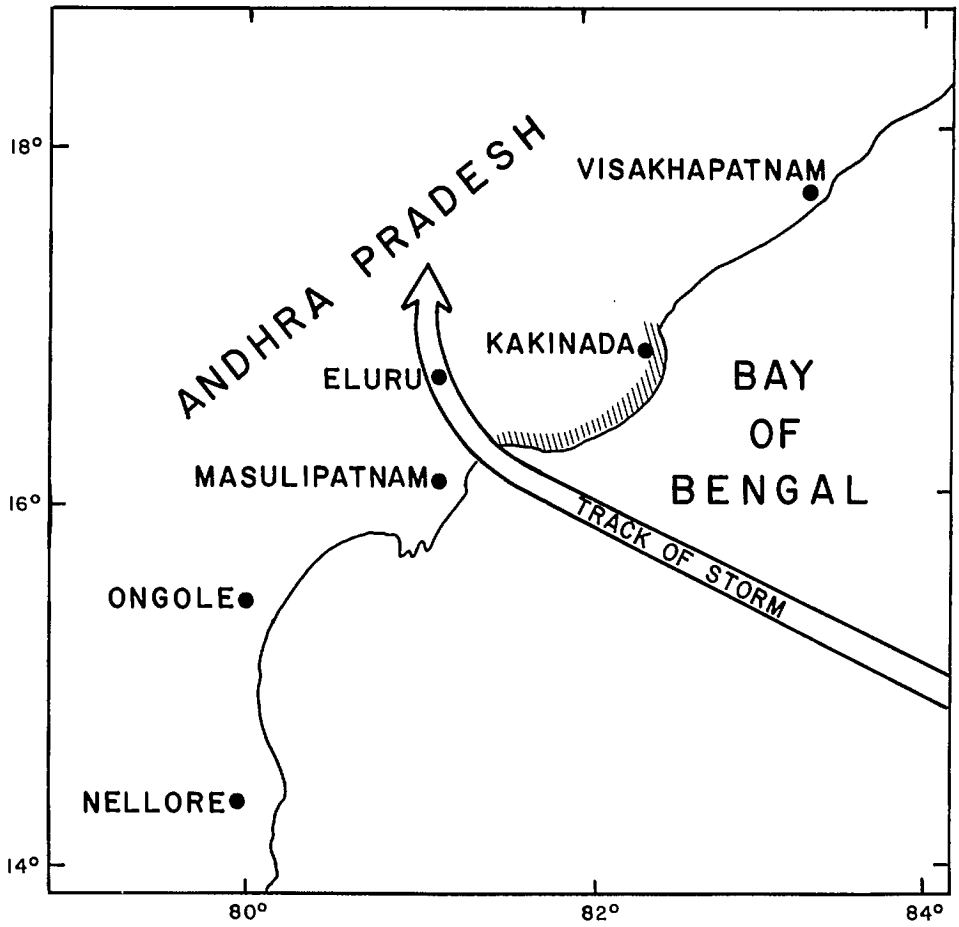

FIG. 6.128. Track of the storm of October 1949 on the southeast coast of India. Hatched area shows the coastline affected by the storm surge. (Rao 1968)

where V_g is the gradient wind, ω is the angular velocity of the earth's rotation, ϕ is the latitude, R is the radius of curvature of the isobars, and ρ is the density of air. It was found that

$$\frac{V}{V_g} = 0.6$$

where V is the wind as measured from ships offshore.

Although storm surges may be of small amplitude at Visakhapatnam, south of it, storm surges could have very large amplitudes. The cyclone of October 28, 1949, made a landfall north of Masulipatnam (Fig. 6.128). Winds up to 90 knots (167 km·h^{-1}) produced storm surges with amplitudes of 3–4 m along a stretch of the coast shown in Fig. 6.128. The storm crossed the coast at the time of high tide (Rao 1968).

Another severe storm struck the Coromandel Coast on November 30, 1952 (Rao 1968). Again, winds up to 90 knots produced surges with amplitudes up to 2.5 m

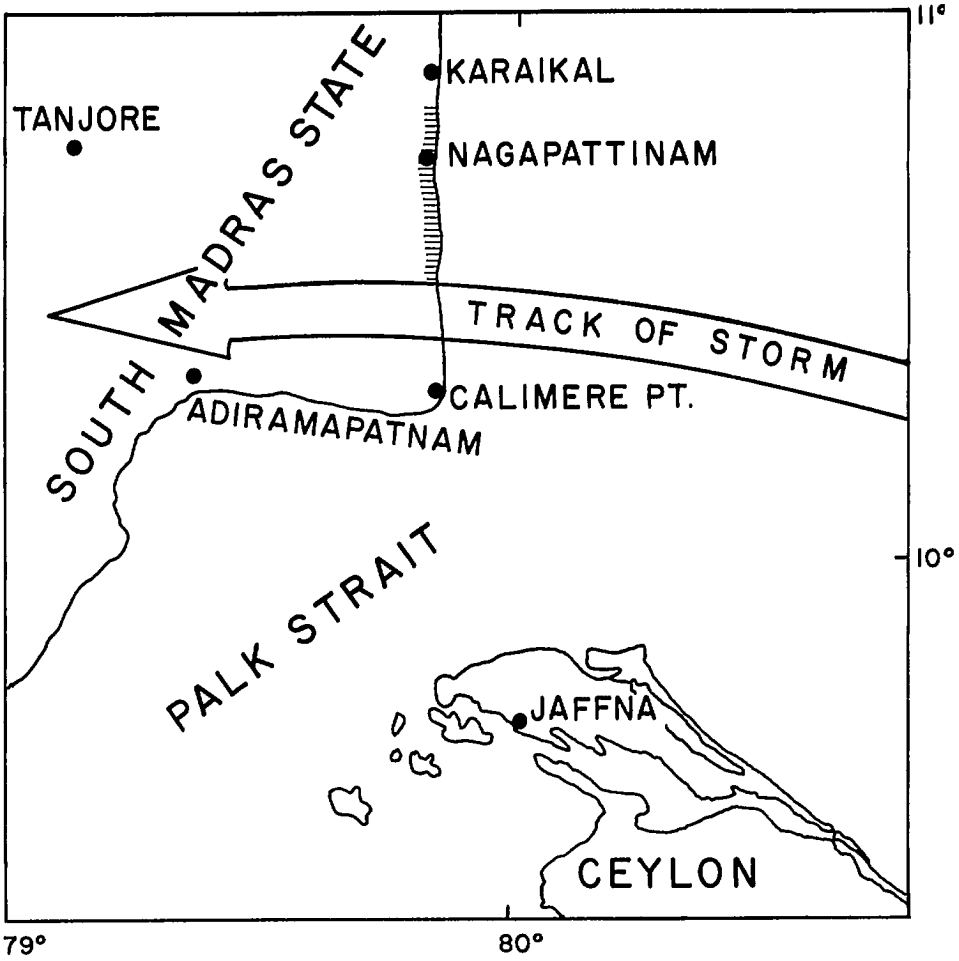

FIG. 6.129. Track of the storm of November 1952 on the southeast coast of India. Hatched area shows the coastline affected by the storm surge. (Rao 1968)

along a stretch of the coast shown in Fig. 6.129. Another severe cyclonic storm traveled towards the west over the northern boundary of the Palk Strait (between India and Sri Lanka) on November 30–December 1, 1955. Two different storm surges occurred (Rao 1968). The first one was along the coast between Point Calimere and Vettaikaran Iruppu and had amplitudes up to 2 m. The second surge occurred between Thambkottai and Kattumavedi with amplitudes over 1 m.

One of the most destructive storm surges in southern India occurred on December 23, 1964 (Fig. 6.55). Winds up to 120 knots (322 $km \cdot h^{-1}$) created storm surges over the islands of Mannar (Sir Lanka) and Rameswaram (India) and the maximum amplitudes of the surges were 5–6 m. This storm exhibited some interesting features: (a) the major surges occurred to the left of the storm track (at Pamban–Dhanushkodi Islands), (b) the surges preceded the arrival of the storm by approximately 3–4 h, (c) although winds up to 80 knots (148 $km \cdot h^{-1}$) were recorded to the west of the Pamban Bridge, no surges

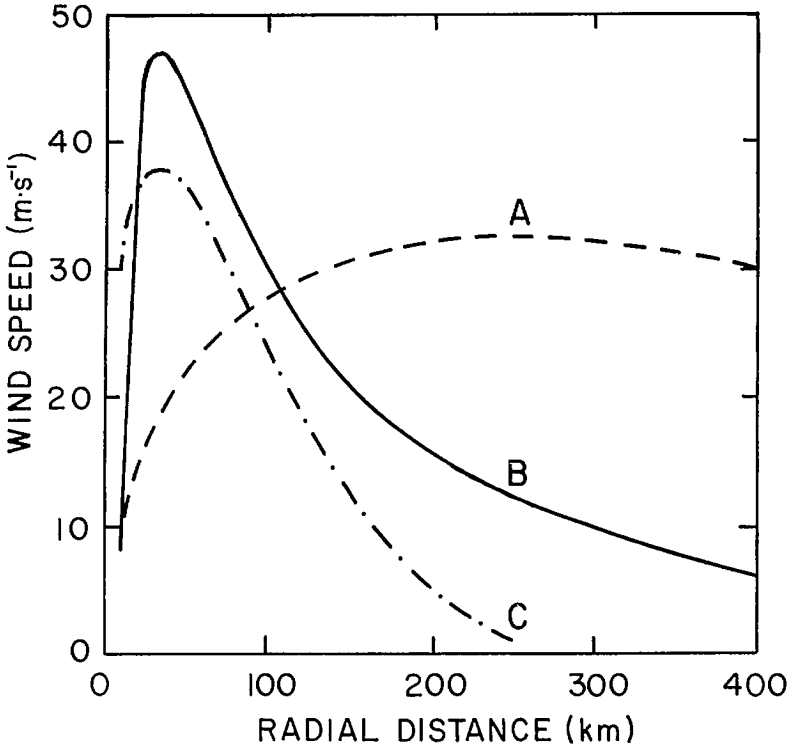

FIG. 6.130. Gradient wind speed versus radial distance. Curve A, R = 350 km; curve B, R = 35 km; curve C, from eq. 6.243. (Holland 1981)

occurred along this part of the coastline.

It was mentioned that the amplitude of storm surges at Visakhapatnam is not significant. Generally, north of Visakhapatnam, the storm surge activity is not severe, except on some stretches of the Orissa coast, until one arrives at the coast of Bangladesh. Saugor Island (India) is situated near the head of the Bay of Bengal where the Hoogly Estuary empties into the Bay. On this island, the surge heights usually range from 1/3 to 1 m (Janardhan 1967).

Johns and Ali (1980) used the following pressure distribution in their simulation of the November 1970 storm surge that caused great devastation in Bangladesh.

$$(6.238) \quad p = p_a - \Delta p \exp\left(-\frac{r}{R}\right)$$

where p is the pressure field at radius r, p_a is the ambient pressure, Δp is the difference between the ambient and central pressures, and R is the e-folding radius of the pressure distribution.

A value of 350 km was given to R. Holland (1980) pointed out that R should be the radius of maximum winds and that a typical value of R should be about 35 km.

The argument that R should be the radius of maximum winds was developed by Holland (1981) as follows. For tropical cyclones, a typical Rossby number will be about 100, in the strongest wind region. One may assume a cyclostrophic balance and write

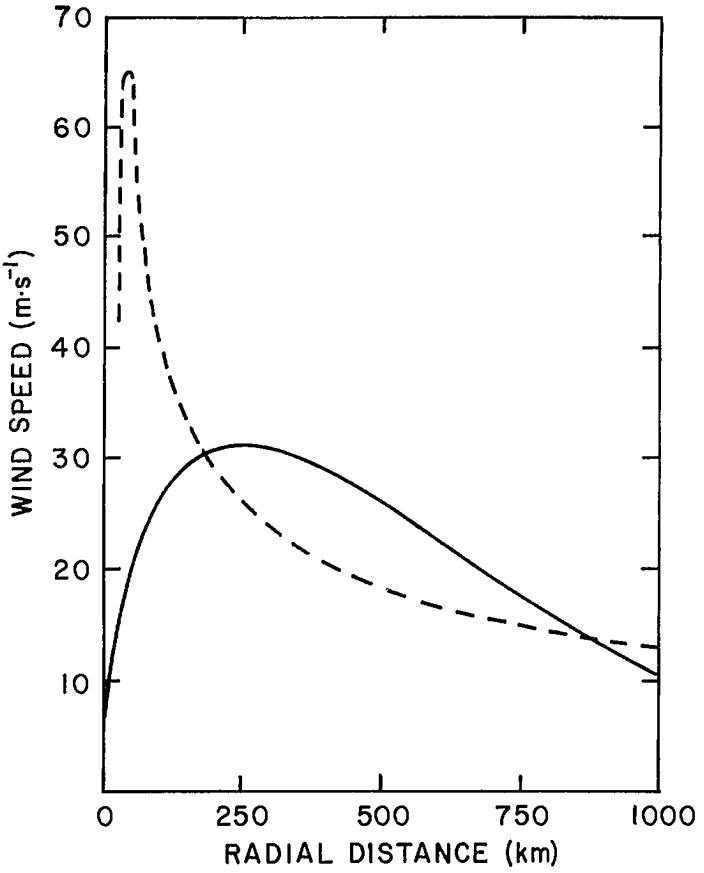

FIG. 6.131. Gradient wind speed versus radial distance. Solid line, using eq. 6.238 and $R = 350$ km; broken line, using eq. 6.143, $R = 40$ km, and $V_m = 65\ \mathrm{m \cdot s^{-1}}$. (Johns and Ali 1981)

$$V_c = \left(\frac{r}{\rho}\frac{\partial p}{\partial r}\right)^{1/2} \tag{6.239}$$

where V_c is the cyclostrophic tangential wind and ρ is the air density. Substituting eq. 6.238 into 6.239 gives

$$V_c = \left[\frac{r\Delta p}{\rho R}\exp\left(-\frac{r}{R}\right)\right]^{1/2} \tag{6.240}$$

A plot of V_c versus r shows a rapid increase in wind speed with radius from the center to a maximum and then a gradual decrease followed by a tangential approach to zero at infinite distance. To determine the radius of maximum winds, eq. 6.240 is differentiated with respect to r and equated to zero:

$$\frac{\partial V_C}{\partial r} = \frac{1}{2}\left[\frac{r\Delta p}{\rho R}\exp\left(-\frac{r}{R}\right)\right]^{1/2}\left(1 - \frac{r}{R}\right)\frac{\Delta p}{\rho R}\exp\left(-\frac{r}{R}\right) \tag{6.241}$$

The nontrivial solution of eq. 6.241 is for $r = R$. Thus, R is the radius of maximum winds.

Wind speed versus radial distance is shown in Fig. 6.130. The wind speed is computed from the gradient wind formula:

$$(6.242) \quad V_g = \left[\frac{r\Delta p}{\rho R} \exp\left(-\frac{r}{R}\right) + \frac{f^2 r^2}{4}\right]^{1/2} - \frac{fr}{2}$$

where V_g is the gradient wind and f is the Coriolis parameter. The following values were used: $\Delta p = 50$ mb, $\rho = 1.2$ km·m^{-3}, $f = 5 \times 10^{-5}$·s^{-1}. In Fig. 6.130, curve A is for $R = 350$ km and curve B is for $R = 35$ km. It can be seen that taking $R = 350$ km gives an incorrect wind field.

Holland (1980) remarked that even with the correct value of R, eq. 6.238–6.242 may not give correct distributions for pressure fields and winds in tropical cyclones. Instead, he suggested the following form:

$$(6.243) \quad p = p_c + \Delta p \exp\left(-\frac{A}{r^B}\right)$$

where p_c is the central pressure and A and B are empirical constants. Usually, B has a value between 1 and 2.5. Then A is determined from the value given to the radius of maximum winds. Curve C of Fig. 6.130 is derived from eq. 6.243 with $A = 207$ and $B = 1.5$.

Johns and Ali (1980) agreed with Holland's (1980) criticism that in their model, the maximum gradient wind occurs at a radial distance of about 250 km. They justified their model by stating that use of $R = 40$ km gives a very low surge response. To account for the role of the wind stress at radial distances of the order of 200 km, they used a representation based on Jelesnianski (1965) with V_{max} for V_R in eq. 6.143. Taking $R = 40$ km and $V_{max} = 65$ m·s^{-1} one can calculate the wind speed for $r = 1000$ km to be 13 m·s^{-1}. Thus, eq. 6.143 also shows a curve similar to curve B of Fig. 6.130.

However, Johns and Ali (1980) did not use the representation in eq. 6.143 because their grid cannot resolve features less than 36 km in length. Hence, they used eq. 6.238 with $\Delta p = 50$ mb and $R = 350$ km. If one takes $f = 5 \times 10^{-5}$·s^{-1}, the gradient wind speed at $r = 250$ km is 30 m·s^{-1}. The representation of the wind field from eq. 6.238 and 6.243 is shown in Fig. 6.131. Basically, what Johns and Ali (1980) did was to use the solid curve of Fig. 6.131 in place of the broken curve to represent the wind field.

6.11 Mesoscale Weather Systems

Hobbs (1981) defined a mesoscale weather system as one with horizontal scales in the range of a few to 1000 km and time scales ranging from several hours to 1 d. Squall lines, thunderstorms, and tornadoes fall into the classification of mesoscale weather systems. Here, squall lines are specifically examined, since, as will be seen later, they can give rise to storm surges.

Squall lines are nonfrontal lines of active thunderstorms, several to some tens of kilometres wide and hundreds of kilometres long, which exist for a considerably longer period than the lifetime of the component cumulonimbus clouds (Ramage 1971).

Stationary as well as traveling mesoscale weather systems such as those that occur over the Great Plains of the United States are classified further into the following: regional scale (200–2000 km), or meso-alpha; squall line scale (20–200 km), or meso-beta; cloud scale (2–20 km), or meso-gamma (Anonymous 1978c).

Regions Where Squall Lines Occur

Squall lines occur in midlatitudes as well in the tropics. They occur mainly over the United States, Central, West, and South Africa, Venezuela, northern India, and northen Australia. In the United States they occur predominantly during spring and summer.

According to Hamilton and Archbold (1945) and Tschirhart (1958), sub-Saharan Africa is a fertile ground for squall lines and, in fact, these account for most of the rainfall. Another area where squall lines occur is the Caribbean Sea. On rare occasions, squall lines can also be observed over the southern part of the North Sea.

Meteorological Aspects

Prior to the enunciation of the frontal theory of cyclones by the Norwegian School of Meteorologists, a squall line was regarded as any line of storms arranged in a general southerly and easterly direction from a depression. Characteristic features of these storms are strong intensity, strong wind gusts, wind shifts, pressure increases, temperature decreases, and heavy rain of the showery type. After the advent of the frontal theory of cyclones, some of these storms were redesignated as cold fronts. The term "squall line" was reserved for the storms in the warm sectors of the cyclones, roughly paralleling the cold front and along which there is intense convective activity.

Harrison and Orendorff (1941) suggested that the squall line was formed by the rain-cooled air of the downdraft. Squall lines develop in air masses that are convectively unstable. Most of the squall lines over the United States develop in regions of warm advection at low levels with neutral or even slight cold advection aloft (Petterssen 1956a, 1956b). A favorable situation for squall line development is when a tongue of warm and moist air from the Gulf of Mexico moves northward over the Great Plains and the Mississippi Valley.

Squall lines may move with speeds of up to $15-18\ \mathrm{m \cdot s^{-1}}$ (faster than the ambient wind). In midlatitudes, especially, they may be embedded in larger scale synoptic weather systems. In such situations, the intense part of the weather might be concentrated only in about 10% of the area of the synoptic system. The life span of a squall line is much shorter than that of the synoptic scale system in which it is embedded (e.g. a few hours versus a few days).

Squall lines have low-level indraft along their forward edge due to rapid motion (Riehl 1979). Individual cumulonimbus clouds in a squall line have life times of at most a few hours. Hence, for a squall line to survive, new convective elements continually replace dissipating elements (Ramage 1971). Squall lines usually become most intense during late afternoons when the convective activity is the highest.

Newton and Newton (1959) and Newton (1967) showed that the continuous exchange of mass between the storm and the surroundings leads to a nonhydrostatic pressure that aids the convection process. On the downshear side the convective elements continually develop whereas on the upshear side they dissipate. Hence, the storm moves in the direction of developing elements and away from dissipating elements.

Over the Central United States the squall lines move 25° to the right of and about $4\ \mathrm{m \cdot s^{-1}}$ slower than the mean wind at the 700-mb level. Squall lines over the midwestern and northeastern parts of the United States deviate 50 and 70°, respectively, to the right of the wind direction at the 700-mb level.

Squall lines usually develop near topographic discontinuities (mountains and valleys). Generally, squall lines tend to dissipate when they cross a coast because cool and

relatively stable surface air suppresses ascent due to buoyancy (Ramage 1971).

In northern India, squall lines occur in the spring and fall (De 1963). In northern Australia, squall lines occur mainly in spring. The West African squall lines resemble those over the United States in the following respects: they tend to develop and are most intense in the afternoon and are most frequent in spring. However, there are certain differences also. The West African squall lines are usually embedded in an environment possessing easterly vertical shear and they travel westward with velocities of up to 10 $m \cdot s^{-1}$. Although the life span of most squall lines is less than 24 h, some persist for several days and travel more than 3000 km. Although most squall lines weaken after crossing a coastline, some do not (e.g. over the warm Guinea current).

Probably the first systematic study of squall lines emerged from the U.S. thunderstorm project during 1946–48. Williams (1948) used the data from the automatic recording stations in Ohio operated by the U.S. Weather Service's cloud physics project to deduce the microstructure of squall lines.

Tepper (1950a, 1950b) described the meteorological features associated with the arrival of an intense squall line at the ground. Initially there is an abrupt rise in the surface pressure, which he referred to as a "pressure jump." Fujita (1955) called it the "pressure surge." Within 1 min after the pressure jump there is a sudden change in the wind direction, which was referred to as "wind shift." Then, the temperature begins to drop rapidly within 2 min after the wind shift. This drop of temperature was referred to as the "temperature break". The peak wind gust, the onset of rain, and the pressure maximum follow the temperature break.

On the other hand, Fujita (1955) described the situation somewhat differently. Following the pressure surge, the thunderstorm high occurs and then the pressure decreases. The low pressure areas following the wake drop in pressure are called wake depressions.

Bedard et al. (1977) and Bedard and Meade (1977) described an inexpensive instrument system that was deployed at the Dulles Airport in Washington, DC, to measure the gust fronts associated with squall lines. NOAA (Anonymous 1978c) described the various modeling activities on squall lines that are being done at the National Severe Storms Laboratory (United States). A model being developed by Fritsch (Anonymous 1978c) incorporates the effects of deep convection and shows how a series of thunderstorms can become organized into groups and how they can influence the winds and pressures in the surroundings. Warm moist air accumulates in front of the squall line, and this leads to a low pressure system at the surface; colder air from the thunderstorm downdraft forms a high pressure area behind the squall line. Presently used weather forecast models cannot resolve the squall lines adequately because the grids used are of the order of 200 km in size.

The official U.S. Weather Service definition of pressure jump (associated with a squall line) is an increase of pressure of more than 0.17 $mb \cdot min^{-1}$ with at least a total increase of 0.7 mb. Tepper (1950) suggested that the detection of the pressure jump can be used as an indication of the movement of the squall line.

Time series data on pressure jumps were published by Tepper (1950), Fujita (1959), and Charba (1974). These data show increases of several millibars in surface pressure during a period of a few minutes. Tepper's (1950) data showed pressure increases of 2.3 mb in 5 min. Williams' (1948) data showed a 2- to 5-mb rise in 5 min. Goff (1975) found an average increase of 2.5 mb in 100 s. Blecker and Andre (1950) found significant pressure increases in 10 min.

As for the speed of travel, Williams (1948) gave a value of 13.4 $m \cdot s^{-1}$, Tepper (1950) found 20.4 $m \cdot s^{-1}$, and Goff (1975) found 10 $m \cdot s^{-1}$. On the other hand, De (1963),

TABLE 6.75. Squall lines over Venezuela. (Betts et al. 1976)

Major axis of squall line (km)	Minor axis of squall line (km)	Life span (min)	Observed track length (km)	Speed of travel ($km \cdot h^{-1}$)
96	32	200	136	51.1
90	46	240	131	38.5
120	27	211	170	55.0
95	20	215	161	59.4
100	30	140	154	52.4
100	31	195	150	52.0

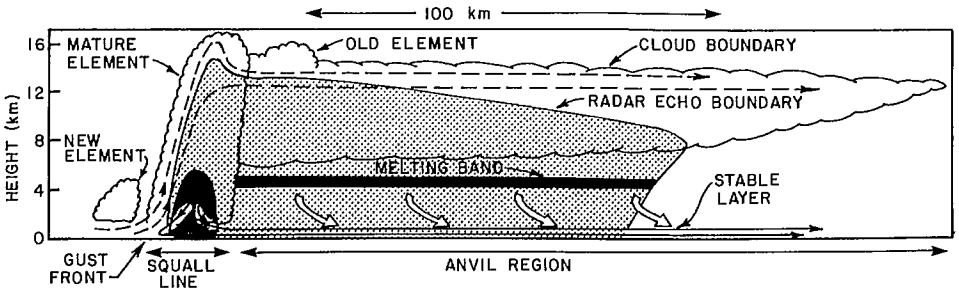

FIG. 6.132. Schematic cross-section through a squall line system. Streamlines show flow relative to the squall line. Broken lines show updraft circulation. Thin solid streamlines show mesoscale downdraft below the base of the anvil cloud. Dark shading shows strong radar echo in the melting band and in the heavy precipitation zone of the mature squall line element. Light shading shows weaker radar echoes. Scalloped line shows visible cloud boundaries. (Houze 1977)

based on a study of 44 squall lines in northern India, found a value of 33 $km \cdot h^{-1}$. He quoted values from other authors ranging from 35 to 40 $km \cdot h^{-1}$. De (1963) also found that the direction of movement of the squall lines is generally within 90° to the right (looking downwind) of the 700-mb wind. They occurred mainly during March–May and their life span varied from 3 to 10 h. Their lengths varied from 40 to 400 km and their speed of travel varied from 20 to 50 $km \cdot h^{-1}$. For comparison, some data on squall lines in Venezuela are listed in Table 6.75.

The cross-section through a squall line system is shown schematically in Fig. 6.132. Important results on squall lines may be found in Lilly (1979), Ogura and Liou (1980), Betts et al. (1976), Zipser (1969, 1977), Houze (1977), Mitchell and Hovermale (1977), Charba (1974), Moncrieff and Miller (1976), and Miller and Betts (1977).

SQUALL LINE FORCING TERMS FOR STORM SURGE CALCULATIONS

Wilson (1978) developed simplified pressure and wind profiles for a "historical maximum squall line" for use in estimating water levels near United States nuclear power plants. One very important point to be made is that, whereas with synoptic scale weather systems (e.g. tropical and extratropical cyclones) usually the wind stress is much more important than the atmospheric pressure gradients, for squall lines, the pressure gradient tems are at least of equal importance and sometimes much bigger than the wind stress terms.

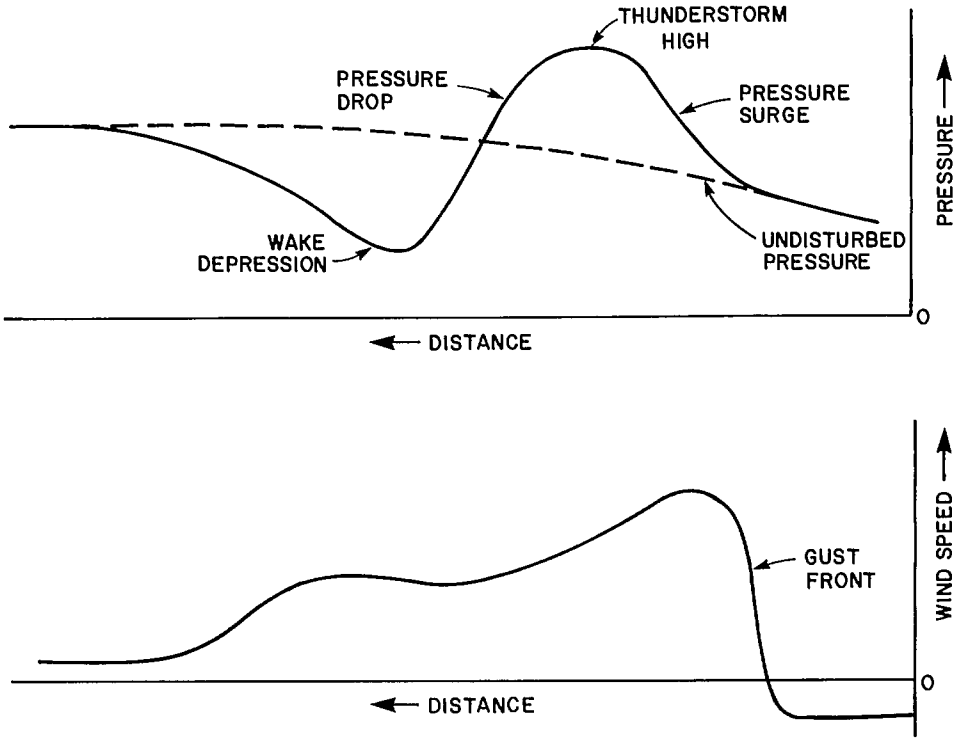

FIG. 6.133. Idealized pressure (top) and wind speed (bottom) field profiles for a squall line system. Negative wind speed denotes inflow into storm system. (Wilson 1978)

Following Fujita (1955), Wilson (1978) developed a simple model for a squall line system, as shown in Fig. 6.133. He also made the following assumptions: (a) the squall line is in a steady state and is in the mature stage, (b) the leading edge of the pressure surge and the gust front move with the same speed (this is in contrast with Fujita's (1955) result that the pressure surge moves with a speed some 40% greater than that of the gust front), and (c) the squall line moves perpendicular to the shoreline.

Making use of these assumptions and the model shown in Fig. 6.133, Wilson (1978) developed the pressure and wind profiles (Fig. 6.134) for a historical maximum squall line. For example, Fujita et al. (1956) gave a value for the pressure gradient of 9 mb in 50 mi (80 km) for a squall line over Nebraska on June 25, 1953, with a sustained post-gust front wind speed of 45 $mi \cdot h^{-1}$ (73 $km \cdot h^{-1}$). In this model Wilson used a value of 50 $mi \cdot h^{-1}$.

It was mentioned that for squall lines the pressure gradient terms are comparable in magnitude with wind stress terms. This is also borne out by the studies of Freeman and Murty (1972) and Murty and Freeman (1973) for the squall line of August 22, 1971, over Lake Huron. For the squall line, a sharp rise of pressure (δp_a) of 4.5 mb and wind (W) of 112.6 $km \cdot h^{-1}$ were deduced from the observations. Taking the average depth (D) of the southern part of Lake Huron as 54.7 m, a horizontal scale (δx) of 8 km, a time interval during which the pressure increased as 5 min, and the speed of travel of the squall line as 96.5 $km \cdot h^{-1}$, the pressure gradient term becomes

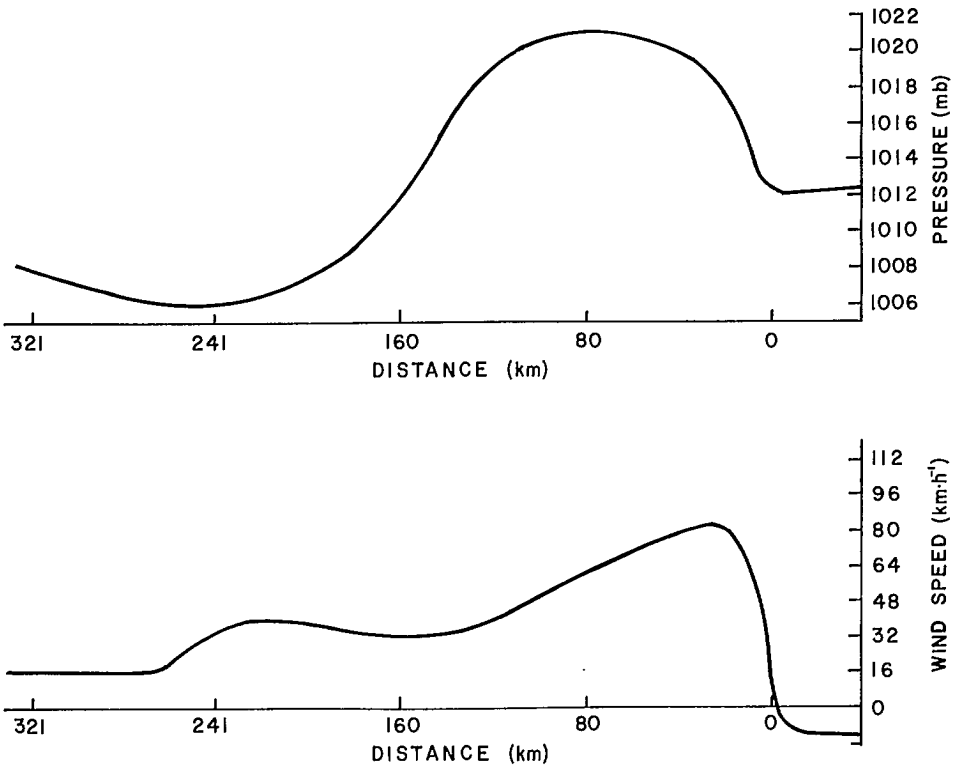

FIG. 6.134. Simplified pressure (top) and wind speed (bottom) profiles for historical maximum squall line system. (Wilson 1978)

$$\frac{1}{\rho} D \frac{\delta p_a}{\delta x} = 34 \text{ cm}^2 \cdot \text{s}^{-2}$$

The wind stress term gives

$$\tau_S = 3 \times 10^{-6} W^2 = 30 \text{ cm}^2 \cdot \text{s}^{-2}$$

For the synoptic scale, the atmospheric pressure gradient as taken from the isobaric plot is a 4-mb change (δp_a) in a 161-km distance (δx). A wind speed (W) of 32 km·h^{-1} is used as a typical value. The pressure gradient term and the wind stress term become 1.5 and 2.4 cm^2·s^{-2}, respectively.

The detailed calculations of the storm surge due to this squall line of August 22, 1971, over Lake Huron will be included in section 7.1. Earlier, the storm surge calculations in idealized situations using the method of characteristics (e.g. Rao 1967, 1969; Murty 1971) were discussed. The calculations of the storm surge in Lake Michigan due to a squall line on June 26, 1954 (Platzman 1958a, 1965a; Irish 1965; Hughes 1965) are included elsewhere in the book. Donn and Balachandran (1969) discussed the water level oscillations in Long Island Sound (east of New York City) due to a squall line on November 23, 1953. Donn (1959) studied the storm surges in Lakes Huron and Erie due to a squall line on May 5, 1952. Krauss (1978) studied the response of a stratified sea to a moving squall line.

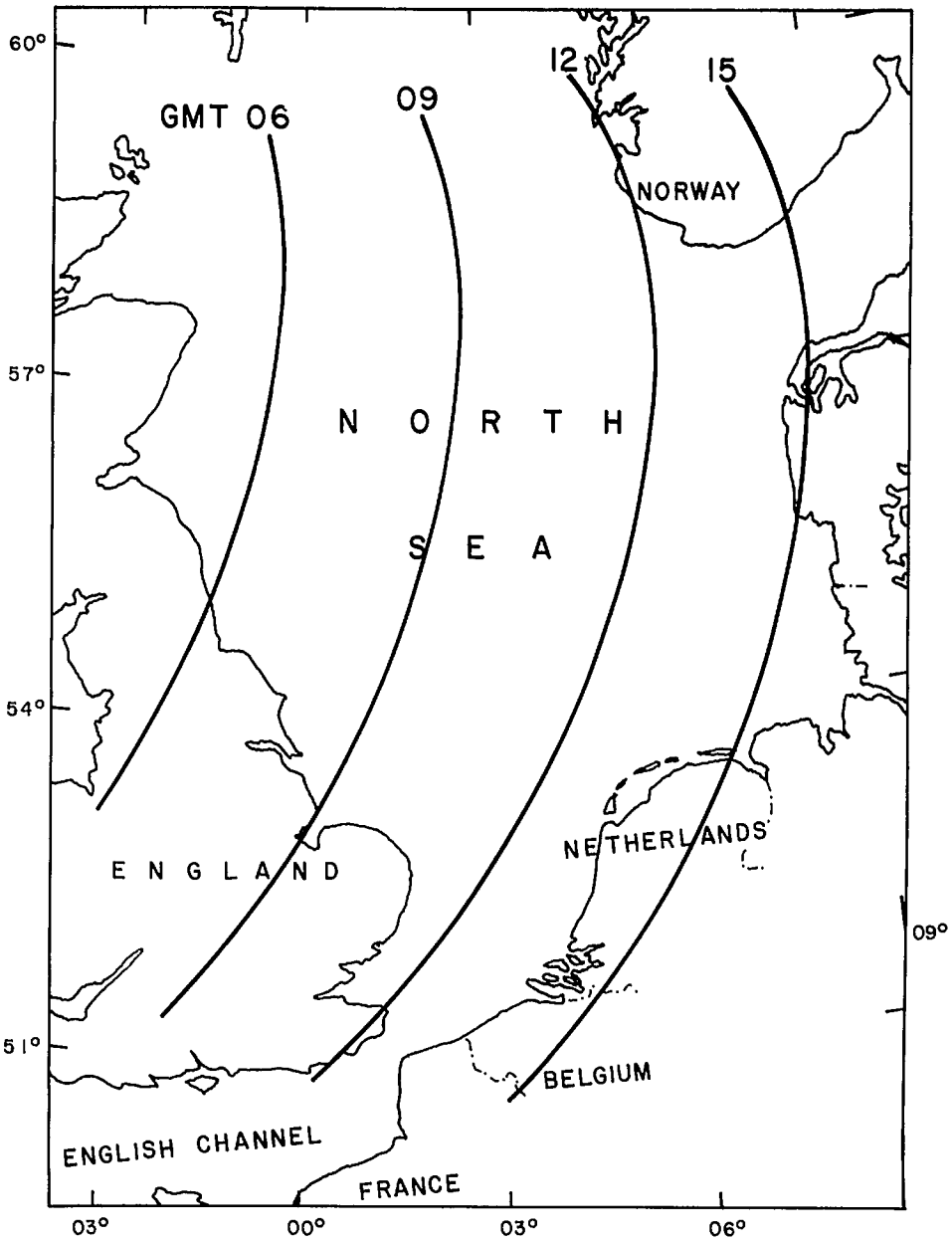

FIG. 6.135. Position of the leading edge of the squall line at four different times (GMT) on December 13, 1956. (Timmerman 1971)

Douglas (1929) made a simple calculation of the water level oscillations in the English Channel due to a squall line on July 20, 1929. Timmerman (1971) studied the water level oscillations (he referred to them as "cold fronts") on the Dutch coast of the North Sea. When the speed of the squall line is between 29 and 36 knots, resonance occurs between the squall line and the long gravity waves in the North Sea, and this leads to water level oscillations. During the period December 13, 1956, to January 4, 1968, 20 squall lines with speeds ranging from 25 to 36 knots traveled over the southern part of the North Sea. The positions of the leading edge of the squall line at four different times on December 13, 1956, are shown in Fig. 6.135.

Chapter 7

Case Studies of Storm Surges on the Globe

7.1 Storm Surges in Canada

Selected storm surge case studies in Canadian waters will be discussed in this section beginning with eastern Canada and proceeding to the west. In Chapter 5 the so-called perigean spring tides and their role in coastal flooding when they occur in conjunction with storm surges were discussed. Cases of coastal flooding in eastern Canada associated with perigean spring tides during the period 1775–1976 are listed in Table 7.1.

Briand (1979) did a statistical study of the storm surges in eastern Canada, making use of an 11-yr data record (1965–75), with emphasis on the St. Lawrence Estuary. In his study he considered the Atlantic Coast of Canada, the Labrador Sea Coast, the Bay of Fundy, the Gulf of St. Lawrence, and the St. Lawrence Estuary. Briand calculated the hourly residues in the standard manner, i.e. by subtracting the predicted astronomical tide from the observed water level. The maximum positive and negative surges together with their return periods are listed for several stations in Table 7.2. The extreme value of the positive surge observed at several stations in each month during the 11-yr period studied is listed in Table 7.3. Similar data for the negative surges are given in Table 7.4.

In Chapter 5, the influence of ice cover on storm surges in eastern Canadian waters was discussed. It was mentioned that whereas positive surges are damped by ice cover, negative surges are not. A storm surge at Pointe-du-Chêne during January 24–27, 1972, is shown in Fig. 7.1. Note the predominantly negative surge during this period when an ice cover exists. Murty and Holloway (1984) showed that ice cover damps positive surges more strongly than negative surges (also see Table 5.20).

The interaction between storm surges and tides in the Thames Estuary was also discussed in Chapter 5. The results of tide–surge interaction in the St. Lawrence Estuary will be considered here (Murty and El-Sabh 1981). Based on Proudman (1957) it can be shown that an estuary is short (with reference to long wave propagation) provided the following two conditions are satisfied:

$$\frac{\sigma L}{c} A \ll 1$$

$$\frac{K\sigma^2 L^3 A}{hc^2} A \ll 1 \tag{7.1}$$

where σ is the angular frequency of the tide, L is the length of the estuary, and $c = \sqrt{gh}$ where g is gravity and h is the average depth of the estuary. The parameter A is defined as

$$A \equiv \frac{B}{2h} \tag{7.2}$$

where B is the tidal amplitude at the mouth. Parameter K is a coefficient of bottom friction and is taken as 0.0025. Note that it is not the physical length alone that determines whether or not an estuary is short, in the sense used by Proudman.

Length L, average depth h, and tidal amplitude B for the two portions of the St. Lawrence Estuary are summarized in Table 7.5. The values of the two Proudman param-

eters defined by eq. 7.1 are also listed for the two sections. Based on these values, the classification into long or short estuary is made in the final column.

The results of Proudman (1957) can be summarized as follows: (a) for a long estuary, for a tide of progressive wave type, maximum surges are associated more with low tide; (b) for a long estuary, for a tide of standing wave type, maximum surges are associated more with high tide; (c) for a short estuary, maximum surges are associated more with high

TABLE 7.1. Cases of coastal flooding in Canada associated with perigean spring tides. Times correspond to 75°W. (Based on Wood 1978)

Date of flooding	Location of flooding	Nearest perigee (date and time)	Nearest syzygy (date and time)
Sept. 9, 1775	Halifax and Newfoundland (Sept. 9–11)	Sept. 8, 1775 (07:00)	Sept. 9, 1775 (10:00)
Oct. 5, 1869	Cobequid Bay, Burncoat Head, and Noel Bay (all in Nova Scotia). Perigean spring tides amplified by Saxby gale	Oct 5, 1869 (02:00)	Oct. 5, 1869 (09:00)
Oct. 25, 1870	Cumberland Basin, N.B.	Oct. 25, 1870 (00:00))	Oct. 24, 1870 (11:00)
Aug. 9, 1873	Pictou, N.S.	Aug. 9, 1873 (06:00))	Aug. 8, 1873 (09:00)
Nov. 1–2, 1877	North Atlantic coast	Nov. 1, 1877 (20:42)	Nov. 5, 1877 (03:48)
Oct. 12, 1887	Moncton, N.B.	Oct. 16, 1887 (13:00)	Oct. 16, 1887 (18:00)
Feb. 8–9, 1895	Halifax, N.S.	Feb. 9, 1895 (08:00)	Feb. 9, 1895 (12:00)
Oct. 8, 1896	Between Amherst, N.S., and Sackville, N.B.	Oct. 7, 1896 (00:00)	Oct. 6, 1896 (17:00)
Nov. 6, 1896	Pictou, N.S., and Charlottetown P.E.I.	Nov. 4, 1896 (12:00)	Nov. 5, 1896 (03:00)
Nov. 27, 1897	Pictou, N.S.	Nov. 24, 1897 (10:00)	Nov. 24, 1897 (04:00)
Oct. 11–12, 1900	Charlottetown and Summertown, P.E.I.	Oct. 8, 1900 (01:00)	Oct. 8, 1900 (08:00)
Apr. 20, 1901	Between Amherst, N.S., and Sackville, N.B.	Apr. 18, 1901 (16:00)	Apr. 18, 1901 (17:00)
May 18, 1901	Between Amherst, N.S., and Sackville, N.B.	May 17, 1901 (02:00)	May 18, 1901 (01:00)
Feb. 3, 1908	Port aux Basques, Nfld., and Harrington Harbor, Que.	Nov. 16, 1914 (23:00)	Nov. 17, 1914 (04:00)
Nov. 20, 1914	Quebec City	Nov. 16, 1914 (23:00)	Nov. 17, 1914 (11:00)
Oct. 1, 1917	Moncton and Sackville, N.B., and Amherst and Windsor, N.S.	Sept. 29, 1917 (13:06)	Sept. 30, 1917 (15:31)
Oct. 31, 1917	Moncton, N.B., and to a lesser extent at Sackville, N.B., and Amherst, N.S.	Oct. 27, 1917 (17:48)	Oct. 30, 1917 (01:19)
Nov. 18, 1918	Batiscan, Que.	Nov. 16, 1918 (22:30)	Nov. 18, 1918 (02:32)
Mar. 4–5, 1931	Halifax, N.S.	Mar. 4, 1931 (05:00)	Mar. 4, 1931 (06:00)
Dec. 11, 1973	Halifax, N.S.	Dec. 10, 1973 (18:00)	Dec. 9, 1973 (21:00)
Mar. 16–17, 1976	Halifax, N.S.	Mar. 16, 1976 (14:00)	Mar. 15, 1976 (22:00)

TABLE 7.2. Extreme positive and negative surges and return periods at selected stations in eastern Canada. (Briand 1979)

Station	Maximum positive surge for which return period determined (cm)	Return period (yr)	Maximum negative surge for which return period determined (cm)	Return period (yr)
Nain, Labrador	100	0.55	120	3.0
West St. Modeste, Labrador	80	1.0	90	0.8
St. John's, Nfld.	90	11.0	80	1.6
Argentia, Nfld.	80	1.3	90	4.0
Port aux Basques, Nfld.	100	2.5	80	3.3
Lark Harbor, Nfld.	80	1.3	120	4.0
Savage Cove, Nfld.	110	3.0	80	6.0
Yarmouth, N.S.	110	3.5	100	7.0
Halifax, N.S.	110	11.0	80	11.0
North Sidney, N.S.	100	5.0	70	1.25
Pictou, N.S.	110	1.4	130	2.3
Charlottetown, P.E.I.	130	4.5	140	4.5
Rustico, P.E.I.	90	—	90	—
St. John, N.B.	110	11.0	100	11.0
Pointe-du-Chêne, N.B.	130	0.5	170	2.0
Pointe Sapin, N.B.	130	3.0	130	3.0
Lonvere Escuminac, N.B.	80	0.4	120	1.0
Rivière-au-Renard, Que.	130	3.5	110	2.3
Harrington Harbor, Que.	110	5.5	80	11.0
Sept-Îles, Que.	90	3.0	120	1.0
Ste-Anne-des-Monts, Que.	130	3.0	150	3.0
Baie-Comeau, Que.	140	3.0	140	3.0
Pointe-au-Père, Que.	130	5.5	140	2.2
Rivière-du-Loup, Que.	130	2.7	190	8.0
Tadoussac, Que.	150	1.4	170	3.5
St-Jean-Port-Joli, Que.	200	2.0	190	6.0
St-Joseph-de-la-Rive, Que.	190	1.7	190	11.0
Lauzon, Que.	270	5.5	220	11.0

tide. Proudman's results were reinterpreted (with justification) to read low tide (or rising tide) and high tide (or falling tide) wherever "low tide" or "high tide" appears in the above statements.

The nature of the tide in the section between Sept-Îles and Tadoussac is more of a standing wave type than of a progressive wave type, whereas between Tadoussac and Quebec City the tide is more of a progressive wave type. The cumulative frequency of surges of a given amplitude associated with a given state of the tide for Tadoussac is listed in Table 7.6. Although the theory does not distinguish between positive and negative surges, they are listed separately. Similar tables were prepared (not shown here) for the other stations. The observed and theoretical results are compared in Table 7.7. Some pertinent data on the surges in the St. Lawrence Estuary are given in Table 7.8.

In Chapter 5, various tidal models for the Bay of Fundy and the Gulf of Maine (e.g. Greenberg 1977) were mentioned. In principle, these could be used as storm surge models with slight modification. However, there is at least one storm surge model available for the Bay of Fundy (Brandon 1981).

Brandon (1981) used a two-dimensional vertically integrated numerical model to study the Bay of Fundy (the Gulf of Maine is not included) and simulated the surge due

TABLE 7.3. Maximum positive surge (cm) observed in each month during the 11-yr period 1965–75 at stations in eastern Canada. (Briand 1979)

Station	Jan.	Feb.	Mar.	Apr.	May	June	July	Aug.	Sept.	Oct.	Nov.	Dec.
Nain, Labrador	100	90	70	90	100	90	100	60	90	90	100	90
West St. Modeste, Labrador	60	20	40	40	40	60	70	60	50	80	70	70
St. John's, Nfld.	60	70	90	60	60	50	50	60	60	60	40	50
Argentia, Nfld.	50	80	70	60	60	70	60	50	60	50	60	80
Port aux Basques, Nfld.	70	80	70	60	300	300	300	40	60	60	80	100
Lark Harbor, Nfld.	80	70	70	70	60	80	60	50	40	80	70	60
Savage Cove, Nfld.	110	90	60	70	70	40	40	40	50	60	60	110
Yarmouth, N.S.	80	70	70	80	50	60	70	50	110	110	60	90
Halifax, N.S.	70	110	70	70	60	60	80	60	60	70	50	90
North Sidney, N.S.	60	100	60	60	50	70	40	40	50	60	60	50
Pictou, N.S.	100	100	80	60	80	100	50	60	60	100	100	110
Charlottetown, P.E.I.	100	110	100	90	70	60	50	50	50	100	80	130
Rustico, P.E.I.	90	40	70	50	50	40	40	40	30	60	70	60
St. John, N.B.	110	100	90	100	70	60	80	60	80	70	100	300
Pointe-du-Chêne, N.B.	60	120	70	60	70	50	50	50	100	130	130	90
Pointe Sapin, N.B.	80	80	80	90	70	60	40	50	60	130	70	90
Lonvere Escuminac, N.B.	80	50	80	70	50	50	50	40	40	60	60	70
Rivière-au-Renard, Que.	70	130	70	80	60	60	80	300	90	80	80	90
Harrington Harbor, Que.	90	100	80	70	40	50	70	60	50	110	80	100
Sept-Îsles, Que.	80	80	90	70	40	300	30	40	60	60	70	80
Ste-Anne-des-Monts, Que.	130	120	100	110	100	90	100	90	90	100	100	90
Baie-Comeau, Que.	140	130	110	100	60	70	70	310	60	70	80	90
Pointe-au-Père, Que.	120	130	100	80	70	50	50	60	310	80	80	100
Rivière-du-Loup, Que.	110	110	120	130	80	310	70	310	70	90	100	100
Tadoussac, Que.	150	120	130	130	70	80	40	310	100	310	90	310
St-Jean-Port-Joli, Que.	170	140	200	120	90	110	70	60	80	100	120	130
St-Joseph-de-la-Rive, Que.	140	130	170	100	70	140	70	80	310	190	100	120
Lauzon, Que.	230	220	270	190	140	120	110	310	120	120	250	230

TABLE 7.4. Maximum negative surge (cm) observed in each month during the 11-yr period 1965–75 at stations in eastern Canada. (Briand 1979)

Station	Jan.	Feb.	Mar.	Apr.	May	June	July	Aug.	Sept.	Oct.	Nov.	Dec.
Nain, Labrador	90	90	110	60	80	90	120	110	90	70	70	90
West St. Modeste, Labrador	80	90	90	60	50	20	10	10	20	30	40	60
St. John's, Nfld.	70	70	50	40	30	30	20	20	50	80	80	80
Argentia, Nfld.	70	70	80	40	30	40	40	50	40	50	70	90
Port aux Basques, Nfld.	60	80	50	60	50	40	30	40	50	60	60	60
Lark Harbor, Nfld.	120	90	50	50	30	60	50	40	40	40	50	80
Savage Cove, Nfld.	80	70	60	50	30	30	30	50	40	50	60	60
Yarmouth, N.S.	80	70	70	70	70	40	60	40	60	50	50	100
Halifax, N.S.	80	60	50	40	30	20	30	70	60	60	50	70
North Sidney, N.S.	70	70	50	30	30	40	30	30	30	40	70	70
Pictou, N.S.	80	120	70	60	50	40	40	40	40	60	80	130
Charlottetown, P.E.I.	140	140	90	50	50	50	40	40	60	70	90	130
Rustico, P.E.I.	60	30	40	40	20	20	20	20	30	50	60	90
St. John, N.B.	100	70	80	80	80	60	60	50	60	60	80	60
Pointe-du-Chêne, N.B.	170	150	100	60	50	40	30	40	40	70	80	90
Pointe Sapin, N.B.	120	90	80	80	40	40	30	40	60	70	70	130
Lonvere Escuminac, N.B.	70	80	50	80	30	40	30	30	40	50	60	120
Rivière-au-Renard, Que.	110	90	70	80	60	60	60	70	50	70	60	80
Harrington Harbor, Que.	80	70	50	40	30	30	60	30	60	50	50	60
Sept-Îsles, Que.	100	120	80	40	40	70	40	40	40	80	70	100
Ste-Anne-des-Monts, Que.	150	90	110	100	100	80	90	110	70	100	90	120
Baie-Comeau, Que.	90	140	90	70	40	80	100	40	60	90	70	120
Pointe-au-Père, Que.	140	140	120	70	60	70	90	80	80	110	140	130
Rivière-du-Loup, Que.	180	180	110	90	50	60	50	190	50	90	100	150
Tadoussac, Que.	150	160	100	80	60	60	50	120	120	100	90	170
St-Jean-Port-Joli, Que.	150	190	170	100	60	60	70	60	110	120	150	180
St-Joseph-de-la-Rive, Que.	180	110	130	80	90	190	60	80	90	150	120	140
Lauzon, Que.	170	200	140	130	100	150	140	90	90	120	130	220

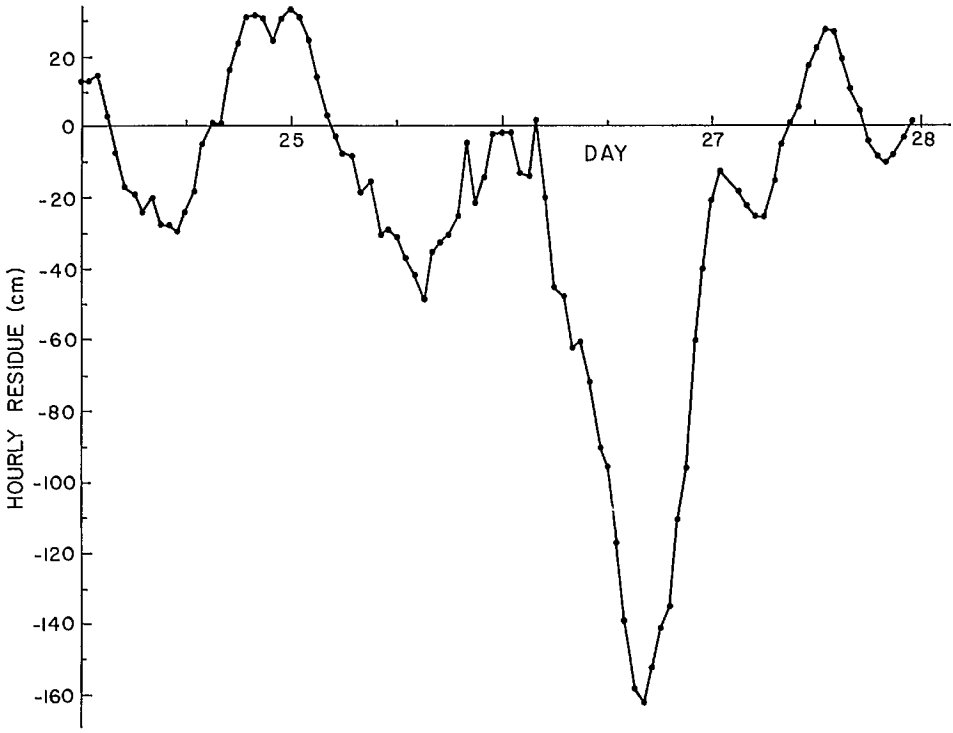

FIG. 7.1. Storm surge at Point-du-Chêne during Janaury 24–27, 1972. (Briand 1979)

TABLE 7.5. Dimensions and classifications of the two sections of the St. Lawrence Estuary.

System	Length (km)	Average depth (cm)	Tide amplitude, B (cm)	Proudman's 1st parameter	Proudman's 2nd parameter	Classification
Sept-Îles to Saguenay River	350	25×10^3	107	0.002	0.007	Short estuary
Saguenay River to Quebec City	193	1800	215	0.12	6.7	Long estuary

to the storm of February 2, 1976 (referred to as the "Groundhog Day Storm"). The calculated surge of 1.3 m at St. John agrees reasonably well with the observed surge of 1.5 m (a statistical method gave a value of only 0.8 m).

The Great Lakes system (Superior, Michigan, Huron, Erie, and Ontario) and their interconnecting rivers and lakes are prone to storm surges not infrequently. The amplitudes and frequency of the surges vary from one lake to another and also from one location to another in the same lake. Since Lake Michigan lies entirely in the United States, storm surges in this lake will not be considered in this section. Also, discussion here will be restricted to the Canadian coast of the Great Lakes system only. Discussion of storm surges in the United States part of the Great Lakes system will be deferred to section 7.2.

Storm surge problems in Lake Erie (the shallowest of the Great Lakes and the one

TABLE 7.6. Number of occasions of positive and negative surges exceeding a given height at Tadoussac during 1965–75. Each hourly reading is treated as one occasion.

State of tide	Surge height (cm)															
	10	20	30	40	50	60	70	80	90	100	110	120	130	140	150	300
	(a) Positive surges															
Low	3806	1763	904	468	260	147	77	48	26	16	10	5	3	2	0	0
Rising	4195	2090	1016	515	263	129	81	61	47	29	12	8	4	3	3	3
High	4063	1843	849	390	185	96	59	33	23	14	3	2	2	2	2	2
Falling	4210	2082	1057	571	315	187	115	60	25	5	3	2	2	0	0	0
	(b) Negative surges															
Low	4466	2046	894	412	192	94	44	22	8	1	0	0	0	0	0	0
Rising	4533	2275	1146	634	324	178	94	56	35	16	5	3	2	1	0	0
High	3441	1513	710	363	205	108	52	34	19	15	13	12	9	7	4	2
Falling	4110	1934	851	385	205	102	53	35	18	12	8	7	5	3	1	0

TABLE 7.7. Comparison between theory and observation of the tide–surge interaction in the St. Lawrence Estuary. H, high tide; L, low tide; R, rising tide; F, falling tide; A, in agreement; D, in disagreement; N, neither agreement nor disagreement.

	State of tide with which the maximum surge is associated		
Station	Theory	Observation	Comparison
Ste-Anne-des-Monts	H–F	F	A
Baie-Comeau	H–F	H	A
Pointe-au-Père	H–F	R–H	N
Tadoussac	H–F	R–H	N
Riviere-du-Loup	L–R	L	A
St-Joseph-de-la-Rive	L–R	H–R	N
St-Jean-Port-Joli	L–R	H	D
St-François	L–R	L–R	A
Quebec City	L–R	L	A

TABLE 7.8. Tidal range and maximum amplitudes of positive and negative surges in the St. Lawrence Estuary.

Station	Spring tidal range (cm)	Amplitude of maximum positive surge (cm)	Amplitude of maximum negative surge (cm)	No. of occurrences of positive surges with amplitude ≥180 cm during the period 1965–75[a]	No. of occurrences of negative surges with amplitude ≥130 cm
Ste-Anne-des-Monts	347	180	140	2(24)	2
Baie-Comeau	402	290	130	2(15)	8
Pointe-au-Père	460	300	130	2(2)	5
Tadoussac	519	300	160	5(11)	16
Riviere-du-Loup	567	300	180	3(3)	21
St-Joseph-de-la-Rive	695	300	250	5(29)	20
St-Jean-Port-Joli	573	190	180	4(34)	33
St-François	686	240	230	17(100)	93
Quebec City	580	300	210	32(157)	20

[a]Value in parentheses is number of occurrences for ≥130 cm.

TABLE 7.9. Casualties due to high water levels in the Great Lakes.

Date	No. of casualties	Date	No. of casualties
Sept. 23, 1679	34	Nov. 9, 1913	251
Nov. 11, 1835	Several hundred	Oct. 20, 1916	55
Oct. 13, 1845	3	Nov. 24, 1918	76
Sept. 8, 1860	287	Nov. 24, 1919	40
Nov. 27–28, 1905	78	Nov. 12, 1940	67

with maximum susceptibility to storm surges) were first considered by Henry (1902) and Garriott (1903). Henry discussed the techniques of computing surges at the eastern end of Lake Erie. Garriott included charts that depicted graphically more than 200 important storms that traversed the Great Lakes during the period 1876–1900 (these charts include United States and Canadian parts of the Great Lakes).

Murty and Polavarapu (1975) reconstructed some major storm surges due to storms that were extensive enough to affect all the Great Lakes. Their study considered the period 1679–1940. The casualties due to high water levels (attributed to storm surges) in the Great Lakes (both in Canada and the United States) during this period are listed in Table 7.9. The casualty toll resulted not only from people drowning near the coast but also from the sinking of ships battered by high waves. This table, at best, is only a partial list and several surges may have been missed. The fact that there is no entry for the eighteenth century is astonishing; it is inconceivable that there were no storm surges on the Great Lakes during a 100-yr duration.

An examination of Table 7.9 shows that all the major storm surges listed occurred during September to November. Irish and Platzman (1961) explained this as due to the convergence of two primary storm tracks from Alberta and Colorado lows in the Great Lakes region. This is due to the southward displacement of the polar front. Also, there is a contribution to cyclogenesis from the Great Lakes themselves.

Of the 10 entries in Table 7.9, the storm surges of 1913, 1916, and 1940 were reconstructed by Murty and Polavarapu (1975). The tracks of these storms considered in this study are illustrated in Fig. 7.2. The notation used in the diagram represents day and time of storm. For example, 10 (1930) means that the center of the storm was at that location at 19:30 on the 10th day of that month. The surface weather chart for 7:30 on November 12, 1940, is given in Fig. 7.3. The extensive size of weather system and the intensive amosphere pressure gradients associated with this can be seen in this diagram. The locations of the water level stations used are shown in Fig. 7.4. The observed and computed maximum surges at various locations are listed in Table 7.10.

Earlier, the effect of rate of growh of the storm on the storm surge was discussed. This is examined in Table 7.11 for the three storms studied here.

The storm surges in Lake St. Clair were briefly discussed earlier. It was mentioned that regression techniques using hourly winds and temperature differences (between air and water) as predictors were reasonably successful in explaining surges with periods equal to or greater than 24 h. However, regression techniques failed to account for water level oscillations in the range of 5–14 h. This failure was attributed to a lack of temporal resolution in the forecast data, since only 1-h lags were allowed.

Hamblin (1978) used lags up to 5 h and also used the impulse response method; i.e. the response of the water level at any given position in the lake to a suddenly imposed wind stress or pressure gradient was calculated. The response functions were expanded in terms of the lowest six gravity modes. The amplitudes of the oscillations were determined from the steady-state solutions of the free surface and the relative phases were determined from the initial conditions. Finite-element methods were used to calculate the characteristic functions of the basin as well as the free surface displacement. Atmospheric stability was also taken into account in determining the wind stress.

More than three dozen storm surges were hindcasted using the regression technique as well as the impulse response method. Some of the results are as follows: (1) when no seiches were present, both methods were reasonably successful for surges with periods longer than 12 h; (2) when seiches with periods of 6 h or greater were present, only the impulse reponse method was successful; (3) when seiches with periods shorter than 6 h

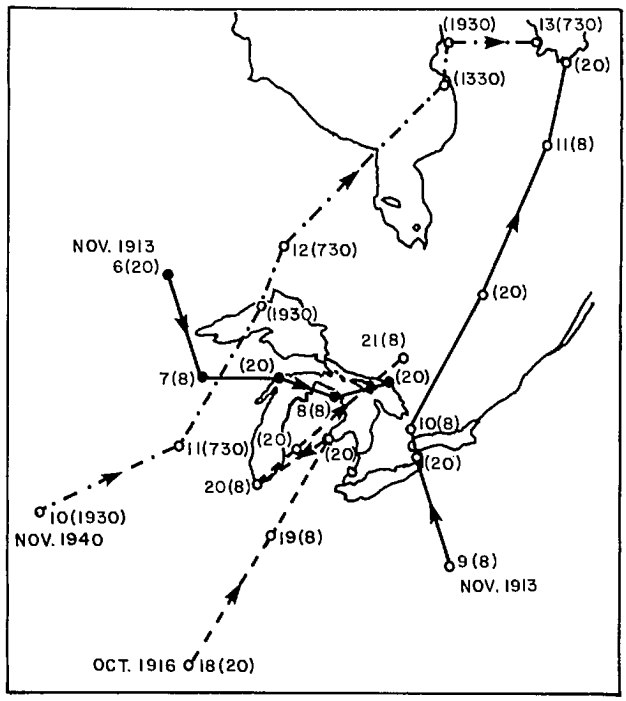

FIG. 7.2. Tracks of three storms in the Great Lakes and surroundings. Numbers denote the dates (numbers in parentheses denote the time (GMT) in hours).

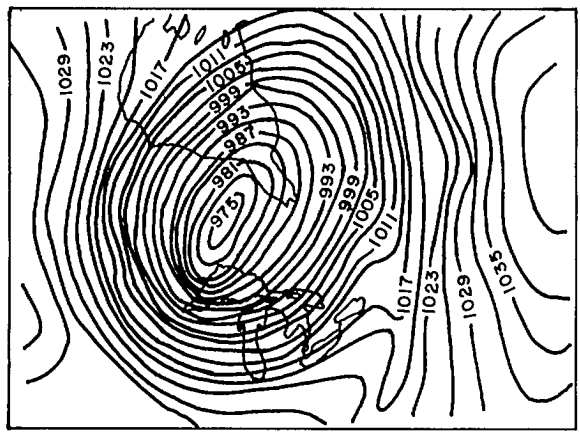

FIG. 7.3. Simplified surface weather chart at 07:30 (GMT) on November 12, 1940. Numbers represent sea level pressures (millibars).

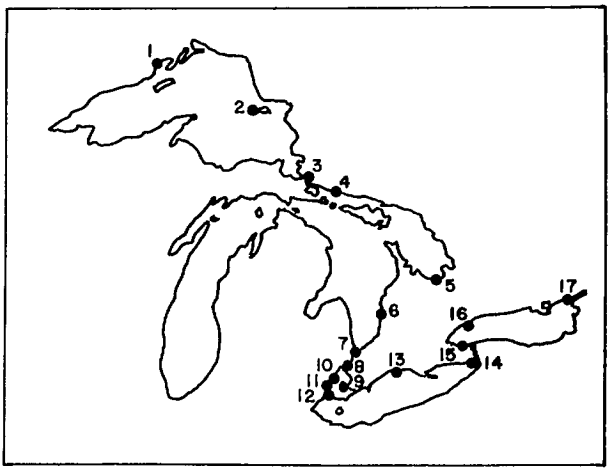

FIG. 7.4. Water level stations used in the storm surge study for the Great Lakes. 1, Port Arthur; 2, Michipicoten; 3, Sault Ste. Marie; 4, Thessalon; 5, Collingwood; 6, Goderich; 7, Point Edward; 8, Port Lambton; 9, Tecumseh; 10, Isle aux Pêches; 11, Fighting Island; 12, La Salle; 13, Port Stanley; 14, Port Colborne; 15, Port Dalhousie; 16, Toronto; 17, Kingston.

were present, both methods failed; (4) when hourly measured wind data were used as input, the predicted surge agreed well with the observed surge, except when there were rapid fluctuations of the water level lasting for several hours. The observed surge and that calculated by both methods, for one case, are compared in Fig. 7.5.

Next, a case study of a storm surge on Lake Huron, in which a squall line played an important role, will be considered. The storm surge of August 22, 1971, in the southern part of Lake Huron was a combination of the effects of an intense and narrow squall line and a cyclonic circulation associated with a low pressure system (Freeman and Murty 1972; Murty and Freeman 1973). The simplified surface weather chart at 19:00 on August 22, 1971 (note that the peak surge occurred at 18:00), is shown in Fig. 7.6a. The track of the low pressure system is also shown and the dots represent 6-h intervals. The storm moved from west–northwest across the southern portion of the lake with a speed of about 80.5 $km \cdot h^{-1}$. With the center of the low to the east of the lake, a fairly steady wind from north–northeast blew along the longitudinal axis of the lake with a fetch almost two thirds of the lake and with an average speed of 32.2 $km \cdot h^{-1}$. Some time before 18:00, the deceleration of a portion of the rapidly advancing cold front produced a squall line with winds peaking to 112.6 $km \cdot h^{-1}$, which is much greater than the steady winds. The squall line, approximately 32 km long and 8 km wide, traveled over Lake Huron from the north–northeast to Sarnia and farther, cutting a 16-km-wide swath inland and causing significant damage onshore.

The water depth contours in the central and southern portions of Lake Huron, as well as the data stations used, are shown in Fig. 7.6b. The 5-min digitized wind speed and direction values at the Grace Church station are shown in Fig. 7.7. The 5-min digitized water level values at Harbour Beach, Goderich, and Fort Gratiot are shown in Fig. 7.8. It was shown in section 6.11 that the pressure gradient and wind stress associated with this squall line were at least an order of magnitude greater than those due to the larger scale cyclonic system.

TABLE 7.10. Recorded and computed[a] water levels at Canadian stations on the Great Lakes.

Date of storm	Station	Observed maximum surge (m)	Calculated maximum surge (m)
November 1913	Port Colborne	1.36	1.40
	Fighting Island	0.48	0.52
	Kingston	0.33	0.27
	Isle aux Pêches	0.28	
	Port Dalhousie	0.20	
October 1916	Port Colborne	1.22	0.88
	Fighting Island	0.71	0.24
	Collingwood	1.64	0.46
	Isle aux Pêches	0.51	0.18
	Goderich	0.39	0.12
	Kingston	0.32	0.15
	Michipicoten	0.24	0.15
	Port Dalhousie	0.20	
	Port Arthur	0.14	
November 1940	Port Colborne	1.43	1.52
	La Salle	0.81	0.46
	Collingwood	0.77	0.73
	Point Edward	0.71	0.76
	Michipicoten	0.70	0.73
	Sault Ste. Marie	0.58	0.64
	Tecumseh	0.54	0.27
	Port Stanley	0.53	0.46
	Goderich	0.51	0.55
	Thessalon	0.39	0.37
	Port Lambton	0.29	
	Kingston	0.24	
	Toronto	0.24	
	Port Arthur	0.19	
	Port Dalhousie	0.18	

[a]Restricted to observed surges greater than 0.3 m.

TABLE 7.11. Effect of the rate of storm growth on the subsequent surge.

Station	1913 storm	1916 storm	1940 storm
Port Colborne (Lake Erie)	Faster growth; range of surge was >1.22 m	Slower growth; range of surge was <0.91 m	Faster growth; range of surge was <1.22 m
Fighting Island (Detroit River)	Slower growth; positive surge was 0.48 m	Faster growth; positive surge was 0.71 m	Station did not exist
Isle aux Pêches	Slower growth; positive surge was 0.28 m	Faster growth; positive surge was 0.51 m	Station did not exist
Michipicoten	Station did not exist	Slower growth; positive surge was 0.24 m	Faster growth; positive surge was 0.70 m

Freeman and Murty (1972) performed statistical analyses of the recorded water levels at Goderich, Harbour Beach, and Fort Gratiot; autocorrelation and cross-correlation coefficients were computed as a function of time lag. The cross-correlograms were used to evaluate the travel times of the squall surge and its subsequent resurgences. The auto-

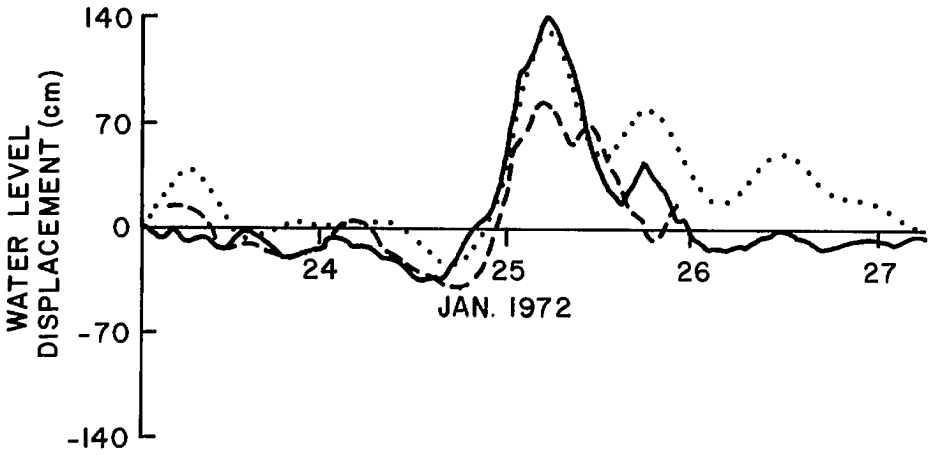

FIG. 7.5. Observed storm surge (solid curve), surge calculated with the regression model (broken curve), and surge calculated with the impulse response model (dotted curve) for the period January 23–27, 1972, at the eastern end of Lake Erie. (Hamblin 1978)

spectra of the three water level records were calculated using the Fast–Fourier Transform (FFT) technique.

To consider the effect of reflections at the coast on the spectra of the water level records, the cepstra were computed using the concepts developed by Bogert et al. (1962). To understand the role of nonlinearities, the bispectra were computed. To determine the variation of energy in each frequency band as a function of time, the total length of the water level record of 5 d for each of the three stations was broken down into four equal parts with the autospectra calculated for the 2-d sections; each section has a 1-d overlap.

The significant periods derived from the autospectra are listed in Table 7.12. Some of these periods were accounted for in terms of the longitudinal and transverse free oscillations of the whole or part of the lake.

Murty and Freeman (1973) extended the earlier study of Freeman and Murty (1972) by using more extensive data (Fig. 7.9). For Mackinaw City the period of 8.33 h (see Table 7.12) agrees well with the 8.8-h period for the first longitudinal mode of Lake Michigan calculated by Rockwell (1966) using a one-dimensional model and by Birchfield and Murty (1974) using a two-dimensional model. Mortimer (1965) found a value of 9.0 h through a statistical analysis of observed water level records. For detailed interpretations of the significant periods see Murty and Freeman (1973).

The lack of significant peaks in the autospectrum for Tobermory verifies that it is located at a nodal point and is sheltered from edge wave excitation. In Chapter 5, edge waves and their role in storm surges were discussed and some examples in the Great Lakes were considered. Another such example is considered here. The edge wave periods, T (Table 7.13), were calculated from the following formula (which can be obtained from eq. 5.132):

$$T = \frac{2\pi U}{g\beta} \tag{7.3}$$

where U is the longshore speed of the squall line, g is gravity, and β is the bottom slope

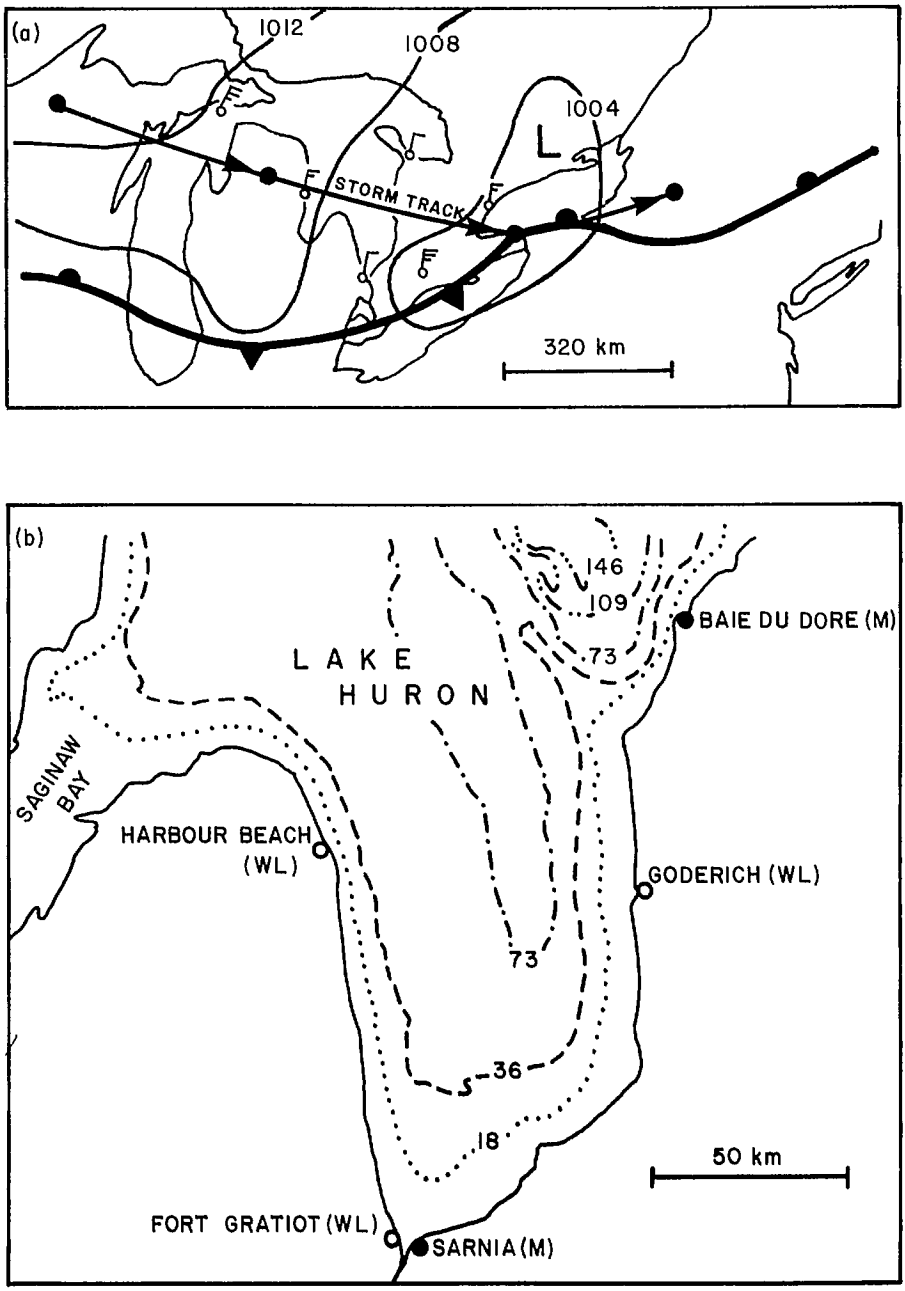

FIG. 7.6. (a) Simplified surface weather chart at 19:00 GMT on August 22, 1971, for the Great Lakes area. Black circles on the storm track show the positions of the center of the low at 6-h intervals. (b) Locations of the various stations (M, meteorological; WL, water level) used in the study. Depth contours (metres) are also shown.

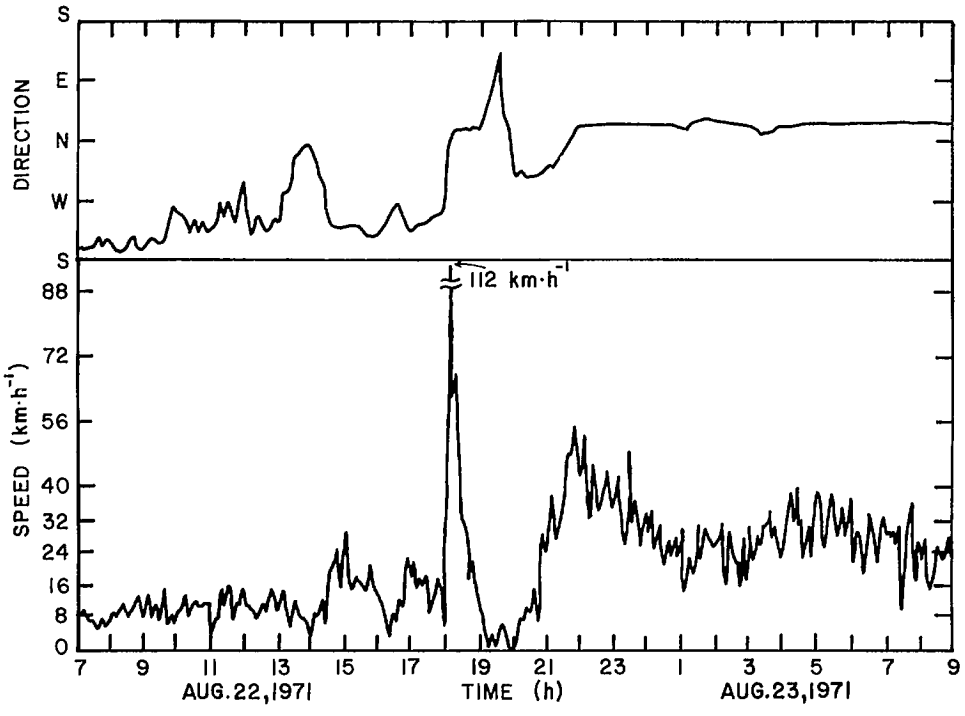

FIG. 7.7. Five-minute digitized wind speed and direction values as obtained from continuous recorders at the Grace Church station.

near the shore. In the water level records described here the shorter periods are due to edge waves and the longer periods are due to gravity modes.

At Fort Gratiot, Tobermory, and Parry Sound, topography coupled with the direction of propagation of the squall line makes edge wave excitation highly unlikely. At Collingwood, the theoretical estimate of 24 min agrees well with the observed period of 22–25 min deduced from the autospectra.

Murty and Freeman (1973) also incorporated the squall line forcing in a two-dimensional time-dependent numerical model. The position of the squall line as a function of time as used in the model is shown in Fig. 7.9. The observed water levels and calculated water levels are shown in Fig. 7.10 and 7.11, respectively, using the forcing due to the large-scale pressure system only and that due to the squall line alone. It can be seen that at Fort Gratiot, the main peak cannot be reproduced unless the forcing due to the squall line is included.

In Chapter 4, statistical techniques for predicting storm surges in the Great Lakes were discussed. Here, a few typical surge profiles at selected stations will be included. The surge profiles for three storms at Collingwood on Lake Huron are given in Fig. 7.12. Surges up to a range of 1.22 m can be seen. The surges at Port Colborne on Lake Erie are given in Fig. 7.13. Surges with ranges greater than 2.44 m can be seen. Surges at Kingsville on Lake Erie are shown in Fig. 7.14 and 7.15. One interesting feature here is the presence of large negative surges.

Helmholtz resonance was discussed in section 5.1. Here, its relevance to storm surges

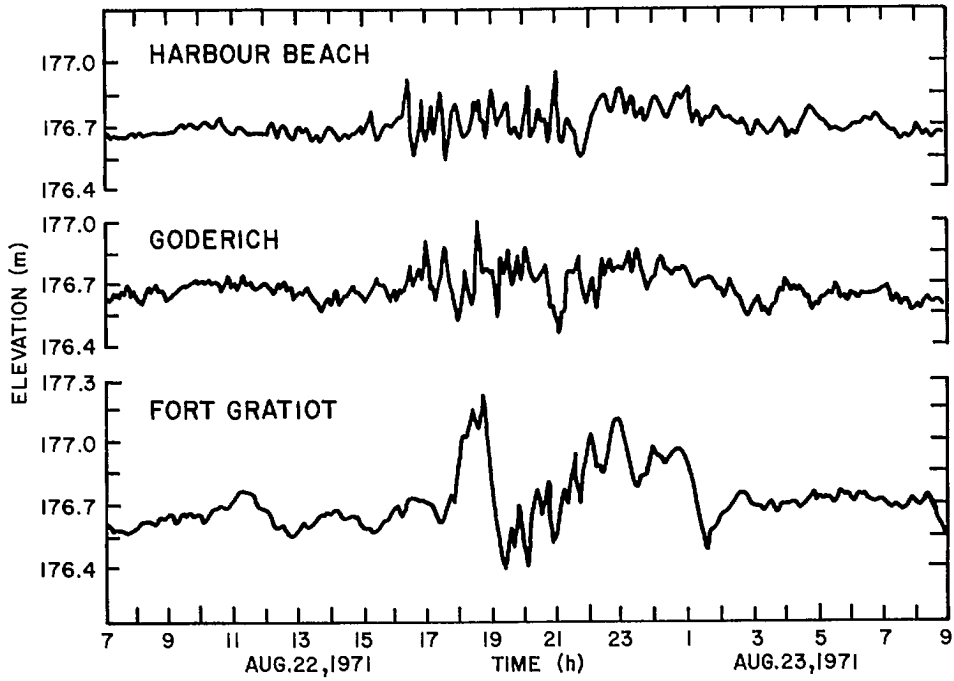

FIG. 7.8. Five-minute digitized water level values as obtained from continuous recorders at three stations on Lake Huron.

in the Great Lakes will be discussed. Freeman et al. (1974) calculated the Helmholtz mode periods for Hamilton Harbor, Toronto Harbor, and Goderich Harbor, and they gave values of 2.5 h, 65 min, and 14 min, respectively, for these three harbors.

During March 17–18, 1973, a storm passed over Lake Huron and the resulting surge caused damage to several ships in Goderich Harbor. This harbor consists of a main berthing basin for commercial ships and a comparatively small basin called Snug Harbor for pleasure craft. Protection to the harbor against wave agitation is provided by two offshore breakwaters. The meteorological situation associated with this storm was studied by Lawford (1977) and the general water level problem in Goderich Harbor was studied by Shaw (1974).

Baird et al. (1976) studied the surge in Goderich Harbor associated with this storm. They showed that the wind waves and seiches were not the main causes of damage in this harbor and the surge was mainly caused by Helmholtz resonance. Recorded water levels in this harbor at a normal time (not during any storm) show clearly an average 14-min period Helmholtz mode. Actually, the period ranged from 13 to 15 min. Note that the independent theoretical calculation by Freeman et al. (1974) gives 14 min as the period of the Helmholtz mode in Goderich Harbor.

A reconstruction of the possible water level changes showed that the contributions to the total surge from wind waves, Helmholtz resonance, and static setup were 2 ft (0.6 m), 4 ft (1.2 m), and 1.2 ft (0.4 m), respectively. The fact that this surge is not an isolated event can be seen from the fact that a surge of 3.7 ft (1.1 m) occurred on March 9, 1974, and the recorded water level for this surge also showed a period of 14 min, which is the Helmholtz period.

TABLE 7.12. Significant periods derived from autospectra of observed water levels in Lake Huron.

Mackinaw City		Harrisville		Harbour Beach		Fort Gratiot		Goderich		Tobermory		Collingwood		Parry Sound		Little Current	
h	min	h	min	h	min	h	min	h	min	h	min	h	min	h	min	h	min
8	21	1	05	6	15	6	15	6	15	No signifi-		12	30	3	08	12	30
3	08	2	30	1	31	2	05	1	00	cant periods		2	16	2	30	6	15
1	55	1	55	1	55	2	47	1	34			6	15				
		5	00	0	38	1	34	0	48			3	35				
		1	23	0	58							0	22				
				1	15							0	25				
				1	40												

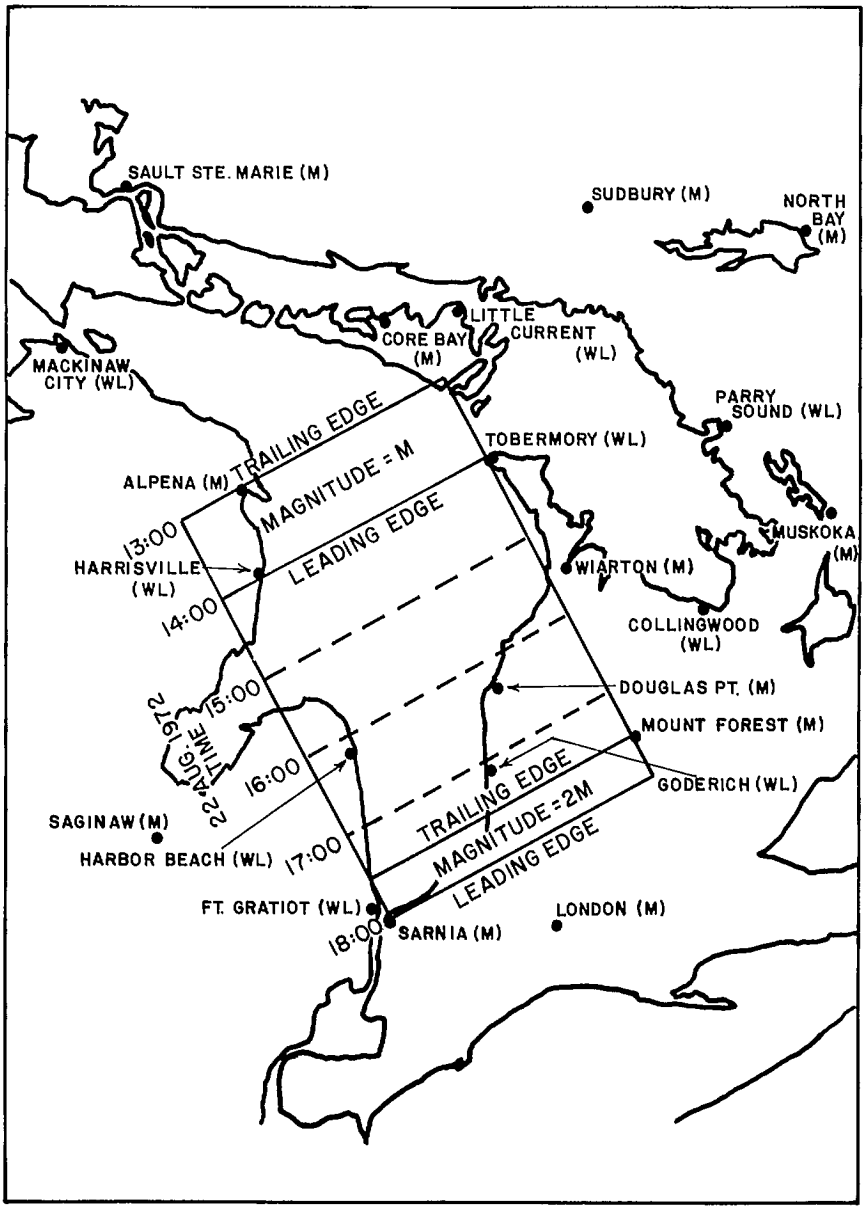

FIG. 7.9. Water level (WL) and meteorological (M) stations on and around Lake Huron. The position of the squall line as a function of time is also shown.

TABLE 7.13. Calculated edge wave periods in Lake Huron.

Station	U (cm·s^{-1})	β	T (min)	L (km)
Harrisville	1000 ± 250	$(2.8 \pm 1) \times 10^{-3}$	38	22.5
Harbour Beach	1300 ± 250	$(4.7 \pm 0.5) \times 10^{-3}$	30	23.3
Fort Gratiot	Cannot be generated			
Goderich	1100 ± 250	$(2.6 \pm 1) \times 10^{-3}$	49	32.2
Tobermory	Cannot be generated			
Collingwood	1200 ± 250	$(5.4 \pm 1) \times 10^{-3}$	24	17.2
Parry Sound	Too far out into harbor			

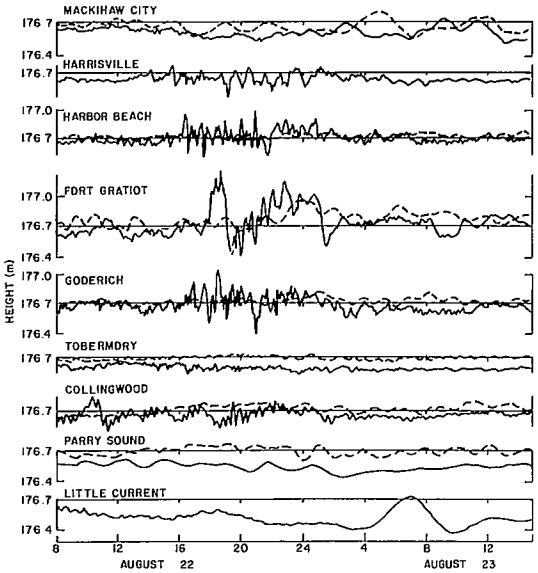

FIG. 7.10. Comparison of observed water levels (solid line) at nine locations on Lake Huron with computed water levels (broken line) due to forcing from the large-scale pressure system alone.

This discussion on the Great Lakes storm surges will conclude with some findings of surveys (Anonymous 1973, 1975) of the damage to the shores of the Great Lakes due to high water levels. The lengths of the coastlines of the Great Lakes and connecting rivers and lakes are listed in Table 7.14. The percentage of the shoreline protected is listed in Table 7.15. The total damage to the United States and Canadian shores of the Great Lakes during the period May 1951–April 1952 is given (dollars) in Table 7.16. Thus, in 1 yr, the total damage was $122.5 million.

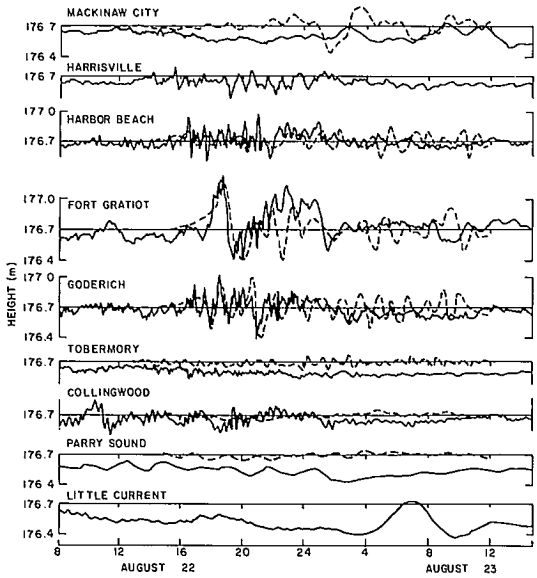

FIG. 7.11. Comparison of observed water levels (solid line) at nine locations on Lake Huron with computed water levels (broken line) due to forcing from the squall line alone.

STORM SURGES IN THE HUDSON BAY–JAMES BAY SYSTEM

Murty (1972) estimated that in the southern part of James Bay, maximum storm surge amplitudes could be as great as 5.7 m. For this estimation he used the following simple formula valid for a rectangular bay of length L and uniform depth h:

$$\eta_{max} = \frac{2L}{gh}\tau \tag{7.4}$$

where g is gravity and τ is the wind stress. Taking $h = 32$ m, $g = 9.8$ m·s^{-2}, and a wind speed of 23 m·s^{-1} gives $\eta_{max} \sim 5.7$ m. Godin (1975) studied four storm surges in James Bay that occurred in 1972.

Godin used the following simple statistical model to calculate the storm surge profiles for these four cases:

$$\eta(t) = \sum_{k=1}^{n} a_k p(t-k) + b_k E(t-k)|E(t-k)| + c_k|E(t-k)| + d_k|S(t-k)| \tag{7.5}$$

where $\eta(t)$ is the storm surge amplitude as a function of time, p is the atmospheric pressure at the centre of James Bay, E and S are the east and south components of the wind, and k is a time lag in units of 6 h. Godin mentioned that the storm surges sometimes penetrate more than 3 mi (4.8 km) inland in James Bay.

Yuen and Murty (1972) studied storm surges in Hudson Bay and James Bay using a time-dependent two-dimensional numerical model. Four different storm tracks over this sytem are illustrated in Fig. 6.73. The storm surge that was simulated in this study is for the storm of October 16–20, 1969. The numbering system for sample water level points (needed for identification in subsequent diagrams) is shown in Fig. 7.16. Also shown are

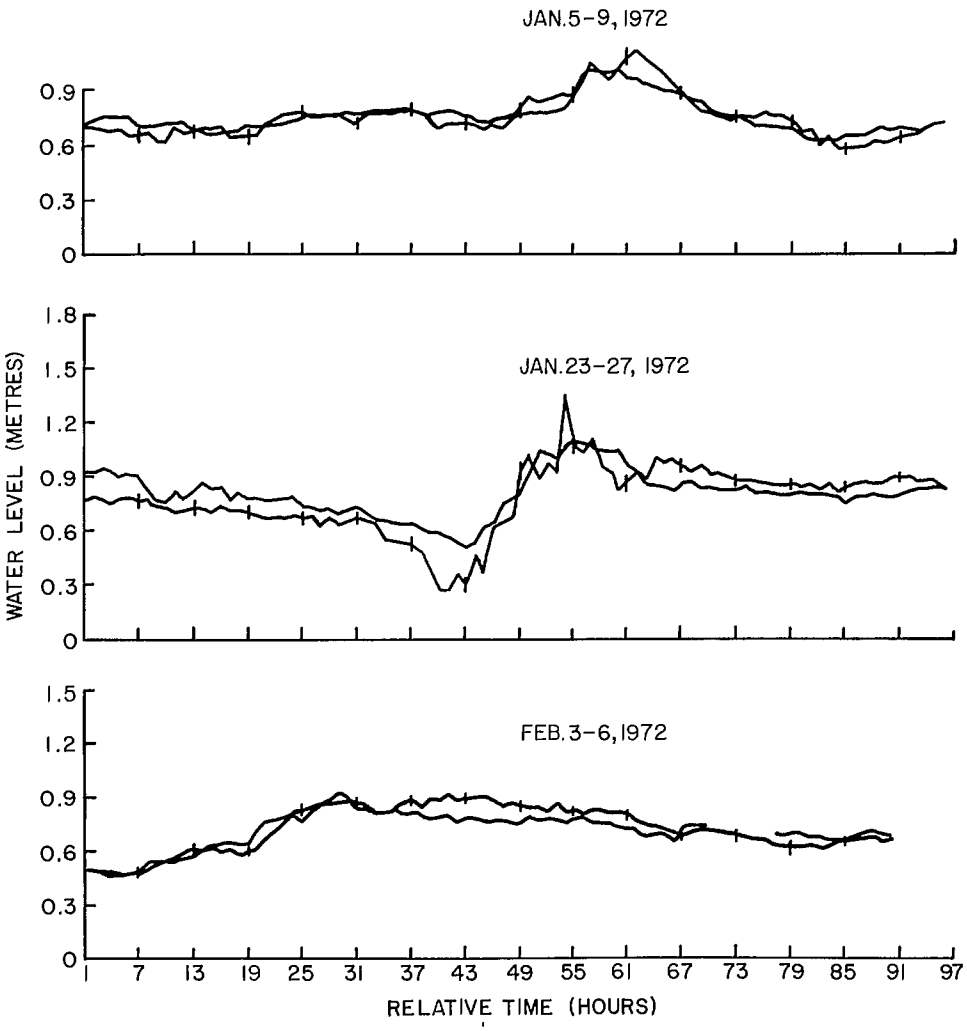

FIG. 7.12. Storm surges at Collingwood on Lake Huron. Curves with vertical ticks are the observed storm surge profiles; the other curves are the predicted profiles. (Venkatesh 1974)

the 10 areas into which the system is divided for the meteorological input data. Since there are only a few weather stations in this region, it was not practical to calculate the meteorological forcing terms at every grid point. Hence, the forcing terms are averaged in each of the 10 regions. The average atmospheric pressure gradients are shown in Fig. 7.17.

The inverse barometer effect is shown in Fig. 7.18. The calculated storm surge and the observed surge at Churchill are compared in Fig. 7.19. Time series plots of water levels around the perimeter of the Hudson Bay–James Bay system are given in Fig. 7.20. The station numbers on the ordinate are those shown in Fig. 7.17. Water level contours at different times are shown in Fig. 7.21. Note the progression of the disturbance round

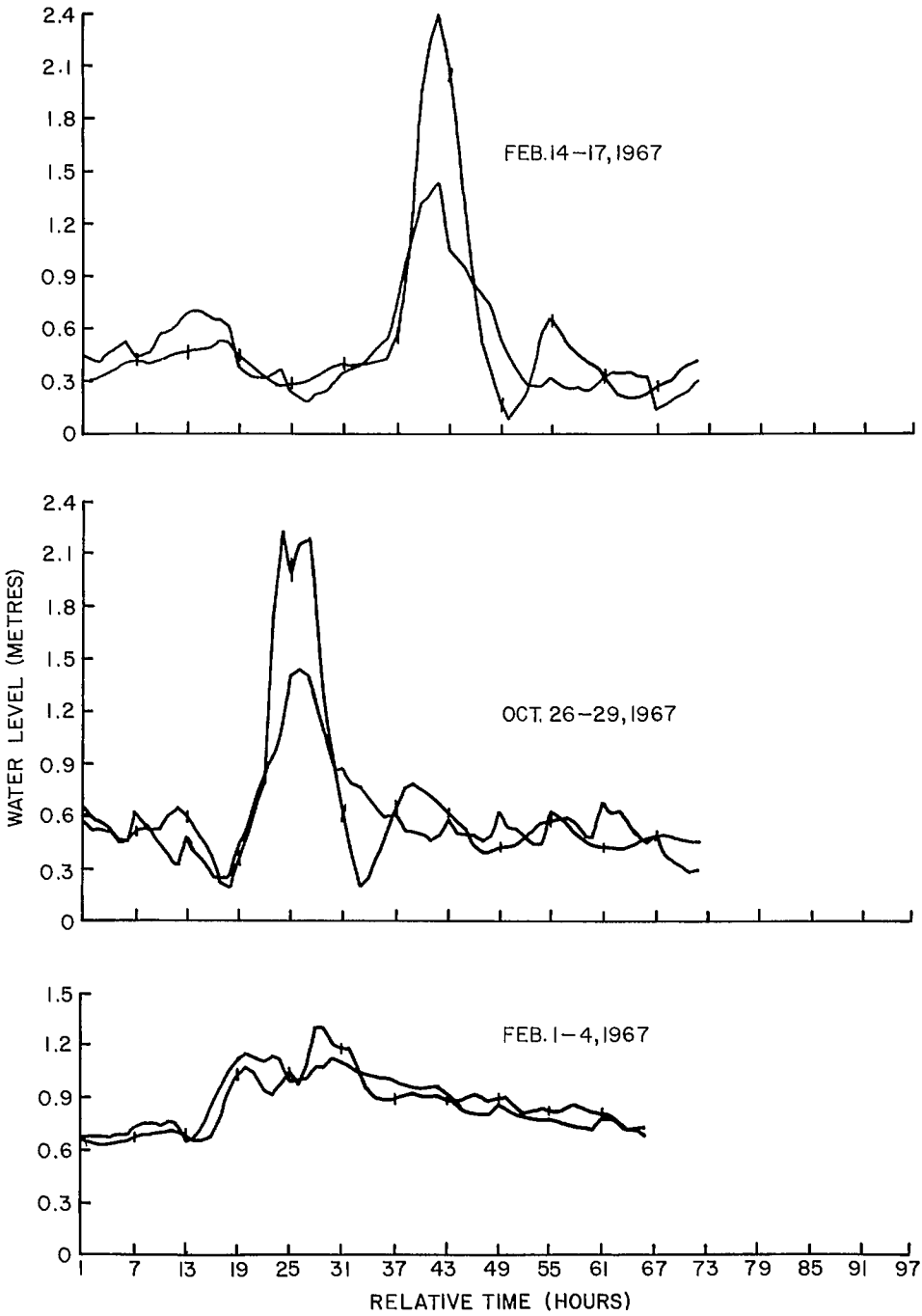

FIG. 7.13. Storm surges at Port Colborne on Lake Erie. See caption to Fig. 7.12 for explanation. (Venkatesh 1974)

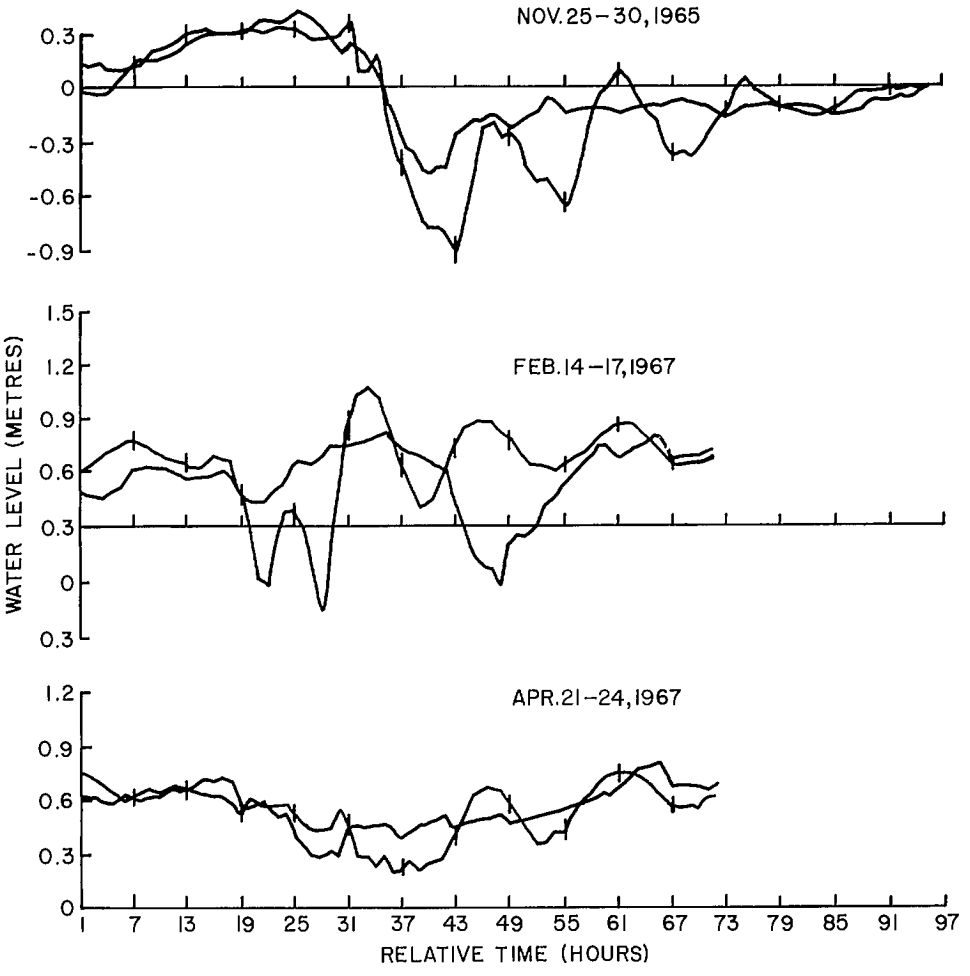

FIG. 7.14. Storm surges at Kingsville on Lake Erie. See caption to Fig. 7.12 for explanation. (Venkatesh 1974)

the perimeter of the system in the anticlockwise direction. The steady depression in the western half of Hudson Bay (100 h and beyond) is due to the persistence of the storm.

Water level contours in James Bay at different times are shown in Fig. 7.22 (again, rotation of the level can be seen). Time series plots of water levels at different locations in James Bay are given in Fig. 7.23. Note the damping of the high-frequency oscillations from the mouth towards the head of James Bay.

STORM SURGES IN LAKE WINNIPEG

Some aspects of the storm surges in Lake Winnipeg (following Hamblin 1976) were discussed in the section on finite-element methods. During the latter half of 1973, hourly wind observations were available at George Island at the northwest end of the lake. Water

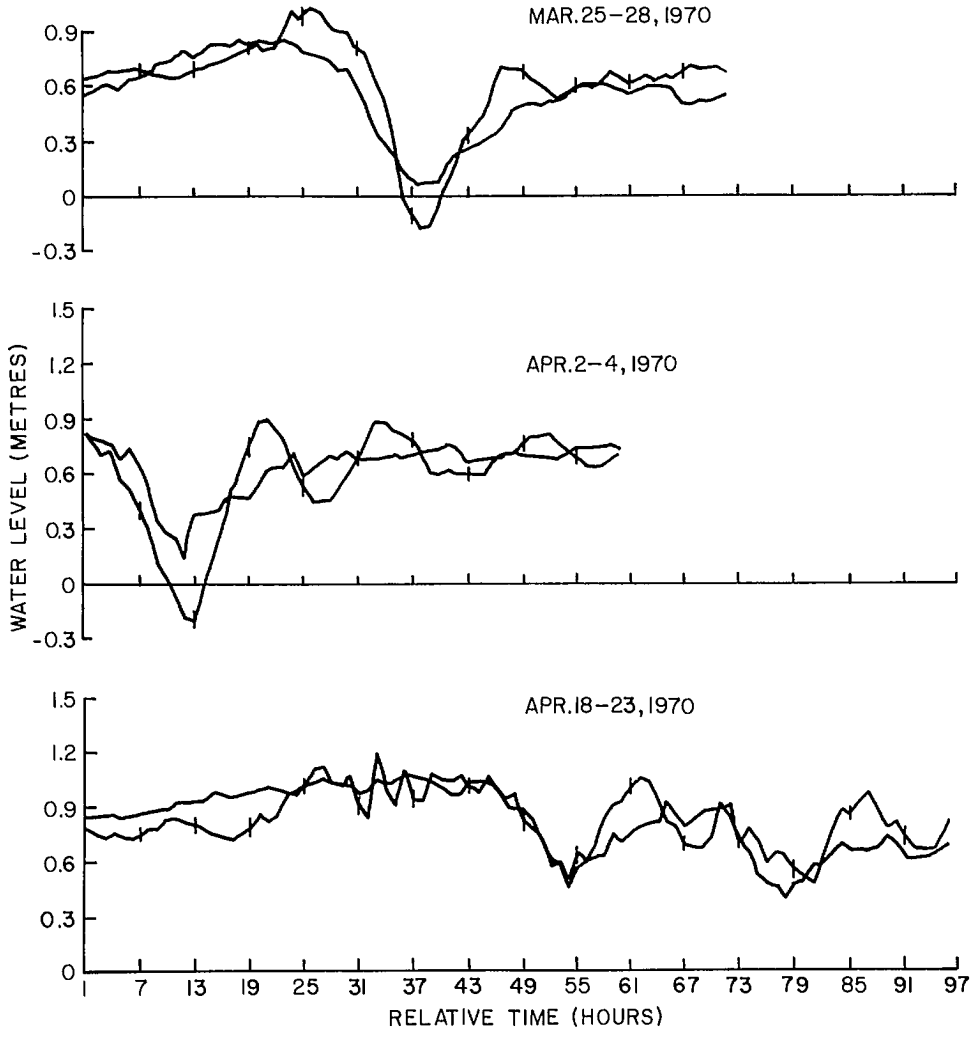

FIG. 7.15. Storm surges at Kingsville on Lake Erie. See caption to Fig. 7.12 for explanation. (Venkatesh 1974)

level data were available at Winnipeg Beach and Victoria Beach, both of these being in the southern part of the lake. During this half-year period, storm surges with amplitudes in excess of 1 m were observed on at least eight different occasions. The computed and observed water levels at these two stations for two different storms are compared in Fig. 7.24.

STORM SURGES IN THE SOUTHERN BEAUFORT SEA

In this system, the southern Beaufort Sea proper will be discussed as well as the Amundsen Gulf, Mackenzie Bay, and Kugmalitt Bay. The general geography of this area

TABLE 7.14. Length of shorelines (km) of the Great Lakes and connecting rivers and lakes. Note that the total length of the shoreline of the Great Lakes is about 18 077 km. (Anonymous 1973)

Shoreline	United States		Canada	
	Mainland	Islands	Mainland	Islands
Lake Superior	1389	615	1394	990
St. Marys River	47	143	106	101
Lake Michigan	2253	383	0	0
Lake Huron	933	414	2044	2769
St. Clair River	45	0	48	8
Lake St. Clair	95	135	114	69
Detroit River	48	63	48	53
Lake Erie	694	69	592	47
Niagara River	58	55	53	5
Lake Ontario	483	45	538	80
St. Lawrence River[a]	243	264	241	303
Total (rounded)	6288	2186	5178	4425

[a]Above Moses–Saunders Power Dam.

TABLE 7.15. Shore protection of the Canadian part of the Great Lakes. (Anonymous 1973)

Type of shore protection	% of shoreline protected			
	Lake Ontario	Lake Erie	Lake St. Clair	Lake Huron
Groynes and jetties	0.28	1.90	2.01	2.20
Dykes	—	—	35.35	—
Offshore breakwaters	0.19	0.73	0.21	0.20
Bulkheads and seawalls	5.43	7.90	29.73	1.70
Unprotected	94.10	89.47	32.70	95.90

TABLE 7.16. Damage (in dollars at 1952 price levels) to the United States and Canadian shores of the Great Lakes due to high water levels during the period May 1951–April 1952. (Anonymous 1973)

Lake	Damage due to inundation	Damage due to wave action	Total damage
Superior (including Upper St. Marys River)	1 506 000	2 853 000	4 359 000
Michigan	1 560 300	29 083 500	30 643 800
Huron (including Lower St. Marys River)	274 700	2 461 500	2 736 200
St. Clair (including St. Clair River and Detroit River)	1 921 700	2 317 800	4 239 500
Erie (including Niagara River above Falls)	4 753 200	7 167 000	11 920 200
Ontario (including Lower Niagara River and St. Lawrence River to International Boundary	1 266 300	6 087 900	7 354 200
Total	11 282 200	49 970 700	61 252 900

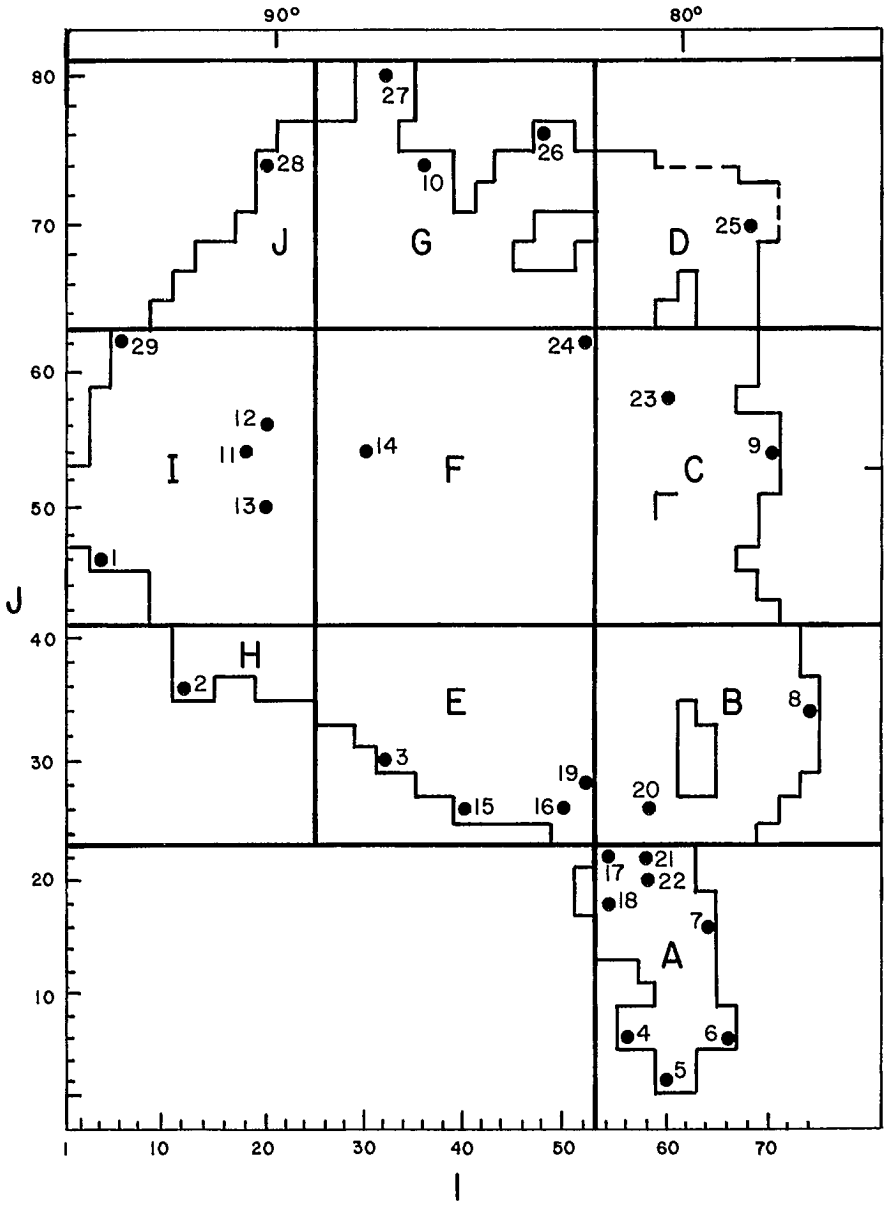

FIG. 7.16. Numbering system for sample water level points, with reference to the time series plots shown in subsequent figures. A–J correspond to the 10 regions in which meteorological forcing terms are averaged.

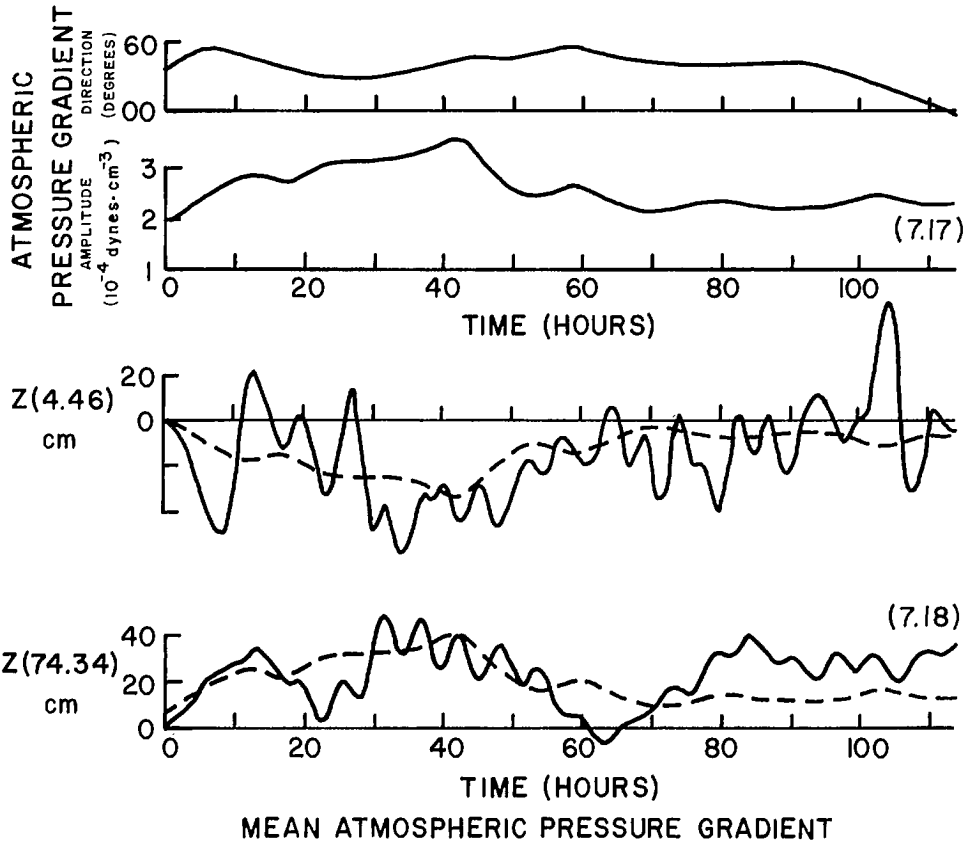

FIG. 7.17–7.18. Mean atmospheric pressure gradient (amplitude and direction) averaged over Hudson Bay (Fig. 7.17) (1 dyne = 20 N) and inverse barometer effect at two stations on Hudson Bay (Fig. 7.18).

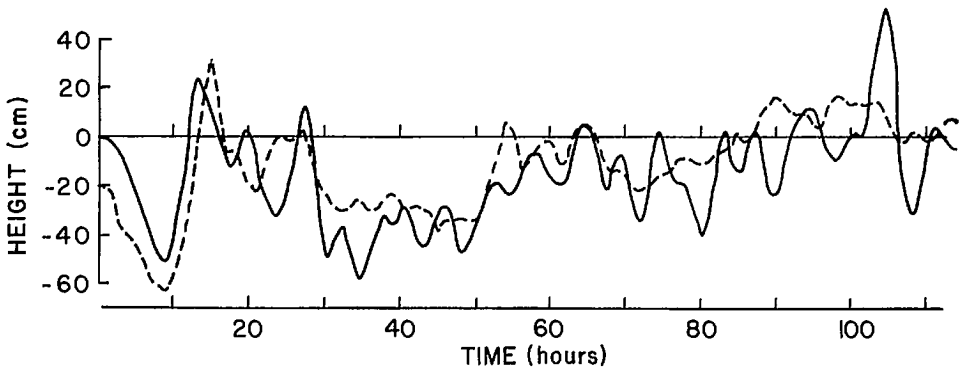

FIG. 7.19. Comparison of observed (solid line) and calculated (broken line) storm surge at Churchill, Manitoba. Time origin is 18:00 (GMT) on October 15, 1969.

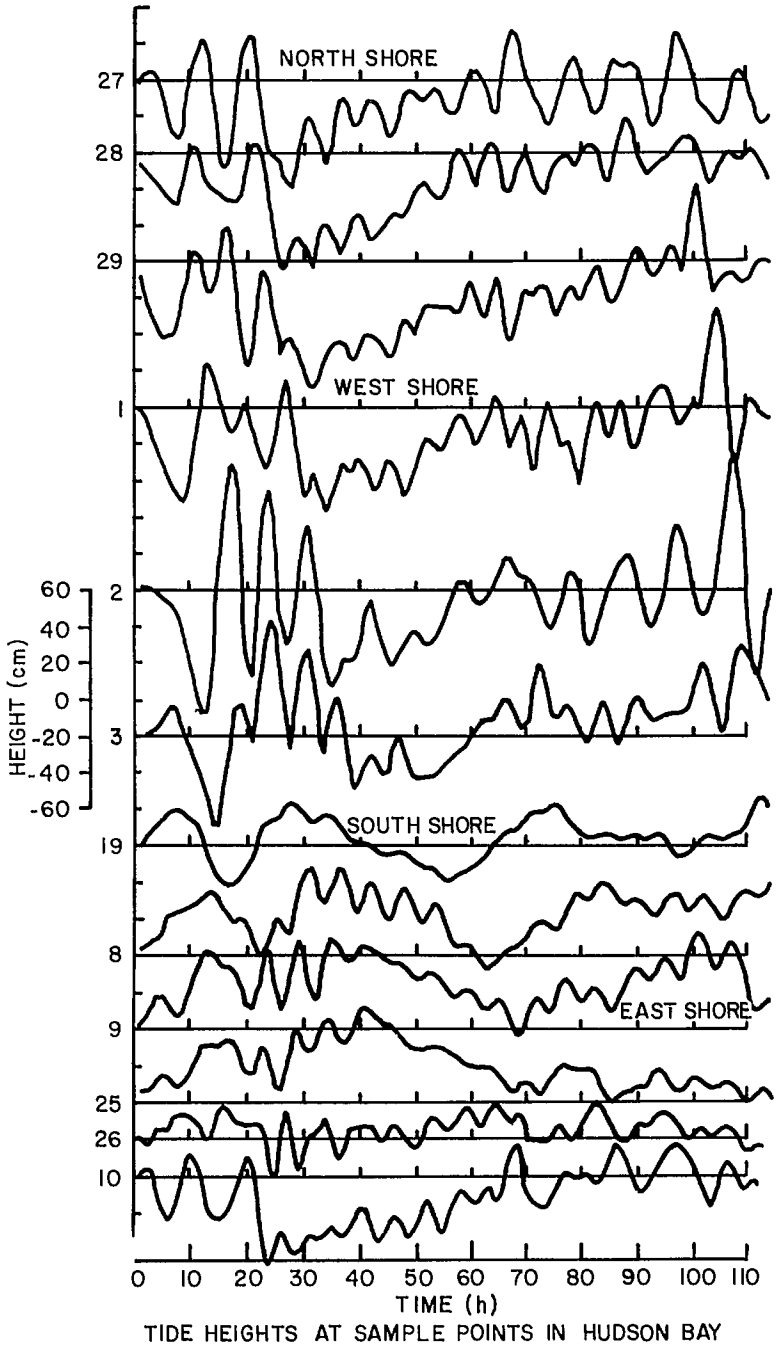

FIG. 7.20. Calculated storm surge profiles at 12 locations around the perimeter of Hudson Bay. The anticlockwise progression of the water level disturbance can be seen.

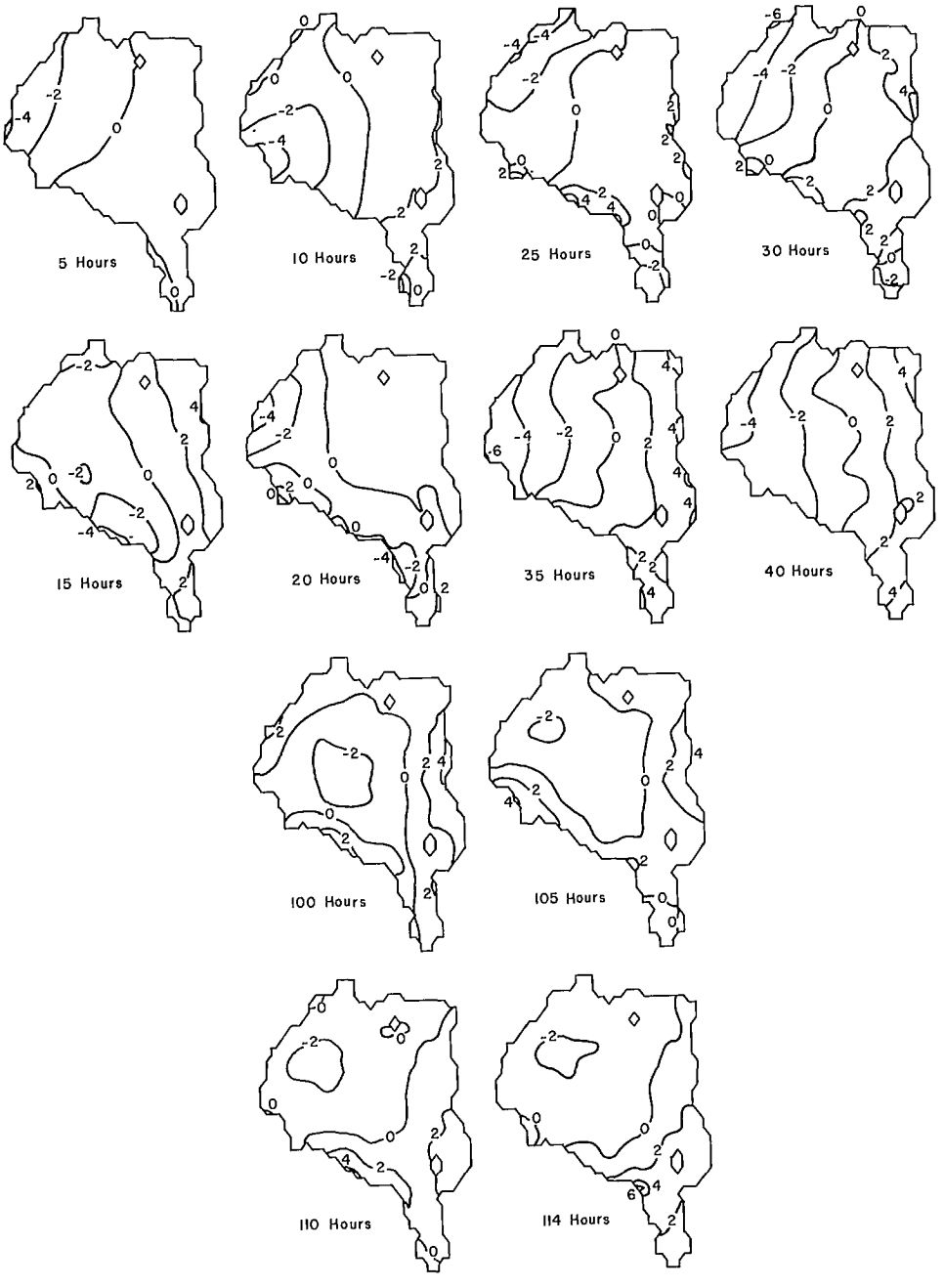

FIG. 7.21. Computed storm surge water level contours in Hudson Bay. Numbers multiplied by 20 give the water levels (centimetres).

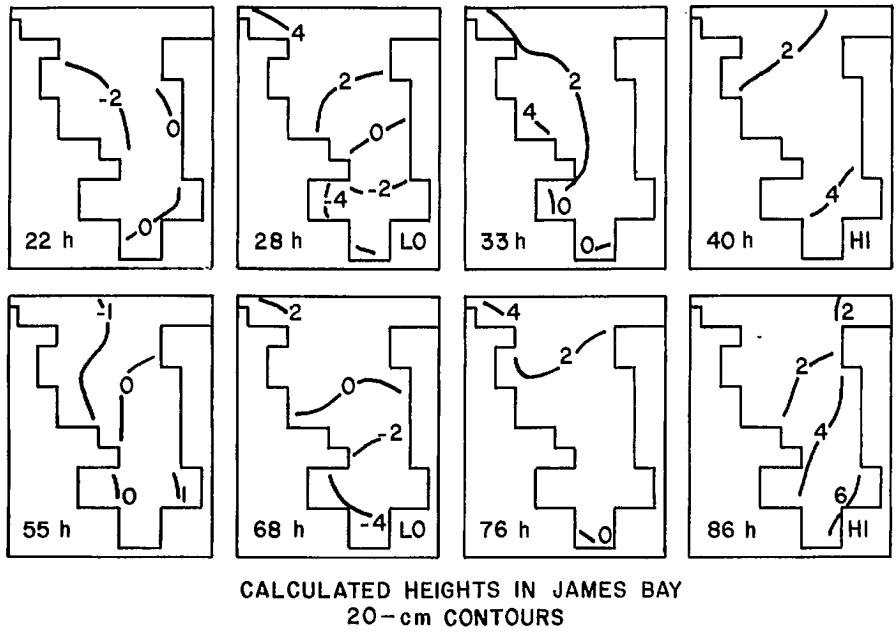

FIG. 7.22. Calculated storm surge water level contours in James Bay. Numbers multiplied by 20 give the water levels (centimetres). This series of diagrams shows the rotation of the water levels in James Bay.

and the area covered by two storm surge numerical models (Henry 1974, 1975; Henry and Heaps 1976) are shown in Fig. 7.25.

The storm surge due to the storm of September 13–16, 1970, was severe in several locations (Anonymous 1971). The following is a summary of the most extreme conditions along the coastline between Herschel Island and Darnley Bay:

Maximum wind velocity	65 mi·h^{-1} gusting to 85 mi·h^{-1} (1 mi·h^{-1} = 1.609 km·h^{-1})
Duration of maximum velocity	4 h
Prevailing wind direction	Northwest
Advance of front	60 mi·h^{-1} (approx.)
Maximum wave height offshore	30 ft } wind waves (1 ft = 0.305 m)
Maximum wave height onshore	5 ft }
Maximum storm surge	8 ft
Astronomical tide	2.5 ft

Along the coast between Herschel Island and Tuktoyaktuk, the wind velocities and the storm surge amplitudes were more or less regular. East of Tuktoyaktuk, the conditions were somewhat irregular with maximum wind velocities up to 50 mi·h^{-1} (80.5 km·h^{-1}) and maximum surge up to 3 ft (0.9 m) in amplitude.

Mackenzie Bay was relatively ice free at this time and the polar ice pack was at least 100 mi (160 km) north of Herschel Island. Thus, this good fetch, combined with high winds and the extensive shallow-water area of the Kugmalitt Bay and Mackenzie Bay plus

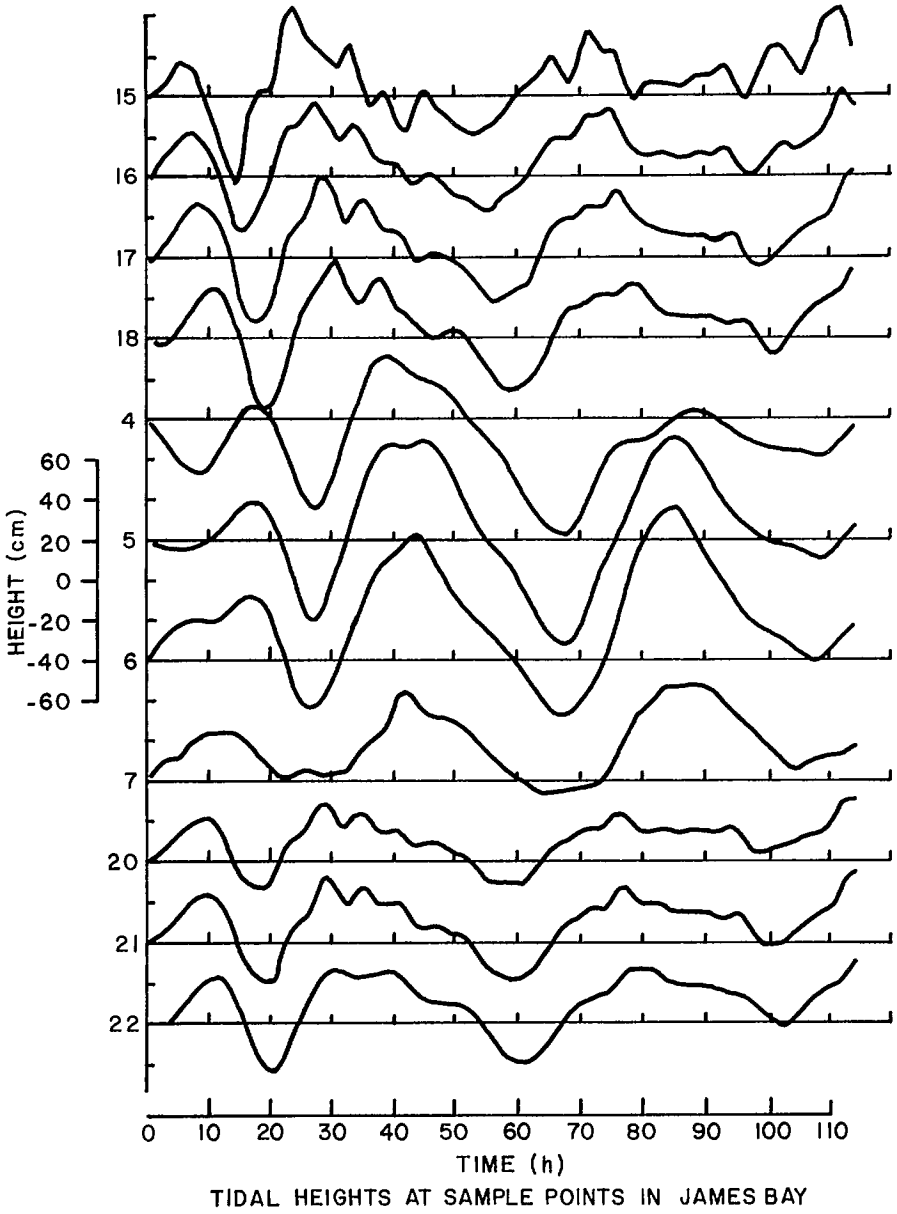

FIG. 7.23. Time series of water levels at various locations in James Bay.

the V-shaped topographies of these bays, amplified the surge in these bays. The fact that this storm surge is not an isolated incident can be seen from the occurrence of at least another storm surge on September 9, 1944, with amplitudes up to 10 ft (3.1 m) (Anonymous 1971). Some theoretical estimates of this storm surge were made (Anonymous 1971) using simple empirical relations of the type discussed in Chapter 4 (see equations 4.201,

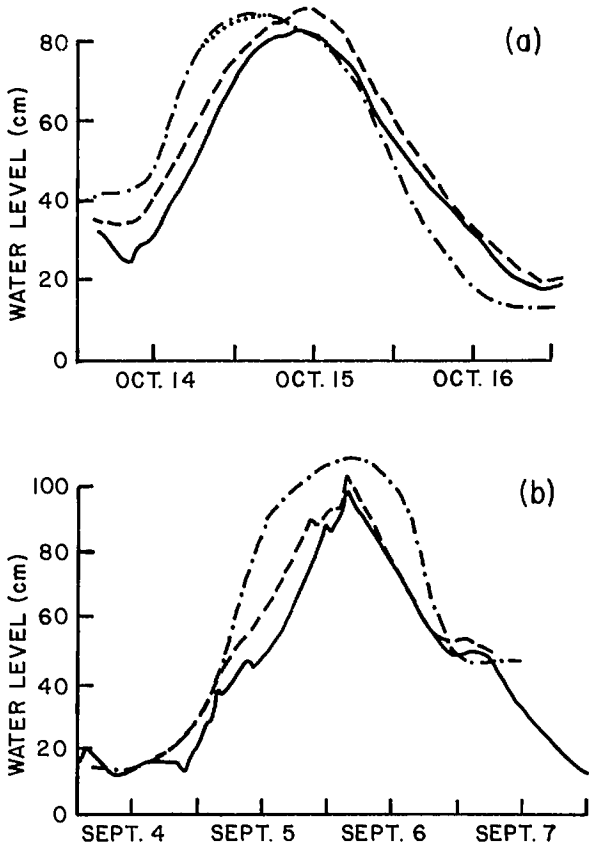

FIG. 7.24. (a) Observed storm surge at Winnipeg Beach in Lake Winnipeg, Manitoba (solid line), for the storm of October 14, 1973, showing calculated water level at Winnipeg Beach (dashed–dotted line) and calculated surge at Victoria Beach (broken line). (b) Observations for the storm of September 4, 1973. (Hamblin 1976)

4.203, 4.250, and 4.252): Herschel Basin (10.7 ft or 3.3 m), Babbage Bight (9.6 ft or 2 m), Horton River (1.9 ft or 0.58 m), and Clapperton Island (3.1 ft or 0.94 m).

Henry (1974) listed all storm surges in the southern Beaufort Sea at Tuktoyaktuk with amplitudes in excess of 1 m for the period 1962–73 (Table 7.17). Based on this information he concluded that maximum amplitudes for positive and negative surges are 2 and 1 m, respectively. Henry (1975) mentioned that in the summer of 1974 no significant surges occurred probably because of an unusually persistent ice cover. Two surges of approximately 1-m amplitudes were recorded in August 1975. The daily extrema of water levels at Tuktoyaktuk for the years 1962, 1963, 1964, and 1974 are shown in Fig. 7.26 (in this diagram, positive extrema of less than 1 m and negative extrema of less than 0.5 m are omitted). A seasonal distribution of the extrema can be noted. Negative surges appear to occur irrespective of the degree of ice cover whereas the suppression of positive surges by the persistent ice cover in 1964 and 1974 can be seen in Fig. 7.26. Observed and calculated surges at four locations in the southern Beaufort Sea are compared in

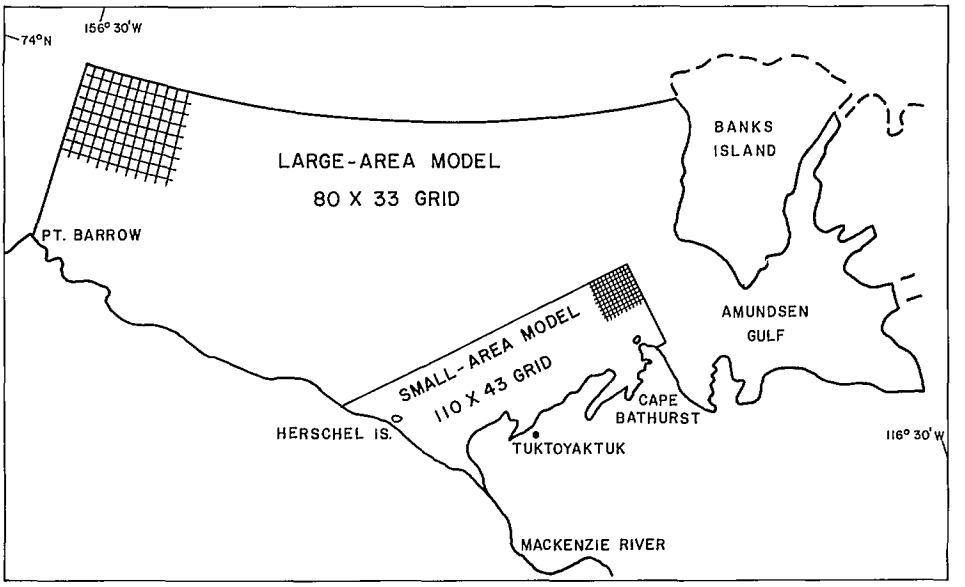

FIG. 7.25. Geography of the Beaufort Sea and the regions covered by the two storm surge models. (Henry 1974)

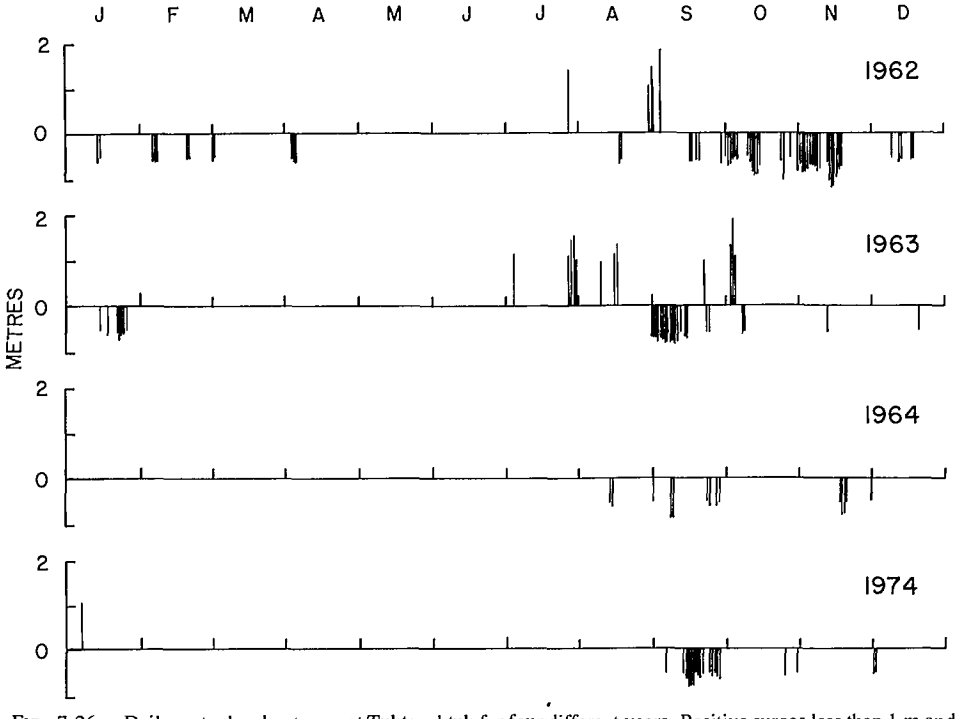

FIG. 7.26. Daily water level extrema at Tuktoyaktuk for four different years. Positive surges less than 1 m and negative surges less than 0.5 m are not shown. (Henry 1975)

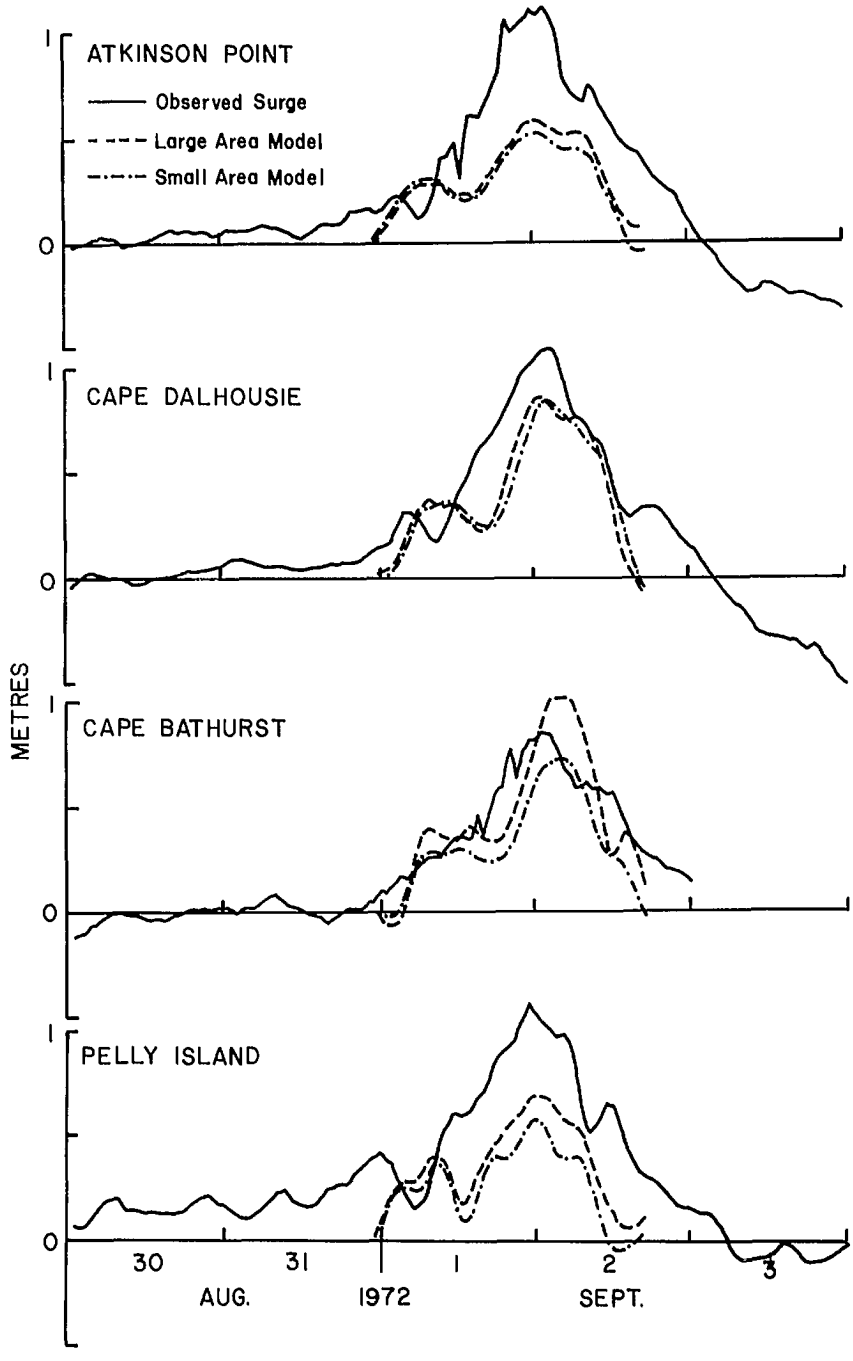

FIG. 7.27. Storm surges in the southern Beaufort Sea for the storm of September 1–3, 1972. (Henry 1975)

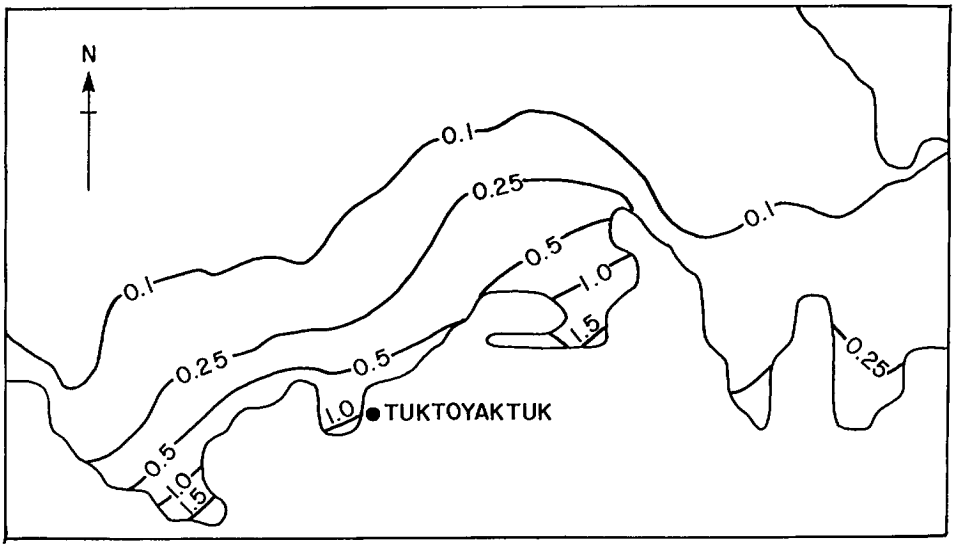

FIG. 7.28. Storm surge water level contours (metres) in the southern part of the Beaufort Sea for the storm of September 1–3, 1972. (Henry 1975)

Fig. 7.27 and maximum elevation contours in the southern Beaufort Sea are shown in Fig. 7.28. For details of the large-area model and small-area model referred to in the diagrams see Henry (1975) and Henry and Heaps (1976).

STORM SURGES ON THE WEST COAST OF CANADA

Although disastrous storm surges do not occur on the west coast of Canada, surges up to 2–3 ft (0.6–0.9 m) can occur. During December 14–18, 1982, a moderate storm surge occurred in the Strait of Georgia followed by some destruction to property. Armstrong (1962) examined the tidal records for the period 1945–61 for Tofino, Prince Rupert, Vancouver Harbour, and Victoria Harbour. For Alert Bay, data for 1949–61 were examined. Based on this study, it was deduced that low pressure systems approaching the British Columbia coast from west to southwest with an average speed of 25–30 knots (46–56 km·h^{-1}) could cause surges. These weather systems cause maximum surges at Tofino, then fill over the Vancouver Island or move northwards to the Queen Charlotte Islands. The surges at Tofino during the period December 1952–March 1959 are summarized in Table 7.18. Surges of similar magnitude could occur at Prince Rupert and in the Queen Charlotte Islands.

7.2 Storm Surges in the United States

This section will begin with a brief description of the tides in selected United States waters and a discussion of the perigean spring tides. East coast hurricane-generated storm surges and Gulf of Mexico hurricane-generated surges will then be discussed followed by special consideration of the Florida coast. Lake Okeechobee surges will be considered in

TABLE 7.17. Storm surges (in excess of 0.9 m) at Tuktoyaktuk (Canada) during summer 1962 to fall 1973. (Henry 1974)

Date	Surge amplitude (m)	Date	Surge amplitude (m)
July 28, 1962	1.37	Sept. 22, 1963	1.01
Aug. 29, 1962	1.04	Oct. 4, 1963	1.89
Aug. 31, 1962	1.43	Oct. 16, 1963	0.91
Sept. 4, 1962	1.83	Aug. 7, 1965	1.37
Oct. 13, 1962	−0.91	Nov. 12, 1965	0.94
Oct. 25, 1962	−1.01	July 18, 1966	0.91
Nov. 14, 1962	−1.16	Sept. 10, 1966	1.13
July 5, 1963	1.19	Oct. 4, 1966	−0.91
July 27, 1963	0.94	Oct. 15, 1966	−1.10
July 28, 1963	1.13	July 24, 1967	1.13
July 30, 1963	1.55	Aug. 13, 1967	1.07
Aug. 4, 1963	0.91	Oct. 3, 1967	0.91
Aug. 10, 1963	1.01	Oct. 12, 1973	1.01
Aug. 17, 1963	1.37		

TABLE 7.18. Storm surges at Tofino, B.C., during December 1952–March 1959. (Based on Armstrong 1962)

Date	Maximum surge (m)	Time of maximum surge (PST)	State of tide at time of maximum surge
Dec. 6, 1952	0.55	21:56	Low water
Dec. 30, 1952	1.01	05:35	Low water
Feb. 12, 1954	0.46	21:36	High water
Feb. 17, 1954	0.52	12:14	High water
Mar. 9, 1954	0.46	09:46	Low water
Nov. 15, 1954	0.34	22:32	Low water
Nov. 19, 1954	0.58	01:26	Low water
Dec. 23, 1954	0.37	10:50	High water
Jan. 15, 1956	0.46	20:11	Low water
Jan. 16, 1956	0.46	02:32	High water
Mar. 2, 1956	0.43	22:08	Low water
Jan. 12, 1959	0.46	02:40	High water
Mar. 29, 1959	0.34	22:07	Low water

detail. Then, case studies of surges in the following water bodies will be considered: Galveston Bay (Texas), Lake Travis (Texas), Mobile Bay (Alabama), Cape Fear Estuary (North Carolina), Chesapeake Bay, New York Bay, and Narragansett Bay. Extratropical surges on the east coast and Great Lakes will be discussed followed by a discussion of the surges on the west coast and Alaska. Finally, surges in the area of the Bahamas, the Gulf Stream area, and other miscellaneous areas will be considered. The section will conclude with probability studies for engineering design, coastal flooding insurance, etc.

TIDES IN SELECTED UNITED STATES WATERS

Tides along the Atlantic and Pacific coasts of the United States are summarized in Tables 7.19 and 7.20, respectively. In Table 7.19, the mean range and highest and lowest

TABLE 7.19. Mean range and highest and lowest tides (m) along the Atlantic and Gulf of Mexico coasts of the United States. (Disney 1955)

Location	Mean range	Highest tide above mean high water		Lowest tide below mean low water	
		Avg. yearly highest	Extreme high	Avg. yearly lowest	Extreme low
Eastport, ME	5.55	1.22	1.52	1.13	1.28
Portland, ME	2.71	0.91	1.31	0.79	1.98
Portsmouth, NH	2.47	0.88	1.19	0.73	0.85
Boston, MA	2.90	0.94	1.31	0.85	1.07
Woodshole, MA	0.55	0.85	2.38	0.55	0.76
Newport, RI	1.07	0.88	3.14	0.58	0.79
Providence, RI	1.40	1.01	4.75	0.73	0.91
New London, CT	0.79	1.07	2.59	0.58	0.91
Willets Point, NY	2.19	1.22	3.02	0.88	1.16
Fort Hamilton, NY	1.43	0.85	1.22	0.91	1.25
New York Battery, NJ	1.34	0.94	1.68	0.85	1.16
Sandy Hook, NJ	1.40	0.94	1.71	0.82	1.13
Atlantic City, NJ	1.25	0.88	1.65	0.79	1.07
Philadelphia, PA	1.77	0.73	1.46	0.91	1.55
Baltimore, MD	0.34	0.82	2.19	0.88	1.37
Washington, DC	0.88	0.94	2.62	0.82	1.04
Norfolk, Sewell Point, VA	0.76	0.85	1.92	0.55	0.82
Southport, NC	1.25	0.73	1.04	0.37	0.58
Charleston, SC	1.55	0.79	1.71	0.64	0.85
Fort Pulaski, GA	2.10	0.85	1.37	0.82	1.25
Fernandina, FL	1.86	0.82	2.38	0.73	1.13
Miami Beach, FL	0.76	0.58	1.19	0.34	0.43
Key West, FL	0.40	0.46	0.76	0.31	0.43
Cedar Key, FL	0.76	0.76	1.07	0.79	1.40
Pensacola, FL	0.40	0.55	2.38	0.40	0.61
Galveston, TX	0.30	0.85	3.08	0.70	1.49

tides at a number of stations are shown. The mean range is the difference in height between mean high water and mean low water. Heights for the highest tides are above the local datum of mean high water whereas the heights for lowest tides are below the local datum of mean low water. Along the Atlantic coast the average yearly highest tide varies from 1.5 to 4.0 ft (0.5−1.2 m) above mean high water whereas the average yearly lowest tide varies from 1.0 to 3.7 ft (0.3−1.1 m) below mean low water (Disney 1955). The range between the average yearly highest tide and average yearly lowest tide at each station may be obtained by adding the heights of the average yearly highest and lowest tides to the mean range for each station. The range between the extreme high and extreme low water levels at each station may be obtained by adding the heights of extreme highest and lowest tides to the mean range for each station.

On the Pacific coast, the datum for hydrographic charts is the mean lower low water (Disney 1955). Because of the large diurnal inequality in the tides (especially in the low waters), this datum is used. For example, at Seattle, one low water of the day may be 10 ft (3.1 m) (or more) lower than the other low water. Thus, there is a special significance on the Pacific coast for mean higher high water and mean lower low water and the range between these two levels. The difference in height between mean higher high water and mean lower low water is known as the great diurnal range (or simply "diurnal range"). The

TABLE 7.20. Diurnal range and highest and lowest tides (m) along the Pacific coast of the United States. (Disney 1955)

Location	Diurnal range	High tide above mean higher high water		Low tide below mean lower low water	
		Avg. yearly highest	Extreme high	Avg. yearly lowest	Extreme low
San Diego, CA	1.77	0.58	0.76	0.58	0.79
La Jolla, CA	1.59	0.58	0.70	0.58	0.76
Los Angeles, CA	1.65	0.58	0.67	0.58	0.79
Santa Monica, CA	1.65	0.61	0.70	0.52	0.76
San Francisco, CA	1.74	0.52	0.76	0.58	0.76
Crescent City, CA	2.10	0.76	0.94	0.70	0.76
Astoria, OR	2.50	0.82	1.19	0.58	0.85
Neah Bay, WA	2.50	0.85	1.22	0.91	1.10
Seattle, WA	3.44	0.70	1.04	1.19	1.40
Friday Harbor, WA	2.35	0.73	1.01	0.98	1.19
Ketchikan, AK	4.70	1.34	1.65	1.37	1.59
Juneau, AK	5.06	1.25	1.59	1.55	1.80
Skagway, AK	5.15	1.37	1.77	1.65	1.86
Sitka, AK	3.02	1.01	1.37	1.01	1.22
Yakutat, AK	3.05	1.07	1.37	1.04	1.31
Seward, AK	3.20	1.04	1.25	1.10	1.31
Anchorage, AK	9.01	1.37	1.77	1.31	1.49
Dutch Harbor Unalaska Island, AK	1.13	0.61	0.88	0.61	0.82
Sweeper Cove, Adak island, AK	1.13	0.67	0.79	0.67	0.88
Massacre Bay, Alta Island, AK	0.01	0.46	0.58	0.55	0.76

diurnal ranges at the highest and lowest tides for several stations on the Pacific coast are listed in Table 7.20. The heights for highest tides are above the local datum of mean higher high water whereas the heights for lowest tides are below the local datum of mean lower low water.

Along the Pacific coast of the continental United States, the average yearly highest tide varies from 1.7 to 2.8 ft (0.5−0.9 m) above mean higher high water whereas the average yearly lowest tide varies from 1.7 to 3.9 ft (0.4−1.4 m) above mean higher high water and the average yearly lowest tide varies from 1.8 to 5.4 ft (0.6−1.6 m) below mean lower low water.

The range between the average yearly highest tide and the average yearly lowest tide in Table 7.20 may be obtained by adding the heights of the average yearly highest and lowest tides to the diurnal range for each station. The range between the extreme high and extreme low water levels at each station can be obtained by adding the heights of extreme highest and lowest tides to the diurnal range of each station.

Some typical tide curves at five locations in the United States are shown in Fig. 7.29. The curves were normalized with reference to the maximum range for each tide station. Hence, in this diagram, the relative ranges are not relevant; it is the characteristics of the tidal curves that are of interest. The curve for New York is a typical semidiurnal curve (two highs and two lows each tidal day of approximately 24 h and 50 min). The curve for Pensacola (Florida) represents a typical diurnal tide (i.e. one high and one low water for

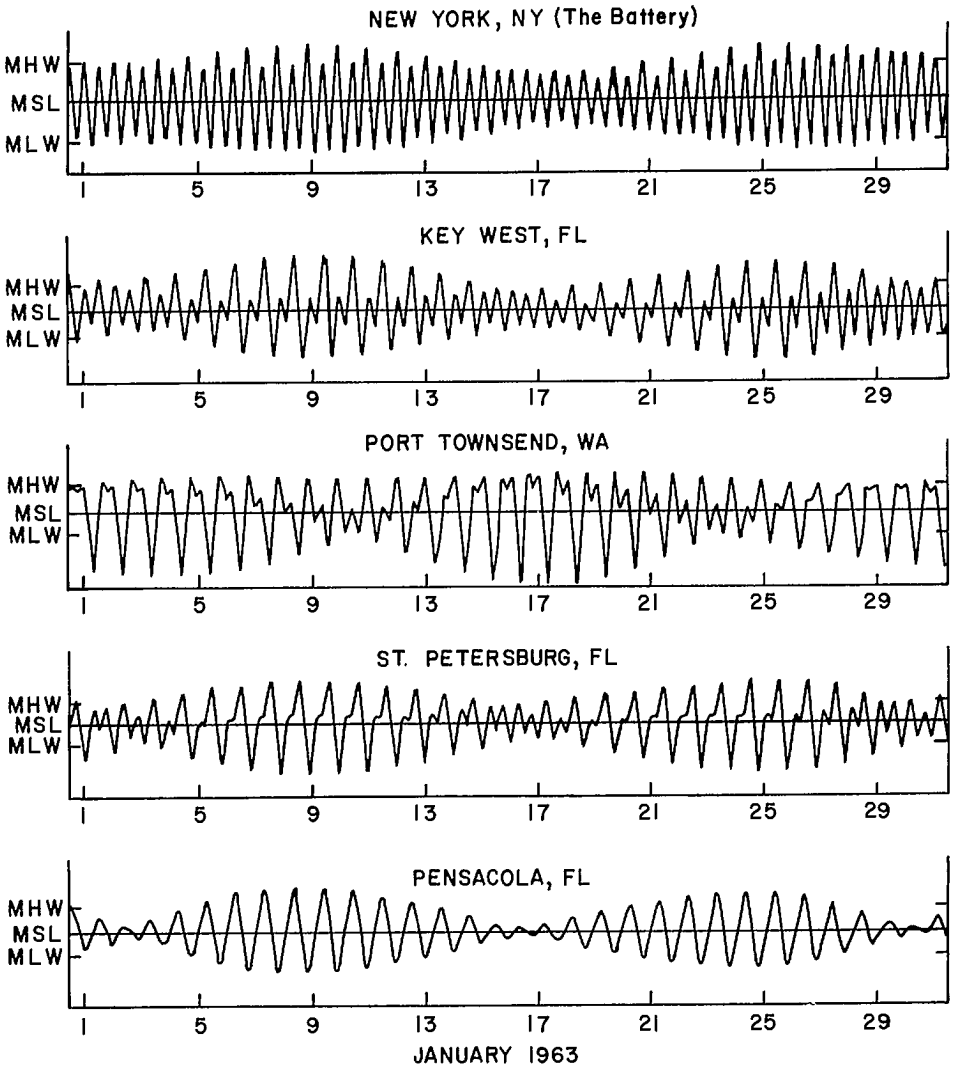

FIG. 7.29. Predicted tide for January 1963 at five locations in the United States. (Harris 1981)

each lunar day). The curves for Key West (Florida) and Port Townsend (Washington State) are of the mixed type. One can see two high and two low waters during each tidal day, although the amplitudes of successive waves are different (except for brief periods near January 15 and 30 for Key West). The curve for St. Petersburg (Florida) is of the vanishing type (i.e. two unequal low and high waters can be seen on most days, but there are other days when one of the tide waves vanishes). The nature of the tide along the coasts of the Gulf of Mexico and Florida is shown in Fig. 7.30.

Redfield (1958) showed that along the east coast of the United States the variation in the range of the tide and time of high water has a direct correlation with the width of

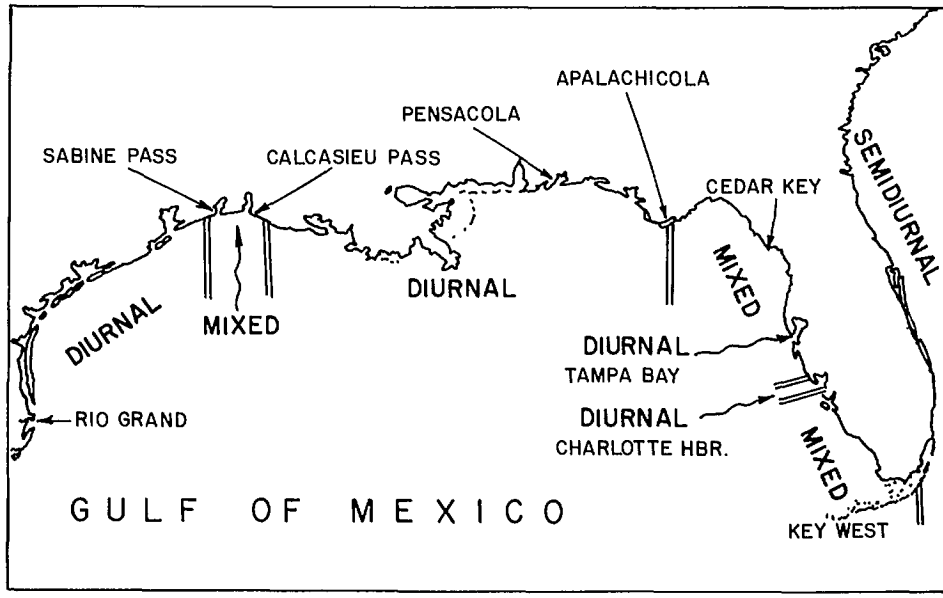

FIG. 7.30. Nature of tides along the coast of the Gulf of Mexico. (Harris 1981)

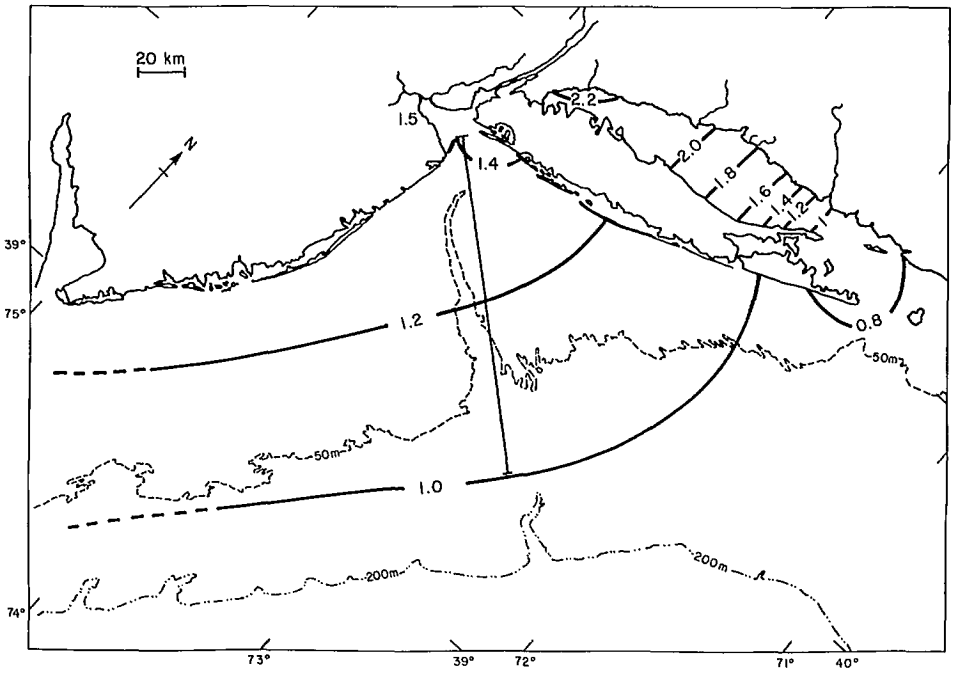

FIG. 7.31. Mean range (metres) of the M_2 tide in the New York Bight and on the shelf. (Swanson 1976)

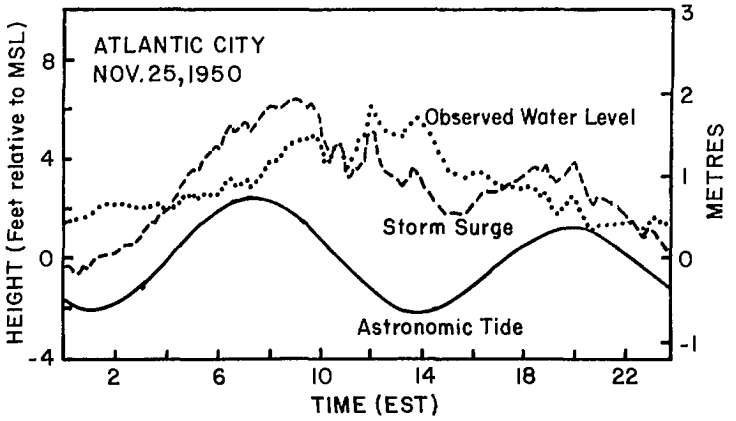

FIG. 7.32. Observed water level, storm surge, and astronomical tide at Atlantic City on November 25, 1950. (Swanson 1976)

the continental shelf. As an example of tides on the shelf and in coastal waters, the New York Bight and outer shelf area are chosen. The mean tidal range for these waters is given in Fig. 7.31.

In section 7.1 for Canadian waters, the importance of the interaction between tides and surges was discussed. Such an interaction is important in United States waters to varying degrees (depending on the location). The tide, surge, and the observed water level at Atlantic City on November 25, 1950, are shown in Fig. 7.32. It can be seen that the maximum surge occurred almost at the time of low tide (Swanson 1976).

The so-called perigean spring tides and their role in coastal flooding were briefly discussed in section 7.1. The cases of coastal flooding in the United States associated with these perigean spring tides (Wood 1978) are listed in Table 7.21.

STORM SURGES DUE TO HURRICANES ON THE EAST COAST OF THE UNITED STATES

Harris (1956) summarized the status of research on hurricane-generated storm surges in the United States up to the early 1950's. He mentioned the study of Cline (1926) as typical of that period. Harris further stated (1956, p. 1):

> Much of the research on storm surges has never been formally published, largely because the people performing the work in relative isolation have not been satisfied with the results. Much of the material which has been published contains a number of questionable statements, mainly in the nature of oversimplification. After the tremendous losses in the northeastern United States due to hurricanes in 1954, congress directed both the U.S. Army Corps of Engineers and the weather bureau to conduct an intensified study of the causes, behavior and methods of forecasting these storms. A large fraction of the available funds are to be spent in studying methods of protection against inundations from the sea.

Thus, one can consider this as the beginning of systematic studies on the storm surges due to hurricanes on the east coast of the United States. First, some factual information will be considered before proceeding to models.

The number of people killed by hurricanes in the United States during 1900–72 is

TABLE 7.21. Representative examples of major coastal flooding along the United States coastline, 1683–1976, related to the near continuous occurrence of perigean spring tides coupled with strong, persistent onshore winds. (Based on Wood 1978)

Serial No.	Date of flooding	Location of flooding	Nearest perigee date and time	Nearest syzygy date and time
1	Mar. 22, 1683 or 1684, or Apr. 1, 1684	Boston, Cambridge, Charlestown, MA	Mar. 31, 1684 (01:00)	Mar. 30, 1684 (21:00)
2	Oct. 19, 1693	From Virginia settlements on the Delmarva peninsula to Long Island, NY	Oct. 29, 1693 (06:00)	Oct. 28, 1693 (23:00)
3	Jan. 15, 1704 or 1705, or Jan. 26, 1705	Boston, Salem, MA; Newport, RI	Jan. 25, 1705 (14:00)	Jan. 25, 1705 (00:00)
4	Feb. 24, 1722 or 1723, or Mar. 7, 1723	Boston, Dorchester, Chatham, Plymouth, Marblehead, Cape Cod, Salem, MA; Hampton, NJ; Falmouth, ME	Mar. 6, 1723 (13:00)	Mar. 6, 1723 (19:00)
5	Jan. 8, 1770	New England, especially near Boston	Jan. 10, 1770 (15:00)	Jan. 11, 1770 (12:00)
6	Dec.4–5, 1786	Boston, Nantucket, MA; New England	Dec. 4, 1786 (15:00)	Dec. 5, 1786 (08:00)
7	Mar. 1–2, 1802	Coast of Massachusetts	Mar. 2, 1802 (23:00)	Mar. 4, 1802 (00:00)
8	Mar. 26, 1803	Portland, ME; Portsmouth, NH; Newburyport, Gloucester, Beverly, Salem, Davensport, Lynn, Boston, Charleston, Cambridge, MA	Mar. 24, 1830 (20:00)	Mar. 24, 1830 (10:00)
9	Dec. 15, 1839	Boston, Newburyport, Plum Island, Salem, Marblehead, Cohasset, Plymouth, Cape Cod, MA	Dec. 18, 1839 (14:00)	Dec. 20, 1839 (21:00)
10	Mar. 1, 1846	Bodie's Island and Hatteras Banks, NC	Feb. 24, 1846 (09:00)	Feb. 25, 1846 (14:32)
11	Sept. 7–8, 1846	Bodie's Island, Hatteras Banks, NC; coastline along Pamplico Sound; Oregon Inlet	Sept. 4, 1846 (17:00)	Sept. 5, 1846 (08:00)
12	Apr. 14–16, 1851	Minot's lighthouse, Cohasset, Scituate Harbor, Dorchester, Deer Island, Shirley Cut, Winthrop, Pleasant Beach, Salem, Gloucester, Boston, MA; Newcastle, NH	Apr. 13, 1851 (13:00)	Apr. 15, 1851 (18:00)
13	Nov. 2, 1861	New Jersey coast between Jersey City and Newark, NJ, and northward to Boston, MA	Nov. 2, 1861 (12:00)	Nov. 2, 1861 (11:00)
14	Oct. 5, 1869	Northern Maine in the vicinity of Eastport	Oct. 5, 1869 (02:00)	Oct. 5, 1869 (09:00)
15	Nov. 1–2, 1877	North Atlantic coast	Nov. 1, 1877 (20:42)	Nov. 5, 1877 (03:48)
16	Oct. 23, 1878	New York City and Coney Island, NY; Brighton Beach, Long Branch, Sandy Hook, NJ; Chester, Greenpoint, Philadephia, PA	Oct. 25, 1878 (01:00)	Oct. 25, 1878 (18:00)
17	Sept. 28, 1882	Long Branch, Highland Beach,	Sept. 26, 1882	Sept. 27, 1882

TABLE 7.21. (*Continued*)

Serial No.	Date of flooding	Location of flooding	Nearest perigee date and time	Nearest syzygy date and time
		Sea Bright, Atlantic Highlands, Ashbury Park, NJ	(14:00)	(00:00)
18	Nov. 24, 1885	Boston, Revere, Winthrop, MA; Long Island, Rockaway Beach, Yonkers, Peekskill, NY; Ashbury Park, Atlantic City, Rahway, NJ	Nov. 25, 1885 (03:30)	Nov. 22, 1885 (16:30)
19	Oct. 13, 1981	Atlantic City, Long Branch, Ashbury Park, Sea Bright, Cape May, Sandy Hook, NJ	Oct. 16, 1891 (13:00)	Oct. 17, 1891 (09:00)
20	June 22, 1894	Cape Hatteras, NC	Jan. 20, 1894 (10:00)	Jan. 21, 1894 (10:00)
21	Feb. 8–9, 1895	Bangor, ME; Portsmouth, NH; Providence, Newport, RI; Gloucester, New Bedford, Cape Cod, Boston, MA; Sandy Hook, NJ; Staten Island, NY	Feb. 9, 1895 (08:00)	Feb. 9, 1895 (12:00)
22	Feb. 8, 1899	New York, NY	Feb. 9, 1899 (09:00)	Feb. 9, 1899 (04:00)
23	Aug. 17, 1899	Newport News, VA, and Virginia coast	Aug. 20, 1899 (17:00)	Aug. 21, 1899 (00:00)
24	Nov. 24, 1901	Ashbury Park, Jersey City, Sandy Hook, Sea Bright, Shrewsbury, NJ; Manhattan, Coney Island, NY; New Haven, Stamford, Greenwich, CT; Chatham, Provincetown, MA	Nov. 25, 1901 (11:00)	Nov. 25, 1901 (20:00)
25	Dec. 26, 1909	Boston, MA	Dec. 23, 1909 (03:48)	Dec. 26, 1909 (16:30)
26	Dec. 17–18, 1914	Long Beach, Balboa, Los Angeles, CA	Dec. 15, 1914 (09:12)	Dec. 16, 1914 (21:35)
27	Apr. 3, 1915	Virginia Beach, Cape Henry, VA; Cape Hatteras, NC	Apr. 1, 1915 (18:48)	Mar. 31, 1915 (00:38)
28	July 13, 1916	Charleston, SC	July 14, 1916 (19:00)	July 15, 1916 (00:00)
29	Apr. 10–12, 1918	Sea Bright, Atlantic City, NJ; Staten Island, Rockaway Beach, southern Long Island, NY	Apr. 10,1918 (05:00)	Apr. 11, 1918 (00:00)
30	Nov. 18, 1918	New York, NY	Nov. 16, 1918 (22:30)	Nov. 18, 1918 (02:33)
31	Nov. 7, 1919	Manhattan, Coney Island, NY	Nov. 8, 1919 (09:00)	Nov. 7, 1919 (19:00)
32	Jan. 11, 1922	Sea Bright, Clifton, Long Branch, NJ	Jan. 14, 1922 (18:48)	Jan. 13, 1922 (09:36)
33	Dec. 8, 1923	Southbend, Raymond, WA	Dec. 6, 1923 (22:00)	Dec. 7, 1923 (21:00)
34	Feb. 11–13, 1926	Los Angeles, Long Beach, San Diego, Capistrano Beach, Ventura, CA	Feb. 12, 1926 (07:00)	Feb. 12, 1926 (12:00)
35	June 28, 1926	Cape Hatteras, NC	June 28, 1926 (04:48)	June 25, 1926 (16:13)
36	Mar. 3–4, 1927	New England coast	Mar. 4, 1927	Mar. 3, 1927
37	Apr. 2, 1927	Atlantic City, NJ, and Delaware	Apr. 1, 1927	Apr. 1, 1927

TABLE 7.21. (*Continued*)

Serial No.	Date of flooding	Location of flooding	Nearest perigee date and time	Nearest syzygy date and time
38	Dec. 5, 1927	Atlantic City, NJ	Dec. 6, 1927 (20:00)	Dec. 8, 1927 (12:32)
39	Apr. 11–12, 1929	Coastal regions of New York and New Jersey	Apr. 12, 1929 (16:30)	Apr. 9, 1929 (15:33)
40	Nov. 18, 1929	Boston, Winthrop, MA	Nov. 19, 1929 (00:48)	Nov. 16, 1929 (19:14)
41	Aug. 23, 1930	From Block Island, NY, to Maine	Aug. 23, 1930 (15:00)	Aug. 23, 1930 (23:00)
42	Jan. 6, 1931	Boston, Cape Cod, Peaked Hill, MA; Hampton, NH	Jan. 6, 1931 (09:48)	Jan. 4, 1931 (08:15)
43	Jan. 6, 1931	Quinault Indian Reservation, Taholah, WA	Jan. 6, 1931 (09:48)	Jan. 4, 1931 (08:15)
44	Mar. 4–5, 1931	Boston, Salem, Winthrop, Revere, Gloucester, Newburyport, MA; Portsmouth, NH; Portland, ME; New Haven, Greenwich, CT; Atlantic City, Jersey City, Ventura, NJ; Rockaway, East Hampton, NY	Mar. 4, 1931 (05:00)	MAr. 4, 1931 (06:00)
45	Apr. 1, 1931	Boston, MA; Flushing, NY; Southhampton, Jersey City, Atlantic City, Long Branch, NJ	Apr. 1, 1931 (17:00)	Apr. 2, 1931 (15:00)
46	Nov. 2, 1932	New York, NY; coast of New Jersey	Oct. 9, 1932 (22:00)	Oct. 29, 1932 (10:00)
47	Nov. 30, 1932	Boston, Winthrop, Cape Cod, Nahant, MA; Hampton Beach, NH	Nov. 27, 1932 (10:00)	Nov. 27, 1932 (20:00)
48	Jan. 27–28, 1933	Atlantic City to Bar Harbor, ME	Jan. 22, 1933 (21:48)	Jan. 25, 1933 (18:20)
49	Apr. 2, 1933	Long Island, NY	Apr. 12, 1933 (06:12)	Apr. 10, 1933 (08:38)
50	Dec. 17, 1933	Aberdeen, Hoquiam, Cosmopolis, Montesano, WA	Dec. 17, 1933 (07:00)	Dec. 16, 1933 (22:00)
51	Aug. 20–22, 1934	Newport Beach, Malibu Beach, Laguna Beach, Balboa, CA	Aug. 23, 1934 (15:00)	Aug. 24, 1934 (15:00)
52	Dec. 8, 1934	Laguna Beach, Newport Beach, Santa Monica, CA	Dec. 8, 1934 (03:00)	Dec. 6, 1934 (12:25)
53	July 16, 1935	Oak Beach, Long Island, NY	July 17, 1935 (21:42)	July 16, 1935 (00:00)
54	Oct. 21–23, 1937	Boston, MA; New York, NY	Oct. 21, 1937 (11:00)	Oct. 19, 1937 (16:48)
55	June 3–5, 1939	Aberdeen, Hoquiam, Neskowin, WA; Marshfield, Astoria, Coos Bay, Seaside, Tillamook, Portland, Delake, OR; Long Beach, CA	Jan. 6, 1939 (06:00)	Jan. 5, 1939 (16:00)
56	Apr. 21, 1940	Boston (Deer Island), Cohasset (Minot's Light and Bassing's Island), Hull, Winthrop, Beachmont, Quincy, MA	Apr. 20, 1940 (14:00)	Apr. 21, 1940 (23:37)
57	Dec. 25–28, 1940	Southbend, Raymond, WA; Delake, Nelscott, OR; Los Angeles, San Pedro, Redondo Beach, Point Fermino, CA	Dec. 25, 1940 (01:00)	Dec. 28, 1940 (15:56)

TABLE 7.21. (*Continued*)

Serial No.	Date of flooding	Location of flooding	Nearest perigee date and time	Nearest syzygy date and time
58	Nov. 30–Dec. 1, 1944	New Bedford, Cape Cod, Chatham, Provincetown, MA; Long Island, NY; Jersey City, Sea Bright, NJ; Mt. Desert Island, ME	Nov. 26, 1944 (23:00)	Nov. 29, 1944 (19:52)
59	Nov. 20, 1945	Portland, Eastport, Machiasport, ME	Nov. 18, 1945 (21:00)	Nov. 19, 1945 (10:00)
60	Jan. 2, 1945	Boston, MA	Dec. 28, 1947 (18:00)	Dec. 27, 1947 (15:27)
61	Jan. 25–26, 1948	Vicinity of San Francisco, CA	Jan. 26, 1948 (06:00)	Jan. 26, 1948 (02:00)
62	Oct. 18, 1949	Long Branch, Sea Bright, NJ	Oct. 21, 1949 (10:00)	Oct. 21, 1949 (16:00)
63	July 17–18, 1951	Long Beach, CA	July 17, 1951 (18:00)	July 18, 1951 (14:00)
64	Dec. 3–4, 1951	San Francisco, Burlingame, CA; Duwamish River, WA	Nov. 30, 1951 (08:00)	Nov. 28, 1951 (20:00)
65	Dec. 29, 1951	San Francisco, San Rafael, CA	Dec. 28, 1951 (18:00)	Dec. 28, 1951 (07:00)
66	Oct. 22–24, 1953	Manhattan, Brooklyn, New Rochelle, NY; Stamford, CT; Boston, MA	Oct. 21, 1953 (11:00)	Oct. 22, 1953 (08:00)
67	Jan.7–8, 1959	Along Hampton Roads and the eastern Piedmont and tidewater portions of Virginia, southern Rhode Island; Cape Cod and coastal Massachusetts and New Hampshire; Wells Beach, ME	Jan. 8, 1958 (19:00)	Jan. 5, 1958 (15:09)
68	Feb. 3–4, 1958	South San Diego Bay, Imperial Beach, Santa Paula, Long Beach, Alamitos Bay peninsula, Santa Monica, Sea Bright, CA	Feb. 5, 1958 (18:00)	Feb. 4, 1958 (03:05)
69	Apr. 1–2, 1958	Boston, Nantucket, Winthrop, Chatham, Lynn, Revere, MA; Portsmouth, NH	Apr. 3, 1958 (15:00)	Apr. 3, 1958 (23:00)
70	Dec. 29, 1959	Atlantic City, NJ; Long Island, NY; Cape Cod, Gloucester, Rockland, Biddeford, MA; Kennebunkport, ME; Rye, NH	Dec. 28, 1959 (20:00)	Dec. 29, 1959 (14:00)
71	Dec. 30, 1959	San Francisco Bay area	Dec. 28, 1959 (20:00)	Dec. 29, 1959 (14:00)
72	Jan. 15, 1961	Atlantic City, Ocean City, NJ; Delaware. A tower was destroyed offshore of New York City in water of depth 18 ft	Jan. 16, 1961 (18:00)	Jan. 16, 1961 (17:00)
73	Jan. 15, 1961	San Buenventura State Park, Ventura County, CA	Jan. 16, 1961 (18:00)	Jan. 16, 1961 (17:00)
74	Mar. 6–7, 1962	Along entire Atlantic coast from South Portland, ME, to South Carolina	Mar. 6, 1962 (04:00)	Mar. 6, 1962 (05:00)
75	Oct. 13, 1962	Local estuaries and bay locations of Washington (e.g. Union); Oregon (e.g. Coos Bay);	Oct. 12, 1962 (23:00)	Oct. 13, 1962 (08:00)

TABLE 7.21. *(Concluded)*

Serial No.	Date of flooding	Location of flooding	Nearest perigee date and time	Nearest syzygy date and time
		northern California (e.g. Humboldt Bay); central California (e.g. Pacifia and Redwood drainage areas)		
76	Nov. 10–14, 1962	Cape May to Sandy Hook, NJ; coastal erosion from Fire Island to Montauk Point (Long Island); New York City; Bridgeport, CT; Nantucket Island, MA; coastal lowlands, ME	Nov. 10, 1962 (09:00)	Nov. 11, 1962 (17:04)
77	Sept. 26, 1965	Capistrano Beach, CA	Sept. 22, 1965 (18:00)	Sept. 24, 1965 (22:18)
78	Apr. 27, 1967	Atlantic City, NJ	Apr. 23, 1967 (14:00)	Apr. 24, 1967 (07:00)
79	Nov. 28–Dec. 3, 1967	Coasts of Massachusetts and and southern New England	Nov. 30, 1967 (09:00)	Dec. 1, 1967 (11:10)
80	Dec. 4–14, 1969	Rincon Point, Ventura, Ocean Beach, Oceanside, Carlsbad, Del Mar, CA	Dec. 10, 1969 (06:00)	Dec. 9, 1969 (04:43)
81	Mar. 5–6, 1970	Capistrano Beach, Newport Beach, CA	Mar. 6, 1970 (05:00)	Mar. 7, 1970 (12:43)
82	Mar. 26, 1971	Virginia Beach, Norfolk, Portsmouth, VA	Mar. 26, 1971 (04:00)	Mar. 26, 1971 (14:00)
83	Apr. 22, 1971	Oxnard Shores, CA	Apr. 23, 1971 (13:00)	Apr. 24, 1971 (23:02)
84	Dec. 3, 1971	Winyah Bay, Georgetown, Pawleys Island, SC	Nov. 30, 1971 (06:00)	Dec. 2, 1971 (02:49)
85	Feb. 18–20, 1972	Along Hampton Roads, VA, to Stamford, CT; Old Orchard Beach, Kennebunkport, Portland, ME	Feb. 17, 1972 (14:00)	Feb. 14, 1972 (19:29)
86	Nov. 20, 1972	Rincon to Oxnard, Oxnard Shores, Hollywood-by-the-sea, CA; also on Nov. 25–26 coastal beaches of Oregon and Washington; Gulf of Mexico	Nov. 20, 1972 (19:00)	Nov. 20, 1972 (18:00)
87	Dec. 11, 1963	Tokeland, Raymond, Southbend, WA; Seaside, Astoria, Newport, OR	Dec. 10, 1973 (18:00)	Dec. 9, 1973 (21:00)
88	Jan. 8, 1974	Santa Barbara, Santa Monica, San Clemente, Newport Beach, Capistrano Beach, Malibu Beach, CA	Jan. 8, 1974 (06:00)	Jan. 8, 1974 (08:00)
89	Mar. 16–17, 1976	Ogunquit, Cranberry Island, Poplam Beach, Saco, Kennebunkport, ME; Newcastle, Rye, Hampton Beach, Portsmouth, NH; Marblehead, Princeton, Plum Island, MA	Mar. 16, 1976 (14:00)	Mar. 15, 1976 (22:00)

listed in Table 1.1. General information on hurricanes is given in Chapter 6. The statistical probability of hurricane strike and storm surge occurrence will be considered at the end of section 7.2.

Wiegel (1964) stated that during the period 1900–55 there were more than 11 750 deaths caused by hurricanes in the United States. The worst storm surge (from the point of view of loss of life) in United States history occurred in September 1900 when more than 6000 people drowned, most of them at Galveston, Texas (Price 1956). During the 14-yr period 1940–53, the loss of life due to hurricane-generated surges over the globe was 3744; 590 of those deaths occurred in the United States (Wiegel 1964).

Dunn (1958) mentioned the years and locations of some of the greatest storm surges on the east coast of the United States: Galveston (1900 and 1915), Tampa Bay (1921), Miami (1926), Palm Beach and Lake Okeechobee (1928, 1949), Florida Keys (1935), and New England, particularly Narragansett Bay (1938, 1954). The maximum storm surge from these was about 12.5 ft (3.8 m) above mean low water.

Dunn (1958, p. 27) compared the storm surge heights along the east coast of the United States and the coast of the Gulf of Mexico and stated:

> Of the 24 best documented storm tides along the coast of the Gulf of Mexico, the maximum storm tide heights averaged 10.3 feet with a range beween 5 and 15 feet. The average maximum reported height of 14 fairly well documented storm tides of the Atlantic coast was 9.7 feet with a range between 3 and 15.5 feet. This group does not include some entering the Florida peninsula where the average height of 15 major storm tides between 1900 and 1955 was 9.8 feet, MSL. The number of documented storm tides is not great enough to attach much significance to the differences between the averages for the various sections given above but because of the predominately shallow coastal waters of the Gulf of Mexico and the concavity of the coastline, a higher average might be expected there. Very high storm tides will occur at the heads of bays and estuaries, particularly when the storm center moves inland on a course at an angle of 90° or less to the coast line (right quadrant).

Harris (1956) and Dunn (1958) mentioned forerunners to storm surges and also resurgences. Redfield and Miller (1957) studied these phenomena in detail and these will be considered now. Also, these authors provided a review of the literature up to 1957; some pertinent information will be extracted.

Between 1635 and 1938 there were at least six major hurricanes on the coast of New England (Tannehill 1950) and between 1938 and 1957 there were at least another six. Since 1874 at least 40 hurricanes passed within 200 nautical miles (370 km) of Rhode Island. Namias (1955) analyzed the tracks of hurricanes and showed that the region most frequently traversed during 1935–55 near the Gulf of Maine was at 40°N, 65°W. One important point made by Redfield and Miller (1957) is that although more than three quarters of the deaths due to hurricanes are caused by the storm surge, until the mid-1950's little attention was paid to the water level problem and all the consideration was given to the meteorological problem.

The data base for the study by Redfield and Miller (1957) is the following: (1) September 21, 1938, (2) September 14–15, 1944, (3) August 31, 1954 (Carol), (4) September 11, 1954 (Edna), (5) October 15–16, 1954 (Hazel). The tracks of these hurricanes are shown in Fig. 7.33. The three phenomena studied were forerunners, hurricane surge, and resurgences.

A forerunner is the gradual rise in sea level along the coast that precedes the arrival of the hurricane, and which may occur while the storm center is at a great distance from the coast regardless of whether or not it reaches the point of observation. The hurricane surge is the sudden and substantial rise in water level that accompanies the violent winds

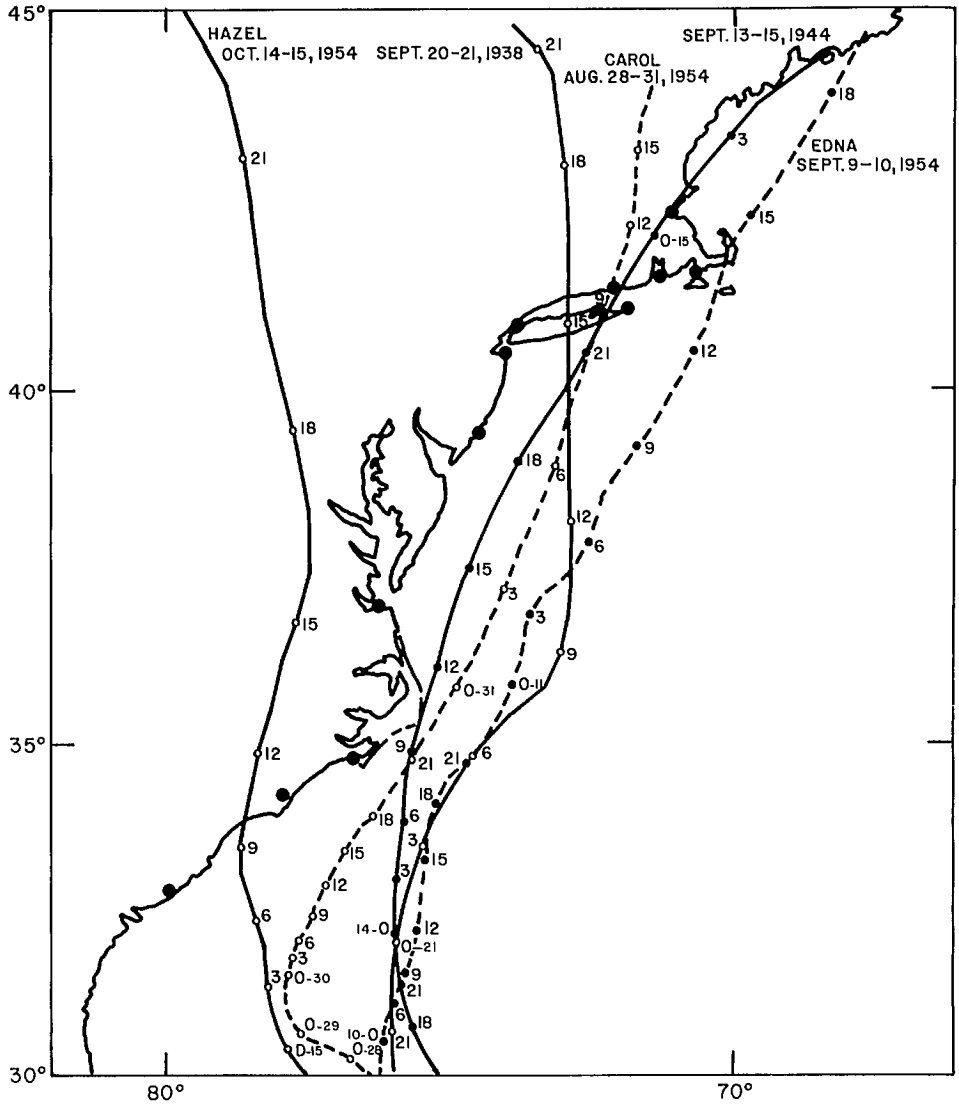

FIG. 7.33. Tracks of some of the hurricanes that affected the New England States. Solid circles show the locations of the tide gauges. Circles on the tracks represent the hours (GMT) and the small numbers denote the dates. (Redfield and Miller 1957)

of the storm. Resurgences include a number of phenomena that occur after the passage of a storm center. They may be attributed in general to the free motion of water in returning to the normal level but are augmented in some cases by wind blowing in a changing direction.

Cline (1920, 1926, 1933) noticed forerunners in the Gulf of Mexico and called attention to their importance in the prediction of the storm arrival. The sea level began to rise (above the predicted tide) 1 or 2 d before the arrival of the storm. Elevations of several

TABLE 7.22. Relation of duration of surge to size and speed of storm. (Redfield and Miller 1957)

Storm	Time (h) half level preceded maximum level	Speed at coast ($km \cdot h^{-1}$)	Diameter of 980-mb isobar (km)	Time (h) pressure <980 mb
1938	1.0–1.5	96	270	3.2
1944	2.1–2.2	67	241	4.2
1954 (Carol)	1.1–1.3	74	183	2.9
1954 (Edna)	2.0–2.3	63	261	4.8
1954 (Hazel)	3.0–5.0	46	261	6.5

feet were noticed before the rapid rise due to the storm surge itself. Cline explained the forerunners as being due to transport of water by the swell that arrives in advance of the hurricanes.

Observations showed that if the tide gauge was within 50 nautical miles (93 km) to the left (in the Northern Hemisphere) of the storm track, or 100 nautical miles (185 km) to its right, the rate of rise of the water level increased to more than 1 $ft \cdot h^{-1}$ beginning 3 or 4 h before the passage of the center. (This rapid rise is the surge whereas the slow gradual rise before this is the forerunner.)

Examples of forerunners can be found in the storm surge records at Atlantic City and Sandy Hook. At Atlantic City during Hurricane Carol of September 1954, the water level began to increase even before the storm passed Cape Hatteras (260 nautical miles or 481 km to the south). This rise continued for 8–12 h at which time the storm center passed over Atlantic City and the wind shifted. Then the water level dropped abruptly and this was followed by resurgences. The hurricane of September 14–15, 1944, traveled close to the coast and the forerunner was not significant. Redfield and Miller (1957) discounted the fall in barometric pressure as the cause of the forerunners. They cited wind as the main agent responsible. The fact that the water levels decreased abruptly when the wind shifted is another piece of evidence, according to them.

After the storm surge itself, on the outer coast, surges up to 8–9 ft (2.4–2.7 m) occurred. At Long Island, and along the coasts of Rhode Island and Massachusetts, water level deviations up to 18 ft (5.5 m) occurred (but part of this was wind-generated waves). However, in Buzzards Bay, Narragansett Bay, Long Island Sound, etc., surges up to 15 ft (4.6 m) have occurred many times. These authors introduced the term "half-level time" to define the time required to develop from one half the maximum to the maximum water level achieved. For hurricanes crossing the coast of New England this time varied from 1.25 to more than 2 h (Table 7.22). This half-level time that defines the sharpness of the surge varies in proportion with the storm speed at the time the storm crosses the coast, as can be seen from Table 7.22. This table also lists the size of the storm as typified by the diameter of the 980-mb isobar and the time during which the pressure was less than 980 mb. This time is roughly twice the half-level time.

The storm surge amplitude (meters) along the ordinate versus distance (nautical miles) from the storm center along the abcissa is given in Fig. 7.34. It can be seen that maximum water levels occurred some 50–70 nautical miles (93–130 km) to the right of

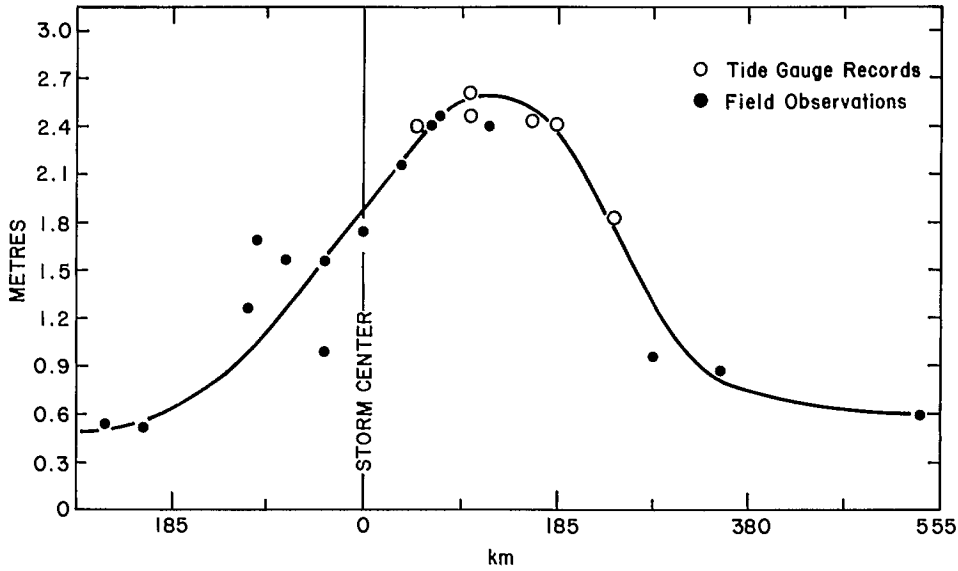

FIG. 7.34. Storm surge amplitude (ordinate) versus distance from storm centre (abcissa). (Redfield and Miller 1957)

the storm center. However, Redfield and Miller (1957) pointed out that the highest water levels following Hurricane Hazel of 1954 occurred close to the storm center, and 40 nautical miles (74 km) to the right they were small. Hubert and Clark (1955) mentioned that for the coast of the Gulf of Mexico the maximum water levels occurred close to the storm center or slightly to its right.

The time of occurrence of the maximum surges with reference to the passage of the storm center differed from one storm to another and from one location to another. If the storm center passed close to a tide gauge, usually, maximum surges occurred within 1 h before or after the storm passage. The differences in the time of occurrence of the maximum surges can be explained by differences in the exposure of the gauges and also by the fact that the wind and pressure centers of a hurricane need not coincide (Myers 1954).

The maximum surges on the southern New England Coast and their times of occurrence following the hurricane of September 21, 1938, are shown in Fig. 7.35 and 7.36, respectively. Similar information for Hurricane Carol of August 31, 1954, is given in Fig. 7.37 and 7.38. Large surges on the coast of southern New England might to some extent be accounted for by the presence of a wide and shallow shelf. This topographic effect is most noticeable between Montauk Point (at the eastern tip of Long Island) and Martha's Vineyard. However, greatest surges and most property damage occurred on the Narragansett Bay coast. Extreme surges up to 13 ft (4 m) were noted at Providence, Rhode Island, in water of depth less than 20 ft (6.1 m).

According to Redfield and Miller (1957), Providence is among the most frequently flooded (due to surges) in the United States. Surges up to 11 ft (3.4 m) were observed in 1944 (but little damage occurred because the maximum surge coincided with low tide); 15-ft (4.6 m) surges were recorded on August 31, 1954, and there was evidence of 12- to 14-ft (3.7–4.3 m) surges in 1815. In Buzzards Bay, surges of 13 ft (4 m) occurred

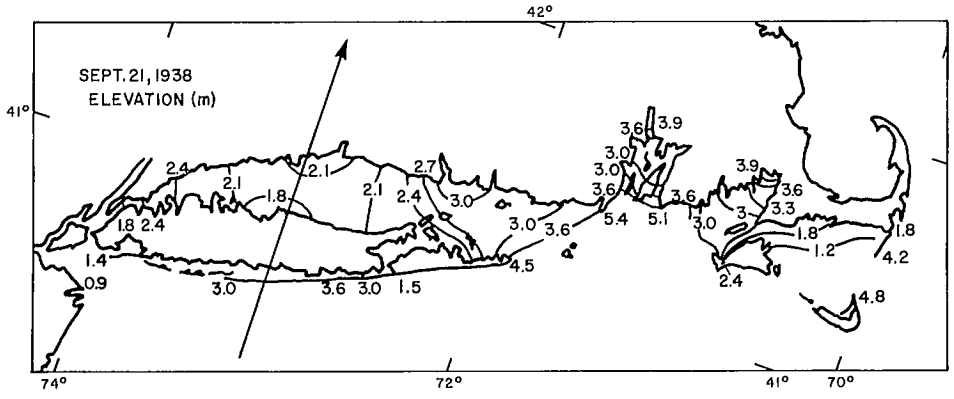

FIG. 7.35. Storm surge heights (metres) on the coast of the southern New England States. The arrow shows the track of the storm of September 21, 1938, that caused this surge. (Redfield and Miller 1957)

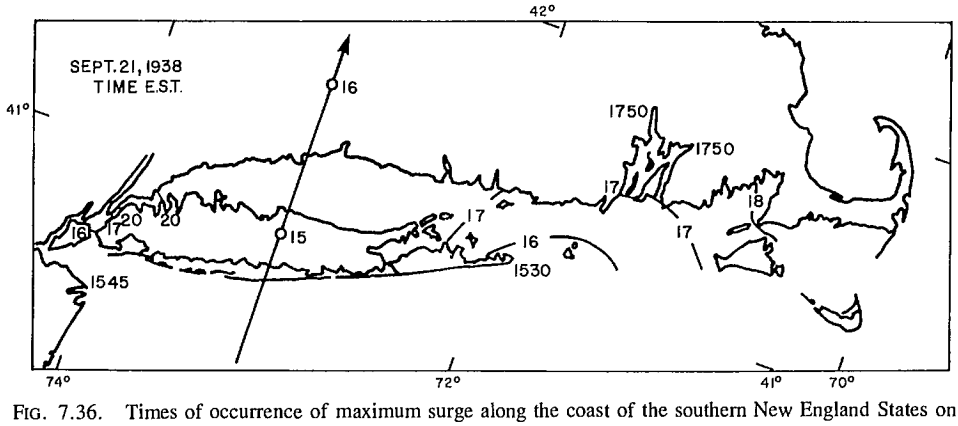

FIG. 7.36. Times of occurrence of maximum surge along the coast of the southern New England States on September 21, 1938. (Redfield and Miller 1957)

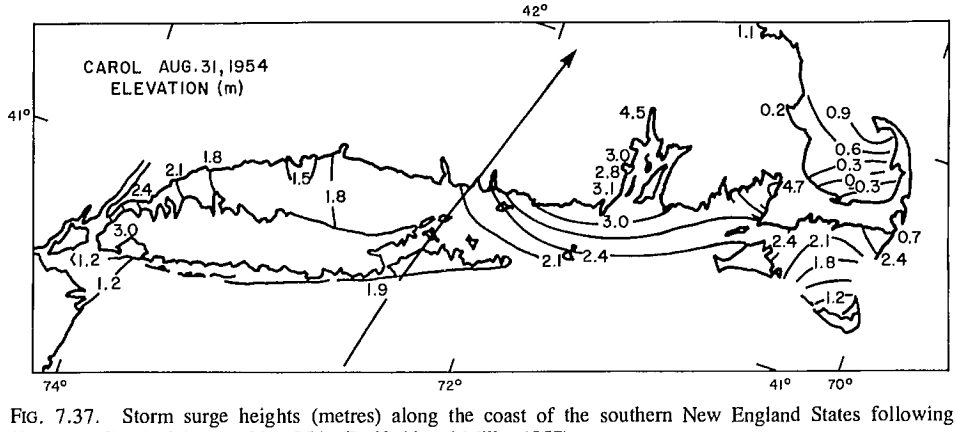

FIG. 7.37. Storm surge heights (metres) along the coast of the southern New England States following Hurricane Carol of August 31, 1954. (Redfield and Miller 1957)

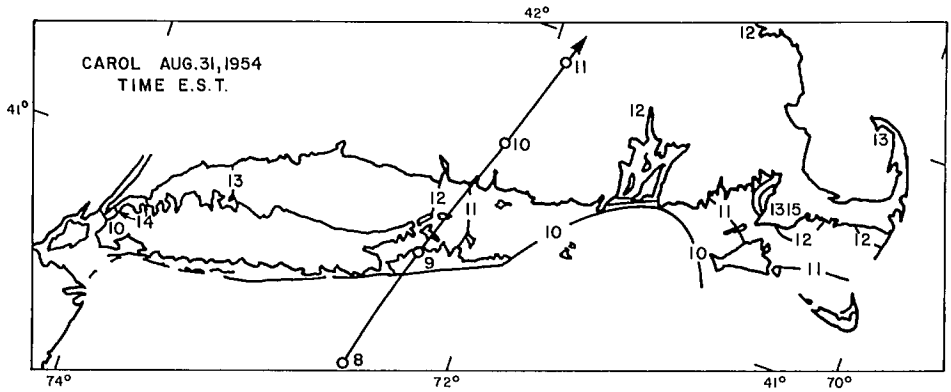

FIG. 7.38. Times of occurrence of maximum surge along the coast of the southern New England States following Hurricane Carol of August 31, 1954. The arrow shows the hurricane track. (Redfield and Miller 1957)

in 1938 and 15-ft (4.6 m) surges were recorded following Hurricane Carol in 1954. A diary entry by Governor Bradford in 1635 (Morison 1952) describes a 20-ft (6.1 m) surge on August 14−15 of that year. There is evidence of negative surges of 1−3 ft (0.3−0.9 m) in Cape Cod Bay and Nantucket Sound. Surges up to 4 ft (1.2 m) were noted at Boston and Portland. North of Cape Cod the amplitudes of surges become small and amount to about 1 ft at Eastport (Maine).

Redfield and Miller (1957) paid particular attention to the resurgences, which are basically free oscillations of the water in trying to return to its normal level. Following Hurricane Carol of August 31, 1954, the damage at the Cape Cod area was a result of the resurgence. In Buzzards Bay, although the main surge had an amplitude of about 12 ft (3.7 m) along the western shore, resurgences with amplitudes up to 15 ft (4.6 m) occurred on the eastern shore. The resurgence following a 1938 hurricane in Buzzards Bay caused great damage and loss of life at Woodshole. In Long Island Sound, resurgences occurred following the hurricanes of September 21, 1938, and August 31, 1954. Tide gauges at Atlantic City and Sandy Hook showed prominent resurgences (Fig. 7.39). After the original surge reaches a maximum, the water level drops abruptly to low values and then increases again in a series of undulations with periods of several hours. These resurgence periods are about 5.5 h at Atlantic City and 7.2 h at Sandy Hook. The attenuation rate of the resurgences at Sandy Hook is about $0.07 \cdot h^{-1}$. Munk et al. (1956) explained these resurgences as due to edge waves.

Storm surges on the east coast of the United States also occur as a result of extratropical cyclones. Some differences between storm surges due to tropical and extratropical storms on the east coast of the United States are listed in Table 7.23.

Some models that were developed with the aim of hindcasting and eventually predicting storm surges will now be considered. The so-called bathystrophic storm surge (Freeman et al. 1957) was discussed earlier. Pararas-Carayannis (1975) used this approach to hindcast surges on the east coast and Gulf of Mexico coast of the United States. The observed and computed surges at three locations are compared in Fig. 7.40. Pararas-Carayannis (1975) simulated surges due to the hurricanes listed in Table 7.24. Pertinent meteorological information is also listed in this table, which is used in the above calculations

Kajiura (1959) examined analytically, as well as empirically, hurricane-generated

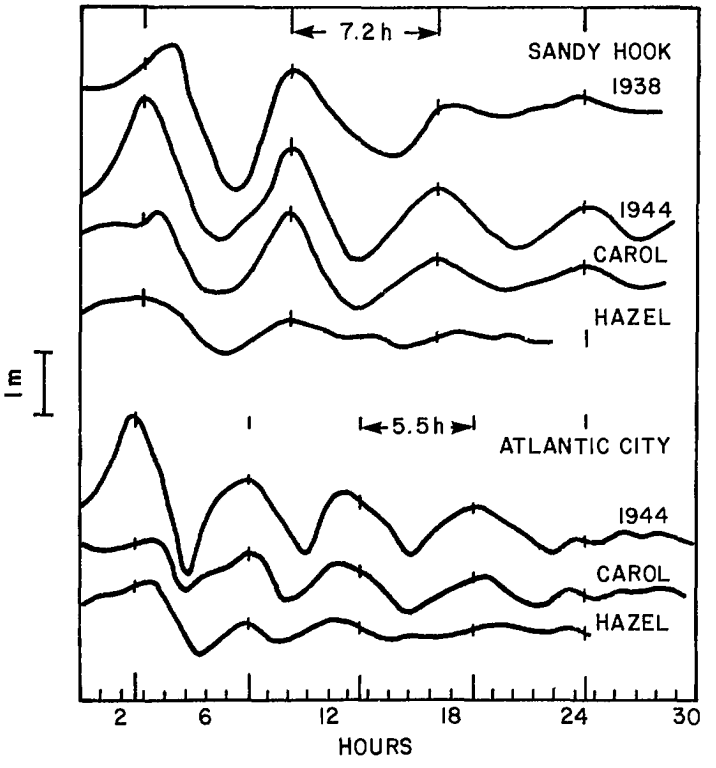

FIG. 7.39. Comparison of resurgences following the passage of several storms at Sandy Hook and Atlantic City. The times were adjusted (for each station) so that the time of occurrence of the first resurgence for the different storms coincide. Vertical ticks denote time separation of 7.2 h for Sandy Hook and 5.5 h for Atlantic City. Ordinate: water level (metres); abcissa: duration of surge (hours). (Redfield and Miller 1957)

surges on continental shelves. Using dimensional analysis he showed that the surge is determined by the following two dimensionless ratios: V/c and L_2/L_1 where V is the speed of movement of the storm, c is the speed of long gravity waves on the shelf, L_2 is the scale of the storm, and L_1 is the width of the shelf. It was shown that for storm scales comparable with or greater than the scale of the shelf, the dynamic response of the water level is significantly influenced by the natural modes of oscillation on the shelf (the dynamic amplification for a one-dimensional case is between 1 and 2). The free oscillations again become important when one considers the transient aspects. Coriolis force becomes relevant if the scale of the disturbance is significant relative to c/f, where f is the Coriolis parameter. When the scale of the shelf is comparable with the scale of the storm, the two-dimensional aspects of hurricanes must be considered.

Other important results from Kujiura's (1959) study are the following. If the storm moves perpendicular to the coastline from the sea, then the maximum surge always occurs a little later than the time of the nearest approach of the storm center to the water level station. For any other type of track, the maximum surge can occur either before or after the storm center approaches nearest to the observing station. When the storm moves inland from the sea, the maximum surge is found to the right of the track. The dynamic

TABLE 7.23. Differences between hurricane-generated and extratropical storm generated surges.

Parameter	Tropical system	Extratropical system
Size of storm	Small	Large
Representation on weather charts	Sometimes difficult to position on weather charts using ordinary weather reports. The vigorous portion of the storm may lie between two observing stations	Easier
Requirement of specialized observations such as satellite, weather reconnaissance, radar, aircraft	Needed	Usually not required. Standard weather reports usually adequate unless mesoscale systems are embedded
Amplitude of surges	Greater. The maximum surge generated in the United States was at Gulfport, MS, following Hurricane Camille in August 1969: 7.5 m	Smaller surges of amplitudes up to 5 m can occur infrequently
Duration of surge	Short (several hours to $\frac{1}{2}$ d)	Long (usually 2–5 d). Severe erosion of coastline can occur
Inland inundation	Large	Little
Length of coastline affected by the surge	Less (usually <160 km)	Several hundred kilometres
Geometry of the storm	Compact and nearly symmetrical	Ill-defined and sprawling geometry
Speed of movement of the storm	Variable	Slow motion generally along a regular track
Pressure gradients and wind stress associated with the storm	Easy to model the driving forces. Could be represented analytically	Difficult to model the driving fields

amplification of the surge is maximum when the track is parallel to the coast and the amplification depends on the duration of the storm as well as V/c.

Actual data of hurricane-generated surges along the Atlantic coast showed that significant surges (up to one third of the maximum surge) occur within 70 nautical miles (130 km) to the left and 110 nautical miles (204 km) to the right of the storm track. The maximum surge usually occurs about 25 nautical miles (46 km) to the right of the track. Unless the storm center is very close to the station, usually the water levels are greater south of Sandy Hook than on the New England coast.

ANALYTICAL–EMPIRICAL MODEL FOR STORM SURGE AMPLIFICATION ON A CONTINENTAL SHELF

Following Kajiura (1959) some simple formulae will be developed to calculate amplification of storm surges on a continental shelf due to resonance, and the results will be applied to actual situations on the east coast of the United States. Kajiura wrote the vertically integrated form of the equation of motion in a vectorial form as follows:

$$\frac{\partial \bar{V}}{\partial t} + g\nabla(\zeta - \zeta^*) + \bar{K} \times (f\bar{V}) = \frac{1}{h}(\bar{\tau}_s - \bar{\tau}_b) \tag{7.6}$$

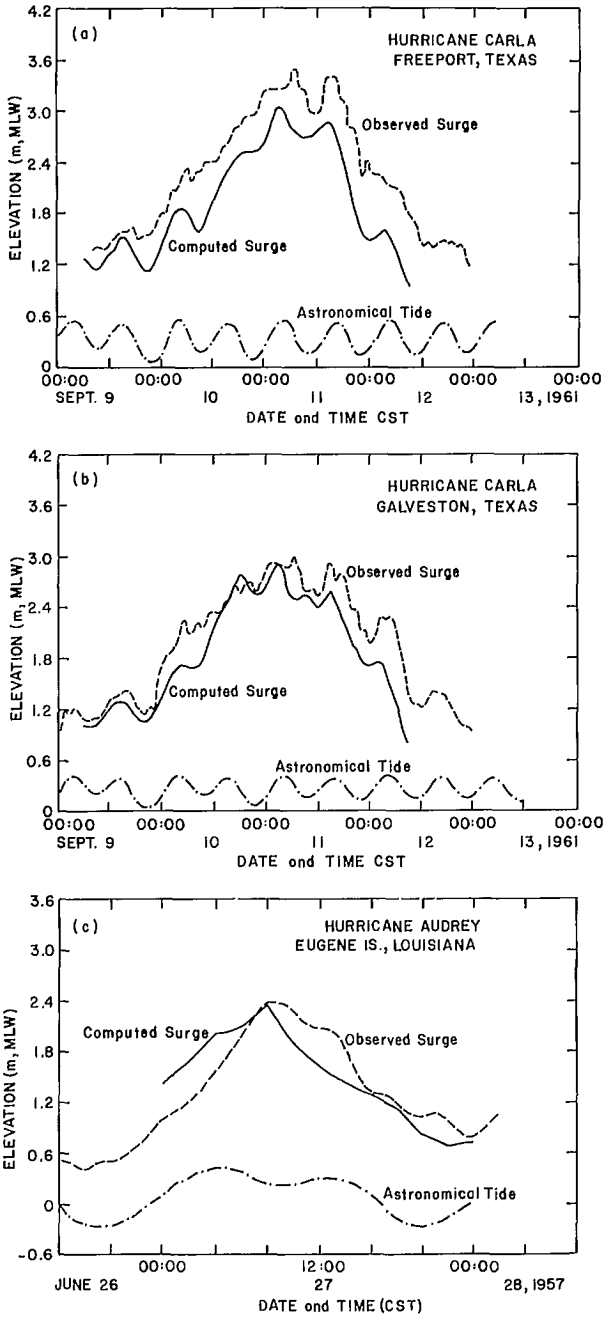

FIG. 7.40. Computed surge (using bathystrophic approach), observed surge, and tide due to (a) Hurricane Carla at Freeport, Texas, (b) Hurricane Carla at Galveston, Texas, and (c) Hurricane Audrey at Eugene Island, Louisiana. (Pararas-Carayannis 1975)

TABLE 7.24. Hurricane parameters in the bathystrophic storm surge study. (Pararas-Carayannis 1975)

Hurricane	Central pressure (mb)	Peripheral pressure (mb)	Radius of maximum winds (km)	Speed of movement ($km \cdot h^{-1}$)	Maximum gradient wind speed ($km \cdot h^{-1}$)
Hurricane of Oct. 3–4, 1949	963.4	1014.2	27.8	20.4	141.6
Carol of Aug. 30–31, 1954	971.6	1013.2	46.3	61.7	152.9
Audrey of June 26–27, 1957	946.5	1005.8	35.2	24.1	152.9
Carla of Sept. 7–12, 1961	936.0	1013.2	85.2	5.6	160.9
Camille of Aug. 15–16, 1969	905.2	1013.2	25.9	24.1	201.2

where $\bar{V}$ is the horizontal velocity vector, $\bar{K}$ is the vertical unit vector, f is the Coriolis parameter, h is the water depth, ζ is the water level deviation, and ζ^* is the atmospheric pressure deficit expressed as water level. The continuity equation is

$$\nabla \cdot (h\bar{V}) = -\frac{\partial \zeta}{\partial t} \tag{7.7}$$

The wind stress $\bar{\tau}_S$ is given by

$$\rho \bar{\tau}_S = K\rho' |U| \bar{U} \tag{7.8}$$

where ρ' is air density, $\bar{U}$ is the wind velocity at 10 m of height, and K is a numerical coefficient that depends on air stability and wind velocity. For the bottom stress $\bar{\tau}_b$ the following linear form is used:

$$\rho \bar{\tau}_b = \rho r \bar{V} \tag{7.9}$$

where r is a friction coefficient with a value of about 0.2 $cm \cdot s^{-1}$ in shallow water.

Taking the y-axis parallel to the coast and the x-axis pointing towards the sea, the boundary condition at the coast is

$$hV_x = 0 \text{ at } x = 0 \tag{7.10}$$

where V_x is the x component of $\bar{V}$. This condition can be written in terms of ζ as

$$\frac{\partial^2}{\partial t \partial x}(\zeta - \zeta^*) + f \frac{\partial}{\partial y}(\zeta - \zeta^*) = \frac{1}{c^2}\left(\frac{\partial \tau_x}{\partial t} + f\tau_y\right) \text{ at } x = 0 \tag{7.11}$$

where $c^2 = gh$ and τ_x and τ_y are the x and y components of $\bar{\tau}_S$. It can be seen from eq. 7.10 that the slope of the water level perpendicular to the coast is related to the integral effect of the longshore wind in contrast with the effect of the on- and off-shore wind, which is instantaneous.

If $x = L$ represents the edge of the shelf and assuming that the water depth is ∞ beyond this edge, then the condition at $x = L$ is

$$\zeta - \zeta^* = 0 \text{ at } x = L \tag{7.12}$$

However, this is not a very realistic condition. On the other hand, one can assume a semi-infinite sea and assume that the waves are divergent at large distances from the source.

The above equations can be nondimensionalized through the following scheme:

$$\begin{aligned} x &= Lx' & \zeta &= T\frac{L}{gH}\zeta' \\ y &= Ly' & \bar{V} &= \frac{T}{H}\frac{L}{V}\bar{V}' \\ h &= Hh' & \alpha &= \frac{fL}{V} \\ t &= \frac{L}{V}t' & \beta &= \frac{r}{H}\frac{L}{V} \\ \bar{\tau} &= T\tau' & \gamma &= \frac{V^2}{gH} \end{aligned} \tag{7.13}$$

Parameters L_1 and L_2 are the scales of the continental shelf and the storm, respectively, which are appropriate for the free and forced waves. The representative velocities would be

$$V_1 = c \text{ and } V_2 = V \tag{7.14}$$

where V is the speed of movement of the storm.

To understand the relative roles played by inertia terms, Coriolis terms, and friction, define

$$\begin{aligned} \alpha_1 &\equiv \frac{fL_1}{c} \\ \alpha_2 &\equiv \frac{fL_2}{c} \\ \beta_1 &\equiv \frac{r}{H}\frac{L_1}{c} \\ \beta_2 &\equiv \frac{r}{H}\frac{L_2}{V} \end{aligned} \tag{7.15}$$

Further, define

$$\frac{f}{c} \equiv \mathcal{K} \tag{7.16}$$

The scale defined by $\mathcal{K}^{-1}$ is important in determining the influence of the Coriolis term, which is obvious from earlier discussion.

An examination of the terms α_2 and β_2 shows that for a rapidly moving small-scale storm, Coriolis terms as well as frictional terms are not important. On the other hand, for a slowly moving storm both are important and should be included. For free and forced waves

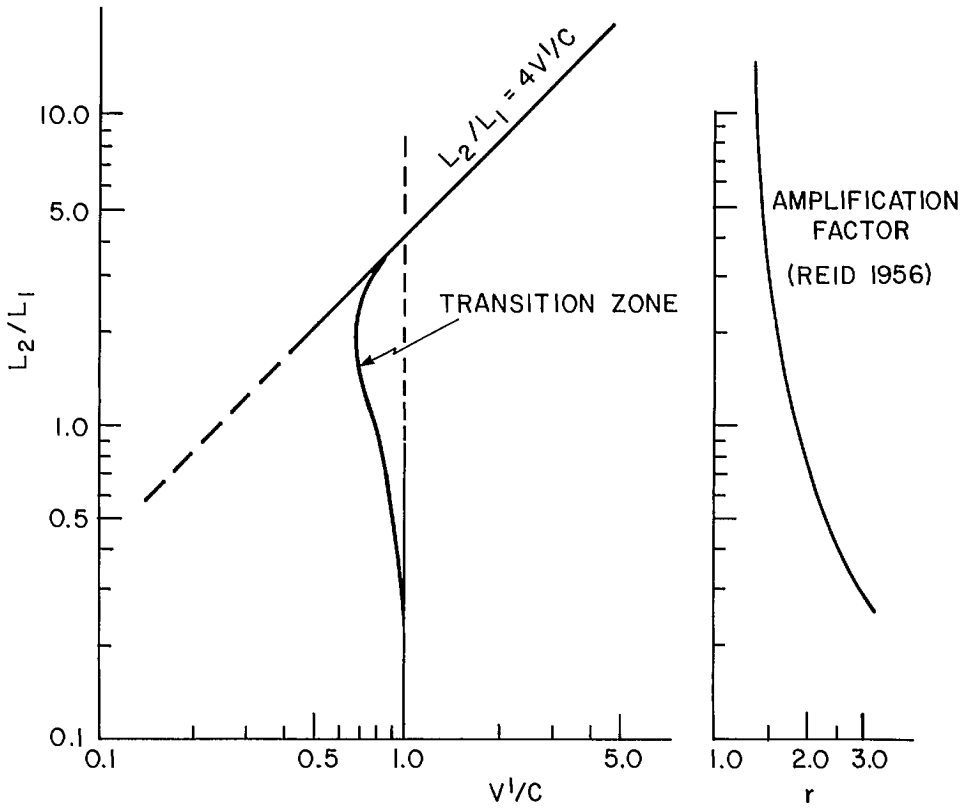

FIG. 7.41. Maximum response of water level at the coast using a one-dimensional model. L_1, width of the shelf; L_2, scale of the storm; $C = \sqrt{gH}$ (g = gravity; H = water depth); V', speed of the storm centre; r, amplification factor. (Kajiura 1959)

$$\gamma_1 = 1 \text{ and } \gamma_2 = \frac{V^2}{c^2} \tag{7.17}$$

Here, γ_2 is related to the dynamic amplification of the forced waves in the ocean. The maximum amplification due to resonance will occur for

$$\frac{L_2}{V} = \frac{4L_1}{c} \tag{7.18}$$

which is the period of the fundamental shelf oscillation. Hence, for this case

$$\gamma_2 = \frac{V^2}{c^2} = \left(\frac{L_2}{4L_1}\right)^2 \tag{7.19}$$

For small values of L_2/L_1, the maximum amplification occurs for $\gamma_2 = 1$, and for large values of L_2/L_1 the maximum amplification can be calculated from eq. 7.19. The maximum response of the water level at the coast as a function of L_2/L_1 is shown in Fig. 7.41. The curve for the amplification factor shown on the right side is taken from Reid (1956). It can be seen that for the one-dimensional case the amplification is between 1.5 and 2 for realistic L_1 and L_2. For the two-dimensional case, the amplification will be somewhat less.

Next, following Kajiura (1959), consider a slowly moving large-scale cyclonic system. Then, the wind field can be assumed to be spatially uniform and commences at $t = 0$. The following form of the wind stress was taken:

$$\left.\begin{aligned} \tau_x &= -\frac{T}{2}\sin(\omega t) \\ \tau_y &= -\frac{T}{2}(1-\cos\omega t) \end{aligned}\right\} \quad \text{for } t \geq 0 \tag{7.20}$$

Initially the water is at rest. Hence

$$\zeta = \frac{\partial \zeta}{\partial t} = 0 \text{ at } t = 0 \tag{7.21}$$

At the coast ($x = 0$) the surge is given by (see Kajiura 1959 for details)

$$\zeta = -\frac{T}{2}\frac{L}{c^2}\left\{(-ft)\frac{\tanh(\mathcal{K}L)}{(\mathcal{K}L)} + \frac{2}{L^2}\sum_{n=1}^{\infty}\frac{f}{\nu_n}\frac{\sin(\nu_n t)}{(\mathcal{K}_n^2+\mathcal{K}^2)} + \left(1-\frac{f}{\omega}\right)\left[-\frac{\tan(\mathcal{K}'L)}{(\mathcal{K}'L)}\sin(\omega t) + \frac{2}{L^2}\sum_{n=1}^{\infty}\frac{\omega}{\nu_n}\frac{\sin(\nu_n t)}{(\mathcal{K}_n^2-\mathcal{K}'^2)}\right]\right\} \tag{7.22}$$

with

$$\mathcal{K}_n = \left(n-\frac{1}{2}\right)\frac{\pi}{L}, \qquad n = 1, 2, 3, \ldots$$

and

$$\begin{aligned} \nu_n^2 &= c^2(\mathcal{K}^2+\mathcal{K}_n^2) \\ \mathcal{K}'^2 &= (\omega^2 - f^2)/c^2 \end{aligned} \tag{7.23}$$

taking

$$c = 20 \text{ m}\cdot\text{s}^{-1}$$

$$f = 10^{-4}\cdot\text{s}^{-1}$$

$$L = 140 \text{ km}$$

$$\frac{\omega}{\nu_1} = 0.9,\ 0.6, \text{ and } 0.3$$

Here, ν_1 is the frequency of the fundamental mode of shelf oscillation. If the wind field changes rapidly, the contribution from the free oscillations is significant, and this is consistent with the observation of resurgences. However, if the wind field varies slowly, the Coriolis terms become important (geostrophic response). The abruptness with which the wind field varies appears to generate certain type of resurgences. The maximum surge appears to occur when the wind blows more or less parallel to the coastline.

Next, following Kajiura (1959), the two-dimensional aspects will be considered. If the scale of the storm is small compared with the shelf width, then the amplitude of the surge is determined by the scale of the storm rather than the shelf width. If the scale of the wind field is greater than the shelf width, then there is significant contribution from the free oscillations of the shelf. If the scale of the storm is small, then the Coriolis terms are not significant.

Consider a symmetric wind field with respect to the center and assume that its divergence is zero. Hence, the surge varies mostly because of the distortion of the circular pattern in the water near the boundary due to the wind stress curl. The tangential component τ_θ and the radial component τ_r of the wind stress in the model hurricane are assumed to be of the following form:

$$\begin{aligned} \tau_r &= 0 \\ \tau_\theta &= T\frac{Kr}{[1 + (Kr)^2]^2} \end{aligned} \tag{7.24}$$

Here, r is the radial distance from the center of the hurricane and T and K are defined with reference to the maximum wind stress $\tau_{\theta_{max}}$ and the distance r_{max} from the center to the maximum wind zone:

$$\begin{aligned} T &= \frac{16}{3\sqrt{3}}\tau_{\theta_{max}} \\ K &= \frac{1}{\sqrt{3}}\frac{1}{r_{max}} \end{aligned} \tag{7.25}$$

The simplified equation for the water level is

$$\frac{\partial^2\zeta}{\partial t^2} - c^2\nabla^2\zeta = 0 \tag{7.26}$$

At the coast ($x = 0$)

$$\frac{\partial\zeta}{\partial x} = \frac{\tau_x}{c^2}$$

At $\sqrt{x^2 + y^2} \to \infty$, ζ should represent a divergent wave. The solution for eq. 7.26 under these conditions is

$$\zeta(x, y, t) = -\int_0^{t+\epsilon}\int_{-\infty}^{\infty}\left[\frac{\tau_x}{c^2}G(x, y, t|x_0, y_0, t_0)\right]_{x_0=0} dy_0 dt_0 \tag{7.27}$$

where the Green function G is defined by

$$G(x, y, t|x_0, y_0, t_0) = G'(x, y, t|x_0, y_0, t_0) + G'(x, y, t|-x_0, y_0, t_0) \tag{7.28}$$

with

$$G'(x, y, t|x_0, y_0, t_0) = \frac{c}{2\pi}\frac{1}{\sqrt{c^2(t - t_0)^2 - (x - x_0)^2 - (y - y_0)^2}} \tag{7.29}$$

for

$$c(t - t_0) \geq \sqrt{(x - x_0)^2 + (y - y_0)}$$

and

$$G'(x, y, t|x_0, y_0, t_0) = 0 \tag{7.30}$$

for

$$c(t - t_0) < \sqrt{(x - x_0)^2 + (y - y_0)^2}$$

The subscript 0 denotes the values of the parameters at the source.

For the steady state, assuming that the center of the storm is located on the coast, it can be shown that the maximum surge is given by

$$\zeta_{max} = \frac{4}{3} \frac{\tau_{\theta_{max}}}{c^2} r_{max} \tag{7.31}$$

and this maximum occurs at a distance of $\sqrt{3}\, r_{max}$ from the center (note that r_{max} is the distance of the maximum winds from the center). This result is quite similar to the one-dimensional case.

For the case of a moving hurricane, taking the origin of the coordinate system at the observing station for the water level, solutions can be written in terms of Green's functions (see Kajiura 1959 for details). This solution shows that the water level responds almost instantaneously to the wind stress when the storm track is perpendicular to the coastline. The time interval between the occurrence of the maximum surge and the passage of the storm center over the station is short.

However, if the storm track is parallel to the coast and if the speed of movement of the storm is close to c (i.e. of the long gravity wave in the water) then the surge will be dynamically amplified. In this situation, unlike in the other case (perpendicular track), the storm duration (i.e. the distance traveled by the storm along the coast) plays an important role because the maximum surge takes considerable time to build up. Thus, the orientation of the storm track is very important in determining the surge. The maximum surge can occur either before or after the nearest approach of the storm center to the observing station. The time interval between the nearest approach of the storm center and the maximum surge depends on the distance of the station from the storm track as well as the orientation of the track.

Kajiura (1959) showed that the dynamic amplifications for the one-dimensional and two-dimensional cases are respectively given by

$$\frac{1}{\left(1 - \frac{V^2}{c^2}\right)}$$

and

$$\frac{1}{\left(1 - \frac{V^2}{c^2}\right)^{1/2}} - 1$$

For a hurricane moving parallel to the coast the amplification is maximum, and it is negligible for a storm moving perpendicular to the coast.

Kajiura (1959) also analyzed the pertinent hurricane-generated storm surge data. The hurricanes that were studied by Kajiura are listed in Table 7.25. In this table, parameter Δp^* is defined as follows. It is the difference in the pressure at 180 nautical miles (333 km) to the right of the hurricane center and the pressure at the center. The maximum observed surge amplitudes at various stations in the three regions are listed in Table 7.26. The identification number for the hurricanes is the same as in Table 7.25.

Other hurricane surge data (not shown in Tables 7.25 and 7.26) indicate that for the hurricane of August 1933, the surge was 6.2 ft (1.9 m) at Hampton Roads and 7.0 ft (2.1 m) at Baltimore. For the September 1938 hurricane, the surge was 9.4 ft (2.9 m) at Willets Points. Along the coast of the Gulf of Mexico greater surges are possible because of the shallow and wide continental shelf to the south of the Louisiana and Texas coasts. The surge following Hurricane Audrey of May 1956 was 12 ft (3.7 m) near Cameron (Louisiana).

TABLE 7.25. Hurricanes used in the study by Kajiura (1959).

Identity No.	Date	Name	Intensity (mb) ΔP^*	
			Region III	Regions I and II
1	Sept. 13–16, 1944		18	27
2	Oct. 17–22, 1944		27	12
3	June 23–28, 1945		20	23
4	Sept. 15–20, 1945		21	13
5	Aug. 25–30, 1949		19	18
6	Aug. 12–16, 1953	Barbara	23	16
7	Aug. 28–Sept. 1, 1954	Carol	30	31
8	Sept. 9–12, 1954	Edna	25	43
9	Oct. 13–17, 1954	Hazel	22	21
10	Aug. 10–14, 1955	Connie	24	22
11	Aug. 16–20, 1955	Diane	26	12
12	Sept. 17–21, 1955	Ione	35	25
13	Sept. 22–29, 1956	Flossy	12	16

Kajiura (1959) plotted positions of storm centers when the surge reached its maximum value or minimum value at a given station (e.g. Wilmington). This diagram (Fig. 7.42) reveals that the time of maximum surge is related to the position of the storm center relative to the observing station in a regular manner for hurricanes. However, if a frontal system exists within the hurricane, or if there is great asymmetry of the pressure field, then the positions of the storms (at the time of peak surge) are distributed irregularly.

To the north of Cape Hatteras, the maximum surge occurs within 1–2 h before or after the time of nearest approach of the storm center if the storm is reasonably symmetric. South of Cape Hatteras, the time intervals vary widely up to 10 h. However, generally, the time of maximum surge appears to be ahead of the time of the nearest approach of the storm center (this is particularly true if the storm track is over land).

Kajiura (1959) calculated the surge heights from the following relation:

$$\zeta = \frac{ra'}{\rho g}\Delta p' = ra\Delta p^* \tag{7.32}$$

where Δp^* is the storm intensity defined above, a' is a numerical coefficient (varies from station to station), and r is the dynamic amplification. If ζ is in feet and Δp^* is in millibars, then a has values in the range of 0.14–0.2. Usually $1.5 < r < 2$ if we take

$$\Delta p^* = 0.55\,(1015 - p_0) \tag{7.33}$$

where p_0 is the minimum pressure (millibars). These agree reasonably well with calculated values by Hoover (1957), Conner et al. (1957), and Harris (1957).

SPLASH MODELS

SPLASH is an acronym for "special program to list amplitudes of surges from hurricanes." SPLASH I deals with landfalling hurricanes and SPLASH II takes care of situations in which the hurricane need not go over land. These models were developed at the Technics Development Laboratory of the U.S. National Weather Service (Jelesnianski 1972, 1974, 1976; Jelesnianski and Barrientos 1975; Barrientos and Jelesnianski 1976,

TABLE 7.26. Observed maximum surges (m) on the east coast of the United States (hurricane identity number same as in Table 7.25). (Kajiura 1959)

	Region I			Region II			Region III			Region III (smoothed)		
Identity No.	Woods Hole	Newport	New London	Montauk	Sandy Hook	Atlantic City	Charleston	Fort Pulaski	Fernandina	Charleston	Fort Pulaski	Fernandina
1	2.04	2.32	1.62	—	1.62	1.55	0.15	—	—	0.15	—	—
2	0.43	0.37	0.46	—	0.79	0.52	1.16	1.83	1.89	1.04	1.43	1.62
3	0.27	0.30	0.34	—	0.34	0.40	0.85	0.94	0.64	0.70	0.73	0.61
4	0.43	0.27	0.30	—	0.70	0.58	1.28	1.19	1.19	1.13	1.10	1.16
5	0.43	0.40	0.30	0.21	0.34	0.30	0.52	1.22	0.88	0.40	0.79	0.55
6	0.24	0.21	0.24	0.30	0.30	0.43	0.18	—	—	0.15	0.12	0.15
7	2.68	2.50	2.07	1.86	0.98	0.76	0.64	0.61	—	0.49	0.43	—
8	1.43	—	0.79	1.16	0.49	0.55	—	—	—	0.27	0.27	—
9	0.40	—	0.76	0.52	0.64	0.88	0.55	0.64	0.64	0.37	0.40	—
							0.37	0.46	0.91			
10	—	—	0.21	0.15	0.82	0.64	0.55	0.52	—	0.40	0.27	—
11	0.27	0.18	0.15	0.15	0.18	0.18	0.46	0.52	0.52	0.34	0.24	—
12	0.24	0.21	0.18	0.21	0.24	0.21	0.37	0.46	0.82	0.18	0.15	—
13	0.21	0.27	0.34	0.34	0.70	0.79	0.40	0.46	0.30	0.40	0.40	0.30

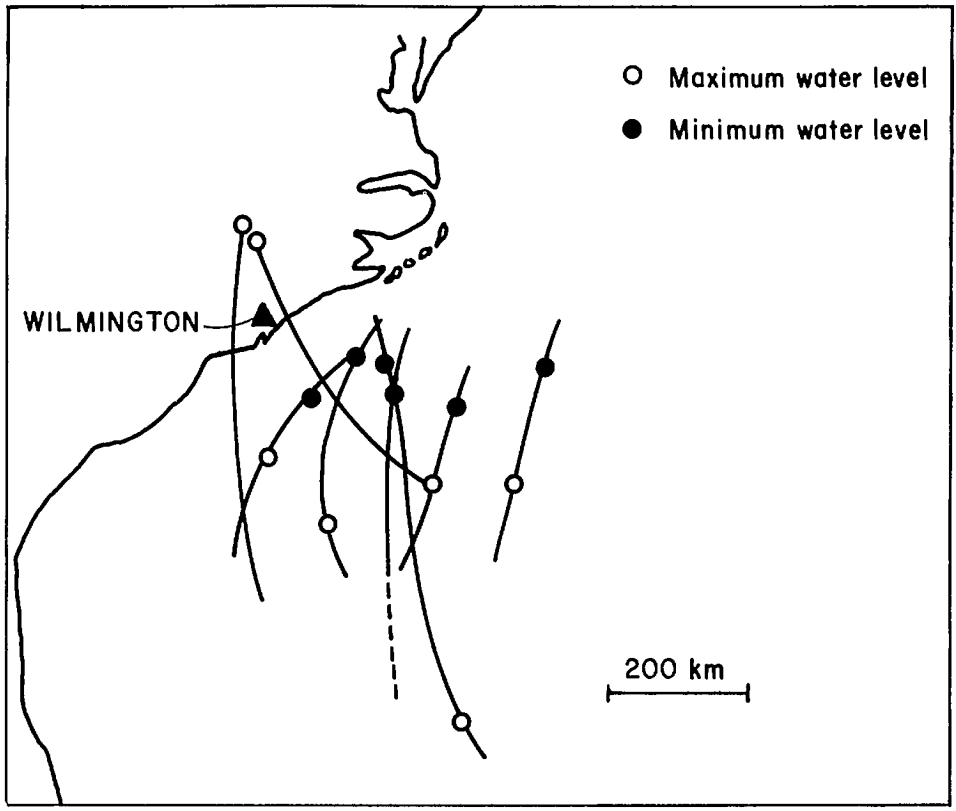

FIG. 7.42. Positions of hurricane centre at the time of maximum (open circle) surge and at the time of minimum (solid circle) surge at Wilmington, North Carolina, for eight different hurricanes. (Kajiura 1959)

1978). This computer program is operationally used at the National Hurricane Center in Miami and is applied to the Atlantic coast and the Gulf of Mexico coast of the United States. The stretch of coast for which these models are used extends about 3000 mi (4827 km) from Brownsville, Texas, to Long Island, New York. Along this coastal stretch, reference stations (for use in hurricane landfall determination) are established with an approximate spacing of 100 mi (161 km).

SPLASH is a numerical storm surge model that involves a linearized version of the transport equations. The geometry of the model is idealized into a rectangle with variable depth. One side of the rectangle is the coast and the other three sides are open boundaries. At the coast the normal transport is zero and at the deepwater open boundary static height is prescribed (this height is zero in the absence of an atmospheric pressure gradient). On the two lateral open boundaries the normal derivative of transport is prescribed to be zero. Depth contours are analyzed on overlapping 600 mi × 72 mi (965 × 116 km) basins. The basins are centered 50 mi apart.

In SPLASH I, which applies to landfalling hurricanes only, the following meteorological input is required: (1) pressure drop $\Delta p = p_\infty - p_0$ where p_∞ is the ambient pressure outside the storm and p_0 is the central pressure of the hurricane, (2) the radius R of maximum winds, (3) the vector storm motion U_S/θ where U_S is the storm speed and

TABLE 7.27. Comparaison of observed maximum surges (m) in the United States with those computed from the nomograms using SPLASH. (Based on Jelesnianski 1972)

Date	Location of peak surge	Computed peak surge	Observed peak surge
Oct. 2, 1893	Mobile, AL	3.32	2.83
Sept. 27, 1894	Charleston, NC	1.59	1.62
Sept. 8, 1900	Galveston, TX	4.60	4.45
Aug. 14, 1901	Mobile, AL	2.07	2.26
July 21, 1909	Galveston, TX	3.54	3.05
Sept. 13, 1912	Mobile, AL	0.91	1.34
Aug. 16, 1915	High Island, TX	3.60	4.24
Sept. 29, 1915	Grand Isle, LA	3.41	2.74
Oct. 18, 1916	Pensacola, FL	1.59	0.91
Sept. 28, 1917	Fort Barrancas, FL	1.77	2.16
Sept. 9, 1919	Key West, FL	2.23	1.98
Oct. 25, 1921	Punta Rassa, FL	3.29	3.32
Aug. 26, 1926	Timbalier Island, LA	3.02	2.99
Sept. 18, 1926	Miami Beach, FL	3.57	3.17
Sept. 20, 1926	Pensacola, FL	2.19	2.74
Sept. 16, 1928	West Palm Beach, FL	2.74	2.96
Sept. 28, 1929	Key Largo, FL	2.23	2.68
Sept. 7, 1933	Brownsville, TX	3.02	3.96
July 25, 1934	Galveston, TX	2.07	1.80
Nov. 4, 1935	Miami Beach, FL	2.01	2.74
July 31, 1936	Panama City, FL	1.71	1.83
Aug. 7, 1940	Colcasieu Pass, LA	1.62	1.62
Aug. 11, 1940	Beaufort, SC	2.44	2.44
Sept. 23, 1941	Sargent, TX	2.35	2.59
Oct. 7, 1941	St. Marks, FL	3.08	1.86
Aug. 30, 1942	Matagorda, TX	2.90	4.27
July 27, 1943	Galveston, TX	1.77	1.10
Oct. 19, 1944	Naples, FL	3.26	3.23
Oct. 20, 1944	Charleston, FL	1.22	1.22
Aug. 27, 1945	Matagorda, TX	1.89	1.95
Aug. 24, 1947	Safine Pass, LA	0.87	0.76
Aug. 17, 1947	Hillsboro Beach, FL	1.95	2.90
Sept. 19, 1947	Biloxi, MS	3.41	3.32
Oct. 15, 1947	Quarantine Station, GA	2.13	1.77
Sept. 4, 1948	Biloxi, MS	1.59	1.55
Aug. 26, 1949	New Jupiter In., FL	1.65	1.25
Oct. 4, 1949	Freeport, TX	3.17	2.74
Aug. 30, 1950	Pensacola, FL	1.16	1.55
Sept. 5, 1950	St. Petersburg, FL	2.10	1.92
Oct. 15, 1954	Southport, NC	3.81	3.90
Aug. 17, 1955	Holden Beach, NC	1.62	1.65
Sept. 24, 1956	Laguna Beach, FL	1.43	2.16
June 27, 1957	Calcasieu Pass, LA	4.82	3.81

θ is the storm direction of motion, and (4) point of landfall. This program assumes that the conditions are steady state, i.e. the size, intensity, and speed of movement are constants.

SPLASH II deals with an unsteady storm. The storm track could have any orientation and the storm need not landfall. The input data consist of (among other things) a 24-h track segment, which is defined by latitude and longitude for five points on the track staggered 6 h apart for a 24-h period. These latitude and longitude data not only define the track but

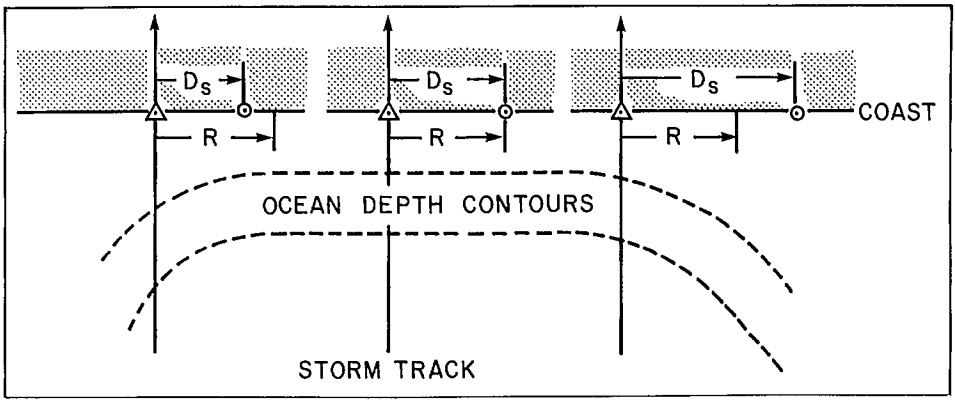

FIG. 7.43. Qualitative illustration showing the varying positions of peak surge on the coast as compared with two-dimensional bathymetry. ⊙, location of peak surge; △, landfall point; R, radius of maximum winds; D_s, distance to peak surge. (Jelesnianski 1972)

also the speed of movement of the storm. Other input data are the radius of maximum winds and pressure drop, which can vary with time.

One very important component in SPLASH is a normalized shoaling correction, which is used to correct the computed surge along the coast if the landfall point is shifted. Shoaling corrections were prepared for the Atlantic and the Gulf coasts by using landfall storms normal to the coast at 16-mi (25.8 km) intervals using a storm speed of 15 mi·h^{-1} (24 km·h^{-1}).

The SPLASH models were verified generally against data from 43 hurricanes during five hurricane seasons. These cases, the dates of occurrence, location of the peak surge, and computed and observed peak surges are listed in Table 7.27. The varying location of the peak surge, depending on the nature of the bathymetry, is shown quantitatively in Fig. 7.43.

Whereas SPLASH I can deal with landfalling hurricanes only, SPLASH II can be applied to a general storm track. Especially the following three types of tracks are considered: (1) landfall storm with its track perpendicular to a straightline coast, (2) an alongshore moving storm (i.e. constant abeam distance of the track from the coast), and (3) a recurving storm (nonlandfall). Slow-moving storms are treated as a special case and a hypothetical storm with the following properties is used: (1) the storm traverses the continental shelf with a speed of less than 8 mi·h^{-1} (12.9 km·h^{-1}), (2) the storm's closest approach to the coast occurs near Miami where there is hardly any continental shelf, and (3) the storm's strength and size (Δp = 100 mb, R = 15 mi·h^{-1} (24 km·h^{-1})) do not change along the track.

Calculations using SPLASH II gave the following results. The maximum surge is not highly sensitive to storm size for landfall storms. However, for nonlandfall storms, the storm size is important because the surge is a function of distance from the coast relative to storm size. When the storm is on the shelf, if the component of the track on the coast is large, the length of the coastline affected by the surge could be very long. For a storm traveling perpendicular to the coast, the component of the track on the coast degenerates to a point, and surges occur only along a small length of the coastline.

One of the main drawbacks of SPLASH II (although it is an improvement over SPLASH I) is that it treats the coast as a straight line and cannot include the curvature of

the coastline. To remove this restriction, Jelesnianski (1976) developed a sheared coordinate system. In this model, a mildly curving coastline (which does not include bays, estuaries, sounds, deltas, capes, spits, etc.) is sheared into a straight line. A surface plane, beginning at the ocean shelf and containing the curved coast as one of the boundaries, is fitted with a curved, nonorthogonal grid. The plane with curved boundaries is then transformed via a sheared coordinate system onto an image rectangle. In this transformed system, one deals with a Cartesian, orthogonal, equally spaced grid in which the coast coincides with grid lines. Jelesnianski (1976) used such a model incorporating the linearized storm surge equations for a 3000-mi (4827 km) coastline beginning at the United States–Mexico border in the Gulf of Mexico to the eastern tip of Long Island in New York. The storm tracks could be curved and the intensity, the size of the storm, and its speed of movement could be variable.

The somewhat idealized SPLASH models are being replaced with a new generation of models referred to as SLOSH (sea, lake, and overland surges from hurricanes). These models are being developed for the east and gulf coasts of the United States. Specifically, the following coastal stretches are being modeled: New Orleans area, Lake Okeechobee, Tampa Bay, Mobile Bay, Galveston area, Charlotte Harbor (Florida), Florida Bay–Biscayne Bay–Florida Keys, Long Island Sound, Chesapeake Bay, Charleston Harbor (South Carolina), Narragansett Bay, Buzzards Bay, Delaware Bay, Pamlico Sound, Massachusetts Bay, Corpus Christi (Texas), Lower Laguna Madre (Texas), Matagorda Bay (Texas), Lake Sabine (Texas), and Pensacola (Florida). Some testing of the SLOSH model during Hurricane Bob in July 1979 showed that the results are quite satisfactory.

Stretched Coordinate Models

Earlier, reference was made to the stretched coordinate models of Birchfield and Murty (1974) and Reid et al. (1977a, 1977b). Wanstrath et al. (1976) used stretched coordinate models for storm surge studies. Three regions of the continental shelf of the Gulf of Mexico and two regions of the east coast of the United States were mapped. These five regions are as follows: (1) western gulf coast: Laguna Madre, Mexico, to Marsh Island, Louisiana; (2) central gulf coast: Matagorda Bay, Texas, to Timbalier Bay, Louisiana; (3) eastern gulf coast: Atchafalaya Bay, Louisiana, to Apalachee Bay, Florida; (4) lower east coast: Cape Kennedy, Florida, to Pamlico Sound, North Carolina; (5) upper east coast: Pamlico Sound, North Carolina, to Penobscot Bay, Maine.

The grid system for the gulf coast is shown in Fig. 7.44. The computed and observed surges at three locations due to Hurricane Camille are compared in Fig. 7.45 and the computed and observed surges at three other locations due to Hurricane Gracie are compared in Fig. 7.46. Reference was already made to the stretched coordinate model of Butler (1979) in which he simulated the surge in Galveston Bay due to Hurricane Carla.

Storm Surges on the Gulf of Mexico Coast (Excluding the Florida Coast)

Up to this point, storm surges along the Atlantic coast and the Gulf of Mexico coast have been studied. The gulf coast will now be considered in some detail. Cline (1920) discussed the storm surges in the Gulf of Mexico due to hurricanes during the 20-yr period 1900–19. The pertinent information for these hurricanes and the storm surges generated is given in Table 7.28.

TABLE 7.28. Hurricanes and storm surges in the Gulf of Mexico during 1900–19.

Date(s) of hurricane	Hurricane	Storm surge
Sept. 1–12, 1900	Hurricane reached Florida Straits on Sept. 5 and moved in a northwesterly direction across the gulf a distance of about 1600 km. Maximum winds observed were 193 $km \cdot h^{-1}$	Surge of 4.6 m at Galveston on Sept. 8; over 6000 people killed; $30 million damage (in 1920 currency)
July 5–10, 1901	Storm of small extent and moderate intensity moved through the Yucatan channel into the Gulf of Mexico on July 7 and reached the Texas coast west of Galveston on July 10	Surge of 1.4 m at Galveston; no damage
Aug. 9–15, 1901	Hurricane first appeared to the north of Cuba on Aug. 9. It moved across southern Florida and into the Gulf of Mexico on the morning of Aug. 11, continued its course westward to 90°W when, during Aug. 14, it recurved and on the morning of Aug. 15 passed northeastward between New Orleans and Port Eads. Hurricane had small diameter but great intensity and its track was unusual	Surge of 1.3 m at Port Eads, 1.7 m at New Orleans, and 2.5 m at Mobile; 10 persons killed; $1 million damage
Sept. 23–27, 1906	Disturbance passed through the Yucatan channel on the morning of Sept. 24, traveled roughly in a straight line, and moved in on the Mississippi coast on the morning of Sept. 27. Hurricane was of large extent and of unusual intensity	Surge of 1.2 m at Port Eads, 3.3 m at Pensacola. At Pensacola 32 people killed and near Mobile 31 killed (it is not known whether some of these deaths were due to the hurricane and not the surge)
July 18–21, 1909	Hurricane moved from the Caribbean Sea though the Yucatan channel on July 18 and moved inland on the Texas coast with its center near Velasco	Surges (amplitudes not known) occurred to the right of the storm center up to Galveston; 4 people killed
Sept. 12–21, 1909	Storm of great extent and unusual intensity. Its effect was felt from east of Pensacola to the west of Galveston. Hurricane passed through the Yucatan channel during Sept. 17 and moved inland on the Louisiana coast on Sept. 20	353 people killed; $6.4 million damage
Oct. 13–18, 1910	Disturbance moved into the Florida Straits on Oct. 14, moved towards the northwest during Oct. 15, southward during Oct. 16, and then eastward to the Florida Straits by the morning of Oct. 17 after which it moved northward over Florida on Oct. 18	Negative surge of 2 m at Tampa
Aug. 13–17, 1915	Storm moved across the western end of Cuba into the Gulf of Mexico during the morning of Aug. 14, traveled in a direct line, and passed inland on the Texas coast a short distance to the left of Galveston on the morning of Aug. 17	$21 million damage
Sept. 2–4, 1915	Disturbance of considerable intensity crossed western Cuba, moved into the east Gulf, and, recurving slowly, moved inland near the mouth of the Apalachicola River during early morning of Sept. 4	Surge of at least 1.5 m at St. Petersburg

TABLE 7.28. (*Concluded*)

Date(s) of hurricane	Hurricane	Storm surge
Sept. 22–30, 1915	One of the most intense hurricanes in the history of the Gulf coast. Hurricane moved through the Yucatan channel during the night of Sept. 27 and, traveling northwestward, moved inland on the Louisiana coast to the left of and near Grand Isle during Sept. 29. Disturbance recurved slowly after crossing latitude 27°N and moved slowly northward	275 persons killed; $13 million damage. Surge heights up to 3.7 m on the coast of Lake Pontchartrain and 3–3.4 m on the Louisiana and Mississippi coasts. Inside Lake Pontchartrain, surges up to 4 m
July 1–6, 1916	Disturbance first appeared in the Caribbean Sea on the afternoon of July 1, moved almost in a straight line through the Yucatan channel on July 3, and reached the Mississippi coast late in the afternoon of July 5. Storm covered considerable area and was of great intensity	Damage at Mobile and along the Alabama coast of $2.5 million; 12 people killed. Damage at Pensacola of $1 million. Maximum surge up to 3.5 m
Aug. 12–19, 1916	Disturbance passed through the Yucatan channel into the Gulf during the night of Aug. 16, advanced northwesterly in nearly a straight line, and moved inland on the Texas coast midway between Corpus Cristi and Brownsville during the afternoon of Aug. 18	15 people killed; $1.8 million damage. Surges greater than 2.1 m at Mobile
Sept. 21–29, 1917	Disturbance moved through the Yucatan channel into the Gulf during the night of Sept. 25 and advanced in a direction a little west of north toward the mouth of the Mississippi River. When within about 80 km of Port Eads the storm began recurving to the right and center, passing about 80 km to the right of Port Eads, and moved inland to the right of Pensacola	Surge of 0.86 m at Pensacola. Surge of 1.77 m at Fort Barancas. Negative surge of 1.52 m at Mobile
Aug. 1–6, 1918	Disturbance moved through the Yucatan channel into the Gulf of Mexico during the night of Aug. 4, traveled in a northwesterly direction, and passed inland over Lake Charles during Aug. 6. Hurricane was small but of marked intensity	$5 million damage and 34 people killed due to the hurricane. Surge of 0.91 m at Morgan City. Surge of 0.86 at Johnson Bayou
Sept. 6–14, 1919	Storm moved through the Yucatan channel into the Gulf during the night of Sept. 25 and advanced in a direction a little west of north toward the mouth of the Mississippi River. When within about 80 km of Port Eads, the storm began recurving to the right and center, passing about 80 km to the right of Port Eads, and moved inland to the right of Pensacola. Storm moved more or less parallel to the coast	284 people killed; more than $20 million damage. Surges of up to 3.7 m occurred

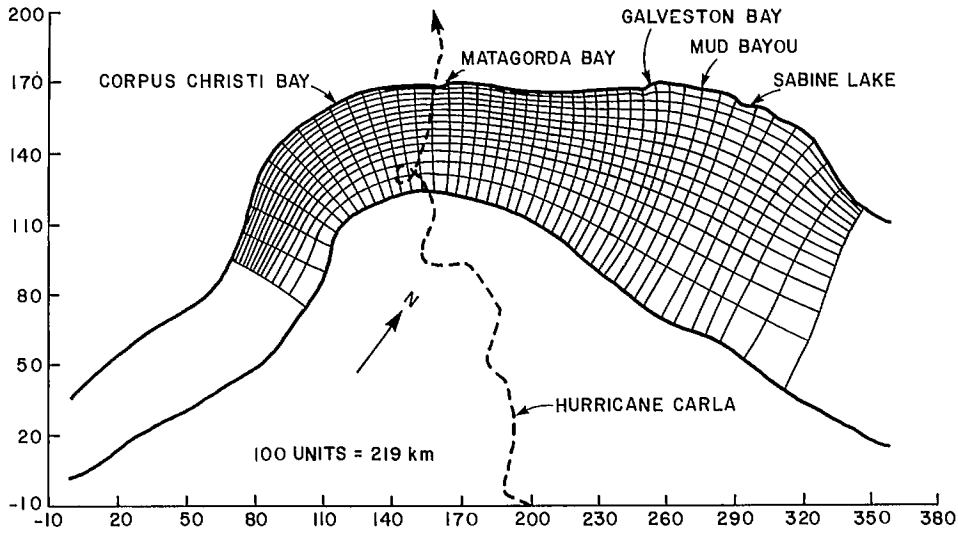

FIG. 7.44. Shelf coordinate system and grid for the Hurricane Carla storm surge simulation. Units = 219 km on the ordinate and abcissa. (Wanstrath et al. 1976)

Following are some results of the study by Cline (1920). During 1900–19, about 7225 people were killed and about $106 million in property damage occurred as a result of hurricanes in the Gulf of Mexico. The storm surge need not be symmetric about the hurricane track because the wind velocities to the left side of the track are much smaller (and less persistent) than on the right side. Peak surges occur a few kilometres to the right and at about the time of the passage of the center of the hurricane. The high water extends for only a short distance to the left of the point where the center of the storm moves inland. High water, however, occurs to the right of the center for a distance of 100–200 mi (161–322 km).

Conner et al. (1957) gave a table of hurricanes and associated surges during the period 1893–1950. This table is reproduced here as Table 7.29. Although this table bears some resemblance to an earlier table (Table 7.27), certain entries are different. Also, in Table 7.29, only the observed surge is included (there is no calculated surge). In addition, the lowest pressure in the hurricane is also listed. Two empirical relations best fit these data. One is

$$(7.34) \qquad h_{\max} = 0.867\,(1005 - p_0)^{0.618}$$

where $h_{\max}$ is the surge height (feet) and p_0 is the lowest central pressure (millibars). The correlation coefficient between $h_{\max}$ calculated and p_0 is 0.66. Another is

$$(7.35) \qquad h_{\max} = 0.154\,(1019 - p_0)$$

In this case the correlation coefficient is 0.68. The differences in the values for the observed surges for the same storms listed in Tables 7.27 and 7.29 are mainly due to different sources.

Hurricane Audrey of 1957 was the first hurricane that caused major storm surges since the organization of the National Hurricane Research Project by the U.S. Weather Bureau. This hurricane crossed the shore near the Texas–Louisiana border on the morning

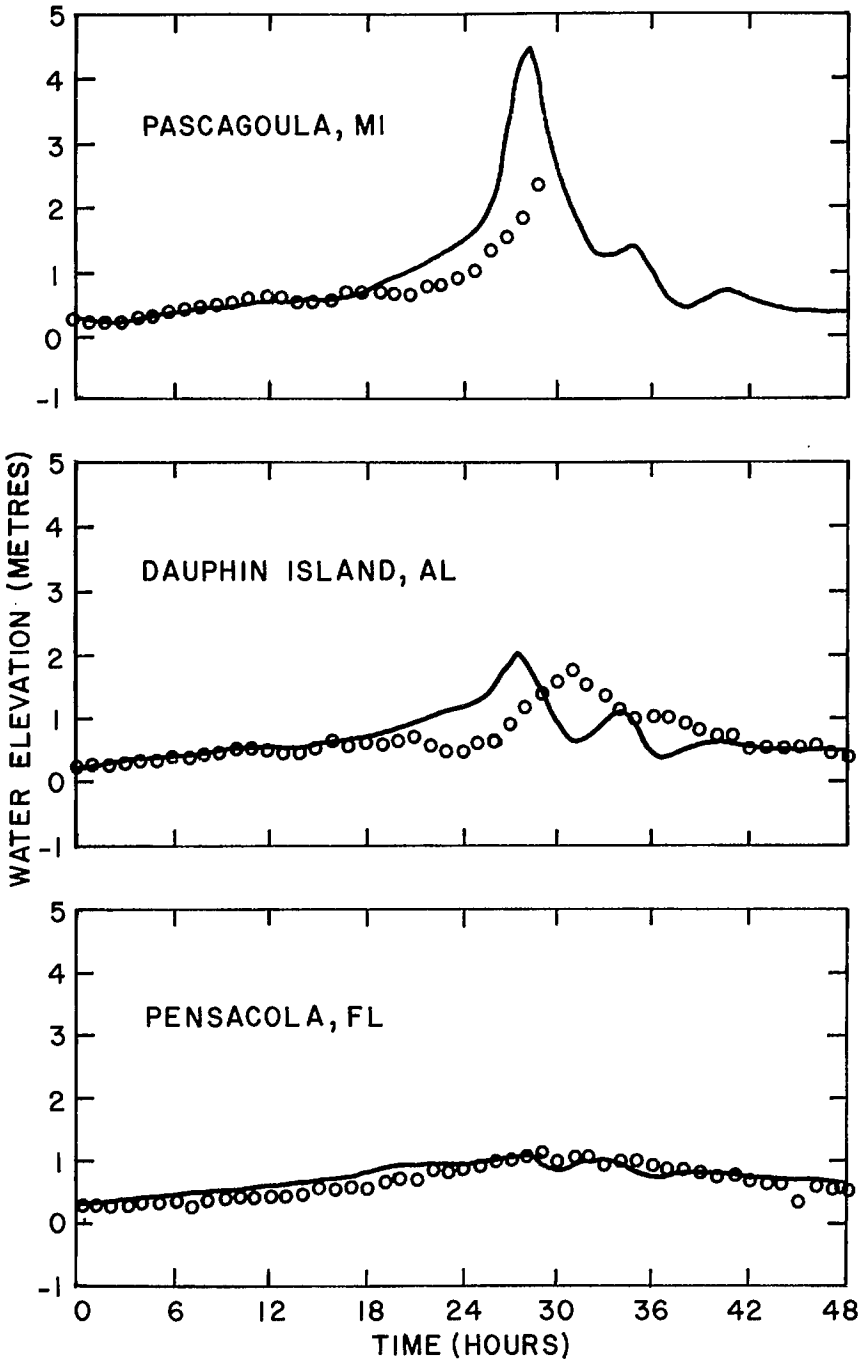

FIG. 7.45. Computed surge (curve) and observed surge (circles) for Hurricane Camille of 1969 at three locations in the United States. (Wanstrath et al. 1976)

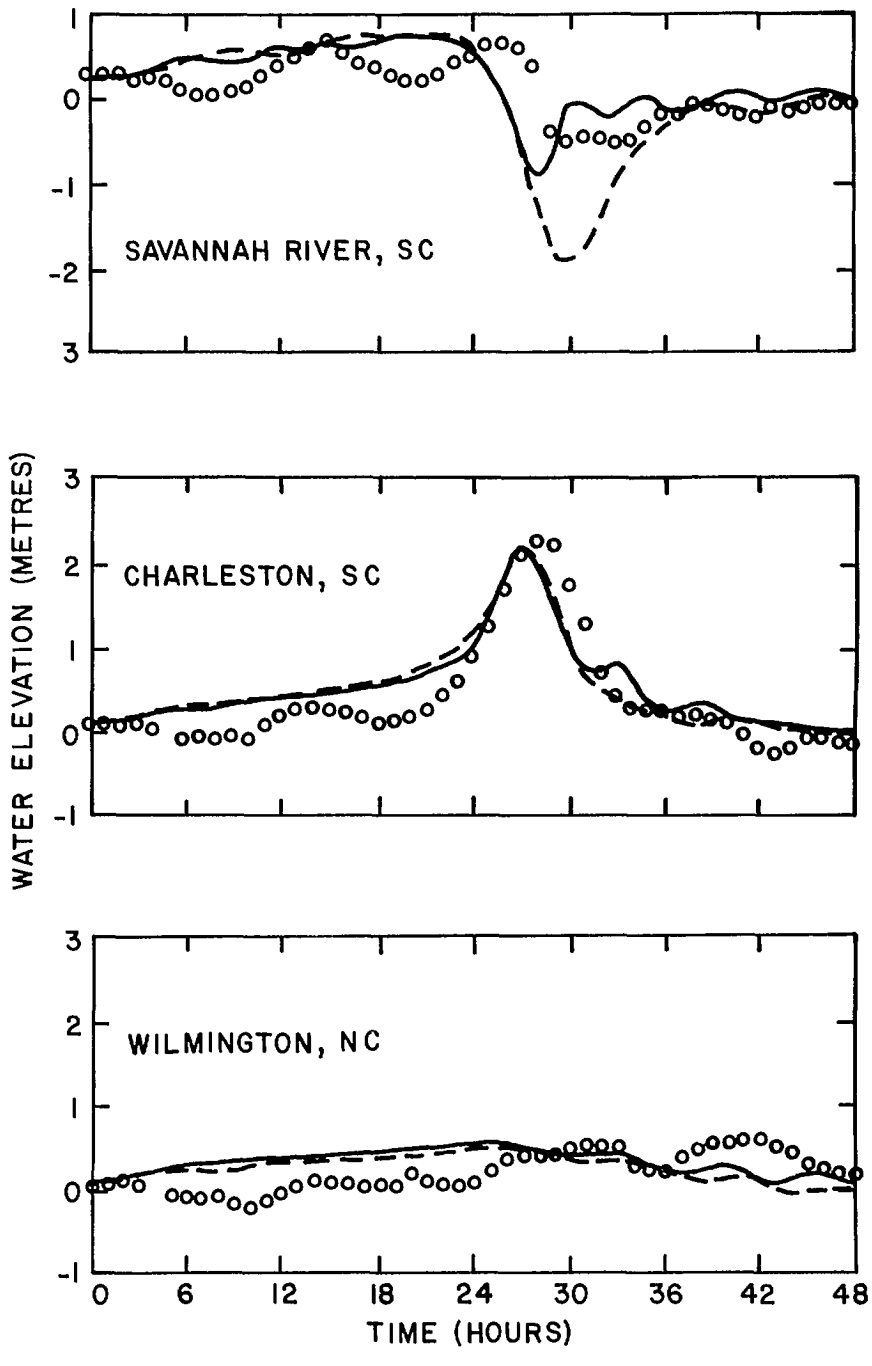

FIG. 7.46. Computed surge (curve) and observed surge (circles) for Hurricane Gracie at three locations in the United States. (Wanstrath et al. 1976)

TABLE 7.29. Lowest central pressures and highest surges of Gulf of Mexico hurricanes. (Connor et al. 1957)

Date	Location of highest surge on open coast	Lowest pressure (mb)	Peak surge (m)
Oct. 2, 1893	Mobile, AL	956	2.56
Sept. 8, 1900	Galveston, TX	936	4.42
Aug. 14, 1901	Mobile, AL	973	2.26
Sept. 27, 1906	Fort Barrancas, FL	965	3.29
July 21, 1909	Galveston, TX	959	3.05
Sept. 20, 1909	Mobile, AL	980	2.38
Sept. 13, 1912	Mobile, AL	993	1.34
Aug. 16, 1915	High Island, TX	953	4.24
Sept. 29, 1915	Grande Isle, LA	944	2.74
July 5, 1916	Fort Morgan, AL	961	1.43
Sept. 28, 1917	Fort Barrancas, FL	964	2.16
Sept. 14, 1919	Port Aransas, TX	948	3.38
Oct. 25, 1921	St. Petersburg, FL	958	2.38
Aug. 25, 1926	Timbalier Bay, LA	959	3.05
Sept. 20, 1926	Pensacola, FL	955	2.32
Sept. 5, 1933	Brownsville, TX	949	3.96
July 25, 1934	Galveston, TX	975	1.80
July 31, 1936	Panama City, FL	964	1.83
Aug. 7, 1940	Calcasieu Pass, LA	974	1.46
Sept. 23, 1941	Sargent, TX	959	3.02
Oct. 7, 1941	St. Marks, FL	981	2.44
Aug. 30, 1942	Matagorda, TX	951	4.51
July 27, 1943	Galveston, TX	975	1.22
Aug. 27, 1945	Matagorda, TX	968	2.23
Aug. 24, 1947	Sabine Pass, LA	992	1.10
Sept. 19, 1947	Biloxi, MS	968	3.38
Sept. 4, 1948	Biloxi, MS	987	1.71
Oct. 4, 1949	Freeport, TX	978	3.17
Aug. 30, 1950	Pensacola, FL	979	1.68
Sept. 5, 1950	Cedar Key, FL	958	1.55

of June 27, 1957. Harris (1958a, 1958b) studied the storm surges associated with this hurricane and gave detailed diagrams of the surge height distribution along the coast.

Marinos and Woodward (1968) used the bathystrophic theory to compute storm surges on the Texas–Louisiana coast. They made use of three storms to calibrate their model and checked it against several other storms. Using several synthetic hurricanes, 100-yr surge hydrographs were also constructed.

Miyazaki (1965) computed the storm surge in the Gulf of Mexico due to Hurricane Carla of September 7–11, 1961, using a time-dependent linearized two-dimensional model. He first used a coarse grid of 48 nautical miles (89 km) for the entire Gulf and then developed a fine-grid model (grid spacing of 9.6 nautical miles or 17.8 km) for the northwestern part where the storm surge was the most significant. In the coarse-mesh model, bottom friction was ignored whereas quadratic bottom friction was used in the fine-mesh model.

Hurricane Carla is an exceptional hurricane in the sense that it moved very slowly (about 7 knots or 13 $km \cdot h^{-1}$). The maximum wind speed was 85–95 knots (137–176 $km \cdot h^{-1}$) and the radius of maximum winds was about 50 nautical miles (93 km). Another remarkable feature of this hurricane is in the generated surge. Along the Texas–Louisiana

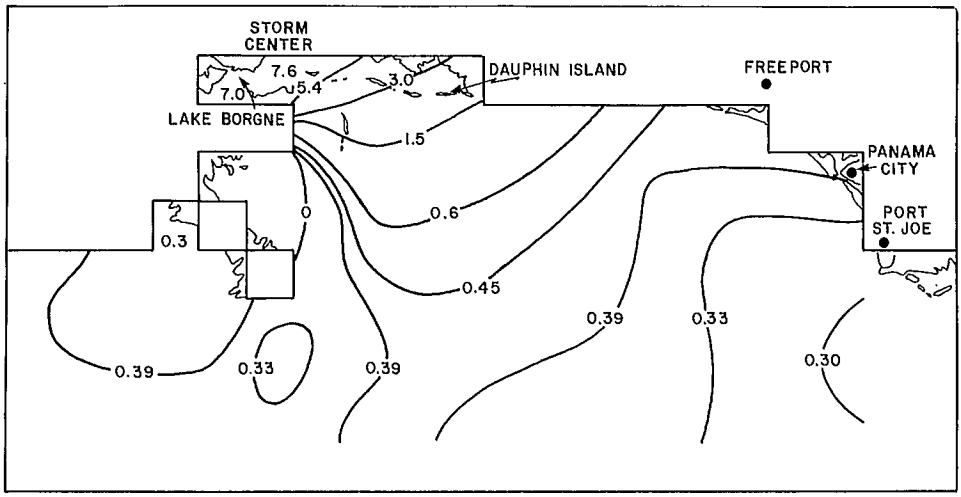

FIG. 7.47. Distribution of the water levels (storm surge wih a 0.25-m tide superimposed) along parts of the coasts of Louisiana, Mississippi, and Alabama due to Hurricane Camille of 1969. (Pearce 1972)

coast the storm surge occurred for almost a 6-d period (September 7–12, 1961). Maximum surge height of about 10 ft. (3.1 m) was estimated on September 10 at Galveston. The calculated surge was compared with the observed surge by Miyazaki (1965) at the following stations: Port Isabel (Texas), Port Aransas (Texas), Freeport (Texas), Pier 21 and Pleasure Pier (both in the Galveston area), Fort Point (Texas), Sabine Pass (Texas), Bayou Rigaud (Louisiana), Humble Oil Platform A (Louisiana), and Pensacola (Florida).

Hurricane Betsy struck the southeastern Louisiana coast on September 9, 1965. It was the most destructive (economically) ever to hit the United States coast up to that time (Goudeau and Conner 1968). Winds reaching up to 125 $mi \cdot h^{-1}$ (201 $km \cdot h^{-1}$) caused a great storm surge resulting in extensive flooding in the Metropolitan area of New Orleans. Goudeau and Connor (1968) also gave detailed diagrams for the storm surge height distribution and flooded areas on the Mississippi River and also in Lake Pontchartrain.

Pearce (1972) developed a two-dimensinal, time-dependent numerical model for studying storm surges in the Gulf of Mexico. He used two different mesh sizes: 16 nautical miles (29.6 km) and 6 nautical miles (11.1 km). These were applied to the surge generated by Hurricane Camille of August 17–22, 1969. There was no significant difference in the results between the smaller grid and larger grid models. Inclusion of the nonlinear advective terms made only a difference of 2% in the surge heights. The model results were insensitive to bottom friction coefficients between 0.005 and 0.02. Pearce (1972) also used a one-dimensional model as well as an analytical model. The distribution of surge heights computed for August 17 at 23:40 is shown in Fig. 7.47. Although in this subsection the Gulf of Mexico was considered as a whole, later subsections will consider parts of this system such as Galveston Bay, Mobile Bay, etc., in detail.

STORM SURGES ALONG THE COAST OF FLORIDA

In this subsection, storm surges along the Gulf of Mexico coast and the Atlantic coast of Florida will be considered. Storm surges in Lake Okeechobee will be considered in the next subsection. Damsgaard and Dinsmore (1975) used a two-dimensional numerical

model to study storm surges in Biscayne Bay, Florida. Their model allows for overtopping of low-lying barrier islands as well as inundation of flood plains. They tested their model against the storm surge generated by Hurricane Betsy of September 8, 1965.

Verma and Dean (1969) also used a two-dimensional model to study storm surges in Biscayne Bay. Their model allows for the inclusion of rainfall. Ross and Jerkins (1977) used two different models to study storm surges in Tampa Bay, Florida. The first model (referred to as USF) was developed at the University of South Florida and is based on the explicit model by Reid and Bodine (1968). The second model is based on the Rand model (Leendertse 1967) and makes use of an implicit–explicit scheme. Based on calculations for Tampa Bay, these authors concluded that the USF model provides a more accurate simulation than the Rand model.

By far the most comprehensive study of storm surges on the Florida coast (which this author could find) is one by Bruun et al. (1962), in which they studied the storm surges in relation to coastal topography. Forty hurricanes during the period 1900–60 that caused significant storm surges along Florida coast are listed in Table 7.30.

Storm Surges in Lake Okeechobee

In an earlier section a storm surge study by Reid et al. (1977a, 1977b) was considered, which treated the extensive vegetation areas of Lake Okeechobee as a canopy. Myers (1954) studied in detail the data from the hurricanes that were pertinent for levee design for this lake (this study was considered in Chapter 6). Here, some studies on storm surges in this lake will be considered. Kivisild (1954) made an extensive study of storm surges in shallow bodies of water and applied this to Lake Okeechobee storm surges.

During the period 1886–1950, the average number of hurricanes reaching Florida was 1.28 per year. The probability that the Okeechobee area would be subjected to winds greater than 75 $mi \cdot h^{-1}$ (121 $km \cdot h^{-1}$) in any given year is 1 in 7. Several tide gauges were located during the Lake Okeechobee project that was organized during the early 1950's. The north–south extent (maximum) of the lake is 30 mi (48 km), the east–west extent (maximum) is 25 mi (40 km), and the total area is 730 mi^2 (1891 km^2). Extensive marsh and vegetation covers the western portion of the lake. The south shore of the lake from St. Lucie Canal to Fisheating Creek is enclosed by levees constructed to an average crown height of 32.5 ft (9.8 m) above mean sea level. On the north shore a levee of the same height extends from 2 mi (3.2 km) southeast of Taylor Creek to Kissimmee River, and this levee protects the town of Okeechobee. The northwest portion of the lake, bordering low, sawgrass marshes, and the northeast shore, bordering comparatively high ground, are unprotected. Ritta, Kreamer, and Torry islands at the southern end of the lake are partially protected by levees but these are insufficient against storm surges such as the hurricane of August 26–27, 1949.

Kivisild (1954) used simple analytical formulae to calculate the surges in Lake Okeechobee. However, for better resolution of the geometry of the lake, he divided it into triangular elements. The pertinent information of the five hurricanes studied by Kivisild (1954) and the related surges is summarized in Table 7.31.

Langhaar (1951) calculated the storm surges in Lake Okeechobee using simple anayltical formulae. These values agreed well with observed surges, which ranged from 3.5 to 10.2 ft (1.1–3.1 m). In this calculation, Langhaar considered the surge at the leeward end of the lake as a superposition of the surge due to seiches and a statical surge that the wind would maintain if it persisted indefinitely. The surge due to the seiche is referred to as the "dynamical surge" and the total surge is the sum of the dynamical and

TABLE 7.30. Major hurricanes affecting Florida, 1903–65. The last four entries are taken from Tetra Tech Inc. (1978) coastal flooding storm surge model, Part 1. Methodology prepared by Tetra Tech Inc. for U.S. Dep. of Insurance Administration, Washington, DC, May 1978. (Bruun et al. 1962)

Index No.	Date of occurrence	Coastal area affected
		Florida Peninsula
1	Sept. 10–16, 1903	Fort Lauderdale and Tampa Bay
2	Oct. 10–23, 1904	West Palm Beach
3	Oct. 11–20, 1906	Florida Keys and Miami
4	Oct. 6–15, 1909	Florida Keys and Miami
5	Oct. 11–13, 1910	Key West to Tampa Bay and Jacksonville
6	Sept. 2–14, 1919	Florida Keys
7	Sept. 27–Oct. 1, 1920	Cedar Key and St. Augustine
8	Oct. 21–23, 1921	Tampa Bay and Daytona Beach
9	July 22–Aug. 2, 1926	Entire east coast
10	Sept. 6–22, 1926	Miami and Everglades to Tampa Bay
11	Aug. 7–10, 1928	Fort Pierce and Cedar Key
12	Sept. 6–20, 1928	West Palm Beach to Jacksonville
13	Sept. 22–Oct. 4, 1929	Florida Keys to Tampa Bay
14	Aug. 31–Sept. 7, 1933	West Palm Beach and Cedar Key
15	Aug. 31–Sept. 8, 1935	Florida Keys to Cedar Key
16	Oct. 30–Nov. 8, 1935	West Palm Beach to Miami and Key West to Fort Myers
17	July 27–Aug. 1, 1936	Miami and Everglades to Tampa Bay
18	Oct. 4–12, 1941	Miami to Florida Keys and Everglades to Cedar Key
19	Oct. 13–21, 1944	Key West to Tampa Bay and Jacksonville
20	Sept. 12–19, 1945	Florida Keys to Miami and northeast coast
21	Oct. 7–9, 1946	Fort Myers to Cedar Key and Jacksonville
22	Sept. 11–19, 1947	Fort Lauderdale and Fort Myers
23	Oct. 9–15, 1947	Key West to Miami
24	Sept. 19–25, 1948	Key West to Fort Myers and Fort Pierce
25	Oct. 4–8, 1948	Florida Keys to Fort Lauderdale
26	Aug. 24–29, 1949	West Palm Beach and Cedar Key
27	Sept. 1–7, 1950	Key West to Cedar Key
28	Oct. 15–19, 1950	Entire east coast
29	Sept. 30–Oct. 7, 1951	Fort Myers and Fort Pierce
30	Oct. 8–10, 1953	Fort Myers and Fort Pierce
		Florida Panhandle
31	Sept. 10–30, 1906	Pensacola
32	Aug. 9–14, 1911	Key West to Pensacola
33	Sept. 11–23, 1912	Tampa Bay to Pensacola
34	Sept. 4, 1915	Key West to Apalachicola
35	July 5, 1916	Pensacola
36	Oct. 12–21, 1916	Pensacola
37	Sept. 21–29, 1917	Pensacola
38	Sept. 13–20, 1924	Panama City ot Apalachicola
39	Sept. 24–26, 1953	Pensacola to Panama City
40	Sept. 9–11, 1960 (Donna)	Florida Keys and South Gulf Coast
41	Aug. 26–29, 1964 (Cleo)	Southeast Florida
42	Sept. 7–11, 1964 (Dora)	Northeast Florida
43	Oct. 8–16, 1964 (Isabell)	Southern Florida
44	Sept. 6–9, 1965 (Betsy)	Southern tip of Florida

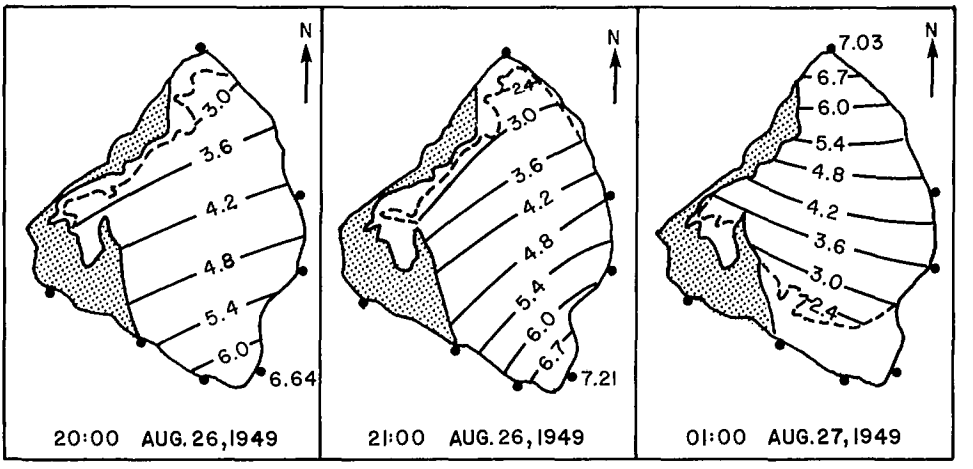

FIG. 7.48. Storm surge height (metres) distribution at three different times in Lake Okeechobee, Florida, due to the hurricane of August 26–27, 1949. (Farrer 1958)

statical surges. Farrer (1958) also used simple analytical formulae to compute storm surges in Lake Okeechobee for the hurricane of August 26, 1949. The water level distribution in the lake at three different times is shown in Fig. 7.48. The shaded area represents the marsh. The irregular triangular grid model of Thacker et al. (1980) was discussed in Chapter 3.

STORM SURGES IN GALVESTON BAY

Reid and Bodine (1968) developed a two-dimensional numerical model for computing storm surges in Galveston Bay. They also allowed for rainfall by including it in the continuity equation. The observed and computed surges at different locations for two different hurricanes are compared in Fig. 7.49 and 7.50.

Butler (1979) also developed a two-dimensional numerical model for storm surge computations in Galveston Bay. The time dependence is treated implicitly in this model. Spatially varying and time-dependent wind fields and rainfall are included. Flooding of low-lying areas is simulated by treating the location of the land–water boundary as a function of the time-varying local water depth. Subgrid barrier effects are also included. Exposed, submerged, and overtopping barriers can be represented in the mesh system; thus, one can allow for the surge waters breaching narrow barriers such as elevated highways, control structures, etc.

One special feature of this model is the employment of a coordinate transformation in the form of a piecewise exponential stretch. This transformation maps prototype space, discretized with a smoothly varying grid, into computational space with a regularly spaced grid, and in the computational space all the derivatives are centered. Through this transformation one can simulate a complex domain by locally increasing grid resolution and also by aligning coordinates along physical boundaries. A smoothly varying grid with continuous first derivatives eliminates the problems usually associated with variable grids. Indeed, Butler (1979) used expansions of grid length in prototype space by a factor of 10.

Butler (1979) wrote the vertically integrated two-dimensional equations of motion and continuity as follows:

TABLE 7.31. Five hurricanes and storm surges in Lake Okeechobee studied by Kivisild (1954).

Date(s) of hurricane	Meteorological information	Storm surge information
Sept. 15–16, 1945	Storm first noted east of the Leeward Islands on Sept. 11; it passed north of Puerto Rico on Sept. 13 and near Turks Island on the night of Sept. 13–14. It began a slow curvature over the great Bahama Banks during the night of Sept. 14–15 and struck Florida with its center passing over the northern end of Key Largo. Highest measured wind velocity was 222 $km \cdot h^{-1}$ at Carysfort Reef, at the southern tip of Florida. Path of the hurricane-intensity winds was only 32–48 km wide, so that only the southwestern shores of Lake Okeechobee received winds of a velocity greater than 121 $km \cdot h^{-1}$. Storm was, in general, of moderate intensity	Maximum surge recorded was about 1.8 m in range
Sept. 16–18, 1947	Hurricane center developed on Sept. 5 in the vicinity of Dakar (French West Africa). It moved about 27 $km \cdot h^{-1}$ on a west–northwest course to the Bahamas where on Sept. 15 it became almost stationary for about 24 h. Center reached the Florida coast at Fort Lauderdale on Sept. 17. Highest recorded wind velocity in Florida was 250 $km \cdot h^{-1}$ at Hillsboro Light near Pompano. Center moved westward across the state at about 16 $km \cdot h^{-1}$ and entered the Gulf of Mexico just north of Naples. Hurricane-force winds were experienced along about 386 km of the Florida east coast, while winds of 160 $km \cdot h^{-1}$ were recorded in a 113-km stretch between Miami and Palm Beach. Hurricane was one of the great storms. Lowest barometric pressure recorded in the Lake Okeechobee area was about 985 mb at Moore Haven	Maximum positive surge of about 2.13 m and a maximum negative surge of 1.22 m
Sept. 21–22, 1948	Hurricane center developed on Sept. 18 between Jamaica and Grand Cayman Islands and moved slowly in a northerly direction passing over Cuba on Sept. 20 with winds greater than 160 $km \cdot h^{-1}$. When the storm center passed over Florida on Sept. 21–22 there appeared to have been several centers, with lulls reported from 64 to 129 km apart normal to the path of the storm. Speed of movement of the storm was 13–16 $km \cdot h^{-1}$. Strongest wind recorded was in gusts of 196 $km \cdot h^{-1}$ at Boca airport near Key West. By the time the Lake Okeechobee region was reached, wind velocities diminished to gusts of about 145 $km \cdot h^{-1}$. Lowest barometric pressure recorded in the Lake Okeechobee area was 962.8 mb	Calculated values much bigger because the bottom friction due to the marsh grass was not taken into account

TABLE 7.31. (*Concluded*)

Date(s) of hurricane	Meteorological information	Storm surge information
Aug. 26–27, 1949	Storm was noticed on Aug. 23 in its formative stage, 201 km northeast of Leeward Islands. Center was well organized by the time it passed North Nassau on Aug. 26 and it intensified as it approached the Florida coast. Strongest winds occurred some distance to the right of the center near Jupiter, FL, where the anemometer failed after reaching an extreme of 246 $km \cdot h^{-1}$. Center passed the northem part of Lake Okeechobee during the early part of the evening of Aug. 26 with wind velocities ranging from 160 to 203 $km \cdot h^{-1}$. In the Lake Okeechobee section it was the worst hurricane felt since the great disastrous hurricane of September 1928	Storm surges with ranges up to 4.27 m were recorded
Oct. 17–18, 1950	Storm formed over the northwestem Caribbean Sea on Oct. 15 and moved northeastward and then northward across Cuba as a small hurricane. Center of the hurricane, about 8 km in diameter, passed directly over Miami on the midnight of Oct. 17–18. Highest recorded wind speed was 201 $km \cdot h^{-1}$. Center crossed northward over Lake Okeechobee during the moming of Oct. 18 with wind gusts up to 153 $km \cdot h^{-1}$. In general, the diameter of this storm was smaller than that of most hurricanes, and sustained wind velocities were barely above the minimum hurricane intensity	Surges with a maximum range of 2.74 m were recorded

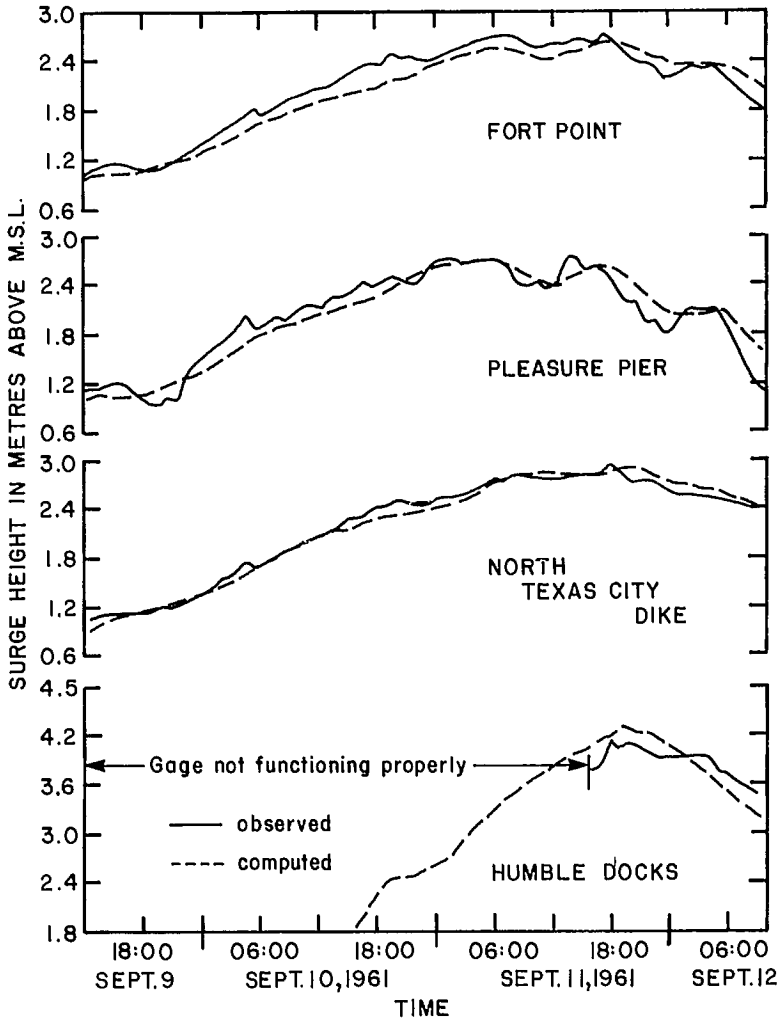

FIG. 7.49. Comparison of observed and computed surges at four different locations in Galveston Bay due to Hurricane Carla of September 9–12, 1961. (Reid and Bodine 1968)

$$(7.36)\quad \frac{\partial U}{\partial t}+\frac{\partial}{\partial x}\left(\frac{U^2}{d}\right)+\frac{\partial}{\partial y}\left(\frac{UV}{d}\right)-fV+gd\frac{\partial}{\partial x}(\eta-\eta_a)+F_x+\frac{gU}{c^2d^2}(U^2+V^2)^{1/2}-de\left(\frac{\partial^2 U}{\partial x^2}+\frac{\partial^2 U}{\partial y^2}\right)=0$$

$$(7.37)\quad \frac{\partial V}{\partial t}+\frac{\partial}{\partial x}\left(\frac{UV}{d}\right)+\frac{\partial}{\partial y}\left(\frac{V^2}{d}\right)+fU+gd\frac{\partial}{\partial y}(\eta-\eta_a)+F_y+\frac{gV}{c^2d^2}(U^2+V^2)^{1/2}-de\left(\frac{\partial^2 V}{\partial x^2}+\frac{\partial^2 V}{\partial y^2}\right)=0$$

$$(7.38)\quad \frac{\partial \eta}{\partial t}+\frac{\partial U}{\partial x}+\frac{\partial V}{\partial y}=0$$

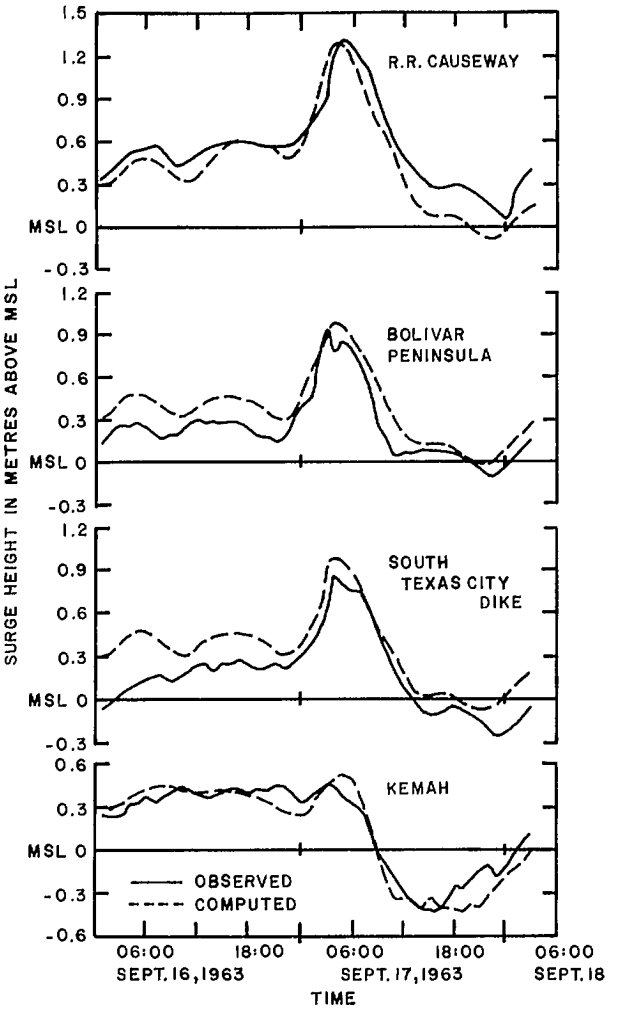

FIG. 7.50. Comparison of computed and observed surges at four locations in Galveston Bay due to Hurricane Cindy of September 16–18, 1963. (Reid and Bodine 1968)

Here, h is the still-water elevation, $d = h + \eta$ is the total water depth, c is the Chézy friction coefficient, e is a generalized eddy viscosity coefficient, R is the rate at which additional water is introduced into or taken out of the water body (rainfall, evaporation), F_x and F_y represent external forcing functions such as wind stress, η is the water surface elevation, and η_a is the hydrostatic elevation corresponding to the atmospheric pressure anomaly.

For each direction a piecewise reversible transformation is independently used to map prototype into computational space. The transformation is of the form

(7.39) $$x = a + b\alpha^c$$

where a, b, and c are arbitrary constants. The equations of motion in the α-space are

$$(7.40)\quad \frac{\partial U}{\partial t} + \frac{1}{\mu_1}\frac{\partial}{\partial \alpha_1}\left(\frac{U^2}{d}\right) + \frac{1}{\mu_2}\frac{\partial}{\partial \alpha_2}\left(\frac{UV}{d}\right) - fV + \frac{gd}{\mu_1}\frac{\partial}{\partial \alpha_1}(\eta - \eta_a) + F_{\alpha_1} + \frac{gU}{C^2 d^2}(U^2 + V^2)^{1/2} - T_1 = 0$$

$$(7.41)\quad \frac{\partial V}{\partial t} + \frac{1}{\mu_1}\frac{\partial}{\partial \alpha_1}\left(\frac{UV}{d}\right) + \frac{1}{\mu_2}\left(\frac{V^2}{d}\right) + fU + \frac{gd}{\mu_2}\frac{\partial}{\partial \alpha_2}(\eta - \eta_a) + F_{\alpha_2} + \frac{gV}{C^2 d^2}(U^2 + V^2)^{1/2} - T_2 = 0$$

$$(7.42)\quad \frac{\partial \eta}{\partial t} + \frac{1}{\mu_1}\frac{\partial U}{\partial \alpha_1} + \frac{1}{\mu_2}\frac{\partial V}{\partial \alpha_2} = R$$

where

$$(7.43)\quad \mu_1 = \frac{\partial x}{\partial \alpha_1} = b_1 c_1 \alpha^{c_1 - 1}$$
$$\mu_2 = \frac{\partial y}{\partial \alpha_2} = b_2 c_2 \alpha^{c_2 - 1}$$

The parameters μ_1 and μ_2 define the stretching of the regular grid into α-space to approximate the study area of real space. The terms T_1 and T_2 represent the transformed flux terms (which are not included in the application to Galveston Bay).

The above model is applied to storm surge computation in Galveston Bay (which is a large shallow bay of area greater than 1000 km^2) due to Hurricane Carla of 1961. The model was calibrated by reproducing the tides. The observed and computed surges at 26 different locations are compared in Table 7.32.

Storm Surges in Pamlico Sound and Cape Fear Estuary

Two important water bodies along the coast of North Carolina are Pamlico Sound in the north and Cape Fear Estuary in the south. In Pamlico Sound the astronomical tides are small (5-cm range) but storm surges could be significant. Roelofs and Bumpus (1953) calculated the surges in this water body using the following simple relation of Keulegan (1951):

$$(7.44)\quad \frac{S}{L} = 3.3 \times 10^{-6}\left[1 + 63\left(\frac{H}{L}\right)^{1/2}\right]\frac{V^2}{gH}$$

where S is the setup (i.e. $h_2 - h_1$, where h_2 and h_1 are the windward and leeward displacements of the water level), L is the length of the water body, V is the wind velocity, and H is the mean depth of the water body. From this formula it was calculated that a southwest wind of about 13 knots (24 km·h^{-1}) is needed to generate a setup of about 1 ft (0.3 m) and a 40-knot (74 km·h^{-1}) wind could produce a surge of 9.8 ft (3 m). This result does not include the funneling effect due to the geometry of the Sound. Northeasterly winds will cause a similar rise along the southwest shore.

Overland and Myers (1976) used a one-dimensional numerical model to calculate the storm surges in Cape Fear Estuary. Some recent dredging operations increased the tidal

TABLE 7.32. Comparison of computed and observed surges (m) at several locations in Galveston Bay due to Hurricane Carla of 1961 (mean absolute error = 0.18 m). (Butler 1979)

Gauge Location	Observed	Computed	Difference
Oyster Creek	3.11	3.29	+0.18
San Luis Pass	3.29	3.05	−0.24
Sea Isle Beach	3.69	3.05	−0.64
Bermuda Beach	3.20	2.99	−0.21
Scholes Field	2.59	2.93	+0.33
Bolivar Beach	2.83	2.83	+0.00
Crystal Beach	2.68	2.87	+0.18
Rollover Beach	2.93	2.83	−0.09
Halls Bayou	4.36	4.30	−0.06
Highway Six	3.84	3.87	+0.03
Sievers Cove	3.23	2.83	−0.39
Dickinson Bayou	3.47	3.60	+0.12
Carbide Docks	3.35	3.17	−0.18
Kemah	4.33	3.90	−0.43
Smith Point	2.99	3.17	+0.18
Oyster Bayou	3.20	3.35	+0.15
Scott Bay	4.33	4.30	−0.03
Humble Docks	4.18	3.84	−0.34
Ananuac	3.78	3.87	+0.09
Wallisville	4.27	4.26	+0.00
Pleasure Pier	2.83	2.87	+0.03
Fort Point	2.74	2.90	+0.15
Pier 21	2.68	2.90	+0.21
Pelican Bridge	2.74	2.87	+0.12
Texas City Dyke (south)	2.90	3.05	+0.15
Texas City Dyke (north)	2.96	3.05	+0.09

TABLE 7.33. Meteorological data for Hurricanes Hazel of 1954, Diane of 1955, and Helene of 1958. (Overland and Meyers 1976)

Hurricane	Central pressure depression (mb)	Radius of maximum winds (km)	Speed of movement ($km \cdot h^{-1}$)	Maximum wind speed ($km \cdot h^{-1}$)
Hazel	66	38.9	53.2	166.7
Diane	30	31.5	22.8	110.4
Helene	65	38.9	24.1	165.9

range at Wilmington, North Carolina. Hence, they used two different depth profiles: the first corresponding to the early 1950's and the second corresponding to the present depths. They generated time histories of the open coast surge from the SPLASH II model for an ensemble of hurricanes, each storm being related to a frequency of occurrence. These time histories are linearly combined with appropriate phases of the astronomical tide at the entrance to Cape Fear River. Three hurricanes were selected: Hazel of 1954, Diane of 1955, and Helene of 1958. The pertinent information for these hurricanes is listed in Table 7.33.

TABLE 7.34. Pertinent information about selected hurricanes affecting Chesapeake Bay. (Bretschneider 1959)

Parameter	Hurricane of Aug. 22–24, 1933	Connie of Aug. 11–13, 1955	Diane of Aug. 15–18, 1955	Hazel of Oct. 14–17, 1957
Track	Just west of Chesapeake Bay's west coast	Just west of Chesapeake Bay's east coast	About 160 km west of Chesapeake Bay's west coast	About 160 km west of Chesapeake Bay's west coast
Radius of maximum winds ($km \cdot h^{-1}$)	86.9	72.4	72.4	57.9
Central pressure anomaly (mb)	28.8	46.4	24.0	56.2
Speed of movement over ocean ($km \cdot h^{-1}$)	46.2	22.2	38.9	101.9
Speed of movement over Chesapeake Bay ($km \cdot h^{-1}$)	24.1	18.5	22.2	66.6
Maximum wind speed over ocean ($km \cdot h^{-1}$)	98.2	115.9	86.9	148.1
Maximum wind speed over Chesapeake Bay ($km \cdot h^{-1}$)	80.5	72.4	56.3	112.7
Peak surge (m) at Hampton Roads, VA	2.01	1.34	0.18	0.55
Peak surge (m) at Gloucester Point, VA	—	1.37	0.70	0.88
Peak surge (m) at Solomon's Island, MD	—	1.28	0.67	0.85
Peak surge (m) at Annapolis, MD	1.77	1.49	0.98	1.28
Peak surge (m) at Baltimore, MD	2.20	1.59	1.13	1.46

STORM SURGES IN CHESAPEAKE BAY

Hurricane-generated storm surges in this water body were studied by Bretschneider (1959). Of all the hurricanes that generated surges in Chesapeake Bay up to 1959, only four are sufficiently well documented: August 22–24, 1933, August 11–13, 1955 (Connie), August 15–18, 1955 (Diane), and October 14–17, 1954 (Hazel).

The pertinent information for the meteorological aspects of these hurricanes as well as the storm surges recorded is given in Table 7.34. Some typical surge profiles in Chesapeake Bay are illustrated in Fig. 7.51 and 7.52.

For computing the surges outside Chesapeake Bay on the open coast, two model hurricanes were selected. The first (referred to as A) is the September 14, 1944, hurricane transposed to the Chesapeake Bay area but not adjusted for filling. For this hurricane, the radius R of maximum winds is 33.5 nautical miles (62 km), the atmospheric pressure anomaly at the center is 2.2 in.Hg (74.5 mb), and the maximum sustained wind speed at R is 105 $mi \cdot h^{-1}$ (169 $km \cdot h^{-1}$). The path of movement over the open ocean was assumed to be perpendicular to the coast and the speed of travel was 15–25 $mi \cdot h^{-1}$ (24–40 $km \cdot h^{-1}$). After crossing the coast, the path of movement curves and proceeds northward along the west side of Chesapeake Bay, and the speed of movement reduces to 12–15 $mi \cdot h^{-1}$ (19–24 $km \cdot h^{-1}$). The second storm (referred to as B) is exactly the same

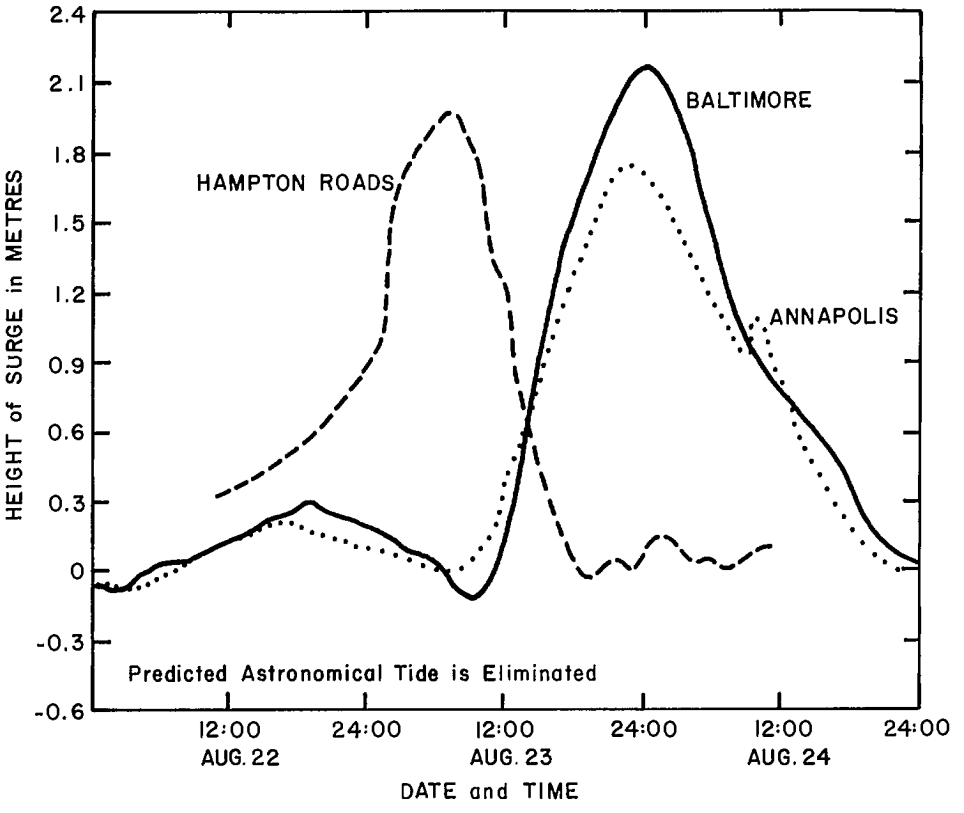

FIG. 7.51. Storm surges at three locations in Chesapeake Bay due to the hurricane of August 22–24, 1933. (Bretschneider 1959)

TABLE 7.35. Computed storm surges in Chesapeake Bay due to hurricanes A and B. These values have an uncertainty of 0.12 m. (Based on Bretschneider 1959)

	Maximum surge (m) due to	
Location	Hurricane A	Hurricane B
Hampton Roads, VA	3.29	3.57
Mouth of York River	3.14	3.44
Mouth of Rappahanock River	2.99	3.26
Mouth of Potomac River	2.77	3.05
Mouth of Severn River	2.53	2.77
Mouth of Patapaco River	2.87	3.11

as A, except that all wind speeds are 5 mi $\cdot$ h^{-1} (8 km $\cdot$ h^{-1}) larger. The results for the surges due to hurricanes A and B are summarized in Table 7.35. The prediction curves for hurricane surges at Washington, DC, are given in Fig. 7.53.

Bodine (1971) used the bathystrophic theory to compute storm surges on an open coast and applied this to the Chesapeake Bay area. In this connection, he pointed to the

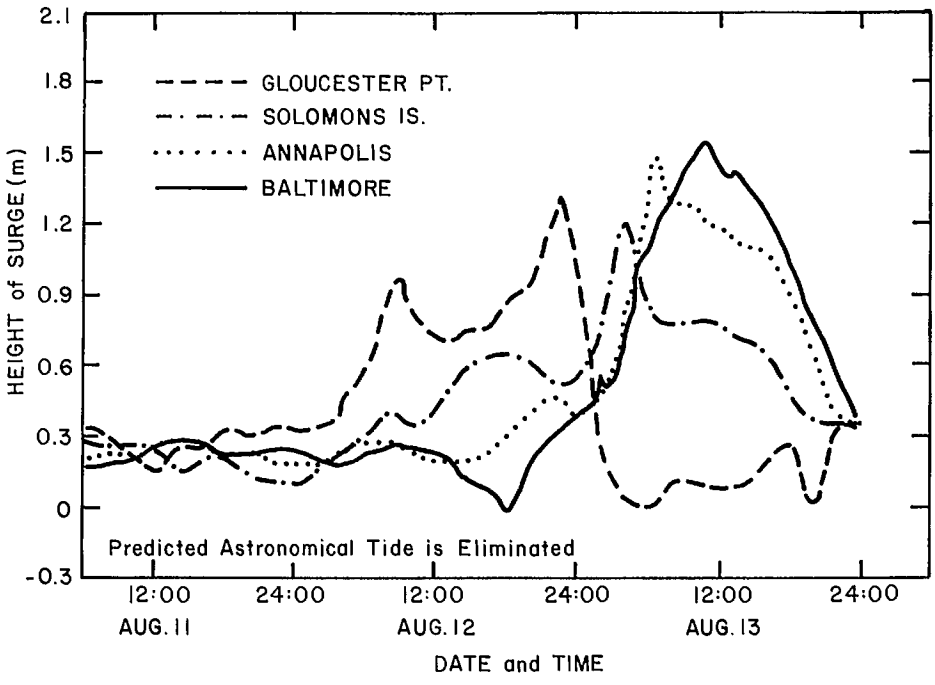

FIG. 7.52. Storm surges at four locations in Chesapeake Bay due to Hurricane Connie of August 11–13, 1955. (Bretschneider 1959)

important effect of interaction between tide and surge, especially when it is recognized that the tidal range can vary from 18.2 ft (5.5 m) at East Port, Maine, to 1.3 ft (0.4 m) at Key West, Florida, and that, generally, the tides along the Atlantic coast of the United States are semidiurnal whereas along the Gulf of Mexico coast they are mainly diurnal.

To give the most probable degree of protection required for any given area, the standard practice is to select a hurricane with a given set of characteristics for the particular geographical location. This will be called a "hypothetical" or "hypohurricane." Also, for such a hurricane the characteristics are taken as invariant and the track is assumed to follow a prescribed path. The U.S. Weather Bureau and the U.S. Army Corps of Engineers jointly established two design storms (which depend on the geographical location) for practical use for coastal engineering purposes. These are the Standard Project Hurricane (SPH) and the Probable Maximum Hurricane (PMH).

Graham and Nunn (1959) defined the SPH as a hypohurricane that is intended to represent the most severe combination of hurricane parameters that is reasonably characteristic of a region, excluding extremely rare combinations. The maximum gradient wind speed in the belt of maximum winds (miles per hour) was determined by the following formulae:

$$\begin{aligned} V_{g_x} &= K(p_n - p_0)^{1/2} - R(0.575f) \\ V_x &= 0.865V_{g_x} + 0.5V_F \end{aligned} \tag{7.45}$$

where $K = 73$, p_n and p_0 are the peripheral and central pressures in inches of mercury, R is the radius of maximum winds in nautical miles, f is the Coriolis parameter in units per

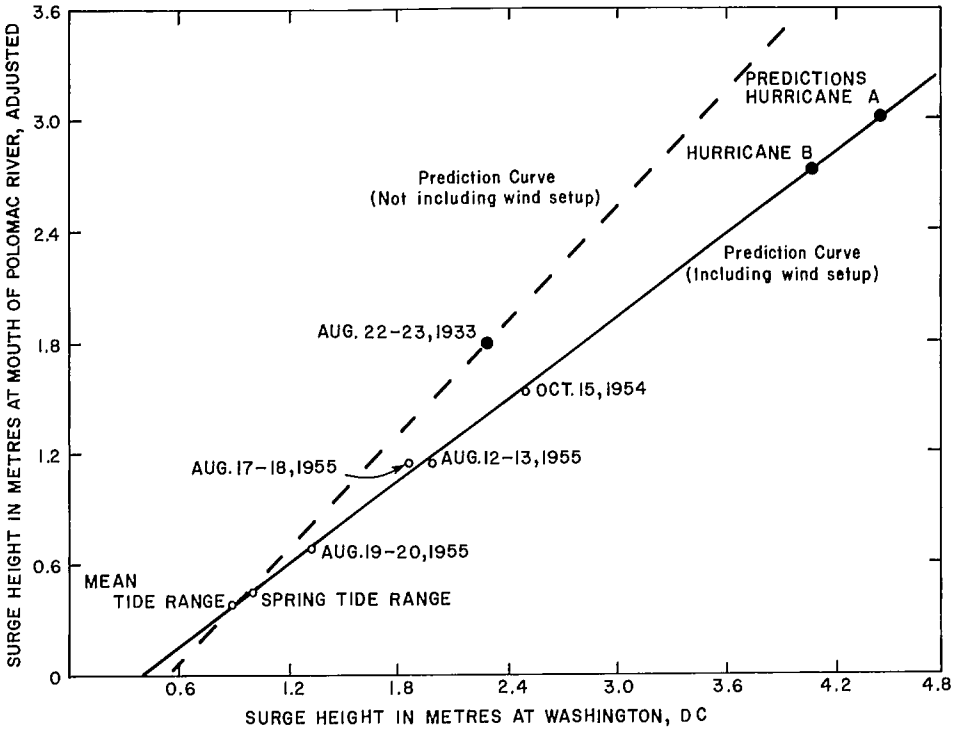

FIG. 7.53. Storm surge prediction curves for hurricane-generated storm surges at Washington, DC. (Bretschneider 1959)

hour, V_F is the speed of movement of the hurricane in miles per hour, and V_x is the maximum wind speed 30 ft (9.1 m) above the water.

For protection of the nuclear power plants, the U.S. Atomic Energy Commission concluded that adequate safety would be provided if the plant site would not be flooded by the surge and surface waves associated with a probable maximum hurricane (PMH). The U.S. Weather Bureau developed the characteristics of the PMH, which is much more severe than the SPH. The PMH was defined as a hypothetical hurricane having that combination of characteristics that will make it the most severe storm that can probably occur in the particular region involved. The hurricane should approach the point under study along a critical path and at an optimum rate of movement. Development of the isovel fields is basically the same for the PMH as for the SPH. The difference essentially is that whereas p_n is taken as the standard sea level pressure of 29.92 in.Hg (1013.2 mb) for the SPH, it is treated as a function of the latitude for the PMH. Also, K is treated as a function of latitude for the PMH whereas it is a constant for SPH. At times it may be desirable to select a design storm other than the SPH or PMH based on the risk or economy factors for a particular location or coastal structure. Using bathystrophic theory, Bretschneider (1959) estimated the peak surge (for a selected storm) at the mouth of Chesapeake Bay to be 13.4 ft (4.1 m).

Pore (1965) studied hurricane-generated storm surges in Chesapeake Bay. He made a distinction between western-type (i.e. hurricanes passing west of the bay) and eastern-type (hurricanes traveling east of the bay) storms. His study showed that the western-type

TABLE 7.36. Storm surge data for western type storms in the Chesapeake Bay region. (Pore 1965)

Date	Surge amplitudes (m) at						Time lag (h) from Norfolk to Baltimore	Storm movement (km) northward in 12 h
	Baltimore	Annapolis	Cambridge	Solomon's Point	Gloucester Point	Hampton Roads		
Oct. 2, 1929	1.19	1.10	—	—	—	0.73	18	352
Aug. 23, 1933	2.13	1.68	—	—	—	1.86	18	315
June 19, 1934	—	—	—	—	—	0.24	—	148
Sept. 18, 1945	0.82	0.73	0.70	0.64	—	0.73	17	389
Aug. 29, 1949	0.52	0.43	0.46	0.24	—	−0.06	—	519
Sept. 1, 1952	1.04	0.88	—	0.49	0.15	0.12	13	241
Oct. 15, 1954	1.40	1.19	—	0.85	0.34	0.46	14	945
Aug. 18, 1955	1.88	0.73	—	0.52	0.52	0.30	21	241

TABLE 7.37. Storm surge amplitudes (m) for eastern type storms in the Chesapeake Bay region. For certain cases, maximum positive and negative surges are listed. (Pore 1965)

Date	Baltimore	Annapolis	Cambridge	Solomon's Point	Gloucester Point	Hampton Roads	Portsmouth
Sept. 16, 1933	0.27	0.30	—	—	—	1.55	—
Sept. 8, 1934	—	—	—	—	—	0.24	—
Sept. 18, 1936	−1.74, 0.40	−1.28, 0.37	—	—	—	1.49	—
Sept. 21, 1938	−0.98, 0.06	−0.67, 0.03	—	−0.43	—	—	0.55
Oct. 24, 1938	0.21	0.21	—	1.8	—	—	0.21
Sept. 1, 1940	0.06	0.06	—	0.06	—	—	0.09
Sept. 14, 1944	−0.64, 0.27	−0.49, 0.21	−0.27, 0.24	−0.18, 0.18	—	1.13	—
June 26, 1945	−0.34, 0.18	−0.24, 0.24	−0.18, 0.27	0.15	—	0.79	—
Aug. 20, 1950	0.21	0.21	0.15	0.18	—	0.24	—
Aug. 14, 1953	−0.79, 0.40	−0.73, 0.34	—	−0.46, 0.34	0.94	1.13	—
Aug. 31, 1954	−0.18, 0.21	0.24	—	0.24	0.49	0.79	—
Sept. 11, 1954	−0.43, 0.15	−0.30, 0.12	—	−0.12, 0.15	0.67	0.88	—
Sept. 27, 1956	0.34	0.58	—	0.64	—	1.13	—
Aug. 28, 1958	−0.37, 0.18	—	—	0.18	—	0.34	—

TABLE 7.38. Storm surge amplitudes (m) as a function of time on the Massachusetts–New York–New Jersey coast during Sept. 21–22, 1938. Time is local time. (Paulsen et al. 1940)

	Sandy Hook, NJ		The Battery, NY		Boston, MA		Mill Neck, NY,
Hour	Sept. 21	Sept. 22	Sept. 21	Sept. 22	Sept. 21	Sept. 22	Sept. 21
01	0.40	−0.49	0.27	−0.21	0.30	0.85	—
02	0.85	−0.37	0.73	−0.18	−0.18	−0.03	—
03	1.19	−0.03	1.13	−0.12	−0.03	−0.49	—
04	1.55	0.58	1.46	0.64	0.49	−0.12	—
05	1.71	1.52	1.59	1.34	1.16	0.24	—
06	1.62	1.74	1.62	1.71	1.92	0.91	—
07	1.34	1.59	1.46	1.71	2.65	1.89	—
08	1.04	1.16	1.22	1.43	3.14	2.80	—
09	0.76	0.76	0.88	1.10	3.20	3.23	—
10	0.49	0.34	0.61	0.61	2.80	2.23	—
11	0.30	0.09	0.37	0.34	2.19	2.80	—
12	0.30	0	0.15	0.09	1.55	2.16	—
13	0.55	−0.03	0.18	0	0.79	1.34	—
14	1.07	0.12	0.55	0	0.21	0.43	—
15	1.80	0.55	1.34	0.30	0.18	−0.24	—
16	2.38	1.01	2.47	0.91	0.91	−0.37	—
17	1.55	1.46	2.04	1.37	1.62	0.15	—
18	0.91	1.74	1.16	1.65	2.13	0.82	—
19	0.24	1.77	1.01	1.74	2.68	1.71	3.54
20	0.09	1.43	0.73	1.65	3.23	2.53	4.60
21	0.76	0.98	0.70	1.34	3.35	3.17	4.02
22	0.79	0.58	1.22	0.91	3.05	3.35	3.78
23	0.24	0.24	0.49	0.52	2.50	3.05	3.69
24	−0.37	0	−0.03	0.21	1.86	2.44	3.66

storms create greater surges in the northern part of the bay whereas the eastern-type storms generate greater surges in the southern portion of the bay. The storm surges resulting from these two types of hurricanes are listed in Tables 7.36 and 7.37.

STORM SURGES ON THE COAST OF NEW JERSEY

The greatest loss of life and property damage on the coast of New England occurred during September 21–22, 1938, as a result of a storm surge generated by a West Indian hurricane coupled with river flooding (due to excessive rainfall). The storm surge amplitude was maximum in Rhode Island with values exceeding 17 ft (5.2 m), and the amplitudes reached record levels all along the coast between New York City and Cape Cod. More than 500 people died (Paulsen et al. 1940) and the property damage exceeded $0.3 billion (at 1938 prices).

The storm surge amplitudes at Sandy Hook on the coast of New Jersey and at three other locations are listed as a function of time in Table 7.38. The surge profiles at Forest Hills and Rockaway Park, both in New York State, are shown in Fig. 1.2 and 1.3.

Pagenkopf and Pearce (1975) developed several storm surge models and applied these to the New Jersey coast. In particular, these authors compared two-dimensional finite-difference and finite-element methods and concluded that, at least for storm surge calculations, there is no particular advantage to preferring one over the other. They also compared their results with bathystrophic storm surge calculations. All these calculations were made for the hurricane of September 14, 1974. The results from the bathystrophic

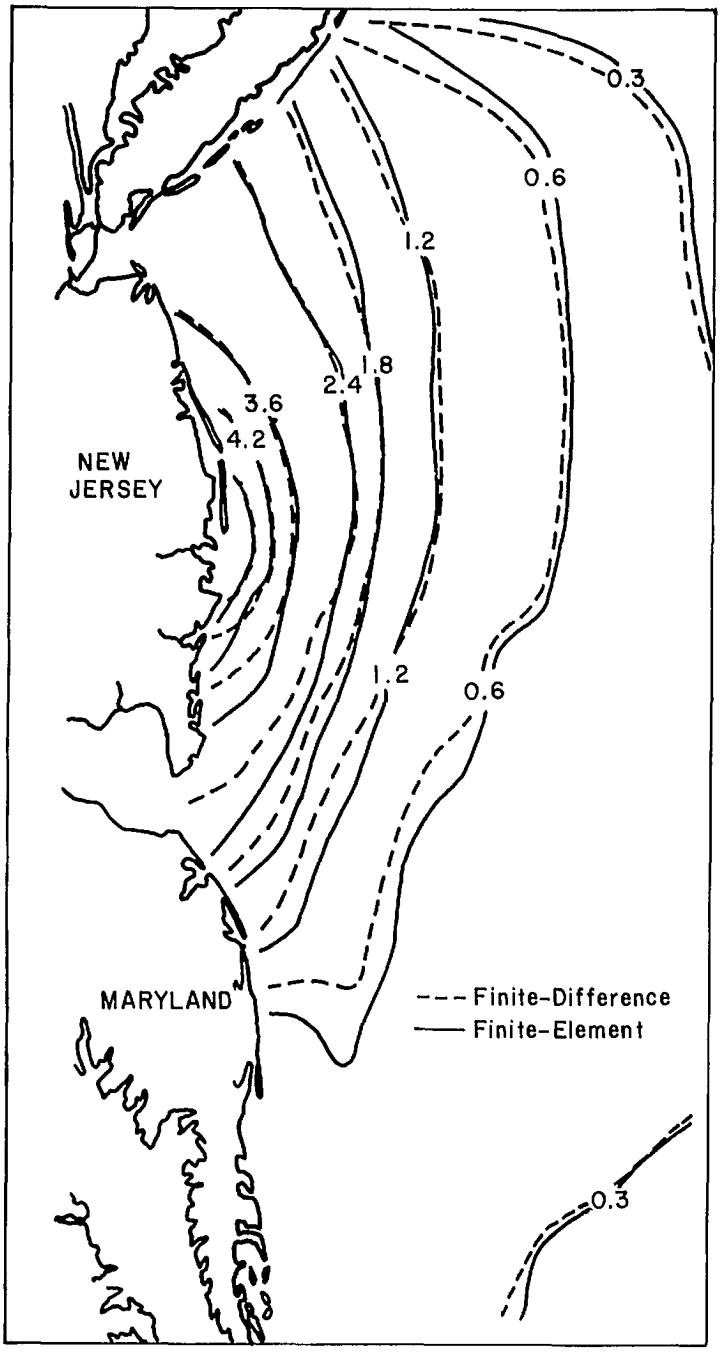

FIG. 7.54. Calculated storm surge heights (metres) along the coast of New Jersey. (Pagenkopf and Pearce 1975)

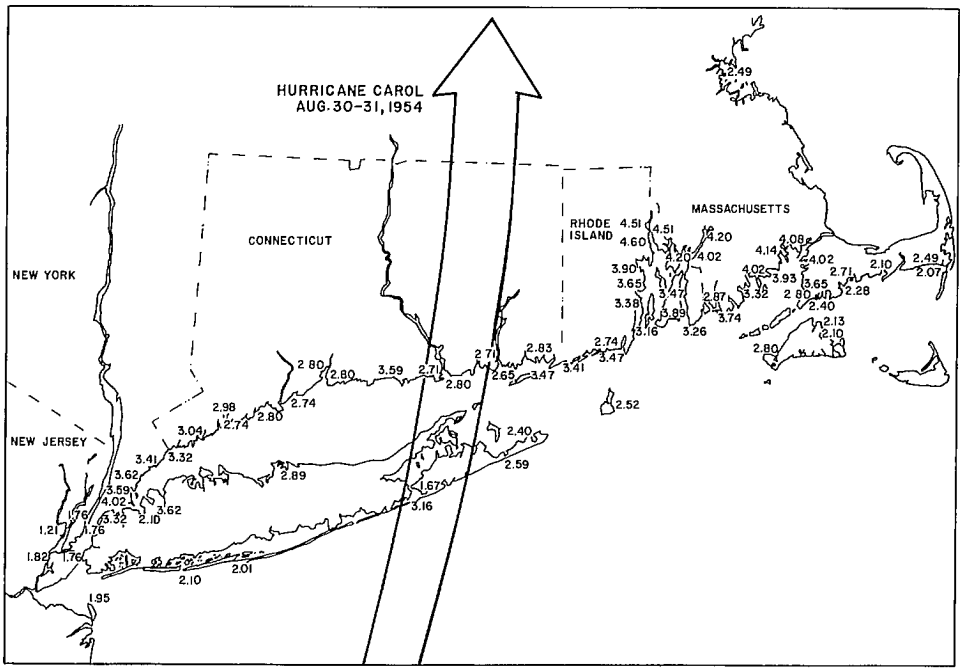

FIG. 7.55. Distribution of storm surge heights (metres) in the New York Bight due to Hurricane Carol of August 30–31, 1954. The arrow shows the hurricane track. (Pore and Barrientos 1976)

calculations are not satisfactory in certain circumstances. The horizontal distributions of storm surge heights computed by the finite-difference and finite-element models are compared in Fig. 7.54.

STORM SURGES IN THE NEW YORK BIGHT

Pore and Barrientos (1976) studied storm surges in the New York Bight due to hurricanes and extratropical cyclones. This subsection will be confined to only hurricane-generated storm surges (extratropical cyclone generated surges will be discussed later). Pore and Barrientos (1976) selected five major hurricanes that affected the New York Bight area: September 21–22, 1938, September 13–15, 1955, August 30–31, 1954 (Carol), September 10–12, 1954 (Edna), and September 12, 1960 (Donna). The storm surge height distributions for the third and fifth hurricanes are given in Fig. 7.55 and 7.56, respectively.

Sethuraman (1979) studied the storm surge due to Hurricane Belle of August 8–10, 1976. The surge at Shinnecock Inlet (Long Island) is shown in Fig. 7.57. This surge occurred near the time of low tide; hence, damage was minimal. The storm surge records showed the three stages discussed earlier, namely, forerunner, surge, and resurgence.

STORM SURGES IN NEW YORK BAY

Kussman (1957) examined the storm surge problem for New York City and surrounding area. The storm surge amplitudes at several locations due to nine hurricanes are

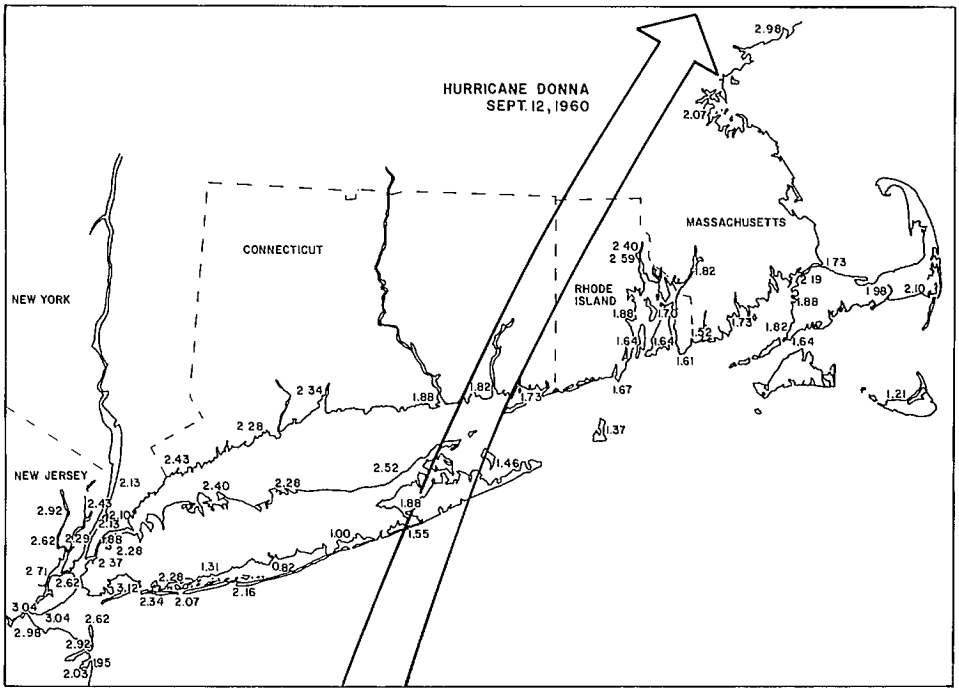

FIG. 7.56. Distribution of storm surge heights (metres) due to Hurricane Donna of September 12, 1960. The arrow shows the hurricane track. (Pore and Barrientos 1976)

listed in Table 7.39. Wilson (1959, 1961) did a comprehensive study of the hurricane-generated storm surge problem in New York Bay. The technique of this study was as follows (Wilson 1961, p. 548):

> A recursion formula is evolved, using the method of finite differences for time increments of 1/3 hour, which relates tide elevation at the bay-mouth with two values of the elevation at 1/3 and 2/3 hour earlier and with values of wind-stress and pressure-gradient driving-force components (directed towards New York Bay from several remote two dimensionally spaced offshore-stations on the continental shelf) at times earlier by the periods taken for free long gravity waves to travel from the stations to the bay-mouth. The formula includes a cumulative forcing function term which allows for the geostrophic influence of the earth's rotation and also for an "edge wave" effect northward along the eastern seaboard. Moreover it takes into account the observed tendencies of hurricane storm tides in New York Bay to develop resurgences at periods of 7 hours with decay rates of 50% amplitude decrease per cycle. The coefficients of the "forcing functions," determined by correlation, tend to represent the storm size and speed and also the dynamic augmentation of the forced wave.

The predicted surge curves at selected locations for a design storm moving with a speed of 35 knots (65 $km \cdot h^{-1}$) are shown in Fig. 7.58. The maximum storm surge amplitude and resurgence amplitude at several locations, due to a designed hurricane, are given in Table 7.40.

TABLE 7.39. Maximum storm surge amplitudes (m) in the New York City area and vicinity due to hurricanes during the period 1938–55. (Kussman 1957)

Location	Sept. 21 1938	Sept. 15, 1944	Nov. 25, 1950	Nov. 7, 1953	Aug. 31, 1954	Sept. 11, 1954	Oct. 15, 1954	Aug. 12–13, 1955	Oct. 14–16, 1955
Fort Hamilton, NY	1.95	2.04	2.29	2.35	1.80	1.31	—	1.37	1.95
Perth Amboy, NJ	2.01	2.26	2.90	2.68	1.77	1.46	1.68	1.62	2.35
Spuyten Duyvil, NY	1.62	1.83	2.13	2.04	1.59	1.22	1.28	1.34	1.80
Lawrence Point, NY	—	—	3.05	3.17	3.32	1.89	1.80	1.59	2.26
The Battery, NY	1.95	1.95	2.26	2.32	1.71	1.16	1.37	1.28	1.80
Sandy Hook, NJ	1.80	2.56	—	2.41	1.86	1.34	1.40	1.25	1.89
Willets Point, NY	3.66	—	—	2.65	3.47	1.95	1.86	1.62	2.38
Montauk (Fort Pond Bay), NY	4.82	2.41	—	1.65	2.41	1.10	0.94	0.64	1.19
New London, CT	2.99	1.86	2.19	1.80	2.65	0.91	1.22	0.76	1.28

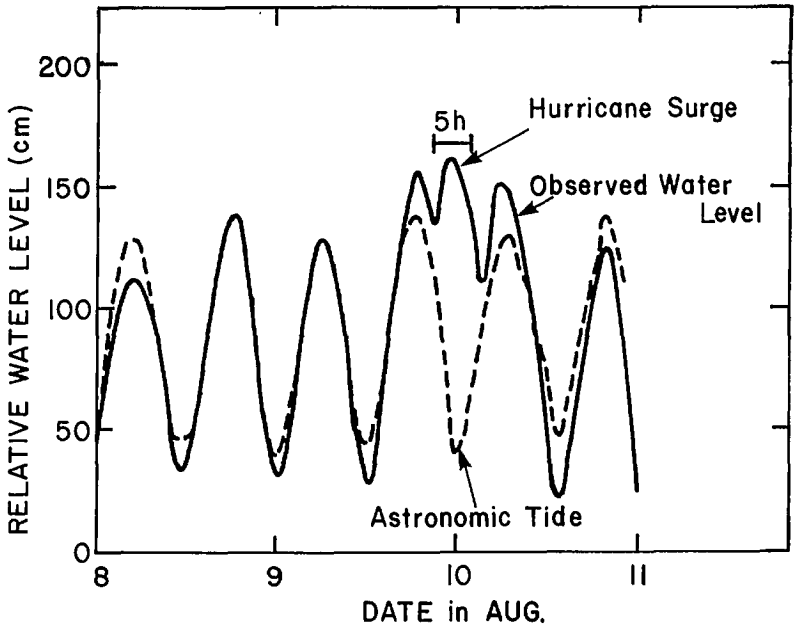

FIG. 7.57. Storm surge and predicted tide at Shinnecock Inlet on Long Island, New York. (Sethuraman 1979)

TABLE 7.40. Predicted maximum storm surge heights due to hurricanes in New York Bay. (Wilson 1959)

	Maximum storm surge height (m)		Maximum first resurgence height (m)	
Station	Surge	Probable error (90% confidence limits)	Resurgence	Probable error (90% confidence limits)
Sandy Hook	2.71	±0.21	1.04	±0.21
Fort Hamilton	2.68	±0.21	1.04	±0.21
Perth Amboy	3.20	±0.30	1.25	±0.30
Elm Park	2.87	±0.46	1.16	±0.46
Whitehall (Battery)	2.53	±0.18 −0.24	1.01	+0.18 −0.24
East Newark	3.11	±0.49	1.25	±0.49
Spuyten Duyvil	2.65	±0.30	1.04	±0.30
Mill Rock	2.99	±1.37[a] −0.91[a]	1.19	+1.37[a] −0.91[a]

[a]The 90% confidence limits are probably better than these for the main surge.

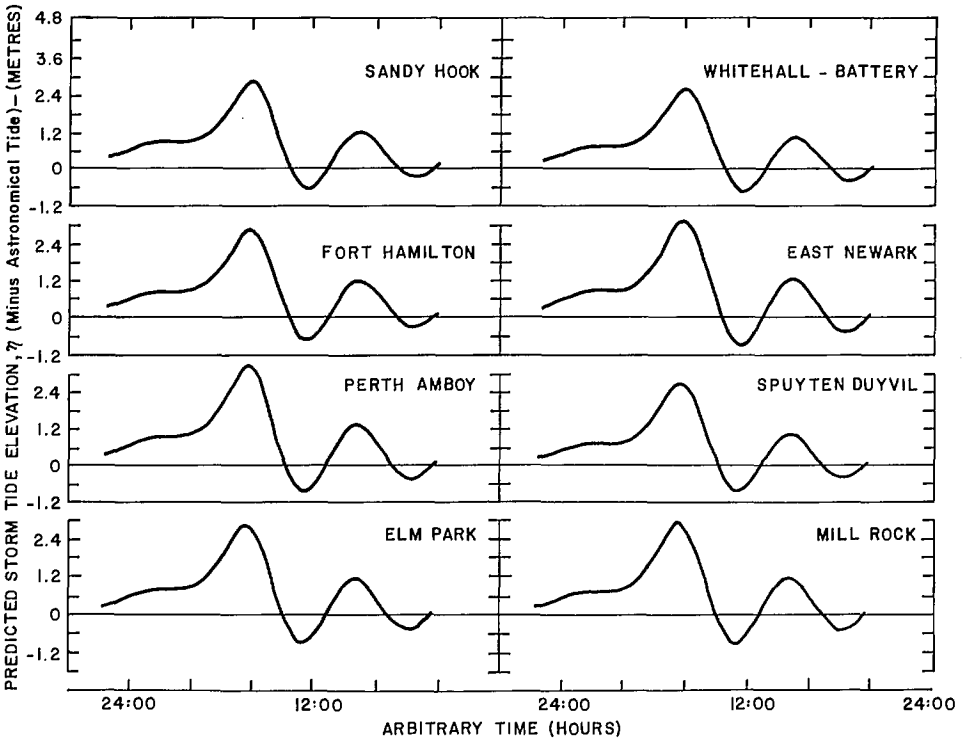

FIG. 7.58. Predicted storm surge heights at various locations in New York Bay for a design hurricane moving with a speed of 65 km·h^{-1}. (Wilson 1959)

STORM SURGES IN NARRAGANSETT BAY

McAleer (1964) studied hurricane-generated storm surges in Narragansett Bay and particularly examined the role of barriers in reducing storm surge levels. The results were arrived at through hydraulic model investigations. Storm surges of up to 10–14 ft (3.0–4.3 m) in amplitude have been observed in Narragansett Bay. A hurricane storm surge in September of 1938 caused $100 million damage and killed 110 people. Ten people were killed in another storm surge during 1954. For some of the major hurricane tracks, Narragansett Bay lies in the dangerous northeast quadrant of the storm.

While some of the major hurricanes move relatively slowly along the southern part of the east coast of the United States, they may move faster when they approach the northern part of the coast. Hence, some storms that were reported as having stalled (or as moving slowly) along the southern east coast suddenly accelerated and caused surges in Narragansett Bay some 8–10 h later.

Numerical and hydraulic models have been used to study the effects of barriers on storm surge amplitudes. The barriers are envisaged as rockfill barriers with large ungated navigation openings across the three entrances to Narragansett Bay. The results indicated that the barriers would reduce the surge amplitudes by 6–7 ft (1.83–2.13 m) over the 120-mi^2 (311 km^2) bay. These barriers will also decrease the mean tidal range somewhat.

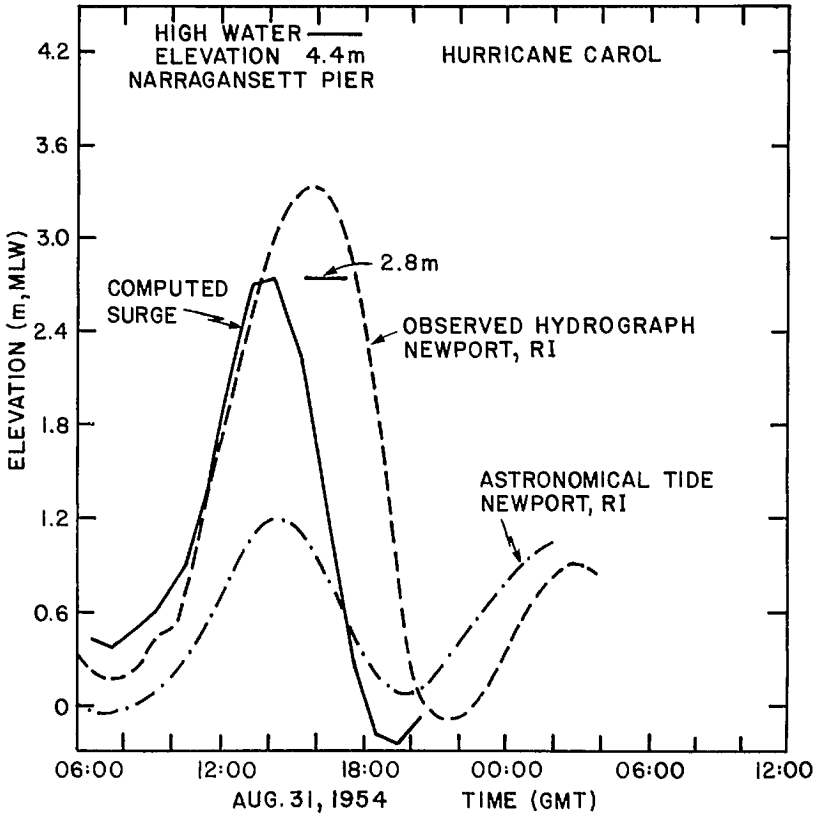

FIG. 7.59. Computed and observed surges at Narragansett Pier due to Hurricane Carol of 1954. (Pararas-Carayannis 1975)

Pararas-Carayannis (1975) used the bathystrophic model to compute the surges at Narragansett Pier, Rhode Island, generated by Hurricane Carol of 1954. This hurricane had a radius of maximum winds of 25 nautical miles (46.3 km) and moved with an average speed of over 33 knots (61 $km \cdot h^{-1}$). Hurricane Carol arrived over Rhode Island at about 10:30 EST on August 31, 1954, with sustained wind speeds up to 90 $mi \cdot h^{-1}$ (145 $km \cdot h^{-1}$) and gusts up to 105 $mi \cdot h^{-1}$ (169 $km \cdot h^{-1}$). At Block Island, gusts up to 130 $mi \cdot h^{-1}$ (209 $km \cdot h^{-1}$) were measured.

Because of its intensity, speed of movement, and arrival at the time of high tide, exceptionally large surges and great destruction occurred. About a third of the city of Providence was under 8–10 ft (2.4–3.0 m) of water for several hours. Pararas-Carayannis (1975) mentioned waves up to 40 ft (12.2 m) in height. Maximum surge at Narragansett Pier was about 12.8 ft (3.9 m). Observed and computed surge profiles at Narragansett Pier are compared in Fig. 7.59.

Extratropical Storm Surges on the East Coast of the United States

In Chapter 6 it was mentioned that at times hurricanes can transform themselves into extratropical cyclones. The circumstances under which this can happen, along with some

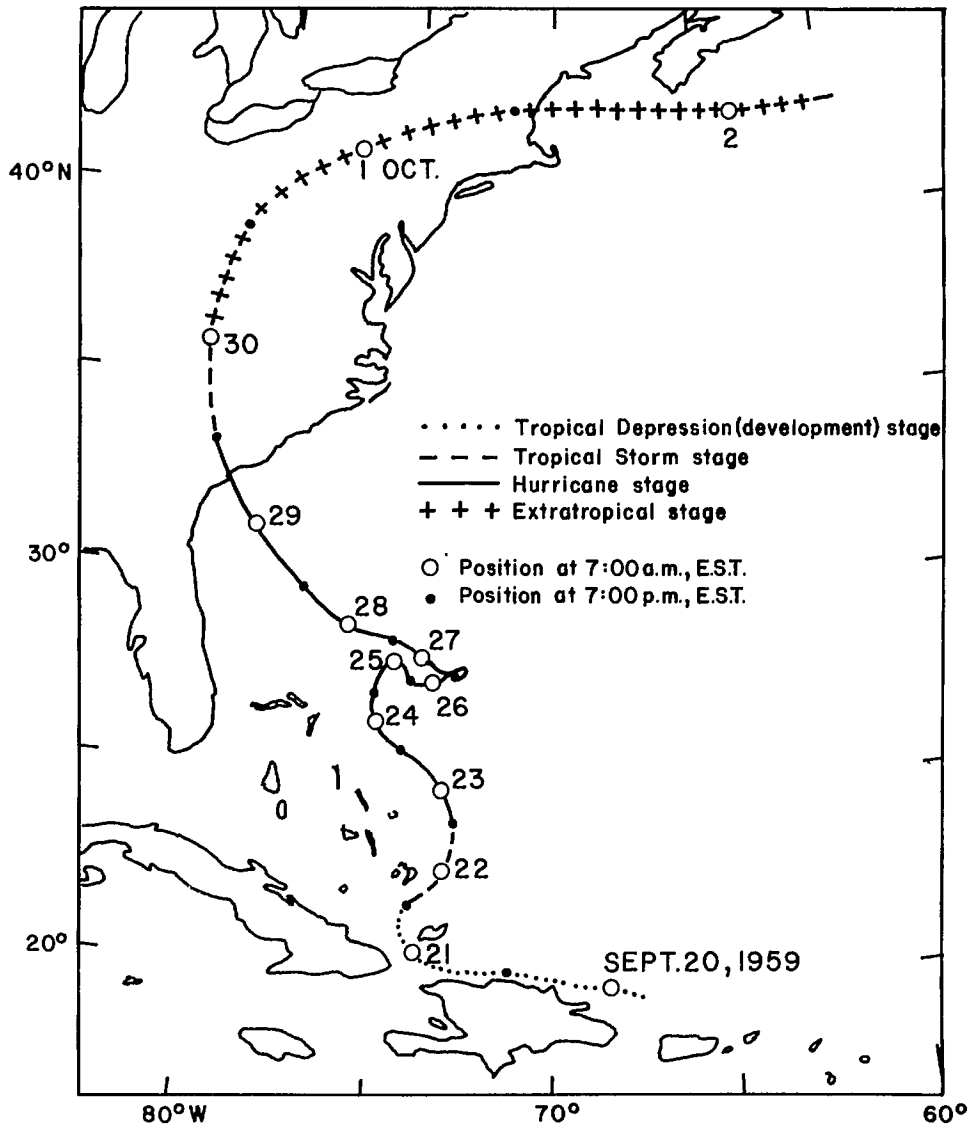

FIG. 7.60. Hurricane Gracie of September 1959 transformed into an extratropical cyclone. The dates are shown along the track. (Harris 1960)

examples, were given. The track of Hurricane Gracie of September 1959 is illustrated in Fig. 7.60. Before September 22 the tropical depression stage and the tropical storm stage are also shown in the diagram. Slightly northwest of Charleston, the hurricane transformed itself into an extratropical cyclone on September 29.

According to O'Brien and Johnson (1963) one of the worst storm surges on the east coast of the United States occurred during March 6–8, 1962. Although it was not called an extratropical cyclone, it really was one and had a diameter of about 1500 mi (2414 km).

TABLE 7.41. Maximum storm surge amplitudes (m) on the east coast of the United States during the storm of Mar. 6–9, 1962. Times given are local times at 75°W. All water levels are with reference to the mean low water. (O'Brien and Johnson 1963)

Location	Maximum water level (surge + tide)	Surge only	Date	Time	Highest water level on record until 1962	Date highest level occurred
New Rochelle, NY	3.66	1.01	6	11:00		
Montauk, NY	1.74	0.94	7	09:36		
Eatons Neck, NY	3.54	1.04	6	23:36		
Port Jeffersen, NY	3.32	1.01	6	23:30		
Willets Point, NY	3.69	1.10	6	11:18		
New York (Battery)	2.83	1.25	6	20:54	3.17	Sept. 12, 1960
Sandy Hook, NJ	3.02	1.37	6	20:24	3.23	Sept. 12, 1960
Atlantic City, NJ	2.77	1.19	6	07:06	2.90	Sept. 14, 1944
Fort Miles, DE	2.96	1.49	6	21:00		
Reedy Point, DE	2.87	1.01	8	00:06		
Philadelphia, PA	2.90	0.98	8	03:12	3.23	Nov. 25, 1950
Washington, DC	1.95	0.94	8	08:54	3.51	Oct. 17, 1942
Sewelles Point, VA	2.44	1.52	7	10:00		
Portsmouth, VA	2.62	1.62	7	10:24		
Wilmington, NC	1.89	0.67	8	23:54		
Myrtle Beach, SC	2.50	0.67	8	21:24		
Charleston, SC	2.50	0.67	8	22:00	3.26	Aug. 11, 1940
Fort Pulaski, CA	2.99	0.52	8	22:06	3.47	Oct. 15, 1947
Femandina, FL	2.56	0.49	8	23:18	4.24	Oct. 2, 1948
Jacksonville, FL	0.98	0.27	9	00:24		
Mayport, FL	1.98	0.40	8	22:30		
Miami, FL	1.31	0.43	8	22:00	1.95	Oct. 18, 1950

The damage due to the storm surge occurred all the way from Florida to southern New England. Another novel feature associated with this surge (unlike with hurricane-generated surges) was the duration of the surge. Whereas the duration of hurricane-generated surges on the same coastal area is usually one to two high tides, this particular surge lasted four to five high tides.

The surge heights and other pertinent information are listed in Table 7.41. This storm, which is referred to as the "Ash Wednesday" east coast storm, was studied in detail by Bretschneider (1964). He cited the occurrence of the surge at the time of the spring tide as partly responsible for the high water level.

The U.S. National Weather Service provides a prediction service for extratropical storm surges (the prediction service for hurricane-generated surges was discussed previously) on the east coast, based on statistical regression models (Pore 1976, 1977). A set of regression equations is derived that relates the surge to atmospheric pressure. A separate regression equation is developed for each tide gauge location. Pore et al. (1975) used 68 historical storms during the period 1956–69. Using sea level weather charts at 6-h intervals, storm surge regression equations were derived for 6-h intervals for 11 locations. Astronomical tide is assumed random in phase. The atmospheric pressure data at these points are used in real time for storm surge prediction.

Pore (1965) developed regression equations for predicting extratropical storm surges in Chesapeake Bay at two locations: Hampton Roads and Baltimore. Wang (1979) studied surges in this water body for the extratropical cyclones of December 1–4, 1974, and April

3–6, 1975. Atmospheric pressure and wind data were used as input. Pore (1964) derived regression relations for extratropical storm surges at Atlantic City. He related the onshore wind components, alongshore wind components, and atmospheric pressure fields with various time lags to the storm surge. In general, the alongshore wind component is found to be more important than the onshore component. Computations using as predictors the components of both wind speed and wind speed squared show both techniques to be about equally satisfactory for practical predictions. Comparison is also made between a one-station model that made use of the meteorological information at Atlantic City alone and a three-station model that included meteorological parameters from Nantucket and Norfolk as well.

The storm surge prediction equation for Atlantic City with the one-station model is

$$S = 13.66 + 0.10V_{-t} - 0.26(p_{-6} - 1000) + 0.30V_{-6} + 0.13V_{-30} \tag{7.46}$$

where S is the surge in tenths of feet, V is the alongshore component of wind in knots, p is the station pressure in millibars, and the subscripts show the time lag in hours.

For the three-station model, the prediction equation is

$$S = 10.60 + 0.36(p_{-6} - 1000)_{ACK} - 0.69(p_{-6} - 1000)_{ORF} + 0.24(V_{-6} + V_{-18})_{ACK} - 0.14(U_{-10})_{ORF} \tag{7.47}$$

where U is the onshore component of wind in knots and ACK and ORF designate the stations Nantucket (Massachusetts) and Norfolk (Virginia), respectively.

Some of the important deductions from this study are as follows: (1) there is no significant difference in the predictability using a linear wind stress law and a quadratic wind stress law, (2) there is a time lag of several hours between the wind and the resulting surge, and (3) the alongshore component of wind is much more important than the onshore component at Atlantic City for generation of extratropical storm surges.

Wilson (1959) studied extratropical storm surges in New York Bay. The distribution of surge heights due to the storm of November 6, 1953, is shown in Fig. 7.61. Pore and Barrientos (1976) studied extratropical storm surges in the New York Bight area. The pertinent information for the six storm surges studied by them is given in Table 7.42. The distribution of surge heights due to the storm of March 1962 is shown in Fig. 7.62.

Donn (1958) developed an empirical prediction scheme for extratropical storm surges on the northen part of the east coast at six locations. The input meteorological data consisted of eight extratropical storms during the period 1952–56. The following are the dates of these storms: January 7, 1952, February 27, 1952, December 22, 1952, January 22, 1953, November 7, 1953, March 16–17, 1956, March 19, 1956, and April 7–8, 1956.

The average lag of the maximum storm surge relative to the time of occurrence of maximum wind at various stations are shown in Table 7.43A and the average lag for each of the storms is given in Table 7.43B. The detailed lags are listed in Table 7.44. It can be seen that, whereas at Willett's Point the maximum surge coincided with the low tide for these cases, at Montauk the maximum surge occurred at the time of high tide. At Atlantic City, Battery, Boston, and Sandy Hook, maximum surges occurred more frequently at the time of low tide than high tide.

Tancreto (1958) used regression techniques to relate maximum value of storm surge at Boston (due to extratropical cyclones) to significant height of wind-generated waves offshore (Fig. 7.63). It can be seen that when the surge height was about 4 ft (1.2 m) the wind wave height was about 34 ft (10.4 m).

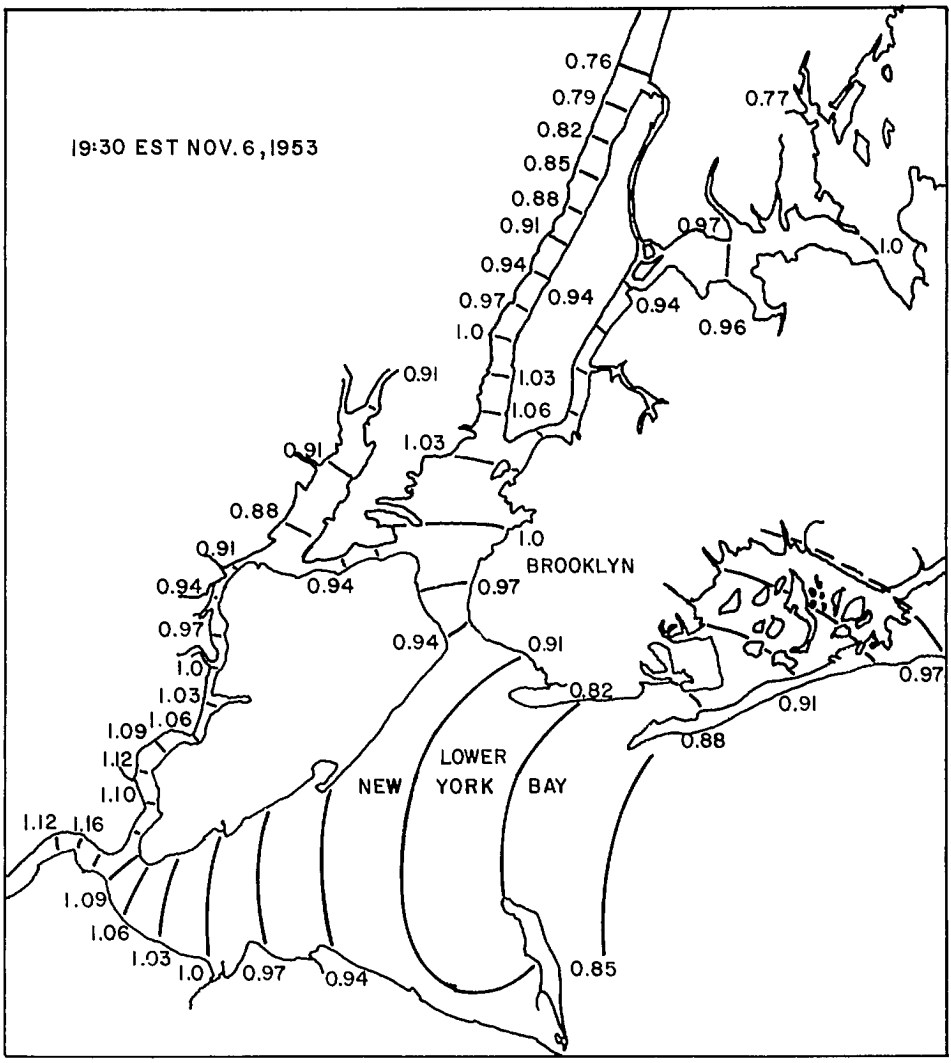

FIG. 7.61. Storm surge heights (metres) in New York Bay at 19:30 (Eastern Standard Time) on November 6, 1953. (Wilson 1959)

STORM SURGES IN THE GREAT LAKES

Storm surges on the Canadian shores of the Great Lakes were considered in section 7.1. The United States part of the Great Lakes will be considered here. The Bulletin of the Beach Erosion Board (1953, special issue No. 2, Corps of Engineers) mentioned that on November 28, 1905, a storm surge of amplitude 2.3 ft (0.7 m) occurred in Duluth Harbor (Lake Superior). In June 1939, a storm surge of 7.4 ft (2.3 m) was noted at Marquette. This bulletin also mentioned that the largest surges in the Great Lakes occur

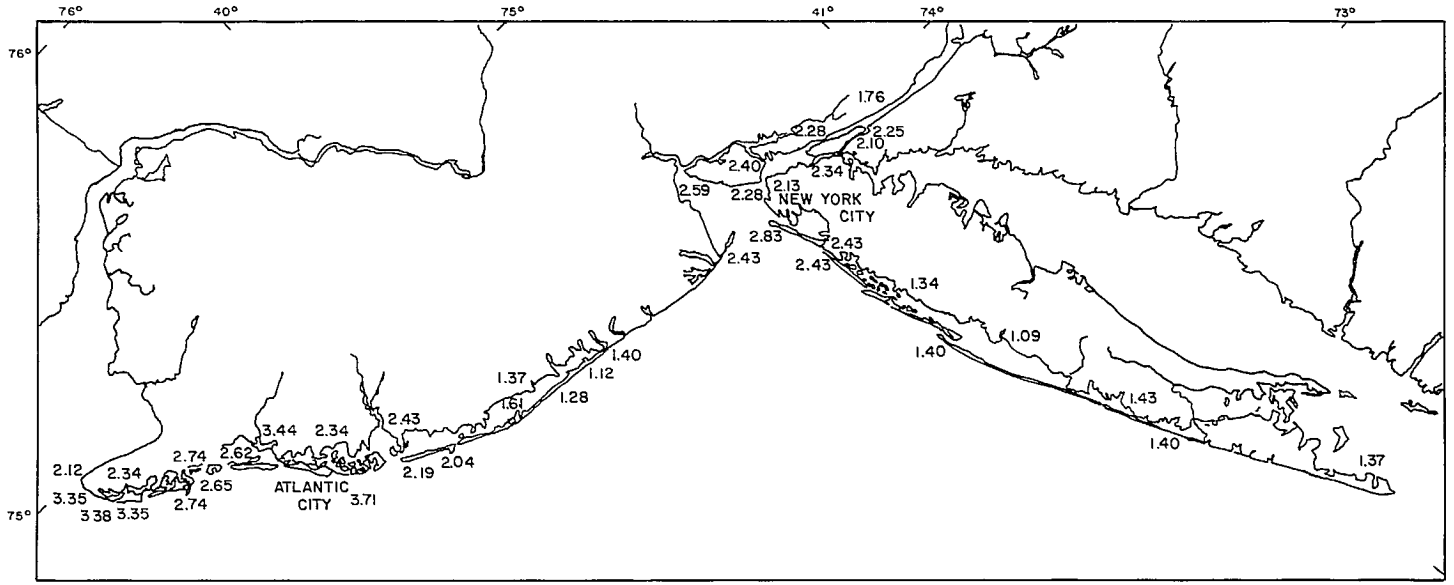

FIG. 7.62. Distribution of storm surge heights (metres) due to the extratropical cyclone of March 6–8, 1962, in the New York Bight area. (Pore and Barrientos 1976)

TABLE 7.42. Episodes of extratropical storm surges in the New York Bight area. Times are EST. (Based on Pore and Barrientos 1976)

Date	Meteorological information	Water level information
Feb. 18–20, 1972	Front of a low pressure system centered over the Great Lakes at 07:00 on Feb. 18, extended southward over eastern Tennessee, Georgia, Alabama, and into the Gulf of Mexico. By 13:00 on Feb. 18 a closed low had formed over Georgia. Further deepening occurred and the storm moved rapidly toward north–northeast to north of Cape Cod at 01:00 on Feb. 20	Storm surge coincided with one of the high tides (two per day). However, it coincided with the lower one. Otherwise, the total water level would have been 0.3 m higher. Extensive damage to coast and region
Nov. 25–26, 1950	Worst storm on record for the eastern United States up to that time. Storm first appeared as a low on a cold front over North Carolina and Virginia. The low deepened considerably before a new low formation became evident at Erie, PA, at 10:30 on Nov. 25. This new center became the main storm and at 19:30 it was near Cleveland with a central pressure of 983 mb. Lowest pressure of 978 mb was reached at 01:30 on Nov. 26. Storm subsequently moved northward	Storm surge occurred during spring tide. Maximum surge at Battery (New York City) was 8.1 ft (2.5 m). Significant interaction between tide and surge
Nov. 6–7, 1953	A low had formed in the northeastern Gulf of Mexico. It moved to off the Georgia–Florida coast by 01:30 on Nov. 6, to Cape Hatteras area by 13:30, and to the Delaware area by 01:30 on Nov. 7. A pressure gradient between the storm's low pressure and a strong high over the Great Lakes brought on extremely high winds north of the storm center	Great storm surges with considerable flooding and flood damage along the mid-Atlantic and New England coasts. Maximum surge at Battery was 5.4 ft (1.6 m)
Mar. 8–9, 1957	Storm closely followed the coast north of Cape Hatteras	Maximum surges of 2.2 ft (0.7 m) at Battery and Atlantic
Mar. 5–8, 1962	At 07:00 on Mar. 5, there was an ill-defined low pressure area with a frontal wave northeast of the Bahamas. Low pressure also extended northwestward through the Carolinas and Virginia. By 07:00 on Mar. 6, the entire low pressure area had deepened, resulting in a long easterly fetch over the western Atlantic north of Cape Hatteras. Storm continued to intensify into an elongated low with a strong northeast wind over a very long fetch	$200 million damage on the coastal areas from southern New England to Florida. Surge coincided with the high tide and also occurred at the time of spring tide. Perigean spring tide also occurred. Variations in maximum water levels of 2–4 ft (0.6–1.2 m) were found within a distance of 0.5 mi. This was the first extratropical storm in which high water marks were observed sufficiently close together to show this variation. Maximum surge values are 6.3 ft (1.9 m) at Breakwater Harbor, DE. Duration of the surge here was over five tidal cycles

TABLE 7.42. *(Concluded)*

Date	Meteorological information	Water level information
Jan. 23–24, 1966	The low developed in the eastern Gulf of Mexico, moved northeast, and was near Cape Hatteras at 01:00 on Jan 23. Later, it moved northeast away from the coast	Large surges and considerable damage along the northern part of the east coast
Nov. 9–12, 1968	Two storms together created surges. The first developed in the Gulf of Mexico and moved northeast along the coast. On Nov. 11 the second storm developed and followed a similar path. Peak wind gusts registered 62 $mi \cdot h^{-1}$ (52 knots) at New York	
Feb. 3–4, 1972	Storm developed near the South Carolina coast and moved rapidly northeastward	Moderate surges in the New York Bight area

TABLE 7.43. Average lag of storm surge at different stations and average lag of storm surge for different storms. (Donn 1958)

Station	Average lag (h)	Storm	Average lag (h)
Atlantic City	5	Jan. 7, 1952	8
Batterry	2	Feb. 27, 1952	1
Boston	4	Dec. 22, 1952	5
Montauk	3	Jan. 21, 1953	1
Sandy Hook	1	Nov. 7, 1953	4
Willets Point	3	Mar. 16, 1956	1
		Mar. 19, 1956	2
		Apr. 8, 1956	1

in Lake Erie (mainly due to its shallowness), especially at Sandusky, Toledo, and Buffalo. An extreme range of 13.7 ft (4.2 m)at Buffalo was mentioned. The highest positive surge at Buffalo observed (up to 1953) was 9.5 ft (2.9 m) on April 1, 1929, and the greatest negative surge was 4.2 ft (1.3 m) on January 30, 1939.

Earlier, the storm surge in the southern part of Lake Michigan due to a squall line on June 25, 1954, was considered. Seven people drowned in Chicago. The storm surge amplitudes at various locations are listed in Table 7.45. This surge was explained as due to resonant coupling between a moving pressure jumpline and the water level in the lake (Harris 1957a, 1957b; Platzman 1958a).

Reference has already been made to the storm surges in Lake Huron. Donn (1959) studied the role of edge waves in the storm surges on Lakes Huron and Erie due to the storm of May 5, 1952. Freeman and Murty (1972) and Murty and Freeman (1973) studied the storm surge in Lake Huron due to the storm of August 22, 1971. Murty and Polavarapu (1975) studied the storm surges in the Great Lakes due to the storms of November 1913, October 1916, and November 1940. Although their study was restricted to the Canadian

TABLE 7.44. Storm surge lags at various locations for different storms. (Donn 1958)

Station	Date	Stage of astronomic tide	Surge lag (h)
Atlantic City	Jan. 7, 1952	Low	14
	Feb. 27, 1952	Low	5
	Dec. 22, 1952	Low	6
	Jan. 22, 1953	Low	4
	Nov. 7, 1953	Low	2
	Mar. 17, 1956	Low	10
	Mar. 19, 1956	Low to high	0
	Apr. 7, 1956	Low	0
Battery	Jan. 7, 1952	Low	8
	Feb. 27, 1952	Low	3
	Dec. 22, 1952	Low	7
	Jan. 22, 1953	Low	−4
	Nov. 7, 1953	High	7
	Mar. 17, 1956	Low	−3
	Mar. 19, 1956	High	0
	Apr. 8, 1956	Low	−2
Boston	Jan. 7, 1952	Low	10
	Feb. 27, 1952	High	5
	Dec. 22, 1952	Low	0
	Jan. 22, 1953	Low	3
	Nov. 7, 1053	Low	2
	Mar. 17, 1956	Low	0
	Mar. 19, 1956	High	10
	Apr. 8, 1956	High	2
Montauk	Jan. 7, 1952	High	5
	Feb. 27, 1952	High	0
	Dec. 22, 1952	High	0
	Jan. 22, 1953	High	6
	Nov. 7, 1953	High	4
	Mar. 17, 1956	High	4
	Mar. 19, 1956	High	2
	Apr. 8, 1956	High	0
Sandy Hook	Jan. 7, 1952	Low	7
	Feb. 27, 1952	Low	−1
	Dec. 22, 1952	Low	6
	Jan. 22, 1953	High	−5
	Nov. 7, 1953	Low	1
	Mar. 17, 1956	Low	−3
	Mar. 19, 1956	High	0
	Apr. 8, 1956	Low	0
Willets Point	Jan. 7, 1952	Low	4
	Feb. 27, 1952	Low	−8
	Dec. 22, 1952	Low	10
	Jan. 22, 1953	Low	−3
	Nov. 7, 1953	Low	6
	Mar. 17, 1956	Low	−3
	Mar. 19, 1956	Low	−1
	Apr. 8, 1956	Low	4

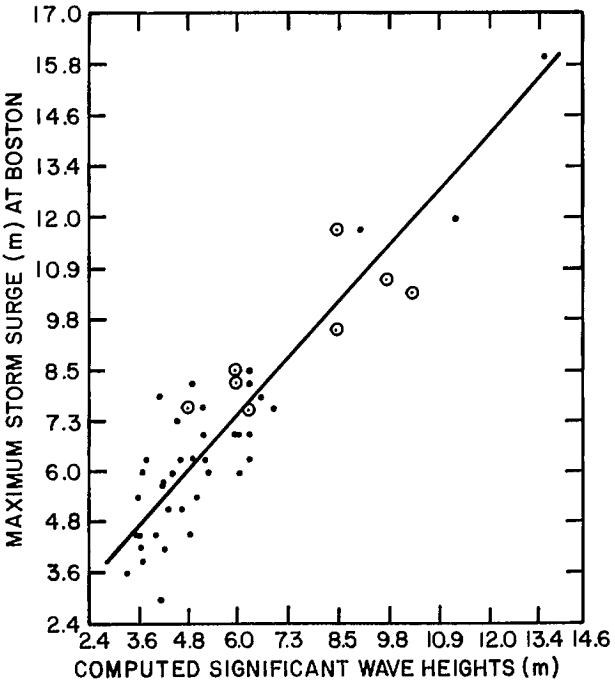

FIG. 7.63. Maximum surge at Boston, Massachusetts, as a function of the computed offshore wind wave heights. The dependent data are plotted as dots and the independent data are plotted as encircled dots. (Tancreto 1958)

TABLE 7.45. Storm surge amplitudes (m) along the south shore of Lake Michigan on June 26, 1954. (Harris 1957a)

Location	Amplitude	Location	Amplitude
Waukegan, IL	0.73	North Avenue, Chicago, IL	2.44[b]
Wilmette, IL	0.98	Chicago River	0.82
Rogers Park Beach, Chicago, IL	1.83	Chicago University campus	0.46
Foster Ave. Beach, Chicago, IL	1.77	79th Street South	0.73
Wilson Ave. Crib, Chicago, IL	1.01	Calumet Harbor	0.58
Montrose Harbor, Chicago, IL	2.07[a]	Gary, IN	0.67
Belmont Harbor, Chicago, IL	2.13	Michigan City, IN	0.91–1.83

[a]May be 2.44.
[b]Estimated.

part of the Great Lakes, these storms were extensive and undoubtedly caused significant surges on the United States shoreline of the Great Lakes also. These storms were extensive enough to affect all five Great Lakes.

Discussion will now concentrate on the storm surges in the United States part of Lake Erie where the most significant surges in the United States part of the Great Lakes occur. One of the earliest studies appears to be by Keulegan (1953). The 22 storm surges on Lake Erie during the period 1900–50 studied by Keulegan (1953) are listed in Table 7.46. A

TABLE 7.46. Storm surges in Lake Erie during the period 1900–50. (Keulegan 1953)

No.	Date	Wind speed, V ($km \cdot h^{-1}$)	ΔH (setup, i.e. surge at Buffalo, surge at Toledo) (m)
1	Nov. 21, 1900	81.3	3.99
2	Oct. 20, 1905	50.5	2.04
3	Oct. 20, 1906	61.6	2.99
4	Jan. 20, 1907	77.4	3.66
5	Dec. 7, 1909	64.5	3.20
6	Dec. 31, 1911	62.6	2.90
7	Jan. 31, 1914	55.8	2.44
8	Dec. 9, 1917	69.5	3.11
9[a]	Dec. 9, 1917	53.3	1.40
10	Dec. 10, 1917	55.2	2.32
11	Dec. 18, 1921	72.6	3.75
12	Dec. 8, 1927	76.3	4.02
13	Dec. 9, 1927	43.8	1.25
14[a]	Dec. 9, 1927	42.0	1.04
15[a]	Dec. 9, 1927	35.6	0.52
16	Apr. 1, 1929	82.6	4.05
17	Jan. 22, 1939	62.4	2.87
18	Sept. 25, 1941	57.5	2.77
19	Jan. 2, 1942	65.0	3.81
20	Jan. 3, 1942	31.4	0.73
21	Nov. 22, 1946	55.0	2.56
22	Mar. 25, 1947	57.5	2.53

[a]Second peak.

plot of the setup ΔH (difference between the water level at Buffalo and at Toledo) and V^2 (wind speed) as a function of time for the storm of December 31, 1911, is given in Fig. 7.64. Correlation of storm surges at Toledo with those at Amherstburg and Gibraltar was reasonably satisfactory. Based on these data, Keulegan (1953) developed a relationship between ΔH and V^2 and used it to compute storm surges for the storms of October 29, 1892, October 14, 1893, September 25, 1941, January 2, 1942, and January 3, 1942. The agreement between observed and computed storm surges for these cases is quite satisfactory.

Hunt (1959) performed a very comprehensive study of the storm surges on Lake Erie. In particular, he paid attention to the role of atmospheric stability in the overwater wind speeds and to the influence of Pelee Point and the islands in the western part of the lake. Finally, he gave a simple method for predicting the surges at Buffalo. The meteorological aspects of this study were considered in Chapter 6.

Hunt (1959) used a stepwise integration by dividing the lake into segments. He drew fetch lines parallel to the wind direction. For most of the southwest storms on Lake Erie, the wind direction is more or less uniform. Thus, the fetch lines will be along the lake's major axis. The lake was then divided into segments, the criterion being that the water depth is more or less uniform in each segment.

The time lag between the wind and the water surface displacement is taken as 1 h. The method of computation is discussed in Anonymous (1955) and Hunt (1954). The

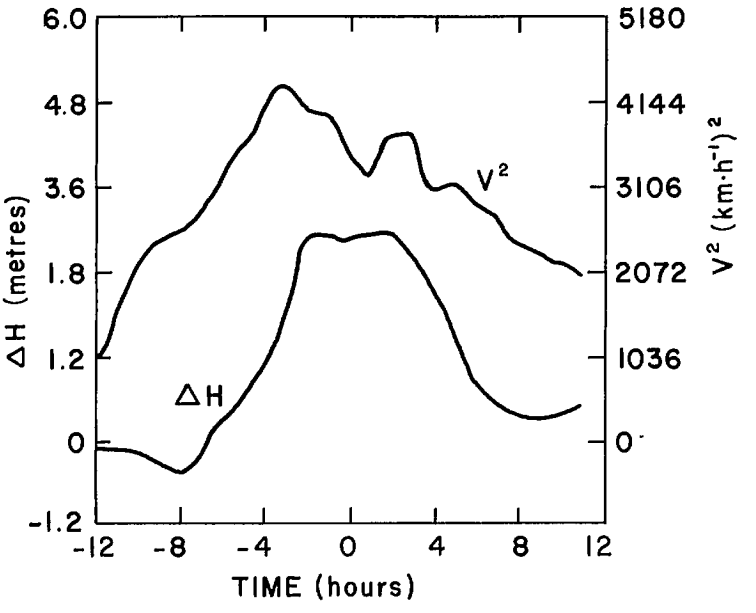

FIG. 7.64. Storm surge setup (ΔH) in Lake Erie and square of wind speed (V) as a function of time for the storm of December 31, 1911. (Keulegan 1953)

computation makes use of the fact that the nodal point is located towards the end from the center of gravity of the lake. It so happens that for lake Erie, for a given wind direction, the position of this nodal point does not depend on the strength of the wind.

The locations of the nodal point and the water level in each segment are determined using the equation

$$\frac{dh}{dx} = \frac{\alpha\tau_S}{\rho g(D+h)} = 1.22 \times 10^{-7} \frac{[U_W - 2 + 0.35(T_A - T_W)]^2}{(D+h)} \tag{7.48}$$

where h is the water level, D is the water depth, U_W is the overwater wind, T_A and T_W are the air and water temperatures, ρ is water density, g is gravity, x is along the axis of the lake, τ_S is the wind stress, and α is defined as

$$\alpha \equiv \frac{\tau_S + \tau_B}{\tau_S} \tag{7.49}$$

where τ_B is the bottom stress. From the above equation a contour map of the water level is made. Then, the volume of the setup is compared with the volume of the drawdown. If they do not agree, the nodal point is moved slightly and the computation is repeated. The Pelee Point topography was included by a 50% reduction of the drawdown in the segment containing the islands. Another interesting result is that, during major storms, the water level at Toledo can be predicted by subtracting 3 ft (0.9 m) from the computed level at Pelee Point.

For the storm of November 8, 1957, the positive surge at Buffalo was 6.5 ft (2.0 m) and the negative surge at Monroe was 5.0 ft (1.5 m). During this storm and several other major west–southwest storms the gauges at the western end of the lake went dry. In the late 1950's the gauge at Toledo was deepened to correct this state. During the storm of

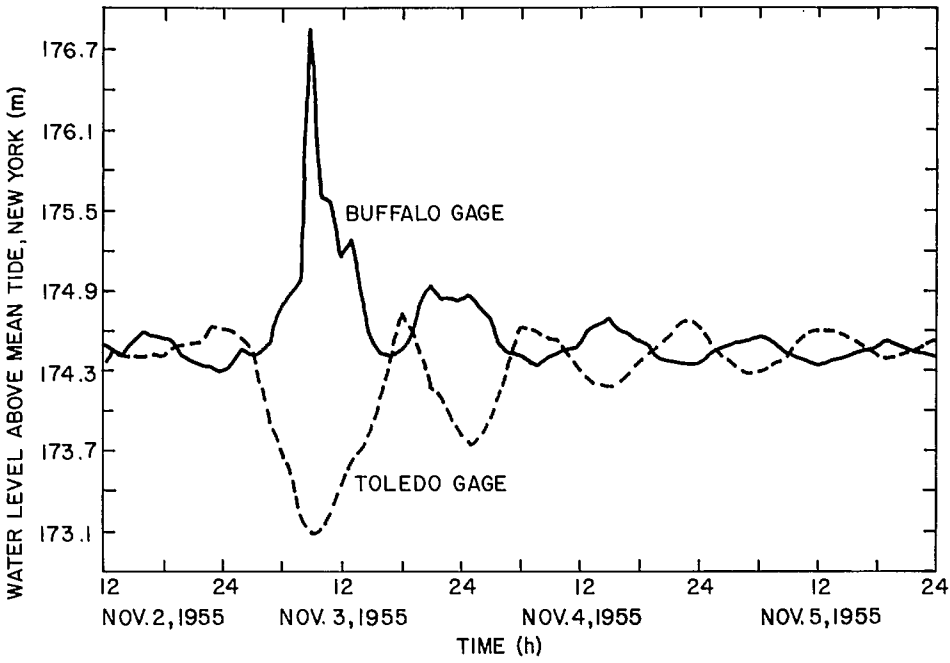

FIG. 7.65. A seiche in Lake Erie resulting from the storm of November 3, 1955. (Hunt 1959)

November 3, 1955, the maximum setup (i.e. water level difference between Buffalo and Toledo) was about 13.2 ft (4.0 m), which consisted of an 8.5-ft (2.6 m) positive surge at Buffalo. Hunt (1959) attributed part of this to seiche action between Long Point and the eastern end of the Lake.

The surge profiles at selected stations for the storm of November 1957 are shown in Fig. 1.4. The seiche that was excited between Buffalo and Toledo by this storm is shown in Fig. 7.65.

Hunt (1959) mentioned that wind setup in Lake Erie causes large surges in the Niagara River. During the storm of November 8, 1957, the water level in the Niagara River rose by 17 ft (5.2 m) in 12 h, and during the same time the flow increased from 118 000 to 253 000 $ft^3 \cdot s^{-1}$ (3341−7163 $m^3 \cdot s^{-1}$). The method of segment computations outlined above appears to work better for Buffalo than for Toledo or Monroe mainly because the Buffalo gauge measures the open water levels and does not respond to the local disturbances. Also, Buffalo is located on the axis of the lake and is not offset, as are Toledo and Monroe. Also, the Pelee Point restriction is too far from Buffalo to have any significant influence. The average error in the calculated maximum setup at Buffalo is only 0.29 ft (0.09 m). A nomogram for computing the positive surge at Buffalo as a function of the wind speed is given in Fig. 7.66.

Harris and Angelo (1963) used statistical regression methods for calculating storm surges on Lake Erie. They mentioned that large storm surges occur at Buffalo more frequently than at any other location in the United States. According to Irish and Platzman (1962) the water level at Buffalo exceeded that at Toledo by at least 6 ft (1.83 m) on 76 separate occasions during the period January 1940−December 1959.

The equation used by Harris and Angelo (1963) is

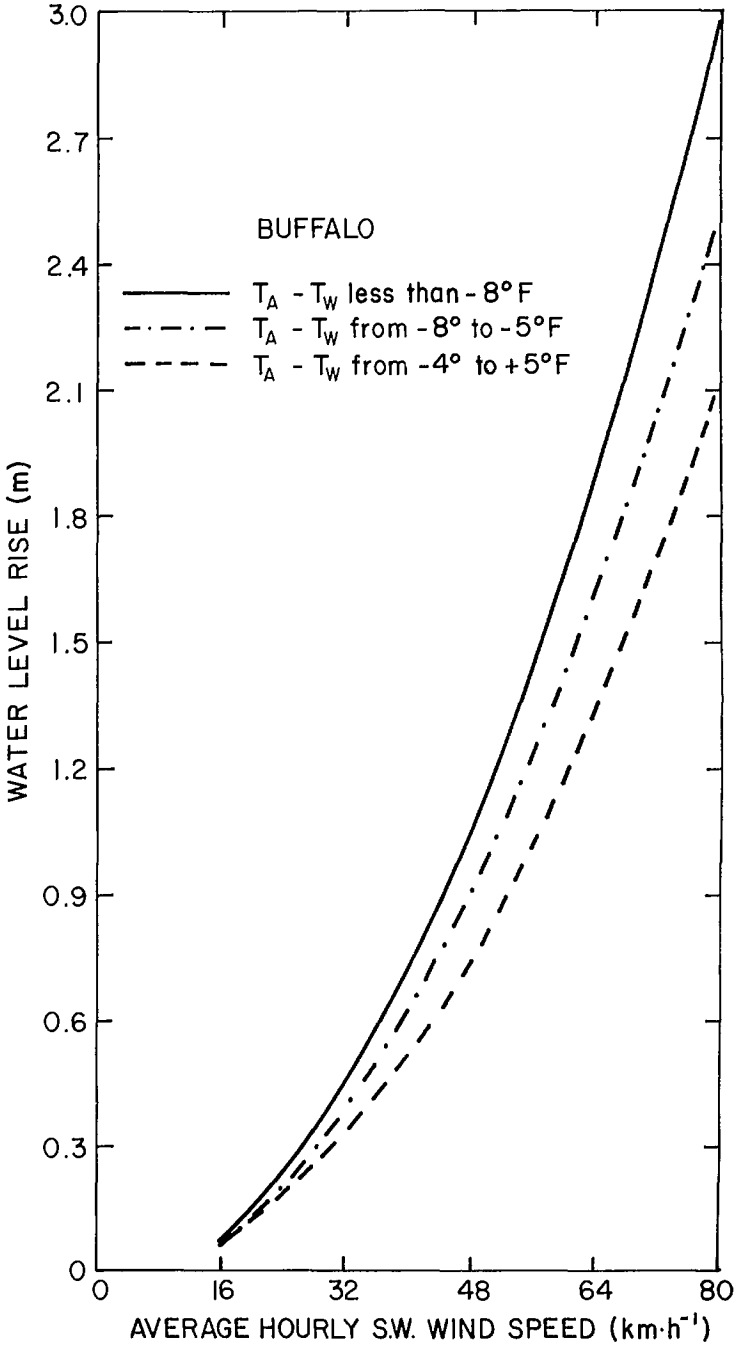

FIG. 7.66. Relationship of water level rise at Buffalo, New York, and the average hourly overland wind speed at Buffalo for southwesterly storms and varying atmospheric conditions. (Hunt 1959)

$$(7.50) \quad h(x_0, y_0, t) = \sum a_{i,j,k}(x_0, y_0) F_{j,k}(t - i\Delta t)$$

where Δt is the time interval between the meteorological observations, i is the number of intervals between the observation and time t, j is an index of the observation station, k is an index indicating the type of observation, $F_{j,k}(t - i\Delta t)$ is the meteorological factor of type k from station j at time $(t - i\Delta t)$, $a_{i,j,k}(x_0, y_0)$ are coefficients that depend on the position (x_0, y_0) for which predictions are desired, and $h(x_0, y_0, t)$ is the predicted surge at time t and location (x_0, y_0). According to these authors, eq. 7.50 contains essentially all the information that is contained in the usual storm surge equations.

The dependent data, i.e. the input data for the regession model for storm surges at Buffalo, consisted of storms on the following dates: November 24, 1942, November 20, 1945, February 12, 1946, December 15, 1946, November 14, 1948, January 17, 1949, January 8, 1950, January 12, 1950, November 14, 1950, March 22, 1951, October 5, 1951, November 2, 1951, December 20, 1951, January 20, 1952, November 24, 1952, February 19, 1953, November 1, 1955, November 15, 1955, and November 3, 1958.

The independent data, i.e. the storms for which the storm surges were computed, were November 30, 1942, December 10, 1943, November 20, 1946, January 19, 1947, November 22, 1947, December 30, 1947, March 1, 1954, September 19, 1954, March 20, 1955, November 14, 1956, and November 19, 1956.

The highest and lowest correlations between observed and predicted surges found were 0.87 and 0.69, respectively. There was no significant difference between the results when a quadratic wind stress law was used instead of a linear stress law. The positive surges at Buffalo were almost always accompanied by negative surges at Toledo. Hence, a similar procedure with some modifications was used for Toledo.

In Chapter 2, the important monograph on Lake Erie storm surges by Platzman (1963) was considered and the works of Richardson (1972) and Richardson and Pore (1969, 1972) were discussed. Pore et al. (1975) deduced that the water level at Buffalo exceeded the monthly mean level by at least 1.4 m once a year and the water level at Toledo dropped by the same amount with the same frequency. This deduction is based on data for the period of 1940–72. Schwab (1978) used a numerical model based on the impulse response function method because this method appears to be more efficient than direct numerical integration of the dynamic equations, if storm surge results are needed at only a few grid points. For hindcast cases, wind observations from the following stations were used: Toledo, Cleveland, Erie, Buffalo, Simcoe, London, and Windsor. Water level data were taken from gauges located at Toledo, Marblehead, Cleveland, Erie, Barcelona, Sturgeon Point, and Stony Point. For actual prediction purposes, wind forecasts at West Erie and East Erie stations issued by the U.S. National Weather Service were used. The surges appear to depend on the two-dimensional structure of the wind field and also on the stability of the atmospheric boundary layer over the lake. For fifteen 5-d hindcast cases at eight water level stations, the overall correlation coefficient between the observed and computed surges was found to be 0.83.

Because water level values are needed only at selected locations for storm surge simulations (not at all the grid points) and since transport components are not really needed, one can use an impulse response method in preference to numerical integration. Also, unlike in numerical integration, no calculation is needed using small time steps. In this method, one represents the components of the meteorological forcing term τ by delta function impulses. Let $g^x(x, y, t)$ and $g^y(x, y, t)$ denote the water level fluctuation resulting from an x impulse and a y impulse, respectively. For the linear case, the water level deviation for arbitrary uniform forcing $\tau(t)$ is given by the convolution integral

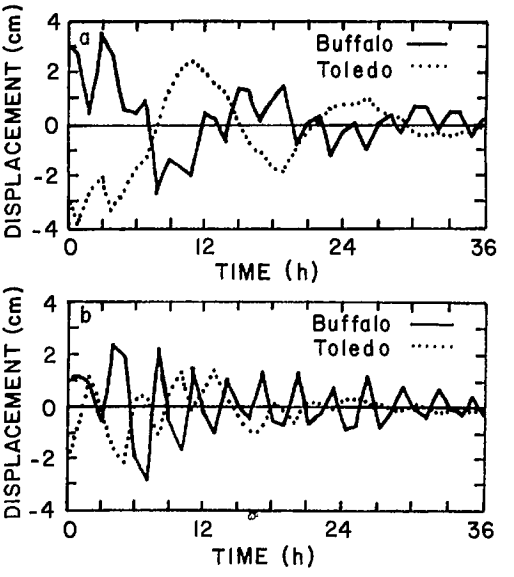

FIG. 7.67. Response functions for 1 dyne·cm^{-2} (1 dyne = 10 N) impulsive wind stress of 1-h duration. (a) Eastward impulse; (b) northward impulse. (Schwab 1978)

$$h(x, y, t) = \int_{-\infty}^{t} g(x, y, t - t')\tau(t')dt' \tag{7.51}$$

where $g = (g^x, g^y)$ is the Green function for the water level.

In practice, in the discretized system, the Green functions can be calculated by permitting the individual stress components to be one unit for the first time step only, integrating forward in time with no forcing and noting the g functions at selected locations. For the time-dependent problem, all one has to do is calculate the discrete analogue of eq. 7.51.

Since the meteorological forcing terms are available at time intervals longer than the time resolution of the impulse response function, the procedure can be somewhat simplified by presumming the discrete g over that period. The response functions due to a spatially uniform wind stress impulse of 1 dyne·cm^{-2}, summed over 1-h periods at Buffalo and Toledo, are given in Fig. 7.67.

To allow for spatial dependence of the wind field, one can follow Platzman (1963) and assign a weighting factor W_i to the m discrete forcing terms:

$$\tau(x, y, t) = \sum_{i=1}^{m} W_i(x, y)\tau_i(t) \tag{7.52}$$

where

$$\sum_{i=1}^{m} W_i(x, y) = 1$$

Here, W_i is taken proportional to the inverse square of the distance from station i. Thus, for the seven meteorological stations used here in the hindcasts, seven response functions

TABLE 7.47. Average monthly and annual frequencies of positive storm surge cases at Buffalo during the period 1940–72. Frequencies are expressed in cases per year. (Pore et al. 1975)

	Storm surge heights (m)					
Month	≥0.61	≥0.91	≥1.22	≥1.52	≥1.83	≥2.13
Jan.	2.31	1.06	0.41	0.16	0.09	
Feb.	1.25	0.31	0.09	0.09	0.03	0.03
Mar.	1.16	0.47	0.37	0.12	0.06	
Apr.	0.72	0.22				
May	0.15	0.06	0.03			
June	0.27	0.03				
July	0.18					
Aug.	0.18					
Sept.	0.70	0.21	0.09	0.03		
Oct.	0.91	0.27	0.09	0.06	0.03	
Nov.	2.85	1.33	0.48	0.21	0.03	
Dec.	2.30	1.12	0.42	0.12	0.03	
Annual	12.98	5.08	1.98	0.79	0.27	0.03

g_i must be calculated for each water level station of interest. Note that the wind-weighting functions W_i are used only for the calculation of g_i. Thus, the water level response for a spatially dependent wind field is

$$(7.53) \qquad h(x, y, t) = \sum_{i=1}^{m} \int_{-\infty}^{t} g_i(x, y, t') \tau_i(t') dt'$$

Hamblin (1979) studied the storm surges in Lake Erie due to the storm of April 6, 1979, which was extensive enough to cause surges at many locations in the Great Lakes. The setup of 4.5 m between Buffalo and Toledo could be the largest ever recorded in Lake Erie. This value can be compared with 4.1 m, which is the maximum setup according to Keulegan (1953) during the period 1900–47, and with 3.9 m according to Irish and Platzman (1962) for the period 1940–59. Maximum wind speeds up to 38 $m \cdot s^{-1}$ were recorded during this storm (April, 1979). This storm also caused surges in Lake St. Clair and Lake Ontario. Schwab (1975) applied the normal mode method to compute storm surges in Lakes Erie and Ontario for the storm of July 22–24, 1972.

Pore et al. (1975) provided statistics on the storm surges of Lake Erie. The average monthly frequencies of positive and negative storm surges at Buffalo and Toledo for the period 1940–72 are listed in Tables 7.47–7.50.

Raney et al. (1979) developed a three-dimensional model from storm surges in Lake Erie and applied it to the possible influence of storm surges on a proposed offshore jet port in Lake Erie.

STORM SURGES ON THE WEST COAST OF UNITED STATES

The west coast has no serious storm surge problems in the strict sense.[6] There are problems associated with wind waves and swell (Todd and Wiegel 1952). In addition,

[6]However, in the months of January and February 1983, major storm surges occurred on the California coast. About 25 people were killed and hundreds of millions of dollars worth of damage to property occurred.

TABLE 7.48. Average monthly and annual frequencies of negative storm surge cases at Buffalo during the period 1940–72. Frequencies are expressed in cases per year. (Pore et al. 1975)

	Storm surge heights (m)					
Month	≤0.61	≤0.91	≤1.22	≤1.52	≤1.83	≤2.13
Jan.	0.41	0.16	0.03			
Feb.	0.16	0.03				
Mar.	0.44	0.06	0.03			
Apr.	0.12					
May	0.03					
June	0.21					
July	0.03					
Aug.	0.03					
Sept.	0.12					
Oct.	0.12					
Nov.	0.18	0.03	0.03			
Dec.	0.45	0.06				
Annual	2.30	0.34	0.09			

TABLE 7.49. Average monthly and annual frequencies of positive storm surge cases at Toledo during the period 1940–72. Frequencies are expressed in cases per year. (Pore et al. 1975)

	Storm surge heights (m)					
Month	≥0.61	≥0.91	≥1.22	≥1.52	≥1.83	≥2.13
Jan.	0.50	0.22	0.06			
Feb.	0.34	0.03				
Mar.	0.94	0.31	0.03			
Apr.	0.47	0.09	0.03	0.03		
May	0.18	0.03				
June	0.21					
July	0.03					
Aug.						
Sept.	0.09	0.03				
Oct.	0.36	0.03				
Nov.	0.48	0.03				
Dec.	0.88	0.12				
Annual	4.48	0.89	0.12	0.03		

seiches and Helmholtz mode could be excited in the bays and harbors due to meteorological causes. Vanoni and Carr (1950) mentioned that wave motion with periods between 1 and 60 min occurs along the entire Pacific coast of the United States. The so-called surging is a serious problem in Long Beach Harbor, California (Herr 1945), and in Depoe Bay, Oregon (Bascom 1950). Wilson (1972) described one such surging case in Long Beach Harbor during August 26–September 14, 1967.

Humphrey and Dorratcague (1976) numerically simulated the storm surges on the northwest coast of the United States. Along the open coast of Clatsop County, Oregon, according to these authors, the maximum levels (estimated for a 100-yr probability) will be a storm surge of 1.2 m, an astronomical tide of 1.4 m, and sea and swell of 3.3 m. One of the largest storm surges on the Pacific northwest coast during the twentieth century

TABLE 7.50. Average monthly and annual frequencies of negative storm surges at Toledo during the period 1940–72. Frequencies are expressed in cases per year. (Pore et al. 1975)

	Storm surge heights (m)					
Month	≤0.61	≤0.91	≤1.22	≤1.52	≤1.83	≤2.13
Jan.	1.62	0.75	0.28	0.09	0.09	
Feb.	1.25	0.31	0.06	0.06	0.03	
Mar.	1.50	0.62	0.37	0.16	0.09	0.03
Apr.	1.09	0.41	0.03			
May	0.39	0.03				
June						
July	0.03	0.03				
Aug.	0.06					
Sept.	0.45	0.09	0.06	0.03		
Oct.	1.18	0.18	0.06	0.03		
Nov.	2.79	1.21	0.63	0.21	0.06	0.03
Dec.	2.24	0.91	0.27	0.09	0.06	
Annual	12.60	4.54	1.76	0.67	0.33	0.06

occurred (not counting the one during January 10–11, 1978) on December 17, 1961. However, this maximum surge of 1.6 m occurred at low tide and, hence, no significant damage was caused.

During the period October 1942–April 1975, there were a total of 200 extratropical cyclones in this area with winds greater than 30 knots (55.6 $km \cdot h^{-1}$) (from directions 165 to 30°S for 4 h or longer). These produced only small surges, if at all. Based on these statistics, Humphrey and Dorratcague (1976) classified the extratropical cyclones on the Pacific northwest coast of the United States as follows (in this classification, the cyclones that generated surges with amplitudes greater than 0.5 m only were considered).

About 50% of these surges are associated with gale force south to southwest winds ahead of cold or occluded fronts of moderate to strong intensity. Usually, the surface low pressure center traveled towards northeast and stalled near Vancouver Island. Occasionally, a blocking Arctic high over the land intensifies the pressure gradient ahead of the front.

Roughly 40% of the surges are associated with strong southwest to west winds south of deep, almost stationary lows on the coast. One of the largest surges ever produced in this area was associated with the storm of December 17, 1961. A simplified version of the surface weather map is shown in Fig. 7.68. The remaining 10% of the surges were associated with complex multiple wave systems.

Storms that did not generate significant surges are the rapidly intensifying deep lows that form just offshore and travel towards the northeast at great speed (e.g. Columbus Day storm of 1962). Although the high winds of these storms cause considerable damage, no significant surges are generated. Even the wind wave action is small due to short wind duration and fetch.

STORM SURGES IN ALASKA

Schafer (1966) used a numerical model to study the storm surge on the northern Alaska coast due to the storm of October 3, 1963, which caused considerable damage and erosion at Barrow. It appears that this was the first major surge since 1901 in this area.

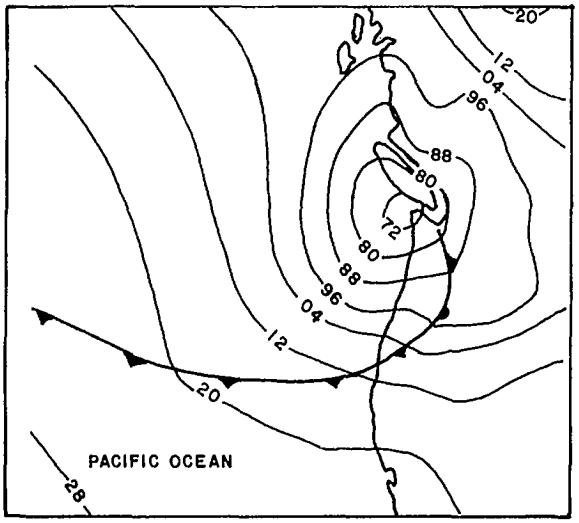

FIG. 7.68. Simplified surface weather chart at 12:00 (GMT) on December 17, 1961, near Vancouver Island on the west coast of Canada. (Humphrey and Dorratcague 1976)

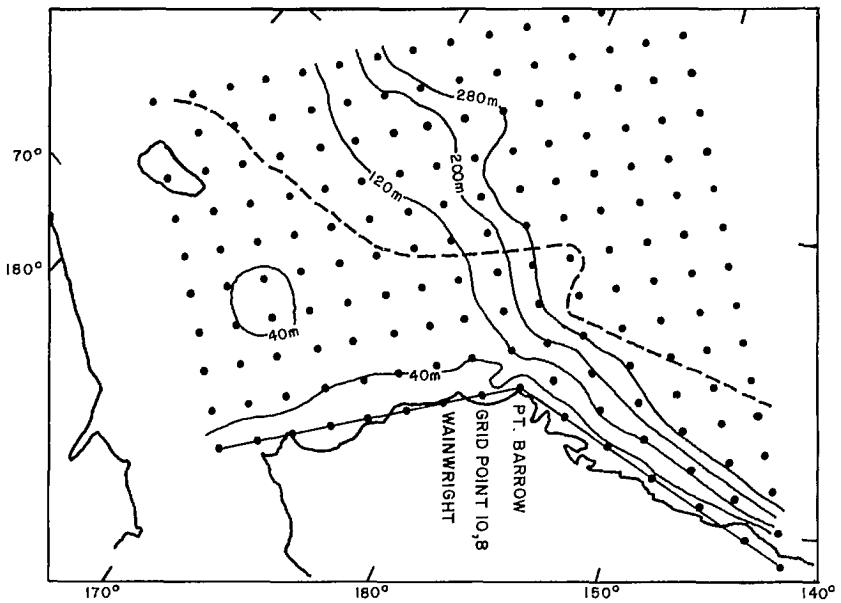

FIG. 7.69. Grid for storm surge computation for the northern coast of Alaska. The broken line represents the boundary of pack ice. (Schafer 1966)

The extratropical cyclone that produced this storm surge had wind speeds of up to 65 $m \cdot h^{-1}$ (105 $km \cdot h^{-1}$). The geography of the area and the pack ice boundary are shown in Fig. 7.69. The open sea boundaries were taken far enough so that the entire fetch for the westerly winds upstream from Barrow is included. Also note that the region of

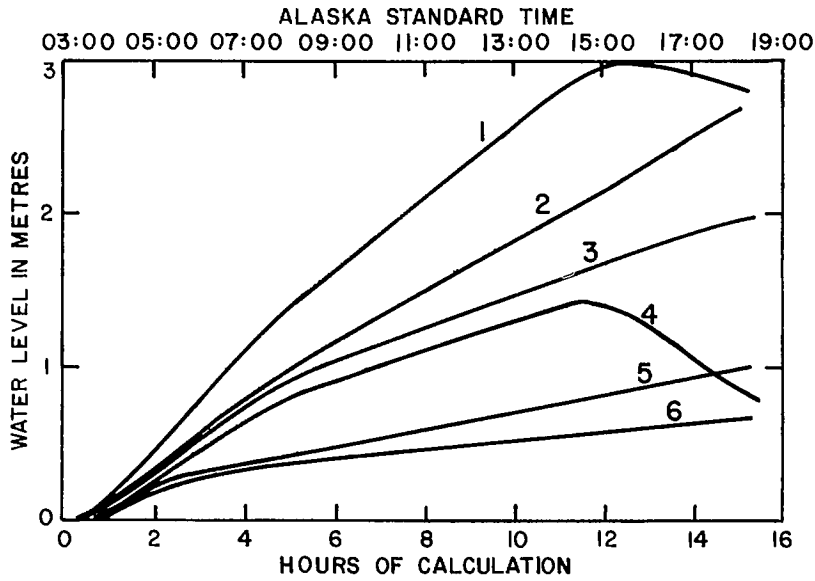

FIG. 7.70. Storm surge at grid point 10,8 (see Fig. 7.69) and at Barrow, Alaska. Curve 1, surge at grid point 10,8 when the observed wind stress was multiplied by 2.0 and used in the calculation; curve 2, same as curve 1 except that the multiplication factor was 1.4; curve 3, same as curve 1 except that the multiplication factor was 1.0; curves 4, 5, and 6, similar to curves 1, 2, and 3 except that these are for Barrow, Alaska. (Schafer 1966)

computation includes parts of the Beaufort Sea and the Chukchi Sea. The western part of the computational region is a shallow shelf, which contributes significantly to the surge. The broken line in Fig. 7.69 shows the edge of the pack ice. It can be seen that there is a wide stretch of open water between the pack ice and the coast.

The calculated storm surge as a function of time at two grid points identified in Fig. 7.69 is given in Fig. 7.70. Curves 3 and 6 indicate that the wind stress, as determined from the weather charts, was used as it was. However, Schafer (1966) had to increase the wind stress (through multiplication factors) to obtain agreement between the computed and observed storm surges. These multiplication factors were 1.4 and 2.0. He justified this multiplication by suggesting that, since the meteorological data in the Arctic are scarce, the analysis from the scanty information obtained from the weather charts could be in error. Note that earlier it was mentioned that numerical modelers generally must increase the wind stress, as obtained from the meteorological observations, to obtain agreement between computed and observed surges.

From the numerical model results, Schafer (1966) concluded that the maximum surge must have occurred near grid point (10,8), which lies in an uninhabited area, and hence, no corroboration is possible. At Wainright, the surge was reported to be 3–3.5 m, which agrees with the calculations. This value is greater than the surge at Barrow.

Hunkins (1965) studied tides and storm surges in the Chukchi Sea. Water level was recorded with a tide gauge at Fletcher's Ice Island (T-3) while it was aground in the Chukchi Sea at 71°55′N and 160°20′W. Here, the mean spring tidal range was 12.5 cm. Storm surges here have a range of about 40 cm. During stationary atmospheric conditions, the storm surge amplitudes agreed with the inverse barometer effect. For moving pressure

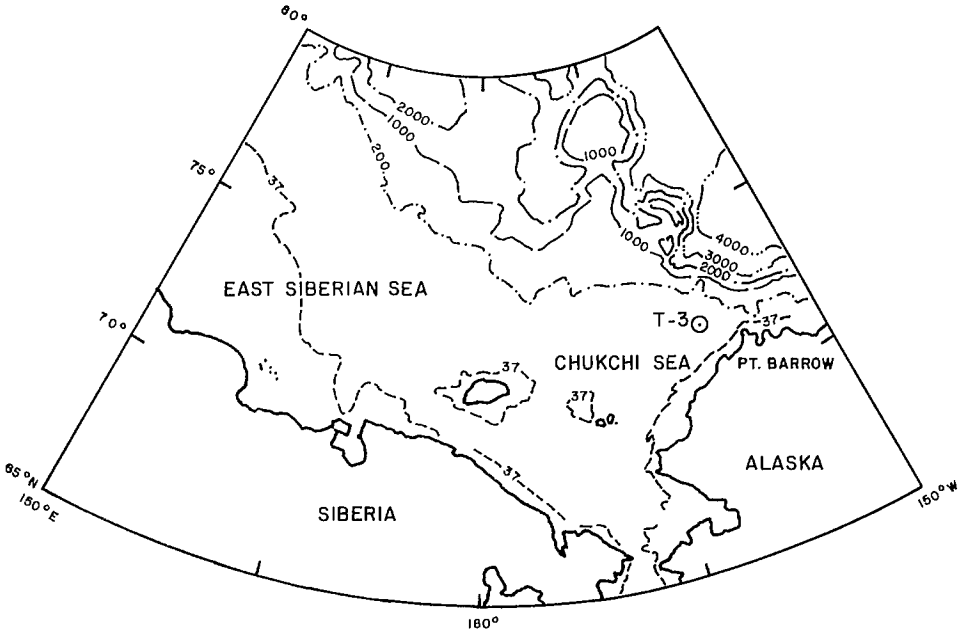

FIG. 7.71. Grounded position of Fletcher's Ice Island (T-3) on the Chuckchi Shelf. Depth contours are in metres. (Hunkins 1965)

systems, however, there was asymmetry in the surge heights, which caused a deviation from the inverse barometer effect.

The Chukchi Sea and Fletcher's Ice Island (T-3) are shown in Fig. 7.71. Hunkins (1965) mentioned that the effect of the pack ice is to increase slightly the wind stress. The storm surge curves obtained after removing the tide from the recorded water level for May 15–June 7, 1961, and for June 11–July 7, 1961, are given in Fig. 7.72. Hunkins explained the asymmetries in the storm surge curves by using a one-dimensional flow model, which has properties similar to a profile through the storm.

Matthews (1971) studied the storm surges on the Arctic Ocean continental shelf. He suggested that storm surges up to 1.5 m in amplitude could occur (here, the mean spring tidal range is 13.6 cm). In winter the enhanced ice cover reduces the wind setup and increases the inverse barometer effect. An intense low pressure system moved north from Siberia and later moved eastwards north of Alaska during October 25–27, 1969, and caused a surge of about 1.3 m at Eluikak Pass on the northernmost point of Alaska.

STORM SURGES IN HAWAII

The Hawaiian Islands are not frequently subjected to storm surges. However, in November 1982, the storm surge caused by Hurricane Eva resulted in extensive damage to the islands of Kaui and Oahu and a few people died. Another major surge occurred in February 1983. Prior to these two surges, major surges occurred in the mid-1950's and some minor ones occurred in the 1970's.

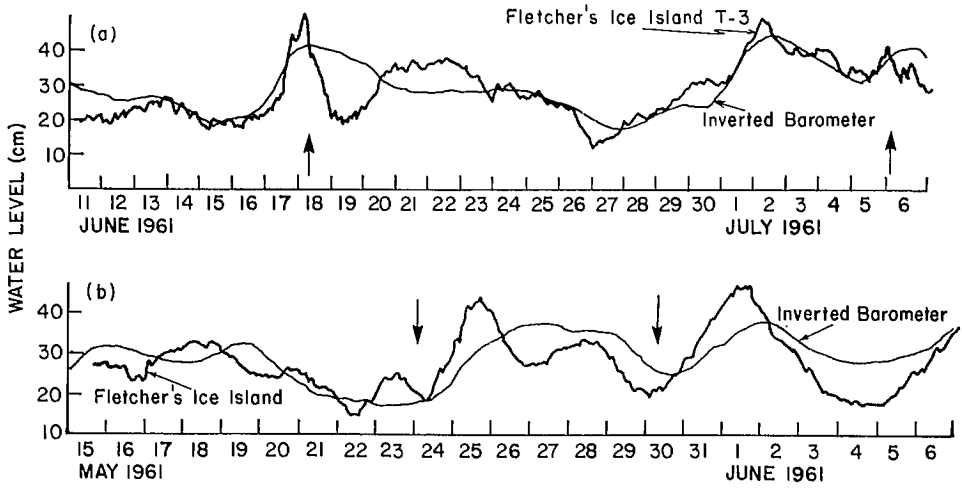

FIG. 7.72. (a) Storm surge heights at Fletcher's Ice Island (T-3) from June 11 to July 7, 1961 (heavy line). The light line is the inverted barometer effect. The two arrows indicate the closest passage of T-3 to two low pressure centres. (b) Storm surge heights at Fletcher's Ice Island (T-3) from May 15 to June 7, 1961 (heavy line). The light line is the inverted barometer effect. The two arrows indicate the closest passage of T-3 to two high pressure centres. (Hunkins 1965)

PLANNING FOR PROTECTION AGAINST STORM SURGES

The number of times destruction was caused by hurricanes on the Gulf Coast and east coast of the United States during the period 1901−55 is given in Fig. 7.73. Simpson and Riehl (1981) discussed hurricane preparedness and plans for protection against hurricanes. Witten (1982) mentioned that the U.S. National Weather Service hopes to compile by 1986 a total of 167 maps covering the entire Gulf of Mexico coast and the east coast of the United States affected by hurricane-generated storm surges. These maps, referred to as "storm evacuation maps," contain information on lake and river basin configuration and water levels, levee systems, roads, evacuation routes, flood-prone zones, high fronts or havens of refuge, populations of cities and towns, etc. Mogolesko (1976) determined the probability of occurrence of a maximum hurricane and its storm surge potential for safety related requirements for nuclear power plants. Earlier, it was seen that the probable maximum hurricane (PMH) is a hypothetical hurricane with the greatest destructive consequences for the locations under question. Seventeen years of tidal data were available at Fort Jefferson, New York (1957−73). Based on high correlations of these data with the data from two nearby Long Island Sound tidal stations, the data are extended to a total of 36 yr by including the years 1938−56. Based on these data, it was estimated that the probability of the occurrence of a PMH is 4×10^{-12}. In other words, the return period is 2.5×10^{11} yr.

Using Gumbels' theory (Gumbel 1958) the return period was determined to be about 10^{12} yr. Mogolesko (1978) felt that 10^{12}-yr return period requirement was too stringent. He felt that a return period of 10^{7} yr was more realistic as far as nuclear power plant safety was concerned. Balloffet et al. (1982) performed a joint probability analysis of storm surges and tides in New York Harbor and Newark Bay.

Richardson (1978) studied shore erosion due to extratropical cyclone generated storm surges on the east coast of the United States. The five cyclones considered by him were

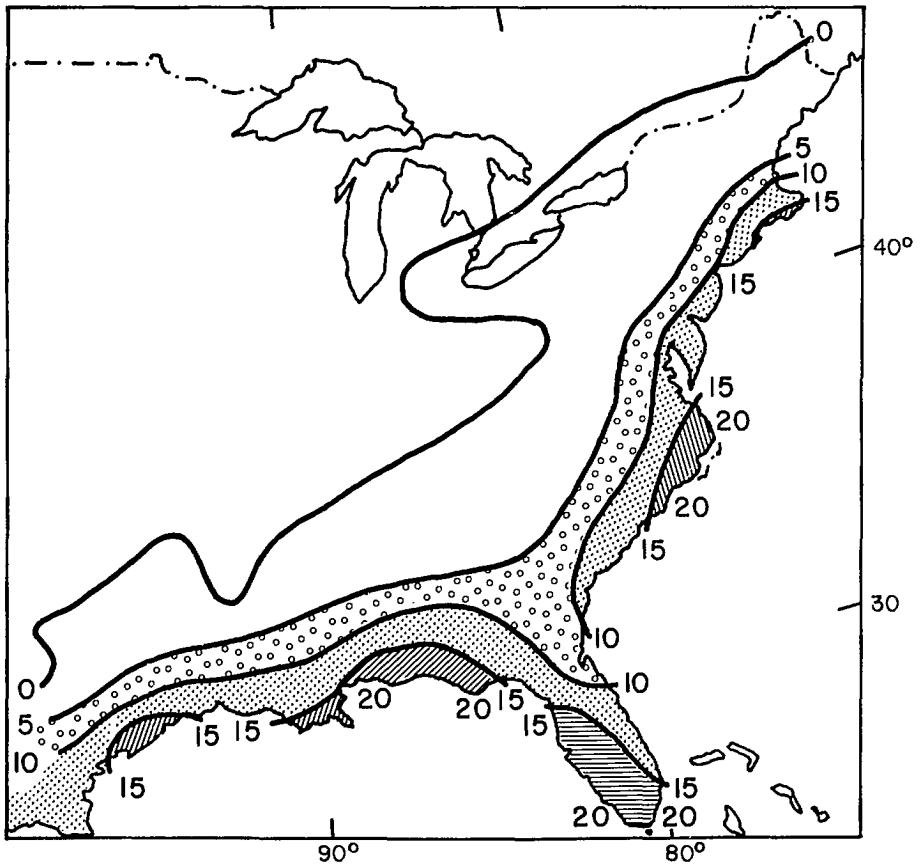

FIG. 7.73. Number of times destruction was caused by hurricanes during the period 1901–55. (Harris 1958a)

(1) March 6–9, 1962, (2) February 19–20, 1972, (3) February 9–11, 1973, (4) March 17–18, 1976, and (5) December 18–19, 1977. Of these, the storms of 1972 and 1976 followed a northeasterly course along the New England coast (path I in Table 7.51) and the other three storms moved off the Carolina coasts in an east–northeasterly direction (path II).

Caldwell (1959) studied shore erosion by storm surges on the Atlantic and Gulf coasts. The results are summarized in Table 7.52. Dolan et al. (1978a, 1978b) studied storm surge erosion along the coast of New Jersey making use of photogrammatic methods. They stated (1978a, p. 21):

> ... a common scale mapping method was developed using historical aerial photography as the data base. Aerial photography of the southern New Jersey coast covering four decades is used to demonstrate the methodology and to provide long-term baseline information on shore dynamics. The data sets include mean erosion rates and variance at 100 meter intervals along the coast. Shore line recession rates along the New Jersey coast are generally less than one meter per year, but for several locations, the rates exceeded 5 meters per year and they vary considerably both within and between the island segments of the New Jersey coast.

TABLE 7.51. Qualitative estimates of beach erosion associated with five extratropical storms. (Richardson 1978)

	Storm				
	Path I		Path II		
State	Feb. 19–20, 1972	Mar. 17–18, 1976	Mar. 6–9, 1962	Feb. 9–11, 1973	Dec. 18–19, 1977[a]
Maine	Severe	Major	Minor	None	None
New Hampshire	Minor	None	Minor	None	None
Massachusetts	Severe	Major	Minor	None	None
Connecticut	Minor	None	Moderate	None	None
Rhode Island	Severe	None	Major	None	None
New York	Minor	None	Severe	None	Minor
New Jersey	None	None	Severe	None	Minor
Delaware	None	None	Severe	None	Major
Maryland	None	None	Severe	Major	Severe
Virginia	None	None	Severe	Severe	Minor
North Carolina	None	None	Severe	Major	None
South Carolina	None	None	Minor	None	None
Georgia	None	None	None	None	None
Florida	None	None	Major	None	None

[a]Preliminary estimates.

TABLE 7.52. Shore erosion due to storm surges. (Based on Caldwell 1959)

Date	Location of eroded coast line	Maximum surge (m)	Duration of surge	Erosion characteristics
Nov. 6–7, 1953	New Jersey	1.83	<2 d	Maximum erosion of the 3-m depth contour was 55 m
Sept. 5, 1950	Florida (Pinellas County)	1.52	>1 d	>100 ft (30.5 m)
Oct. 4–5, 1948	Virginia	2.07	~3 d	30.5 m
Sept. 21, 1938	Long Island	2.74		37 m
June 27, 1957 (Hurricane Audrey)	Louisiana coast (south of St. Charles)	3.05		38 m
Aug. 26–27, 1949	Lake Okeechobee	2.07	2.6 h	18.3 m

These authors designed the OGAS (orthogonal grid address system) for the rapid and systematic acquisition of shoreline and storm penetration information from historical aerial photographs at 100-m intervals along the coast. From these photographs, the movement of the high water line (HWL) is studied statistically. In these studies the shoreline is defined for operational purposes as the high water line and the storm surge penetration line is defined as the line that separates the active, nonvegetated sand areas from the areas of continuous strands of grass and shrub. The mean rate of change in the storm surge penetration line and shoreline for the southern New Jersey coast during the period 1930–71 is given in Fig. 7.74.

Yang et al. (1970) studied the probability of hurricane-generated storm surges at Breakwater Harbor, Lewes, Delaware, making use of Gumbel's theory (Gumbel 1958) and Wemelsfelder's theory (Wemelsfelder 1961). First, results obtained using Gumbel's theory will be considered. From mean sea level records, monthly maximum levels were

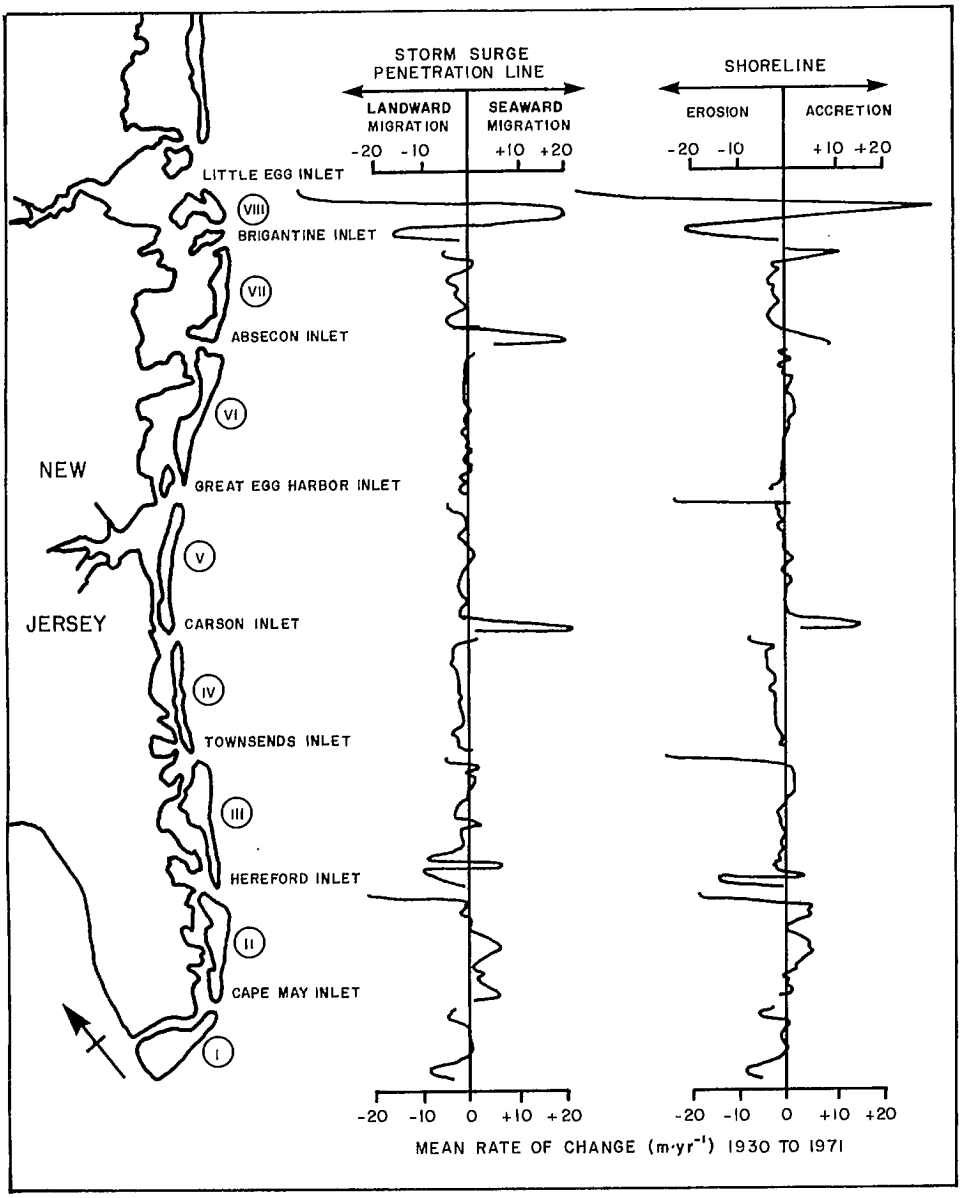

FIG. 7.74. Mean rate of change (metres per year) in storm surge penetration line and shoreline for the southern New Jersey coast from 1930 to 1971. (Dolan et al. 1978b)

obtained at Breakwater Harbor for the period 1953–69. The goal is to predict the probability of occurrence of high water levels based on these data. From the data, the maximum height in each year (365 d) was noted. This is treated as a random variable and is denoted by X. The probability that X is less than or equal to a certain quantity x is the same as the probability that all 365 daily water levels are less than or equal to x. Next, assume that

the random daily levels are independent of each other and have a common probability distribution. Then

$$(7.54) \quad F_X(x) = [F_{X_0}(x)]^n$$

where X_0 denotes the random daily level and $n = 365$. Thus, if the probability distribution $F_{X_0}(x)$ of the random daily level X is known, then using eq. 7.54, the probability distribution of the annual maxima can be determined. Gumbel's theory shows that

$$(7.55) \quad F_X(x) = e^{-\alpha(x-\mu)}$$

provided the number of random daily levels is great, i.e. provided n is a large number. Here, parameters α and μ can be determined by plotting all the data on an extreme probability graph and then fitting a straight line to these data.

The basic difference between Gumbel's theory and Wemelsfelder's theory is in the initial treatment of the data and in the presentation of the results. In the latter theory, instead of selecting the annual maximum out of 365 daily values, one counts the number of exceedances of high water levels in the total period for which observations are available. Thus, unlike in Gumbel's theory (in which there is only one value for each year), in Wemelsfelder's theory, there could be several values in any given year exceeding a specified water level. In Wemelsfelder's theory, one plots this number ν per year against the corresponding water level H, and this plot is referred to as a frequency curve. Then one can use the Poisson probability distribution, according to which the probability p of no exceedance of a level in a given period T is

$$(7.56) \quad p = e^{-\nu T}$$

where ν is now the average rate of exceedance that can be obtained from the frequency curve. The probability of exceeding the specified level is

$$(7.57) \quad q = 1 - e^{-\nu T}$$

Since this probability implies a chance of failure, it is defined as risk. Thus, a relation is obtained between the risk q, the design period T, and the design water level H. The mean rate ν is a function of H through the frequency curve. In Wemelsfelder's theory, the results are presented in a two-dimensional plot, i.e. the abcissa is T, the ordinate is H, and the curves are for various risks q.

The results from Gumbel's theory for Breakwater Harbor and Atlantic City are shown in Fig. 7.75 and 7.76, respectively. In these diagrams the ordinate is the water level and the bottom abcissa is the probability distribution of the asymptote of the annual extremes (i.e $F_X(x)$). The top abcissa is the return period in years. The plotted points are data points. The line in the center is the prediction based on Gumbel's theory. For example, for Breakwater Harbor, the height of 11 ft (3.4 m) has a probability of 0.9 of not being exceeded in any one future year, and on an average it will be exceeded once every 10 yr. Similarly, a height of 12.2 ft (3.7 m) has a chance of 0.98 of not being exceeded in any given year, and on an average it will be exceeded once every 50 yr. The two curves on either side of the central curve are referred to as "control curves" and they form a band. These curves denote the allowable deviation of data points from the central line. If all data points fall within the band, then Gumbel's theory is supposed to be valid.

The frequency curves for Breakwater Harbor and Atlantic City are shown in Fig. 7.77 and 7.78, respectively. The results from Wemelsfelder's theory for Breakwater Harbor are given in Fig. 7.79. In Fig. 7.79, the ordinate is the water level and the abcissa is the design period in years. For example, at Breakwater Harbor, in 50 yr the level of 13.5 ft (4.1 m)

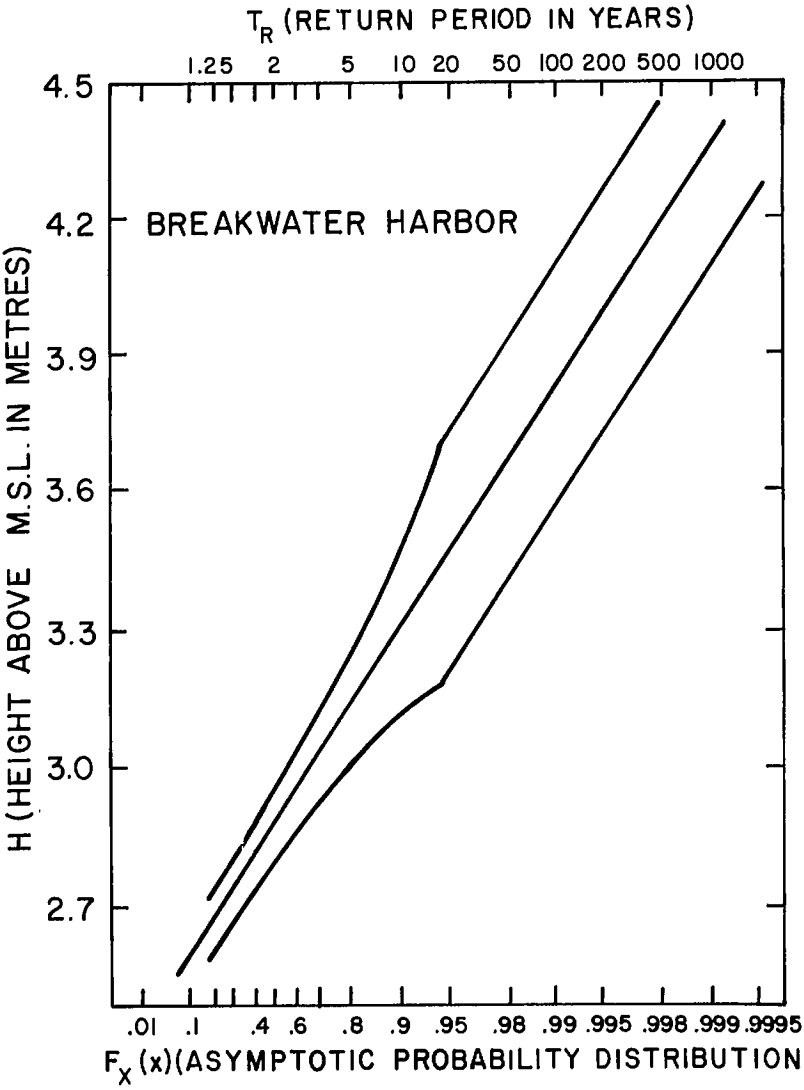

FIG. 7.75. Storm surge probability curves for Breakwater Harbor, Delaware. (Yang et al. 1970)

will be exceeded with a probability (or risk) of 10%, 15.3 ft (4.7 m) with a risk of 1%, and 17.2 ft (5.2 m) with a risk of 0.1%.

Yang et al. (1970), based on their study, concluded that there are certain shortcomings in Wemelsfelder's theory. They stated (1970, p. 2016):

> . . . we could not find a clear ground rule for making the count of exceedances. Suppose that a severe hurricane hits a coastal area for three days with highest water levels on the first and third day. Such an event may be counted as two if the unit of time intervals is a day, counted as 1 if it is a month, or counted as 1 if the entire hurricane unit is counted as a unit.

Another drawback that both theories share is that neither one can take into account

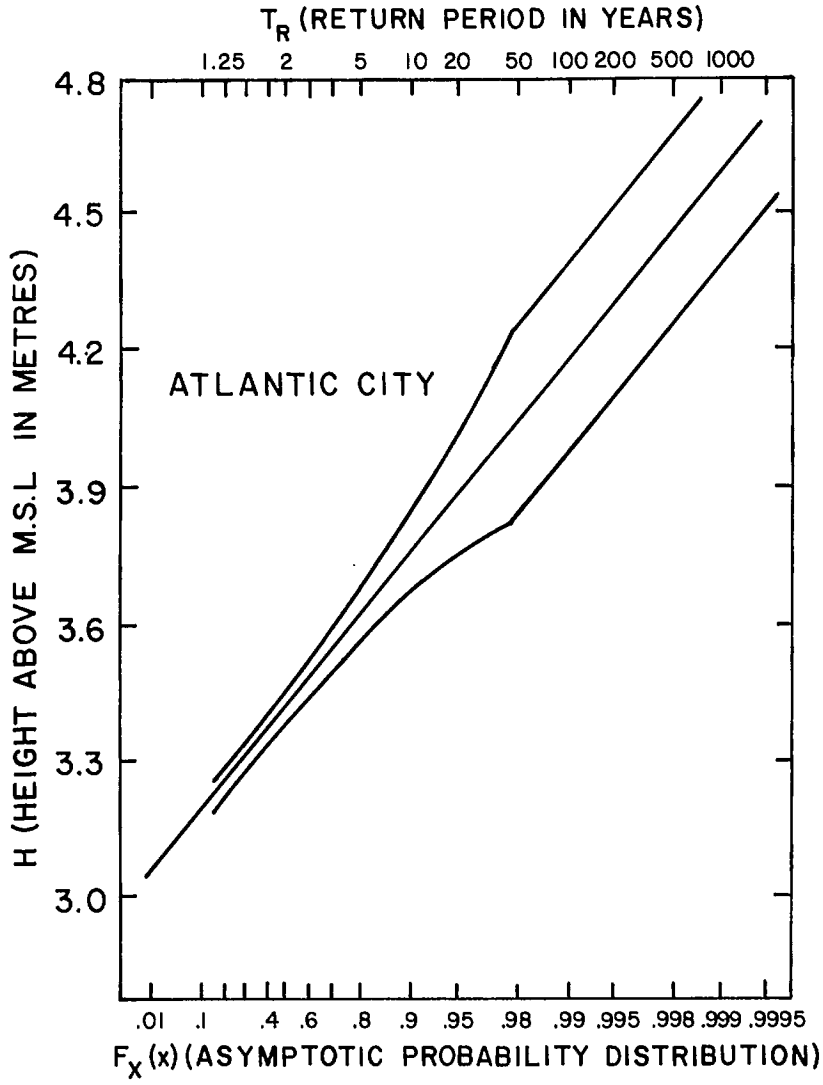

FIG. 7.76. Storm surge probability curves for Atlantic City, New Jersey. (Yang et al. 1970)

the duration of occurrence of the high water levels, which is a very significant parameter for coastal damage. As has been seen in the above study, the total water level is considered (i.e. tide + surge) rather than the surge alone. It might be better to consider the surge alone but one must consider in detail the (nonlinear) interaction between the tide and the surge.

Fallah et al. (1977) extended the earlier study of Yang et al. (1970) to determine the storm surge probability at Breakwater Harbor, Delaware. In this study they recognized the fact that since long-term water level data are not available, one can deduce this from long-term meteorological data through the use of a hydrodynamic model. Thus, a combined statistical (for the meteorological part) and hydrodynamic model is developed. These authors mentioned that Bretschneider (1959) was the first one to use a similar model

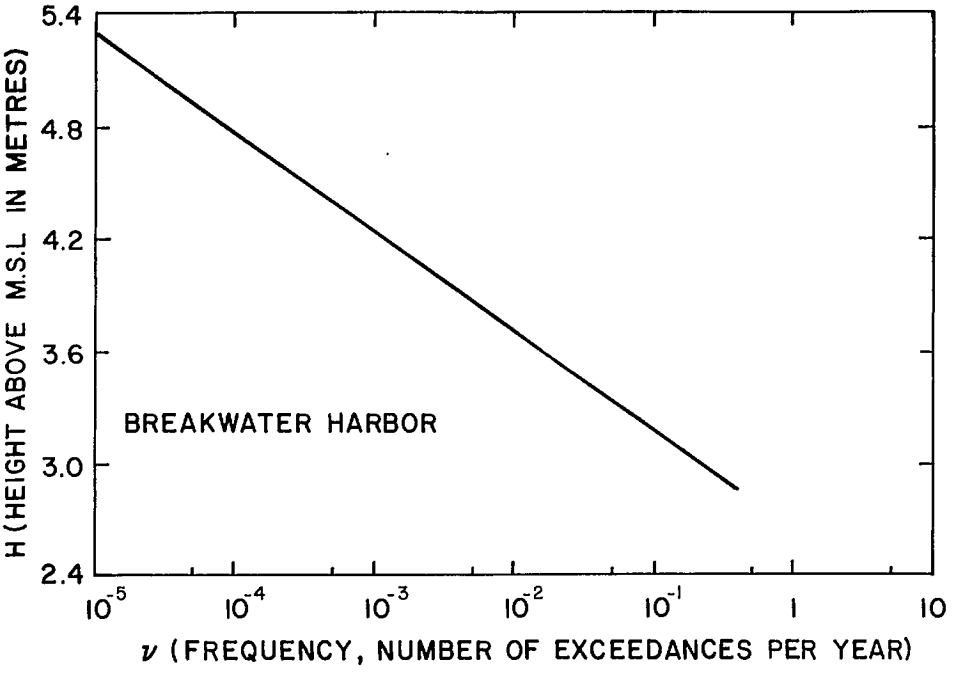

FIG. 7.77. Storm surge frequency curve for Breakwater Harbor, Delaware. (Yang et al. 1970)

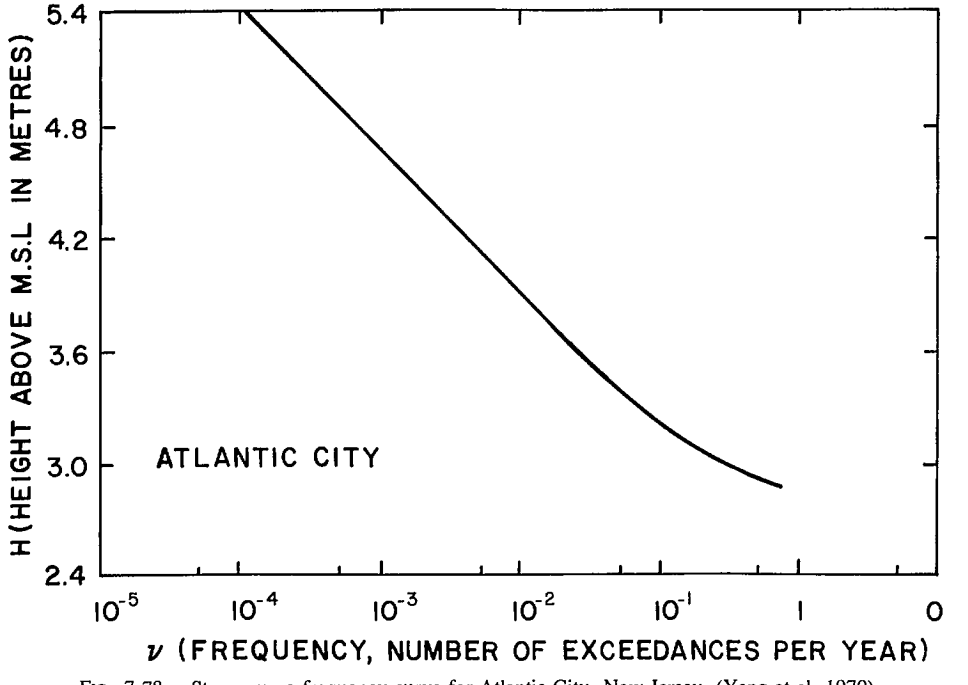

FIG. 7.78. Storm surge frequency curve for Atlantic City, New Jersey. (Yang et al. 1970)

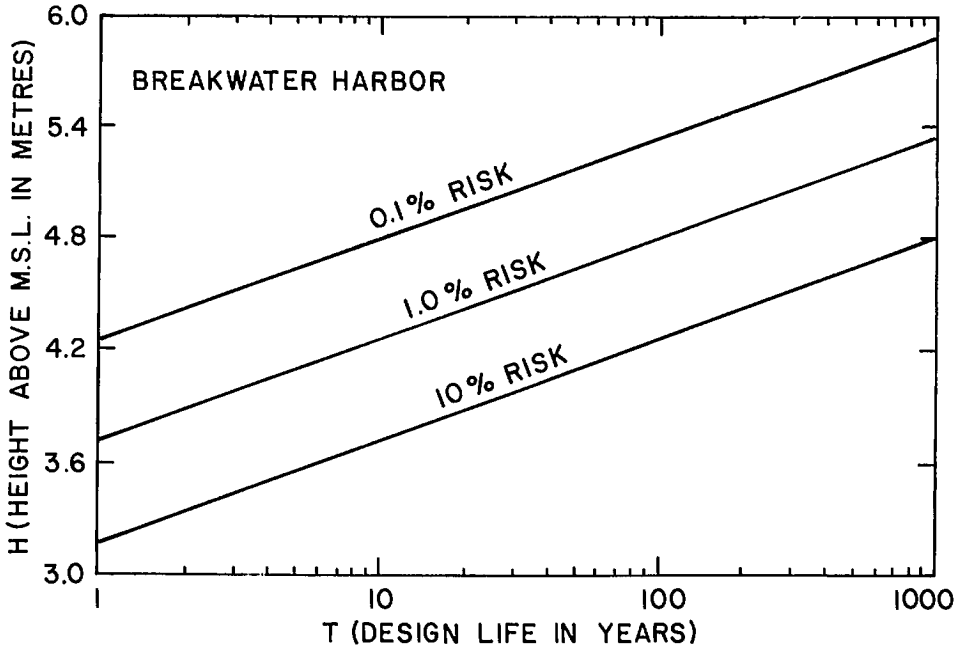

FIG. 7.79. Wemelsfelder risk curves for Breakwater Harbor, Delaware. (Yang et al. 1970)

for Delaware Bay and Chesapeake Bay.

The statistical model used is based on Monte Carlo simulation and consists of the following six steps: (1) estimate the statistical distribution of historical hurricanes and hurricane parameters; (2) generate artificial hurricanes associated with the set of random hurricane parameters; (3) compute the surge heights associated with each artificial hurricane by a suitable hydrodynamic model; (4) combine the hurricane surge with astronomical tide; (5) generate a random total water level (surge + tide); (6) construct extreme value distribution based on yearly maxima.

Bretschneider (1972) gave hurricane data for the Delaware coast for 70 yr. This was used along with the tidal data from Myers (1970). Storm surge data are taken for the period 1953–74 from the U.S. Geological Survey. The hydrodynamic model used was SPLASH II (discussed earlier). There are a total of 792 sample years in this simulation from which important data on the surge + tide and their frequency of occurrence are extracted. These values are plotted on extreme value probability paper (Fig. 7.80). The bottom abcissa is the probability distribution function, i.e. the probability that the yearly extreme is equal to or less than the indicated value. The top abcissa is the return period in years.

In Fig. 7.80 comparison is made among the results obtained by Yang et al. (1970) for Breakwater Harbor, by Myers (1970) for Atlantic City, by the Corps of Engineers (1972) for Rehoboth Beach, Delaware, and the present results. The results from the Corps of Engineers and by Myers appear to be overly conservative.

Myers (1975) studied storm tide frequencies due to hurricanes along the coast of Carolina. The technique that was used in this study has been used by NOAA for similar studies for other parts of the east coast and Gulf Coast of the United States with the aim of providing technical information for the Federal Insurance Agency. Specifically, storm

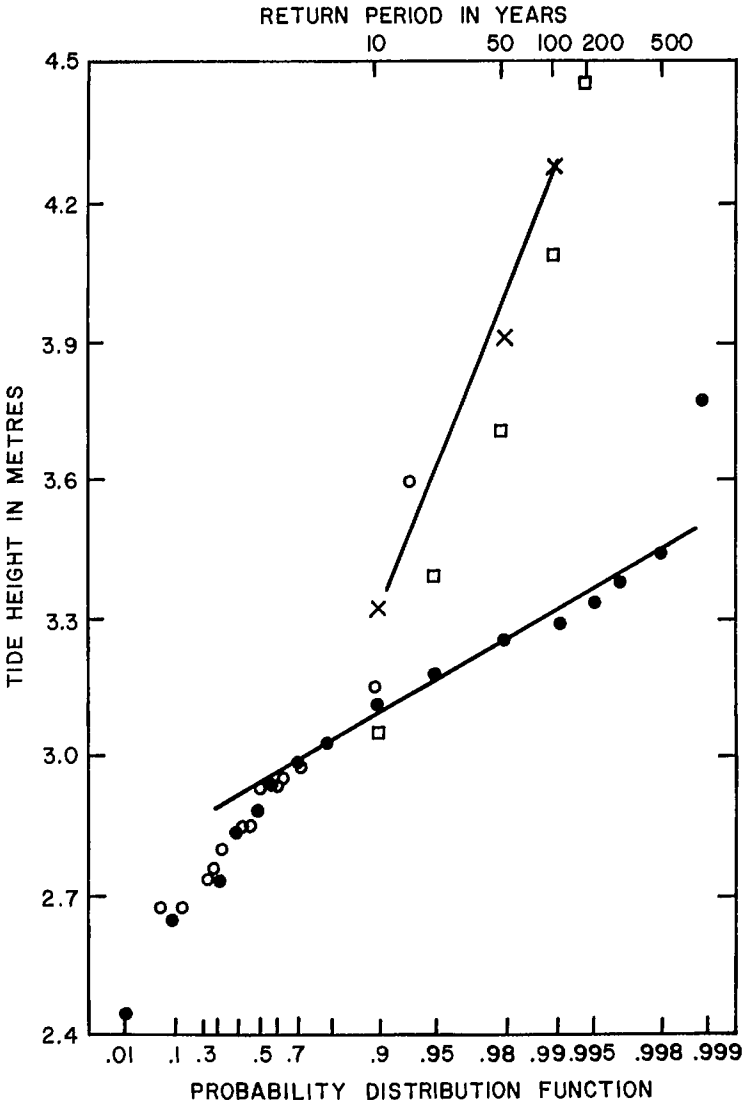

FIG. 7.80. Maximum storm surge heights, their probability of occurrence, and return periods for Breakwater Harbor, Delaware. ●, Urban Development (1976) simulation (792 yr); □, Myers (1970) model for Atlantic City; ○, Yang et al. (1970); ×, Corps of Engineers model (1972). (Fallah et al. 1977)

tide (here, storm tide refers to storm surge plus astronomical tide) levels with return periods (or recurrence intervals) of 10–500 yr are examined. The so-called "joint probability method of tide-frequency analysis" used here consists of three steps: (1) determination of the climatology of hurricane characteristics; (2) development of a hydrodynamic model to calculate storm tide levels on the coast due to hurricanes; (3) synthesizing this information into storm tide frequency analysis.

In this study the astronomical tide and the storm surge are simply added and the

(nonlinear) interactions are not considered. The time of occurrence of the surge relative to the tide is very important. Hurricane Gracie of September 29, 1959, produced a maximum surge of 8.3 ft (2.5 m), which occurred at the time of low tide on the lower South Carolina coast. Hence, the total storm tide was only 5.6 ft (1.7 m) at Charleston, South Carolina. Had the surge occurred some 6 h later, the total storm tide would have been 11.2 ft (3.4 m). Hurricane Hazel of October 15, 1954, struck Myrtle Beach and produced a surge at the time of high tide. Had the surge occurred at the time of low tide, the storm tide would have been 6 ft (1.83 m) smaller. In this joint probability method, it is assumed that the hurricane arrival time is independent of the state of the tide.

The climatological data used are central pressure of the hurricane, radius of maximum winds, directional approach to the coast, and forward speed. Some of the major hurricanes used in this study and the relevant information are listed in Table 7.53. Based on the hurricane data, probability distribution functions were derived for radius of maximum winds, hurricane forward speed, and direction of forward motion. The hydrodynamic model used is SPLASH II. The maximum storm surges for 17 cases at Charleston are given in Table 7.54.

Next, the Florida coast will be considered. It is only affected by hurricanes and not extratropical cyclones. Bruun et al. (1962) related Florida's coastal topography to its storm surges and stated (p. 1):

> Practically all of the East Coast of Florida consists of a barrier island chain broken occasionally by inlets. At Cape Canaveral the ocean beach is the greatest distance from the mainland — about 15 miles [24 km]... South of Miami Beach, Keys extend southwestward to Key West and small islands continue to Dry Tortugas ... Mangrove swamps comprise the coastline from Cape Sable to Cape Romano on the lower west peninsula. From Cape Romano to Anclote Keys the outer shore of the Gulf is formed of barrier islands, mostly low and without sand dunes. North of Anclote Keys the Gulf shoreline consists of tidal flats through Apalachee Bay ... A barrier island system continues on the northwest of Apalachee Bay. However, between St. Andrew Bay and Choctawhatchee Bay the Gulf Beach is on the mainland for approximately 80 kilometers, an unusual but not unique feature in Florida's coastal topography.

Bruun et al. (1962) mentioned that hydraulic models for studying storm surges have been constructed for Sarasota Bay, Bakers Haulover Inlet (near Miami), Lake Worth Inlet, and Boca Raton Inlet. Based on these hydraulic studies, diagrams for return periods of storm surges (5- to 100-yr range) were developed for 15 coastal sections. A statistical analysis was performed of all available data. The frequency curves for six locations on the east coast of Florida are shown in Fig. 7.81 and the frequency curves for four locations on the west coast of Florida are shown in Fig. 7.82.

Mariner's Weather Log (Vol. 22, No. 5, Sept. 1978, p. 345–346) reported the results of a survey on the effectiveness of hurricane warnings: "When Hurricane Eloise hit the Florida panhandle in 1975, 100 000 Gulf Coast residents left their homes, fleeing inland in the face of 125 mph [201 kph] winds and 18 foot [5.5 m] storm tides. But many thousands either would not or could not move ... "

A few days after the storm, a cooperative study between the U.S. National Weather Service and the Social Science Research Center at Mississippi State University put a survey team into the area to learn more about the perceptions and reactions of persons to a hurricane threat and weather warning messages. This was a followup to a similar effort conducted by these two groups following Hurricane Camille in 1969. Three of the important findings were as follows. (1) Newcomers are more likely to evacuate when faced with a hurricane warning than are residents of the area for 5 yr or more. (2) There is a lack of understanding by coastal residents of the nature of a hurricane and its dangers. Hurri-

TABLE 7.53. Some of the important storm surges on the coast of South Carolina up to 1959. (Based on Myers 1975)

Date	Meteorological information	Oceanographical information
Sept. 4–5, 1686	A hurricane struck the Charleston area	Severe destruction. An interesting historical aspect is given by Ludlam (1963): "A hurricane struck the Charleston area causing severe destruction to the new colony, but it also benefitted the colony by disrupting a Spanish attack on the lower Carolina settlements. The Spanish landed near North Edisto Island and struck toward Stuart Town near Beaufort on September 4th. That evening the wind picked up to a gale, driving two of the Spanish galleys so high on land that they had to be abandoned and the attack called off"
Sept. 16 (or 14), 1700	A hurricane wrecked the ship *Rising Sun* in Charleston Harbor with the loss of all onboard	Streets were flooded in Charleston
Sept. 16–17, 1713		70 people drowned north of Charleston
Aug. 13, 1728	A tropical cyclone	Great damage; 23 ships were driven ashore in Charleston Harbor
Sept. 15, 175?	Most intense hurricane in the Charleston area during colonial times (i.e. before 1776)	Several people killed
Sept. 30–Oct. 1, 1752	A severe tropical cyclone	Damage along the South Carolina coast
Oct. 7–8, 1783	A major storm on the South Carolina coast	Great damage to shipping
Sept. 19, 1787		A great storm surge drowned 23 people at Charleston
Oct. 19–20, 1797	A tropical cyclone	Flooding in Charleston
Sept. 7, 1804	A severe hurricane moved inland between Savannah and Charleston and caused great damage to the coasts of Georgia and South Carolina and then moved to sea again	More than 500 people drowned in South Carolina
Aug. 27, 1813	A tropical storm near Charleston. Exceptionally high winds	Very large storm surges

TABLE 7.53. (*Continued*)

Date	Meteorological information	Oceanographical information
Sept. 10, 1820	A destructive hurricane passed inland just north of Georgetown	A storm surge of 1.22 m at Georgetown
Sept. 27, 1822	A small but severe hurricane entered the coast between Georgetown and Charleston	Great storm surge at Georgetown. Several hundred people drowned
Sept. 4, 1834		Record storm surges at Georgetown. Duration was about 12 h
Aug. 7–8, 1854	Hurricane approached the United States from the south–southeast after moving through the northern Bahamas	Edisto Island, near Charleston, suffered severely, as did Port Royal and Beaufort to the south. The massive extent of the disturbance can be guessed from the vast inundations that took place in the Winyah Bay area of Georgetown county
Aug. 27, 1881	A major hurricane. Winds up to 87 $km \cdot h^{-1}$	More than 700 people killed by storm surge. Surges up to 5 m
Aug. 25, 1885	Hurricane moved inland near Savannah on a northerly course and passed to the west of Wilmington. As a result of this destructive storm, it was proposed that a weather reporting system be set up in the West Indies and Mexico	South Carolina coast severely damaged. About 90% of the houses in Charleston destroyed; 21 people killed in Charleston
Aug. 27–28, 1893	A severe hurricane passed over the coasts of Georgia and lower South Carolina. The storm moved through central South Carolina on a northerly course passing from about Savannah to a little west of Charlotte	About 2000 people killed. Maximum surge of 6 m at Savannah Beach, GA. Surges of 3.3 m at Edisto Beach, 2.6 m at Charleston
Aug. 28, 1911	A severe hurricane moved inland between Savannah and Charleston. Winds up to 130 $km \cdot h^{-1}$ at Charleston	Surges up to 2.2 m at Charleston; 17 people killed
Aug. 11, 1940	Storm entered the coast from the southeast striking between Savannah and Beaufort	34 people killed in the storm surges. Surge of 4.3 m at Beaufort. Storm surges of up to 3 m at the outlying islands of St. Helena, Hilton Head, Doufuskie, and Pinckney. Surge of 4.1 m at the southern tip of Edisto Island. Surge of 2.6 m on Folly Island. Surge of 2.7 m at Charleston

TABLE 7.53. *(Concluded)*

Date	Meteorological information	Oceanographical information
Oct. 15, 1954	Hurricane Hazel entered the coast just north of Myrtle Beach and was one of the most destructive hurricanes in terms of property damage. Hurricane winds hit the coast between Georgetown and Cape Lookout. Highest wind gust at Myrtle Beach was 171 $km \cdot h^{-1}$. After devastating the coast, the hurricane moved across North Carolina with diminishing winds, passing through Virginia and heading northward toward Lake Ontario and Canada. Lowest recorded barometric pressure of 938 mb was at Little River Inlet on the South Carolina–North Carolina border	Advance warnings enabled people to evacuate the threatened areas and only one person was killed in South Carolina. Every fishing pier from Myrtle Beach to Cedar Island (a distance of 274 km) was destroyed. Surges of 5 m at Holden Beach Bridge and Calabash. Surge of 5.2 m at Cherry Grove Beach. Surge of 4.7 m at Myrtle Beach. Surges greater than 4 m at Surfside and Garden City. Surges of 3 m on Pawleys Island
Sept. 29, 1959	Hurricane Gracie entered the Beaufort County coast at about 11:30 a.m. on Sept. 29 and the eye of the hurricane passed over St. Helena about 16 km north of Beaufort. Lowest pressure of 950 mb at Beaufort. Hurricane followed a path north–northwest to Bamberg and then changed to west and passed west of Columbia	Storm surge coincided with low tide at Charleston. Even then, considerable damage occurred

TABLE 7.54. Storm surges due to hurricanes affecting Charleston, SC, during 1893–1964. (Meyers 1975)

Date	Maximum storm surge (m)	Date	Maximum storm surge (m)
Aug. 28, 1893	2.72	Aug. 17, 1955 (Diane)	1.59
Aug. 11, 1940	2.44	Sept. 11, 1960 (Donna)	1.52
Aug. 27–28, 1911	2.41	Sept. 18–19, 1955 (Ione)	1.34
Sept. 27–28, 1894	2.13	Aug. 11, 1955 (Corrine)	1.31
Sept. 29, 1959 (Gracie)	1.83	Oct. 15, 1954 (Hazel)	1.28
Oct. 15, 1947	1.83	Aug. 29–30, 1954 (Carol)	1.28
July 14, 1916	1.80	Aug. 30, 1952 (Able)	1.22
Oct. 20, 1944	1.77	Sept. 27, 1958 (Helen)	1.19
Sept. 18, 1928	1.71		

cane winds were by far the most feared element of the storm, and this was the reason given by most people for evacuating, mentioned about three times as often as fear of water. This lack of understanding of, and respect for, storm surges is particularly significant in that 90% of all hurricane deaths are from drowning. (3) The majority of those interviewed in the Eloise Survey were satisfied with the U.S. National Weather Service's warnings and their distribution by public safety agencies and the news media.

White and Haas (1975) assessed the storm surge risk in Florida from the point of view of evacuation, a portion of which is presented (p. 30):

> [It] ... is a large, slow-moving, wet hurricane making a landfall south of Miami. Specifically, it is a hurricane with a central pressure of 925 mb and radius of maximum winds of 15 miles [24 km]. This is equivalent to Donna (1960), Carla (1961) and Betsy (1965) and much less severe than the Keys storm of 1935, which drowned 730 people in that area. It passes just south of Key Biscayne and moves onshore at 15 mph [24 kph] at the new residential community of Saga Bay ... Under these conditions, the National Hurricane Center in Coral Gables issues a warning for residents of Key Biscayne, Virginia Key and South Miami to evacuate. Such a warning is normally made with at least 12 hours of daylight remaining before the predicted landfall of the hurricane ... Not all of the 12 hours of warning are available for evacuation. As much as 6 hours prior to a slow-moving hurricane's landfall, storm surge may cause tides to begin rising, thereby flooding some low points on roadways used for evacuation, and bringing automobile traffic to a halt. Even before the storm surge hits its peak at the coast, traffic is snarled by a combination of congestion, weather, flat tires, and automobile accidents ... The drawbridge[7] represents another weak link in the escape route ... Severing of the causeway for any reason means large fatalities from storm surge in the trapped population. The five to ten foot land elevations afford minimal shelter from the wind-driven storm surge waves of 10-15 ft. along the right side of the hurricane. Mainlanders also experience severe difficulties in their attempts to evacuate. A storm surge 6 hours in advance of the hurricane's center catches many residents still preparing to leave ... Saga Bay is an excellent example of how the hurricane disaster potential is exacerbated by coastal development. Elevation of the Saga Bay area varies from sea level to 5 ft. above mean sea level. In order to meet Federal housing

[7]Key Biscayne and Virginia Key are about 5 mi (8 km) off the coast of South Miami. The elevations of these areas above mean sea level range from 2 to 3 ft, with an average of approximately 10 ft. Rickenbacker Causeway, a 2-mi bridge across Biscayne Bay bisected by a drawbridge, connects Key Biscayne and Virginia Key with the mainland.

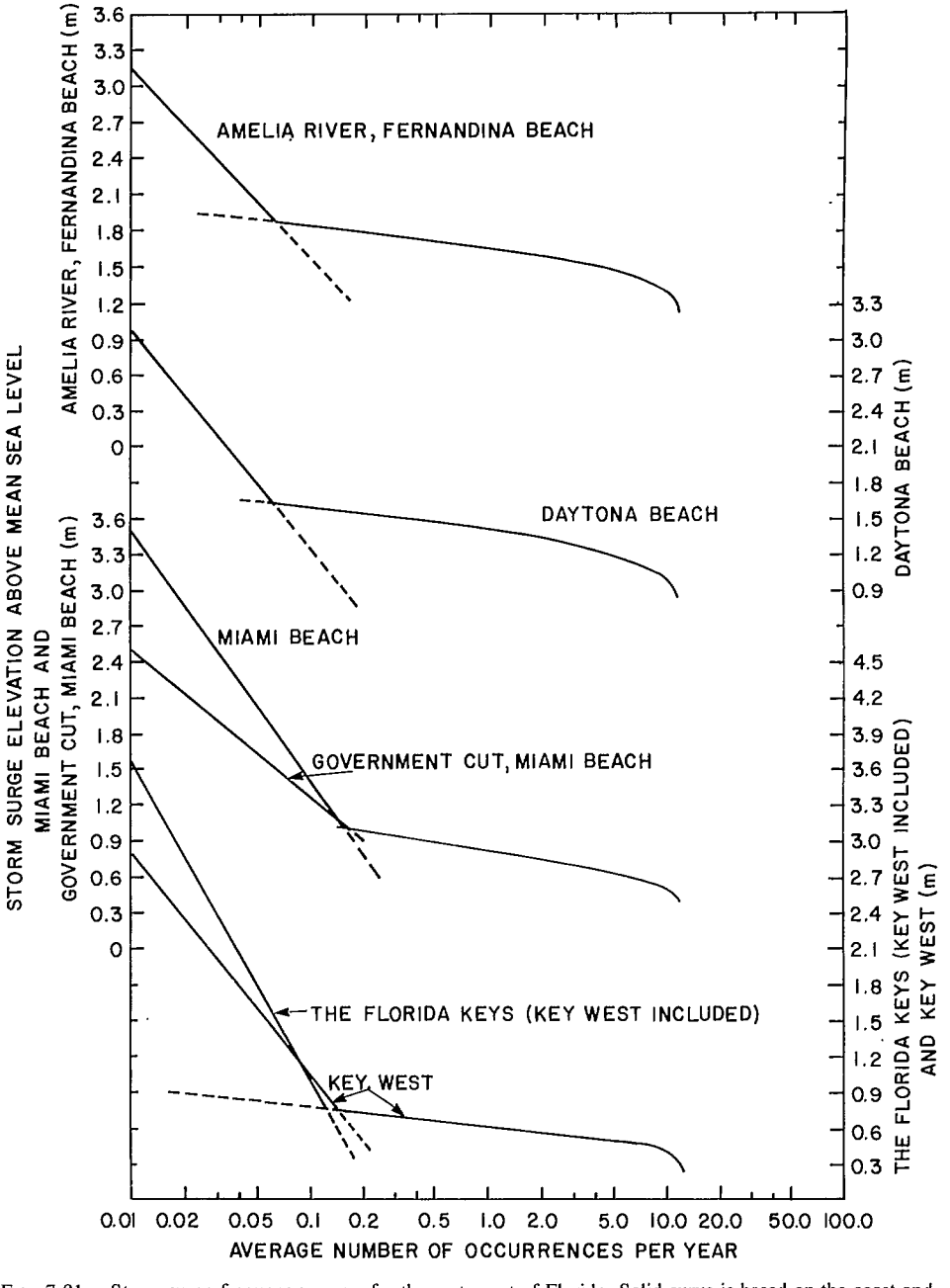

FIG. 7.81. Storm surge frequency curves for the east coast of Florida. Solid curve is based on the coast and Geodetic Survey data. Broken curve is based on the Corps of Engineers data. (Bruun et al. 1962)

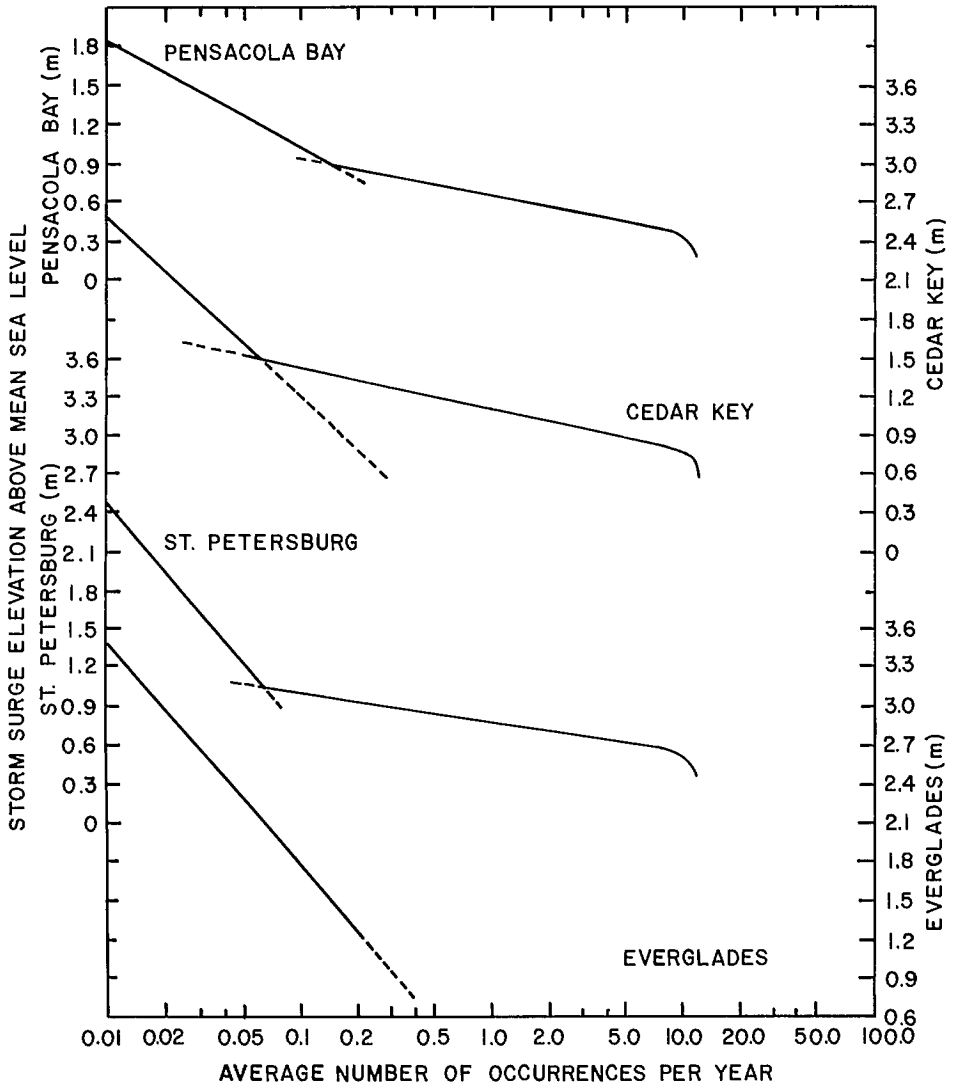

FIG. 7.82. Storm surge frequency curves for the west coast of Florida. See Fig. 7.81 for explanation.(Bruun et al. 1962)

regulations, houses are elevated 5 ft. above m.s.l. on fill dug from nearby manmade lakes. The developers also tore out the mangroves along the coast, which are unsightly and ill-smelling. These mangroves formerly provided one of the few effective barriers to storm surge, and the smooth cleared beaches that are being built invite the unrestrained sweep of storm surge across the entire area.

The south and east coasts of the United States are illustrated in Fig. 7.83. The small numbers 1−58 refer to 58 segments of the coast, each 50 mi (80 km) wide. The numbers in the top belt give the percentage probability of hurricane winds (i.e. winds exceeding 73 $m \cdot h^{-1}$ or 33 $m \cdot s^{-1}$) occurring in any year. The numbers in the bottom belt give the

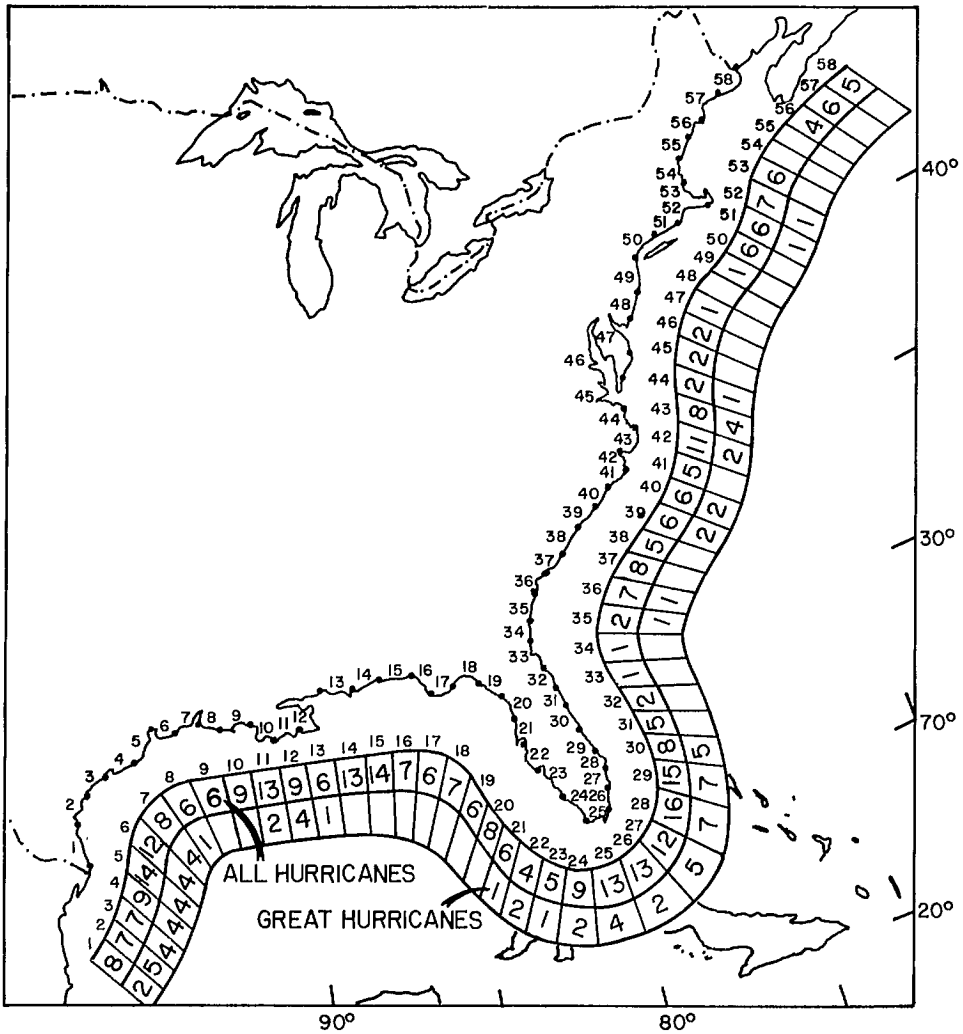

FIG. 7.83. Cyclone risk along the United States coast. The small numbers on the coastline as well as outside denote 58 segments, each 80 km long. The large numerals in the top belt denote the percentage probability of winds exceeding 33 $m \cdot s^{-1}$ in any year. The large numbers in the bottom belt show the percentage probability of winds exceeding 56 $m \cdot s^{-1}$ in any year. (Simpson and Lawrence 1971)

probability that winds will exceed 125 $mi \cdot h^{-1}$ (56 $m \cdot s^{-1}$). The cost of damage for the period 1934–70 is given in Fig. 7.84. For other useful information, see Friedman (1975, 1977) and Tubbesing (1979).

The Bulletin of the American Meteorological Society (Vol. 60, No. 6, June 1979, p. 683) says that five storm evacuation maps designed to facilitate evacuation of persons from endangered areas along the coast of Florida from Jacksonville to Cape Canaveral have been recently prepared by NOAA. These maps show emergency evacuation routes, areas subject to flooding from hurricanes and other storms, and areas that might provide safety for evacuees. More details can be found in Witten (1982).

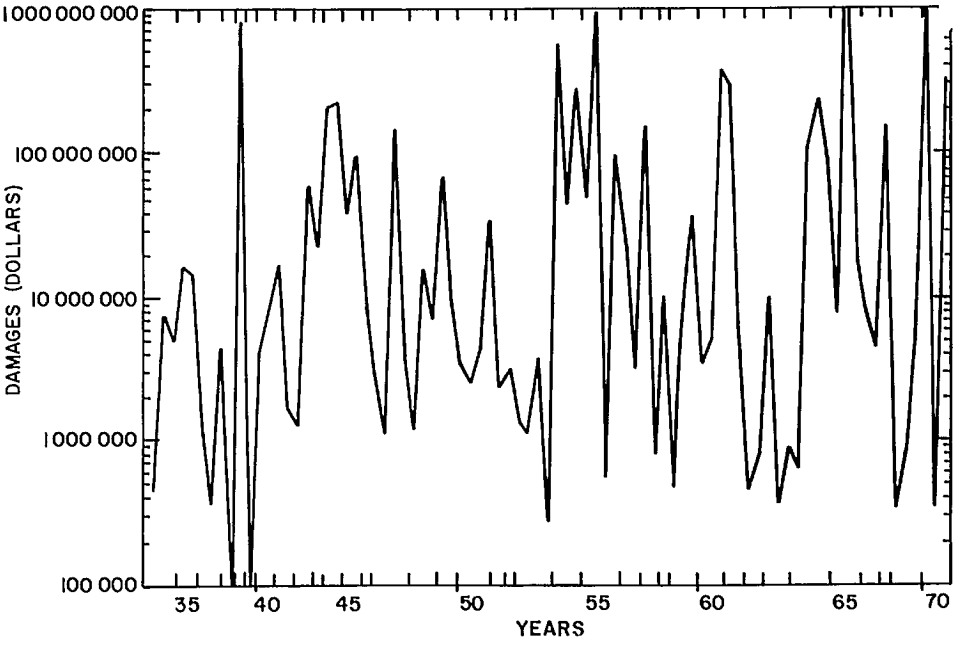

FIG. 7.84. Damage from hurricanes and storm surges (in U.S. dollars) versus year for the period 1934–70 in the United States. (White and Haas 1975)

In 1971 the Florida State Legislature enacted a law and set up guidelines for beach front construction in Florida (Collier 1978). It is desirable to have similar guidelines for all coastal areas in the world vulnerable to storm surges. The Florida Sea Grant Marine Advisory Program (FMAP) recently expanded the scope of marine advisory services to include natural disaster preparedness (Leahy 1979). Leahy (1979) stated some of the problems peculiar to Florida from the point of view of storm surges (p. 18):

> Florida with 1,350 miles (2,173 km) of coastline and a shoreline of nearly 8,500 miles (13,680 km) 50 estuaries, 50 inlets and a lengthy inter-coastal water way ...

There were 54 hurricanes between 1900 and 1975, the last one hitting the north coast between Fort Walton Beach and Panama City in September 1975. But since that time the state's population has increased by 1.8 million, with an estimated 1979 population of over 9 million, many of whom never experienced a hurricane. There is no point in the state of Florida that is more than 70 mi (113 km) from salt water. It is estimated that 78% of all residents live on or near the coast.

Tetra Tech. Inc. (1978) evaluated storm surge risk to the coast of Florida with the goal of determination of coastal flood levels having recurrence intervals of 10, 50, 100, and 500 yr with an accuracy of ± 0.5 ft (0.15 m). They recognized two classes of methodology: historical and synthetic. In the first approach, either the worst case on record or a statistical analysis of all historical events is used. This approach is satisfactory provided the length of the data record is large. For engineering design purposes, a typical historical storm may be used to determine design criteria. This storm may be given different landfall locations, different arrival times with reference to the tide, etc., and one can use a synthetic or joint probability method. In these methods, historical data of *individual storm parameters* (and not just the storm surge amplitude) are used. The

statistical distributions of the storm parameters that determine the surge amplitudes are examined collectively as well as individually. From these distributions, a large sample of synthetic storms can be created that resemble the historical storms. Through this procedure one can simulate several thousand years of storms and then estimate the storm surge recurrence intervals.

In this study the basic data consisted of 44 hurricanes during the period 1903–65 (see Table 7.30). The storm parameters used are the central pressure, the radius of maximum winds, the forward speed of the storm, its direction of travel, and the point at which it crosses the coast (or the distance offshore if its track is parallel to the coast). Each of these parameters is subjected to statistical analysis to determine its probability of occurrence. Several hundred storms are synthesized from these statistical distributions and the corresponding pressure and wind fields are determined, and the storm surge is computed using a model that allows for coastal flooding. The astronomical tide is then statistically combined (with random phase) with the computed surge. The influence of rainfall was also considered. This effect is significant inland in the rivers and inlets. The results of this study are summarized in Fig. 7.85. Further results can be found in Taylor (1980).

Next to be considered is the coast of Louisiana. Shaw (1929) discussed the storm surge hazard to New Orleans. New Orleans missed great destruction from the storm surges of September 20, 1909, August 17, 1915, and September 29, 1915, mainly because of its location relative to the storm tracks. However, if the tracks had slightly shifted to the east, great destruction would have occurred. The levees are 10 ft (3 m) high, whereas a storm surge height of 13 ft (4 m) occurred only a few kilometres away from New Orleans.

Crawford (1979) described the results of storm surge calculations for the southeast coast of Louisiana using the model SLOSH (Jelesnianski and Chen 1979). This section of the coast is vulnerable to severe storm surges. Recent examples are Hurricane Betsy of 1965 and Hurricane Camille of 1969. This model calculates the sea, lake, and overland surges and includes the complex levee systems and the water bodies Lake Maurepas, Lake Pontchartrain, Lake Borgne, Lake Salvador, Breton Sound, and Barataria Bay. In the results, flooding (F) was referred to as water levels less than 3 ft (0.91 m) above average ground levels, major flooding (MF) as between 3 and 7 ft (0.91–2.1 m) above average ground levels, and catastrophic flooding (CF) as more than 7 ft (2.1 m) above average ground levels. A total of nine tracks were simulated over three directions: south–southwest, south, and southeast.

The results form the numerical model were summarized by Crawford (1979) in great detail for each geographic location. For example, for storms from the south–southwest he stated:

> CF is possible on the western side of the Mississippi River Levee System from near Buras northwest to the storm track . . . MF is possible west and north of Lake Maurepas . . . There is strong evidence that the Mississippi River Levee System may increase flood potentials at locations on the upwind or stormside while lessening the potentials downwind of the river levees . . .

This paper is very useful from a practical point of view.

Next, storm surge risk on the Texas coast will be considered beginning with Galveston where more than 6000 people were killed by a storm surge in 1906, which to date is the biggest single natural disaster in United States history. Galveston Island is a long, narrow barrier beach that runs parallel to the Texas coast some 2 mi (3.2 km) away across Galveston Bay. The city of Galveston occupies the eastern end of the island (Hughes 1979). In most of the residential areas, the average height of the street above sea level ranged from 4 to 7 ft (1.2–2.1 m). A hurricane that originated in the tropical Atlantic

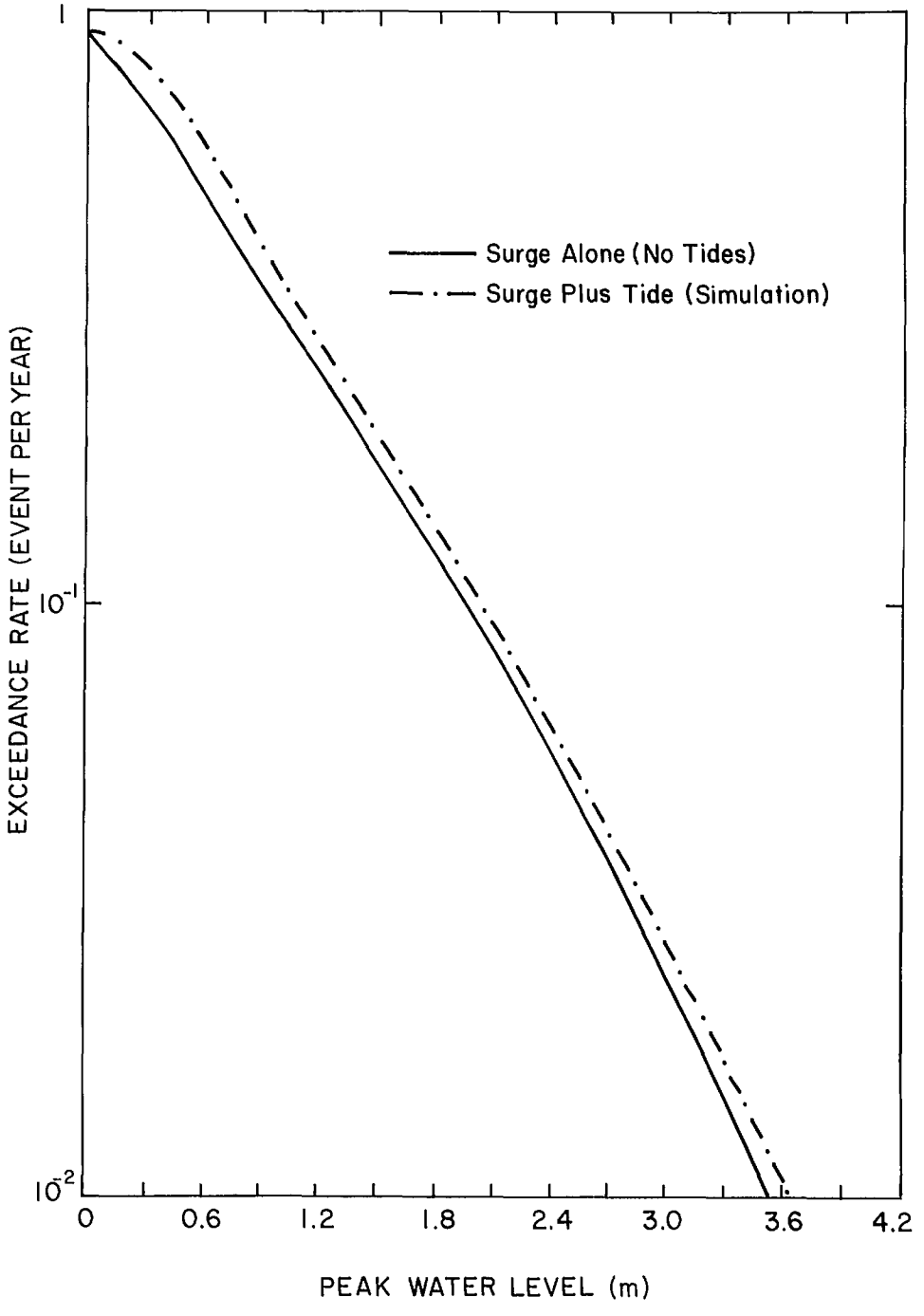

FIG. 7.85. Flood level exceedance rates due to storm surges along the coast of Florida. (Tetra Tech. Inc. 1978)

west of Cape Verde Islands on August 27, 1906, moved on to the Galveston area by September 8 and caused a great storm surge. The waters from Galveston Bay (to the north of the city) and the waters from the Gulf of Mexico (to the south of the city) converged and submerged the entire city. Storm surges of up to at least 10 ft (3 m) invaded the city.

Davis (1963) studied the problem of design of hurricane flood protection works near Texas City, located on Galveston Bay. The design hurricane for a given coastal area is defined as a hurricane with a recurrence interval of 100 yr. For the Gulf of Mexico coast, in the Galveston area, the design hurricane has the following characteristics: maximum wind velocity (30 ft above the water surface) = 101 mi·h^{-1} (162.5 km·h^{-1}); radius from the center to the region of maximum winds = 14 nautical miles (25.9 km); forward speed of the hurricane = 11 knots (20.4 km·h^{-1}); central barometric pressure = 27.52 in.Hg (931.94 mb); asymptotic barometric pressure = 29.92 in.Hg (101.32 mb). This design hurricane would generate a storm surge of amplitude 15 ft at Galveston.

The following formula was used for the computation of the storm surge:

$$(7.58) \qquad N_m = K\frac{T}{c_1}\left(\frac{d_1}{d_0}\right)^{0.25} W_m^2 S$$

where N_m is the maximum rise in water level (feet) caused by the wind stress, d_1 is the mean water depth at the seaward edge of the continental shelf just landward of the sharp increase in slope on the continental shelf (feet), d_0 is the mean water depth at the shoreward edge of the continental shelf just seaward of the sharp increase in slope near shore zone (feet), K is a wind stress parameter whose value is taken as 3.0×10^{-6}, $T = B/\bar{c}$, where B is the breadth (feet) of the continental shelf between d_1 and d_0, and $\bar{c} = \frac{1}{2}(c_0 + c_1)$ (feet per second), where $c_0 = \sqrt{g d_0}$ and $c_1 = \sqrt{g d_1}$, W_m is the maximum sustained wind speed (feet per second) 30 ft above the water surface, and S is a response factor depending on the ratio of fetch length to breadth of continental shelf and the ratio of the forward speed of the hurricane to the propagational speed of the free wave.

In computing the surge at Galveston, the following values are used: $d_0 = 36$ ft (10.9 m), $d_1 = 180$ ft (54.9 m), $B = 110$ nautical miles (203 km), and $T = 3.39$ h. These give from eq. 7.58

$$(7.59) \qquad N_m = 1.55 \times 10^{-3} W_m^2 S$$

where W_m is in miles per hour. Calibration against two storm surges (one in 1900 and another in 1915) gave a better formula:

$$(7.60) \qquad N_m = 1.69 \times 10^{-3} W_m^2 S$$

In formula 7.60, W_m was taken as 99 mi·h^{-1} and S as 0.82 to give $N_m = 13.5$ ft (4.1 m).

The rise in water level N_p (feet) due to reduction in atmospheric pressure is computed from

$$(7.61) \qquad N_p = 1.14\Delta p \times 0.63$$

where 1.14 is a factor to convert inches of mercury to feet of water, Δp is the difference between atmospheric pressure at the center of the storm and the asymptotic pressure, and 0.63 is a factor to reduce the pressure difference to a difference at the zone of maximum wind. For the design storm, $\Delta p = 29.92 - 27.54 = 2.38$. Using eq. 7.61 gives $N_p = 1.7$ ft. The tidal range at Galveston is only 1.5 ft (0.5 m).

The design storm surge at Texas City was estimated to have about the same amplitude as at Galveston (about 15 ft or 4.9 m) but with a slight time lag. The following amplitudes for storm surges were actually observed at Texas City: 14.5 ft (4.42 m) for the storm in

TABLE 7.55. Characteristics of the full hurricanes for the Texas coast during 1900–49. Parameters P and E are storm surge potential and wind wave energy index, respectively. Parameter E is the product of the radius of maximum winds and the central pressure deficit and is in units of km·mb^{-1}. The storm surge potential was estimated by the authors (Reid and Wilson 1954) in F.P.S. units. In C.G.S. units some multiplicative factors occur. Since the absolute value of this potential is not important (it is only the relative values that are relevant), the original values as given by the authors are retained here. (Reid and Wilson 1954)

Date	Nearest place of landfall	Radius of maximum winds, R (km)	Central pressure deficit, ΔP (mb)	Storm surge potential, P	Wave energy index, E
Sept. 7, 1900	Galveston	25.9	76.9	3.64	1991.7
July 21, 1909	Bay City	34.3	50.8	2.83	1742.4
Aug. 16, 1915	Freeport	57.1	62.0	3.73	3540.2
Aug. 18, 1916	Sarita	64.4	64.7	3.96	4166.7
Sept. 14, 1919	Sarita	139.1	42.7	3.47	5939.6
June 22, 1921	Port Lavaca	31.5	58.9	3.11	1855.4
June 28, 1929	Port Lavaca	24.1	43.7	2.33	1053.2
Aug. 13, 1932	Freeport	21.2	70.4	3.20	1492.5
Aug. 4, 1933	Brownsville	44.6	37.6	1.96	1677.0
Sept. 4, 1933	Brownsville	54.7	64.0	3.78	3500.8
Aug. 7, 1940	Port Arthur	20.4	38.9	2.04	793.6
Sept. 23, 1941	Freeport	38.9	42.3	2.55	1645.5
Aug. 30, 1942	Port Lavaca	33.5	62.3	3.29	2087.1
July 27, 1943	Port Bolivar	30.6	38.3	2.23	1172.0
Aug. 27, 1945	Port Aransas	32.5	45.4	2.58	1475.5
Oct. 4, 1949	Freeport	51.5	34.9	2.38	1797.4

1900, 12.7 ft (3.87 m) for the storm of 1915, and 11.7 ft (3.57 m) for the storm of 1961.

Reid and Wilson (1954) performed a comprehensive study on the storm surges and wind-generated waves for the Texas coast. According to these authors, hurricane statistics are fairly accurate since the year 1866, and prior to that, statistics were available only on the significant hurricanes. During the period 1886–1954, there were 50 hurricanes that were significant. Thus, a rate of 50 hurricanes in 89 yr or one hurricane every 1.78 yr is a typical rate for the Texas coast. Based on more accurate data for the period 1900–49, it was deduced that the frequency of occurrence of fully developed hurricanes on the Texas coast is 16/30 of the rate given above, i.e. the modified rate is one hurricane per 15 yr for 100 statute miles (161 km) of the coast.

A hurricane index is developed for classifying hurricanes. The two parameters used are R, the radial distance from the storm center to the region of maximum wind speed, and Δp, the anomaly of pressure from normal at the storm center (i.e. normal pressure minus central pressure). Since both these parameters together determine the storm surge amplitude, a single index could be constructed through some combination of these.

A storm tide potential p is defined as

$$p = (\Delta p)^n R^{1-n} \tag{7.62}$$

where n depends on the slope of the shelf and the range of values of Δp and R. Basically, p is proportional to the maximum surge generated by a hurricane, provided the shelf topography can be approximated by a uniform slope, at least to a depth where the wind effect becomes negligible. Until it is calibrated, the absolute value of p has no meaning; only relative values of p for two storms describe the relative potential for generating storm surges. The values of R, Δp, and the index p for various hurricanes on the Texas coast during the period 1900–49 are listed in Table 7.55. In the last column is listed a wave energy index E, which represents the potential for generating wind-generated waves.

TABLE 7.56. Summary of the characteristics of synthetic hurricanes on the coast of Texas. S_0, initial storm surge (m); T_r, return period of storm (yr); CPI, central pressure index or the estimated minimum pressure for a particular hurricane (mb); R, distance from storm center to the region of maximum wind speed (km); V_{ex}, maximum cyclostrophic wind speed ($km \cdot h^{-1}$); V_{gx}, maximum gradient wind speed ($km \cdot h^{-1}$); V_x, estimated maximum overwater wind speed at 10-m height. (Masch et al. 1970)

S_0	T_r	CPI	R	V_{ex}	V_{gx}	V_x
0.61	100	929.2	22.2	185.9	182.9	168.9
0.61	75	931.3	23.2	182.6	179.5	166.2
0.61	50	934.6	24.1	180.9	177.7	164.5
0.61	30	939.0	25.0	174.1	170.9	158.6
0.46	20	944.1	25.9	167.3	164.0	152.8
0.46	15	946.2	26.9	164.0	160.6	149.3
0.46	10	953.6	27.8	155.5	152.1	142.3
0.30	5	967.2	28.7	138.6	135.1	127.3
0.30	3.3	976.6	29.6	114.9	111.4	107.0

Again, the absolute values have no meaning until they are calibrated. This index is defined as

(7.63) $$E = (\Delta p)R$$

Masch et al. (1970) analyzed the hurricane-generated storm surges at Padre Island, Texas. They developed a set of synthetic hurricanes with specified sizes, rates of travel, wind fields, and pressure fields. Using numerical models the offshore form of the surge was first computed and then the profile of the surge at Padre Island was determined for each synthetic hurricane. The results are summarized in Table 7.56.

Earlier, classification of storms by storm tide and wave energy indices was discussed. Reid (1957a) extended the earlier study of Reid and Wilson (1954) and showed that the logarithms of these indices have approximately a Gaussian distribution. The results for the storm tide potential are summarized in Fig. 7.86.

Bodine (1969), based on 19 hurricanes since the year 1900, derived storm surge frequencies for the entire coast of Texas. He also made use of synthetic hurricanes that he generated based on prescribed values of central pressure index, forward speed, and radius of maximum winds. He also considered the surge frequency, not only on the open coast, but also in inland bays. His basic data are given in Table 7.57. Surge height versus distance along the open coast is plotted in Fig. 7.87. The terms left and right in the figure are the directions as seen from the ocean. These surge profiles will not apply for hurricanes approaching and crossing the coast at a small angle to the coastline.

The results of the analysis for the entire Texas coast are shown in Fig. 7.88. Here, H is the surge height for the particular hurricane and H_B is the surge height for a beta-hurricane, which is derived by the parameters in Table 7.58. Simpson and Freeman (1976) studied the coastal hazard potentials for Texas. They identified hazard zones as a function of anticipated flood stages inland, and they described methods for routing the storm surge flood waters.

TIDE–SURGE INTERACTION

It was mentioned earlier that the astronomical tide is quite significant in the northern parts of the east coast of the United States and it becomes less and less important as we proceed south and also along the Gulf coast. It was also mentioned that in the storm surge

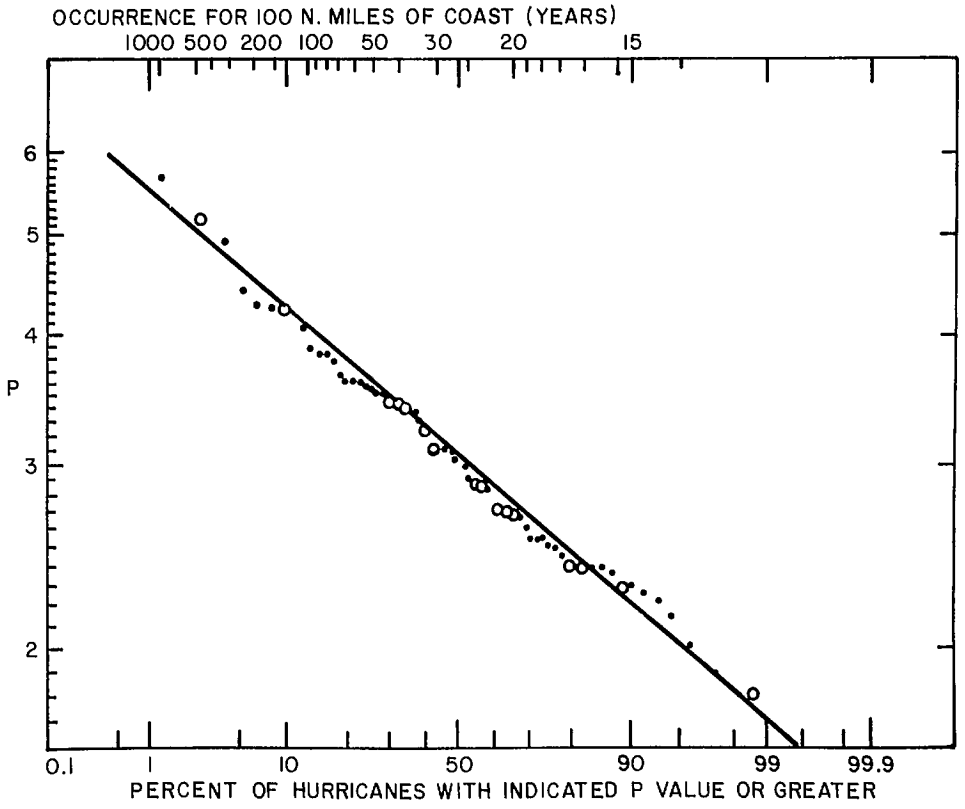

FIG. 7.86. Storm tide potential P versus percentage of hurricanes with indicated P value or greater and occurrence for 100 nautical miles (185 km) of coastline in years. (Reid 1957b)

studies in the United States, the problem of tide–surge interaction has not received adequate attention, as, for example, in the North Sea. Either the tide and surge are linearly added or added with random phases. However, it does not necessarily mean that these studies are inaccurate. All one can say is that it is better to show at first that nonlinear interactions between tide and surge are not important in a given coastal region before using simple linear superposition.

Earlier, a study by Myers (1970) was referred to in which a joint probability method of analysis for Atlantic City and Long Island was used. One result that followed from this study is shown in Fig. 7.89 giving the return periods for storm tides of different amplitudes due to different types of storms.

Tayfun (1979) studied the problem of joint occurrences of a tide with a rare phenomenon such as a storm surge or a tsunami. He also assumed that the two events (i.e tide and surge) are independent (and thus did not allow for mutual interaction). He took into account the transient nature of the primary event (i.e. the storm surge) by defining an equivalent magnitude in terms of an average over the duration of the primary event.

At a given coastal location, during a period of t yr, let $z_1, z_2, \ldots, z_n$ denote the maximum water levels (here $i = 1, 2, \ldots, N$) due to the joint occurrence of a storm surge and the astronomical tide. Our goal is to determine the probability distribution of the largest intensity:

TABLE 7.57. Parameters for Texas hurricanes used in the study by Bodine (1969).

Date of landfall	Approximate location of landfall	Central pressure (mb)	Radius of maximum winds (km)	Speed of movement of hurricane ($km \cdot h^{-1}$)	Open coast peak surge estimated (m)	Return period between events of this surge amplitude (yr)
Sept. 8, 1900	Galveston	936.0	25.9	18.5	3.35	280
July 21, 1909	Freeport	958.7	35.2	22.2	2.74	16
Aug. 16, 1915	Galveston	952.9	59.3	20.4	3.87	8
Aug. 18, 1916	Mustang Island	948.2	64.8	20.4	2.80	7
Sept. 14, 1919	Port Aransas	948.2	37.0	37.0	3.38	184
June 22, 1921	Port O'Connor	953.9	31.5	20.4	2.16	13
June 28, 1929	Port O'Connor	969.2	24.1	27.8	0.91	63
Aug. 13, 1932	Freeport	942.4	22.2	27.8	1.86	792
Aug. 4, 1933	Port Isabel	975.3	46.3	18.5	1.37	11
Sept. 5, 1933	Port Isabel	948.9	37.0	14.8	3.35	93
Aug. 7, 1940	Galveston	973.9	20.4	14.8	0.64	135
Sept. 23, 1941	Freeport	958.7	38.9	24.1	2.90	17
Aug. 30, 1942	Port O'Connor	950.6	33.3	25.9	3.05	38
July 27, 1943	Port Bolivar	974.6	29.6	14.8	0.91	22
Aug. 27, 1945	Port Aransas	967.5	33.3	7.4	2.74	52
Oct. 4, 1949	Freeport	978.0	51.9	20.4	2.38	3
June 25, 1959	Galveston	984.4	31.5	9.3	0.85	43
Sept. 11, 1961	Port O'Connor	936.0	48.2	7.4	3.75	289
Sept. 17, 1963	High Island	995.9	55.6	18.5	1.28	3

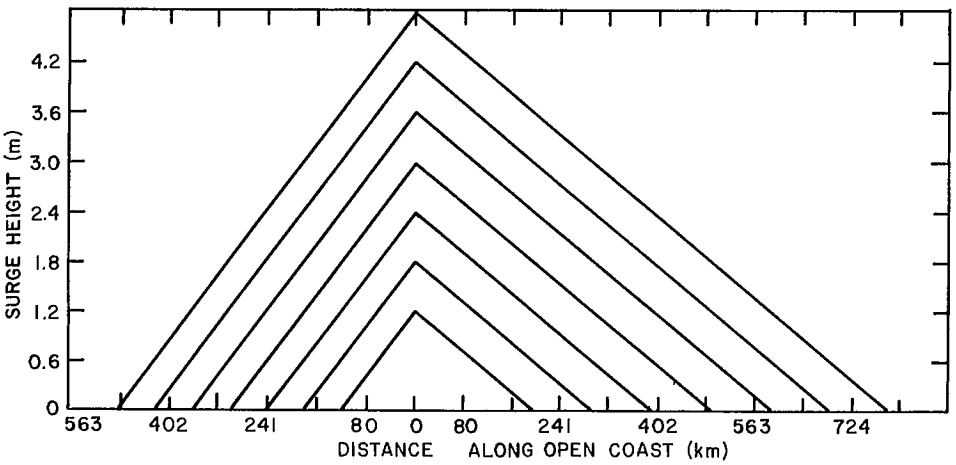

FIG. 7.87. Surge height versus distance along the Gulf of Mexico and coast of Texas. (Bodine 1969)

(7.64) $\hat{z} = \max(z_i; i = 1, \ldots, N)$

where N is a random variable, which is assumed to be governed by the Poisson distribution:

(7.65) $$P_N(n; t) = \frac{(\sigma t)^n}{n!} \exp(-\sigma t)$$

where

(7.66) $P_N(n; t) = \text{prob}[N = n \text{ in } (0, t)]$

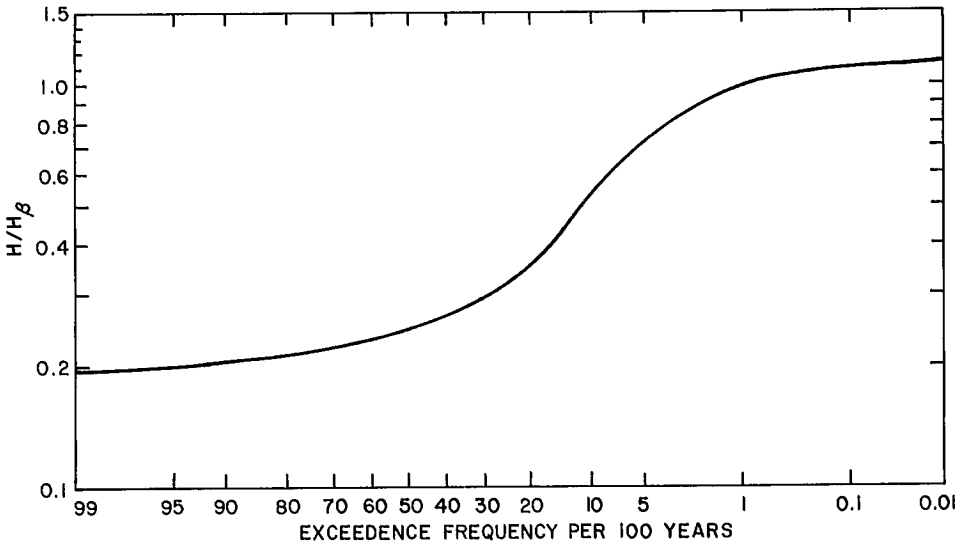

FIG. 7.88. Generalized storm surge frequency curve for the coast of Texas. (Bodine 1969)

TABLE 7.58. Parameters for the β hurricane. (Bodine 1969)

Location in Texas	Central pressure of hurricane (mb)	Radius of maximum winds (km)			Forward speed of movement of hurricane ($km \cdot h^{-1}$)		
		Small	Medium	Large	Slow	Medium	Large
Port Arthur	932.6	13.0	25.9	50.0	7.4	20.4	51.9
Galveston	931.9	13.0	25.9	48.2	7.4	20.4	51.9
Bay City	930.9	11.1	24.1	46.3	7.4	20.4	51.9
San Antonio Bay	929.6	11.1	24.1	44.4	7.4	20.4	51.9
Sarita	927.2	11.1	22.2	42.6	7.4	20.4	51.9
Brownsville	923.8	11.1	20.4	37.0	7.4	20.4	51.9

and σ is the mean occurrence rate of storm surges with the assumption that $z_i (i = 1, \ldots, N)$ are independent observations from a population with the probability law

(7.67) $\quad \text{prob}\,(z_i \leq z) = P_z(z);\ i = 1, \ldots, N$

One can show that the cumulative distribution of the largest intensity $\hat{z}$ has the form

(7.68) $\quad P_{\hat{z}}(z) = \exp\{-\sigma t[1 - P_z(z)]\}$

Define the time interval between the exceedances of a value z as the waiting time $W_{\hat{z}}(z)$ for the level z. The mean value of $W_{\hat{z}}(z)$ is

(7.69) $\quad \bar{W}_{\hat{z}}(z) = \{\sigma[1 - P_z(z)]\}^{-1}$

$\bar{W}_{\hat{z}}(z)$ is referred to as the return period. The inverse of the return period

(7.70) $\quad R_{\hat{z}}(z) = \sigma[1 - P_z(z)]$

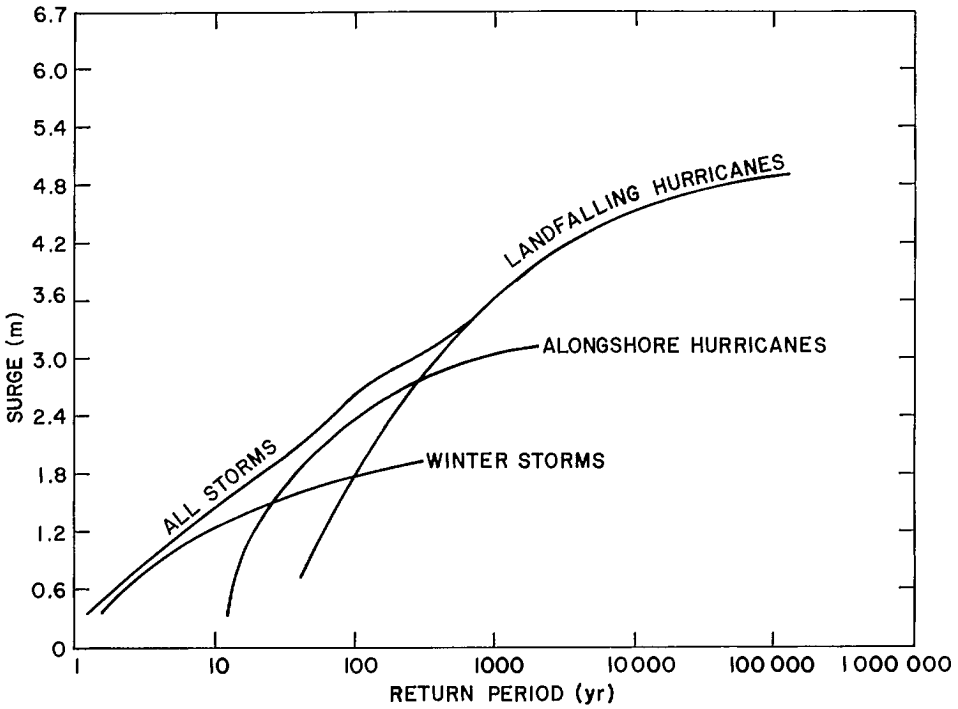

FIG. 7.89. Storm surge height versus return period for Atlantic City, New Jersey. (Myers 1970)

is the recurrence rate, i.e. the number of times the largest intensity $\hat{z}$ exceeds the level z per unit time.

The input data consist of the mean occurrence rate σ of the primary event (for the location under consideration) and the parent distribution P_z for the peak flood levels

$$z = \max [A(t) + S(t)] \tag{7.71}$$

where $A(t)$ is the astronomical tide and $S(t)$ is the storm surge. Thus, the goal is to estimate P_z in terms of the probability distributions of A and S. This is done in a two-step procedure: (1) the distribution is estimated through a synthetic simulation technique (such as the joint probability method, see Ho 1976a, 1976b, 1977) and (2) the resulting distributions are modified to include the effects of the local astronomical tide. Tayfun (1979) developed an analytical procedure for this second step.

WEST COAST AND ALASKA SURGES

Storm surges are a rare phenomenon on the Pacific coast of the United States. However, there are instances when great damage is done by them on the west coast.

Two intense storms moved into the Gulf of Alaska during October 20–31, 1977, and produced extreme damage on the Pacific northwest coast of the United States. Wind waves and swell up to 33 ft (10 m) in height occurred. Storm tides (tide + surge) up to 9.2 ft (2.8 m) occurred at South Beach, Newport, on the Oregon coast.

During 1977–78, four major storms occurred over southern California doing great

damage (Pappas 1978). During the storm of January 10–11, 1978, storm tides of up to 7 ft (2.1 m) in height occurred at Redondo Beach. Part of the damage during the storm of February 9–10, 1978, was caused by a squall line. Mudslides, flooding, and surges occurred during the storm of February 28–March 6, 1978, in southern California. The rock slides and mudslides continued to May 1978 because of weakened mountain slopes. The towns of Tijuana and Ensenada in northern Baja California were also heavily damaged.

This section will conclude with a discussion on storm surges in the United States with the findings from three important recent reports. The first is published by the National Academy of Sciences (1975) and examines the question of "how best to estimate the height of coastal surges from hurricanes." The second report is prepared by the Hydrology Committee of the U.S. Water Resources Council's storm surge assessment work group. The third report is the proceedings of a storm surge workshop organized by the National Weather Service in 1978. The results from the National Academy of Sciences report are considered first.

The National Academy of Sciences report specifically examines the following features: (1) reviews hurricane parameters and surge and coastal water characteristics, in addition to height, that can influence the height and areal extent of inland flooding; (2) describes various methods available for use in estimating the characteristics of hurricane-induced coastal surges; (3) recommends methods for estimating the characteristics of coastal surges from hurricanes to be used for the purposes of the National Flood Insurance Program during the immediate future; (4) identifies fundamental areas in need of further study and research to improve the adequacy of the recommended methods for predicting the characteristics of coastal surges from hurricanes.

This report concludes that the current approach to determining the height and areal extent of inland flooding having probabilities of annual occurrence of 0.1, 0.02, etc., on the coastline and of projecting these results inland is inadequate. It suggests that the SPLASH models of NOAA currently provide the soundest basis for determining the temporal and spatial characteristics of hurricane surges along open, unbroken coastlines of the Atlantic and Gulf coasts. According to this report, the method of joint probabilities provides the soundest basis for assigning a probability of occurrence to the temporal and spatial characteristics of a surge produced by a hurricane and to the total height of the resulting storm waters (surge + tide).

It also suggests that the ability to model and predict hurricane surge heights within estuaries, bays, lagoons, and other semi-enclosed tidal waters and in adjacent low-lying lands must be improved. Required are not only general models but specific ones for each separate body of water for which such a model would be needed.

The report lists the following four areas that require the attention of researchers: (1) the assumption of independence among storm parameters, (2) the assumption of independence among surge, astronomical tide, and other initial water conditions, (3) the feedback effect of flooding of low-lying coastal areas on surge height and growth rate at shore, and (4) the effect of the presence of bays and estuaries on the surge at points along the coast away from the entrance to the bays and estuaries.

The Hydrology Committee of the U.S. Water Resources Council examined the state-of-the-art storm surge modeling. This committee examined the following models: (1) SPLASH of NOAA, (2) SSURGE developed at Texas A & M University, (3) the FIA (Federal Insurance Agency) model developed by Tetra Tech. Inc., and (4) the bathystrophic model. This report concludes that, whereas adequate meteorological input data exist, sufficient surge data do not exist to both calibrate and verify surge simulations.

The recommendations from the proceedings of the NOAA's storm surge workshop are too detailed to list here; however, this important document is recommended for further study.

Before closing this section on storm surges in the United States, it is worth reiterating that in the twentieth century alone, hurricanes (and accompanying storm surges) killed more than 45 000 people in the regions surrounding the Caribbean Sea and the Gulf of Mexico (about 15 000 killed in the United States) and caused more than $12 billion worth of damage in the United States. Although the number of deaths directly attributable to hurricanes has decreased recently (due to better warning systems and awareness), the amount of damage is not on the decline. For example, Hurricanes Betsy (1965) and Camille (1969) each did more than $1.4 billion damage in the United States. For comparison, it may be pointed out that in the 18 nations of the Economic and Social Commission for Asia and the Pacific region (ESCAP), during 1961–75, the damage was estimated to be upwards of $36 billion (at 1975 price levels), which amounts to about $3 billion annually. Of this $36 billion damage, $21 billion damage occurred in Japan, more than $7 billion damage in India, and about $4.5 billion damage in Bangladesh (Sen 1978).

In the United States, during 1900–80, three catastrophic hurricanes occurred (ranking 5 on the Saffir–Simpson scale). These are the 1935 Labor Day storm (that destroyed the Florida Keys), Hurricane Camille in 1969, and Hurricane Allen in 1980. The storms that originate in August and September have longer lives (2 wk) compared with those originating in June–July and October–November. These latter ones originate in the Caribbean Sea and the Gulf of Mexico and do not live longer than 7 d due to the shorter distance traveled before landfall.

7.3 Storm Surges in Europe

In section 6.9, the meteorological problems associated with storm surges in European waters were introduced. Here, case studies of storm surges in several water bodies in Europe and environs will be considered.

Storm Surges in the North Sea (Including the Thames Estuary)

In this subsection, the surges before 1953 will be considered. The disastrous surge of January 31–February 2, 1953, will be considered separately. In Chapter 6, storm surges in the Thames Estuary were listed (Table 6.64) as well as the meteorological situations associated with these. The storm surge at Southend (near the mouth of the Thames Estuary) during January 12–16, 1916, is shown in Fig. 7.90a. For comparison, the surge at Dunbar (which is located farther north on the east coast of the United Kingdom) is also shown. The surge profiles at Southend and Dunbar during November 24–28, 1917, are given in Fig. 7.90b. The reason for showing surges at Southend and Dunbar together is to make the point that, in the early literature (before the computer era) on North Sea surges, predictions along the east coast of the United Kingdom were made using correlations of the surges at these two locations. Similar results for two other storms are shown in Fig. 7.90c and 7.90d.

Douglas (1929) mentioned a storm surge in the English channel due to a squall line on July 20, 1929. A simple analytic theory gave an amplitude comparable with the observed. Bowden (1957) mentioned that, in the southern part of the North Sea, the greatest elevation tends to occur along a line from Harwich to Flushing. The surface then

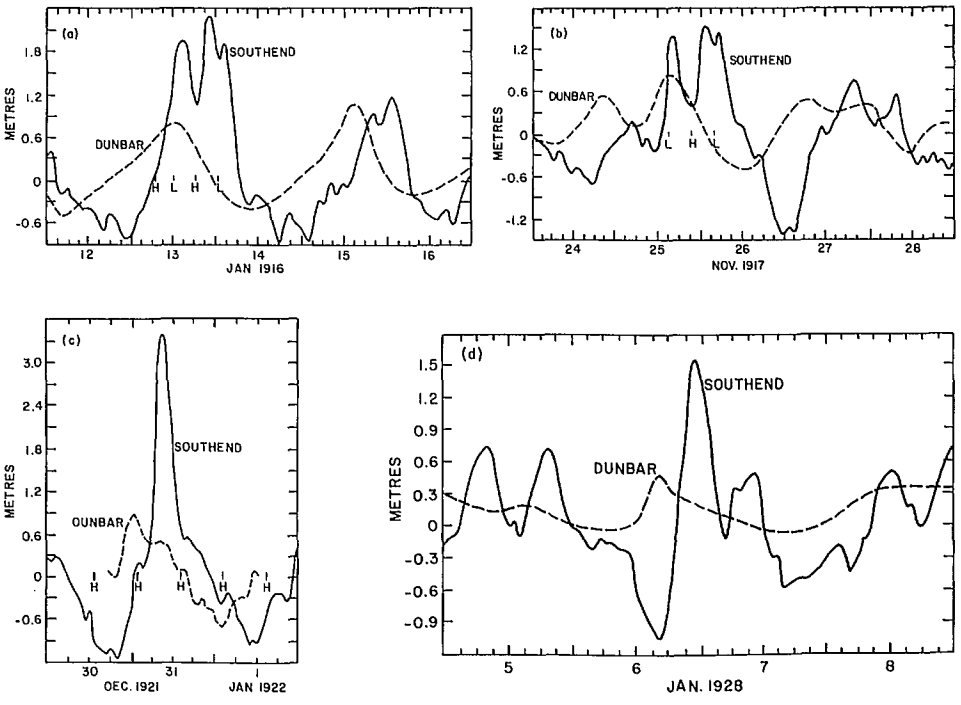

FIG. 7.90. Storm surges at Southend and Dunbar, U.K., during (a) January 12–16, 1916, (b) November 24–28, 1917, (c) December 30, 1921– January 2, 1922, and (d) January 5–8, 1928. (Doodson 1929)

slopes downward towards the Strait of Dover due to the flow of water into the English Channel.

The surge profiles along the western side of the North Sea during January 6–10, 1949, are shown in Fig. 7.91A, beginning at Aberdeen and ending at Newhaven. The surge profiles along the eastern boundary of the North Sea during the same period are given in Fig. 7.91B. One can see a counterclockwise progression of the disturbance with about the same travel speed as that of the diurnal tide (Fig. 7.92). The interaction between the tide and surge appears to be small (note that in the Thames Estuary the tide–surge interaction is significant).

Rossiter (1959) developed empirical relationships for prediction of storm surges at Aberdeen, Immingham, Southend, River Tyne entrance, Lowestoft, King's Lynn, and Newhaven. The observed and computed surges at Immingham for one storm are compared in Fig. 7.93. It can be seen that there is reasonably good agreement.

NEGATIVE SURGES IN THE NORTH SEA

Rossiter (1971a, 1971b) drew attention to the navigational hazard posed to large ships in the southern North Sea due to negative storm surges. Doodson (1947) mentioned that negative surges occurred at Dunbar and Southend during the storms of November 10–13, 1929, January 1–3, 1928, and October 17–21, 1935.

Geelhoed (1973) studied negative storm surges in the southern part of the North Sea, with particular attention to the Sandettie Bank and the Brand Ridge areas because of the

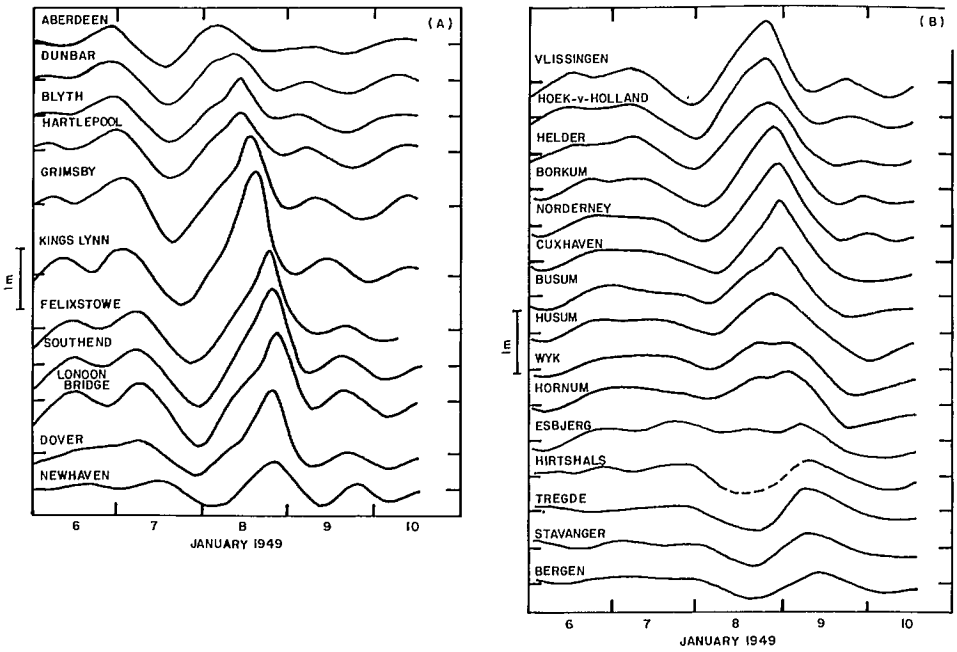

FIG. 7.91. Storm surge profiles at stations along the (A) western boundary of the North Sea and the (B) eastern boundary of the North Sea during January 6–10, 1949. (Charnock and Crease 1957)

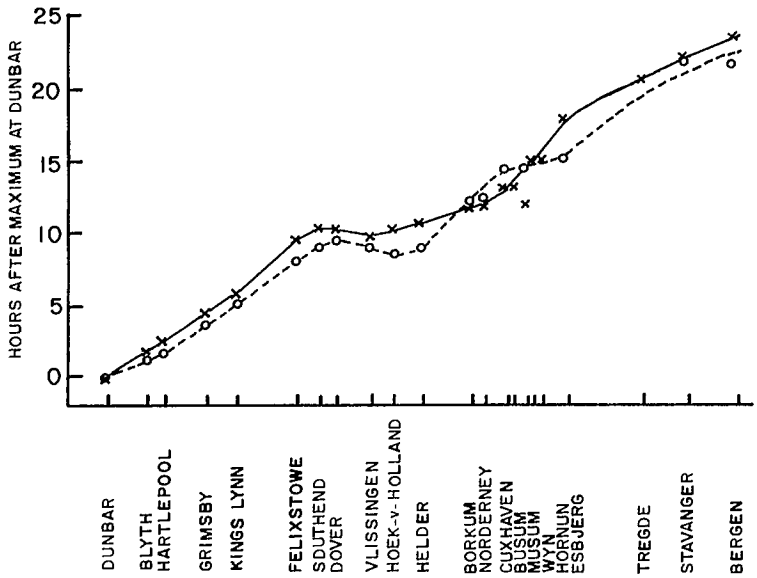

FIG. 7.92. Progress of storm surge and diurnal tide around the North Sea. (Charnock and Crease 1957)

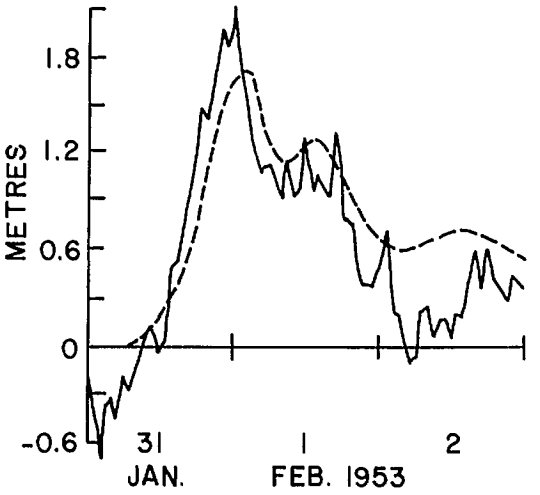

FIG. 7.93. Observed (solid line) and computed (broken line) storm surges at Immingham, U.K., during January 31–February 2, 1953. (Rossiter 1959b)

TABLE 7.59. Frequency of negative storm surges in the southern part of the North Sea. (Geelhoed 1973)

Location	Amplitude (cm) of negative surge that can occur (at the time of low water) with the frequency per year of			Amplitude (cm) of negative surge that can occur (at the time of high water) with the frequency per year of		
	10	1	10^{-1}	10	1	10^{-1}
Hook of Holland	50	83	117	50	80	111
Flushing	46	75	103	47	80	113
Dunkerque	44	68	92	46	75	105
Dover	43	69	96	47	79	111

shallow water depths there. The data source consisted of 50 yr of data for the stations of Hook of Holland and Flushing, 4.7 yr of data for Dunkerque, and 20.1 yr of data for Dover. The results of a frequency analysis are summarized in Table 7.59. This table must be interpreted as follows. For example, at Hook of Holland, negative surges of amplitudes up to 50 cm occur on the average about 10 times per year; negative surges with amplitudes up to 83 cm occur once a year and negative surges of amplitudes up to 117 cm occur only once in 10 yr. The differences between the negative surges at low and at high waters are not significant.

Negative surges predominantly occur in winter. Southerly to westerly winds produce negative surges at Dover whereas at Hook of Holland, southerly to easterly winds cause negative surges. Largest negative surges occur at Southend (up to 2.3 m) and at Tilbury (up to 2.8 m). At other stations, negative surges with amplitudes of 1.0–1.5 m occur. Geelhoed (1973) attributed the differences in the amplitudes of the negative surges at various locations to topographic differences.

TABLE 7.60. Calculated amplitudes (m) of storm surges at three locations in the southern part of the North Sea for three different wind fields. (Based on Geelhoed 1973)

Type of wind field ($83\ km \cdot h^{-1}$)	Amplitude (m) of surge at		
	Sandettie	Brown Ridge	Hook of Holland
Easterly	−0.8	−0.7	−1.3
Westerly	+0.8	+0.7	—
Southerly	−1.9	−1.8	−2.1

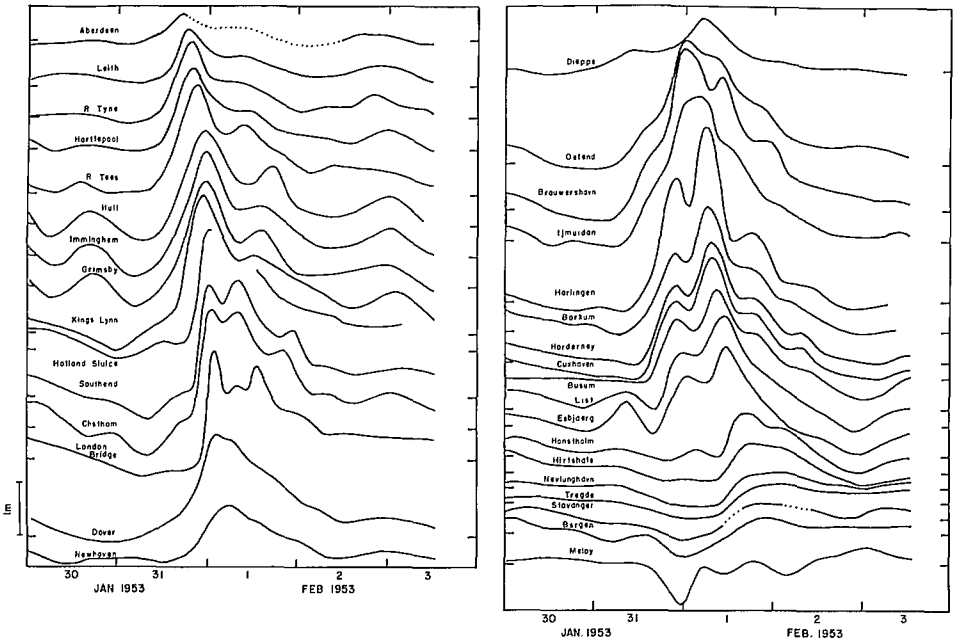

FIG. 7.94. Storm surges at various locations around the North Sea during January 30–February 3, 1953. (Rossiter 1954)

Westerly winds appear to cause negative surges exclusively on the east coast of the United Kingdom whereas easterly winds could cause negative surges exclusively on the coast of the Netherlands. On the other hand, southerly winds can cause negative surges on both coasts simultaneously (and indeed in the whole southern part of the North Sea). The calculated negative surges at three locations for three different wind fields are summarized in Table 7.60.

THE STORM SURGE OF JANUARY 31–FEBRUARY 2, 1953

The track of the storm that produced this major surge is shown in Fig. 6.107. In Fig. 7.93 the surge at Immingham is shown and compared with the calculated surge. The observed surges at various locations around the North Sea are shown in Fig. 7.94. The propagation of the surge through the English Channel from the North Sea is shown in Fig. 7.95.

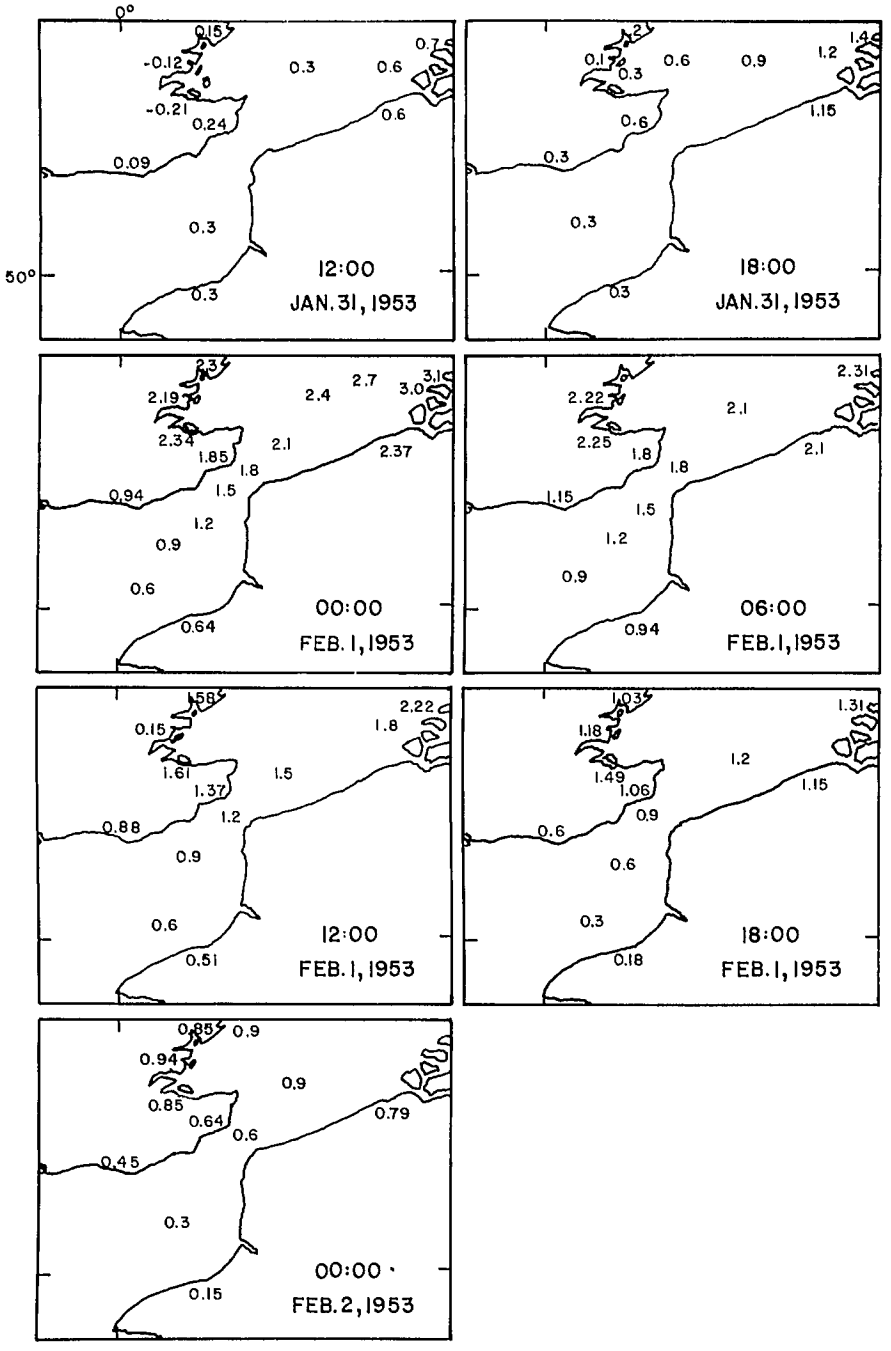

FIG. 7.95. Storm surge heights (metres) in the English Channel during January 31–February 1, 1953. (Rossiter 1954)

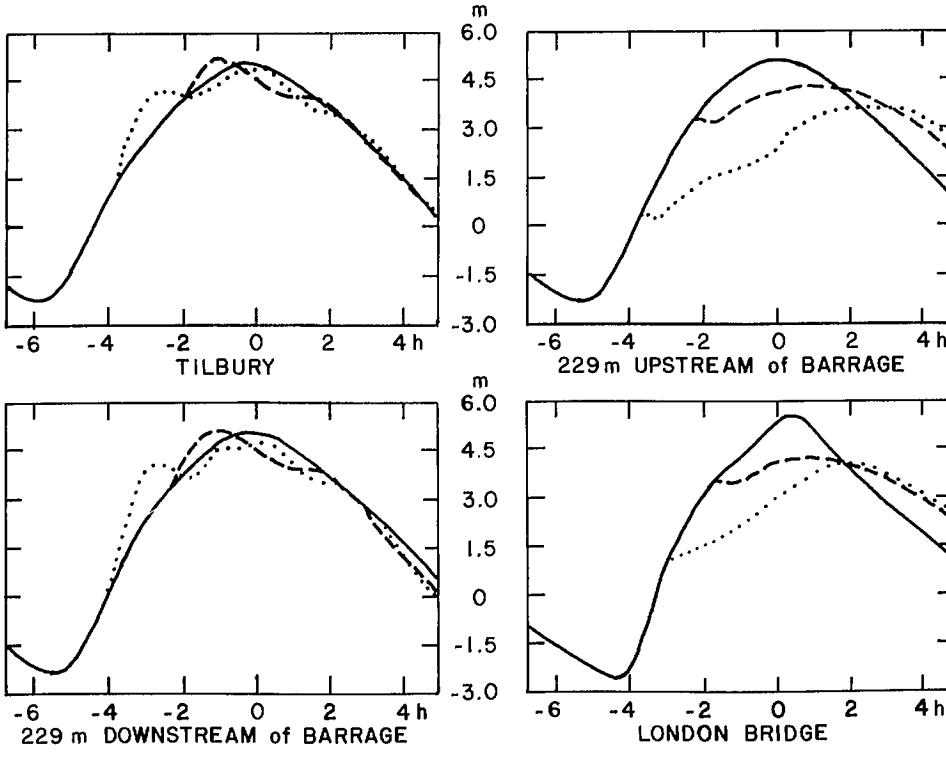

FIG. 7.96. Influence of 90% closing of the barrage on storm surges in the Thames Estuary. Solid line, observed surge during January 30–February 1, 1953; broken line, barrage closed 2 h before high water; dotted line, barrage closed 4 h before high water. (Allen et al. 1955)

Allen et al. (1955) performed hydraulic model studies to simulate this surge in the Thames Estuary. The model had the following features: horizontal linear scale, 1/3000; vertical linear scale, 1/120; vertical exaggeration, 25; time scale, 1/273.8; velocity scale, 1/10.95; discharge scale, $1/(3.943 \times 10^6)$. In the model the tides were generated by an electronically controlled pneumatic displacer.

Tests were also run on the effect of a surge-reducing barrage, located near Purfleet in Long Reach. The barrage was lowered at 1, 2, 3, 4, and 5 h before the occurrence of high water at the site of the barrage. The amount of closure was varied from 50 to 90% of the cross-sectional area of the estuary at mean tide level. Other tests were run with 80 and 100% closures. The effects of the barrage for 90 and 100% closures at four different locations are illustrated in Fig. 7.96 and 7.97, respectively. Results are shown for two closure times (2 and 4 h before high water). For comparison, the observed surge during the January–February 1953 case is also shown. These results appear to indicate that the barrage would have some effect in reducing storm surge levels.

STORM SURGES IN THE NORTH SEA AFTER 1953

Following the disastrous storm surge of January 30–February 2, 1953, in the North Sea, the storm surge warning service for the east coast of the United Kingdom was

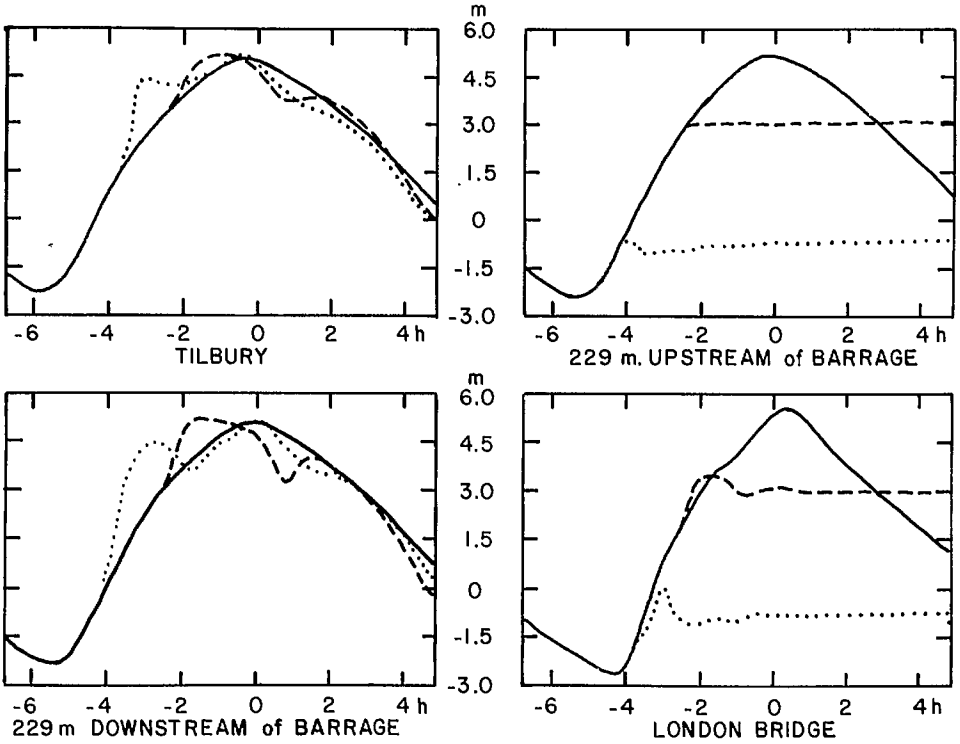

FIG. 7.97. Influence of 100% closing of the barrage on storm surges in the Thames Estuary. Solid line, observed surge during January 30–February 1, 1953; broken line, barrage closed 2 h before high water; dotted line, barrage closed 4 h before high water. (Allen et al. 1955)

improved further. Hunt (1972) discussed the activities of the storm surge warning service. The following eight stations are treated as reference ports: Stornoway, Wick, Aberdeen, Tyne entrance, Immingham (on the Humber station), Lowestoft, Harwich (after 1970, this was replaced by Walton in Essex), and Southend. The storm surge at these locations during September 28–29, 1969, is shown in Fig. 7.98. One can see the propagation of a negative surge southward along the east coast of the United Kingdom. This was followed by a positive surge with peak values of 2.2 ft (0.67 m) at Stornoway and 7.4 ft (2.26 m) at Southend.

Multiregression techniques were used to determine the significant storm surge generating parameters at the above ports. At Stornoway, the atmospheric pressure gradient must be considered to predict the surge generated northwest of Scotland. At all the other ports, the wind stress and the southward propagation of the surge were important.

Prediction formulae were developed for 12- and 4-h predictions. For the 4-h prediction the rms error was 0.4 ft (0.12 m) (a little less than 0.4 ft for the stations on the northern port and slightly greater than 0.4 ft for the southern stations). For example, the 4-h prediction formula for Southend is

$$(7.72) \qquad S = 0.29 + 73S_L + 0.38S_I - 0.57S_{L-3} + 0.007V_{t-6}^{330}$$

where S is the peak surge at Southend (feet), S_L and S_I are the peak surges at Lowestoft

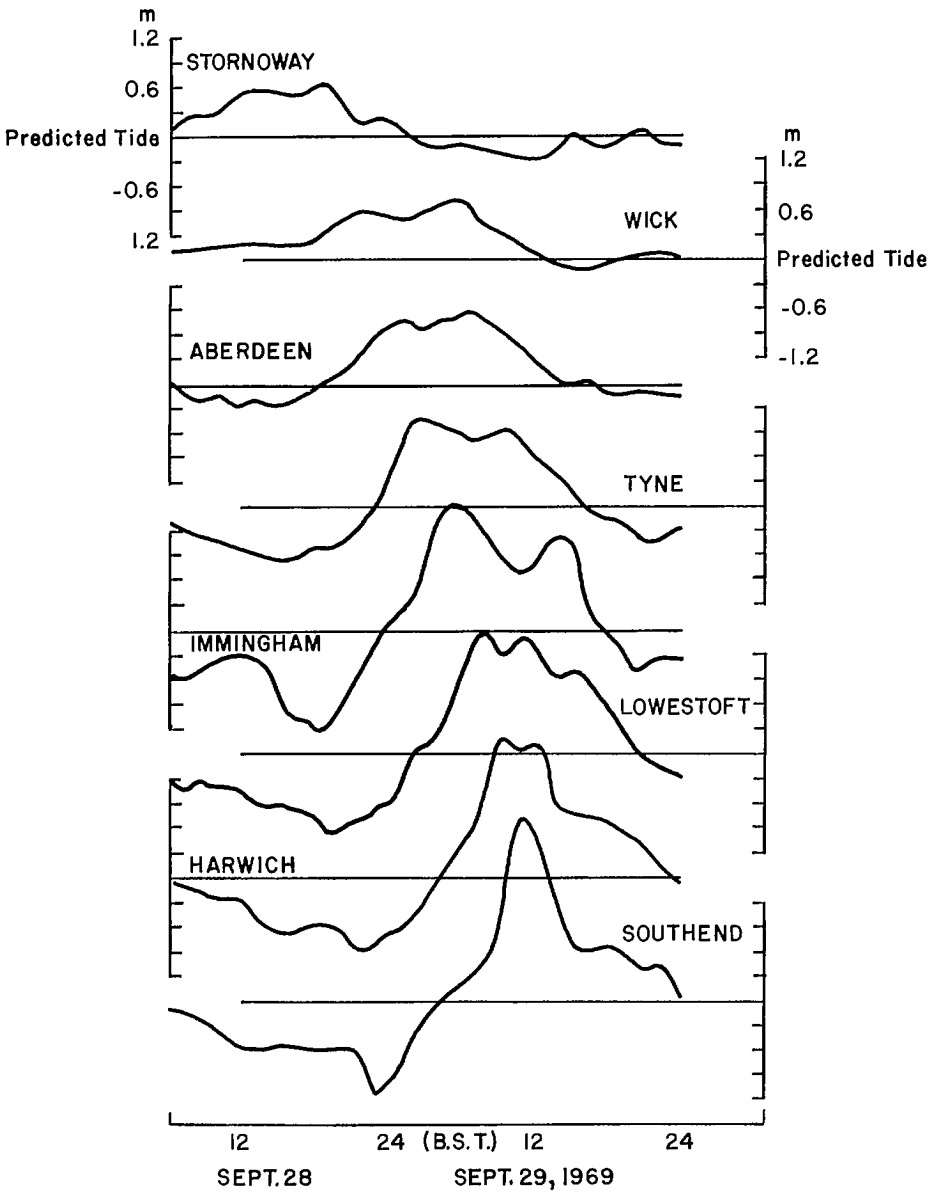

FIG. 7.98. Storm surge at the reference ports (of the U.K. Storm Surge Warning Service) during September 28–29, 1969. (Hunt 1972)

and Immingham (note that high water occurs at Lowestoft and Immingham some 3 and 7 h before it occurs at Southend), S_{L-3} is the surge at Lowestoft some 3 h before high water at Lowestoft (this is a parameterization for the tide–surge interaction), and V_{I-6}^{330} is the 333° component of the geostrophic wind (knots) in an area off Immingham and Lowestoft.

Following the 1953 disastrous storm surge, several numerical models for the North

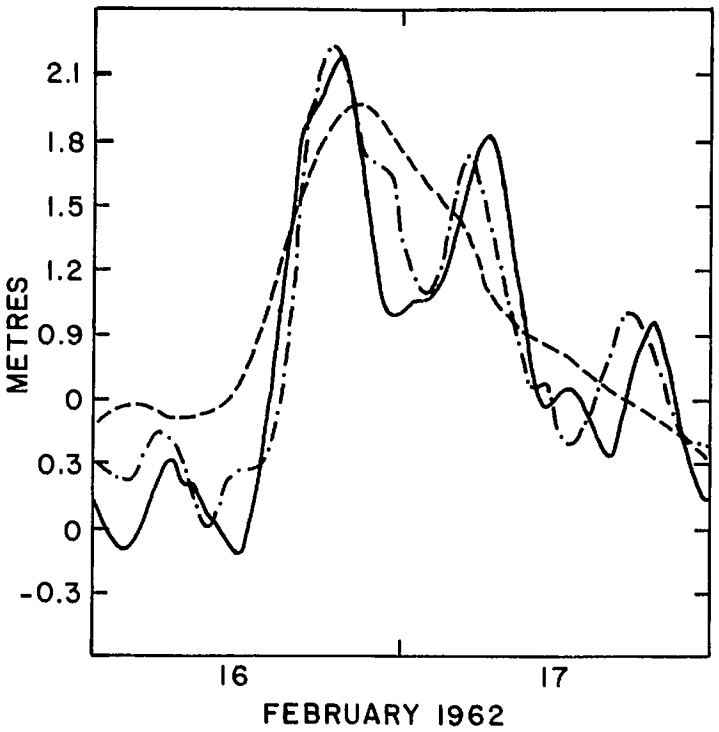

FIG. 7.99. Comparison of observed and computed surges at Southend, U.K., during February 16–17, 1962. Solid line, observed surge; broken line, computed surge using a linear model; dashed–dotted line, computed surge using a nonlinear model. (Rossiter 1971)

Sea and Thames Estuary were developed. Results from a linear model and a nonlinear model are compared with the observed surge of February 16–17, 1962, at Southend in Fig. 7.99.

A major storm surge occurred in the southern part of the North Sea and in the Thames Estuary during January 31–February 1, 1983, exactly 30 yr after the major surge of 1953. The meteorological conditions were somewhat different in these two cases. The surge of 1983 was potentially as destructive as the one of 1953. However, because of considerable improvement in storm surge warning services and the development of coastal protection works and the Thames Estuary barrier, loss of life and damage to property were considerably less than in 1953.

MODELING OF STORM SURGES IN THE NORTH SEA (INCLUDING THE THAMES ESTUARY)

Certain models have already been considered for the North Sea in different sections. Ishiguro (1976a) showed through electronic analog models that atmospheric pressure gradient generated surges are important in the North Sea (Table 7.61). Ishiguro (1976b) gave diagrams of estimated peak surges for different wind speeds. Contours of surge height for a wind speed of 36 $m \cdot s^{-1}$ are illustrated in Fig. 7.100.

Davies and Flather (1977) computed the storm surge in the North Sea for the case of

TABLE 7.61. Comparison of the amplitudes of pressure gradient generated and wind stress generated surges in the North Sea. (Ishiguro 1976a)

Wind direction (degrees)	Wind duration (h)	Wind speed ($m \cdot s^{-1}$)	Pressure gradient ($mb \cdot 100\ km^{-1}$)	Pressure-generated surge, Y_p (cm)	Wind-generated surge, Y_w (cm)	Y_p/Y_w (%)
22	30	10	2.3	8	33	24
		20	4.5	16	130	12
		30	6.7	23	293	8
		40	9.0	32	520	6
112	10	10	2.3	10	15	67
		20	4.5	20	60	33
		30	6.4	30	135	22
		40	9.0	40	240	17

April 1–6, 1973, using several different numerical models. The features of these models are summarized in Table 7.62 and the rms errors at various locations for these models are listed in Table 7.63.

Prandle and Wolf (1978a, 1978b) used parallel numerical models to study the modification of the tide due to surge and vice versa in the southern part of the North Sea. The tide and the surge before and after interaction for the case of October 19, 1970, are shown in Fig. 7.101. The interactions at Lowestoft and Southend for the event of January 31–February 1, 1953, are shown in Fig. 7.102 and 7.103, respectively. The contours of the interaction in the southern part of the North Sea are shown in Fig. 7.104.

Flather (1980) summarized the status of a real-time storm surge prediction scheme for the North Sea. In this scheme, the meteorological forcing terms are obtained in real time as output of a 10-level primitive equation atmospheric model. In the storm surge model, a coarse model covers the whole of the Northwest European continental shelf. Models with finer resolution for the southern bight, eastern part of the English Channel, and the Thames Estuary are being developed. The contours of the surge at 03:00 GMT on January 12, 1978, are shown in Fig. 7.105. Hamilton (1979) used a conformal coordinate stretched model for storm surge propagation through the English Channel. For some recent works, see Peregrise (1981), Townsend (1981), Golding (1981), Flather (1981), Davies (1981), Wolf (1981), Horner (1981), and Walden (1982).

STORM SURGES IN THE IRISH SEA

In section 6.9, the meteorological situations leading to storm surges in the Irish Sea were discussed. The storm surge at Liverpool during December 29, 1921, to January 2, 1922, and the pressure data are shown in Fig. 7.106. Creswell (1929) gave storm surge amplitudes at Holyhead, Belfast, Fleetwood, and Preston for the surge of October 20–24, 1928. These range from 1 ft 7 in. (48 cm) to 4 ft 7 in. (140 cm). However, a surge on October 29, 1927, had amplitudes of 7 ft 8 in. (2.34 m) at Fleetwood and 10 ft 2 in. (3.1 m) at Preston. For this event, the amplitudes at Holyhead and Belfast were 3 ft 4 in. (1.04 m) and 3 ft 2 in. (0.97 m), respectively.

During the storm surge event of January 31, 1957, the surge amplitude at Liverpool reached a peak value of 3 ft whereas another event on February 4, 1957, produced a surge with an amplitude of 5.8 ft (1.76 m). Another surge event of January 11–12, 1962, produced surges up to 5.5 ft (1.68 m) at Liverpool and up to 6.5 ft (1.98 m) at Avonmouth.

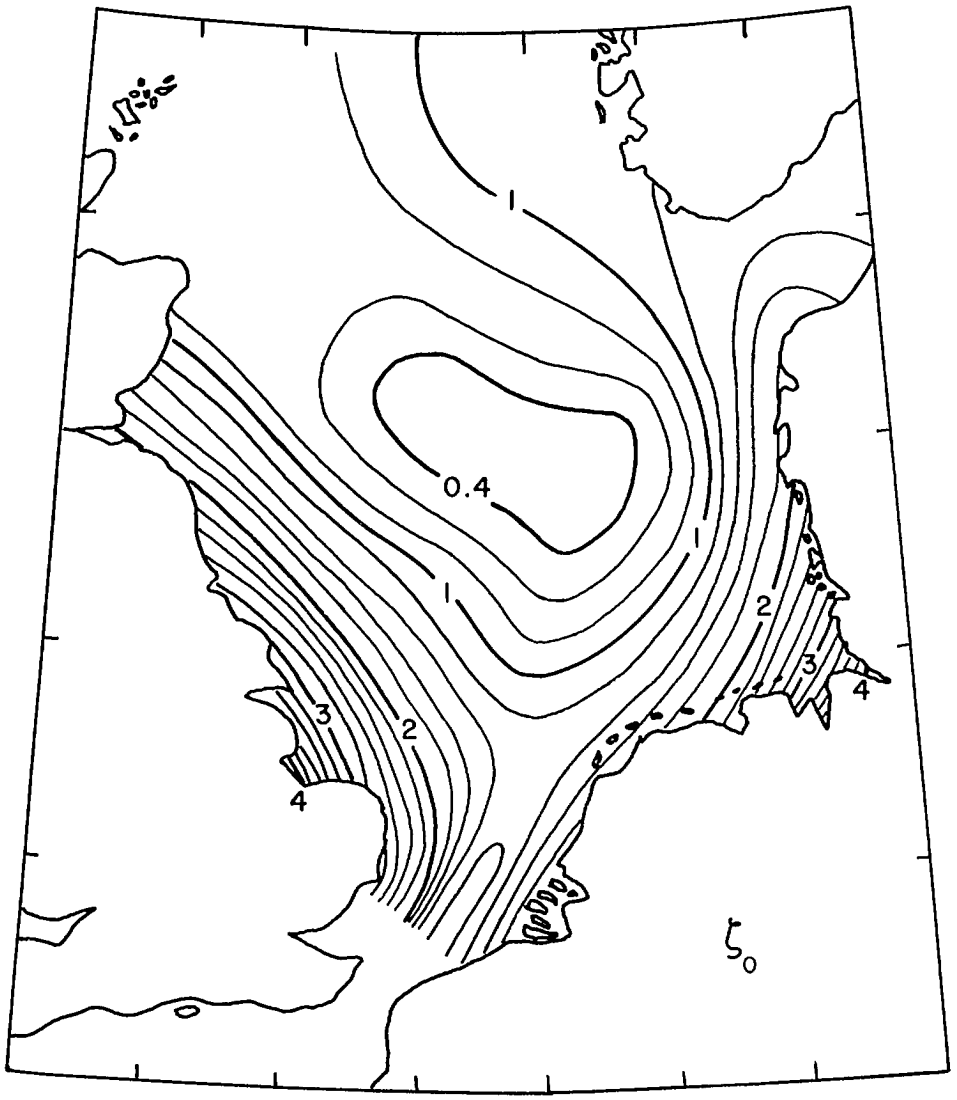

FIG. 7.100. Storm surge heights in the North Sea for a wind speed of 36 $m \cdot s^{-1}$ blowing for 10 h. (Ishiguro 1976b)

The surges at Milfordhaven and Avonmouth during November 29–30, 1954, are shown in Fig. 7.107.

Corkan (1952) mentioned that localized northerly winds over the Irish Sea will lower the water level everywhere in this waterbody, with the minimum lowering occurring at Liverpool. Strong southerly winds near the southern entrance to the Georges Channel will produce only small surges at locations such as Cork and Newlyn. After several hours, the general level rises in the Irish Sea. On the other hand, when a depression exists south of Ireland (with strong southerly winds blowing steadily) over the Bay of Biscay, surges up

TABLE 7.62. Features of the different models for the North Sea used in the simulation of the storm surge of Apr. 1–6, 1973. (Davies and Flather 1977)

Calculation	Model	Open boundary condition	Surge input	Tidal input
a	Shelf	Radiation	Hydrostatic	None
b	North Sea	Elevation specified	Hydrostatic	None
c	Shelf	Radiation	Hydrostatic	$M_2 + S_2$
d	North Sea	Elevation specified	Hydrostatic	$M_2 + S_2$
e	North Sea	Elevation specified	From calculation c + observations from Wick	$M_2 + S_2$

TABLE 7.63. Root-mean-square errors (cm) for calculations using models a to e (see Table 7.62) for the storm surge of Apr. 2–6, 1973. (Davies and Flather 1977)

Port	a	b	c	d	e
Wick	18.1	12.6	13.5	12.6	0.0
Aberdeen	20.3	13.7	15.9	13.3	10.9
North Shields	22.5	17.7	17.0	16.6	16.3
Inner Dowsing	26.9	27.5	21.2	27.1	25.2
Immingham	26.6	25.6	19.5	20.8	18.2
Lowestoft	29.8	28.5	25.0	27.5	25.3
Walton-on-Naze	34.3	31.2	27.2	29.0	26.8
Southend	42.9	38.6	33.9	35.1	33.0
Ostende	36.1	34.0	25.1	30.3	26.7
Ijmuiden	42.3	40.6	34.6	35.4	33.3
Terschelling	32.3	31.8	27.2	27.3	26.4
Cuxhaven	48.0	45.0	37.4	40.2	38.4
Esbjerg	32.6	29.0	23.3	24.1	21.2

to 1–2 ft (0.3–0.6 m) could occur inside the region bordered by a hypothetical line joining Cork to Newlyn.

Heaps and Jones (1975) simulated the storm surge in the Irish Sea for the event of January 10–18, 1965, using a two-and-a-half-dimensional model. The surge profiles at several locations in the Irish Sea (observed and computed) are shown in Fig. 7.108. The horizontal distribution of the storm surge heights at two different times is given in Fig. 7.109.

Heaps and Jones (1979) simulated the storm surges in the Irish Sea for the events of November 11–15, 1977, and January 2–3, 1976, and compared these with the event of January 13–17, 1965. They paid particular attention to the time of occurrence of the peak surge relative to the times of high and low water. The tide and surge (computed and observed) at Liverpool and at Workington are shown in Fig. 7.110 and 7.111, respectively. McIntyre (1979) used an analytical model to simulate the storm surge of January 1–3, 1976, in the Celtic Sea (south of Ireland). Amin (1982) modeled the tides and surges on the west coast of the United Kingdom.

STORM SURGES IN BELGIUM, THE NETHERLANDS, GERMANY, AND DENMARK

Up to this point, the storm surges in the western and southwesten part of the North Sea have been considered. Now, the surges along the southern and eastern coasts will be

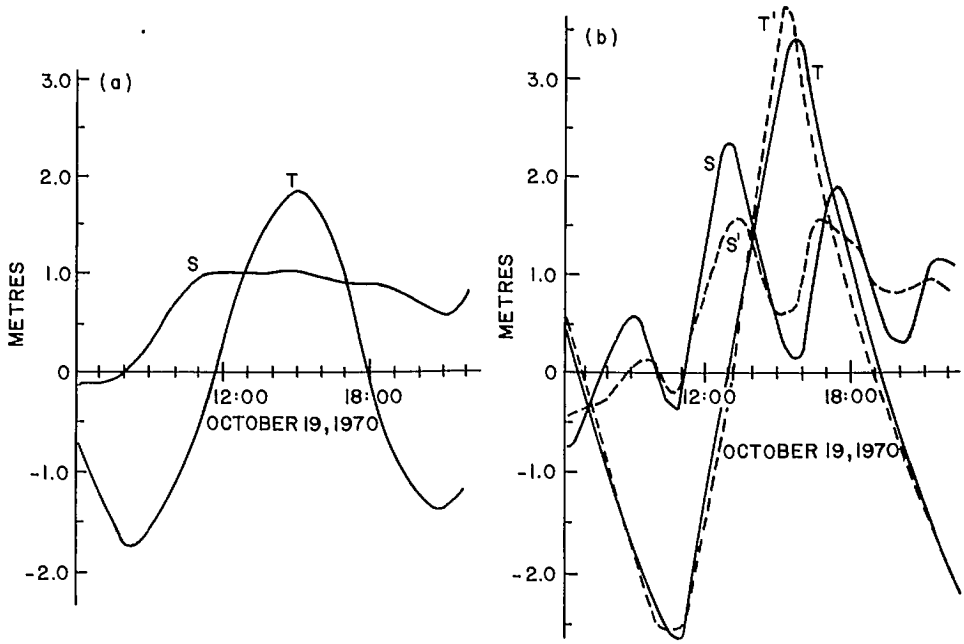

FIG. 7.101. Tide–surge interaction at (a) Walton–Margate (mouth of the model) and (b) Tower Pier. T, tide; S, surge; T′, tide modified due to interaction with surge. S′, surge modified due to interaction with tide. (Prandle and Wolf 1978)

considered. The horizontal distribution of the storm surge amplitudes at three different times during January 31–February 2, 1953, in the North Sea is given in Fig. 7.112. Maximum amplitudes up to 3 m occurred on the Belgian and Netherlands coasts. Amplitudes up to 2.5 m occurred on the coast of France, whereas amplitudes up to 2 m were found in the German Bight. On the Danish coast the maximum amplitudes were about 1 m. Calculated (Davies and Flather 1977) and observed surges at five locations along the south and west coasts of the North Sea for the surge of April 2–6, 1973, are compared in Fig. 7.113.

Adam (1979) described the real-time storm surge forecasting system for the coast of Belgium. The meteorological aspects of this model were considered in section 6.9. The surges that are significant on the coast of Belgium originate from the northwest. A surge wave travels from North Shields to Ostend in approximately 12 h. Thus, using the forecasted value of the surge at North Shields, one can provide an 18- to 24-h advance warning for the Belgium coast. One of the deficiencies of the model is its overestimation of the amplitudes of positive surges and underestimation of the amplitudes of negative surges.

STORM SURGES ON THE COAST OF THE NETHERLANDS

In section 6.9, the works of Gallé (1915) and Schalkwijk (1947) were discussed. The storm surge amplitudes along the coast of the Netherlands during the major storm surge of January 31–February 1, 1953, were greater than those on the east coast of the United Kingdom (Ufford 1953). Surge amplitudes up to 9 ft (2.74 m) occurred along the coasts

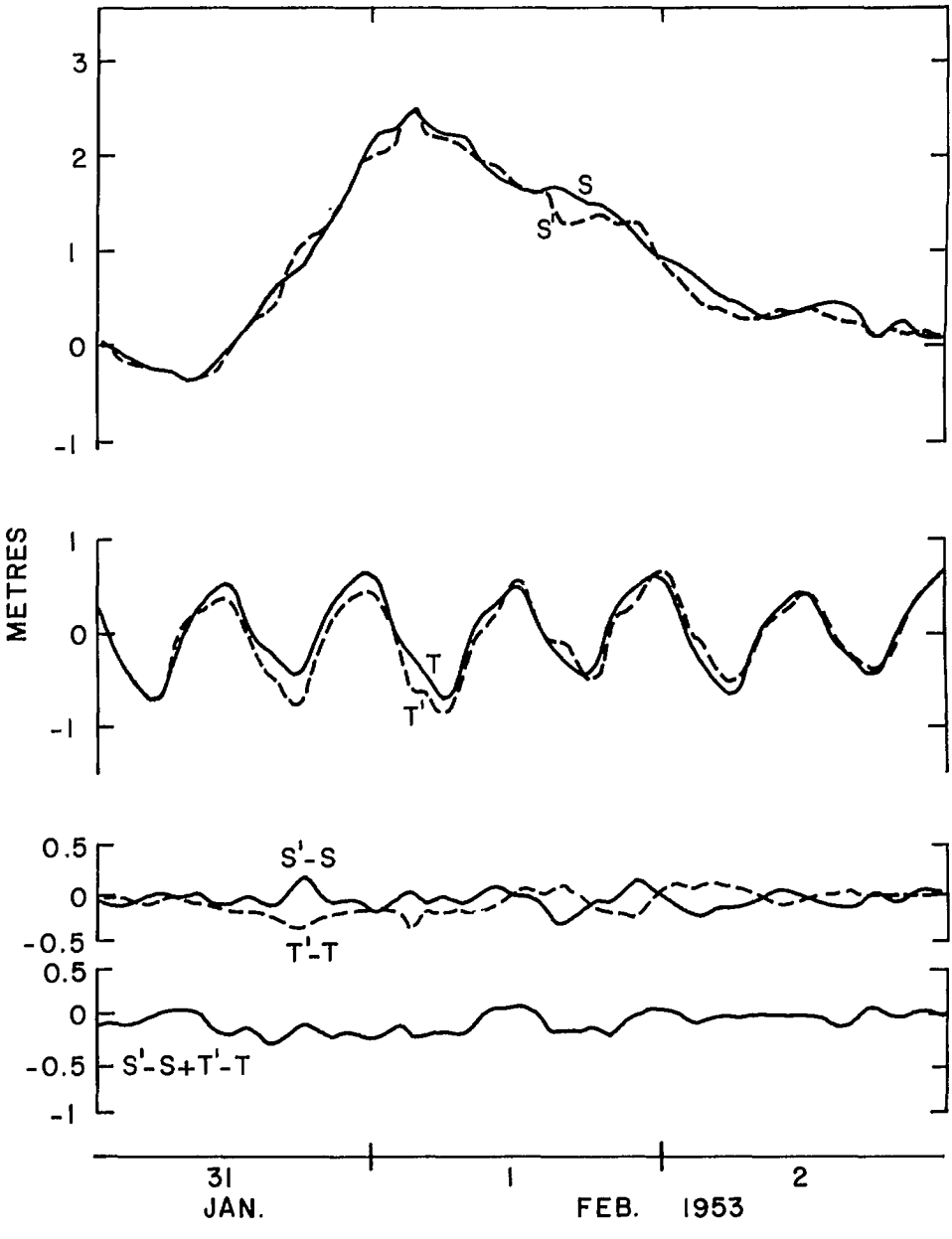

FIG. 7.102. Tide–surge interaction at Lowestoft, U.K. See Fig. 7.101 for explanation. (Prandle and Wolf 1978)

of the provinces of Zeeland and Zuid-Holland, with a peak surge of 9.6 ft (2.93 m) occurring at Hellevoetsluis. In the Scheldt Estuary the amplitudes were even greater. At Berger op Zoom the amplitude was about 11 ft (3.35 m).

The water level rose above the dykes, and about 50 dykes collapsed and at least 1800

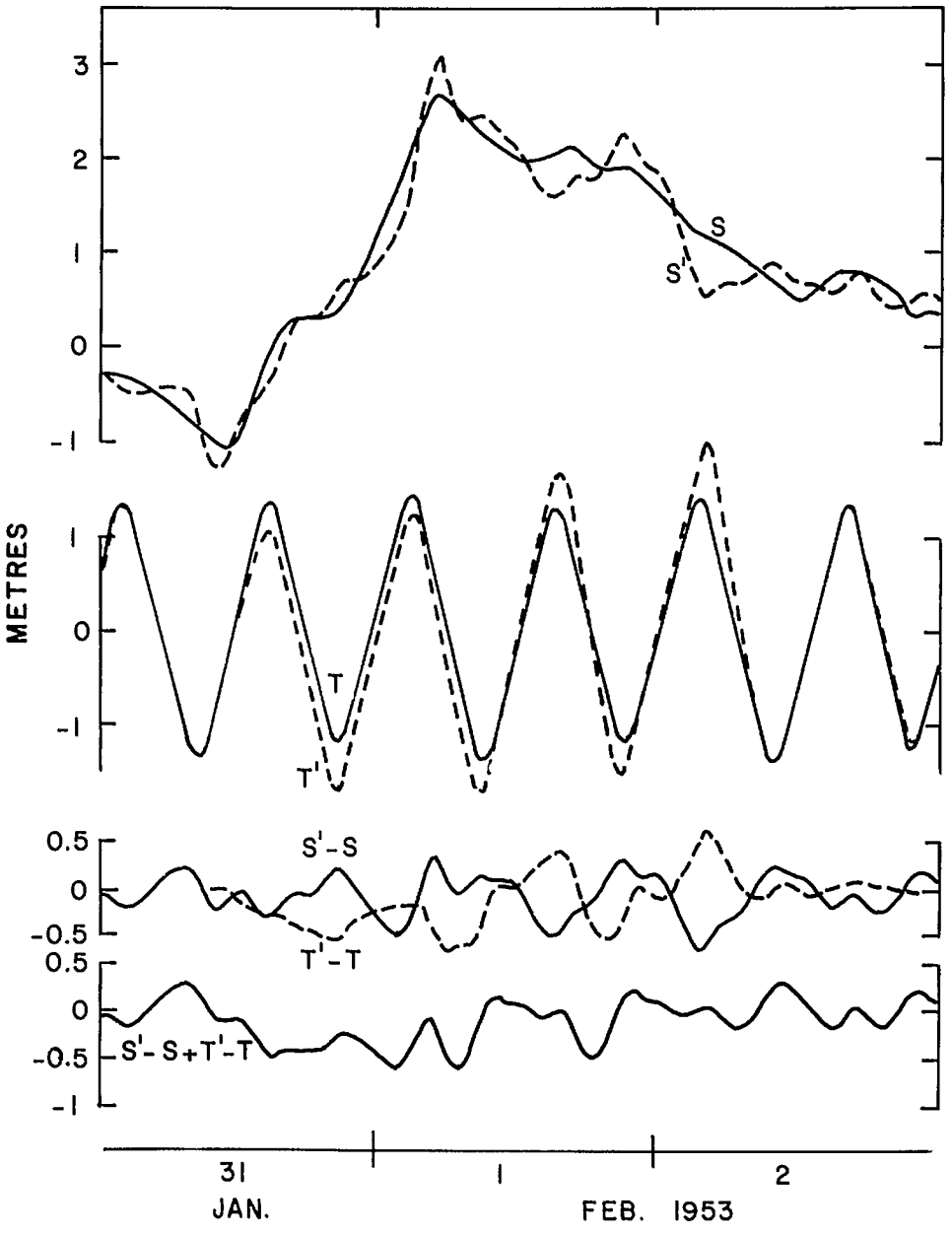

FIG. 7.103. Tide–surge interaction at Southend, U.K. See Fig. 7.101 for explanation. (Prandle and Wolf 1978)

people died. The damage exceeded £100 million (at 1953 prices). Ufford (1953) mentioned that this was the biggest surge since the one on November 18, 1421, when at least 10 000 people died. Since the time tide gauges were set up in 1890, the surge of 1953 was

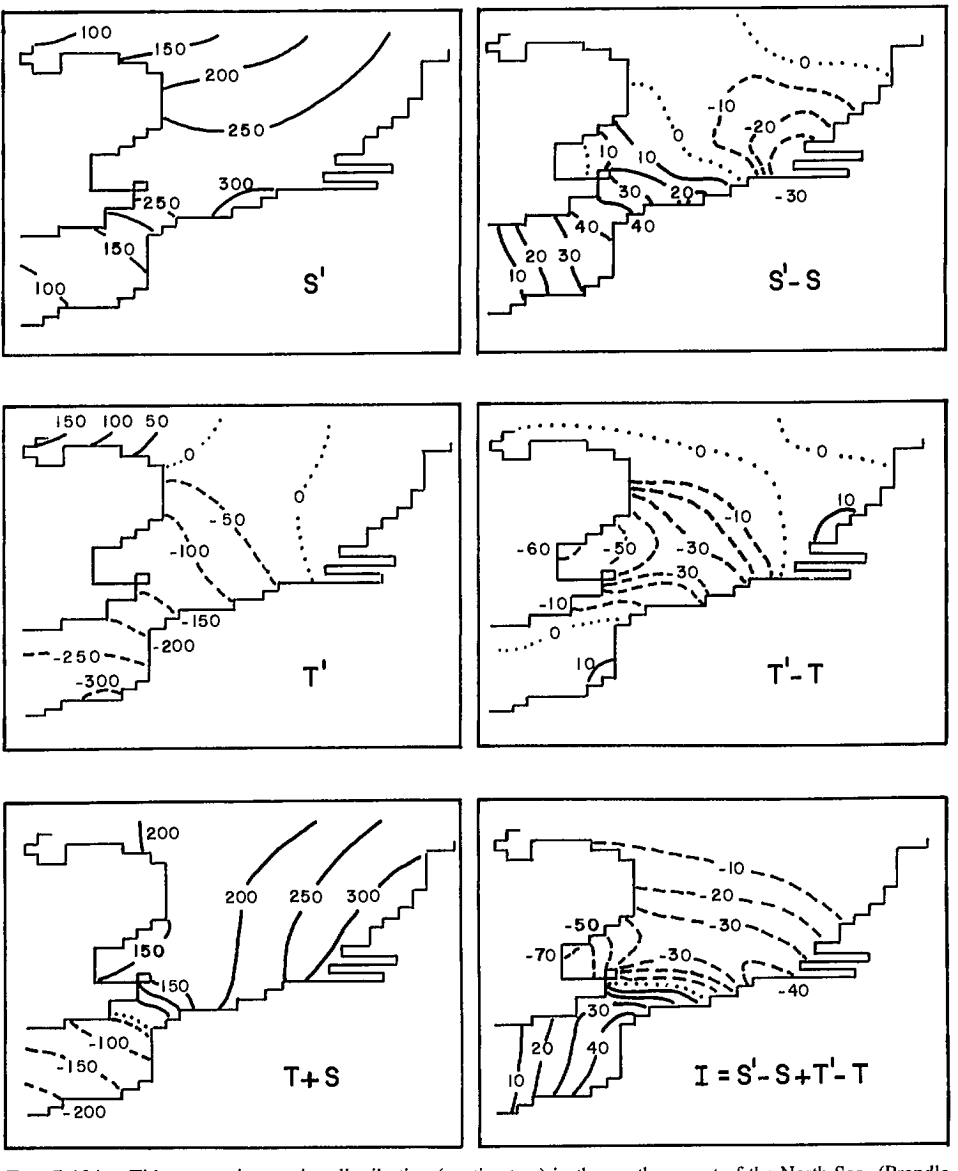

FIG. 7.104. Tide–surge interaction distribution (centimetres) in the southern part of the North Sea. (Prandle and Wolf 1978)

2 ft greater on the average than any other surge during the period 1890–1953. The extent of the flooding on the coast of the Netherlands is shown in Fig. 7.114.

Weenink (1956) studied the so-called twin storm surges that occurred on December 21 and 24, 1954. The observed surge and that computed through an equilibrium wind assumption are shown in Fig. 7.115.

Timmerman (1971) showed that moving cold fronts over the southern part of the North Sea can produce a sudden increase of water level on the Netherlands coast (he uses

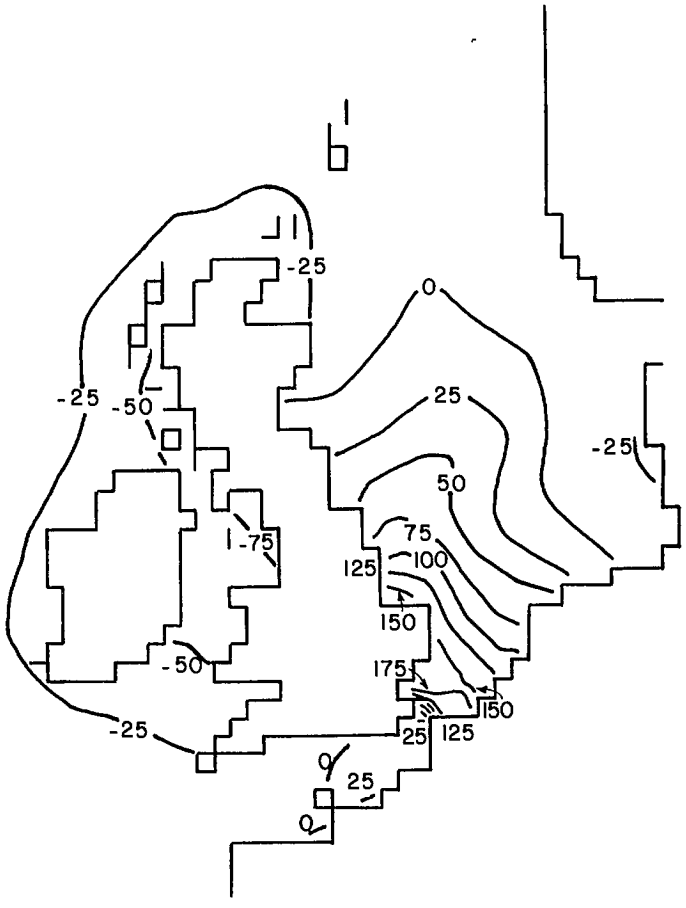

FIG. 7.105. Spatial distribution of surge elevation (centimetres) at 03:00 (GMT) on January 12, 1978, in the northwest continental shelf of Europe. (Flather 1980)

the rather inappropriate term "gust bump" to refer to these water level increases). These increases in the water level occur only when the speed of propagation of the cold front lies between 29 and 36 knots ($54-67\ km \cdot h^{-1}$). This suggests resonance between the traveling atmospheric disturbance and the long surface gravity waves in the water body. He numerically simulated the event of December 13, 1956.

One can obtain some idea of the time scale and amplitudes of the gust bumps from Fig. 7.116. One can clearly see the bump at Katwuk at 11 a.m. on March 27, 1966. The locations of these stations can be seen in Fig. 7.117. Similar sudden water level increases for the event of December 13, 1956, are shown in Fig. 7.118.

Dronkers (1961) discussed the plan of the Delta works project to reduce storm surge amplitudes in the southwest part of the Netherlands. He stated (p. 603):

> . . . this entails the closure of three large sea arms situated between western Scheldt and Rotterdam waterway and will bring about radical changes in the tidal movement and storm flood levels of the estuaries and tidal rivers . . . Three big dams to be built [see Fig. 7.119] in the mouths of eastern Scheldt, Brouwershavense Gat and Haringvliet,

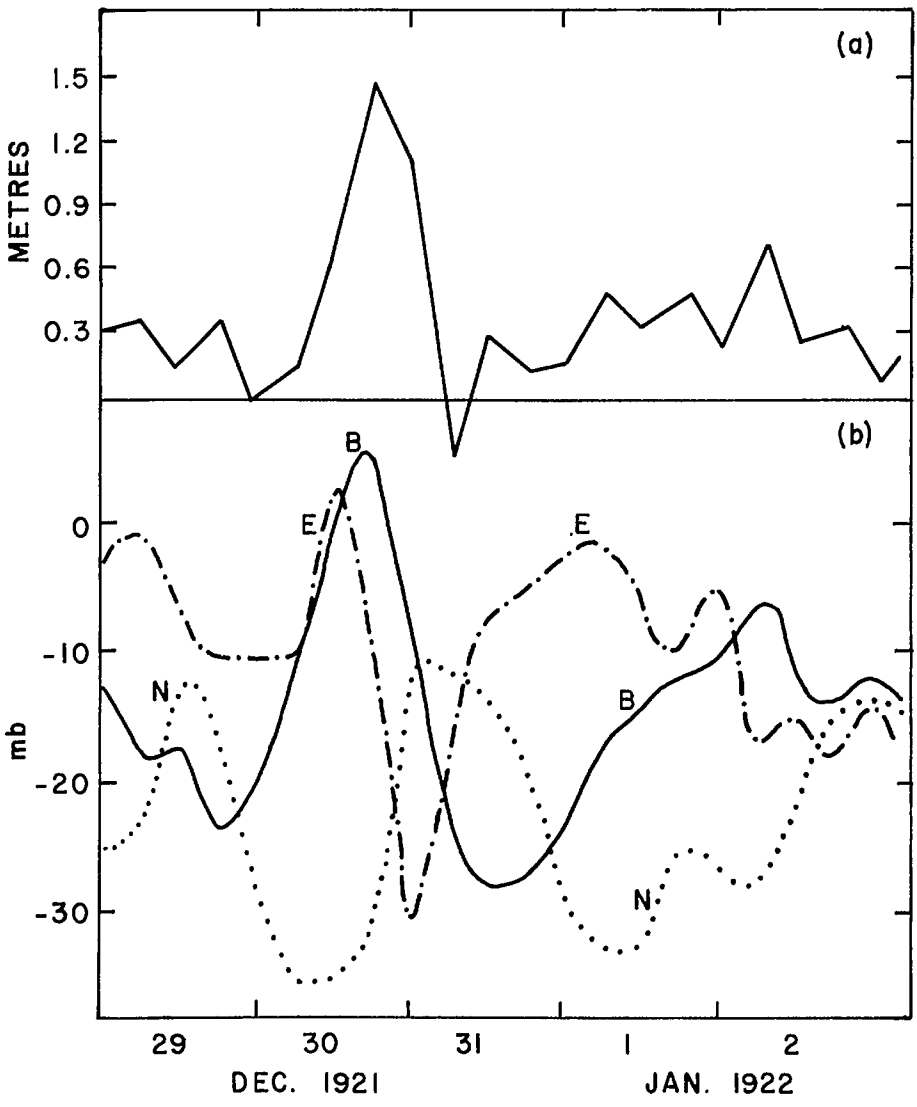

FIG. 7.106. (a) Storm surge at Liverpool, U.K., during December 29, 1921–January 2, 1922. (b) Curve B shows the fall of the atmospheric pressure at Liverpool; curves E and N, respectively, denote the east and north pressure gradients (millibars per 800 km). (Doodson and Dines 1929)

as well as two smaller ones to be constructed further inland . . . The waters of the delta will then be divided into two separate basins by means of a dam in the Yolkerak. The southern basin will be entirely cut off from the sea, becoming a fresh water lake. The northern, comprising the mouths of the Rhine and the Meuse, will remain in communication with the sea, because the Rotterdam waterway must stay open for shipping. Consequently, the tides and storm surges will still be able to penetrate inland via this mouth, but they can cause high water levels in the waterway only; in the rest of the basin their effect will be considerably weakened . . .

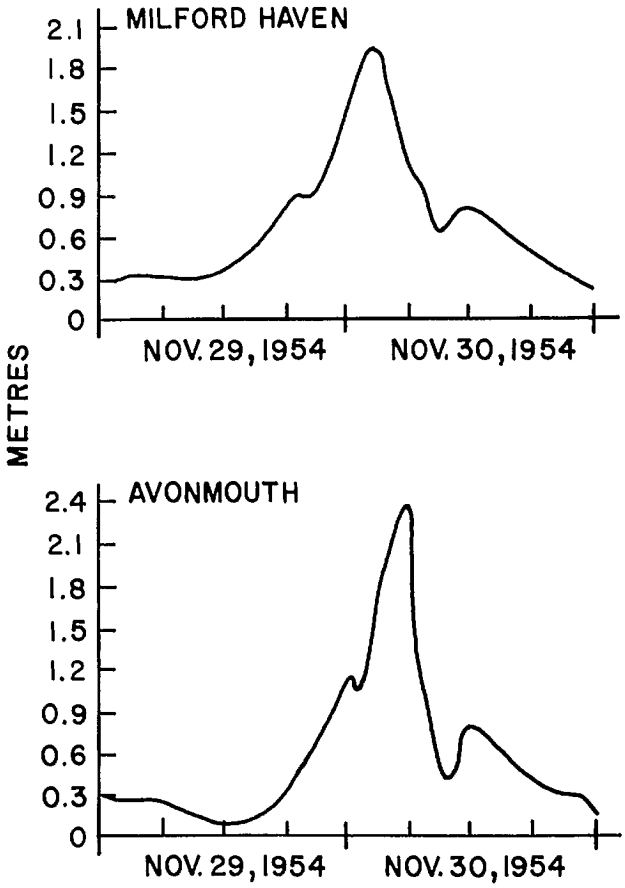

FIG. 7.107. Storm surges at Milford Haven and Avonmouth, U.K., during November 29–30, 1954. (Heaps 1967)

The projected influence of the Delta works on the high water and low water levels is shown in Fig. 7.120. The storm surge amplitudes are expected to be reduced by several feet. The possible modification of the frequency of high water levels at Dordrecht is shown in Fig. 7.121.

Langerak et al. (1979) discussed the status of this project as existed in 1978. They stated (p. 1049):

> In the mid-1950's the Netherlands government embarked on a massive construction program, called the delta plan. Its purpose was to enhance protection from floods caused by the North Sea in the estuaries of the Rhine, Meuse and Scheldt. According to the plan, all connections to the sea were to be closed by dams, except the New waterway to Rotterdam and the western Scheldt. In 1974 all dams and dikes were complete except the dam closing off the eastern Scheldt from the sea. In view of growing opposition to a complete closure, plans were revised in 1976, and instead of the dam, a storm surge barrier will be constructed. This barrier will reduce the tidal range in the eastern Scheldt and will be closed during storm surges.

Some recent information on the status of this project can be seen in Anonymous (1982).

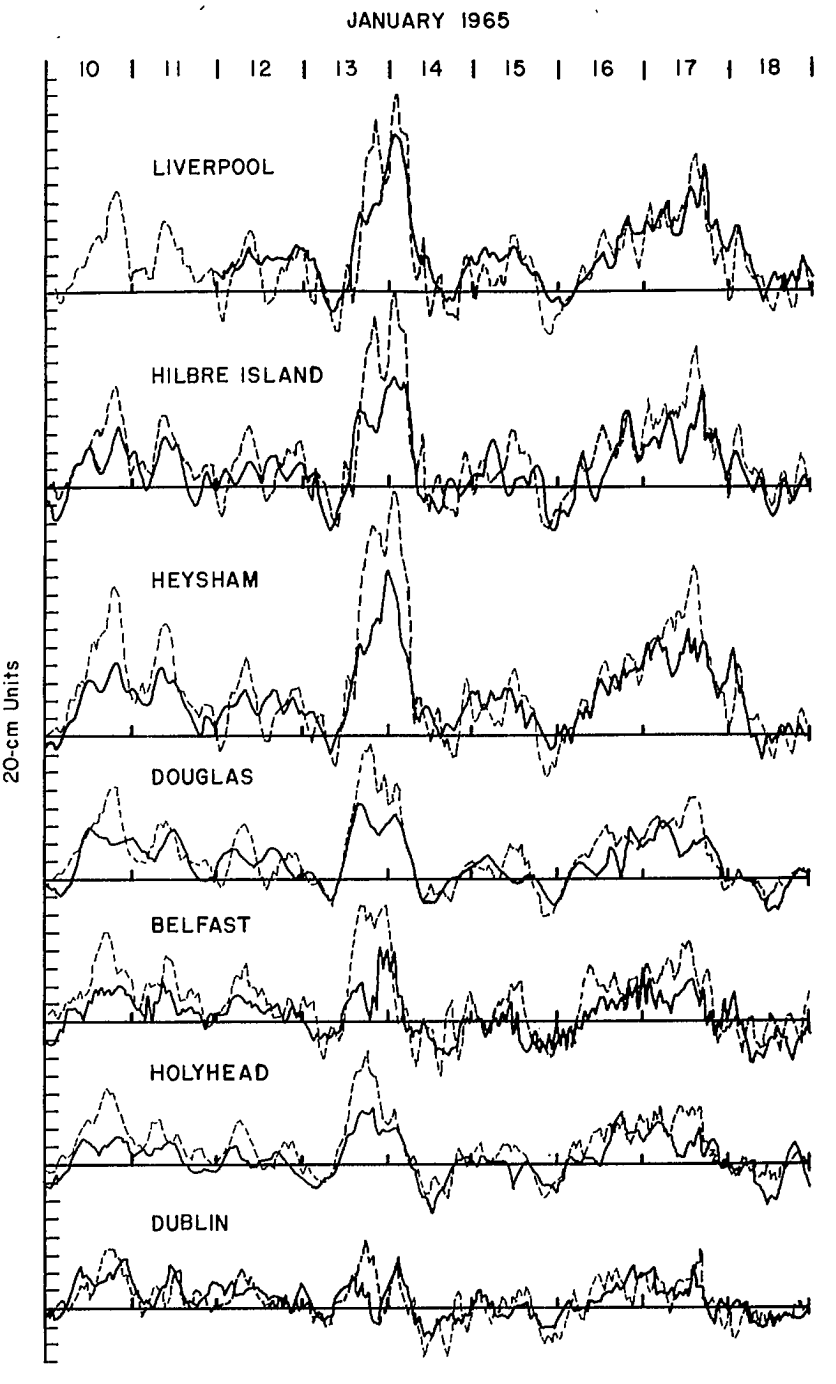

FIG. 7.108. Storm surges at various locations around the Irish Sea during January 10–19, 1965. (One unit = 20 cm along the ordinate). (Heaps and Jones 1975)

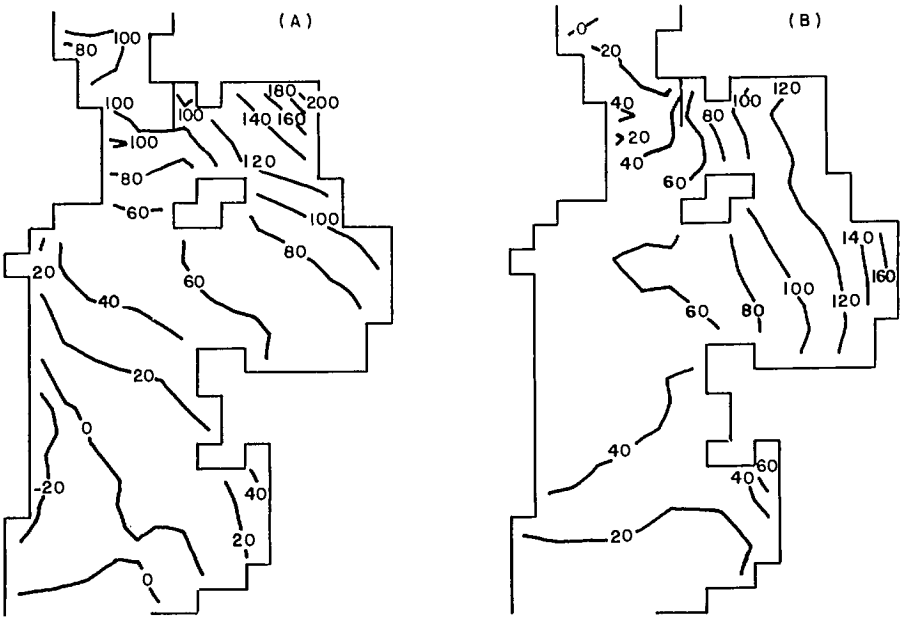

FIG. 7.109. Distribution of storm surge heights (centimetres) in the Irish Sea on January 14, 1965, at (A) 00:00 and (B) 04:00. (Heaps and Jones 1975)

Langerak et al. (1979) developed a numerical model for computing tides and storm surges for this area. The semidiurnal tide propagates along the coast of the Netherlands in a northeasterly direction and the amplitude reduces from 1.90 m at Blankenberghe to about 0.85 m at Scheveningen.

STORM SURGES IN THE GERMAN BIGHT

Tomczak (1950) discussed the storm surge of February 9–10, 1949, in the North Sea. The greatest effect of the surge was on the coast of North Friesland. One interesting feature was that the storm center remained almost stationary off the island of Sylt on the 9th and blocked the outflow of water northwards from the German Bight. The maximum amplitudes of the water level at several locations are listed in Table 7.64.

Siefert (1968, 1978) studied storm surges in the Elbe River. His study involved a total of 130 surges since 1900, and he developed a technique with which the shape of the surge curve can be predicted 6 h in advance to an accuracy of ±0.2 m. He used the results from hydraulic model studies, and his scheme can predict surges at Hamburg 6–8 h in advance to an accuracy of ±0.25 m and the time of the peak surge to within ±30 min. He also considered tide–surge interaction in the Elbe River and showed how the surge modifies the tide. Another important point made was that, following improvements (for navigation) in the Ems, Weser, and Elbe rivers, the amplitudes of storm surges have increased in general.

Engel (1979) described the status of the operational storm surge prediction system for West Germany as existed in 1978. Using numerical models for the meteorological forcing terms as well as for storm surges in the North Sea, the surge of January 3, 1978, was

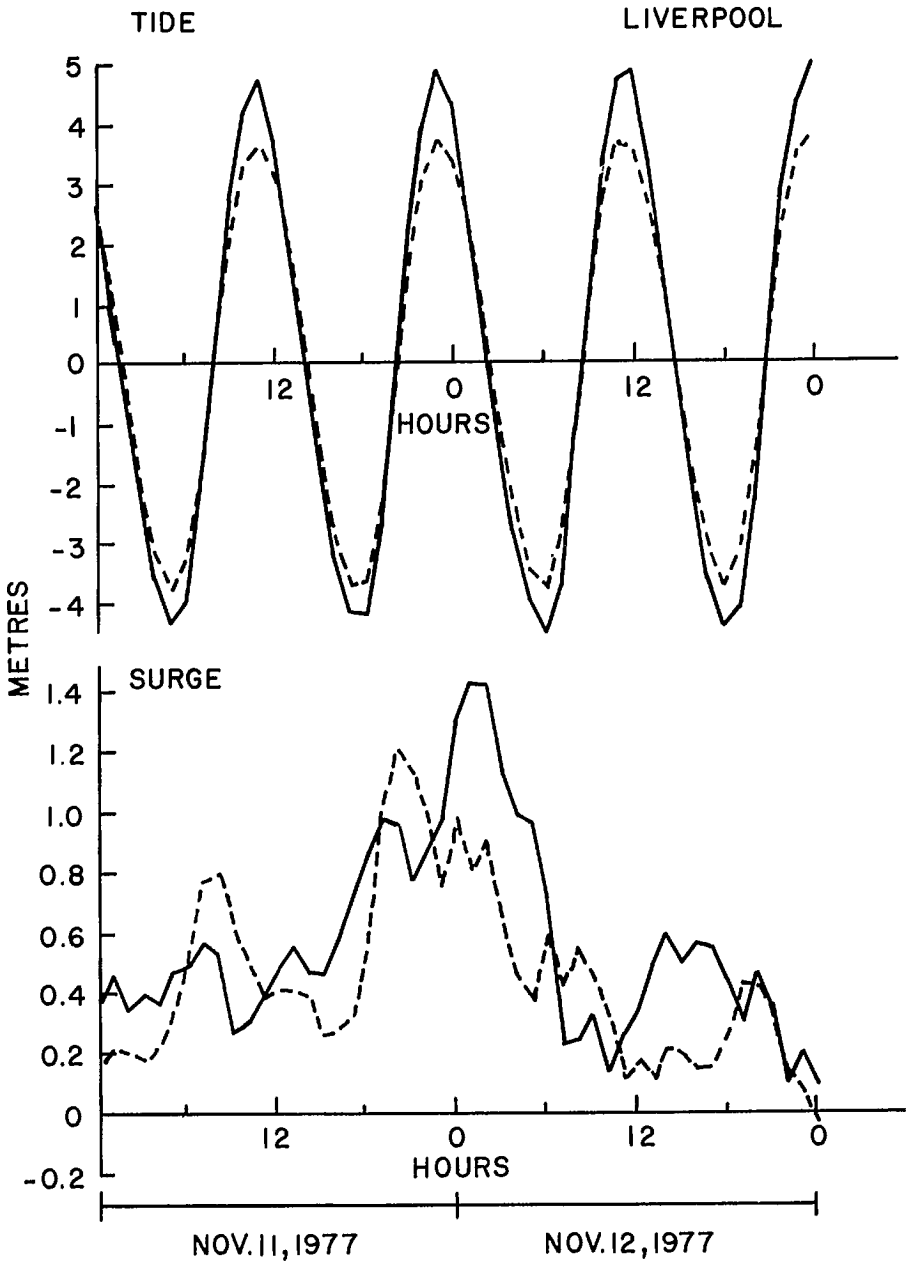

FIG. 7.110. Top: observed (solid line) and computed (broken line) tide at Liverpool during November 11–12, 1977. Bottom: observed (solid line) and computed (broken line) surge at Liverpool for the same period. (Heaps and Jones 1980)

reasonably well simulated. The agreement between observed and hindcasted surges was better than the agreement between observed and predicted surges. Maximum errors occurred in the German bight. These errors are attributed to the errors in the predicted geostrophic winds due to underestimating the atmospheric pressure gradients.

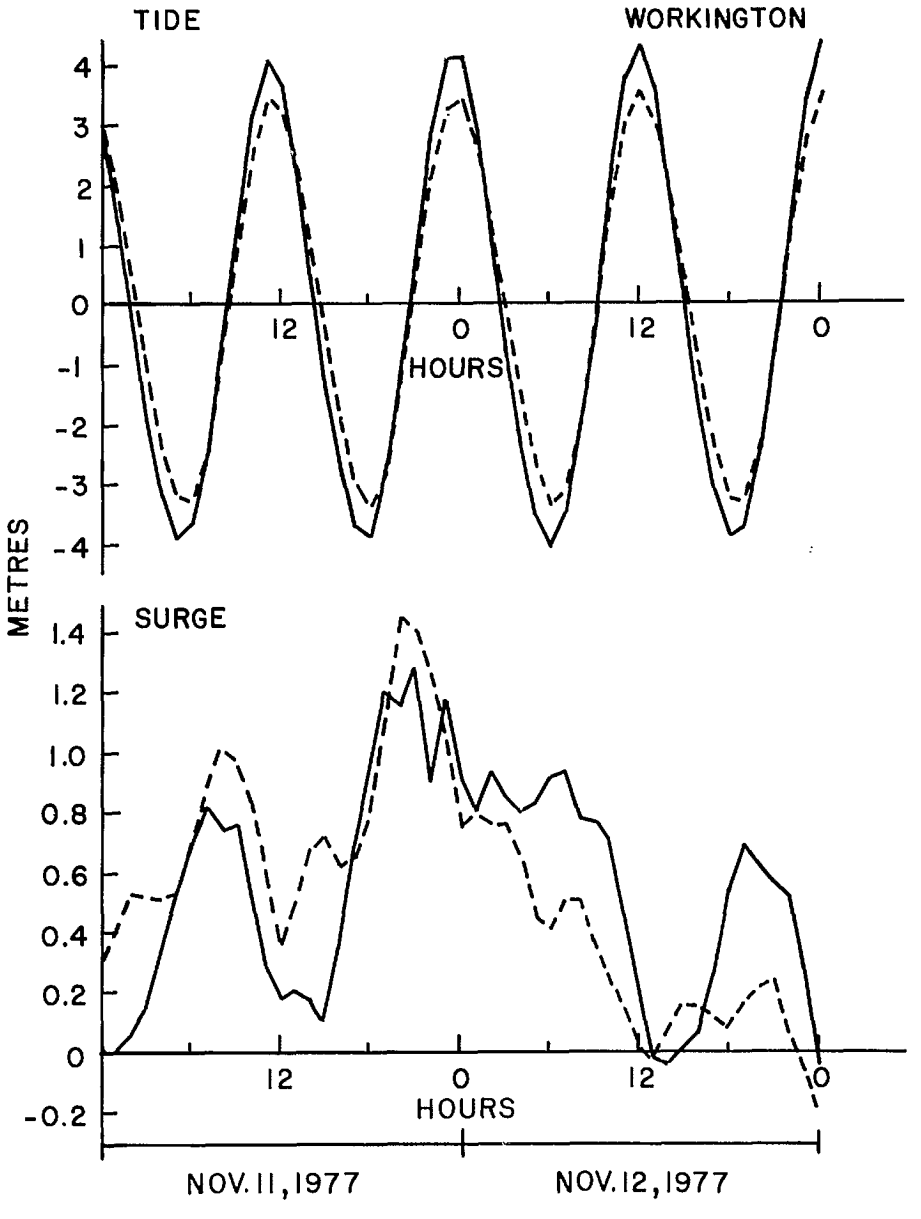

FIG. 7.111. Tide and storm surge at Workington, U.K. See Fig. 7.110 for explanation. (Heaps and Jones 1980)

Göhren (1976) studied currents in the tidal flats in the German Bight. Note that these tidal flats could be as wide as 20 km. He showed that the currents can increase from the normal 30 $cm \cdot s^{-1}$ to as much as 120 $cm \cdot s^{-1}$ during storm surges. The destructive storm

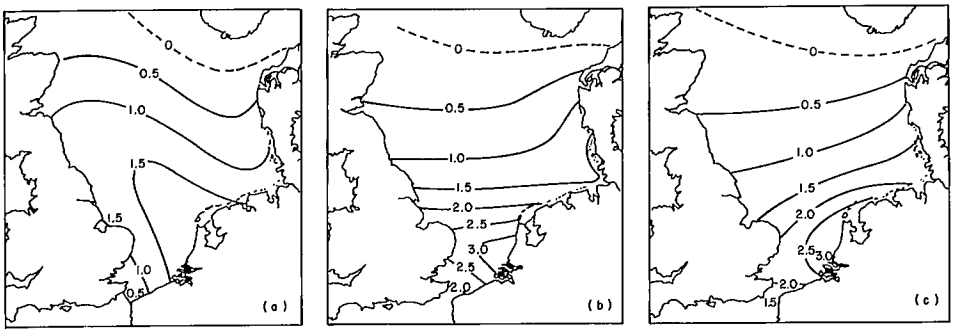

FIG. 7.112. Distribution of storm surge amplitudes (metres) in the North Sea during January 31–February 1, 1953, at (a) 18:00 (GMT) on January 31, (b) 00:00 (GMT) on February 1, and (c) 06:00 (GMT) on February 1. (Groen and Groves 1962)

surges on the North Sea coast of Germany during February 16–17, 1962, December 6–7, 1973, and January 3, 1976, prompted Zschau et al. (1978) to develop a storm surge forecasting technique by measuring the inland crustal tilt and the deflection of the local vertical due to the buildup of the surge. These authors, using a vertical pendulum, measured such tilts with precision and according to them there is advance information about the storm surge in these tilt measurements. The rationale for this is explained below.

There is an indirect effect of tides on tidal gravity, tilt, and strain measurements. Since this effect depends on the elasticity of the crust and the upper mantle, this effect has been used to determine their elastic properties. However, in the regions where the elastic properties are known better than the tides, the inverse problem of determining the tides from measurements of tidal gravity on the land has been used. Zschau et al. (1978) used this inverse approach of determining the storm surge from tilt measurements made inland. According to them, the additional water mass of the surge has three different effects on these measurements: (1) the deflection of the vertical due to the gravitational attraction of the water mass, called the Newtonian tilt; (2) the tilt of the surface due to the loading and unloading of the sea floor, called the primary loading tilt; (3) the secondary deflection of the vertical due to the redistributions of mass caused by the loading and unloading, called the secondary loading tilt.

The secondary loading tilt, generally, is small compared with the primary tilt and it can be combined with the loading tilt. Note that the Newtonian tilt and the primary tilt cause a deflection of a vertical pendulum tiltmeter and also tilt its casing.

The storm surge of December 6–7, 1973, at Büsum on the west coast of Schleswig-Holstein is shown in Fig. 7.122. A maximum amplitude of about 3 m was attained. The measured tilt at Kiel-Rehmsberg and also the astronomical tide are shown. It can be seen that the tilt curve matches the storm surge curve except for a 12-h phase advance. This phase advance is explained as due to the amphidromic component of the North Sea surge, which takes roughly a day to propagate in a counterclockwise direction from Scotland along the coasts of the United Kingdom, Belgium, the Netherlands, Germany, and Denmark to Norway.

This same technique was used to simulate four major, two moderate, and three minor surges during November–December 1973. The predictions (Fig. 7.123) 9, 6, and 3 h ahead had average errors of 29, 18, and 11 cm, respectively, in the maximum storm surge amplitudes.

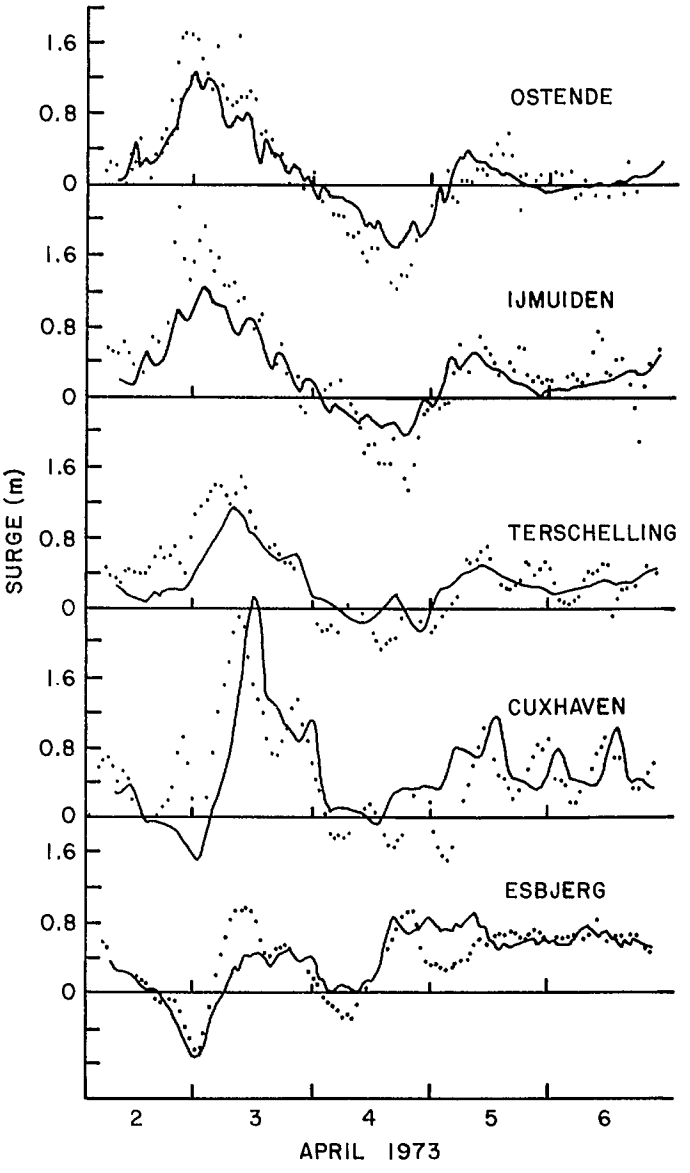

FIG. 7.113. Computed (solid line) and observed (dots) storm surges at five locations on the south and west coasts of the North Sea during April 2–6, 1973. (Davies and Falther 1977)

STORM SURGES IN DENMARK

Egedal (1957) examined the storm surges at Randers on the east coast of Jutland. Depressions traveling over Jutland from the west cause north–northeasterly winds, which generate surges on the east coast of Jutland. Another area where surges are generated by

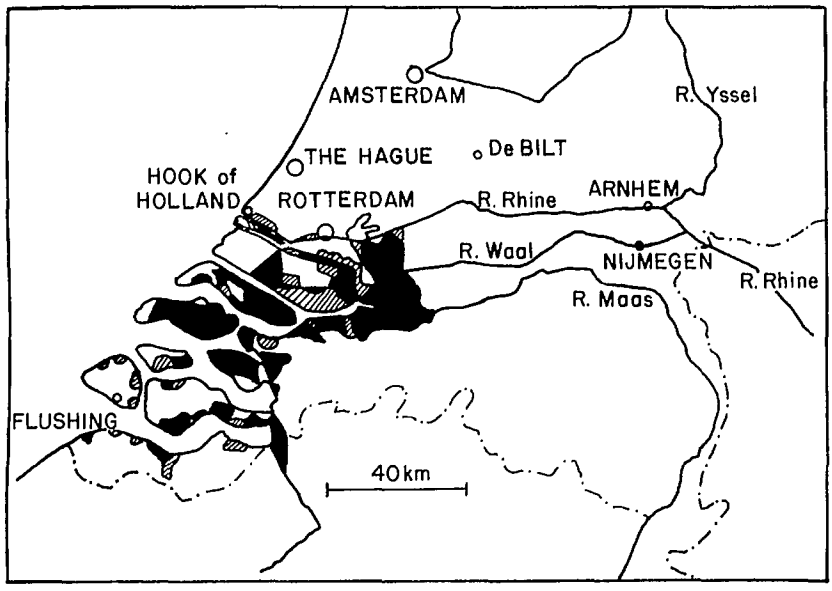

FIG. 7.114. Extent of flooding on the coast of the Netherlands due to the storm surge of January 31–February 1, 1953. Dark areas show regions that were flooded until March 1953. Hatched areas are those that were reclaimed after the flooding. (Ufford 1953)

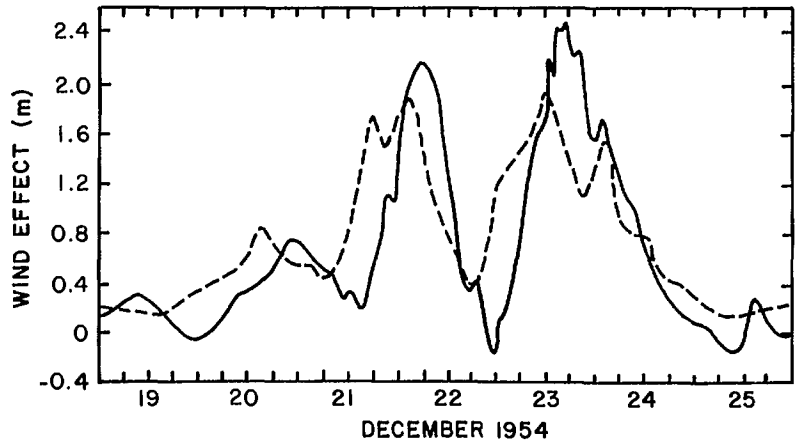

FIG. 7.115. Twin surges of the North Sea in December 1954 as recorded at the Hook of Holland (solid line). Broken line shows the computed surge using the equilibrium wind effect. (Weenink 1956)

such a weather system is the Island of Funen (Fyn). Egedal remarked that as far as storm surges are concerned, there are similarities between the east coast of Jutland and the east coast of the United Kingdom.

Ringe-Jørgensen (1958) studied the storm surges along the North Sea coast of Denmark. The tidal amplitude varies from about 1.5 m near the Danish–German bound-

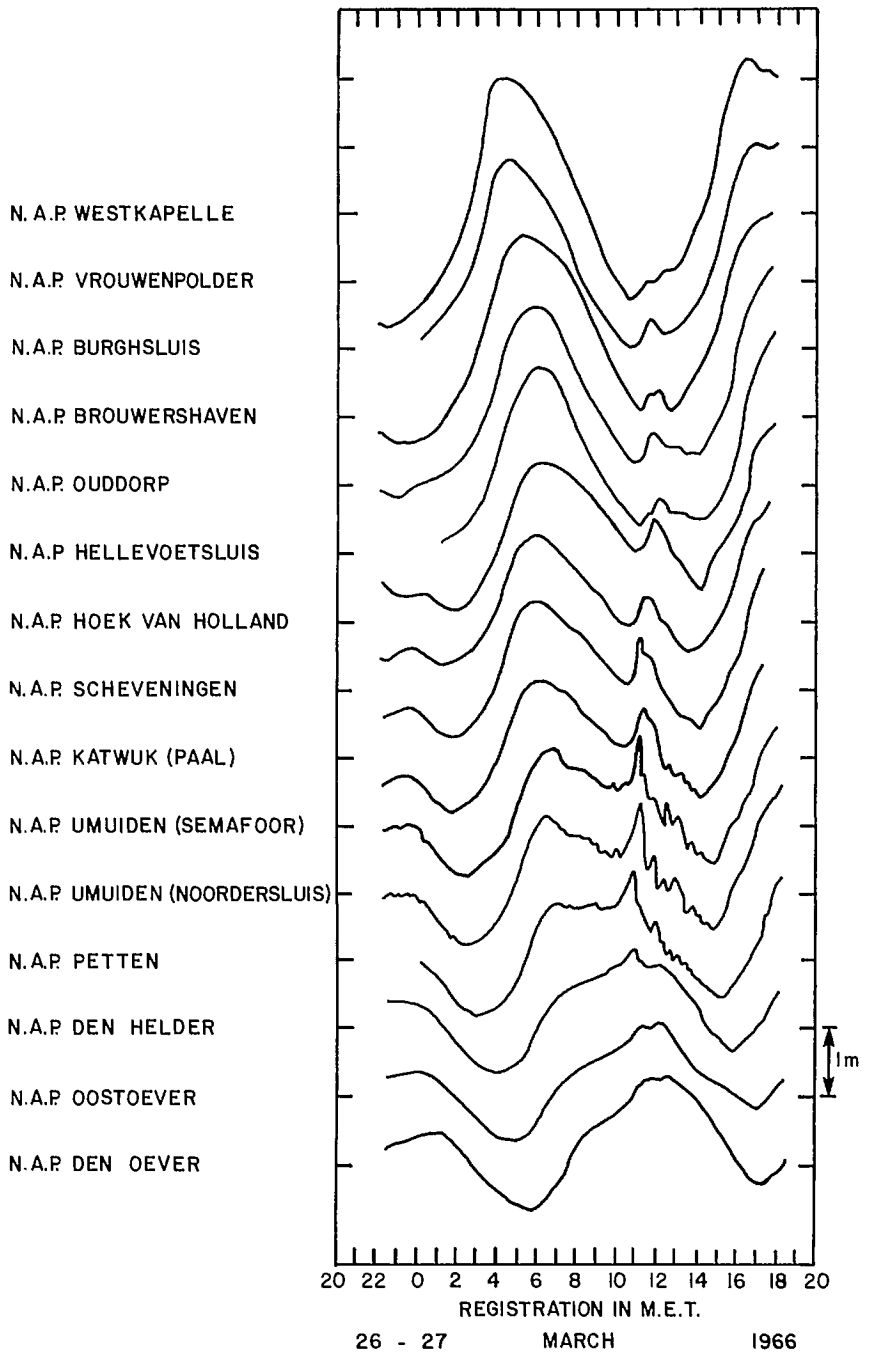

FIG. 7.116. Sudden water level changes (gust bumps) during March 27, 1966, at several locations on the Netherlands coast. (Timmerman 1971)

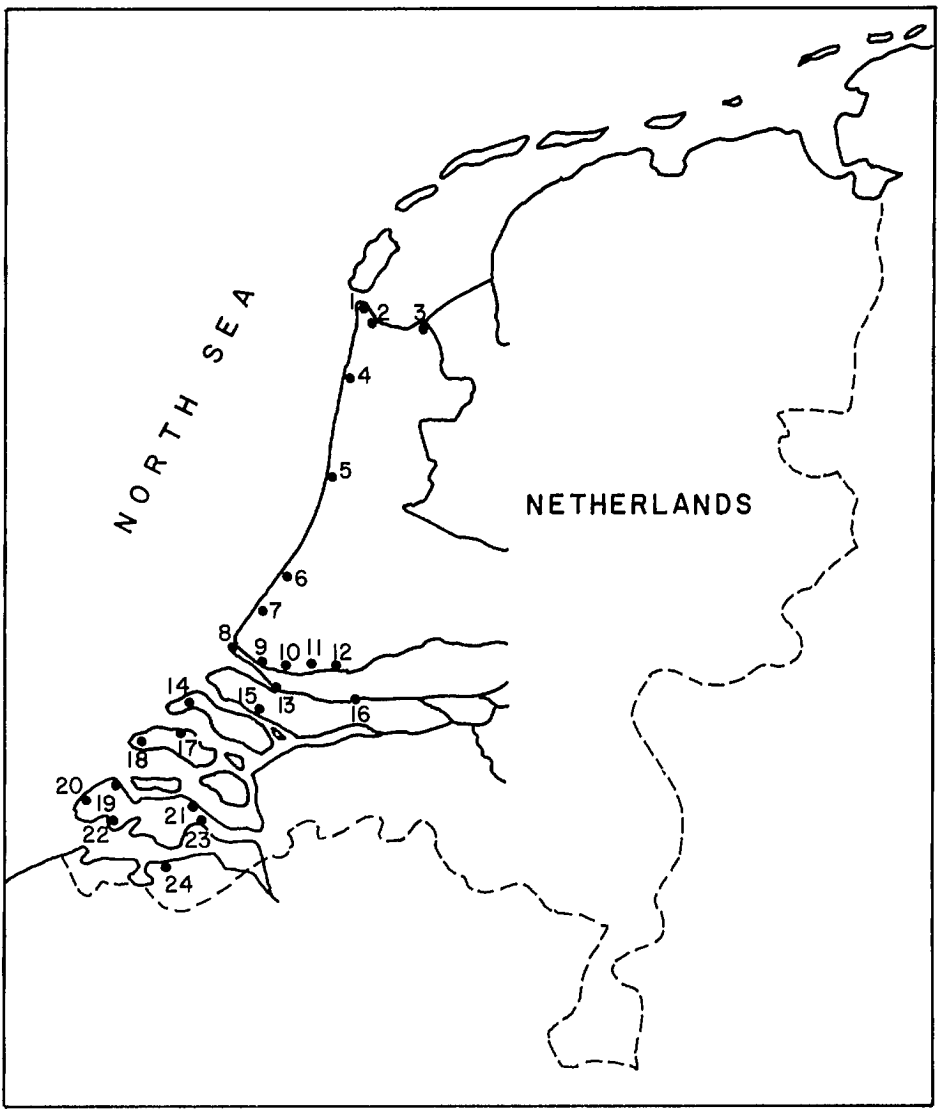

FIG. 7.117. Netherlands coast showing the locations of the tide gauge stations used in the storm surge study. 1, Den Helder; 2, Oostoever; 3, Den Oever; 4, Petten; 5, Umuiden; 6, Katwuk aan Zee; 7, Scheveningen; 8, Hoek van Holland; 9, Maassluis; 10, Vlaardingen; 11, Rotterdam; 12, Krimpen aan den Lek; 13, Spukenisse; 14, Ouddorp; 15, Hellevoetssluis; 16, Dordrecht; 17, Brouwershaven; 18, Burghsluis; 19, Vrouwenpolder; 20, Westkapelle; 21, Wemeldinge; 22, Vlissingen; 23, Hansweert; 24, Terneuzen. (Timmerman 1971)

ary to about 0.4 m at Thyborön. This study suggested that a meteorological situation similar to that of the January 31–February 2, 1953, event could cause surges with amplitudes up to 3.4 m at Harlingen (Holland) and only about 1 m at Hanstholm (50 km north of Thyborön). The influence of the Norwegian Ditch appears to prevent the occurrence of very large amplitude surges at Thyborön but permits the occurrence of a large

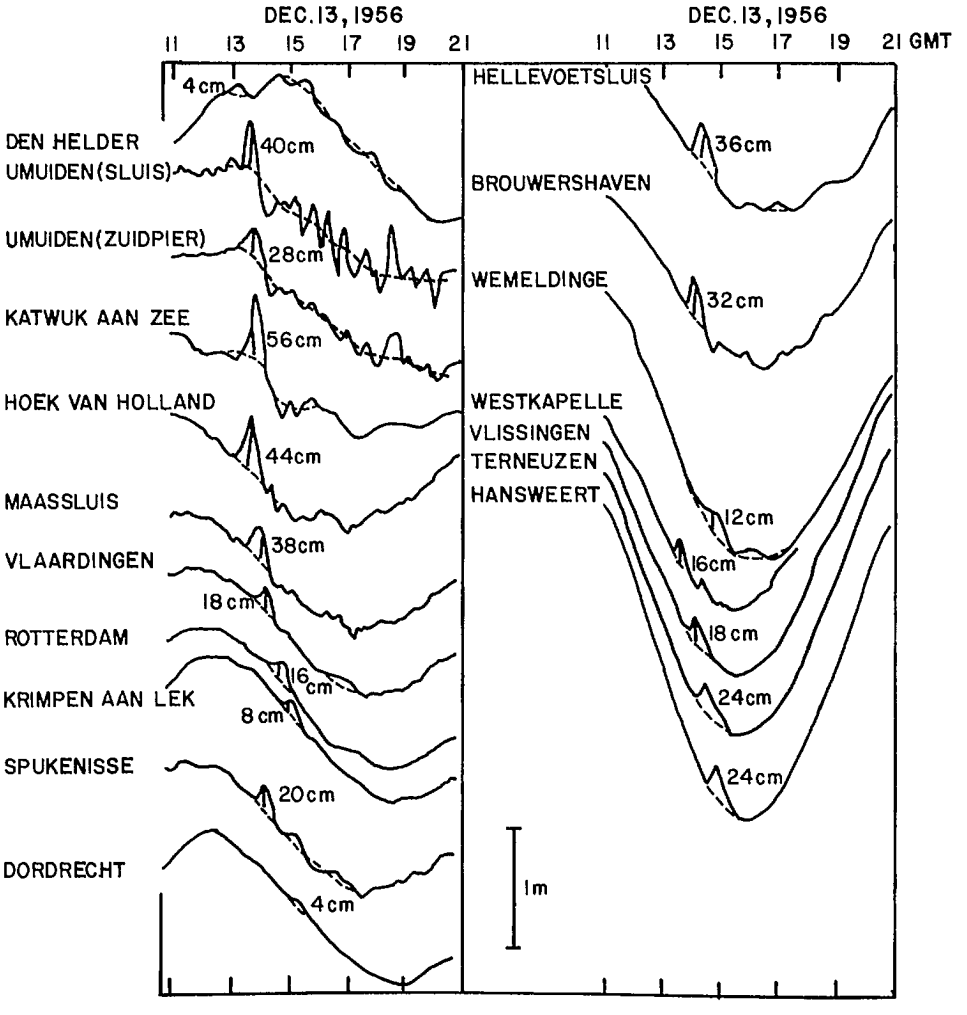

FIG. 7.118. Sudden water level changes (gust bumps) at several locations on the Netherlands coast on December 13, 1956. (Timmerman 1971)

number of moderate surges.

Lundbak (1956) studied the storm surge of January 31–February 2, 1953, on the coast of Denmark. The surge at Esbjerg is shown in Fig. 7.124. He mentioned that one of the worst storm surges on the Danish coast occurred November 12–14, 1872, in which there was great damage and loss of life on the island of Lolland. The storm surge of October 10–11, 1634, was supposed to have killed more than 6000 people. This surge cut the German island, Nordstrand, into two separate islands, which were later named Pellworm and Nordstrand.

LaCour (1917a) studied the storm surge of January 15–16, 1916. He gave tables of the surge amplitudes at 46 locations at every hour from 12:00 on the 15th to 00:00 on the 17th. He also gave several diagrams showing the winds, currents, and the water level at

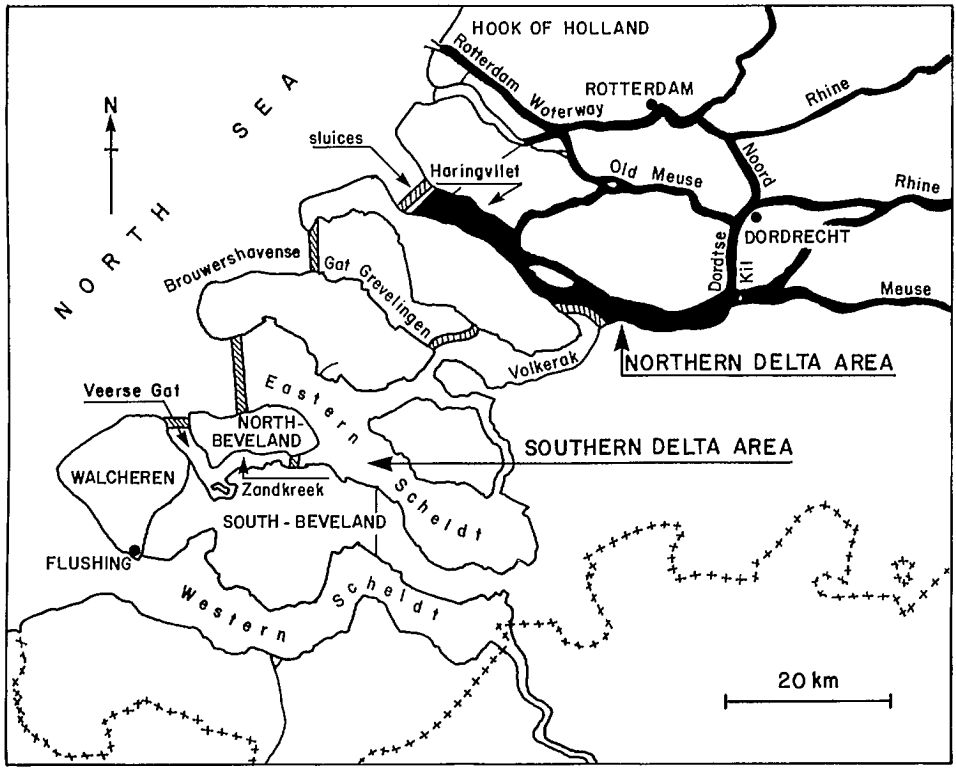

FIG. 7.119. Plan of the Delta project to reduce storm surge and tide levels on the coast of the Netherlands. (Dronkers 1961)

various times. Peak surges up to 1.9 m occurred. The distribution of the storm surge heights at 06:00 January 16, 1916, is given in Fig. 7.125.

STORM SURGES IN NORWAY

Gjevik and Røed (1974) mentioned that catastrophic surges occurred at the island of Grip (a small island on the west coast of Norway), which were discussed by Helland (1911). Major surges occur also at the Island of Ona. Johansen (1959) studied the surge along the southeast coast of Norway. Gjevik and Røed (1974) studied the following three surges on the Norwegian west coast: November 2, 1971, December 30, 1972, and December 31, 1972. The surge curves at three locations for the three cases together are shown in Fig. 7.126 and 7.127, respectively. The peak surge amplitudes at six locations for the first case are given in Table 7.65.

Martinsen et al. (1979) developed a numerical model to simulate storm surges on the west coast of Norway. The observed surges at five locations and those calculated from the numerical model including bottom stress are compared in Table 7.66.

STORM SURGES IN SWEDEN

Bergsten (1955) studied the relationship between winds and the water levels on the

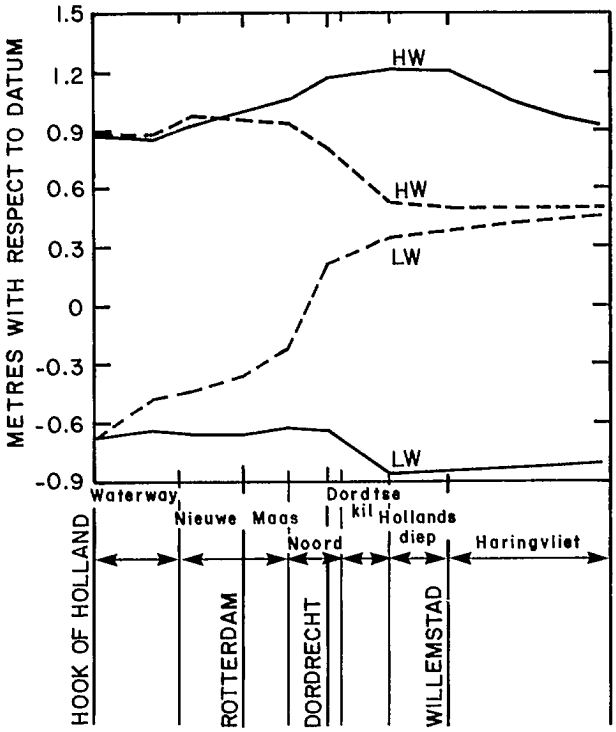

FIG. 7.120. High water (HW) and low water (LW) levels before and after the Delta plan on the coast of the Netherlands. The solid curve shows the situation before the Delta plan and the broken curve shows the estimated values when the plan is realized. (Dronkers 1961)

coasts of Sweden. He stated (p. 132–133):

> Generally, the water level in the South Baltic rises when the winds are northerly, and falls when they are southerly . . . The consequence is that on the south coasts of Skane and Blekinge offshore winds will raise the water level, and winds from the sea will reduce it . . . Another consequence is that the water level in the Sound and the Belts will be greatly changed in height; e.g., SW gales are blowing, as these will lower the water level in the South Baltic, and raise it on the west coast. The difference between the levels in the South Baltic and the west coast may in extreme cases be as much as a couple of meters. As far as the Sound is concerned, the difference is concentrated to the very short distance from Limhamn to Klagshamn, where a submarine bank runs from the Swedish to the Danish side, constituting the boundary between the Baltic and the western seas. Northeasterly gales reverse these conditions.

The surges at five locations on the Baltic coast of Sweden for the storm surge of January 2–5, 1954, are shown in Fig. 7.128. This surge was generated by a northerly gale. The surge at Björn on January 3 is particularly interesting because it shows that the Aland archipelago acts as a strong barrier to the southward flow of water.

Welander (1961) simulated the storm surge at Ystad using the so-called influence method and compared it with the observed surge for the case of the September 15–20, 1948, event. The observed and computed surges are shown in Fig. 7.129. Svansson (1958) compared observed and calculated surges at Varberg for the event of December 5–12, 1932 (Fig. 7.130).

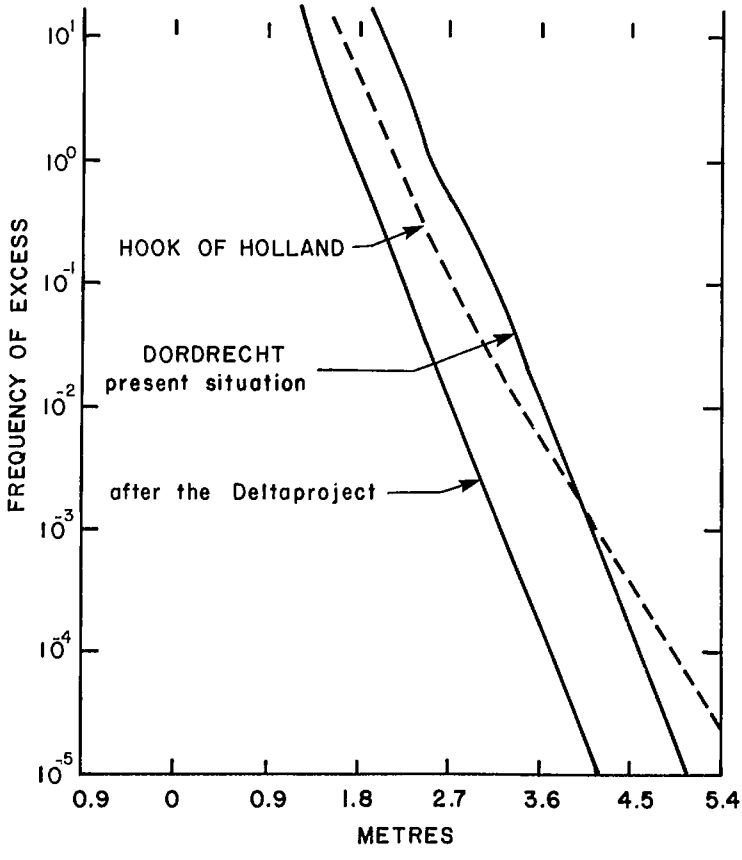

FIG. 7.121. Frequency of excess of high water levels on the coast of the Netherlands. (Dronkers 1961)

TABLE 7.64. Maximum water levels during the storm surge of Feb. 9–10, 1949, on the coast of Germany. (Tomczak 1950)

Station	Amplitude (m)	Station	Amplitude (m)
Borkum	2.4	Bremerhaven	3.9
Noderney	3.0	Cuxhaven	4.2
Emden	3.3	Büsum	4.8
Wilhelmshaven	3.4	Husum	5.6

STORM SURGES IN THE BALTIC SEA

In Chapter 3, the one-dimensional model of Svansson and Szaron (1975) for the Baltic Sea was discussed. Observed and computed surges at several locations for the storm surge event of August 1–5, 1964, are compared in Fig. 7.131.

Henning (1962) numerically simulated the surge of January 3–4, 1954, in the Baltic Sea. This surge caused maximum elevations up to 1.7 m in the western part of the Baltic Sea. The surface weather chart at 06:00 GMT on January 5, 1954, is given in

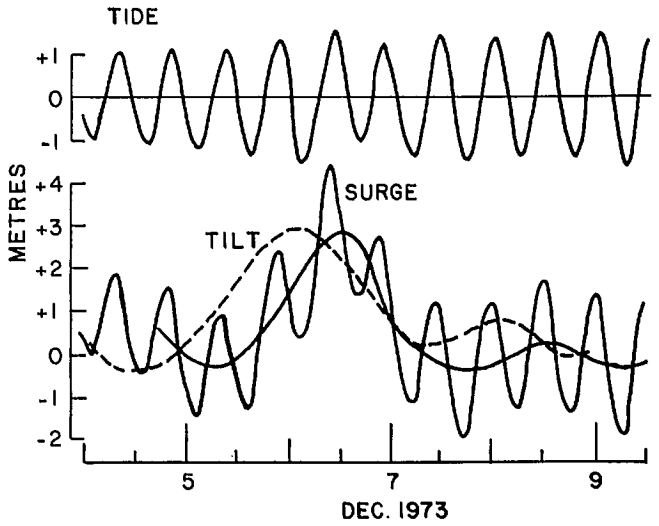

FIG. 7.122. Tide and surge on the coast of Germany during December 6–7, 1973. Top: tide at Büsum; bottom: solid curve shows the surge at Büsum and the broken curve shows the tilt at Kiel-Rehmsberg. (Zschau 1977)

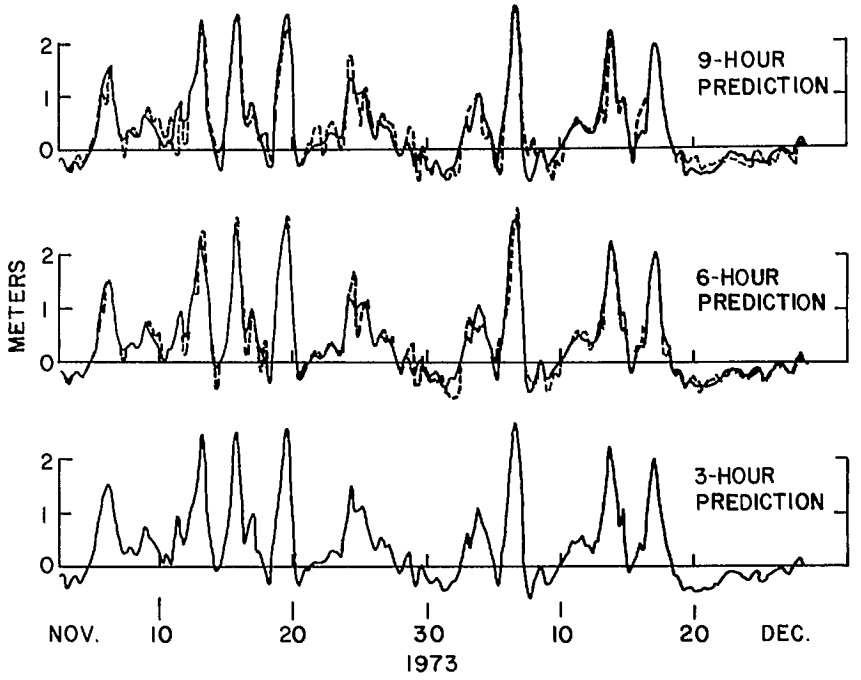

FIG. 7.123. Hindcast of storm surges for Büsum from tilt measurements at Keil-Rehmsberg 9, 6, and 3 h in advance. Solid line: observed surge; broken line: hindcasted surge. (Zschau and Kumpel 1979)

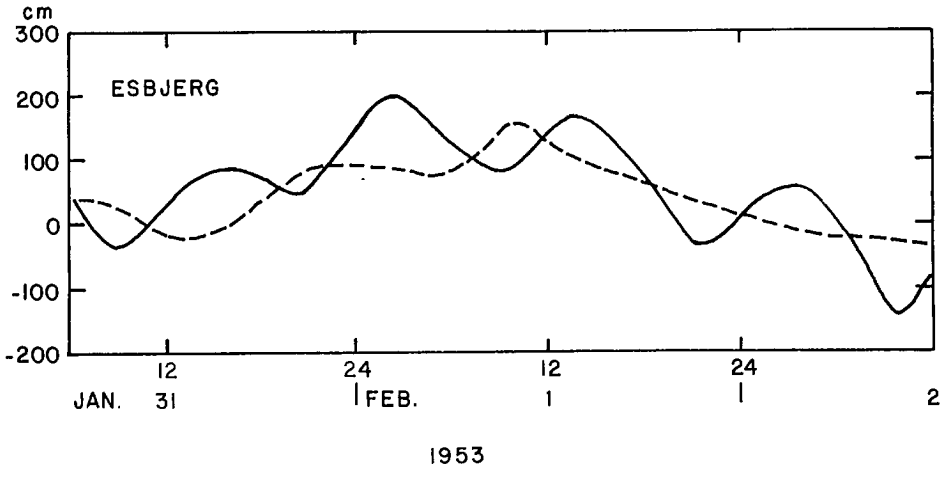

FIG. 7.124. Water level at Esberg on the North Sea during January 31–February 2, 1953. Solid line: total water level (surge plus tide); broken line: storm surge only. (Lundbak 1956)

Fig. 7.132. The distributions of the surge heights at two different times are shown in Fig. 7.133 and 7.134. Observed and computed surges at five locations are compared in Fig. 7.135. Some relevant data on this surge are given in Table 7.67.

Wroblewski (1978) used stochastic techniques to simulate the following surges at Nowyport (on the Poland coast of the Baltic Sea): January 17, 1955, February 15, 1962, February 18, 1962, and February 21, 1962. Demel (1934) studied the surges of 1930 and 1931 on the Baltic coast of Poland.

For the literature on storm surges in the early part of this century in the Baltic, see Krüger (1910). Lisitzin (1974) examined the influence of ice cover on storm surges in the Baltic Sea (discussed earlier).

STORM SURGES IN FRANCE

The North Sea coast of France was discussed earlier. Here, the Atlantic and Mediterranean sea coasts of France will be considered. LaCour (1917b) studied the storm surges at Brest (on the Atlantic coast of France) for the period 1861–1905. It appears that no significant surges occurred.

Fabry (1909) studied the surge near Marseille (on the Mediterranean Sea coast of France) of June 15, 1909. The surge amplitude was between 0.4 and 0.8 m and an earthquake might have caused this, making this water level oscillation a tsunami rather than a storm surge. Some water level oscillations can occur in this region due to landslides.

Crepon (1974) studied water level oscillations on the Mediterranean coast of France. Note that in this area, the tidal range is rather small (less than 1 m). Crepon applied his analytical theory to study the water levels at Sète located on the Mediterranean coast of France. Here, the continental shelf is about 100 km wide and 90 m deep and there are no significant orographic influences on the wind field. The observed and computed water levels at this location for the period January–March 1969 are compared in Fig. 7.136. Some storm surge effects could be seen around the following dates: January 3–4, February 17–22, February 27, and March 21–23. It is interesting to note that the

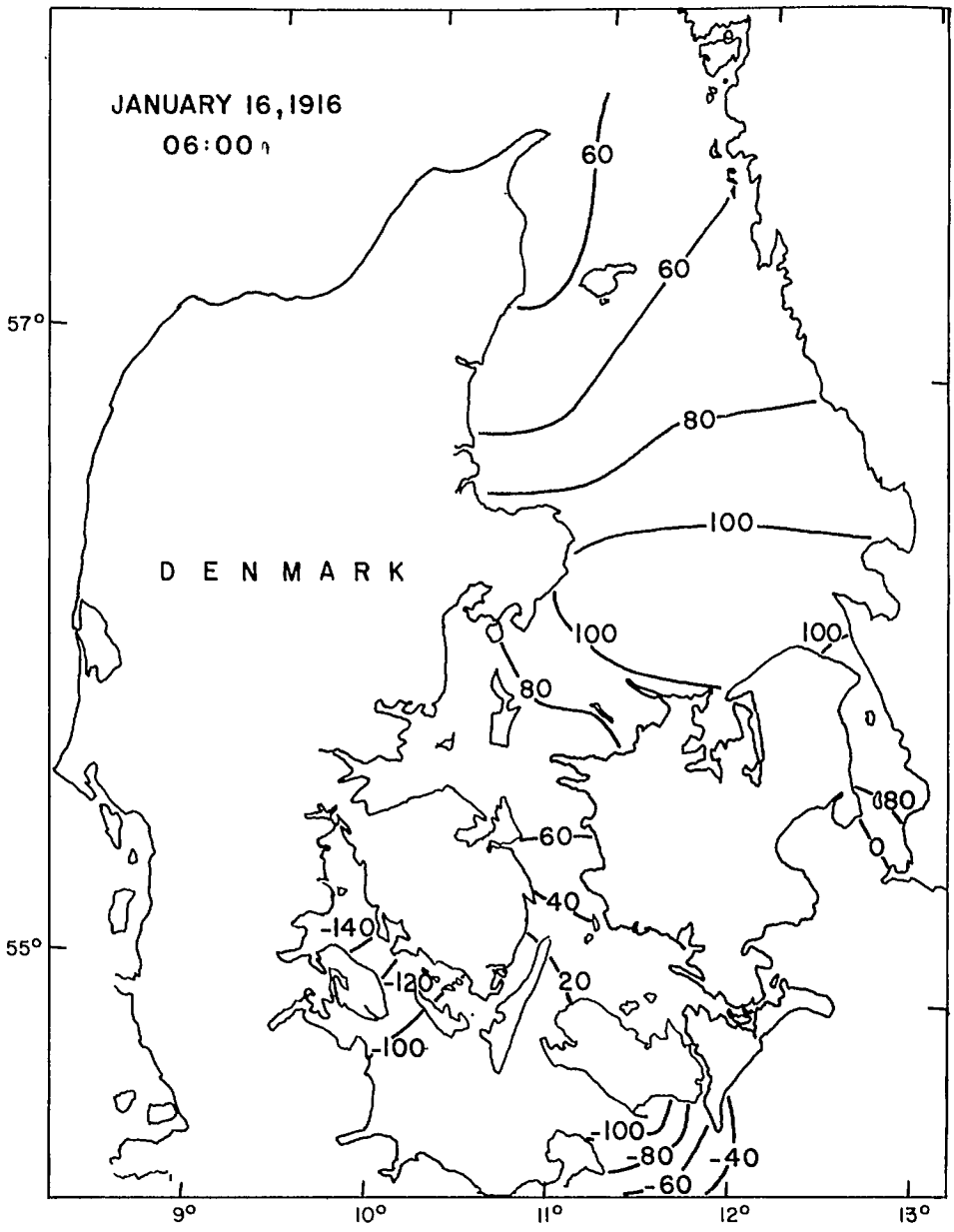

FIG. 7.125. Storm surge amplitudes along the east coast of Denmark at 06:00 on January 16, 1916. (LaCour 1932)

calculated water levels are systematically lower than the observed values. Also, the observed maximum values were about 0.5 m. One may conclude that storm surges are probably not significant in France except on the North Sea coast.

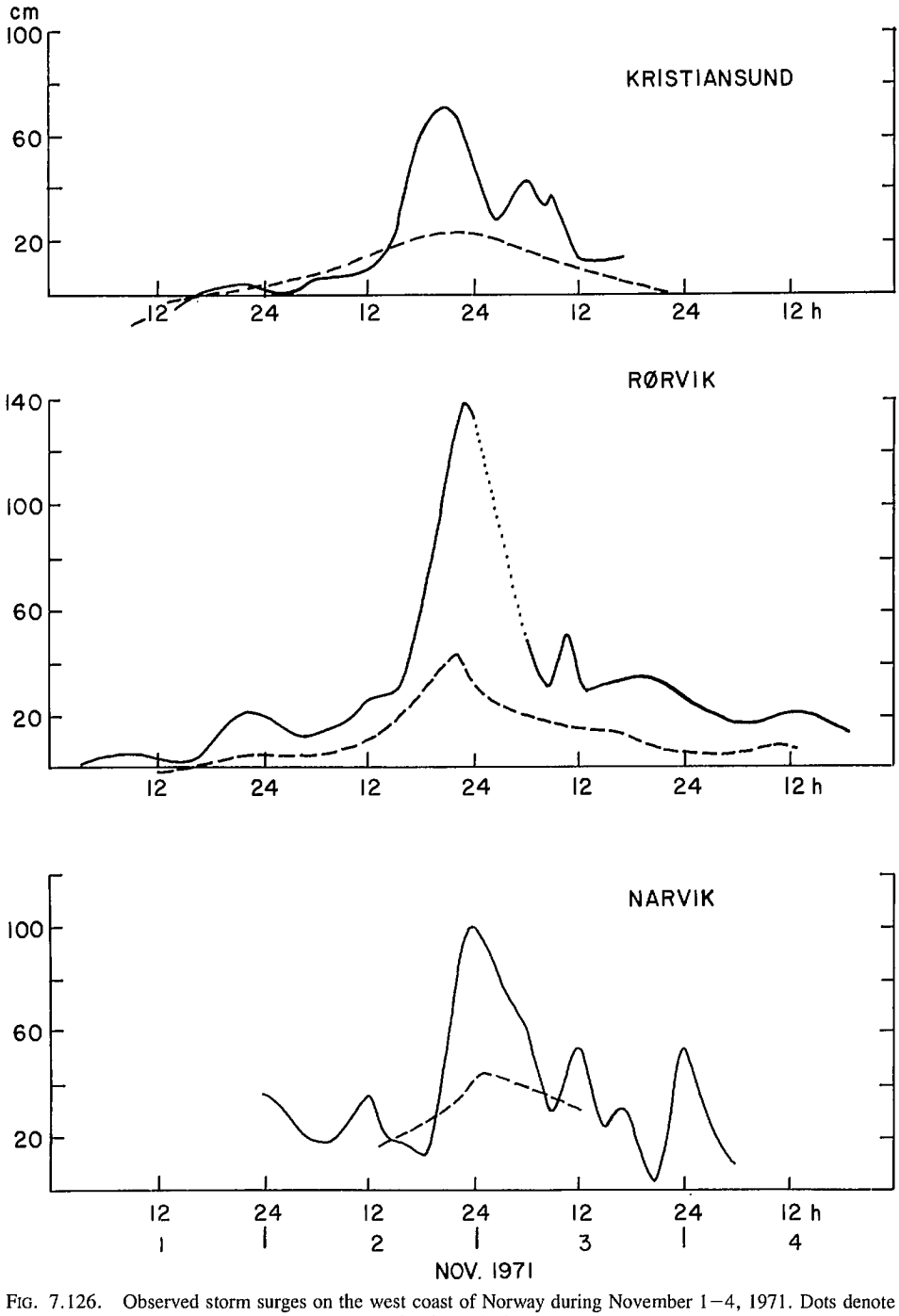

FIG. 7.126. Observed storm surges on the west coast of Norway during November 1–4, 1971. Dots denote missing observations. Broken curve represents the theoretical surge due to the atmospheric pressure gradient only. (Gjevik and Røed 1974)

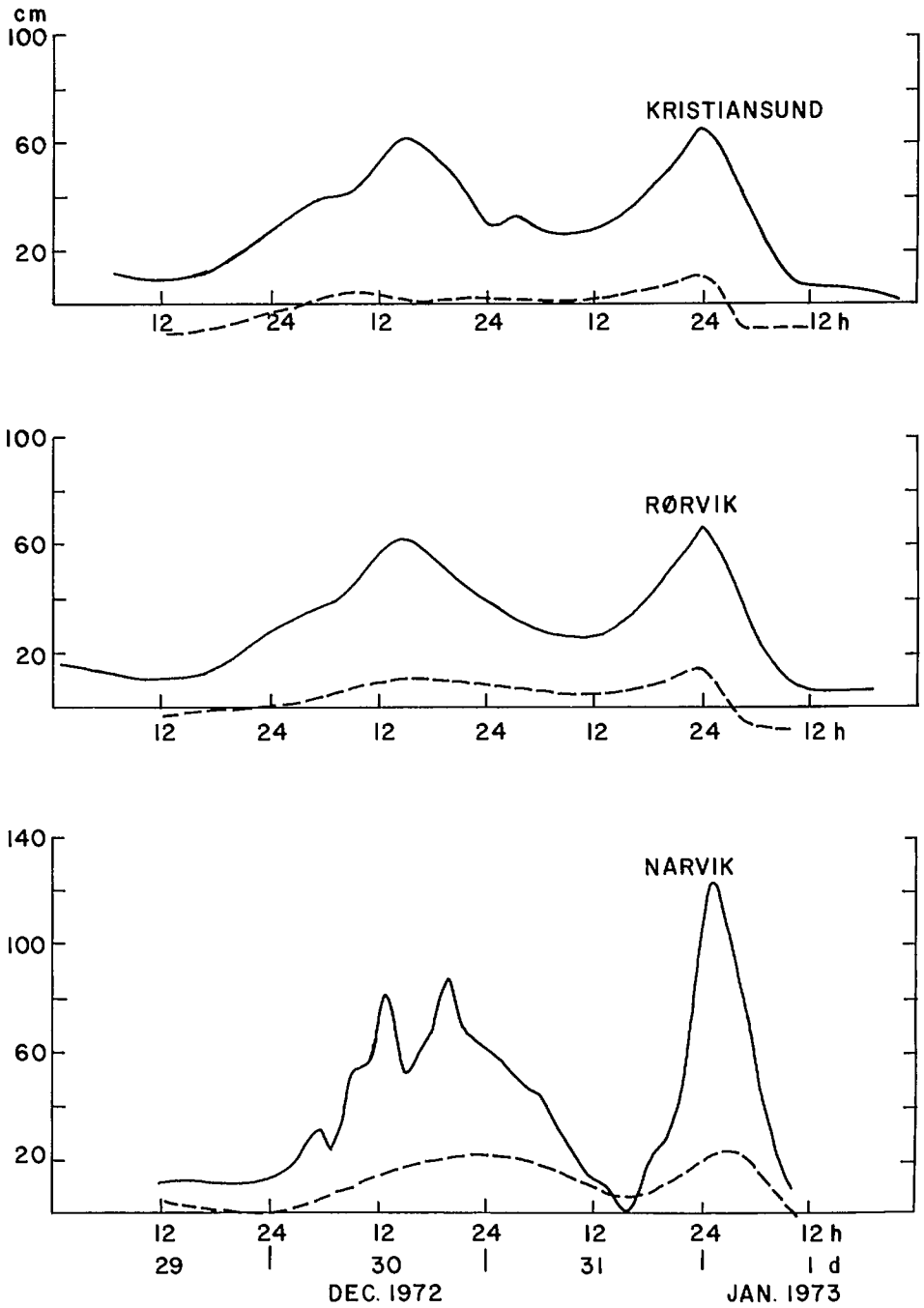

FIG. 7.127. Observed storm surges on the west coast of Norway during December 29, 1972–January 1, 1973 (solid line). Broken line shows the theoretical surge due to the atmospheric pressure gradient only. (Gjevik and Røed 1974)

TABLE 7.65. Peak storm surge amplitudes at certain locations on the west coast of Norway for the surge of Nov. 2, 1971. (Gjevik and Røed 1974)

Location	Observed peak surge (m)
Alesund	0.40
Heimsjø	0.75[a]
Trondheim	1.00
Sandnessjøen	1.20
Hammerfest	0.40
Tromsø	0.50

[a]This value does not agree with that given by Martinsen et al. (1979). See Table 7.66.

TABLE 7.66. Comparison of observed and calculated peak surge amplitudes on the west coast of Norway for the surge of Nov. 2, 1971. (Martinsen et al. 1979)

	Peak surge (m)	
Location	Observed	Computed
Kristiansund	0.7	0.98
Heimsjø	1.0	1.08
Rørvik	1.4	1.40
Sandnessjøen	1.2	1.47
Tromsø	0.5	0.65

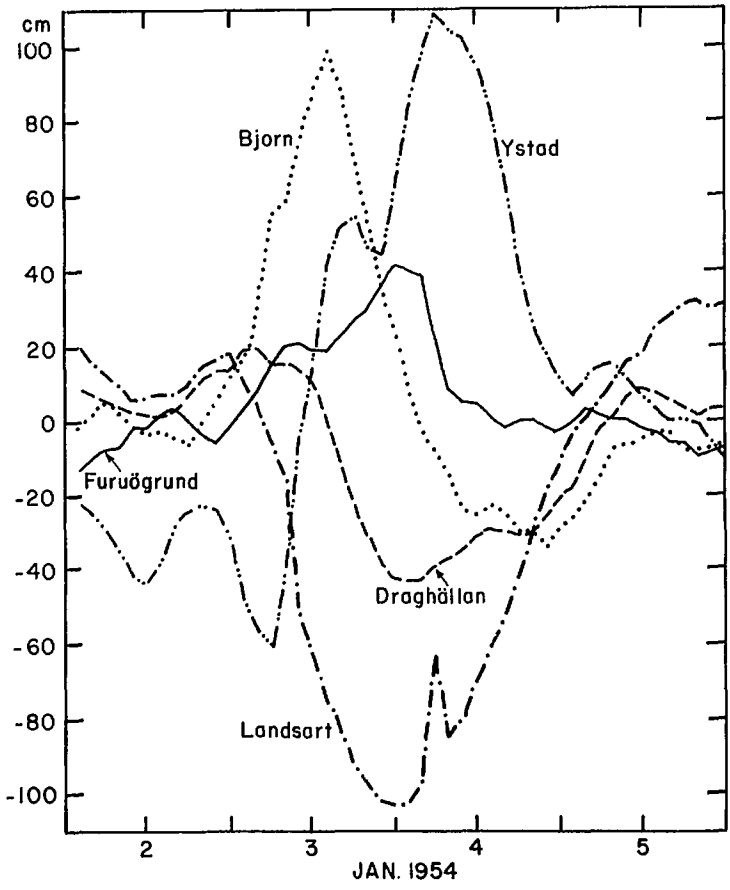

FIG. 7.128. Observed storm surges on the Baltic Sea coast of Sweden during January 2–5, 1954. (Bergsten 1955)

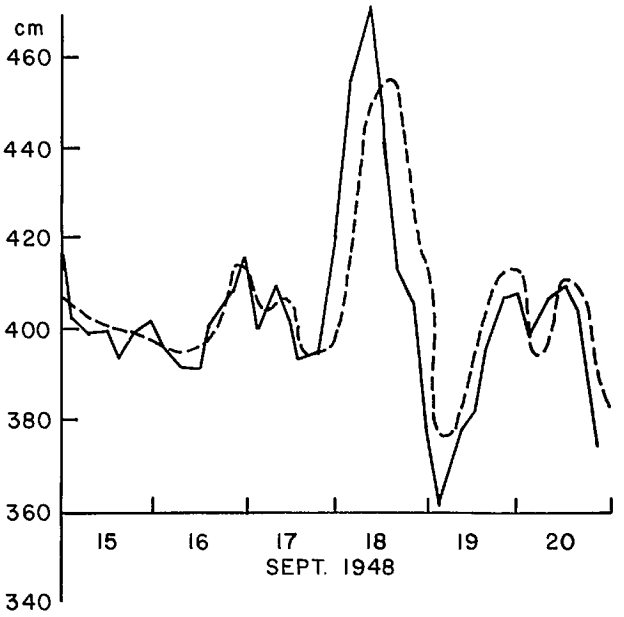

FIG. 7.129. Observed (solid line) and computed (broken line) storm surges at Ystad (Sweden) during September 15–20, 1948. (Welander 1961)

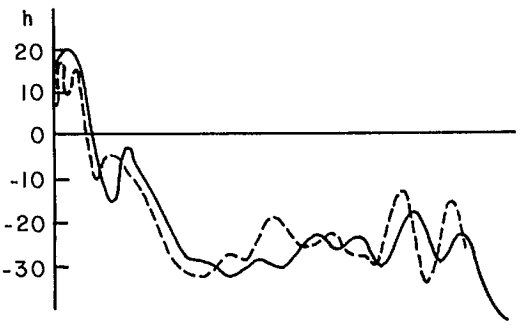

FIG. 7.130. Observed (solid line) and computed (broken line) storm surges at Varberg (Sweden) during December 5–12, 1932. (Welander 1961)

STORM SURGES IN PORTUGAL

Storm surges can occur on the northen part of the Atlantic coast of Portugal (Morais and Abecasis 1975). A surge during January 16–17, 1973, did considerable damage in the Leixoes Harbor. The damage was severe because the surge occurred at the time of spring tide. The center of a low pressure system passed over Leixoes and its exceptionally long duration of 24 h generated very large wind waves.

In the surge record, waves with periods between 4 and 40 min attained significant amplitudes. Leixoes Harbor exhibits a seiche with a 4-min period, which was amplified

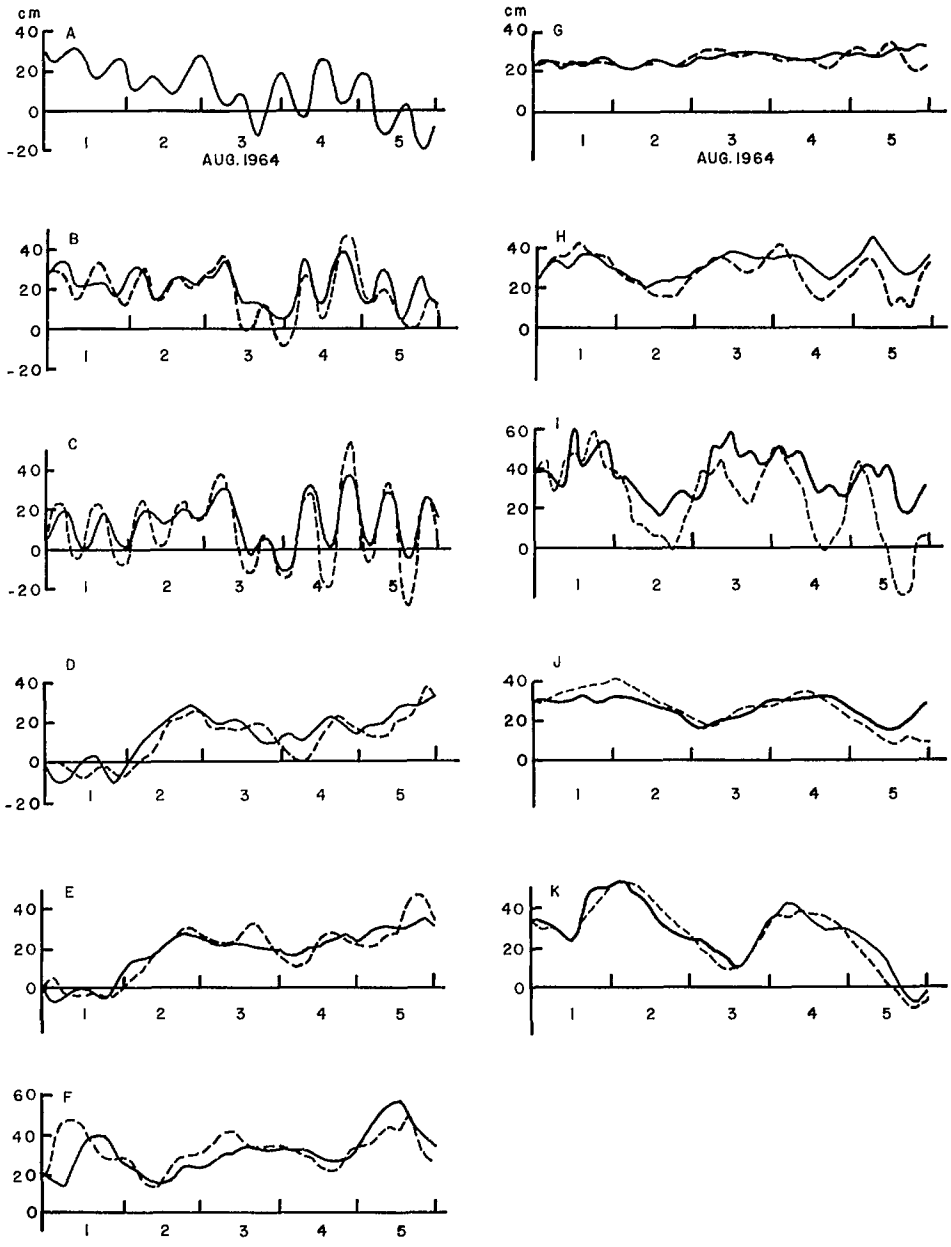

FIG. 7.131. Observed (solid line) and computed (broken line) storm surges at various locations along the Baltic Sea. (Svansson and Szaron 1975)

by resonance. There is evidence of the occurrence of a Helmholtz mode type motion also.

Storm surges occurred again in January and February 1974 but the damage was minimal. Hydraulic model tests were run to simulate these.

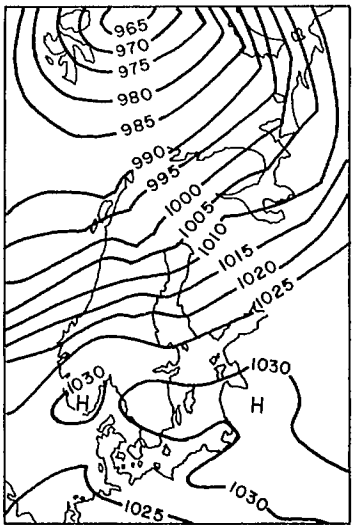

FIG. 7.132. Simplified surface weather chart at 06:00 (GMT) on January 5, 1954, for the Baltic Sea area. (Henning 1962)

STORM SURGES IN ITALY

In Italy, storm surges occur along the Ligurian Sea coast, the Tyrrhenian Sea coast, and the Adriatic Sea coast. On February 18, 1955, a cyclone caused great damage to the breakwater in Genoa Harbor (Grimaldi 1955; D'Arrigo 1955). Strong winds from the southwest generated wind waves with greater than 7-m amplitudes and possibly also a storm surge. Some of the water level problems in the Ligurian Sea associated with weather systems were discussed in section 6.9.

In section 6.9, some of the storm surge problems at Venice were considered. Tomasin and Frasetto (1979) studied the surge of April 21–22, 1967 (Fig. 7.137). What makes the problem more complicated is a seiche with a period of about 1 d that can be excited by weather systems. Such a seiche during February 16–20, 1967, is shown in Fig. 7.138. Observed and computed surges at Venice for February 12, 1972, are shown in Fig. 7.139. In the fall of 1982, major storm surges occurred at Venice and Trieste causing considerable damage.

In 1975 the Italian government devised a plan to reduce the effects of tides and storm surges at Venice by constructing barriers to narrow the entrances to the lagoon on which Venice lies (Vittori and Tampieri 1979).

STORM SURGES IN THE ADRIATIC SEA

Stravisi (1972) used a one-dimensional numerical model to simulate hypothetical storm surges in the Adriatic Sea. Storm surge amplitudes at two different times are shown in Fig. 7.140. Tebaldi (1973) studied the nonlinear aspects of storm surge generation in a rectangular bay of the dimensions of the Adriatic Sea. Zore (1955) stuided the seiches and water level oscillations due to weather systems in the Bay of Kastela. Surges and seiches wth amplitudes from 20 to 60 cm occurred on the following dates: September

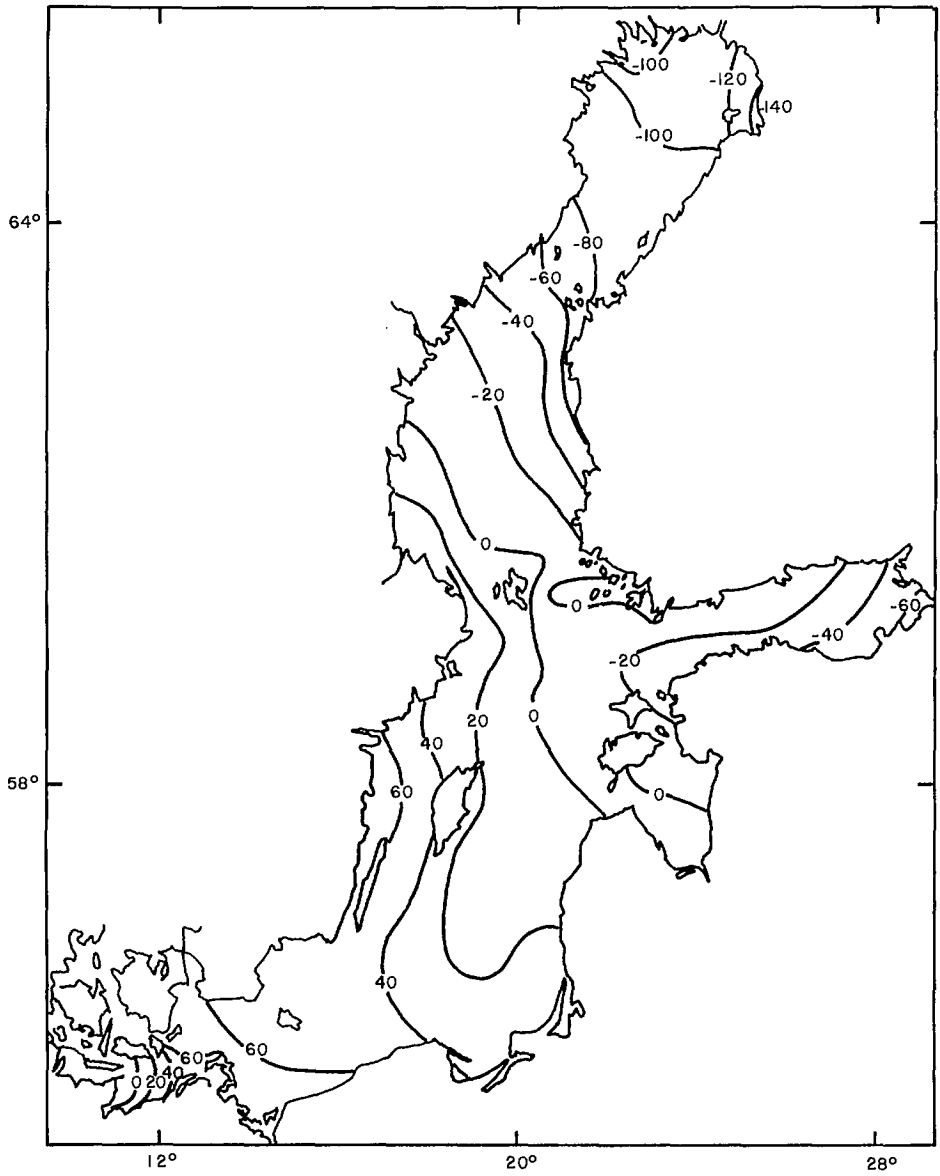

FIG. 7.133. Distribution of storm surge amplitudes (centimetres) in the Baltic Sea at 20:00 (GMT) on January 3, 1954. (Henning 1962)

14–15, 1949, November 24–25, 1949, December 14–15, 1949, January 18–19, 1951, April 17, 1952, and May 8–9, 1952.

STORM SURGES IN THE AEGEAN SEA

Wilding et al. (1980) studied tides and storm surges in the northwestern part of the

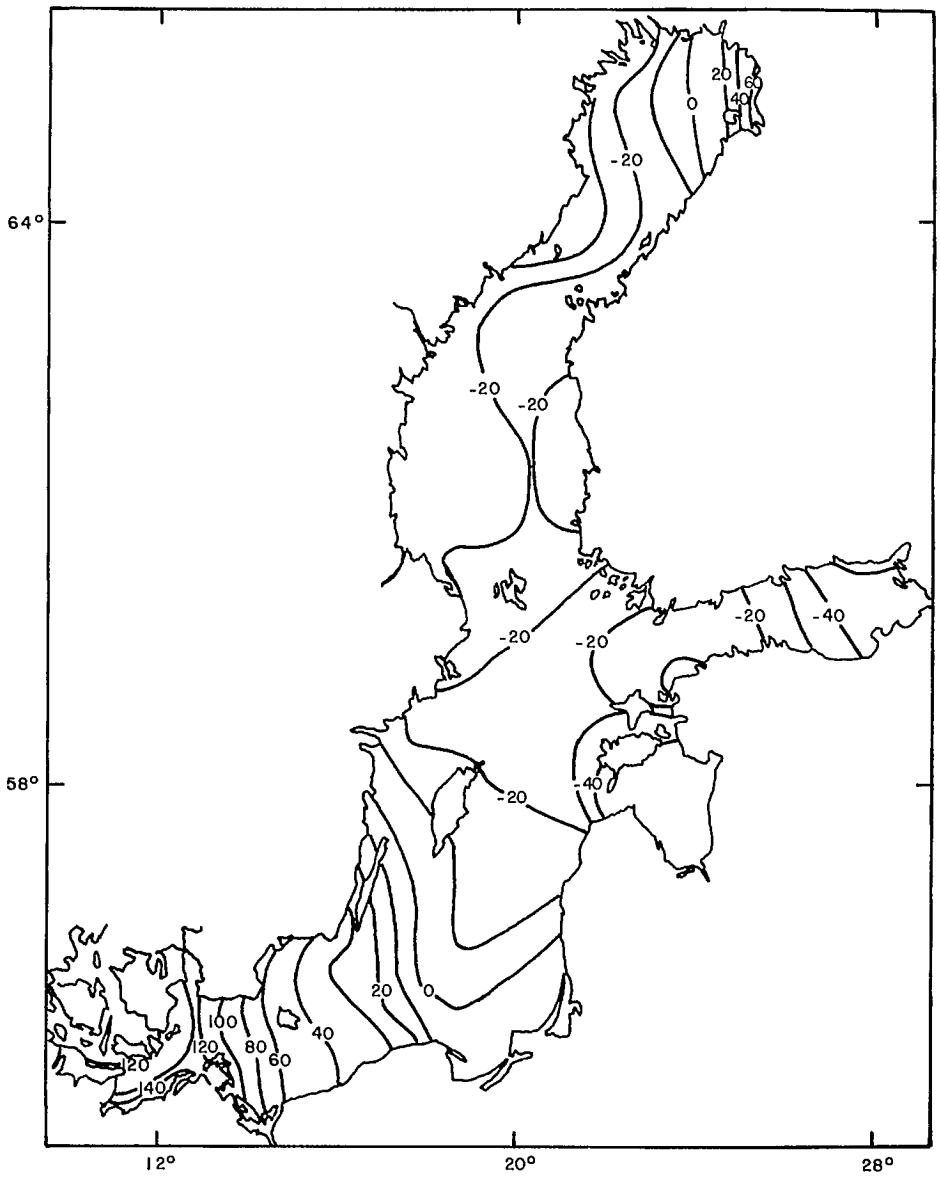

FIG. 7.134. Distribution of storm surge amplitudes (centimetres) in the Baltic Sea at 14:00 (GMT) on January 4, 1954. (Henning 1962)

Aegean Sea. The geography of this area is shown in Fig. 7.141. The tides are rather small in this water body, as can be seen from Table 7.68. The surges during August 20–23, 1975, at three locations are shown in Fig. 7.142. The power spectrum of half-hourly water level records is given in Fig. 7.143. Predominant periods of 2.68 and 2.40 h can be seen.

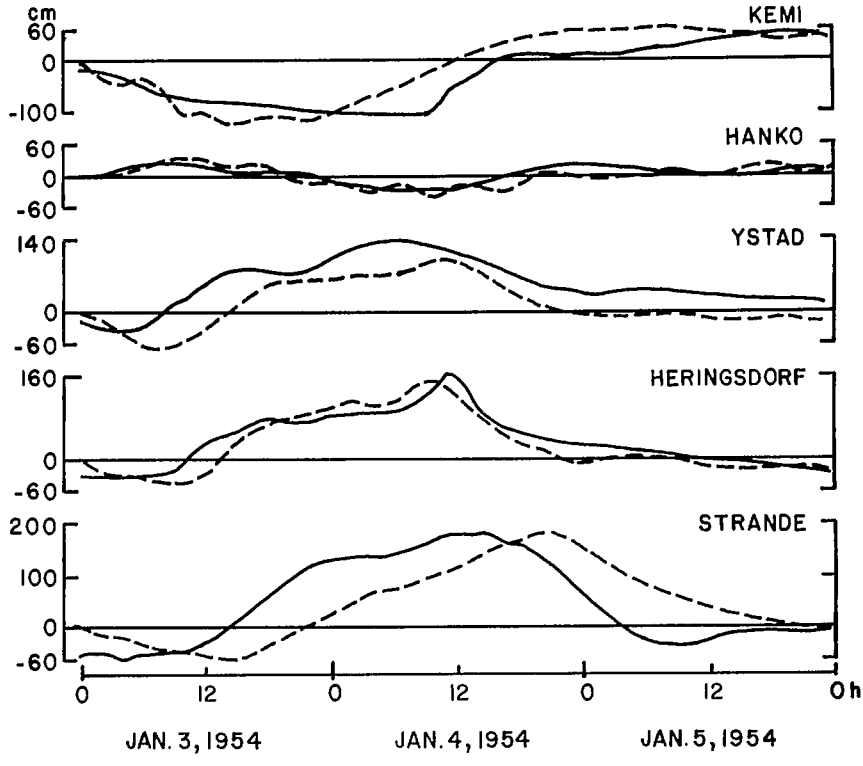

FIG. 7.135. Observed (solid line) and computed (broken line) storm surges in the Baltic Sea during January 3–5, 1954. (Henning 1962)

TABLE 7.67. Comparison between observed and computed storm surges in the Baltic Sea for the event of Jan. 3–4, 1954. (Henning 1962)

Water level gauge	Time of maximum elevation (observed)		Surge (cm)	
	Day	Time (GMT)	Observed	Computed
Degerby	3	8:00	47	52
Landsort	4	0:00	51	77
Kungholmsfort	4	8:00	100	105
Ystad	4	5:00	171	164
Heringsdorf	4	11:00	195	197
Saßnitz	4	11:00	183	171
Kap Arkona	4	10:00	187	193
Darßer Ort	4	12:00	190	195
Warnemünde	4	13:00	224	192
Wismar	4	14:00	291	192
Travemünde	4	15:00	283	192
Gedser	4	12:00	231	186
Langballigau	4	12:00	236	262
Strande	4	15:00	239	236

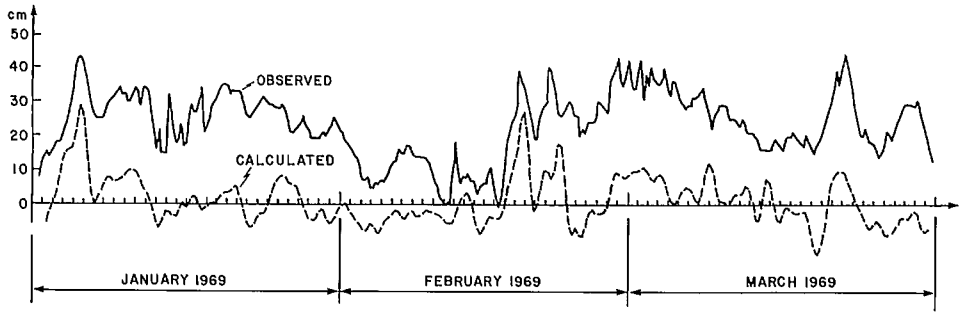

FIG. 7.136. Observed and calculated water levels at Séte (on the Mediterranean coast of France) for the period January–March 1969. (Crepon 1974)

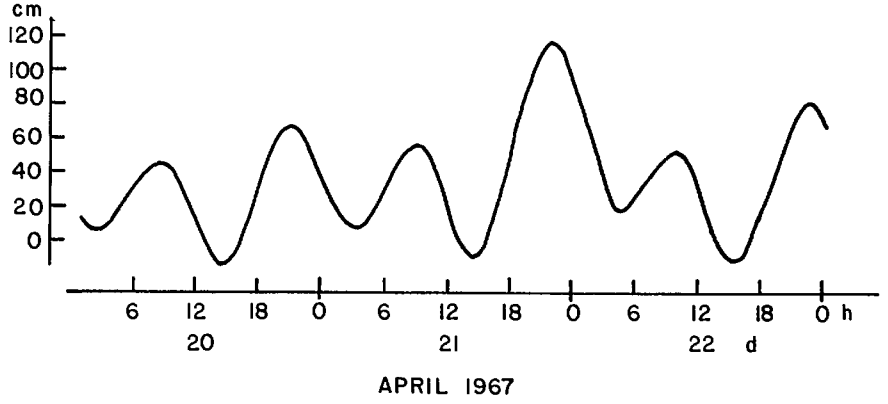

FIG. 7.137. Recorded water level (tide plus surge) at Venice, Italy, during April 20–22, 1967. Time is GMT − 1. (Tomasin and Frasetto 1980)

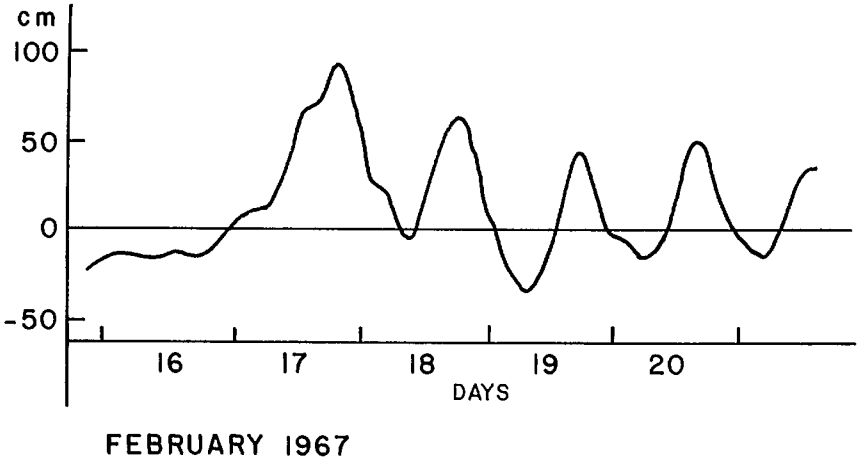

FIG. 7.138. Seiche at Venice, Italy, with a period of approximately 24 h. (Tomasin and Frasetto 1979)

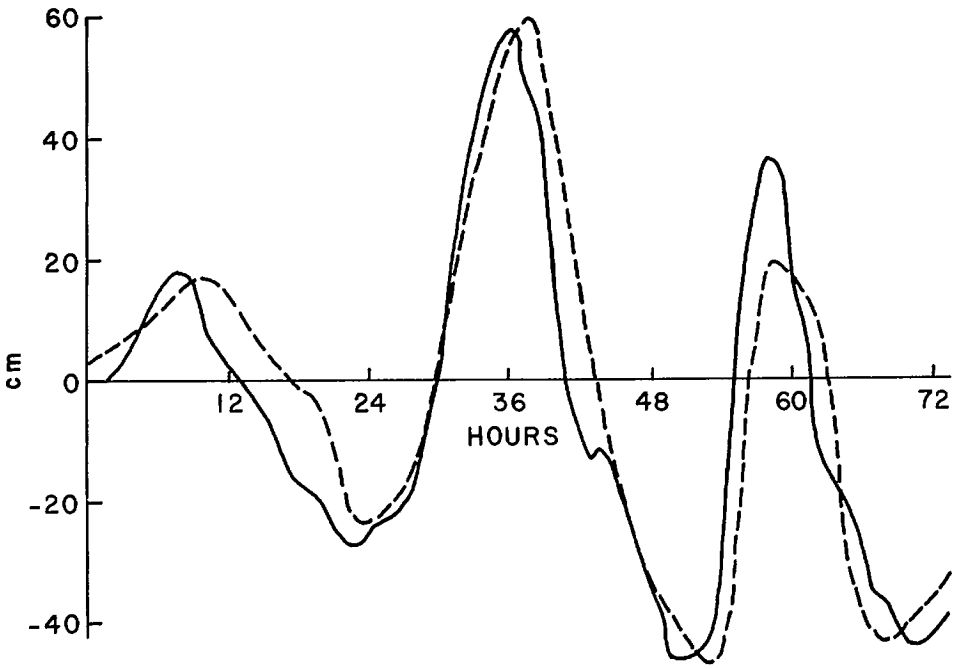

FIG. 7.139. Computed (broken line) and observed (solid line) surges at Venice during February 12–15, 1972. Time is hours from the starting time of 03:00 (GMT) on February 12, 1972. (Tomasin and Frasetto 1979)

PLANNING FOR PROTECTION AGAINST STORM SURGES IN EUROPE

The background and the considerations that went into planning for protection against storm surges in the United Kingdom, the Netherlands, and Germany will be discussed in this subsection.

In the United Kingdom serious consideration was given to protection against storm surges following the disastrous event of January 31–February 2, 1953. In these floods at least 309 people died, 24 000 houses were destroyed, 200 large industrial premises were flooded and damaged, and 16 000 acres (1 acre = 0.405 ha) of land was inundated. In this event, the maximum surge was about 9 ft (2.74 m) and this was compounded by high-amplitude wind waves. The flooded areas on part of the east coast of the United Kingdom are illustrated in Fig. 7.144.

Following this event, a recommendation was made to provide storm surge warnings each season beginning on September 15 and ending on April 30. The storm surge hazard is assumed to be on the increase because the southeast coast of the United Kingdom is estimated to be sinking (with reference to the mean sea level) by as much as 1 ft (0.305 m) per century. However, there are long stretches of natural protection against storm surges on the east coast of the United Kingdom such as dunes and shingle ridges. Over the years, about 1270 mi (2044 km) of manmade earthen and other types of barriers were also added.

Flooding in the Thames Estuary is also a serious problem. For example, in the 1953 event, at least 30 000 acres of land was inundated. Following this event, several runs were made in a hydraulic model on the effect of increasing the heights of barriers in Kent and

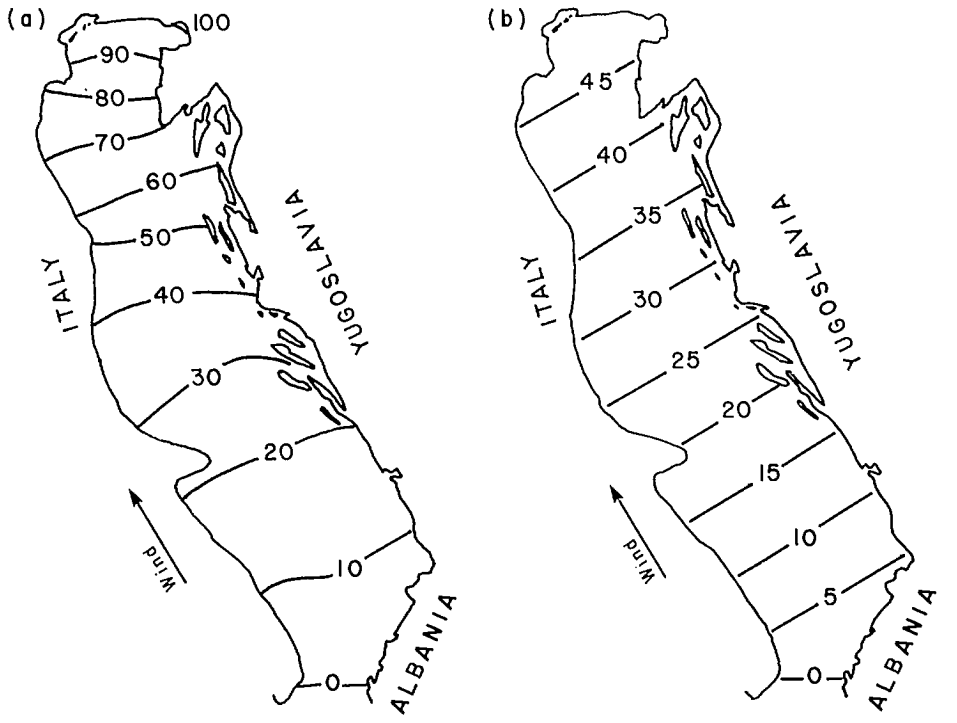

FIG. 7.140. Distribution of the amplitudes (centimetres) of a hypothetical storm surge in the Adriatic Sea at (a) 10 h and (b) 11 h after the start of wind stress application. (Stravisi 1972)

Essex by 3–4 ft (0.91–1.22 m). The results showed that this might increase the water level, for example, in central London. Two alternate possibilities were considered.

One scheme calls for the construction of a barrier across the estuary, leaving gaps for ships to pass through. The disadvantage of this is the belief that this will deteriorate the estuary as an ecosystem. A second and possibly better scheme calls for the construction of a suitable structure across Long Reach (between Purfleet and Greenhithe). This structure will be provided with gates that can be closed during high floods.

Jensen (1953a, 1953b) discussed qualitatively the changes in the North Sea coastline going back to 2000 B.C. He also discussed the dykes that were built during the last several centuries against flooding.

Farquharson (1953) studied the storm surges at Sheerness and Southend going back to 1820 (when tide gauges were put in). The records were more or less complete except for a break from 1858 to 1867. He made the point that the frequency of occurrence of major surges gradually increased during the period 1820–1953. Regarding their monthly distribution, November–January (Table 7.69) had the highest frequency.

Pugh and Vassie (1979) studied the statistics of extreme sea levels in the North Sea and Irish Sea, making use of the probabilities of tide and surge occurrences. This technique enables one to estimate the probability of occurrence of extreme levels, using the probability of tide and surges separately based on a few years of data. Let the total water level ξ be the sum of a tidal component x, a surge component y, and a mean sea level z_0. Then

$$\xi(t) = x(t) + y(t) + z_0 \tag{7.73}$$

FIG. 7.141. Geography of the Aegean Sea. (Wilding et al. 1980)

TABLE 7.68. Tides in the Aegean Sea. (Wilding et al. 1980)

Location	Mean spring range (cm)	Mean neap range (cm)
Port Salonica	32.4	9.6
Saint Trias	29.0	6.6
Krini	29.6	4.4
Mihaniona	29.4	5.0
Kavoura	29.0	4.6

The tidal part can be expressed as

$$x(t) = \sum_{n=1}^{N} H_n \cos(\sigma_n t + V_n - g_n) \tag{7.74}$$

where H_n is the amplitude of each tidal constituent, σ_n is the frequency of the tidal constituent, V_n is the equilibrium phase, and g_n is the phase lag of the constituent on the equilibrium tide.

It is assumed that tides and surges can occur independently, and the total probability $p(\xi)$ for the tide and surge together can be written as

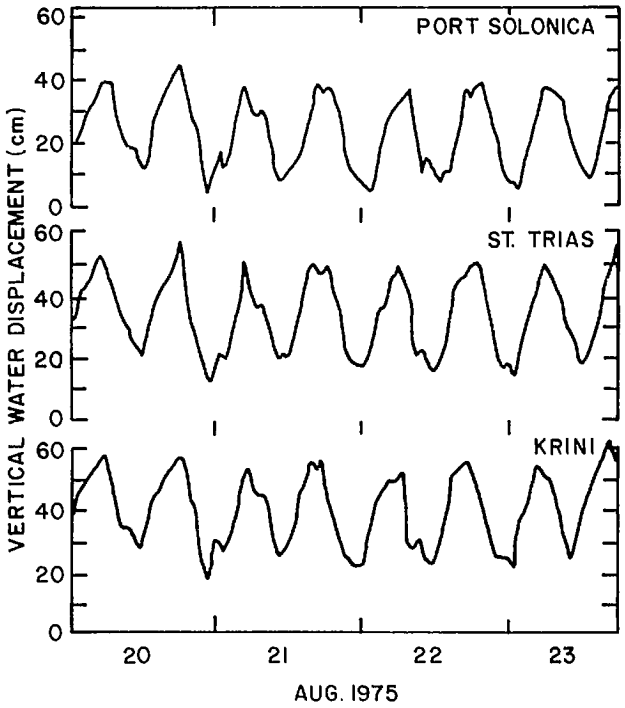

FIG. 7.142. Water level oscillations during August 20–23, 1975, at three locations in the Aegean Sea. (Wilding et al. 1980)

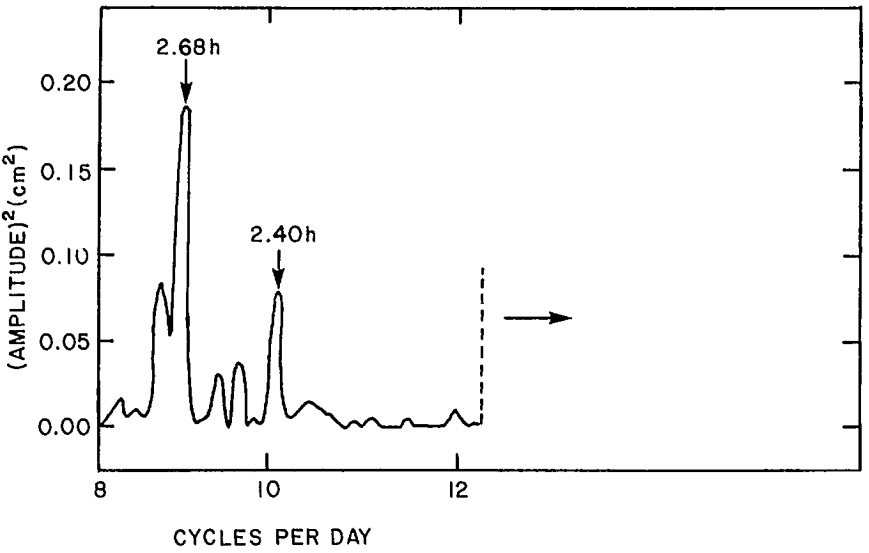

FIG. 7.143. Power spectrum of half-hourly water level data at Port Solonica (Aegean Sea). (Wilding et al. 1980)

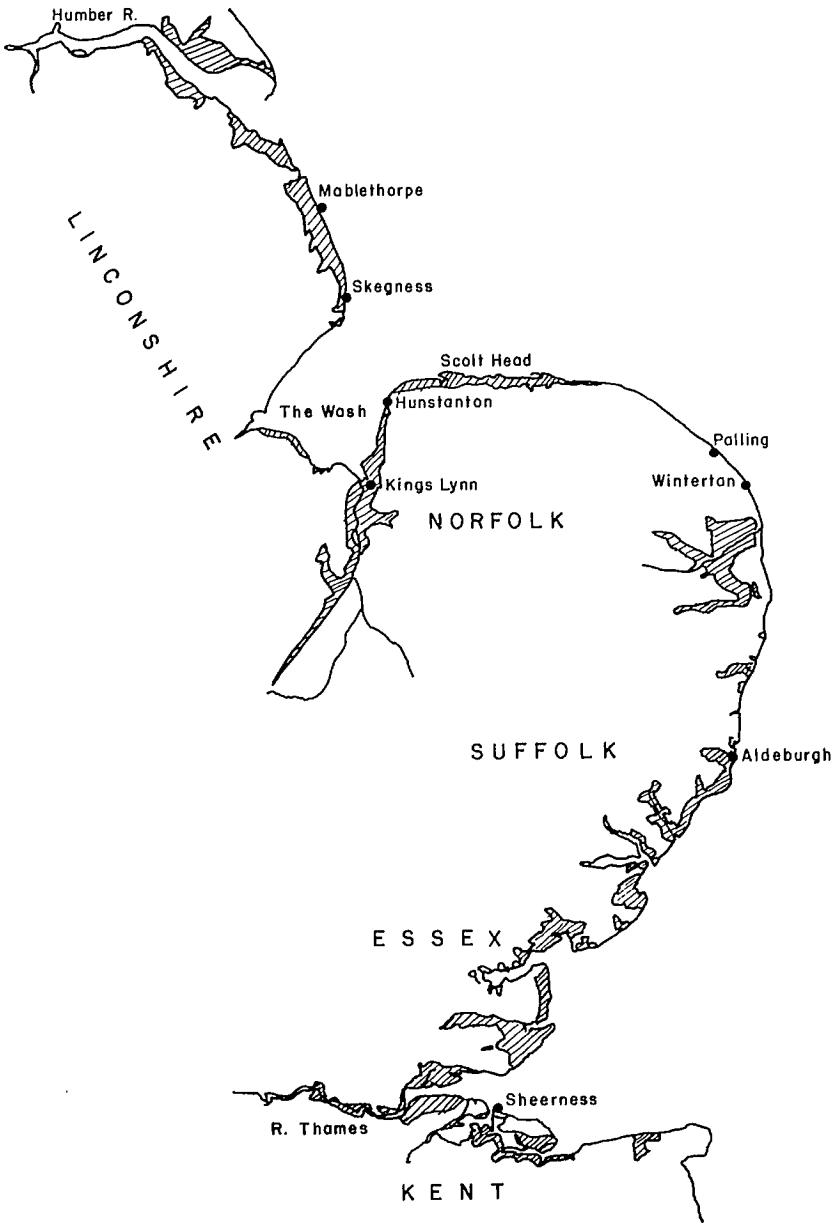

FIG. 7.144. Areas inundated by the storm surge of January 31–February 1, 1953, on the east coast of the United Kingdom. (Jensen 1953a)

$$p(\xi) = \int_{-\infty}^{\infty} p_t(\xi - y) p_s(y) dy \tag{7.75}$$

where $p_t(x)$ is the probability density function for the tide and $p_s(y)$ is the probability density function for the surge.

TABLE 7.69. Monthly distribution of the 49 major storm surges (with amplitudes in excess of 3.35 m at Sheerness, U.K.) during the period 1934–53 on the east coast of the United Kingdom. (Farquharson 1953)

Month	No. of occurrences	Month	No. of occurrences
October	3	January	10
November	12	February	6
December	11	March	7

TABLE 7.70. Return periods (yr) for positive storm surges at selected stations in the British Isles. Note that Lerwick has been offset relative to the mean level by 1 m to fit in the table. (Pugh and Vassie 1979)

Level above MSL (m)	Newlyn	Fishguard	Malin Head	Stornoway	Lerwick[a]	Aberdeen
3.6	1670					
3.5	311	926				
3.4	74	261				
3.3	20	81		762		
3.2	5.9	26		182		
3.1	1.9	8.7		50		863
3.0	0.7	3.1	1520	15		248
2.9		1.1	392	4.9		80
2.8			109	1.7	1520	27
2.7			35	0.6	199	9.8
2.6			12		27	3.6
2.5			4.4		4.8	1.4
2.4			1.7		1.0	

[a]Lerwick levels are related to mean sea level + 1 m.

TABLE 7.71. Return periods (yr) for negative storm surges at selected stations in the British Isles. Note that Lerwick has been offset relative to the mean level by 1 m to fit in the table. (Pugh and Vassie 1979)

Level above MSL (m)	Newlyn	Fishguard	Malin Head	Stornoway	Lerwick[a]	Aberdeen
−2.3			1.3			
−2.4			5.6		1.1	
−2.5		0.8	28		7.2	
−2.6		3.4	178		56	0.7
−2.7		18	1655		641	2.6
−2.8		101				12.4
−2.9		584		0.6		64
−3.0	1.3			2.0		316
−3.1	6.6			7.0		1590
−3.2	42			28		
−3.3	335			120		
−3.4				560		
−3.5						
−3.5						

[a]Lerwick levels are related to mean sea level −1 m.

TABLE 7.72. Positive and negative maximum sea levels (m) due to surge and tide that can occur at six locations in the United Kingdom during 50- and 100-yr return periods. (Pugh and Vassie 1979)

	50 yr		100 yr	
Location	Maximum positive level	Maximum negative level	Maximum positive level	Maximum negative level
Newlyn	3.38	3.32	3.43	3.37
Fishguard	3.27	2.78	3.33	2.80
Malin Head	2.75	2.55	2.80	2.59
Stornoway	3.10	3.31	3.18	3.34
Lerwick	1.65	1.60	1.68	1.65
Aberdeen	2.87	2.89	2.93	2.94

The probablity of a particular level can be obtained from the cumulative distribution function $F(\eta)$:

$$(7.76) \qquad F(\eta) = \int_{\eta}^{\infty} p(\xi)d\xi$$

The return period for the level η is $1/F(\eta)$ provided the time series that represents the surge is not autocorrelated. For a negative surge (exposure of low levels), rather than eq. 7.76, one can write

$$(7.77) \qquad F(\eta) = \int_{-\infty}^{\eta} p(\xi)d\xi$$

Using this technique, Pugh and Vassie (1979) determined the return periods for positive and negative extreme levels for six locations on the United Kingdom coast (Tables 7.70 and 7.71).

The maximum positive and negative levels that can occur at these six stations during a 50- and a 100-yr period are given in Table 7.72.

Mantz and Wakeling (1979) studied the probability of extreme levels on the coast of Norfolk due to the combined action of rainfall and storm surges to obtain design heights for safe riverbank crest levels. They gave the following simple relations for the Yare Basin:

$$(7.78) \qquad \frac{Q_R}{A} = \left\{ \frac{\left[\frac{Q_R(1)}{A}\right] - 0.5}{5.48} \right\} x + 0.5$$

where Q_R/A is the short-term areal discharge for any extreme value reduced variate x. The constant 0.5 $m^3 \cdot km^{-2}$ is the mean daily base flow ($x = 0$) for the total catchment and the constant 5.48 represents the x value for a return period of 242 d (a surge year).

Similarly, a short-term (less than 1 yr) surge level prediction is needed for the joint occurrence analysis. This is given by

$$(7.79) \qquad S_H = \left[\frac{S_H(1) - 0.5}{5.48} \right] x + 0.5$$

where S_H denotes the short-term surge level for any extreme value reduced variate x. The constant of 0.5 m is a daily height that could be exceeded ($x = 0$) and the constant 5.48 represents the x value for a return period of 242 d.

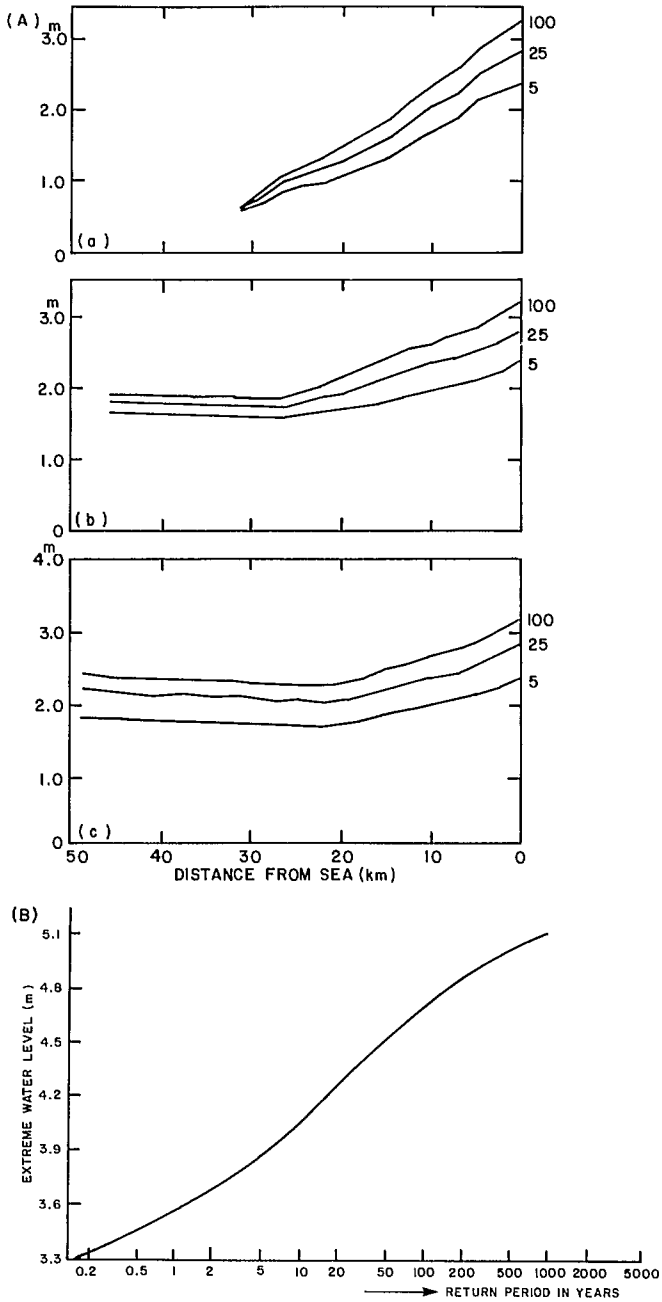

FIG. 7.145. (A) Maximum water level from combined tide and surge that can occur in the basins of (a) Bure, (b) Yare, and (c) Waveney on the southeast coast of the United Kingdom. These water levels are predicted for 100-, 25-, and 5-yr events. (Mantz and Wakeling 1979) (B) Return period versus extreme water level on the coast of Essex. (Ackers and Ruxton 1975)

If T_Q is the return period for the rain flood and T_R is the return period for the surge flood, then the joint return period is

$$T_{QR} = \frac{242}{J_T} T_Q T_R \tag{7.80}$$

where J_T is the average duration during which a flood could occur. Note that

$$J_T = \bar{Q}_T + \bar{Q}_R \tag{7.81}$$

where $\bar{Q}_T$ and $\bar{Q}_R$ are the average durations of rain floods and surge floods. The maximum water levels that can occur from rainfall and surges together in three basins on the southeast coast of the United Kingdom within periods of 525 and 100 yr are given in Fig. 7.145A. The return periods for storm surges on the Essex coast are given in Fig. 7.145B.

Ackers and Ruxton (1975) studied the probability of extreme water levels due to tides and surges on the Essex coast including the effect of wind waves. The results for return periods for up to 5000 yr (using the year 1971 as a base year) are summarized in Fig. 7.146. One has to be very careful in using results of this nature where the extrapolation is thousands of years.

Graff and Blackman (1979) analyzed the water level data for the south coast of England. The data for 10 locations varied from 16 to 125 yr. They used the so-called Jenkinson (1955) method in which the return period T of a given water level h can be written as

$$T = -\frac{1}{\ln p} \text{ or } \ln T = -\ln(-\ln p) = x \tag{7.82}$$

where p is the probability that the annual maxima are less than h. The curve between h and x can be approximately represented by

$$x = \frac{1}{K} \ln \frac{(h - h_c)}{(1 - a)} \tag{7.83}$$

where K, h_c, and a are constants to be determined from the data. The parameter K is a measure of the type of data distribution:

$$K = \begin{cases} <0, \text{ curve bends upwards:} & \text{type I} \\ =0, \text{ curve is a straight line:} & \text{type II} \\ >0, \text{ curve bends downwards:} & \text{type III} \end{cases} \tag{7.84}$$

The results show that along the south coast of the United Kingdom beginning in the west and proceeding towards the east, the curve changes from type III to type II and then to type I (Fig. 7.146).

Prandle (1980) used the analogy between AC circuit theory and hydrodynamics to study the influence of barriers on the tidal regimes. He showed that for the Thames Estuary, barriers located between North Woolwich and Chelsea Bridge will slightly increase the M_2 tidal range. On the other hand, in the Bristol Channel, barriers downstream of Newport will slightly reduce the M_2 tidal range.

Lindström (1979) used the word "turbation" to denote an interesting feature in the sand ridges along the coast of northern Brittany. He stated:

> Sand ridges ... contain alternating beds of coarse and fine to medium sand 4 to 10 meters above normal reach of highest spring tides. They were deposited in the Holocene, largely during the last centuries, by sand charged storm surges ...

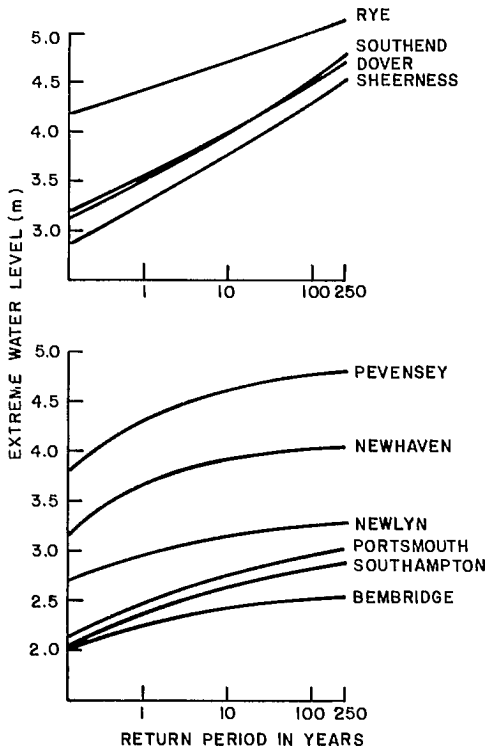

FIG. 7.146. Return period versus extreme water level for selected stations along the south coast of the United Kingdom. (Graff and Blackman 1979)

Regarding the storm surge flooding problem in the Netherlands, the highest point in the extreme southeastern part of the country is about 1000 ft (305 m) above mean sea level whereas the western and northern parts of the country (constituting 40% of the area of the Netherlands) would be submerged due to tides but for the protection afforded by dykes. The lakes and bays that were reclaimed by pumping out water are all below sea level by 19–23 ft.

Storm surges in 1825, 1894, 1906, 1916, and 1953, with amplitudes up to 3 m, caused terrible destruction. The event of January 31–February 2, 1953, flooded 400 000 acres (Edwards 1953) and affected a population of 665 000 in the Netherlands, as well as destroying thousands of houses and killing thousands of animals. Earlier, the so-called "delta plan" that was put into operation in the Netherlands as protection against storm surges was discussed.

Wemelsfelder (1961) established frequency curves for storm surges in the Netherlands. Edelman (1972) studied the beach profiles before and after a storm surge event to estimate the amount of erosion. The surge profiles before and after a storm surge are shown in Fig. 7.147.

The AB portion of the profile is represented by

$$y + 0.90 = 0.415\sqrt{x + 4.70} \tag{7.85}$$

where y is the depth below the highest level of the storm surge and x is the distance from

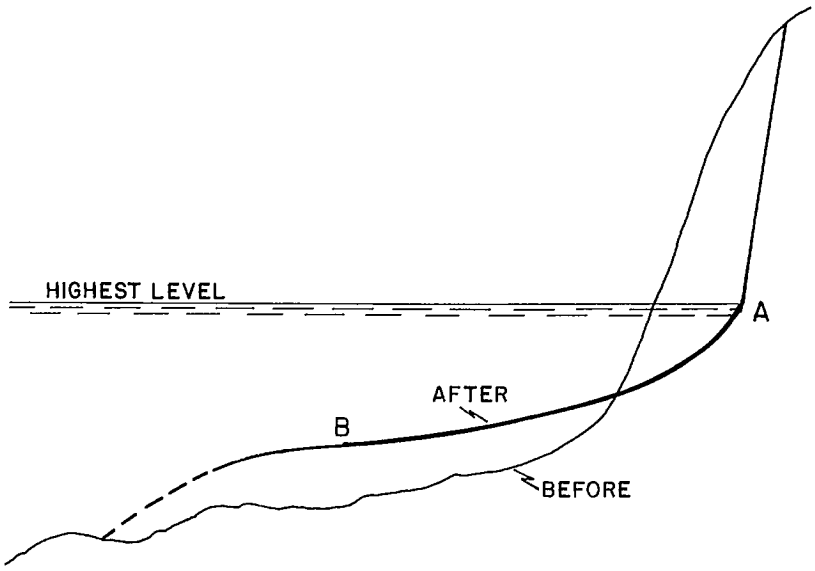

FIG. 7.147. Hypothetical beach profile before and after a storm surge occurrence. (Edelman 1972)

the water line A. Note that $x = 0$ and $y = 0$ gives point A and $x = 100$ m and $y = 3.35$ m gives point B.

To represent the total beach profile after the storm surge, Edelman (1972) tried the cubic formula

$$y = ax^3 - bx^2 + cx \tag{7.86}$$

where a, b, and c must be determined from the data. Edelman (1972) concluded that it is not possible to extrapolate seaward the AB portion of the curve.

van de Graaff (1979) studied dune erosion due to storm surges on the Netherlands coast. He also simulated the events in a hydraulic model. He stated that the primary defense against storm surges in the Netherlands are the dunes. The storm surge of 1953 caused erosion in the width of the dunes by as much as 20–30 m. The average amount of erosion was 100 m^3 per 1-m length of coastline.

Based on hydraulic test results, the following form was assumed for the beach profiles after a storm surge:

$$z = 0.415(x + 4.5)^{0.5} - 0.88 \tag{7.87}$$

where z is the depth (metres) below the maximum water level during the surge and x is the distance (metres) from the intersection of the beach profile and the maximum water level. The simulated dune erosion is shown as a function of time in Fig. 7.148. Based on these tests it was deduced that storm surges with amplitudes of up to 3.8 m could cause erosion at the rate of 160 $m^3 \cdot m^{-1}$ whereas for surges with amplitudes of up to 5 m, the rate could be about 225 $m^3 \cdot m^{-1}$.

Fohrboter (1979) studied the frequencies of extreme storm surges on the coast of West Germany and advanced the hypothesis that storm surge activity is on the increase in the German Bight. To support this contention he stated that after the disastrous 1953 storm

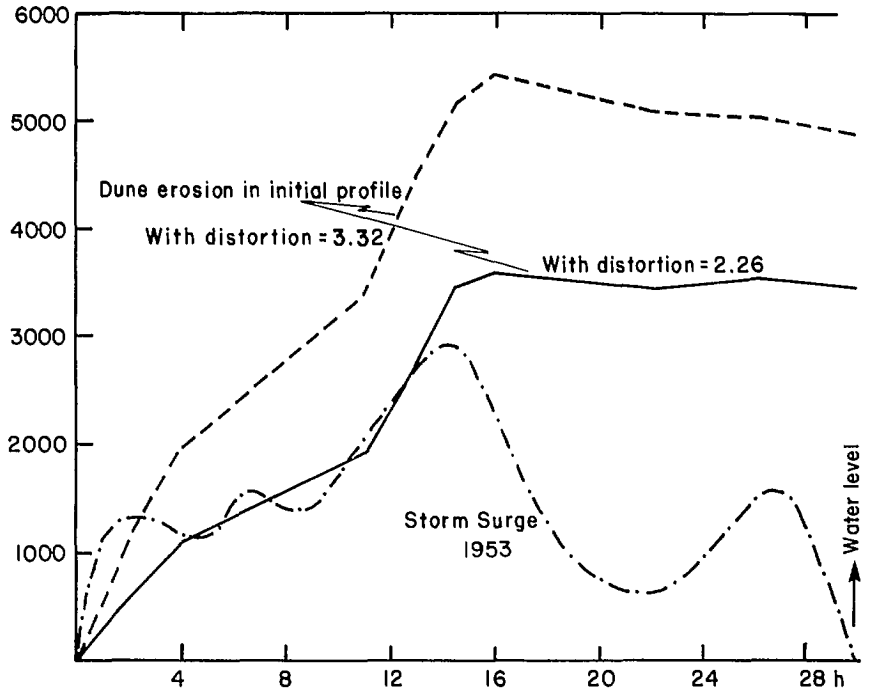

FIG. 7.148. Hydraulic model results of dune erosion due to storm surges on the coast of the Netherlands. Time is after the start of the surge. The ordinate is the volume of erosion in a model test (in arbitrary units). The distortion referred to is the distortion in the hydraulic model. In these tests, a maximum surge amplitude of 5 m is assumed. (van de Graaff 1979)

surge in the Netherlands, the next major one was in Germany in 1962. Another one in November 1972 did extensive damage all along the coastline from France to Poland. Then, six storm surges occurred in November–December 1973, and two major surges occurred in January 1976.

Fohrboter (1979) suggested that the classical extrapolation techniques for return periods might not be applicable in this situation because the time series (representing the storm surge data) is not stationary but changing with time. At three locations on the North Sea coast of Germany, storm surge records are available for long periods: Cuxhaven for 1813–1976 (Fohrboter's study does not consider data subsequent to 1976), Wilhelmstaven for 1854–1976, and Husum for 1867–1971. Using two different models, he showed that there is a general increase of storm surge activity beginning in the 1950's.

Barthel (1979) showed that significant wind wave activity can occur in the German Bight. One must include this in predicting the total water level.

7.4 Storm Surges Elsewhere than in Canada, the United States, and Europe

STORM SURGES IN BERMUDA

Redfield and Miller (1957) studied hurricane-generated storm surges at Bermuda due

to the storm of October 7, 1948. They could account for the storm surge in terms of the inverse barometer effect. The surge amplitude was only 0.6 ft (0.18 m). The hurricanes of September 13, 1948, and September 17, 1953, produced similar surges. These low amplitudes for the surges are consistent with the concept of low amplitudes for long waves in deep water (noting that Bermuda is a small island and there is no wide shelf surrounding it).

However, major surges can occur occasionally. Surges of up to 6 ft (1.83 m) in amplitude occurred at St. George's due to the hurricanes of September 12–13, 1899, September 21, 1922, and October 22, 1926.

Storm Surges in the Caribbean Sea Region

Hurricanes and storm surges cause significant death and damage in the nations of the Caribbean Sea region. Of the four nations Haiti, Cuba, The Dominican Republic, and Honduras, maximum effects occurred in Haiti (Funk 1980) where about 8400 people were killed in the twentieth century. In 1963 alone, Hurricane Flora caused 5000 deaths. Hurricane David of August 29, 1979, killed 56 people in Dominica.

Hurricanes originating in the Caribbean Sea south of 15°N, especially in the month of August, are a potential threat to Jamaica. Hurricane Allen of August 4–7, 1980, produced major storm surges that caused great devastation in Jamaica (Blake 1981). Winds of up to 45 $m \cdot s^{-1}$ generated storm surges with amplitudes up to 12 m at Manchioneal and Galina. Most of the northern coast of Jamaica was struck by surges of amplitudes between 4 and 8 m. There is evidence that the surge penetrated several kilometres inland. The damage was estimated to be about $126 million. About 75% of the banana crop, 95% of the fishing industry equipment on the north coast, and more than 800 houses were destroyed.

The storm surge of June 12, 1979, made poeple aware of what to expect and this helped in the safe evacuation of people during the 1980 surge.

Storm Surges in Mexico

Mexico is affected by storm surges on its Gulf of Mexico coast. Usually, the hurricane tracks over the Gulf of Mexico are such that they strike the United States rather than Mexico. However, on rare occasions, storm surges do occur on the Mexican coast also. On the Pacific coast of Mexico, also, storm surges occur rather infrequently. The storm surge due to Hurricane Paul of September 30, 1982, killed 24 people and caused considerable damage on the Baja California coast. In this hurricane, winds up to 240 $km \cdot h^{-1}$ were reported.

Storm Surges in Barbados

Barbados and other islands of the Lesser Antilles are not usually subjected to storm surges, but they do have severe problems from swell and wind waves. There is a broad reef shelf surrounding Barbados and this makes the problem worse. The swell action is not associated with local storms from the Caribbean Sea but is due to intense extratropical cyclones in the North Atlantic Ocean (Donn and McGuinness 1959).

Swell with amplitudes up to 20 ft (6.1 m) can occur quite frequently. Between December 1957 and October 1958, at least four occasions of major swell activity occurred.

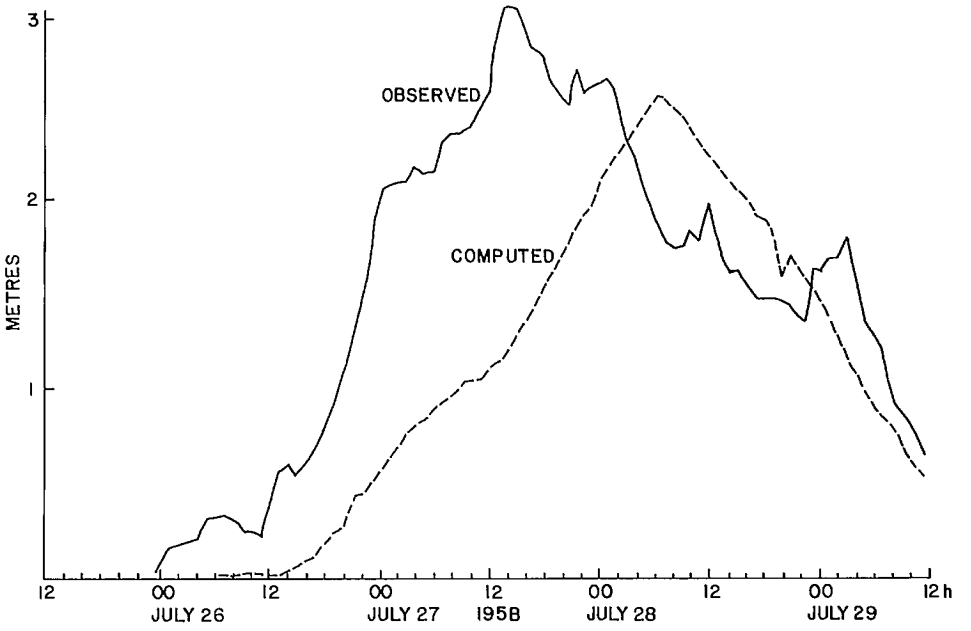

FIG. 7.149. Observed and computed storm surges at Palermo (Buenos Aires) during July 26–29, 1958. (Alvarez 1973)

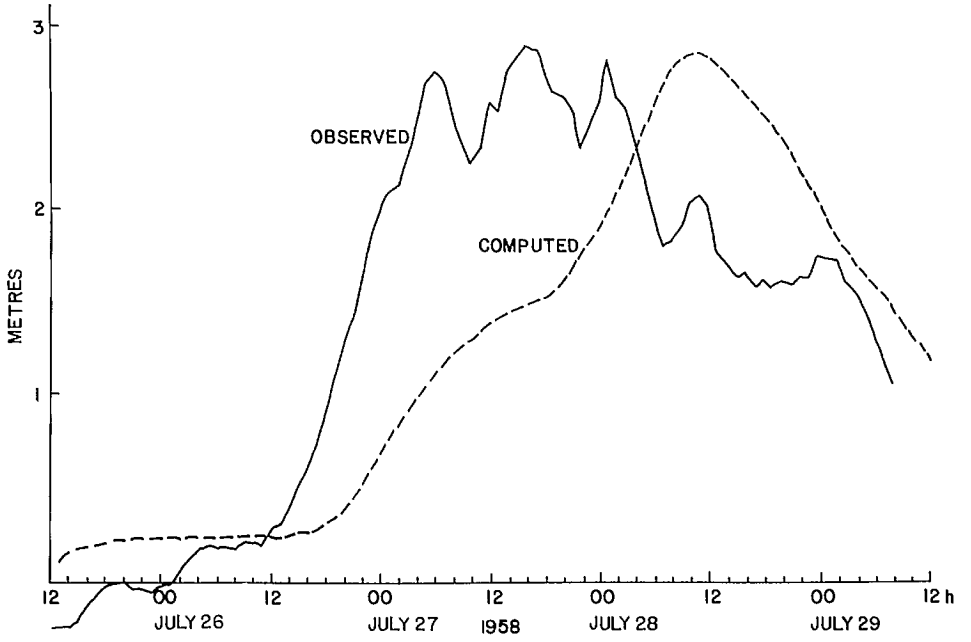

FIG. 7.150. Observed and computed storm surges at Martin Garcia during July 26–29, 1958. (Alvarez 1973)

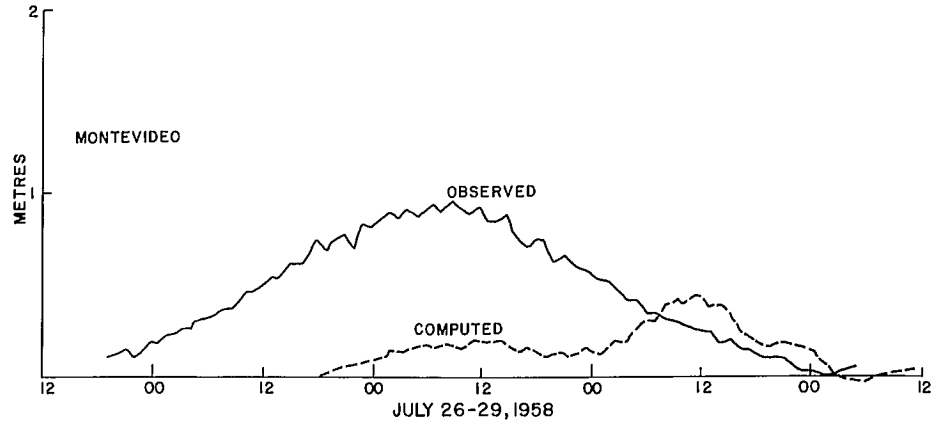

FIG. 7.151. Observed and computed storm surges at Montevideo during July 26–29, 1958. (Alvarez 1973)

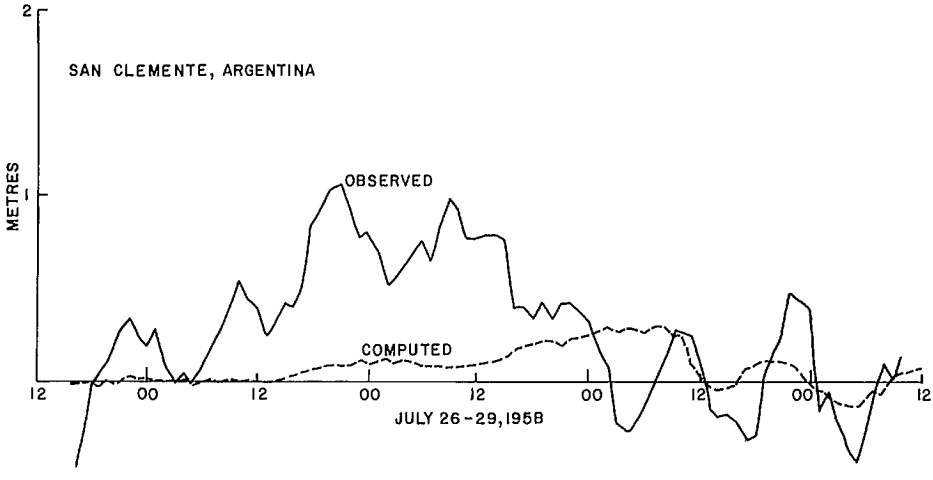

FIG. 7.152. Observed and computed storm surges at San Clemente (Argentina) during July 26–29, 1958. (Alvarez 1973)

STORM SURGES IN SOUTH AMERICA

Alvarez (1973) studied storm surges in Rio de la Plata, which is a water body bordering the South Atlantic Ocean between the south coast of Uruguay and the east coast of Argentina (Buenos Aires is situated on the south coast of this water body and Montevideo is on its north coast). The observed and computed surges during July 25–29, 1958, at Palermo (near Buenos Aires) are compared in Fig. 7.149 and similar data are shown for Martin Garcia in Fig. 7.150. The computed and observed surges at Montevideo and San Clemente for the same dates are shown in Fig. 7.151 and 7.152. It can be seen that the computed values are systematically smaller than the observed values. The differ-

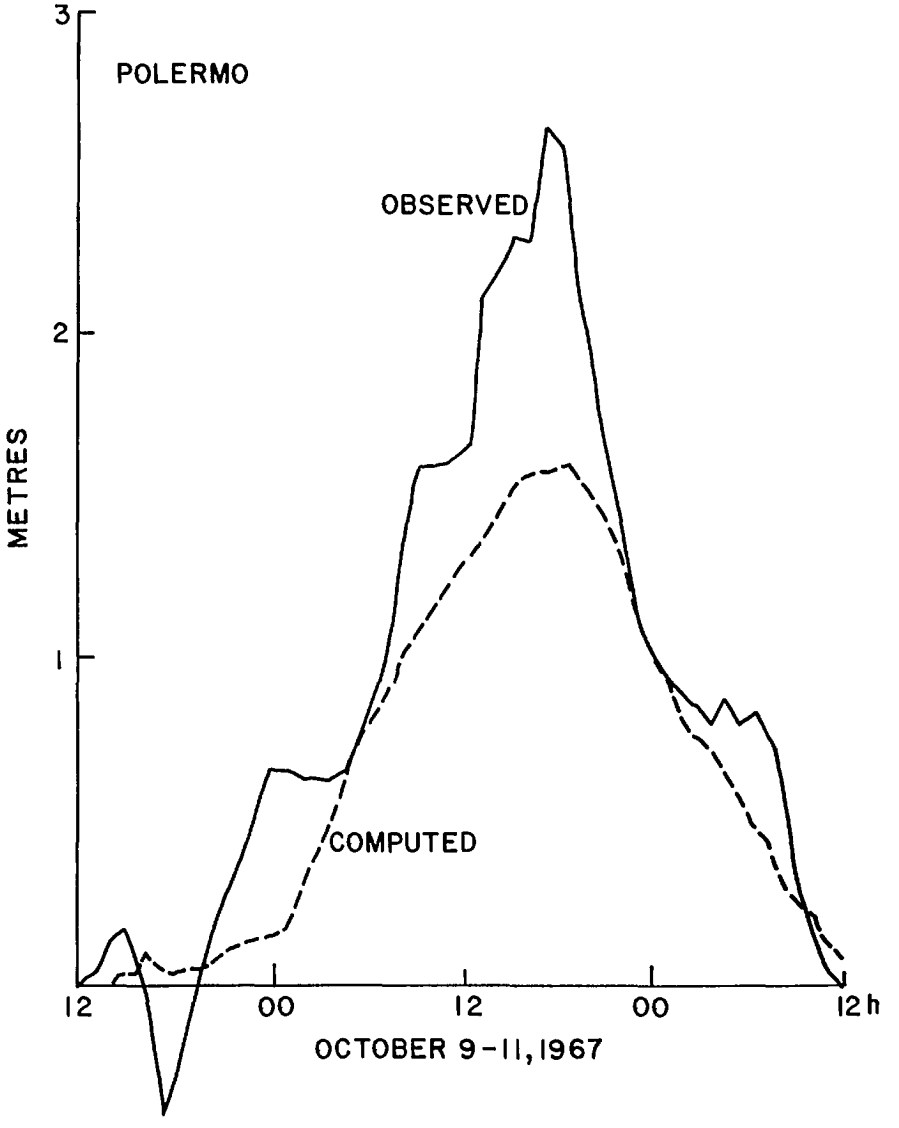

FIG. 7.153. Observed and computed storm surges at Palermo (Buenos Aires) during October 9–11, 1967. (Alvarez 1973)

ences are somewhat severe at Montevideo and San Clemente.

Alvarez (1973) also simulated the storm surge of October 10–12, 1967. The computed and observed surges at Palermo, Martin Garcia, Montevideo, and Torre Oyarvide are compared in Fig. 7.153–7.156, respectively. In this case the agreement between computed and observed surges is somewhat better, especially at Martin Garcia. Also, the computed surges are generally smaller than the observed surges.

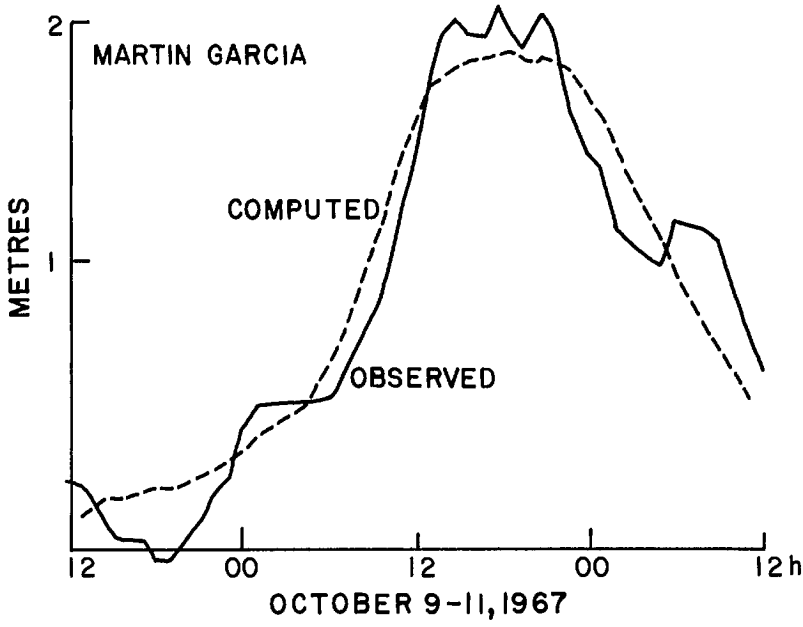

FIG. 7.154. Observed and computed storm surges at Martin Garcia during October 9–11, 1967. (Alvarez 1973)

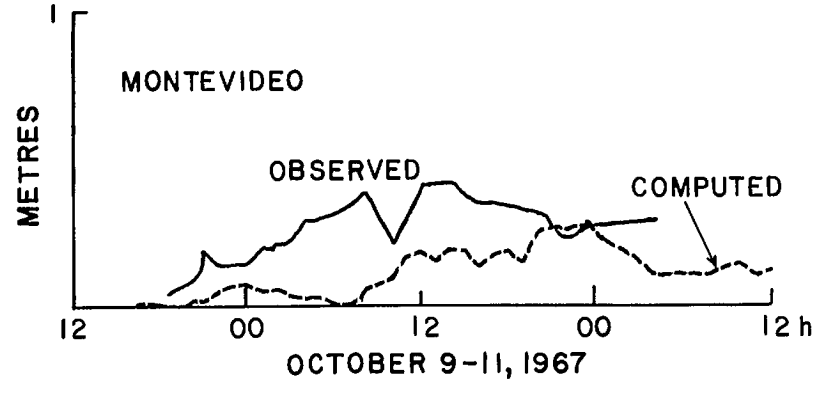

FIG. 7.155. Observed and computed storm surges at Montevideo during October 9–11, 1967. (Alvarez 1973)

STORM SURGES IN MARIANAS, AMERICAN SAMOA, SOLOMON ISLANDS, AND TONGA

Redfield and Miller (1957) mentioned that near the island of Mille in the Marianas, a storm surge of 12–15 m occurred in 1905 due to a buildup of the surge in a lagoon 25 nautical miles (46 km) long.

Gallagher (1973) studied the nonlinear distortion produced to the tidal regime due to openings of restricted depth. He showed that the tides in the Pala Lagoon in American

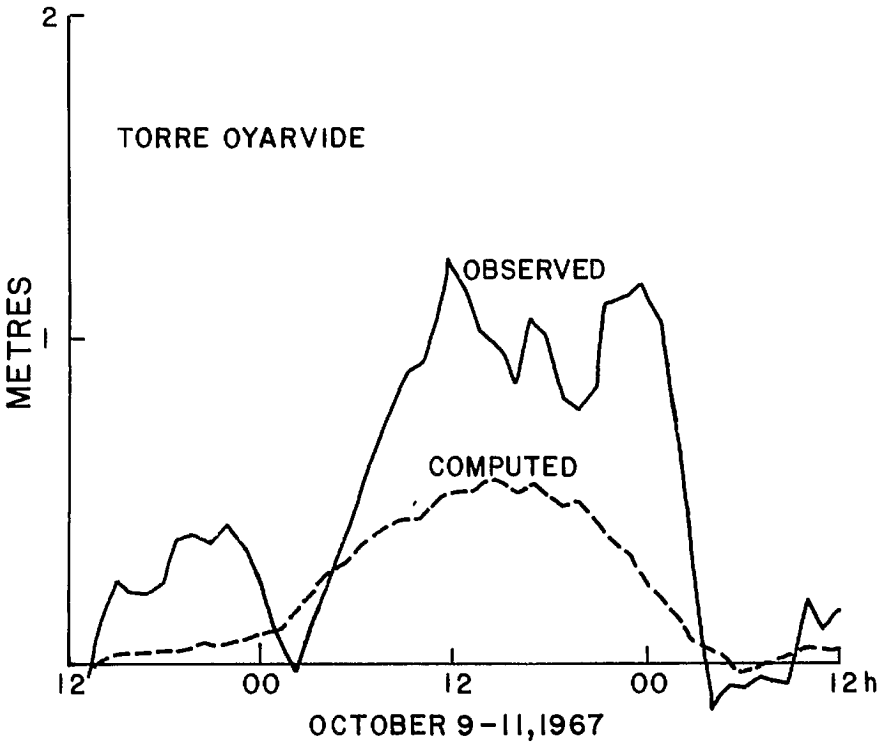

FIG. 7.156. Observed and computed storm surges at Torre Oyarvide during October 9–11, 1967. (Alvarez 1973)

Samoa and the Main Lagoon on Christmas Island (in the latter case, very severely) are distorted. Similar behavior is expected for other long waves such as storm surges and tsunamis.

Grover (1967) studied storm surges in the Solomon Islands, which is a rare phenomenon there. Cyclones forming in the Coral Sea region and intensifying in the area south and east of the Solomons could cause surges occasionally. The storm surge of January 1952 caused some destruction on the west coast of Guadalcanal and at Malaita. The amplitude of the surge (at the time of low tide) at Honiara was about 3.5 ft (1.07 m). Winds greater than 85 $mi \cdot h^{-1}$ (137 $km \cdot h^{-1}$) were recorded there during this event.

The surge caused serious erosion in a swath 60 m wide. Interesting topographic changes took place in the coastal waters. Grover (1967) mentioned that some villages that withstood severe tsunamis during a half-century period were obliterated by this surge.

A major storm surge occurred during March 3–4, 1982, in Tonga Island in the South Pacific (which is located about 4025 km northeast of Sydney, Australia), and the surge amplitude was at least 1.3 m (*The Citizen*, March 4, 1982, Ottawa, Ont.). Winds up to 276 $km \cdot h^{-1}$ coupled with the surge caused great devastation and killed several people.

STORM SURGES IN NEW ZEALAND

Severe storm surges generally do not occur on the coasts of New Zealand. Gilmour (1963) reported a surge of 0.78 m at Bluff Harbour; Agnew (1966) found surges of up to

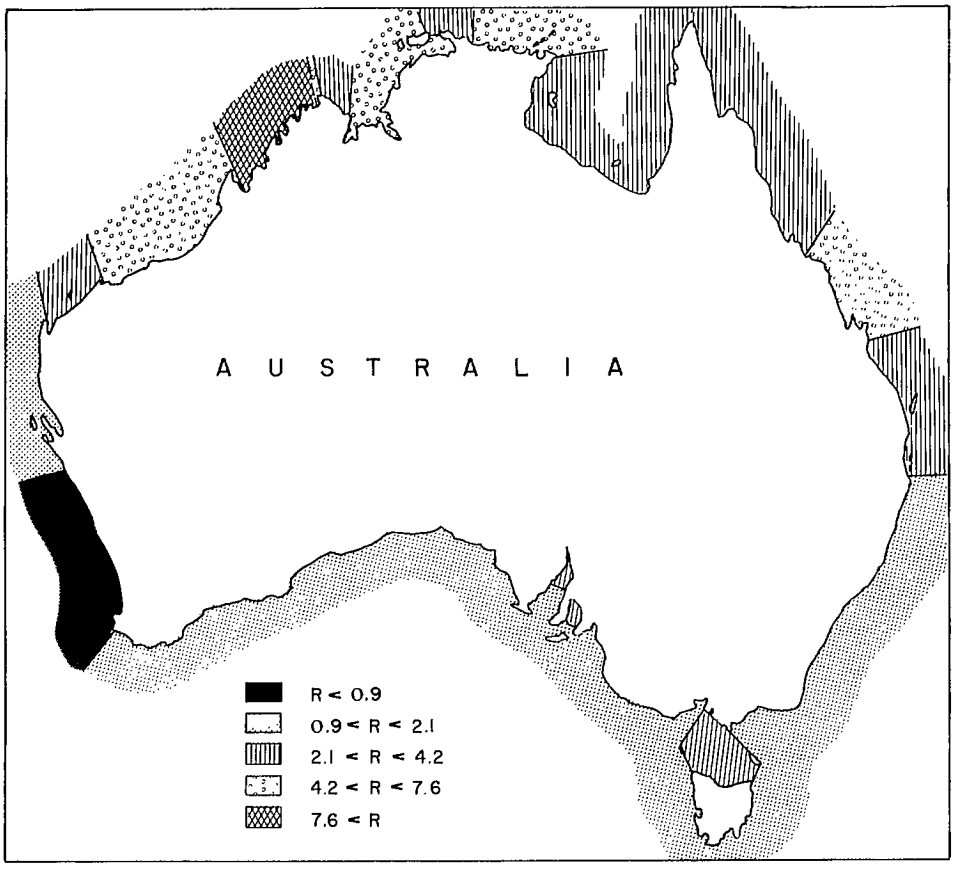

FIG. 7.157. Tidal range R (metres) along the Australian coast. (Easton 1970)

0.8 m on the west coast of the North Island during July 1965. Two cyclones in April 1972 produced surges up to 0.3 m on the east coast of New Zealand (Pickrill 1972). Heath (1979) mentioned that due to the windy climate of New Zealand, departures from isostatic equilibrium are quite common.

Although storm surge amplitudes are small on the New Zealand coast, they cause considerable erosion (Gibb 1976, 1977), e.g. in the Bay of Plenty on the west coast of the North Island and all along the east coast of the North Island (north of Auckland).

Heath (1979) studied three storm surges: April 9–10, 1968, on the east coast of the North Island, July 30–August 1, 1975, on the east coast of the South Island, and September 11–13, 1976, on the west coast of the North Island. These three are the major storm surge events in New Zealand during the period 1968–78. The maximum surge in these events was about 0.6 m.

STORM SURGES IN AUSTRALIA

Since tide–surge interaction could be important, some tidal information will be presented for the coasts of Australia. The tidal range around the Australian coast is shown

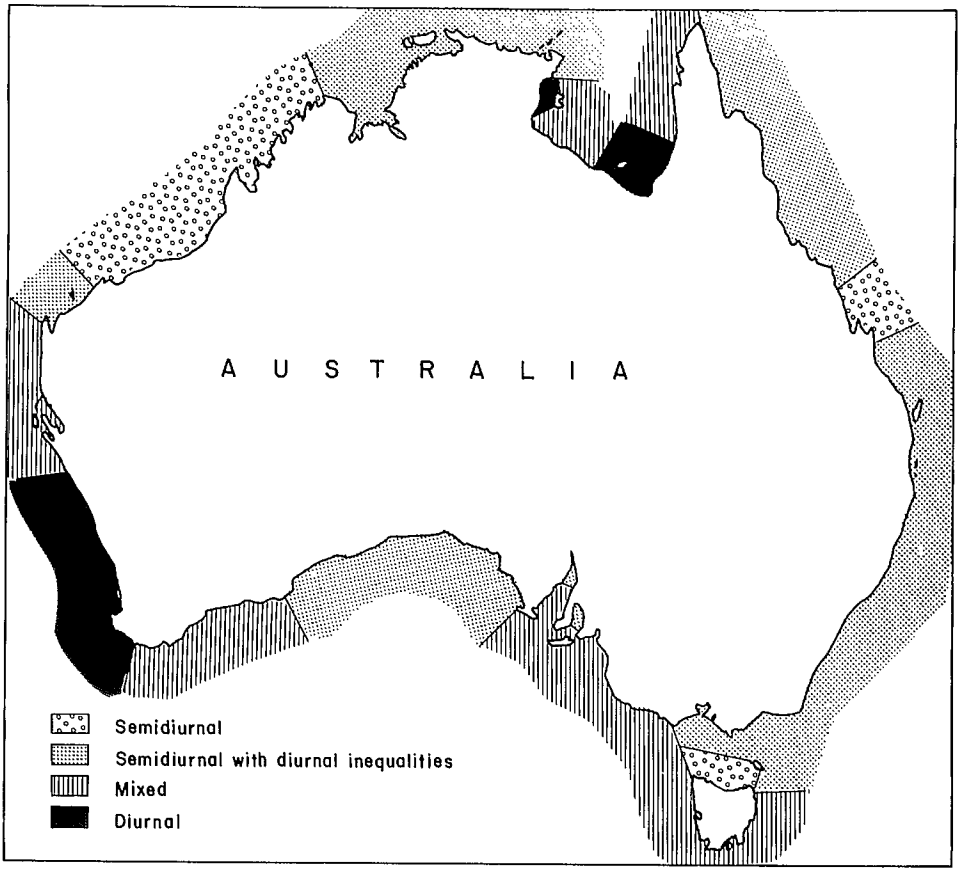

FIG. 7.158. Tidal types along the Australian coast. (Easton 1970)

in Fig. 7.157 and the types of tides are shown in Fig. 7.158.

Hopley and Harvey (1979) studied storm surges in Australia. They questioned the accuracy of the 12.2-m surge in Bathurst Bay in 1899 (Whittingham 1958) and the 7.01-m surge at Groote Eylandt in 1923 (Whittingham 1958). However, they mentioned that several surges with amplitudes greater than 3 m occur in eastern Queensland, Gulf of Carpentaria, and western Australia. These authors used the Jelesnianski (1972) scheme to compute the amplitudes of the surges. The maximum surge height h_c was calculated from

$$h_c = h_S \frac{V_p}{87} F_D \tag{7.88}$$

where h_S is the precomputed surge height based on cyclone parameters (see the SPLASH model of Jelesnianski 1972), V_p is a correction factor based on maximum wind field and pressure drop, and F_D is a depth correction factor for local bathymetry.

Surge amplitudes are generally small on the Australian coastline, with the highest levels usually occurring on the Queensland coast, particularly south of Fraser Island. Storms moving parallel to the west and east coasts of Australia produce edge waves. It is observed that these edge waves tend to amplify the crest of the surge waves on the west

coast of Australia, whereas on the coast of Queensland, they tend to amplify the trough. Negative surges also predominantly occur on the Queensland coast.

Storm surge profiles at several locations along the Australian coast are shown in Fig. 7.159. The maximum surge (3 m) in this diagram was at Townsville due to Cyclone Althea during December 22–25, 1976. Hopley and Harvey (1979) analyzed the contributions from the forerunner, effects of wind stress and pressure gradients, and semidiurnal and diurnal tides to the total water level during storm surge events for six regions of Australia. These results are summarized in Table 7.73.

These authors also calculated the peak surge occurrence probability curves for 19 locations around the northern coast of Australia. Brisbane and Noosa have the lowest surge risk. Two locations with the greatest surge risk are Townsville and Karumba. These results, however, change somewhat when one superimposes the tide on the surge. The greatest risk will then be at Milner Bay, followed by Carnarvon, Townsville, and Centre Island. These surge risk results are summarized in Table 7.74.

Nelson (1975) listed 30 major tropical cyclones that caused surges of amplitudes of at least 0.5 m on the north coast of Australia during the period 1880–1970. Hurricane Tracey of December 25, 1974, did great damage near Darwin. Das et al. (1978) pointed out that although the central pressure was as low as 955 mb and wind gusts attained 200 $km \cdot h^{-1}$, the peak surge was only 1.6 m. Russell (1898) reported that storm surges occurred at Sydney and Newcastle on the coast of New South Wales from storms passing over the Bass Strait. These surges contained waves with periods of about 26 min. Similar phenomena occurred in Lake George. In Chapter 4, the statistical models developed by Tronson and Noye (1973) for the Adelaide area were considered.

Mackey and Whittingham (1956) studied the storm surges at Port Hedland on the northwest coast of Australia for the events of November 14–20, 1955, and February 24–March 2, 1956. The observed and predicted tides and the observed surge for the latter case are shown in Fig. 7.160.

Storm Surges in Japan

Storm surges in the bays on the coast of Japan are slightly less severe than, for example, in the Bay of Bengal and the Gulf of Mexico but they cause great damage and loss of life when they strike the densely populated coasts of Tokyo Bay, Osaka Bay, Ise Bay, etc. Tables 6.71 and 6.72 list the important storm surges in Japan. Miyazaki (1975) mentioned that storm surge records in Japan generally exhibit three features: the forerunner, the main surge, and the resurgence. The surge profiles at Nagoya and Toba along the coast of Ise Bay due to the typhoon of September 26–27, 1959, are given in Fig. 7.161. Forerunners with amplitudes of 20–30 cm can be seen. Resurgences with periods of about 7 h can also be seen. Miyazaki (1975) also estimated the return periods of surges with different maximum amplitudes at six locations in Japan. These results are summarized in Table 7.75.

Unusual storm tracks can occur in the Japan area. The track of Typhoon Orchid of September 1980 is illustrated in Fig. 7.162. This track is remarkable because it shows three loops. Nakayama (1972) described the telemetering system for the tsunami and storm surge warning service provided by the Japan Meteorological Agency. As of 1972 there were a total of 60 coastal tide gauge stations in this system. Next, storm surge events will be considered in several different bays along the coast of Japan, beginning with Tokyo Bay and proceeding southwest. Note that the storm surge problem on the west coast of Japan (facing the Sea of Japan) is less severe than along the Pacific coast of Japan.

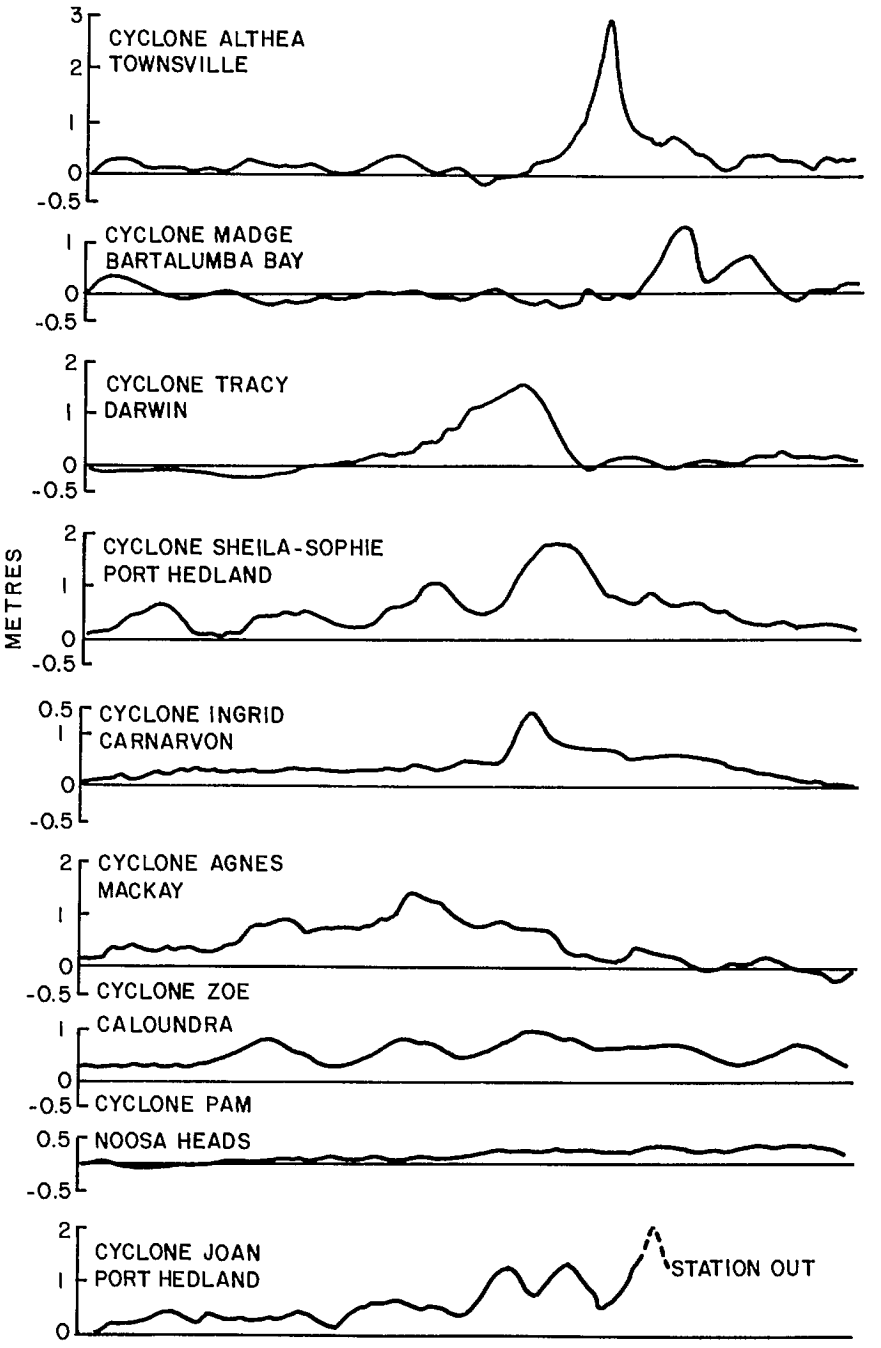

FIG. 7.159. Storm surge profiles at some locations due to selected hurricanes on the coast of Australia. Total length of the abcissa is 72 h, with the exception of Cyclone Tracey, for which it is only 18 h. (Hopley and Harvey 1979)

TABLE 7.73. Percentage contribution of various factors to the total water level during storm surge events in Australia. (Hopley and Harvey 1979)

Region	No. of surges analyzed	Forerunner	Wind and pressure	Semidiumal tide	24-h diumal tide	Other sources
South Queensland	22	40.4	31.5	14.1	10.0	4.0
North Queensland	28	27.1	29.1	23.8	10.9	9.1
Gulf of Carpentaria	15	29.1	44.1	3.9[a]	23.8	—
Northwest (Broome-Darwin)	4	15.7	31.4	37.2	4.7	9.0
Central Western Australia (Port Hedland–Camarvon)	8	50.3	25.5	9.7	5.8	8.7
Southwest Australia	7	74.5	14.7	1.3	3.2	6.3

[a]Without Melville Bay.

TABLE 7.74. Maximum surge heights (m) that can occur in 10, 100, and 1000 yr at any point along a 100-km coastline centered at specific locations on the coast of Australia. (Hopley and Harvey 1979)

Station	10 yr	100 yr	1000 yr
Brisbane	0.15	0.43	0.73
Noosa	0.20	0.50	0.83
Bundaberg	1.40	2.80	4.15
Gladstone	1.30	2.50	3.78
MacKay	1.40	2.40	3.40
Townsville	1.45	3.25	4.90
Caims	1.03	1.78	2.55
Thursday Island	1.25	2.50	3.70
Weipa	0.60	1.30	2.00
Karumba	2.25	3.20	4.15
Centre Island	1.41	2.22	3.00
Milner Bay	1.40	2.25	3.15
Melville Bay	1.50	2.40	3.30
Darwin	1.65	2.30	2.90
Wyndham	1.50	2.73	3.60
Broome	1.10	1.75	2.38
Port Hedland	1.50	2.78	3.70
Camarvon	0.80	1.46	2.10
Geraldton	0.60	1.15	1.64

Miyazaki et al. (1961) used numerical models to compute the storm surges in Tokyo Bay, Ise Bay, and Osaka Bay. They reconstructed the meteorological forcing terms for the Ise Bay typhoon of September 1959. The pressure–distance and wind–distance relations are shown in Fig. 7.163 and 7.164, respectively.

Simulations were made for the following cases: (1) surges in Ise Bay due to the Ise Bay typhoon of September 1959, (2) surges in Tokyo Bay due to the typhoon of October 1, 1917, and Typhoon Kitty of September 1949, and (3) surges in Osaka Bay due to the Muroto typhoon of September 1934 and Typhoon Jane of September 1950.

The horizontal distribution of the storm surge amplitudes in Tokyo Bay due to the typhoon of October 1917 is given in Fig. 7.165. Computed and observed surges at Kishiwada and Osaka due to Typhoon Jane are compared in Fig. 7.166. The spectrum of the storm surge at Kobe due to Typhoon Jane is shown in Fig. 7.167.

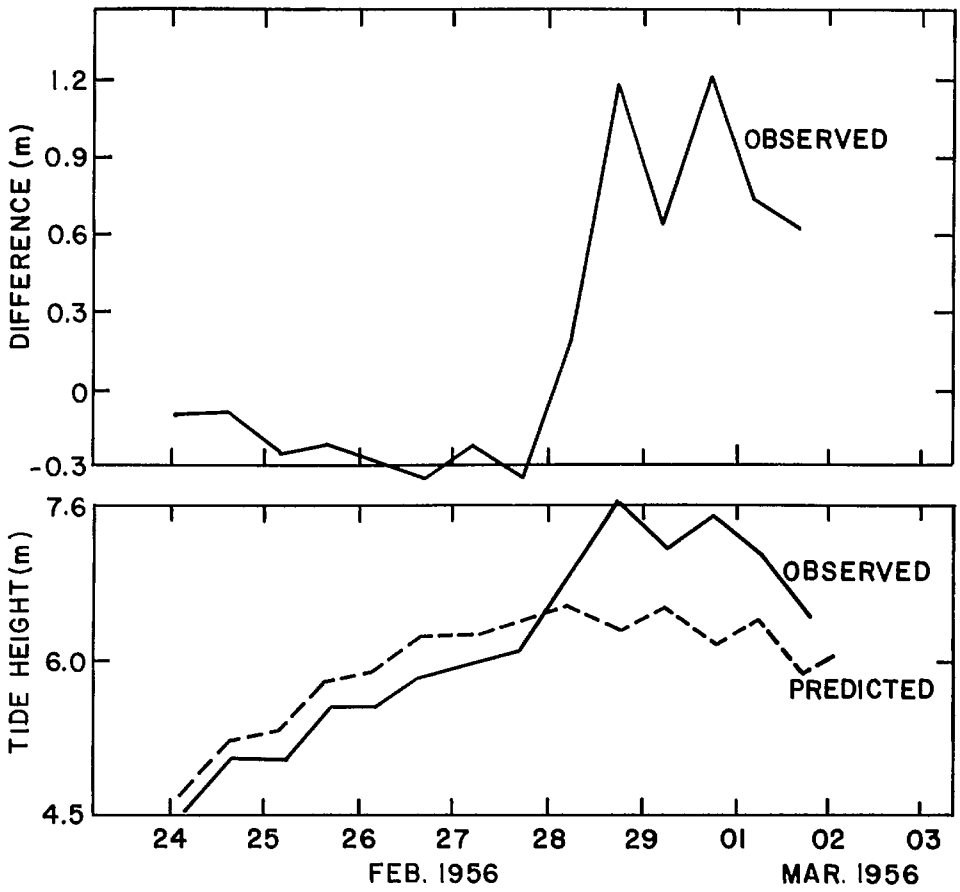

FIG. 7.160. Observed surge (top) and observed and predicted tides (bottom) at Port Hedland on the northwest coast of Australia during February 24–March 2, 1956. (Mackey and Whittingham 1956)

Ito et al. (1965) developed a two-dimensional numerical model for storm surges in Tokyo Bay and the outer shelf using multiple grids. They also studied the problem of tide–surge interaction and the influence of a dyke (with an opening) in Tokyo Bay (north of a line connecting Kawasaki and Kisarazu) on the storm surges in the bay. They simulated the surges due to the October 1, 1917, typhoon and also due to the Ise Bay typhoon of September 1959.

They found the following empirical relation for the maximum water level η_{max} in that part of the bay protected by the dyke:

$$\eta_{max} = a + m \log A \tag{7.89}$$

where A is the cross-sectional area of the opening, a is a constant that depends on the point of observation, and m is another constant almost independent of location.

Runs were made with the numerical model for openings with widths of 20 m to 2 km and also for a case of two openings, each 0.5 km wide. The results tend to show that the maximum surge amplitudes in the inner bay (i.e. protected by the dyke) decrease when a dyke is present. Also, the maximum surge amplitude decreases for smaller widths of the

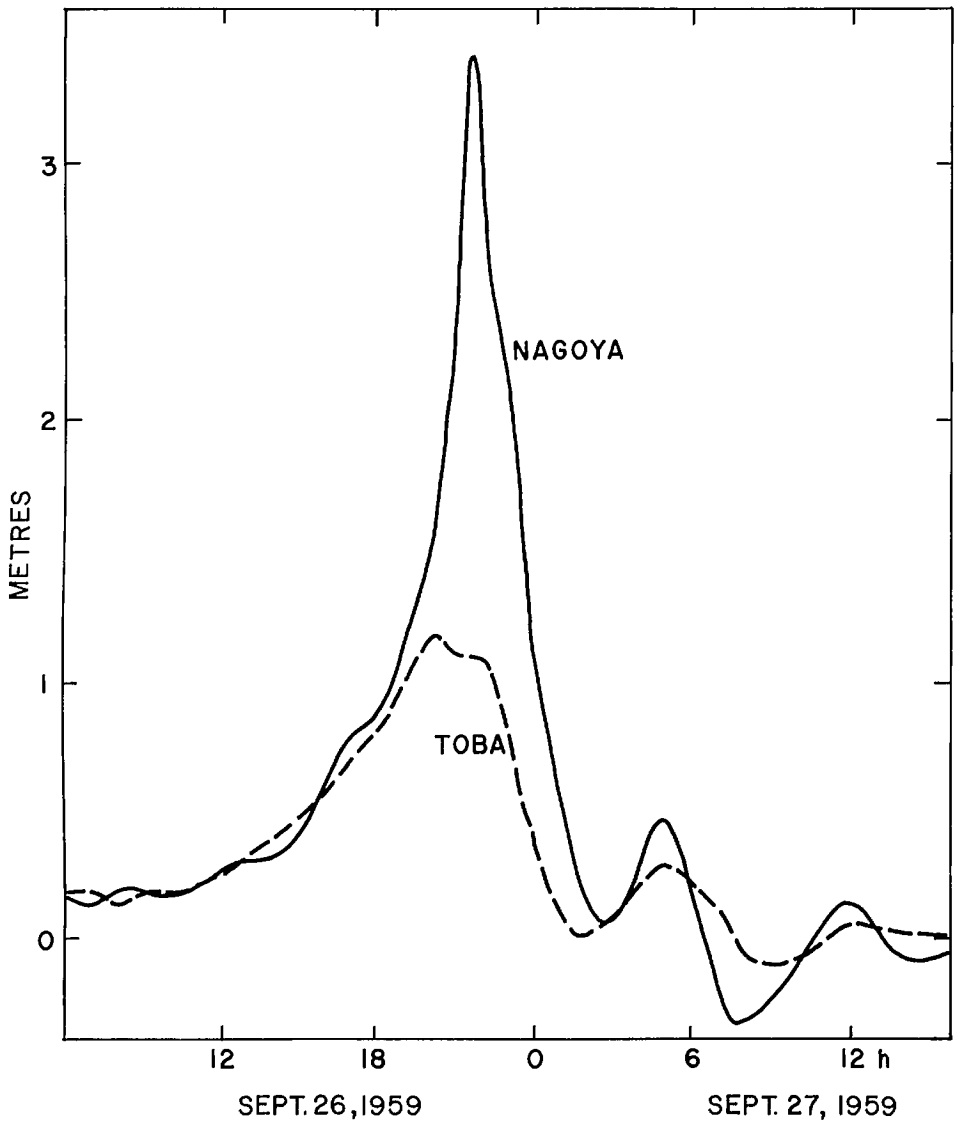

FIG. 7.161. Storm surges at Nagoya and Toba on Ise Bay, Japan, due to the typhoon of September 26–27, 1959. Note the forerunners and the resurgences in addition to the main surge. (Miyazaki 1975)

opening (Fig. 7.168). Several runs were made to compute the tide–surge interaction. A linear superposition of the tide and surge tends to overestimate the total water level, as can be seen from Fig. 7.169.

Kawahara et al. (1980) used a finite-element model to compute storm surges in Surugawan Bay due to the typhoon (No. 6626) of September 24, 1966. The maximum surge produced was about 1 m. After the disastrous storm surge of September 1959 in Ise Bay, a breakwater was constructed in the inner part of the bay to protect the Nagoya district

TABLE 7.75. Return periods of storm surges in Japan. (Miyazaki 1975)

Location	Maximum surge observed (m)	Return period (yr) for surges with peak amplitude of at least		
		0.5 m	1.0 m	2.0 m
Tokyo	2.1	1.0	8	35
Yokohama	1.1	1.4	19	—
Nagoya	3.4	0.6	3	15
Osaka	3.1	0.7	3	10
Kobe	2.2	1.0	6	30
Beniya (on the Ariake Sea)	2.5	—	7	17

(Nakamura et al. 1964). These authors also performed hydraulic model tests. The tests showed that the breakwater will not significantly alter the tide but will reduce the surge considerably in the inner part of the bay.

The Muroto typhoon of September 21, 1934, caused major storm surges in Lake Biwa (northeast of Osaka). The southern portion of this lake is very shallow with an average depth of only 3.4 m. Surges up to 2.4 m in amplitude were generated (Nomitsu 1935).

Miyazaki (1955) studied storm surges in the Kobe Harbor. During the period 1925–54, a total of at least 34 storm surges occurred in this harbor. The Muroto typhoon of September 21, 1934, produced a surge of amplitude 2.2 m. Typhoon Jane of September 3, 1950, produced a surge of 1.7 m; the Makurazaki typhoon of September 18, 1945, as well as another typhoon on September 26, 1954, produced surges up to 1.5 m.

Miyazaki (1955) gave the following return periods for surges of amplitude 1.0, 1.5, 2.0, and 2.0 m in Kobe harbor: 5, 24, 105, and 455 yr. The frequency distribution of storm surges (with amplitudes greater than or equal to 0.5 m) in Kobe Harbor by month is given in Fig. 7.170. Of a total of 32 storm surges studied, 22 were caused by tropical cyclones and the remaining 10 were caused by extratropical cyclones. Further, any surges with amplitudes greater than 0.8 m were exclusively produced by tropical cyclones.

Osaka Bay is frequently subjected to severe storm surges. The Muroto typhoon of September 21, 1934, killed 2593 people and 110 000 houses were destroyed in Osaka alone. The central pressure of this typhoon was the lowest ever recorded at a land station (912 mb). Wind velocities of up to 60 $m \cdot s^{-1}$ created maximum water levels of 4.6 m, and surges with amplitudes of up to 2.3 m inundated large areas (Matsuo 1934). Osaka Harbor (and several others) was heavily damaged and individual ships of up to 3145 t in weight were carried ashore by the surge. The total weight of the ships carried ashore in Osaka Harbor was about 23 000 t. The envelope of maximum surge amplitude at several locations along Osaka Bay due to Typhoon Nancy of 1961 is shown in Fig. 7.171.

Hayami et al. (1955) performed hydraulic model experiments to study the propagation of a storm surge as a bore in the rivers and canals near Osaka City and concluded that the embankment under construction (1955) would provide some protection but not total protection from storm surges. Murota (1963) also performed hydraulic model studies for Osaka Bay and concluded that construction of a breakwater would actually increase the amplitudes of storm surges due to increased seiche action. Ueno (1981) used SPLASH and also a numerical model to simulate the storm surge of August 21, 1970, in Tosa Bay, which produced surges up to 2 m in amplitude. He also used a two-layer model to include the effect of stratification.

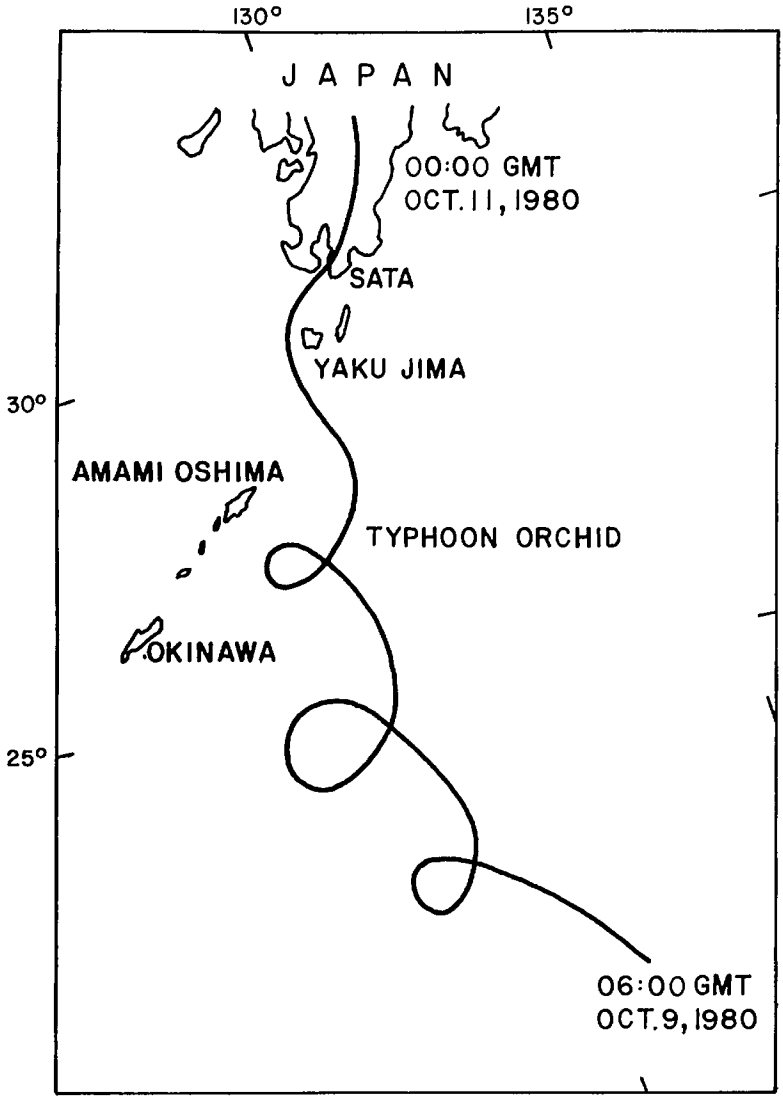

FIG. 7.162. Track of Typhoon Orchid during October 9–10, 1980. (Joint Typhoon Warning Center 1981)

STORM SURGES IN KOREA

Storm surges are not a serious problem in the Sea of Japan. Hence, the west coast of Japan and the east coast of Korea are not prone to major storm surges. However, storm surges occur in the Yellow Sea and the Po Hai Sea. Thus, storm surges on the west coast of Korea deserve attention.

On the southern part of the Korean peninsula, the tidal range in the Yellow Sea is about 4 m and it increases to about 10 m in the northern part (An 1980). The typhoons

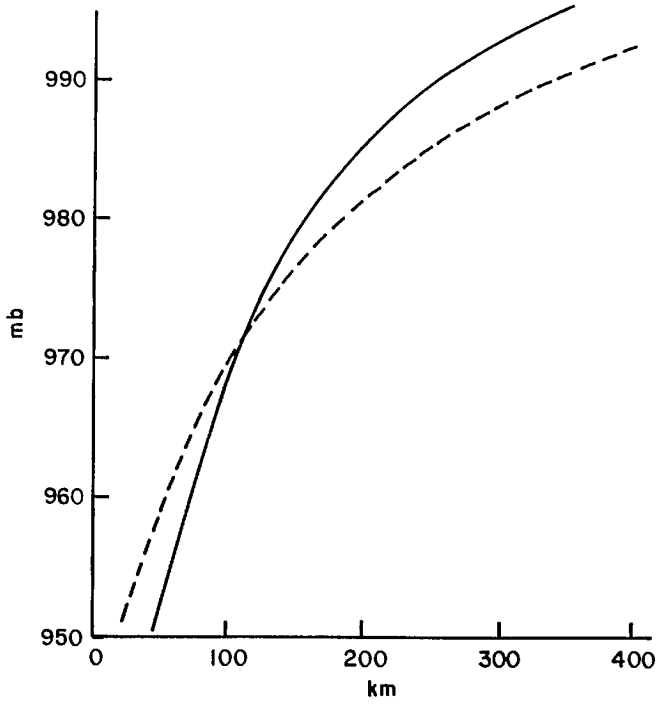

FIG. 7.163. Atmospheric pressure versus distance from the typhoon center for the Ise Bay typhoon of September 1959. Solid curve is obtained using Fujita's formula and the broken curve is from Takahasi's formula. (Miyazaki et al. 1961)

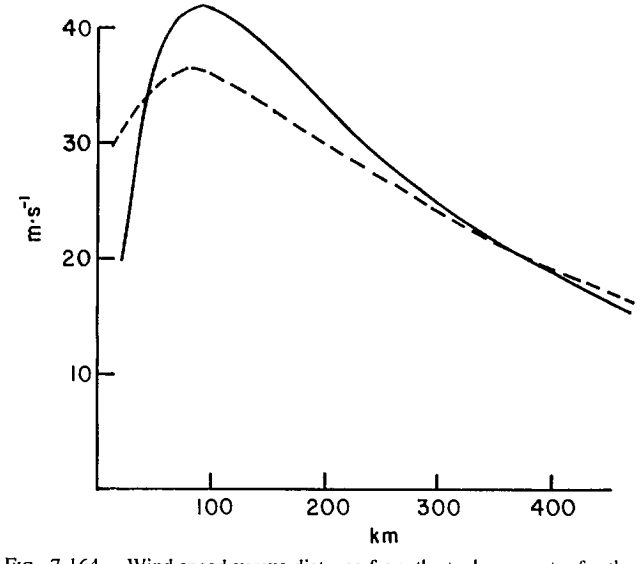

FIG. 7.164. Wind speed versus distance from the typhoon center for the Ise Bay typhoon of September, 1959. Solid curve is from Fujita's formula and the broken curve is from Takahasi's formula. (Miyazaki et al. 1961)

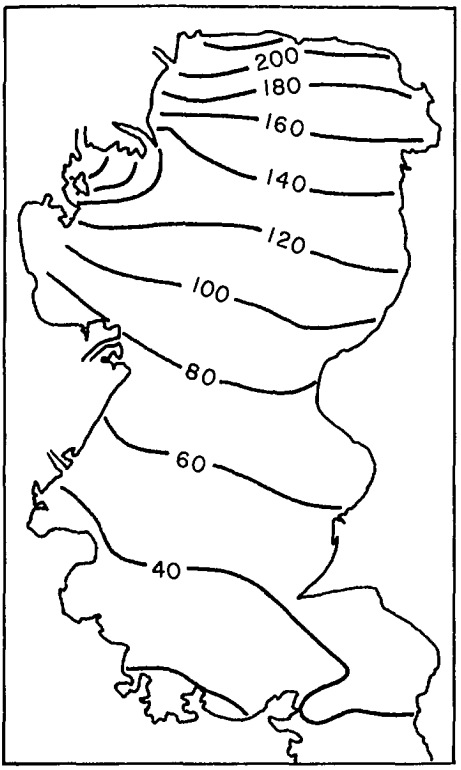

FIG. 7.165. Distribution of storm surge heights (centimetres) in Tokyo Bay at 04:00 on October 1, 1917. (Miyazaki et al. 1961)

that pass over Korea are usually less severe than those that affect Japan.

The observed storm surge at Inchon (tidal range here is about 7 m) during August 30–31, 1970, due to Typhoon Billie is shown in Fig. 7.172. The track of this typhoon is shown in Fig. 7.173. An (1980) used a two-dimensional numerical model to simulate this storm surge. The range (trough to crest) of the storm surge at Inchon was about 1.4 m. At Mokpo and Kunsan, the range was only about 0.4 m. On July 29, 1965, a storm that struck the west coast of Korea generated an unusually large surge of 5.2 m (Das et al. 1978).

STORM SURGES IN CHINA

Storm surges up to 6 m can occur occasionally on the coast of China, with surges up to 2–3 m occurring quite frequently. Tseng-Hao and Shih-Zao (1975) used a numerical model to compute storm surges in the Po Hai Sea. Jin-Chuan and Guang (1979) developed empirical techniques for hourly predictions of surges due to typhoons on the southeastern coast of China. Their study involved predictions for the following tidal stations: Shacheng, Sansha, Xiamen, Dongshan, Shantou, and Shanwei. The total number of surges considered by them was more than 1000. They used the empirical formulae thus developed operationally since 1977. The hourly predicted and observed surges at three locations due

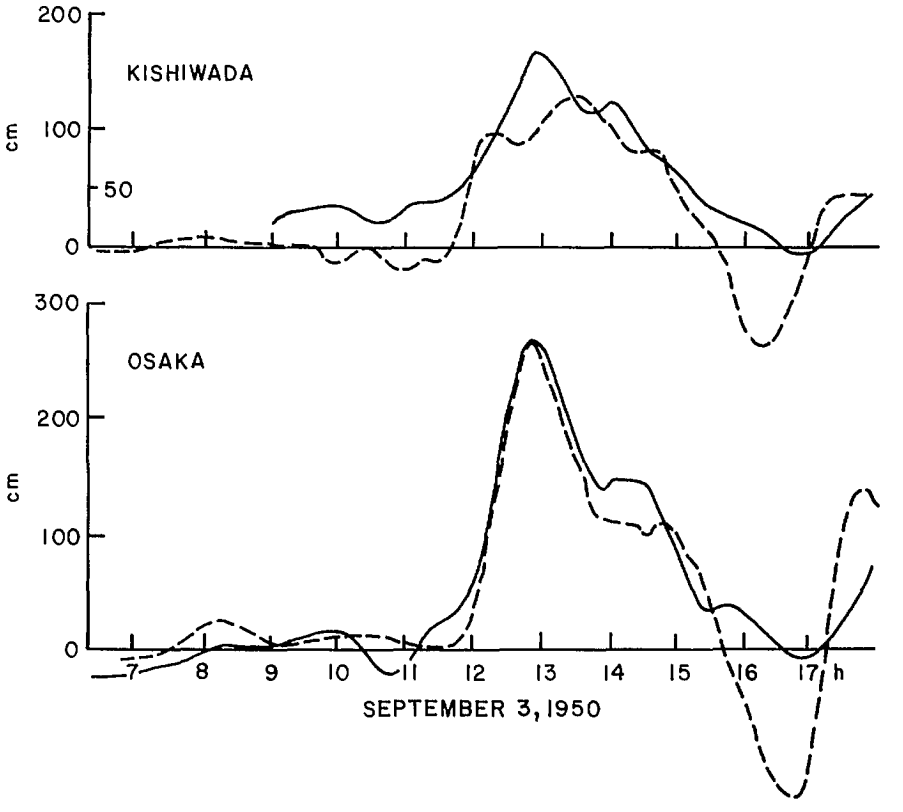

FIG. 7.166. Observed (solid line) and computed (broken line) storm surges at Kishiwada and Osaka due to Typhoon Jane of September 1950. (Miyazaki et al. 1962)

to typhoon 7908 of August 2, 1979, are compared in Table 7.76. Jin-Chuan and Guang (1979) gave surge profiles for the 24 most important storm surges on the southeastern coast of China during the 1970's. Five of these profiles are given in Fig. 7.174–7.178. C. Tseng-Hao and F. Shih-Zao (unpublished data) developed numerical models for storm surge prediction on the east coast of China.

STORM SURGES IN HONG KONG

Storm surges are reasonably severe in Hong Kong (see section 6.10). In section 6.10, the three different types of surges and the empirical formulae for predicting them (Chan and Walker 1979) were discussed. The return periods for surges of different amplitudes (Bell 1961), computed using Gumbel's methods and using data from maximum hourly winds, are listed in Table 7.77. Silvester (1971) studied storm surges in Hong Kong and developed empirical relations. The pressure deficits and observed storm surges at North Point, Hong Kong Harbor, for seven different typhoons are listed in Table 7.78.

Lau (1980b) used the SPLASH model to compute storm surges at North Point and in Tolo Harbor for events of tropical cyclone passages across the northern part of the South China Sea. This study used 93 historical storms during the period September 1906–June

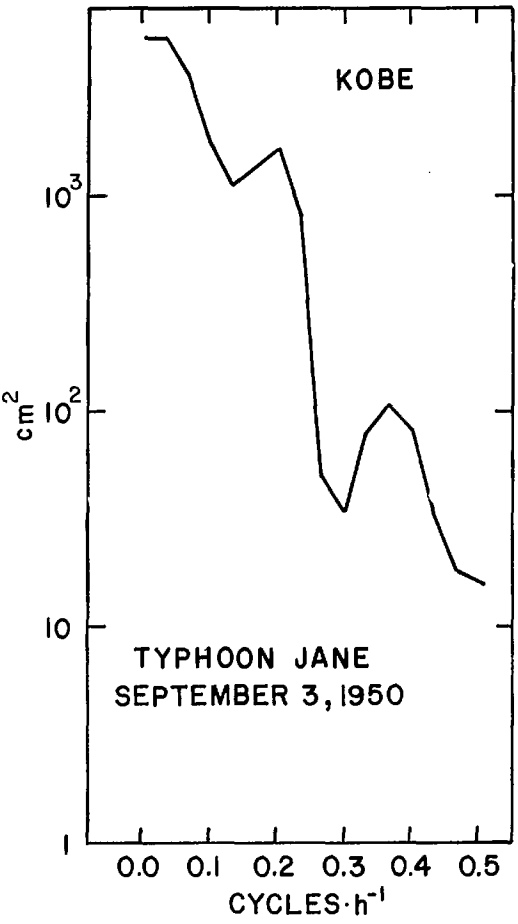

FIG. 7.167. Power spectrum of the storm surge at Kobe due to Typhoon Jane of September 3, 1950. (Das et al. 1978)

1976 that generated storm surges in Hong Kong. The standard storm of the SPLASH model gives an open-coast peak surge of 1.92 m at North Point. Nomograms for the surge height at North Point are given in Fig. 7.179–7.183, respectively, as a function of the central pressure of the storm, storm direction, storm speed, radius of maximum winds, and distance of nearest approach of storm.

Lau (1980a) mentioned that the storm surge problem is getting worse in Hong Kong with more and more people crammed into reclaimed low-lying areas. A typhoon surge on September 2, 1937, killed 11 000 people, and several villages around Tolo Harbor were destroyed. Typhoon Wanda of September 1, 1962, killed 127 people. Lau (1980a, 1980b) summarized the empirical relations developed by Cheng (1967) and Chan (1976). He also included a table from Peterson (1975) in which joint probabilities for certain combinations of tides and surges at Tolo Harbor and North Point were listed. Finally, Lau (1980a) developed a series of numerical models for computing surges in different areas of Hong Kong and environs. Observed and computed water levels at Tai Po Kau due to Typhoon

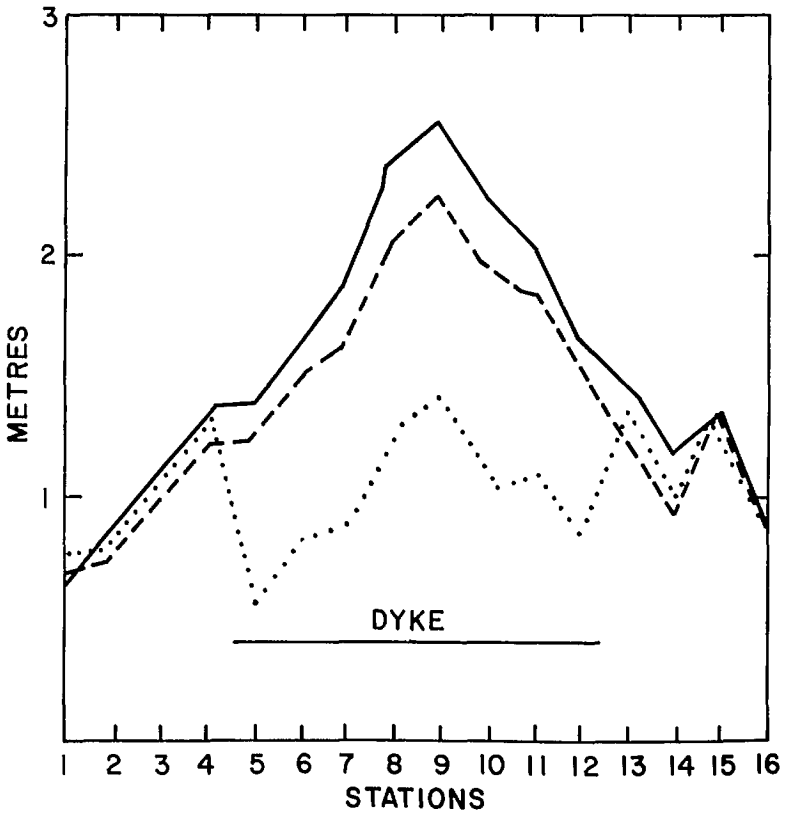

FIG. 7.168. Computed envelope of peak storm surge in Tokyo Bay after the construction of a dyke. Solid line: without dyke; broken line: with dyke having an opening of 2 km width; dotted line: with dyke having an opening of 0.5 km width. Stations: 1, Kurihama; 2, Yokosuka; 3, Yokohama; 4, Kawasaki South; 5, Kawasaki North; 6, Tokyo; 7, Urayasu; 8, Funabashi; 9, Chiba; 10, Goi; 11, Anegasaki; 12, Narawa; 13, Kisarazu; 14, Futtsu; 15, Isone; 16, Kaiho II. (Ito et al. 1965)

Elaine of October 29–30, 1974, are compared in Fig. 7.184. Computed and observed water levels at Tai Po Kau due to Typhoon Elsie of October 14–15, 1975, are compared in Fig. 7.185.

Das et al. (1978) mentioned that storm surges occur at the rate of three to four per year in Hong Kong Harbor. Thirty-five surges with amplitudes from 0.2 to 1.8 m occurred there during 1954–64 (Cheng 1967). Typhoon Wanda of September 1962 produced a surge of about 3.2 m at Tai Po Kau (farther inland from Hong Kong Harbor), whereas the peak surge in Hong Kong Harbor was 1.8 m.

STORM SURGES IN THE PHILIPPINES

During the period 1907–31, there were 43 significant storm surges in the Philippines (Das et al. 1978). A storm of October 15–16, 1912, struck the towns of Leyte and Cebu and apparently caused 9-m surges at Sogod Norte in the Lisayan Islands (Barrientos 1978). Typhoon Irma of October 24–26, 1981, caused major surges and destroyed one village.

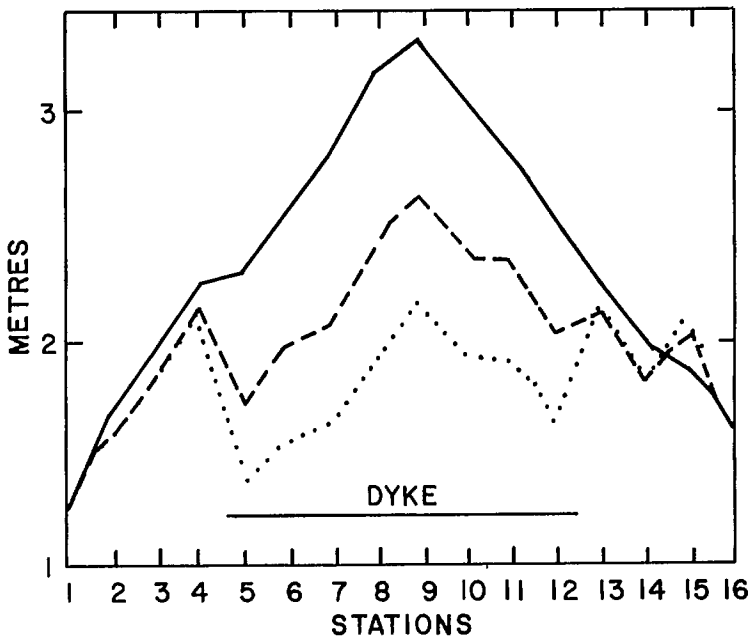

FIG. 7.169. Calculated envelope of total water level (surge plus tide) in Tokyo Bay. Solid line: without dyke; broken line: with dyke having an opening of 1 km width and tide and surge linearly superimposed; dotted line: with dyke having an opening of 1 km width with nonlinear interaction between tide and surge included. See Fig. 7.168 for station names. (Ito et al. 1965)

Storm surges occur in the Sulu Sea, which is a water body on the southeastern corner of the South China Sea. Surges up to 1.22 m in amplitude and with periods of up to 75 min occur in this water body (Haight 1928).

STORM SURGES IN VIETNAM

Storm surges occur on the east coast of North Vietnam and on the east and south coasts of South Vietnam. Nickerson (1971) used SPLASH models to study these surges. One of the worst storm surges in human history occurred in 1881 in which about 300 000 people were killed in the area surrounding Haiphong (LaCour 1917c).

STORM SURGES IN THE BAY OF BENGAL

As mentioned earlier, storm surges are an extremely serious hazard along the coast of the Bay of Bengal, particularly for Bangladesh and India and, to a lesser extent, Burma, Thailand, and Sri Lanka. Except for certain oral statements to the effect that a given storm would produce a surge of about half the amplitude in the Gulf of Thailand compared with a surge in the Bay of Bengal, this author has not been able to find any related literature. Das et al. (1978) stated that peak surges of up to 4 m have been reported on the coast of Thailand. They also stated that Thailand experiences one to two major surges per year.

Similarly, although storm surges have occurred occasionally in Sri Lanka (the most

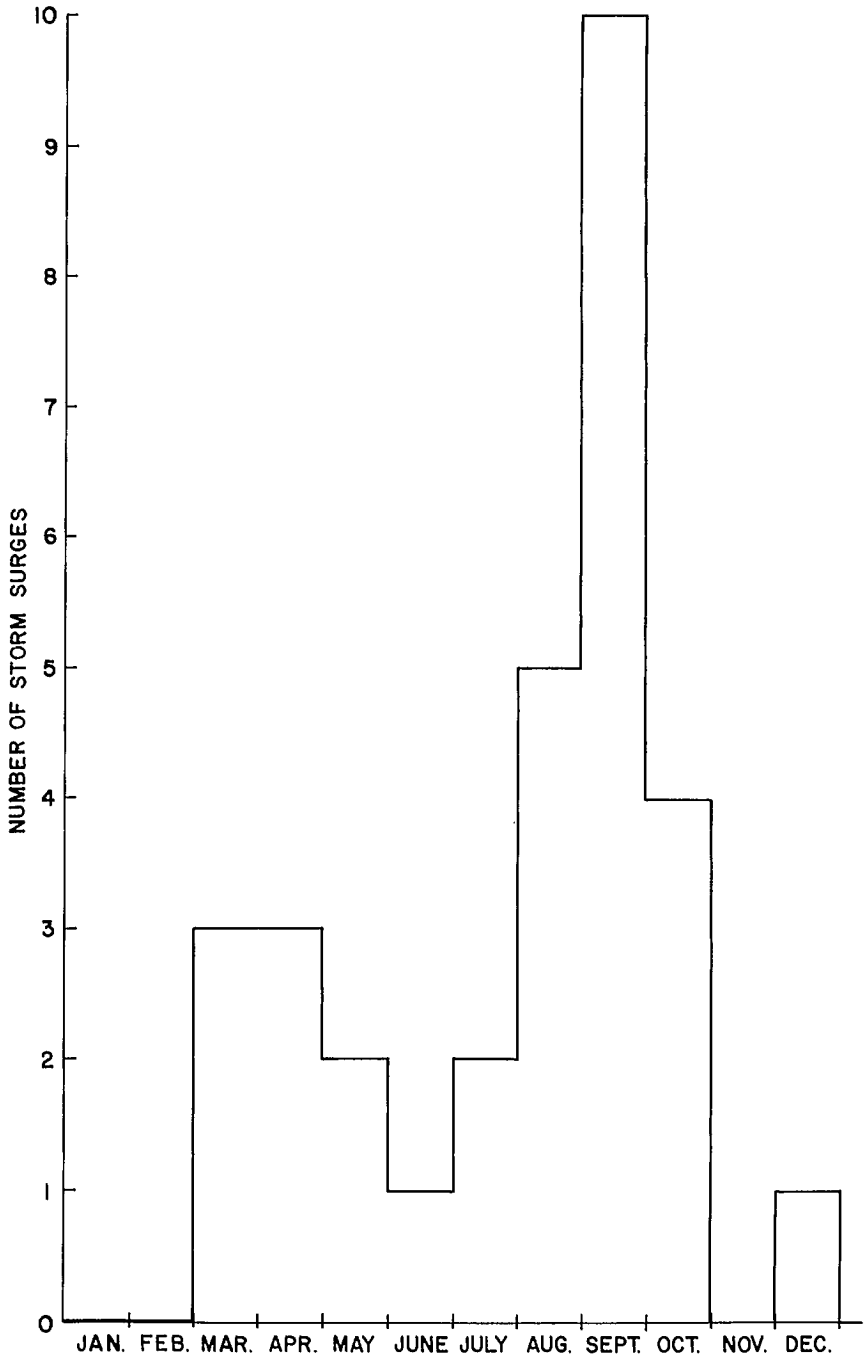

FIG. 7.170. Storm surge frequency distribution in Kobe Harbor for the period 1925–54. Surges with amplitudes smaller than 0.5 m are not included.

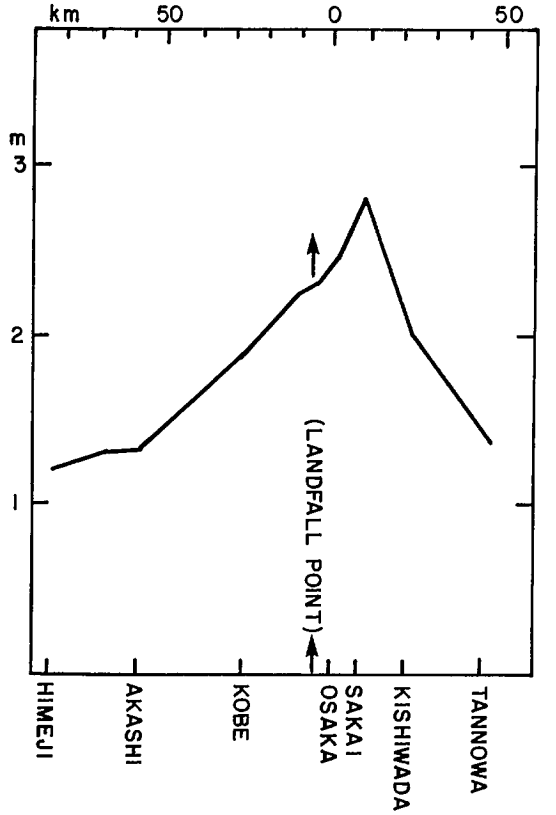

FIG. 7.171. Peak surge envelope at stations along Osaka Bay due to Typhoon Nancy of 1961. (Das et al. 1978)

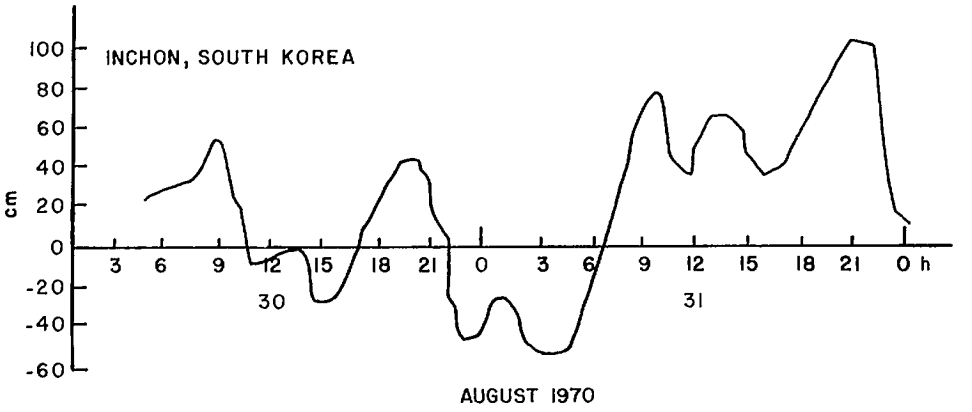

FIG. 7.172. Storm surge at Inchon, South Korea, during August 30–31, 1970, due to Typhoon Billie. Time is Korean Standard Time. (An 1980)

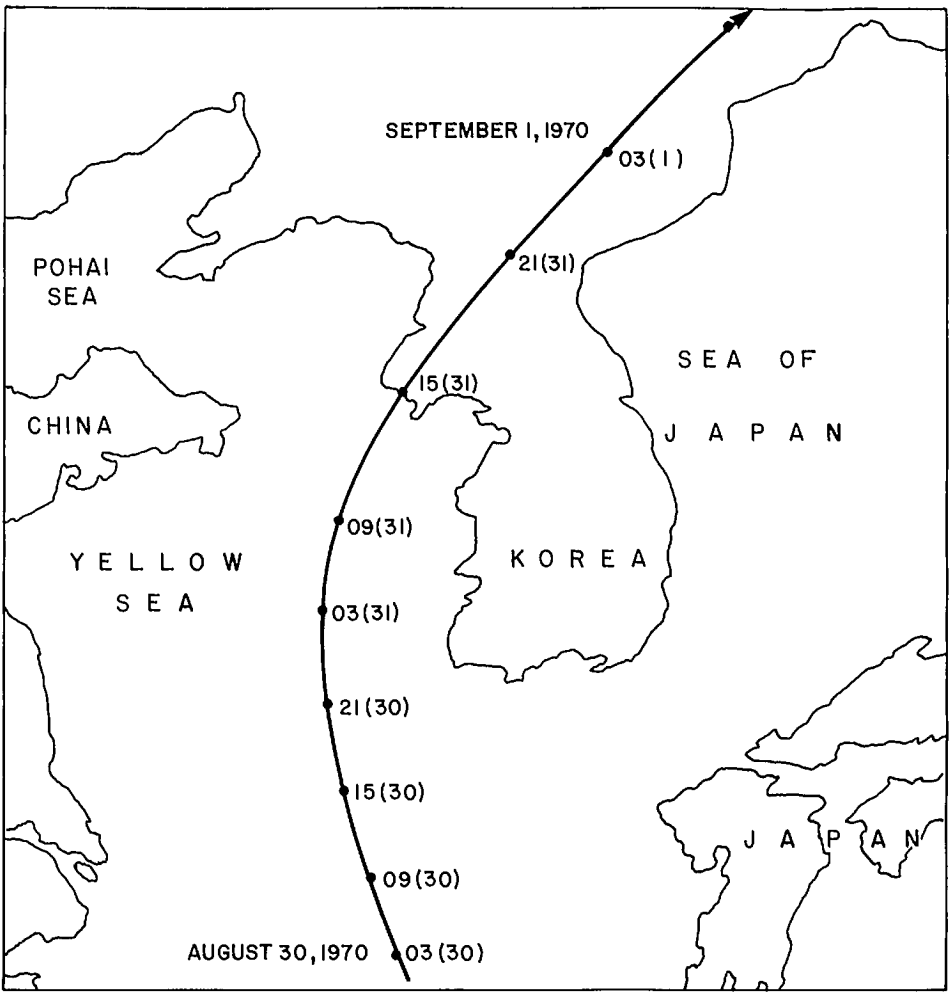

FIG. 7.173. Track of Typhoon Billie during August 30–September 1, 1970. Time is Korean Standard Time. Numbers in the parentheses are the dates. (An 1980)

recent one being in November 1978, which killed 373 people and caused extensive damage (80 000 houses destroyed) on the northeast coast of Sri Lanka), this author could not find any pertinent literature. Hence, the storm surge problem on the Bay of Bengal coasts of Thailand and Sri Lanka will not be considered. Discussion in the following subsections will concentrate on the surges on the Bay of Bengal coasts of Burma, Bangladesh, and India.

STORM SURGES IN BURMA

During May 16–18, 1967, a severe storm surge struck the Rangoon area and killed about 100 people and destroyed 800 villages. In the 1970's, four severe cyclones struck

TABLE 7.76. Predicted and observed storm surges at three locations in China due to Typhoon 7908 of August 2, 1979. (Jin-Chuan and Guang 1974)

Time (h) GMT	Storm surges (cm) at					
	Shantou		Xiamen		Chongwu	
	Observed	Predicted	Observed	Predicted	Observed	Predicted
05	95	106	84	105	78	99
08	158	163	88	107	61	75
10	201	223	91	95	47	65
11	187	199	92	87	35	60
14	66	100	27	43	21	40

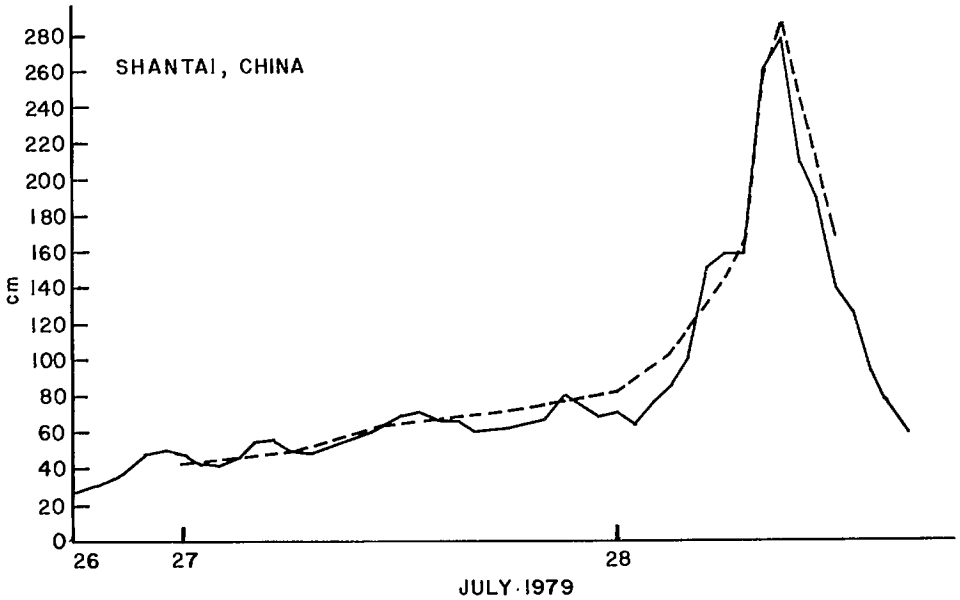

FIG. 7.174. Observed (solid line) and computed (broken line) surges at Shantow, China, during July 26–29, 1979. (Jin-Chuan and Guang 1979)

the Burmese coast and caused storm surges. Storm surge generating cyclones usually develop in the Bay of Bengal during the premonsoon (e.g. the May 1968 and May 1975 cyclones that caused surges on the Burmese coast) or during the postmonsoon season (November–December). The storm surge due to the May 1975 cyclone killed 303 people and thousands of cattle and destroyed about 28 000 houses in Burma (Cho 1980).

In Burma, tidal and storm surge data are available at about 10 stations beginning with the 1960's. The peak surge envelope for the cyclone of May 1968 is shown in Fig. 7.186. The distribution of the maximum surge along the Irrawaddy River for the cyclone of May 1975 is given in Fig. 7.187. The duration of the surge is given as a function of distance (Fig. 7.188) in the Irrawaddy River for the May 1975 event. The storm surge problem in Burma is important in the shallow-water areas of the Arakan coast. The storm surge due to the May 1975 event penetrated at least 60 mi (100 km) into the river systems and also

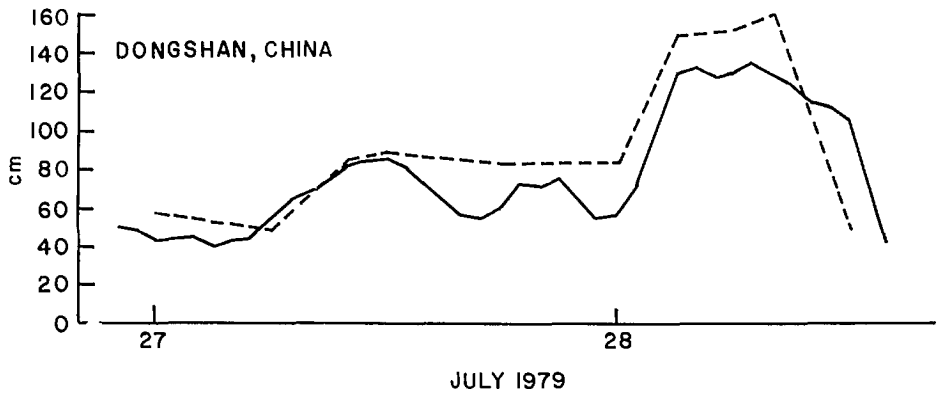

FIG. 7.175. Observed (solid line) and computed (broken line) surges at Dongshan, China, during July 27–28, 1979. (Jin-Chuan and Guang 1979)

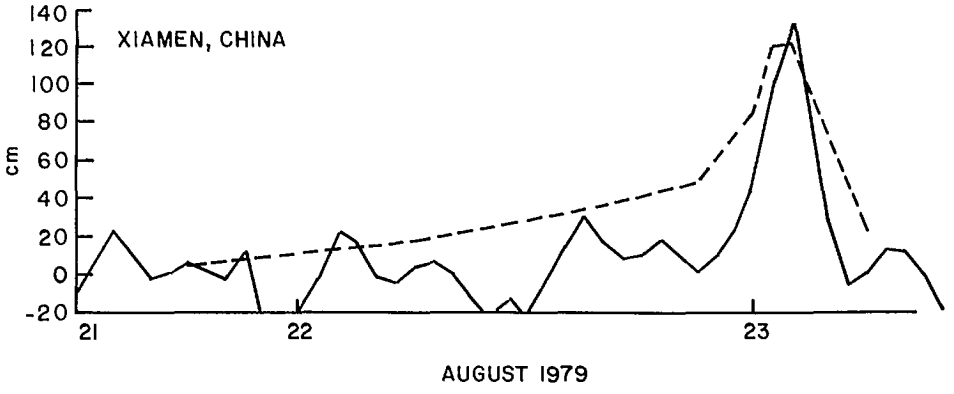

FIG. 7.176. Observed (solid line) and computed (broken line) surges at Xiamen, China, during August 21–23, 1979. (Jin-Chuan and Guang 1979)

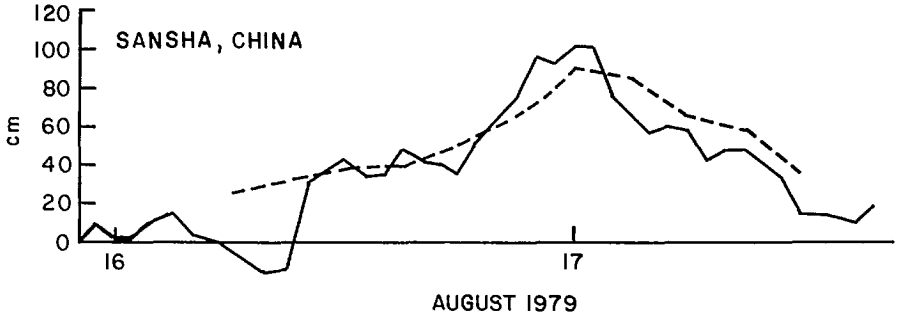

FIG. 7.177. Observed (solid line) and computed (broken line) surges at Sansha, China, during August 16–17, 1979. (Jin-Chuan and Guang 1979)

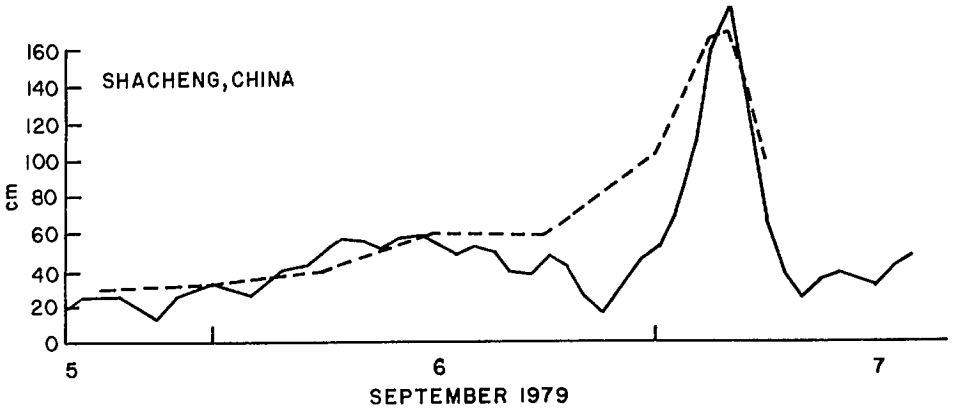

FIG. 7.178. Observed (solid line) and computed (broken line) surges at Shacheng, China, during September 5–7, 1979. (Jin-Chuan and Guang 1979)

TABLE 7.77. Return periods for extreme storm surges in Hong Kong. (Bell 1961)

Surge amplitude (m)	Return period (yr)	Surge amplitude (m)	Return period (yr)
1.6	10	2.4	200
1.8	20	2.7	500
2.0	50	2.9	1000
2.2	100		

TABLE 7.78. Observed storm surge amplitudes and pressure deficits in typhoons that affected Hong Kong (North Point). (Silvester 1971)

Typhoon	Date	Pressure deficit (mb)	Observed surge amplitude (m)
Wanda	Sept. 1962	61	0.62
Faye	Sept. 1963	17	0.17
Viola	May 1964	21	0.21
Ida	Aug. 1964	38	0.39
Ruby	Sept. 1964	45	0.46
Sally	Sept. 1964	24	0.24
Shirley	Aug. 1968	44	0.45

caused inland flooding (Lwin 1980).

Odd (1980) studied the storm surges in the Irrawaddy Delta area of Burma making use of hydraulic and numerical models. In this connection, he questioned the validity of the tide and surge data at Elephant Point. The surge time histories at several stations during May 5–8, 1975, are shown in Fig. 7.189. The distribution of the surge is given as a function of distance (Fig. 7.190) along the coast from the Bassein River entrance. Odd concluded that the surge amplitudes as well as the amplitude of the semidiurnal tide increase rapidly east of the China Bakir because of the shallowness and funnel shape of

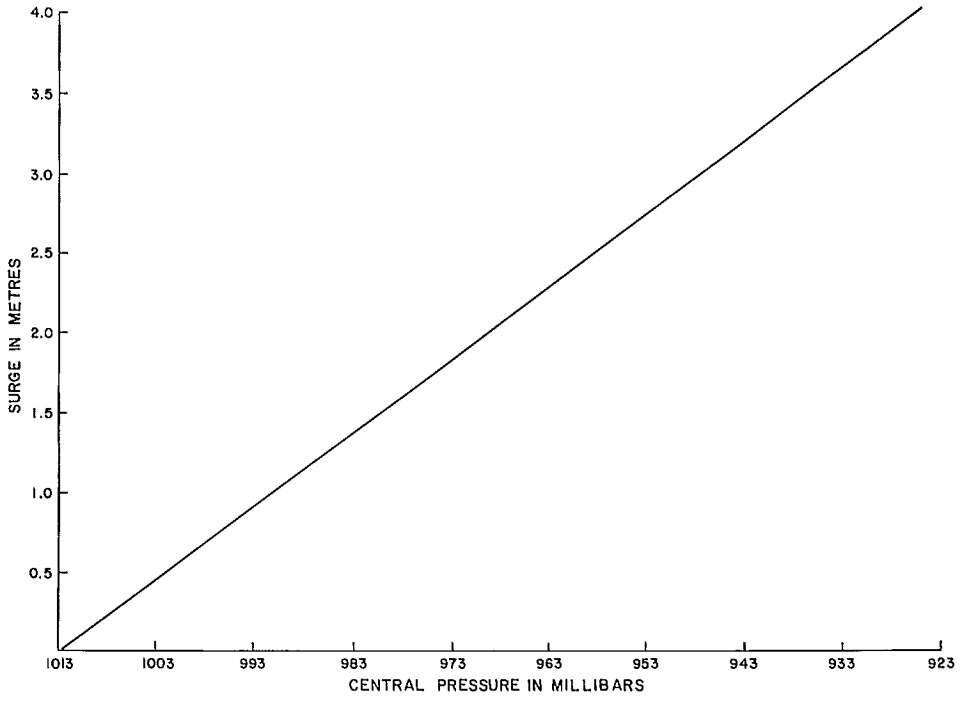

FIG. 7.179. Surge amplitude versus central pressure of storm for North Point in Hong Kong Harbor. (Lau 1980b)

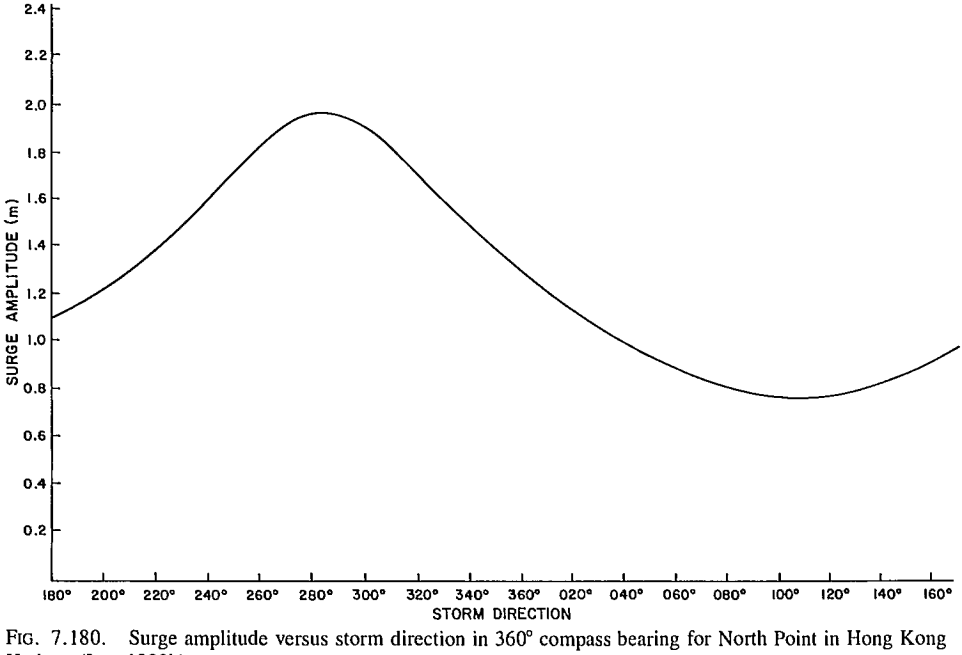

FIG. 7.180. Surge amplitude versus storm direction in 360° compass bearing for North Point in Hong Kong Harbor. (Lau 1980b)

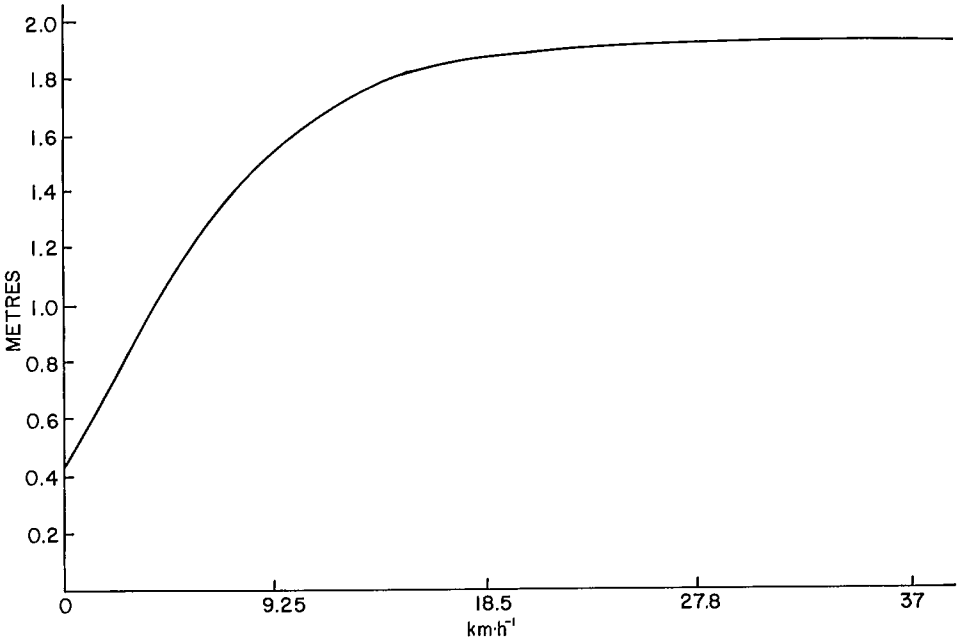

FIG. 7.181. Storm surge amplitude versus storm speed for North Point in Hong Kong Harbor. (Lau 1980b)

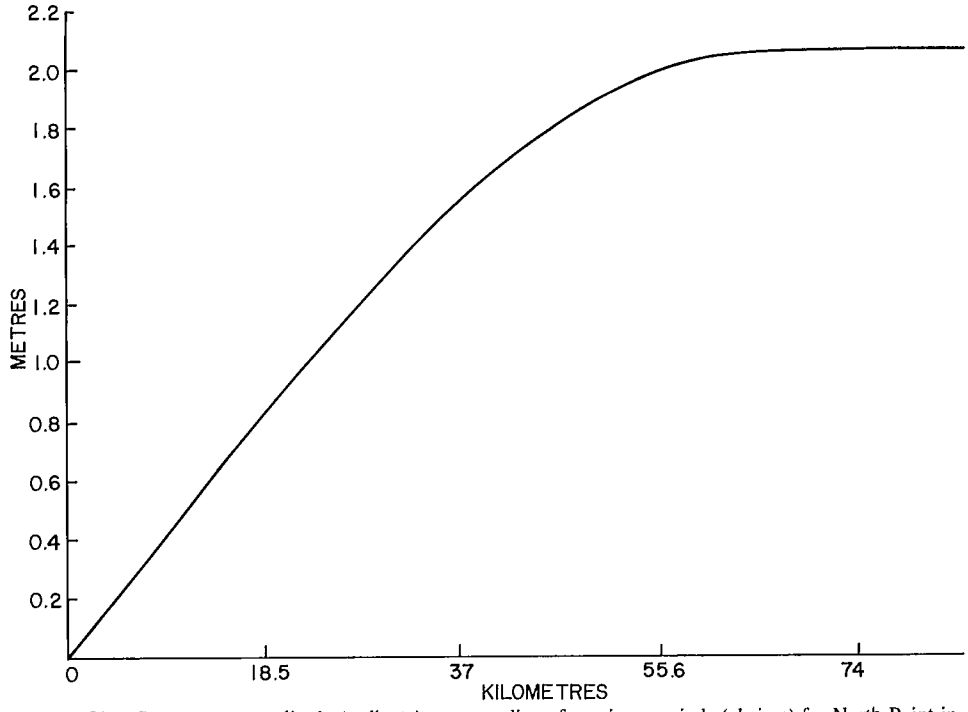

FIG. 7.182. Storm surge amplitude (ordinate) versus radius of maximum winds (abcissa) for North Point in Hong Kong Harbor. (Lau 1980b)

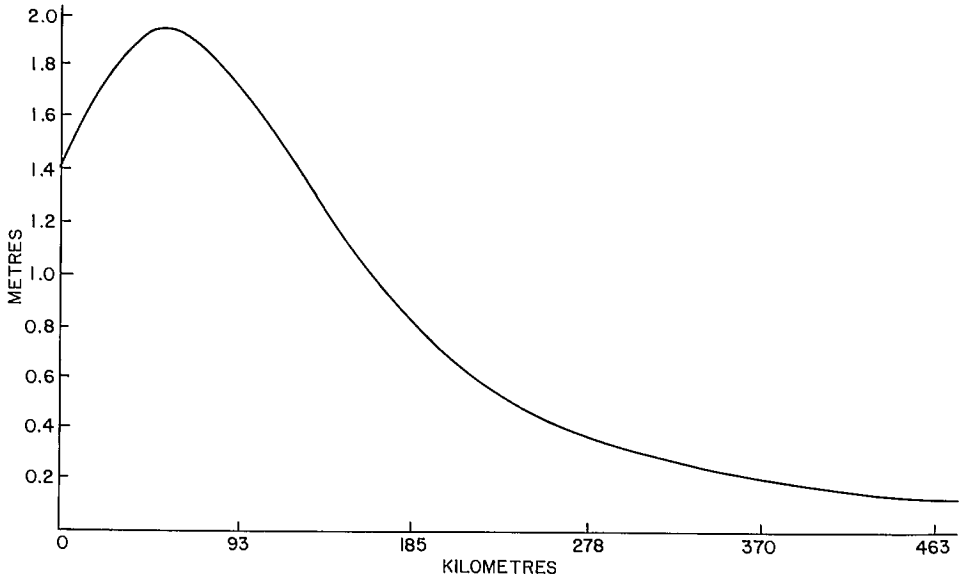

FIG. 7.183. Storm surge amplitude (ordinate) versus distance from the nearest approach of storm for North Point in Hong Kong Harbor. (Lau 1980b)

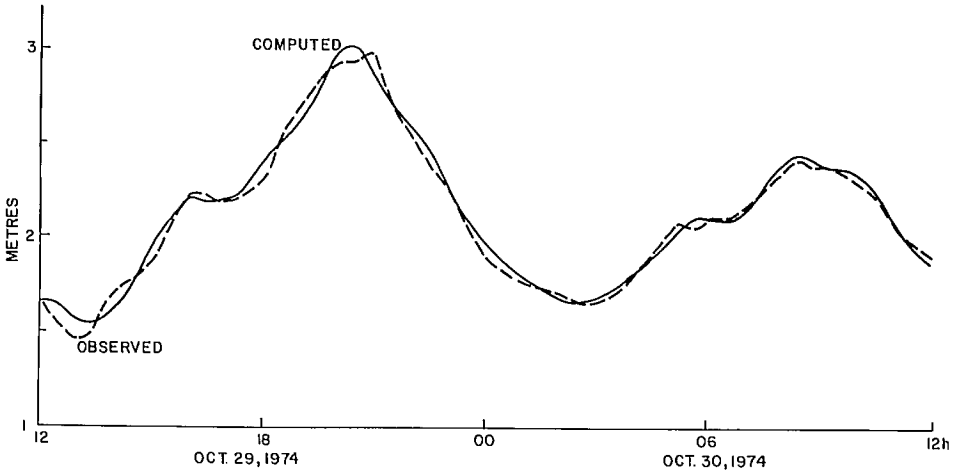

FIG. 7.184. Computed (solid line) and observed (broken line) water levels at Tai Po Kau due to Typhoon Elaine of October 29–30, 1974. Time is Hong Kong Standard Time. (Lau 1980a)

the Gulf of Martaban. The maximum expected surge levels from a hypothetical storm (one in a 100-yr event) are shown in Fig. 7.191.

Regarding protection from storm surges, Odd (1980) mentioned that it would be impractical to build embankments high enough to contain the waters from a peak surge occurring with spring tides. Instead, he proposed that each polder should contain special

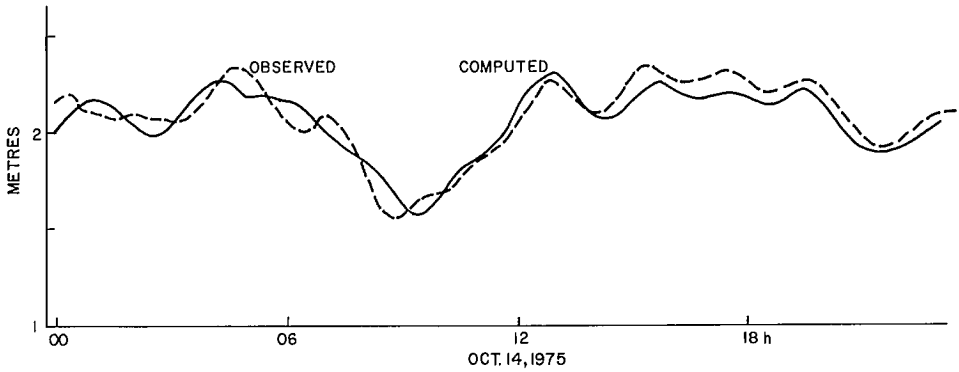

FIG. 7.185. Computed (solid line) and observed (broken line) water levels at Tai Po Kau due to Typhoon Elsie of October 14–15, 1975. Time is Hong Kong Standard Time. (Lau 1980a)

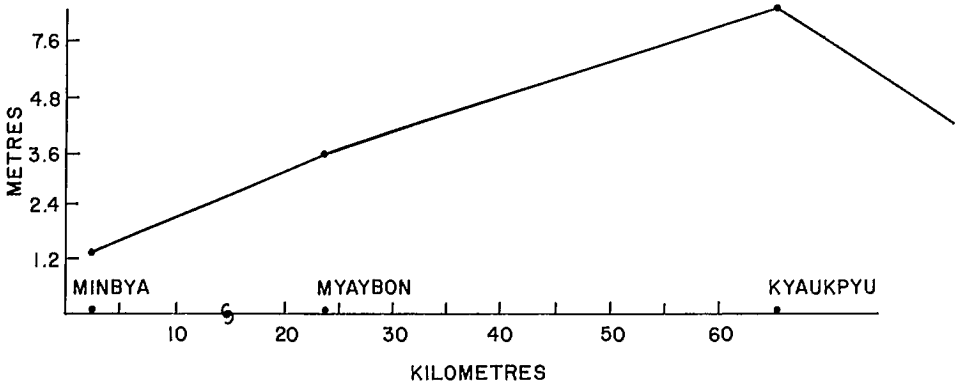

FIG. 7.186. Peak surge envelope on the Burmese Coast for the storm of May 1968. The ordinate is surge amplitude and the abcissa is distance along the coast. (Cho 1980)

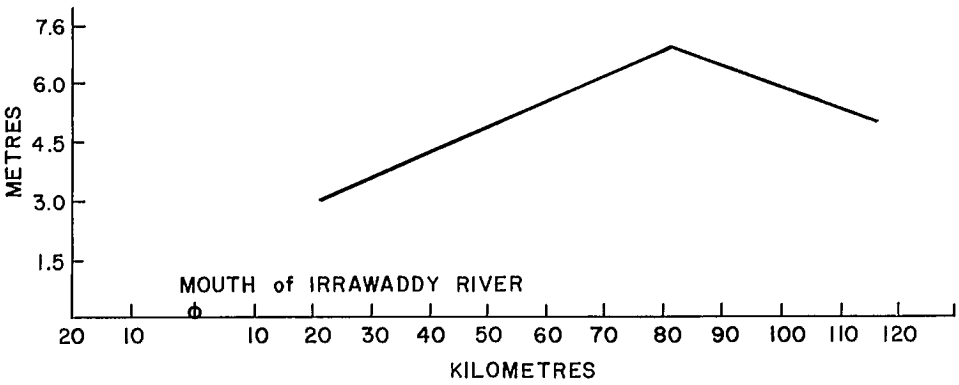

FIG. 7.187. Distribution of the maximum surge along the Irrawaddy River for the storm of May 5–8, 1975. The ordinate is the surge amplitude and the abcissa is distance along the river. (Cho 1980)

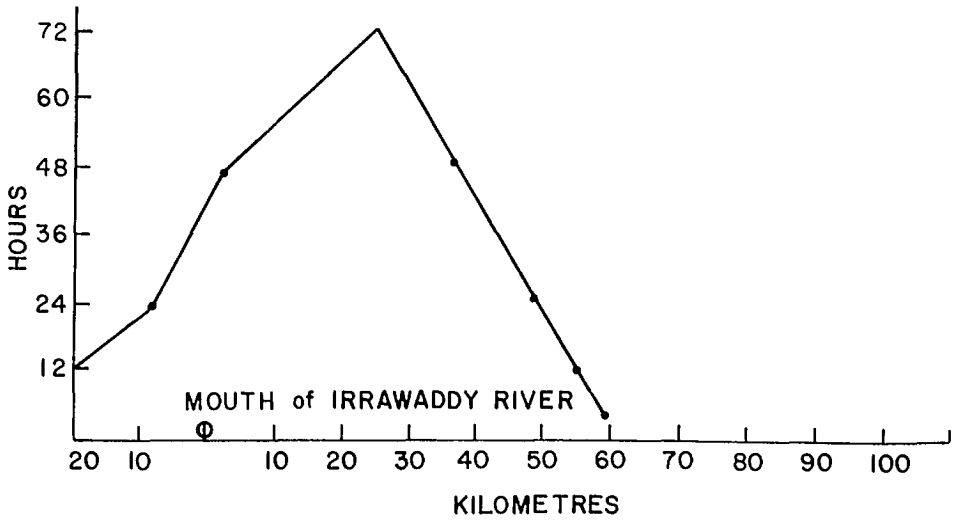

FIG. 7.188. Surge duration versus distance along the Irrawaddy River for the storm of May 5–8, 1975. (Cho 1980)

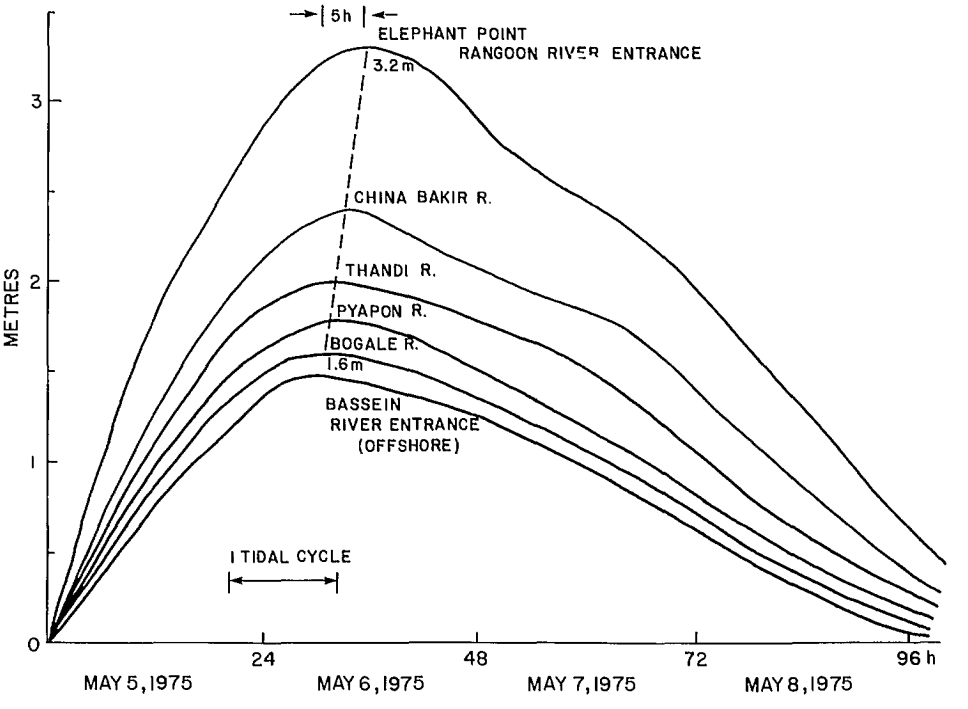

FIG. 7.189. Storm surge amplitude versus time for the storm of May 5–8, 1975, along the Burmese coast. (Odd 1980)

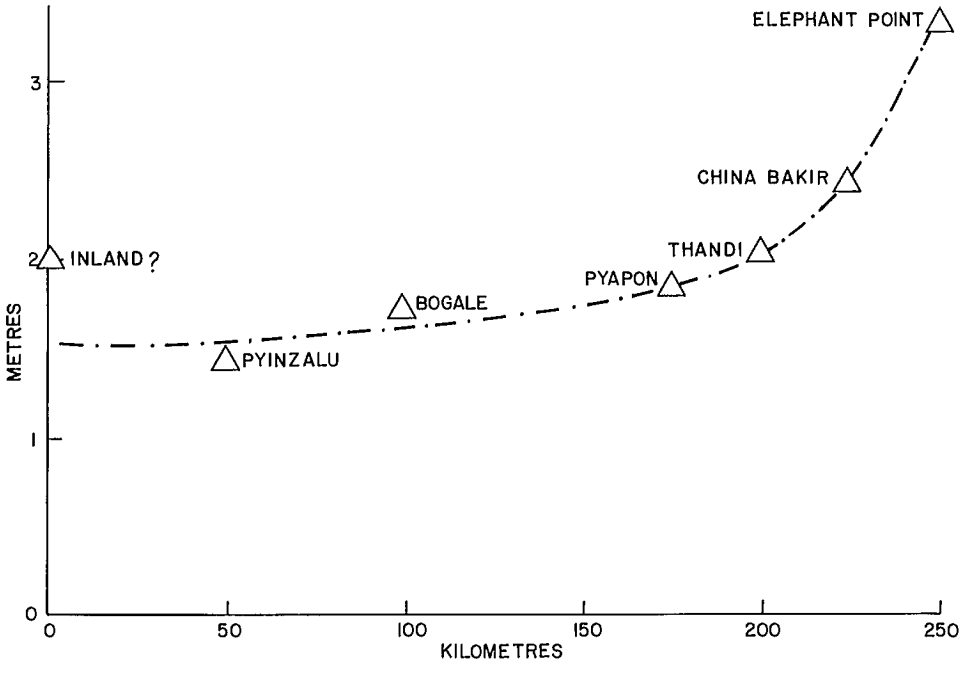

FIG. 7.190. Peak surge amplitude (ordinate) versus distance along the coast from the Bassein River entrance for the storm of May 6, 1975, on the Burmese coast. (Odd 1980)

low lengths of embankments, which could be allowed to spill waters into the polders so that minimum damage is caused.

In the villages prone to storm surges on the Arakan coast of Burma, artificial earthern mounds have already been constructed.

STORM SURGES IN BANGLADESH

It is probably not incorrect to say that Bangladesh suffered more from storm surges than any other country. Ali (1980d) summarized the main factors contributing to the disastrous storm surges on the coast of Bangladesh: (1) shallow water, (2) convergence of the bay, (3) high astronomical tide, (4) thickly populated low-lying islands, (5) favorable cyclone track, and (6) innumerable number of inlets and a few large estuaries and rivers. Except in the eastern and southeastern parts of the country (where there are hills) most of the land is flat. Many places, although 100 mi (160 km) from the sea, are not more than 30 ft (9.1 m) above sea level. A rise of a few feet in sea level can bring large areas of land under water (Gill 1975).

Another peculiar problem is the topographical changes that appear to occur in decadal periods in the courses of the rivers and tributaries. The storm surge problem became worse after the Assam earthquake of August 1950 because millions of tons of material from the mountains was dislodged by the earthquake, which ultimately found its way into the river systems and caused raising of the bottom by as much as 14 ft (4.3 m) in certain locations.

The approximate number of people killed in Bangladesh because of storm surges is listed in Table 7.79. For comparison, a storm surge in 1881 in China supposedly killed

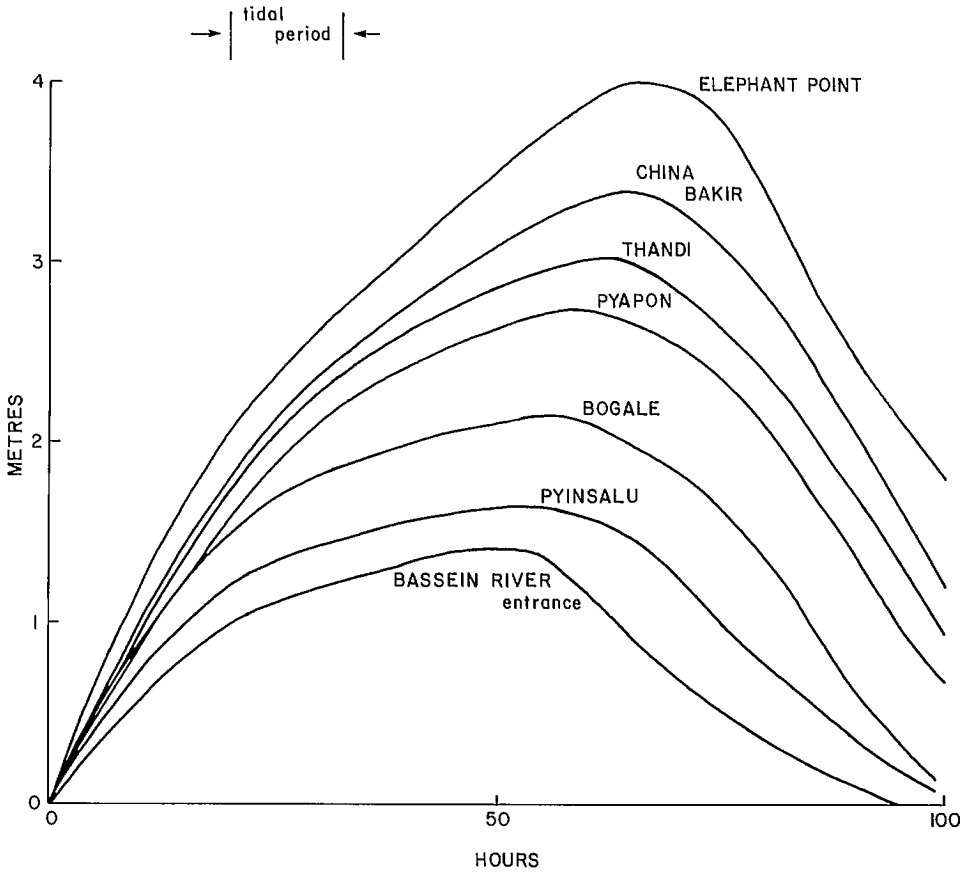

FIG. 7.191. Peak surge amplitude versus time for a hypothetical 100-yr design storm on the Burmese coast. (Odd 1980)

TABLE 7.79. Number of people killed in Bangladesh due to storm surges. Only those cases in which the number is more than 5000 are included.

Year	Estimated approximate No. of deaths
1822	40 000
1876	100 000
1897	175 000
1912	40 000
1919	40 000
1960	15 000
1963	11 520
1965	19 279
1970	>200 000

TABLE 7.80. Damage in Bangladesh (in addition to human death toll) due to the November 1970 cyclone and storm surge. (Frank and Hussain 1971)

Damage	Toll
Population affected	4.7 million
Crop loss	U.S.$63 million
Loss of cattle	280 000
Loss of poultry	500 000
Houses damaged	400 000
Schools damaged	3 500
Fishing boats (marine) destroyed	9 000
Fishing boats (inland waters) destroyed	90 000

TABLE 7.81. Partial list of storm surges in Bangladesh during the period 1876–1970. Values listed are total water levels.

Date of cyclone	Maximum wind speed ($km \cdot h^{-1}$)	Pressure drop (mb)	Observed maximum water level (m)
Oct. 27–Nov. 1, 1876			13.7
Oct. 31, 1897			
Nov. 1, 1912			
Sept. 20–25, 1919			
May 1926			
May 1941			
May 1942			
Oct. 21–24, 1958	88.5		1.8
Oct. 7–10, 1960	128.8	16	6.1
Oct. 30–31, 1960	209.2	35	9.1
May 6–9, 1961	148.1		8.8
May 27–30, 1961	144.8		8.8
May 25–29, 1963	201.2		9.1
May 10–12, 1965	160		5.8
May 31–June 1, 1965			7.6
Dec. 11–15, 1965	209.2		6.9
Sept. 27–Oct. 1, 1967	144.8		9.6
Oct. 10–11, 1967	144.8		8.8
Oct. 22–24, 1967			7.6
May 8–10, 1968			4.6
Oct. 10, 1969			7.3
May 5–7, 1970			4.9
Nov. 13, 1970	22.1		9.1

TABLE 7.82. Observed water levels (tide + surge) in metres at six locations in Bangladesh. (Ali 1980d)

Date	Khulna	Barisal	Sandwip	Chittagong	Chandpur	Companigonj
May 12, 1965	—	2.84	2.90	—	2.53	2.21
May 31, 1965	2.25	2.44	3.73	—	3.80	7.13
Oct. 11, 1967	2.59	—	—	2.92	—	8.75
Oct. 24, 1967	2.44	—	—	1.89	—	7.61
May 10, 1968	—	—	2.78	3.38	—	4.74
Oct. 10, 1969	2.61	—	7.21	3.20	4.27	4.63
Oct. 23, 1970	3.02	3.47	—	—	4.74	4.21
Nov. 12, 1970	—	2.67	3.86	5.58	4.09	5.58
Sept. 30, 1971	3.08	3.04	—	—	5.03	4.21
Oct. 20, 1976	—	4.64	3.00	3.17	3.54	5.02

300 000 people. A surge in Japan in 1923 killed 250 000 people. Another surge in Japan in 1960 killed 5000 people. A surge in 1780 in the Antilles killed 22 000 people and one in the Cuba–Haiti area in 1963 killed 7196 people (Frank and Hussain 1971).

The November 13, 1970, storm surge was supposed to be the worst on record in Bangladesh. The death toll was initially estimated to be over a million people. Later estimates brought it down to 500 000, then 300 000, and finally 200 000. Whatever the

TABLE 7.83. Some pertinent details for storm surges at Chittagong, Bangladesh. (Flierl and Robinson 1972)

Date	Storm speed ($km \cdot h^{-1}$)	Maximum observed wind speed ($km \cdot h^{-1}$)	Astronomical tide (m)	Observed sea level (m)	Maximum surge (m)
Oct. 11, 1960	20	161	1.5	6.0	4.5
Oct. 31, 1960	38	193	0.0	6.6	6.6
May 9, 1961	38	161	1.2	4.8	3.6
May 30, 1961	22	161	0.6	—	—
May 29, 1963	40	209	0.3	—	—
Nov. 6, 1965	42	161	1.2	—	—
Dec. 15, 1965	32	161	0.3	—	—
Nov. 13, 1970	20	161	1.8	6.0–9.0	4.2–7.2

correct toll may be, this storm surge event created a new awareness of tropical cyclones in general and of storm surges in particular, not only in Bangladesh but all over the world. In a storm surge event of this magnitude, there is not only the human death toll but there are other damages as well. The damage in Bangladesh due to this storm surge is listed in Table 7.80. The salt water from the sea flooded the land during the surge event, leaving much salt on the land, which for 4–5 yr after the event affected crops until rains finally washed away the salt.

There are at least 36 known cases of storm surges in Bangladesh during the period 1800–1979. A partial list is given in Table 7.81 for the period 1876–1970. It is quite probable that some of the entries in the table are wrong. Also, sometimes the total water level (i.e. tide + surge) is reported as surge.The observed water levels during storm surge events at six different locations in Bangladesh during the period 1965–76 are listed in Table 7.82. The storm surges and the pertinent meteorological and tidal information at Chittagong for the period 1960–70 are given in Table 7.83. Ali (1980d) summarized the numerical models that have been developed for storm surges on the coast of Bangladesh. Probably the first model is by Das (1972) for the coasts of India and Bangladesh, and he simulated the surge due to the November 1970 cyclone. This was extended by Das et al. (1974). They investigated the effect of the central pressure drop and the speed of movement of the cyclone. Nomograms were given for the peak surge for three different tracks. This work will be considered under the subsection Storm Surges in India. Flierl and Robinson (1972) also developed a linear model specifically for the coast of Bangladesh. A nomogram for practical purposes was also prepared.

In Chapter 3, the nonlinear model of Johns and Ali (1980) was considered. The area modeled is shown in Fig. 3.7 and the track of the November 1970 cyclone is shown in Fig. 6.63. Das (1980) used a nonlinear model to study the tide–surge interaction in the Meghna Estuary.

Ali (1980) stated that about one third of the area of Bangladesh is penetrated by tides (through estuaries and rivers). Maximum tidal range (up to 20 ft or 6.1 m) and surges are found in the Meghna Estuary (see Table 7.82).

Tide–surge interactions during the November 1970 event are shown in Fig. 7.192–7.194. It can be seen that at Patenga, maximum surge occurred at the time of high tide whereas at Amtali the peak surge occurred after the occurrence of high tide. However, at Kaikhali the peak water level elevation is smaller than due to the tide alone. Ali (1980d) ascribed this to the effect of the offshore wind component, which drives the water from the rivers located to the west of the cyclone track. The two small peaks in the

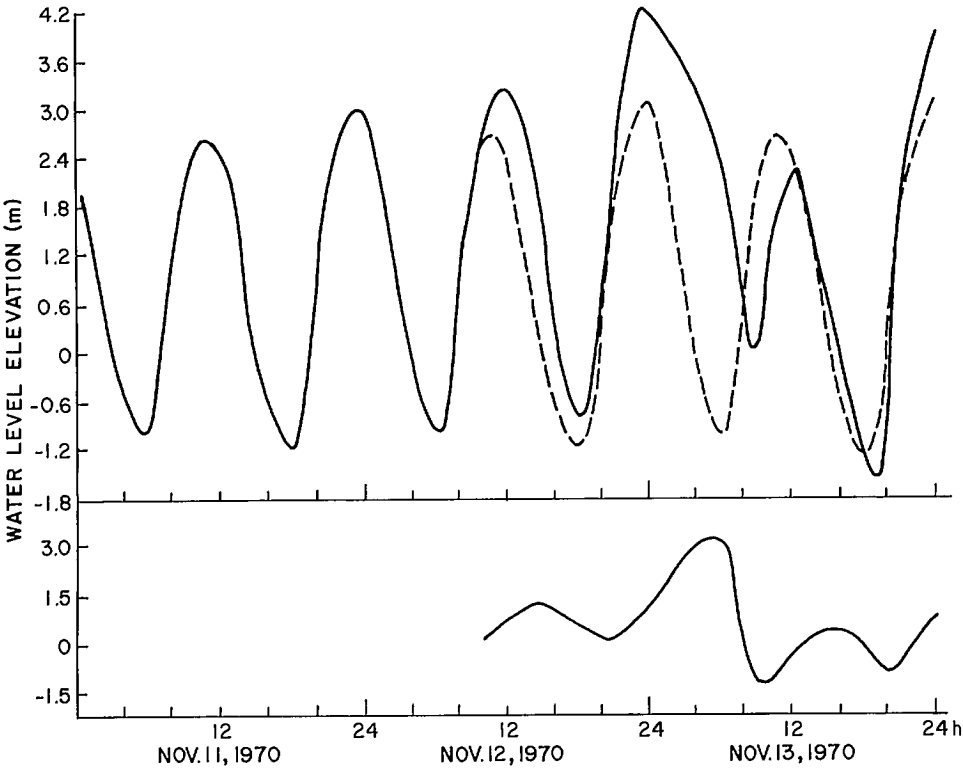

FIG. 7.192. Water level at Patenga, Bangladesh, during November 11–13, 1970. Top: observed water level (tide plus surge) is shown by the solid line and the computed water level by the broken line; bottom: observed storm surge. (Ali 1980c)

total elevation near the time of high tide are probably due to the tide–surge interaction.

Murty and Henry (1982) and Henry and Murty (1982) developed a series of numerical models for tides and surges in the Bay of Bengal. The regions covered by the various regular grid models are shown in Fig. 7.195. The irregular triangular grid that has also been used is shown in Fig. 7.196. The computed water level (tide + surge) at Sagar Island and the Pussur River entrance is shown in Fig. 7.197. The contours of the computed surge are shown in Fig. 7.198.

Islam (1971) discussed the storm surge protection problem in Bangladesh. He mentioned the construction of various types of raised platforms (Machan, Killa, etc.) for people and animals. Kibria (1980) discussed the planned delta works to protect the Bangladesh coast from storm surges.

STORM SURGES ON THE BAY OF BENGAL COAST OF INDIA

Like Australia, India is also prone to storm surges on both its east and west coasts, although the frequency and severity of surges is greater on the east coast. Some important storm surges (from the point of view of loss of life) on the Bay of Bengal coast of India are listed in Table 7.84. This list, which is based on various sources, might not be totally

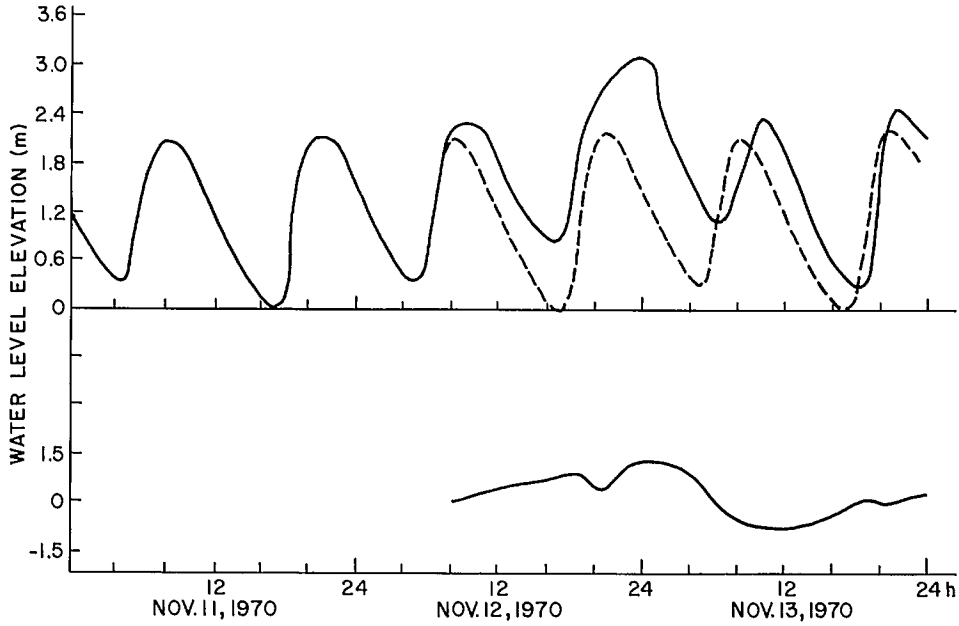

FIG. 7.193. Water level at Amtali, Bangladesh, during November 11–13, 1970. See Fig. 7.192 for explanation. (Ali 1980c)

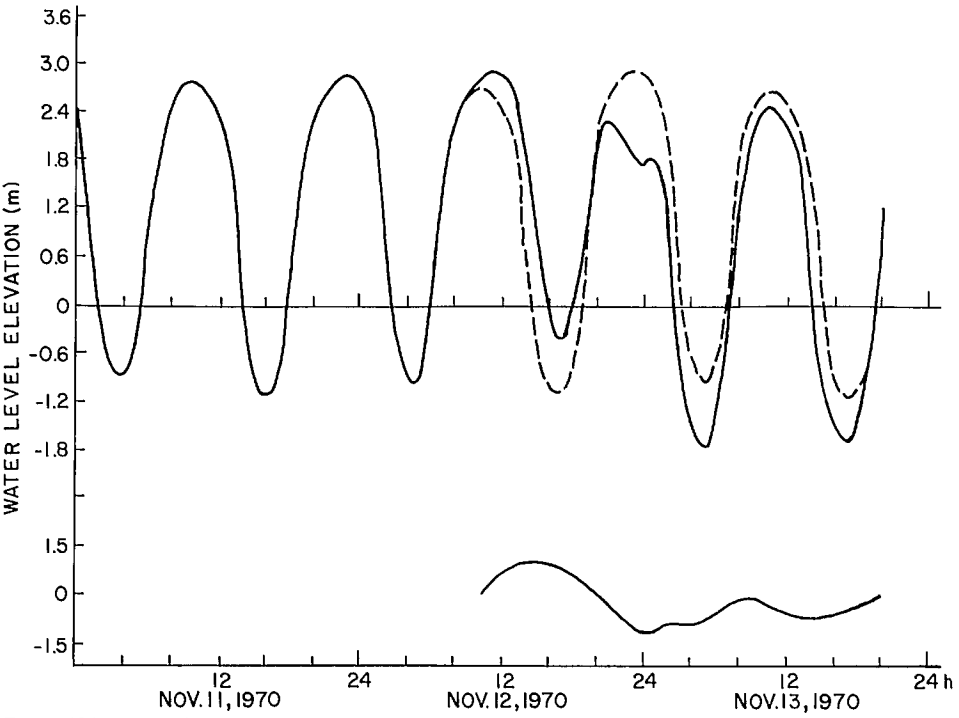

FIG. 7.194. Water level at Kaikhali, Bangladesh, during November 11–13, 1970. See Fig. 7.192 for explanation. (Ali 1980c)

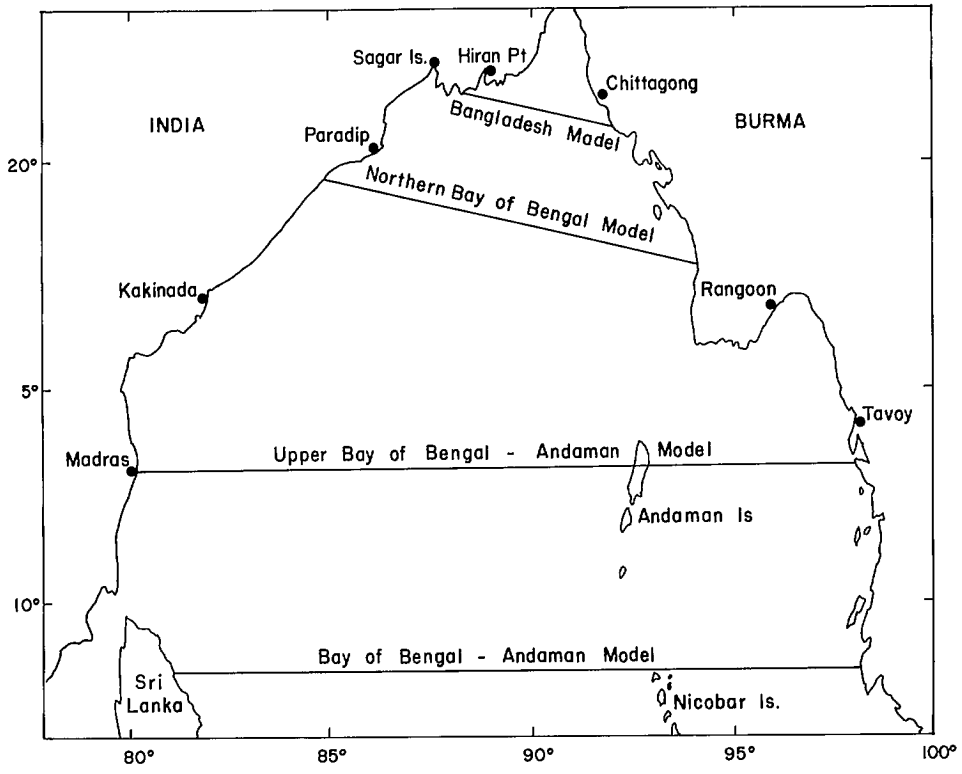

FIG. 7.195. Open southern boundaries of the four regular square grid tidal–storm surge models for the Bay of Bengal.

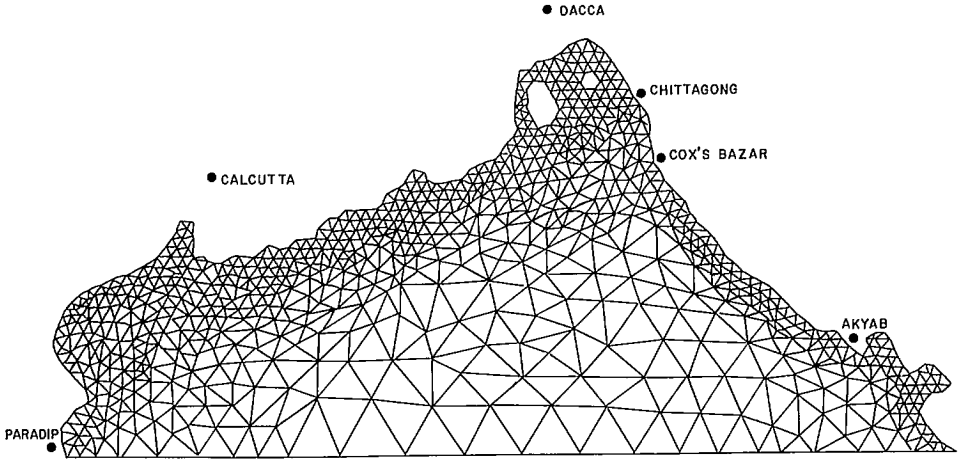

FIG. 7.196. Irregular triangular grid model for tides and storm surges in the northern part of the Bay of Bengal.

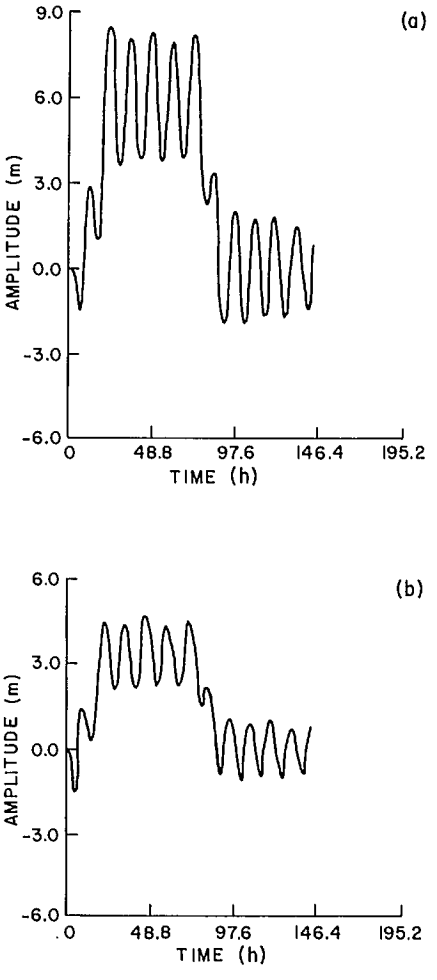

FIG. 7.197. Calculated water level (tide plus surge) at (a) Sagar Island and at (b) the Pussur River entrance in the Bay of Bengal for a hypothetical storm modeled after the November 1970 storm.

correct. Also, in this list, several minor surges in which less than 100 people were killed are excluded.

Some pertinent information on six storm surges at Saugor Island (in the northwestern part of the Bay of Bengal) during the period 1948–55 is given in Table 7.85. This table also compares the observed surges with those computed using simple empirical formulae (Janardhan 1967).

Rao and Mazumdar (1966) and Rao (1968) used empirical relations to calculate storm surges on the east coast of India, south of 17°N. Topography near the shore and wind waves were also included in the calculations. Based on these calculations, Rao (1968) classified the east coast of India (and the coasts of Bangladesh and Burma for comparison) into three types. These results are summarized in Table 7.86. In this table, the values listed

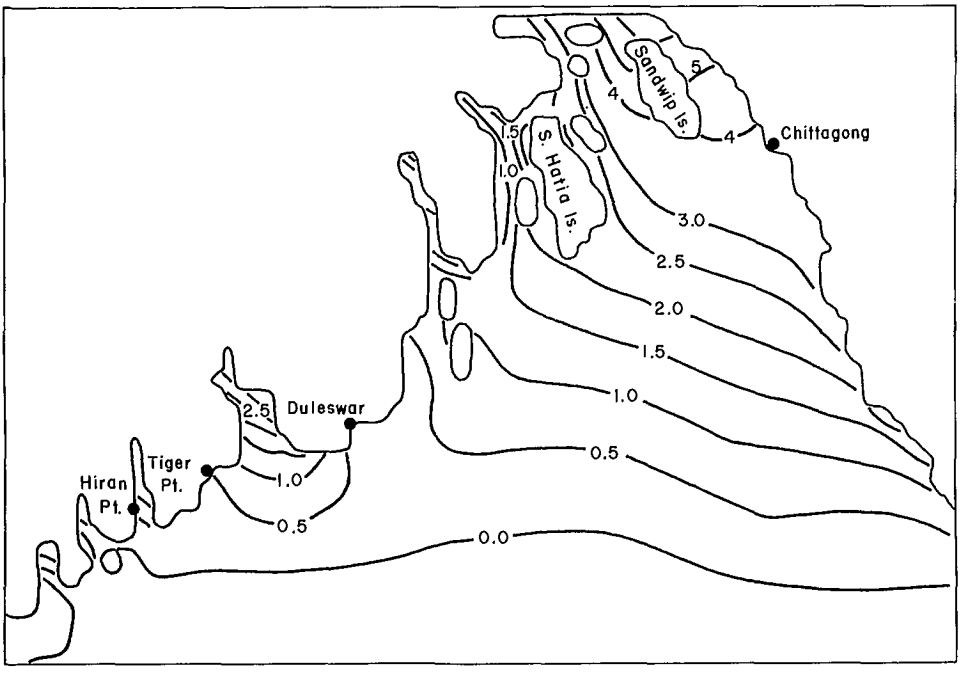

FIG. 7.198. Storm surge heights in the northern part of the Bay of Bengal from a hypothetical storm modeled after the November 1970 storm.

under "storm surge amplitude" pertain to a storm with winds up to 40 $m \cdot s^{-1}$. The values listed under "total water level" include the peak surge plus the wind waves.

Classification of types A, B, and C is as follows. For a type A coastline, the maximum total water level is less than or equal to 2 m during storm surge events, for type B the amplitude is between 2 and 5 m, and for type C the amplitude is greater than 5 m. This classification is shown in Fig. 7.199 for the east and west coasts of India (the west coast of India will be considered in the next subsection). The storm surge considered here is the piling up of the water due to wind stress. The inverse barometer effect is not included here, since according to Rao (1968), it does not exceed 0.5 m anywhere on the east coast of India.

This classification into types A, B, and C has been verified to a certain extent by comparison with actual data (Table 7.87). Thus, type C belts are the most prone to major storm surges. It can be seen from Fig. 7.199 that there are four such belts on the coasts of the Indian subcontinent (Rao 1968). Two are as follows.

1) The coastal belt around the head of the Bay of Bengal, approximately to the north of 20°N. The frequency of cyclones is high here and the storm tracks are usually favorable for generating maximum surges, especially in the Sunderbans.

2) South Coromandel coast around the Palk Bay. Although the frequency of storms striking this region is somewhat smaller than for the first belt, the major storms that strike this coast usually produce major surges.

The other two belts are on the west coast of the subcontinent and will be considered in the next subsection.

TABLE 7.84. Storm surges on the Bay of Bengal coast of India.

Year	Month	Day	Location where storm crossed the coast	Area affected by storm surges	Peak surge (m)	Loss of life
1737	Oct.	7–11	Mouth of Hoogly	Sunderbans	12	300 000
1789	Dec.		Kakinada			20 000
1833						50 000
1839						20 000
1864	Oct.		Mouth of Hoogly	Calcutta and surroundings	12	50 000
1864	Nov.		Masulipatnam	Masulipatnam and surroundings		40 000
1885	Sept.		False Point	North Orissa	7	Several thousand
1927			Nellore	Andhra		300
1942	Oct.		West Sunderbans	West Bengal	5 m at Midnapore (64 km inland on a river)	40 000
1952	Nov.		Negapottinam	South Coromandel coast and northern shores of Palk Bay	3	Few thousand
1964	Dec.		Adirampatnam	South Coromandel coast and west shores of Palk Bay	6	1 000
1969	Nov.		Andhra	Andhra		200
1971	Oct.		Orissa	Orissa		10 000
1977	Nov.		Chirala	Divi and surroundings	5	20 000

TABLE 7.85. Storm surges at Saugor Island, India, during 1948–55. (Janardham 1967)

Date	Distance of storm center to Saugor Island (km)	Observed peak surge (m)	Computed peak surge (m)	State of tide at time of peak surge
Aug. 14, 1948	306	0.34	0.43	High
Aug. 15, 1948	402	0.43	0.40	Low
July 25, 1951	306	0.85	0.98	Low
July 05, 1952	418	0.34	0.34	High
Aug. 03, 1953	306	0.46	0.46	High
Sept. 30, 1955	217	0.46	0.46	High

There is a short, type C belt near Nizampatnam Bay. (For interest, it might be mentioned that this author was born in a small village about 8 km from here and spent the first 14 yr of his life here.) The Andhra cyclone of November 1977 produced major surges in this general area and killed several thousand people. The east coast of India, between 14 and 16.5°N, is in the type B category. Also, the Coromandel coast between Point Calimere and Karikal falls into this category.

Ghosh (1977) used the SPLASH model (Jelesnianski 1972) for the east coast of India. He prepared nomograms for calculating peak surges based on pressure drop, radius of

TABLE 7.86. Maximum possible storm surge amplitudes and total water levels (surge + wind waves) at selected locations on the east coast of India. The hypothetical storm has a wind speed of 40 $m \cdot s^{-1}$. A, total water level <2 m; B, 2–5 m; C, >5 m. A few locations in Bangladesh and one in Burma are included for comparison. (Rao 1968)

Location	Favorable wind direction	Storm surge amplitude (m)	Storm surge + wind wave (total water level) (m)	Classification
Dhanushkodi	NNE	4.8	8.2	C
Rameswaram	SE	6.8	11.3	C
Pamban	NNW	4.4	7.3	C
Devipatnam	E	4.5	7.5	C
Adirampatnam	SSE	5.1	8.5	C
Point Calimere	SSE	4.2	7.0	C
Nagapattinam	E	1.5	2.5	B
Karikal	E	0.3	1.3	A
Madras	ENE	1.5	2.5	B
Nizampatnam	SW	4.5	7.4	C
Mouth of Krishna River	SE	1.6	2.7	B
Narasapur	S	1.7	2.9	B
Sacromento Shoals (outer sand banks)	SSE	1.4	2.3	B
Kakinada (outer sand banks)	E	0.6	1.0	A
Visakhapatnam	SE	0.7	1.2	A
Kalingapatnam	E	1.1	1.8	A
Gopalpur	SE	0.9	1.5	A
Mouth of Devi River	SE	0.8	1.3	A
False Point	SE	1.9	3.2	B
Balasore	SE	3.0	5.0	C
Mouth of Hoogly River	S	6.5	10.8	C
Mouth of Matla River	S	5.0	8.4	C
Mouth of Baleswar River (Bangladesh)	S	6.9	11.5	C
Mouth of Meghna River (Lakhichar Island, Bangladesh)	SSE	8.0	13.4	C
Cox Bazar (Bangladesh)	WSW	3.2	6.3	C
Mouth of Faaf River (Burma)	SW	3.2	5.3	C

maximum winds, vector motion of the storm, and bathymetry offshore. The nomograms were prepared separately for the northern part (where the slope of the shelf is small) and for the remaining part of the coast (where the slope is large). A separate nomogram is presented to include the tidal effects on the northern part of the coast where the tidal range is large. Two typical nomograms prepared in this manner are shown in Fig. 7.200. Some of the tropical cyclones that generated storm surges on the Bay of Bengal coast of India during the period 1967–74 are listed in Table 7.88.

Das (1972) used a numerical model to compute storm surges in the Bay of Bengal, which is probably the first numerical model developed for this area. Das et al. (1974) extended this model to simulate the storm surge due to the cyclone of November 13, 1970,

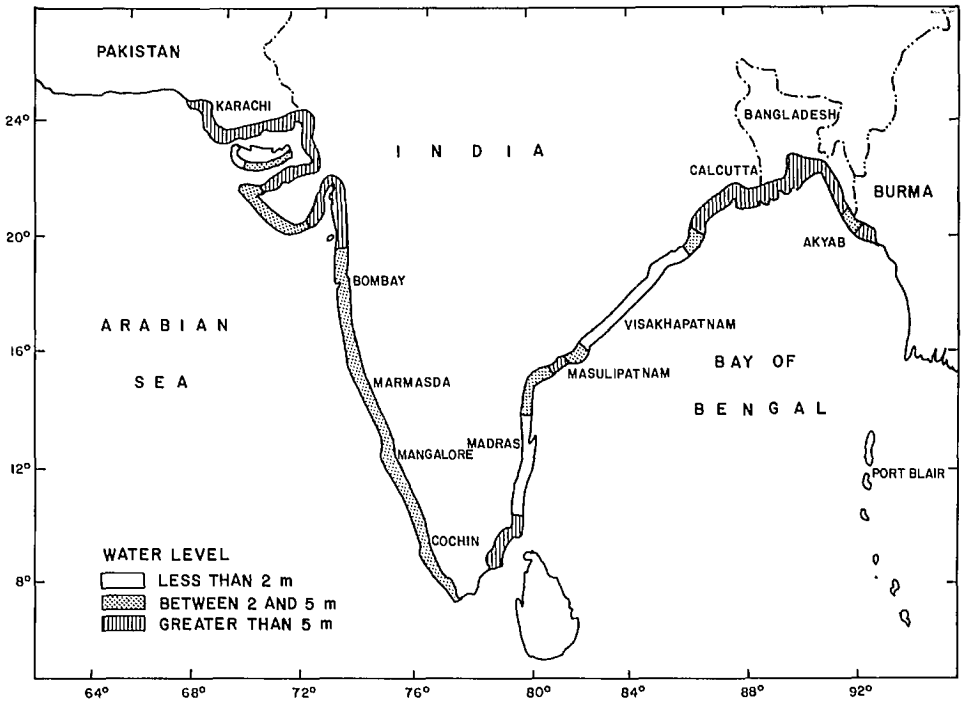

FIG. 7.199. Classification of the Bay of Bengal and the Arabian Sea coasts of India.

TABLE 7.87. Relationship between type of coastline and occurrence of storm surges on the coast of India. A, surge + wind wave amplitudes <2 m; B, 2–5 m; C, >5 m. Data are mainly for the period 1949–66. (Rao 1968)

Type of coast	Intensity of storm	No. of storms that affected the coast	No. of storms that caused major storm surges
A	Moderate	13	—
	Severe	12	—
B	Moderate	19	—
	Severe	6	4
C	Moderate	1	—
	Severe	3	3

which caused great loss of life and destruction in Bangladesh. They used a two-dimensional linear model and telescoping grids. The grid scheme used for three different types of tracks is illustrated in Fig. 7.201. Nomograms for the storm surge as a function of the storm intensity and the speed of movement of the storm are given (for the three tracks shown in Fig. 7.201) in Fig. 7.202.

The relationship between the storm surge amplitude η and the storm intensity Δp and speed of movement of storm c was expressed as

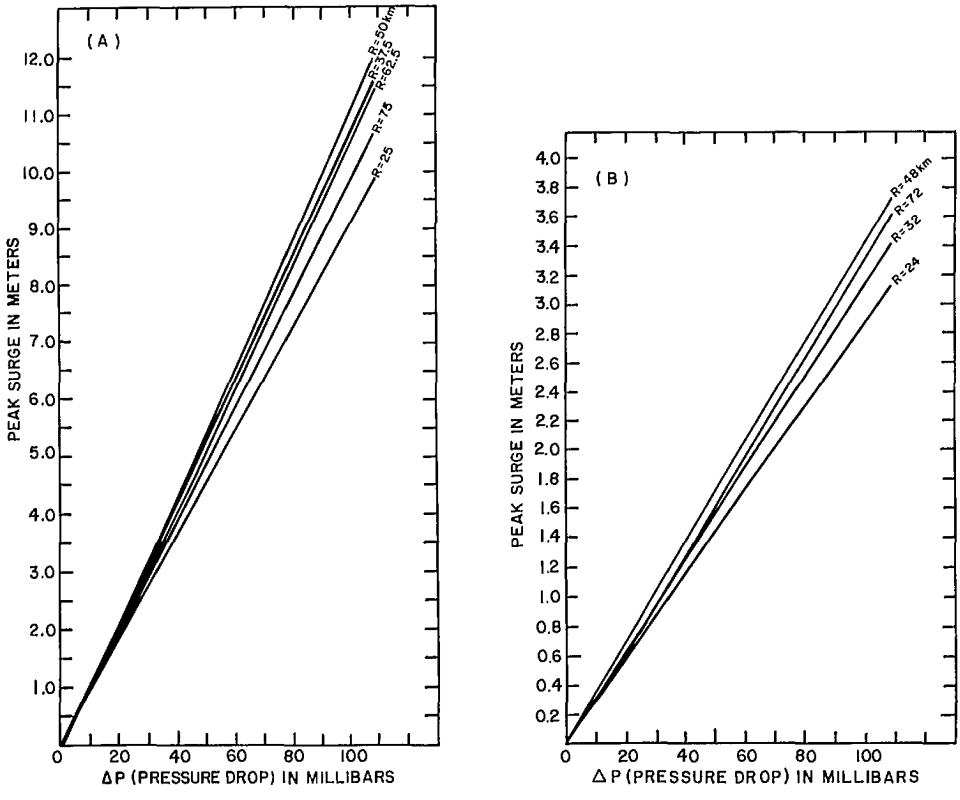

FIG. 7.200. Nomogram of peak storm surge as a function of pressure drop and radius of maximum winds for the (A) northern part and the (B) southern part of the east coast of India. (Ghosh 1977)

TABLE 7.88. Tropical cyclones striking India during 1967–74 that generated major storm surges. Estimated tide listed is the amplitude of the tide at the time of peak surge. However, the peak elevation listed in the last column (which is a combination of tide and surge) need not have occurred at the time of peak surge. (Das 1980)

Date	Location of landfall	Central pressure (mb)	Pressure deficit (mb)	Maximum wind speed ($km \cdot h^{-1}$)	Computed surge (m)	Estimated tide (m)	Peak elevation (m)
Oct. 9, 1967	Puri	970	40	167	2.5	0	3.1
Nov. 7, 1969	Kakinada	968	42	176	2.6	0	3.1
Oct. 30, 1971	Paradeep	970	40	167	2.5	0.9	6.0
Setp. 10, 1972	Baruva	945	65	204	3.8	−0.8	3.4
Sept. 11, 1976	Contai	972	38	148	2.0	1.4	3.0
Nov. 19, 1977	Chirala	909	101	259	4.0	0.3	5.0
May 12, 1979	Kavali	954	56	189	2.7	0.6	3.0
May 7, 1970	Cox's Bazar (Bangladesh)	977	33	148	2.3	0.2	3.4
Nov. 12, 1970	Hatia (Bangladesh)	940	70	222	4.1	2.0	5.5
Nov. 28, 1974	Chittagong (Bangladesh)	974	36	161	3.1	0.2	4.0

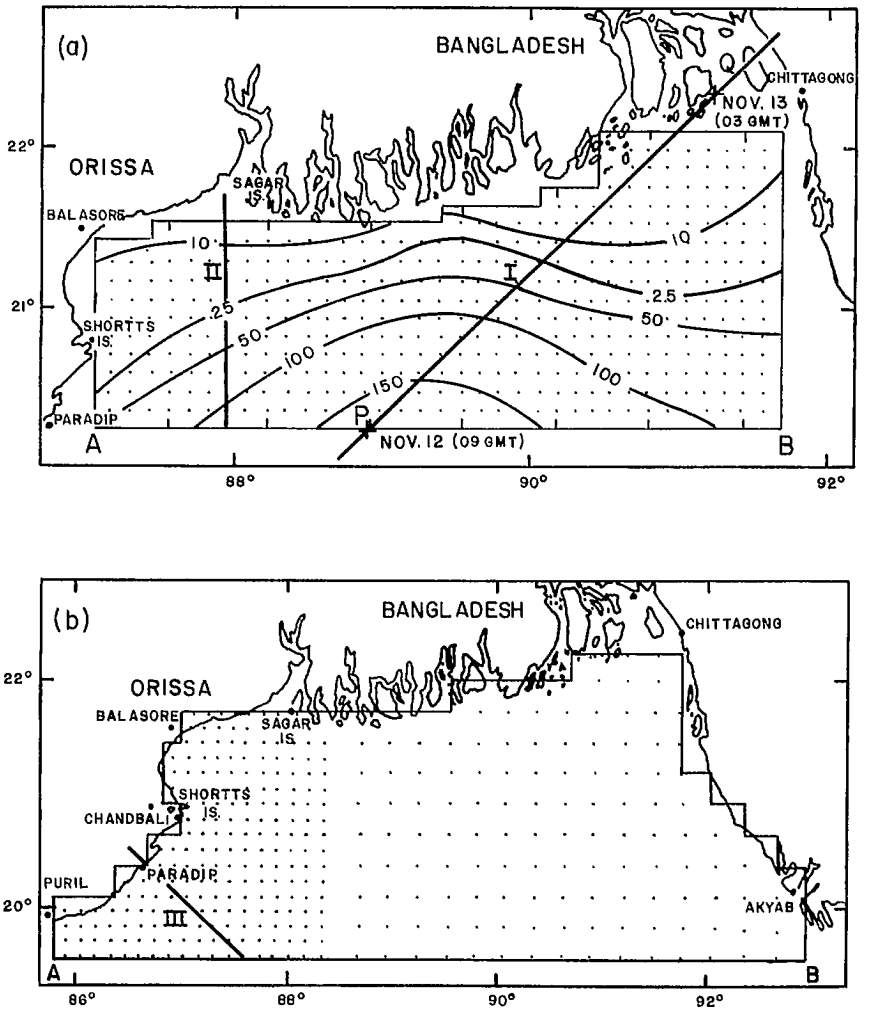

FIG. 7.201. (a) Grids for storms moving northeast (I) and north (II). Contours represent water depth (metres). (b) Grids for storms moving northwest (III). (Das et al. 1974)

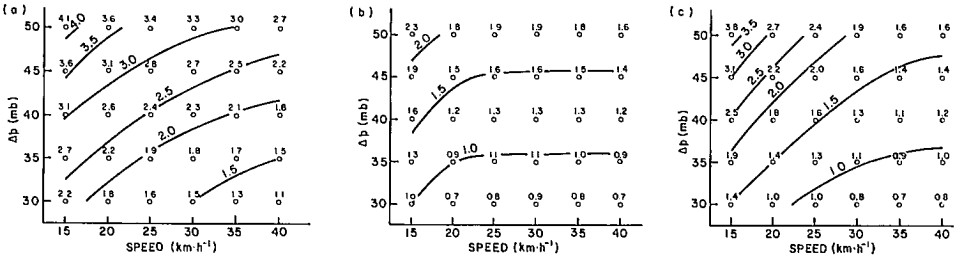

FIG. 7.202. Storm surge amplitude (metres) as a function of storm intensity (millibars) and speed C of storm movement for the (a) northeast track (I), (b) northward track (II), and (c) northwest track (III) of Fig. 7.201. (Das et al. 1974)

TABLE 7.89. Numerical values of the constants A_0, A_1, and A_2 of eq. 7.90 for the three different tracks shown in Fig. 7.201. (Das et al. 1974)

Track	A_0 ($\times 10^2$)	A_1 ($\times 10^4$)	A_2 ($\times 10^2$)
Northeast	9.59	−0.91	−4.60
North	2.88	3.08	−1.20
Northwest	8.24	−1.60	−5.15

$$\eta = A_0 \Delta p + A_1 (\Delta p)^2 + A_2 c \tag{7.90}$$

The numerical values of the constants A_0, A_1, and A_2 are listed for the three different tracks (shown in Fig. 7.201) in Table 7.89. These authors concluded that linear superposition of tide and surge would overestimate the water level by about 1 m.

Das (1980) included nonlinear advective terms and improved the model of Das et al. (1974), and the computational area was also enlarged. This model, which includes the tide–surge interaction in a more realistic manner, gave water levels that agreed better with observed levels. Natarajan and Ramanathan (1980) developed a nonlinear finite-element model and used the same computational area and storm tracks as in Das et al. (1974). Johns et al. (1981) and Dube et al. (1981) simulated the November 1977 storm surge on the Andhra coast of India.

STORM SURGES IN THE ARABIAN SEA

Rao (1968) studied the storm surges on the Arabian Sea coast of India (and Pakistan). Classification of this coast into types A, B, and C is given in Fig. 7.199. Previously, it was mentioned that on the Bay of Bengal coast of the subcontinent, there are two dangerous zones (type C). On the Arabian coast, also, there are two dangerous zones. The first one includes the Konkan coast to the north of 18°N and the coastal belt around the Gulf of Cambay.

In this belt, the frequency of storms striking the coast is low (over a 75-yr period, only four storms struck the coast between 18 and 19°N and only three storms struck between 19 and 21°N). Here, the tidal range is quite large (e.g. 8 m at Bombay and 11 m at Cambay). Unless peak surge occurs close to the time of high tide, no major water level oscillations may occur in this belt. It should be emphasized that, even though the Arabian Sea coast experiences major storm surges much less frequently than the Bay of Bengal coast, the reason there are two dangerous belts is the manner of the classification into types A, B, and C. This classification does not include the frequency of occurrence. It only deals with the maximum water level to be expected in the event of major storms, however infrequently they may occur.

The second dangerous belt stretches from Dwarka (India) to Karachi (Pakistan). This region includes the extensive marshy areas (mostly unpopulated) known as the "Rann of Kutch." In this belt, also, the frequency of storms is low and the tracks are not usually favorable for major surge development. However, on the rare occasion when they do occur, storm surges several metres in amplitude could result.

Rao (1968) mentioned that the extensive marshlands of the Rann of Kutch are subject to large storm surges with the onset of the strong westerlies of the southwest monsoon season. The entire west coast of India south of 18°N falls into the type B category. In this

TABLE 7.90. Peak surge amplitude and maximum water level (surge + wind wave) that can occur for a storm with maximum winds of 40 $m \cdot s^{-1}$ on the Arabian Sea coast of the Indian subcontinent. Classification: B, total water level 2–5 m; C, >5 m. (Rao 1968)

Location	Favorable wind direction	Peak surge amplitude (m)	Maximum value of total water level (m)	Classification
Mutham Point (Nagercoil)	SW	1.4	2.3	B
Cochin	W	1.6	2.7	B
Calicut	WSW	2.1	3.5	B
Mangalore	WSW	1.8	3.0	B
Bhatkal	WSW	2.7	4.5	B
Panjim	WSW	1.7	2.8	B
Devgad	WSW	1.5	2.5	B
Ratnagiri	W	1.8	3.0	B
Harnaf	WSW	1.7	2.8	B
Mouth of Rajpuri River (Murud)	W	3.1	5.2	C
Mouth of Patel Ganga River	W	4.3	7.2	C
Bombay	W	1.5	4.5	B
Agashi Bay	W	4.2	7.0	C
Dahapu	W	4.0	6.7	C
Bulsar Kheri	W	4.5	7.5	C
Suvali Point	WSW	3.3	5.5	C
Mindola	WSW	5.2	8.7	C
Mal Bank	S	4.3	7.2	C
Mahuva Road	SE	2.0	3.4	B
Jafarabad	SSE	3.1	5.2	C
Diu	SSE	2.2	3.7	B
Veeraval	SW	1.5	2.5	B
Porbandar	SSW	1.6	2.7	B
Dwaraka	SW	1.6	2.7	B
Balachin	W	5.1	8.5	C
Rann of Kutch	WSW	3.9	6.5	C
Wari Creek	SSW	4.0	6.7	C
Mouth of Indus River	S	3.0	5.0	C
Karachi	S	3.5	5.8	C

area, also, the frequency of storms is low (only four major storms in 75 yr). Also, the tracks are not generally favorable for major surge development. The coast around the Kathiawar Peninsula between Diu and Dwaraka belongs to the type B category. The major surge amplitudes that can occur here are about 1.5 m and are about half the tidal range here. In this area the frequency of storms is high, but usually they are not intense (not of hurricane strength).

The peak storm surge amplitudes, maximum total water level (surge + wind waves), and the classification (into type A, B, or C) at several locations on the west coast of India and the coast of Pakistan are listed in Table 7.90. A partial list of major storm surges on the Arabian sea coast is given in Table 7.91. The track of the Kutch cyclone of June 1964 and the areas where surges occurred are shown in Fig. 7.203. Rao (1968, p. 239) stated:

> Even though the storm moved closer to the B-type areas between Jafarabad and Porbander than to the C-type area between Jafarabad and Bhavanagar, damages by storm surges were reported from the latter strip and practically none from the former. Storm surges of a minor order were also reported from the B-type area between

TABLE 7.91. Partial list of major storm surges on the Arabian coast of the Indian subcontinent during 1782–1977. Only those cases in which major destruction and loss of life occurred are included. (Rao 1968)

Year	Month	Day	Area of landfall	Area of major storm surges	No. of people killed
1782	Apr.	20–21	South Saurashtra coast	Gulf of Cambay	Several thousand
1851	May		32 km west of Karachi	Karachi and environs	
1920	June		Veeraval	Gulf of Cambay	
1964	June		Naliya	North and south shores of the Gulf of Kutch	
1977	Nov.	22	Karwar	Karwar and environs	

Porbander and Dwaraka. The maximum damage occurred in the C-type area around the Gulf of Kutch at the time when the storm was crossing the coast near Naliya, when westerly gales swept across the area and heavy swells rolled up the Gulf.

To summarize, although frequency of storms and storm surges is less in the Arabian Sea than in the Bay of Bengal, major destructive surges can occur occasionally. Newspaper reports mentioned that a major storm towards the end of October 1981 generated significant surges in the Kathiawar Peninsula and killed about 300 people. Note that the number of cyclones in the Bay of Bengal over a given period is about four times the number in the Arabian Sea; however, only about one quarter of the Bay of Bengal storms mature into severe storms, whereas about 40% of the Arabian Sea storms can become severe storms.

STORM SURGES IN THE USSR

Moderate storm surges occur in the Black Sea, the Okhotsk Sea, the Pacific coast of the USSR, the East Siberian Sea, and the Chukchi Sea. Large surges (up to 6 m in amplitude) can occur in Lake Baikal. Winds from north of this lake can produce surges that sometimes take only a few minutes to develop.

In section 6.10, the work of Lappo and Rozhdestvenskiy (1977, 1979) was discussed in which they considered the lag of storm surges with reference to the atmospheric systems. Their work was for the northwest part of the Pacific Ocean in general and for the Pacific coast of the USSR near the Kurile Islands in particular. They considered the contribution of the static surge to the total water level deviation and developed the important concept of the hysteresis loop (Fig. 6.123). The lag between the atmospheric forcing and the storm surge could be anywhere between 5 and 18 h on this part of the USSR coast.

Mustafin (1969) studied the storm surges in the East Siberian and Chuckchi seas with the particular aim of predicting the surges at Cape Schmidt. Based on 192 cases during the summer period (July–October) for 1951–55, in which the surges at Cape Schmidt and in Ambarchik Inlet exceeded 30 cm (both positive and negative surges), he prepared the following regression relationships:

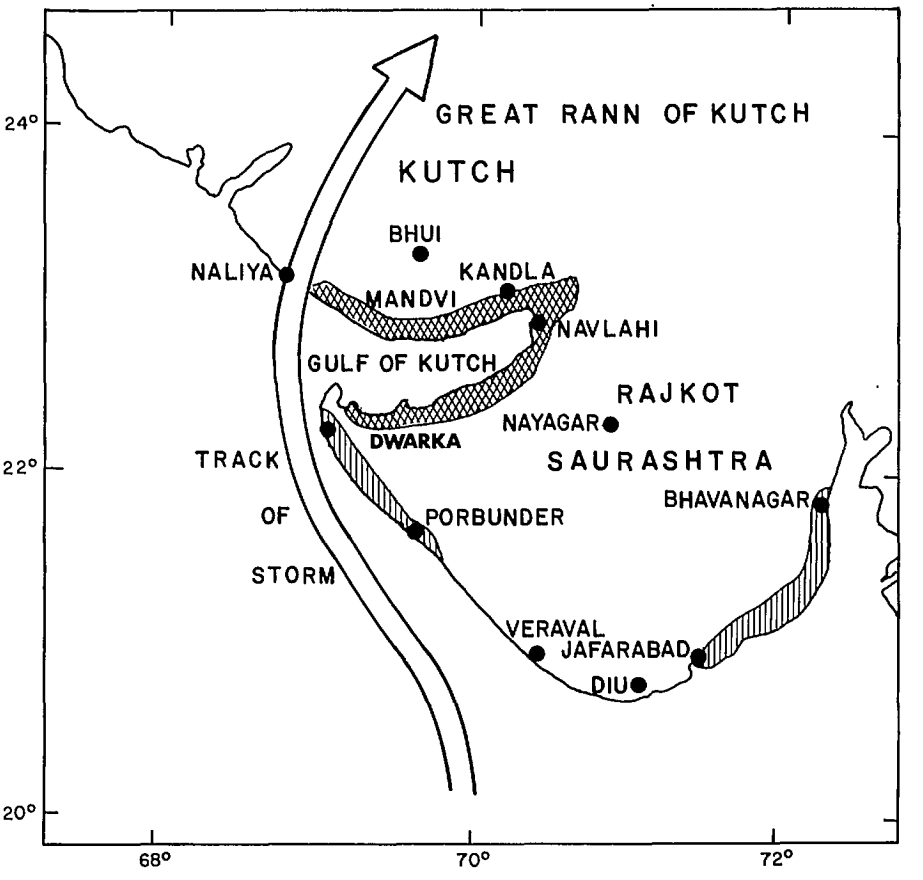

FIG. 7.203. Track of the Kutch cyclone of June 1964 on the west coast of India. Single-hatched area is affected by minor surges; double-hatched areas are affected by major surges. (Rao 1968)

$$\Delta h_{\text{Schm}} = a_1 \Delta p_1 \cos \alpha_1 + a_2 \Delta p_2 \cos \alpha_2 + a_3 \Delta h_{\text{Amb}} \tag{7.91}$$
$$R = 0.94 \pm 0.001, \qquad \Sigma = 21$$

$$\Delta h_{\text{Schm}} = a_4 \Delta h_{\text{Amb}} b_1 \tag{7.92}$$
$$r = 0.90 \pm 0.01, \qquad \Sigma = 26$$

$$\Delta h_{\text{Schm}} = a_5 \Delta p_1 \cos \alpha_1 + a_6 \Delta h_{\text{Amb}} b_2 \tag{7.93}$$
$$R = 0.93 \pm 0.004, \qquad \Sigma = 23$$

$$\Delta h_{\text{Schm}} = a_7 \Delta p_2 \cos \alpha_2 + a_8 \Delta h_{\text{Amb}} b_3 \tag{7.94}$$
$$R = 0.92 \pm 0.007, \qquad \Sigma = 24$$

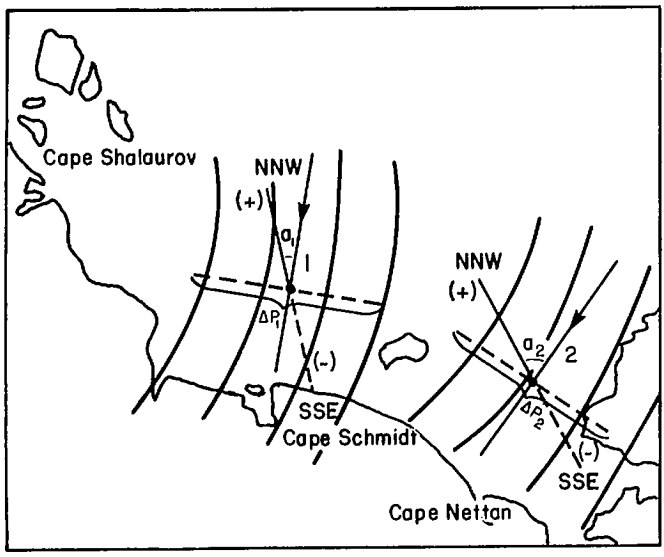

FIG. 7.204. Determination of the quantities Δp_1 and Δp_2 and the wind current direction from the isobars at points 1 and 2 (see eq. 7.91–7.95). a_1 and a_2 are the angles between the wind current direction (arrows) and the effective refluxing–fluxing direction north–northwest to south–southeast. The angles are acute and determine positive components (+) of Δp_1 and Δp_2 at the time of sea level fluxing motions and negative components (−) at the time of sea level refluxing wind directions. (Mustafin 1969)

$$\Delta h_{\text{Schm}} = a_9 \Delta p_1 \cos \alpha_1 + a_{10} \Delta p_2 \cos \alpha_2 + b_4 \tag{7.95}$$
$$R = 0.88 \pm 0.01, \qquad \Sigma = 29$$

where Δh_{Schm} is the deviation (centimetres) of the nonperiodic factor in the sea level at Cape Schmidt from the mean annual navigational level, precalculated with an average forewarning period of 12–13 h upward (+) and downward (−); Δh_{Amb} is the deviation (centimetres) of the actual sea level in Ambarchik Bay from the mean annual navigational level upward (+) and downward (−); Δp_1 and Δp_2 are the respective pressure differences (millibars) at points 1 and 2 at a distance of 600 km (6 cm on a 1 : 10 000 000 scale map) along lines perpendicular to the isobaric trend (Fig. 7.204 of this chapter and Fig. 7 of Mustafin 1969); α_1 and α_2 are the angles between the wind direction along the isobars and the line running north–northwest and south–southeast (Fig. 7.204 of this chapter and Fig. 7 of Mustafin 1969); $a_1, \ldots, a_{10}$ are constants; $b_1, \ldots, b_4$ are free terms; R and r are multiple and partial correlation coefficients and their probable errors; and Σ is the mean square root error (centimetres) of the regression equation.

Parameters Δp_1, Δp_2, α_1, α_2, etc., needed here are determined as shown in Fig. 7.204. One of the interesting features of this study is that, in contrast with the universally used technique of determining the atmospheric pressure gradients along constant directions, here, these gradients are calculated along variable directions but at preselected locations in the waterbody.

Mustafin's (1969) study was done for nine locations on the Siberian coast. Since knowing the water level at one location in advance might help the prediction at other

TABLE 7.92. Correlation coefficients between the storm surges at various locations on the East Siberian Sea and Chuckchi Sea coasts. (Mustafin 1969)

	Cape Shalaurov	Ambarchik Inlet	Rau-Chua	Pevek	Cape Billings	Cape Schmidt	Cape Vankarem	Kolyuchin Island	Cape Nettan
Cape Shalaurov	1	0.86	0.83	0.85	0.82	0.75	0.70	0.84	0.77
Ambarchik Inlet		1	0.95	0.97	0.79	0.80	0.74	0.83	0.70
Rau-Chua			1	0.97	0.88	0.87	0.86	0.80	0.74
Pevek				1	0.85	0.90	0.67	0.81	0.85
Cape Billings					1	0.86	0.83	0.71	0.77
Cape Schmidt						1	0.84	0.84	0.91
Cape Vankarem							1	0.78	0.81
Kolyuchin Island								1	0.85
Cape Nettan									1

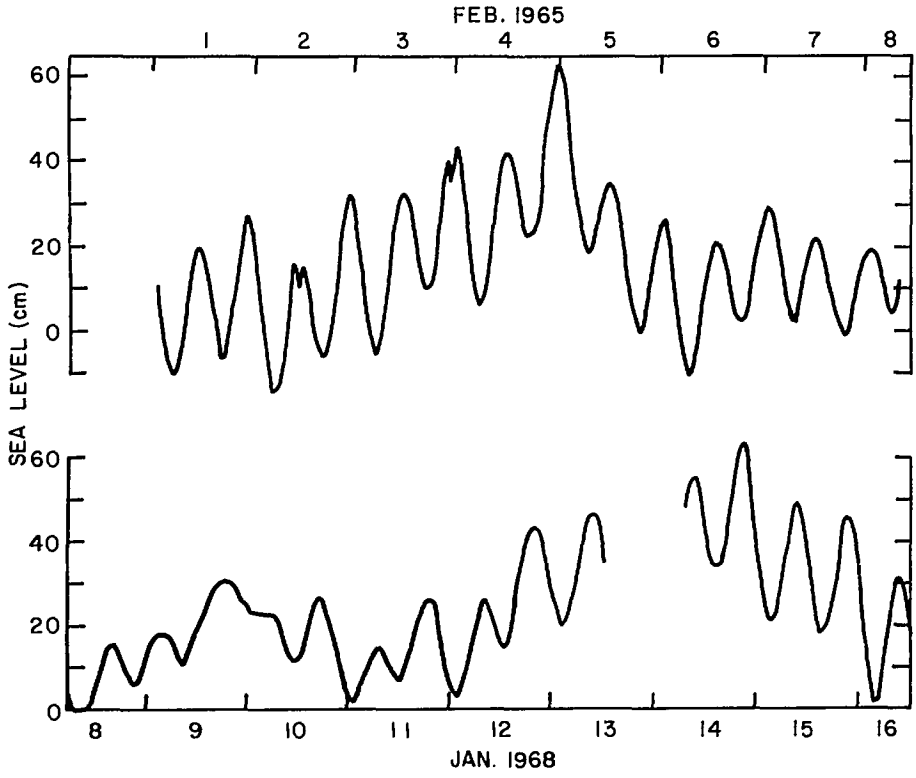

FIG. 7.205. Storm surges at Ashdod, Israel. Examples are shown of gradual changes in several days. Top: February 1–8, 1965; bottom: January 8–16, 1968. (Striem 1974)

locations, Mustafin (1969) tabulated the correlation coefficients for the water levels between these stations. These are shown in Table 7.92. On this coast, the surges appear to lag the meteorological forcing by about 12 or 13 h.

STORM SURGES IN ISRAEL

Striem (1974) studied the storm surges at Ashdod on the Mediterranean coast of Israel using the data for a 6-yr period (1965–70). The tide here is mainly semidiurnal with a range of less than 1 m.

The data for this study were selected whenever the daily mean sea level exceeded the average level by at least 20 cm and when there was a storm present. The storm surges at Ashdod for two events (February 1–8, 1965, with peak surge during the 4th and 5th and January 1968 with peak surge during the 14th) are shown in Fig. 7.205.

Striem (1974) used the term "storm surge" to denote the changes in sea level at Ashdod during a period of several days due to storms in the eastern part of the Mediterranean Sea and the term "storm set-up" to denote the rapid changes in the water level during a few hours. Three examples of these storm setups are shown in Fig. 7.206.

The six largest positive storm surges at Ashdod during the period of this study are summarized in Table 7.93. The six largest negative storm surges at Ashdod are listed in

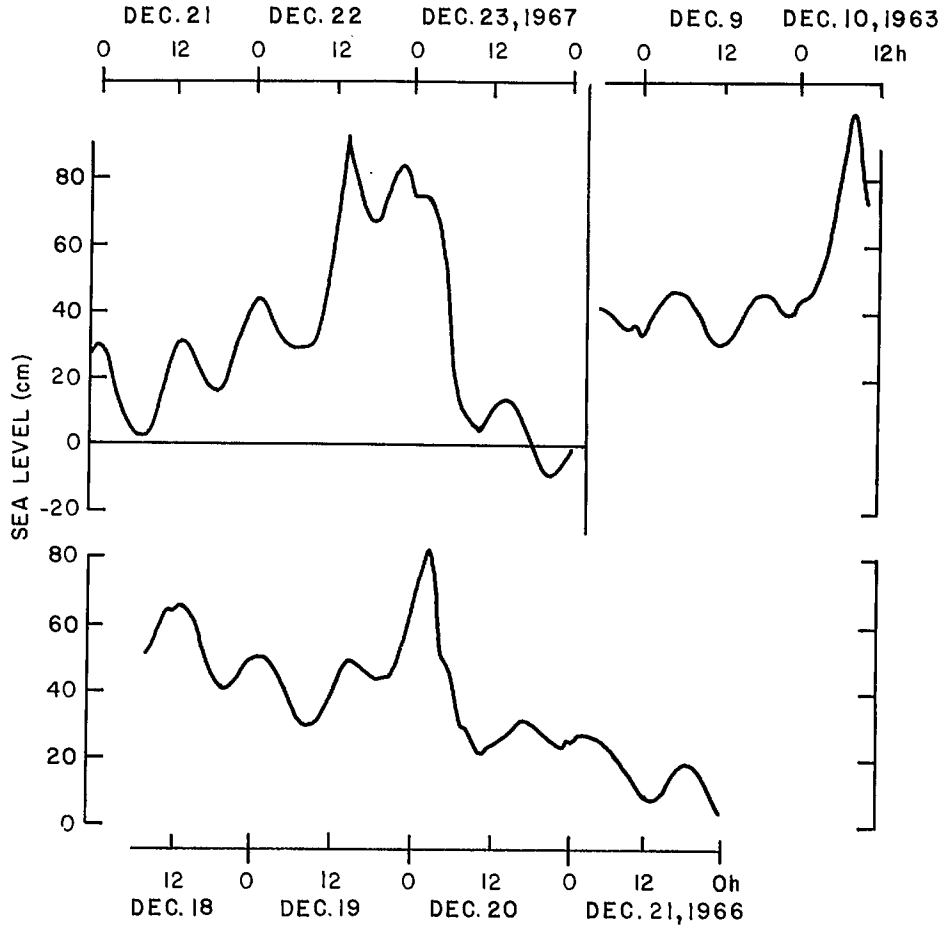

FIG. 7.206. Storm surges at Ashdod, Israel. Examples are shown of rapid changes. Top left: December 21–23, 1967; top right: December 9–10, 1963; bottom: December 19–21, 1966. (Striem 1974)

TABLE 7.93. Six largest positive storm surges at Ashdod, Israel, during 1965–70. (Striem 1974)

Date	Amplitude of surge (cm)
Dec. 10, 1963	100
Dec. 22, 1967	93
Dec. 20, 1966	83
Feb. 5, 1965	63
Mar. 26, 1967	63
Jan. 14, 1968	63

TABLE 7.94. Six largest negative storm surges at Ashdod, Israel, during 1965–70. (Striem 1974)

Date	Amplitude of surge (cm)
Jan. 29, 1964	51
Mar. 24, 1966	46
Mar. 26, 1968	45
Feb. 12, 1968	42
Oct. 16, 1970	41
Apr. 12, 1968	40

Table 7.94. The factors that cause the sea level to rise and fall at Ashdod are summarized in Tables 7.95 and 7.96, respectively. It was found that the storm surges at Ashdod basically are gradual changes in the daily mean sea level and that these changes could be

TABLE 7.95. Factors contributing to the rise of sea level at Ashdod, Israel. (Striem 1974)

Factor	Time of occurrence	Approx. maximum rise of sea level (cm)
(a) High of spring tides	Vernal equinox	+26
(b) High of the seasonal fluctuation	Midsummer	+10
(c) High annual mean sea level		+7
(d) Rise due to daily inequality of the tides		+5
Total of effects not due to wind		+48
(e) Storm surges	Winter	+40
(f) Storm setup	Winter	+40

TABLE 7.96. Factors contributing to the lowering of sea level at Ashdod, Israel. (Striem 1974)

Factor	Time of occurrence	Approx. maximum fall in sea level (cm)
(a) Extreme low of spring tides	Vernal equinox	−26
(b) Low of the seasonal fluctuation	End of spring	−10
(c) Low of annual levels		−6
(d) Lowering due to daily inequality of the tides		−5
Total of effects not due to wind		−47
(e) Lowering due to eastern (offshore) winds (or down-surge after onshore storms)		−15 (or −30)
Possible lowering due to occurrence of all factors		−62 (or −77)

linearly correlated with daily mean values of wind wave heights and wind velocities at the shore.

STORM SURGES IN EGYPT

Storm surges occur in the Suez Canal and also on the Mediterranean coast of Egypt. Murty and El-Sabh (1981) studied the storm surges at Port Said at the northern end of the Suez Canal and at Port Suez at the southern end of the canal using the data for 1966.

The length of the Suez Canal is about 175 km and the average depth is 15 m. At Port

TABLE 7.97. Number of occasions (treating each hourly value as one case) when positive and negative storm surges at Port Said, Egypt, exceeded prescribed amplitudes in 1966.

State of tide	Surge height (cm)									
	10	20	30	40	50	60	70	80	90	100
Positive surges										
Low tide	253	189	90	28	9	5	1	1	1	1
Rising tide	236	137	51	10	1	0	0	0	0	0
High tide	237	131	44	2	0	0	0	0	0	0
Falling tide	246	175	82	26	6	2	1	0	0	0
Negative surges										
Low tide	19	7	3	2	0	0	0	0	0	0
Rising tide	16	9	3	2	1	1	0	0	0	0
High tide	12	5	1	1	1	1	1	1	1	1
Falling tide	13	5	0	0	0	0	0	0	0	0

Said the tide is cooscillating with the eastern part of the Mediterranean Sea and has an amplitude of 25 cm. At Port Suez the tide is from the Red Sea and has an amplitude of 75 cm. Based on these features the Suez Canal can be classified into a long estuary, in the Proudman sense (discussed earlier under Tide–Surge Interaction in the North Sea and in the St. Lawrence Estuary).

Treating each hourly surge value as one case, the number of occasions when positive and negative surges exceeded prescribed values at Port Said and Port Suez is given in Tables 7.97 and 7.98, respectively. Earlier, it was seen that Proudman's (1957) theory suggested that for a long estuary, for a tide of progressive wave type, maximum surges are associated predominantly with low tide (or rising tide), and for a tide of standing wave type, maximum surges are associated predominantly with high tide (or falling tide). Observations for 1966 showed that the theoretical results of Proudman, when interpreted for the Suez Canal, agreed with the observations at Port Said but not with those at Port Suez.

STORM SURGES IN MALAGASY REPUBLIC (MADAGASCAR)

Earlier, it was mentioned that tropical cyclones travel nearby and sometimes traverse Malagasy Republic. The only study this author could find on the storm surges in this region is by LaCour (1935). In principle, storm surges could occur along the long east and west coasts of this island (about 1500 km in length). However, favorable cyclone tracks usually generate surges on the east coast of the island, where the tidal range is small (less than 80 cm).

Storm surges appear to be more frequent on the east coast than on the west coast. Also, surges on the east coast are more important south of Tamtave then north of it. Although surges are more frequent on the east coast the amplitudes usually are rather small (20 cm or less). However, the March 1927 event near Tamtave was a major surge and caused some destruction. Major surges could occur at Tuléar on the southern part of the west coast (e.g. the event of January 1933). A partial list of storm surges on the east and west coasts of Malagasy Republic is given in Table 7.99. Das et al. (1978) stated that cyclonic storms in the Island of La Réunion in the South Indian Ocean often produced exceptionally heavy rain. Instances of heavy rain accompanied by surges of 4.6 m have been reported from this island.

Storm Surges in South Africa

Storm surges in the strict sense of the word are rare on the coasts of South Africa. However, harbor surging occurs associated with the passage of weather systems (Wilson 1954) as, for example, at Cape Town near the southern tip on the west coast of South Africa. Another extremely interesting phenomenon that occurs near the east coast of South Africa is the so-called "giant wave." This will be considered in some detail after discussion of harbor surging.

Frontal depressions from the South Atlantic Ocean create swell on the western and southern coasts of South Africa, which in turn is responsible for harbor surging. Wilson (1954) pointed out that in this region of the globe, prominent cold fronts stretch in crescent form some 1000−1500 mi (1609−2414 km) north of the depression center.

Table Bay (near Cape Town) exhibits seiches with periodicities of 62, 51, 33−26, 23−17, 14−12, 11−10, and 9.8 −9.4 min (Wilson 1954). Some of these periods agree with the higher harmonics of the oscillation of the South Atlantic Ocean lying between the mid-Atlantic Ridge and the west coast of South Africa. The prominent seiches in the quasi-basin between the breakwater and the shore are those with periods from 14 to 9.4 min.

Wilson (1954) considered the seiches in Duncan Basin and Victoria Basin. He made certain recommendations for reducing the surging problem.

Next, the so-called giant waves (also referred to as "freak waves," "episodic waves," and "killer waves") that occur in several locations on the globe, but most prominently near the east coast of South Africa, will be considered. Smith (1976, p. 417) stated:

> During the closure of the Suez Canal a number of ships, particularly oil tankers, have reported extensive damage caused by giant waves off the southeast coast of South Africa (Mallory, 1974; Sturm, 1974; Sanderson, 1974). Two particularly unfortunate vessels are the "World Glory" which broke in two and sank in June 1968, and the "Neptune Sapphire" which lost 60 m of its bow section in August 1973. We can only speculate that giant waves may account for many of the ships which have been lost without trace off this coast. When returning from the Persian Gulf the tankers take advantage of the rapid Agulhas current, and all except one of the eleven incidents listed by Captain Mallory (1974) involved vessels riding on the current. By examining weather charts, Mallory showed that when the incidents occurred the dominant wind-produced waves were opposed by the current.

James (1974), who reported similar phenomena along the north wall of the Gulf Stream, offered a qualitative explanation by suggesting that the effect of an opposing current on the waves is to decrease their wavelength and thus increase their amplitude. Smith (1976) developed a mathematical theory for giant waves beginning with the non-linear form of the Schrödinger equation.

Regarding the specific location on the southeast coast of South Africa where these waves occur, Mallory (1974, p. 99) stated:

> . . . considerable damage to vessles when steaming in a southwesterly direction down the east coast between Durnford Point and Great Fish Point. . . It is safe to say that many other ships must have experienced abnormal waves off the South African coast between Durnford Point and Cape Recife . . .

Schumann (1980) confirmed that the giant waves are from the southwest and the most dangerous situations occurred when the low pressure systems were moving along the coast in a northeasterly direction. He suggested that the giant waves are big swells propagating from a southerly or southwesterly direction around South Africa and moving into the Agulhas current.

TABLE 7.98. Number of occasions (treating each hourly value as one case) when positive and negative storm surges at Port Suez, Egypt, exceeded prescribed amplitudes for positive surges and 10–90 cm for negative surges in 1966.

State of tide	Surge height (cm)														
	10	20	30	40	50	60	70	80	90	100	110	120	130	140	150
Positive surges															
Low tide	172	111	75	44	32	16	8	3	3	3	3	3	2	1	1
Rising tide	191	110	76	38	13	7	6	6	3	1	0	0	0	0	0
High tide	121	57	18	5	2	1	1	1	1	0	0	0	0	0	0
Falling tide	174	107	50	34	27	23	10	3	0	0	0	0	0	0	0
Negative surges															
Low tide	84	66	46	32	16	11	3	0	0						
Rising tide	104	69	45	45	14	21	1	0	0						
High tide	117	69	59	49	40	24	6	0	0						
Falling tide	113	84	55	27	38	9	9	2	1						

TABLE 7.99. Partial list of storm surges in Malagasy Republic before 1935. Note that this study is based mainly on the data for the year 1934 and a few examples before that. (Based on LaCour 1935)

Date	Remarks
Feb. 21, 1893	Storm center passed 50 km north of Tamtave (east coast) at Foulpointe. Major surges at Hastie Point in Tamtave
Mar. 1927	Cyclone passed near Tamtave. Surge south of Tamtave in the region of Pangalanes. Railway bridge collapsed at Nossi-Vé. Smaller surges north of Tamtave
Jan. 1933	Major surge at Tuléar on the Bay of Austine (southern part of the west coast)
Jan. 8–9, 1934	Cyclone made landfall on the east coast of Nosy-Varika and Mananjary (300 km south of Tamtave). Cyclone originated 200 km south of Réunion Island
Jan. 13–19, 1934	Negligible surge. Cyclone track northeast of Tamtave
Jan. 29–Feb. 1, 1934	Track 800 km southeast of Tamtave. Cyclone traveled from Réunion to Fort Dauphin (near the southern end of the east coast). Small surge at Tamtave
Feb. 23–27, 1934	Cyclone in the Mozambique channel traveled from north to south. Passed near Cape St. Andre on the west coast. This generated a 200-cm positive surge and a 10-cm negative surge at Tamtave
Mar. 4–8, 1934	A 20-cm negative surge at Tamtave. Could not be traced to any cyclone
Mar. 13–14, 1934	Local cyclone of small diameter in the Bay of Antongil (130 km north of Tamtave). Cyclone crossed the island from east to west. A 10-cm positive surge at Tamtave
Mar. 23–25, 1934	Cyclone from the Indian ocean. Small surge

Schumann (1980, p. 29) also included the official warning on the hydrographic charts for this region. It states in part:

> Abnormal waves of up to twenty meters in height, preceded by a deep trough, may be encountered in the area between the edge of the continental shelf and twenty miles to seaward thereof. These can occur when a strong southwesterly wind is blowing, the sea is rough and the barometric pressure is low . . . [T]he necessary evasive action is to stay clear of the area seaward of the edge of the continental shelf.

Schumann stated further that this well-established rule (i.e. staying clear of the edge of the continental shelf) gave rise to the belief that the bottom topography plays an important part in generating the giant waves. He suggested that the bottom topography plays only a minor indirect role. He stated (p. 29):

> The Agulhas current hugs the edge of the African continent, and since it extends to depths well below 1,000 meters, it generally does not intrude onto the shelf regions, but tends to lie just offshore of the shelf edge. Consequently the core of the current is usually found where the giant waves are most likely to occur.

References

Not all references contained in this list appear in the text

ABBOTT, M. B. 1969. Aspects of an analysis of a difference scheme, Appendix in Sobey 1970. p. 27–29.

ABBOTT, M. B., J. A. BERTELSEN, AND I. R. WARREN. 1976. Modelling of storm surges in stratified flow. Proc. 15th Coastal Eng. Conf., July 11–17, 1976, Honolulu, HI. ASCE, New York, NY. 4 p.

ABBOTT, M. B., A. DANESGAARD, AND G. S. RODENHUIS. 1973. System 21, Jupiter: a design system for two-dimensional nearly-horizontal flow. J. Hydraul. Res. 11: 1–28.

ABRAHAM, G. 1961. Hurricane storm surge considered as a resonance phenomenon, p. 585–602. *In* J. W. Johnson [ed.] Proc. 7th Coastal Eng., Conf. Aug. 1960, The Hague. Chap. 31. Council on Wave Research, The Engineering Foundation, New York, NY.

ACCAD, Y., AND C. L. PEKERIS. 1978. Solution of the tidal equations for the M_2 and S_2 tides in the world oceans from a knowledge of the tidal potential alone. Philos. Trans. R. Soc. London Ser. A 290: 235–266.

ACCERBONI, E., AND B. MANCA. 1973. Storm surges forecasting in the Adriatic Sea by means of a two-dimensional hydrodynamical numerical model. Boll. Geofis. Teor. Appl. 15: 3–22.

ACKERS, P., AND T. D. RUXTON. 1975. Extreme levels arising from meteorological surges. Proc. 14th Coastal Eng. Conf., June 24–28, 1974, Copenhagen. ASCE, New York, NY. p. 69–86.

ADAM, Y. 1979. Belgian real-time system for the forecasting of currents and elevations in the North Sea, p. 411–425. *In* J. C. J. Nihoul [ed.] Marine forecasting. Proc. 10th Int. Liège Colloq. Ocean Hydrodyn. Elsevier Scientific Publishing Company, Amsterdam, Netherlands.

AGNEW, R. 1966. Storm tides in the Tasman Sea, New Zealand. J. Geol. Geophys. 9: 239–242.

ALAKA, M. A. 1976. Climatology of Atlantic tropical storms and hurricanes, p. 479–508. *In* W. Schwerdtfeger [ed.] Climates of Central and South America. Elsevier Scientific Publishing Company, Amsterdam, Netherlands.

ALEXANDER, G., G. A. GEORGE, AND R. JAMBUNATHAN. 1974. Cyclones and depressions of 1973 — Bay of Bengal and Arabian Sea. Indian J. Meteorol. Hydrol. Geophys. 25: 347–362.

ALEXANDER, G., N. S. B. RAO, AND R. JAMBUNATHAN. 1976a. Cyclones and depressions of 1974 — Bay of Bengal and Arabian Sea. Indian J. Meteorol. Hydrol. Geophys. 27: 113–126.

1976b. Cyclones and depressions of 1974 — Bay of Bengal and Arabian Sea. Indian J. Meteorol. Hydrol. Geophys. 28: 3–20.

ALI, A. 1980a. The dynamic effects of barometric forcing on storm surges in the Bay of Bengal. Mausam 31(4): 517–522.

1980b. A numerical model for the prediction of storm surges in the Bay of Bengal. Presented at the Indo–French school on recent advances in computer techniques in meteorology, biomechanics, and applied systems, New Delhi, Feb. 4–13, 1980.

1980c. Some experiments with a numerical model developed for the prediction of storm surges in the Bay of Bengal, p. 162–169. Symp. Typhoons, Oct. 6–11, 1980, Sanghai. (Preprint volume)

1980d. Storm surges in Bangladesh. Report to W.M.O. Workshop on storm surges, Nov. 10–15, 1980, Rangoon. 13 p.

ALLEN, F. H., W. A. PRICE, AND C. V. INGLIS. 1955. Model experiments on the storm surge of 1953 in the Thames Estuary and the reduction of future surges. Proc. Inst. Civ. Eng. (U.K.) Part III. 4: 48–82.

ALLEN, W. T. R., AND B. S. V. CUDBIRD. 1971. Freeze-up and break-up dates of water bodies in Canada. Report CLI-1-71, Can. Meteorol. Ser., Toronto, Ont. 144 p.

ALVAREZ, J. A. 1973. Numerical prediction of storm surges in the Rio de la Plata area. Ph.D. thesis, University of Buenos Aires, Buenos Aires, Argentina. 70 p. plus tables and figures.

AMADORE, L. A. 1972. An evaluation of the accuracy of some objective techniques for predicting tropical cyclone movement in the western North Pacific. Tech. Ser. No. 14, W.M.O./U.N.D.P. Project. 74 p.

AMIN, M. 1978. A statistical analysis of storm surges in Torres Strait. Aust. J. Mar. Freshwater Res. 29: 479–496.

1982. On analysis and forecasting of surges on the west coast of Great Britain. Geophys. J. R. Astron. Soc. 68: 79–94.

AMOROCHO, J., AND J. J. DEVRIES. 1980. A new evaluation of the wind stress coefficient over water surfaces. J. Geophys. Res. 85: 433–442.

AN, M. B. 1980. A survey of storm surges along the West Coast of the Korean Peninsula. Report to the W.M.O. Workshop on storm surges, Nov. 10–15, 1980, Rangoon. 12 p.

ANANTHAKRISHNAN, R. 1964. Tracks of storms and depressions in the Bay of Bengal and the Arabian Sea, 1877–1960. Indian Meteorol. Dep., New Delhi.

ANGELL, J. K., J. KORSHOVER, AND G. F. COTTEN. 1969. Quasi-biennial variations in the centers of action. Mon. Weather Rev. 97(12): 867–872.

ANISIMOVA, Y. P., Y. N. BELOV, A. A. SPERANSKAYA, A. A. ARD, AND V. S. SHANDIN. 1981. Model of an atmospheric vortex. Izv. Atmos. Oceanic Phys. 17(7): 567–570.

ANNETTE, P. 1976. Recent events concerned with importing objective aids to predict tropical cyclone motion. Australian Bureau of Meteorology, Meteorological Note No. 90. Melbourne, Australia.

ANONYMOUS. 1954. Coastal flooding in Britain. Nature (London) 174: 193–195.

1955. Waves and wind tides in shallow lakes and reservoirs. Project CW-167, University of Florida, Jacksonville, FL.

1956. Report of the Ice Observing and Forecast Program. Spec. Publ. U.S. Navy Hydrographic Office, Washington, DC.

1957. Bibliography on generation of currents and changes of surface-level in oceans, seas and lakes by wind at atmospheric pressure, 1726–1955. Publ. Sci. No. 18, IUGG, Gotenborg, Sweden. 76 p.

1958. Oceanographic atlas of the Polar Seas. U.S. Navy Hydrographic Office, Washington, DC. 149 p.

1964. Tracks of storms and depressions in the Bay of Bengal and the Arabian Sea, 1877–1960. Indian Meteorol. Dep., New Delhi, Mar. 1964. 167 p. plus appendices.

1966. Techniques for forecasting wind waves and swell. Publ. No. 604, U.S. Navy Hydrographic Office, Washington, DC. 37 p.

1967. Mar. Weather Log 10(4): 206.

1971. Investigation of the storm of September 13–16, 1970, MacKenzie Delta region, Beaufort Sea. Engineering Programs Branch, Dep. Public Works, Ottawa, Ont., Nov. 1971.

1973. Regulation of the Great Lakes water levels. Appendix C. Shore property. Report to the International Joint Commission by the Great Lakes Level Board, Dec. 7, 1973.

1974. Navigation season extension studies, Montreal–Lake Ontario section, St. Lawrence River, winter 1973–74. Ministry of Transport, Canadian Marine Transportation Administration. 18 p. plus charts.

1975. Canada/Ontario Great Lakes shore damage survey. Tech. Rep., Environment Canada, Ottawa, Ont., Oct. 1975. 97 p.

1978a. What's in a name? A detailed look at the practice of assigning names to hurricanes which might include Carol, Edna, Hazel, or Saxby. NOAA 8(3): 13–17.

1978b. Present techniques of tropical storm surge prediction. Rep. No. 13. Marine Science Affairs. W.M.O. No. 500, Geneva. 87 p.

1978c. A trigger for great stores? Mysteries of the mesoscale. NOAA 8(1): 42–45.

1979. Operational techniques for forecasting tropical cyclone intensity and movement. W.M.O. No. 528, Geneva, Switzerland.

ANTHES, R. A. 1972. Development of asymmetries in a three-dimensional numerical model of the tropical cyclone. Mon. Weather Rev. 100: 461–476.

1977. Hurricane model experiments with a new cumulus parameterization scheme. Mon. Weather Rev. 105: 287–300.

ANTHES, R. A., S. L. ROSENTHAL, AND J. W. TROUT. 1971a. Preliminary results from an asymmetric model of the tropical cyclone. Mon. Weather Rev. 99: 744–758.

1971b. Comparisons of tropical cyclone simulations with and without the assumption of circular symmetry. Mon. Weather Rev. 99: 759–766.

AOKI, T. 1979. A statistical prediction of the tropical cyclone position based on persistence and climatological factor in the western North Pacific (the PC method). Geophys. Mag. 38(4): 17–27.

ARAKAWA, A. 1966. Computational design for long-term numerical integration of the equations of fluid motion: two-dimensional incompressible flow. Part 1. Comput. Phys. 1: 119–143.

1972. Design of the U.C.L.A. general circulation model, numerical simulation of weather and climate. Department of Meteorology, University of California, Los Angeles, CA.

ARAKAWA, H., AND V. R. LAMB. 1981. A potential enstrophy and energy conserving scheme for the shallow water equations. Mon. Weather Rev. 109: 18–36.

ARAKAWA, H. 1963. Typhoon climatology as revealed by data of the Japanese Weather Service, p. 633–639. Proc. of a Seminar on Tropical Cyclones, Tokyo. Japan Meteorological Agency, Tokyo, Japan.

1969. Climates of northern and eastern Asia, p. 12–173. World survey of climatology. Vol. 8. Elsevier Scientific Publishing Company, Amsterdam, Netherlands.

ARCHIBALD, D. C. 1945. Intense storm tracks over Hudson Bay, the eastern Nova Scotia coast and the Grand Banks. Report of the Meteorological Branch, Department of Transport, Toronto, Ont. 9 p.

ARMSTRONG, J. B. 1962. The effect of meteorological conditions on sea level. Circular 3747, Tec-429, Nov. 1, 1962, Vancouver Meteorol. Off., Vancouver, B.C. 12 p.

ASSEL, R. A. 1976. Great Lakes ice thickness prediction. J. Great Lakes Res. 2(2): 248–255.

ATKINSON, G. D., AND C. R. HOLLIDAY. 1977. Tropical cyclone minimum sea level pressure/maximum sustained wind relationship for the western North Pacific. Mon. Weather Rev. 105: 421–427.

BACKHAUS, J. 1976. Zur hydrodynamik im flachwassergebiet, ein numerisches modell. Dtsch. Hydrogr. Z. 29: 222–238.

1979. First results of a three-dimensional model on the dynamics in the German Bight, p. 333–349. *In* J. C. J. Nihoul [ed.] Marine forecasting. Proc. 10th Int. Liège Colloq. Ocean Hydrodyn. Elsevier Scientific Publishing Company, Amsterdam, Netherlands.

BAER, F. 1979. Numerical hurricane prediction, p. 488–544. *In* H. Riehl [ed.] Climate and weather in the tropics. Chap. 11. Academic Press, New York, NY.

BAINES, P. G. 1974. On the drag coefficient over shallow water. Boundary-Layer Meteorol. 6: 299–303.

BAIRD, W. F., N. G. FREEMAN, AND T. S. MURTY. 1976. Reconstruction of the high water levels in Goderich Harbour during March 17–18, 1973. Report prepared by Environment Canada to the Department of Justice, Ottawa, Ont. 6 p.

BALLENZWEIG, E. M. 1959. A practical equal-area grid. J. Geophys. Res. 64: 647–651.

BALLOFFET, A., M. L. SCHEFFLER, AND T. F. SERGI. 1982. Frequency of tidal storm surge at New York Harbor (New York) and Newark Bay (New Jersey). Coastal Eng. 6: 281–298.

BANDYOPADHYAY, K. K., AND N. C. MAZUMDAR. 1967. Design of a tidal channel friction simulator. Int. J. Electron. 23(6): 519–531.

1969a. Scaling of tidal channel parameters for the construction of an electronic analogue model. Int. J. Electron. 26: 145–152.

1969b. Error in the propagation characteristics of the lumped analogue model of a tidal channel. Int. J. Electron. 27: 231–235.

1970. Design of a tidal channel inertia simulator. Int. J. Electron. 28: 533–545.

BANKS, J. E. 1974. A mathematical model of a river–shallow sea system used to investigate tide, surge and their interaction in the Thames–southern North Sea region. Philos. Trans. R. Soc. London Ser. A 275: 275–609.

BANSAL, R. K., AND R. K. DATTA. 1974. A statistical approach method of forecasting the movement of cyclonic storms in the Bay of Bengal. Indian J. Meteorol. Geophys. 25(3–4): 391–397.

BARNES, F. A., AND C. A. M. KING. 1953. The Lincolnshire coastline and the 1953 storm flood, p. 141–160. Proc. Conf. North Sea Floods.

BARNETT, T. P. 1968. On the generation, dissipation and prediction of ocean wind waves. J. Geophys. Res. 73: 513–530.

BARRIENTOS, C. S. 1970. An objective method for forecasting winds over Lake Erie and Lake Ontario. E.S.S.A. Tech. Memo. WBTM TDL-34, Aug. 1970, Silver Spring, MD.

1971. An objective method for forecasting winds over Lake Erie and Lake Ontario, p. 401–411. Proc. 14th Conf. Great Lakes Res. Int. Assoc. Great Lakes Res., Ann Arbor, MI.

BARRIENTOS, C. S., AND J. CHEN. 1974. Storm surge shoaling corrections along the east coast. Report to the Federal Insurance Administration, U.S. Department of Housing and Urban Development. 16 p.

BARRIENTOS, C. S., AND C. P. JELESNIANSKI. 1973. Storm surge shoaling corrections along the Gulf Coast. Report to the Federal Insurance Administration, U.S. Department of Housing and Urban Development. 26 p.

1976. SPLASH — A model for forecasting storm surges. Proc. 15th Coastal Eng. Conf., July 11–17, 1976, Honolulu, HI. ASCE, New York, NY. (Abstr.)

1978. SPLASH — A model for forecasting tropical storm surges, p. 941–958. Proc. 15th Coastal Eng. Conf., June 24–28, 1976, Copenhagen, Denmark. ASCE, New York, NY.

BARRY, R. G., AND R. J. CHORLEY. 1970. Atmosphere, weather and climate. Holt, Rinehart and Winston, Inc., New York, NY. 70 p.

BARTHEL, V. 1979. Analysis of storm tide waves, 1016–1029. Proc. 16th Coastal Eng. Conf., Aug. 27–Sept. 3, 1978, Hamburg, W. Germany. ASCE, New York, NY.

BASANO, L., AND L. PAPA. 1978. Correlation of the free oscillation of the Ligurian Sea with meteorological perturbations: a preliminary investigation. Boll. Geofis. Teor. Appl. 20(79): 223–234.

BASCOM, W. 1950. Surging in Depoe Bay, Oregon. Bulletin of the Beach Erosion Board (Washington, DC) 4: 32–39.

BASTE, M. 1954. La raz de marée du 31 janvier 1953 en mer du Nord. Les dommages causés sur la côté orientale de la Grande Bretagne, Navires ports et chantiers. Aug. 1954. p. 699–705.

BATES, J. 1977. Vertical shear of the horizonal wind speed in tropical cyclones. Tech. Memo, ERL-WMPO-39, NOAA, National Weather Service, Silver Spring, MD.

BAYNTON, H. W. 1979. The case for doppler radars along our hurricane affected coasts. Bull. Am. Meteorol. 60(9): 1014–1037.

BEDARD, A. J., W. H. HOOKE, AND D. W. BERAN. 1977. The Dulles Airport pressure-jump detector array for gust front detection. Bull. Am. Meteorol. Soc. 58(2): 920–926.

BEDARD, A. J., AND H. B. MEADE. 1977. The design and use of sensitive pressure-jump sensors to detect thunderstorm gust fronts. Part 1: Pressure-jump detector design. J. Appl. Meteorol. 16(10): 1049–1055.

BELL, G. J. 1961. Surface winds in Hong Kong typhoons. Proc. U.S.–Asian Symp. Typhoons, Baguio, Philippines.

1962. Predicting the movement of tropical cyclones in the region of the China Sea, p. 195–198. Proc. Interreg. Semin. Trop. Cyclones, Tokyo, Japan.

1979. Severe tropical storm Agnes, July 1978. Mar. Weather Log 23: 227–230.

BENGTSSON, L., H. BOLTGER, AND M. KANAMITSU. 1982. Simulation of hurricane-type vortices in a general circulation model. Tellus 34: 440–457.

BENNETT, J. R. 1977. A three-dimensional model of Lake Ontario's summer circulation. I. Comparison with observations. J. Phys. Oceanogr. 7: 591–601.

BENTON, G. S., AND M. A. ESTOQUE. 1954. Water vapor transfer over the North American continent. J. Meteorol. 11: 462–477.

BENWELL, G. R., A. J. GADD, J. F. KEERS, M. S. TIMPSON, AND P. W. WHITE. 1971. The Bushby–Timpson 10-level model on a fine mesh. Sci. Pap. No. 32, Meteorol. Off., London, England. 23 p.

BERGERON, T. 1954. The problem of tropical hurricanes. Q. J. R. Meteorol. Soc. 80(344): 131–164.

BERGSTEN, F. 1955. Winds and water levels on the coasts of Sweden. Geogr. Ann. Band 37: 119–140.

BERRY, M. O., P. M. DUTCHAK, M. E. LALONDE, J. A. W. MCCULLOCH, AND I. SAVDIE. 1975. Weather, waves and icing in the Beaufort Sea. Tech. Rep. No. 21, Beaufort Sea Project, Dec. 1975, Department of the Environment, Victoria, B.C. 57 p.

BERSON, F. A. 1949. Summary of a theoretical investigation into the factors controlling the instability of long waves in zonal currents. Tellus 1(4): 44–52.

BETTS, A. K., R. W. GROVER, AND M. W. MONCRIEFF. 1976. Structure and motion of tropical squall lines over Venezuela. Q. J. R. Meteorol. Soc. 2: 395–404.

BHALME, H. N. 1972. Trends and quasi-biennial oscillation in cyclonic disturbances. Indian J. Meteorol. Hydrol. Geophys. 23: 355–358.

BHALTACHARJEC, P., AND A. C. DE. 1976. Cyclonic storm of August 14–15, 1974, in the Bay of Bengal–A radar study. Indian J. Meteorol. Hydrol. Geophys. 27: 9–14.

BIGELOW, F. H. 1904. The mechanism of countercurrents of different temperatures in cyclones and anticyclones. Mon. Weather Rev. 31: 1–72.

BILELLO, M. A. 1964. Method for predicting river and lake ice formation. J. Appl. Meteorol. 3: 38–44.

BIRCHFIELD, G. E., AND B. P. HICKIE. 1977. The time-dependent response of a circular basin of variable depth to a wind stress. J. Phys. Oceanogr. 7: 691–701.

BIRCHFIELD, G. E., AND T. S. MURTY. 1974. A numerical model for wind-driven circulation in Lakes Michigan and Huron. Mon. Weather Rev. 102(2): 157–165.

BJERKNES, J. 1919. On the structure of moving cyclones. Geofys. Publ. 1(1): 1–8.

1937. Die Theorie der aussertropisepen Zyklonenbildung. Meteorol. Z. 54: 460–466.

BJERKNES, J., AND H. SOLBERG. 1921. Meteorological conditions for the formation of rain. Geofys. Publ. 2(3): 1–61.

1922. Life cycle of cyclones and the polar front theory of atmospheric circulation. Geofys. Publ. 3(1): 1–18.

BLACKFORD, B. L. 1966. A simple two-dimensional electrical analog model for wind-driven circulation in the Gulf of St. Lawrence. J. Fish. Res. Board Can. 23(9): 1411–1438.

BLAKE, J. T. 1981. Jamaica's encounter with Hurricane Allen. W.M.O. Bull. 30(2): 101–104.

BLANFORD, H. F. 1883. Indian Meteorologist's Vade-Mecum, Government of India, Calcutta, India.

BLASIUS, W. 1875. Storms, their nature, classification and laws. Porter and Coates Publishers, Philadelphia, PA. 342 p.

BLECKER, W., AND J. M. ANDRÉ. 1950. Convective phenomena in the atmosphere, J. Meteorol. 7: 195–209.

BLUMBERG, A. F. 1976. A two-dimensional numerical model for the simulation of partially well-mixed estuaries. *In* M. Wiley [ed.] Estuarine processes. Vol. 11. Academic Press, New York, NY. 428 p.

BLUMBERG, A. F., AND G. L. MELLOR. 1980. A coastal ocean numerical model, p. 203–219. *In* J. Sündermann and K. P. Holz [ed.] Mathematical modelling of estuarine physics. Springer-Verlag, Berlin. 265 p.

BLUMEN, W. 1967. On nonlinear geostrophic adjustment. J. Atmos. Sci. 24: 325–332.

1972. Geostrophic adjustment. Rev. Geophys. Space Phys. 10: 485–528.

BODINE, B. R. 1969. Hurricane surge frequency estimated for the Gulf Coast of Texas. U.S. Army Coastal Eng. Res. Cent. Tech. Memo. 26: 32 p.

1971. Storm surge on the open coast: fundamentals and simplified prediction. U.S. Army Coastal Eng. Res. Cent. Tech. Memo. 35: 55 p.

BOERMAN, W. E. 1953. The storm floods in the Netherlands, p. 178–189. Proc. Conf. North Sea Floods.

BOGERT, B. P., M. J. R. HEALY, AND J. W. TUKEY. 1962. The frequency analysis of time series for echoes: cestrum, pseudo-autocavariance, cross-cepstrum and sappe-cracking, p. 209–243. Proc. Symp. Time Series Anal. John Wiley & Sons, New York, NY.

BOLDUC, P. A. 1974. Point Petre storm surge simulation, p. 358–368. Proc. 17th Conf. Great Lakes Res. Int. Assoc. Great Lakes Res., Ann Arbor, MI.

BOLIN, B. 1953. The adjustment of a non-balanced velocity field towards geostrophic equilibrium in a stratified fluid. Tellus 5: 373–385.

BOOK, D. L., J. P. BORIS, AND K. HAIN. 1975. Flux corrected transport. II. Generalization of the method. J. Comput. Phys. 18: 248–283.

BOWDEN, K. F. 1953a. Note on wind drift in a channel in the presence of tidal currents. Proc. Soc. London Ser. A 219: 426–446.

1953b. Storm surges in the North Sea. Weather 8: 82–84.

1957. The effect of flow through the Strait of Dover on storm surges in the North Sea. Assoc. Oceanogr. Phys. Publ. Sci. No. 18: 61.

1965. Horizontal mixing in the sea due to a shearing current. J. Fluid Mech. 21: 83–95.

BOWDEN, K. F., L. A. FAIRBAIRN, AND P. HUGHES. 1959. The distribution of shearing stresses in a tidal current. Geophys. J. R. Astron. Soc. 2: 288–305.

BOWIE, E. H., AND R. H. WEIGHTMAN. 1914. Types of storms of the United States and their average movements. Mon. Weather Rev. Suppl. No. 1: 37 p. plus 114 charts.

BOWMAN, M. J., A. C. KIBBLEWHITE, AND D. E. ASH. 1980. M_2 tidal effects in Greater Cook Strait, New Zealand. J. Geophys. Res. 85(C5): 2728–2742.

BOX, G. E. P., AND G. M. JENKINS. 1970. Time series analysis: forecasting and control. Holden-Day, Inc., San Francisco, CA.

BRADBURY, D. 1954. Frequencies of cyclones and anticyclones and high and low zonal indexes. Department of Meteorology, University of Chicago, Chicago, IL. (Manuscr.)

BRADBURY, T. A. M. 1949. An account of a tropical cyclone in the Arabian Sea. October 1948, U.K. Meteorol. Off., Bracknell. (Manuscr.)

BRADDOCK, R. D. 1977. An analysis of the common stilling well tide gauge. Appl. Math. Res. Rep. No. 86, University of Queensland, Australia.

1980. Response of a conventional tide gauge to a tsunami. Mar. Geod. 4(3): 223–236.

BRAND, S. 1971. The effects on a tropical cyclone of colder surface waters due to upwelling and mixing produced by a tropical cyclone. J. Appl. Meteorol. 10: 865–874.

1978. The Typhoon Havens Research Program at the Naval Environmental Prediction Research Facility, p. 325–332. Proc. 11th Tech. Conf. Hurricanes Trop. Meteorol. Dec. 13–16, 1977, Miami Beach, FL. Am. Meteorol. Soc.

BRAND, S., AND J. W. BLELLOCH. 1976. Typhoon Havens Handbook for the Western Pacific and Indian Oceans. Naval Environmental Prediction Research Facility, Monterey, CA, June 1976.

BRAND, S., J. W. BLELLOCH, D. A. MAUTNER, AND R. M. DE ANGELIS. 1977a. Hong Kong as a typhoon haven. Mar. Weather Log 21(6): 362–371.

BRAND, S., M. E. BROWN, AND R. M. DE ANGELIS. 1977b. Guam as a typhoon haven. Mar. Weather Log 21(2): 80–89.

1978a. Kaohsiung, Taiwan, as a typhoon haven. Mar. Weather Log 22(2): 71–78.

BRAND, S., C. A. BUENAFE, AND H. D. HAMILTON. 1981. Comparison of tropical cyclone motion and environmental steering. Mon. Weather Rev. 109: 908–909.

BRAND, S., J. A. DOUGLAS, AND R. M. DE ANGELIS. 1979. Manila as a typhoon haven. Mar. Weather Log 23(5): 297–305.

BRAND, S., R. J. GRAFF, AND R. M. DE ANGELIS. 1978b. Tokyo Bay as a typhoon haven. Mar. Weather Log 22(6): 387–395.

BRAND, S., AND C. P. GUARD. 1979. An observational study of extratropical storms evolved from tropical cyclones in the western North Pacific. J. Meteorol. Soc. Jpn. 57(5): 479–483.

BRAND, S., J. M. LONG, J. W. BLELLOCH, AND G. D. HAMILTON. 1974. Environmental Prediction Research Facility, U.S. Navy, Monterey, CA, Tech. Pap. No. 11-74: 20 p.

1975. A tropical cyclone analog program for the North Indian Ocean. Mon. Weather Rev. 103: 258–261.

BRAND, S., D. K. RUDOLPH, AND R. M. DEANGELIS. 1980. Pusan as a typhoon haven. Mar. Weather Log 24(5): 337–343.

BRANDON, E. W. 1981. An operational storm surge model for the Bay of Fundy, Internal Report, Atmospheric Environment Service, Halifax, N.S. 8 p.

BREBBIA, C. A., AND P. W. PARTRIDGE. 1976. Finite element simulation of water circulation in the North Sea. Appl. Math. Model. 1: 101–107.

BRENNAN, F. E., AND P. J. SMITH. 1978. The climatology of cyclones and anti-cyclones in the upper Mississippi and Ohio River Valleys and Great Lakes region, 1950–74. Proc. Indiana Acad. Sci. 87: 391–402.

BRENNAN, W. J. 1981. Storm stalking with a hurricane historian. NOAA 11 (3): 9–11.

BRETSCHNEIDER, C. L. 1957. Hurricane design wave practices. Proc. ASCE J. Waterways Harbors Div. 83 (WW2).

1959. Hurricane surge predictors for Chesapeake Bay, Corps of Engineers, Washington, DC, Sept. 1959, Tech. Rep. AD 699408: 51 p.

1964. The Ash Wednesday east coast storm, March 5–8, 1962. A hindcast of events, causes and effects, p. 617–659. Proc. 9th Coastal Eng. Conf., Lisbon, June 1964, ASCE, New York, NY.

1966a. Engineering aspects of hurricane surge. A. T. Ippen [ed.] *In* Estuary and coast line hydrodynamics, p. 231–256. McGraw-Hill Inc., New York, NY.

1966b. A bibliography on storm surges and related subjects. Rept. SN-134-12, Office of Naval Research, Washington, DC, Aug. 1966. 48 p.

1967. Storm surges, p. 341–418. Advances in hydroscience. Vol. 4. Academic Press, New York, NY.

1972. Revision to *Hurricane design wave practices*, p. 167–196. Proc. 13th Coastal Eng. Conf. ASCE, New York, NY.

1975. The envelope wave spectrum. Proc. 3rd Int. Conf. Port Ocean Eng. Under Arctic Conditions. University of Fairbanks, Fairbanks, AK.

BRETSCHNEIDER, C. L., AND R. E. ROCHELEAU. 1979. An evaluation of extreme wave climate at Keapole Point, Hawaii, p. 152–173. Proc. 16th Coastal Eng. Conf., Aug. 27–Sept. 3, 1978, Hamburg, W. Germany, ASCE, New York, NY.

BRIAND, J. M. 1979. Étude des vagues de tempête des eaux de l'est du Canada et de l'estuaire du Saint-Laurent. M.Sc. thesis, Department of Oceanography, University of Quebec, Rimouski, Que. 252 p.

1980. Étude descriptive des amplitudes des ondes de tempête de l'est du Canada et de l'estuaire du Saint-Laurent. Department of Oceanography, University of Quebec, Rimouski, Que. 263 p.

BROGDON, N. J. 1969. Galveston Bay hurricane surge study. Report 1. Effects of proposed barriers on hurricane surge heights. Hydraulic Model Investigation, Tech. Rep. H-69-12, U.S. Army Eng. Dist., Vicksburg, MS.

BROWN, A. L. 1954. An analytical method of ice potential calculation. Tech. Rep. TR-5, U.S. Navy Hydrographic Office, Washington, DC, Sept. 1954. 13 p.

BROWN, H. E., AND R. J. YOUNKIN. 1973. The National Meteorological Center's performance in the forecasting of a winter storm, February 19–20, 1972. Bull. Am. Meterol. Soc. 54: 525–535.

BROWN, R. A. 1981. Modelling the geostrophic drag coefficient for AIDJEX. J. Geophys. Res. 86(C3): 1989–1994.

BROWN, P. S., AND J. P. PANDOLFO. 1978. Merging finite difference schemes having dissimilar time-differencing operators. Mon. Weather Rev. 106: 268–270.

BRUNT, A. T., AND J. HOGAN. 1956. The occurrence of tropical cyclones in the Australian region, p.5–18. Proc. Trop. Cyclone Symp., Brisbane, December 1956. Bureau of Meteorology, Melbourne, Australia.

BRUUN, P., T. Y. CHIU, F. GERRITSEN, AND W. H. MORGAN. 1962. Storm tides in Florida as related to coastal topography. Florida Eng. Ind. Exp. Stat. Res. Issue. 16 p.

BRYAN, K. 1966. A scheme for numerical integration of the equations of motion on an irregular grid free of nonlinear instability. Mon. Weather Rev. 194: 39–40.

BRYSON, R. A., AND F. K. HARE [ed.] 1974. Climates of North America, p. 31–360. World survey of climatology. Vol. II. Elsevier Scientific Publishing Company, Amsterdam, Netherlands.

BUDGELL, W. P., AND A. EL-SHAARAWI. 1979. Time series modelling of storm surges in a medium sized lake, p. 197–218. *In* J. C. J. Nihoul [ed.] Marine forecasting. Proc. 10th Int. Liège Colloq. Ocean Hydrodyn. Elsevier Scientific Publishing Company, Amsterdam, Netherlands.

BUGDEN, G. 1976. Ice movement and modification in the Gulf of St. Lawrence. M.Sc. thesis, Department of Oceanography, Dalhousie University, Halifax, N.S. 117 p.

BUNKER, A. F., AND L. V. WORTHINGTON. 1976. Energy exchange charts of the North Atlantic Ocean. Bull. Am. Meteorol. Soc. 57: 670–678.

BURNS, B. M. 1973. The climates of the MacKenzie Valley. Beaufort Sea. Vol. 1. Atmospheric Environment Service, Toronto, Ont. 227 p.

BURRIDGE, D. M., AND A. J. GADD. 1976. The Meteorological Office operational 10-level numerical weather prediction model (December 1975). Sci. Pap. No. 34, Meteorol. Off., London, England. 39 p.

BURROUGHS, L. D., AND S. BRAND. 1973. Speed of tropical storms and typhoons after recurvature in the western North Pacific Ocean. J. Appl. Meteorol. 12(3): 452–458.

BURTON, I., R. W. KATES, AND G. F. WHITE. 1978. The environment as a hazard. Oxford University Press, New York, NY. 235 p.

BÜSCHING, F. 1977. Energy spectrum of irregular surface waves, p. 539–559. 15th Int. Coastal Eng. Conf., July 11–17, 1976, Honolulu, HI. ASCE, New York, NY.

1979. Anomalous dispersion of fourier components of surface gravity waves in the near shore area, p. 152–173, 247–267. Proc. 16th Coastal Eng. Conf., Aug. 27–Sept. 3, 1978. Hamburg, W. Germany. ASCE, New York, NY.

BUTLER, H. L. 1979. Coastal flood simulation in stretched coordinates, p. 1030–1048. Proc. 16th Coastal Eng. Conf., Aug. 27–Sept. 3, 1978, Hamburg, W. Germany. ASCE, New York, NY.

CACCHIONE, D. A., AND D. E. DRAKE. 1982. Measurements of storm-generated bottom stresses on the continental shelf. J. Geophys. Res. 87: 1952–1960.

CAHN, A. 1945. An investigation of the free oscillations of a simple current system. J. Meteorol. 2(2): 113–119.

CALDWELL, J. M. 1959. Shore erosion by storm waves. U.S. Beach Erosion Board Misc. Rep. 1-59.

CARDONE, V. J., D. B. ROSS, AND M. R. AHRENS. 1977. An experiment in forecasting hurricane generated sea states, p. 688–695. Proc. 11th Tech. Conf. Hurricanes Trop. Meteorol. Dec. 13–16, 1977, Miami Beach, FL. Am. Meteorol. Soc., Boston, MA.

CARR, J. H. 1952. Long-period waves or surges in harbors, Proc. A.S.C.E. Vol. 7–8, Sep. No. 123: 1–16.

CARRIER, G. F. 1971. The intensification of hurricanes. J. Fluid Mech. 49: 145–158.

CARTWRIGHT, D. E. 1960. Report on the work of the National Institute of Oceanography, October 1959 to April 1960. Adv. Comm. Oceanogr. Meterol. Res., Godalming, U.K.

1968. A unified analysis of tides and surges round North and East Britain. Philos. Trans. R. Soc. London Ser. A 263: 1–55.

CARTWRIGHT, D. E., A. C. EDDEN, R. SPENCER, AND J. M. VASSIE. 1980. The tides of the northeast Atlantic Ocean. Philos. Trans. R. Soc. London Ser. A 298: 87–139.

CARTWRIGHT, D. E., AND C. M. YOUNG. 1974. Seiches and tidal ringing in the sea near Shetland. Proc. R. Soc. London Ser. A: 111–128.

CATCHPOLE, A. J. W., AND D. W. MOODIE. 1974. Changes in the Canadian definitions of break-up and freeze-up. Atmosphere 12(4): 133–138.

CESELSKI, B. F. 1974. Cumulus convection in weak and strong tropical disturbances. J. Atmos. Sci. 31: 1241–1255.

CHAKRAVORTHY, K. C. 1956. Calm centers of storms originating in the Bay of Bengal, p. 171–175. Proc. Trop. Cyclone Symp., Brisbane, Dec. 1956. Bureau of Meteorology, Melbourne, Australia.

CHAKRAVORTHY, K. C., AND S. C. BASU. 1956. How to predict recurvature of storms in the Bay of Bengal, p. 359–365. Proc. Trop. Cyclone Symp., Brisbane, Dec. 1956. Bureau of Meteorology, Melbourne, Australia.

CHAN, H. F. 1976. A study of the characteristics of storm surges at Hong Kong. M.Philos. thesis, University of Hong Kong, Hong Kong.

CHAN, H. F., AND G. O. WALKER. 1979. Empirical studies of the peak surge due to tropical storms at Hong Kong. J. Oceanogr. Soc. Jpn. 35: 110–117.

CHAN, J. C. L., W. C. GRAY, AND S. Q. KIDDER. 1980. Forecasting tropical cyclone turning motion from surrounding wind and temperature fields. Mon. Weather Rev. 108: 778–792.

CHAN, M. Y. 1978. Satellite photographs as an aid to forecast tropical cyclone recurvature. Tech. note 44, Royal Observatory, Hong Kong.

CHANDRASEKHAR, S. 1942. Principles of stellar dynamics. University of Chicago Press, Chicago, IL.

CHANG, C. B., D. J. PERKEY, AND C. W. KREITZBERG. 1981. A numerical case study of the squall line of May 6, 1975. J. Atmos. Sci. 38: 1601–1615.

CHANG, S. W. J. 1981. The impact of satellite-sensed winds on intensity forecasts of tropical cyclones. Mon. Weather Rev. 109: 539–553.

CHANG, S. W. J., AND R. V. MADALA. 1980. Numerical simulation of the influence of sea surface temperature on translating tropical cyclones. J. Atmos. Sci. 37: 2617–2630.

CHARBA, J. 1974. Application of gravity current model to analysis of squall line gust front. Mon. Weather Rev. 102: 140–156.

CHARNEY, J. G. 1947. The dynamics of long waves in a baroclinic westerly current. J. Meteorol. 4(5): 135–162.

1955. The generation of oceanic currents by wind. J. Mar. Res. 14 (4): 477–498.

CHARNEY, J. G., AND A. ELIASSEN. 1964. On the growth of the hurricane depression. J. Atmos. Sci. 21: 68–75.

CHARNOCK, H. 1955. Wind stress on a water surface. Q. J. R. Meteorol. Soc. 81: 639–640.

CHARNOCK, H., AND J. CREASE. 1957. Recent advances in science. North Sea surges. Sci. Prog. 45: 494–511.

CHARNOCK, H., AND T. H. ELLISON. 1967. The boundary layer in relation to large scale motions of the atmosphere and ocean. Proc. Study Conf. G.A.R.P., I.C.S.U./I.U.G.G./W.M.O., and C.O.S.P.A.R./ Appendix 3: 11 p.

CHEN, H. S. 1981. A finite element model of storm surge and circulation for Chesapeake Bay and its Atlantic nearshore, p. 815–819. Oceans '81 conference record. Vol. 2. Institute of Electrical and Electronics Engineers. 1222 p.

CHEN, M., A. ASHLEY, D. DIVOKY, AND L. S. HWANG. 1977. Draft report coastal flooding handbook. Part I: Methodology. Tetra Tech. Rep. TC-612-10-1, Tetra Tech. Inc. Pasadena, CA, May, 1977.

CHENG, R. T. 1972a. Numerical investigation of lake circulation around islands by the finite-element method. Int. J. Num. Methods Eng. 5: 103–112.

1972b. Numerical solution of the Navier–Stokes equations by the finite-element method. Phys. Fluids 15: 2098–2105.

1974. On the study of convective–dispersion equation, p. 29–48. *In* J. T. Oden et al. [ed.] Finite element methods in flow problems. University of Alabama Press, Hunstville, AL.

1978. Modelling of hydraulic systems by finite elernent methods, p. 207–284. *In* V. T. Chow [ed.] Advances in hydroscience. Vol. 11. Academic Press, New York, NY.

CHENG, R. T., T. M. POWELL, AND T. M. DILLON. 1976. Numerical models of wind-driven circulation in lakes. Appl. Math. Model. 1(3): 141–159.

CHENG, R. T., AND C. TUNG. 1970. Wind driven lake circulation by the finite element method, p. 891–903. Proc. 13th Conf. Great Lakes Res. Int. Assoc. Great Lakes Res.

CHENG, T. T. 1967. Storm surges in Hong Kong, p. 1–16. Tech. Note 26, Royal Observatory, Hong Kong.

CHIN, P. C. 1970. The control point method for prediction of tropical cyclone movement. Tech. Note 30, Royal Observatory, Hong Kong. 25 p.

1972. Tropical cyclone climatology for the China Seas and western North Pacific from 1884 to 1970. Report of the Royal Observatory, Hong Kong. 4 p. plus charts.

1976. A diagnostic approach in tropical cyclone movement forecasting by objective techniques. Reprint No. 63, Royal Observatory, Hong Kong. 6 p. plus charts.

1977. The Royal Observatory tropical cyclone prediction program. Occas. Pap. No. 37, Royal Observatory, Hong Kong. 19 p.

CHO, H. A. 1980. Methods of observation of storm surges and astronomical tides. Report to the W.M.O. Workshop on storm surges, Nov. 10–15, 1980, Rangoon. 7 p.

CHOI, B. H. 1980. A tidal model of the Yellow Sea and the eastern China Sea. Report No. 80–0, Korea Ocean Research and Development Institute, Seoul, South Korea. 72 p.

CHOUDHURY, A. M. 1978. Rose petals for tropical cyclones. Nucl. Sci. Appl. Ser. A II: 1–7.

CHOUDHURY, A. M., AND A. ALI. 1974. Prediction of storm surge heights associated with cyclones affecting Bangladesh — a preliminary investigation. Nucl. Sci. Appl. Ser. B 7: 118–120.

CHRISTIANSEN, H., AND W. SIEFERT. 1979. Storm surge prediction by combined wind and tide data, p. 965–974. Proc. 16th Coastal Eng. Conf., Aug. 27–Sept. 3, 1978, Hamburg, W. Germany. ASCE New York, NY.

CHRYSTAL, G. 1905. On the hydrodynamical theory of seiches (with bibliography on seiches). Trans. R. Soc. Edinburgh 41(3): 599–649.

1906. Investigation of the seiches of Loch Earn by the Scottish Loch Surveys, Parts I and II. Trans. R. Soc. Edinburgh 45(2): 361–396.

1908. An investigation of the seiches of Loch Earn by the Scottish Loch Survey. 5. Mathematical appendix on the effect of pressure disturbances upon the seiches in a symmetric parabolic lake. Trans. R. Soc. Edinburgh 46(5): 455–517.

CHU, K. K., S. T. WANG, AND H. P. PAO. 1978. Surface wind fields and moving tracks of typhoons when encountering the Island of Taiwan, p. 84–87. Proc. 11th Tech. Conf. Hurricanes Trop. Meteorol., Dec. 13–16, 1977, Miami Beach, FL. Am. Meteorol. Soc., Boston, MA.

CHUNG, Y. S., K. A. HAGE, AND E. R. REINELT. 1976. On the lee cyclogenesis and airflow in the Canadian Rocky Mountains and the East Asian Mountains. Mon. Weather Rev. 104: 879–891.

CLARK, J. D. 1978a. Rapid developing east Pacific tropical cyclones, p. 642–644. Proc. 11th Tech. Conf. Hurricanes Trop. Meteorol. Dec. 13–16, 1977, Miami Beach, FL. Am. Meteorol. Soc., Boston, MA.

1978b. Rapidly developing eastern North Pacific tropical cyclones. Mar. Weather Log 22 (5): 325–327.

CLARKE, A. J., AND D. S. BATTISTI. 1980. The effects of continental shelves on tides. Ocean Modelling, June 1980. p. 7.

CLARKE, D. J. 1974. Three dimensional storm surge computations. Geophys. J. R. Astron. Soc. 39: 195–199.

CLINE, I. M. 1920. Relation of changes in storm tides on the coast of the Gulf of Mexico to the centre and movement of hurricanes. Mon. Weather Rev. 48: 127–146.

1926. Tropical cyclones. Macmillan and Co., Ltd., New York, NY.

1933. Tides and coastal currents developed by tropical cyclines. Mon. Weather Rev. 61: 36–38.

COLDING, A. 1880. Det. Kong. Dan. Selsk. Skrifter. Natur. Math. (Afh.) 5, Raekke XI, 3: 247.

1881. Det. Kong. Dan. Selsk. Skrifter. (Afh.) 6, Raekke I: 243.

COLE, J. D. 1968. Perturbation methods. *In* Applied mathematics. Blaisdell Press, New York, NY. 260 p.

COLEMAN, F. 1972. Frequencies, tracks and intensities of tropical cyclones in the Australian region 1909–1969. Commonwealth Bureau of Meteorology, Melbourne, Australia. (Meteorological summary)

COLLIER, C. A. 1978. Guidelines for beachfront construction in Florida. Ocean Eng. 5: 309–320.

COLLINS, J. I., AND M. J. VIEHMAN. 1971. A simplified empirical model for hurricane wind felds. Offshore Technol. Conf. Apr. 1971, Houston, TX. (Preprint Vol. 1)

COLUCCI, S. J. 1976. Winter cyclone frequencies over the eastern United States and adjacent western Atlantic. Bull. Am. Meteorol. Soc. 57: 548–553.

CONNOR, J. J., AND C. A. BREBBIA. 1976. Finite elements for fluid flow. Butterworths Press, London, England.

CONNOR, J. J., AND J. D. WANG. 1973. Mathematical models of the Massachusetts Bay. Part I. Finite element modelling of two-dimensional hydrodynamical circulation. Rep. No. 172, Department of Civil Engineering, M.I.T., Cambridge, MA. 57 p.

CONNOR, W. C., R. H. KRAFT, AND D. L. HARRIS. 1957. Empirical methods for forecasting the maximum storm tide due to hurricanes and other tropical storms. Mon. Weather Rev. 85(4): 113–116.

COOPER, C., AND B. PEARCE. 1980. On the forcing mechanisms affecting the bottom shear stress in coastal waters. J. Phys. Oceanogr. 10: 1870–1876.

1982. Numerical simulations of hurricane-generated currents. J. Phys. Oceanogr. 12, 1071–1091.

COOPER, P. F. 1975. Movement and deformation of the landfast ice of the southern Beaufort Sea. Tech. Rep. No. 37, Beaufort Sea Project, Dec. 1975. Department of the Environment, Victoria, B.C. 16 p.

COOPERMAN, A. I., AND H. E. ROSENDAL. 1963. Mean five day pressure pattern of the Great Atlantic Coast Storm, March 1962. Mon. Weather Rev. 91: 337–344.

CORKAN, R. H. 1948. Storm surges: their importance in modern tidal science and some results of a recent investigation, p. 266–271. U.K. Dock and Harbour Authority, Feb. 1948.

CORKAN, R. H. 1950. The levels in the North Sea associated with the storm disturbance of January 8, 1949. Philos. Trans. R. Soc. London Ser. A 242(853): 493–525.

1952. Storm effects in the Irish Sea, p. 170. Proc. I.U.G.G. Gen. Assem., Aug. 1951, Bergen, Proces-Verbaux, No. 5. (Abstr.)

CRANDALL, S. H. 1956. Engineering analysis — a survey of numerical procedures. McGraw-Hill Publications, New York, NY. 417 p.

CRAWFORD, K. C. 1979. Hurricane surge potentials over southeast Louisiana as revealed by a storm surge forecast model: a preliminary study. Bull. Am. Meteorol. Soc. 60(5): 422–429.

CREAN, P. B. 1978. A numerical model of barotropic mixed tides between Vancouver Island and the mainland and its relation to studies of the estuarine circulation, p. 283–313. *In* J. C. J. Nihoul [ed.] Hydrodynamics of estuaries and fjords. Proc. 9th Int. Liège Colloq. Ocean Hydrodyn. Scientific Publishing Company, Amsterdam, Netherlands.

CREASE, J. 1955. Propagation of long waves due to atmospheric disturbances on a rotating sea. Proc. R. Soc. London, Ser. A 233: 556–569.

1956. Long waves on a rotating earth in the presence of a semi-infinite boundary. J. Fluid Mech. 1: 86–96.

CREPON, M. 1974. The influence of wind on sea level. Manuscr. Rep. Mus. Natl. Hist. Nat. Paris. 8 p.

CRESWELL, M. 1928. Wind and tidal height in the Irish Sea. Mar. Obs. 5: 206–213.

1929. Wind and tidal height in the Irish Sea. Mar. Obs. 6: 226–227.

CROWLEY, W. P. 1970. A numerical model for viscous, free surface, barotropic wind driven ocean circulations. J. Comput. Phys. 5: 139–168.

CRUTCHER, H. L. 1971a. Atlantic tropical cyclone statistics. NASA Contract Rep., NASA-CR-61335. George P. Marshall Space Flight Center, Huntsville, AL. 16 p. plus appendices.

1971b. Atlantic tropical cyclone strike probabilities. NASA Contract Rep., NASA-CR-61361. George P. Marshall Space Flight Centre. 13 p. plus 2 appendices.

CRUTCHER, H. L., AND L. R. HOXIT. 1973. South Indian tropical cyclone strike probabilities. U.S. Naval Weather Service Command, Washington, DC. 91 p.

CRUTCHER, H. L., AND M. L. NICODEMUS. 1973. South Indian tropical cyclone vector mean charts. U.S. Naval Weather Service Command, Washington, DC. 56 p.

CRUTCHER, H. L., M. L. NICODEMUS, AND M. J. CHANGERY. 1978. Tropical storm accelerations, p. 466–471. Proc. 11th Tech. Conf. Hurricanes Trop. Meteorol., Dec. 13–16, 1977, Miami Beach, FL. Am. Meteorol. Soc., Boston, MA.

CRUTCHER, H. L., AND G. QUAYLE. 1974. Mariners worldwide climatic guide to tropical storms at sea. Published by the direction of the Commander, U.S. Naval Weather Service Command, NAVAIR, 50-1C-61, Superintendent of Documents, U.S. Government Printing Office, Washington, DC. 114 p. plus 311 charts.

CRUTCHER, H. L., AND F. T. QUINLAN. 1971. Atlantic tropical cyclone vector mean charts. Published by the direction of the Commander, U.S. Naval Weather Service Command, National Climatic Center, Asheville, NC. 7 p. plus charts.

CRY, G. W. 1965. Tropical cyclones of the North Atlantic Ocean. Tech. Pap. No. 55, U.S. Weather Bureau, Washington, DC. 148 p.

CSANADY, G. T., AND P. T. SHAW. 1980. The evolution of a turbulent Ekman layer. J. Geophys. Res. 85: 1537–1547.

DALLAS, W. L. 1891a. Cyclone memoirs — Part IV. Government of India, Calcutta, India.

1891b. An inquiry into the nature and course of storms in the Arabian Sea and a catalogue and brief history of all recorded cyclones in that sea from 1648 to 1889. India Meteorol. Dep. Cyclone Mem. 4: 301–424.

DAMSGAARD, A., AND A. F. DINSMORE. 1975. Numerical simulation of storm surges in bays, p. 1533–1551. Proc. Symp. Model. Techn. Vol. 2, Sept. 3–5, 1975, San Francisco, CA. ASCE, New York, NY.

DANARD, M. B. 1971. A numerical study of the effects of long wave radiation and surface friction on cyclone development. Mon. Weather Rev. 99(11): 831–839.

1977. Computing winds in Barrow Strait, N.W.T., and vicinity. Prepared for C.R.E.P., Department of National Defense, Victoria, B.C., by Atmospheric Dynamics Corporation, R.R.1, Elmira, Ont., Mar. 1977. 24 p.

DANARD, M. B., AND G. E. ELLENTON. 1980. Physical influences on east coast cyclongenesis. Atmosphere–Ocean 18(1): 65–82.

DANARD, M. B., AND G. V. RAO. 1972. Numerical study of the effects of the Great Lakes on a winter cyclone. Mon. Weather Rev. 100(5): 374–382.

D'ARRIGO, A. 1955. The recent damage to the Genoa Breakwater: the effect of sea conditions on vertical walls, p. 53–57. U.K. Dock and Harbour Authority, June 1955.

DAS, P. K. 1972. Prediction model for storm surges in the Bay of Bengal. Nature (London) 239: 211–213.

1980. Storm surges in the Bay of Bengal, p. 171–183. Proc. Symp. Typhoons, Oct. 6–11, 1980, Shanghai, China.

1981. Storm surges in the Bay of Bengal. Proc. Indian Acad. Sa-Eng. 4: 269–276.

DAS, P. K., C. A. GEORGE, AND R. JAMBUNATHAN. 1972. Cyclones and depressions of 1971 — Bay of Bengal and Arabian Sea. Indian J. Meteorol. Geophys. 23: 453–466.

1973. Cyclones and depressions of 1972 — Bay of Bengal and Arabian Sea. Indian J. Meteorol. Geophys. 24: 327–344.

DAS, P. K., M. MIYAZAKI, AND C. P. JELESNIANSKI. 1978. Present techniques of tropical storm surge prediction. W.M.O. No. 500, Geneva, Switzerland. 87 p.

DAS, P. K., M. C. SINHA, AND V. BALASURBRAMANYAM. 1974. Storm surges in the Bay of Bengal. Q. J. R. Meteorol. Soc. 100 (425): 437–449.

DATTA, R. K. 1969. A study on the movement of May cyclonic storms in the Bay of Bengal, Bull. Nat. Inst. Sci. India 38(2): 943–958.

DAVIES, A. M. 1976. A numerical model of the North Sea and its use in choosing locations for the deployment of offshore tide gauges in the JONSDAP 76 oceanographic experiment. Sonderd. Dtsch. Hydrogr. 29(1): 11–24.

1980. Numerical sea model wth two-dimensional and three-dimensional regions dynamically connected. Dtsch. Hydrogr. Z. 33(1): 1937.

1981. Three-dimensional modelling of surges, p. 45–74. *In* D. H. Peregrine [ed.] Floods due to high winds and tides. Academic Press, London. 109 p.

DAVIES, A. M., AND R. A. FLATHER. 1977. Computation of the storm surge of 1 to 6 April 1973, using numerical models of the northwest European continental shelf and the North Sea. Dtsch. Hydrogr. Z. 30(5): 139–162.

1978. Application of numerical models of the Northwest European continental shelf and the North Sea to the computation of storm surges of November to December 1973. Dtsch. Hydrogr. Z. Ergänzunscheft Reihe A, Nr 14: 7–72.

DAVIES, A. M., AND G. K. FURNES. 1980. Observed and computed M_2 tidal currents in the North Sea. J. Phys. Oceanogr. 10: 237–257.

DAVIS, A. B. 1963. Design of hurricane flood protection works in the upper Texas coast, p. 563–577. *In* J. W. Johnson [ed.] Proc. 8th Coastal Eng. Conf., 1962, Mexico City, Mexico. Chap. 33. Council on Wave Resources, The Engineering Foundation, New York, NY.

DAVIS, P. A., W. F. EVANS, R. L. MANCUSO, AND D. E. WOLF. 1976. Height positioning of cloud motions from infra-red tracking, p. 211–213. Proc. Symp. Meteorol. Obs. Space; their contribution to F.G.G.E., COSPAR.

DAWSON, J. 1977. Freak ocean waves are episodic. New Sci. 73(1033): 7–9.

DE, A. C. 1963. Movement of pre-monsoon squall lines over Gangetic West Bengal as observed by radar at Dum Dum Airport. Indian J. Meteorol. Geophys. 14: 37–45.

DEACON, E. L. 1957. Wind profiles and the shearing stress — an anomaly resolved. Q. J. R. Meteorol. Soc. 83: 537–540.

DEAN, C. H. 1969. The attenuation of ocean waves near the ocean/pack ice boundary. Proc. Symp. Antarctic Oceanogr. Science Committee on Antarctic Resources, Santiago, Chile, Sept. 13–16, 1966. W. Heffer, Cambridge, U.K.

DEAN, R. G. 1964. Long wave modification by linear transitions. Proc. Soc. Civ. Eng., Waterways and Harbors Division. 90(WWi): 1–29.

DE ANGELIS, R. M. 1977a. Hurricane alley. Mar. Weather Log 21(1): 16–18.

1977b. Hurricane alley. Mar. Weather Log 21(2): 91–93.

1977c. Hurricane alley. Mar. Weather Log 21(3): 170–173.

1978a. Hurricane alley. Mar. Weather Log 22(1): 21–23.

1978b. Hurricane alley. Mar. Weather Log 22(3): 182–183.

1978c. Hurricane alley. Mar. Weather Log 22(4): 265–266.

1978d. Hurricane alley. Mar. Weather Log 22(5): 337–339.

1979a. Hurricane alley. Mar. Weather Log 23(1): 21–22.

1979b. Hurricane alley. Mar. Weather Log 23(2): 91–94.

1979c. Hurricane alley. Mar. Weather Log 23(4): 247–249.

DEARDORFF, J. W. 1968. Dependence of air–sea transfer coefficients on bulk stability. J. Geophys. Res. 73: 2549–2557.

1972. Parameterization of the planetary boundary layer for use in general circulation models. Mon. Weather Rev. 100: 93–106.

DEBNATH, L., AND A. K. CHATTERJEE. 1979. Nonlinear mathematical model of the propagation of tides in interlacing channels. Comput. Fluids 7: 1–12.

DEFANT, A. 1924. Die Gezeiten des Atlantischen ozeans und des Arktischen Meeres. Ann. Hydrogr. Mar. Meteorol. 52. 153–166, 177–184.

1961. Physical oceanography. Vol. 2. Pergamon Press, Inc., New York, NY. 598 p.

DEMEL, K. 1934. Les oscillations du Niveau de la Mer à Hel (côte polonaise de la battique) en fonction des vents. Kosmos LIX(3): 135–146.

DEPPERMAN, C. E. 1947. Notes on the origin and structure of Philippines typhoons. Bull. Am. Meteorol. Soc. 28: 399–404.

DESAI, B. N. 1967. On the formation, direction of movement and structure of the Arabian Sea cyclone of May 20–29, 1963. Indian J. Meteorol. Geophys. 18(1): 61–68.

DE VEAUX, E. J. 1955. Meteorological trend and the apparent rise in sea level along the South Carolina coast. Mon. Weather Rev. 85(10): 217–224.

DEVRIES, J., AND J. AMOROCHO. 1980. Wind set up effects in large open channels. J. Waterway Port Coastal Ocean Div., Proc. Soc. Civ. Eng. 126 (WW3): 319–334.

DEWOLFE, D. L. 1979. Offshore tidal measurements. Proc Tidal Workshop, Nov. 1–3, 1977, p. 55–61 Manuscr. Rep. No. 52, Marine Sciences Directorate, Ottawa, Ont.

DIAZ, H. F., AND R. G. QUAYLE. 1978. The 1976–1977 winter in the contiguous United States in comparison with past records. Mon. Weather Rev. 103: 1393–1421.

DICKINSON, R. R. 1979. Weather and circulation of August 1979 — Early stages of two destructive Atlantic hurricanes. Mon. Weather Rev. 107: 1558–1564.

DICKSON, R. R., AND J. NAMIAS. 1976. North American influences on the circulation and climate of the North Atlantic sector. Mon. Weather Rev. 104: 1255–1265.

DIETRICH, G. 1944a. Die Gezeiten des Weltmeeresals Geographische Erscheinung. Z. Gesamte Erdk. 3: 69.

1944b. Die Schwingungssysteme der halb und eintägigen Tiden in den ozeanen. Veroeff. Inst. Meereskunde, Univ. Berlin.

DINES, J. S. 1929. Meteorological conditions associated with high tides in the Thames, p. 27–39. Geophys. Mem. No. 47. Meteorological Office, Air Ministry, London, U.K.

DINES, W. H. 1912. Geophysical memoirs. No. 2. Meteorological Office, Air Ministry, London, U.K.

DINGLE, A. N., AND C. YOUNG. 1965. Computer applications in the atmospheric sciences. Rep. to N.S.F., grant G-25204, June 1965., Department of Meteorology and Oceanography, University of Michigan, Ann Arbor, MI. 35 p.

DINGLE, A. N., AND C. YOUNG. 1965. Computer applications in the atmospheric sciences. Rep. to N.S.F., grant G-25204, June 1965, Department of Meteorology and Oceanography, University of Michigan, Ann Arbor, MI. 35 p.

DISNEY, L. P. 1955. Tide heights along the coasts of the United States. Proc. Am. Soc. Civ. Eng. Sep. No. 666, Hydraulics Division. 9 p.

DOBSON, G. M. B. 1963. Exploring the atmosphere. Clarendon Press, Oxford, U.K. 209 p.

DOHLER, G. C. 1967a. The accuracy of tide predictions within Canadian waters. Proc. Symp. Tides, Monaco, Apr. 28–29, 1967, p. 129–153. Organized by the International Hydrographic Bureau, UNESCO Publication.

1967b. Tides in Canadian waters. Department of Energy, Mines, and Resources, Ottawa, Ont. 14 p.

DOLAN, R., B. HAYDEN, AND J. HEYWOOD. 1978a. A new photogrammetric method for determining shoreline erosion. Coastal Eng. 2: 21–39.

1978b. Analysis of coastal erosion and storm surge hazards. Coastal Eng. 2: 41–58.

DONELAN, M. A. 1975. On the coupling between wind and waves. Tech. Rep. Canada Center for Inland Waters, Burlington, Ont. 42 p.

1977. Are aquatic micrometeorologists delivering the goods or is the over-water drag coefficient far from constant? Proc. Symp. Model. Transport Mech. Oceans Lakes. Canada Center for Inland Waters, Burlington, Ont. Oct. 6–8, 1975. Manuscr. Rep. No. 43, Marine Sciences Directorate, Ottawa, Ont.

1979. On the fraction of wind momentum retained by waves, p. 141–159. *In* J. C. J. Nihoul [ed.] Marine forecasting. Elsevier Scientific Publishing Company, Amsterdam, Netherlands.

1982. The dependence of the aerodynamic drag coefficient on wave parameters, p. 381–387. First International Conference on Meteorology and Air–Sea Interaction of the Coastal Zone, The Hague, 1982. Preprints. American Meteorological Society, Massachusetts. 404 p. (Manuscr.)

DONN, W. L. 1958. An empirical basis for forecasting storm tides. Bull. Am. Meteorol. Soc. 39(12): 640–647.

1959. The Great Lakes storm surge of May 5, 1952. J. Geophys. Res. 64(2): 191–198.

DONN, W. L., AND N. K. BALACHANDRAN. 1969. Coupling between moving air pressure disturbance and the sea surface. Tellus 21: 701–706.

DONN, W. L., AND M. EWING. 1956. Stokes' edge waves in Lake Michigan. Science (Washington, DC) 124(3234): 1238–1242.

DONN, W., AND W. T. MCGUINNESS. 1959. Barbados storm swell. J. Geophys. Res. 64(12): 2341–2349.

DONN. W., R. ROMMER, F. PRESS, AND M. EWING. 1954. Atmospheric oscillations and related synoptic patterns. Bull. Am. Meteorol. Soc. 35: 301–309.

DOODSON, A. T. 1924. Meteorological perturbations of sea level and tides. Geophys. Suppl. R. Astron. Soc. London 1: 124–127.

1929. Report on Thames floods, p. 1–26. Geophys. Mem. No. 47. Meteorological Office, Air Ministry, London, U.K.

1947. Storm surges. Int. Hydrogr. Rev. 24: 108–120.

1956. Tides and storm surges in a long uniform gulf. Proc. R. Soc. London Ser. A 237: 325–343.

DOODSON, A. T., AND J. S. DINES. 1929. Meteorological conditions associated with high tides in the Thames. Geophys. Mem. No. 47. U.K. Meteorological Office, London. 26 p.

DOOLEY, H. D. 1971. Some mechanisms for the generation of residual current flow off the Scottish east coast. Dtsch. Hydrogr. Z. 24: 268–283.

DORER, H., AND S. H. LIE. 1973. Surge computation in a navigation canal with lateral offtake — comparison to field measurements, p. 153–158. Proc. C. R. Vol. 5, 15th Congr. Int. Assoc. Hydraul. Res. Istanbul, Turkey.

DOUGLAS, S. K. M. 1929. The line squall and channel wave of July 20, 1929. Meteorol. Mag. 64: 187–189.

DRONKERS, J. J. 1961. The investigations of the tides and storm surges for the Delta Works in the southwestern part of the Netherlands, p. 603–616. *In* J. W. Johnson [ed.] Proc. 7th Coastal Eng. Conf., Aug. 1960, The Hague. Chap 32. Council on Wave Resources, The Engineering Foundation, New York, NY.

DUNN, G. E. 1958. Hurricanes and hurricane tides, p. 19–29. *In* J. W. Johnson [ed.] Proc. 6th Coastal Eng. Conf., Dec. 1957, Florida. Council on Wave Resources, The Engineering Foundation, New York, NY.

DUNN, G. E., AND B. I. MILLER. 1960. Atlantic hurricanes. Louisiana State University Press, Baton Rouge, LA.

DUNNAVAN, G. M., AND J. W. DIERCKS. 1980. An analysis of Supertyphoon Tip, October 1979. Mon. Weather Rev. 108: 1915–1923.

DUNN-CHRISTENSEN, J. T. 1971. Investigation on the practical use of a hydrodynamic numerical model for calculation of sea level variations in the North Sea, the Skageraak and the Kattegat. Dtsch. Hydrogr. Z. 24: 210–227.

1975. The representation of the surface pressure field in a two-dimensional hydrodynamic model for the North Sea, the Skagerrak and the Kattegat. Dtsch. Hydrocr. Z. 28: 97–116.

DURNING, P. J. 1971. Prediction of maximum wave height from historical data. Proc. Offshore Technol. Conf. Pap. No. 1343: 165–172.

DVORAK, V. F. 1973. A technique for the analysis and forecasting of tropical cyclone intensities from satellite pictures. NO.A.A. Tech. Memo. NESS-15, Revision of TM NESS-36, Feb. 1973. 19 p.

1975a. Tropical cyclone intensity analysis and forecasting from satellite imagery. Mon. Weather Rev. 102: 420–430.

1975b. Tropical cyclone intensity analysis and forecasting. Mar. Weather Log 19(4): 199–206.

DVORAK, V. R., AND S. WRIGHT. 1978. Tropical cyclone intensity analysis using enhanced infra-red satellite data, p. 268–273. Proc. 11th Techn. Conf. Hurricanes Trop. Meteorol., Dec. 13–16, 1977, Miami Beach, FL. Am. Meteorol. Soc., Boston, MA.

DVORKIN, E. N., B. A. KAGAN, AND G. P. KLESHYAVA. 1972. The calculation of the tide motions in the Arctic seas. Izv. Akad. Nauk. SSSR Fiz. Atmos. Okeana 8: 298–306. (In Russian)

EADY, E. T. 1949. Long waves and cyclone waves. Tellus 1(3): 33–52.

EASTON, A. K. 1970. The tides of the continent of Australia. Ph.D. thesis, Horace Lamb Center, Flinders University of South Australia, Bedford Park, South Australia. 326 p.

1972. Tides in Hudson Strait. Rep. B1-R-72-6, Bedford Institute of Oceanography, Dartmouth, N.S. 14 p.

EDELMAN, T. 1972. Dune erosion during storm conditions, p. 405–407. Abstr. 13th Int. Conf. Coastal Eng., July 10–14, 1972. Vancouver, B.C.

EDWARDS, K. C. 1953. The storm floods of February 1, 1953, p. 161–164. A note on the River Trent. Proc. Conf. North Sea Floods, London, U.K.

EGEDAL, J. 1957. Some remarks on storm surges in interior Danish waters. Proces Verbaux Assoc. Oceanogr. Phys. Publ. Sci. No. 18: 200–201.

EINARSSON, T. 1972. Discussion. *In* T. Carlsson [ed.] Sea ice. National Research Council of Reykjavik, Iceland.

EKMAN, V. W. 1905. On the influence of the earth's rotation on ocean currents. Ark. Mat. Astron. Fys. 2(4).

1923. Veber Horizontal cirkulation bei winderzeuøgten Meeres Strömungen. Ark. Mat. Astron. Fys. 17: 26.

ELAHI, K. Z., AND K. RASHID. 1981. A mathematical model of the Northern Arabian Sea. Ocean Manage. 6: 149–158.

ELAHI, K. Z., AND J. SÜNDERMANN. 1979. The wind driven circulation in the Northern Arabian Sea. p. 2708–2714. Proc. 16th Coastal Eng. Conf. Aug. 27–Sept. 3, 1978, Hamburg, W. Germany. Vol. 3. Chap. 165. ASCE, New York, NY.

ELIASSEN, A. 1956. A procedure for numerical integration of the primitive equations of the two-parameter model of the atmosphere. Sci. Rep. No. 4, Department of Meteorology, U.C.L.A., Los Angeles, CA. 53 p.

ELIOT, J. 1882. An account of 46 storms in the Bay of Bengal for the period 1877–1881. Indian Meteorol. Mem. 2: 217–448.

1887. An account of 55 storms in the Bay of Bengal for the period 1882–1886. Indian Meteorol. Mem. 4: 163–172.

1890. Handbook of cyclonic storms in the Bay of Bengal. Publ. Indian Meteorol. Dep., Calcutta, India.

1900. Cyclonic storms in the Bay of Bengal. Rep. Indian Meteorol. Dep., Calcutta, India.

ELLIOTT, A. J. 1976. A numerical model of the internal circulation in a branching tidal estuary. Spec. Rep. 54. Chesapeake Bay Institute, Johns Hopkins University (Report 76–7, June 1976). 85 p.

EL-SABH, M. I. 1969. Seasonal hydrographic variations in the Suez Canal after the completion of the Aswan High Dam. Kiel. Meeresforsch. Inst. Meeresk. Univ. XXV (1): 18 p.

ELSBERRY, R. L. 1979. Applications of tropical cyclone models. Bull. Am. Meteorol. Soc. 60(7): 750–762.

ENGEL, M. 1979. Numerical storm surge forecasting, p. 976–985. Proc. 16th Coastal Engineering Conf., Aug. 27–Sept. 3, 1978, Hamburg, W. Germany. Vol. 1. ASCE, New York, NY.

ERASLAN, A. H. 1974. A transient, two-dimensional discrete-element model for far field analysis of thermal discharges in coastal regions. Proc. Conf. Therm. Pollut. Anal., Virginia Polytechnique Institute and State University, Blacksburg, VA.

ESTOQUE, M. A., AND J. M. GROSS. 1979. Diurnal wind and temperature variations over Lake Ontario. Mon. Weather Rev. 106: 1742–1746.

EVA, C., AND L. PAPA. 1978. High frequency loading effects by the Ligurian Sea — A statistical investigation. Phys. Earth Planet. Inter. 16: 352–360.

FABRY, L. 1909. Sur une oscillation de la mer Constatée le 15 juin 1909 dans le port de Marseille. C.R. 149: 324–325.

FAIRBAIRN, L. A. 1954. The semi-diurnal tides along the equator in the Indian Ocean. Philos. Trans. R. Soc. London Ser. A 247(927): 191–212.

FAIRCHILD, J. C. 1956. Model study of wave set-up induced by hurricane waves at Narragansett Pier, Rhode Island. Memo. HUR-7-4, Mar. 1, 1956. Hydrometeorological section, U.S.W.B., Wind over Narragansett and Buzzards Bay in hurricane of September 21, 1938, for aid in consideration of design hurricane.

FALCONER, R. A. 1980. Numerical modelling of tidal circulation in harbors, p. 31–48. J. of the Waterway, Port, Coastal and Ocean Division. Proc. ASCE, Feb. 1980, WWi.

FALLAH, M. H., J. N. SHARMA, AND C. Y. YANG. 1977. Simulation model for storm surge probabilities, p. 934–940. Proc. 15th Coastal Eng. Conf., July 11–17, 1976, Honolulu, HI. ASCE, New York, NY.

FANDRY, C. B. 1981. Development of a numerical model of tidal and wind driven circulation in Bass Strait. Aust. J. Freshwater Res. 32: 9–29.

FARQUHARSON, W. I. 1953. Storm surges on the east coast of England, p. 14–27. Proc. Conf. North Sea Floods.

1970. Tides, tidal streams and currents in the Gulf of St. Lawrence. 2nd ed. Part I. Tides and tidal streams. A.O.L. Rep. 1970–75. Bedford Institute of Oceanography, Dartmouth, N.S. 145 p.

FARRER, L. A. 1958. Wind tides in Lake Okeechobee, p. 134–136. *In* J. W. Johnson [ed.] Proc. 6th Coastal Eng. Conf., Dec. 1957, FL. Chap. 7. Council on Wave Resources, The Engineering Foundation, New York, NY.

FEIT, D. M., AND C. S. BARRIENTOS. 1974. Great Lakes wind forecasts based on model output statistics, p. 725–732. Proc. 17th Conf. Great Lakes Res., Hamilton, Ont.

FEIT, D. M., AND N. A. PORE. 1978. Objective wind forecasting and verification on the Great Lakes. J. Great Lakes Res. 4(1): 10–18.

FERTUK, J., J. W. SHYKER, AND W. H. W. HUSBAND. 1971. Numerical estimation of ice growth as a function of air temperature, wind speed and snow cover. Trans. Can. Soc. Mech. Eng. Tech. Note: 1–6.

FETT, R. W. 1964. Aspects of hurricane structure: new model considerations, suggested TIROS and Project Mercury observations. Mon. Weather Rev. 92(2): 43–60.

FETT, R. W., AND S. BRAND. 1975. Tropical cyclone movement forecasts based on observations from satellites. J. Appl. Meteorol. 14: 452–465.

FINDLATER, J., T. N. S. HARROWER, G. A. HOWKINS, AND H. L. WRIGHT. 1966. Surface and 900 mb wind relationships. Sci. Pap. No. 23. Meteorological Office, London, U.K. 41 p.

FINIZIO, C., S. PALMIERI, AND A. RICCUCCI. 1972. A numerical model of the Adriatic for the prediction of high tides at Venice. Q. J. R. Meteorol. Soc. 98: 86–104.

FINLAYSON, G. A., AND L. E. SCRIVEN. 1965. The method of weighted residuals and its relation to certain variational principles for the analysis of transport processes. Chem. Eng. Sci. 20.

FISCHER, G. 1959. Ein numerisches Verfahren zur Errechnung von Windstau und Gezeiten in Randmeeren. Tellus 11: 60–76.

1965a. A survey of finite difference approximations to the primitive equations. Mon. Weather Rev. 93: 1–10.

1965b. Comments on some problems involved in numerical solutions of tidal hydraulics equations. Mon. Weather Rev. 93: 110–111.

1965c. On a finite difference scheme for solving the primitive equations for a barotropic fluid with application to the boundary current problem. Tellus 17: 405–412.

1979. Results of a 36-hour storm surge prediction of the North Sea for January 3, 1976, on the basis of numerical models. Dtsch. Hydrogr. Z, 32(3): 89–99.

FITZ-ROY, R. 1863. Weather book: a manual of practical meteorology. London, U.K.

FIX, G. J. 1975. Finite element models for ocean circulation problems, S.I.A.M. J. Appl. Math. 29(3): 371–387.

FJELDSTAD, J. E. 1929a. Ein Beitrag zur Theorie der winderzeugh Meeresströmungen (a contribution to the theory of wind generated ocean currents). Gerlands Beitr. Geophys. 9: 237–247.

1929b. Contributions to the dynamics of free progressive tidal waves. Sci. Res. Norweg. North Polar Exped. Maud (1918–1925) 4(3): 3–80.

1930. Ein problem aus der windstrom theorie zeits für Angew. Math. Mem. No. 10: 121–137.

FJORTOFT, R. 1950. Application of integral theorems in deriving criteria of stability of laminar blows and of baroclinic circular vortex. Geofys. Publ. 17(5): 1–52.

FLATHER, R. A. 1976a. Practical aspects of the use of numerical models for storm surge prediction. Rep. No. 30. Institute of Oceanographic Sciences, Bidston, U.K.

1976b. Results from a storm surge prediction model of the northwest European continental shelf for April, November and December 1973. Rep. No. 24. Institute of Oceanographic Sciences, Bidston, U.K. 32 p.

1976c. A tidal model of the northwest European continental shelf. Mem. Soc. R. Sci. Liêge 10: 141–164.

1976d. The development of mathematical models for tides and storm surges in shallow seas, p. 23–48. Mathematical models in geophysics. Proc. Moscow Symp., Aug. 1971. IAHS-AISH Publ. No. 116. 215 p.

1979. Recent results from a storm surge prediction scheme for the North Sea, p. 385–409. *In* J. C. J. Nihoul [ed.] Marine forecasting. Proc. 10th Int. Liège Colloq. Ocean Hydrodyn. Elsevier Oceanography Series No. 25, Amsterdam, Netherlands.

1980. Recent results from a storm surge prediction scheme for the North Sea, p. 385–409. *In* J. C. J. Nihoul [ed.] Proc. 10th Int. Liège Colloq. Ocean Hydrodyn. Elsevier Scientific Publishing Company, Amsterdam, Netherlands.

1981. Practical surge prediction using numerical models, p. 21–43. *In* D. H. Peregrine [ed.] Floods due to high winds and tides. Academic Press, London. 109 p.

FLATHER, R. A., AND A. M. DAVIES. 1975. The application of numerical models to storm surge prediction. Inst. Oceanogr. Sci. Rep. No. 16.

1976. Note on a preliminary scheme for storm surge prediction using numerical models. Q. J. R. Meteorol. Soc., 102(431): 123–132.

1978. On the specification of meteorological forcing in numerical models for North Sea storm surge prediction with application to the surge of January 2–4, 1976. Dtsch. Hydrogr. Z. Reihe A, Nr 15: 7–51.

FLATHER, R. A., AND N. S. HEAPS. 1975. Tidal computations for Morecambe Bay, Geophys. J. R. Astron. Soc. 42: 489–518.

FLATHER, R. A., AND R. PROCTOR. 1982. The west coast surge prediction experiment 1981–82. Inst. Oceanogr. Sci. Rep. 150: 83 p.

1983. Prediction of North Sea storm surges using numerical models: recent developments in the U.K., p. 299–317. *In* J. Sundermann and W. Lenz [ed.] North Sea dynamics. Springer-Verlag, Berlin.

FLATTERY, T. W. 1967. Hough functions. Ph.D. thesis, Department of the Geophysical Sciences, University of Chicago, Chicago, IL. 168 p.

FLIERL, G., AND A. R. ROBINSON. 1972. Deadly surges in the Bay of Bengal, dynamics and storm tide tables. Nature (London) 239: 213–215.

FOFONOFF, N. P. 1962. Dynamics of ocean currents, p. 323–395. *In* M. N. Hill [ed.] The sea. Vol. 1. Physical oceanography. Interscience Publishers, New York, NY.

FOHRBOTER, A. 1979. Frequencies and probabilities of extreme surges: On the time-dependent changes of the probability of extreme storm floods at the German North Sea coast. Proc. of the 16th Coastal Eng. Conf., August 27–Sept. 3, 1978, Hamburg, vol. 1, ASCE, New York, 949–964.

FONG, S. W., AND N. S. HEAPS. 1978. Note on quarter-wave tidal resonance in the Bristol Channel. Inst. Oceanogr. Sci. Rep. No. 63: 11 p. plus figs. (Manuscr.)

FOREL, F. A. 1982. Le Leman (collected papers). Two volumes. Rouge, Lausanne, Switzerland.

FOREMAN, M. G. G., L. M. DELVES, I. BARRODALE, AND R. F. HENRY. 1980. On the use of the Proudman–Heaps tidal theorem. Geophys. J. R. Astron. Sci. 63: 467–478.

FORRISTALL, G. Z. 1974. Three-dimensional structure of storm-generated currents. Geophys. Res. 79(18): 2721–2729.

1978. On the statistical distribution of wave heights in a storm. J. Geophys. Res. 83(C5): 2353–2358.

1980. A two-layer model for hurricane-driven currents on an irregular grid. J. Phys. Oceanogr. 10: 1417–1438.

FORRISTALL, G. Z., R. C. HAMILTON, AND V. J. CARDONE. 1977. Continental shelf currents in tropical storm Delia: observations and theory. J. Phys. Oceanogr. 7: 532–546.

FORTAK, H. 1962. Concerning the general vertically averaged hydrodynamic equations with respect to basic storm surge equations. Natl. Hurricane Res. Project Rep. 51: 70 p.

FORTNER, L. E. 1958. Typhoon Sarah, 1956. Bull. Am. Meteorol. Soc., 39: 633–639.

FORTUNE, M. 1980. Properties of African squall lines inferred from time-lapse satellite imagery. Mon. Weather Rev. 108: 153–168.

FOX, W. T., AND R. A. DAVIS. 1979. Computer model of wind, waves and long shore currents during a coastal storm. Math. Geol. 11(2): 143–164.

FRANCIS, J. R. D. 1951. The aerodynamic drag of a free water surface. Proc. R. Soc. London Ser. A 206: 387.

FRANK, N. L. 1978. Tropical systems — a ten year summary, p. 455–458 Proc. 11th Tech. Conf. Hurricanes Trop. Meteorol., Dec. 13–16, 1977, Miami Beach, FL. Am. Meteorol. Soc., Boston, MA.

FRANK, N. L., AND G. CLARK. 1980. Atlantic tropical system of 1979. Mon. Weather Rev. 108: 966–972.

FRANK, N. L., AND S. A. HUSSAIN. 1971. The deadliest tropical cyclone in history. Bull. Am. Meteorol. Soc. 52: 438–444.

FRANK, W. M. 1977a. The structure and energetics of the tropical cyclone. Part I: Storm structure. Mon. Weather Rev. 105: 1119–1135.

1977b. The structure and energetics of the tropical cyclone. Part II: Dynamics and energetics. Mon. Weather Rev. 105: 1136–1150.

FREEMAN, J. C. 1951. The solution of nonlinear meteorological problems by the method of characteristics, p. 421–433. Compendium of meteorology, Am. Meteorol. Soc., Boston, MA.

FREEMAN, J. C., AND L. BAER. 1956. Graphical computation of storm tides. Report to U.S.W.B., Contact No. CWb-8687. (Unpublished)

1957. The method of wave derivatives. Trans. Am. Geophys. Union 38(4): 483–494.

FREEMAN, J. C., L. BAER, AND G. H. JUNG. 1957. The bathystrophic storm tide. J. Mar. Res. 16: 12–22.

FREEMAN, N. G., P. F. HAMBLIN, AND T. S. MURTY. 1974. Helmholtz resonance in harbours of the Great Lakes, p. 399–411. Proc. 17th Conf. Great Lakes Res. Int. Assoc. Great Lakes Res. Proc. 15: 766 p.

FREEMAN, N. G., AND T. S. MURTY. 1972. A study of a storm surge on Lake Huron, p. 565–582. Proc. 15th Conf. Great Lakes Res.

1976. Numerical modelling of tides in Hudson Bay. J. Fish Res. Board Can. 33: 2345–2361.

FRIEDMAN, D. G. 1975. Computer simulation in natural hazard assessment. Monogr. No. NSF-RS-E-75-002. Institute of Behavioral Science, University of Colorado, Boulder, CO. 194 p.

1977. Assessment of the magnitude of the hurricane hazard, p. 294–301. Proc. 11th Tech. Conf. Hurricanes Trop. Meteorol., Dec. 13–16, 1977, Miami Beach, FL Am. Meteorol. Soc., Boston, MA.

FUJITA, T. 1952. Pressure distribution in a typhoon. Geophys. Mag. 23.

1955. Results of detailed synoptic studies of squall lines. Tellus 4: 405–436.

1959. Precipitation and cold air production in meso-scale thunderstorm systems. J. Meteorol. 16: 454–466.

FUJITA, T., H. NEWTON, AND M. TEPPER. 1956. Mesoanalysis: an important scale in the analysis of weather data. U.S. Weather Bur. Res. Pap. No. 39: 83 p.

FUJITA, T., E. W. PEARL, AND W. E. SHENK. 1975. Satellite-tracked cumulus velocities. J. Appl. Meteorol. 14: 407–413. New York, N.Y.

FUJITA, T., K. WATANOBE, AND T. IZAWA. 1969. Formation and structure of equatorial anticyclones caused by large scale cross-equatorial flows determined by ATS-1. J. Appl. Meteorol. 8: 649–667.

FUJIWHARA, S. 1921. The natural tendency towards symmetry of motion and its application as a principle of meteorology. Q. J. R. Meteorol. Soc. 47: 287–293.

FULKS, J. R. 1951. The instability line, p. 647–652. Compendium of meteorology, Am. Meteorol. Soc., Boston, MA.

FUNK, B. 1980. Hurricane! Natl. Geogr. Sept. 1980: 346–379.

FUNKE, E. R., AND N. L. CROOKSHANK. 1979. A hybrid model of the St. Lawrence River Estuary, p. 2855–2869. Proc. 16th Coastal Eng. Conf., Aug. 27–Sept. 3, 1978, Hamburg, W. Germany.

GABY, D. C., AND K. O. POTEAT. 1973. ATS-3 satellite derived low level winds: a provisional climatology. J. Appl. Meteorol. 12: 1054–1061.

GALLAGHER, B. 1973. Model for nonlinear tides in small basins with openings of restricted depth. J. Hydraul. Res. 78(27): 6395–6400.

GALLAGHER, R. H., AND S. T. K. CHAN. 1973. Higher order finite element analysis of lake circulation. Comp. Fluids 1: 119–132.

GALLAGHER, R. H., J. A. LIGGET, AND S. T. K. CHAN. 1973. Finite element shallow lake circulation analysis. J. Hydraul. Res. Div. ASCE 99(HY7): 1083–1098.

GALLÉ, P. H. 1915. On the relation between the departures from the normal in the strength of the trade winds of the Atlantic Ocean and those in the water level and temperature in the northern European seas. Proc. K. Ned. Akad. Wet. Ser. B Phys. Sci. 17: 1147–1158.

1925. On the relation between wind or current and mean sea level in the Indian and the Atlantic oceans and the adjacent seas. Proc. K. Ned. Akad. Wet. Ser. B Phys. Sci. 28(6–10): 905–918.

GALT, J. A. 1971. A numerical investigation of pressure-induced storm surges over the Continental Shelf. J. Phys. Oceanogr. 1: 82–91.

GARABEDIAN, P. R. 1964. Partial differential equations. John Wiley & Sons, New York, NY. 672 p.

GARCIA, A. W., AND J. R. HOUSTON. 1974. Tsunami run-up prediction for southern California coastal communities. U.S.A. Tsunami Res. Sump., Wellington, New Zealand. R. Soc. N. Z. (and UNESCO) Bull. 15: 5–16.

GARRATT, J. R. 1977. Review of drag coefficients over oceans and continents. Mon. Weather Rev. 105: 915–929.

GARRETT, C. J. R. 1970. Bottomless harbours. J. Fluid Mech. 43(3): 433–449.

1975. Tides in gulfs. Deep-Sea Res. 22: 23–25.

GARRETT, C. J. R., AND D. A. GREENBERG. 1977. Predicting changes in tidal regime: the open boundary problem. J. Phys. Oceanogr. 7(2): 171–187.

GARRIOTT, E. B. 1903. Storms of the Great Lakes. U.S.W.B. Bull. K, Washington, DC. 9 p. plus 968 charts.

GASTRELL, J. E., AND H. F. BLANFORD. 1866. Report on the Calcutta Cyclone on October 5, 1864. Government of India, Calcutta, India.

GATES, L. W. 1959. On the truncation error, stability and convergence of difference solutions of the barotropic vorticity equation. J. Meteorol. 16: 556–568.

GEDNEY, R. T., AND W. LICK. 1972. Wind driven currents in Lake Erie. J. Geophys. Res. 77: 2715–2723.

GEELHOED, P. T. 1973. Negative surges in the southern North Sea. Int. Hydrogr. Rev. L(1): 61–73.

GEISLER, J. E. 1970. Linear theory of the response of a two layer ocean to a moving hurricane. Geophys. Fluid Dyn. 1: 249–272.

GEISLER, J. E., AND R. E. DICKINSON. 1972. The role of variable Coriolis parameter in the propagation of inertia–gravity waves during the process of geostrophic adjustment. J. Phys. Oceanogr. 2: 263–272.

GELCI, R., AND E. DEVILLAZ. 1970. Le calcul numérique de l'état de la mer. Houille Blanche 25: 117–126.

GENTILLI, J. 1971. Climates of Australia and New Zealand, p. 86–222. World survey of climatology. Vol. 13. Elsevier Scientific Publishing Company, Amsterdam, Netherlands.

GENTRY, R. C. 1964. Forecasting the movement of tropical cyclones, p. 683–701. *In* J. W. Hutchings [ed.] Proc. Symp. Trop. Meteorol. New Zealand Meteorological Service, Wellington, N.Z.

GENTRY, R. C., E. RODGERS, J. STERANKA, AND W. E. SHENK. 1978. Equivalent blackbody temperatures of cloud tops and tropical cyclone intensity, p. 274–279. Proc. 11th Tech. Conf. Hurricanes Trop. Meteorol., Dec. 13–16, 1977, Miami Beach, FL. Am. Meteorol. Soc., Boston, MA.

GEORGE, K. J. 1980. Anatomy of an amphidrome. Hydrogr. J. 18: 5–12.

GEORGE, J. E., AND W. M. GRAY. 1977. Tropical cyclone recurvature and nonrecurvature as related to surrounding wind height fields. J. Appl. Meteorol. 16: 34–42.

GEORGE, K. J., AND D. K. THOMAS. 1976. Two notable storm surges of the South coast of England. Hydrogr. J. 2(4): 13–16.

1978. The "Morning Cloud " storm surge in the English Channel. Weather 33: 227–235.

GERRITSEN, F. 1962. Surface wind stress over water as related to wave action. *In* M. A. Alaka [ed.] Proc. 2nd Tech. Conf. Hurricanes, June 27–30, 1961, Miami Beach, FL. Nat. Hurricane Res. Proj. Rep. No. 50. Part I. U.S. Weather Bureau, Washington, DC. 266 p.

GHOSH, S. K. 1977. Prediction of storm surges in the east coast of India. Indian J. Meteorol. Hydrol. Geophys. 28(2): 157–168.

1980. The intensity of the Andhra Cyclone of 1977. Indian Meteorological Department, New Delhi, India. 6 p.

GIBB, J. G. 1976. Coastal erosion along Wellington's west coast. Soil Water 13 (3): 6–7.

1977. Late quaternary sedimentary processes at Ohiwa Harbour, eastern Bay of Plenty, with special reference to property loss. Tech. Publ. No. 5. Water and Soil division, Ministry of Works and Development, Wellington. 16 p.

GILL, S. M. 1975. The discovery of Bangladesh. The Offington Press, Melksham, U.K. 138 p.

GILL, A. E., AND A. J. CLARKE. 1974. Wind-induced upwelling, coastal currents and sea level changes, Deep-Sea Res. 21: 325–345.

GILLIES, D. K. A. 1959. Winds and water levels on Lake Erie. R. Meteorol. Soc., Can. Branch Publ. Vol. 9. No. 1: 12–24. Toronto, Ont.

GILMAN, C. S., AND V. A. MYERS. 1958. Winds and pressures in hurricanes, p. 1–18. *In* J. W. Johnson [ed.] Proc. 6th Conf. Coastal Eng., Dec. 1957, Florida. Council on Wave Research, The Engineering Foundation, New York, NY.

GILMOUR, A. E. 1963. Note on the relation between high sea level and atmospheric pressure at Bluff Harbour, N.Z. J. Geol. Geophys. 6: 582–586.

GJEVIK, B. 1978. Sea level changes along the coast of Norway. Nat. Univ. Forlaget (Oslo) 4: 147–159.

GJEVIK, B., AND L. P. RØED. 1974. Storm surges along the western coast of Norway. Rep. No. 7, Oct. 1974, Institute of Geophysics, University of Oslo, Oslo, Norway.

1976. Storm surges along the western coast of Norway. Tellus 28: 166–182.

GLOVER, R. E., D. J. HEBERT, AND C. R. DAWM. 1953. Application to a hydraulic problem. Trans. Am. Soc. Civ. Eng. 118: 1010–1027.

GODIN, G. 1965a. Some remarks on the tidal motion in a narrow rectangular sea of constant depth. Deep-Sea Res. 12: 461–468.

1965b. The M_2 tide in the Labrador Sea, Davis Strait and Baffin Bay. Deep-Sea Res. 12: 469–477.

1966a. Daily mean sea level and short-period seiches. Int. Hydrogr. Rev. 43: 75–89.

1966b. The tides in the Labrador Sea, Davis Strait and Baffin Bay. Manuscr. Rep. No. 2. Marine Science Branch, Ottawa, Ont. 15 p.

1972. The analysis of tides. University of Toronto Press, Downsview, Ont. 264 p.

1974. The tide in eastern and western James Bay. Arctic 27(2): 104–110.

1975. Les vagues de tempête dans la Baie James. Nat. Can. 102: 219–228.

1977. Identification and classification of tidal records through pattern recognition. Manuscr. Rep. No. 42. Marine Sciences and Information Directorate, Department of Fisheries and Oceans, Ottawa, Ont. 45 p.

1980a. Cotidal charts for Canada. Manuscr. Rep. No. 55. Marine Sciences and Information Directorate, Department of Fisheries and Oceans, Ottawa, Ont. 93 p.

1980b. Modification of the tide in the Canadian Arctic by an ice cover. Manuscr. Rep. No. 56. Marine Sciences and Information Directorate, Department of Fisheries and Oceans, Ottawa, Ont. 29 p.

GODIN, G., AND F. G. BARBER. 1980. Variability of the tide at some sites in the Canadian Arctic. Arctic 33(1): 30–37.

GOFF, R. C. 1975. Thunderstorm outflow kinematics and dynamics. NOAA Tech. Mem. ERL-NSSL-75: 63 p.

GÖHREN, H. 1976. Currents in tidal flats during storm surges, p. 959–970. Proc. 15th Coastal Eng. Conf., July 11–17, 1976, Honolulu, HI. ASCE, New York, NY.

GOLDING, B. 1981. The meteorological input to surge and wave prediction, p. 9–20. *In* D. H. Peregrine [ed.] Floods due to high winds and tides. Academic Press, London. 109 p.

GOLDMAN, J. L., AND T. USHIJIMA. 1974. Decrease in hurricane winds after landfall. J. Struct. Div. 100(STi): 129–141.

GOLDSBOROUGH, G. R. 1913. The dynamical theory of the tides in a polar basin. Proc. London Math. Soc. 14(2): 31–66.

1952. A theory of North Sea surges. Mon. Not. R. Astron. Soc. Geophys. Suppl. 6: 365–371.

GORDON, R. L. 1982. Coastal ocean current response to storm winds. J. Geophys. Res. 87: 1939–1951.

GOUDEAU, D. A., AND W. C. CONNOR. 1968. Storm surge over the Mississippi River Delta accompanying Hurricane Betsy 1965. Mon. Weather Rev. 96(2): 118–124.

GRAF, W. H., AND J. P. PROST. 1979. The aerodynamic drag: experiments on Lake Geneva, p. 303–312. *In* H. Graf and C. H. Mortimer [ed.] Hydrodynamics of lakes. Proc. Symp. Oct. 12–13, 1978, Lausanne, Switzerland. Elsevier Scientific Publishing Company, Amsterdam, Netherlands.

GRAFF, J. 1981. An investigation of the frequency distributions of annual sea level maxima at ports around Great Britain. Estuarine Coastal Shelf Sci. 12: 389–449.

GRAFF, J., AND D. L. BLACKMAN. 1979. Analysis of maximum sea levels in southern England, p. 931–948. Proc. 16th Coastal Eng. Conf., Aug. 27–Sept. 3, 1978, Hamburg, W. Germany. Vol. 1. ASCE, New York, NY.

GRAHAM, H. E., AND D. E. NUNN. 1959. Meteorological considerations pertinent to standard project hurricane, Atlantic and Gulf coasts of the United States. National Hurricane Res. Proj. Rep. No. 33, U.S. Weather Bureau and Army Corps. of Engineers, Washington, DC.

GRAMMELVEDT, A. 1969. A survey of finite difference schemes for the primitive equations for a barotropic fluid. Mon. Weather Rev. 97: 384–404.

GRANT, W. D., AND O. S. MADSEN. 1979. Combined wave and current interaction with a rough bottom. J. Geophys. Res. 84: 1797–1808.

GRAY, W. M. 1978a. Hurricanes: their formation, structure and likely role in the torpical circulation, p. 155–218. *In* D. B. Shaw [ed.] Meteorology over the tropical oceans. Royal Meteorol. Soc., Bracknell, U.K.

1978b. Tropical disturbance to cyclone transformation, p. 27–34. Proc. 11th Tech. Conf. Hurricanes Trop. Meteorol., Dec. 13–16, 1977, Miami Beach, FL. Am. Meteorol. Soc., Boston, MA.

1978c. Tropical cyclone motion and steering flow relationships in the western Atlantic and in the western Pacific, p. 472–477. Proc. 11th Tech. Conf. Hurricanes Trop. Meteorol., Dec. 13–16, 1977, Miami Beach, FL. Am. Meteorol. Soc., Boston, MA.

1978d. Cyclone intensity determination through upper troposphere reconnaissance, p. 288–293. Proc. 11th Tech. Conf. Hurricanes Trop. Meteorol., Dec. 13–16, 1977, Miami Beach, FL. Am. Meteorol. Soc., Boston, MA.

1979. Tropical cyclone intensity determination through upper tropospheric aircraft reconnaissance. Bull. Am. Meteorol. Soc. 60(9): 1069–1074.

GRAY, W. G., AND D. R. LYNCH. 1977. Time stepping schemes for finite element tidal model computations. Adv. Water Resour. 1(2): 83–95.

1979. On the control of noise in finite element tidal computations: a simi-implicit approach. Comput. Fluids 7: 47–67.

GRAY, W. G., AND G. F. PINDER. 1976. On the relationship between the finite element and finite difference methods. Int. J. Numer. Methods Eng. 10: 893–923.

GRAY, W. M., AND D. J. SHEA. 1973. The hurricane's inner core region, II. Thermal stability and dynamical characteristics, J. Appl. Meteorol. 30(8): 1565–1576.

GRECO, L., P. CALCI, AND F. VISIOLI. 1957. The effect of long period waves in ports and their origin. Proc. 19th Int. Navig. Congr. 1957. Sect. II. Communications 1: 119–143.

GREENBERG, D. A. 1975. Mathematical studies of tidal behavior in the Bay of Fundy. Ph.D. thesis, University of Liverpool, Liverpool, U.K. 139 p.

1976. Mathematical description of the Bay of Fundy – Gulf of Maine numerical model. Tech. Note 16, Marine Environmental Data Service, Ottawa, Ont.

1977. Mathematical studies of tidal behavior in the Bay of Fundy. Rep. No. 46, Marine Sciences Directorate, Ottawa, Ont.

1979. A numerical model investigation of tidal phenomena in the Bay of Fundy and Gulf of Maine. Mar. Geod. 2(2): 161–187.

GREENSPAN, H. P. 1956. The generation of edge waves by moving pressure distributions. J. Fluid Mech. 1: 574–592.

1970. A note on edge waves in a stratified fluid. Stud. Appl. Math. 49(4): 381–388.

GRIFFITHS, J. F. 1972. Climates of Africa, p. 80–481. World survey of climatology. Vol. 10. Elsevier Scientific Publishing Company, Amsterdam, Netherlands.

GRIMALDI, M. 1955. Disastrous cyclone damage at Genoa; causes of the breakwater failure examined, p. 117–121. Dock and Harbour Authority, Italy, Aug. 1955.

GROEN, P., AND G. W. GROVES. 1962. Surges, p. 611–646. *In* M. N. Hill [ed.] The sea. Chap. 7. Physical oceanography. Vol. 1. John Wiley & Sons, New York, NY.

GROENING, H. U. 1960. Die tropische zyklone von 2–25 Mai 1959 im Arabischen Meer. Seewart 21(2): 66–72.

GROTKOP, G. 1973. Finite element analysis of long period water waves. Comput. Methods Appl. Mech. Eng. 2(2): 147–157.

GROVE, A. T. 1953. The sea flood on the coasts of Norfolk and Suffolk, p. 164–170. Proc. Conf. North Sea Floods. Institute of Civil Engineers, London, U.K.

GROVER, J. C. 1967. Storm surge effects in the Solomon Islands, p. 43–46. Proc. Symp. Tsunamis Storm Surges, Aug. 25–26, 1966. Committee for the Pacific Science Congress, Tokyo, Japan.

GROVES, G. W., AND G. NIEMEYER. 1975. A numerical simulation of the wind-driven water circulation on the Sunda Shelf. Penelitian Indones. (Mar. Res. Indones.) 14: 31–47.

GUMBEL, E. J. 1958. Statistics of extremes. Columbia University Press, New York, NY. 375 p.

GUNTHER, E. B. 1977. Eastern North Pacific tropical cyclones, 1976. Mar. Weather Log 21(3): 143–154.

1978. Eastern North Pacific tropical cyclones, 1977. Mar. Weather Log 22(3): 157–166.

1979. Eastern North Pacific tropical cyclones, 1978. Mar. Weather Log 23(3): 152–165.

GUPTA, R. N., AND R. K. DATTA. 1971. Tracking tropical storms in the Bay of Bengal by storm analog techniques using computer. Vayer Mandal (continues Indian J. Meteorol. Hydrol. Geophys.) 1: 125–127.

HAIGHT, F. J. 1928. Unusual tidal movements in the Sulu Sea. Mil. Eng. 20: 471–475.

HALL, M. 1916. Notes on hurricanes, earthquakes and other physical occurrences in Jamaica up to the commencement of the Weather Service, 1880, with brief notes in continuation up to the end of 1915. Jam. Meteorol. Serv. No. 455.

HAMBLIN, P. F. 1969. Hydraulic and wind-induced circulation in a model of a Great Lake, p. 567–582. Proc. Great Lakes Conf., International Association for Great Lakes Research, Toronto, Ont.

1972. Some free oscillation of a rotating natural basin. Ph.D. thesis, University of Washington, Seattle, WA. 97 p.

1976. Seiches, circulation and storm surges of an ice-free Lake Winnipeg. J. Fish Res. Board Can. 33: 2377–2391.

1978. Storm surge forecasting methods in enclosed seas. Pap. No. 126. Summ. 16th Int. Conf. Coastal Eng., Aug. 27–Sept. 3, 1978, Hamburg, W. Germany. ASCE, New York, NY.

1979a. An analysis of the wind drag over lakes. Canada Center for Inland Waters, Burlington, Ont. (Unpubl. Rep. June 1979)

1979b. Great Lakes storm surge of April 6, 1979. J. Great Lakes Res. 5(3–4): 312–315.

1979c. Storm surge forecasting methods in enclosed seas, p. 998–1015. Proc. 16th Coastal Eng. Conf. 1978, Hamburg, W. Germany. Vol. 1. Germany. American Society of Civil Engineers, New York, NY. 3060 p.

HAMBLIN, P. F., AND W. P. BUDGELL. 1973. Wind-induced water level changes on the southeastern shoreline of Lake St. Clair. C.C.I.W. Pap. No. 12: 10 p.

HAMILTON, J. 1978. The quarter-diurnal tide in the English Channel. Geophys. J. R. Astron. Soc. 53: 541–552.

1979. Finite difference storm surge prediction. Dtsch. Hydrogr. Z. 32(6): 267–278.

HAMILTON, P. 1975. A numerical model of the vertical circulation of tidal estuaries and its application to the Rotterdam Waterway. Geophys. J. R. Astron. Soc. 40: 1–21.

1976. On the numerical formulation of a time-dependent multilevel model of an estuary, with particular reference to boundary conditions, p. 347–364. *In* M. Valey [ed.] Estuarine processes. Vol. II. Academic Press, New York, NY.

HAMILTON, R. A., AND J. W. ARCHBOLD. 1945. Meteorology of Nigeria and adjacent territory. Q. J. R. Meteorol. Soc. 71: 231–262.

HAMMOND, B. 1980. Developing low pressure areas over the northeastern Pacific: how well are they forecast? Pac. Reg. Tech. Note 80-029, Sept. 12, 1980. Pacific Weather Center, Vancouver, B.C. 5 p.

1981. Developing low pressure areas over the northeastern Pacific: how well are they forecast? Pac. Reg. Tech. Note 81-014, 1981. Pacific Weather Center, Vancouver, B.C. 5 p.

HANSEN, U. A. 1978. Wave set-up in the surf zone, p. 1071–1083. Proc. 16th Coastal Eng. Conf., Aug. 27–Sept. 3, 1978, Hamburg, W. Germany. Vol. 1. ASCE, New York, NY.

HANSEN, W. 1949. Die halbtägigen Gezeiten im Nordatlantisepen Ozean. Dtsch. Hydrogr. Z. 2: 44–61.

1956. Theorie zur Errechnung des Wasserstandes und de Stromüngen in Tandmeeren nebst Anwendungen. Tellus 8: 287–300.

1962. Hydrodynamical methods applied to oceanographic problems, p. 25–34. Proc. Symp. Math. Hydrodyn. Methods Phys. Oceanogr., 1961. Institut für Meereskunde der Universität Hamburg, Hamburg, W. Germany.

1966. The reproduction of the motion of the sea by means of hydrodynamical numerical methods. Mitt. Inst. Meereskund. Univ. Hamburg Nr 5.

HARDER, J. A., AND F. D. MASCH. 1961. Non-linear tidal flows and electric analogues. ASCE J. Waterways Harbors Coastal Eng. Div. 87: 28–39.

HARDER, J. A., AND J. D. NELSON. 1966. Analog modeling the California Delta tidal system. ASCE J. Hydraul. Div. 22: 1–10.

HARDING, J., AND A. A. BINDING. 1978. The specification of wind and pressure fields over the North Sea and some areas of the North Atlantic during 42 gales from the period 1966 to 1976. Inst. Oceanogr. Sci. Rep. No. 55: 17 p. plus appendices. (Manuscr.)

HARLEY, W. S. 1978. Trends and variations of mean temperature in the lower troposphere. Mon. Weather Rev. 106: 413–416.

HARRIS, D. L. 1953. Wind tides and seiches in the Great Lakes, p. 25–51. Proc. 14th Coastal Eng. Conf., Sept. 1953, Chicago, IL.

1956. Some problems involved in the study of storm surges. Natl. Hurricane Res. Proj. Rep. No. 4. U.S. Weather Bureau, Washington, DC. 16 p.

1957a. The effect of a moving pressure disturbance on the water level in a lake. Meteorol. Monogr. 2(10): 46–57.

1957b. The hurricane surge. Proc. 6th Coastal Eng. Conf. Council on Wave Research, The Engineering Foundation, Berkeley, CA.

1958a. The hurricane surge, p. 96–114. *In* J. W. Johnson. Proc. 6th Coastal Eng. Conf., Dec. 1957, Florida. Chap. 5. Council on Wave Research, The Engineering Foundation, Berkeley, CA.

1958b. Hurricane Audrey storm tide. Natl. Hurricane Res. Proj. Rep. No. 23. U.S. Weather Bureau, Washington, DC. 15 p.

1959. An interim hurricane surge forecasting guide. Natl. Hurricane Res. Proj. Rep. No. 32. U.S. Weather Bureau, Washington, DC.

1960. Hurricane Gracie storm surge. Natl. Hurricane Res. Proj. Rep. U.S. National Weather Service, Washington, DC. 20 p.

1961. Comments on "The prediction of hurricane storm tides in New York Bay" by B. W. Wilson, U.S. Army Corps of Engineers, Beach Erosion Board. Tech. Mem. No. 120-A: 1–12.

1962. The equivalence between certain statistical prediction methods and linearized dynamical methods. Mon. Weather Rev. 90: 331–340.

1967. A critical survey of the storm surge prediction problem, p. 47–64. Proc. Symp. Tsunamis Storm Surges. The 11th Pacific Science Congress, Tokyo, 1966. Committee for the Pacific Science Congress, March 1967, Tokyo.

1981. Tides and tidal datums in the United States. Spec. Rep. No. 7, Feb. 1981. Coastal Engineering Research Center, U.S. Army Corps of Engineers. Fort Belvar, Va. 382 p.

HARRIS, D. L., AND A. ANGELO. 1963. A regression model for storm surge prediction. Mon. Weather Rev. 91: 710–726.

HARRIS, D. L., AND C. P. JELESNIANSKI. 1964. Some problems involved in the numerical solutions of tidal hydraulic equations. Mon. Weather Rev. 92: 409–422.

HARRIS, R. A. 1904. Manual of tides. IVb. Report to the superintendent. U.S. Coast and Geodetic Survey, Washington, DC. 313 p.

1908. Seiches in lakes, bays, etc. Manual of tides. Part V. Chap. IX. Appendix 6. U.S. Coast and Geodetic Survey, Washington, DC.

1911. Arctic tides. U.S. Coast and Geodetic Survey, Washington, DC. 103 p.

HARRISON, E. J. 1973. Three-dimensional numerical simulations of tropical storms utilising nested fine grids. J. Atmos. Sci. 30: 1528–1543.

1981. Initial results from the Navy two-way interactive nested tropical cyclone model. Mon. Weather Rev. 109: 173–177.

HARRISON, H. T., AND W. K. ORENDORFF. 1941. Pre-frontal squall lines. United Airlines Meteorol. Circ. No. 16: 12 p.

HASSE, L. 1974a. Note on the surface-to-geostrophic wind relationship from observations in the German Bight. Boundary-Layer Meteorol. 6: 197–201.

1974b. On the surface to geostrophic wind relationship at sea and the stability dependence of the resistance law. Beitr. Phys. Atmos. 47: 45–55.

HASSE, L., AND V. WAGNER. 1971. On the relationship between geostrophic and surface wind at sea. Mon. Weather Rev. 99: 255–260.

HASSELMAN, K. 1982. The Marsen experiment: principal results and conclusions, p. 391. First Int. Conf. Meteorol. Air–Sea Interact. Coastal Zone, 1982, The Hague, Netherlands. American Meteorological Society, Boston, MA. 404 p. (Preprint)

HASSELMAN, K., D. B. ROSS, P. MULLER, AND W. SELL. 1976. A parametric wave prediction model. J. Phys. Oceanogr. 6(2): 200–228.

HAUGH, L. D., AND C. E. P. BOX. 1977. Identification of dynamic regression (distributed lag) models connecting two time series. J. Am. Stat. Soc. 72: 121–130.

HAUGUEL, A. 1978. A combined FE–BIE method for water waves. Pap. No. 115. Summ. 16th Int. Conf. Coastal Eng., Aug. 27–Sept. 3, 1978, Hamburg, W. Germany.

HAURWITZ, B. 1935. The height of tropical cyclones and the eye of the storm. Mon. Weather Rev. 63: 45–49.

1951. The slope of lake surfaces under variable wind stresses. AD699402, Corps of Engineers. Washington, DC. 23 p.

HAURWITZ, B., AND J. M. AUSTIN. 1944. Climatology. McGraw-Hill Publications, New York, NY. 410 p.

HAY, F. M., AND J. LAING. 1954. The storm of January 31–February 1, 1953. Mar. Obs. 24(164): 87–91.

HAYAMI, S., K. YANO, S. ADACHI, AND H. KUNISHI. 1955. Experimental studies on meteorological tsunamis travelling up the rivers and canals in Osaka City, p. 1–47. Bull. No. 9, Disaster Prevention Research Institute, Kyoto University, Kyoto, Japan.

HAYDEN, B. P. 1980. Atlantic coast extratropical cyclones: characteristic frequency patterns and their secular variation, p. 192–197. Second Conf. Coastal Meteorol., Los Angeles, CA. American Meteorological Society, Boston, MA. (Preprint)

1981a. Secular variation in Atlantic coast extratropical cyclones. Mon. Weather Rev. 109: 159–167.

1981b. Cyclone occurrence mapping: equal area or raw frequencies? Mon. Weather Rev. 109: 168–172.

HAYFORD, J. F. 1922. Effects of winds and of barometric pressures on the Great Lakes. Carnegie Institution of Washington, Washington, DC. 133 p. plus 16 plates.

HEAPS, N. S. 1965. Storm surges on a continental shelf. Philos. Trans. R. Soc. London Ser. A 257: 351–383.

1967. Storm surges, oceanography and marine biology. Oceanogr. Mar. Biol. Annu. Rev. 5: 11–47.

1969. A two-dimensional numerical sea model. Philos. Trans. R. Soc. London Ser. A. 275: 93–137.

1972. On the numerical solution of the three-dimensional hydrodynamical equations for tides and storm surges. Mem. Soc. R. Sci. Liège Collect. Huit 2: 143–180.

1973. Three-dimensional numerical model of the Irish Sea. Geophys. J. R. Astron. Soc. 35: 99–120.

1974. Development of a three-dimensional numerical model of the Irish Sea. Rapp. P.-V. Reun. Cons. Int. Explor. Mer. 167: 147–162.

1975. Resonant tidal cooscillations in a narrow gulf. Arch. Meteorol. Geophys. Bioklimatol. Ser. A 24: 361–384.

1977. Development of storm-surge models at Bidston. Inst. Oceanogr. Sci. Rep. No. 53. 30 p. plus figures. (Manuscr.)

1981. Three-dimensional model for tides and surges with vertical eddy viscosity prescribed in two layers. I. Mathematical formulation. Geophys. J. R. Astron. Soc. 64: 291–302.

HEAPS, N. S., AND J. E. JONES. 1975. Storm surge computations for the Irish Sea using a three-dimensional numerical model. Mem. Soc. R. Sci. Liège Collect. Huit 6(7): 289–333.

1979. Recent storm surges in the Irish Sea, p. 285–319. *In* J. C. J. Nihoul [ed.] Marine forecasting. Proc. 10th Liège Colloq. Ocean Hydrodyn. Elsevier Oceanographic Series No. 25, Amsterdam, Netherlands.

1981. Three-dimensional model for tides and surges with vertical eddy viscosity prescribed in two layers. II. Irish Sea with bed friction layer. Geophys. J. R. Astron. Soc. 64: 303–320.

HEATH, R. A. 1974. Sea level oscillations in Wellington Harbour. N.Z. J. Mar. Freshwater Res. 8(2): 403–414.

1975. Surface oscillations of Lake Wakatipu, New Zealand, N.Z. J. Mar. Freshwater Res. 9(2): 223–238.

1978. Atmsopherically induced water motions off the west coast of New Zealand. N.Z. J. Mar. Freshwater Res. 12(4): 381–390.

1979. Significance of storm surges on the New Zealand coast. N.Z. J. Geol. Geophys. 22(2): 259–266.

1981. Variations in the semi-diurnal tidal admittance near New Zealand. Deep-Sea Res. 28A(8): 847–858.

HEATHCOTE, R. L., AND B. G. THOM. 1979. Natural hazards in Australia. Proceedings of a symposium held in May 1976. Australian Academy of Science, Canberra, Australia. 531 p.

HEATHERSHAW, A. D. 1982. Some observations of currents in shallow water during a storm surge. Estuarine Coastal Shelf Sci. 14: 635–648.

HEBERT, P. J. 1979. Empirical techniques, p. 11.3.1–11.3.20. Operational techniques for forecasting tropical cyclone intensity and movement. Chap. 3. WMO No. 528, Geneva, Switzerland.

1980. Atlantic hurricane season of 1979. Mon. Weather Rev. 108: 973–990.

HEFFERMAN, R. F. 1972. Hurricane heat potential of the North Atlantic and North Pacific oceans. M.Sc. thesis, Naval Post Graduate School, Monterey, CA.

HELD, G., AND H. J. C. VAN DEN BERG. 1977. A pre-frontal squall line on November 14, 1975. Arch. Meteorol. Geophys. Bioklimatol. Ser. A 26: 361–379.

HELLAND, A. 1911. Norges land og folk, Romsdals Amt., Kristiania, Norway.

HELLSTROM, B. 1941. Wind effect on lakes and rivers. R. Inst. Technol. Bull. 41. Stockholm, Sweden.

HELMHOLTZ, H. 1888. Über atmosphärische Bewegungen, I. Akad. Ber., Berlin.

1889. Über atmosphärische Bewegungen, II. Akad. Ber., Berlin.

HENDERSON, G., AND N. B. WEBBER. 1977. Storm surge in the U.K. south coast. Dock & Harbour Auth. 58. 21–22.

1978. Waves in a severe storm in the central English Channel. Coastal Eng. 2: 95–110.

HENNING, D. 1962. Computation of a storm surge in the Baltic Sea, p. 257–263. Proc. Symp. Math. Hydrodyn. Methods. Physical Oceanography, University of Hamburg, Hamburg, W. Germany.

HENRY, A. J. 1902. Wind velocity and fluctuations of water level on Lake Erie. Bull. U.S. Weather Bureau, Washington, DC. 22 p. plus 12 charts.

HENRY, R. F. 1974. Storm surges. Interim Rep., Beaufort Sea Project. Institute of Ocean Sciences, Sidney, B.C. 6 p.

1975. Storm surges. Tech. Rep. No. 19, Beaufort Sea Project. Department of the Environment, Victoria, B.C. 41 p.

1982. Automated programming of explicit shallow-water models. Part I. Linearized models with linear or quadratic friction. Pac. Mar. Sci. Rep. 3, Dec. 1981. Institute of Ocean Sciences, Department of Fisheries and Oceans, Victoria, B.C. 70 p.

HENRY, R. F., AND M. G. G. FOREMAN. 1977. Numerical model studies of semi-diumal tides in the southem Beaufort Sea. Pac. Mar. Sci. Rep. 77–11. Institute of Ocean Sciences, Department of Fisheries and Oceans, Victoria, B.C. 71 p.

HENRY, R. F., AND N. S. HEAPS. 1976. Storm surges in the southern Beaufort Sea. J. Fish. Res. Board Can. 33: 2362–2376.

HENRY, R. F., AND T. S. MURTY. 1982. Tides in the Bay of Bengal. p. 541–550. *In* G. A. Keramidas and C. A. Brebbia [ed.] Proc. Int. Conf. Comput. Methods Exp. Meas., June 30–July 2, 1982, Washington, DC. Springer-Verlag, New York, NY.

HERR, D. L. 1944. Final report of the Los Angeles–Long Beach Harbor Surge Investigation at the U.S. Naval Drydocks, Terminal Island, San Pedro, CA.

1945. Pacific Ocean surge in Los Angeles–Long Beach Harbor. J. Am. Soc. Nav. Eng. 57(3): 350–375.

HIDAKA, K. 1932. Explication théorique des seiches dans la Baie d'Ôsaka. Mem. Imp. Mar. Obs. 5: 41–49.

1933. Nonstationary ocean currents. Part I. Mem. Imp. Mar. Obs. 5: 141–266.

1953. Wind-driven sea level change of a shallow sea over a continental shelf. Tech. Rep. No. 9. Department of Oceanography, Texas A&M University, College Station, TX. 24 p.

HIDAKA, K., AND M. YASUI. 1948. On the seiches of Lake Inawashiro. Geophys. Mag. XV(2–4): 45–49.

HIGUCHI, H., H. YASUDA, AND N. HAYAKAWA. 1978. Experimental study on scale effect of tidal model. Pap. No. 113. Summ. 16th Int. Conf. Coastal Eng., Aug. 27–Sept. 3, 1978, Hamburg, W. Germany.

HINSMAN, D. E. 1977. Preliminary results from the Fleet Numerical Weather Central tropical cyclone model. Proc. 3rd Conf. Numer. Weather Predict., Omaha, NB.

HO, F. P. 1976a. Hurricane tide frequencies on the Atlantic coast, p. 886–905. Proc. 14th Coastal Eng. Conf., June 24–28, 1974, Copenhagen, Denmark. ASCE, New York, NY.

1976b. Hurricane tide frequencies on the Atlantic coast, p. 19–22. Abstr. 15th Coastal Eng. Conf., July 11–17, 1976, Honolulu, HI. ASCE, New York, NY.

1977. Hurricane tide frequencies on the Atlantic coast, p. 886–905. Proc. 15th Coastal Eng. Conf., ASCE, New York, NY.

HO, F. P., R. W. SCHWERDT, AND H. B. GOODYEAR. 1975. Some climatological characteristics of hurricanes and tropical storms, gulf and east coast of the United States. Tech. Mem. Natl. Weather Serv. 15: 5 p.

HO, F. P., AND R. J. TRACEY. 1975. Storm tide frequency analysis for the coast of North Carolina, north of Cape Lookout. NOAA Tech. Mem. NWS-HYDRO-27, National Weather Service, Silver Spring, MD. 46 p.

HOBBS, P. V. 1981. The Seattle Workshop on extratropical cyclones: a call for a national cyclone project. Bull. Am. Meteorol. Soc. 62(2): 244–254.

HODUR, R. M. 1981. Operational tropical cyclone model results in the Pacific during 1979. Mon. Weather Rev. 109: 648–652.

HOLLAND, G. J. 1980. An analytic model of the wind and pressure profiles in hurricanes. Mon. Weather Rev. 108: 1212–1218.

1981. Comments on "The numerical modelling of storm surges in the Bay of Bengal" by B. Johns and M. A. Ali. 1980. Q. J. R. Meteorol. Soc. 106: 1–18. Q. J. R. Meteorol. Soc. 107: 268–270.

HOLLAND, G. L. 1969. Some theoretical aspects on the study of storm surges. Rep. No. 11. Marine Sciences Branch, Department of Energy, Mines and Resources, Ottawa, Ont. 85 p.

1970. Effects of the rate of storm growth on subsequent surge elevations. J. Fish. Res. Board Can. 27: 2223–2227.

HOLLIDAY, C. 1969. On the maximum sustained winds occurring in Atlantic hurricanes. E.S.S.A. Tech. Mem. SR-45, U.S. Weather Bureau, Southern Region, Fort Worth, TX. 6 p.

1972. Operations of the joint typhoon warning centre, Mar. Weather Log 16(6): 350–355.

HOLLIDAY, C. R., AND A. H. THOMPSON. 1979. Climatological characteristics of rapidly intensifying typhoons. Mon. Weather Rev. 107: 1022–1034.

HOLLOWAY, J. L. 1958. Smoothing and filtering of time series and space fields. Adv. Geophys. 4: 351–389.

HOLMBOE, J. 1945. Dynamic meteorology. John Wiley & Sons, New York, NY. 378 p.

HOLZ, K. P. 1977. Hybrid models, a study on their principle and realization. Proc. 7th Conf. I.A.H.R. 6: 674–678.

HOMSI, A. 1978. Wave climate in some zones off the Brazilian coast, p. 114–133. Proc. 16th Coastal Eng. Conf., Hamburg, W. Germany. ASCE, New York, NY.

HONSYÙ, K. 1932. Statistical investigation on the effect of winds and air pressure on the height of sea level at some tidal stations in Japan. Geophys. Mag. 6: 123–145.

HOOVER, R. A. 1957. Empirical relationships of the central pressures in hurricanes to the maximum surge and storm tide. Mon. Weather Rev. 85: 167–174.

HOPE, J. R. 1979. Tropical cyclone climatology, p. 1.2.1–1.2.10. Operational techniques for forecasting tropical cyclone intensity and movement. Chap. 2. Rep. No. 528. WMO, Geneva, Switzerland.

HOPE, J. R., AND C. J. NEUMANN. 1969. Climatology of Atlantic tropical cyclones by 2.5 degree latitude/longitude boxes. ESSA Tech. Mem. SR-44, U.S. Weather Bureau, Washington, DC.

1970. An operational technique for relating the movement of existing tropical cyclones to past tracks. Mon. Weather Rev. 98: 925–933.

1978. A survey of world wide tropical cyclone prediction models, p. 367–374. Proc. 11th Tech. Conf. Hurricanes Trop. Meteorol., Dec. 13–16, 1977, Miami Beach, FL. American Meteorological Society, Boston, MA.

HOPLEY, D., AND N. HARVEY. 1979. Regional variation in storm surge characteristics around the Australian coast: a preliminary investigation, p. 164–185. Proc. Conf. Nat. Disasters Australia. Australian Academy of Science, Canberra, Australia.

HORNER, R. W. 1981. Flood prevention works with specific reference to the Thames Barrier, p. 95–106. *In* D. H. Peregrine [ed.] Floods due to high winds and tides. Academic Press, London, U.K. 109 p.

HOSLER, C. L., AND L. A. GAMAGE. 1956. Cyclone frequencies in the United States for the period 1905 to 1954. Mon. Weather Rev. 84: 388–390.

HOUGH, L. D., AND G. F. P. BOX. 1977. Identification of dynamic regression (distributed lag) models connecting two time series. J. Am. Stat. Soc. 72: 121–130.

HOUGHTON, J. T. 1978. The role of satellites in the tropical observing system, p. 261–273. *In* D. B. Shaw [ed.] Meteorology over the tropical oceans. Royal Meteorological Society, Bracknell, U.K.

HOUSTON, J. R. 1978. Interaction of tsunamis with the Hawaii Islands calculated by a finite element numerical model. J. Phys. Oceanogr. 8: 93–102.

HOUZE, R. A. 1977. Structure and dynamics of a tropical squall line system. Mon. Weather Rev. 105: 1540–1567.

HOVERMALE, J. B., AND R. E. LIVEZEY. 1978. Three-year performance characteristics of the NMC hurricane model, p. 122–125. Proc. 11th Tech. Conf. Hurricanes Trop. Meteorol., Dec. 13–16, 1977, Miami Beach, FL. American Meteorological Society, Boston, MA.

HOWARTH, M. J. 1975. Current surges in St. Georges Channel. Estuarine Coastal Mar. Sci. 3: 57–70.

HOWARTH, M. J., AND J. E. JONES. 1981. A comparison of numerical model and observed currents during a storm surge period. Estuarine Coastal Shelf Sci. 12: 655–663.

HUBERT, L. F. 1955. Frictional filling of hurricanes. Bull. Am. Meteorol. Soc. 36(9): 440–445.

1976. Wind determination from geostationary satellites, p. 211–213. Proceedings of a Symposium on Meteorological Observations from Space: their contributions to F.G.G.E., C.O.S.P.A.R.

HUBERT, L. F., AND G. B. CLARK. 1955. The hurricane surge. Interim Rep., June 1955. U.S. Weather Bureau, Washington, DC. 34 p.

HUBERTZ, J. M., AND J. J. WANSTRATH. 1979. A comparison of two numerical storm surge prediction models. Can. Mar. Sci. Dir. Manuscr. Rep. Ser. No. 53: 117–124.

HUEBNER, K. H. 1974. Finite element method — stress analysis and much, much more. Mach. Des. 46: 92–103.

HUGHES, L. A. 1952. On the low-level wind structure of tropical storms. J. Meteorol. 9: 422–428.

1965. The prediction of surges in the southern basin of Lake Michigan. Part III. The operational basis for prediction. Mon. Weather Rev. 93(5): 292–296.

HUGHES, P. 1979. Galveston. It was America's worst natural disaster. Could it happen again? N.O.A.A. 9(3): 8–13.

HUMPHREY, J. H., AND D. E. DORRATCAGUE. 1976. Numerical simulation of storm surges on the Pacific Northwest coast, p. 91–93. Proc. Conf. Coastal Meteorol., Sept. 21–23, 1976. Virginia Beach, VA. American Meteorological Society, Boston, MA.

HUNKINS, K. L. 1965. Tide and storm surge observations in the Chukchi Seas. Limnol. Oceanogr. 10: 29–39.

HUNT, I. A. 1954. The effect of the wind on liquid surfaces. Ph.D. thesis, University of Grenoble, Grenoble, France.

1959. Winds, wind set-ups and seiches on Lake Erie. Res. Rep. Nos. 1 and 2, January 1959. U.S. Lake Survey, Detroit, MI. 59 p.

HUNT, R. D. 1972. North Sea storm surges. Mar. Obs. 42: 115–124.

HUNTER, H. E., E. B. RODGERS, AND W. E. SHENK. 1981. An objective method for forecasting tropical cyclone intensity using Nimbus-5 electrically scanning microwave radiometer measurements. J. Appl. Meteorol. 20: 137–145.

HUNTLEY, J. E., AND J. W. DIERCKS. 1981. The occurrence of vertical tilt in tropical cyclones. Mon. Weather Rev. 109(8): 1689–1700.

HURLEY, J. C. 1954. Statistics on the movement of and deepening of cyclones in the Middlewest. Mon. Weather Rev. 82: 116–122.

HUSTEAD, A. D. 1955. An empirical method of forecasting meteorological produced tidal departures from the normal astronomical tide in the Norfolk, Virginia, tidal basin for a specific wind direction. Intern. Rep. U.S. Weather Bureau, Washington, DC. 5 p.

HUTCHINSON, D. L. 1912. The Saxby Gale, p. 253–259. Transactions of the Royal Canadian Institute for Sciences, Toronto, Ont.

ICHIYE, T. 1949. On the model experiment of a tsunami in the Osaka Bay. Umi-to-Sora 26(5–6): 4–7. (In Japanese)

1950. A note on the friction terms in the equation of ocean currents. Oceanogr. Mag. 2: 49–52.

1962. National Hurricane Research Project Rep. No. 50: 255–266. U.S. Weather Bureau, Washington, DC.

INDIAN METEOROLOGICAL DEPARTMENT. 1964. Tracks of storms and depressions over the Bay of Bengal and the Arabian Sea (1877–1960); also supplement (1961–1970). Indian Meteorological Department, Poona, India.

1979. Tracks of storms and depressions in the Bay of Bengal and the Arabian Sea (1877–1970). Indian Meteorological Department, Poona, India. 186 p. + 2 append.

INTERNATIONAL ASSOCIATION FOR THE PHYSICAL SCIENCES OF THE OCEAN. 1976. Symposium on storm surges. P.-V. Int. Assoc. Phys. Sci. Ocean 14: 166–171.

INTERNATIONAL COUNCIL FOR THE EXPLORATION OF THE SEA. 1962. Mean monthly temperature and salinity of the surface layer of the North Sea and adjacent waters from 1905–1954. Charlottenlund Slot.

IPPEN, A. T., AND D. R. F. HARLEMAN. 1966. Tidal dynamics in estuaries. *In* A. T. Ippen [ed.] Estuary and coastline hydrodynamics. Chap. 10. McGraw-Hill Publications, New York, NY.

IRISH, S. M. 1965. The prediction of surges in the southern basin of Lake Michigan. Part II: A case study of the surge of August 3, 1960. Mon. Weather Rev. 93(5): 282–291.

IRISH, S. M., AND G. W. PLATZMAN. 1961. An investigation of the meteorological conditions associated with extreme wind tides on Lake Erie. U.S. Weather Bur. Tech. Rep. No. 4. Department of Meteorology, University of Chicago, May 1961. 35 p.

1972. An investigation of meteorological conditions associated with extreme wind tides on Lake Erie. Mon. Weather Rev. 90: 39–47.

ISHIGURO, S. 1950. An experimental analysis method for forced oscillations of water in a lake or sea (1st report). Oceanogr. Meteorol. 4(2–4): 59–64.

1956. An electronic method for recording and analysing ocean waves. Parts 1, 2, and 3. Ph.D. thesis, University of Tokyo, Tokyo, Japan. 292 p.

1959. A method of analysis of long wave phenomena in the ocean using electric network models. I. The earth's rotation ignored. Philos. Trans. R. Soc. London Ser. A 251: 303–340.

1962. An electronic analog method for tides and storm surges and some applications to the North Sea, p. 265–269. Proc. Symp. Math. Hydrodyn. Methods Phys. Oceanogr., Hamburg, 1961. Inst. fur Meereskunde, University of Hamburg, Hamburg, W. Germany.

1963. Tidal analogues. Encycl. Dictionary Phys. 7: 351–353.

1966a. Storm surges in the North Sea. Pap. No. 25(III). Advisory Comittee on Oceanographic and Meteorological Research. 57 p.

1966b. Storm surges in the North Sea: an electric model approach. Rep. No. 4. National Institute of Oceanography, Wormley, U.K. 57 p.

1967. Storm surges in the North Sea. Pap. No. 27(III). Advisory Committee on Oceanographic and Meteorological Research. 197 p.

1968. International dictionary of geophysics, p. 1059–1062. Vol. 2. Pergamon Press, London, U.K.

1972a. Electronic analogues in oceanography. Oceanogr. Mar. Biol. Annu. Rev. 10: 27–96.

1972b. An electronic model for tides and storm surges in the North Sea. Institute of Ocean Sciences Internal Report. 234 p.

1976a. Pressure-generated surges in the North Sea. Rep. No. 35. Institute of Oceanographic Sciences, Wormley, U.K. 26 p.

1976b. Highest surge in the North Sea. Rep. No. 36. Institute of Oceanographic Services, Wormley, U.K. 31 p.

ISHIGURO, S., AND A. FUJIKI. 1954. An analysing method for the oscillations of water in a bay or lake, using an electronic analogue computer. Oceanogr. Meteorol. Nagasaki 6: 114–118.

1955. An analytical method for the oscillations of water in a bay or a lake, using an electric network and an electronic analog computer. J. Oceanogr. Soc. Jpn. 11: 191–197.

ISLAM, M. A. 1971. Human adjustment to cyclone hazards: a case study of Char Jabbar. Working paper No. 18. Department of Geography, University of Dacca, Dacca, Bangladesh. 34 p.

ISOZAKI, I. 1970a. An investigation on the variations of sea level due to meteorological disturbances on the coast of the Japanese Islands. 5. Storm surges on the coast of the Kanto and Tokai districts. Pap. Meteorol. Geophys. 21: 1–32.

1970b. An investigation on the variations of sea level due to meteorological disturbances on the coast of the Japanese Islands. 6. Storm surges on the coasts of the Inland Sea and Osaka Bay. Pap. Meteorol. Geophys. 21: 291–322.

1970c. An investigation of the variations of sea level due to meteorological disturbances on the coast of the Japanese Islands. 7. Storm surges on the coast of West Japan facing the Pacific and the East China Sea. Pap. Meteorol. Geophys. 21: 421–448.

ITO, T., M. HIRONO, J. WATANABE, AND K. HINO. 1965. Numerical prediction on typhoon tide in Tokyo Bay, p. 686–712. Chap. 43. Proc. 9th Conf. Coastal Eng., June 1964, Lisbon. ASCE, New York, NY.

ITO, Y., K. TANIMOTO, AND T. KIHARA. 1966. Storm surge in Surugawan Bay. Proc. Res. Inst. Harbor Transp. 95–145.

JACOBSEN, J. P. 1915. Hydrographical investigations in foveroc waters; Cruise of the M/S *Margrethe* in 1913. Kommission HOS C. A. Reitzel, Copenhagen. 47 p.

JAMART, B. M., AND D. F. WINTER. 1978. A new approach to the computation of tidal motions in estuaries, p. 261–282. *In* J. C. J. Nihoul [ed.] Hydrodynamics of estuaries and fjords. Elsevier Oceanography Series No. 23, Amsterdam, The Netherlands.

1979. Finite element computation of the barotropic tides in Night Inlet, B.C., p. 283–290. *In* H. J. Freeland, D. M. Farmer, and C. D. Levings [ed.] Fjord oceanography. Plenum Press, New York, NY. 715 p.

JAMES, R. W. 1974. Dangerous waves along north wall of the Gulf Stream. Mar. Weather Log 18(6): 363–366.

JAMISON, M. V. 1956. Typhoon research and forecasting methods in the 1st weather wing, United States Air Force, p. 97–102. Proc. Trop. Cyclone Symp., December 1956, Brisbane. Bureau of Meteorology, Melbourne, Australia.

JANARDHAN. S. 1967. Storm-induced sea level changes at Saugor Island situated in the north Bay of Bengal. Indian J. Meteorol. Geophys. 18: 205–212.

JANJIC, Z. I. 1974. A stable centered difference scheme free of two-grid interval noise. Mon. Weather Rev. 102: 319–323.

JAPAN METEOROLOGICAL AGENCY. 1977. Outline of operational numerical weather prediction at Electronic Computation Center, Japan Meteorological Agency. 71 p.

JARRELL, J. D., S. BRAND, AND D. S. KIEKLIN. 1978. An analysis of western North Pacific tropical cyclone forecast errors. Mon. Weather Rev. 106: 925–937.

JARRELL, J. D., D. J. MAUCK, AND R. J. RENARD. 1975. Forecasting tropical cyclone motion over the northeastern Pacific by an analog scheme. Mon. Weather Rev. 103: 674–684.

JARRELL, J. D., AND W. L. SOMERVELL. 1970. A computer technique for using typhoon analogs as a forecast aid. Tech. Pap. No. 6–70. U.S. Weather Research Facility, Norfolk, VA. 39 p.

JARRELL, J. D., AND R. A. WAGONER. 1973. The 1972 typhoon analog program, NAVENVPRED-RSCHFAC. Tech. Pap. 1-73. Naval Postgraduate School, Environmental Prediction Research Facility, Monterey, CA. 38 p.

JAYARAMAN, S. 1961. Tests of randomness of occurrence of depressions; storms in the Bay of Bengal. Indian J. Meteorol. Geophys. 12: 529–530.

JEFFREYS, H. 1923. The effect of a steady wind on the sea level near a straight shore. Philos. Mag. 46: 114–125.

JELESNIANSKI, C. P. 1965. A numerical calculation of storm tides induced by a tropical storm impinging on a continental shelf. Mon. Weather Rev. 93: 343–360.

1966. Numerical computations of storm surges without bottom stress. Mon. Weather Rev. 94: 379–394.

1967. Numerical computations of storm surges with bottom stress. Mon. Weather Rev. 95: 740–756.

1970. Bottom stress time history in linearized equations of motion for storm surges. Mon. Weather Rev. 98: 462–478.

1972. SPLASH I. Landfall storms. NOAA Tech. Mem. NWS-TDL-46. NOAA, Washington, DC. 52 p.

1974. SPLASH (Special Program to List Amplitudes of Surges from Hurricanes) II. General track and variant storm conditions. NOAA Tech. Mem. NWS-TDL-52. NOAA, Washington, DC. 50 p.

1976. A sheared coordinate system for storm surge equations of motion with a mildly curved coast. NOAA Tech. Mem. NWS-TDL-61. NOAA, Washington, DC. 52 p.

1978. Storm surges, p. 185–192. *In* Geophysical predictions. National Academy of Sciences, Washington, DC.

1979. Dynamical model to predict storm surges and overload flooding in bays and estuaries, Bull. Am. Met. Soc. 60(10): 1248.

JELESNIANSKI, C. P., AND C. S. BARRIENTOS. 1973. Storm surge model for Puerto Rico. A report to the Federal Insurance Administration, U.S. Department of Housing and Urban Development. 16 p.

1975. A preliminary view of storm surges before and after storm modifications for alongshore moving storms. Techniques Development Lab., NWS-TDL-58. National Weather Service, Silver Spring, MD. 16 p.

JELESNIANSKI, C. P., AND J. CHEN. 1979. SLOSH (Sea, Lake and Overland Surges from Hurricanes). Report of the Techniques Development Laboratory, National Weather Service, Silver Spring, MD.

JELESNIANSKI, C. P., AND A. D. TAYLOR. 1973. A preliminary view of storm surges before and after storm modifications. NOAA Tech. Mem. ERL-WMPO-3. NOAA, Washington, DC. 33 p.

JENKINSON, A. F. 1955. The frequency distribution of the annual maximum (or minimum) values of meteorological elements. Q. J. R. Meteorol. Soc. 81: 158–171.

JENSEN, H. A. P. 1953a. Tidal inundations past and present. Part I. Changing sea level. Weather 8(3): 85–89.

1953b. Tidal inundations past and present. Part II. The extent of the inundation. Weather 8(4): 108–113.

JIN-CHUAN, C., AND C. GUANG. 1979. A dynamic model for hourly predictions of typhoon surges along the southeastern coast of China. Contribution (October 1979) of the Department of Oceanography, Amoy University, Fujian, China. 24 p.

JOHANSEN, S. 1959. On the effect of meteorological conditions upon the height of the sea level at the coast of southern Norway. Meteorol. Ann., 4(14). Det Norske Meteorologiske Institut, Norway.

JOHNS, B., AND A. ALI. 1980. The numerical modelling of storm surges in the Bay of Bengal. Q. J. R. Meteorol. Soc. 106(447): 1–18.

1981. Reply to J. Holland comment on paper by B. Johns and M. A. Ali "The numerical modelling of storm surges in the Bay of Bengal." Q. J. R. Meteorol. Soc. 107: 271–272.

JOHNS, B., S. K. DUBE, U. C. MOHANTY, AND P. C. SINHA. 1981. Numerical simulation of the surge generated by the 1977 Andhra cyclone. Q. J. R. Meteorol. Soc. 107: 919–934.

JOHNSON, D. H. 1964. Weather systems of west and central Africa, p. 339–346. *In* J. W. Hutchings [ed.] Proc. Symp. Trop. Meteorol. New Zealand Meteorol. Service, Wellington, N.Z.

JOINT TYPHOON WARNING CENTER. 1977. Annual typhoon report, U.S. Fleet Weather Central, Joint Typhoon Warning Center, Guam, COMNAVMARINAS, Box 17, FPO San Francisco, CA. 96630. 125 p. (NIIS AD-AOSS)

1978. Western North Pacific typhoons 1977. Mar. Weather Log 22(4): 237–254.

1979. Western North Pacific typhoons 1978. Mar. Weather Log 23(5): 306–319.

1981. Western North Pacific typhoons 1981. Mar. Weather Log 25(4): 237–252.

JONES, R. W. 1977. A nested grid for a three-dimensional model of a tropical cyclone. J. Atmos. Sci. 34: 1528–1553.

JONSSON, I. G. 1965. Friction factor diagrams for oscillatory boundary layers. Coastal Eng. Lab. Tech. Univ. Denmark, Basic Res. Prog. Rep. No. 10: 10–21.

1966. Wave boundary layers and friction factors, p. 127–148. Proc. 10th Conf. Coastal Eng. ASCE, New York, NY.

JORDAN, E. S. 1952. An observational study of upper wind circulation around tropical storms. J. Meteorol. 9(5): 340–346.

JOY, J. W. 1965. U.S. Defence Atomic Support Agency Rep. No. 1678: 128 p.

1966. Practical use of electrical networks to simulate or predict seiche conditions in harbors, p. 87–114. Prog. Santa Barabara Coastal Eng. Conf. 1965. ASCE, New York, NY.

KABBAJ, A., AND C. LEPROVOST. 1980. Nonlinear tidal waves in channels. A perturbation method adapted to the importance of quadratic bottom friction. Tellus 32: 143–163.

KAGAN, B. A. 1967a. A three-dimensional model of the tidal flow in a ice-covered sea. Atmos. Oceanic Phys. 3(5): 526–536.

1967b. Tidal ice drift. Atmos. Oceanic Phys. 3(8): 881–889.

1968. Gidrodinamiceskie modeli prelivnych diviszenij V more (Hydrodynamical models of tidal motion in the sea). Gidrometeorolog. Izd. 218 5 m. Abb., Leningrad, USSR.

KAJIURA, K. 1956. A forced wave caused by atmospheric disturbances in deep water. Tech. Rep. 133-1. Department of Oceanography and Meteorology, Texas A&M University, College Station, TX. 32 p.

1959. A theoretical and empirical study of storm induced water level anomalies. Tech. Rep. 59-23F. Department of Oceanography and Meteorology, Texas A&M University, College Station, TX. 97 p.

1964. On the bottom friction in an oscillatory current. Bull. Earthquake Res. Inst. 42: 147–174.

KASAHARA, A. 1961. A numerical experiment on the development of a tropical cyclone. J. Meteorol. 18: 259–282.

1969. Simulation of the earth's atmosphere. N.C.A.R. Manuscr. 69-27: 42 p.

KAWABATA, Y., AND M. FUJITO. 1951. Elevation of the sea surface caused by typhoons. J. Meteorol. Soc. Jpn. W.N.D. Ser. 29(2): 37–43.

KAWAHARA, M., K. HASEGAWA, AND Y. KAWANAGO. 1977. Periodic tidal flow analysis by finite element perturbation method. Comput. Fluids 5: 175–189.

KAWAHARA, M., S. NAKAZAWA, S. OHMORI, AND T. TAGAKI. 1980. Two-step explicit finite element method for storm surge propagation analysis. Int. J. Numer. Methods Eng. 15: 1129–1148.

KAWAKAMI, N. 1923. The secondary undulations of the oceanic tides in the Bay of Miho. Mem. Kobe Mar. Obs. 1: 131–136.

KEEGAN, T. J. 1958. Arctic synoptic activity in winter. J. Meteorol. 15: 513–521.

KEEN, R. A. 1977. The response of Baffin Bay ice conditions to changes in atmospheric circulation patterns, p. 963–971. *In* D. B. Muggeridge [ed.] Proceedings of the 4th International Conference on Port and Ocean Engineering under Arctic Conditions, Memorial University, Sept. 26–30, 1977, St. John's, Nfld. Vol. 11.

KEERS, J. F. 1968. An empirical investigation of interaction between storm surge and astronomical tide on the east coast of Great Britain. Dtsch. Hydrogr. Z. 21: 118–125.

KEULEGAN, G. H. 1938. Laws of turbulent flow in open channels. J. Res. U.S. Nat. Bur. Stand. 21.

1951. Wind tides in small enclosed channels. J. Res. U.S. Nat. Bur. Stand. 46: 358–381.

1952. The form factor in wind tide formulas. National Bureau of Standards. Rep. No. 1835.

1953. Hydrodynamic effects of gales on Lake Erie. J. Res. U.S. Nat. Bur. Stand. 50: 99–109.

KIBEL, I. A. 1955. On the adaptation of air motion to the geostrophic law. Dokl. Akad. Sci. SSR 104: 60–63. (In Russian)

KIBRIA, A. M. M. 1980. Protection of Bangladesh against cyclone generated surges, p. 759–769. *In* P. Karasudhi, A. S. Balsubramanyam, and W. Karoknukalchou [ed.] Engineering for protection from natural disasters. John Wiley & Sons Ltd., Chichester, U.K.

KIELMANN, J., AND Z. KOWALIK. 1980. A bottom stress formulation for storm surge problems. Oceanol. Acta 3: 51–58.

KING, D. B., AND O. H. SHEMDIN. 1978. Radar observations of hurricane wave directions, p. 209–226. Proc. 16th Coastal Eng. Conf., Hamburg, W. Gemany. Vol. 1. ASCE, New York, NY.

KINSMAN, B. 1965. Wind waves. Prentice-Hall, Englewood Cliffs, NJ. 676 p.

KINTANAR, R. L., L. A. AMADORE, AND R. P. LAO. 1979. Tropical cyclone hazard in the Philippines. Typhoon Moderation Research and Development Office, Philippine Atmospheric, Geophysical and Astronomical Services Administration, Quezon City, Philippines, December 1979, Rep. TM RDO-3: 38 p.

KITAIGORODSKII, S. A. 1968. On the calculation of the aerodynamic roughness of the sea surface. Atmos. Oceanic Phys. 4: 498–502.

KITAIGORODSKII, S. A., AND M. M. ZASLAVSKII. 1974. A dynamical analysis of the drag conditions at the sea surface. Boundary-Layer Meteorol. 6: 53–61.

KIVISILD, H. R. 1954. Wind effects on shallow bodies of water with special reference to Lake Okeechobee. UDC 551.481.115.551.556, Goteborg, Elanders Boktryckeri Aktiebolag.

KLEIN, W. H. 1957. Principal tracks and mean frequencies of cyclones and anticyclones in the Northern Hemisphere. Res. Pap. No. 40. U.S. Weather Bureau, Washington, DC. 22 p. + 72 charts.

1958. The frequency of cyclones and anticyclones in relation to the mean circulation. J. Meteorol. 15: 98–102.

KLEINSTREUER, C., AND J. T. HOLDEMAN. 1980. A triangular finite element mesh generator for fluid dynamic systems of arbitrary geometry. Int. J. Num. Methods Eng. 15: 1325–1334.

KONDO, H., K. SAITO, Y. MAMIYA, AND M. HARA. 1982. On the conservation of the energy of low-frequency waves in iterative time integration schemes. J. Meteorol. Soc. Jpn. 60(2): 824–829.

KOOPMAN, G. 1963. Schwallerscheinungenam October 16–17, 1963, in der Deutschen Bucht. Dtsch. Hydrogr. Z. 16: 231.

KORSHOVER, J. 1967. Climatology of stagnating anticyclones east of the Rocky Mountains, 1936–1965. Public Health Service Publ. No. 999-AP-34. U.S. Department of Health, Education, and Welfare.

KOTESWARAM, P. 1961. Cloud patterns in a tropical cyclone in the Arabian Sea viewed by TIROS I meteorological satellite. Inst. Geophys. Sci. Rep. No. 2, contract AF10-604-6156. University of Hawaii.

KOTESWARAM, P., AND S. GASPER. 1956. The surface structure of tropical cyclones in the Indian Area. Indian J. Meteorol. Geophys. 7(4): 339–352.

KOWALIK, Z. 1969. Wind-driven circulation in a shallow sea with application to the Baltic Sea. Acta Geophys. Pol. 17(1): 13–38.

1972. Wind-driven circulation in a shallow stratified sea. Sonderd. Dtsch. Hydrogr. Z. 25(6): 265–278.

KOWALIK, Z., AND N. BICH HUNG. 1977. On a system of hydrodynamic equations for certain oceanographical problems in the region of the earth's pole and the stability of its solution. Oceanologia 7: 5–20.

KOWALIK, Z., AND N. UNTERSTEINER. 1978. A study of the M_2 tide in the Arctic Ocean. Dtsch. Hydrogr. Z. 31(6): 216–229.

KRAFT, R. H. 1961. The hurricane's central pressure and highest wind. Mar. Weather Log 5: 157.

KRAMER, J. 1976. Safety of dykes against storm floods and wave run-up; p. 23–25. Abstr. 15th Coastal Eng. Conf., July 11–17, 1976, Honolulu, HI. ASCE, New York, NY.

KRAMER, M. P. 1955. Bibliography on storm surges. Am. Meteorol. Soc. 6(3).

KRAUSS, E. B. 1967. Wind stress along the sea surface, p. 13–255. *In* H. E. Landsberg and J. van Miegham [ed.] Advances in geophysics. Vol. 12. Academic Press, New York, NY.

1972. Atmosphere–ocean interaction. Clarendon Press, Oxford, U.K.

1978. The response of a stratified viscous sea to moving meterological fronts and squall lines. Dtsch. Hydrogr. Z. 31(1): 16–29.

KRISHNAMURTI, T. N., M. KANAMITSU, B. CESELSKI, AND M. B. MATHUR. 1973. Florida State University's tropical prediction model. Tellus 25: 523–535.

KRISHNAMURTI, T. N., R. J. PASCH, AND P. ARDANUY. 1980. Prediction of African waves and specification of squall lines. Tellus 32: 215–231.

KREUGER, D. W. 1959. A relation between the mass circulation through hurricanes and their intensity. Bull. Am. Meteorol. Soc. 40(4): 182–189.

KRÜGER, G. 1910. Über Sturmfluten an den Deutschen Küsten der westlichen Ostee. XII. Japresberiept der Geogriges. zw. Greifswald.

KULLENBERG, G. E. B. 1976. On vertical mixing and the energy transfer from the wind to the water. Tellus 28: 159–165.

KUMAR, S., AND K. PRASAD. 1973. An objective method for the prediction of tropical storm movement in the Indian Seas. Indian J. Meteorol. Hydrol. Geophys. 24(1): 31–34.

KUO, H. L. 1949. Dynamic instability of two-dimensional nondivergent flow in a barotropic atmosphere. J. Meteorol. 6(2): 105–122.

1965. On the formation and intensification of tropical cyclones through latent heat release by cumulus convection. J. Atmos. Sci. 22: 40–63.

KUO, H. L., AND T. ICHIYE. 1977. A numerical study of the response of a barotropic ocean to a moving hurricane. Tellus 29: 561–571.

KURIHARA, Y. 1965a. On the use of implicit and iterative methods for the time integration of the wave equation. Mon. Weather Rev. 93: 33–46.

1965b. Budget analysis of a tropical cyclone simulated in an axisymmetric numerical model. J. Atmos. Sci. 22: 25–59.

KURIHARA, Y., AND M. A. BENDER. 1980. Use of a movable nested mesh model for tracking a small vortex. Mon. Weather Rev. 108: 1792–1809.

KURIHARA, Y., AND R. E. TULEYA. 1974. Structure of a tropical cyclone developed in a three dimensional numerical simulation model. J. Atmos. Sci. 31: 893–919.

1981. A numerical simulation study of the genesis of a tropical storm. Mon. Weather Rev. 109(8): 1629–1653.

KUSSMAN, A. S. 1957. The storm surge problem in New York City, p. 751–763. Proceedings of the New York Academy of Science, Section of Oceanography and Meteorology, New York, NY.

KWIZAK, M., AND A. J. ROBERT. 1971. A semi-implicit scheme for grid point atmospheric models of the primitive equations. Mon. Weather Rev. 99: 32–36.

LACOUR, D. 1917a. Conditions anormales du niveau de la mer dans les eaux danoises les 15 et 16 janvier 1916, p. 30–117. Annales de la Commission des Raz-de-Marée. Publikationer fra det danske meteorologiske Institut Middelelser, Nr 4. Copenhagen, Denmark.

1917b. Sur la variation du niveau moyen de la mer à Brest (France) en fonction de la pression atmospherique, p. 22–34. Annales de la Commission des Raz-de-Marée. Publikationer fra det danske meteorologiske Institut Middelelser, Nr 4. Copenhagen, Denmark.

1917c. Raz de Marée aux Pays-Bas et leurs previsions, p. 116–129. Annales de la Commission des Raz-de-Marée. Publikationer fra det danske meteorologiske Institut Meddelelser, Nr 4. Copenhagen, Denmark.

1932. Conditions anormales du niveau de la mer dans les lava danoises les 15 et 16 janvier 1916. Ann. Comm. Raz-de-Marée 2: 30–117.

1935. Madagascar: note sur les marés et courants cotiers produits apr les cyclones tropicaux. Ann. Comm. Raz-de-Marée 5: 67–89.

LAGRANGE, J. L. 1781. Memoire sur la théorie du mouvement des fluides. Nouv. Mem. Acad. R. Berlin, Oeuvres 4.

LAJOIE, F. A., AND N. NICHOLLS. 1974. A relationship between the direction of movement of tropical cyclones and the structure of their cloud systems. Tech. Rep. No. 11: 22 p. Bureau of Meteorology, Australia.

LAKTIONOV, A. F. 1960. K. Voprosu o Vliyanii l'da na Prilivno-Otlivnyye Yavleniya (The problem of the effect of ice on tidal phenomena). Problemy Arktiki i Antarktiki (Leningrad) No. 5: 53–58. Translated by M. Shessers, U.S. Naval Oceanographic Office, Washington, DC. 11 p.

LAM, D. C. L. 1977. Comparison of finite element and finite difference methods for nearshore advection–diffusion transport models, p. 115–129. *In* W. G. Gray, G. F. Pinder, and C. A. Brebbia [ed.] Finite elements in water resources. Pentech Press, London, U.K.

LAMB, H. 1945. Hydrodynamics. Dover, New York. 738 p.

1953. Hydrodynamics. 6th ed. Cambridge University Press, London and New York. 590 p.

1980. Climate fluctuations in historical times and their connexion with transgressions of the sea, storm floods and other coastal changes, p. 251–290. *In* A. Verhulst and M. K. E. Gottschalk [ed.] Transgressies en Occupatiegeschiedenis in de kustgebieden van Nederland en Belgie. Belgisches Centrum voor Landelijke Geschiedenis Publ. No. 66.

LAMMING, S. D. 1975. Some characteristics of hurricanes in the western Caribbean. Meteorol. Inst., Barbados, West Indies. 24 p.

LANDSBERG, H. E. 1978. Geophysical predictions: overview and recommendations. Eos 59(7): 710–718.

LANE, F. W. 1965. The elements rage, p. 1–38. Chilton Co., Philadelphia, PA.

LANGERAK, A., M. A. M. DERAS, AND J. J. LEENDERTSE. 1979. Adjustment and verification of the Randdelta II model, p. 1049–1069. Proc. 16th Coastal Eng. Conf., Aug. 27–Sept. 3, 1978, Hamburg, W. Germany. Vol. 1. ASCE, New York, NY.

LANGHAAR, H. L. 1951. Wind tides in inland waters, p. 278–296. Proc. 1st Mid-winter Conf. Fluid Dyn. J. W. Edwards and Co., Ann Arbor, MI.

LAPPO, S. S., AND A. Y. ROZHDESTVENSKIY. 1977. An estimate of the energy transferred to the ocean by a moving atmospheric pressure disturbance. Atmos. Oceanic Phys. 13(2): 120–124.

1979. Calculation of the energy transferred by the atmosphere to a meteorological ocean tide. Atmos. Oceanic Phys. 15(12): 907–911.

LARSON, S., AND T. LAEVASTU. 1969. Numerical analysis and forecasting of sea and swell in semi-enclosed seas and in coastal areas with actual examples for the South China Sea and the Mediterranean Sea. Tech. Note No. 50, July 1969. Fleet Numerical Weather Central, Monterey, CA. 18 p.

LAU, R. 1977. Report on the Tolo Harbour storm surge numerical modelling investigation. Physical Oceanography Unit, Royal Observatory, Hong Kong.

1980a. Storm surge investigations and the use of vertically integrated hydrodynamical models. Tech. Note No. 53, Jan. 1980. Royal Observatory, Hong Kong. 42 p.

1980b. Evaluating peak storm surge heights and high sea levels from SPLASH outputs. Tech. Note No. 54, Feb. 1980. Royal Observatory, Hong Kong. 30 p.

LAUWERIER, H. A. 1955. The motion of a shallow sea under influence of a nonstationary wind. Math. Cent. Rep. TW 31. Amsterdam, The Netherlands.

1957a. Rapp. Afd. Toegep. Math. Cent. Rep. TW 41. Amsterdam, The Netherlands. 31 p.

1957b. Exponential wind fields. Math. Cent. Rep. TW 42. Amsterdam, The Netherlands. 9 p.

1962. Some recent work of the Amsterdam Mathematical Center on the hydrodynamics of the North Sea, p. 13–24. Proc. Symp. Math. Hydrodyn. Math. Phys. Ocean. University of Hamburg, Hamburg, W. Germany.

LAUWERIER, H. A., AND B. R. DAMSTÉ. 1963. The North Sea problem. 8. A numerical treatment. Proc. K. Ned. Akad. Wet. Ser. A 66: 167.

LAW, C. R. 1975. Storm surges in the English Channel. Hydrogr. J. 2: 30–34.

LAWFORD, R. G. 1977. A study of meteorological events which occurred on March 17th and 18th, 1973, in the vicinity of Goderich, Ontario. Int. Rep. SSU-77-6. Ontario Region of Atmospheric Environment Service. 19 p.

LAWRENCE, M. B. 1977. North Atlantic tropical cyclones, 1976. Mar. Weather Log 21(2): 63–72.

1978a. North Atlantic tropical cyclones, 1977. Mar. Weather Log 22(2): 79–84.

1978b. Atlantic hurricane season of 1977. Mon. Weather Rev. 106: 534–545.

1979a. Atlantic hurricane season for 1978. Mon. Weather Rev. 107: 477–491.

1979b. North Atlantic tropical cyclones, 1978. Mar. Weather Log 23(2): 76–85.

LAX, P., AND R. RICHTMEYER. 1956. Survey of the stability of linear finite difference equations. Commun. Pure Appl. Math. 9: 267–293.

LAX, P. D., AND B. WENDROFF. 1960. Systems of conservation laws. Commun. Pure Appl. Math. 13: 217–237.

LEAHY, T. M. 1979. Disaster preparedness for Floridians. NOAA Tech. Rep. NMFS Circ. (3): 16–19.

LEBLOND, P. H., AND L. A. MYSAK. 1978. Waves in the ocean. Elsevier Oceanography Series 20, Amsterdam, The Netherlands. 602 p.

LEE, J. J., AND F. RAICHLEN. 1972. Oscillations in harbors with connected basins. J. Waterways Harbors Coastal Eng. Div. Proc. ASCE Issue WWZ, Aug. 1972. Vol. 98: 311–332.

LEENDERTSE, J. J. 1967. Aspects of a computational model for long-period water wave propagation. RM-5294-PR, May 1967. The Rand Corporation, Santa Monica, CA.

1970. A water quality simulation model for well mixed estuaries and coastal seas. Vol. I. Principles of computation. RM 6230-RC, Feb. 1970. The Rand Corporation, Santa Monica, CA.

LEENDERTSE, J. J., AND E. C. GRITTON. 1971. A water quality simulation model for well mixed estuaries and coastal seas. Vol. II. Principles of computation. RM-6230-RC. The Rand Corporation, New York. R-708-NJC.

LEIMKUHLER, W., J. J. CONNOR, J. WANG, G. CHRISTODOWLOW, AND S. SUNDGREN. 1975. Two-dimensional finite element dispersion model, p. 1467–1486. Proc. Symp. Model. Tech. Volume II. Sept. 3–5, 1975, San Francisco, CA. ASCE, New York, NY.

LEIPPER, D. F., AND J. JENSEN. 1971. Changes in energy input from the sea into hurricanes. Bull. Am. Meteorol. Soc. 52: 9–28.

LEIPPER, D. F., AND D. VOLGENAU. 1972. Hurricane heat potential of the Gulf of Mexico. J. Phys. Oceanogr. 2: 218–224.

LEITH, C. E. 1965. Numerical simulation of the earth's atmosphere. Math. Comp. Phys. 4: 1–28.

LENNON, G. W. 1963. The identification of weather conditions associated with the generation of major storm surges along the west coast of the British Isles. Q. J. R. Meteorol. Soc. 89: 381–394.

1971. Sea Level instrumentation, its limitations and the optimization of the performance of conventional gauges in Great Britain. Int. Hydrog. Rev. 48(2): 129–147.

LE PROVOST, C. 1978. A new approach for tidal computations, p. 1104–1121. Summ. 16th Int. Conf. Coastal Eng., Aug. 27–Sept. 3, 1978, Hamburg, W. Germany. Pap. No. 112.

LETTAU, V. H. 1932. Seiches des Frishehen Haffes. Ann. Hydrogr. Mar. Meteorol. 229–240.

LEVESQUE, L. 1977. Étude du modèle mathématique de la propagation des marées dans l'estuaire du Saint-Laurent. Cahier d'information No. 2. Section d'Oceanographie, Université du Québec à Rimouski, Rimouski, Que. 161 p.

LEY, G. W., AND R. L. ELSBERRY. 1976. Forecasts of Typhoon Irma using a nested grid model. Mon. Weather Rev. 104: 1154–1161.

LIECHTY, K. R. 1972. Intensity changes of tropical cyclones in the western North Pacific Ocean during 1960–69. M.Sc. thesis, Naval Postgraduate School. 136 p.

LIEK, W. 1976. Numerical models of lake currents. Ecol. Ser. EPA-600/3-76-020. U.S. Environmental Protection Agency, Washington, DC. 140 p.

LIGHTHILL, J., AND R. P. PEARCE [ed.] 1981. Monsoon dynamics. Cambridge University Press, Cambridge, U.K. 735 p.

LIGHTHILL, M. J. 1969a. Dynamic response of the Indian Ocean to onset of the southwest monsoon. Philos. Trans. R. Soc. London Ser. A 265: 45–92.

1969b. Unsteady wind-driven ocean currents. Q. J. R. Meteorol. Soc. 95: 675–688.

LILAND, D. M. 1975. Surges in ice covered channels. M.Sc. thesis, University of Alberta, Calgary, Alta. 108 p.

LILLY, D. K. 1961. A proposed staggered grid system for numerical integration of dynamic equations. Commun. Pure Appl. Math. 9: 267–293.

1965. On the computational stability of numerical solutions of time-dependent nonlinear geophysical fluid dynamics problems. Mon. Weather Rev. 93: 11–26.

1979. The dynamical structure and evolution of thunderstorms and squall lines. Annu. Rev. Earth Planet. Sci. 7: 117–161.

LINDSTRÖM, M. 1979. Storm surge turbation. Sedimentology 26: 115–124.

LINSLEY, R. K., M. A. KOHLER, AND J. L. H. PAULHUS. 1949. Applied hydrology. McGraw-Hill Publications, New York, NY. 689 p.

LISITZIN, E. 1974. Sea level changes. Elsevier Oceanographic Series No. 8, New York, NY. 273 p.

LIU, S. K., AND J. J. LEENDERTSE. 1979. A three-dimensional model for estuaries and coastal seas. Vol. VI. Bristol Bay simulations. R-2405-NOAA, Sept. 1979. The Rand Corporation, Santa Monica, CA. 121 p.

LONG, B. L. 1979. Forecasting hurricane waves. Mar. Weather Log 23(1): 1–10.

LONGUET-HIGGINS, M. S., AND R. W. STEWART. 1962. Radiation stress and mass transport in gravity waves with application to surf betas. J. Fluid Mech. 13: 481–504.

1963. A note on wave set-up. J. Mar. Res. 21: 4–10.

1964. Radiation stress in water waves: a physical discussion with applications. Deep-Sea Res. 11: 529–562.

LOOMIS, H. G. 1970. A method of setting up the eigenvalue problem for the linear, shallow water wave equation for irregular bodies of water with variable water depth and application to bays and harbors in Hawaii. Hawaii Inst. Geophys. HIG-70-32, NOAA-JTRE-16. 9 p.

1972. A package program for time-stepping long waves into coastal regions with application to Haleiwa Harbor, Oahu. Hawaii Inst. Geophys. HIG-72-21, NOAA-JTRE-79. 33 p.

1973. A new method for determining normal modes of irregular bodies of water with variable depth. Hawaii Inst. Geophys. HIG-73-10, NOAA-JTRE-86. 27 p.

LUDLAM, D. M. 1963. Early American hurricanes 1492–1870. American Meteorological Society, Boston, MA. 198 p.

LUNDBAK, A. 1956. The North Sea storm surge of February 1, 1953: its origin and development. Int. Hydrogr. Rev. 33(1): 185–196.

LWIN, T. 1980. Review of methods of storm surge prediction currently used in Burma. Report to the W.M.O. Workshop on storm surges, Nov. 10–15, 1980. Rangoon, Burma. 8 p.

LYDOLPH, P. E. 1977. Climates of the Soviet Union, p. 17–196. *In* World Survey of Climatology. Vol. 7. Elsevier Press, Amsterdam, The Netherlands.

LYNCH, D. R. 1980. Moving boundary numerical surge model. J. Waterway Port Coastal Ocean Div. Proc. 106 (WW3): 425–428.

LYNCH, D. R., AND W. G. GRAY. 1978a. Finite element simulation of shallow water problems with moving boundaries. Resource Policy Center, Thayer School of Engineering, Dartmouth College, Hanover, N.H., DSD No. 221. *Reprinted from* C. Brebbia, W. G. Gray, and G. F. Pinder [ed.] Finite elements in water resources II. Pentech Press Limited, Plymouth, U.K. 20 p.

1978b. Analytic solutions for computer flow model testing, J. Hydraul. Div. HY10. Proc. Am. Soc. Civ. Eng. 1409–1428.

1979. A wave equation model for finite element tidal computations. Comput. Fluids 7: 207–228.

1980a. An explicit model for two-dimensional tidal circulation in triangular finite element elements. WAVETL User's Manual, U.S. Geological Survey, Water Resources Investigations 80-42: 63 p.

1980b. Finite element simulation of flow in deforming regions. J. Comput. Phys. 36(2): 135–153.

LYNDE, R. E. 1976. Storm tides along the New England coast, p. 88–90. Proc. Conf. Coastal Meteorol, Sept. 21–23, 1976, Virginia Beach, VA. American Meteorological Society, Boston, MA.

MACKEY, G. W., AND H. E. WHITTINGHAM. 1956. Sea and swell in tropical cyclones, p. 413–431. Proc. Trop. Cyclone Symp., Dec. 1956, Brisbane. Bureau of Meteorology, Melbourne, Australia.

MADALA, R. V., AND S. A. PAIESEK. 1975. Numerical simulation of asymmetric hurricanes on a β-plane with vertical shear. Tellus 27: 453–468.

MADSEN, O. S. 1977. A realistic model of the wind-induced Ekman boundary layer. J. Phys. Oceanogr. 7: 248–255.

MAKAROV, V. A. 1963. A project involving an electrical model for the study of tidal phenomena, p. 173–179. Papers of the 2nd conference on the problem: interaction between the atmosphere and the hydrosphere in the North Atlantic. Gidrometeorologicheskii Institut, Leningrad. 282 p.

MAKAROV, V. A., AND A. B. MENZIN. 1965. An investigation of the propagation of long waves in channels of variable cross-section by the method of electric modelling. Tr. Leningr. Gidrometeorol. Inst. 20: 194–197.

1967. The determination of the periods of the natural oscillations of a fluid in basins by means of an electrical model. Tr. Leningr. Gidrometeorol. Inst. 24: 167–168.

1970. The use of electrical analog models for studying dynamic processes in the sea. Okeanologia 10: 815–819.

MALKIN, W. 1959. Filling and intensity changes in hurricanes over land. National Hurricane Research Project Rep. No. 34. U.S. Weather Bureau, Washington, DC. 18 p.

MALKUS, J. S., AND H. RIEHL. 1960. On the dynamics and energy transformation in steady state hurricanes. Tellus 12: 1–20.

MALLORY, J. K. 1974. Abnormal waves on the southeast coast of South Africa. Int. Hydrogr. Rev. 51: 99–129.

MANSFIELD, D. A. 1974. Polar lows: the development of baroclinic disturbances in cold air outbreaks. Q. J. R. Meteorol. Soc. 100: 541–554.

MANTZ, P. A., AND H. L. WAKELING. 1979. Forecasting flood levels for joint events of rainfall and tidal surge flooding using extreme value statistics. Proc. Inst. Civ. Eng. 67(2): 31–50.

MARCHUK, G. I. 1977. Methods of numerical mathematics. Nauka Press. (In Russian).

MARGULES, M. 1905. Über die Energie der Stürme. Jahrb. K. K. Zentralbl. Meteorol. W. Geodyn. (Wien). Bd. XL.

MARINOS, G., AND J. W. WOODWARD. 1968. Estimation of hurricane surge hydrographs. J. Waterways Harbors Div. Proc. ASCE WW2: 189–216.

MARKHAM, W. E. 1974. Ice climatology in the Beaufort Sea. Interim report of Beaufort Sea Project Study G1, Dec. 1974. Department of Environment, Victoria, B.C. 3 p.

MARMER, H. A. 1926. The tides. Appleton Press, New York.

MARTINSEN, E. A. 1978. A numerical storm surge model related to the western coast of Norway. Candreal, University of Oslo, Oslo, Norway. 67 p.

1981. The barotropic current due to storm surges along the coast of Norway, p. 500–517. *In* R. Saetre and M. Mork [ed.] The Norwegian Coastal Current. Vol. 2. University of Bergen, Bergen, Norway. 759 p.

MARTINSEN, E. A., B. GJEVIK, AND L. P. RØED. 1979. A numerical model for long barotropic waves and storm surges along the western coast of Norway. J. Phys. Oceanogr. 9: 1126–1138.

MASCH, F. D., J. R. BRANDES, F. T. HILL, AND W. A. WHIE. 1970. Analysis of hurricane tide at Padre Island, Texas, p. 2031–2050. Proc. 12th Coastal Eng. Conf., Sept. 13–18, 1980, Washington, DC. Chap. 123. ASCE, New York, NY.

MATANO, H., AND M. SEKIOKA. 1971a. On the synoptic structure of Typhoon Cora, 1969, as the compound system of tropical and extra-tropical cyclones. J. Meteorol. Soc. Jpn. 49: 282–295.

1971b. Some aspects of the extra-tropical transformation of a tropical cyclone. J. Meteorol. Soc. Jpn. 49: 736–743.

MATHESON, K. M. 1967. The meteorological effect on ice in the Gulf of St. Lawrence. Manuscr. Rep. No. 3, Sept. 1967. Marine Sciences Center, McGill University, Montreal, Que. 110 p.

MATHUR, M. B. 1972. Simulation of an asymmetric hurricane with a fine mesh multiple grid primitive equation mode. Ph.d thesis, Florida State University, Tallahassee, FL.

1974. A multiple grid primitive equation model to simulate the development of an asymmetric hurricane (Israel, 1964). J. Atmos. Sci. 31: 371–393.

MATSUMOTO, S. 1961. A note on geostrophic adjustment and gravity wave in the atmosphere. J. Meteorol. Soc. Jpn. 39: 18–28.

MATSUO, H. 1934. Typhoon damage in Japan caused by record high tide. Engineering News-Rec. 13: 656–657.

MATTHEWS, J. B. 1971. Long period gravity waves and storm surges on the Arctic Ocean continental shelf, p. 332–333. Proceedings of the Joint Oceanographic Assembly, 1970.

MAZUMDAR, S. 1965. Study of a cyclonic spell in the Indian Seas. W.M.O. Tech. Note 69: 141–161.

MAZURÉ, J. P. 1937. The computation of tides and storm surges in Maritime rivers. Ph.d. thesis, Technical University of Delft, Delft, The Netherlands.

MCALEER, J. B. 1964. Hurricane studies for Narragansett Bay, p. 660–685. Proc. 9th Conf. Coastal Eng., June 1964, Lisbon. ASCE, New York, NY.

MCLURE, D. J. 1970. Dynamic forecasting of Lake Erie water levels. Rep. No. 70-250 H, May 1970. Hydro Electric Power Commission of Ontario, Research Division, Toronto, Ont. 62 p.

MCCOWAN, J. 1894. On the highest wave of permanent type. Philos. Mag. 38: 351–358.

MCINTYRE, R. J. 1979. Analytic models for west coast storm surges, with application to events of January 1976. Appl. Math. Model. 3: 89–98.

MCKNOWN, R., AND COLLABORATORS. 1952. Fifth annual report of the typhoon post analysis board. Anderson Airforce Base, Guam.

MEANS, L. 1952. On thunderstorm forecasting in the Central United States. Mon. Weather Rev. 80: 145–170.

1954. A study of the mean southerly wind-maximum in low levels associated with a period of summer precipitation in the Middle West. Bull. Am. Meteorol. Soc. 35: 166–170.

MEI, C. C., AND H. S. CHEN. 1975. Hybrid-element method for water waves, p. 63–81. Symp. Model. Tech. 2nd Annu. Symp. ASCE, Sept. 3–5, 1975, San Francisco, CA.

MERIAN, J. R. 1828. Über die Bewegung tropfbarer Flussigkeiten in Gefassen, Basel. (In von der Mühll. Math. Ann. 27: 575).

MESERVE, J. M. 1974. U.S. Navy Marine climatic atlas of the world. North Atlantic Ocean. Vol. 1. U.S. Naval Weather Service Command. 369 p.

MESINGER, F. 1973. A method for construction of second order accuracy difference schemes permitting no false two grid interval wave in the height field. Tellus 25: 444–458.

MESINGER, F., AND A. ARAKAWA. 1976. Numerical methods used in atmospheric models. WMO, GARP Publ. No. 17: 64 p.

MEYER, R. E. 1971. Resonance of unbounded water bodies, p. 189–227. *In* W. H. Reid [ed.] Mathematical problems in the geophysical sciences. Vol. 1. American Mathematical Society, Providence, RI.

MICHELATO, A. 1975. Numerical computation of surges induced by southern winds in the Adriatic Sea. Boll. Geofis. Teor. Appl. 18: 322–334.

MIHALJAN, J. M. 1963. The exact solution of the Rossby adjustment problem. Tellus 15: 150–154.

MILES, J. H., AND W. H. MUNK. 1961. Harbor paradox. J. Waterways Harbors Div. Proc. ASCE. WW2: 111–130.

MILES, J. W. 1971. Resonant response of harbors: an equivalent circuit analysis. J. Fluid Mech. 46(2): 241–265.

1974. Harbor seiching. Annu. Rev. Fluid Mech. 6: 17–35.

MILES, J. W., AND Y. K. LEE. 1975. Helmholtz resonance of harbors. J. Fluid Mech. 67(3): 445–464.

MILLER, A. R. 1957. The effect of steady winds on sea level at Atlantic City. Meteorol. Monogr. Am. Meteorol. Soc. 2: 24–31.

MILLER, B. I. 1958. On the maximum intensity of hurricanes. J. Meteorol. 15: 184–195.

1963. On the filling of tropical cyclones overland. Natl. Hurricane Res. Proj. Rep. No. 66. U.S. Weather Bureau. Washington, DC. 82 p.

1964. A study of the filling of Hurricane Donna 1960 overland. Mon. Weather Rev. 92: 389–406.

1969. Experiment in forecasting hurricane development with real data. ESSA. Tech. Mem. ERLTM-NHRL-85, Miami, FL.

MILLER, B. I., AND P. P. CHASE. 1966. Prediction of hurricane motion by statistical methods. Mon. Weather Rev. 94: 399–406.

MILLER, B. I., P. P. CHASE, AND B. R. JARVINEN. 1972. Numerical prediction of tropical weather systems. Mon. Weather Rev. 100: 825–835.

MILLER, B. I., E. C. HILL, AND P. P. CHASE. 1968. Revised techniques for forecasting hurricane motion by statistical methods. Mon. Weather Rev. 96: 540–548.

MILLER, B. I., AND P. L. MOORE. 1960. A comparison of hurricane steering levels. Bull. Am. Meteorol. Soc. 41: 59–63.

MILLER, F. R., AND R. N. KESHAVAMURTY. 1968. Structure of an Arabian Sea summer monsoon system. East-West Center Press, Honolulu, HI. 94 p.

MILLER, M. J., AND A. K. BETTS. 1977. Travelling convective storms over Venezuela. Mon. Weather Rev. 105: 833–848.

MILLER, R. G. 1958. The screening procedure: a statistical procedure for screening predictors in multiple regression. Part II, p. 86–95. *In* B. Shorr [ed.] Studies in statistical weather prediction. Contract No. AF19 (604)1590, Travelers Weather Research Center, Hartford, CT.

MISHRA, D. K., AND G. R. GUPTA. 1976. Estimation of maximum wind speeds in tropical cyclones occurring in Indian Seas. Indian J. Meteorol. Hydrol. Geophys. 27: 285–290.

MITCHELL, K. E., AND J. B. HOVERMALE. 1977. A numerical investigation of the severe thunderstorm gust front. Mon. Weather Rev. 105: 657–675.

MIYAKODA, K. 1962. Contribution to the numerical weather prediction computation with finite difference. Jpn. J. Geophys. 3(1): 75–190.

MIYAZAKI, M. 1951a. On the relation among wind speed, tangential stress and roughness parameters of the sea surface. Oceanogr. Mag. 3: 17–21.

1951b. Averaged wind stress relation on the sea surface. Oceanogr. Mag. 3(2): 75–77.

1952. On the sea level variations accompanied with the travelling atmospheric disturbances. Oceanogr. Mag. 4(1): 1–11.

1955. Storm surges at the Kobe Harbour (Part I). Oceanogr. Mag. 7(1): 11–19.

1957. On storm surges which recently struck the Japanese coast. Oceanogr. Mag. 9(2): 209–225.

1965. A numerical computation of the storm surge of Hurricane Carla 1961 in the Gulf of Mexico. Oceanogr. Mag. 17: 109–140.

1967. Storm surges along the Japanese coast and their prediction, p. 74. Proc. Sump. Tsunamis Storm Surges, Aug. 25–26, 1966. The 11th Pacific Science Congress, Tokyo, Japan.

1971. Storm surges and their frequencies along the Japanese coast. Bull. Coastal Oceanogr. 9(7): 29–30. (In Japanese)

1975. Characteristics of storm surges induced by typhoons along the Japanese coast. *In* Typhoon modification. Proc. WMO Tech. Conf., Oct. 15–18, 1974, Manila. WMO 408: 37–44.

1976. Numerical simulation of storm surges induced by typhoons, p. 18–22. Mathematical models in geophysics. Proceedings of the Moscow Symposium, 1971. IASH-AISH Publ. No. 116: 215 p.

1978. Prediction of storm surges along the Japanese coast. Weather Resour. Ser. (U.N.) 49: 24–25.

MIYAZAKI, M., T. VENO, AND S. UNOKI. 1961. Theoretical investigations of typhoon surges along the Japanese coast. Oceanogr. Mag. 13: 51–75.

1962. Theoretical investigation of typhoon surges along the Japanese coast (II). Oceanogr. Mag. 13(2): 103–117.

MOGOLESKO, F. J. 1976. Assessment of coastal flooding due to the probable maximum hurricane, p. 10–15. Proc. Conf. Coastal Meteorol. Sept. 21–23, 1976. Virginia Beach, VA. American Meteorological Society, Boston, MA.

MONCRIEFF, M. W., AND M. J. MILLER. 1976. The dynamics and simulation of tropical cumulonimbus and squall lines. Q. J. R. Meteorol. Soc. 102: 373–394.

MOOLEY, D. A. 1980a. Severe cyclonic storms in the Bay of Bengal, 1877–1977. Mon. Weather Rev. 108: 1647–1655.

1980b. Suitable probability model for severe cyclonic storms striking the coast around the Bay of Bengal, p. 349–357. *In* S. Ikeda et al. [ed.] Statistical climatology: developments in atmospheric science. Rep. No. 13. Elsevier Scientific Publishing Company, Amsterdam, The Netherlands.

MORAIS, C. C., AND F. ABECASIS. 1975. Storm surge effects at Leixoes, p. 98–111. Proc. 14th Coastal Eng. Conf., June 24–28, 1974, Copenhagen, Denmark. Chap. 3. ASCE, New York, NY.

MORRISON, S. F. 1952. Of Plymouth plantation. W. Bradford [ed.] Knopf Press, New York, NY. 448 p.

MORTIMER, C. H. 1965. Spectra of long surface waves and tides in Lake Michigan and at Green Bay, Wisconsin. Proc. 9th Conf. Great Lakes Res. Publ. No. 13. International Association for Great Lakes Research, University of Michigan, Ann Arbor, MI.

MOWLA, K. G. 1968. Cyclogenesis in the Bay of Bengal and Arabian Sea. Tellus 20: 151–162.

MUIR, L. R. 1978. Bernoulli effects on pressure-activated water level gauges. Int. Hydrogr. Rev. 60(2): 111–119.

MUKHERJEE, A. L., J. M. KORKHAV, AND V. SRINVASAN. 1961. On some sea surface characteristics in relation to storm development over Arabian Sea. Indian J. Meteorol. Geophys. 12(4): 598–603.

MUNK, W. H., F. SNODGRASS, AND G. F. CARRIER. 1956. Edge waves on the continental shelf. Science, (Washington, DC) 123(3187): 127–132.

MUNN, R. E. 1969. Seasonal trends in the frequencies of storm winds over Lake Superior and the Gulf of St. Lawrence. Atmosphere 7(5): 144–147.

MUROTA, A. 1963. The model study on the validity of the large breakwaters in the Osaka Bay against storm surges. Technol. Rep. Osaka Univ. 13(555): 173–189.

MURRAY, R., AND C. P. W. MARSHALL. 1955. The storms and associated storm surges of December 21–23, 1954. Meteorol. Mag. 84: 333–341.

MURTY, T. S. 1971. The response of a lake with a depth-discontinuity to a time-dependent wind stress. Arch. Meteorol. Geophys. Bioklimatol. Ser. A 20: 55–66.

1972. Circulation in James Bay, p. 143–193. Manuscr. Rep. No. 24. Marine Sciences Branch, Department of the Environment, Ottawa, Ont.

1977. Seismic sea waves — tsunamis. Bull. Fish. Res. Board Can. 198: 337 p.

MURTY, T. S., AND F. B. BARBER. 1973. An assessment of ice transport in the Hudson Bay region, p. 441–450. Proceedings of the 2nd International Conference on Port and Ocean Engineering under Arctic Conditions. Reykjavik, University of Iceland.

MURTY, T. S., AND M. I. EL-SABH. 1981. Interaction between storm surges and tides in shallow waters. Mar. Geodes. 5: 19–33.

MURTY, T. S., M. I. EL-SABH, AND J. M. BRIAND. 1979. Storm surge amplitudes in the St. Lawrence Estuary. J. Can. Hydrogr. Assoc. 20: 8–10.

1981. Statistics of extreme storm surges in eastern Canadian water bodies, p. 1184–1188. Proc. Oceans — 81 Conf. Sept. 16–18, 1981, Boston, MA. Institute of Electrical and Electronics Engineers, New York, NY. 1222 p.

MURTY, T. S., AND N. G. FREEMAN. 1973. Applications of the concepts of edge waves and numerical modelling to storm surge studies on Lake Huron. Proc. 16th Conf. Great Lakes Res. Int. Assoc. Great Lakes. Res. 16: 533–548.

MURTY, T. S., AND R. F. HENRY. 1983. Tides in the Bay of Bengal. J. Geophys. Res. 88: 6069–6076.

MURTY, T. S., G. A. MCBEAN, AND B. MCKEE. 1982. Explosive cyclogenesis in the northeast part of the Pacific Ocean. Proc. 9th Conf. Weather Forecasting Analysis, June 28–July 1, 1982. American Meteorological Society, Boston, MA.

1983. Explosive cyclogenesis over the Northeast Pacific Ocean. Mon. Weather Rev. 111. 5: 1131–1135.

MURTY, T. S., AND R. J. POLAVARAPU. 1975. Reconstruction of some of the early storm surges on the Great Lakes. J. Great Lakes Res. 1(1): 116–129.

1979. Influence of an ice layer on the propagation of long waves. Mar. Geodes. 2(2): 99–125.

MURTY, T. S., AND S. D. SMITH. 1973. A box model of ice transport in the Gulf of St. Lawrence. Rep. Ser. BI-R-73-9, July 1973. Bedford Institute of Oceanography, Dartmouth, N.S. 17 p.

MURTY, T. S., AND J. D. TAYLOR. 1975. Free oscillations in bays and harbors, p. 874–877. Proc. Symp. Modelling Tech., Sept. 3–5, 1975, San Francisco, CA. ASCE, New York, NY.

MURTY, T. S., AND G. HOLLOWAY. 1984. Influence of marginal ice cover on storm surges. J. Waterway Port Coastal Ocean Eng. American Society of Civil Engineers, New York, NY.

MUSTAFIN, N. V. 1969. Methods of computative forecasting of nonperiodic oscillations in the sea level. Oceanol. 8: 414–421.

MYERS, V. A. 1954. Characteristics of United States hurricanes pertinent to levee design for Lake Okeechobee, Florida. Hydrometeorol. Rep. No. 32, March 1954. U.S. Weather Bureau, Washington, DC. 106 p.

1957. Maximum hurricane winds. Bull. Am. Meteorol. Soc. 38(4): 227–228.

1970. Joint probability method of tide frequency analysis applied to Atlantic City and Long Beach Island, N.J. U.S. Dep. Commer. Weather Bureau, ESSA Tech. Memo. WBTM HYDRO II: 109 p.

1975. Storm tide frequencies on the south Carolina coast. U.S. National Weather Service. NOAA Tech. Rep. NWS-16: 90 p.

MYERS, V. A., AND W. MALKIN. 1961. Some properties of hurricane wind fields as deduced from trajectories, p. 1–45. Natl. Hurricane Res. Rep. No. 49. U.S. Weather Bureau, Washington, DC.

NAKAMURA, M., H. SHIRAISHI, AND Y. SASAKI. 1964. A model study on tide and storm surge due to a typhoon in Ise Bay. Coastal Eng. Jpn. 8: 45–63.

NAKANO, M. 1949. On the secondary undulations of tides caused by cyclonic storms. Oceanogr. Mag. 1(1): 13–32.

NAKAYAMA, M. 1972. On the PCM-FS-FM tide telemetering system for warning of tsunamis and storm surges. Oceanogr. Mag. 23(2): 59–67.

NAMIAS, J. 1955. Secular fluctuations in vulnerability to tropical cyclones in and off New England. Mon. Weather Rev. 83: 155–162.

NATARAJAN, R., AND N. RAMANATHAN. 1980. Estimation of storm surges in a bay. Presented at the Indo-French School on Recent Advances in Computer Techniques in Meteorology, Bio-Mechanics and Applied Systems, Feb. 4–13, 1980. New Delhi, India.

NATIONAL ACADEMY OF SCIENCES. 1975. Methodology for estimating the characteristics of coastal surges from hurricanes. Prepared by the panel on Coastal Surges from Hurricanes, Science and Engineering Committee on Prevention and Mitigation of Flood Losses. Building Research Advisory Board, National Research Council. 34 p.

NEKRASOV, A. V. 1962. Computation and construction of M_2 tidal chart in the Norwegian and Greenland Sea by the Hansen's method. Tr. Leningr. Gidrometeorol. Inst. 16: 49–57. (In Russian)

NELSON, R. C. 1975. Tropical cyclone storm surges in Australia 1880 to 1970, p. 193–197. Proc. 2nd Aust. Conf. Coastal Ocean Eng., Queensland, Australia.

NEUMANN, C. J. 1969. Probability of tropical cyclone induced winds at N.A.S.A. Manned Space-craft Centre. ESSA Tech. Memo. WBTM-SOS-4: 46 p.

1972. An alternate to the HURRAN tropical cyclone forecast system. NOAA Tech. Memo. NWS-SR-62. Fort Worth, TX. 32 p.

1979. Statistical techniques. *In* Operation techniques for forecasting tropical cyclone intensity and movement. Chap. 4. No. 528, World Meteorological Organization, Geneva, Switzerland.

1981. Some characteristics of Atlantic tropical cyclone forecast errors. Mar. Weather Log 25(4): 231–236.

NEUMANN, C. J., AND G. W. CRY. 1978. A revised Atlantic tropical cyclone climatology. Mar. Weather Log 22(4): 231–236.

NEUMANN, C. J., G. W. CRY, E. L. CASO, AND B. R. JARVINEN. 1978. Tropical cyclones of the North Atlantic Ocean, 1871–1977. National Climatic Center, Asheville, NC. 170 p.

NEUMANN, C. J., AND D. A. HILL. 1976. Computerized tropical cyclone climatology. Mar. Weather Log 20(5): 257–262.

NEUMANN, C. J., J. R. HOPE, AND B. I. MILLER. 1972. A statistical method of combining synoptic and empirical tropical cyclone prediction systems. NOAA Tech. Memo. NWS-SR-63: 32 p.

NEUMANN, C. J., AND M. B. LAWRENCE. 1975. An operational experiment in the statistical dynamical prediction of tropical cyclone motion. Mon. Weather Rev. 103: 665–673.

NEUMANN, C. J., AND P. W. LEFTWICH. 1977. Statistical guidance for the prediction of eastern North Pacific tropical cyclone motion — part I. NOAA Tech. Memo. NWS-WR-124: 32 p.

NEUMANN, C. J., AND G. S. MANDAL. 1978. Statistical prediction of storm motion: motion over the Bay of Bengal and Arabian Sea. Indian J. Meteorol. Hydrol. Geophys. 29(3): 487–500.

NEUMANN, C. J., AND J. M. PELISSIER. 1981a. Models for the prediction of tropical cyclone motion over the North Atlantic: an operational evaluation. Mon. Weather Rev. 109: 522–538.

1981b. An analysis of Atlantic tropical cyclone forecast errors 1970–1979. Mon. Weather Rev. 109: 1248–1266.

NEUMANN, C. J., AND E. A. RANDRIANARISON. 1976. Statistical prediction of tropical cyclone motion over the Southwest Indian Ocean. Mon. Weather Rev. 104(1): 76–85.

NEUMANN, G. 1948. Uber den Tangentialdruck des Winds und die Rauhikheit der Meeresoberfläche. Z. Meteorol. 2: 7–8.

NEWMAN, B. W., A. R. MARTIN, AND W. R. WILKIE. 1956. Occurrence of tropical depressions and cyclones in the Australian region during the summer of 1955–56, p. 25–55. Proc. Trop. Cyclone Symp., Dec. 1956, Brisbane, Australia. Bureau of Meteorology, Melbourne, Australia.

NEWTON, C. W. 1950. Structure and mechanism of the prefrontal squall line. J. Meteorol. 7: 210–222.

1967. Severe convective storms. Adv. Geophys. 12: 257–308.

NEWTON, C. W., AND H. R. NEWTON. 1959. Dynamical interactions between large convective clouds and environment with vertical shear. J. Meteorol. 16: 483–496.

NICKERSON, J. W. 1971. Storm-surge forecasting. Tech. Rep. AD-751 578, Apr. 1971. Navy Weather Research Facility, Norfolk, VA. 91 p.

NIEMEYER, G. 1979a. Long wave model independent of stability criteria. J. Waterway Port Coastal Ocean Div. WWI: 51–65.

NIEMEYER, H. D. 1979b. Wave climate study in the region of the east Frisian Islands and coast, p. 134–151. Proc. 16th Coastal Eng. Conf., Hamburg, W. Germany, ASCE, New York, NY.

NIHOUL, J. C. J. 1975. Modelling of marine systems. Elsevier Press, Amsterdam, The Netherlands.

1977. Three-dimensional model of tides and storm surges in a shallow well mixed continental sea. Dyn. Atmos. Oceans. 2: 29–47.

1978. Hydrodynamics of estuaries and fjords. Proc. 9th Int. Liège Colloq. Ocean Hydrodyn., Elsevier Press, Amsterdam, The Netherlands. 546 p.

1979. Marine forecasting. Proc. 10th Int. Liège Colloq. Ocean Hydrodyn. Elsevier Press, Amsterdam, The Netherlands. 493 p.

NIHOUL, J. C. J., AND F. C. RONDAY. 1975. The influence of the tidal stress on the residual circulation: application to the southern bight of the North Sea. Tellus 27: 484–489.

1976a. Mathematical hydrodynamical models for the study of marine circulation and dispersion of pollutants in a shallow sea, p. 447–472. *In* R. Glowinski and J. L. Lions [ed.] Computing methods in applied sciences. Springer-Verlag, Heidelberg, W. Germany.

1976b. Hydrodynamical models of the North Sea: a comparative assessment. Mem. Soc. R. Sci. Liège 10: 61–96.

NOBLE, R. M., AND J. A. HENDRICKSON. 1974. Calibration of a hurricane storm surge program, p. 87–97. Proc. 14th Coastal Eng. Conf., June 24–28, 1974, Copenhagen, Denmark. ASCE, New York, NY.

NOMITSU, T. 1933a. A theory of the rising stage of drift current in the ocean. I. The case of no bottom current, Mem. Coll. Sci. Kyoto Imp. Univ. Ser. A 16(2): 161–175.

1933b. On the development of the slope current and the barometric current in the ocean, I. The case of no bottom current. Mem. Coll. Sci. Kyoto Imp. Univ. Ser. A 16(2): 203–242.

1934. Mem. Coll. Sci. Kyoto Imp. Univ. Ser. A 17: 249–280.

1935. Surface fluctuations of Lake Biwa caused by the Muroto typhoon. Mem. Coll. Sci. Kyoto Imp. Univ. Ser. A 18(5): 221–238.

NOMITSU, T., AND T. TAKEGAMI. 1934. Coast effect upon the ocean current and sea level. I. Steady state Mem. Coll. Sci. Kyoto Imp. Univ. Ser. A 17: 93–141.

NORTON, W. R., I. P. KING, AND G. T. ORLOB. 1973. A finite-element model for lower granite reservoir. Prepared for Walla Walla district, U.S. Army Corps of Engineers. Rep. No. 10560. Water Resources Engineers Inc., March 1973.

NOYE, B. J. 1968. The frequency response of a tide well. Proc. 3rd Aust. Conf. Hydraul. Fluid Mech. Institute of Engineers, Sydney, Australia.

1972. Meteorological tides and storm surges around Australia. Aust. Mar. Sci. Bull. 40: 17–24.

1974a. Some nonlinear effects of the conventional tide well. J. Mar. Res. 32.

1974b. Frequency response of a linear tide well system. J. Mar. Res. 32.

1974c. Improved interpretations of tide well records. J. Mar. Res. 32.

1977. Wind-induced circulation and water level changes in lakes, p. 135–145. *In* C. A. Brebbia [ed.] Applied numerical modelling. Halstead Press, London, U.K.

NOYE, B. J., AND K. C. S. TRONSDN. 1978. Finite difference schemes applied to the simulation of tides and currents in gulfs, p. 285–355. *In* B. J. Noye [ed.] Numerical simulation of fluid motion. North-Holland Publishing Co., Amsterdam, The Netherlands.

NUNEZ, E., AND W. M. GRAY. 1978. A comparison between West Indies hurricanes and Pacific typhoons, p. 528–534. Proc. 11th Tech. Conf. Hurricanes Trop. Meteorol., Dec. 13–16, 1977, Miami Beach, FL. American Meteorological Society, Boston MA.

OAKLAND, H. 1970. On the adjustment towards balance in primitive equation weather prediction models. Mon. Weather Rev. 98: 271–279.

O'BRIEN, M. P., AND J. W. JOHNSON. 1963. The March 1962 storm on the Atlantic coast of the United States, p. 555–562. *In* J. W. Johnson [ed.] Proc. 8th Coastal Eng. Conf., Nov. 1962, Mexico City. Chap. 32. Council on Wave Research, The Engineering Foundation, Berkeley, CA.

OBUKHOV, A. M. 1949. On the question of the geostrophic wind. Izv. Akad. Nauk SSSR Ser. Geogr. Geofiz. 13: 281–306. (In Russian)

1957. O tochnosti predvychislenia advektionyklu izmenenii polei pri chislenom prognoze pogody. Izv. Akad. Nauk SSSR Ser. Geofiz. 9: 1133–1141.

O'CONNOR, J. F. 1964. Hemispheric distribution of 5-day mean 700 mb circulation centers. Mon. Weather Rev. 92: 303–315.

ODD, N. 1980. Mathematical model studies of the Irrawaddy Delta. Hydraulics Research Station, Wallingford, U.K. 7 p.

OGURA, S. 1925. Effect of atmospheric pressure on sea level in western part of the North Pacific Ocean. Jpn. J. Astron. Geophys. 11: 209–231.

OGURA, Y. 1964. Frictionally-controlled, thermally-driven circulations in a circular vortex with application to tropical cyclones. J. Atmos. Sci. 21: 610–621.

OGURA, Y., AND M. T. LIOU. 1980. The structure of a mid-latitude squall line: a case study. J. Atmos. Sci. 37: 553–567.

OKADA, M., AND K. MIYOSHI. 1933. Experimental studies of the water movement in coastal regions of the sea. I. Tidal oscillations in Sagami Bay. J. Imp. Fish. Inst. 29(1): 15–98.

1935. Experimental studies of the water movement in coastal regions of the sea. II. Tidal oscillations in Sagami Bay (II). J. Imp. Fish. Inst. 24–45: 253–263.

ÖKLAND, H. 1958. False dispersion as a source of integration errors. Sci. Rep. No. 1. Norske Meteorological Institute, Oslo, Norway.

OOYAMA, K. 1964. A dynamical model for the study of tropical cyclone development. Geoffis. Int. 4: 197–198.

1969. Numerical simulation of the life cycle of tropical cylones J. Atmos. Sci. 26: 3–40.

ORLOB, G. T. 1972. Mathematical modelling of esturial systems, p. 1–127. *In* A. K. Biswas [ed.] Proc. Int. Symp. Model. Tech. Water Resour. Syst., May 9–12, 1972. Vol. 1. Environment Canada, Ottawa, Ont.

ORSZAG, S. A. 1971. On the elimination of aliasing in finite differencing schemes by filtering high wave number components. J. Atmos. Sci. 28: 1074.

ORTT, F. L. 1897. De invloed vap zinel en luchtdruk op de getijden. K. Inst. Ingen. Verb. 1896–1897: 117–130 (Nature (London) 56: 80–84).

OTTER, J. R. H., AND A. S. DAY. 1960. Tidal flow computations. Engineer 209: 177–182.

OVERLAND, J. E. 1975. Estimation of hurricane storm surge in Apalachicola Bay, Florida. Tech. Rep. NWS17, June 1975, N.W.S., Silver Spring, MD. 66 p.

OWEN, A. 1980a. The tidal regime of the Bristol channel: a numerical modelling approach. Geophys. J. R. Astron. Soc. 62: 59–75.

OWEN, T. B. 1980b. Hurricane preparedness: a team effort. NOAA Magazine, May–June 1980. p. 5.

PAGENKOPF, J. R., AND B. R. PEARCE. 1975. Evaluation of techniques for numerical calculation of storm surges. Rep. No. 199, Feb. 1975. Department of Civil Engineering, MIT, Cambridge, MA. 120 p.

PALMÉN, E. 1932. Versuch zur bestimmung des Tangentialdruckes des Windes aut die Meeresoberfläche miltels Wasserstandsbeobachtungen. Ann. Hydrogr. Mar. Meteorol. Heft XI, Berlin.

1949. On the formation and structure of tropical hurricanes. Geophysics 3.

1936. Uber die von einem Stationaren Wind verusachte Wasserstauung bericht 15B. Hydd. Konferenz der Baltischen Staaten, Finland.

1951. The aerology of extratropical disturbances, p. 599–620. Compendium of Meteorology, American Meteorological Society, Boston, MA.

1955. Improved terrain effects in barotropic forecasts. Mon Weather Rev. 83: 327–342.

PALMÉN, E. H., AND E. LAURIA. 1938. Über die Einwirkung eines Sturmes auf den Hydrographiscen zustand in nordliche osteegebiet. Soc. Sci. Fenn. Comm.

PALMÉN, E., AND C. W. NEWTON. 1969. Atmospheric circulation systems: their structure and physical interpretation, p. 515–522. Academic Press, New York, NY.

PALMIERI, S., C. FINIZIO, AND R. COZZI. 1976. The contribution of meteorology to the study and prediction of high tides in the Adriatic. Boll. Geofis. Teor. Appl. 19(71): 191–198.

PANT, P. S., A. R. RAMAKRISHRAN, AND R. JAMBUNATHAN. 1980. Cyclones and depressions over the Indian Seas in 1977. Mausam (formerly Indian J. Meteor. Hydrol. Geophys.) 31(3): 337–356.

PANT, P. S., V. SRINIVASAN, AND R. JAMBUNATHAN. 1978. Cyclones and depressions in the Indian Seas in 1976. Indian J. Meteorol. Hydrol. Geophys. 29: 613–628.

PAPA, L. 1977. The free oscillations of the Ligurian Sea computed by the H–N method. Dtsch. Hydrogr. Z. 30(3): 81–90.

PAPPAS, R. G. 1978. The 1977–78 southern California winter. Mar. Weather Log 22(5): 317–324.

PARARAS-CARAYANNIS, G. 1975. Verification study of a bathystrophic storm surge model. Tech. Memo. No. 50, May 1975. U.S. Army Corps of Engineers, Coastal Engineering Research Center, Fort Belvar, VA. 248 p.

PARKE, M. E., AND M. C. HENDERSHOTT. 1980. M_2, S_2, K_1 models of the global ocean tide on an elastic earth. Mar. Geodes. 3: 379–408.

PASKAUSKY, D. F., AND D. L. MURPHY. 1973. Two-dimensional numerical prediction of wind surge in Lake Erie, p. 808–817. Proc. 16th Conf. Great Lakes Res. Int. Assoc. Great Lakes Res. 16: 1068 p.

PATZERT, W. C. 1972. Seasonal variations in structure and circulation in the Red Sea. Tech. Rep. HIG-72-13, Aug. 1972. Hawaii Institute of Geophysics, University of Hawaii, Honolulu, HI. 58 p.

PAULSEN, C. G., B. L. BIGWOOD, A. W. HARRINGTON, C. W. HARTWELL, AND H. B. KINNISON. 1940. Hurricane floods of September 1938. U.S. Geological Survey, Water Supply Pap. 867. U.S. Government Printing Office, Washington, DC. 555 p.

PEARCE, B. R. 1972. Numerical calculation of the response of coastal waters to storm systems — with application to Hurricane Camille of August 17–22, 1969. Tech. Rep. No. 12, Aug. 1952. Coastal and Oceanographic Engineering Lab. University of Florida, Gainesville, FL. 152 p.

PEARCE, B. R., AND C. K. COOPER. 1981. Numerical circulation model for wind induced flow. J. Hydraul. Div. Proc. Am. Soc. Civ. Eng. 107(HY3), 285–302.

PEARSON, C. E., AND D. F. WINTER. 1977. On the calculation of tidal currents in homogeneous estuaries. J. Phys. Oceanogr. 7: 520–531.

PEDGLEY, D. E. 1969. Cyclones along the Arabian Coast. Weather 24: 456–468.

PEIMU, W., X. YONGSHUI, L. YANCHU, C. YUXIA, AND C. JILIANG. 1982. Nonlinear numerical computations on storm surges at the Taiwan Strait. Acta Oceanol. Sinica 1(2): 195–203.

PELISSIER, J. M. 1979. Dynamical techniques. *In* Operational techniques for forecasting tropical cyclone intensity and movement. Chap. 5. WMO No. 528: 11.r.1–11.5.11.

PERLROTH, I. 1967. Hurricane behavior as related to oceanographical environmental conditions. Tellus 19: 258–268.

1969. Effects of oceanographic media on equatorial Atlantic hurricanes. Tellus 21: 230–244.

PETERS, S. P. 1954. Some meteorological aspects of North Sea floods, with special reference to February 1953. Proc. Conf. North Sea Floods. Weather 9(2): 28–36.

PETERSON, P. 1975. Storm surge statistics. Tech. Note No. 20. Royal Observatory, Hong Kong.

PETTERSSEN, S. 1950. Some aspects of the general circulation of the atmosphere. Cent. Proc. R. Meteorol. Soc. London: 120–155.

1956. Weather analysis and forecasting. Vol. I and II. 2nd ed. McGraw-Hill Publications, New York, NY. 428 p.

1969. Introduction to meteorology. McGraw-Hill Publications, New York, NY. 333 p.

PHILLIPS, D. W., AND J. A. W. MCCULLOCH. 1972. The climate of the Great Lakes Basin. Climatol. Stud. No. 20. Atmospheric Environment Service, Environment Canada, Toronto, Ont. 40 p. + diagrams.

PHILLIPS, E. F. 1959. The association of spherics with tropical cyclones. Aust. Meteorol. Mag. 26: 76–85.

PHILLIPS, N. A. 1960. Numerical weather prediction, p. 43–90. *In* F. L. Alt [ed.] Advances in computers. Vol. 1. Academic Press, New York, NY.

PHILLIPS, O. M. 1978. Ocean means and extremes, p. 1–10. Proc. S.T.A.R. Symp., Apr. 26–20, 1978. Pap. No. 1. Society of Naval Architects and Marine Engineers, New York, NY.

PICKRILL, R. A. 1972. Storm surge on the east coast of New Zealand. M.A. thesis, Geography Department, University of Canterbury, Canterbury, New Zealand.

PIDDINGTON, H. 1851. The sailor's handbook for laws of storms. 4th ed. Government of India, Calcutta, India.

PIERSON, W. J., L. J. TIEK, AND L. BAER. 1966. Computer based procedure for preparing global wave forecasts and wind field analysis capable of using wave data obtained from a spacecraft, p. 499. Proc. 6th Symp. Naval Hydrodyn., Washington, DC.

PIFER, B. E. 1977. User assumptions in tropical cyclone research, p. 310–314. Proc. 11th Tech. Conf. Hurricanes Trop. Meteorol., Dec. 13–16, 1977, Miami Beach, FL. American Meteorological Society, Boston, MA.

PIKE, A. C. 1972. Improved barotropical hurricane track prediction by adjustment of the initial wind field. NOAÀ Tech. Memo. NWS-SR-66.

PLATE, D. J., AND P. WENGEFELD. 1979. Exchange processes at the water surface, p. 277–301. *In* W. H. Graf and C. H. Mortimer [ed.] Hydrodynamics of lakes. Proc. Symp., Oct. 12–13, 1978, Lausanne, Switzerland. Elsevier Press, Amsterdam, The Netherlands.

PLATZMAN, G. W. 1954. The computational stability of boundary conditions in numerical integration of the vorticity equation. Arch. Meteorol. Geophys. Bioklamatol. Ser A 7: 29–40.

1958a. A numerical computation of the surge of June 26, 1954, on Lake Michigan. Geophysica 6: 407–438.

1958b. The lattice structure of the finite-difference primitive and vorticity equations. Mon. Weather Rev. 86: 285–292.

1963. The dynamic prediction of wind tides on Lake Erie. Meteorol. Mongr. 4(26): 44 p.

1964. An exact integral of complete spectral equations for unsteady one dimensional flow. Tech. Rep. 16. Department of Geophysical Sciences, University of Chicago, Chicago, IL. 28 p.

1965a. The prediction of surges in the southern basin of Lake Michigan. Part I. The dynamical basis for prediction. Mon. Weather Rev. 93: 275–281.

1965b. The daily variation of water level on Lake Erie. Report No. 19 to the NSF, Nov. 1965. Department of Geophysical Sciences, University of Chicago, Chicago, IL. 41 p.

1967. A procedure for operational prediction of wind set-up on Lake Erie. Tech. 11. E.S.S.A. contract E-91-67(N). University of Chicago, Chicago, IL.

1971. Ocean tides and related waves. Lectures for the American Mathematical Society, 1970. Summer seminars on mathematical problems in the geophysical sciences, held at Rensselaer Polytechnic Institute, Troy, NY. 94 p. (Also *In* W. H. Reid [ed.] Mathematical problems in the geophysical sciences. Vol. 14. Part 2. p. 239–291.)

1972. Two-dimensional free oscillations in natural basins. J. Phys. Oceanogr. 2(2): 117–138.

1974. Normal modes of the Atlantic and Indian oceans. Tech. Rep. 25. Department of Geophysical Sciences, University of Chicago, Chicago, IL. 83 p.

1975. Normal modes of the Atlantic and Indian oceans. J. Phys. Oceanogr. 5: 201–222.

1978. Normal modes of the world ocean. Part I. Design of a finite element barotropic model. J. Phys. Oceanogr. 8(3): 323–343.

1979. Effects of multiple connectivity on a finite element barotropic model. J. Phys. Oceanogr. 9(6): 1276–1283.

1981. Some response characteristics of finite element tidal models. J. Comput. Phys. 40(1): 36–63.

POLLARD, M. 1978. North Sea surge. The story of the east coast floods of 1953. Lavenham: Terence Dalton Ltd., Lavenham, U.K. 136 p.

PORE, N. A. 1964. The relation of wind and pressure to extra-tropical storm surges at Atlantic City. J. Appl. Meteorol. 3: 155–163.

1965. Chesapeake Bay extratropical storm surges. Chesapeake Sci. 6(3): 172–182.

1973. Marine conditions and automated forecasts for the Atlantic Coastal storm of February 18–20, 1972. Mon. Weather Rev. 101: 363–370.

1976. Automated forecasting of extra-tropical storm surges, p. 16–18. Abstr. 15th Coastal Eng. Conf., July 11–17, 1976, Honolulu, HI. ASCE, New York, NY.

1977. Automated forecasting of extra-tropical storm surges, p. 906–920. Proc. 15th Coastal Eng. Conf., July 11–17, 1976, Honolulu, HI. ASCE, New York, NY.

PORE, N. A., AND C. S. BARRIENTOS. 1976. Storm surge. *In* Marine ecosystem analysis (MESA). New York Bight Atlas Monogr. No. 6, Feb. 1976. New York Sea Grant Institute, Albany, NY. 44 p.

PORE, N. A., AND R. A. CUMMINGS. 1967. A Fortran program for the calculation of hourly values of astronomical tide and time and height of high and low water. ESSA Tech. Memo. WBTM-TDL-6. U.S. Department of Commerce, Washington, DC. 17 p.

PORE, N. A., J. M. MCCLELLAND, C. S. BARRIENTOS, AND W. E. KENNEDY. 1971. Wave climatology for the Great Lakes. NOAA Tech. Memo. NWS-TDL-40, Feb. 1971. 61 p.

PORE, N. A., H. P. PERROTTI, AND W. S. RICHARDSON. 1975. Climatology of Lake Erie storm surges at Buffalo and Toledo. NOAA Tech. Memo. NWS-TDL-54. 27 p.

POSEY, C. A. 1981. Forging new tools for hurricane forecasters. NOAA 11(3): 15–16.

PRANDLE, D. 1974. A numerical model of the southern North Sea and River Thames. Rep. No. 4. Institute of Oceanographic Sciences, Bidston, U.K. 25 p.

1975. Storm surges in the southern North Sea and River Thames. Proc. R. Soc. London Ser. A 344: 509–539.

1978. Residual flows and elevations in the southern North Sea. Proc. R. Soc. London Ser. A 359: 189–228.

1980. Modelling of tidal barrier schemes: an analysis of the open boundary problem by reference to open circuit theory. Estuarine Coastal Mar. Sci. 11: 53–71.

PRANDLE, D., AND N. CROOKSHANK. 1972. Numerical model studies of the St. Lawrence River. Rep. No. 12764. Division of Mechanical Engineering, National Research Council of Canada, Ottawa, Ont.

1974. Numerical model of the St. Lawrence Estuary. J. Hydraul. Div. ASCE Vol. 100. Proc. Pap. 10472: 517–529.

PRANDLE, D., E. R. FUNKE, N. L. CROOKSHANK, AND R. RENNER. 1980. The use of array processors for the numerical modelling of tidal estuary dynamics, p. 2413–2432. Proc. 17th Int. Conf. Coastal Eng., Mar. 23–28, 1980, Sydney, Australia. Am. Soc. Civil Eng., New York, NY.

PRANDLE, D. AND J. WOLF. 1978a. The interaction of surge and tide in the North Sea and River Thames. Geophys. J. R. Astron. Soc. 55: 203–216.

1978b. Surge–tide interaction in the southern North Sea. p. 161–185. *In* J. C. J. Nihoul [ed.] Proc. 9th Int. Liège Colloq. Ocean Hydrodyn. Elsevier, Amsterdam, The Netherlands.

PRANDTL, L. 1932. Meteorologische Anwendung der Strömungslehre. Beitr. Phys. Frei. Atmos. 19: 185.

PRICE, W. A. 1956. Hurricanes affecting the coast of Texas from Galveston to Rio Grande. Tech. Memo. No. 78, Mar. 1956. Beach Erosion Board, Corps of Engineers. 17 p.

PRIESTLEY, C. H. B. 1951. A survey of the stress between the ocean and atmosphere. Aust. J. Sci. Res. A4: 315–328.

PROCTOR, R. 1981. Tides and residual circulation in the Irish Sea: a numerical modelling approach. Ph.D. thesis, University of Liverpool, Liverpool, U.K.

PROCTOR, R., AND H. H. PEECK. 1983. First comparison of operational storm surge models for the North Sea. (Unpublished manuscript.)

PROUDMAN, J. 1929. The effects on the sea of changes in atmospheric pressure. Mon. Not. R. Astron. Soc. Geophys. Suppl. 2: 197–209.

1944. The tides of the Atlantic Ocean. Mon. Not. R. Astron. Soc. Geophys. Suppl. 104: 244–256.

1953. Dynamic oceanography. Methuen and Co. Ltd., London, U.K. 409 p.

1954a. Note on the dynamical theory of storm surges. Arch Meteorol. Geophys. Bioklimatol. Ser. A 3.

1954b. Note on the dynamics of storm surges. Mon. Not. R. Astron. Soc. Geophys. Suppl. 7: 345–351.

1954c. Note on the dynamics of storm surges. Mon. Not. R. Astron. Soc. Geophys. Suppl. 7: 44–48.

1955a. The propagation of tide and surge in an estuary. Proc. R. Soc. London Ser. A 231: 8–24.

1955b. The effect of friction on a progressive wave of tide and surge in an estuary. Proc. R. Soc. London Ser. A 233: 407–418.

1957. Oscillations of tide and surge in an estuary of finite length. J. Fluid Mech. 2: 371–382.

1958. On the series that represent tide and surge in the Thames. J. Fluid Mech. 3(4): 411–417.

PROUDMAN, J., AND A. T. DOODSON. 1924a. Time-relations in meteorological effects on the sea. Proc. London Math. Soc. 24: 140–149.

1924b. The principal constituent of the tides in the North Sea. Philos. Trans. R. Soc. London Ser. A 224: 185–219.

PUDOV, V. D. 1979. Influence of the heat content of the upper layer of the ocean on typhoon trajectories. Oceanography 19(6): 662–665.

PUGH, D. T. 1982. Estimating extreme currents by combining tidal and surge probabilities. Ocean Eng. 9: 361–372.

PUGH, D. T., AND J. M. VASSIE. 1976. Tide and surge propagation offshore in the Dowsing region of the North Sea. Dtsch. Hydrogr. Z. 29(5): 163–213.

1979. Extreme sea levels from tide and surge probability, p. 911–930. Proc. 16th Coastal Eng. Conf., Aug. 27–Sept. 3, 1978, Hamburg, W. Germany. Vol. 1. ASCE, New York, NY.

1980. Applications of the joint probability method for extreme sea level computations. Proc. Inst. Civ. Eng. 69: 959–975.

PUNIIANI, A. L. 1971. Dynamic forecasting of Lake Erie levels under storm conditions. Rep. No. 71-233-k, June 1971. Research Division, Ontario Hydro.

QUINN, F. H. 1980. Wind stress effects on Detroit River discharges. J. Great Lakes Res. 6(2): 172–175.

RABE, K., AND S. BRAND. 1977. Numerical simulation of sea states around tropical cyclones, p. 680–687. Proc. 11th Tech. Conf. Hurricanes Trop. Meteorol., Dec. 13–16, 1977, Miami Beach, FL. American Meteorological Society, Boston, MA.

1980. A numerical simulation of an occurrence of extreme sea states within a typhoon. J. Meteorol. Soc. Jpn. 58(5): 394–402.

RAGHAVENDRA, V. K. 1973. A statistical analysis of the number of tropical storms and depressions in the Bay of Bengal during 1890 to 1969. Indian J. Meteorol. Geophys. 24: 125–130.

RAICHLEN, F. 1966. Harbor resonance, p. 281–340. *In* A. T. Ippen [ed.] Estuary and coastline hydrodynamics. Chap. 7. McGraw-Hill Publications, New York, NY.

RAISIRCAR, N. C. 1956. A climatological study of storms and depressions in the Bay of Bengal. Indian J. Meteorol. Geophys. 7: 157–160.

1958. A climatological study of storms and depressions in the Bay of Bengal. Mem. Indian Meteorol. Dep. 30(5).

RAMAGE, C. S. 1962. The subtropical cyclone. J. Geophys. Res. 67: 1401–1411.

1971. Monsoon meteorology. Academic Press, New York, NY. 296 p.

1973. The typhoon of October 1970 in the south China Sea: intensification, decay and ocean interaction. Environmental Prediction Research Facility, Monterey, CA.

RAMAN, K., R. VENKATARAMAN, AND A. A. RAMASASTRY. 1967. Unusually large number of cyclonic storms in the Bay of Bengal during the post-monsoon season of 1966. Indian J. Meteorol. Hydrol. Geophys. 18: 1015–1037.

RAMANADHAM, R., AND R. VARADARAJULU. 1965. Storm tides at Visakhapotnam. Indian J. Pure Appl. Phys. 3(5): 173–176.

RAMMING, H. G. 1972. Reproduction of physical processes in coastal areas, p. 2197–2216. Proc. 13th Conf. Coastal Eng., Vancouver, B.C. ASCE, New York, NY.

1976. A nested North Sea model with fine resolution in shallow coastal areas. Mem. Soc. R. Sci. Liège 10: 9–26.

RAMMING, H. G., AND Z. KOWALIK. 1980. Numerical modelling of marine hydrodynamics. Applications to dynamic physical processes. Elsevier Oceanographic Series No. 26. Elsevier, Amsterdam, The Netherlands. 368 p.

RAMSEIER, R. O., W. J. CHUBBIAK, M. R. VANT, AND R. B. GRAY. 1974. Distribution of ice thickness in the Beaufort Sea. Interim report of Beaufort Sea Project Study G3, Dec. 1974. Department of Environment, Victoria, B.C. 7 p.

RAMSTER, J. W. 1977. Development of cooperative research in the North Sea: the origins, planning and philosophy of JONSDAP 76. Mar. Policy 1: 318–325.

RAMSTER, J. W., AND K. P. KOLTERMANN. 1976. Report of the working group on permanent, moored current-meter stations in the North Sea. Int. Counc. Explor. Sea Coop. Res. Rep. No. 53: 150 p.

RANEY, D. C., D. L. DURHAM, AND H. L. BUTLER. 1979. Application of a three-dimensional storm surge model, p. 77–86. *In* W. H. Graf and C. H. Mortimer [ed.] Hydrodynamics of lakes. Elsevier, Amsterdam, The Netherlands. 360 p.

RAO, D. B. 1967. Response of a lake to a time-dependent wind stress. J. Geophys. Res. 72(6): 1697–1708.

1969. Effect of travelling disturbances on a rectangular bay of uniform depth. Arch. Meteorol. Geophys. Bioklimatol. Ser. A 18: 171–190.

1973. Spectral methods of forecasting storm surges. Hydrol. Sci. Bull. 18: 311–316.

1974. Transient response of shallow enclosed basins by the method of normal modes. Sci. Ser. No. 38, CCIW: 30 p.

RAO, D. B., AND T. S. MURTY. 1970. Calculation of the steady state wind-driven circulations in Lake Ontario. Arch. Meteorol. Geophys. Bioklimatol. Ser. A 19: 195–210.

RAO, D. B., AND D. J. SCHWAB. 1974. Two-dimensional normal modes in arbitrarily enclosed basins on a rotating earth: application to Lakes Ontario and Superior. Spec. Rep. No. 19. Center for Great Lakes Studies, University of Milwaukee, Milwaukee, WI. 69 p.

RAO, K. N., AND S. JAYARAMAN. 1958. Frequency of depressions and cyclones. Indian J. Meteorol. Geophys. 9: 233–250.

RAO, M. P. 1978. Cyclones, p. 36–39. Home Life, December 1978.

RAO, N. S. B. 1968. On some aspects of local and tropical storms in the Indian area. Ph.d. thesis, University of Jadavapur, Jadavapur, India. 262 p.

RAO, N. S. B., AND S. MAZUMDAR. 1966. A technique for forecasting storm waves. Indian J. Meteorol. Geophys. 17(3): 333–346.

RATNAM, V., AND P. S. NAYAR. 1966. Floods due to storm surges associated with cyclonic storms. Indian J. Meteorol. Geophys. 17: 363–368.

RAYCHOUDHURI, S. N., Y. H. SUBRAMANYAN, AND R. CHELLAPPA. 1959. A climatological study of storms and depressions in the Arabian Sea. Indian J. Meteorol. Geophys. 10(3): 283–290.

READ, S. 1975. Dynamical aspects of the wind storm of August 1, 1975. N.Z. Meteorol. Serv. Tech. Note.

REDFIELD, A. C. 1953. Interference phenomena in the tides of the Woodshole region. J. Mar. Res. 12: 121–140.

1958. The influence of the Continental Shelf on the tides of the Atlantic coast of the United States. J. Mar. Res. 17: 432–448.

REDFIELD, A. C., AND A. R. MILLER. 1955. Memo on water levels accompanying Atlantic coast hurricanes. W.H.O.I. Ref. No. 55–28, June 1955. (Manuscript)

1957. Water levels accompanying Atlantic coast hurricanes, *In* Interaction of sea and atmosphere. Met. Monogr. 2(10): 1–23.

REED, R. J. 1979. Cyclogenesis in polar air streams. Mon. Weather Rev. 107: 38–52.

REICHARD, R. P., AND B. CELIKOL. 1978. Application of a finite element hydrodynamic model to the Great Bay Estuary system, New Hampshire, U.S.A., p. 349–372. *In* J. C. J. Nihoul [ed.] Hydrodynamics of estuaries and fjords. Elsevier Oceanography Series No. 23, New York, NY.

REID, R. O. 1955. On the classification of hurricanes by storm tide and wave energy indices. Paper presented at May 1955 meeting, A.G.U. and A.M.S. A.M.S. Meteorol. Monogr. No. 10.

1956. Approximate response of water level on a sloping shelf to a wind fetch which moves towards shore. Tech. Memo No. 83. Beach Erosion Board, Corps of Engineers.

1957a. Forced and free surges in a narrow basin of variable depth and width: a numerical approach. Rep. No. 57–25T. Department of Oceanography, Texas A&M University, College Station, TX.

1957b. Modification of the quadratic bottom stress law for turbulent channel flow in the presence of surface wind stress. Tech. Memo. No. 93. Beach Erosion Board, Corps of Engineers. 33 p.

1958. Effect of Coriolis force on edge waves. I. Investigation of normal modes. J. Mar. Res. 16: 109–141.

1975. Comment on "Three-dimensional structure of storm-generated currents" by G. Z. Forristall. J. Geophys. Res. 80(9): 1184–1187.

REID, R. O., AND B. R. BODINE. 1968. Numerical model for storm surges in Galveston Bay. Proc. Am. Soc. Civ. Eng. J. Waterways Harbors Div. 94(WW1): 33–57.

REID, R. O., AND C. L. BRETSCHNEIDER. 1953. Surface waves and offshore structures. Technical Rep. No. 38-0, Oct. 1953. Texas A&M Research Foundation. 33 p. + 11 plates.

REID, R. O., AND A. C. VASTANO. 1966. Orthogonal coordinates for analysis of long gravity waves near islands. Santa Barbara Specialty Conference in Ocean Engineering. Proc. Soc. Civ. Eng. 1–20.

REID, R. O., A. C. VASTANO, AND T. J. REID. 1977a. Development of Surge II Program with application to the Sabine–Calcasieu area for Hurricane Carla and design hurricanes. Tech. Pap. No. 77–13, Nov. 1977. U.S. Army Corps of Engineers, Coastal Eng. Research Center, Fort Belvoir, VA. 218 p.

REID, R. O., A. C. VASTANO, R. E. WHITAKER, AND J. J. WANSTROTH. 1977b. Experiments in storm surge simulation, p. 145–168. *In* E. D. Goldberg, I. N. McCave, J. J. O'Brien, and J. H. Steele [ed.] The sea. Vol. 6. Chap. 5. Wiley Interscience Publication, New York, NY. 1048 p.

REID, R. O., AND R. E. WHITAKER. 1976. Wind driven flow of water influenced by a canopy. Pap. 11926. J. Waterways Coastal Eng. Div. Proc. Am. Soc. ASCE Civ. Eng. 102 (WW1): 61–77.

REID, R. O., AND B. W. WILSON. 1954. Compendium of results of storm tide and wave analysis for full hurricane conditions at Freeport, Texas. Texas A&M Project No. 91, Ref. 54–64F: 45 p.

REITAN, C. H. 1974. Frequencies of cyclones and cyclogenesis for North America, 1951–1970. Mon. Weather Rev. 102: 861–868.

1979. Trends in the frequencies of cyclone activity over North America. Mon. Weather Rev. 107: 1684–1688.

REMUS, M. D. 1979. Winter navigation: an overview. Great Lakes Commun. 9(5): 1–6.

RENARD, R. J. 1968. Forecasting the motion of tropical cyclones using a numerically derived steering current and its bias. Mon. Weather Rev. 96(7): 453–469.

RENARD, R. J., S. G. COLOGAN, M. J. DALEY, AND S. K. RINARD. 1973. Forecasting the motion of North Atlantic tropical cyclones by the objective MOHATT scheme. Mon. Weather Rev. 101: 206–214.

RESIO, D. T., AND C. L. VINCENT. 1977. Estimation of winds over the Great Lakes. J. Waterway Port Coastal and Ocean Div. Proc. Am. Soc. Civ. Eng. WW2: 265–283.

REYNOLDS, G. 1956. A wind analysis for the northern Irish Sea. Q. J. R. Meteorol. Soc. 82: 469–480.

RICHARDSON, L. F. 1922. Weather prediction by numerical process. Cambridge University Press, London and New York.

1925. How to solve differential equations approximately by arithmetic. Math. Gaz. 12: 415–421.

RICHARDSON, W. S. 1972. Evaluation of Lake Erie storm surge forecasts for 1971 to 1972 Lake Erie storm surge season. Enclosure to a letter dated August 9, 1972, to Mr. C. Dunn.

1978. Extra-tropical storm-related beach erosion. Mar. Weather Log 22: 149–153.

RICHARDSON, W. S., AND N. A. PORE. 1969. A Lake Erie storm surge forecasting technique. Tech. Memo. WBTM-TDL-24. U.S. Weather Bureau, Silver Spring, MD. 23 p.

RICHARDSON, W. S., AND N. A. PORE. 1972. Weather Service Program in Lake Erie storm surge forecasting, TDL, Sept. 1972. NOAA, 11 p.

RICHARDSON, W. S., AND D. J. SCHAWB. 1979. Comparison and verification of dynamical and statistical Lake Erie storm surge forecasts. NOAA Tech. Memo. NWS-TDL-69: 19 p.

RICHTMEYER, R. D. 1957. Difference methods for initial value problems. No. 4. Inter-science, New York, NY.

RICHTMEYER, R. D. 1963. A survey of difference methods for non-steady fluid dynamics. NCAR Tech. Notes 63–2: 25 p.

RICHTMEYER, R. D., AND K. W. MORTON. 1967. Difference methods for initial value problems. Wiley Interscience, New York, NY.

RIEDEL, H. P., AND F. L. WILKINSON. 1976. Numerical modelling — an aid to assessing field data, p. 30–33. Abstr. 15th Coastal Eng. Conf., July 11–17, 1976, Honolulu, HI. ASCE, New York, NY.

RIEHL, H. 1954. Tropical meteorology. McGraw-Hill Publications, New York, NY. 392 p.

1956. Sea surface temperature anomalies and hurricanes. Bull. Am. Meteorol. Soc. 37: 413–417.

1963. Some relations between wind and thermal structure of steady state hurricanes. J. Atmos. Sci. 20: 276–287.

1979. Climate and weather in the tropics. Academic Press, New York, NY. 611 p.

RINGE-JØRGENSEN, C. 1958. High-water problems on the Danish North Sea coast, p. 115–133. *In* J. W. Johnson [ed.] Proc. 6th Conf. Coastal Eng., Dec. 1957, Florida. Council on Wave Research, The Engineering Foundation.

ROBERT, A. J. 1966. The integration of a low order spectral form of the primitive meteorological equations. J. Meteorol. Soc. Jpn. Ser. 2, 44: 237–245.

ROBERTS, K. V., AND N. O. WEISS. 1966. Convective difference schemes. Math. Comp. 20: 272–299.

ROBIN, G. D. Q. 1963. Wave propagation through fields of pack ice. Philos. Trans. R. Soc. London Ser. A 255: 313–339.

ROBINSON, A. H. W. 1953a. The storm surge of January 31–February 1, 1953, and the associated meteorological and tidal conditions, p. 134–141. Proc. Conf. North Sea Floods.

1953b. The sea floods around the Thames Estuary, p. 170–176. Proc. Conf. North Sea Floods. Institute of Civil Engineers, London, U.K.

ROBINSON, A. R., A. TOMASIN, AND A. ARTEGIANI. 1973. Flooding of Venice: phenomenology and prediction of the Adriatic storm surge. Q. J. R. Meteorol. Soc. 99: 688–692.

ROBINSON, I. S. 1979. The tidal dynamics of the Irish and Celtic seas. Geophys. J. R. Astron. Soc. 56: 159–197.

ROCKWELL, D. C. 1966. Theoretical free oscillations of the Great Lakes, p. 352–368. Proc. 9th Conf. Great Lakes Res. Great Lakes Res. Div. Publ. No. 15. University of Michigan, Ann Arbor, MI.

RODGERS, E., R. C. GENTRY, W. E. SHENK, AND V. OLIVER. 1978. The benefits of using short interval satellite imagery to derive winds for tropical cyclones, p. 653–660. Proc. 11th Tech. Conf. Hurricanes Trop. Meteorol. Dec. 13–16, 1977, Miami Beach, FL. American Meteorological Society, Boston, MA.

RØED, L. P. 1979. Storm surges in stratified seas. Tellus 31: 330–339.

RØED, L. P., AND J. J. O'BRIEN. 1981. Geostrophic adjustment in highly dispersive media: an application to the marginal ice zone. Geophys. Astrophys. Fluid Dyn. 18: 263–278.

ROELOFS, E. W., AND D. R. BUMPUS. 1953. The hydrography of Pamlico Sound. Woods Hole Oceanogr. Inst. Collect. Repr. No. 547: 181–205.

RONDAY, F. C. 1976. Modèles hydrodynamiques. Rapport final programme National Belge sur l'Environment, Proj. Mer 3.

RONDY, D. R. 1969. Great Lakes ice atlas. U.S. Lake Surv. Res. Rep. No. 5.6.

ROSENTHAL, S. L. 1964. Some attempts to simulate the development of tropical cyclones by numerical methods. Mon. Weather Rev. 92: 1–21.

1970. A circularly symmetric primitive equation model of tropical cyclone development containing an explicit water vapour cyclone. Mon. Weather Rev. 98: 643–663.

1971. The response of a tropical cyclone model to variations in boundary layer parameters, initial conditions, lateral boundary conditions and domain size. Mon. Weather Rev. 10: 767–777.

1978. Numerical simulation of tropical cyclone development with latent heat release by the resolvable scales. 1. Model description and preliminary results. J. Atmos. Sci. 35: 258–271.

ROSS, B. E., AND P. JERKINS. 1977. A comparison of the application of two computer models of Tampa Bay, Florida, p. 91–101. *In* C. A. Brebbia [ed.] Applied numerical modelling. Proc. 1st Int. Conf. Appl. Numer. Model., July 11–15, 1977, University of Southampton, Southampton, U.K. John Wiley & Sons Ltd., New York, NY.

ROSS, D. 1979. Observing and predicting wind and wave conditions, p. 407–420. I.O.C. Workshop Rep. No. 17. Suppl. Pap. submitted to the Joint I.O.C./W.M.O. Seminar on Oceanographic Products and the I.G.O.S.S. Data Processing Services System, Moscow, USSR, Apr. 2–6, 1979.

ROSSBY, C. G. 1936. On frictional force between air and water and on the occurrence of a laminar boundary layer next to the surface of the sea. Pap. Phys. Oceanogr. 3(4): 1.

1937. On the mutual adjustment of pressure and velocity distributions in certain simple current systems I. J. Mar. Res. 1: 15–28.

1938. On the mutual adjustment of pressure and velocity distributions in certain simple current systems II. J. Mar. Res. 1: 239–263.

ROSSBY, C. G., AND R. B. MONTGOMERY. 1935. The layer of frictional influence in wind and ocean currents. Pap. Phys. Oceanogr. 3(3): 1.

ROSSITER, J. R. 1954. The North Sea storm surge of January 31 and February 1943. Philos. Trans. R. Soc. London Ser. A 251: 139.

1959a. A method for extracting storm surges from tidal records. Sonder. Dtsch. Hydrogr. Z. 12(3): 117–127.

1959b. Research methods of forecasting storm surges on the east and south coasts of Great Britain. Q. J. R. Meteorol. Soc. 85: 262–277.

1961. Interaction between tide and surge in the Thames. Geophys. J. R. Astron. Soc. 6: 29–53.

1971. Long period waves: seiches, surges and tides in coastal waters, p. 155–168. *In* D. A. Howells, I. P. Haigh, and C. Taylor [ed.] Dynamic waves in civil engineering. Wiley Interscience, New York, NY. 575 p.

ROSSITER, J. R., AND G. W. LENNON. 1965. Computation of tidal conditions in the Thames by the initial value method. Proc. Inst. Civ. Eng. 31: 25–56.

ROUCH, J. 1944. La variation du niveau de la mer en fonction de la pression atmosphérique. D'après les observations du pourquoi pas dans l'Antarctique? Bull. Inst. Oceanogr. (Monaco) 1–5.

ROY, J. H. L., J. ROFFEY, AND N. E. GERBIER. 1963. Report on aerial surveys in the Arabian Peninsula. FAO, UNSF Desert Locust Project Rep. OP/3.

RUMNEY, G. R. 1969. Climatology and the world's climates. The Macmillan Company, London. 656 p.

RUNCHAL, A. K. 1975. Numerical model for storm surge and tidal run-up studies. Symposium on modelling techniques, Sept. 3–5, 1975, San Francisco, CA. p. 1516–1534. Vol. 11. ASCE, New York, NY.

RUSSELL, H. C. 1898. The source of periodic waves. Nature (London) 62: 493–494.

SADLER, J. E. 1962. The first hurricane track determined by meteorological satellite. Indian J. Meteorol. Geophys. 13(1): 29–44.

SADLER, J. E., AND R. E. GIDLEY. 1973. Tropical cyclones of the North Indian Ocean. UHMET-73-02, Mar. 1973. Department of Meteorology, University of Hawaii at Manoa, Honolulu, HI.

SANDERS, F., A. L. ADAMS, N. J. R. GORDON, AND W. D. JENSEN. 1978. A study of forecast errors in a barotropic operational model for predicting paths of tropical storms, p. 389–396. Proc. 11th Tech. Conf. Trop. Meteorol., Dec. 13–16, 1977, Miami Beach, FL.

SANDERS, F., AND R. W. BURPEE. 1968. Experiments in barotropic hurricane track forecasting. J. Appl Meteorol. 7(3): 313–323.

SANDERS, F., AND J. R. GYAKUM. 1980. Synoptic–dynamic climatology of the "bomb." Mon. Weather Rev. 108: 1589–1606.

SANDERS, F., A. C. PIKE, AND J. P. GAERTNER. 1975. A barotropic model for operational prediction of tropical storms. J. Appl. Meteorol. 14(3): 265–280.

SANDERSON, R. M. 1974. The unusual waves off Southeast Africa. Mar. Obs. 44: 180–183.

SATER, J. E., A. G. RONHOUDE, AND L. C. VAN ALLEN. 1971. Arctic environment and resources. No. 736. Arctic Institute of North America, Washington, DC. 184 p.

SAUNDERS, P. M. 1976. On the uncertainty of wind stress curl calculations. J. Mar. Res. 34: 155–160.

1977. Wind stress on the ocean over the eastern continental shelf of North America. J. Phys. Oceanogr. 7: 555–566.

SAVILLE, T. 1953. Wind set-up and waves in shallow water. Tech. Memo. No. 27. U.S. Beach Erosion Board, Washington, DC.

1961. Experimental determination of wave set-up. Proc. 2nd Tech. Conf. Hurricanes. Natl. Hurricane Res. Proj. Rep. No. 50: 242–252.

SCHAFER, P. J. 1966. Computation of a storm surge at Barrow, Alaska. Arch. Meteorol. Geophys. Biolkimatol. Ser. A 15(3–4): 372–393.

SCHALKWIJK, W. F. 1947. A contribution to the study of storm surges on the Dutch coast. K. Ned. Meteorol. Inst. De Bilt, No. 125, Medeelingen Envertandelingen Ser. B (7): 111 p.

SCHLOEMER, R. W. 1954. Analysis and synthesis of hurricane wind patterns over Lake Okeechobee, Florida. Hydrometeorol. Rep. No. 31, Mar. 1954. U.S. Weather Bureau, Washington, DC. 49 p.

SCHMITZ, H. P. 1962. On external surges and special meteoro-hydrographical problems in computing storm surges in adjacent seas and lakes by physical methods, p. 89. Mitt. Inst. Meereskd. Univ. Hamburg Nr. 1. Proc. Symp. Math. Hydrogyn. Meth. Phys. Oceanogr.

1965. Modellrechnungen zur deepwater-surge-Entwieklung-das external surge problem. Dtsch. Hydrogr. Z. 18: 49.

SCHOLER, H. A. 1958. Tides in rivers and coastal inlets. J. Inst. Eng. Aust. 30: 125–136.

1960. Inst. Eng. Aust. 32: 14–24.

SCHÖNFELD, J. C. 1955. Tides and storm surges in a shallow sea. C.S.D. 55-3-N: 35 p.

SCHÖNFELD, J. C., AND H. J. STROBAND. 1961. Getijonderzoek door middel van de hydraulisch-elektrische analogie. (Tidal research by means of the hydraulic-electric analogy.) Delta Comm. Rep. 4: 211–230.

SCHÖNFELD, J. C., AND C. M. VERHAGEN. 1959. Development of the tidal analogue technique in Holland, p. 376–380. Proc. 2nd Int. Analogue Comput. Meet., Sept. 1–6, 1959, Strasburg, France.

SCHUMANN, E. H. 1980. Giant wave anomalous seas of the Agulhas current, p. 27–31. Oceans, July 1980.

SCHWAB, D. J. 1975. A normal mode method for predicting storm surges on a lake. Spec. Rep. No. 20. Center for Great Lakes Studies, University of Wisconsin, Milwaukee, WI. 50 p.

1978. Simulation and forecasting of Lake Erie storm surges. Mon. Weather Rev. 106: 1476–1487.

1982. An inverse method for determining stress from water level fluctuations. Dyn. Atmos. Oceans 6(4): 251–278.

SCHWERDT. R. W. 1976. Revised values of parameters for the probable maximum hurricane and standard project hurricanes, p. 126–127. Proc. Conf. Coastal Meteorol., Sept. 21–23, 1976, Virginian Beach, VA. American Meteorological Society, Boston, MA.

1978. Reduction of overwater wind speed when intense hurricanes move overland, p. 490–495. Proc. 11th Tech. Conf. Hurricanes Trop. Meteorol. Dec. 13–16, 1977, Miami Beach, FL. American Meteorological Society, Boston, MA.

SCHWIDERSKI, E. W. 1978a. Global ocean tides. Part I. A detailed hydrodynamical interpolation model. NSWC/DL TR-3866, Sept. 1978. Naval Surface Weapons Center, Dahlgren Lab, Dahlgren, VA. 88 p.

1978b. Hydrodynamically defined ocean bathymetry. NSWC/DL TR-3888, Nov. 1978. Naval Surface Weapons Center, Dahlgren Lab, Dahlgren, VA. 57 p.

1979. Global ocean tides. Part II. The semidiurnal principle lunear tide (M_2). Atlas of tidal charts and maps. NSWC TR 79-414, Dec. 1979. Naval Surface Weapons Center, Dahlgren Lab, Dahlgren, VA. 15 p.

1980a. Ocean tides. Part I. Global ocean tidal equations. Mar. Geodes. 3: 161–217.

1980b. Ocean tides. Part II. A hydrodynamical interpolation model. Mar. Geodes. 3: 219–255.

1980c. On charting global ocean tides. Rev. Geophys. Space Phys. 18(1): 243–268.

SCHWOLKWYK, W. F. 1947. A contribution to the study of storm surges on the Dutch Coast. K. Ned. Meteorol. Inst. Bull. No. 125. Med. Ver. Ser. B 1(7): 1–111.

SEAY, D. N. 1964. Annual typhoon report, 1963, p. 6–11. Fleet Weather Central, Guam.

SEKIOKA, M. 1970. On the behavior of cloud patterns as seen on satellite photographs in the transformation of a typhoon in to an extra-tropical cyclone. J. Meteorol. Soc. Jpn. 48: 224–233.

1972a. A kinematical consideration on behavior of a front within a typhoon area. Arch. Meteorol. Geophys. Bioklimatol. Ser. A 21: 1–12.

1972b. A note on the extratropical transformation on a typhoon in relation with cold outbreaks. Arch. Meteorol. Geophys. Bioklimatol. Ser. A 21: 413–418.

SEN, S. N. 1978. Introduction, p. 1.1-1–1.1-6. *In* P. K. Das, M. Miyazaki, and C. P. Jelesnianski [ed.] Present techniques of tropical storm surge prediction. WMO No. 500: 87 p.

SETHURAMAN, S. 1979. Atmospheric turbulence and storm surge due to Hurricane Belle (1976). Mon. Weather Rev. 107: 314–321.

SHARAF EL DIN, S. H., AND Z. A. MOURSY. 1977. Tide and storm surges on the Egyptian Mediterranean coast. Rapp. P.-V. Reun. Cons. Int. Explor. Mer 24(2): 33–37.

SHAW, A. M. 1929. An estimate of storm tide hazards to New Orleans. Eng. New Rec. 102(8): 698–702.

SHAW, SIR NAPIER. 1921. Forecasting weather. 2nd ed. British Meteorological Office, London, U.K.

SHAW, S. L. 1979. Central North Pacific tropical cyclones, 1978. Mar. Weather Log 23(3): 166–172.

SHAW, V. K. 1974. Surge study, Goderich Harbour, Ontario. Marine Engineering Design and Construction Branch, Department of Public Works, Ottawa, Ont. 25 p.

SHEA, D. I., AND W. M. GRAY. 1973. The hurricane's inner core. J. Atmos. Sci. 30(11): 1544.

SHEETS, R. C. 1969. Some mean hurricane sounding. J. Appl. Meteorol. 8: 134–146.

SHEETS, R. C., AND N. E. LASEUR. 1978. Project Stormfury: present status — future plans, p. 280–287. Proc. 11th Tech. Conf. Hurricanes Trop. Meteorol., Dec. 13–16, Miami Beach FL.

SHENG, Y. P., AND W. J. LICK. 1972. The wind driven currents in a partially ice covered lake. FTAS/TR-72-78. School of Engineering, Case Western Reserve University, Cleveland, OH. 70 p.

SHIPLEY, A. M. 1963. On measuring long waves with a tide gauge. Dtsch. Hydrogr. Z. 16(3): 16–19.

SHRIFFLER, J. H., AND F. S. BINKOWSKI. 1981. Observations of pressure jump lines in the mid-west, August 10–12, 1976. Mon. Weather Rev. 109(8): 1713–1725.

SHULEYKIN, V. V. 1978. Calculation of the development and dissipation of hurricanes and the main waves produced by hurricanes. Gidrometeoizdat Press, Leningrad, USSR. 96 p.

SHULTS, G. J. 1981. Hurricane structure and the zero potential vorticity approximation. Mon. Weather Rev. 109: 324–329.

SHUMAN, F. G. 1957. Numerical methods in weather prediction. II. Smoothing and filtering. Mon. Weather Rev. 85: 357–361.

1974. Analysis and experiment in nonlinear computational stability. Difference and spectral methods for atmospheric and ocean dynamics problems. Proc. Symp. Novosibirsk. Part I: 51–81.

SHUMAN, F. G., J. A. BROWN, AND K. CAMPANA. 1972. A new explicit differencing system for primitive equations. Paper presented at the Am. Geophys. Union, Spring Meeting, Washington, DC. Trans. Am. Geophys. Union 33: 386. (Abstr.)

SHUMAN, F. G., AND J. B. HOVERMALE. 1968. An operational six layer primitive equation model. J. Appl. Meteorol. 7: 525–547.

SHUMAN, F. G., AND J. D. STACKPOLE. 1968. Note on the formulation of finite difference equations incorporating a map scale factor. Mon. Weather Rev. 96(3): 157–161.

SIBUL, O. J. 1955. Laboratory study of wind tides in shallow water. Tech. Memo. No. 61, Aug. 1955. Beach Erosion Board, Corps of Engineers. 50 p.

SIBUL, O. J., AND J. W. JOHNSON. 1957. Laboratory study of wind tides in shallow water. Pap. No. 1210. J. Waterways Harbors Div. Proc. Am. Soc. Civ. Eng. WW1: 32 p.

SIEFERT, W. 1968. Sturmflutvorpersage für den Tidebereich der Elbe aus dem Verlaut der Windstaukurve in Cuxhaven. Mitt. Franzius Int. TV Hanover H30.

1978. Storm surge prediction in tidal rivers: a new conception, p. 986–997. Vol. 1. Proc. 16th Coastal Eng. Conf., Aug. 27–Sept. 3, 1978, Hamburg, W. Germany. ASCE, New York, NY.

SIELECKI, A. 1968. An energy-conserving difference scheme for the storm surge equations. Mon. Weather Rev. 96: 150–156.

SIELECKI, A., AND M. G. WURTELE. 1970. The numerical integration of the nonlinear shallow water equations with sloping boundaries. J. Computat. Phys. 6: 219–236.

SIKKA, D. R., AND R. SURYANARAYANA. 1972. Forecasting the movement of tropical storms, depressions in the Indian region by a computer oriented technique using climatology and persistence. Indian J. Meteorol. Hydrol. Geophys. 23(1): 35–40.

SILVESTER, R. 1969. Tides and long period waves on continental margins, p. 113–130. Proc. 13th Congr. Int. Assoc. Hydraul. Res., Aug. 31–Sept. 5, 1961. Vol. 3.

1971. Computation of storm surge, p. 1995–2010. Proc. 12th Conf. Coastal Eng. Vol. 3. ASCE, New York, NY.

1974. Coastal engineering II: Sedimentation, estuaries, tides, effluents, and modelling, p. 178–191. Developments, in geotechnical engineering. 4B. Elsevier North Holland, New York, NY.

SIMMONS, H. B. 1964. Protection of Narragansett Bay from hurricane surges. Summary report. Hydraulic model investigation, U.S. Army Engineer Division, New England, Oct. 1964. Tech. Rep. No. 2-662: 48 p. + tables and figures.

SIMONS, T. J. 1973a. Development of three-dimensional numerical models of the Great Lakes. Sci. Ser. No. 12. Inland Waters Directorate, Canada Center for Inland Waters, Burlington, Ont. 26 p.

1973b. Comparison of observed and computed currents in Lake Ontario during Hurricane Agnes, June 1972, p. 831–844. *In* Proceedings of the 16th Conference on Great Lakes Research. Proc. Int. Assoc. Great Lakes Reg. 16: 1068 p.

1975. Effective wind stress over the Great Lakes derived from long term numerical model simulations. Atmosphere 13(4): 169–179.

1978. Wind driven circulations in the Southwest Baltic. Tellus 30: 272–283.

1979. Storm surge modelling, p. 113–116. Proc. Symp. Long Waves Ocean. Manuscr. No. 53. Marine Sciences Directorate, Department of Fisheries and Environment, Ottawa, Ont.

1980. Circulation models of lakes. Bull. Fish Res. Board Can. 203: 146 p.

SIMON-TOV, M. 1974. A time-dependent, two-dimensional mathematical model for simulating the hydraulic, thermal and water quality characteristics in shallow water bodies. ORNL-TM-4626. Oak Ridge National Lab, Tennessee.

SIMPSON, R. H. 1952. Exploring the eye of Typhoon Marge 1951. Bull. Am. Meteorol. Soc. 33: 286–298.

1971. The decision process in hurricane forecasting. NOAA. Tech. Memo. NWS-SR-63: 35 p.

SIMPSON, R. H., AND J. C. FREEMAN. 1976. Coastal hazard potentials. Proc. Conf. Coastal Meteorol., Sept. 21–23, 1976, Virginian Beach, VA. American Meteorological Society, Boston, MA.

SIMPSON, R. H., AND M. B. LAWRENCE. 1971. Atlantic hurricane frequencies along the U.S. coastline. NOAA Tech. Memo. N.W.S. SR-58. Washington, DC.

SIMPSON, R. H., AND H. RIEHL. 1981. The hurricane and its impact. Louisiana State University Press, Baton Rouge, LA. 398 p.

SMITH, A. A. 1962. Hydraulic models involving tides and tidal currents. Engineer 214: 532–535.

SMITH, R. 1976. Giant waves. J. Fluid Mech. 77(3): 417–431.

SMITH, S. D. 1980. Wind stress and heat flux over the ocean in gale force winds. J. Phys. Oceanogr. 10: 709–726.

SMITH, S. D., AND E. G. BANKE. 1975. Variation of the sea surface drag coefficient with wind speed. Q. J. R. Meteorol. Soc. 101: 665–673.

SNEYERS, R. 1953. La tempête et le débordement de la mer du 1er février 1953. Ciel Terre 69(3–4): 97–108.

SOBEY, R. J. 1970. Finite difference schemes compared for wave-deformation characteristics in mathematical modelling of two-dimensional long-wave propagation. Tech. Memo No. 32, Oct. 1970. U.S. Army Corps of Engineers, Coastal Engineering Research Center. 29 p.

1978. Wind wave frequencies in a tropical cyclone region, p. 76–96. Proc. 16th Coastal Eng. Conf. Hamburg, W. Germany. Chap. 3. ASCE, New York, NY.

SOBEY, R. J., B. A. HARPER, AND G. M. MITCHELL. 1981. Numerical modelling of tropical cyclone storm surge, p. 725–745. Proc. 7th Coastal Eng. Conf., Mar. 23–28, 1980, Sydney, Australia. Vol. 1. ASCE, New York, NY.

SOETJE, K. C., AND C. BROCKMANN. 1983. An operational numerical model of the North Sea and the German Bight. *In* J. Sundermann and W. Lenz [ed.] North Sea dynamics. Springer-Verlag, Berlin.

SOLBERG, H. 1936. Le mouvement d'inertie de l'atmosphère stable et son rôle dans la théorie des cyclones. P.-V. Meteorol., I.U.G.G., Intern II: 66–82. Edinburgh, U.K.

SOMMERFELD, A. 1949. Partial differential equations. Academic Press, New York, NY. 333 p.

STEERS, J. A. 1954. The east coast floods: January 31–February 1, 1953. Proc. Conf. North Sea Floods. Weather 9(2): 280–298.

STERNECK, R. V. 1919. Die Gezeitenerscheinungen in der Adria. Densepr. Akad. Wiss. Wien. 96: 277–324.

1920. Die Gezeiten der Ozeane, Stiz. Ber. Akad. Wiss. Wien. 129: 131–150.

STEWART, J. Q. 1962. The Great Atlantic coast tides of March 5–8, 1962. Weatherwise 15: 117–120.

STEWART, R. W. 1961. The wave drag of wind over water. J. Fluid Mech. 10: 189–194.

1974. The air–sea momentum exchange. Boundary-Layer Meteorol. 6: 151–167.

STOKES, G. G. 1847. On the theory of oscillatory waves. Trans. Cambridge Philos. Soc. 8: 441.

STORM TIDE WARNING SERVICE. 1980. Storm Tide Warning Service extends forecasts. Dock Harbour Auth. 61(714): 4–6.

STRAVISI, F. 1972. A numerical experiment on wind effects in the Adriatic Sea, p. 187–196. Accad. Naz Lincei, Estratto dal fase 2. Ser. VIII. February 1972, Rome.

1973. Analysis of a storm surge in the Adriatic Sea by means of a two-dimensional linear model. Atti Accad. Naz. Lincei Rend. Cl. Sci. Fis. Mat. Nat. Ser. VIII 54(2): 243–260.

STRIEM, H. L. 1974. Storm surges and unusual sea levels on Israel's Mediterranean Coast. Int. Hydrogr. Rev. 51: 59–70.

STURM, H. 1974. Giant waves. Ocean 2(3): 98–101.

SUCHMAN, D., AND D. W. MARTIN. 1976. Wind sets from S.M.S. images: an assessment of quality for G.A.T.E. J. Appl. Meteorol. 15: 1265–1278.

SUNDQVIST, H. 1970a. Numerical simulation of the development of tropical cyclones with a ten layer model. Part I. Tellus 22: 359–390.

1970b. Numerical simulation of the development of tropical cyclones with a ten level model. Part II. Tellus 22: 504–510.

SUOMI, V. E. 1969. Recent developments in satellite techniques for observing and sensing the atmosphere, p. 222–234. *In* G. A. Corby [ed.] The global circulation of the atmosphere. Royal Meteorological Society, Bracknell, U.K.

SUTCLIFFE, R. C. 1936. Surface resistance in atmospheric flow. Q. J. R. Meteorol. Soc. 62: 3–14.

1947. A contribution to the problem of development. Q. J. R. Meteorol. Soc. 73: 370–383.

SVANSSON, A. 1958. Some computations of water heights and currents in the Baltic. Tellus 11(2): 232–238.

1972. Canal models of sea level and salinity variations in the Baltic and adjacent waters. Rep. No. 26. Series Hydrography, Fishery Board of Sweden, Lund, Sweden. 72 p.

SVANSSON, A., AND J. SZARON. 1975. Sea level computations of the Baltic with a 20 canal model. Tellus 27: 596–605.

SVENSSON, U. 1979. The structure of the turbulent Ekman layer. Tellus 31: 340–350.

SVERDRUP, H. U. 1926. Dynamics of tides on the North Siberian Shelf: results from the Maud expedition. Geophys. Publ. 4(5): 1–75.

SVERDRUP, H. U., M. W. JOHNSON, AND R. H. FLEMING. 1946. The oceans, their physics, chemistry and general biology. Prentice-Hall, New York, NY. 1060 p.

SVERDRUP, H. U., AND W. H. MUNK. 1947. Wind, sea and swell: theory of relations for forecasting. H. P. Publ. No. 601. U.S. Navy.

SWAMINATHAN, D. R. 1966. The extra-ordinary path of the Bay of Bengal storm of December 7–15, 1965, in relation to the Tiros 10 satellite observations and the upper tropospheric wind field. Indian J. Meteorol. Geophys. 20: 357–360.

SWANSON, R. L. 1976. Tides. *In* Marine ecosystem analysis (MESA). New York Bight Atlas, Monogr. No. 4, Jan. 1976. New York Sea Grant Institute, Albany, NY. 32 p.

TAKAHASHI, K. 1939. Distribution of pressure and wind in a typhoon. J. Meteorol. Soc. Jpn. 17: 417–421.

1952. Techniques in typhoon forecast. Geophys. Mag. 24: 1–8.

TAKEGAMI, T. 1934. The boundary value problem of the wind current in a lake or sea. Mem. Coll. Sci. Kyoto Imp. Univ. Ser. A 17: 305–318.

1936. A study of the effect of a local wind on the sea surface. Mem. Coll. Sci. Kyoto Imp. Univ. Ser. A 19: 109–130.

1938. A study of the effect of a travelling atmospheric disturbance upon the sea surface. Mem. Coll. Sci. Kyoto Imp. Univ. 21: 55–74.

TAKEHASI, R. 1934. Seiches and surface waves in Ofunato Bay and two other bays. Bull. Earthquake Res. Inst. Tokyo Imp. Univ. Suppl. 1: 198–217.

TALJAARD, J. J. 1967. Development, distribution and movement of cyclones and anticyclones in the Southern Hemisphere during the I.G.Y. J. Appl. Meteorol. 6: 973–987.

TANG, F. L. W., S. W. J. CHANG, AND S. H. OW. 1978. Wind induced water surface set-up and drift currents, p. 841–858. Proc. 16th Coastal Eng. Conf., Aug. 27–Sept. 3, 1978, Hamburg, W. Germany. Vol. 1. ASCE, New York, NY.

TANCRETO, A. E. 1958. A method for forecasting the maximum surge at Boston due to extra-tropical storms. Mon. Weather Rev. 86: 197–200.

TANNEHILL, I. R. 1944. Hurricanes. Princeton University Press, Princeton, NJ. 269 p.

1950. Hurricanes. Princeton University Press, Princeton, NJ. 304 p.

TAYFUN, M. A. 1979. Joint occurrences in coastal flooding. J. Waterway Port Coastal Ocean Div. Proc. Am. Soc. Civ. Eng. WW2: 107–123.

TAYLOR, C., AND J. DAVIS. 1972. Tidal and long wave propagation — a finite element approach. C/R/189/72. Department of Civil Engineering, University College of Swansea, U.K.

TAYLOR, C., AND P. HOOD. 1973. A numerical solution of the Navier–Stokes equations using the finite element technique. Comput. Fluids 1: 73–100.

TAYLOR, G. I. 1915. Eddy motion in the atmosphere. Philos. Trans. R. Soc. Ser. A 215: 1–26.

1916. Skin friction of the wind on the earth's surface. Proc. R. Soc. London Ser. A 92: 196–199.

TAYLOR, J. D. 1975. Note on map projections. M.E.D.S. Tech. Note No. 7, May 1975. Fisheries and Marine Service, Environment Canada, Ottawa, Ont. 13 p.

TAYLOR, P. A., AND P. R. GENT. 1978. A numerical investigation of variations in the drag coefficient for the air flow above water waves. Q. J. R. Meteorol. Soc. 104: 979–988.

TAYLOR, R. B. 1980. Simplified methods for the prediction of hurricane surge and water run-up. Mar. Tech. Soc. J. 14(3): 20–26.

TEBALDI, C. 1973. Numerical study of nonlinear storm surges. Pure Appl. Geophys. 3: 2346–2357.

TEPPER, M. 1950a. A proposed mechanism of squall lines: the pressure jump-line. J. Meteorol. 7(1): 21–29.

1950b. On the generation of pressure jump lines by the impulsive addition of momentum to simple current systems. J. Meteorol. 12(4): 287–297.

TERADA, K. 1939. On "tsunami" or destructive sea waves excited by a travelling typhoon. Mem. Imp. Mar. Obs. Kobe, Japan 7(2): 209–230.

1912. Secondary undulations of tides caused by cyclonic storms. Proc. Tokyo Math-Phys. Soc. 2nd Ser. 6: 196–201.

TERADA, T., AND S. YAMAGUTI. 1928. On the effect of cyclones upon sea level. Proc. Imp. Acad. Jpn. 28: 478–480.

TETRA TECH. INC. 1978. Coastal flooding storm surge model. Part I: Methodology. Prepared by Tetra Tech. Inc. for the U.S. Department of Insurance Administration, Washington, DC. May 1978.

THACKER, W. C. 1977. Irregular grid finite difference techniques: simulations of oscillations in shallow circular basins. J. Phys. Oceanogr. 7: 284–292.

1978a. Comparison of finite element and finite difference schemes. Part I: One dimensional gravity wave motion. J. Phys. Oceanogr. 8: 676–679.

1978b. Comparison of finite element and finite difference schemes. Part II: Two-dimensional gravity wave motion. J. Phys. Oceanogr. 8: 680–689.

1978c. Irregular grid finite difference techniques for storm surge calculations for curving coastlines. *In* J. C. J. Nihoul [ed.] Marine forecasting. Proc. 10th Int. Liège Colloq. Ocean Hydrodyn. Elsevier Oceanogr. Ser. 25: 261–283.

1980a. A brief review of techniques for generating irregular computational grids. Int. J. Numer. Methods Eng. 15: 1335–1341.

1980b. A geodesic finite difference method for curved domains: simulations of tidal motion on a sphere. J. Comput. Phys. 37: 355–370.

THACKER, W. C., A. GONZALEZ, AND G. E. PUTLAND. 1980. A method for automating the construction of irregular computational grids for storm surge forecast models. J. Comput. Phys. 37: 371–387.

THIEL, V. G. 1964. Die Sturmflut der Nord und Ostsee vom 16. und. 17. Februar 1962. Dtsch. Hydrogr. Z. 17(4): 174–178.

THIJSSE, J. T. 1938. On wind effects. U.S. Waterways Exp. Stn. Bull. 2: 213–222.

THOM, H. C. S. 1960. The distribution of annual storm frequency. J. Geophys. Res. 65: 213–222.

THOMAS, J. H. 1975. A theory of steady wind-driven currents in shallow water with variable eddy viscosity. J. Phys. Oceanogr. 5: 136–142.

THOMPSON, W. J., R. L. ELSBERRY, AND R. G. READ. 1981. An analysis of eastern North Pacific tropical cyclone forecast errors. Mon. Weather Rev. 109(9): 1930–1938.

TICKNER, E. G. 1957. Effects of bottom roughness on wind tide in shallow water. Tech. Memo. No. 95, May 1957. Beach Erosion Board, Corps of Engineers. 25 p.

1960. Effects of reefs and bottom slopes on wind set-up in shallow water. Tech. Memo. No. 122, Nov. 1960. Beach Erosion Board, Corps of Engineers. 20 p.

1961. Transient wind tides in shallow water. Tech. Memo. No. 123, Jan. 1961. Beach Erosion Board, Corps of Engineers. 48 p.

TIMCHALK, A., L. F. HUBERT, AND S. FRITZ. 1965. Wind speeds from TIROS pictures of storms in the tropics. U.S. Weather Bur. Meteorol. Satellite Lab. Rep. No. 33.

TIMMERMAN, H. 1971. On the connection between cold fronts and gust bumps. Dtsch. Hydrogr. Z. 24(4): 159–172.

1975. On the importance of atmospheric pressure gradients for the generation of external surges in the North Sea. Dtsch. Hydrogr. Z. 28(2): 62–71.

1979. Forecasting meteorological effects on water levels on a routine basis with a numerical model. Dtsch. Hydrogr. Z. 32: 190–203.

TODD, D. K., AND R. L. WIEGEL. 1952. Near-coastal storms and associated waves. Trans. Am. Geophys. Union 33(2): 217–225.

TOMASIN, A. 1972. Autoregressive prediction of sea level in the northern Adriatic. Riv. Ital. Geofis. 21: 211–214.

TOMASIN, A., AND R. FRASETTO. 1979. Cyclogenesis and forecast of dramatic water elevations in Venice. *In* J. C. J. Nihoul [ed.] Marine forecasting. Proc. 10th Int. Liège Colloq. Ocean Hydrodyn. Elsevier Oceanogr. Ser. 25: 427–438.

TOMCZAK, V. G. 1950. Die Sturmfluten vom 9. und 10. Februar 1949 an der Deutschen Nordseeküste. Dtsch. Hydrogr. Z. 3(3–4): 227–240.

1952a. Der Einfluss der Küstengestalt und des Norgelagerten Meeresbodens aut den windbedingten Anstau des Wassers. Part I. Dtsch. Hydrogr. Z. 5(2–3): 114–131.

1952b. Der Einfluss der Küstengestalt und des Norgelagerten Meeresbodens aut den windbedingten Anstau des Wassers. Part II. Dtsch. Hydrogr. Z. 5(5–6): 277–284.

TOWNSEND, J. 1975. Forecasting 'negative' storm surges in the Southern North Sea. 45: 27–35.

1979. The storm surge of January 11–12, 1978. Meteorol. Mag. 108: 147–153.

TREWARTHA, G. T. 1968. An introduction to climate. McGraw-Hill Publications, New York, NY. 408 p.

TRONSON, K. 1975. The hydraulics of South Australian Gulf System II. Resonances. Aust. J. Mar. Freshwater Res. 26: 363–374.

TRONSON, K., AND B. J. NOYE. 1973. A statistical model for prediction of storm surges on the Adelaide foreshore, p. 190–196. Proc. 1st Aust. Conf. Coastal Eng., May 1973, Sydney, Australia.

TSCHIRHART, G. 1958. Les conditions aérologiques à l'avant des lignes de grains en Afrique Equatoriale. Meteorol. Natl. Monogr. Roll. 28 p.

TSE, S. Y. W. 1966. A new method for the prediction of typhoon movement using the 700 mb chart. Q. J. R. Meteorol. Soc. 92: 239–253.

TSENG-HAO, C., AND F. SHIH-ZAO. 1975. A preliminary study on the mechanism of shallow water storm surges. Sci. Sin. 18(2): 242–261.

TUBBESING, S. K. 1979. Natural hazards data resources: uses and needs. Monogr. No. 27. Institute of Behavioral Sciences, University of Colorado, Boulder, CO. 160 p.

UENO, T. 1964. Nonlinear numerical studies on tides and surges in the central part of Seto Inland Sea. Oceanogr. Mag. 16: 53–124.

1981. Numerical computations of the storm surges in Tosa Bay. J. Oceanogr. Soc. Jpn. 37: 61–73.

UFFORD, H. A. Q. 1953. The disastrous storm surge of February 1. Weather 8(4): 116–120.

UNITED NATIONS EDUCATIONAL, SCIENTIFIC AND CULTURAL ORGANIZATION. 1967. Annual summary of information on natural disasters, 1967. Paris, France.

1968. Annual summary of information on natural disasters, 1968. Paris, France.

1969. Annual summary of information on natural disasters, 1969. Paris, France.

1970. Annual summary of information on natural disasters, 1970. Paris, France.

UNITED STATES ARMY COMMITTEE ON TIDAL HYDRAULICS. 1980. Evaluation of numerical storm surge models. U.S. Army Comm. Tidal Hydraul. Tech. Bull. No. 21: 70 p.

UNITED STATES WATER RESOURCES COUNCIL: HYDROLOGY COMMITTEE. 1979. Report of the Storm Surge Assessment Working Group.

UNOKI, S. 1959. An investigation on meteorological tides in the neighboring seas of Japan. IV. General features of regional distribution and seasonal variation. Oceanogr. Mag. 11(1): 51–63.

URSELL, F. 1952. Edge waves on a sloping beach. Proc. R. Soc. London Ser. A 214: 79–97.

UUSITALO, S. 1960. The numerical calculation of wind effect on sea level elevations. Tellus 12(4): 427–435.

VAN DE GRAAFF, J. 1979. Dune erosion during a storm surge. Coastal Eng. 1: 99–134.

VAN DORN, W. G. 1953. Wind stress on an artificial pond. J. Mar. Res. 12: 249–276.

VAN HAMME, J. L. 1979. Observations and studies of the cyclogenesis in the Ligurian Sea, p. 493–509. I.O.C. Workshop Rep. No. 17. Supplement papers submitted to the Joint I.O.C./W.M.O. seminar on oceanographic products and the I.G.O.S.S. data processing and services system, Apr. 2–6, 1979, Moscow.

VAN LOON, H., AND J. WILLIAMS. 1976a. The connection between trends of mean temperature and circulation at the surface: part I. Winter. Mon. Weather Rev. 104: 265–280.

1976b. The connection between trends of mean temperature and circulation at the surface: part II. Summer. Mon. Weather Rev. 104: 1003–1011.

VANONI, V. A., AND J. H. CARR. 1950. Harbor surging, p. 60–68. Proc. 1st Conf. Coastal Eng., Berkeley, CA.

VAN VEEN, J. 1938. Water movement in the Straits of Dover. J. Cons. Cons. Int. Explor. Mer. 13: 7–38.

1946. Electrische nabvotsing van getijden. Ingenier No. 3: 4 p.

1947a. Analogy between tides and A.C. electricity. Engineer 184: 498–544.

1947b. Analogie entre marées et courants alternatifs. Houille Blanche 5: 474–490.

1947c. The calculation of tides in new channels. Trans. Am. Geophys. Union 28(6): 861–866.

VASTANO, A. C., AND R. O. REID. 1967. Tsunami response for islands: verification of a numerical procedure. J. Mar. Res. 25(2): 129–139.

1970. Tsunami response for islands: comparison of the hydraulic and numerical approaches. J. Mar. Res. 28(3): 345–356.

VEIGAS, K. W. 1961. Prediction of 12, 24 and 36 hour displacement of hurricanes by statistical methods. Final report GWB9807. Travelers Weather Research Center, Hartford, CT. 36 p.

1962. Development of prediction equations for hurricane movement. Final report CWB10170. Travelers Weather Research Center, Hartford, CT. 59 p.

1966. The development of a statistical–physical hurricane prediction model. Final report CWB-10966. Travelers Weather Research Center, Hartford, CT. 19 p.

VEIGAS, K. W., R. G. MILLER, AND G. M. HOWE. 1959. Probabilistic prediction of hurricane movements by synoptic climatology. Occas. Pap. Meteorol. No. 2, Travelers Weather Research Center, Hartford, CT. 54 p.

VOYT, S. S. 1974. Long waves and tides, p. 33–51. *In* P. S. Lineykin [ed.] I.T.O.G.I. Summaries of scientific progress. Oceanology. Vol. 2. G. K. Hall and Co., Boston, MA.

VENKATESH, S. 1974. The development of manual techniques for the real time prediction of storm surges on the Great Lakes. Report prepared for the Department of Environment under contract No. OS3-0248, July 1974. CCIW, Burlington, Ont. 136 p.

VENKATESH, S., AND M. B. DANARD. 1976. A model for computing small scale wind variations over a water surface. Report of the Atmospheric Dynamics Corp., Dec. 1976, Elmira, Ont. 45 p.

VERBER, J. L. 1960. Long and short period oscillations in Lake Erie. Division of Shore Erosion, Department of Natural Resources, Ohio. 80 p. + figures.

VERMA, A. P., AND R. G. DEAN. 1969. Numerical modelling of hydromechanics of bay systems, p. 1069–1087. *In* Civil engineering in the oceans. Part II. ASCE Conf., Dec. 10–12, 1969, Miami Beach, FL.

VERONIS, G. 1956. Partition of energy between geostrophic and non-geostrophic oceanic motions. Deep-Sea Res. 3: 157–177.

VERONIS, G., AND H. STOMMEL. 1956. The action of variable wind stresses on a stratified ocean. J. Mar. Res. 15: 43–75.

VILLAIN, C. 1952. Carte des lignes cotidals dans les océans. Ann. Hydrogr. 3: 269.

VITTORI, O., AND F. TAMPIERI. 1979. Venice: sea–lagoon exchange in a modified tide regime. Science (Washington, DC) 204(4390): 261–264.

WACHHOLZ, E. R. 1961. Annual typhoon report 1960, p. 204–207. Fleet Weather Central, Joint Typhoon Warning Center, Guam.

WADATI, K., AND T. HIRONO. 1954. Storm tides caused by typhoons. Proc. UNESCO Symp. Typhoons: 31–48.

WADHAMS, P. 1972. Measurement of wave attenuation in pack ice by inverted echo sounding, p. 255–260. *In* T. Carlsson [ed.] Sea ice. National Research Council of Reykjavik, Reykjavik, Iceland.

1973. Attenuation of swell by sea ice. J. Geophys. Res. 78(18): 3552–3563.

WAKE, A., AND R. R. RUMER. 1979. Modelling ice regime of Lake Erie. J. Hydraul. Div. Proc. Soc. Civ. Eng. HY7: 827–844.

WALKER, E. R. 1977. Aspects of oceanography in the Archipelago. I.O.S. note, Aug. 3, 1977. 186 p.

WALLEN, C. C. 1970. Climates of northern and western Europe, p. 9–205. World survey of climatology. Vol. 5. Elsevier Press, Amsterdam, The Netherlands.

WALMSLEY, J. L. 1966. Ice cover and surface heat fluxes in Baffin Bay. Publ. No. 84, Oct. 1966. Arctic Meteorology Research Group, Department of Meteorology, McGill University, Montreal, Que. 94 p.

WALTERS, R. A., AND R. T. CHENG. 1980a. Calculations of estuarine residual currents using the finite element method. *In* D. H. Norrie [ed.] Proc. 3rd Int. Conf. Finite Elem. Flow Probl. University of Calgary, Calgary, Alta.

1980b. Accuracy of an estuarine hydrodynamic model using smooth elements. Water Resour. Res. 16(1): 187–195.

WALTON, R., AND B. A. CHRISTENSEN. 1980. Friction factors in storm surges over inland areas. J. Waterways Port Coastal Ocean Div. Proc. Am. Soc. Civ. Eng. WW2: 261–271.

WANG, D. P. 1979. Extratropical storm surges in the Chesapeake Bay, p. 323–332. *In* J. C. J. Nihoul [ed.] Marine forecasting. Proc. 10th Int. Liège Colloq. Ocean Hydrodyn. Elsevier Oceanogr. Ser. Elsevier Press, Amsterdam, The Netherlands.

WANG, D. P., AND D. W. KRAVITZ. 1980. A semi-implicit two-dimensional model of estuarine circulation. J. Phys. Oceanogr. 10: 441–454.

WANG, G. 1954. The development and movement of typhoons, Proc. UNESCO Symp. Typhoons: 165–174.

1956. An objective method of forecasting typhoon movement. Tech. Rep. No. 1. First Sea Wing, U.S. Air Force.

1960. A method in regression equations for forecasting the movement of typhoons. Bull. Am. Meteorol. Soc. 41(3): 115–124.

1978. Sea level pressure profile and gusts within a typhoon circulation. Mon. Weather Rev. 106: 954–960.

WANG, J. D. 1977. Comments on "Irregular grid finite-difference techniques: simulations of oscillations in shallow circular basins." J. Phys. Oceanogr. 7: 932–933. Reply by W. C. Thacker. J. Phys. Oceanogr. 7: 933–934.

WANG, J. D., AND J. J. CONNER. 1975a. Mathematical modelling of near coastal circulation. Rep. No. MIT SG75-13, Apr. 20, 1975. Sea Grant Program, MIT. 272 p.

1975b. Finite element model of two payer coastal circulation, p. 2401–2420. Proc. Coastal Eng. Conf., 1975, Copenhagen, Denmark. Chap. 141. Vol. 3.

WANSTRATH, J. J. 1976. Storm surge simulation in transformed coordinates. Vol. 11: Program documentation. Tech. Rep. No. 76–3, Nov. 1976. Coastal Engineering Research Center, U.S. Army Corps of Engineers, Fort Belvoir, VA. 176 p.

1977a. An open coast storm surge model wth inland flooding, p. 676–679. Proc. 11th Tech. Conf. Hurricanes Trop. Meteorol., Dec. 13–16, 1977, Miami Beach, FL. American Meteorological Society, Boston, MA.

1977b. Near shore numerical storm surge and tidal simulation. Tech. Rep. H-77-17. U.S. Army Engineer Waterways Experiment Station, CE, Vicksburg, MS.

WANSTRATH, J. J., R. E. WHITAKER, R. O. REID, AND A. C. VASTANO. 1976. Storm surge simulation in transformed coordinates. Vol. 1: Theory and application. Tech. Rep. No. 76–3, Nov. 1976. Coastal Engineering Research Center, U.S. Army Corps of Engineers, Fort Belvoir, VA. 166 p.

WASSERMAN, S. E., AND D. B. GILHOUSEN. 1976. Prediction of meteorological factors related to beach erosion at New Jersey and Long Island, N.Y. J. Appl. Meteorol. 15(4): 313–318.

WATTS, I. E. M. 1959. The effect of meteorological conditions on tide height at Hong Kong. Tech Memo. No. 8. Royal Observatory, Hong Kong. 30 p.

1969. Climates of China and Korea. p. 1–117. Chap. 1. *In* H. Arakawa [ed.] Climates of northern and eastern Asia. Survey of climatology. Vol. 8. Elsevier, New York and Amsterdam.

WEARE, T. J. 1976a. Finite element or finite difference methods for the two dimensional shallow water equations. Comput. Methods Appl. Mech. Eng. 7: 351–357.

1976b. Instability in tidal flow computational schemes. J. Hydraul. Div. Proc. Am. Soc. Civ. Eng. 102(HY5): 569–580.

WEATHERLY, G. L. 1977. Bottom boundary layer observations in the Florida current, p. 237–254. *In* J. C. J. Nihoul [ed.] Bottom turbulence. Elsevier Press, Amsterdam, The Netherlands.

WEBB, D. J. 1976. A model of continental shelf resonances. Deep-Sea Res. 23: 1–15.

1981. Numerical model of the tides in the Gulf of Carpentaria and the Arafura Sea. Aust. J. Mar. Freshwater Res. 32: 31–44.

WEENINK, M. P. H. 1956. The twin storm surges during December 21–24, 1954: a case of resonance. Dtsch. Hydrogr. Z. 9: 240–249.

WEENINK, M. P. H., AND P. GROEN. 1958a. A semi-theoretical, semi-empirical approach to the problem of finding wind effects on water levels in a shallow, partly enclosed sea. I. K. Ned. Akad. Wet. Abdeeking Nat. Proc. Sect. Sci. Ser. B: Phys. Sci. 6(3): 198–204.

1958b. A semi-theoretical, semi-empirical approach to the problem of finding wind effects on water levels in a shallow, partly enclosed sea. II. K. Ned. Akad. Wet. Abdeeking Nat. Proc. Sect. Sci. Ser. B: Phys. Sci. 6(3): 205–213.

WELANDER, P. 1956. On the wind action on shallow seas with particular reference to the problem of numerical sea level prediction. Institute of Meteorology, University of Stockholm, Stockholm, Sweden.

1957. Wind action on a shallow sea: some generalizations of Ekman's theory. Tellus 9: 45–52.

1961. Numerical prediction of storm surges, p. 315–317. *In* H. E. Landsberg and J. van Miegham [ed.] Advances in geophysics. Vol. 8. Academic Press, New York, NY.

WEMELSFELDER, P. J. 1954. The disaster in the Netherlands caused by the storm flood of February 1, 1953, p. 258–271. Proc. 4th Conf. Coastal Eng.

1961. On the use of frequency curves of storm floods, p. 617–632. *In* J. W. Johnson [ed.] Proc. 7th Conf. Coastal Eng. Aug. 1960, The Hague. Council on Wave Research, The Engineering Foundation.

WENXIN, S., F. SHIZUO, AND Q. ZENGHAS. 1982. Numerical study on the Bohai Sea wind surges — the zeroth-order dynamic model. Acta Oceanol. Sin. 1(2): 175–188.

WHEWELL, W. 1833. Essay towards a first approximation to a map of cotidal lines. Philos. Trans. R. Soc. London Ser. A 1: 147.

WHITAKER, R. E., R. O. REID, AND A. C. VASTANO. 1973. Drag coefficient at hurricane wind speeds as deduced from numerical simulation of dynamical water level changes in Lake Okeechobee, Fla. Tech. Rep. 73–13–T. Department of Oceanography, Texas A&M University, College Station, TX.

WHITE, G. F., AND J. E. HAAS. 1975. Assessment of research on natural hazards. MIT Press, Cambridge, MA. 487 p.

WHITTINGHAM, H. 1958. The Bathurst Bay hurricane and associated storm surge. Aust. Meteorol. Mag. 23: 14–36.

1968. The Douglas Manson tropical cyclone of 1923, p. 79–88. *In* Tropical cyclones in the Northern Australian regions for 1964–65 season. Bureau of Meteorology, Melbourne, Australia.

WIEGEL, R. L. 1964. Oceanographical engineering. Prentice-Hall Inc., Englewood Cliffs, NJ. 532 p.

WILDING, A. J. 1980. Storm surges in Swansea Bay, p. 101–113. *In* M. B. Collins, F. T. Banner, P. A. Taylor, S. J. Wakefield, and A. E. James [ed.] Industrialised embayments and their environmental problems. A case study of Swansea Bay. Pergamon Press, Oxford, U.K. 614 p.

WILDING, A., M. COLLINS, AND G. FERENTINOS. 1980. Analyses of sea level fluctuations in Thermaicos Gulf and Salonica Bay, Northwestern Aegean Sea. Estuarine Coastal Mar. Sci. 10: 325–334.

WILLIAMS, D. T. 1948. A surface micro-study of squall-line thunderstorms. Mon. Weather Rev. 76: 239–246.

WILLIAMS, G. P. 1965. Correlating freeze-up and break-up with weather conditions. Can. Geotech. J. 11(4): 313–326.

WILLIAMS, K. T., AND W. M. GRAY. 1973. Statistical analysis of satellite-observed trade wind cloud clusters in the western North Pacific. Tellus 25: 313–336.

WILLIAMS, N. V., AND V. T. BUCHWALD. 1974. Resonator activity of the tides in the gulfs of Carpentaria and Thailand. Tech. Rep. Department of Mathematics, University of New South Wales, Kensington, New South Wales. 9 p.

WILSON, B. W. 1954. Harbor surging at Cape Town, South Africa. Dock Harbor Auth. Mar. 1954: 329–333.

1957a. Fundamentals of wave motion. *In* Oceanographic principles of coastal and offshore engineering. Chap. 3. Special Course Notes, Texas A&M University, College Station, TX.

1957b. Origin and effects of long period waves in ports. Proc. 19th Int. Navig. Congr., 1957, Sect. II: Commun. 1: 13–61.

1958. Hurricane wave statistics for the Gulf of Mexico, p. 68–94. *In* J. W. Johnson [ed.] Proc. 6th Conf. Coastal Eng., Dec. 1957, Florida. Council on Wave Research, The Engineering Foundation.

1959. The prediction of hurricane storm tides in New York Bay. Rep. No. 165-3, Oct. 1959. Department of Oceanography and Meteorology, Texas A&M University, College Station, TX.

1960. The prediction of hurricane storm tides in New York Bay. Tech. Memo. No. 120. Beach Erosion Board, U.S. Army Corps of Engineers, Washington, DC.

1961. The prediction of hurricane storm tides in New York Bay (discussion). Tech. Memo. No. 120-A. Beach Erosion Board, U.S. Army Corps of Engineers, Washington, DC.

1972. Seiches. Adv. Hydrosci. 8: 1–94.

WILSON, J. W. 1978. Meteorological considerations for use in storm surge models. Presented at the 58th annual meeting of the American Meteorological Society, Feb. 1, 1978, Savannah, GA.

WINCHESTER, P. 1979. Disaster relief operations in Andhra Pradesh, southern India, following the cyclone in November 1977. Disasters 3(2): 173–177.

WITTING, R. 1908. Untersuchungen zur Kenntnis der Wasserbewegungen und der Wasserumsetzung in den Finnland umgeben den Meeren, Finnlandsche. Hydrogr. Biol. Unters 2: 181–244.

WITTMAN, W., AND M. D. BURKHART. 1973. Sea ice. Part 2: Ice distribution and forecast services, North America Arctic waters. Mar. Weather Log 17(6): 343–355.

WOLF, J. 1978. Interaction of tide and surge in a semi-infinite uniform channel, with application to surge propagation down the east coast of Britain. Appl. Math. Model. 2: 245–253.

1981. Surge–tide interaction in the North Sea and River Thames, p. 75–94. *In* D. H. Peregrine [ed.] Floods due to high winds and tides. Academic Press, London, U.K. 109 p.

WOOD, J. F. 1978. The strategic role of perigean spring tides in nautical history and North American coastal flooding, p. 1635–1976. U.S. Dep. Commer., NOAA. 538 p.

WORLD METEOROLOGICAL ORGANIZATION. 1975. Typhoon modification. WMO No. 408. Geneva, Switzerland. 141 p.

1978. Present techniques of tropical storm surge prediction. Rep. No. 13. Marine Science Affairs, WMO No. 500. Geneva, Switzerland. 87 p.

WROBLEWSKI, A. 1978. Stochastic computations of Baltic storm surges in Nowy Port. Pap. No. 135. Summ. 16th Int. Conf. Coastal Eng., Aug. 27–Sept. 3, 1978, Hamburg, W. Germany.

WU, J. 1969. Fraide number scaling of wind stress coefficients. J. Atmos. Sci. 26: 408–413.

1980. Wind stress coefficients over sea surface in neutral conditions — a revisit. J. Phys. Oceanogr. 10: 727–740.

WURTELE, M. G., J. PAEGLE, AND A. SIELECKI. 1971. The use of open boundary conditions with the storm surge equations. Mon. Weather Rev. 99(6): 537–544.

WÜST, G. 1920. Die Verdunstung auf dem Meere. Veroeff. Inst. Meereskd. Univ. Berlin Ser. A 6: 73.

YAMAGUTI, S. 1929. On the effect of cyclones upon sea level. Bull. Earthquake Res. Inst. 7(1): 115–132.

YAMASAKI, M. 1968. Numerical simulation of tropical cyclone development with the use of primitive equations. J. Meteorol. Soc. Jpn. 46: 178–201.

1977. A preliminary experiment of the tropical cyclone without parameterizing the effects of cumulus convection. J. Meteorol. Soc. Jpn. 55(Ser. II): 11–31.

YANG, C. Y., A. M. PARISI, AND W. S. GAITHER. 1970. Statistical prediction of hurricane storm surge, p. 2011–2030. Proc. 12th Coastal Eng. Conf., Sept. 13–18, 1970, Washington, DC.

YEH, G. T. 1979. Comparisons and verifications of storm surge analysis with emphasis on moving boundary conditions. Can. Mar. Sci. Dir. Manuscr. Rep. Ser. 53: 125–139.

YEH, G. T., AND F. K. CHOU. 1979. Moving boundary numerical surge model. J. Waterway Port Coastal Ocean Div. Proc. Am. Soc. Civ. Eng. WW3: 247–263.

YEH, G. T., AND F. F. YEH. 1976. A generalized model for storm surges, p. 921–933. Proc. 15th Int. Conf. Coastal Eng. July 7–11, 1976, Honolulu, HI. Vol. 1. Chap. 54.

YOUNG, J. A. 1968. Comparative properties of some time differencing schemes for linear and nonlinear oscillations. Mon. Weather Rev. 96: 357–364.

YUEN, K. B. 1967. The effect of tidal barriers upon the M_2 tide in the Bay of Fundy. Marine Science Branch, Department of Energy, Mines and Resources, Ottawa, Ont. 53 p.

YUEN, K. B., AND T. S. MURTY. 1972. A preliminary study of storm surges in Hudson Bay, p. 215–235. Proc. 13th Conf. Coastal Eng. ASCE, New York, NY.

ZAHEL, W. 1973. The diurnal K_1 tide in the world ocean — a numerical investigation. Pure Appl. Geophys. 109: 1819–1825.

1977. The influence of solid earth deformations on semidiurnal and diurnal oceanic tides, p. 98. *In* P. Brosche and J. Sündermann [ed.] Tidal friction and earth's rotation. Springer-Verlag, New York, NY.

ZEHR, R. 1976. Tropical disturbance intensification. Pap. No. 259. Department of Atmospheric Science, Colorado State University, Fort Collins, CO.

ZIENKEWICZ, O. C. 1971. The finite element method in engineering sciences. McGraw-Hill Publications, New York, NY.

ZIPSER, E. J. 1969. The role of organized unsaturated convective downdrafts in the structure and rapid decay of an equatorial disturbance. J. Appl. Meteorol. 8: 799–814.

1977. Mesoscale and convective scale downdrafts as distinct components of squall line structure. Mon. Weather Rev. 105: 1568–1589.

ZISHKA, K. M., AND P. J. SMITH. 1980. The climatology of cyclones and anticyclones over North America and surrounding ocean environs for January and July, 1950–77. Mon. Weather Rev. 108: 387–401.

ZORE, M. 1955. On the seiches occurring in the Bay of Kastela. Acta Adriat. 7(3): 31–37.

ZSCHAU, J. 1977. Prediction of storm surges from marine loading tilt measured inland from the sea, p. 787–801. *In* M. Bonatz and P. Melchior [ed.] Proc. 8th Int. Symp. Earth Tides, Sept. 19–24, 1977, Bonn, W. Germany. Institut für Theoretische Geodäsie der Universität Bonn.

ZSCHAU, J., U. CAROW, AND R. MEIBNER. 1978. A new geophysical method in forecasting storm surges. Pap. No. 137. Summ. 16th Int. Conf. Coastal Eng., Aug. 27–Sept. 3, 1978, Hamburg, W. Germany. ASCE, New York, NY.

ZSCHAU, J., AND H. J. KÜMPEL. 1979. Prediction of storm surges using vertical pendulums. Geophys. Astrophys. Fluid Dyn. 13: 245–252.

ZUBOV, N. N. 1938. Marine water and ice. Moska Gidrometeoizdat. 453 p.

1943. Arctic ice. (Translated from Russian into English by the U.S. Navy Oceanographic Office and the American Meteorological Society)